

C55-612-771/v.2

A UNITED STATES
DEPARTMENT OF
COMMERCE
PUBLICATION

U.S. DEPARTMENT OF COMMERCE
National Oceanic and Atmospheric Administration

COLLECTED REPRINTS-1971
Volume II

ATLANTIC OCEANOGRAPHIC
AND METEOROLOGICAL LABORATORIES





U.S. DEPARTMENT OF COMMERCE

Peter G. Peterson, Secretary

NATIONAL OCEANIC AND ATMOSPHERIC ADMINISTRATION

Robert M. White, Administrator

ENVIRONMENTAL RESEARCH LABORATORIES

Wilmot N. Hess, Director

Collected Reprints—1971

Volume II

ATLANTIC OCEANOGRAPHIC AND METEOROLOGICAL LABORATORIES

ISSUED JULY 1972

Atlantic Oceanographic and Meteorological Laboratories
Miami, Florida 33149

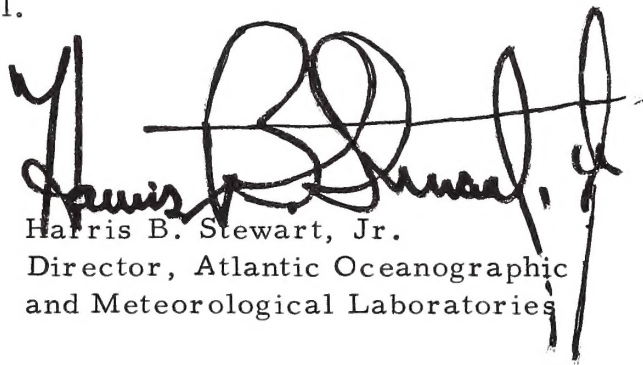
For sale by the Superintendent of Documents, U. S. Government Printing Office, Washington, D. C. 20402

FOREWORD

An increased understanding of the ocean and its processes, of the underlying geological and geophysical structures, and of the overlying atmosphere and its interactions with the sea will result in man's increased ability to deal intelligently with the problems of this environment.

The scientific and technical accomplishments of the National Oceanic and Atmospheric Administration's Environmental Research Laboratories are contributing to this understanding. Because the published results of the Atlantic Oceanographic and Meteorological Laboratories are broadly scattered through the literature, they are being brought together in a series of annual publications. These provide a convenient summary of the results of the work of these laboratories for researchers and interested laymen alike.

This volume, the sixth in the series, contains the published results of NOAA's Atlantic Oceanographic and Meteorological Laboratories for the year 1971.



Harris B. Stewart, Jr.
Director, Atlantic Oceanographic
and Meteorological Laboratories



Digitized by the Internet Archive
in 2012 with funding from
LYRASIS Members and Sloan Foundation

CONTENTS

VOLUME I

General

1. Apel, John R.
Wave Interactions in Solid State Plasmas: Book Review.
Physics Today 24, No. 2, p. 47.
2. Stewart, Harris B. Jr.
CICAR - An International Oceanographic Program in the
Caribbean: Oceanic Citation Journal 8, No. 5, 2-5.
3. Stewart, Harris B. Jr.
Ecological Aspects of Industrial Development: Muse
News 11, No. 12, 411-413.
4. Stewart, Harris B. Jr.
Exploring America's Mediterranean: NOAA 1, No. 2, 9-11.
5. Stewart, Harris B. Jr.
Man and the Sea: Book Review. Bulletin of the American
Meteorological Society 52, No. 8, 739-740.
6. Stewart, Harris B. Jr.
Non-Food Resources as Viewed by: Federal Oceanographic
Research: Third Proceedings of the Third Sea Grant
Conference, sponsored by Oregon State University,
March 1970, 47-48.
7. Stewart, Harris B. Jr.
Ocean Symposium: AAAS Symposia Annual Meeting: Phila-
delphia. Science 174, No. 4012, 964-965.
8. Staff
Satellite Data Requirements of Atlantic Oceanographic
and Meteorological Laboratories for Studies of Ocean
Physics and Solid Earth. NOAA TR ERL 225-AOML 5.

Physical Oceanography

9. Chew, Frank, and G. A. Berberion
A Determination of Horizontal Divergence in the Gulf Stream Off Cape Lookout: *Journal of Physical Oceanography* 1, No. 1, 39-44.
10. Hansen, Donald V.
Oceanography for the 1970's. *The Science Teacher* 38, No. 1.
11. Hansen, Donald V.
Oceans from Space: Book Review. *Bulletin of the American Meteorological Society* 52, No. 8, 738-739.
12. Low, James K., and George A. Maul
Precise Two-Point STD Calibrations: *Marine Technology Society Journal* 5, No. 5, 22-33.
13. Zetler, Bernard D.
Earth Tides. *McGraw-Hill Yearbook of Science Technology*, 174-177.
14. Zetler, Bernard D., and George A. Maul
Precision Requirements for a Spacecraft Tide Program: *Journal of Geophysical Research* 76, No. 27, 6601-6605.
15. Zetler, Bernard D.
Radiational Ocean Tides Along the Coasts of the United States: *Journal of Physical Oceanography* 1, No. 1, 34-38.
16. Zetler, Bernard D., D. Cartwright, and W. Munk
Tidal Constants Derived from Response Admittances: *Sixth International Symposium on Earth Tides, Strasbourg 1969*, 1-4.
17. Zetler, Bernard D.
Tide: *Encyclopedia Americana*, 731-735.
18. Zetler, Bernard D.
Tsunamis and the Seismic Sea Wave Warning System: *Man and the Sea*, American Museum of Natural History, 301-306.

Meteorology

19. Anthes, Richard A.
A Numerical Model of the Slowly Varying Tropical Cyclone in Isotropic Coordinates: Monthly Weather Review 99, No. 8, 617-635.
20. Anthes, Richard A.
Iterative Solutions to the Steady-State Axisymmetric Boundary-Layer Equations under an Intense Pressure Gradient: Monthly Weather Review 99, No. 4, 261-268.
21. Anthes, Richard A.
Numerical Experiments with a Slowly Varying Model of the Tropical Cyclone: Monthly Weather Review 99, No. 8, 636-643.
22. Anthes, Richard A.
The Development of Asymmetries in a Three-Dimensional Numerical Model of the Tropical Cyclone: NOAA Tech Memo ERL NHRL-94.
23. Anthes, Richard A.
The Response of a Three-Level Axisymmetric Hurricane Model to Artificial Redistribution of the Convective Heat Release: NOAA Tech Memo ERL NHRL-92.
24. Anthes, Richard A., Stanley L. Rosenthal, and James W. Trout
Preliminary Results from an Asymmetric Model of the Tropical Cyclone: Monthly Weather Review 99, No. 10, 744-758.
25. Anthes, Richard A., James W. Trout, and Stellan S. Ostlund
Three-Dimensional Particle Trajectories in a Model Hurricane: Weatherwise 24, No. 4, 174-178.
26. Anthes, Richard A., James W. Trout, and Stanley L. Rosenthal
Comparisons of Tropical Cyclone Simulations With and Without the Assumption of Circular Symmetry: Monthly Weather Review 99, No. 10, 759-766.
27. Black, Peter G.
Cumulonimbus Modification of Tropical Nature: Bulletin of the American Meteorological Society 52, No. 7, 562-565.

28. Black, Peter G., and Richard A. Anthes
On the Asymmetric Structure of the Tropical Cyclone Outflow Layer: Journal of Atmospheric Sciences 28, No. 8, 1348-1366.
29. Carlson, Toby N.
A Detailed Analysis of Some African Disturbances: NOAA Tech Memo ERL NHRL-90.
30. Carlson, Toby N.
Weather Note: An Apparent Relationship Between the Sea-Surface Temperature of the Tropical Atlantic and the Development of African Disturbances into Tropical Storms: Monthly Weather Review 99, No. 4, 309-310.
31. Carlson, Toby N., and Robert C. Sheets
Comparison of Draft Scale Vertical Velocities Computed from Gust Probe and Conventional Data Collected by a DC-6 Aircraft: NOAA Tech Memo ERL NHRL-91.
32. Gentry, R. Cecil
To Tame a Hurricane: Science Journal, 49-55.
33. Koss, Walter James
Numerical Integration Experiments with Variable-Resolution Two-Dimensional Cartesian Grids Using the Box Method: Monthly Weather Review 99, No. 10, 725-738.
34. Rosenthal, Stanley L.
The Response of a Tropical Cyclone Model to Variations in Boundary Layer Parameters, Initial Conditions, Lateral Boundary Conditions and Domain Size: Monthly Weather Review 99, No. 10, 767-777.
35. Rosenthal, Stanley L., and Michael S. Moss
Numerical Experiments of Relevance to Project Stormfury: NOAA Tech Memo ERL NHRL-95.
36. Rosenthal, Stanley L., and Michael S. Moss
The Responses of a Tropical Cyclone Model to Radical Changes in Data Fields During the Mature Stage: NOAA Tech Memo ERL NHRL-96.

37. Scott, William D.
Aerosol Sampling and Data Analysis with the NCAR Counter: The Second International Workshop on Condensation and Ice Nuclei sponsored by National Science Foundation, August 1970, 49-52.
38. Scott, William D., Robert M. Cunningham, Robert G. Knollenberg, and William R. Cotton
Symposium on the Measurements of Cloud Elements: Bulletin of the American Meteorological Society 52, No. 9, 889-890.
39. Sugg, Arnold L., Leonard G. Pardue, and Robert L. Carrodus
Memorable Hurricanes of the United States Since 1873: NOAA Tech Memo NWS SR-56.

Volume II

Meteorology (continued)

40. Staff
Project Stormfury 1970 Annual Report.
41. Trout, James W., and Richard A. Anthes
Horizontal Asymmetries in a Numerical Model of a Hurricane: NOAA Tech Memo ERL NHRL-93.
42. Barday, Robert J.
Free-Air Gravity Anomalies South of Panama and Costa Rica (NOAA Ship Oceanographer - August 1969): NOAA Tech Memo ERL AOML-14.
43. Bassinger, B. G., R. N. Harbison, and L. Austin Weeks
Marine Geophysical Study Northeast of Trinidad-Tobago: The American Association of Petroleum Geologists Bulletin 55, No. 10, 1730-1740.
44. Bennett, Richard H., and Douglas N. Lambert
Rapid and Reliable Technique for Determining Unit Weight and Porosity of Deep-Sea Sediments: Marine Geology 11, 201-207.

45. Bennett, Richard H., Douglas N. Lambert, and Paul J. Grim
Tables for Determining Unit Weight of Deep-Sea Sediments from Water Content and Average Grain Density Measurements: NOAA Tech Memo ERL AOML-13.
46. Dietz, Robert S.
North Atlantic-Geology and Continental Drift (A Symposium): Marine Technology Society Journal 5, No. 5, 33.
47. Dietz, Robert S.
Shatter Cones (Shock Fractures) in Astroblemes: Meteoritics 6, No. 4, 258-259.
48. Dietz, Robert S.
Sudbury Astrobleme: A Review. Meteoritics 6, No. 4, 259-260.
49. Dietz, Robert S.
The Sea: Ideas and Observations on Progress in the Study of the Seas. Book Review American Scientist 59, No. 5, 627.
50. Dietz, Robert S.
Those Shifty Continents: Sea Frontiers 17, No. 4, 204-212.
51. Dietz, Robert S., and K. D. Emery
Portrait of a Scientist: Francis Shepard. Earth-Science Reviews 7, No. 1, A9-A15.
52. Dietz, Robert S., and John C. Holden
Pre-Mesozoic Oceanic Crust in the Eastern Indian Ocean (Wharton Basin): Nature 229, No. 5283, 309-312.
53. Dietz, Robert S., John C. Holden, and Walter P. Sproll
Geotectonic Evolution and Subsidence of Bahama Platform: Reply. Geological Society of America Bulletin 82, 811-814.
54. Dietz, Robert S., and Harley J. Knebel
Trou Sans Fond Submarine Canyon: Ivory Coast, Africa: Deep Sea Research 18, 441-447.

55. Freeland, George L., and Robert S. Dietz
Plate Tectonic Evolution of Caribbean - Gulf of
Mexico Region: Nature 232, 20-23.
56. Keller, George H.
Engineering Properties of North Atlantic Deep-Sea
Sediments: Interocean '70 2, 65-71.
57. Keller, George H.
Mass Properties of the Sea Floor in a Selected Depositional Environment: Proceedings Civil Engineering in the Oceans II, Miami Beach, December 1969, 857-877.
58. Lattimore, R. K., L. Austin Weeks, and L. W. Mordock
Marine Geophysical Reconnaissance of Continental Margin North of Paria Peninsula, Venezuela: The American Association of Petroleum Geologists Bulletin 55, No. 10, 1719-1729.
59. Peter, George and Omar E. DeWald
Deformation of the Sea Floor off the North-west Coast of the United States: Nature Physical Science 232, No. 31, 97-98.
60. Peter, George, Barrett H. Erickson, and Paul J. Grim
Magnetic Structure of the Aleutian Trench and Northeast Pacific Basin (1968): The Sea, Ed. A. E. Maxwell, Published by Wiley-Interscience, 4, pt. 2, 191-222, 1971. John Wiley & Sons, Inc., 1971.
61. Rona, Peter A.
Bathymetry Off Central Northwest Africa: Deep Sea Research 18, 321-327.
62. Rona, Peter A.
Deep Sea Salt Diapirs: Letter to editor Geotimes, p. 8.
63. Rona, Peter A.
Depth Distribution in Ocean Basins and Plate Tectonics: Nature 231, 179-180.
64. Starr, Robert B., and Robert G. Bassinger
Marine Geophysical Observations of the Eastern Puerto Rico-Virgin Islands Region: Trans-Fifth Caribbean Geological Conference, Geology Bulletin No. 5, Queens College Press, 25-29.

65. Weeks, L. Austin, and Robert K. Lattimore
Continental Terrace and Deep Plain Offshore Central
California: Marine Geophysical Research 1, 145-161.
66. Weeks, L. Austin, R. K. Lattimore, R. N. Harbison,
B. G. Bassinger, and G. F. Merrill
Structural Relations Among Lesser Antilles, Venezuela,
and Trinidad-Tobago: The American Association of
Petroleum Geologists Bulletin 55, No. 10, 1741-1752.

Sea-Air Interaction

67. Hanson, Kirby J.
Studies of Cloud and Satellite Parameterization of
Solar Irradiance at the Earth's Surface: Proceedings
of the Miami Workshop on Remote Sensing March 29-31,
1971, Miami, Florida, 133-148.
68. McAlister, E. D., William McLeish, and Ernst A. Corduan
Airborne Measurements of the Total Heat Flux from the
Sea during BOMEX: Journal of Geophysical Research 76,
No. 18, 4172-4180.
69. Nordbert, W., J. Conway, Duncan B. Ross, and T. Wilheit
Measurements of Microwave Emission from a Foam-
Covered Wind-Driven Sea: Journal of Atmospheric
Sciences 28, No. 3, 429-435.
70. Ostapoff, F.
Introductory Remarks - Sea-Air Interaction Instrumen-
tation: IEEE Transactions on Geoscience Electronics
GE-9, No. 4, 197-198.
71. Ostapoff, F.
Ocean-Atmosphere Interaction in the Caribbean Sea:
Viewed from the Oceanographer Side: Proceedings Sym-
posium on Investigations and Resources of the Caribbean
Sea and Adjacent Regions, 137-145.
72. Shinnars, Willard W., Gerald E. Putland, and Peter B.
Connors
Tests of Modified Radiosonde Hygristor Duct: NOAA
Tech Memo ERL AOML-15.



U.S. DEPARTMENT OF THE NAVY
J. H. CHAFEE, Secretary

Naval Weather Service Command
W. J. KOTSCH, Rear Admiral, USN, Commander



U. S. DEPARTMENT OF COMMERCE
M. H. STANS, Secretary

National Oceanic and Atmospheric Administration
R. M. WHITE, Administrator

PROJECT STORMFURY ANNUAL REPORT 1970

MIAMI, FLORIDA
MAY 1971

Project STORMFURY was established by an Interdepartmental agreement between the Department of Commerce and the Department of Defense, signed July 30, 1962. Additional support has been provided by the National Science Foundation under Grant NSF-G-17993.

This report is the ninth of a series of annual reports to be prepared by the Office of the Director in accordance with the Project STORMFURY interdepartmental agreement.

Additional copies of this report may be obtained from:

U. S. Naval Weather Service Command
Department of the Navy
Washington Navy Yard
Washington, D. C. 20390

or

National Hurricane Research Laboratory
P. O. Box 8265, University of Miami Branch
Coral Gables, Florida 33124.

NOTICE

The National Hurricane Research Laboratory and the Naval Weather Service Command, do not approve, recommend, or endorse any proprietary product or proprietary material mentioned in this publication. No reference shall be made to either organization or to this publication in any advertising or sales promotion which would indicate or imply that the National Hurricane Research Laboratory or the Naval Weather Service Command approves, recommends, or endorses any proprietary product or material mentioned herein, or which has as its purpose an intent to cause directly or indirectly the advertised product to be used or purchased because of this publication.

TABLE OF CONTENTS

	Page
INTRODUCTION	1
HISTORY AND ORGANIZATION	2
PROJECT STORMFURY ADVISORY PANEL	3
PUBLIC AFFAIRS	4
PYROTECHNIC DEVICES - SILVER IODIDE	4
AREAS OF OPERATIONS	5
PLANS FOR FIELD OPERATIONS - 1970	5
FIELD OPERATIONS	8
RESEARCH ACTIVITIES	10
OPERATIONAL AND RESEARCH DATA COLLECTION	12
OUTLOOK FOR 1971	13
REFERENCES AND SPECIAL REPORTS	14
APPENDIX A. Report On Meeting Of Project Advisory Panel	A-1
APPENDIX B. A Hypothesis For Modification Of Hurricanes	B-1
APPENDIX C. Hurricane Modeling At The National Hurricane Research Laboratory (1970)	C-1
APPENDIX D. Summary Of Preliminary Results From An Asymmetric Model Of The Tropical Cyclone	D-1
APPENDIX E. Response of STORMFURY Cloudline Cumuli To AgI And AgI·NaI Ice Nuclei From A Solution-Combustion Generator	E-1
APPENDIX F. Measurements Of Vertical Motion In The Eyewall Cloud Region Of Hurricane Debbie	F-1
APPENDIX G. An Estimate Of The Fraction Ice In Tropical Storms	G-1
APPENDIX H. Ice-Phase Modification Potential Of Cumulus Clouds In Hurricanes	H-1
APPENDIX I. Use Of Light Aircraft In STORMFURY Activities	I-1
APPENDIX J. Use Of Echo Velocities To Evaluate Hurricane Modification Experiments	J-1

	Page
APPENDIX K. A Summary Of Radar Precipitation Echo Heights In Hurricanes	K-1
APPENDIX L. Project STORMFURY Experimental Eligibility In The Western North Pacific	L-1

PROJECT STORMFURY ANNUAL REPORT - 1970

INTRODUCTION

The apparently successful seeding operations on Hurricane Debbie in 1969 made it most urgent that similar experiments be carried out on a 1970 storm to provide further evaluation of the effectiveness of the technique. The 1970 hurricane season, however, produced no tropical cyclones which were eligible for seeding experiments. In spite of this, or perhaps because of it, the 1970 season was undoubtedly the most productive research period for Project STORMFURY to date.

Even though no eligible storm developed, the STORMFURY forces did operate together during dry-run exercises, cloud-line experiments, and on a data-gathering mission in Tropical Storm Dorothy. The dry-run exercises were conducted from the Naval Station Roosevelt Roads, Puerto Rico, on 21 through 24 July, and these were followed immediately by the cloudline exercises during the last 6 days of the month. The STORMFURY forces were again deployed to Puerto Rico when it appeared on 19 August that Tropical Storm Dorothy might develop into a hurricane and move into the Caribbean. Even if she did not intensify and become eligible for a modification experiment, she could still have provided a good storm for a STORMFURY monitoring mission if her intensity remained sufficiently stable. On this basis, the STORMFURY forces moved to Puerto Rico on 20 August. Dorothy, however, started to weaken after crossing the island of Martinique, and the operation reverted to a data-gathering mission to provide badly needed information on a tropical wave.

With the lack of eligible storms in 1970, the hurricane research efforts were intensified and carried out without operational interruptions. The results of these various research activities are extremely interesting particularly as they relate to future STORMFURY operations, and the more significant results are given in the Appendices to this report. Of special interest in this connection is Appendix B which details a new and better explanation for the apparent success of the 1969 "Debbie" experiments than was possible with the pre-existing hypothesis.

The optimism generated by the "Debbie" work also resulted in increased emphasis being placed on the Project by the Government. In 1970 Project STORMFURY was designated a National Pilot Project by the Interdepartmental Committee for Atmospheric Science (ICAS), and some additional STORMFURY funding was made available in the FY-1971 budget of the Department of Commerce.

HISTORY AND ORGANIZATION

Project STORMFURY is a joint Department of Commerce (NOAA)-Department of Defense (Navy) program of scientific experiments designed to explore the structure and dynamics of tropical cyclones and their potential for modification. The Project which was formally established in 1962 has as its principal objective experimentation directed towards changing the hurricane's energy exchange by strategic seeding from aircraft with silver iodide crystals. The crystals are dispensed from pyrotechnic devices developed by the U.S. Navy. The hypothesis calls for a measurable decrease in the maximum wind velocities near the center of the storm. Navy and NOAA scientists and aircraft, supplemented by those of the U.S. Air Force, have cooperated in STORMFURY experimental operations since 1961 when the first informal agreement was proposed. To date, the experiments conducted by the Project consist of:

- Hurricane Esther - seeded in 1961 - Single seeding
- Hurricane Beulah - seeded in 1963 - Single seeding
- Tropical Cumulus Cloud Seedings - 1963
- Tropical Cumulus Cloud Seedings - 1965
- Tropical Cloudline Seedings - 1968
- Tropical Cloudline Seedings - 1969
- Hurricane Debbie Seedings - 1969 - Multiple seeding
- Tropical Cloudline Seedings - 1970.

Since 1962, only two hurricanes have been seeded¹. The results of the Hurricane Debbie multiple seeding experiments conducted on 18 and 20 August 1969, were extremely encouraging in that a decrease in the maximum wind velocity of the hurricane was observed on both days. Although by no means conclusive, these observations coupled with radar and other meteorological data strongly suggest that a modification to Hurricane Debbie was achieved. The exact amount of effect caused by seeding is still very difficult to determine due to the natural fluctuations which occur in each tropical cyclone.

The initial 1962 Project STORMFURY agreement between the Department of Commerce and the Department of the Navy covered 3 years and was renewed annually from 1965 to 1968. The 1969 renewal was extended to cover a 3 year period.

¹ See Project STORMFURY Annual Reports 1963 through 1969.

Dr. Robert M. White, NOAA Administrator, and Rear Admiral W. J. Kotsch, U.S. Navy, Commander Naval Weather Service Command, had overall responsibility for the cooperatively administered project.

The Project Director in 1970 was Dr. R. Cecil Gentry, Director of the National Hurricane Research Laboratory (NHRL), Miami, Florida. The Alternate Director was Dr. Harry F. Hawkins, also of NHRL. The Assistant Project Director and Navy Project Coordinator was Captain L. J. Underwood, U.S. Navy, Commanding Officer of the Fleet Weather Facility, Jacksonville, Florida (FLEWEAFAC JAX). The Alternate to the Assistant Project Director was Commander J. O. Heft, U.S. Navy, also of FLEWEAFAC JAX. Mr. Jerome W. Nickerson, Navy Weather Research Facility, Norfolk, Virginia (WEARSCHFAX), was Technical Advisor to the Navy; Dr. S. D. Elliott, Jr., Naval Weapons Center, China Lake, California, was NWC Project Officer; Mr. Max Edelstein, Naval Weather Service Command Headquarters, Washington, D.C., was assigned liaison duties representing the Navy; and Mr. William D. Mallinger (NHRL) was assigned liaison duties for the Project Director and NOAA and acted as Data Quality Control Coordinator.

PROJECT STORMFURY ADVISORY PANEL

The Advisory Panel of five members is representative of the scientific community and provides guidance through its consideration of various scientific and technical problems involved with the project. Their recommendations have proved to be of great value to the project since its inception.

The Panel reviews results from previous experiments, proposals for new experiments and their priorities, and makes recommendations concerning the effectiveness of data collection and evaluation, eligibility criteria for storms to be seeded, and other items as applicable.

During 1970, the Advisory Panel consisted of the following prominent scientists: Professor Noel E. LaSuer, Chairman (Florida State University), Professor Jerome Spar (Department of Meteorology and Oceanography, New York University), Professor Edward Lorenz (Department of Meteorology, Massachusetts Institute of Technology), Professor Charles L. Hosler (Dean, College of Earth and Mineral Sciences, Pennsylvania State University), and Professor James E. McDonald (Institute of Atmospheric Sciences, University of Arizona).

The Panel met in Miami on 29 and 30 September 1970 to discuss numerical hurricane modeling research and the simulated seeding experiments with the hurricane models conducted by Dr. S. L. Rosenthal and his group at NHRL.

The Panel again met in Washington, D.C., on 28-30 January 1971. The first day, the Panel members participated in a briefing to NOAA about research on "Decision Analysis of Hurricane Modification" done at the Stanford Research Institute. The Panel meeting on 29 and 30 January was attended by representatives from cooperating agencies and included full discussions of research on past experiments and future plans for the Project. Professor Lorenz resigned from the Panel in October due to the pressure of other work in which he is engaged. He was replaced by Professor Norman A. Phillips (Department of Meteorology, Massachusetts Institute of Technology). Recommendations from the Panel meetings in Miami, Florida, and Washington, D.C., are included in this report as Appendix A.

PUBLIC AFFAIRS

A coordinated press release and fact sheet for STORMFURY were distributed to the media prior to the experimental season. Although no hurricane seeding opportunities occurred, the public affairs team was prepared to operate with a plan similar to that used during the "Debbie" experiments of 1969. Two seats on the Project aircraft were to be made available on a pool basis to media representatives. One seat was to go to a reporter and the other to a cameraman representing TV networks. Additional seats for the media may be possible for future operations if sufficient interest for additional coverage becomes apparent.

PYROTECHNIC DEVICES - SILVER IODIDE

The pyrotechnics prepared for the 1970 season were similar to the STORMFURY I unit used in the 1969 seeding experiments, but incorporated several improvements that made them safer to handle. This new unit, developed under the leadership of Dr. Pierre St. Amand of the Naval Weapons Center, China Lake, California, was provisionally designated WMU-2(XCL-1)/B.

The new unit is fired from the same type of rack and cartridge case as is the STORMFURY I round. Its pyrotechnic grain is also similar in composition and performance to that of the earlier unit, but it incorporates pressure relief, bore-safety, and time delay functions that will permit it to be certified for general use in all appropriate racks and aircraft without special supervision.

More details of the pyrotechnics used can be found in Appendix D of the 1969 Project STORMFURY Annual Report.

AREAS OF OPERATIONS

Eligible areas for experimentation in 1970 were the Gulf of Mexico, the Caribbean Sea, and the southwestern North Atlantic region.

Operations in these areas were limited by the following guideline: A tropical cyclone was considered eligible for seeding as long as there was only a small probability (10 percent or less) of the hurricane center coming within 50 miles of a populated land area within 18 hours after seeding.

There are two primary reasons for not seeding a storm near land. First, a storm seeded further at sea will have reverted to its natural state prior to affecting a land area. Second, large changes in the hurricane structure occur when it passes over land. These land-induced modifications would obscure the short period effects expected to be produced by the seeding experiments and greatly complicate the scientific evaluation of the results.

PLANS FOR FIELD OPERATIONS - 1970

The period 20 July to 31 October was established for STORMFURY operations in 1970. The following aircraft were planned as STORMFURY forces during the season:

1. Navy Weather Reconnaissance Squadron Four
Four WC-121N's
2. Marine All-Weather Attack Squadron Two Two Four
Four A-6 Intruders

3. NOAA Research Flight Facility
 - Two DC-6's
 - One B-57
 - One C-54 (replaced by a C-130 during the season)
4. Air Force 53rd Weather Reconnaissance Squadron
 - Two WC-130's
5. Air Force 55th Weather Reconnaissance Squadron
 - One WC-135
6. Air Force 58th Weather Reconnaissance Squadron
 - One RB-57F
7. Naval Air Test Center
 - One P3
8. Naval Weapons Center
 - One Cessna 401.

Operations Plan No. 1-70 was provided to participants. It covered flight operations, communications, instrument calibration and use, data collection and distribution, logistic and administrative procedures, airspace reservations agreements, and public affairs.

The plan also provided for a series of fall-back research missions to be used when no eligible hurricane was available for seeding after deployment of project forces. These research missions are primarily data gathering or storm monitoring missions in unseeded cloud systems or storms.

As recommended by the STORMFURY Advisory Panel, first priority was given to the eyewall experiment in order to gain additional data which could be correlated with those collected during the 1969 "Debbie" seeding experiments.

This multiple seeding of the clouds in the annulus radially outward from the maximum hurricane winds calls for five seedings at 2-hour intervals. Each seeding consists of dropping 208 pyrotechnic units along a radially outward flight path, starting just outside the radius of maximum winds. The hypothesis in 1969 and early 1970 stated that the introduction of freezing nuclei (silver iodide crystals produced by the pyrotechnics) into the clouds in and around the eyewall should cause a chain of events that includes the release of latent heat, warming of the air outside the central core, changes in temperature and pressure gradients, and a reduction in maximum winds. Data from several experiments and individual cases are needed before definite conclusions regarding the validity of this hypothesis can be assumed.

Because the magnitude of natural variations in hurricanes is sometimes as large as the hypothesized artificially induced changes, it is frequently difficult to distinguish between the two.

Second priority was given to the rainsector and third to the rainband experiments. The rainsector experiment is designed to test whether some of the latent energy in the air flowing toward the center of the hurricane can be intercepted and released while it is still between 50 and 100 miles from the center. If successful, this experiment should result in the dispersal of the energy over a larger area rather than concentration near the center. Clouds in a 45-degree sector between 50 and 75 miles radius are seeded to stimulate growth. This sector is selected because it is an area where an abundance of warm moist tropical air is being carried by the low-level winds toward the clouds nearer the center of the storm. If cloud growth in this sector causes moist air to ascend to the outflow layer at a relatively large radius, some of the energy normally released near the center of the storm would be released at greater radius and could result in a reduction in the storms' wind maxima.

All suitable clouds in the designated sector are seeded while monitoring aircraft continue to collect data to document changes in storm structure or intensity. The seedings are made in four periods of 50 minutes each, separated by non-seeding periods of 50 minutes.

The Rainband Experiment has the same objectives as does the Rainsector Experiment and, in addition, should permit the opportunity to study the interaction of seeded clouds with other clouds in the same and nearby rainbands. Clouds are seeded along a rainband (a line of clouds spiraling around and toward the center of the storm) at 50 to 150 miles from the storm center. Seeding of such a rainband may produce a dispersion of the energy of the hurricane over a larger area and should provide information and data needed to improve the design of other modification experiments. The rainband experiment provides data needed for studies of cloud interactions. A rainband can be selected that is well removed from the central vortex area and not obscured by the main cloud system of the hurricane. This selection facilitates visual observations.

The Advisory Panel has recommended that cloudline experiments continue to be conducted in order to collect data vital to the understanding of the dynamics of clouds organized into systems such as rainbands. These experiments can be conducted when there are no hurricanes and should provide additional opportunities for evaluation of seeding effects. During these experiments, tests of various seeding agents and dispersing techniques can also be conducted. Cloudline experiments were scheduled for 24-31 July 1970, in the military operational areas near Puerto Rico.

Project STORMFURY field experiments are extremely complex operations that require extensive planning and effective coordination. During the multiple seeding experiments, there are as many as 12 aircraft simultaneously operating in the hurricane circulation. Safety of the aircraft and personnel is paramount throughout the experiment. It is obvious that training, professionalism, and dedication are vital to safe and successful operations in the weather extremes encountered. Radars, cameras, radios, and data collection systems must be in peak operating condition. The seeder aircraft must be carefully and accurately vectored by radar and voice communications for the seeding runs. Teamwork is mandatory. For these reasons, it is also imperative that dry-run exercises be conducted prior to operations in a hurricane environment. This dry-run also provides opportunities for testing equipment and procedures, and for crew training.

FIELD OPERATIONS

Dry-runs were conducted from the Naval Station Roosevelt Roads, Puerto Rico, on 21 and 23 July, following a general briefing on 20 July. Participating in the dry-runs were aircraft from the Navy Weather Reconnaissance Squadron FOUR (VW-4), NAS Jacksonville, Florida; NOAA's Research Flight Facility, Miami, Florida; Marine All-Weather Attack Squadron Two Two Four (VMA-AW-224), MCAS Cherry Point, North Carolina; Air Force 53rd Weather Reconnaissance Squadron, Ramey AFB, Puerto Rico; and the 55th Weather Reconnaissance Squadron, McClellan AFB, Sacramento, California.

Also taking part were scientists from the Naval Weather Service Command Headquarters, Washington, D.C.; Naval Weapons Center, China Lake, California; Fleet Weather Facility, Jacksonville, Florida; Navy Weather Research Facility, Norfolk, Virginia; University of Miami, Coral Gables, Florida; and NOAA's National Hurricane Research Laboratory, Coral Gables, Florida.

Dry-run exercises for the STORMFURY eyewall experiment were conducted on 21 July and for the rainsector/rainband experiment on 23 July. Extensive individual debriefs of each flight were made followed by a general critique covering the total operations after each experiment.

A series of cloudline type experiments were carried out at the conclusion of the dry-runs with a portion of the forces. (The Marine A-6 aircraft, the Air Force WC-135, and two of the Navy WC-121N's were released.) Flight operations were carried out on 24, 27, 28, 29, 30, and 31 July, utilizing three types of seeding aircraft (Cessna 401, DC-6, B-57). See appendix I for report on the Cessna 401 operations.

The DC-6 was used on the last three operating days to seed with various silver iodide compositions generated from a burner attached to the wing. A report on these operations is included as appendix E.

On 19 August, Tropical Storm Dorothy developed east of the Caribbean Sea and was predicted to move into the Caribbean on the 20th. In anticipation that the storm would either intensify into a hurricane or remain stable enough in intensity as a tropical storm to serve as a fit subject for a STORMFURY monitoring mission, the forces (with the exception of seeder aircraft) were requested to deploy to Puerto Rico on 20 August. The monitoring mission was to include the flight patterns used to monitor a seeded hurricane. These data collected in an unseeded storm were to be used for comparison purposes and for research on the natural variability of storms.

The Research Flight Facility flew a three-plane mission of the monitoring type on 21 August, and the other project aircraft (less seeders) arrived for the major effort on Saturday, 22 August.

After crossing Martinique, Dorothy started weakening slowly. On Friday, the 21st, there was still a closed circulation, but the Research Flight Facility aircraft had difficulty orienting their flight patterns about the broad weak center. By Saturday, the 22nd, the storm had reverted to a tropical wave with maximum winds of about 45 knots. The STORMFURY monitoring mission was then changed to a fall-back research flight mission which collects data at several levels on a tropical wave. These data should prove to be very valuable for studying the structure of easterly waves, for data of this type have been extremely rare in the past.

Forces performed in an outstanding manner throughout the dry-run exercises, the cloudline experiments, and the Tropical Storm Dorothy operations. The fall-back exercise gave the first opportunity to work with all three of the Air Force participants (WC-130, WC-135, RB57F). Several problems were found in data collection and were resolved as a result of experience gained during these operations.

RESEARCH ACTIVITIES

Progress in the hurricane modification work was quite considerable in 1970 even though nature did not provide a suitable hurricane for a field experiment. This progress was due to the efforts of the research workers, and their findings provide a much broader and firmer base for the future work of the Project. This research took place primarily at the National Hurricane Research Laboratory, Coral Gables, Florida; the Navy Weather Research Facility, Norfolk, Virginia; and at cooperating Universities. Appendices B through L are reports on some of these STORMFURY research efforts.

Appendix B "A hypothesis for modification of hurricanes," by Drs. R. C. Gentry and H. F. Hawkins, explains the new hypothesis on hurricane modification experiments that was developed this year. The article summarizes the evolution of ideas concerning the use of freezing nuclei for modifying hurricanes, explains how the new hypothesis accounts for the apparently favorable results from the experiments on Hurricanes Esther (1961), Beulah (1963), and Debbie (1969), and discusses some of the questions concerning hurricane modification which still need to be answered either by the theoretical investigations or by the field experiments.

Appendix C "Hurricane modeling at the National Hurricane Research Laboratory, 1970," by Dr. S. L. Rosenthal, reviews the NHRL's more significant achievements in the general area of time-dependent hurricane modeling. Dr. Rosenthal discusses the specific problem of modeling a Debbie-like field experiment and summarizes efforts less directly related to the development of time-dependent models. He also outlines investigations planned by this group for the next few years.

Appendix D "Summary of the preliminary results from an asymmetric model of the tropical cyclone," by Dr. R. A. Anthes, Dr. S. L. Rosenthal, and J. W. Trout, shows that the asymmetrical hurricane model reproduces many observed features of the three-dimensional tropical cyclone. Realistic portrayals of

spiral rainbands and the strongly asymmetric structure of the outflow layer are obtained. The kinetic energy budget of the model compares favorably with empirical estimates and also shows the loss of kinetic energy by truncation errors to be very small. Large-scale horizontal asymmetries in the outflow are found to play a significant role in the radial transport of vorticity during the mature stage and are of the same magnitude as the transport by the mean circulation. In agreement with empirical studies, the outflow layer of the model storm shows substantial areas of negative absolute vorticity and anomalous winds.

Appendix E "Response of STORMFURY cloudline cumuli to AgI and AgI·NaI ice nuclei from a solution-combustion generator," by E. E. Hindman, II., Dr. S. D. Elliott, Jr., Dr. W. G. Finnegan, and B. T. Patton, studies the responses of cumulus clouds to silver iodide seedings during the 1970 STORMFURY cloudline operations and compares the effectiveness of two different silver iodide solutions burned in a solution-combustion generator.

Appendix F "Measurements of vertical motion in the eyewall cloud region of Hurricane Debbie," by Dr. T. N. Carlson discusses the estimates of cumulus cloud vertical motions recorded by an RFF DC-6 aircraft while flying in Hurricane Debbie. The accuracy of the vertical motions obtained is discussed, and various factors which may affect the accuracy are explained.

Appendix G "An estimate of the fraction ice in tropical storms," by Dr. W. D. Scott and C. K. Dossett, presents estimates of fraction ice in tropical storms collected in Tropical Storm Inga and Tropical Depression No. 14 as obtained through the use of the foil impactor and formvar replicator.

Appendix H "Ice phase modification potential of cumulus clouds in hurricanes," by D. A. Matthews, presents an examination of ice-phase modification potential of cumulus clouds. Predicted results of modification potential by a one-dimensional steady-state cumulus model are used to test the suggestion (Gentry, 1971) that an important effect on hurricanes may be realized by seeding the less fully developed cumulus cells that are located slightly outward from the mammoth clouds in the inner eyewall. Mr. Matthews's paper also describes the decreases in surface pressure, the increases in rainfall, and the increases in cloud top height as derived from model simulation of the ice-phase modification. In the calculations, he uses 87 temperature soundings observed within 100 n miles of hurricane eyes and five average hurricane soundings prepared by Sheets (1969).

Appendix I "Use of light aircraft in STORMFURY activities," by Dr. S. D. Elliott, Jr., and Dr. W. G. Finnegan, describes the use of contractor-operated light aircraft in Project STORMFURY dry-run and cloudline experiments and offers conclusions and recommendations involving the use of light aircraft in future STORMFURY activities.

Appendix J "Use of echo velocities to evaluate hurricane modification experiments," by P. G. Black, examines radar echo velocities computed over the entire storm for six time intervals before and during the seeding of Hurricane Debbie on 20 August 1969. He finds that mean echo speeds equaled or exceeded cyclostrophic winds computed from 12,000-ft D-value data as well as measured 12,000-ft winds after a correction for water motion was applied to the original "Doppler winds." Mr. Black further examines mean echo crossing angles to determine their variations and angular rotation in relation to the storm's major and minor axes.

Appendix K "A summary of radar precipitation echo heights in hurricanes," by H. V. Senn, surveys radar height data and hurricane case histories to determine likely occurrence of clouds that can be significantly modified in various sectors of a hurricane. This information suggests that clouds exist in hurricanes of the type that the new hypothesis (app. B) suggests are needed in the hurricane modification work.

Appendix L "Project STORMFURY experimental eligibility in the Western North Pacific," by W. D. Mallinger, updates and reviews numbers of typhoons eligible for Pacific STORMFURY experiments. This study strongly indicates that both Guam and Okinawa must be available as bases for Project forces in order to expect a profitable number of experimental storms during a 3-month operation.

OPERATIONAL AND RESEARCH DATA COLLECTION

Data collection procedures appeared adequate for the Project. While problems with radar still existed on some of the Project aircraft, continuous efforts were made during the season to improve these observational tools.

Two special Polaroid cameras (CU-5) were purchased and modified for use on the Air Force WC-130 aircraft radar. Although automatic time-lapse radar cameras are preferred, the Polaroid cameras produced good research data where none had been previously available from these aircraft.

The Research Flight Facility conducted several research missions in tropical circulations, but the 1970 hurricane season was generally one in which few good data collection opportunities occurred.

A one-plane mission was flown into Hurricane Ella in the far southwest Gulf of Mexico on 11 September.

A three-plane, five-level mission was flown into Tropical Storm Felice on 15 September. Felice was almost up to minimal hurricane force, and wind gusts as high as 64 knots were noted as it passed to the south of the Mississippi Delta region.

A three-plane, five-level mission on 2 October and a two-plane mission on 3 October were flown in Tropical Depression No. 14 as it passed through the eastern Caribbean.

Processing of STORMFURY films was again accomplished at a commercial firm in Miami. Some experiments in reducing costs by obtaining work prints to satisfy requirements for duplicates were attempted, but technical difficulties in processing were encountered. These difficulties are now believed to be surmounted, and a modified version of this procedure will be tried during the 1971 STORMFURY season.

OUTLOOK FOR 1971

Project STORMFURY operations are expected to be very similar to those planned for 1970. It is likely that the dry-run exercises will be conducted from the Naval Station Roosevelt Roads, Puerto Rico, followed by a series of cloud-line experiments with forces based at Barbados.

Continued emphasis will be placed on repeating the "Debbie" type experiment and conducting monitoring missions in unseeded storms for comparisons purposes.

Project aircraft will be essentially the same as in 1970, except that a WP-3 weather reconnaissance aircraft belonging to Navy Weather Reconnaissance Squadron FOUR (VW-4) is expected to participate in STORMFURY missions for data collection and for additional use and evaluation as a seeder aircraft.

REFERENCES AND SPECIAL REPORTS

- Anthes, R. A., S. L. Rosenthal, and J. W. Trout (1970): Numerical simulation of a hurricane. *Proceedings of the Meteorological Technical Exchange Conference*, 21-24 September, Annapolis, Md., U.S. Naval Weather Service Command.
- Anthes, R. A. (1971): The response of a 3-level axisymmetric hurricane model to artificial redistribution of convective heat release. Technical Memorandum ERLTM-NHRL, No. 92, NOAA, Dept. of Commerce, NHRL, Miami.
- Black, P. G., and T. T. Fujita (1970): In- and outflow field of Hurricane Debbie as revealed by echo and cloud velocities from airborne radar and ATS-III pictures. *Proceedings of the 14th Annual Conference on Radar Meteorology*, Tucson, Ariz. November, pp. 353-358.
- Black, P. G., H. V. Senn, and C. L. Courtright (1971): Some airborne radar observations of precipitation tilt, bright band distribution, and eye configuration changes during the 1969 multiple seeding experiments in Hurricane Debbie. Submitted for publication in the *Monthly Weather Review*.
- Carlson, T. N., and R. C. Sheets (1971): Comparison of draft scale vertical velocities computed from gust probe and conventional data collected by a DC-6 aircraft. Technical Memorandum ERLTM-NHRL No. 91, NOAA, U.S. Dept. of Commerce, NHRL, Miami, Fla.
- Gentry, R. C. (1970): Progress on hurricane modification research - October 1969 to October 1970. Presented at the *Twelfth Interagency Conference on Weather Modification*, October 28-30, Virginia Beach, Va.
- Gentry, R. C. (1970): Hurricane modification - Experiments and prospects. Presented at *Hurricane Foresight Conference*, New Orleans, La., April 30, and distributed by the New Orleans States-Item.
- Gentry, R. C. (1970): Modification experiments on Hurricane Debbie, August 1969. *Proceedings of the Second National Conference on Weather Modification*, American Meteorological Society, pp. 205-208.
- Gentry, R. C. (1970): The hurricane modification project: Past results and future prospects. *Proceedings of the Seventh Space Congress*, April 22-24, Cocoa Beach, Fla.

- Gentry, R. C. (1970): Modifying the great storm on earth -- the hurricane. *Underwater Science and Technology Journal*, December, pp. 204-214.
- Gentry, R. C. (1971): To tame a hurricane. *Science Journal*, 7, (1), January, pp. 49-55.
- Gentry, R. C. (1971): Hurricane. *McGraw-Hill Yearbook of Science and Technology*, pp. 232-234.
- Hawkins, H. F. (1971): Modifying the hurricane. Submitted for publication in *UMSCHAU* (German publication), April.
- Hawkins, H. F. (1971): Comparison of results of the Hurricane Debbie (1969) modification experiments with those from Rosenthal's numerical model simulation experiments. *Monthly Weather Review*, 99, (5), May, pp. 427-434.
- Mallinger, W. D. (1970): Project STORMFURY operations and plans. *Mariners Weather Log*, 14, (5), September, pp. 262-266.
- Underwood, L. J. (1970): Project STORMFURY operations 1970. Presented at the *Twelfth Interagency Conference on Weather Modification*, October 28-30, Virginia Beach, Va.

APPENDIX A

REPORT ON MEETING OF PROJECT STORMFURY ADVISORY PANEL

Miami, Florida

29-30 September 1970

INTRODUCTION

In response to the recognition of the increasing importance of computer simulation of both "natural" and "seeded" hurricanes to the interpretation and design of Project STORMFURY field experiments, the Advisory Panel met at NHRL on 29-30 September to undertake a more intensive evaluation of models developed by Rosenthal and colleagues at NHRL. From this assessment, several conclusions and recommendations emerged.

EVALUATION OF HURRICANE MODELING

Results of computer simulations of natural hurricanes were available from two models: the improved symmetric (two-dimensional) model with explicit water cycle and air-sea energy exchanges and better horizontal resolution of 10 km, as well as preliminary results from a simplified asymmetrical (three-dimensional) model which neglects interaction with the environment, has constant Coriolis parameter, and rather coarse vertical and horizontal resolution. Simulation of seeded hurricanes was carried out solely with the use of the symmetrical model. Varying augmented heating rates were applied at different radial increments both continuously and intermittently for 10 hours in an attempt to simulate the multiple eyewall experiment of Project STORMFURY.

From a study of these results the Panel reached the following conclusions:

- (1) Within the limitations imposed by symmetry and convective parameterization, the simulation of the natural hurricane is impressively realistic. The distributions of temperature, pressure, and horizontal and vertical motion of the model storm compare favorable with those observed in typical mature hurricanes in nature.

- (2) Within the limitations of the simple asymmetrical model given above, plus the recognition that some asymmetry is introduced artificially by round-off errors and boundary geometry, an asymmetrical structure develops in a manner and with a structure that is not unrealistic. When averaged in the azimuthal direction, the structure is sufficiently similar to the symmetrical analog to give increased confidence in the validity of the symmetrical model. The favorable comparison of model storm structures with observation lends credence to the simulation of seeded hurricane structure. In spite of the realistic simulation of hurricane structure, the Panel noted that neither the symmetrical nor the asymmetrical model is able to give any information on the effects of internal or external influences on the motion of natural or seeded hurricanes.
- (3) The essential result which emerges from the seeding simulation is the formation of a new wind maximum and zone of strongest upward motion at a greater radius than those existing in the natural model storm if the augmented heating rate is added *outside* these pre-existing maxima. Only minor differences in this essential result appear in experiments with different augmented heating rates at different radii.
- (4) This new wind maximum which forms in the seeded storm is weaker than the model control by about 10 percent. Larger reductions of wind speed occur at the radius of maximum wind of the control storm and smaller increases occur at radii beyond the new maximum. The decreases in wind speed are associated with decreased horizontal temperature gradients in the upper and middle troposphere and weakened surface pressure gradients together with the fact that inflowing air rises at a greater radius, thus acquiring smaller tangential relative momentum. The augmented heating also increases the static stability which is associated with smaller rates of release of latent heat and conversion of available potential to kinetic energy.
- (5) Evidence from available simulations has, so far, always indicated that seeding at radii outside the original wind maximum results in reduction of the maximum winds. However, the augmented heating associated with the simulated seeding results in an *increase* in the *total* kinetic energy of the hurricane winds by about 20 percent. Since this could result in a significant increase in the

storm surge, we caution against conclusions that seeding does not make the storm "worse." Furthermore, "simulated seeding" *inside* the original radius of maximum winds results in a slight *increase* of strongest winds.

- (6) The augmented heating rates used to simulate seeding probably cannot be realized in nature solely from release of latent heat of fusion. The most reasonable analog in nature is the possibility that convective clouds in the region just outside the existing eyewall could be stimulated by seeding to more active growth and intensity thus replacing the previous eyewall with a new one at a greater radius. Augmented heating from enhanced condensation, plus freezing in such circumstances, probably exceeds the augmented heating rates used in the seeding simulations.

RECOMMENDATIONS

Based upon the above conclusions, the Advisory Panel makes the following recommendations with regard to Project STORMFURY:

Recommendation ONE: More detailed diagnostic studies of existing simulations of seeding should be carried out to verify the tentative conclusions reached above as to the mechanisms of the seeding influences. In particular, other quantities than those now available should be studied with greater time resolution.

Reasons: It is essential to understand the seeding simulations in as great detail as possible to gain confidence in the results and for comparison with field experimental results.

Recommendation TWO: Development of the asymmetrical (three-dimensional) model should be continued with the ultimate objective of modeling the nonstationary hurricane as it moves through and interacts with the larger scale environment. When this has been achieved for natural storms, simulation of seeding should be carried out.

Reasons: Only with such a model it is possible to investigate interactions between the hurricane and its environment and remove the constraint of axial symmetry. Furthermore, simulation of seeding in only one sector of the storm will be possible, as well as investigating the possible effects of seeding on the motion of hurricanes.

Recommendation THREE: Further simulations of seeding should be made with the symmetrical (two-dimensional) model to supplement the diagnostic studies of existing seeding simulations recommended above.

Reasons: Additional information on varying augmented heating rates and radii of seeding is needed. It is also anticipated that the diagnostic studies will reveal points in need of further clarification.

Recommendation FOUR: The resources of the computer simulation group under Dr. Rosenthal at NHRL should be augmented by: (a) two Ph.D. level scientists with appropriate qualifications, and (b) computer facilities of greater speed and capacity.

Reasons: Although excellent progress has been made by this group in the past 2 years, the experiments recommended above will require additional personnel and computer facilities to accelerate this rate of progress in the next 2 years.

Recommendation FIVE: Available radar data should be studied in an attempt to verify the existence of convective clouds just outside existing eyewalls with a structure susceptible to enhanced growth through seeding. Results from Hurricane Debbie should be reviewed once more from this point of view.

Reasons: If verified, the existence of such clouds and their enhancement by seeding would provide a sounder hypothesis for STORMFURY field experiments.

Recommendation SIX: Radar and cloud physics instrumentation on the research aircraft should be further improved to give more quantitative information on the distribution of convective and other clouds and all phases of water in the hurricane.

Reasons: The essence of possible modification of hurricanes rests in the questions of influencing the intensity and organization of convection and the associated phase changes of water. Unless more and better data can be acquired on these questions, residual doubt will always remain in the interpretation of experimental results.

Professor Noel E. LaSeur, Chairman
Dean Charles L. Hosler
Professor James E. McDonald
Professor Edward N. Lorenz
Professor Jerome Spar

10 November 1970

RECOMMENDATIONS OF THE ADVISORY PANEL FOR PROJECT STORMFURY

Washington, D.C.

February, 1971

INTRODUCTION

In the course of the meeting of the Advisory Panel for Project STORMFURY held in Washington, D.C., 28-30 January 1971, two aspects of Project activities emerged which need immediate action if necessary planning is to be accomplished. These are: the proposed operations of Project STORMFURY in the Pacific during the summer of 1972; and the acquisition, outfitting, and testing of alternate seeding aircraft. Because of the immediacy of these problems, the Advisory Panel is issuing these recommendations; further recommendations on other aspects of Project activities discussed will be forthcoming.

Recommendation ONE: The Panel recommends that appropriate agencies of the government intensify efforts to solve the financial, logistic, diplomatic, and other problems associated with proposed operations of Project STORMFURY in the typhoon region of the Western North Pacific Ocean during the summer of 1972.

Reasons: The increased opportunities for STORMFURY experiments to be expected from the typically greater frequency of Pacific typhoons in a large, sparsely populated oceanic region fully justify the expense and effort required to move Project operations to that area. There is every reason to believe that experimental results obtained in Pacific typhoons will be completely valid for Atlantic hurricanes.

Recommendation TWO: The Panel recommends that Project STORMFURY continue efforts to acquire, outfit, and test alternate seeding aircraft with the following capabilities: increased capacity to carry Project personnel and seeding pyrotechnics; increased range and time "on-station" in the storm; and capability to seed at levels in the range from 25,000 ft to 30,000 ft or at lower levels if suitable temperatures for seedings exist.

Reasons: The Panel considers it undesirable for the Project to have to rely on seeder aircraft from external units. In the past, available aircraft have lacked capacity for Project personnel to fly on-board, and thus provide better

control of the time and place of seeding. They have also lacked range, capability for multiple seeding without refueling, and were limited to high altitudes. Acquisition by the Project of aircraft with the recommended capabilities could eliminate significant uncertainties inherent in the presently available planes.

Professor Noel E. LaSeur, Chairman
Dean Charles L. Hosler
Professor James E. McDonald
Professor Jerome Spar

APPENDIX B

A HYPOTHESIS FOR MODIFICATION OF HURRICANES

R. Cecil Gentry and Harry F. Hawkins
National Hurricane Research Laboratory

INTRODUCTION

The encouraging results from the Hurricane Debbie modification experiments of August, 1969 (Gentry, 1970a) have stimulated research on many problems related to hurricane modification experiments. One of the more interesting developments during 1970 was a new hypothesis which accounted for results from the "Debbie" experiments and offered a more acceptable rationale that details how seeding a hurricane can cause a reduction in its maximum intensity.

R. H. Simpson proposed in 1961 that hurricanes might be modified by introducing freezing nuclei into the massive cloud wall surrounding the center of a hurricane. His hypothesis was set forth in a number of papers (e.g., Simpson and Malkus, 1965; 1964b). It suggested that there was sufficient supercooled water (particularly in the "chimney" area) which, if suddenly frozen, would release enough latent heat of fusion to permit increasing the cloud temperatures 1 to 2°C. By assuming that there was an effective lid on top of the storm and using a hydrostatic model, he calculated that the maximum pressure gradient in the storm might be reduced by 10-15 percent if the heating effects could be confined to a selected area. He further hypothesized that this would be accompanied by a similar percentage reduction in the maximum winds.

In 1968, a hurricane model developed by S. L. Rosenthal was used for some preliminary experiments relative to the modification hypothesis (Gentry, 1969). In these experiments, seeding of the clouds was simulated by assuming that the seeding would result in enhanced heating of the seeded clouds sufficient to change the temperature at the rate of 2°C per $\frac{1}{2}$ hour for $\frac{1}{2}$ hour. That is, the seeding was *simulated* by increasing the heating function in a specified volume of the storm. In the model, heat was added at 500 mb and 300 mb, the levels where introduction of artificial freezing nuclei would most likely result in freezing of significant amounts of water. Calculations were then made with the model to

determine in which portion of the storm addition of heat would most likely result in reduction of the maximum winds; in an: (1) annular band radially inward from the maximum winds, (2) annular band spanning the radius of maximum winds, or (3) annular band radially outward from the radius of maximum winds. The answer from the model was that reductions were most likely when the heat was added radially outward from the maximum winds.

Based on these experiments with the model, crude as they were, the seeding pattern for the experiment was redesigned. Formerly, the seeding aircraft crossed the eye of the hurricane and started dropping the pyrotechnic silver iodide generators at the inner edge of the eyewall. The run continued radially outward for 15 to 25 miles (Simpson and Malkus, 1964a). Prior to the 1969 hurricane season, this pattern was altered to have the run start about 3 miles radially outward from the inner edge of the eyewall (past the ring of maximum winds) and continue on for 15-25 miles. This meant a relatively small change in the annular band seeded because there was about an 85 percent overlap in this pattern and the one used in the earlier seeding runs on hurricanes.

Debbie was seeded five times at 2-hour intervals on 18 August 1969, and again on 20 August (Gentry, 1970b). The operational plan called for the seeding runs to be from the radius of maximum wind outward for 15-25 miles (the spread was somewhat a function of the reaction time of the man in the seeder aircraft and the turbulence encountered). When operations are conducted, it is frequently difficult for the Project Director in the command-control aircraft to know the exact location of the radius of maximum winds, but he does have a good radar picture of the hurricane. R. Sheets, National Hurricane Research Laboratory, has studied the flight data collected by the Research Flight Facility and the National Hurricane Research Laboratory during the last 14 years, and has concluded that in mature hurricanes the most likely radius for the maximum winds was 2 or 3 miles radially outward from the inner edge of the eyewall (as seen by radar)¹.

By the time of the Debbie experiments, S. L. Rosenthal had made several improvements in the hurricane model. The encouraging results from the field experiments put much greater emphasis on all phases of the research effort, and a new series of experiments simulating the modification effects were made with the more sophisticated model (Rosenthal, 1970).

¹ Personal communication.

The new experiments also simulated the modification experiment by assuming that seeding would add heat to the clouds. It was again found that a reduction in maximum winds was most likely if the heat was added radially outward from the radius of maximum winds. Several variations were run in which changes were made in the intensity of the enhanced heating function, in the radial bands at which it was applied, and in the length of time of application. There were also experiments to consider whether the heating should be applied continuously or in pulses to simulate the multiple seeding experiments conducted on Debbie.

In general, the results showed that a reduction in maximum winds was most likely if the heat were added radially outward from the radius of maximum winds. They also showed that there was little difference in the reactions between heat added continuously and heat added in pulses. Larger amounts of enhanced heating caused quicker responses in the wind field, but eventually the reduction in maximum winds became about the same. There did seem to be a lower limit to the rate at which heat should be added below which no significant change in the maximum winds occurred within 10 to 20 hours (Rosenthal, 1971).

During the 1968, 1969, and 1970 seasons, the National Hurricane Research Laboratory with the assistance of the Research Flight Facility of NOAA made some measurements of the liquid- and solid-water content of hurricane clouds (Sheets, 1969).

These measurements were limited in number because of the infrequency of hurricanes within range of the aircraft bases and due to failure of measuring equipment. Nevertheless, some information became available on how much heat might be furnished hurricane clouds by introducing freezing nuclei. One tentative conclusion was that there was possibly enough supercooled water in the major eyewall clouds to furnish latent heat to change the temperature 1 or 2°C if all this liquid was frozen "simultaneously." There was considerable doubt about whether the average supercooled water content over the entire seeded band was sufficient to account for the heating rates suggested by Rosenthal's model runs through heat of fusion alone. On the other hand, it is extremely dangerous to transfer the quantitative aspects of model runs, whether in terms of heating rates, reaction times, or whatever, into direct experimental values. The runs should be used as qualitative guides only.

When the multiple seedings were considered, however, there appeared to be too little supercooled water for the latent heat of fusion to be an adequate sole heat source. Once the liquid in the clouds has been frozen, one cannot keep refreezing it to get more heat. Only by introducing fresh supercooled water into the clouds can one get the additional heat by this mechanism. Simple calculations suggest that heating rates through the release of latent heat of fusion would be 1 to 2 orders of magnitude less than the amount calculations with Rosenthal's hurricane model suggest is needed if one is to get significant reductions in the maximum winds within 4 to 10 hours. In further view of the fact that there appears to be a lower limit below which the heating has no apparent effect, this limited small heat source gave serious concern to the scientists involved.

A new hypothesis for the source of the enhanced heating has been developed. We have reviewed the seeding procedures used in the Hurricane Esther, 1969 (Simpson et al., 1963), Hurricane Beulah, 1963 (Simpson and Malkus, 1964a), and Hurricane Debbie, 1969 (Gentry, 1970a, b) experiments and believe that the changes observed in each of these storms may be accounted for much more reasonably by the new hypothesis than by the original hypothesis. It provides for an improved interpretation of the Debbie results without requiring any *drastic* revision of the seeding patterns used in the hurricane experiments. If this hypothesis is confirmed, however, it will permit changes in the seeding patterns and seeding altitudes to allow more efficient use of the Project aircraft that are likely to be available in future years.

A NEW SEEDING HYPOTHESIS

The new explanation reemphasizes that the seeding should be done radially outward beyond the tallest clouds in the eyewall and at radii greater than that of either the greatest ascending motion or the maximum winds. The first goal of the seeding with silver iodide crystals is to cause freezing of supercooled water droplets in towering cumulus with tops at temperatures of -5 to -20°C and to release the latent heat of fusion. In the old explanation, the latter was the main reaction expected. In the new explanation, it is the initiation of a bigger reaction, i.e., the trigger that sets off a chain reaction. The latent heat of fusion is expected to increase the buoyancy of the towers to cause greater growth of the ascending plumes in the clouds, and ultimately *to result in condensation or sublimation of extra water vapor* at the radii of the seeding. Either of the latter

two processes can release many times as much heat as would be released by merely freezing the supercooled water droplets in the clouds. The stimulation of cloud growth at these radii accomplishes two ends: it allows the clouds to grow vertically up into the outflow layer so that air "circulating through this duct" never penetrates to smaller radii, and at the same time it increases the heat release at the radii of seeding. Obviously, air which is thus diverted upward never spirals on into the eyewall and is therefore unable to contribute its heat and angular momentum to maintaining the old ring of maximum winds.

Thus, one purpose of seeding the clouds outside the old eyewall is to develop a "new eyewall" at a greater radius. If this is accomplished, and most of the air flowing inward ascends at a larger radius, lower maximum wind speeds should result simply from conservation of angular momentum. H. Sundqvist (1970), who has also developed a hurricane model, recently expressed this same idea when he wrote, "Regarding the radial distribution of heating by condensation, we can conclude that the farther from the centre the maximum is, the farther from the centre will the maximum radial wind occur. And from absolute angular momentum considerations it is clear that the earlier (coming from the outside) the inflow ceases the less will the tangential wind be."

A first reaction to this proposal may be, "Hurricane clouds already extend to great heights. How can one make them grow taller?" In the eyewall this may indeed be difficult, but in all other regions it may be quite practical. H. V. Senn (app. K) studied RHI (vertical profiles of radar targets) radar pictures of hurricanes. He found many echoes whose tops were between 20,000 and 30,000 ft. Such clouds occupied much of the outer portions of the hurricane, and there were many even within 5 n miles outward from the inner edge of the eyewall. His data show that more than 50 percent of the echoes within 30 n miles of the center have tops in this range. These data are not adequate support for any strong conclusions, but Senn found nothing to indicate that most echoes in the vital annular ring naturally grew to the top of the troposphere. Thus, current radar data suggest it is possible to make the cumuliiform clouds grow sufficiently to cause extra condensation (sublimation) of water vapor in the region where the simulation experiment with the Rosenthal model indicates that application of the enhanced heating function results in the greatest reduction in maximum winds.

Scientists in the Naval Weapons Center at China Lake, California (St. Amand, 1970; Schleusener et al., 1970), the Experimental Meteorology Laboratory of NOAA (Simpson and Woodley, 1971), Pennsylvania State University (Davis, 1966;

Davis et al., 1968) and other groups have all shown conclusively that under certain conditions, cumulus clouds, including those in the tropics, can be made to grow both vertically and horizontally by seeding and in some cases can be made to grow explosively.

The cloud environment in a hurricane is different from the mean tropical atmosphere, but there are reasons for believing that clouds outside the eyewall in a hurricane also can be made to grow by seeding. R. Sheets (1969a) using the cloud model developed at the Experimental Meteorology Laboratory (Simpson and Wiggert, 1969) has made computations as to the seedability of hurricane clouds using the mean soundings he developed for different radii (surface pressure) in hurricanes. Using assumptions considered reasonable, he calculated that cumuliform clouds similar to those found beyond the eyewall of hurricanes might be expected to grow considerably more than 5000 additional feet after being seeded. D. A. Matthews obtained similar results using a different cloud model (app. H).

A radar picture showing a vertical slice through the left rear quadrant of Hurricane Debbie, 20 August 1969, is shown in figure B-1. This picture was taken by one of the Navy's APS-45 (3 cm) radars. It shows the eyewall and the fine scale structure of some of the rainbands. The echoes from this picture have been reproduced in the right side of figure B-2. Note that the eyewall, 40 n miles from the aircraft (A/C), extends to at least the top of the scope which is at 40,000 ft. The other echoes end below 30,000 ft. The difference cannot be explained by attenuation because the radar saw through these echoes to the eyewall. Other aircraft in the area reported clouds from near sea level to above 40,000 ft, so there must have been stratiform clouds between the radar echoes throughout the area represented by the picture except in the eye of the storm. The echoes in the pictures presumably are associated with clouds that have the stronger ascending currents and the greater liquid-water content.

The left side of figure B-2 illustrates the basic factors considered in simulating the modification experiment with Rosenthal's model (1970b). The enhanced heating function was such as to change the temperature at the rate of $4^{\circ}\text{C hour}^{-1}$ and was applied at 300 mb and 500 mb. The temperatures do not actually change this much because the extra heat is rapidly dispersed to other portions of the storm. Considering the levels used in the model and interpolations between levels, this means that the enhanced heating affects the layer between 600 mb and 250 mb or a layer 350 mb thick.

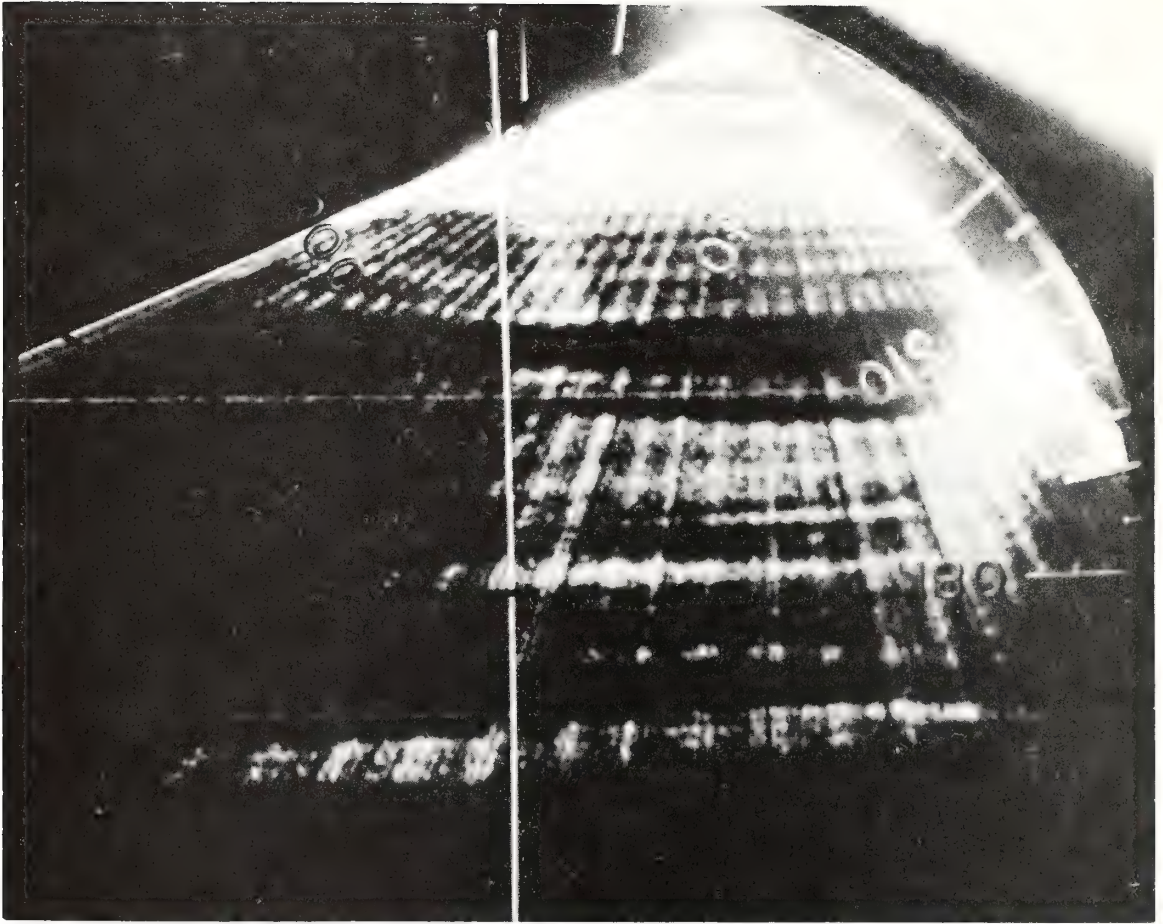


Figure B-1. Photo of the rainbands and southern eyewall of Hurricane Debbie, 20 August 1969, taken by the APS-45 (X-Band) radar operating in RHI mode on U.S. Navy Reconnaissance aircraft. The white line shows 20,000 ft elevation. The tallest echo (about 40 n miles from aircraft) is the eyewall.

Consider any vertical column 1 cm^2 in cross section and extending through a depth of 350 mb. Then the enhanced heating function calls for adding $0.0934 \text{ cal sec}^{-1}$ to this column. In the reproduction of the radar band just to the right of the column (fig. B-2), some potential for growth is suggested. The specific humidity at the top of the radar echo was about 5.5 g kg^{-1} of air. If by seeding, one could initiate the release of latent heat of fusion and sufficient increase in cloud buoyancy to cause the ascending column to rise about 2000 additional feet, the specific humidity at the top would then be 4.5 g kg^{-1} . That is, 1 extra gram of water vapor would be sublimated or condensed and would release up to

HURRICANE "DEBBIE" AUGUST 20, 1969

SIMULATING A HURRICANE MODIFICATION EXPERIMENT

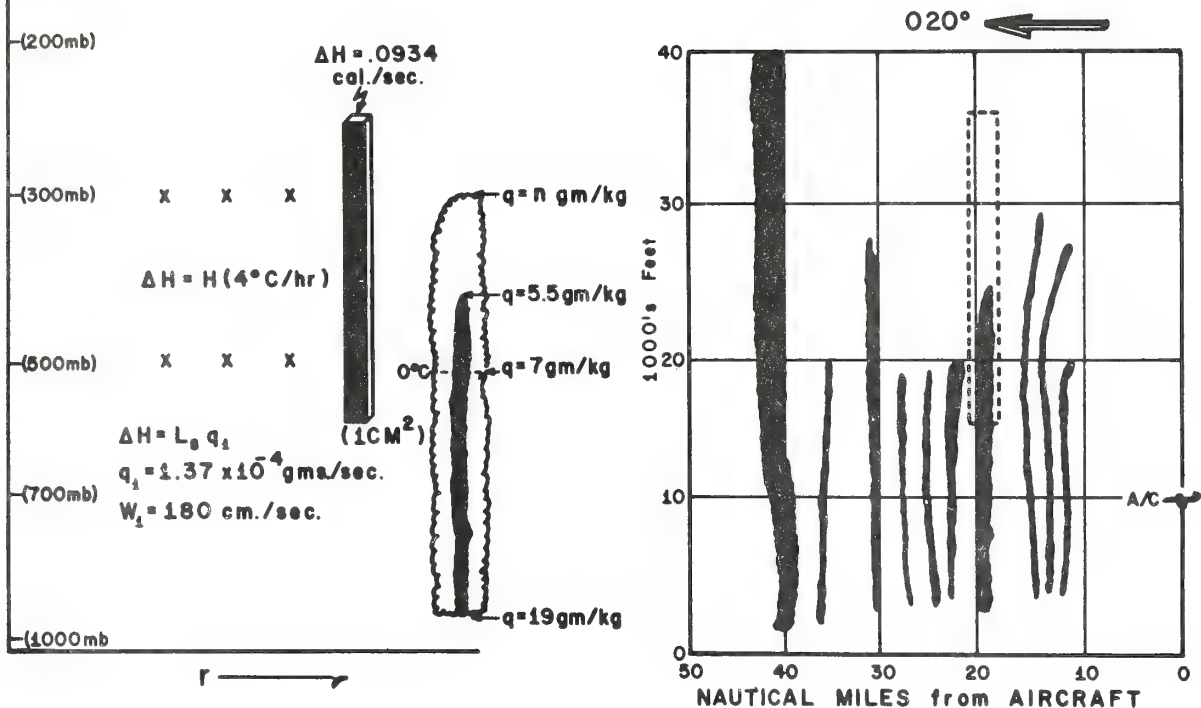


Figure B-2. Radar echoes from the original picture reproduced in Fig. 1 are in the right side of the diagram. The center of Hurricane Debbie was about 50 n miles north-northwest of the aircraft. The eyewall (40 n miles from aircraft) extended higher than 40,000 ft (limit of the radarscope). The left portion refers to calculations of amount of heat that can be released by seeding and to the amount of heat required for modification of a hurricane in the simulation experiment with a theoretical model (see text).

678 cal to warm the air column. We can make a rough check on whether this mechanism can furnish sufficient heat at the rate suggested by the calculations with the numerical models. If we assume that for each kilogram of air entering the base of the clouds, seeding causes 1 extra gram of water vapor to sublimate, we can calculate the vertical velocity needed to provide for the enhanced heating. For the entire annulus affected by the seeding an average vertical velocity of 180 cm sec⁻¹ is needed at 600 mb to provide the required air flow. This is believed to be a conservative value based both on results from the modeling experiments and measurements

made of the divergence fields in hurricanes. Obviously updrafts will be stronger in the clouds in order for the average vertical velocity to be 180 cm sec^{-1} . Since we do not have accurate estimates of the percentage of the area that is covered by the active convective towers, we cannot state precisely what the average updraft speeds will be, but order of magnitude type calculations again suggest values that are in line with observations. Thus, it seems reasonable that the amount of heat required under the assumption of an enhanced heating function sufficient to cause temperature change at rates of $4^{\circ}\text{C hour}^{-1}$ can be provided by the latent heat of sublimation (or condensation) if the seeding will cause the clouds to grow an additional few thousand feet.

The U.S. Air Force Air Weather Service will make special efforts in 1971 to release dropsondes at radii outside the eyewall of tropical cyclones to provide data needed to make more reliable computations of the seedability (difference in height of seeded cloud and expected natural growth of the same cloud) of hurricane clouds outside the eyewall.

Qualitative support is provided by Rosenthal's modeling results to the idea that adding heat above the freezing level and outside the eyewall can cause a new eyewall to develop at a greater radius. In part of the volume in the model where the enhanced heating was applied, "natural factors" started operating and 13 times as much heat was released in the model computations as was added due to the artificial enhancement of the heating function. For the volume as a whole, the natural enhancement as represented by the increases in enthalpy was approximately 10 times as great as that added by the enhanced heating function (Rosenthal, 1971). This is further evidence that there is a latent instability present which can be triggered by properly applied heating.

The increased "natural" heating in the model is explained by what happened to the vertical motion in the "modified" model hurricane. Initially, the maximum updraft velocities were located between the 15 and 25 km radii. After the enhanced heating was applied between radii of 25-45 km, a new maxima of vertical motion developed there, and within less than 10 hours, the original maxima had disappeared. The shift to the radii of enhanced heating resulted in much greater condensation at those radii. Since the total volume of the annulus increases when its radii increases, the same vertical velocity results in a larger total rainfall for the modified storm. A detailed analysis of the vertical motion fields revealed two maxima for a short period, one at the radius of the original maximum, and the other at the radii

of the enhanced heating function. Eventually the latter became the larger, and a new eyewall (or at least the maximum vertical velocity) developed at the greater radii. Once the inflowing air at the low levels started ascending at the larger radii, the calculations with the model indicated a reduction in maximum winds. Winds at the new maximum wind radius were stronger than the old winds at that radius but less than the old maximum winds.

Examination of the seeding runs made in the various hurricanes that have been seeded, that is, Esther (1961), Beulah (1963), and Debbie (1969), reveals they were all seeded in *roughly* the same radial band or annulus. In the earlier cases, the seeding run started at the inner edge of the eyewall and in Debbie started at a point about 3 n miles radially outward from the inner edge of the eyewall. All seeding runs extended radially outward 14 to 30 n miles and most extended about 20 n miles. The new hypothesis suggests that the seeding run should start at a point about 5 n miles radially outward from the inner edge of the eyewall and go outward for 15 to 30 n miles. This constitutes an even smaller change in the radii from those used in the Debbie experiment than the changes from the seeding radii used for the 1961 and 1963 experiments to those of the Debbie experiment.

The present plans for the seeding and those used in the Debbie experiment call for the pyrotechnics to produce a curtain of silver iodide crystals from about 33,000 ft down to the freezing level. If the new hypothesis is correct, the seeding might be equally effective if the silver iodide generators produced the crystals from some lower level, for example, 27,000 ft, down to the freezing level.

QUESTIONS NEEDING BETTER ANSWERS

While the new hypothesis does suggest better answers to some of the questions that have been asked by critics of the hurricane modification experiments, there are still several questions which have not been adequately answered. A few of these are discussed in the following paragraphs:

- (1) The basic question, of course, is, will the modification experiment work and, if so, under what conditions? Thus far we have been seeking answers to this question from the modeling experiments with back-up from information derived from the Hurricane Debbie experiments. While the latest version of the hurricane model does simulate many

features of hurricanes very well (Rosenthal, 1970), its developer says it is still in some respects a rather crude model. It should not be depended upon for final, authoritative, and quantitative answers about what results to expect from a modification experiment on an actual hurricane. More experience with this and more sophisticated models is needed.

- (2) How do we get the freezing nuclei into the clouds where they are most likely to produce results? There are two problems here. The first involves getting the seeder airplane to the right position to put freezing nuclei into the clouds. While pilots are very experienced in flying aircraft through hurricanes, it is difficult for them to identify and fly to the portion of the cloud having the strongest updraft and to drop the silver iodide without encountering hazardous flight conditions. The second question is what happens to the silver iodide freezing nuclei that are released in a cloud without an ascending current. Presumably, they are swept around the storm by the winds. Are they entrained into the next updraft that they pass or do they skirt around it? Senn et al. (1971) and Hawkins and Rubsam (1968) have presented data about the radar bright band which suggest that there are already many naturally created ice crystals in the hurricane clouds outside of the active updrafts. If so, the artificial freezing nuclei that do not get into the updrafts initially may be mixed with the natural ice crystals and have little influence on later developments.
- (3) The most difficult question we have had to answer in the Debbie and earlier experiments is how to evaluate the results. It is comparatively simple to determine whether the storm weakens or intensifies. It is difficult to learn whether the seeding caused the change or whether the change was a result of natural forces. The new explanation for why the seeding should work offers opportunities, however, for answering this question. We have a sequence of events which should occur: (a) There are convective clouds present which contain supercooled water and relatively few natural freezing nuclei. (b) These clouds do not extend to the top of the hurricane. (c) Seeding these clouds with silver iodide causes them to grow. (d) When the clouds grow, the temperature increases slightly in the area of the seeding. (e) A new eyewall starts to develop in that area. The radar on aircraft currently assigned to the Project can be used to monitor the clouds and record changes in the clouds in the seeded band for several hours to see if they grow at proper times and at rates expected to result from the seeding. If changes occur in conformance with the hypothesis, this would be very convincing evidence that the seeding contributed to these changes and to simultaneous changes in the wind speed.

- (4) Where does water vapor come from that is condensed (or sublimated) to provide the heat required in the new hypothesis? In the simulation experiment made with the Rosenthal model, it was assumed that the enhanced heat came from releasing the latent heat of fusion from water already in the volume. In the new version of the hypothesis, we must account for new supplies of water vapor being condensed in greater quantities at greater radii, and this vapor must come either from the ocean, the low atmospheric levels, or from some mid-level portion of the storm. Anthes (1971) has investigated this problem and concluded that the reduction in the maximum winds that the model suggests will take place varies greatly depending on the origin of the water vapor that goes into the growing seeded clouds. S. L. Rosenthal discusses in appendix C, another method of simulating the seeding in the modeling experiments. Perhaps these new experiments he is planning will answer this question. In any case, this is a problem that will require much more research on both the hurricane and cloud scales of motion and their interactions.
- (5) As has already been mentioned, there is a need to know more about the seedability of hurricane clouds. That is, can they be made to grow taller and larger by seeding? How numerous are they, how high should they grow, what volumes of low-level air might they divert?

FUTURE PLANS

The Air Weather Service (USAF) has already issued instructions to the hurricane hunter squadrons in the Atlantic and Pacific to make special efforts to get dropsonde data from the 300-mb level in tropical cyclones in the annulus, 5 to 40 miles radially outward from the inner edge of the eyewall. These data will make possible more definitive computations of the seedability of the hurricane clouds.

The Navy, NOAA, and Air Force aircraft will make extra efforts to get consistent radar coverage not only of experimental hurricanes, but also of nonexperimental hurricanes. The latter data will be used for establishing a range of natural variability that can be compared with the changes occurring in experimental hurricanes following seedings. The Navy aircraft have radar especially well-designed for this task. The radar data should also provide more information about the number and location of clouds that have seedability.

The Research Flight Facility and the National Hurricane Research Laboratory will continue their efforts to get more information about the amount and distribution of the liquid- and solid-water contents of the hurricane clouds.

As outlined in appendix C, greatly increased efforts will be devoted to improving the theoretical models of hurricanes.

Finally, every effort will be made to conduct additional modification experiments on hurricanes. These are necessary. No matter how the theoretical models are improved, and no matter how much cloud physics, radar, and other data are accumulated, they in themselves will be insufficient (for the foreseeable future) to determine whether we can modify hurricanes. The final answer will have to come from experiments on real storms.

ACKNOWLEDGEMENTS

Many people have contributed to the development of the new hypothesis. Some of these have been referenced in this paper. The first presentation of a preliminary version of the new hypothesis was made by the senior author at a meeting of the STORMFURY Advisory Panel on 29 September 1970. Many improvements in the hypothesis were suggested at that time. Among those participating were Professor Noel E. LaSeur, Professor Charles Hosler, Professor Edward Lorenz, Professor James E. McDonald, Professor Jerome Spar, Dr. Stanley Rosenthal, Dr. Harry F. Hawkins, Dr. Richard Anthes, Mr. William Mallinger, Mr. Peter Black, and Dr. William Cotton.

This presentation of the hypothesis is the work of the writers and any deficiencies should be attributed to them. If, however, the hypothesis proves to have great merit, credits should be shared with the ones listed above and the many people whose research has been referenced herein.

In addition, credit should be given to the scientists and technicians of the National Hurricane Research Laboratory (NOAA), Research Flight Facility (NOAA), Navy Weather Research Facility, and the Navy and Air Force Hurricane Hunter Squadrons who collected, processed, and analyzed the data needed to support the new ideas.

REFERENCES

- Anthes, R. A. (1971): The response of a 3-level axisymmetric hurricane model to artificial redistribution of convective heat release. Technical Memorandum ERLTM-NHRL No. 92, NOAA, Dept. of Commerce, NHRL, Miami, Fla.
- Davis, L. G. (1966): Alternation of buoyancy in cumuli. Ph.D. Thesis, The Pennsylvania State University, University Park, Penn.
- Davis, L. G., J. I. Kelley, A. Weinstein, and H. Nicholson (1968): Weather modification experiments in Arizona. NSF Report 12A and Final Report NSF GA-777, Department of Meteorology, The Pennsylvania State University, University Park, Penn. 129 pp.
- Gentry, R. C. (1969): Project STORMFURY. *AMS Bulletin*, 50, (6), June, pp. 404-409.
- Gentry, R. C. (1970a): Hurricane Debbie modification experiments, August, 1969. *Science*, 168, pp. 473-475.
- Gentry, R. C. (1970b): The hurricane modification project: Past results and future prospects. *Project STORMFURY Annual Report 1969*, U.S. Department of Navy and U.S. Department of Commerce, Appendix B.
- Rosenthal, S. L. (1970a): A circularly symmetric primitive equation model of tropical cyclone development containing an explicit water vapor cycle. *Monthly Weather Review*, 98, (9) September, pp. 643-663.
- Rosenthal, S. L. (1970b): A circularly symmetric, primitive equation model of tropical cyclones and its response to artificial enhancement of the convective heating functions. *Monthly Weather Review*, 99, (5), May, pp. 414-426.
- Schleusener, R. A., P. St. Amand, W. Sand, and J. A. Donnan (1970): Pyrotechnic production of nucleants for cloud modification. *Journal of Weather Modification*, 2, (4), May, pp. 98-117.
- Sheets, R. C. (1969): Computations of the seedability of clouds in a hurricane environment. *Project STORMFURY Annual Report 1968*, U.S. Department of Navy and U.S. Department of Commerce, Appendix E.

- Sheets, R. C. (1969): Preliminary analysis of cloud physics data collected in hurricane Gladys, 1968. *Project STORMFURY Annual Report 1968*, U.S. Department of Navy and U.S. Department of Commerce, Appendix D.
- Simpson, J., and V. Wiggert (1969): Models of precipitation cumulus towers. *Monthly Weather Review*, 97, (7), July, pp. 471-489.
- Simpson, J., and W. L. Woodley (1971): Seeding cumulus in Florida--New 1970 results. *Science*, 172, (3979), April 9, pp. 117-126.
- Simpson, R. H., M. R. Ahrens, and R. D. Decker (1963): A cloud seeding experiment in Hurricane Esther, 1961. *National Hurricane Research Project Report No. 60*, Weather Bureau, U.S. Department of Commerce, Washington, D.C., 30 pp.
- Simpson, R. H., and J. S. Malkus (1964a): A cloud seeding experiment in Hurricane Beulah, 1963. *Project STORMFURY Annual Report 1963*, U.S. Department of Navy and U.S. Department of Commerce, Appendix E.
- Simpson, R. H., and J. S. Malkus (1964b): Experiments in hurricane modification. *Scientific American*, 211, pp. 27-37.
- Simpson, R. H., and J. S. Malkus (1965): Hurricane modification: Progress and prospects, 1964. *Project STORMFURY Annual Report 1964*. U.S. Department of Navy and U.S. Department of Commerce, Appendix A.
- St. Amand, P. (1970): Techniques for seeding tropical cumulus clouds. AMS Second National Conference on Weather Modification, April, Santa Barbara, Cal.
- Sundqvist, H. (1970): Numerical simulation of the development of tropical cyclones with a ten-level model. Part I. *Tellus*, XXII, Nov. 4, pp. 359-390.

APPENDIX C

HURRICANE MODELING AT THE NATIONAL HURRICANE RESEARCH LABORATORY (1970)

Stanley L. Rosenthal
National Hurricane Research Laboratory

INTRODUCTION

The major achievement of this period has been the development of a working, asymmetric model of the hurricane (app. D). Substantial progress has, however, also been made in other areas. Brief summaries of these efforts will be given in later sections of this appendix.

Section 2 reviews our more significant achievements in the general area of time-dependent hurricane modeling. Section 3 reviews the specific problem of modeling a Debbie-like field experiment. Section 4 summarizes efforts less directly related to the development of time-dependent models. Section 5 outlines investigations planned by the group for the next few years.

TIME-DEPENDENT MODELS

(a) The Asymmetric Model: As already noted, progress with this model has been sufficient to warrant a separate discussion (app. D) in this year's annual report. An expanded version of appendix D (Anthes, Rosenthal, Trout, 1970) will appear in the *Monthly Weather Review*. A second paper which compares results of the asymmetric model with a symmetric analog of equivalent vertical resolution has also been accepted for publication (Anthes, Trout, and Rosenthal, 1970).

Computing economics dictate rather coarse vertical and horizontal resolution for the asymmetric model. The atmosphere's vertical structure is represented by only three layers and horizontal spacing of grid points is 30 km. The radial extent of the computational domain is approximately 435 km. The version used to obtain the results shown in appendix D did not contain an explicit water vapor cycle. Although the model allows azimuthal variations, the hurricane

remains an isolated, stationary vortex on an f-plane similar in fashion to the circularly symmetric models. Like the circularly symmetric models, this model is a theoretical tool with no potential for dealing skillfully with real data.

Despite obvious deficiencies due to the lack of adequate resolution, the model reproduces many of the observed asymmetrical features of the hurricane. Realistic portrayals of spiral rainbands are obtained. The anticyclonic eddies of the upper troposphere are reproduced as are the observed areas of negative absolute vorticity and anomalous winds.

Since the preparation of appendix D, the asymmetric model has been generalized to include an explicit water vapor cycle and has been recoded for a staggered horizontal grid. The latter reduces local truncation error without either increasing the number of grid points or reducing the spacing between them. A number of experiments have been conducted with the revised model and results even more promising than those described in appendix D have been obtained. These data are now undergoing careful study.

Despite the realism of the results and despite the increased accuracy obtained through horizontal staggering of variables, the model continues to suffer from a lack of adequate resolution. Improvement of the vertical resolution appears to be economically beyond our reach. There is a possibility, on the other hand, that horizontal resolution, at least in the inner core of the hurricane, may be improved through the use of horizontally variable grids.

Two such grid systems have been designed and tested at NHRL. One of these (Anthes, 1970a) is an analytical transformation from a non-orthogonal, variable mesh in physical space to an orthogonal constant mesh in a computational space. This system possesses the following characteristics: (a) The size of a grid element varies smoothly from a minimum value at the center of the array to a maximum along the boundary. (b) Since the variable grid is derived from an analytical transformation, the degree of variability is easily changed. (c) In the limiting case, the variable grid collapses to the familiar two-dimensional, square grid. (d) The distortion associated with the non-orthogonality of the variable grid is minimum at the center and maximum along the boundaries. (e) The machine programming is relatively simple. On the other hand, the transformed equations do contain more non-linear terms than the original equations which may be a source of difficulty in very long integrations.

The second type of variable grid (Koss, 1970) is composed of a central core of equal area square grid elements surrounded by 'square annuli' of square grid elements of even larger size. The construction defines a family of variable grids. A degenerate member of the family is the familiar "telescope" grid which has been discussed in the literature with reference to local forecasting by numerical methods. However, other members of the family, in which the sizes of grid squares increase rather gradually outward from the central core, seem to be more suitable for the hurricane problem. The advantages of Koss's approach are that Cartesian coordinates are used and, hence, neither transformation terms nor additional nonlinear terms appear in the hydrodynamic equations. A further advantage is that mass and momentum integrals are preserved to within time differencing errors since the equations are expressed in flux form and variable transformation coefficients (similar to map-scale factors) do not appear. The major disadvantage is that machine coding is extremely laborious.

Numerical tests (Anthes, 1970a; Koss, 1970) indicate that both types of variable grids show promise for the hurricane problem. Further tests are planned for both systems.

Two other studies related to the asymmetric model are in progress. It has been suggested that the vertical staggering of variables (see app. D) may severely distort the basic CISK mechanism which drives the model hurricane. While the realism of the results counteracts this suggestion, we are investigating the matter through a linear analysis. The analysis requires solution of a ninth order characteristic equation with complex coefficients. Results are not yet available.

Output data from the asymmetric model are being examined in detail in an attempt to gain greater physical insight into the asymmetric structure of the model storm. With circularly symmetric initial and boundary conditions, the calculation should remain circularly symmetric for all time. Asymmetries are introduced through the initialization procedure and by the fact that the boundaries are not quite circular. Both of these effects tend to excite wave number 4 and, to a lesser extent, wave number 8. However, during the asymmetric stage of the numerical integration, virtually all of the circular variance is contained in wave numbers 1 and 2. An exception to this occurs quite close to the outer boundary where wave number 4 is most significant. The circular variance near the boundary is quite small and, hence, wave number 4, over-all, is rather insignificant.

While the growth of the symmetric part of the systems is understandable from earlier work with symmetric models, and while the dominance of wave numbers 1 and 2 over higher wave numbers is empirically reasonable, we would like to know more about the physical mechanisms involved. The investigation involves a program of harmonic analysis in an attempt to understand the behavior of the governing equations in the spectral domain.

(b) The Seven-Level Symmetric Model: The basic design of this model, as well as typical results to be expected, were documented in three reports which appeared during the year (Rosenthal, 1970a, 1970b, 1970c).

The only significant revisions during the past year (and since the experiments discussed in the papers cited above) are concerned with the boundary layer formulation. Whereas air-sea exchanges of sensible and latent heat had been simulated by some rather pragmatic constraints on the Ekman layer temperatures and humidities, these energy exchanges are now computed explicitly through the bulk aerodynamic method. The constant drag coefficient used in previous experiments has been replaced with Deacon's empirical relationship.

The revised model was used for a number of experiments (Rosenthal, 1970d) in which boundary layer parameters, initial conditions, lateral boundary conditions, and computational domain size were varied.

When the drag coefficient is varied during the immature stage, the response of the model follows linear theory, and growth is more rapid with larger drag coefficients. However, the ultimate intensity reached by model storms varies inversely with drag coefficient. In the mature stage, small decreases of drag coefficient lead to stronger peak winds; but when the drag coefficient is reduced by large amounts, peak winds diminish. In the latter situation, there is insufficient low-level convergence to sustain convection in the storm core.

Oceanic evaporation was found to be an essential ingredient without which immature storms would not develop and mature storms could not sustain themselves. The air-sea exchange of sensible heat was of lesser importance and only small changes occurred when this energy source was completely suppressed. The relative importance of the air-sea exchanges of sensible and latent heat can be explained rather easily (Rosenthal, 1970d).

Comparisons between experiments with open and mechanically closed lateral boundaries show these boundary conditions to be extremely important. For computational domains of 2000 km or less, model storms with closed lateral boundaries are less intense than their counterparts with open lateral boundaries. The intensity of closed systems increases markedly with domain size, while that of open systems varies only slowly with domain size. The experiments indicate that differences due to lateral boundary conditions might be minimized if the computational domain exceeded 2000 km.

Experiments conducted with open lateral boundaries revealed that the structure and intensity of the mature stage of the model cyclone is relatively insensitive to variations in the scale and intensity of the initial perturbation. The time required to reach the mature stage is, however, quite sensitive to these factors.

MODELING AND GUIDANCE FOR PROJECT STORMFURY (1970)

Appendix C of the 1969 Project STORMFURY Annual Report summarized a number of calculations performed with the seven-level symmetric model in which extremely crude attempts were made to simulate a Debbie-like field experiment. (A revised version of that summary appears in the *Monthly Weather Review* (Rosenthal, 1970e).) Additional calculations of this type have been carried out during the last few months and provide results which differ in varying degrees from those reported on last year.

Before proceeding with a discussion of these differences, some words of caution are in order. These comments arise from having an additional year of thought and discussion devoted to the simulation problem. Rosenthal (1970e) pointed out that the assumption of circular symmetry precluded direct comparisons between model calculations and specific real tropical cyclones. It was our feeling at that time, and it continues to be our feeling, that the model should only be considered representative of some sort of "average" hurricane. We pointed out that real hurricanes are strongly influenced by interactions with neighboring synoptic systems and that these interactions may vary markedly in character from storm to storm and cannot realistically be modeled with a symmetric, isolated vortex.

The calculations discussed in Rosenthal (1970d), raise additional questions concerning certain aspects of the model. In previous reports (Rosenthal, 1970e, for example) we have shown the model to yield a highly realistic storm structure during the mature stage. However, since the model has not and cannot be tested using real observations as initial conditions, we cannot examine the model's realism with regard to the time required for it to pass through a series of transients as it proceeds from one slowly varying state to another. Furthermore, Rosenthal (1970d) showed that the time required for a model storm to reach its mature stage varied by several days according to the values of several rather arbitrary parameters (see discussion in Time Dependent Models p. C-1).

Both the field experiments and the model simulations involve adding a small perturbation to a mature hurricane with the hope that it will be unstable. Since no clear-cut theoretical path for establishing the model's credibility with regard to small perturbations is at hand, and since we cannot be entirely certain that Debbie's changes were produced by the seeding, the realism of the model's response to artificial enhancement of the heating functions must also remain an open question. This will be discussed later in this section.

A major difficulty with regard to interpretation of model simulations is related to the so-called "new hypothesis" (discussed elsewhere in this report, see app. B). The artificial enhancement of the model heating functions, which was designed on the basis of the old hypothesis, appears, from a conceptual point of view, to be inconsistent with the new hypothesis.

Under the old hypothesis, the source of this additional heat was attributed to the freezing of supercooled water in the upper tropospheric portions of tall Cb. In the model calculations, this was represented by adding a fixed amount of heat to the upper troposphere over periods of several hours. While valid arguments could be raised concerning the reality of the magnitude of this heat source and the length of time over which it was added, we could at least visualize a clear relationship between the model procedure and the postulated real atmospheric process.

The hurricane could be pictured as a system which continually generates new Cb whose upper tropospheric positions consist of supercooled water. The seeding operation could then be visualized as a process in which this newly generated supercooled water is continually frozen through artificial nucleation. With this view of the field experiment, it is

not unreasonable to attempt a simulation by adding fixed amounts of heat (intended to be the released heat of fusion) to the upper troposphere at each time step for some period of time.

Under the new hypothesis, however, heat of fusion released through silver iodide nucleation is considered only as a stimulus for increasing the buoyancy of Cb (outward from the main eyewall) which by natural processes would reach only to middle tropospheric levels. Under this hypothesis, the major source of energy for modification purposes is sought in the additional condensation and/or sublimation heating released as the seeded clouds grow to upper tropospheric levels.

The difficulty with a simulation relevant to the new hypothesis is that all model Cb which originate in the boundary layer reach upper tropospheric levels by natural processes. This stems from the fact that the model Cb are comprised of undilute ascent. Entrainment is not taken into account. With the current version of the model, therefore, the eyewall region differs from other regions of the storm in *cloud concentration but not in cloud depth*.

Simulation of the new hypothesis is then not easily visualized unless one adopts a highly philosophical attitude. One can, however, argue as follows. The basic feature of the new hypothesis is the stimulation of tall convection at radii larger than that of the eyewall in the hope of diverting some of the boundary layer inflow thus reducing the supply of moisture and angular momentum to the eyewall region. In the field experiment, this is to be accomplished by causing relatively short clouds to become tall as described in a previous paragraph. In the model, where all clouds are tall, a conceivable analogue to the field experiment is to increase the *concentration* of tall clouds at the corresponding radii. Once this point of view has been accepted, the means by which model convection is stimulated becomes rather arbitrary.

The addition of a fixed amount of heat as in Rosenthal (1970e) is only one of many possibilities. Others include arbitrary changes of boundary layer convergence, changes of the humidity patterns, and changes in static stability. Of course, these alterations can also be made in various combinations.

While calculations of the Rosenthal (1970e) type can still provide helpful information for Project STORMFURY if properly interpreted, clearly literal comparisons between the calculations and the Debbie experiment are unwarranted. Aside from the arbitrary procedures used to simulate seeding,

the questions concerning the response time of the model raised earlier in this section must be considered as must the lack of interaction with other synoptic features.

It is abundantly clear that we must strive to provide more direct numerical tests of the new hypothesis. To achieve this end, it will be essential to include entrainment and some simple representation of the more significant microphysical processes. It may also be necessary to make improvements in the modeling of the interactions between the Cb and hurricane scales. This will be a high priority item for the next year.

In the meantime, calculations of the old type will continue. These have and will continue to provide useful information when compared against each other. As noted earlier, differences of varying degree have arisen between the calculations reported on last year and those performed in recent months. Some of these differences are probably attributable to a revision of the model during the intervening period. This revision consisted of replacement of the constant drag coefficient (3×10^{-3}) by Deacon's empirical relationship (see discussion in Section 2). The latter gives a linear dependence on wind speed, and values of 3×10^{-3} are not reached until winds approach 50 m sec^{-1} .¹ A second source of the differences may well be that model response to the heating enhancement is dependent on the initial conditions. A series of controlled experiments is planned to study this aspect of the problem.

To make meaningful comparisons between the results presented in the 1969 report and those obtained more recently, the former are briefly summarized below. Heating rates were increased at 500 and 300 mb by $1 \text{ kj-ton}^{-1} \text{ sec}^{-1}$ (*normal heating*), $3 \text{ kj-ton}^{-1} \text{ sec}^{-1}$ (*large heating*), and $9 \text{ kj-ton}^{-1} \text{ sec}^{-1}$ (*extreme heating*) for 10-hour intervals at various radii. The radial intervals selected were 25, 35, and 45 km (*small radii* experiments) and 35, 45, and 55 km (*large radii* experiments). The sea-level wind maximum for the control experiment was at 20 km. Hence, in both the *small* and *large radii* experiments, the heat was applied at radii beyond the sea-level wind maximum. The center of the eyewall for the control experiment was at 25 km radius. The *small radii* calculations, therefore, add heat from the eyewall center outward whereas the *large radii* experiments do not add heat at the eyewall center. Experiments were also conducted in which heat was added from the eyewall center inward.

¹ For a discussion of the effect of this change on the typical results to be expected from the model, the reader is referred to Rosenthal (1970d).

Small and *large radii* experiments were consistent in showing the development of a new eyewall at 35 km and destruction of the original eyewall. A new surface-wind maximum was consistently formed at a radius of 40 km, and the original maximum (at 20 km) was eventually destroyed. In general, the newly formed maximum was about 5 m sec^{-1} less intense than the original.

With *normal heating at small radii*, the time required for the new wind maximum to become established was about 8 hours. Differences between *small* and *large radii* experiments with *normal heating* were minor. In both of these experiments, however, prior to the development of the new wind maximum, winds stronger than the control were found at all radii. *Extreme heating* experiments differed from *normal heating* calculations only in response time. *Extreme heating at large radii* gave results which differed from *extreme heating at small radii* also only in response time. With *extreme heating at large radii*, the new surface-wind maximum was established within 2 hours. *Extreme heating at small radii* required 4 hours to establish the new velocity maximum. Prior to this time, surface winds in the modified calculation were as large as 5 m sec^{-1} greater than in the control. Application of the extreme heating rate inside the radius of maximum wind resulted in surface wind increases of 3 m sec^{-1} . However, when the artificial heating was terminated, the system recovered to a state close to that of the control within 4 hours. In contrast, the *large* and *small radii* experiments reached rather stable configurations which were maintained even after the artificial heating was terminated.

While the general evolution of the sea-level winds in the experiments described above was in the sense predicted by either the "old" or the "new" hypothesis, the model's behavior at 700 mb raised some questions. The sense of the 700 mb changes was more or less similar to those changes at sea level. However, the 700 mb responses were more rapid and extreme. The early intensification found at the surface was even more pronounced at 700 mb. The new wind maximum, when formed at 700 mb, was generally more intense than the original maximum until after termination of the enhanced heating.

The major difference between the experimental results just summarized and those obtained more recently is that for a given rate and location of heating, the response times are greater and the magnitudes of the responses are less in the new calculations. In the new experiments, normal heating at *small radii* requires 14 hours to develop the new wind maximum at sea level. Furthermore, in all of the new experiments, the new wind maximum is generated only 10 km outward from the

original maximum. In the old calculations the displacement was 20 km. In the old calculations, with the *normal heating* rate, the magnitude and timing of the response were similar for both *large* and *small radii* experiments. In the new calculations, *normal heating* at *large radii* generates the new sea-level wind maximum about 6 hours earlier than does *normal heating* at *small radii*. Calculations with the $\frac{1}{4}$ the *normal heating* rate at *small radii* shows an ultimate effect similar to that obtained for the experiments with *normal heating*. However, approximately $3\frac{1}{2}$ days of enhanced heating are required to obtain the effect.

Despite the differences which have been emphasized in the last few paragraphs, the experiments do show a consistent pattern which is useful for the design of field experiments. Enhancement of the upper tropospheric heating functions for a sufficiently long period at *radii greater* than the eyewall center and surface wind maximum will ultimately produce a new eyewall and a new, less intense, sea-level wind maximum at radii greater than those of the "naturally" occurring features. The time required to produce these changes is reduced as the rate of heating enhancement is increased. Application of enhanced heating from the eyewall center inward or only at the eyewall center will result in stronger winds at sea level. In this case, the eyewall and the wind maximum will remain at the natural locations.

OTHER INVESTIGATIONS

Anthes (1970b) examined the role of azimuthal asymmetries in satisfying the mean angular momentum budget for the steady-state hurricane.

Anthes (1970c) developed a circularly symmetric model in isentropic coordinates to study the effects of differential heating on the dynamics and energetics of the steady-state tropical cyclone. From specified heating functions, he obtained nearly steady-state solutions for the mass and momentum fields. These solutions were then used to evaluate the available potential energy cycle for the theoretical hurricane. The major results of this investigation will appear in the *Monthly Weather Review* (Anthes, 1970d, 1970e).

Anthes (1970f) examined the problem of truncation error in the calculation of vertical motions at the top of the Ekman layer under an imposed hurricane-like, circularly symmetric pressure field.

Black and Anthes (1971) constructed detailed wind analyses of the outflow layer for four hurricanes and one tropical storm. Harmonic analysis of these data, together with that of the composite storms of Miller and Izawa, shows wave numbers 1 and 2 to account for most of the circular variance in the momentum and kinetic energy fields.

FUTURE PLANS

High priority will be given the development of a more sophisticated cloud representation to be used with the seven-level, circularly symmetric hurricane model so that closer simulations of the "new" STORMFURY hypothesis may be performed.

Simulations of hurricane seeding will be carried out with the asymmetric hurricane model during the next year.

Horizontal resolution in the central portions of the asymmetric hurricane model may be improved through recoding for one of the variable mesh systems discussed in Section 2. Beyond this, the next logical step would seem to be removal of the stationary, isolated vortex assumptions. This will be a major step and will increase our computing requirements by an order of magnitude.

We envision a model in which a fine mesh moves with the hurricane center through a coarse mesh on which the large-scale synoptic patterns are forecast. This type of model will not only serve as a theoretical tool but also will have the potential for real hurricane forecasting. Whether or not this potential will ever be realized will, to a major extent, be dependent upon the development of real time observational techniques for providing adequate high resolution initial data (~10 km horizontal resolution) in the hurricane vortex.

To develop such a model, important background investigations will be required. The mathematical and physical considerations for linking a moving fine mesh with a stationary coarse mesh in the framework of a primitive equation model will require extensive research. The problem of hurricane displacement forecasting by dynamic methods must be reexamined. It is not clear whether the characteristic errors of the existing filtered (primarily barotropic) models are primarily a result of erroneous initial data or physical simplifications.

While these problems must ultimately be faced in the real data context, it is our feeling that the most promising start lies with the use of hypothetical initial data and a philosophical attitude similar to that adopted for our earlier work.

REFERENCES

- Anthes, R. A. (1970a): Numerical experiments with a two-dimensional horizontal variable grid. *Monthly Weather Review*, 98, (11), November, pp. 810-822.
- Anthes, R. A. (1970b): The role of large-scale asymmetries and internal mixing in computing meridional circulations associated with steady-state hurricanes. *Monthly Weather Review*, 98, (7), July, pp. 521-529.
- Anthes, R. Z. (1970c): A diagnostic model of the tropical cyclone in isentropic coordinates. ERLTM-NHRL Technical Memorandum No. 89, ESSA, U.S. Dept. of Commerce, NHRL, Miami, Fla., 147 pp.
- Anthes, R. A. (1970d): A numerical model of the steady-state tropical cyclone in isentropic coordinates. Paper accepted for publication in the *Monthly Weather Review*.
- Anthes, R. A. (1970e): Numerical experiments with a steady-state model of the tropical cyclone. Paper accepted for publication in the *Monthly Weather Review*.
- Anthes, R. A. (1970f): Iterative solutions to the steady-state axisymmetric boundary layer equations under an intense pressure gradient. Paper accepted for publication in the *Monthly Weather Review*.
- Anthes, R. A., S. L. Rosenthal, and J. W. Trout (1970): Preliminary results from an asymmetric model of the tropical cyclone. Accepted for publication in the *Monthly Weather Review*.
- Anthes, R. A., J. W. Trout, and S. L. Rosenthal (1970): Comparisons of tropical cyclone simulations with and without the assumption of circular symmetry. Accepted for publication in the *Monthly Weather Review*.

- Black, P. G., and R. A. Anthes (1971): On the asymmetric structure of the tropical cyclone outflow layer. Paper submitted to the *Monthly Weather Review*.
- Koss, W. J. (1970): Numerical integration experiments with variable resolution two-dimensional Cartesian grids using the box method. Accepted for publication in the *Monthly Weather Review*.
- Rosenthal, S. L. (1970a): A survey of experimental results obtained from a numerical model designed to simulate tropical cyclone development. ERLTM-NHRL Technical Memorandum No. 88, ESSA, U.S. Dept. of Commerce, NHRL, Miami, Fla., 78 pp.
- Rosenthal, S. L. (1970b): Experiments with a numerical model of tropical cyclone development. Some effects of radial resolution. *Monthly Weather Review*, 98, (2), February, pp. 106-120.
- Rosenthal, S. L. (1970c): A circularly symmetric primitive equation model of tropical cyclone development containing an explicit water vapor cycle. *Monthly Weather Review*, 98, (9), September, pp. 643-663.
- Rosenthal, S. L. (1970d): The response of a tropical cyclone model to variations in boundary layer parameters, initial conditions, lateral boundary conditions, and domain size. Accepted for publication in the *Monthly Weather Review*.
- Rosenthal, S. L. (1970e): A circularly symmetric, primitive equation model of tropical cyclones and its response to artificial enhancement of the convective heating functions. *Monthly Weather Review*, 99, (5), May, pp. 414-426.

APPENDIX D

SUMMARY OF PRELIMINARY RESULTS FROM AN ASYMMETRIC MODEL OF THE TROPICAL CYCLONE¹

Richard A. Anthes, Stanley L. Rosenthal, and James W. Trout
National Hurricane Research Laboratory

ABSTRACT

A three layer, primitive equation model of an isolated stationary tropical cyclone is constructed. The major difference between this and previously published models is the elimination of the assumption of circular symmetry. The release of latent heat by the organized cumulus convection is parameterized by use of techniques previously shown to give realistic results in symmetrical models. In particular, the total release of heat in a vertical column is given by the horizontal convergence of water vapor in the Ekman layer, and the vertical distribution of the heating follows the proposals made by Kuo (1965). In this preliminary calculation, water vapor content is not forecast but, rather, is treated implicitly as was the case for the earlier circularly symmetric models.

The results show that the model reproduces many observed features of the three-dimensional tropical cyclone. Realistic portrayals of spiral rainbands and the strongly asymmetric structure of the outflow layer are obtained. The kinetic energy budget of the model compares favorably with empirical estimates and also shows the loss of kinetic energy to truncation errors to be very small.

Large scale horizontal asymmetries in the outflow are found to play a significant role in the radial transport of vorticity during the mature stage and are of the same magnitude as the transport by the circulation.

In agreement with empirical studies, the outflow layer of the model storm shows substantial areas of negative absolute vorticity and anomalous winds.

¹ This report summarizes a more complete version to be published in the *Monthly Weather Review* in 1971.

INTRODUCTION

Axisymmetric numerical models have simulated the life cycle of tropical cyclones with a large degree of realism (Ooyama, 1969; Yamasaki, 1968a, 1968b; Rosenthal, 1970b). They have also yielded valuable insight into hurricane dynamics, energetics, and the important problem of parameterizing the latent heat released in organized cumulus convection. With this background, and with ever increasing computer capability, it is not premature to begin the study of the asymmetric features of the hurricane. Among the more notable of these are the upper tropospheric outflow layer, the rainbands, hurricane motion, and the interactions between the hurricane and nearby synoptic systems.

To incorporate all of these features in a single numerical model is an extremely ambitious goal that will require further investigation. The model developed here represents an isolated stationary vortex and appears to be the logical first step beyond the axisymmetric models. For computational economy, we have limited the model to three vertical levels, a coarse horizontal resolution of 30 km, and a relatively small domain of radius 435 km.

DESIGN OF MODEL

The equations of motion are written in σ coordinates (Phillips, 1957) on an f -plane, where f , the Coriolis parameter, is appropriate to approximately 20°N ($5 \times 10^{-5} \text{ sec}^{-1}$). The equations of motion, continuity equation, thermodynamic equation, and hydrostatic equation are identical to those employed by Smagorinsky et al. (1965) for general circulation studies. The basic equations are given in Anthes et al. (1971a), hereafter referred to as I, and are not repeated here.

STRUCTURE OF THE MODEL

The vertical structure of the model is shown by figure D-1a. The atmosphere is divided into upper and lower layers of equal pressure depth and a thinner Ekman boundary layer. The information levels for the dynamic and thermodynamic variables (fig. D-1a) are staggered according to the scheme used by Kurihara and Holloway (1967).

The horizontal mesh (fig. D-1b) is rectangular with a uniform spacing of 30 km. The lateral boundary points approximate a circle, and all boundary points are contained between radii of 450 and 435 km. All variables are defined at all grid points on the σ -surfaces.

THE FINITE DIFFERENCE EQUATIONS








The finite difference analogs to the horizontal derivatives are similar to those in Grammeltvedt's (1969) scheme "B". The vertical portion of the differencing scheme is identical to that of Kurihara and Holloway (1967) with the exception that potential temperature rather than temperature is interpolated where needed. The details are given in I.

For adiabatic, inviscid flow in a laterally closed domain with $\sigma = 0$ at $\sigma = 0$ and 1, Kurihara and Holloway showed this system to conserve the finite difference analog to

$$\int_x \int_y \int_0^1 p^* \left[C_p T + \frac{u^2 + v^2}{2} \right] d\sigma dy dx. \quad (D.1)$$

VERTICAL DIFFUSION OF MOMENTUM

Although vertical transport of horizontal momentum by the cumulus-scale motions has been shown to be an important element in maintaining the observed structure of hurricanes (Gray, 1967; Rosenthal, 1970b), this effect is not included in the preliminary calculations reported on here. Therefore,

VERTICAL STRUCTURE			
VARIABLE		K	P(mb)
$\sigma = 0$		1	0
Ψ, T		1 1/2	225
σ, ϕ		2	450
Ψ, T		2 1/2	675
σ, ϕ		3	900
Ψ, T		3 1/2	957.5
$\phi = \sigma = 0$		4	1015

(a)

HORIZONTAL STRUCTURE - Northwest Section

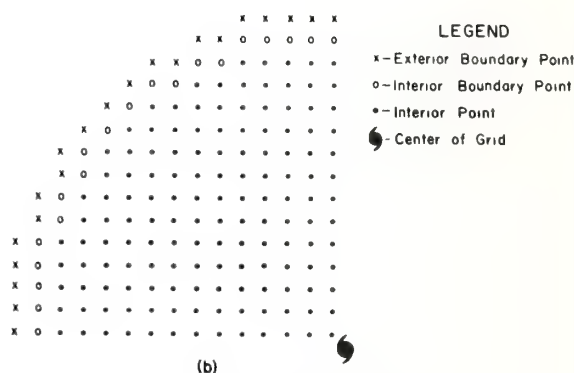


Figure D-1. (a) Vertical information levels; (b) Northwest quadrant of the horizontal grid.

vertical diffusive and "frictional" effects in this experiment are due to the vertical transports of horizontal momentum by subgrid scale eddies smaller than the cumulus scale. The most important aspect of these terms is the surface drag which produces frictional convergence in the cyclone boundary layer and, therefore, a water vapor supply which controls the parameterized cumulus convection (Charney and Eliassen, 1964; Ooyama, 1969; Rosenthal, 1970b).

The surface drag is modeled using the well-known quadratic stress law, and a constant value of 3×10^{-3} was adopted for C_D . For the remaining σ -levels we use the Austausch formulation with the Rossby-Montgomery formulation adopted for the vertical kinematic coefficient of eddy viscosity, K_z (Smagorinsky et al., 1965). The details are given in I.

LATERAL MIXING TERMS

After Smagorinsky et al. (1965), the lateral exchange of horizontal momentum by subgrid scale eddies is written

$$F_H(\vec{V}) = \frac{\partial}{\partial x} \left(K_H \frac{\partial p^* \vec{V}}{\partial x} \right) + \frac{\partial}{\partial y} \left(K_H \frac{\partial p^* \vec{V}}{\partial y} \right) \quad (D.2)$$

where \vec{V} is the horizontal vector velocity, p^* is surface pressure, and K_H is the horizontal coefficient of eddy viscosity.

Preliminary tests, as well as calculations with a symmetrical analog to this model (Anthes et al., 1971b) revealed that neither a constant value of K_H nor Smagorinsky's (1965) variable K_H (proportional to the magnitude of the total deformation of the horizontal motion) provided acceptable results.

The formulation ultimately adopted was

$$K_H = C_1 |V| + C_2 \quad (D.3)$$

where $C_1 = 10^3$ and $C_2 = 5 \times 10^3 \text{ m}^2 \text{ sec}^{-1}$.

While this selection was based primarily on the results of numerical tests, the form was suggested by the encouraging results obtained from symmetrical models (Rosenthal, 1970b; Yamasaki, 1968b) which employed upstream differencing of advection terms with forward time steps. This scheme introduces a computational viscosity (Molenkamp, 1968) which is similar to the variable portion of (D.3).

Although (D.3) is not terribly satisfying from a physical point of view, it does afford a useful interim representation of the statistical effect of horizontal interactions between the momentum fields of the cumuli and macroscale. More satisfying formulations are dependent on the success of future theoretical and observational studies of these interactions.

The preliminary tests also indicated that adequate results can be obtained if the lateral diffusion of heat is computed with a constant thermal diffusivity (K_T) of $5 \times 10^4 \text{ m}^2 \text{ sec}^{-1}$. The lateral mixing term in the thermodynamic equation was, therefore, expressed in the form

$$F_H(T) = p * K_T \left(\frac{\partial^2 T}{\partial x^2} + \frac{\partial^2 T}{\partial y^2} \right), \quad (\text{D.4})$$

where T is temperature.

TIME INTEGRATION

A number of experiments were conducted for the purpose of selecting a method of time integration. Comparisons were made between the usual leap-frog method, the two-step Lax-Wendroff scheme (Richtmyer and Morton, 1967), and the Matsuno (1966) simulated forward-backward scheme. With viscous and diabatic effects included, the Matsuno technique was clearly superior to the other schemes tested. This conclusion was based on intuitive meteorological inspection of the test results. Presumably, the superiority of the Matsuno scheme is due to its severe damping of high temporal frequencies. Since this model has very limited vertical resolution, the high-frequency inertia-gravity waves (particularly, the external gravity wave) are probably overly excited by the diabatic heating. The Matsuno damping may, then, compensate for this effect.

LATERAL BOUNDARY CONDITIONS

The small domain size and the irregular boundary make the choice of lateral boundary conditions extremely important. Preliminary experimentation showed that realistic results could be obtained for steady-state pressure and temperature on the boundary and a variable momentum based on extrapolation outward from the interior of the domain.

LATENT HEAT RELEASED IN ORGANIZED CUMULUS CONVECTION

As already noted, this preliminary experiment does not contain an explicit water cycle. Because of this, the convective adjustments of macroscale temperature are parameterized as they were in the original version of Rosenthal's (1969) symmetric model. The formulation contains ingredients suggested by previous investigators - particularly, Charney and Eliassen (1964); Kuo (1965); Ogura (1964); Ooyama (1969); Syōno and Yamasaki (1966); Yamasaki (1968a, b).

The basic characteristics of this convective adjustment are summarized as follows:

1. Convection occurs only in the presence of low-level convergence and conditional instability for air parcels rising from the surface.
2. All the water vapor that converges in the boundary layer rises in convective clouds, condenses, and falls out as precipitation.
3. All the latent heat thus released is made available to the macroscale flow.
4. The vertical distribution of this heating is such that the macroscale lapse rate is adjusted towards the pseudo-adiabat appropriate to ascent from the surface.

Empirical justification for these characteristics is presented by Rosenthal (1969).

The convective adjustment, described above, applies only when the atmosphere is conditionally unstable; i.e., the cloud temperature, T_c , exceeds the environmental temperature, T . In mature hurricanes, however, prolonged and intense cumulus convection substantially reduces parcel buoyancy and lapse rates approach the moist adiabatic. Under these circumstances, significant amounts of nonconvective precipitation (and, hence, latent heat release) may occur (Hawkins and Rubsam, 1968). Since, in this experiment, water vapor is not explicitly forecast, it is necessary to parameterize this effect.

The parameterization of nonconvective latent heat release under nearly moist adiabatic conditions proceeds as follows. Whenever $(T_c - T) < 0.5^\circ\text{C}$ in the middle or upper tropospheric layers, this quantity is arbitrarily set to 0.5°C . Under a nearly moist adiabatic lapse rate, therefore, $T_c - T = 0.5^\circ\text{C}$ at both levels, and the latent heat is partitioned equally between the upper and lower troposphere. Therefore, latent heat is released in the column as long as a water vapor supply from the boundary layer is present.

The value of specific humidity, q , in the boundary layer, needed for the evaluation of the moisture convergence, is assumed to be given by

$$q = \text{minimum} \left\{ \begin{array}{l} 0.90 \quad q_s \\ 0.020 \end{array} \right\} \quad (\text{D.5})$$

where q_s is the saturation specific humidity. The upper boundary of 0.020 avoids excessive moisture values at points close to the storm center in the late stages of development when warm temperatures associated with an "eye" appear.

Finally, the surface humidity and temperature are required to establish the pseudoadiabatic appropriate to parcel ascent from the surface.

The surface temperature, T^* , is computed by a downward extrapolation from the temperature at level $k = 7/2$ assuming a constant lapse rate between the dry and moist adiabatic rates. The surface specific humidity, q^* , is obtained from q through the assumption that the relative humidity is constant in the boundary layer.

AIR-SEA EXCHANGE OF SENSIBLE HEAT

The sensible heat flux at the air-sea interface is assumed to obey the bulk aerodynamic relationship. It is further assumed that the heat flux decreases linearly with σ until it reaches a value of zero at the $k = 3$ level. This gives

$$p^* \dot{Q}_{k=7/2}^s = \left\{ \begin{array}{ll} \frac{g C_p C_E |V| \rho^* (T_{\text{sea}} - T^*)}{\sigma_4 - \sigma_3}, & T_{\text{sea}} > T^* \\ 0, & T_{\text{sea}} \leq T^* \end{array} \right\} \quad (\text{D.6})$$

where $Q_{k=7/2}^S$ is the sensible heat added per unit mass and time at $k=7/2$. The exchange coefficient C_E is taken equal to C_D (0.003); $T_{sea} = 302^\circ K$ is used for the experiment discussed below.

INITIAL CONDITIONS

The initial conditions consist of an axisymmetric vortex in gradient balance. The minimum pressure is 1011 mb and the environmental pressure on the lateral boundaries is 1015 mb, yielding a maximum gradient wind of 18 m sec^{-1} at a radius of 240 km.

EXPERIMENTAL RESULTS

The history of the cyclone is summarized by figure D-2 which shows the evolution of the minimum surface pressure and the maximum wind speed in the boundary layer ($k = 7/2$). Due

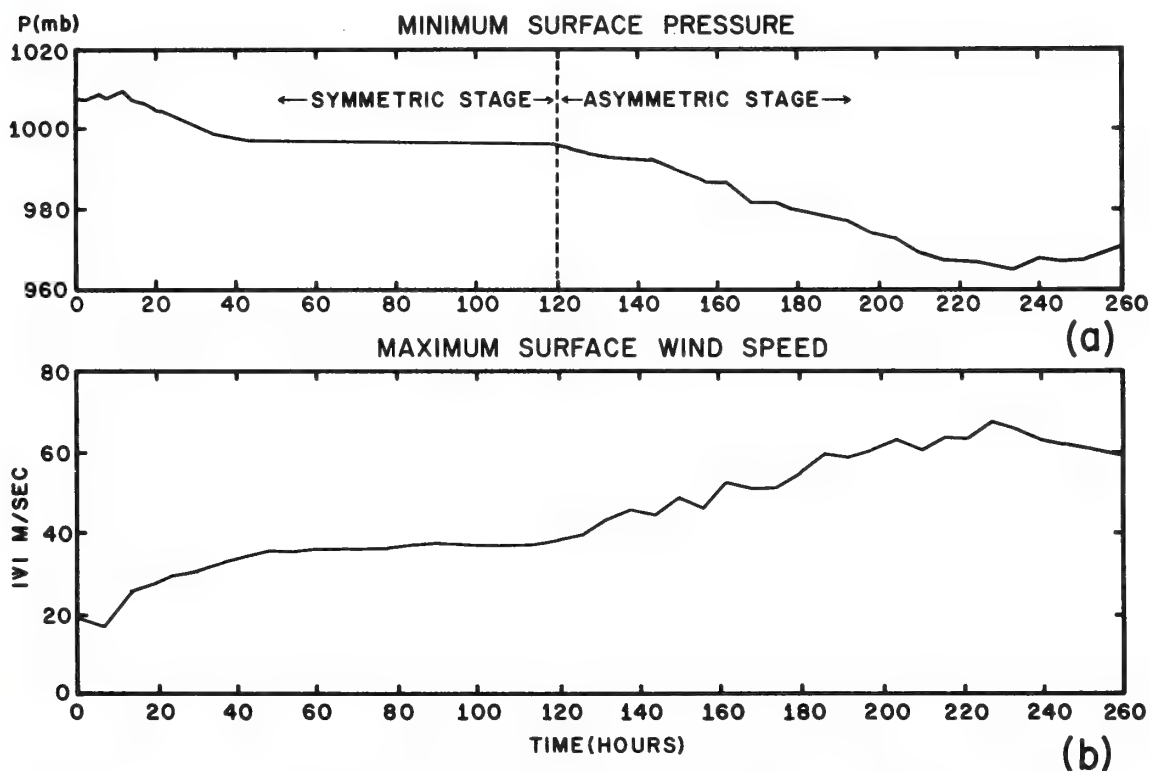


Figure D-2. Time variation of the minimum surface pressure and the maximum surface wind speed.

to the substantial strength of the initial vortex, a short "organizational phase" of only 12 hours is needed before steady intensification begins. Hurricane force winds appear at about 40 hours and, thereafter, the relatively weak storm remains in a quasi-steady state until about 120 hours. At this point, a second period of intensification begins and the maximum wind eventually exceeds 60 m sec^{-1} . The unsteady nature of the storm during this period seems to be related to the development of pronounced asymmetries (especially in the out-flow region). These asymmetries are discussed in detail later.

Figure D-3 shows the temporal variations of the components of the kinetic energy budget. The sum of, (1) the conversion of potential to kinetic energy ($C(K)$), (b) the flux

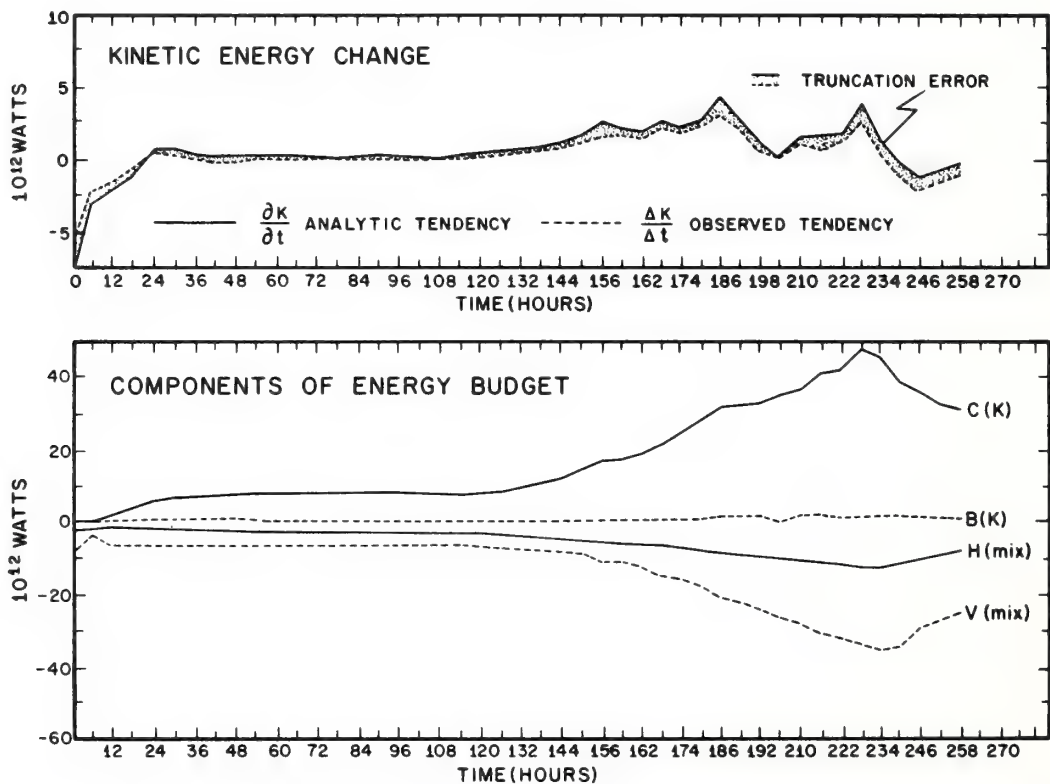


Figure D-3. (a) Time variation of the observed kinetic energy ($\Delta k/\Delta t$) and the change computed from the kinetic energy equation ($\partial k/\partial t$): (b) Time variation of individual components of the kinetic energy tendency: $C(k)$ is the conversion of potential to kinetic energy, $B(k)$ is the flow of kinetic energy through the lateral boundary, $H(mix)$ is the loss of kinetic energy through lateral eddy viscosity, $V(mix)$ is the loss of kinetic energy through vertical eddy viscosity and includes the effect of surface drag friction.

of kinetic energy across the lateral boundary ($B(K)$), (3) the dissipation due to lateral mixing ($H(\text{mix})$), and (4) the dissipation due to vertical mixing ($V(\text{mix})$) equals the "analytic" kinetic energy tendency ($\partial k / \partial t$). Also shown by figure D-3 are the observed rates of change of kinetic energy ($\Delta k / \Delta t$). The difference between $\partial k / \partial t$ and $\Delta k / \Delta t$ is a measure of the truncation error and, as figure D-4 shows, this difference is quite small. Furthermore, the individual components of the budget are reasonable when compared to empirical estimates (Hawkins and Rubsam, 1968; Miller, 1962; Palmén and Riehl, 1957; and Riehl and Malkus, 1961).

For purposes of discussion, it is convenient to divide the history of the storm into two stages. From the initial instant until about 120 hours, all features are quite symmetric with respect to the storm center. During this period, there is neither evidence of a banded structure in the rainfall (analogous to rainbands in real hurricanes) nor does the

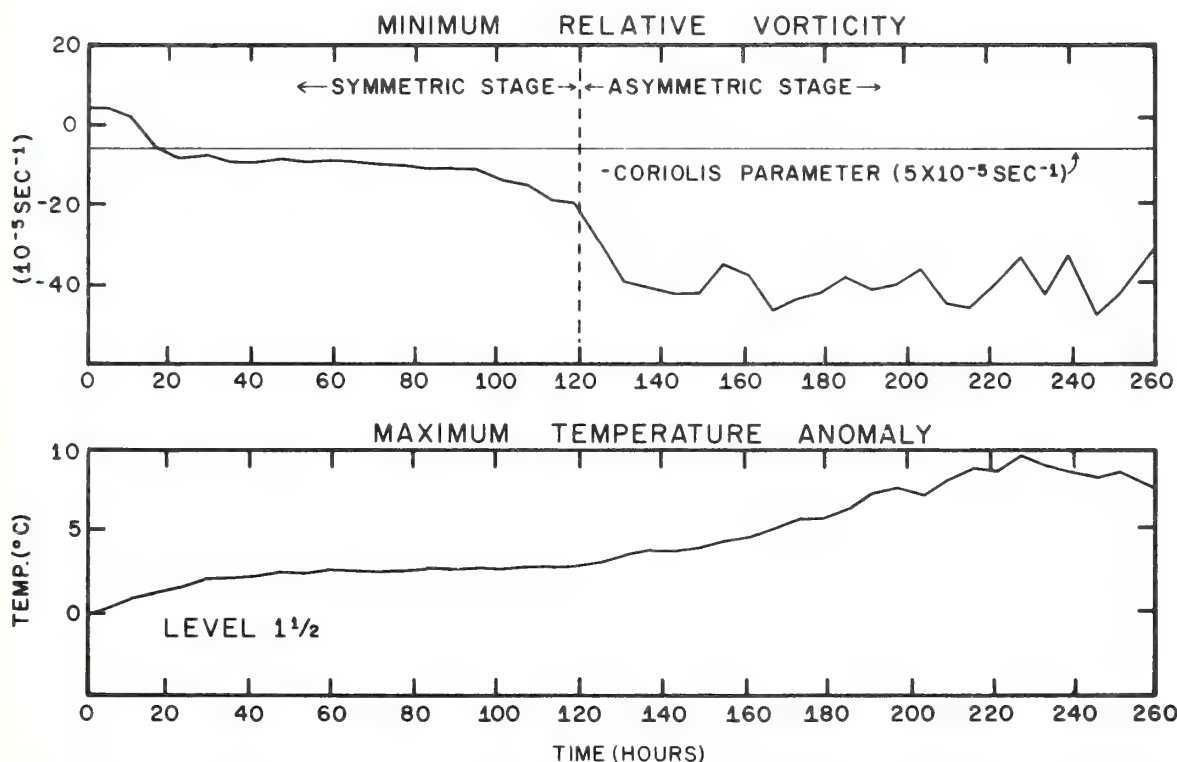


Figure D-4. (a) Time variation of the minimum relative vorticity in upper troposphere (level $1\frac{1}{2}$); (b) Time variation of the maximum temperature anomaly (departure of temperature from the steady-state value at the lateral boundary) in the upper troposphere (level $1\frac{1}{2}$).

upper tropospheric outflow show any preference for particular quadrants. We refer to this interval as the "early symmetric stage." After 120 hours, the upper outflow is quite asymmetric while the rainfall and vertical motions show distinct patterns analogous to the spiral rainbands found in real storms. We refer to this period as the "asymmetric stage." The "symmetric" and "asymmetric" stages refer to the model calculation only, and, because of the arbitrary nature of the initial conditions, are not meant to have direct counterparts in natural storms.

EARLY, SYMMETRIC STAGE OF THE MODEL STORM

A representative view of the structure during this period is provided by the data at 84 hours. The region of hurricane force winds is very small, extending only about 75 km from the center. Gale force winds extend outward to 150 km. The maximum tangential and radial winds are 34.0 m sec^{-1} and -19.4 m sec^{-1} , respectively, yielding an inflow angle of about 29 degrees.

The circulation in the upper troposphere (level $1\frac{1}{2}$) shows a fairly symmetric outflow pattern. Cyclonic outflow occurs inside a radius of about 200 km. Beyond 200 km, the circulation is anticyclonic, reaching a maximum velocity of about 6 m sec^{-1} around the outer boundary. The figures are shown in I.

Dynamic (or inertial) instability of the upper tropospheric outflow has been suggested by Alaka (1961, 1962, 1963) and others as a contributory factor in the intensification of tropical cyclones. An approximate necessary condition for this instability is given by

$$\zeta_a \left(\frac{2|\vec{V}|}{R} + f \right) < 0 \quad (\text{D.7})$$

where $|\vec{V}|$ is the wind speed, R is the radius of curvature of the streamlines, and ζ_a is the absolute vorticity.

Strictly speaking, this criterion for instability refers to horizontal parcel displacements normal to a streamline and is derived under the assumption that the velocity and pressure fields are invariant along the streamline. A

necessary criterion for a closely related instability is

$$\left(\frac{\partial v_{\lambda}}{\partial r} + \frac{v_{\lambda}}{r} + f \right) \left(\frac{2v_{\lambda}}{r} + f \right) < 0 . \quad (D.8)$$

The criterion (D.8) relates to the instability of horizontal symmetric fluid ring displacement in a symmetric vortex.

A third type of dynamic instability is governed by the necessary condition that the radial gradient of the absolute vorticity of the tangential flow have at least one zero. That is, the condition

$$\frac{\partial}{\partial r} \left\{ \frac{\partial v_{\lambda}}{\partial r} + \frac{v_{\lambda}}{r} + f \right\} = 0 , \quad (D.9)$$

is satisfied somewhere in the fluid system. This is a necessary condition for asymmetric (azimuthally varying) horizontal perturbations to be unstable.

At the initial instant, when the flow is nearly symmetric and tangential, (D.7) and (D.8) become equivalent. Since the initial data satisfy neither condition, these instabilities do not contribute to the very early intensification. On the other hand, (D.9) is satisfied even in the initial data since there is a maximum of cyclonic vorticity close to the center of the storm and a vorticity minimum (maximum of anticyclonic relative vorticity) at a radius of approximately 345 km. This should favor the growth of wave-like perturbations in the azimuthal direction. Since weak waves of this type are present in the initial data due to round-off differences, and since, as already noted, substantial symmetry is retained for the first 120 hours, it is clear that the instability is either quite weak or that it is being counteracted by other effects such as those due to eddy viscosity.

Figure D-4 shows the time evolution of the minimum value of relative vorticity in the upper level within 350 km of the storm center. During the initial deepening stage the minimum value of absolute vorticity becomes slightly negative. However, this occurs after the intensification and only over a small region.

The term $(2|\vec{V}|/R + f)$ was also evaluated for several times during the first 120 hours. These calculations revealed only small patches of anomalous winds. We, therefore, also feel that the instabilities represented by (D.7) and (D.8) played no significant role in the early symmetric stage of the model storm.

Azimuthally averaged vertical cross sections provide an adequate description of the storm structure during the early symmetric stage. Mean cross sections² for the tangential wind, radial wind, and the temperature departure at 84 hours are shown by figure D-5. These cross sections reveal a structure very typical of that of a weak hurricane (Hawkins and Rubsam, 1968).

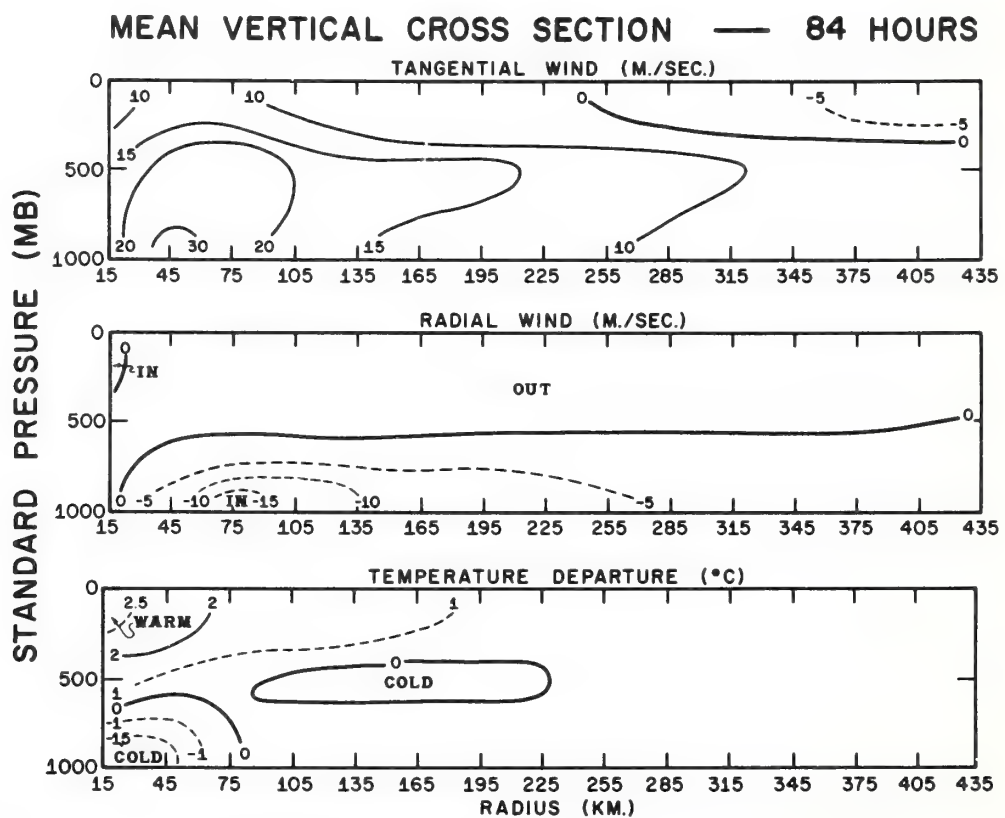


Figure D-5. Azimuthal mean vertical cross sections for the tangential wind, the radial wind, and the temperature anomaly at 84 hours. Isotherms are labeled in °C; isotachs are labeled in $m\ sec^{-1}$.

² The circular averages were computed through linear interpolation of gridpoint values to a polar grid with a radial increment of 30 km and an angular increment of 22.5 degrees.

The vertical motion at the top of the boundary layer at 84 hours shows a nearly circular region of upward motion that extends from the center to about 180 km. Maximum velocities of about $-140 \text{ mb hour}^{-1}$ (about 0.4 m sec^{-1}) occur in a ring near the center. Weak subsidence occurs in the environment beyond 180 km. The strongest upward velocities occur in the middle troposphere (level 5/2) and reach $-230 \text{ mb hour}^{-1}$ (about 0.7 m sec^{-1}). These values appear reasonable for averages over a 30 km interval of a weak hurricane (Carlson and Sheets, 1971).

The average rainfall over the inner 100 km, computed by conversion of the total release of latent heat in a column to the equivalent water depth, is 65 cm day^{-1} which is comparable with the estimates made by Riehl and Malkus (1961) for Hurricane Daisy (1958). The total release of latent heat at this time is $5.0 \times 10^{14} \text{ W}$. This also compares favorably with empirical estimates (Anthes and Johnson, 1968). Finally, the rainfall pattern at 84 hours shows no evidence of spiral bands.

Figure D-6 shows surface pressure profiles for various times along one radius from the center of the grid. Since the surface isobars are very nearly circular, these profiles provide an adequate description of the surface pressure field. The minimum value at 84 hours (995 mb) is quite realistic for a maximum wind of 32 m sec^{-1} (Colón, 1963). The general shapes of the profiles agree well with observations (Fletcher, 1955; Miller, 1963).

The early symmetric period may be summarized as follows. After a short period of development (about 24 hours), a quasi-steady state is reached in which the model storm closely resembles a weak hurricane. The circulation is nearly axisymmetric. Air spirals inward in the low levels, ascends in a narrow ring, and flows outward in the upper levels. The outflow becomes anticyclonic beyond 200 km. However, the absolute vorticity in the outflow layer is positive except in small areas. The central pressure, temperature anomalies, rainfall rates, and the components of the kinetic energy budget are all reasonable for a weak hurricane.

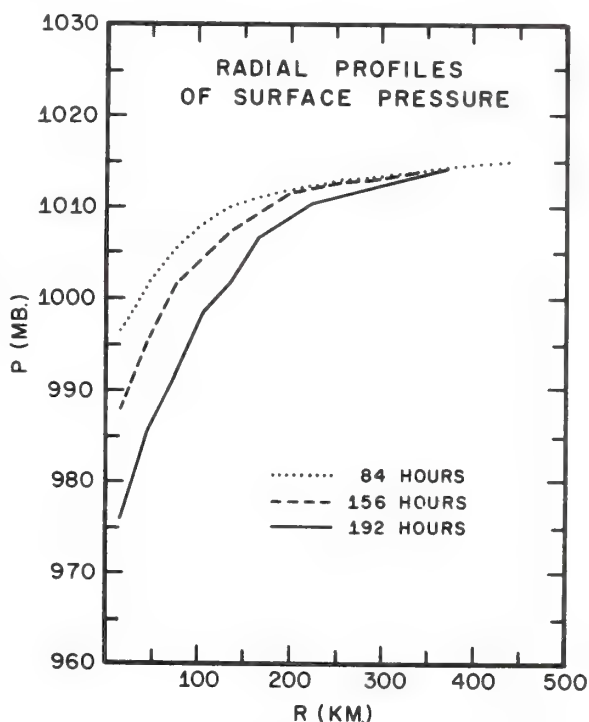


Figure D-6. Radial profiles of surface pressure along an east-west axis at 84, 156, and 192 hours.

ASYMMETRIC STAGE OF THE MODEL

As shown by the central pressure, maximum wind speed, and maximum temperature anomaly (figs. D-3 and D-4), the storm begins a second period of intensification at about 120 hours. The low-level inflow at 156 hours is still fairly symmetric, but shows an increased intensity over that at 84 hours. The maximum wind speed is now 46 m sec^{-1} , hurricane force winds extend outward to 80 km, and gale force winds to 210 km. The average angle of inflow has increased to 38 degrees.

In contrast to the symmetric inflow, the outflow occurs in a highly asymmetric fashion (figs. D-7 and D-8). Outflow occurs in two quadrants, and several small eddies are located about the main center. This asymmetric nature of the outflow is typical of many hurricanes (e.g., Alaka, 1961, 1962; Miller, 1963).

The vorticity at level 3/2 shows large regions of negative absolute vorticity, with minimum values about $-30 \times 10^{-5} \text{ sec}^{-1}$. This is in contrast with the vorticity pattern at 84 hours. These regions are transient. They form and reform in various sectors of the outflow level. This unsteady behavior of the outflow is probably related closely to the oscillations in the central pressure and maximum surface wind during the latter portions of the computation (fig. D-2). It is noted that negative absolute vorticity is an observed feature of hurricane outflow (Alaka, 1962) and even appears as a feature of composite mean storms (Izawa, 1964).

The presence of large values of negative absolute vorticity suggests the presence of one or more of the types of dynamic instability discussed in the previous subsection. Since the condition (D.8) refers to symmetric instability and since (D.9) is satisfied in the initial data without noticeable effect, attention was focused on the condition (D.7). The quantity, $2|\vec{V}|/R$, was computed for level 3/2 at 156 hours. In contrast to the early stages, anomalous winds are found to cover substantial areas of the domain and negative values of $2|\vec{V}|/R$ exceed $40 \times 10^{-5} \text{ sec}^{-1}$. The presence of anomalous winds in hurricane outflow has been documented by Alaka (1961).

The role of dynamic instability in the development of tropical cyclones has been subjected to prolonged debate and will not be discussed in detail here. We merely note that the second period of intensification in this model calculation appears to be related to the development of areas of dynamic instability. If we refer to figure D-9, we note that the minimum vorticity in the outflow layer shows a sudden decrease at about 100 hours. The second period of deepening (as measured by central pressure and maximum winds) *follows* this decrease in absolute vorticity by about 20 hours.

STREAMLINES

LEVEL $1\frac{1}{2}$

156 HOURS

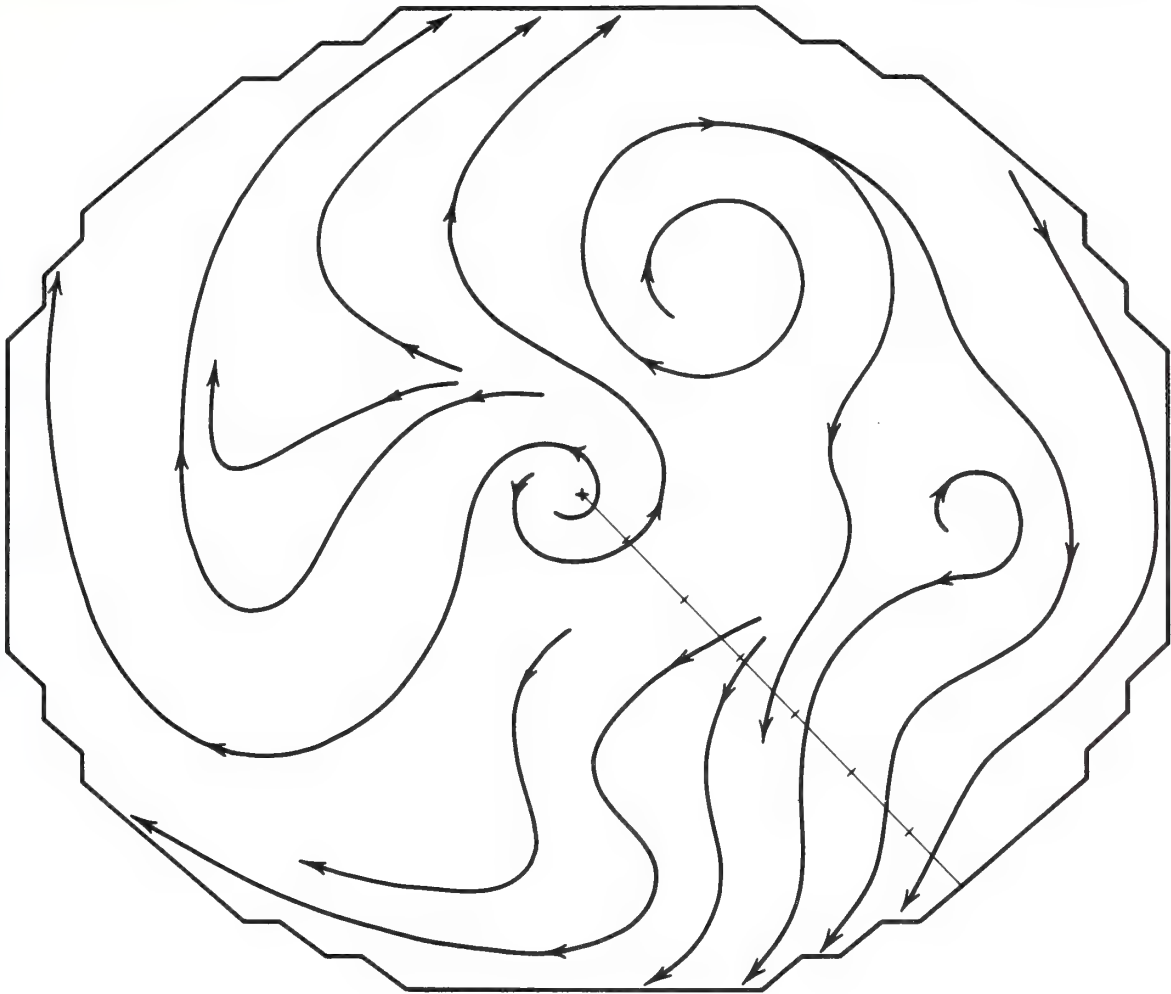


Figure D-7. Streamline analysis for the upper troposphere (level $1\frac{1}{2}$) at 156 hours.

Coincident with the formation of asymmetries in the outflow is the appearance of spiral bands of rising motion which closely resemble hurricane rainbands. The vertical motion pattern at level $3\frac{1}{2}$ (fig. D-9) shows two bands of upward motion which begin at the edge of the domain and spiral inward toward the primary ring of upward motion near the center. The maximum vertical velocity near the center is $-440 \text{ mb hour}^{-1}$ (about 1.5 m sec^{-1}).

The precipitation pattern, shown in figure D-10, resembles a radar picture of a mature hurricane (e.g., Colón, 1962; Coló et al., 1961). Strong convection occurs near the center in an irregular circle corresponding to an "eyewall."

ISOTACHS (M/SEC.)

LEVEL $1\frac{1}{2}$

156 HOURS

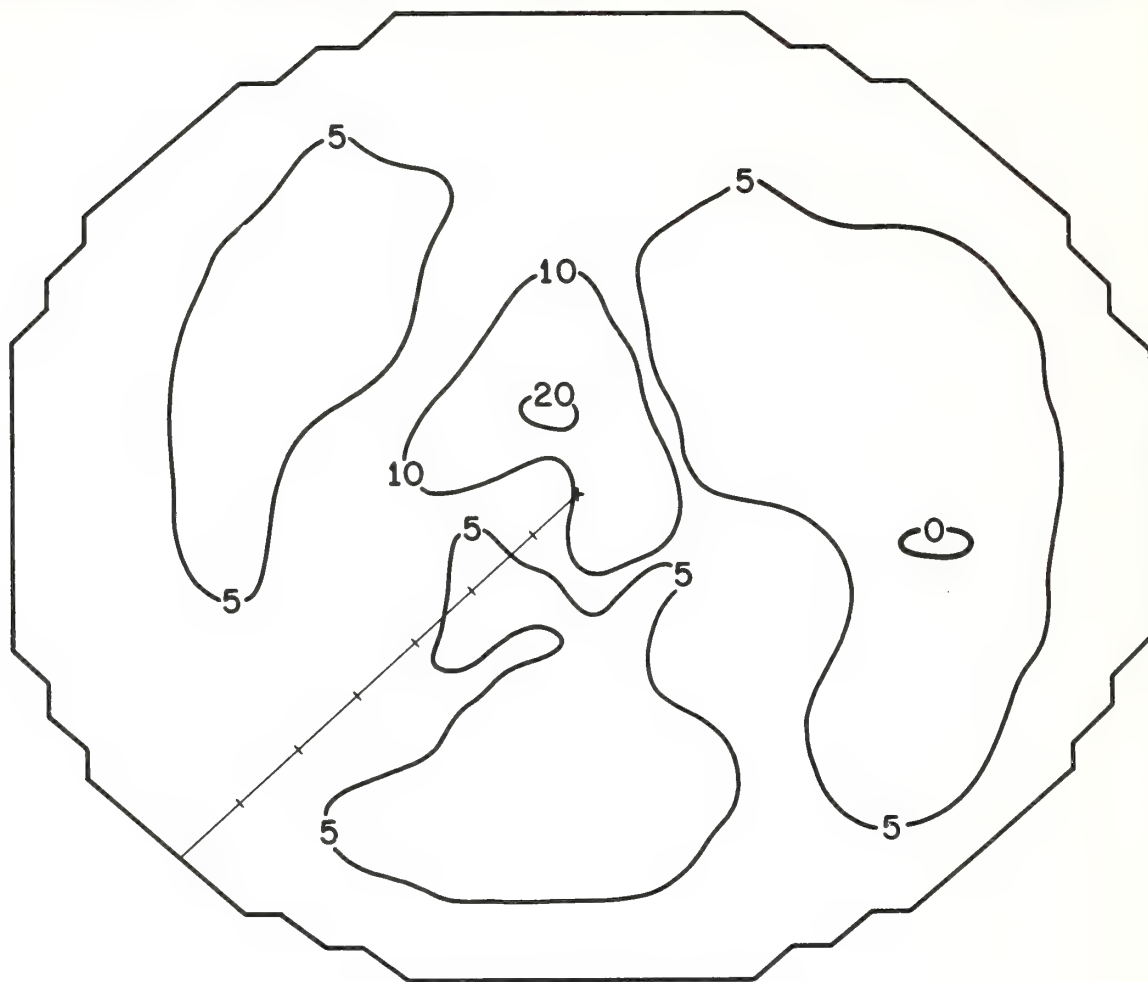


Figure D-8. Isotach analysis for the upper troposphere (level $1\frac{1}{2}$) at 156 hours. Isopheths are labeled in $m\ sec^{-1}$.

Maximum rainfall rates in this region are over $100\ cm\ day^{-1}$. Two bands of weaker convection spiral in toward the center. The rainfall rates in the spiral bands are much less than those near the center of the storm, averaging only about $3\ cm\ day^{-1}$.

The fact that the spiral bands do not appear in the model calculation until the symmetry of the outflow pattern has been destroyed suggests that the generation of the bands and the breakdown of the outflow pattern may be related. As we have noted above, the loss of symmetry in the outflow appears to be associated with dynamic instability. It should

OMEGA (ω)(CB./HOUR)LEVEL $3\frac{1}{2}$

156 HOURS

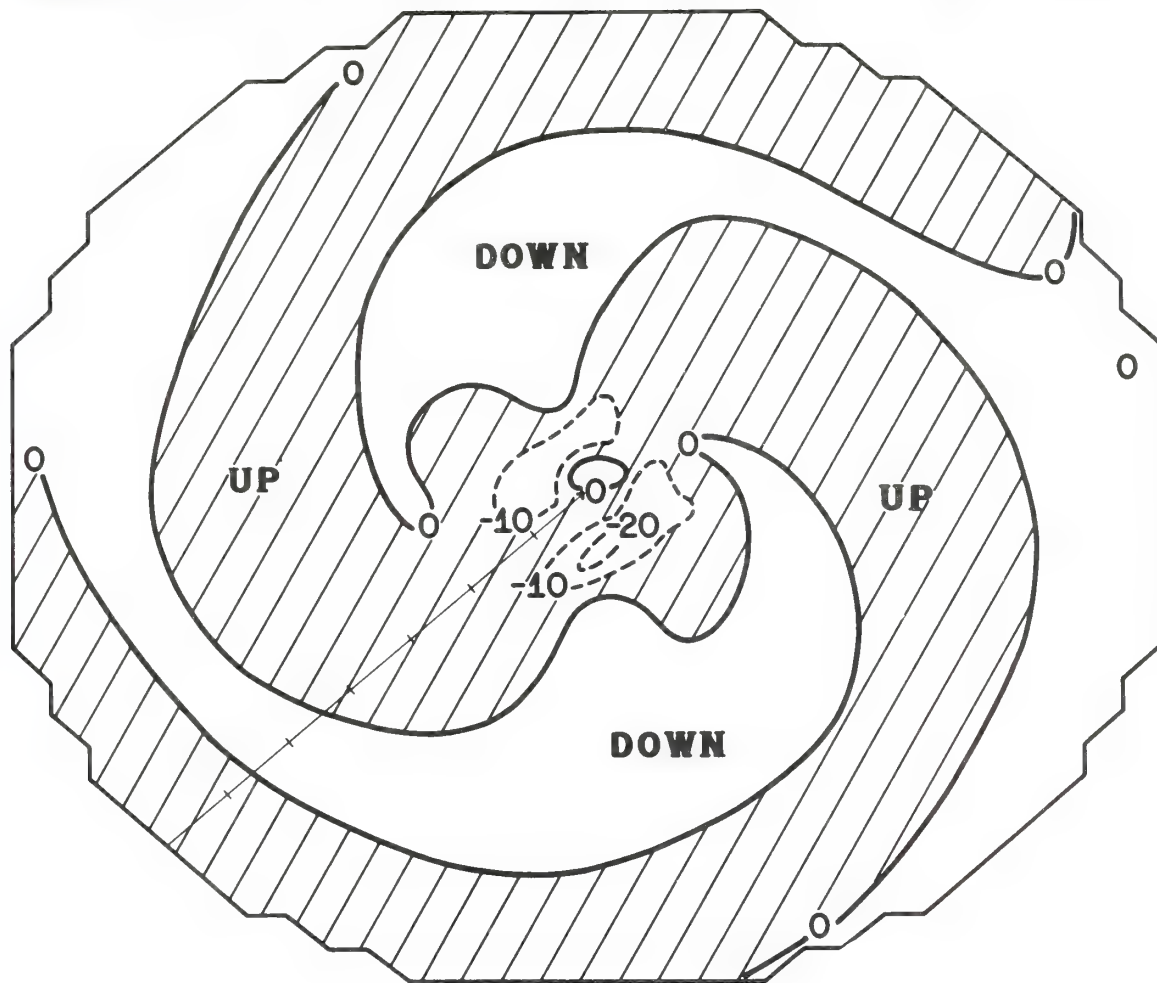


Figure D-9. Individual rate of change of pressure ($\omega = dp/dt$) for level $3\frac{1}{2}$ at 156 hours. Isophleths are labeled in units of $cb\ hour^{-1}$.

be emphasized, however, that this linkage is merely speculation at this time and will be pursued further when we have had the opportunity to perform experiments with greater horizontal resolution.

In a recent paper, Anthes (1970) hypothesized that large scale asymmetries between radii of 400 and 1000 km from the hurricane center may play an important role in satisfying the angular momentum budget of the mature hurricane. The mean radial flux of vorticity may be written

$$A \equiv \overline{v_r} \frac{\lambda}{\zeta_a} + \overline{v_r} \frac{\lambda}{\zeta_a} \quad (D.10)$$

RAINFALL RATES

(CM./DAY)

156 HOURS

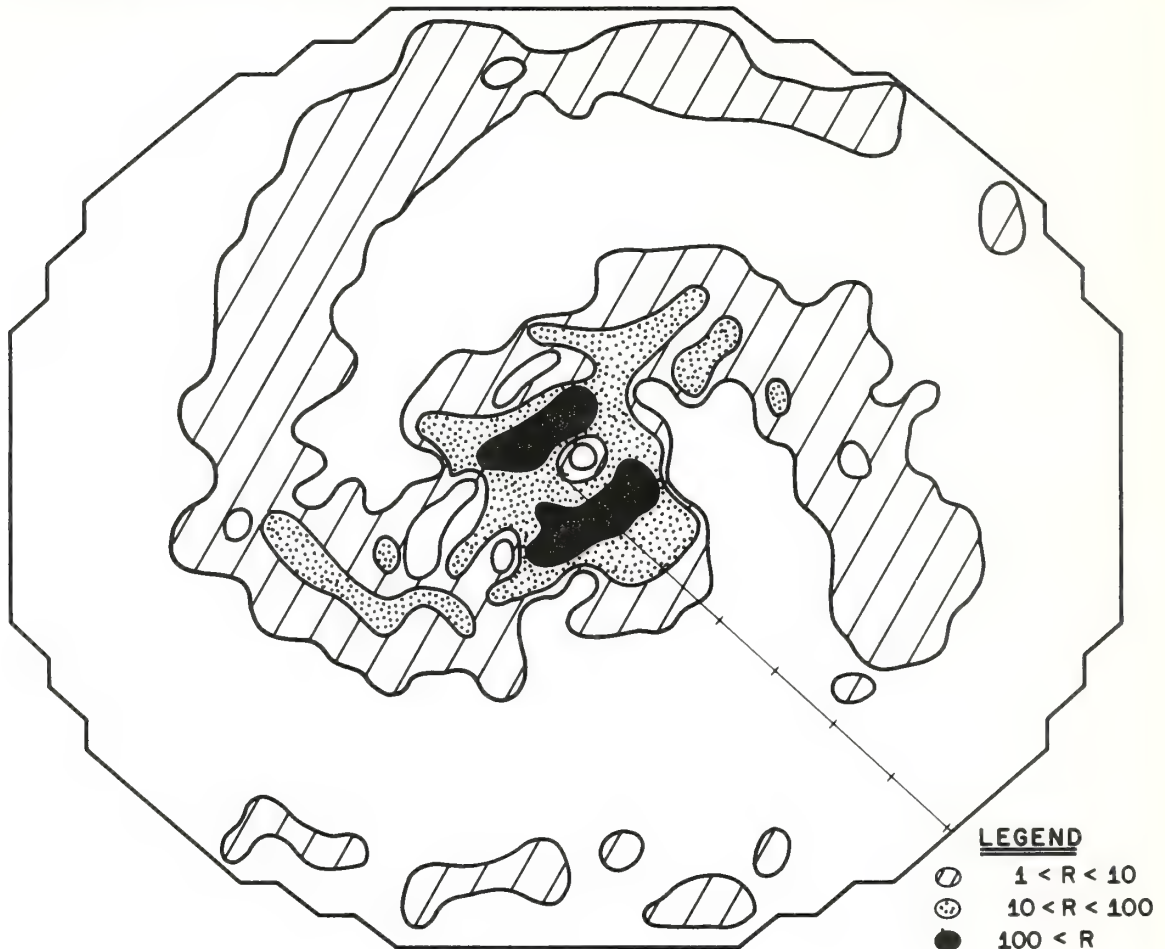


Figure D-10. Rainfall rates (cm day^{-1}) computed from the total release of latent heat at 156 hours. Isopheths are labeled in units of cm day^{-1} .

where the $(\overline{\quad})^\lambda$ operator refers to the azimuthal mean at a given radius and $(\quad)'$ refers to departures from this mean. Figure D-11 shows the radial profiles of $\overline{v_r' \zeta_a'}^\lambda$ and $\overline{v_r^\lambda \zeta_a^\lambda}$ computed for the model storm at 192 hours. Both mean and eddy transports of vorticity are positive inside 200 km. Beyond 200 km, however, where the vertical motion is small, there is a negative correlation between outflow and absolute vorticity, and the eddy flux very nearly balances the mean flux from there to the limit of the domain.

Although the maximum value of $\overline{v_r' \zeta_a'}^\lambda$ in figure D-11 is $-70 \times 10^{-4} \text{ cm sec}^{-2}$, which is about half the maximum value found by Anthes (1970), the qualitative agreement is good.

Figure D-12 shows the azimuthally averaged vertical cross sections at 156 hours. The mean tangential and radial circulations are more intense than at 84 hours (see fig. D-5). The temperature section shows an increase in mean temperature anomaly from 2.5 to 4.1°C and a reduction in the low-level cold core maximum from -1.5°C to -1.0°C . The weak middle-level cold region located between 105 and 225 km at 84 hours has disappeared by 156 hours.

In summary, beginning at about 100 hours, substantial areas of negative absolute vorticity appear in the upper level and the outflow pattern becomes asymmetric. Rainbands appear during this asymmetric stage. The storm is considerably less steady than during the earlier, symmetric stage, and the central pressure and maximum winds oscillate with a period of about 6 hours. This unsteady behavior appears to be related to the transient behavior of the regions of negative vorticity in the outflow layer.

From the time of appearance of the asymmetries at 120 hours, more or less continuous deepening occurs until the storm reaches a maximum intensity at about 230 hours (see fig. D-3). At this time the storm corresponds to a strong hurricane, with a central pressure of 963 mb and a maximum wind speed of 65 m sec^{-1} . The lapse rate in the inner region is very nearly pseudoadiabatic at this time. After 230 hours, the storm begins to slowly fill and the calculation is terminated at 260 hours.

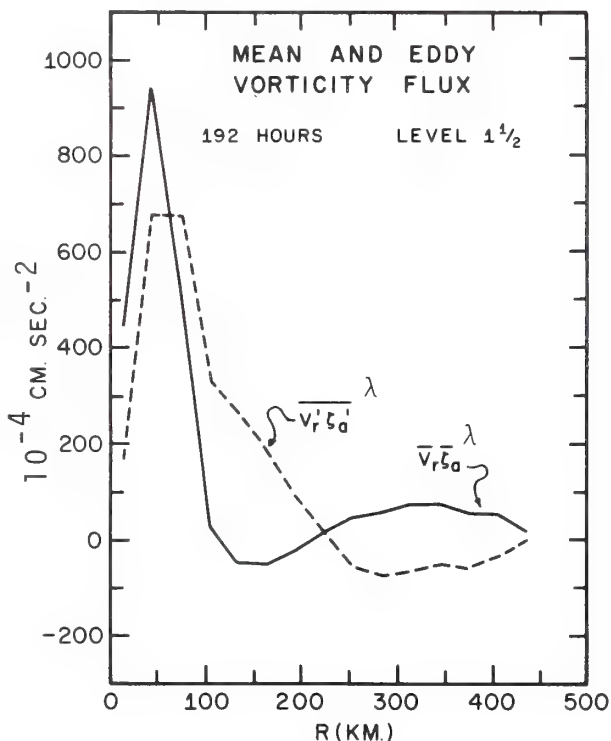


Figure D-11. Azimuthal mean $(\overline{v_r' \zeta_a'})^\lambda$ and eddy $(\overline{v_r' \zeta_a'})^\lambda$ horizontal vorticity flux in the upper troposphere (level $1\frac{1}{2}$) at 192 hours.

MEAN VERTICAL CROSS SECTION — 156 HOURS

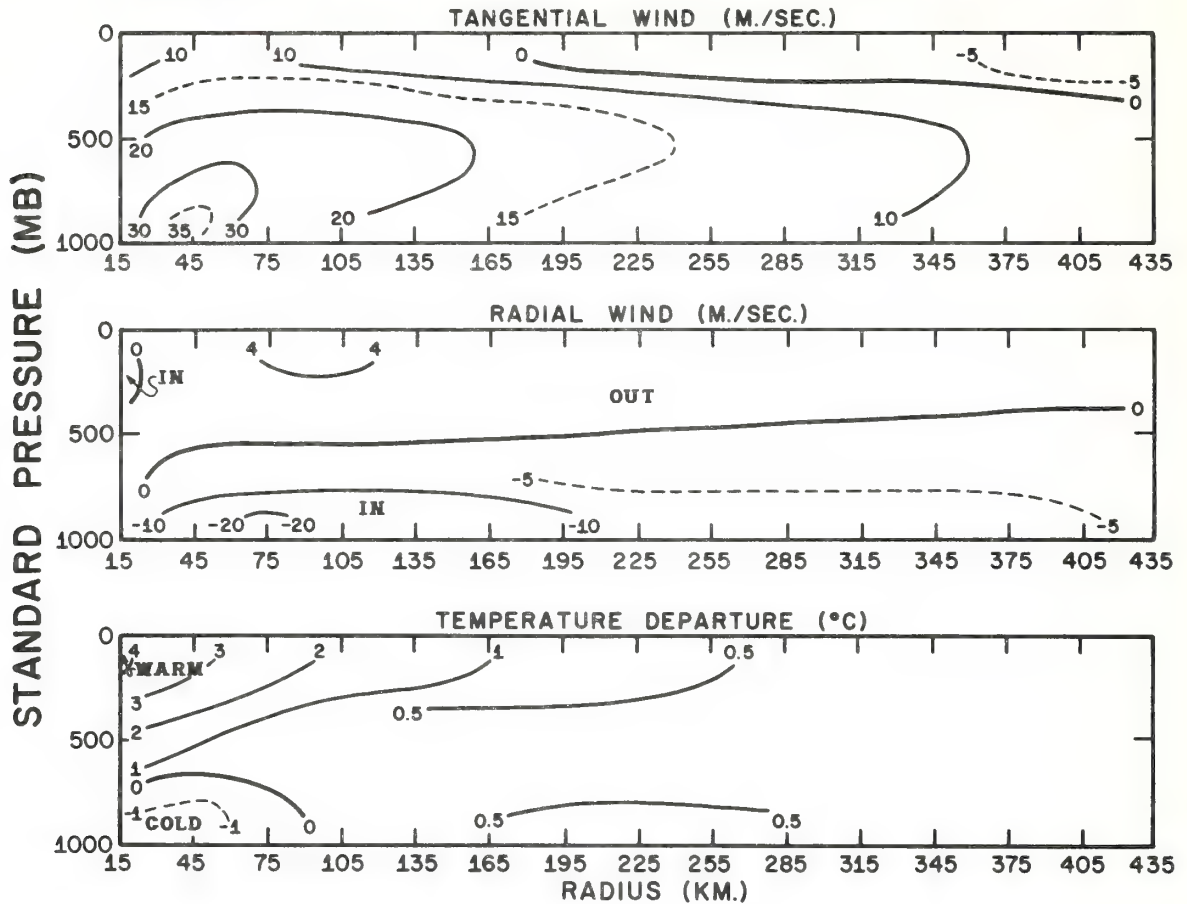


Figure D-12. Azimuthal mean-vertical cross sections for the tangential wind, the radial wind, and the temperature anomaly at 156 hours. Isotherms are labeled in °C. Isotachs are labeled in m sec^{-1} .

SUMMARY AND CONCLUSIONS

Preliminary results show that the model is capable of reproducing many observed features of the three-dimensional tropical cyclone. Rather realistic simulations of spiral rainbands and the strongly asymmetric structure of the outflow are obtained.

Despite a relatively coarse horizontal resolution of 30 km, the model produces a storm with maximum winds exceeding 65 m sec^{-1} and a kinetic energy budget which compares favorably with empirical estimates.

In the mature, asymmetric stage of the storm, substantial regions of negative absolute vorticity, anomalous winds, and dynamic instability are present in the upper troposphere. There is a suggestion that the breakdown of the early symmetry of the flow as well as the deepening which takes place during the asymmetric stage are related to the dynamic instability. Large scale, horizontal asymmetries in the outflow are found to play a significant role in the transport of vorticity during the mature stage. Beyond 200 km, the eddy transport of vorticity is opposite in sign and nearly equal in magnitude to the mean transport.

REFERENCES

- Alaka, M. A. (1961): The occurrence of anomalous winds and their significance. *National Hurricane Research Project Report No. 45*, U.S. Weather Bureau, Washington, D.C., June, 25 pp.
- Alaka, M. A. (1962): On the occurrence of dynamic instability in incipient and developing hurricanes. *National Hurricane Research Project Report No. 50*, U.S. Weather Bureau, Washington, D.C., March, pp. 51-56.
- Alaka, M. A. (1963): Instability aspects of hurricane genesis. *National Hurricane Research Project Report No. 64*, U.S. Weather Bureau, Washington, D.C., June, 23 pp.
- Anthes, R. A., and D. R. Johnson (1968): Generation of available potential energy in Hurricane Hilda (1964). *Monthly Weather Review*, 96, (5) May, pp. 291-302.
- Anthes, R. A. (1970): The role of large-scale asymmetries and internal mixing in computing meridional circulations associated with steady-state hurricanes. *Monthly Weather Review*, 98, (7) July, pp. 521-529.
- Anthes, R. A., S. L. Rosenthal, and J. W. Trout (1971): Preliminary results from an asymmetric model of the tropical cyclone. Accepted for publication in the *Monthly Weather Review*.
- Anthes, R. A., J. W. Trout, and S. L. Rosenthal (1971): Comparisons of tropical cyclone simulations with and without the assumption of circular symmetry. Accepted for publication in the *Monthly Weather Review*.

- Carlson, T. C., and R. C. Sheets (1971): Comparison of draft scale vertical velocities computed from gust probe and conventional data collected by a DC-6 aircraft. Technical Memorandum ERLTM-NHRL No. 91, NOAA, U.S. Dept. of Commerce, Miami, Fla.
- Charney, J. G., and A. Eliassen (1964): On the growth of the hurricane depression. *Journal of the Atmospheric Sciences*, 21, (1), January, pp. 68-75.
- Colón, J. A., and Staff NHRL (1961): On the structure of Hurricane Daisy, 1958. *National Hurricane Research Project Report No. 46*, U.S. Weather Bureau, Washington, D.C., October, 102 pp.
- Colón, J. A. (1962): Changes in the eye properties during the life cycle of tropical hurricanes. *National Hurricane Research Project Report No. 50*, U.S. Weather Bureau, Washington, D.C., March, pp. 341-354.
- Colón, J. A. (1963): On the evolution of the wind field during the life cycle of tropical cyclones. *National Hurricane Research Project Report No. 65*, U.S. Weather Bureau, Washington, D.C., November, 36 pp.
- Fletcher, R. D. (1955): Computation of maximum surface winds in hurricanes. *Bulletin of the American Meteorological Society*, 36, (6), June, pp. 247-250.
- Grammeltdedt, A. (1969): A survey of finite-difference schemes for the primitive equations. *Monthly Weather Review*, 97, (5), May, pp. 384-404.
- Gray, W. M. (1967): The mutual variation of wind, shear, and baroclinicity in the cumulus convective atmosphere of the hurricane. *Monthly Weather Review*, 95, (5), February, pp. 55-73.
- Hawkins, H. F., and D. T. Rubsam (1968): Hurricane Hilda, 1963 II: Structure and budgets of the hurricane on October 1, 1964. *Monthly Weather Review*, 96, (9), September, pp. 617-636.
- Izawa, T. (1964): On the mean wind structure of typhoon. *Technical Note No. 2*, Typhoon Research Laboratory, Meteorological Research Institute, Tokyo, Japan, March, 19 pp.

- Kuo, H. L. (1965): On formation and intensification of tropical cyclones through latent heat release of cumulus convection. *Journal of the Atmospheric Sciences*, 22, (1), January, pp. 40-63.
- Kurihara, Y., and J. L. Holloway (1967): Numerical integration of a nine-level global primitive equation model formulated by the box method. *Monthly Weather Review*, 95, (8), August, pp. 509-530.
- Matsuno, T. (1966): Numerical integrations of the primitive equations by a simulated backward difference method. *Journal of the Meteorological Society of Japan*, 44, (1), February, pp. 76-83.
- Miller, B. I. (1962): On the momentum and energy balance of Hurricane Helene (1958). *National Hurricane Research Project Report No. 53*, U.S. Weather Bureau, Washington, D.C., April, 19 pp.
- Miller, B. I. (1963): On the filling of tropical cyclones over land. *National Hurricane Research Project Report No. 66*, U.S. Weather Bureau, Washington, D.C., December, 82 pp.
- Molenkamp, C. R. (1968): Accuracy of finite difference methods applied to the advection equation. *Journal of Applied Meteorology*, 7, (2), April, pp. 160-167.
- Ogura, Y. (1964): Frictionally controlled, thermally driven circulations in a circular vortex with application to tropical cyclones. *Journal of the Atmospheric Sciences*, 21, (6), November, pp. 610-621.
- Ooyama, K. (1969): Numerical simulation of the life cycle of tropical cyclones. *Journal of the Atmospheric Sciences*, 26, (1), January, pp. 3-40.
- Palmén, E., and H. Riehl (1957): Budget of angular momentum and kinetic energy in tropical cyclones. *Journal of Meteorology*, 14, (2), March, pp. 150-159.
- Phillips, N. A. (1957): A coordinate system having some special advantages for numerical forecasting. *Journal of Meteorology*, 14, (2), April, pp. 184-185.
- Richtmyer, R. D., and K. W. Morton (1967): Difference methods for initial-value problems. Second edition, *Interscience*, New York, 405 pp.

- Riehl, H., and J. S. Malkus (1961): Some aspects of Hurricane Daisy, 1958. *Tellus*, 13, (2), May, pp. 181-213.
- Rosenthal, S. L. (1969): Numerical experiments with a multi-level primitive equation model designed to simulate the development of tropical cyclones: Experiment I. Technical Memorandum ERLTM-NHRL No. 82, ESSA, U.S. Dept. of Commerce, Miami, Fla., January, 33 pp.
- Rosenthal, S. L. (1970): A circularly symmetric, primitive equation model of tropical cyclone development containing an explicit water vapor cycle. *Monthly Weather Review*, 98, (9), September, pp. 643-663.
- Smagorinsky, J., S. Manabe, and J. L. Holloway, Jr. (1965): Numerical results from a nine-level general circulation model of the atmosphere. *Monthly Weather Review*, 93, (12), December, pp. 727-768.
- Syōno, S., and M. Yamasaki (1966): Stability of symmetrical motions driven by latent heat release by cumulus convection under the existence of surface friction. *Journal of the Meteorological Society of Japan*, Ser. 2, 44, (6), December, pp. 353-375.
- Yamasaki, M. (1968a): A tropical cyclone model with parameterized vertical partition of released latent heat. *Journal of the Meteorological Society of Japan*, 46, (3), June, pp. 202-214.
- Yamasaki, M. (1968b): Detailed analysis of a tropical cyclone simulated with a 13-layer model. *Papers in Meteorology and Geophysics*, 19, (4), December, pp. 559-585.

APPENDIX E

RESPONSE OF STORMFURY CLOUDLINE CUMULI TO AgI AND AgI·NaI ICE NUCLEI FROM A SOLUTION-COMBUSTION GENERATOR

Edward E. Hindman, II
Navy Weather Research Facility

Shelden D. Elliott, Jr., and William G. Finnegan
Naval Weapons Center

and

Bradley T. Patton
Research Flight Facility

INTRODUCTION

The existing basis for reducing destructive hurricane winds has been the seeding of eyewall cumulus clouds with silver iodide ice nuclei (Simpson and Malkus, 1964; Gentry, 1970). Recent investigations (Woodley, 1970; Gentry, 1971) suggest that less fully developed cumuli at slightly greater distances outward from the present eyewall seeding location may be more responsive to seeding than eyewall cumulus clouds. The responses of such cumuli to silver iodide seedings were studied during the 1970 STORMFURY cloudline operation.

In addition, at the suggestion of Naval Weapons Center, China Lake, California, a special experiment to compare the effectiveness of two different silver iodide solutions was conducted during the 1970 STORMFURY cloudline operation. Silver iodide-sodium iodide-acetone and silver iodide-ammonium iodide-acetone solutions were burned in the solution-combustion generator designed by Patton (1970). Vonnegut (1949, 1950) discovered that combustion products from both solutions were effective ice nuclei. Recent evidence (Finnegan et al., 1971) suggests that the sodium solution produces *complexed* nuclei (AgI·NaI), and the ammonium solution produces *uncomplexed* nuclei (AgI). Laboratory and field evidence (Donnan et al., 1970; Auer and Veal, 1970) have shown that this difference in nucleus structure affects the nucleus activation; the AgI nuclei become active at -5°C and the AgI·NaI nuclei become active at -10°C when both nuclei are released in the warmer-than-freezing regions of cumulus clouds. Furthermore, when both nuclei are released in clouds at -5°C the AgI nuclei are the more active.

PROCEDURE

A NOAA-Research Flight Facility (RFF) DC-6 aircraft was utilized for both seeding the cloudline cumuli and monitoring the effects of seeding. The NOAA-RFF solution-combustion generator (Patton, 1970) was used to produce the ice nuclei (see fig. E-1). The nuclei delivery rate was nearly equivalent to the rate ($\sim 1 \text{ g sec}^{-1}$) of the WMU-2 pyrotechnic flares presently used in hurricane seedings.

The cloud response to the nuclei was indicated by simultaneous in-cloud measurements of vertical motions and liquid-water contents (LWC) and ice-water contents (IWC). NOAA-National Hurricane Research Laboratory (NHRL) derived the vertical-motion values from the DC-6 aircraft pitch-angle and

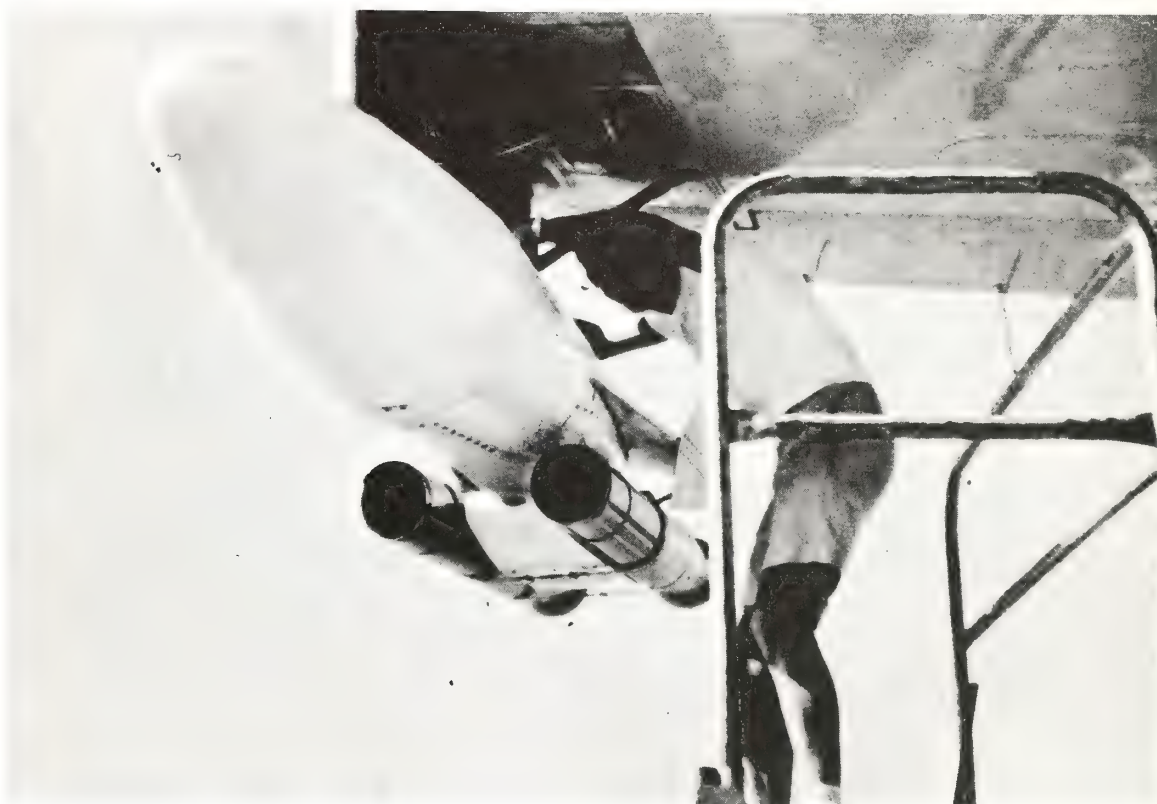


Figure E-1. The NOAA-Research Flight Facility solution-combustion ice nuclei generator is pictured mounted on the NOAA-RFF DC-6 (N8539C). The seeding solution is contained in the tank and the solution is burned in the two cylindrical chambers. The resulting ice nuclei exhaust from the rear of the chambers.

radio-altimeter data (Carlson and Sheets, 1971). The LWC and IWC of the precipitation size particles ($\text{dia} \geq 200 \mu\text{m}$) were determined by Navy Weather Research Facility (WEARSCHFAC) from NOAA-NHRL foil impactor data (Hindman, 1970)(see fig. E-2). The water contents of the cloud size particles ($\text{dia} < 200 \mu\text{m}$) can be reduced from simultaneously gathered formvar replicator data in a manner similar to the analysis of foil impactor data and will be accomplished at a later data. Results will be described in a subsequent report. These results should provide an important follow-on to previous studies of IWC increases in cumulus clouds that were attributed to seeding (Todd, 1965; Sax, 1969; and Weinstein and Takeuchi, 1970).



Figure E-2. The Meteorology Research, Inc., foil impactor is pictured mounted on the NOAA-RFF DC-6(N8539C). The particle impressions from this impactor are analyzed by Navy Weather Research Facility to produce liquid-water and ice-water contents and liquid and ice particle size-distribution.

The water-content values were computed from particle size-distributions which were reduced from foil impactor data using a CALMA 302 digitizer, a UNIVAC 1107 computer, and a Calcomp plotter. The digitizer was used to code particle sizes and type onto magnetic tapes which were processed on the computer. The resulting water-contents and size-distributions were displayed by means of the plotter. The vertical-motion values were retrieved from data cards provided by NOAA-NHRL.

The procedure of seeding and monitoring 1970 STORMFURY cloudline cumuli is illustrated in figure E-3. Seeding was conducted at $+5^{\circ}\text{C}$ in the Cloud I experiment and monitoring penetrations were made at 0°C and -5°C , 14 and 27 minutes after seeding, respectively. Immediately following the -5°C monitoring penetration in Cloud I, seeding was conducted on the first -5°C penetration of the Cloud II experiment. Subsequently, two monitoring penetrations were made through Cloud II, both at -5°C at intervals of 15 and 30 minutes after seeding, respectively.

The AgI nuclei were tested on 29 and 30 July, and the AgI-NaI nuclei were tested on 31 July. The procedure outlined in figure E-3 was followed on all 3 days. The flight path in the Cloud I experiment tested the effectiveness of both nuclei when released in the warmer-than-freezing cloud region. The flight path in the Cloud II experiment tested both nuclei when released in the subcooled region of the clouds.

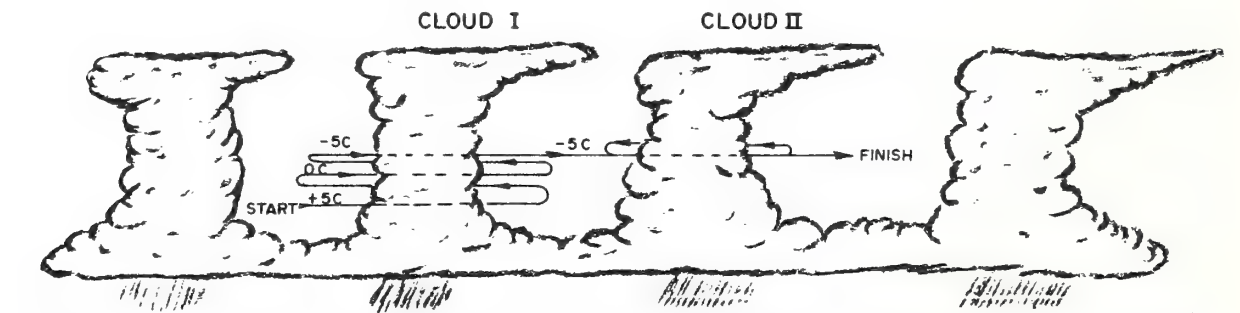


Figure E-3. Procedure for seeding and monitoring STORMFURY cloudline cumuli, 29, 30, 31 July 1970. Seeding was done at $+5^{\circ}\text{C}$ in Cloud I and monitoring passes were made at 0°C and -5°C . Seeding was done on the first pass at -5°C in Cloud II. Two counter-clockwise monitoring passes then were made at -5°C in Cloud II. Cloud I tested warm-cloud release of ice nuclei and Cloud II tested cold-cloud release of ice nuclei.

RESULTS

An example of the average liquid and ice particle size-distributions computed from the foil impactor data gathered in Cloud I is given in figure E-4. The largest particles were ice suggesting that ice particle growth by accretion was more effective than liquid particle growth by coalescence.

Simultaneous foil impactor and vertical-motion data were gathered on each penetration of Cloud I on 29 and 31 July. An example of the water-content and vertical-motion results from these data is presented in figure E-5. The average LWC and IWC for the precipitation size particles ($\text{dia} \geq 200 \mu\text{m}$) are plotted along with the vertical-motion values. Positive water-content deviations indicate the precipitation core within the cloud. The vertical-motion values are studied to diagnose the extent of the interaction of cloud dynamical and microphysical processes. Similar results from Cloud II are not presented because the analysis of these data has not been completed.

The average LWC and IWC of the precipitation-size particles were computed from the water-content data gathered during the 0°C and -5°C monitoring passes of the Cloud I experiment on 29 and 31 July. The values are presented in table E-1. The IWC was greater than the LWC on all passes.

All precipitation measurements (total, LWC and IWC) were considerably larger on the 29 July Cloud I experiment than in the 31 July experiment.

FLIGHT 700729-A, CLOUD I, PASS 2
INITIAL TIME 160731Z
TEMPERATURE $+1^\circ\text{C}$ ALT. 15,000FT

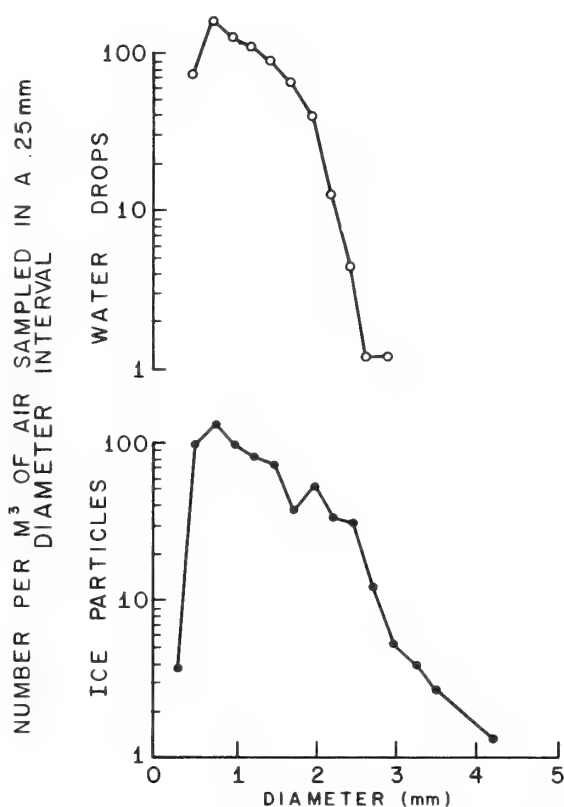


Figure E-4. Liquid and ice particle size-distribution averaged along the 0°C monitoring pass of Cloud I, 29 July 1970 are shown. The unknown particles (u) and small particles (s) contain both ice and liquid particles but are too small to differentiate between either ice or water.

FLIGHT 7700729-A, CLOUD I, PASS 2
 INITIAL TIME 160731Z
 TEMPERATURE + 1°C ALT. 15,000FT.

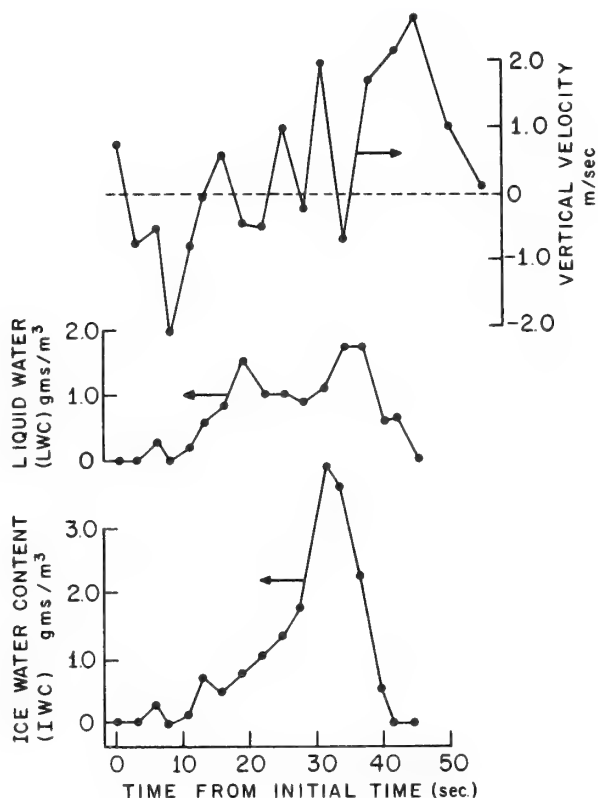


Figure E-5. Navy Weather Research Facility water-content deviations about the average water-content value are plotted with the simultaneously observed NOAA-NHRL vertical-motion values. The data are from the 0°C monitoring-pass of Cloud I on 29 July 1970. The initial time is the time the aircraft entered the cloud. The aircraft flew at 100 m sec⁻¹; as a result, 10 sec on the time equals 1 km. The average LWC and IWC values are 0.715 and 0.958 g m⁻³, respectively.

On both days, however, the absolute precipitation amounts (total, LWC and IWC) at the lower level (0°C) were from five fold to an order of magnitude greater than at the upper level (-5°C), and the percentage of liquid content with respect to ice content was greater at the lower level. These figures indicate that the layer between 0°C and -5°C was an active precipitation formation region and that the increases in both the LWC and the IWC between -5°C and 0°C may indicate significant contributions from both coalescence and accretion.

The ratio of the LWC to the IWC at the 0°C level was approximately the same on both days but was somewhat lower at the -5°C level for the AgI experiment, suggesting effects of seeding which will be discussed in more detail.

While these results are quite useful, their reanalysis in conjunction with cloud particle distributions from the formvar replicator data should contribute to improved understanding and improved parameterization of microphysical processes in numerical simulation models.

Table E-1. Average Liquid-Water and Ice-Water Content of Precipitation ($g\ m^{-3}$).

Test Day	Nuclei	CLOUD I Experiment*					
		Monitoring Level					
		0°C			-5°C		
		LWC	IWC	LWC/IWC	LWC	IWC	LWC/IWC
29 July 1970	AgI	0.715	0.958	0.75	0.074	0.188	0.39
31 July 1970	AgI•NaI	0.078	0.106	0.74	0.010	0.022	0.45

* Cloud II Experiment data not reduced yet

The average vertical motions were computed and the maximum updrafts were isolated from the vertical-motion data gathered on all passes in the Cloud I and Cloud II experiments on 29 and 31 July. The values are presented in table E-2. The maximum positive vertical-motion and updrafts for all passes occurred during the seeding pass and then tapered off during the monitoring passes.

Table E-2. Observed Average Vertical Motion/Observed Maximum Updrafts ($m\ sec^{-1}$).

Test Day	Nuclei	Experiment					
		CLOUD I			CLOUD II		
		Seed +5°C	Monitor 0°C -5°C		Seed -5°C	Monitor -5°C -5°C	
29 July 1970	AgI	3.0/ 9.3	0.5/ 3.5	1.0/ 4.0	1.0/ 6.2	0.3/ 2.6	0.8/ 4.0
31 July 1970	AgI•NaI	1.5/ 7.5	0.7/ 5.2	0.2/ 2.5	2.7/ 8.2	2.7/ 5.7	-0.3/ 2.1

DISCUSSION

Cloud I contained an average maximum updraft of $5\ m\ sec^{-1}$ (averaged from table E-2) on both 29 and 31 July. Assuming a majority of the ice nuclei were transported in this updraft, the nuclei would have reached the 0°C level, the -5°C level, and the -10°C level in 3 minutes, 7 minutes, and 10 minutes, respectively, after the seeding time. The DC-6

aircraft reached the 0° and -5° levels 14 and 27 minutes after seeding, respectively. Hence, it is likely that most of the seeding material had been carried up and through these levels prior to the aircraft penetration.

The precipitation resulting from seeding, however, may have been observed at the -5°C level in Cloud I on 29 July. The median mass diameter of the ice precipitation particles observed at -5°C was approximately 1.5 mm. These ice particles were estimated to grow from ice nuclei to 1.5 mm in 17 minutes in the observed in-cloud conditions (-5°C, 1 g m^{-3} LWC) (Hindman and Johnson, 1970). The particles' fall velocity after 17 minutes of growth was estimated to be faster than the updraft, thus permitting the particles to settle from the rising seeding region. Assuming that a majority of AgI nuclei are activated in 3 minutes after the seeded region passed -5°C, then the total time from seeding to grow 1.5 mm ice particles is 7 min + 3 min + 17 min = 27 minutes which is the time it took the aircraft to reach the -5°C level.

The LWC/IWC ratio illustrated in table E-1 shows that the 0°C passes in Cloud I on 29 and 31 July had similar LWC/IWC ratios. The -5°C passes, however (which presumably measure the seeding effects on the precipitation), had a lower ratio on the 29th (0.39) than on the 31st (0.45). The higher relative ice content of the AgI-seeded cloud (29th) at -5°C compared to that of the AgI·NaI-seeded cloud (31st) suggests that the aircraft may have intercepted the ice precipitation particles settling from the region of the cloud affected by the AgI.

Random interpretation error of approximately ± 19 percent has been estimated when differentiating between ice and water particle impressions from the foil sampler. The difference in the LWC/IWC ratio is slightly greater than the possible random error, therefore the difference is considered real.

It would not be expected that the ice precipitation settling from the region of Cloud I affected by the AgI·NaI would be intercepted. These particles formed at and below -10°C and probably did not overcome the updraft to reach the -5°C level in the 27-minute interval between seeding and the monitoring passes. Simpson (1970) recently showed that precipitation assumed to result from seeding was observed on radar within 10 minutes at 6 km below the seeded region. This remarkably short period of time was possible because a 4 m sec^{-1} downdraft assisted the precipitation in falling from the formation level (6-7 km above cloud base) to the observation level (1 km above cloud base).

Significant decreases in the average vertical motion after seeding were measured in both the AgI and AgI·NaI experiments in Cloud II (see table E-2). An unexpected reduction was registered in the AgI-seeded cloud on the first monitoring pass followed by a restoration trend on the second monitoring pass. In contrast, the AgI·NaI-seeded cloud showed a slight decrease during the first monitoring pass but a more significant reduction during the second monitoring pass.

Admittedly the vertical motion values constitute a limited sample and the magnitudes are near the data's noise level. If these observations are considered somewhat credible, they still present a paradox and suggest certain weaknesses in current parcel and bubble theories of convection. The theories may not adequately explain the paradoxical decrease in updrafts following seeding. A more rigorous application of the hydrodynamic and thermodynamic equations integrated with a more realistic microphysical parameterization may be required for adequate simulation of cumulus convective processes. Such a formulation is currently being considered at WEARSCHFAC which would explain the sequence of events in the Cloud II experiments according to the suggested processes below.

For both seedings in Cloud II, the average vertical velocities were measured below the region in which the artificial nuclei increased natural glaciation. The decreases in updrafts following these seedings suggest that the initial effects of seeding decrease the stability and increase the updrafts in and above the increased glaciation region while increasing the stability and suppressing the updrafts below this region. In the AgI experiment the increased release of the latent heat of fusion would take place directly above the seeding and sensing levels because these nuclei become active at -5°C . Hence the suppressing effects on the updrafts would be noticed rather quickly. Such was the case on the first monitoring penetration, and perhaps the effect began to diminish by the time of the second pass because the updrafts increased. In the AgI·NaI experiment, the increased release of the latent heat of fusion would take place at higher levels than in the AgI experiment because the AgI·NaI are less active than the AgI nuclei. The impact on the updrafts would be delayed, which is consistent with the trend of values shown in the Cloud II experiment in table E-2.

These processes suggest the following cycle of events which may occur after a cumulus cloud is seeded:

- a. The seeding material will be carried upward with increased glaciation taking place at the level according to the activation of the seeding material

- and will be followed by increased condensation and increased precipitation.
- b. Initially, the increased release of latent heat will augment the updrafts in and above the increased glaciation level and suppress updrafts below this level.
 - c. Subsequently, the net effect of the whole process will warm the cloud core as well as create a divergent outflow in the upper levels. The warming and outflow will decrease the surface pressure which will cause an increased inflow at the lower levels and produce a general increase in upward motion throughout the cloud.

This cycle suggests prospects of developing a rationale for increasing cloud growth by successive pulsed seedings. Empirical evidence compiled by St. Amand (1969) indicates that pulsed seedings may increase cloud growth and merge individual clouds into cloud systems. While the cycle is not properly reflected in current simple cloud models, its physical reasoning is qualitatively consistent.

An advantage of glaciating tropical cumuli with AgI ice nuclei rather than AgI·NaI ice nuclei is illustrated in figure E-6. Illustrated are cloud vertical motions that were simulated with a numerical cumulus model described by Matthews in this report (app. H). The vertical motions decrease to zero at 6.3 km for the natural cloud assumed to glaciate at -25°C , indicating a cloud top at 6.3 km. The cloud seeded with AgI·NaI ice nuclei also did not grow more than 6.3 km. The cloud reached the -6°C level but needed to grow to roughly the -10°C level before the AgI·NaI ice nuclei would increase natural glaciation and increase cloud growth. The cloud seeded with AgI ice nuclei, however, grew to 11 km because these nuclei increased natural glaciation at the -5°C level. This glaciation boosted the cloud past the 6.3 km level it would have grown to naturally.

CONCLUSIONS

Ice-water content data and vertical-motion data from two cloudline cumuli seeded with AgI ice nuclei tentatively indicate that the cumuli began to glaciate at approximately -5°C . Similar data from two other cloudline cumuli seeded with AgI·NaI indicate that the cumuli began to glaciate at a colder temperature, possibly -10°C . These tentative conclusions are in agreement with previous laboratory results

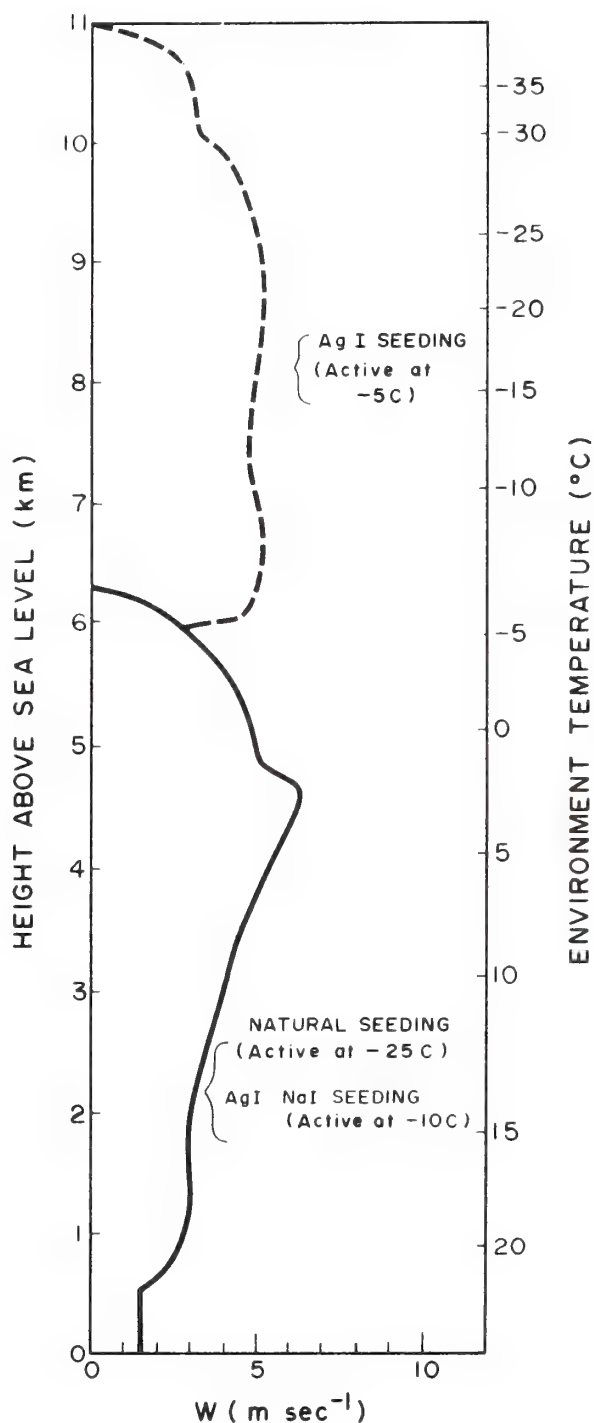
Donnan et al. (1970) and field results of Auer and Veal (1970). This agreement suggests that given a choice of acetone solutions to burn in a solution-combustion generator, the AgI-NH₄-acetone solution would be the choice if glaciation at temperatures near -5°C is desired.

Vertical-motion data from two cloudline cumuli seeded and monitored at the -5°C level suggest that the initial effects of seeding may have suppressed the updrafts below the regions of increased glaciation and heating.

Further testing, however, is needed to confirm these preliminary conclusions. The extremely limited number of seeded clouds prevented a statistically significant sample. Furthermore, the lack of control clouds prevented objective comparisons of the seeded clouds with those developing naturally.

The operational data gathered from the NOAA-RFF solution-combustion generator indicated that the device can be used routinely to seed STORMFURY cloudline cumuli.

Figure E-6. Effect of seeding on updrafts in a cumulus cloud in a hurricane environment, as simulated by Matthews (1971) using a one-dimensional cumulus model. Cloud base diameter was assumed to be 3 km. The atmospheric sounding, from which cloud growth was simulated, was from the 996-999 mb pressure region of a hurricane.



RECOMMENDATIONS

1. Conclusions derived from the evaluation of 1970 STORMFURY cloudline data presented in the report are limited by the preliminary nature of the experiments. Subsequent experiments should be more extensive to determine if the initial effect of seeding tropical cloudline cumuli is the suppression of updrafts.

2. The need for shorter time-separation between seeding and monitoring passes and the need for monitoring passes above the seeding level suggest a dual-aircraft experiment.

3. The difficulty in executing monitoring passes in rapid succession and monitoring passes above the seeding level indicates the desirability of having an aircraft that can stay within the core and rise at approximately the same speed as the seeded updraft. The cloud physics instrumented NCAR SGS 2-32 sailplane (Schribner, 1966) is suited for these flight requirements. This aircraft would be able to seed the core of the rising air and continuously monitor the seeding effects. Results from such flights would illustrate how thoroughly the seeding is glaciating the available supercooled water and provide a measure of the effects of seeding on vertical accelerations. These results should contribute to a much needed improvement in the parameterization of seeding effects in numerical cloud models.

REFERENCES

- Auer, A. H., Jr. and D. Veal (1970): Evaluation of cloud seeding devices in an outdoor laboratory. *Project Report, Naval Weapons Center Contract N66001-70-C-0639*, November, (on file, Naval Weapons Center (code 602), China Lake, California).
- Carlson, T. N., and R. C. Sheets (1971): Comparison of draft scale vertical velocities computed from gust probe and conventional data collected by a DC-6 aircraft. Technical Memorandum ERLTM-NHRL No. 91, NOAA, Dept. of Commerce, NHRL, Miami, Fla.
- Donnan, J. A., D. N. Blair, W. G. Finnegan and P. St. Amand (1970): Nucleation efficiencies of $\text{AgI-NH}_4\text{I}$ and AgI-Nai-Acetone solutions and pyrotechnic generators as a function of LWC and generator flame temperature. A Preliminary Report. *The Journal of Weather Modification*, 2, pp. 155-164.

- Finnegan, W. G., P. St. Amand and L. A. Burkardt (1971): An evaluation of ice nuclei generator systems. Submitted to *Science*.
- Gentry, R. C. (1970): Hurricane Debbie modification experiments, August 1969. *Science*, 164, pp. 473-475.
- Gentry, R. C. (1971): Progress on hurricane modification research-October 1969 to October 1970. Presented at *Twelfth Interagency Conference on Weather Modification*, October 28-30, Virginia Beach, Va.
- Hindman, E. E., II (1970): Cloud particle samples and water contents from a 1969 STORMFURY cloudline cumulus. *Project STORMFURY Annual Report 1969*, U.S. Dept. of Navy and U.S. Dept. of Commerce, Appendix F.
- Hindman, E. E., II and D. B. Johnson (1970): Numerical simulation of ice hydrometeor development. Preprints - *Conference on Cloud Physics*. American Meteorological Society, Boston, Mass., pp. 63-64.
- Patton, B. T. (1970): Preliminary report on the Patton mark series generators. On file at NOAA-RFF, Miami, Fla., 5 pp.
- Sax, R. I. (1969): The importance of natural glaciation of the modification of tropical maritime cumuli by silver iodide seeding. *Journal of Applied Meteorology*, 8, pp. 92-104.
- Schribner, K. (1966): The explorer. *Journal Soaring Society of America*, pp. 12-13.
- Simpson, J. (1970): On the radar-measured increase in precipitation within ten minutes following seeding. *Journal of Applied Meteorology*, 9, pp. 318-320.
- Simpson, R. H., and J. S. Malkus (1964): Experiments in hurricane modification. *Scientific American*, 211, p. 27.
- St. Amand, P. (1969): Weather modification techniques development. Appears in "A Summary of the U.S. Navy Program and FY-1969 Progress in Weather Modification and Control." *WEARSCHFAC Technical Paper No. 26-69*, pp. 38-39.
- Todd, C. J. (1965): Ice crystal development in a seeded cumulus cloud. *Journal of Atmospheric Science*, 4, pp. 70-78.

- Vonnegut, B. (1949): Nucleation of supercooled water clouds by silver iodide smokes. *Chemical Review*, 44, pp. 277-289.
- Vonnegut, B. (1950): Techniques for generating silver iodide smoke. *Journal of Colloid. Sciences*, 5, p. 377.
- Weinstein, A. I., and D. M. Takeuchi (1970): Observation of ice crystals in a cumulus cloud seeded by vertical-fall pyrotechnics. *Journal of Applied Meteorology*, 9, pp. 265-268.
- Woodley, W. L. (1970): Precipitation results from a pyrotechnic cumulus seeding experiment. *Journal of Applied Meteorology*, 9, pp. 242-257.

APPENDIX F

MEASUREMENTS OF VERTICAL MOTION IN THE EYEWALL CLOUD REGION OF HURRICANE DEBBIE

Toby N. Carlson

National Hurricane Research Laboratory

INTRODUCTION

Vertical motions on a cumulus cloud scale (1 to 100 km) can be estimated using various parameters recorded by the RFF DC-6 aircraft (Carlson and Sheets, 1971). The formula used to obtain the drift scale vertical velocity, W , is

$$W = V_t (\alpha_d - \theta_d) + W_p, \quad (F.1)$$

where V_t is the true air speed, α_d and θ_d are the angle of attack and pitch angle of the aircraft with respect to the equilibrium values of these angles, and W_p is the aircraft vertical velocity. In the DC-6 aircraft, the latter is determined by differentiating the radio-altimeter values to give change in aircraft height with time. The true airspeed and pitch angle are directly measured; the equilibrium value of the pitch angle must be continuously determined since it is found to drift slowly with time.

The equilibrium pitch angle, θ_e , is determined by assuming that the mean vertical motion throughout a given straight line pass is zero for short passes through cumulus clouds; in longer passes, such as straight line radial legs through hurricanes, it is assumed that W is zero when averaged over a longer interval, L , (~50 to 75 miles); a variable θ_e is thereby determined at the mid-point of a sliding scale of length L which will be shorter than the length of the pass. Inspection of the vertical motion trace may indicate that the vertical velocity averaged over L need not be zero, in which case the zero vertical velocity axis should be adjusted by eye; for example, if the values fail to approach zero in the undisturbed environment of a cumulus cloud or in the center of the hurricane eye. The angle of attack is not measured but is computed indirectly from the equation of motion for aircraft lift. In practice during flights in hurricanes,

the basic 1 sec digital values are converted to a 6 sec block average in order to minimize noise in the data. For cumulus clouds, a weighted 4 sec (binomially smoothed) running mean is used.

PROFILE OF VERTICAL MOTION IN HURRICANE DEBBIE (1969)

The draft scale vertical motion computations were determined for all radial legs in Hurricane Debbie on 18 and 20 August 1969, by the 39-C DC-6 aircraft which was the only aircraft capable of making such measurements on those occasions. Of the 10 radial penetrations made on the 20th, and of seven made on the 18th by this aircraft a total of eight and five passes, respectively, were made along a southwest-northeast azimuth. Most of the penetrations began and ended about 70 km from the center and all of them penetrated both of the eyewalls and the inner clear region of the eye.

Examination of the individual vertical motion profiles showed that there was considerable variability from pass to pass due to the rapidly shifting echo patterns. In order to arrive at a composite picture for the storm, the vertical motion profiles for the southwest-northeast legs were arithmetically averaged together for the eight passes on the 20th and the five passes on the 18th. Each radial leg from the eye was averaged with respect to the point of entry of the aircraft into (or from) the eyewall cloud from (or into) the clear eye. Except for the outer portions of the eyewall cloud region in figure F-1 where there were fewer observations, the composite profiles of vertical motion represent an average of eight or five points, respectively, for the 20th and 18th. (The inner portion of the clear eye was composited separately and is not shown here.)

Both profiles show some similarity in that a broad domain of rising motion is found in the eyewall cloud region which is surrounded by a more narrow ring of descending (or nearly neutral) vertical motion near the eyewall (and just inside the eye) and also on the outer edges of the wall cloud region. The strength of the updrafts appeared to be about the same on the 18th as on the 20th, although the storm had deepened appreciably in the interval. In figure F-1, the maximum ascent was $2-3 \text{ m sec}^{-1}$ (strongest in the southwest sector), while the mean rising motion averaged over the rising annulus was about 1 m sec^{-1} on both days. Because the vertical motion measurements were made from a series of passes which spanned only a few hours, it is difficult to

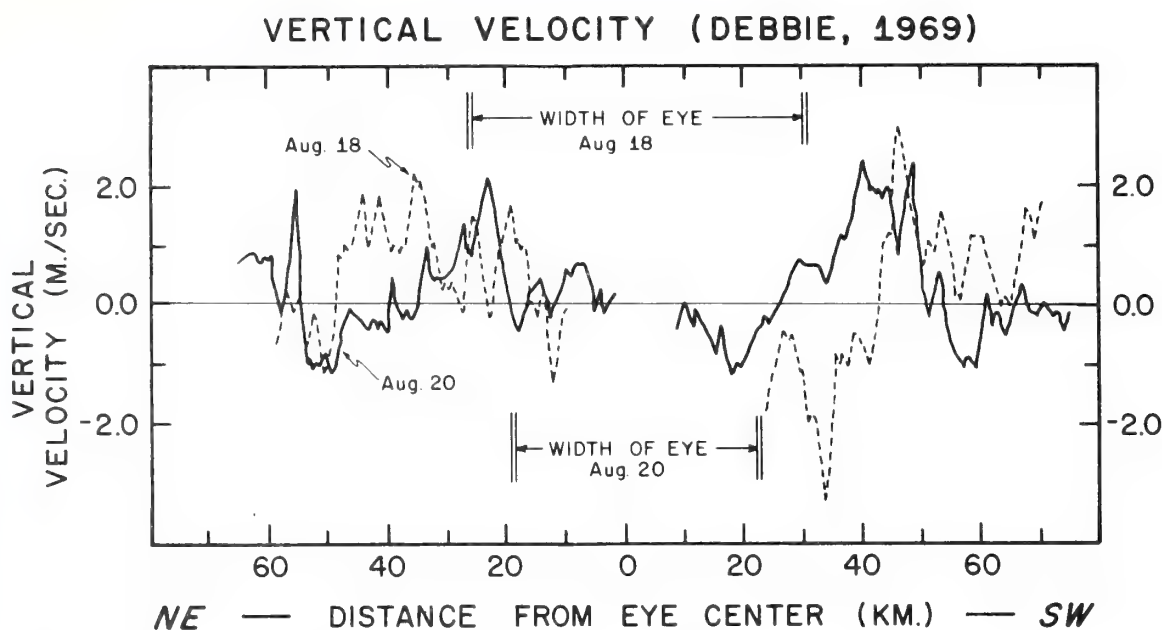


Figure F-1. Composited vertical velocity profile for Hurricane Debbie as determined from the RFF 39-C DC-6 aircraft. The profile represents an average of 8 radial legs on 20 August 1969, and 5 radial legs on 18 August, which were on a northeast-southwest azimuth. Compositing was done with respect to the inner face of the eyewall cloud, the mean positions of which are indicated by the width of the eye.

assess the effects of seeding on the updraft profile in Hurricane Debbie. The composite profiles, however, demonstrate the possible use of vertical motions in evaluating seeding experiments (see app. E in this report).

ACCURACY OF THE VERTICAL MOTIONS

Carlson and Sheets (1971) have discussed deficiencies in the measurement of draft scale vertical motion and the accuracy of the calculations, based on a comparison with simultaneous measurements made with the RFF gust probe system in a series of test passes through individual cumulus clouds. Their results indicate that the measurement accuracy depends on the scale in question and on the intensity of the turbulent motions (the variance of W). Reliability of the measurements is considered to be greatest for updrafts on the scale of the cumulus cloud (1 to 10 km) and for strong vertical motions.

But for scales of motion a kilometer or less, the uncertainty decreases rapidly with decreasing wavelength of the updraft. A possible noise frequency (that of aircraft oscillation) may exist with a frequency of 5-10 sec and an amplitude of about 0.5 m sec^{-1} . Absolute errors appear to increase with increasing intensity of the vertical motions, but the percent error in a particular draft profile decreases with the amplitude of the draft, and the uncertainty is probably a small fraction of the amplitude value when the peak value exceeds a few meters per second. Conversely, the percentage error for a particular updraft or downdraft profile decreases with increasingly weaker vertical motions and may become comparable to the amplitude of the motions themselves in weak cumulus or in clear air where the maximum draft speeds are a meter per second or less. A minimum uncertainty of $0.4\text{-}0.8 \text{ m sec}^{-1}$ may be present even in clear air where the vertical velocity variance is of this order. In composites such as the one shown for Debbie (fig. F-1), the noise may be canceled to some extent; therefore, the magnitude of the broad profile of updrafts and downdrafts may have more significance than it would have had in an individual pass.

Vertical motions are also adversely affected by sharp turns and during significant changes in aircraft altitude brought about by the pilot attempting to climb or descend. For that reason the calculations are felt to have some validity only in straight line (or radial) passes flown at a constant level where the power setting changes by the pilot are kept to a minimum. Occasional power setting changes, which are necessarily made by the pilot in penetrating intense cumulus updrafts of the eyewall cloud of a hurricane, are detrimental to the measurements but are not considered to be critical in determining the basic draft profile. Power setting changes are also made during cloud seeding runs when the silver iodide burner is operated on board the DC-6 aircraft. In the future, an angle of attack vane will be mounted on the aircraft which will hopefully improve the measurements of vertical velocity since, at present, α_d is not accurately known.

REFERENCE

Carlson, T. N., and R. C. Sheets (1971): Comparison of draft scale vertical velocities computed from gust probe and conventional data collected by a DC-6 aircraft. Technical Memorandum ERLTM-NHRL No. 91, NOAA, Dept. of Commerce, NHRL, Miami, Fla.

APPENDIX G

AN ESTIMATE OF THE FRACTION ICE IN TROPICAL STORMS

W. D. Scott and C. K. Dossett
National Hurricane Research Laboratory

INTRODUCTION

With the present concept of the modification of tropical storms, a considerable amount of supercooled water must exist above the freezing level in the storm cloud system. This thinking precludes modification of the storm if the supercooled water has already frozen and turned to ice. Hence, an estimate of the ice content of the clouds at levels between 0° and -20°C would help us assess the probability of being able to modify the storm, and, perhaps, give an *a posteriori* judgment on the success of a seeding mission.

We currently have acquired three instruments that should give an estimate of ice concentration during a flight into a storm. These are the foil impactor, the continuous particle replicator, and the ice particle counter. The foil impactor has been described in previous STORMFURY Reports (see Sheets, 1969; Hindman, 1970) and some data from the cloud-line experiments are presented in this report by Hindman (app. E). The particles are impacted on a strip of aluminum foil and the size and character of the particles are derived from the impressions they make.

The ice particle counter was recently acquired through a contract with Mee Industries, Altadena, California. It uses an optical technique which measures the scintillations or "twinkles" ice crystals make when they reflect light off their secular faces. It is now undergoing calibration tests, but preliminary test results indicate that it can count ice particles in real time with a 75 percent or better reliability even in the worst case when large water drops are present in the sample.

The continuous particle (formvar) replicator is a device which captures cloud particles (i.e., droplets, raindrops, and ice crystals) and forms plastic replicas of them on a 16-mm motion picture film. The device currently in operation was also manufactured by Mee Industries. Its essential features are nearly identical to the instrument manufactured by

Meteorology Research, Inc., and described by Sheets (1969); the instrument and its basic principles have been used for years, and several different versions of it are presently being used (see for example: MacCready and Todd, 1964; Spyers-Duran and Braham, 1967; Ruskin, 1967; Patrick and Gagin, 1971). It has several deficiencies, but it does seem reasonable that the instrument can be used to obtain a subjective estimate of the fraction ice in clouds, i.e., that fraction of the total hydrometeor population considered to be ice. With the continued operation of the instrument in hurricanes and tropical storms, a large quantity of in-cloud data has been amassed. In this report some of the more recent data are considered, and the fraction ice at different levels in these storms estimated.

THE FLIGHT TRACKS

The aircraft flight tracks on which the data were taken are presented in figures G-1a, G-1b, and G-1c and are represented by arrows. On figures G-1a and G-1b the orientation and the relative locations of the clouds are preserved;

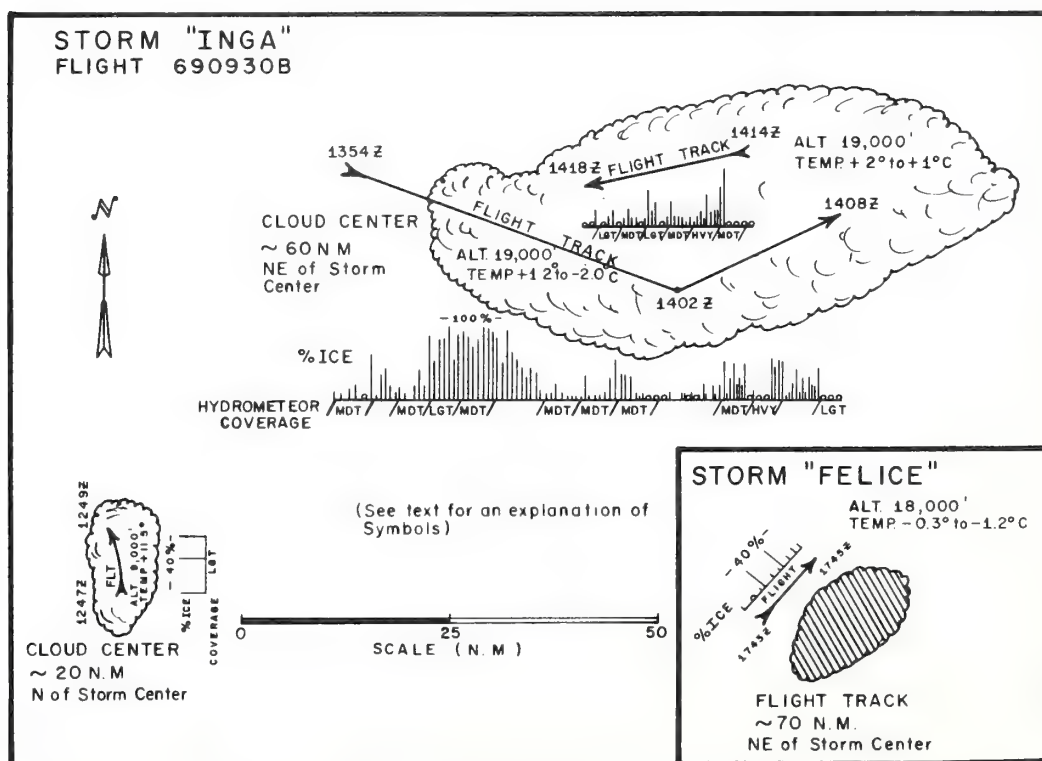


Figure G-1a. Sampling locations in Tropical Storms "Inga" and "Felice."

STORM: TD # 14
FLIGHT: 701002A

CLOUD CENTER
~150 N.M. E
from Storm Center

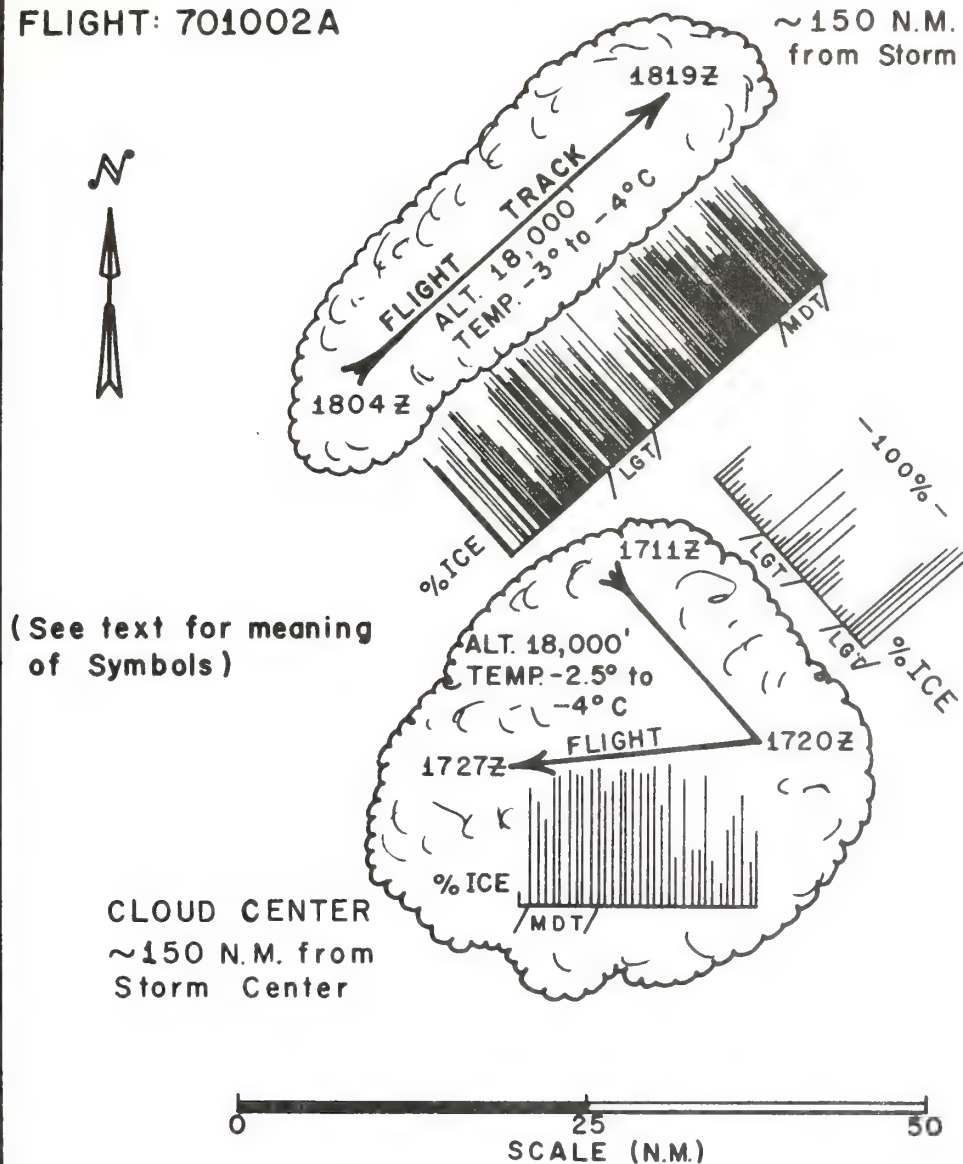


Figure G-1b. Sampling locations in Tropical Depression Number 14.

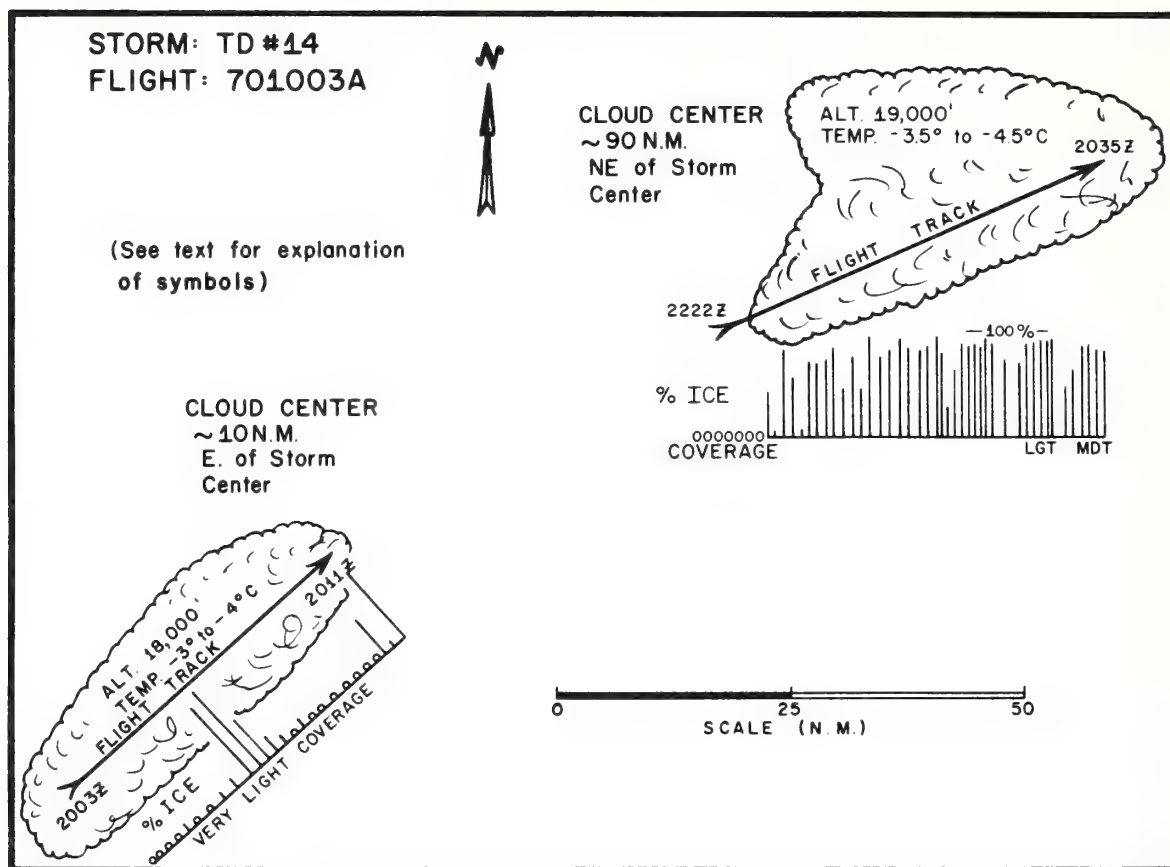


Figure G-1c. Sampling locations for Tropical Depression Number 14.

on figure G-1c the two clouds were slightly farther apart than is shown. The cloudy shapes represent the approximate extent of visible cloudiness, and the crosshatched area on figure G-1a is the area where a significant radar echo was observed. The scale is constant on all the figures; altitudes, temperatures, and the relationship of each cloud to the storm center are indicated.

A summary of all the results is shown in figure G-2. At the time the data were taken Tropical Storm Inga was increasing in intensity and had just produced hurricane-force winds. "Felice" appeared to be developing into a hurricane but it never became one. Tropical Depression No. 14 never did reach the status of a tropical storm, but the same storm system had flooded the island of Barbados and subsequently caused massive flooding in Puerto Rico.

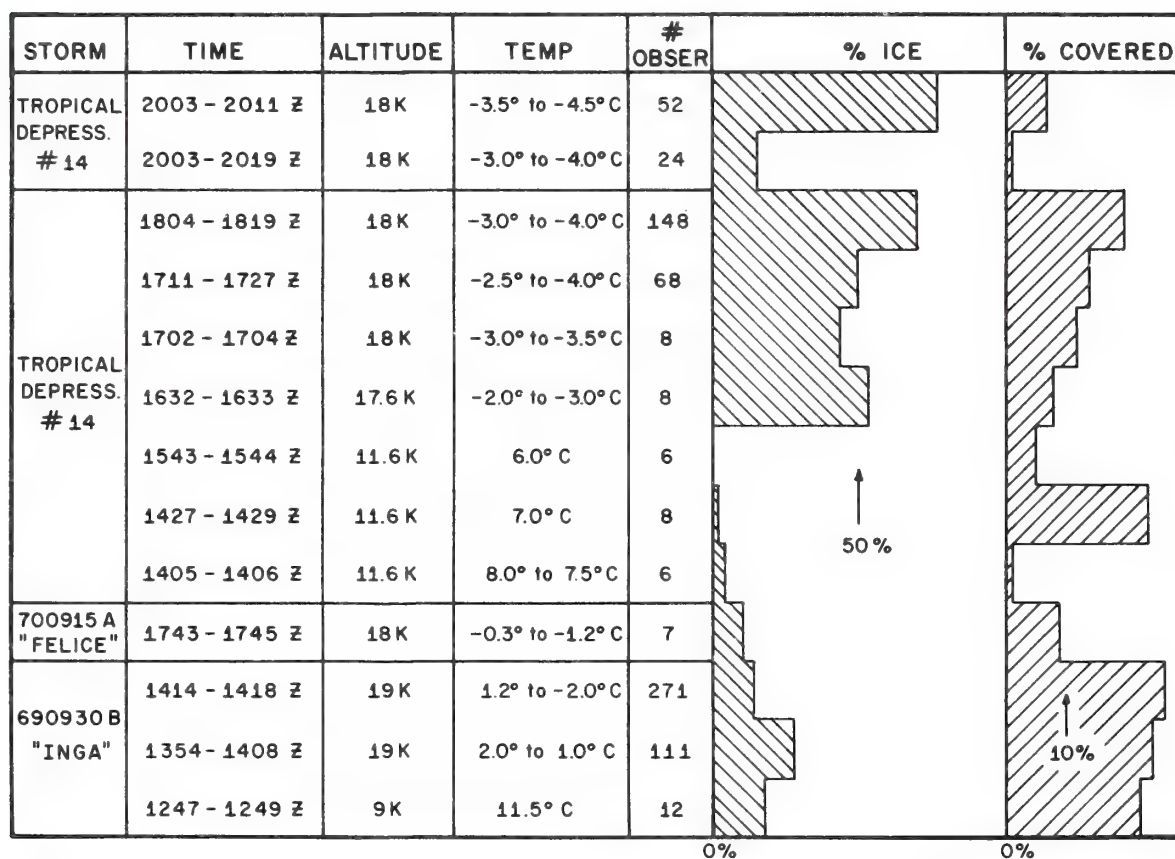


Figure G-2. Storm data.

THE ESTIMATED FRACTION ICE

The data were interpreted by viewing the projected image of the replaced crystals with a 16-mm motion picture projector. The magnification was such that 1 mm of distance on the film was projected to make 8 inches on the screen. All particles that appeared to have a crystalline character were assumed to be ice. That is, any particle with a non-spherical shape was assumed to be ice. As overall judgment was made on a single frame; one frame in approximately every 200 frames was chosen. The estimates of fraction ice are shown in detail in figures G-1a, G-1b, and G-1c. The bars represent the fraction ice which is the fraction of the total hydrometeor population that was considered ice. Below the abscissas are shown the relative quantity of hydrometeors that were sampled in terms of coverage of the 16-mm film. The blank areas indicate very light coverage. The circles represent hydrometeor samples that contained no detectable ice; the vacant spaces between the bars indicate either that no sample was taken, that there was an insufficient number of hydrometeors to estimate the fraction ice, or that the sample was too poor to make a judgment.

Several small clouds in the same general position relative to Tropical Depression No. 14 are not shown on figure G-1b. A sample taken from 1406Z to 1407Z in clear air showed the presence of cloud droplets with what appears as a small amount of ice. In this instance there were three small clouds showing radar returns within 10 n miles. An in-cloud sample taken between 1427Z and 1428Z indicated a moderate amount of liquid water and little ice. A third sample between 1632Z and 1633Z was taken outside the visible cloud and contained only ice in small quantities; again, a cloud with a radar echo was within 10 n miles. Of these samples, all were taken between the 6° and 8°C levels except the last which was taken between -2° and -3°C and, accordingly, contains mostly ice.

DISCUSSION

The observations of appreciable quantities of both liquid and solid hydrometeors outside the cloud boundaries is interesting and may shed light on the possibility of natural seeding by nearly glaciated clouds. It also points to the intangible character of a cloud boundary. At this time, however, in many of the samples, the possibility still exists

that there is an improper time correlation. An electronic counter with a digital readout is currently being added to the instrument which should help to alleviate this problem in future flights.

Figure G-3 shows a plot of the estimated fraction ice at different temperatures. The vortex temperatures may be as much as 1°C in error and most likely are a little low. The data indicate that a large portion of ice is present at the warmer temperatures (below the -5°C elevation level). Of course, the data may merely reflect the age of the storm since all the data at the colder temperatures are from Tropical Depression No. 14, and it was passing through a temporary dissipation stage at the time. It is interesting, however, that the data for Tropical Depression No. 14 are corroborated by simultaneous samples taken by the foil impactor (Meteorology Research, Inc.). The foil samples showed a large number of remarkably detailed impressions of stellar and needle crystals (see fig. G-4). These crystals did not appear in the formvar samples; but numerous, smaller, amorphous ice pieces were replicated.

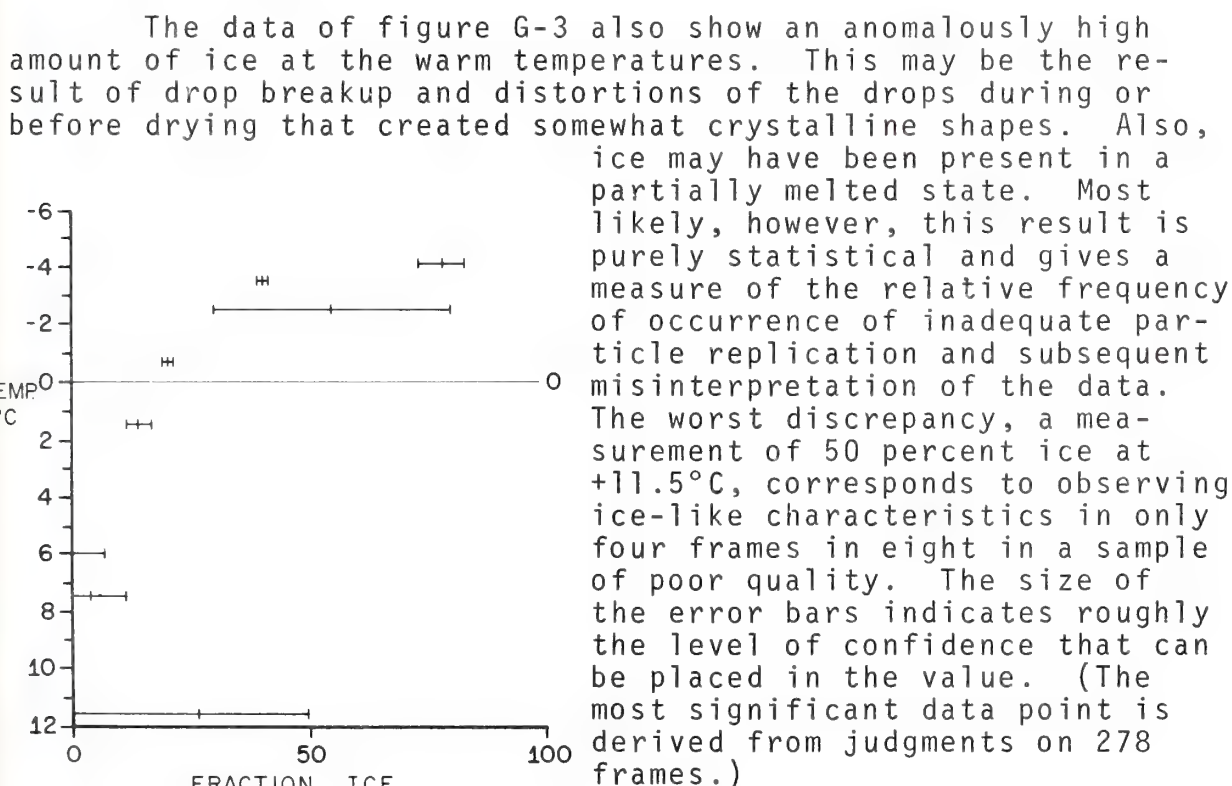


Figure G-3. Fraction ice at different temperatures in tropical storms.

All the data were processed without knowledge of the flight levels, and in Tropical Storm Inga, the analysis was

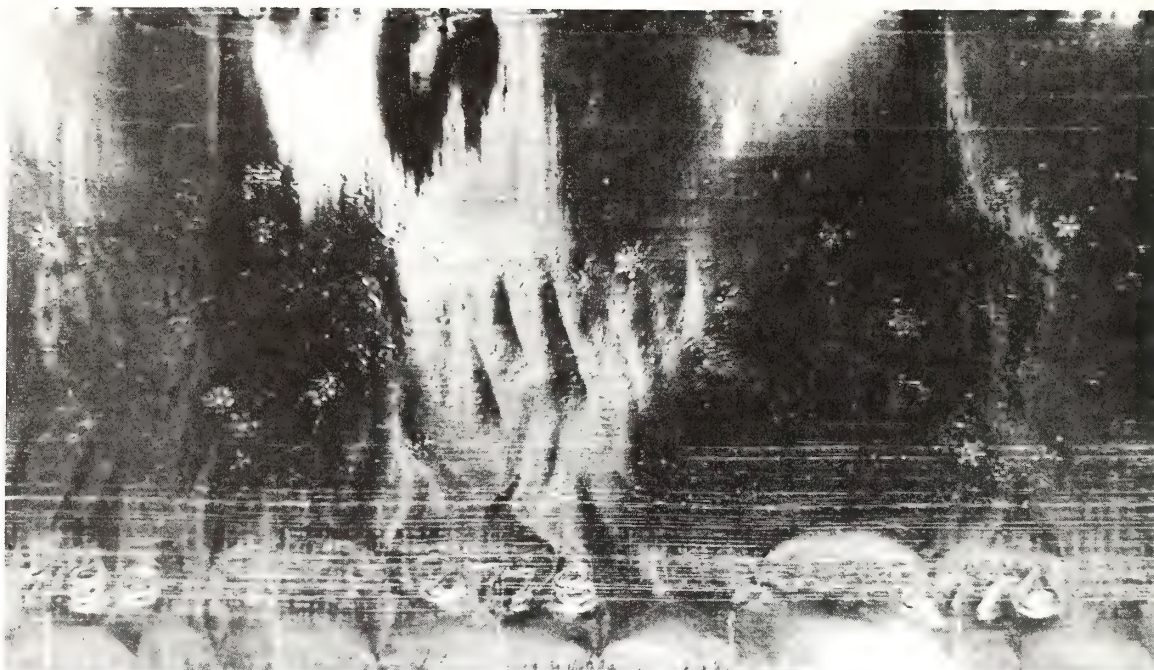


Figure G-4. Impressions of stellar and needle ice crystals on the foil impactor.

repeated by both authors independently on alternate, but staggered, frames. The results are shown in figure G-5, and the data points with the error bars represent this comparison. Another comparison was made between samples in Tropical Depression No. 14, in flights at the same temperature but at slightly different times. These data are represented by the triangles.

The airborne continuous particle replicator has been criticized on several points, including: (a) the nonstatistical size of the sample; (b) the possibility of particle breakup producing misleading numbers of ice particles; and (c) the unknown collection efficiency of the sampling boom due to pressure fluctuations and flow in and out of the boom. Niemann and Mee (1970) have completed the analysis of the 1968 cloud hydrometeor data for the Experimental Meteorology Laboratory. Occasionally they found gross discrepancies in the data, even as regards the presence or absence of ice. Figure G-5 presents an appraisal of the possible data handling problems as the usefulness of the instrument is limited by one's ability to interpret the data it presents. It appears that the criticisms above (a, b, and c) are not limiting

the value of the data, but instead, the possibility of misjudgments of the data themselves are involved. Figure G-5, all in all, says that occasionally one can expect to misinterpret the data (perhaps 10 to 20 percent of the time) but, accepting this error, the device can be used to estimate the fraction ice.

CONCLUSIONS

These data indicate that considerable amounts of ice can occur in tropical storms at temperatures above -5°C , an observation in agreement with the work of Ruskin (1967) but in contradiction to the findings of Sheets (1969) using data from Hurricane Gladys. However, the data presented here are of a limited nature and may not apply to mature storms. But, as data from more storms are analyzed and our instruments and data reduction techniques are improved, our estimates of the fraction ice in tropical storms should become more reliable.

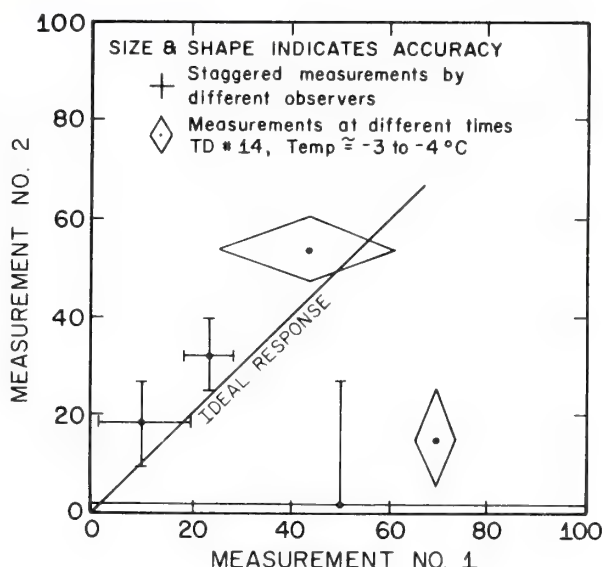


Figure G-5. The accuracy of the measurement of the fraction ice with the continuous particle replicator.

REFERENCES

- MacCready, P. B., and C. J. Todd (1964): Continuous particle sampler. *Journal of Applied Meteorology*, 3, pp. 450-460.
- Niemann, B. L., and T. R. Mee (1970): Analysis of cloud particle samples for ESSA-NRL cumulus experiments. *Final Report to Experimental Meteorology Branch*, ESSA, Miami, Fla., Contract E22-96-69(N), p. 8.
- Patrick, J., and A. Gagin (1971): Ice crystals in cumulus clouds--preliminary results, Studies of the microphysical aspects of cloud processes leading to the formation of precipitation. *Report No. 4, The Hebrew University of Jerusalem*, Dept. of Meteorology, Cloud and Rain Physics Laboratory.

- Ruskin, R. E. (1967): Measurements of water-ice budget charges at -5°C in AgI-seeded tropical cumulus. *Journal of Applied Meteorology*, 6, pp. 72-81.
- Sheets, R. C. (1969): Preliminary analysis of cloud physics data collected in Hurricane Gladys (1968). *Project STORMFURY Annual Report 1969*, U.S. Dept. of Navy and U.S. Dept. of Commerce, Appendix D.
- Spyers-Duran, P. A., and R. R. Braham, Jr. (1967): An airborne continuous cloud particle replicator. *Journal of Applied Meteorology*, 6, pp. 1108-1113.

APPENDIX H

ICE-PHASE MODIFICATION POTENTIAL OF CUMULUS CLOUDS IN HURRICANES

David A. Matthews
Navy Weather Research Facility

INTRODUCTION

An examination of ice-phase modification potential of cumulus clouds in a hurricane environment is presented. The modification potential is defined as the difference between natural and modified (1) rainfall, (2) surface pressure, (3) cloud virtual temperature departure from the environment, (4) vertical velocity maximum, and (5) height of cloud tops. The modification potential is predicted by a one-dimensional steady-state cumulus model (Weinstein and Davis, 1968; Lowe et al., 1971). Modification potential results are used to test the suggestions (Gentry, 1971) that increased effects may be realized by seeding less fully developed cumulus cells that are displaced slightly outward from the present eyewall seeding area.

This paper will describe the decreases in surface pressure, the increases in rainfall, and the increases in cloud top height as derived from model simulation of ice-phase modification using 87 soundings observed within 100 n miles of hurricane eyes as well as five average hurricane soundings from Sheets (1969).

CLOUD MODEL

The Pennsylvania State University-Navy Weather Research Facility one-dimensional cumulus model (Lowe et al., 1971) was used to determine the modification potential. This model performs an integration of the vertical equation of kinetic energy for a rising cloud tower (a rising parcel in the cloud core). The basic physical assumptions of the model are as follows:

- (1) None of the physical parameters investigated varies with time.

- (2) The cloud tower examined has the form of an entraining jet.
- (3) Entrainment is inversely proportional to the cloud tower radius.
- (4) Vertical acceleration is expressed as a function of buoyancy forces and drag forces.
- (5) Cloud buoyancy is generated by latent heat of condensation up to the level of nucleation. At this level, latent heat of fusion from freezing all liquid water stimulates buoyancy. Subsequent growth is solely a result of the released heat of deposition.
- (6) Cloud base is located at the convective condensation level (CCL) based on surface temperature and dew point values.
- (7) Seeding is simulated by freezing all liquid water at a specified temperature.

Seeding was simulated by using two nucleation temperatures, permitting an examination of the effects of different seeding materials. Temperatures of -5°C and -10°C simulated seeding by an $\text{AgI-NH}_4\text{I}$ -acetone system and an AgI-NaI -acetone system, respectively (see app. E).

Cloud core radii were selected to correspond with those selected by Sheets (1969). Cloud bases located at the CCL were found to be in agreement with those assumed by Sheets; however, they were generally about 200 m higher (see table H-1).

Table H-1. A Comparison of Cloud Bases Selected by Sheets (1969) and Those Corresponding to the Convective Condensation Level (CCL) for the Same Five Average Soundings. Sample Size from Which the Average Soundings Were Compiled Is Also Shown.

Surface Pressure (mb)	Cloud Base Sheets	CCL (m)	Sample Size
$P < 995$	200	443	8
$995 \leq P \leq 999$	200, 300	415	12
$1000 \leq P \leq 1004$	300, 500	492	19
$1005 \leq P \leq 1009$	500, 750	720	26
$1010 \leq P \leq 1014$	500, 750	997	22

DISCUSSION OF MODIFICATION POTENTIAL RESULTS

Table H-2 presents average values of model results and the modification potential for five average hurricane soundings presented by Sheets (1969). The results of three cloud radii (1.5, 3.2, 5.0 km) and three nucleation temperatures (-5° , -10° , -25°C) are presented. The -5° and -10°C temperatures simulated artificial modification by AgI and AgI·NaI ice nuclei, respectively; the -25°C temperature simulated natural freezing.

Average values of cloud model results for the modified clouds in table H-2(a) show increases over values for the natural cloud. In table H-2(b) a comparison of seeding with AgI ice nuclei (-5°C) and AgI·NaI ice nuclei (-10°C) shows significant increases in the average values over those of natural nucleation. The rainfall and surface pressure values in table H-2(c) for the -5°C nucleation temperature are 8 and 63 percent higher, respectively, than those values at -10°C . This difference indicates that the AgI ice nuclei may be expected to be somewhat more effective than AgI·NaI ice nuclei in glaciating clouds. The use of a seeding material active

Table H-2. Modification Potential Results

Nucleation Temp. ($^{\circ}\text{C}$)	(a) Average Values From the Natural Cloud ¹ and the Modified Clouds ²														
	-5	-10	-25	-5	-10	-25	-5	-10	-25	-5	-10	-25	-5	-10	-25
Radius (km)	Rainfall (in)			Base Press. Change (mb)			Cloud Top (m)			Virt. Temp. Depart. ($^{\circ}\text{C}$)			Max. Vel. (m sec ⁻¹)		
1.5	3.3	2.9	2.2	0.5	0.4	0.2	11094	10174	8254	1.9	1.9	1.7	4.4	9.4	9.3
3.2	5.2	5.1	4.8	1.3	1.3	1.0	13050	13174	12454	3.6	3.5	3.4	13.8	13.0	11.9
5.0	5.9	5.7	5.6	2.3	2.1	1.7	14094	13814	13854	4.2	4.4	4.2	17.4	18.2	14.9
Nucleation Temp. ($^{\circ}\text{C}$)	(b) Differences in Average Values Between the Modified Clouds and the Natural Cloud														
	-5	-10	-5	-10	-5	-10	-5	-10	-5	-10	-5	-10	-5	-10	-10
1.5	1.1	0.7	0.2	0.2	2840	2400	0.5	0.3	0.6	0.7					
3.2	0.4	0.3	0.2	0.3	750	720	0.2	0.2	3.1	2.1					
5.0	0.3	0.1	0.6	0.4	400	-50	0.3	0.2	3.7	3.2					
Nucleation Temp. ($^{\circ}\text{C}$)	(c) Average Percent Changes of Modification Potential														
	-5	-10	-5	-10	-5	-10	-5	-10	-5	-10	-5	-10	-5	-10	-10
1.5	50%	42%	187%	124%	40%	32%	46%	19%	7%	7%					
3.2	9%	8%	58%	60%	10%	9%	7%	6%	25%	16%					
5.0	9%	4%	34%	21%	3%	-.2%	10%	8%	25%	22%					

¹ Nucleation temperature -25°C .

² Nucleation temperature -5° , -10°C .

at warmer temperatures also enables modification of smaller clouds (whose tops have reached -5°C levels but not -10°C levels) earlier in their development than does material having colder activation temperatures.

The greatest change in potential occurs in clouds of 1.5 km radius. This relationship is to some extent the property of one-dimensional steady-state models and, at best, is qualitatively valid. The explanation for the relationship is as follows:

- (1) In the model the initial effect of the additional latent heat of fusion from seeding will decrease the hydrometeor concentration by evaporation. The total increase in rainfall is directly dependent upon the vertically integrated increase of hydrometeor content; hence, the net effect of seeding must produce sufficient cloud growth to increase upper level hydrometeor content to more than offset the effect of increased warming at the glaciation level.
- (2) The maximum growth of unseeded small radii clouds is often limited by the higher entrainment rates which prevent growth through small, stable stratifications in the ambient atmosphere. Whereas lesser entrainment rates of unseeded larger radii clouds permit them to penetrate these small, stable layers and grow up to the tropopause. Hence, the increased buoyancy from seeding permits the smaller radii clouds to push through any stable layers, thus resulting in a large net growth and increase of total hydrometeor content.
- (3) Large radii clouds, however, which in the unseeded state already have tops at the tropopause, will grow only slightly through seeding. As a result, many larger radii clouds in one-dimensional model experiments show a net decrease in total hydrometeor content (see Lowe et al., 1971). While this is a qualitatively valid relationship, strict quantitative interpretation of one-dimensional model results, in this respect, is not valid. These models do not accommodate the increased outflow at the top of these large clouds and do not permit a net increase in the total upward flux of saturated air. However, experience supports the validity of the qualitative aspects of model results.

Within the limitations of the one-dimensional model and the sounding data used, the modification potential of average cloud top heights shows increases in cloud top heights of 2800 m for 1.5 km and 750 m for 5.0 km cloud-core radii.

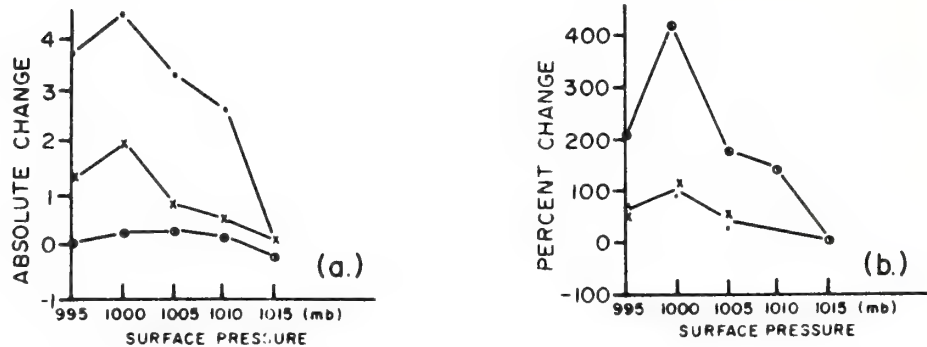
Examination of modification potential as a function of sounding location relative to the hurricane center was accomplished by five surface pressure categories corresponding to those of Sheets (1969) (see table H-1). Sheets derived five average hurricane soundings corresponding to these categories. Cloud model results of modification potential for these five surface pressures are presented in figures H-1(a), H-1(b), and H-2(a), and H-2(b). The 87 soundings were also divided into five groups according to the same surface pressure categories. Each sounding within a group was examined with the model, and the modification potential within each group was averaged. Figures H-1(c), H-1(d), H-2(c), and H-2(d) present the average modification potential of the five groups of soundings.

Figures H-1 and H-2 indicate that for clouds of 1.5 km radii there may be a preferred pressure location for optimum modification potential in hurricanes. In figures H-1(a) and H-1(b), this preferred location appears at a surface pressure of 1000 mb. The pattern of increasing modification potential from 1015 mb to 1005 mb is, however, probably more important than the individual maximum at 1000 mb. This pattern is consistent for all plots of modification potential in these figures both for five average soundings and for average modification potential for five groups of soundings. This pattern is also consistent for the three cloud radii examined and the two modification nucleation temperatures. This consistency of pattern adds further support to a relationship between optimum modification potential and location with respect to the hurricane center.

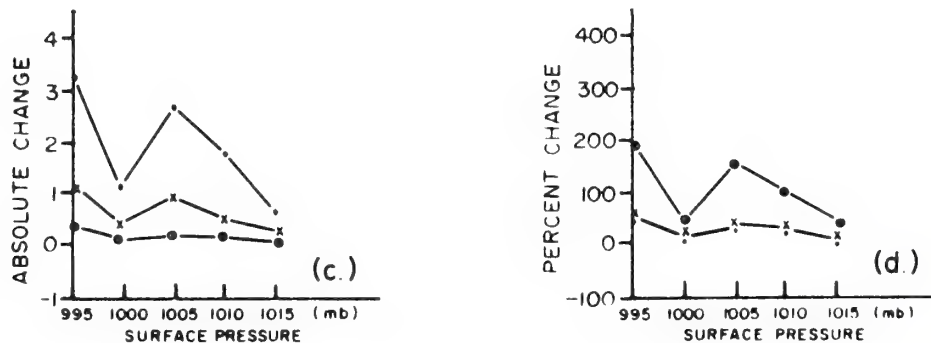
The pattern of high modification potential at 995-1005 mb suggests the existence of cumuli which have vertical growth arrested by small stable stratifications induced in the ambient air, but which are high enough to permit the unseeded cloud tops to reach nucleation temperature. Sounding data were not available with lower pressures to check the potential at smaller radii. The pattern of decrease of potential with further increasing pressure (to 1010 mb), however, suggests that stable stratifications and upper level dryness restrict the cloud tops to levels below the required nucleation temperature in which case the clouds would not respond to silver iodide seeding. This restriction in cloud tops is consistent with the pattern of tropical hurricane structures discussed by Palmen and Newton (1970).

CLOUD RADIUS = 1.5 km
NUCLEATION TEMPERATURE = -5°C

MODIFICATION POTENTIAL OF 5 AVERAGE SOUNDINGS



MODIFICATION POTENTIAL OF 5 GROUPS OF INDIVIDUAL SOUNDINGS

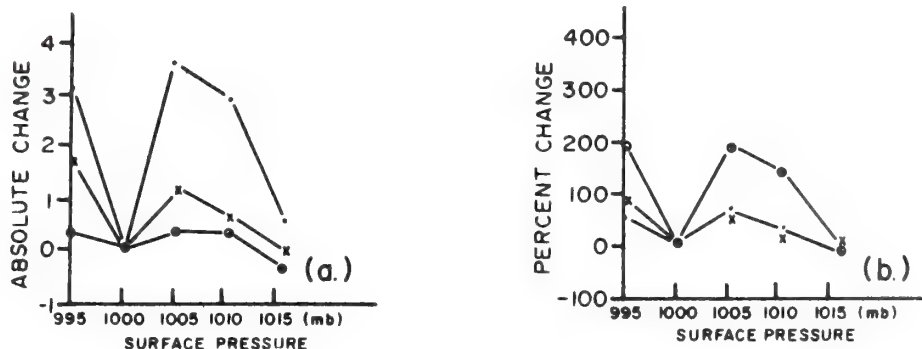


ΔZ , CLOUD TOP CHANGE (km) —•—
 ΔR , RAINFALL CHANGE (in) —x—
 ΔP , CLOUD BASE PRESSURE CHANGE (mb) —o—

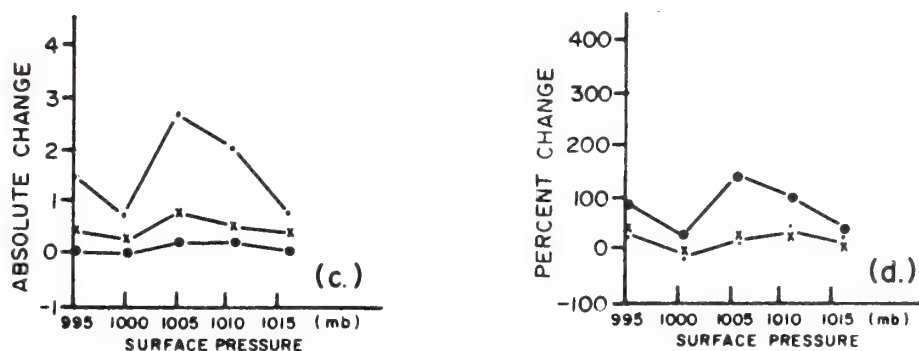
Figure H-1. Modification potential vs. surface pressure (-5°C nucleation temperature). Modification potential is divided into three categories: Cloud top change from natural cloud top, rainfall change, and surface pressure changes for clouds modified at -5°C . Both values of modification potential (a, c) and percentage changes (b, d) in modification potential are shown for five average soundings (a, b) and five groups of individual soundings (c, d).

CLOUD RADIUS = 1.5 km
NUCLEATION TEMPERATURE = -10°C

MODIFICATION POTENTIAL OF 5 AVERAGE SOUNDINGS



MODIFICATION POTENTIAL OF 5 GROUPS OF INDIVIDUAL SOUNDINGS



ΔZ , CLOUD TOP CHANGE (km) —•—
 ΔR , RAINFALL CHANGE (in) —x—
 ΔP , CLOUD BASE PRESSURE CHANGE (mb) —o—

Figure H-2. Modification potential vs. surface pressure (-10°C nucleation temperature). Modification potential is divided into three categories: Cloud top change from natural cloud top, rainfall change, and surface pressure changes for clouds modified at -5°C . Both values of modification potential (a, c) and percentage changes (b, d) in modification potential are shown for five average soundings (a, b) and five groups of individual soundings (c, d).

CONCLUSIONS

Significant increases in cloud growth, precipitation, and surface pressure change indicated by a one-dimensional model appear to support the latest STORMFURY hypothesis which postulates these increases from seeding. However, the effect of these increases on the storm's maximum winds still needs to be demonstrated.

Preferred seeding distances from the eye appear to exist in the hurricane environment. These may be a function of seeding material, cloud top temperature, and cloud radii.

RECOMMENDATIONS

(1) A detailed study of modification potential of various regions of the hurricane should be made using dropsonde data and cloud models. Such a study would provide valuable information on regions of optimum modification potential. Dropsonde data should be collected from the 100- to 200-mb level down to the surface. These soundings could be made using a WC-135 flying at 40,000 ft in a large "figure-eight" pattern centered on the hurricane eye. Dropsondes made every 10 minutes during a 1-hour pattern would provide sounding data at systematic intervals from the eye in different regions of the hurricane.

(2) Improved convective models would help define optimum seeding regions and levels for hurricane abatement. Direct transmission of dropsonde data from reconnaissance aircraft to ground computer facilities would enable real-time cloud model analysis of modification potential throughout seeding operations.

(3) A study of cloud top temperatures throughout a hurricane would also provide information on which regions have optimum cloud populations for modification.

(4) The feasibility of warm cloud modification prior to cold cloud modification should be examined because warm cloud modification may permit growth of small warm clouds to temperatures at which cold cloud modification will be effective. The combined use of warm cloud and cold cloud modification techniques would permit selective seeding in all regions without cloud top temperature restrictions.

REFERENCES

- Gentry, R. C. (1971): Progress on hurricane modification research-October 1969 to October 1970. Presented at *Twelfth Interagency Conference on Weather Modification*, October 28-30, Virginia Beach, Va.
- Lowe, P. R., D. C. Schertz and D. A. Matthews (1971): A climatology of cumulus seeding potential for the Western United States. *WEARSCHFAC Technical Paper No. 4-71*, 78 pp.
- Palmén, E., and C. Newton (1969): *Atmospheric Circulation Systems*. Academic Press, N.Y., pp. 471-522.
- Sheets, R. C. (1969): Computations of the seedability of clouds in the environment of a hurricane. *Project STORMFURY Annual Report 1968*, U.S. Dept. of Navy and U.S. Dept. of Commerce, Appendix E.
- Weinstein, A. I., and L. G. Davis (1968): A parameterized model of cumulus convection. *Report No. 11 to NSF*, NSFGA-777, 41 pp.

APPENDIX I

USE OF LIGHT AIRCRAFT IN STORMFURY ACTIVITIES

Dr. S. D. Elliott, Jr., and Dr. William G. Finnegan
Naval Weapons Center

INTRODUCTION

During the past three STORMFURY operating seasons, the Naval Weapons Center (NWC) has made one or two Navy-leased or contractor operated light aircraft available to the program for use during dry-run and cloudline experiment periods. This type of aircraft has provided a mainstay to other NWC programs in weather investigation and modification, and the opportunity was welcomed, both to pass on NWC experience in the effective employment of such aircraft to other STORMFURY participants, and to assess their utility in the STORMFURY operational context. As a result of three seasons' experience, some conclusions may be drawn on this topic and some recommendations offered for future STORMFURY activities.

BACKGROUND

In 1965 and 1966, NWC participation in STORMFURY included making available an A3B jet aircraft and crew to augment the RA3B's of VAP 62 in their employment as seeders. This aircraft and its military crew participated in both dry-runs, in the 1965 cumulus cloud experiments (Simpson et al., 1965) and in the aborted deployments for Betsy in 1965 (STORMFURY Annual Report 1965) and Faith in 1966 (STORMFURY Annual Report 1966). Unfortunately, the NWC A3B was lost in 1967 on a cross-country flight.

In 1967 the Naval Air Facility (NAF), China Lake, made arrangements for long-term leasing of a Cessna 210 single-engine, high-wing, four-place aircraft (fig. I-1). Equipped with retractable landing gear, full IFR instrumentation, a built-in oxygen system, and a turbo-charged engine, this 210, registry number N6877R, was capable of airspeeds in excess of 200 mph, altitudes exceeding 30,000 feet, and flight durations of 5 hours or more. Special meteorological instrumentation was installed, and external racks designed to accommodate a variety of attached and air-dropped pyrotechnic



Figure I-1. Navy-leased Cessna 210(77R). Streamlined rack for STORMFURY type air-dropped flares on port wing, boom for burn-in-place flares on starboard wing.

nucleant generators. This aircraft and similar contractor-operated aircraft provided economical and flexible tools for the development and assessment of weather modification techniques in numerous experimental projects.

The 1968 STORMFURY schedule (Project STORMFURY, Operation Plan No. 1-68) called for a dry-run exercise based at Naval Station Roosevelt Roads, Puerto Rico, with a briefing session on Monday, 5 August, and eyewall and rainband dry-runs on the 6th and 7th, the latter also to incorporate a test of the proposed cloudline experiment procedures. Cessna 210(77R) was flown to Puerto Rico for the week of 5-9 August and provided orientation and indoctrination for STORMFURY participants in current Navy-developed seeding techniques.

For 1969, the cloudline exercises were expanded to a full-scale experimental program scheduled to take place during the period 9 through 19 September (Project STORMFURY, Operation Plan No. 1-69). For this program, NWC made available two contractor-operated Cessna 401 low-wing, twin-engine, six-to-eight place aircraft (fig. I-2), having performance comparable to that of the 210 but with considerably greater

payload capacity. One 401, N3220Q, operated by Meteorological Operations, Inc., of Hollister, California, was equipped with a prototype meteorological data sensing and recording system developed by the NWC Aviation Ordnance Department, leaving only three seats available for passengers. The second 401, N32210Q, operated by Weather Service, Inc., Norman, Oklahoma, had five seats available. The twin-engine configuration of the 401 permits the use of a nose-mounted radar, and both aircraft were equipped with Bendix RDR-100 K-band weather avoidance radar systems covering a 90 degree forward sector to 80 n miles distance. Both aircraft were also equipped to carry and dispense 52 STORMFURY III air-dropped flares, externally similar to the STORMFURY I units used on Hurricane Debbie, but loaded with a shorter burning grain of EW-20 pyrotechnic mixture better suited to the cloudline operational environment (Project STORMFURY Annual Report, 1969). Other aircraft scheduled to participate in these exercises were the two NOAA DC-6's, two Navy WC-121N's, and a USAF WC-130.

All forces gathered at Naval Station Roosevelt Roads on 8 September. Cloudline experiments were conducted on 7 days during the period 9 through 18 September. The normal procedure was for the USAF WC-130 to depart Ramey AFB about 0900 local to scout the assigned operating areas for suitable cloud



Figure I-2. Cessna 401(20Q) in flight over NAVSTA Roosevelt Roads, Puerto Rico (STORMFURY Cloudline Experiments, September 1969).

groups. When these were located, within a range of 100 to 250 n miles to the northeast or southeast of Roosevelt Roads, the WC-121N's and DC-6's departed to take up their stations and establish radar surveillance and traffic control patterns (WC-121N's at 4,000 and 7,000 ft, on racetrack paths parallel to and to either side of the cloudline) and instrumented penetration and photographic tracks (DC-6's at cloud base and 18,000 ft, in a squared "figure-eight" around and through the target group). The first 401 departed the base shortly afterward, rendezvoused with the other aircraft once the latter's pre-seeding flight patterns had been established, and spent 60 to 90 minutes alternately seeding updrafts and growing cells at 18-19,000 ft (-5°C to -7°C) and withdrawing to clear the area for penetration by the upper-level DC-6. If conditions warranted, the second 401 was called out from Roosevelt Roads about 90 minutes after the first, and either continued seeding the selected group or joined the other aircraft at a newly selected target. The two 401's participated in six (20Q) and five (21Q) missions, flying a total of 30.5 hours, normally carrying three Project officials and observers each. Approximately 125 STORMFURY III flares were fired into cloudline targets. In addition to seeding and indoctrination in seeding procedures, the 401's provided photographic and visual coverage of the experiment and aided in target selection. Only limited use of the instrument package installed aboard 20Q was made, but the potentialities of the system and procedures for its maintenance and use under field conditions were established. Otherwise, aircraft performance was excellent, only one mission being aborted due to a pyrotechnic rack wiring problem aboard 20Q; 21Q was, however, able to take over and complete the mission. In addition, both 401's were used on a stand-down day for a 1.5-hour air-to-air photography mission, yielding valuable motion picture footage which has since been incorporated in NWC documentary films. The aircraft were also used for several logistic flights to transport personnel and equipment between Roosevelt Roads and San Juan.

Operationally, the cloudline experiments were regarded as entirely successful in achieving their primary purpose of establishing the flight patterns, and communications and control procedures to be used in future STORMFURY operations. Additionally, valuable meteorological data were secured on the behavior of natural and artificially modified linear cloud arrays similar to hurricane rainbands. Finally, most of the key personnel in the STORMFURY program were directly exposed to Navy developed procedures for selecting and seeding individual clouds, which would not have been possible with the high-performance A6 jet seeder aircraft. The success of the cloudline experiments was thus due in no small measure to the availability and capabilities of 20Q and 21Q (Project STORMFURY Annual Report, 1969).

1970 DRY-RUN/CLOUDLINE OPERATIONS

For 1970, the STORMFURY Cloudline exercises were scheduled for the period 24-31 July, immediately following the dry-run exercises 20-23 July at Naval Station Roosevelt Roads (Project STORMFURY Operation Order No. 1-70). During the previous year, one of the NOAA DC-6's (39C) as well as the B-57 had been equipped to dispense STORMFURY pyrotechnic flares of the WMU-2 type, while the DC-6 additionally carried an RFF-developed acetone-burning nucleant generator. It was therefore decided that only one Cessna 401 (21Q) would be brought by the NWC staff, equipped for air-dropped flares but without a data-collecting system in order to retain maximum seating space. The Cessna arrived in Puerto Rico on the evening of Wednesday, 23 July. On the 24th and 25th it flew four training missions, during which various military and civilian personnel involved in ordnance development, seeding, and operational activities connected with STORMFURY received intensive indoctrination in seeding procedures. On the 26th, a project stand-down day, members of the NWC staff flew an experimental mission to test two newly developed types of air-dropped flares under consideration for future STORMFURY applications. On the 27th, 28th, and 29th, 21Q participated in cloudline experiments together with the two DC-6's, the B-57, two WC-121N's, and the WC-130. On the evening of the 29th, the Cessna departed for China Lake, to meet other commitments. In summary, 21Q made a total of eight training and experimental flights, for a total duration of 17.7 hours, during which approximately 80 rounds of various types of pyrotechnic flares were fired. In addition, several photographic and logistic flights were conducted. These light aircraft thus once again provided a significant contribution to STORMFURY training and experimental activities.

CONCLUSIONS

Experience with the use of light aircraft in connection with STORMFURY activities, as cited above, leads to certain conclusions regarding their utility in the following fields:

(a) *Training.* NWC-sponsored light aircraft provided training in seeding techniques pertinent to the hurricane environment for key STORMFURY personnel during one flight in 1968 and four in 1970, in connection with the dry-run exercises. The cloudline experiments in 1969 and 1970 provided further opportunities for such indoctrination. This was accomplished at much lower cost (\$50 per flight hour for the single-engined 210, and \$100 per hour for the 401 twin), and

with much greater flexibility than would have been the case had the larger aircraft employed in STORMFURY hurricane operations been used for this task. This use should definitely be continued during future STORMFURY seasons.

(b) *Independent Experiments.* As exemplified by the pyrotechnic tests conducted on 26 July 1970 and by some of the tests carried out during the 1969 and 1970 cloudline exercises, these light aircraft are ideal for preliminary testing of novel seeding materials and techniques, operating either alone, or in conjunction with at most, two other aircraft. It is essential that such tests be planned to permit maximum flexibility in operations, since the results obtained have only limited predictability. Such tests will undoubtedly be carried out in future seasons, as new nucleant-generating systems are developed.

(c) *Organized Experiments.* The utility of the light aircraft in complex, preplanned operations involving several other airplanes is more limited, although still substantial. Although the Cessna 210 and 401 aircraft have performance capabilities not significantly inferior to the DC-6's and WC-121N's and superior in the case of altitude, their limited flight duration (4½ to 5 hours for over-water operations with a full passenger load, and 2 to 3 hours of oxygen for high altitude flight) requires their use in relays (as in 1969, and with the B-57 in 1970) for protracted experiments. Similarly, their maximum effective operating radius at sea of approximately 250 miles, when coupled with the requirement that experimental activities be conducted at least 100 n miles at sea (to avoid complications inherent in the use of controlled airspace) limits their usefulness when suitable clouds are scarce. It should be noted, however, that high-performance aircraft such as the A6 and B-57 are similarly limited in flight duration, although not in range. Available navigation and radio equipment (VHF only) are also unsuited for long range use at sea. Within these limitations, however, continued use of light aircraft in cloudline experiments appears desirable.

(d) *Hurricane Operations.* It is doubtful whether light aircraft of this class would be of any utility in an actual hurricane seeding operation, except possibly in a situation in which outlying rainbands pass relatively close to a suitable operating base.

(e) *Miscellaneous.* On many occasions during the last 3 years, the NWC-provided aircraft provided an inexpensive, rapid, and flexible means for transporting personnel and equipment. They also proved highly effective in obtaining photography for both documentation and data assessment purposes.

It thus appears that continued use of at least one light aircraft (preferably twin-engined for safety and performance reasons) is desirable for future STORMFURY seasons, at least in connection with dry-run, cloudline and equivalent activities. The Naval Weapons Center, plans to continue providing this capability.

REFERENCES

- Simpson, J., et al. (1965): *STORMFURY Cumulus Seeding Experiment, 1965*, Preliminary Summary, Project STORMFURY Report No. 1-65. U.S. Navy/Weather Bureau, 1 November.
- STORMFURY Staff (1966): *Project STORMFURY Annual Report, 1965*. U.S. Dept. of Navy and U.S. Dept. of Commerce.
- STORMFURY Staff (1967): *Project STORMFURY Annual Report, 1966*. U.S. Dept. of Navy and U.S. Dept. of Commerce.
- STORMFURY Staff (1968): *Project STORMFURY Operation Plan No. 1-68*. U.S. Fleet Weather Facility, Jacksonville, Florida. p. D-1.
- STORMFURY Staff (1969): *Project STORMFURY Operation Plan No. 1-69*. U.S. Fleet Weather Facility, Jacksonville, Florida. p. G-1.
- STORMFURY Staff (1970): *Project STORMFURY Annual Report, 1969*. U.S. Dept. of Navy and U.S. Dept. of Commerce.
- STORMFURY Staff (1970): *Project STORMFURY Operation Order No. 1-70*. U.S. Fleet Weather Facility, Jacksonville, Florida. pp. D-I-1, D-V-1.

APPENDIX J

USE OF ECHO VELOCITIES TO EVALUATE HURRICANE MODIFICATION EXPERIMENTS

Peter G. Black

National Hurricane Research Laboratory

ABSTRACT

Echo velocities computed from airborne radar at six time intervals over the entire storm before and during the seeding of Hurricane Debbie on 20 August 1969, reveal that mean echo speeds equaled or exceeded cyclostrophic winds computed from 12,000-ft. D-value data as well as measured 12,000-ft winds after a correction for water motion was applied. In the time period from just before seeding began to just after seeding ended, azimuthal mean echo speed increases ranging from 30 knots at the 100 n mile radius to 10 knots in the outer eyewall were found. In this same period, the mean echo crossing angle changed from 5 degrees inward to 5 degrees outward at the 100 n mile radius. Deviations about the azimuthal mean echo speed and crossing angle indicated that wave number 2 accounted for nearly all of the variance around the storm's circumference at all radii. The deviations remained fixed in time between radii of 25 and 150 n mile, but rotated with the major axis in the inner and outer eyewalls. It is suggested that these echo motions approximate the air flow in the lower levels of the hurricane.

INTRODUCTION

For some time attention has been focused on the symmetrical features of the hurricane circulation, with the only asymmetry on the scale larger than that of the rainbands being introduced by the motion of the storm. Aircraft and ship data collected in storms have been too sparse in space and time to

adequately describe other asymmetries of these larger scales. Considerable time variation in wind speed profiles on the rainband scale and smaller through several hurricanes has been measured. This has been attributed to the "natural variation" in storm intensity. However, it is a distinct possibility that the time change in these wind speed profiles can be partly due to the advection of horizontal asymmetries. Furthermore, in hurricane modification experiments, the possibility exists that the seeding location relative to horizontal asymmetries may have an important bearing on the outcome of the experiment.

Therefore, in this report, an attempt has been made to define the low-level asymmetries in a hurricane and their change with time using the motion of small precipitation echoes. Ten-minute time periods were used to define a motion field over a portion of the hurricane circulation within 150 n miles of the storm center. Several of these time periods were composited to give an average 1-hour motion field over the entire hurricane circulation. Radial and azimuthal profiles of the echo speed and crossing angle were constructed for 6 one-hour time periods. These profiles were compared with aircraft wind measurements where they were available.

Many authors have computed echo velocities in hurricanes and attempted to relate these velocities to winds at a particular level. Ligda (1955) used land based radar in Florida to compute echo velocities in the hurricane of 23-28 August 1949. He coined the term "spawinds" to refer to the motion of isolated convective cells since he said they correlated well with the 700 mb winds. Senn et al. (1960a, 1960b) and Senn (1963, 1965) have done extensive work on the calculation of echo velocities within Hurricanes Edna of 1954; Connie, Diane, and Ione of 1955; Audrey of 1957; Daisy and Helene of 1958; Debra of 1959; and principally, Donna of 1960. He found systematic variations in echo velocity with azimuth around the storm, with day vs. night, with land vs. sea, with storm speed, and with echo crossing angle. Senn compared echo velocities with aircraft winds and found that in general the echoes moved slower than the winds at all levels. Watanabe (1963) computed echo velocities in Typhoon Nancy of 1961 from a ground based radar on Okinawa. He found very good agreement between the echo velocities near rawinsonde stations and the mean wind between cloud base and cloud top.

Fujita (1959) used airborne radar to compute echo velocities in Hurricane Carrie of 1957. His technique involved placing each radar photograph at the aircraft position given by the Doppler navigation system and then tracing the successive position of various radar echoes. However, any error in

the Doppler fix will result in an error in the echo velocity. Jordan (1960) also used airborne radar to compute echo velocities in Hurricane Daisy of 1958. He used the hurricane center as a reference point for his calculations. He noted relatively good agreement between his echo velocities within the eyewall region and aircraft measured winds at 13,000 ft.

The above authors have shown that no unique relationship appears to exist between echo velocities and winds at a particular level. This may appear to be a severe limitation in using echo velocities to evaluate hurricane seeding experiments. However, the data presented in the next section will show that this shortcoming is not so bad as it may seem, especially when the proposed mechanism governing echo motion, presented in a later section, is taken into consideration.

DATA ANALYSIS

In this study, airborne radar data collected during the seeding experiment in Hurricane Debbie, 20 August 1969, were used. Echo velocities over a 10-minute period were computed from primarily the Air Force APS-64, 3-cm radar on board a WB-47 flying at 39,000 ft. Echo velocities were also computed from the Navy APS-20, 10-cm radar on board a WC-121N flying at 1,000 ft. See Black et al. (1971) for the specifications of these radars. Fujita's movie-loop technique was used to construct picture sequences using airborne radar photographs taken at 30-sec intervals which had been registered with respect to the hurricane center and true north. This technique yields extremely accurate results since 30 sec continuity on the echo motion can be obtained, and any errors in positioning the photographs with respect to the same fixed point and orientation (namely the hurricane center and true north, respectively) will be immediately obvious by a jump in the echo position when projected in movie form on a screen.

Short period oscillations in the storm speed during the 10-minute interval used for computing echo velocities are not thought to be large enough to bias the echo velocities by more than 1 or 2 knots. Senn (1965) has indicated average fluctuations in the speed of Hurricane Donna on the order of about 5 knots in 1 hour with maximum fluctuations on the order of 10 knots in 1 hour. Such fluctuations were not detected in the motion of Hurricane Debbie. However, errors in aircraft navigation and eye location were such that they could have existed.

Usually, four or five 10-minute average echo velocity fields were composited to obtain the echo velocity field characteristic of a 1-hour time interval. The short period storm motion fluctuations should be sufficiently random to cancel out when the 1-hour composites are compared with each other.

ECHO VELOCITY PROFILES

One-hour echo velocity composites were prepared for the time periods 1100-1200Z, 1600-1700Z, 1700-1800Z, 1800-1900Z, 1900-2000Z, and 2000-2100Z. Usable data were not available for any other time periods. The above times cover a period from 1 hour before seeding began (about 1200A) to 1 hour after seeding ended (about 2000Z).

The storm was divided into four quadrants defined by perpendicular lines oriented 45 degrees to the left and right of the storm motion vector (310 degrees in this case). All the echo velocity vectors within each quadrant were then composited into radial profiles of speed and crossing angle (defined as positive inward). The resulting scatter diagrams for selected time periods are shown in figures J-1 to J-3. The mean scatter was about 10 knots for the speed and about 10 degrees for the crossing angle, which is well within the scatter that would be introduced by short period fluctuations in the storm speed. A portion of this scatter (perhaps half) can be accounted for by azimuthal variations in echo velocity as will be seen in a later section.

Relative wind profiles measured by RFF aircraft at 12,000 ft as well as computed cyclostrophic wind profiles were superimposed, where available, in the left and right quadrants. The cyclostrophic winds were computed from

$$C = \sqrt{rg \frac{\Delta D}{\Delta r}} \quad (J.1)$$

where r is the radius from the storm center, Δr was chosen as 2 n miles, and ΔD was the D-value gradient which was subjectively smoothed. Relative winds based on reports from Navy aircraft at 1,000 ft, 6,000 ft, and 10,000 ft are also plotted where available.

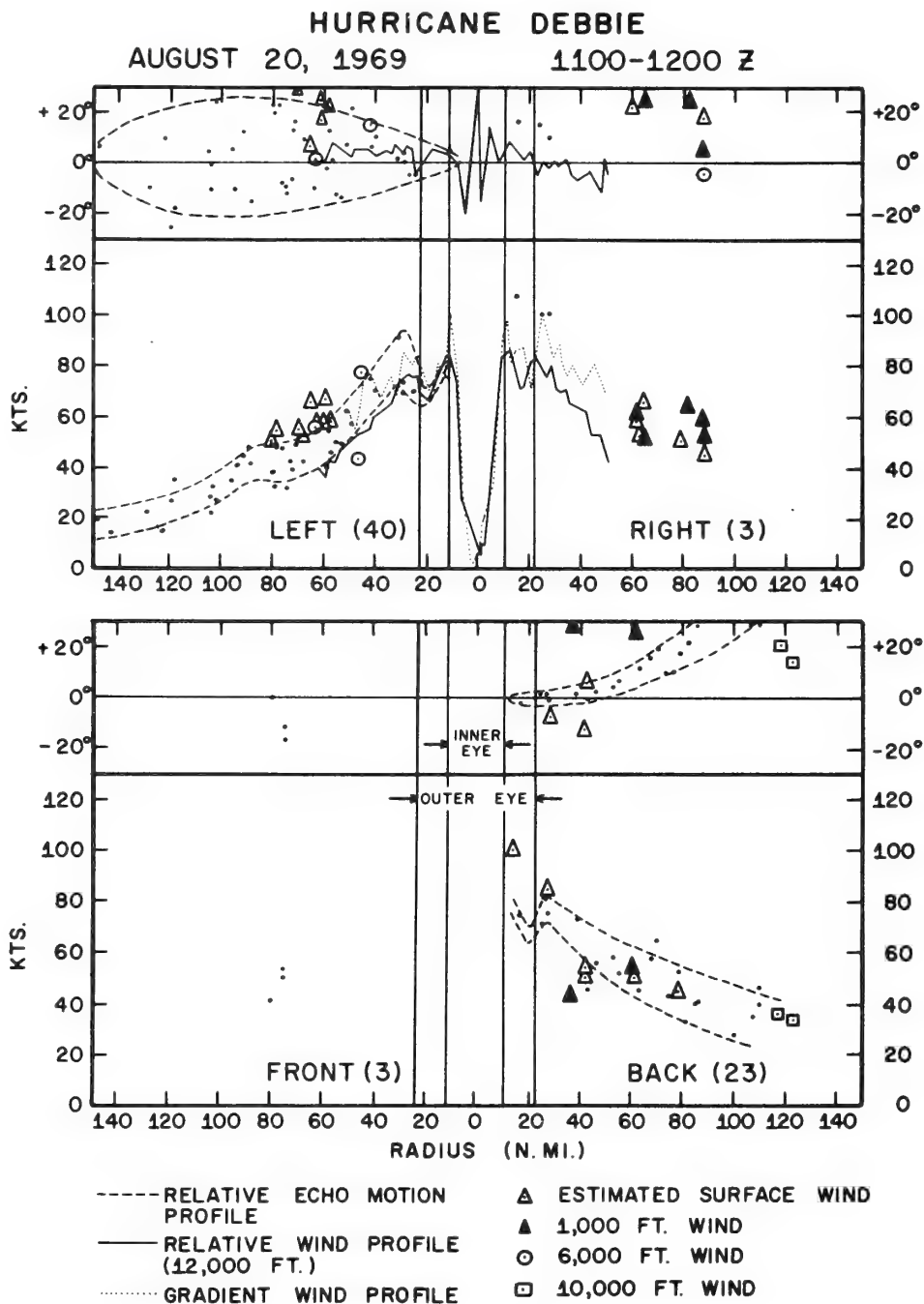


Figure J-1. Relative echo speed (bottom panel) and crossing angle (top panel) profiles compared with relative 12,000-ft wind and cyclostrophic wind profiles, as well as scattered surface, 1,000 ft, 6,000 ft, and 10,000 ft relative wind reports for 1100 to 1200Z, 20 August 1969. The vertical lines indicate the inner edges of the inner and outer eye-walls.

HURRICANE DEBBIE

AUGUST 20, 1969 1600-1700 Z

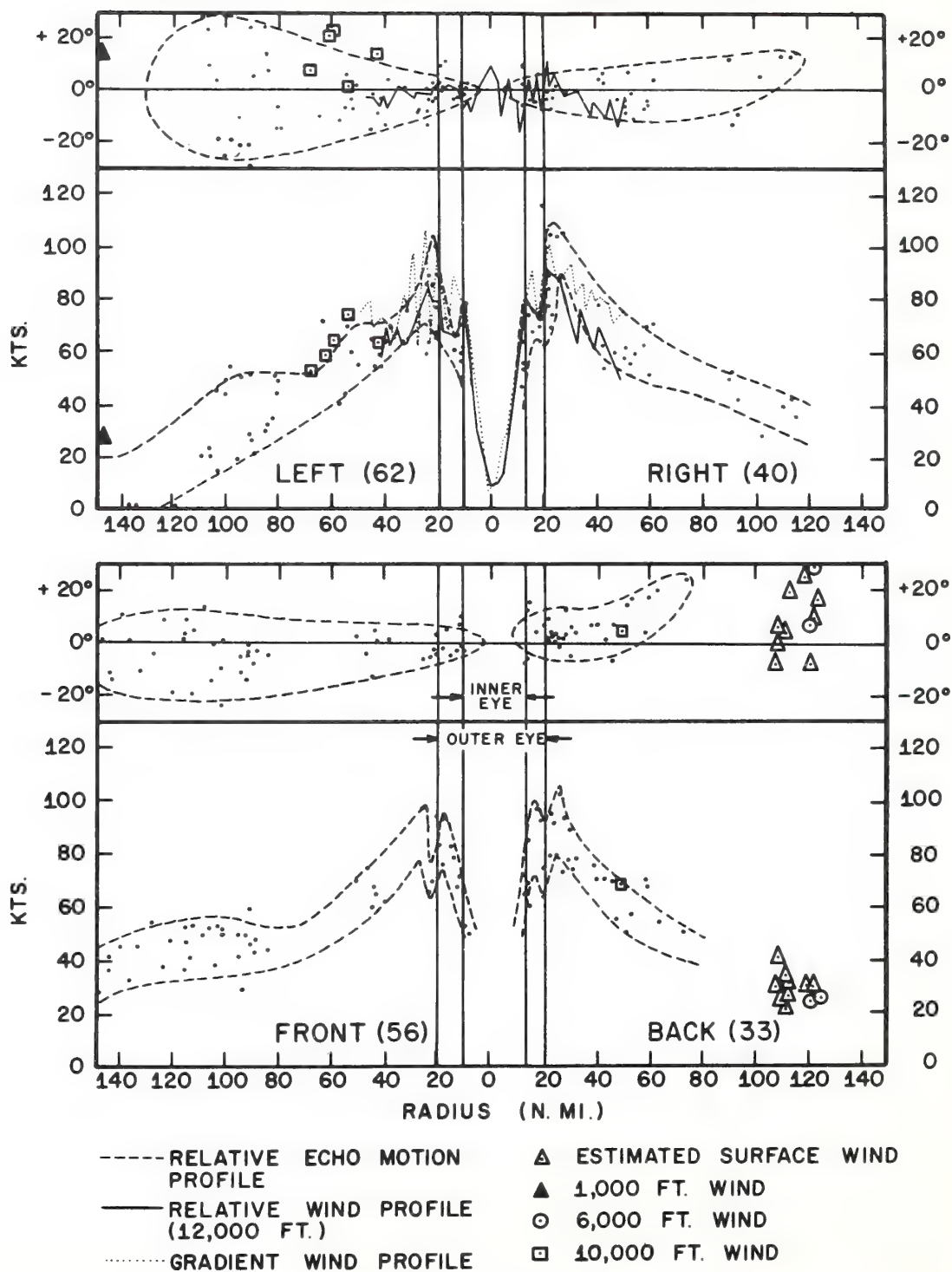


Figure J-2. Same as figure 1 except for the time period from 1600 to 1700Z, 20 August 1969.

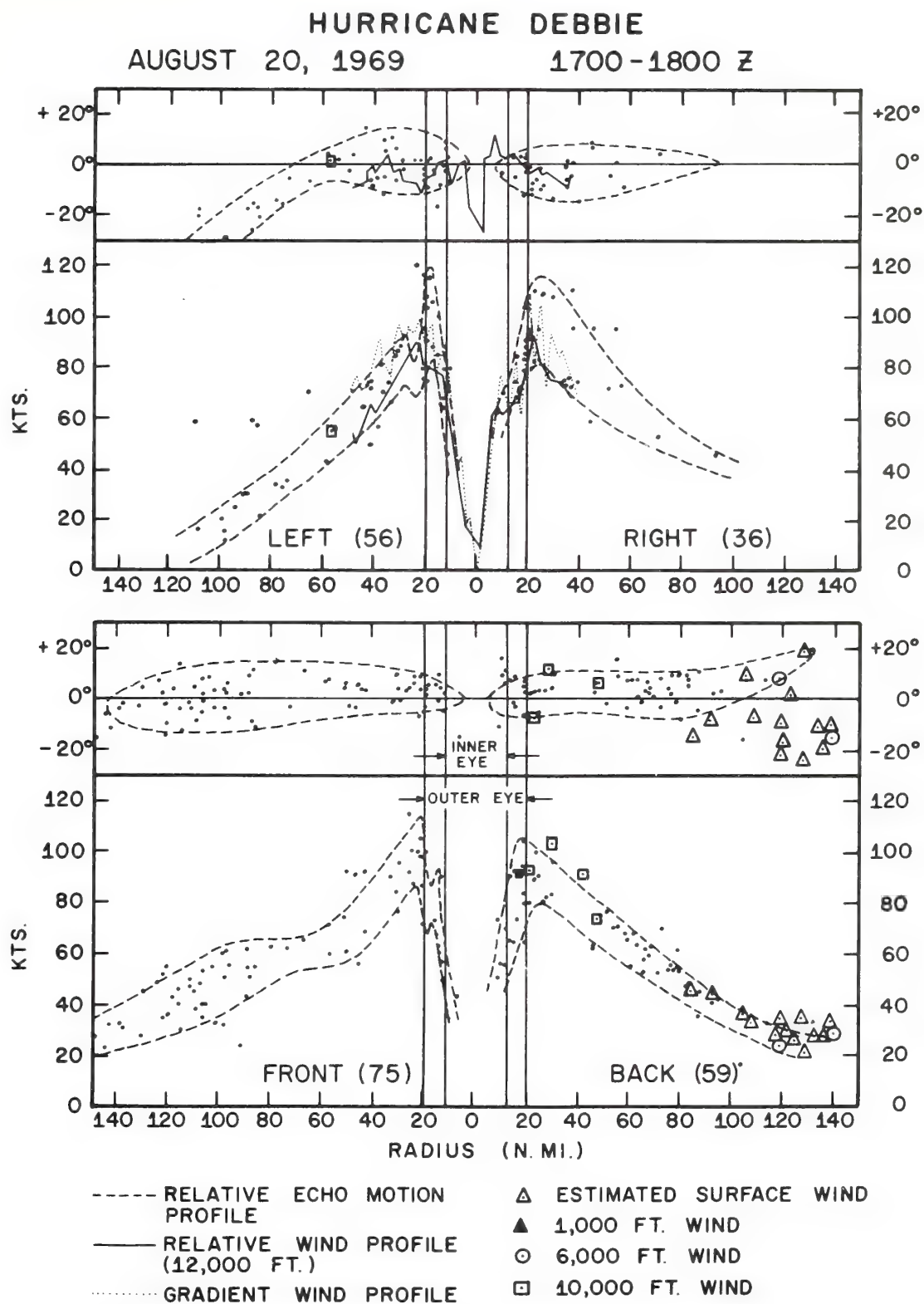


Figure J-3. Same as figure 1 except for the time period from 1700 to 1800Z, 20 August 1969.

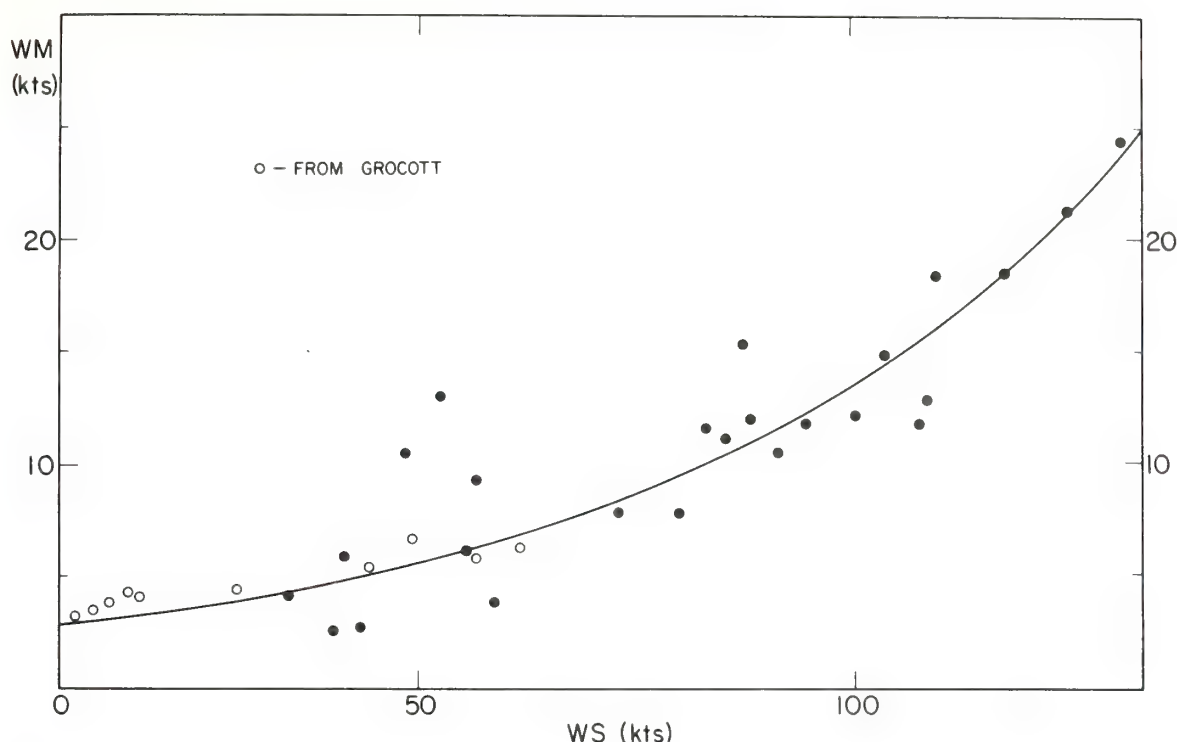
The mean location of the inner edge of the inner and outer eyewalls during the hour is indicated by the vertical lines. Seeding times, radii, and azimuths are given in table J-1.

The results indicate that the mean relative echo speeds are generally in balance with the cyclostrophic winds at 12,000 ft. However, in some cases, the relative echo speeds exceed the cyclostrophic winds by about 5 knots (e.g., left quadrant, 30-40 n miles radius, fig. J-1; and right quadrant, 30-50 n miles radius, fig. J-3). The measured relative winds at 12,000 ft appeared to be about 10 knots less than the mean relative echo speeds and the cyclostrophic winds out to a radius of 40 n miles. Where data are available beyond that radius, there appears to be much closer agreement between the profiles.

The discrepancy between the relative winds and the cyclostrophic winds might possibly be explained by the effects of the moving sea surface on the airborne Doppler radar used to measure the aircraft ground speed from which the winds are calculated. Figure J-4 represents an extension of Grocott's (1963) work by Black et al. (1967) in relating sea surface movement to wind speed. Using data from Hurricane Flora of 1963, the data of Grocott were extended to hurricane force winds. Figure J-4 indicates that for wind speeds ranging from 75 knots to 100 knots (corresponding to those measured within 40 n miles of Hurricane Debbie) a water motion of from 5 to 10 knots or more would be possible. The water motion has been shown to be nearly parallel to the wind out to at least twice the radius of maximum wind (22 n miles in the case of Debbie). The Doppler winds would thus be an underestimate of the true wind by 5 to 10 knots or more within 40 n miles of the storm center. When this correction is applied, the relative measured winds become equal to and in some cases slightly greater than the cyclostrophic winds.

Table J-1. Seeding Times and Locations for Hurricane Debbie, 20 August 1969.

Seeding Time (Z)	Range Interval (n miles)	Azimuth (from true North)
115630-115830	15-22	022-001
140140-140330	12-25	044-034
161345-161545	11-25	357-351
175750-175950	12-27	018-010
195350-195620	18-34	356-359



A time history of the mean relative echo speed and crossing angle profiles is given in figure J-5. The figure indicates that the echo speeds tend to increase with time at radii of from 40 to 150 n miles in all quadrants of the storm. The increase was on the order of 10 to 20 knots. This result is consistent with the results of Hawkins (1971) which indicated an increase in the winds in the left quadrant at radii from 75 to 200 n miles of 10 to 15 knots from well before to well after the seeding experiment. This result is further substantiated by the time change of the azimuthal mean echo speed given in a later section.

It should be noted that the echo speeds fall off most rapidly in the left quadrant, reaching a mean value of about 10 knots at 150 n miles radius. A sharp shear line has been shown to exist in this quadrant at radii larger than 150 n miles by the low-level streamline analysis of Fujita and Black (1970), based on low cloud motions. The echo speeds fall off to about 30 knots at 150 n miles radius in the right and back quadrants. This result is also illustrated clearly in the azimuthal profiles.

Figure J-5 also shows that the crossing angle becomes more negative with time in all quadrants, indicating the echoes are tending to move outward more as time progresses. Of special note is the change evident in the back quadrant where crossing angle changes from 20 degrees inward at 75 n miles radius before seeding to 15 degrees outward after seeding are evident.

These results tend to be in the sense anticipated by the numerical modification experiments of Rosenthal (1971) which predicted an increase in the winds outside the seeded eyewall region, even as the maximum wind was reduced and moved outward. Therefore, these results appear to support the contention that a modification of Hurricane Debbie was indeed achieved.

A POSSIBLE MECHANISM GOVERNING ECHO MOTIONS IN A HURRICANE

Some clarification is needed concerning the mechanism responsible for the observed echo velocities. It was mentioned earlier that in some cases, agreement was found between echo speeds and the 700 mb winds. This is probably fortuitous. Watanabe (1963) has suggested, using rawinsonde data, that echo velocities agree best with the mean wind between the echo base and the echo top, which Senn (see app. K) has shown is generally not much higher than 30,000 ft. This

HURRICANE DEBBIE - AUGUST 20, 1969

TIME HISTORY OF ECHO MOTION PROFILES

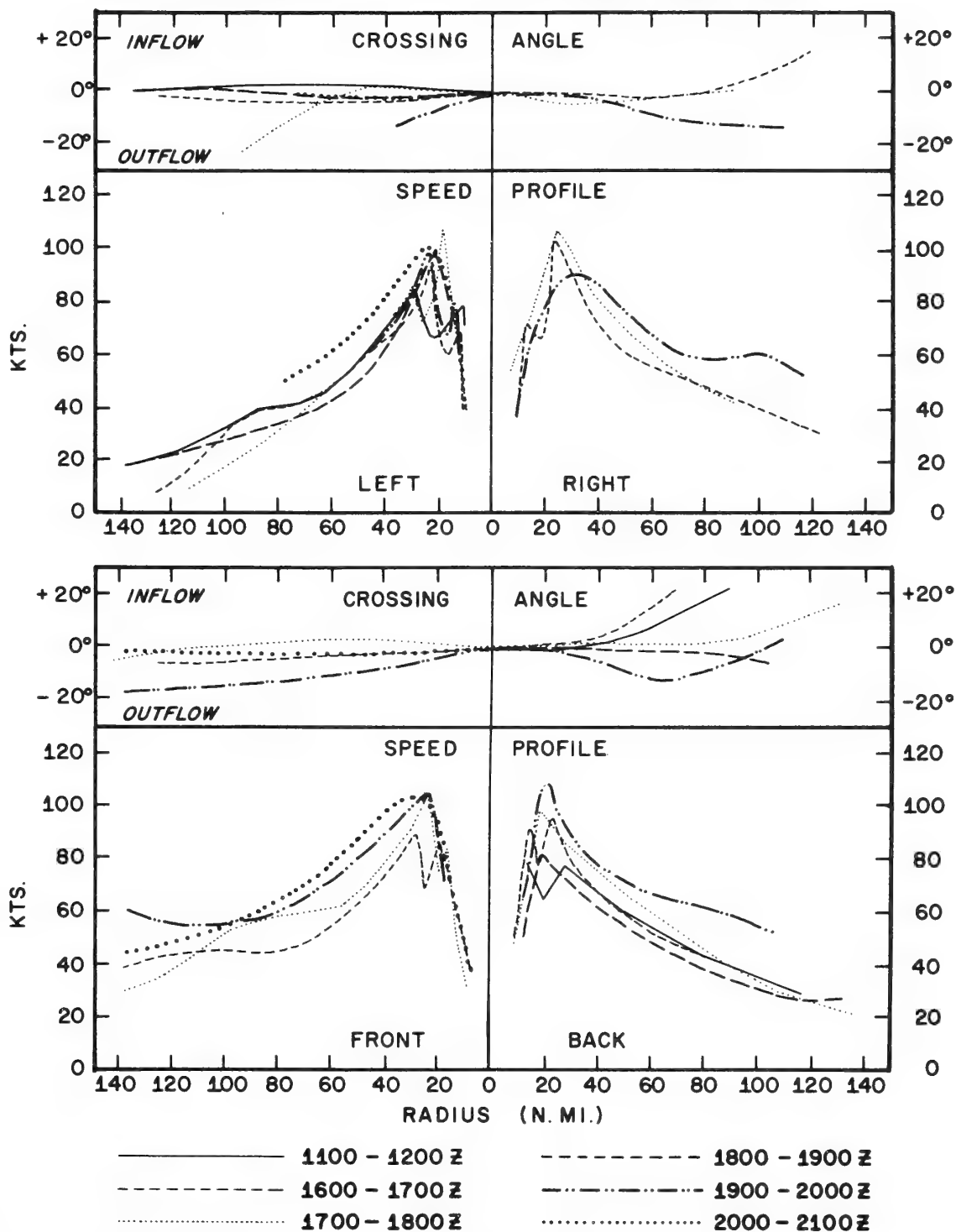


Figure J-5. Time change of echo speed and crossing angle profiles for four quadrants of Hurricane Debbie.

mean wind, in many cases, appears to be nearly that at 10,000 ft (about 700 mb). However, Senn (1965) has observed that in general, echoes move fast early in their lifetime and slower later in their lifetime. Watanabe, in order to account for the scatter in his data about the 700 mb wind, suggests he was observing echo velocities at different stages in their lifetime, and hence moving at different velocities.

It is now suggested that the reason for the above reported behavior could be that the growing echo, sustained by a substantial vertical velocity (probably greater than 10 m sec^{-1}), moves with the horizontal momentum of the inflowing air near cloudbase. Even though the vertical profile of the echo may be tilted, due to vertical wind shear, the echo boundary, as outlined by Gentry et al. (1970), will still move with the low-level wind speed as long as the vertical velocity is sustained. In fact Senn (1966) and Black et al. (1971) have used the vertical tilt of radar echoes to infer the shear, assuming precipitation particles were falling at their terminal velocities. Therefore, at all levels in which the radar is observing actively growing convective echoes, the echo boundary of an actively growing echo will move with the low-level speed. The present data indicate this since most of it was taken from an aircraft at 39,000 ft, and the resultant echo velocities agreed best with the low-level winds. The echo motion data of Jordan (1960), which were representative of the level from 20,000 to 30,000 ft, also tended to agree better with the lower-level winds.

In the case of precipitation falling through weak diluted updrafts (on the order of 1 or 2 m sec^{-1}), the tilt of the echo would still be in the same sense as outlined in the above paragraph, but more tilted. In this case, the echo boundary could be expected to move with nearly the speed of the wind at the precipitation generating level. However, this type of echo tends to be more diffuse than the actively growing one and hence harder to follow. Therefore, most of the echoes used in this study were most probably near their mature stage.

If the above argument is valid, most of the echoes probably represent the flow in the inflow layer, modified slightly by entrainment. Trends in the mean echo velocities in particular quadrants or range intervals should therefore indicate trends in the low-level flow field. Deviations from the mean echo velocities around the circumference of the storm at different radii are then a measure of the asymmetries in the low-level flow.

THE LOW-LEVEL ASYMMETRIC STRUCTURE OF HURRICANE DEBBIE AS REVEALED BY ECHO VELOCITIES

Study of the variation in echo velocity with azimuth in Hurricane Debbie is presently underway. Preliminary results indicate the following:

- (1) The mean echo speeds around the circumference of the storm at range intervals of 18-28 n miles (outer eyewall), 28-50 n miles, 50-75 n miles, and 75-150 n miles increased with time as shown in figure J-6. Increases from $\frac{1}{2}$ hour before seeding began until $\frac{1}{2}$ hour after seeding ended ranged from 30 knots at the outermost range interval to 10 knots in the outer eyewall. The echo speeds decreased in this time period in the range interval from 10-15 n miles (inner eyewall) by about 20 knots.
- (2) Superimposed on the upward trend beyond the inner eyewall was a shorter period fluctuation, indicated by the thin solid lines on figure J-6. At each range interval, a 5-10 knot increase appeared to follow each seeding followed by a slightly smaller decrease until the next seeding, when another increase occurred. Therefore, there appear to be three time scales of echo motion: (a) the long period trend over several hours, (b) the shorter period fluctuations with a period of an hour or two, and (c) the deviations about the mean with a period of less than 1 hour.
- (3) The echo speed deviations from the mean averaged about 11 knots. At the two outer range intervals, the deviations increased with time. At the three inner range intervals, the deviations decreased with time.
- (4) The mean crossing angle around the circumference of the storm decreased at all range intervals, indicating less inflow in the time period studied. This is shown in figure J-7. The largest decrease occurred in the outer range interval where a change of from about 5 degrees inward to about 5 degrees outward was measured. At the other range intervals the decrease was about 5 degrees inward to about zero. The average maximum deviations from the mean generally tended to decrease during the time period studied. The average maximum deviation during the time period was about 8 degrees, the largest deviations occurring at the outermost range interval.

HURRICANE "DEBBIE" AUGUST 20, 1969

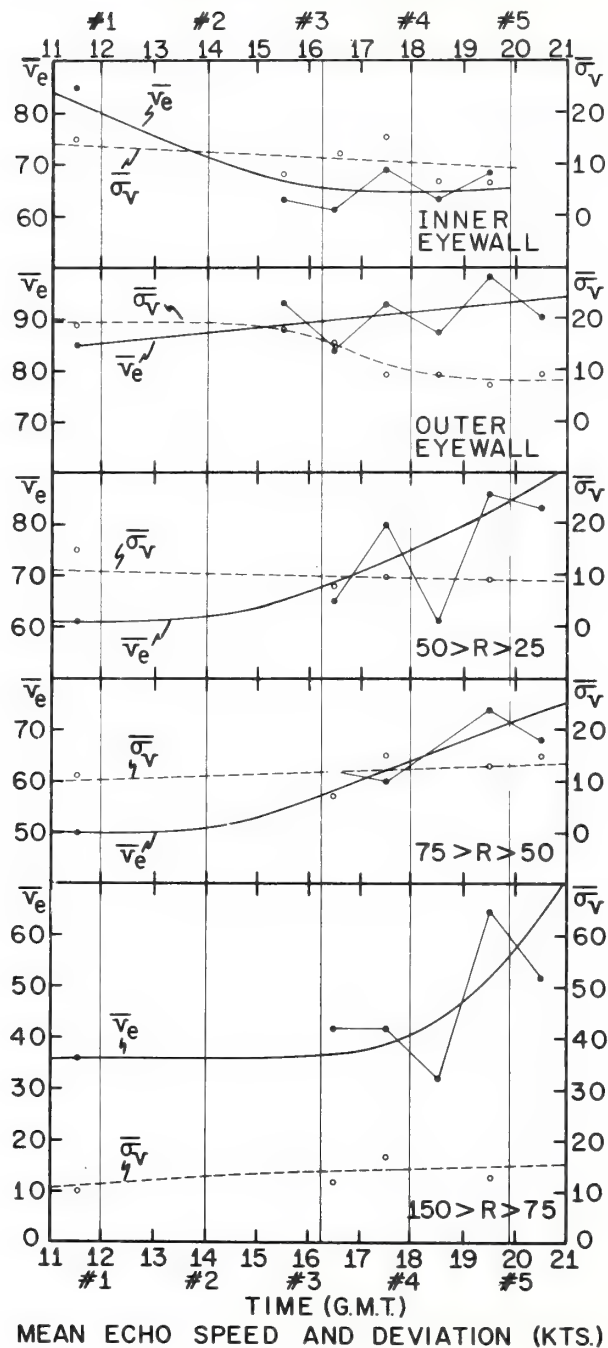


Figure J-6. Azimuthally averaged echo speeds at selected range intervals together with the mean maximum deviations about the azimuthal mean. Scale for the mean values (solid circles) is on the left and the scale for the deviations (open circles) is on the right. The thin vertical lines indicate the seeding times.

HURRICANE "DEBBIE" AUGUST 20, 1969

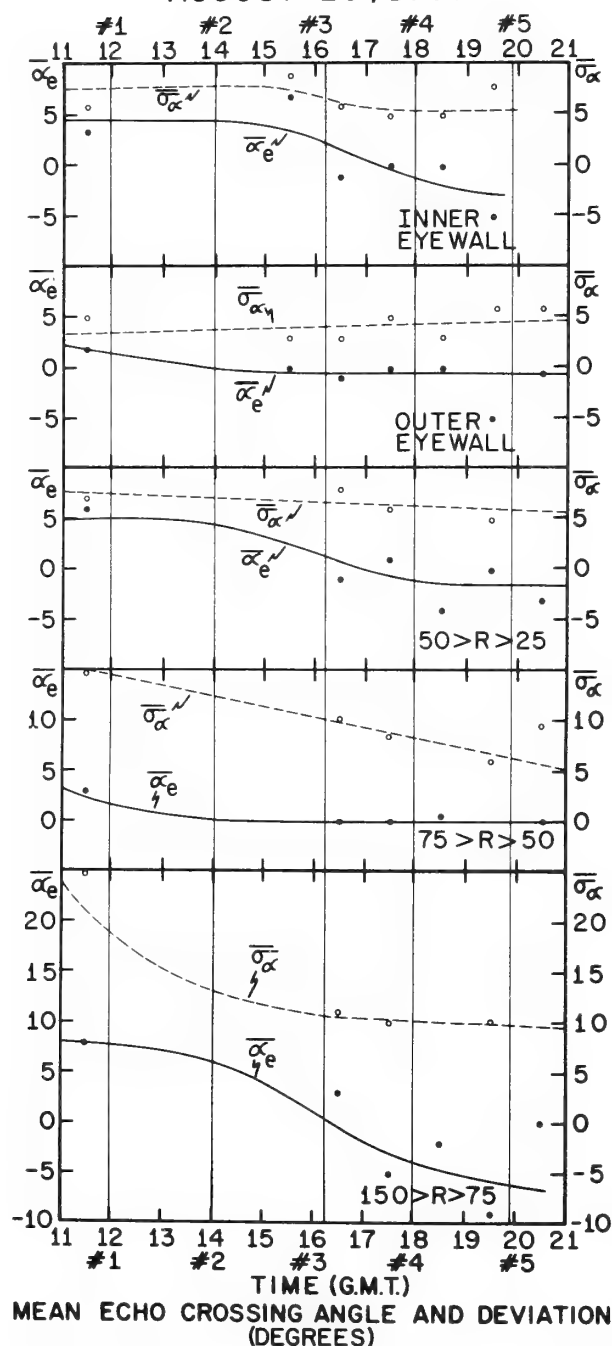


Figure J-7. Azimuthally averaged echo crossing angles at selected range intervals together with the mean maximum deviations about the azimuthal mean. Scale for the mean values (solid circles) is on the left and the scale for the deviations (open circles) is on the right. The thin vertical lines indicate the seeding times.

- (5) When the echo speed deviations from the mean were plotted as a function of azimuth, wave number 2 appeared to be the dominant wave number at all radius intervals and time periods studied. This was true also when the crossing angle deviations were plotted as a function of azimuth.
- (6) The general tendency was for the positive echo speed deviations in the outer three range intervals to be located in the front and right rear quadrants with negative deviations in the right front and left quadrants, as shown in figure J-8.
- (7) The phase of the crossing angle deviations was almost exactly one-half wavelength out of phase with the speed deviations in each of the outer three range intervals. This meant that negative crossing angle deviations (outward moving echoes) were most common in the left front and rear quadrants, with positive crossing angle deviations (inward moving echoes) located in the rear and right front quadrants. This means that the speed maxima and minima are located at the position of zero crossing angle. Likewise, the maximum inward and outward crossing angles occur at the mean echo speed. Furthermore, as the echo speed is decelerating downstream the crossing angle is outward, and as the echo speed is accelerating downstream, the crossing angle is inward.
- (8) Figure J-9 illustrates how the speed and crossing angle deviations around the inner and outer eyewalls tended to rotate cyclonically with time nearly matching the rotation rate of the major axis as described by Black et al. (1971). Following each of the last three seedings the relative location of the major axis, speed maximum, and crossing angle maximum changed as each decelerated by different amounts during the time period from 15 minutes after seeding to 1 hour after seeding and then accelerating, maintaining their new phases until the next deceleration. The significance of this is not known at present. However, it seems quite significant that, except for the period of about an hour after each seeding, the rate of rotation of the speed and crossing angle deviations nearly matches that of the major axis.
- (9) The relation between the phases of the speed and crossing angle deviations was not as clear-cut as the outer radius intervals, but generally the speed maxima corresponded with crossing angle minima (outward motion).
- (10) The faster moving, outward moving echoes in the inner and outer eyewall regions tended to be correlated with more solid looking echoes when compared with a PPI radar composite at the same time interval, while the slower moving, inward moving echoes tended to be correlated with the portion of the eyewall broken into individual cells, which tended to protrude into the eye occasionally. This

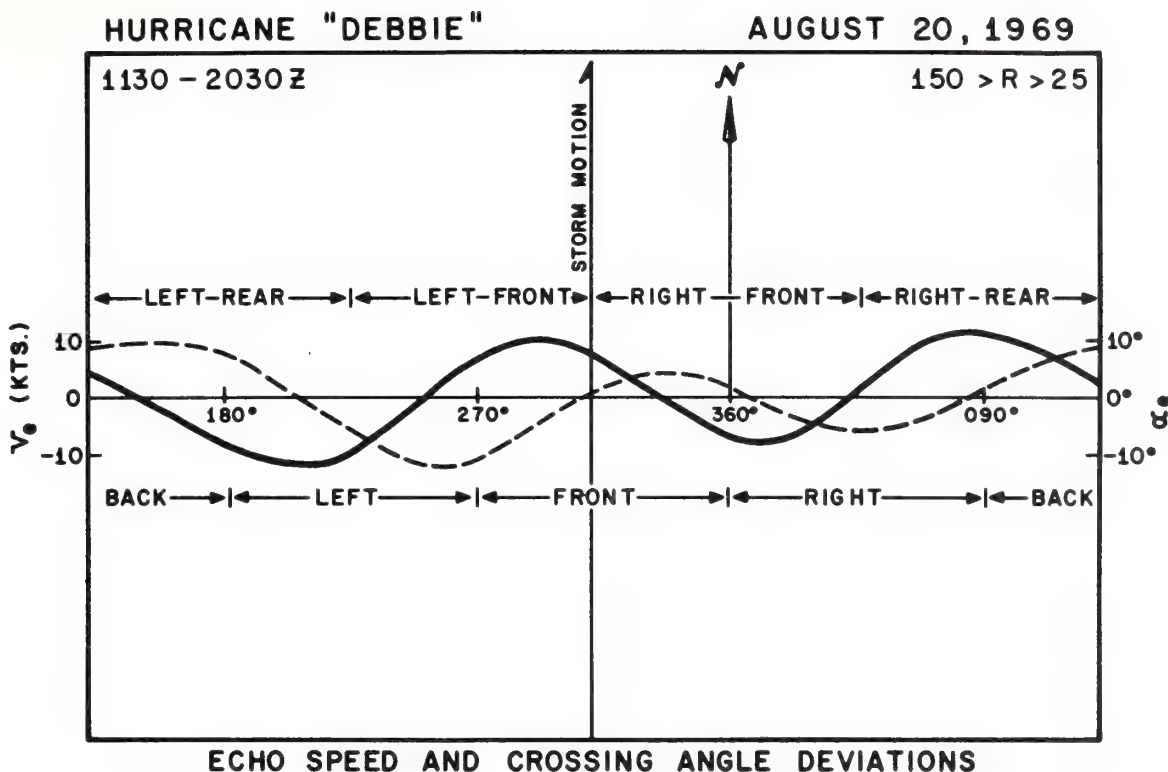


Figure J-8. Azimuthal variation of echo speed (solid curve) and crossing angle (dashed curve) beyond the eyewall during the time period studied.

result is in agreement with echo velocity analyses of the eyewall region of Hurricane Carrie by Fujita (1959), of Hurricane Daisy by Jordon (1960), and of Hurricane Celia by Fujita (1971).

CONCLUSIONS

Further study is needed relating the horizontal asymmetries in the low- and middle-level motion fields to the asymmetric structure of the radar echoes and their motion with time. It is anticipated that further study of the motion of radar echoes in a hurricane should yield relationships between preferred regions of convergence and divergence and the appearance of radar echoes at a given time, especially in the eyewall region. If such a relationship is forthcoming, it might greatly improve the implementation of hurricane seeding

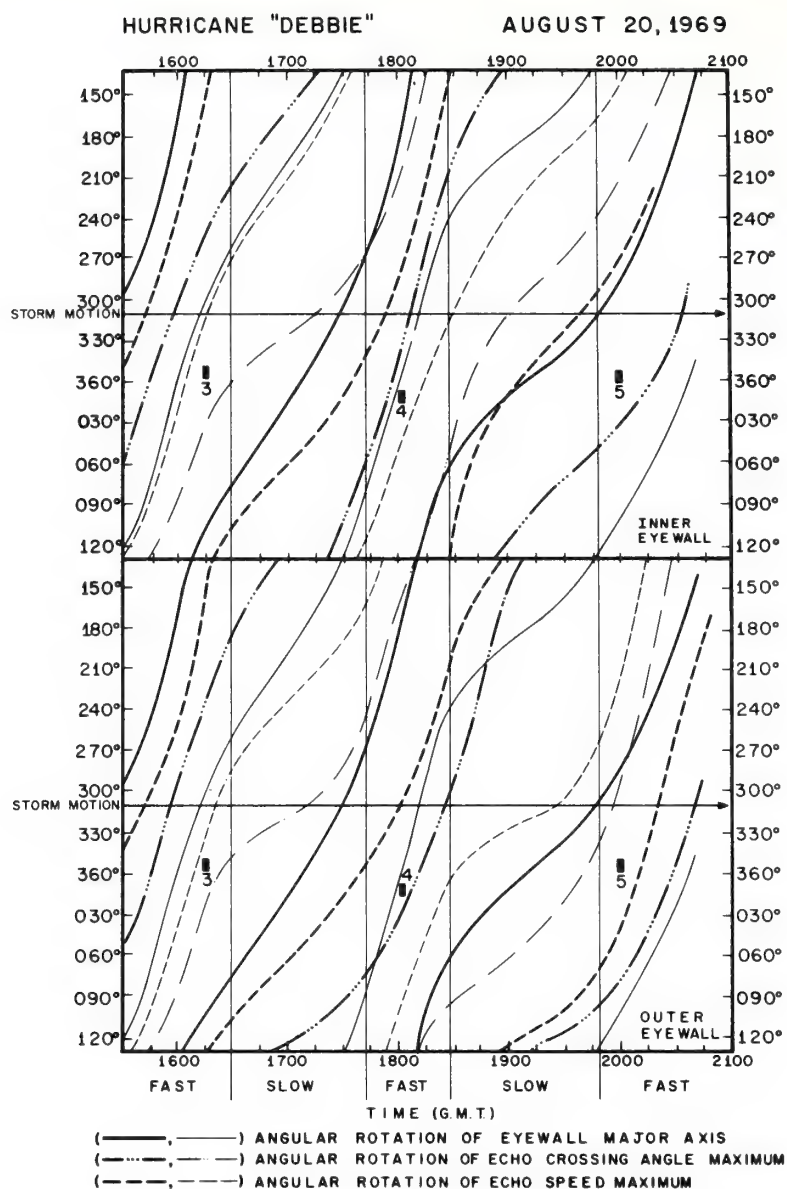


Figure J-9. Angular rotation of the eyewall major axis initially in the front quadrant together with the echo speed and crossing angle maxima initially just upstream from this major axis position are all indicated by thick lines. The position of the major axis initially in the rear quadrant together with the echo speed and crossing angle maxima just upstream are indicated by thin lines.

The top panel is the rotation rates for the inner eyewall and the bottom panel is the rotation rates for the outer eyewall. Black rectangles indicate the seeding time and location for the third, fourth, and fifth seedings. Thin vertical lines delineate the slow moving time periods following each seeding from the fast moving time periods.

experiments since the appearance of the eyewall region on radar could then be used to direct seeding aircraft to the locations where the seeding agent will be most effective.

REFERENCES

- Black, P. G., J. J. O'Brien and B. M. Lewis (1967): Ocean motion beneath a hurricane and its influence on the operation of airborne Doppler radar. Fifth Technical Conference on Hurricanes and Tropical Meteorology, Caracas, Venezuela, November.
- Black, P. G., H. V. Senn and C. L. Courtright (1971): Some airborne radar observations of precipitation tilt, bright band distribution and eye configuration changes during the 1969 multiple seeding experiments in Hurricane Debbie. Submitted to *Monthly Weather Review*.
- Fujita, T. T. (1959): A computation method of velocity of individual echoes inside hurricanes. Final Report CWB 9530, May, 7 pp.
- Fujita, T. T., and H. Grandoso (1968): Split of a thunderstorm into anticyclonic and cyclonic storms and their motion as determined from numerical model experiments. *Journal of Atmospheric Sciences*, 25, (3), May, pp. 416-438.
- Fujita, T. T. (1971): private communication.
- Gentry, R. C., T. T. Fujita and R. C. Sheets (1970): Aircraft, spacecraft, satellite and radar observations of Hurricane Gladys, 1968. *Journal of Applied Meteorology*, 9, (6), December, pp. 837-850.
- Grocott, D. F. H. (1963): Doppler correction for surface movement. *Journal of the Institute for Navigation*, 16, pp. 57-63.
- Hawkins, H. F. (1971): Comparison results of the Hurricane Debbie, 1969, modification experiments with those from Rosenthal's numerical model simulation experiments. *Monthly Weather Review*, 99, (5), May, pp. 427-434.
- Jordon, C. L. (1960): Spawinds for the eyewall of Hurricane Daisy of 1958. *Proceedings of the Eighth Weather Radar Conference*, April 11-14, pp. 219-226.

- Ligda, M. G. H. (1955): Analysis of motion of small precipitation areas and bands in the hurricane of August 23-28, 1949. *Technical Note No. 3*, Massachusetts Institute of Technology, 41 pp.
- Rosenthal, S. L. (1971): A circularly symmetric, primitive equation model of tropical cyclones and its response to artificial enhancement of the convective heating function. *Monthly Weather Review*, 99, (5), May, pp. 414-426.
- Ross, D. (1971): private communication.
- Senn, H. V. (1960): The mean motion of radar echoes in the complete hurricane. *Proceedings of the Eight Weather Radar Conference*, April 11-14, pp. 427-434.
- Senn, H. V., H. W. Hiser and R. D. Nelson (1960): Studies of the evolution and motion of radar echoes from hurricanes. Final report, U.S. Weather Bureau, *Report No. 8944-1*, August.
- Senn, H. V. (1963): Radar precipitation echo motion in Hurricane Donna. *Proceedings of the Third Technical Conference on Hurricanes and Tropical Meteorology*, June 6-12.
- Senn, H. V., and J. A. Stevens (1965): A summary of empirical studies of the horizontal motion of small radar precipitation echoes in Hurricane Donna and other tropical storms. *Technical Note 17-NHRL-74*, November, 55 pp.
- Senn, H. V. (1966): Precipitation shear and bright band observations in Hurricane Betsy, 1965. *Proceedings of the Twelfth Weather Radar Conference*, American Meteorological Society, October, pp. 447-453.
- Watanabe, K. (1963): Vertical wind distribution and weather echo (in the case of the typhoon). *Proceedings of the Tenth Weather Radar Conference*. April 22-25, pp. 222-225.

APPENDIX K

A SUMMARY OF RADAR PRECIPITATION ECHO HEIGHTS IN HURRICANES

Harry V. Senn

Rosenstiel School of Marine and Atmospheric Science
University of Miami

INTRODUCTION

In recent years the need for three-dimensional radar precipitation data in hurricanes has increased greatly. This is due partly to requirements of the National Weather Service for such information on existing storms, partly to satisfy the interests of those who must reconnoiter the storms with aircraft, but most importantly to fill gaps in the knowledge necessary for intelligent planning and execution of attempts to significantly modify hurricanes.

A large amount of height data and many case histories are available for various types of storms which occur over the United States because of the presence of radars capable of making observations. Some land-based RHI data on hurricanes exist for storms approaching or over land, but these cases are not typical of over-water situations in the tropics. Furthermore, such data are rarely obtained with radars having optimum vertical beamwidths (1 degree or less), transmitting frequencies, peak power, or data recording equipment. For instance, in several hurricanes which affected the southeast coast of Florida, each of the WSR-57 radars at Miami and Key West obtained only two or three Polaroid RHI photographs for later analysis. The sparsity of RHI data was due to lack of automatic data gathering equipment. During the same period, many days of routine, excellent PPI data were collected.

Unfortunately, RHI data for hurricanes farther from land are even more limited. Although nearly optimum airborne equipment has existed for almost two decades, Project STORM-FURY impetus was necessary before the APS-45 radars aboard the WC-121N reconnaissance aircraft were capable of obtaining documented RHI data useful to researchers.

The following is an attempt to summarize the RHI data from all sources on hurricanes in an attempt to arrive at a model which might be used to help determine where one might profitably direct modification efforts.

HURRICANES PRIOR TO 1958

Early observations by Wexler (1947), Ligda (1951), Jordan and Stowell (1955) either do not even mention radar echo top observations or they report on heights in a single narrow area of interest without indicating the general height population in hurricanes. Probably the most complete early report on echo heights was by Kessler and Atlas (1956) on Hurricane Edna, 1954, using the TPQ-6, FPS-4, and FPS-6 radars. However, the observations were made at latitudes and times in the life history of the storm that they were most probably not representative of hurricanes in more tropical latitudes.

HURRICANE DAISY, 1958

Jordan et al. (1960) presented many features of Hurricane Daisy, 1958, including some RHI radar data taken in and near the eyewall region. They found the maximum echo tops to be about 65,000 ft with echoes "away from the eye..." less than 45,000 ft. "Daisy" was a very well formed storm just northeast of the Bahama Islands at the time. The eye was open with classically clear blue skies above it, and the precipitation pattern fairly typical (Senn and Hiser, 1959) except for the fact that the eyewall was open to the west and the heaviest precipitation, as well as spiral bands, had rotated to the southern regions.

HURRICANE JUDITH, 1959

In 1960, Senn et al. presented RHI data taken on the University of Miami MPS-4 radar on minimal Hurricane Judith, 1959, a small, late season storm. However, "Judith" was not typical of most hurricanes in either PPI or RHI pattern configurations.

HURRICANE DONNA, 1960

Jordan and Schatzle (1961) published the first RHI picture of the eye taken on the U.S. Navy's APS-45 airborne radar when reporting on the "Double Eye of Hurricane Donna." Although the picture did not show it, they described the inner eyewall echo tops as 45,000 ft with the outer eyewall topped

near 30,000 ft. Using the land-based University of Miami's MPS-4 radar, Senn and Hiser (1961) presented the first comprehensive data on echo tops in a major storm at sub-tropical latitudes. Table K-1 summarizes the heights of 3709 echoes in the four quadrants of Hurricane Donna based on the direction of motion of the storm. (Since this was northerly during most of the period of observation, little difference would be apparent if the reference line were north.) It is interesting to note that over 95 percent of the echoes observed had tops of less than 30,000 ft and over 78 percent had tops below 20,000 ft. However, it is just as obvious that more than one-third of all echoes had tops above the melting level. Assuming this storm was typical with respect to bright band echoes, probably only a small fraction of those above the bright band were active towers; the rest had reached or passed the mature stages. In the absence of sufficient RHI data, Senn et al. (1963) attempted to use far more voluminous "Donna" PPI data using range variations to indicate approximate echo heights for comparisons with observed winds. The technique was somewhat rewarding in the absence of other better data but obviously did not produce echo heights to the accuracy limits of an RHI radar, so no detailed comparisons with other storm data are presented.

HURRICANE DEBRA, 1961

Bigler and Hexter (1960) used CAPPI techniques to show the echo coverage at "standard," 10,000, 20,000, and 30,000 ft levels in Hurricane Debra (1961) as viewed by the 3-cm CPS-9

Table K-1. Number of Echoes by Height, Range, and Quadrant From MPS-4 Radar, Hurricane Donna, 1960.

Quad. Range*	0-89°				90-179°				180-269°				270-359°				TOTAL	% OF TOTAL
	<45	55	65	75	<45	55	65	75	<45	55	65	75	<45	55	65	75		
02-10	19	7	4	2	2	5	5	6	5	7	2	1	25	11	9	4	114	03.1
12-20	293	154	97	41	250	214	151	97	325	172	119	53	348	330	170	97	2801	75.5
22-30 **	76	33	27	12	85	55	27	9	100	32	36	11	79	52	44	23	701	18.9
32-40	8	8	9	4	6	2	4	9	4	0	1	2	4	6	0	1	68	01.8
42-50	2	5	4	2	2	6	0	0	1	0	1	0	0	2	0	0	25	00.7
TOTAL	398	207	141	61	345	282	187	121	435	211	159	67	456	291	223	125	3709	100.0

* Range from storm center nautical miles.

**HT.K'

FROM: Senn and Hiser (1961).

radar. Although this radar is subject to very appreciable attenuation in such situations, the data are interesting from several points of view. Very few echoes exceeded 30,000 ft. Some of those that did were in the northeast portion of the eye; others were 25 to 50 miles north; but the largest area is about 50 miles long and 50 miles west of the storm center. This is the area which has fewer and less intense echoes in normal storms (Senn and Hiser, 1959). However, "Debra" was under increasing influence from land areas and no longer typical of an over-water, undisturbed low latitude formation.

HURRICANE CLEO, 1963

Echo heights were studied by Senn (1965) in all regions of Hurricane Cleo again using the land-based University of Miami's MPS-4 radar. He found the median heights of echoes 30-40 miles from the storm center to be 20,000 ft with some cores in that region extending significantly higher. At greater ranges, heights were mostly lower; and nearer the eye the frequency of higher precipitation towers was greater. In the eyewall, towers generally exceeded 28,000 ft with some above 32,000 ft. Figures K-1 and K-2 are typical views of "Cleo" PPI and RHI data superimposed. In that study most active portions of spiral bands had tops on the order of 20,000 to 25,000 ft near the eye. Heights were 15,000 ft farther out in the rainshield, and generally the same in spiral band tails except for their cores which occasionally were found at 25,000 ft, once to 33,000 ft.

HURRICANE BETSY, 1965

Hurricane Betsy (1965) echoes were studied both from the land-based University of Miami's radars and the APS-45 airborne set by Senn (1966). In fact, this was the first comprehensive study of most quadrants and ranges of a storm in a completely over-water environment. Unfortunately, when the APS-45 RHI data were gathered on 1 September 1965, "Betsy" was a minimal hurricane gradually increasing in intensity. However, the Betsy precipitation pattern was much more normal than Cleo's in 1963. The Betsy echo heights occasionally exceeded 40,000 ft in the eyewall, and the echoes tended to be higher in the front of the storm; whereas, in Cleo they were higher in the right rear. Figures K-3 and K-4 show typical Betsy composites of echo heights superimposed on PPI presentations, and figures K-5 and K-6 show breakdowns of echo heights within 20 miles of the eyewall.

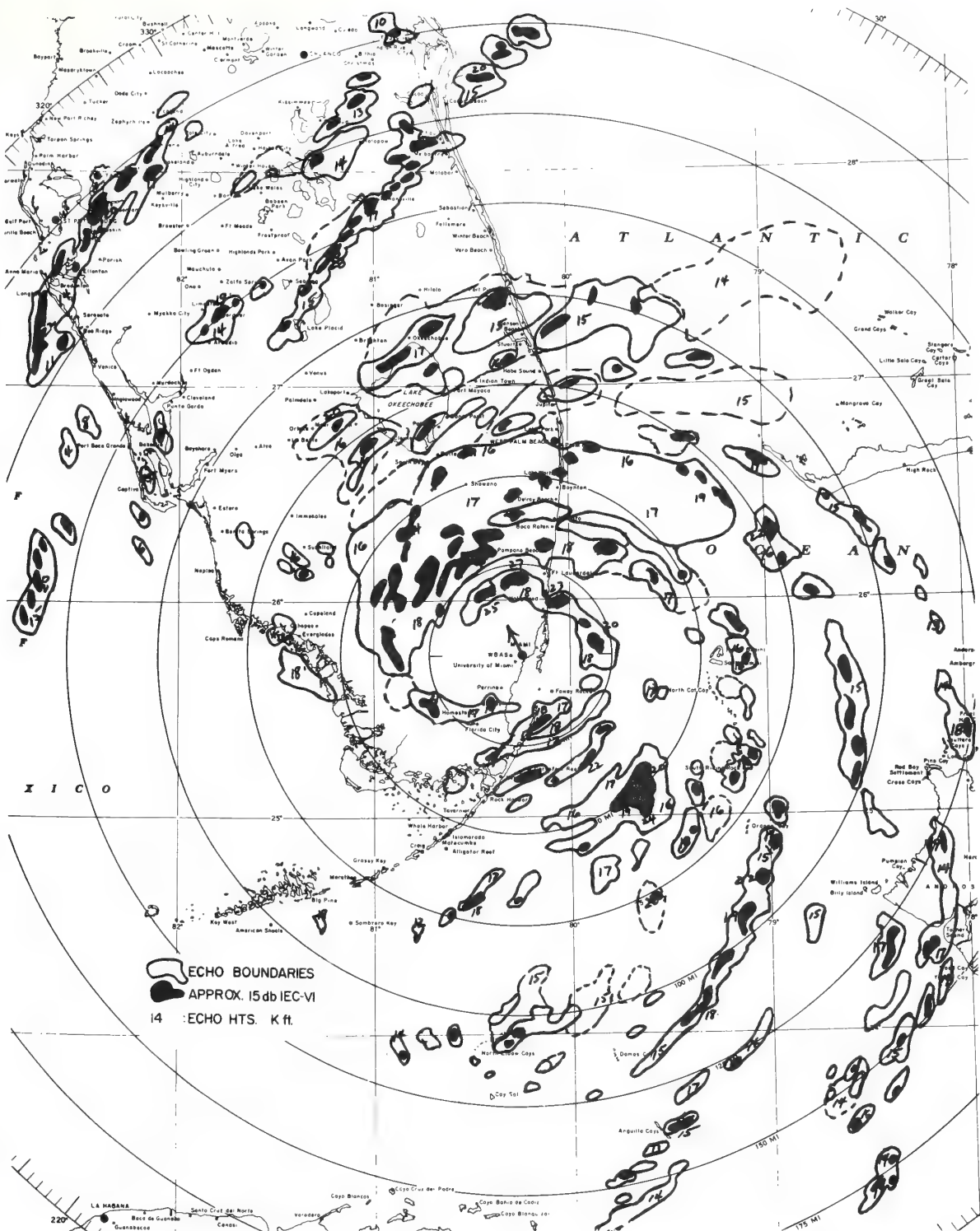


Figure K-1. Composite of typical PPI and RHI Cleo data 26-27 August 1964 from University of Miami MPS-4 radar.



Figure K-2. Hurricane Cleo, 26 August 1964, 2130 EST, UM/10-cm PPI with IEC; heights in k ft from MPS-4; Circle includes eyewall precipitation; eye diameter 14 miles.

HURRICANE INEZ, 1966

Hurricane Inez (1966) echoes were also studied by Senn (1967) using an IEC device on the University of Miami's RHI radar. "Inez" was moving southwest toward the Florida Keys and was a most unusual, asymmetrical hurricane. Figures K-7 and K-8 show that some echoes exceeded 60,000 ft while almost all of the heaviest cores exceeded 20,000 ft. Almost the entire precipitation pattern consisted of a rather intense band of weather to the east and southeast of the storm center over the warm Straits of Florida waters with the entire western quadrants precipitation free. A further breakdown of

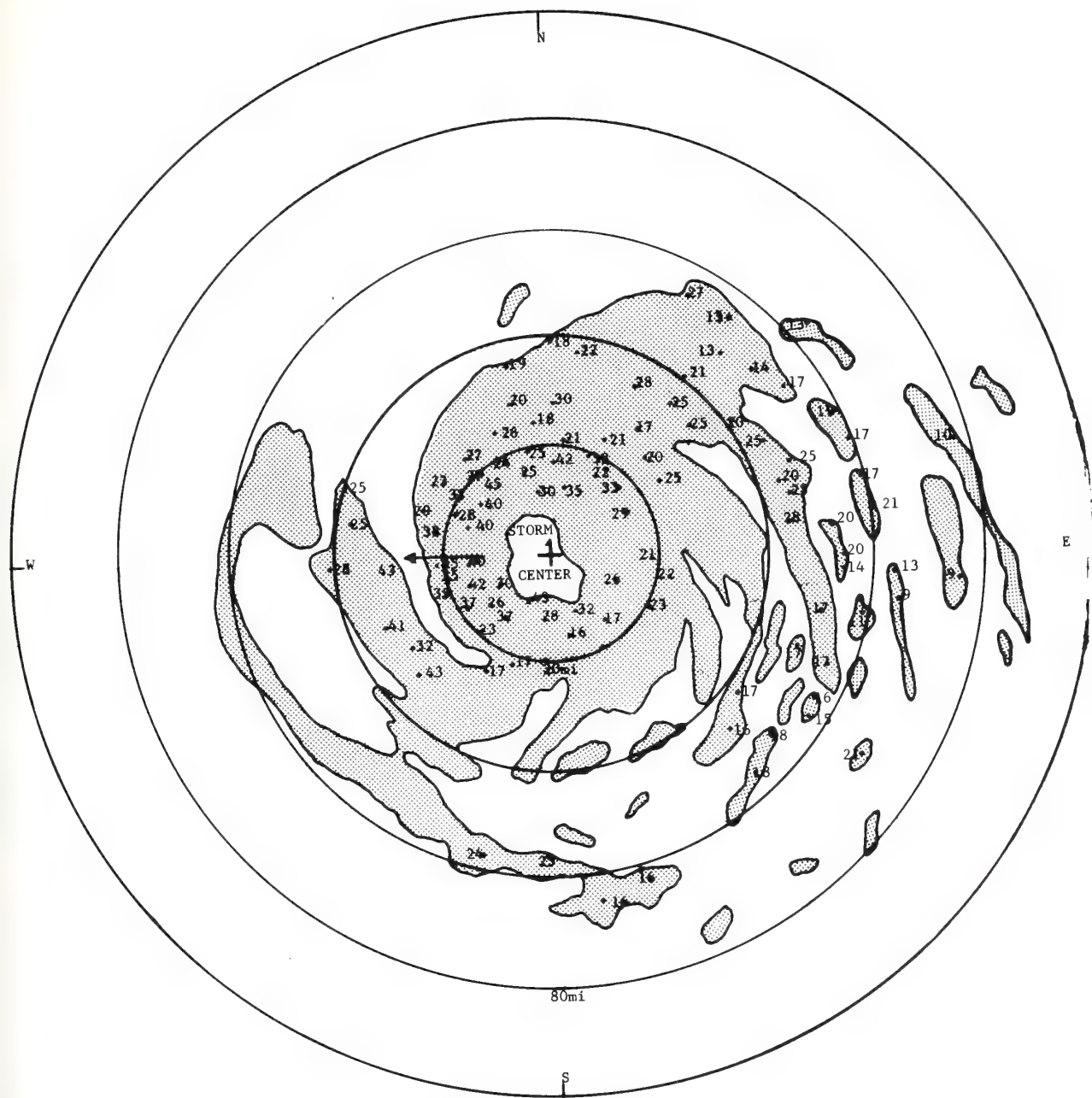


Figure K-3. Hurricane Betsy PPI with echo heights in k ft, APS-45, 1 September 1965.

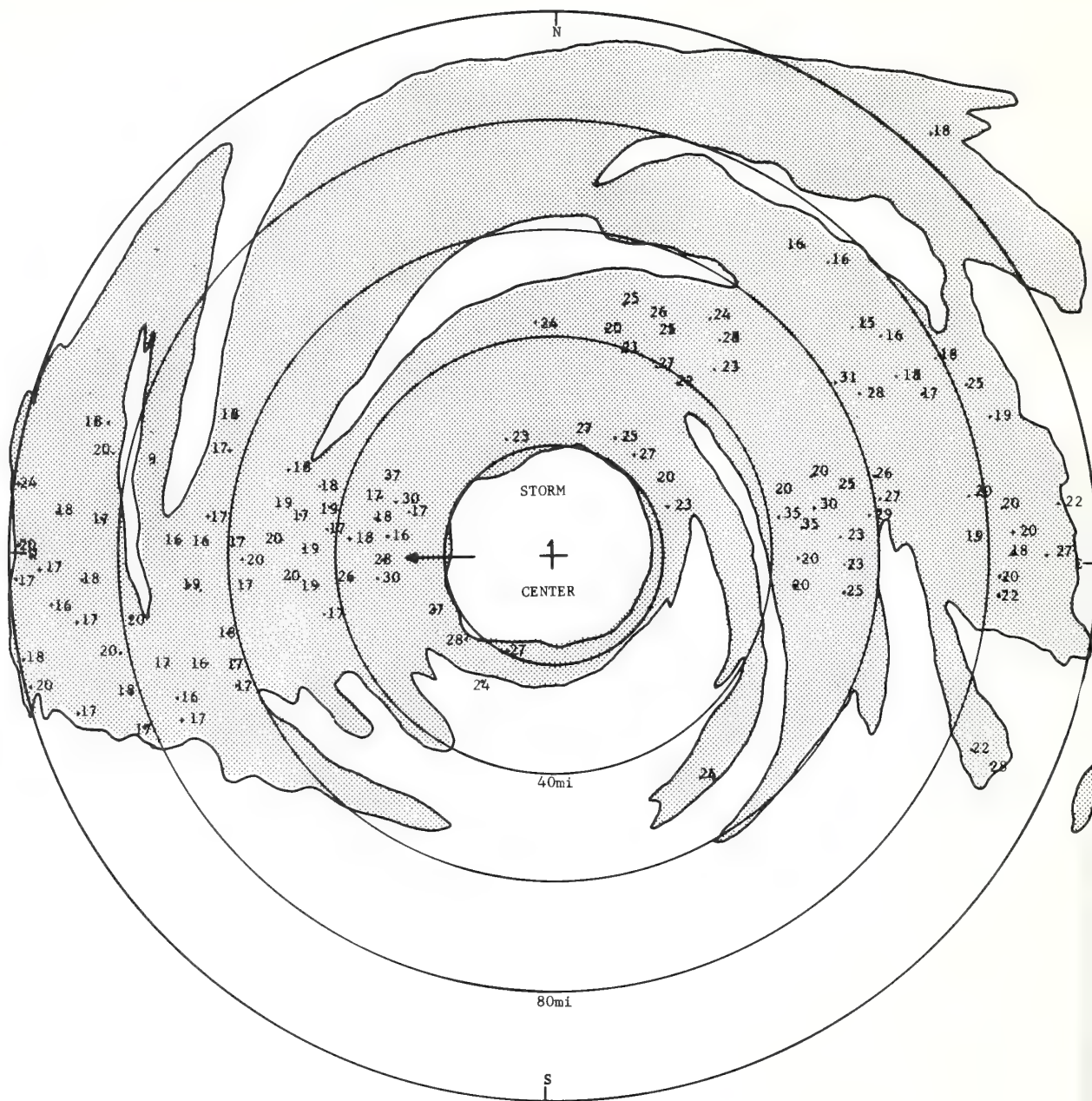


Figure K-4. Hurricane Betsy PPI with echo heights in k ft, MPS-4, 7 and 8 September 1965.



0849 - 1433 Z

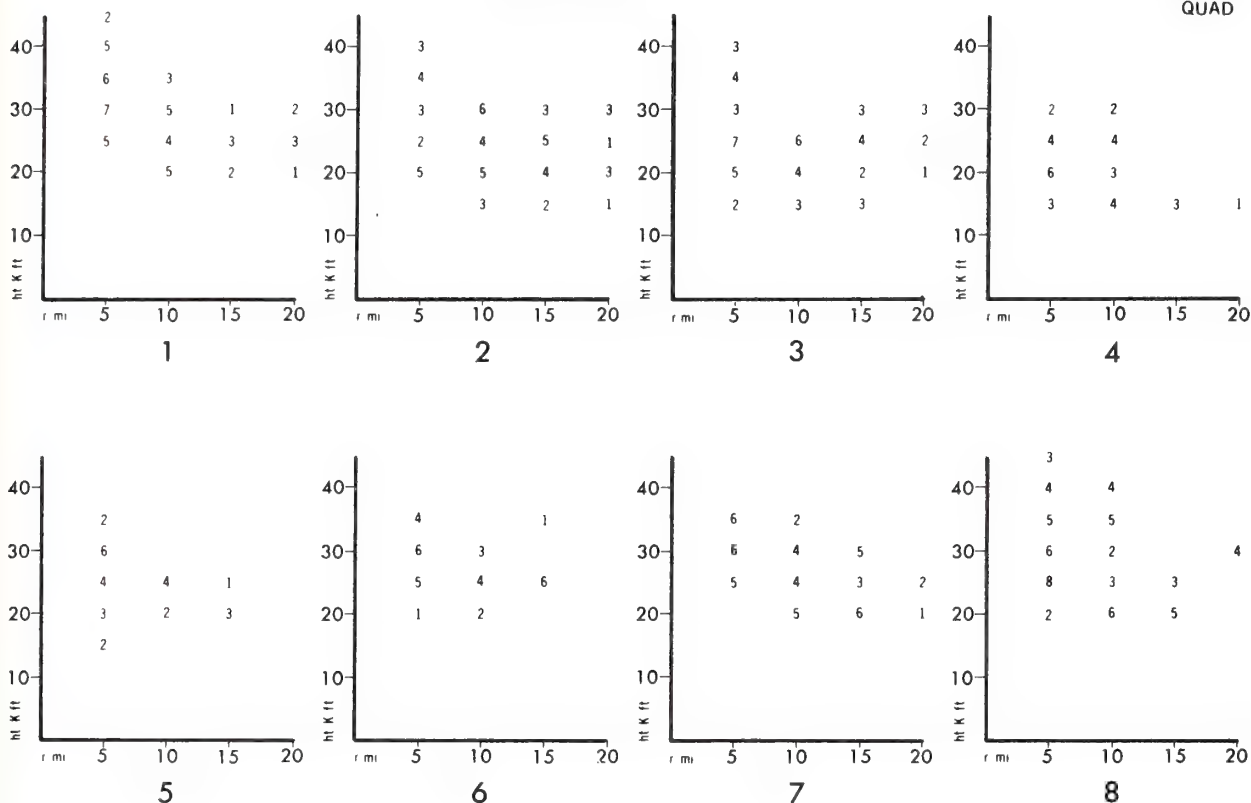


Figure K-5. Number and height of echoes within 20 miles of eyewall by quadrant in Hurricane Betsy, 1 September 1965, APS-45.

heights by quadrant and range within 20 miles of the eyewall was made using data from an earlier period northeast of Miami and these are shown in figure K-9.

HURRICANE FAITH, 1966, AND HURRICANES BEULAH AND HEIDI, 1967

Also underway is a study of echo tops in Hurricanes Faith (1966), Beulah and Heidi (1967) using the APS-45 data. However, these data are seriously lacking in important details and are expected to yield only general results. Some of these are discussed and shown in the summary.

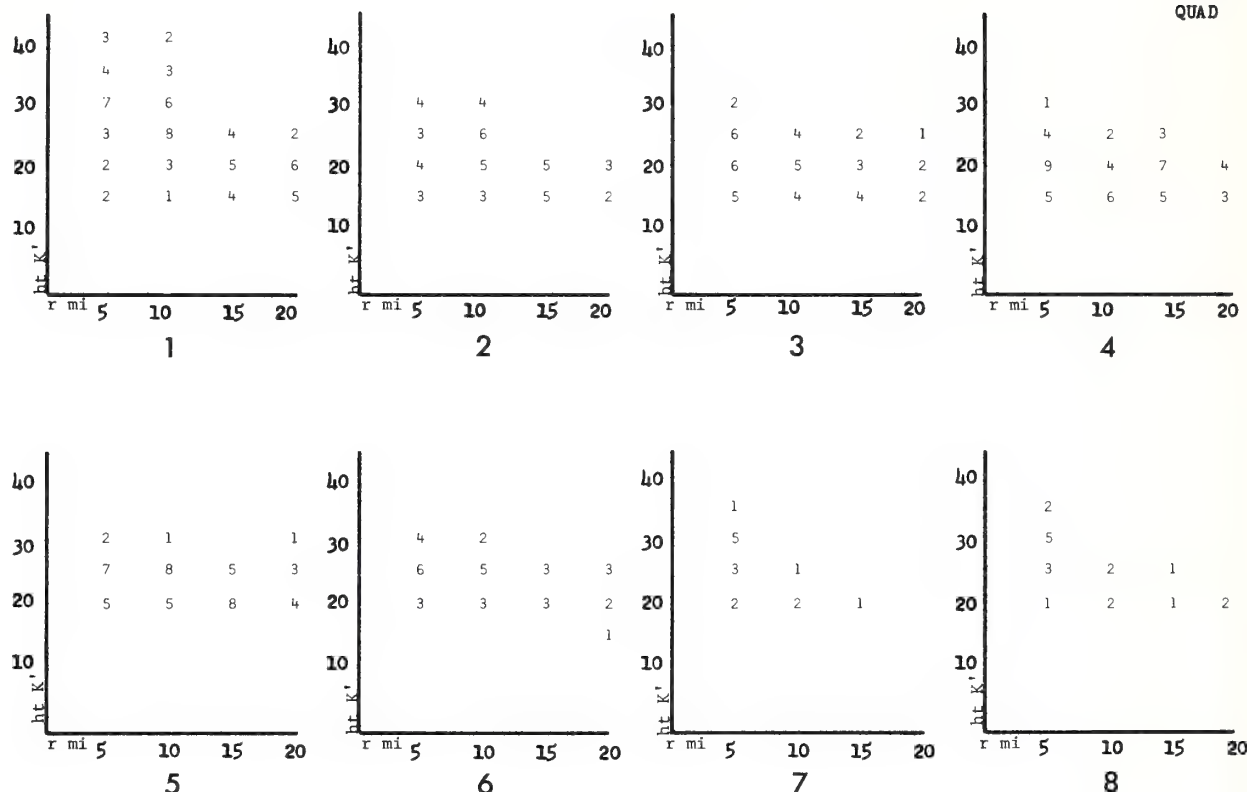


Figure K-6. Number and height of echoes within 20 miles of eyewall by quadrant in Hurricane Betsy, 8 September 1965, MPS-4, 0012-1140Z.

HURRICANE DEBBIE, 1969

Hurricane Debbie (1969) was studied by Senn and Court-right (1970), but results are only available for the eyewall region at present. These are shown on figures K-10 and K-11. A more complete study of the echo tops using the APS-45 air-borne data is underway.

SUMMARY

Figure K-12 summarizes the number of echoes by height categories for five storms, all over water and below 26°N latitude. Note that the data are not comparable in the sense



Figure K-7. Hurricane Inez, 4 October 1966, 0750 EST, UM/10-cm PPI with IEC; heights in k ft from MPS-4; circle includes eyewall precipitation; eye diameter 20 miles.

that although all echoes were found within 20 n miles of the eyewall (not the storm center), the number of echoes is a function of the flight path, quality of data collected, etc., as well as the actual height population produced in the storm. Consequently, the data for each category are also given in percentages of the total for that storm.

Although echoes penetrate significantly above 30,000 to 35,000 ft at greater ranges, a summary of the composite figures presented above shows that most of the taller echoes are within 20 n miles of the eyewall. Frequency distributions show the vast majority of all echoes to have tops in the 15,000 to 30,000 ft categories at all ranges. Generally, one should have no trouble finding echoes in the 20,000 to 25,000 ft category in and near the eyewall.

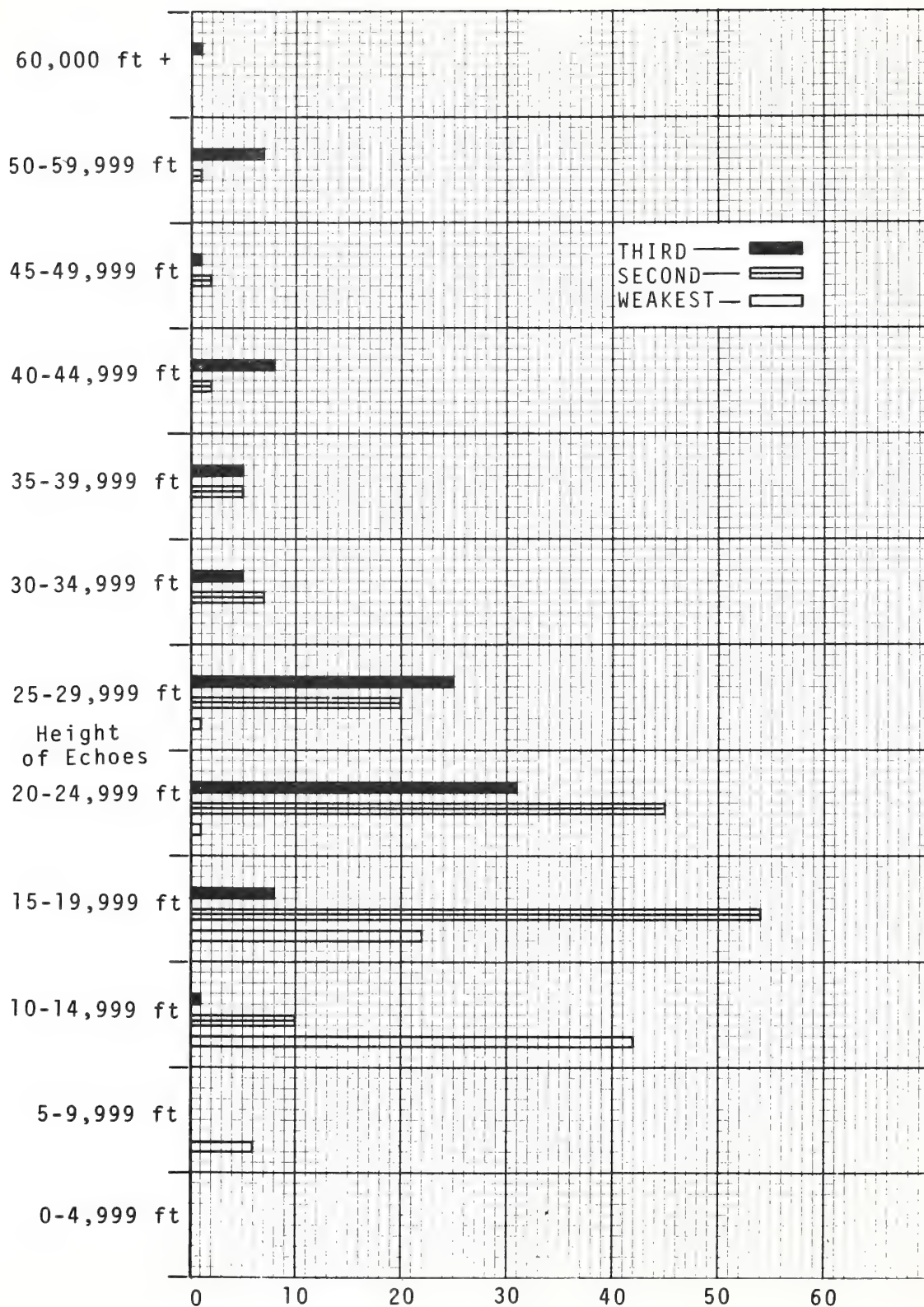


Figure K-8. Number and height of Hurricane Inez echoes in each of three iso-echo contour intensities.

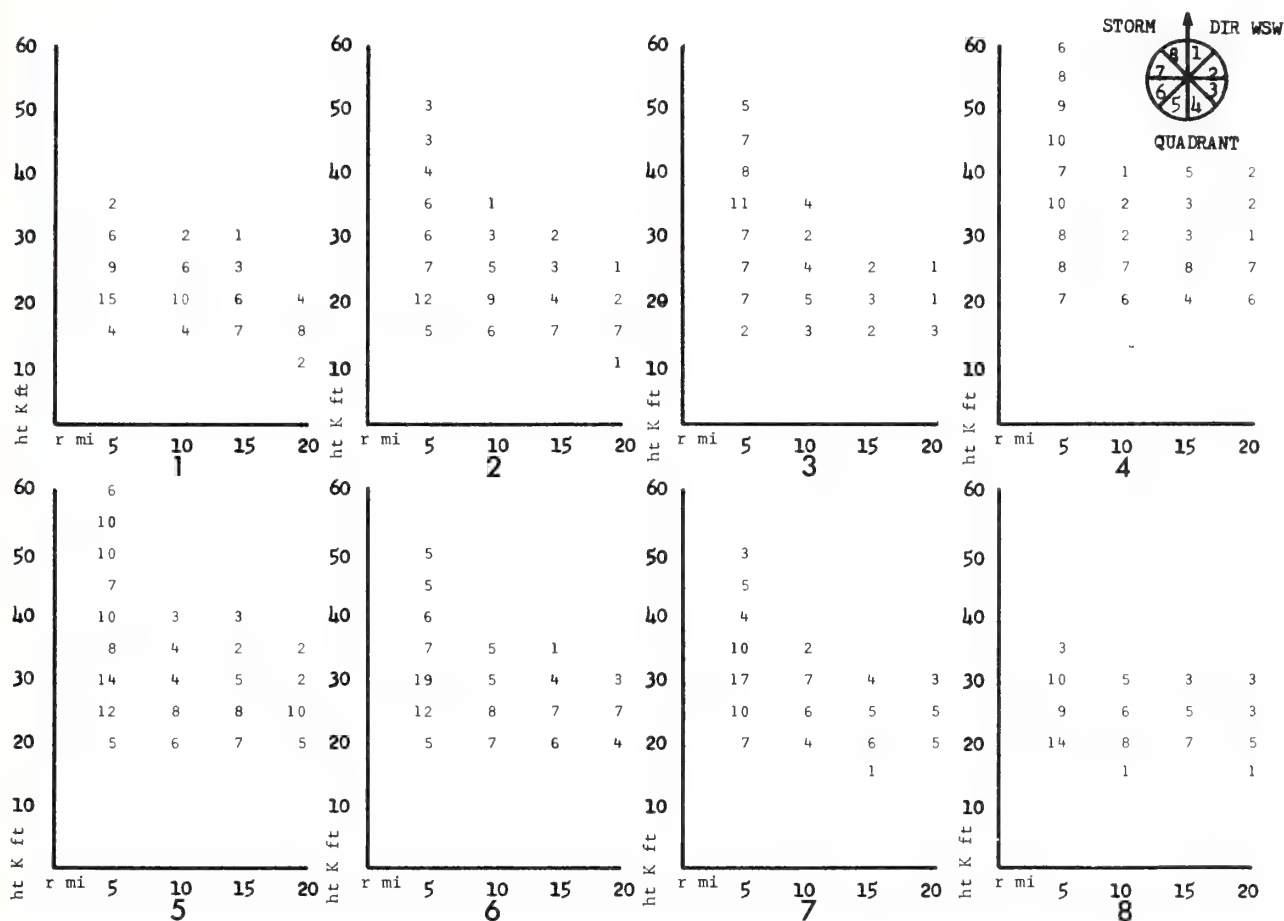
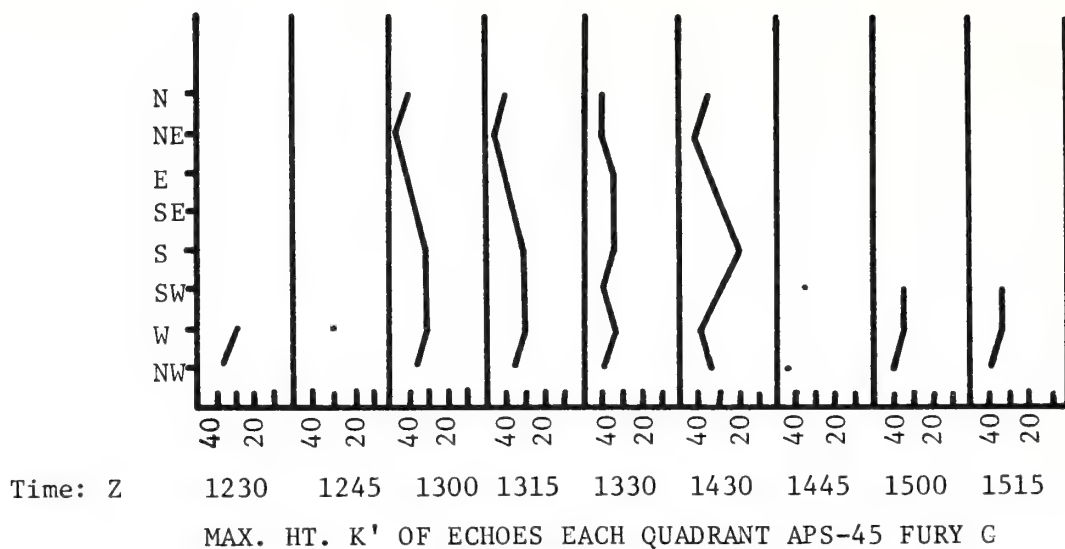
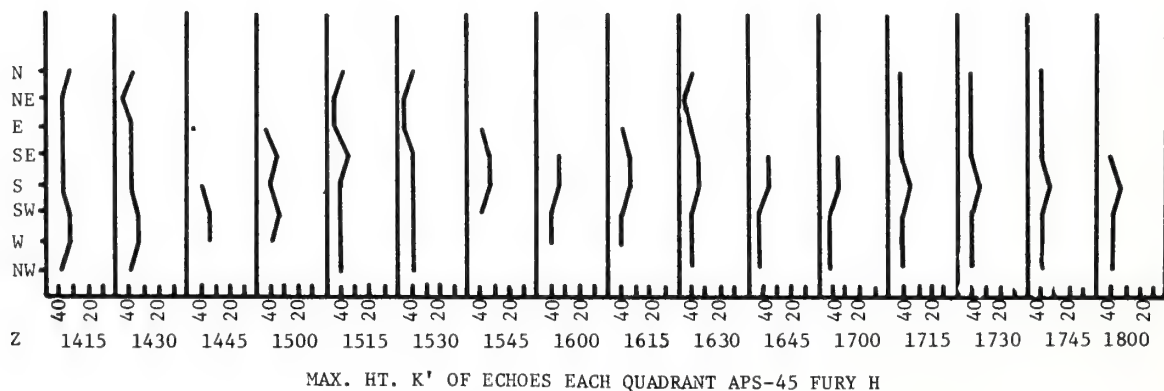


Figure K-9. Number and height of echoes within 20 miles of eyewall by quadrant in Hurricane Inez, 4 October 1966, MPS-4, 0030-2340Z.

Not shown in these figures, but deduced from earlier work, is the fact that, except when a storm is approaching land, the echo height populations remain relatively stationary with respect to the direction of storm motion rather than exhibiting a rotation around the storm center. It is not yet clear whether that also holds with respect to north, since most of the storms that could be considered representative were headed westerly or northerly when the observations were made. The tallest echoes, likewise, appear to be to the east and north of the storm center, and the south (or general rear) quadrants have the weakest, lowest echoes (sometimes not at all).



*Figure K-10. Height of eyewall echoes, Hurricane Debbie
18 August 1969.*



*Figure K-11. Height of eyewall echoes, Hurricane Debbie
20 August 1969.*

	≤ 15 K'	> 15 K' ≤ 30 K'	> 30 K'
Debbie F/H 8-20-69	8 8 (12%)	2 6 7 (38%)	3 5 1 (50%)
Debbie F/G 8-20-69	7 2 (13%)	2 1 3 (39%)	2 5 9 (48%)
Debbie F/G 8-18-69	5 1 (10%)	1 8 2 (38%)	2 4 9 (52%)
Heidi '67	5 1 (24%)	8 3 (39%)	7 7 (37%)
Beulah '67	3 2 (19%)	6 0 (36%)	7 4 (45%)
Faith '66	1 9 (16%)	5 8 (50%)	3 9 (34%)
Cleo '64	3 8 (22%)	7 1 (41%)	6 4 (37%)

Figure K-12. Number and percent of echoes by height within 20 miles of eyewall.

CONCLUSIONS

If one is looking for precipitation towers on the order of 20,000 to 25,000 ft outside the eyewall of a normal mature hurricane, he should find them in the north and east quadrants. A good RHI radar is a necessity, however, in a brief analysis of such clouds prior to any modification attempts since these quadrants are generally badly messed up by multi-layers of clouds, ample regions of "bright bands" (indicating melting hydrometers), etc., which make action purely on the basis of visual observations subject to uncertainty.

In fact, some of the above data lead to some rather perplexing questions regarding the seeding hypothesis used in Project STORMFURY. We have found the bright band in most quadrants and ranges of several hurricanes, as indicated in another paper in process. The results above show widespread echoes at heights where one expects glaciation, and certainly high level reconnaissance photos and satellite observations show an abundance of cirrus. However, one is also impressed with the general convective nature most echoes have on the RHI scope, many times in close proximity to the bright band. These observations suggest that echoes exist in all stages of generation and dissipation; but they do little to help answer the question of whether there is enough mixing of ice nuclei in the wall cloud regions of interest to significantly alter the possible effects of seeding active towers there. The results above show widespread echoes at heights where one expects glaciation, and certainly high level reconnaissance photos and satellite observations show an abundance of cirrus. However, one is also impressed with the general convective nature most echoes have on the RHI scope, many times in close proximity to the bright band. These observations suggest that echoes exist in all stages of generation and dissipation; but they do little to help answer the question of whether there is enough mixing of ice nuclei in the wall cloud regions of interest to significantly alter the possible effects of seeding active towers there.

Unfortunately, it is not possible to draw a series of PPI-RHI composites for any storm found in a relatively undisturbed tropical over-water environment simply because the data are too limited to date. Consequently, it seems essential that every effort be made to obtain such records with the only airborne radar presently capable of gathering high quality RHI data, the Navy APS-45. Secondarily, more effort should be made to gather RHI data on WSR-57's, the new WMO supplied RC-32B weather radars in the Lesser Antillies, and others, in an attempt to better describe this most important hurricane precipitation pattern dimension, including the bright band and shear in every sector of the storm.

REFERENCES

- Bigler, S. G., and P. L. Hexter, Jr. (1960): Radar analysis of Hurricane Debra. *Proceedings 8th Weather Radar Conference*, American Meteorological Society, Cal., April, pp. 25-32.

- Jordan, C. L., D. A. Hurt, and C. A. Lowrey (1960): On the structure of Hurricane Daisy on 27 August 1958. *Journal of Meteorology*, American Meteorological Society, 17, pp. 337-348.
- Jordan, C. L., and F. J. Schatzle (1961): The 'Double Eye' of Hurricane Donna. *Monthly Weather Review*, 89, (9), September, pp. 354-356.
- Jordan, H. M., and D. J. Stowell (1955): Some small-scale features of the track of Hurricane Ione. *Monthly Weather Review*, 83, (9), September, pp. 210-215.
- Kessler, E., and D. Atlas (1956): Radar-synoptic analysis of Hurricane Edna, 1954. *Geophysical Research Papers No. 50*, A.F.C.R.L., Bedford, Mass., July, p. 113.
- Ligda, M. G. H. (1951): Radar storm detection. *Compendium of Meteorology*, American Meteorological Society, Boston, Mass., pp. 1265-1289.
- Senn, H. V. (1963): Radar precipitation echo motion in Hurricane Donna. *Proceedings 3rd Technical Conference on Hurricanes and Tropical Meteorology*. A.M.S., A.G.I., and M.G.I. and M.G.U., Mexico City, Mexico, June 6-12, R.S.M.A.S. Contr. No. 463.
- Senn, H. V. (1965): The three-dimensional distribution of precipitation in Hurricane Cleo. *4th Technical Conference on Hurricanes and Tropical Meteorology*. A.M.S., Miami Beach, Fla., November.
- Senn, H. V. (1966): Precipitation shear and bright band observations in Hurricane Betsy, 1965. *Proceedings 12th Weather Radar Conference*, October 17-20, Oklahoma City, Okla., R.S.M.A.S. Contr. No. 710.
- Senn, H. V. (1967): Radar Hurricane Research, Final Report, ESSA, NHRL Contract No. E22-84-67(N), *Report No. 8208-1*, September, DDC AD 821-860.
- Senn, H. V., and H. W. Hiser (1959): On the origin of hurricane spiral bands. A.M.S., *Journal of Meteorology*, 16, (4), August, pp. 419-426, R.S.M.A.S. Contr. No. 215.
- Senn, H. V., H. W. Hiser, and R. D. Nelson (1960): Studies of the evolution and motion of radar echoes from hurricanes 1 July 1959 to 30 June 1960, Final Report. U.S. Weather Bureau, Contract CWB-9727, *Report No. 8944-1*, August.

- Senn, H. V., and H. W. Hiser (1961): Effectiveness of various radars in tracking hurricanes. *Proceedings 2nd Technican Conference on Hurricanes*, A.M.S., Miami Beach, Fla., June, pp. 101-114, R.S.M.A.S. Contr. No. 318.
- Senn, H. V., and C. L. Courtright (1970): Radar Hurricane Research, Final Report, ESSA, NHRL, Contract No. E21-41-70(N), October.
- Wexler, H. (1947): Structure of Hurricanes as determined by radar. *Annals of N.Y. Academy Sciences*, 48, September 15, pp. 821-944.

APPENDIX L

PROJECT STORMFURY EXPERIMENTAL ELIGIBILITY IN THE WESTERN NORTH PACIFIC

William D. Mallinger
National Hurricane Research Laboratory

INTRODUCTION

Project STORMFURY, the interagency project for hurricane modification experiments, was formally organized in 1962. Since that time the operating areas authorized and the eligibility rules have been changed several times progressively toward further relaxations of the seeding restrictions. The rules for this area eligibility for seeding were last changed in 1970 and are now as follows: "A storm or hurricane in the southwest North Atlantic, the Caribbean Sea, or the Gulf of Mexico is eligible for seeding as long as the forecast states that there is a small probability (10 percent or less) of the hurricane coming within 50 n miles of a populated land area within 18 hours after seeding." To date only the Atlantic Ocean area has been utilized to seed the three hurricanes upon which experiments have been conducted (Esther, 1961; Beulah, 1963; and Debbie, 1969).

Studies of statistical probabilities of eligible hurricanes and typhoons under the older eligibility rules were made and published in the STORMFURY Annual Reports for 1968 and 1969. These reports covered the Atlantic, Caribbean, and Gulf of Mexico areas; the eastern Pacific hurricane regions; and the western North Pacific area. The hurricanes occurring in the eastern North Pacific area (off the west coast of Mexico) are not considered to be suitable experimental targets for STORMFURY seeding and will not be further discussed in this report. An update to include 1970 cases under the new 18-hour rule for the Atlantic areas will be included for purposes of comparison with the seeding opportunities in the Western Pacific. This comparison is particularly important because proper bases for operations in the Pacific are needed if there is to be a sufficient increase in experimental opportunities to justify the Project's move to the Pacific.

ATLANTIC OCEAN, CARIBBEAN SEA, AND
GULF OF MEXICO STORMFURY AREAS

Figure L-1 shows the eligible areas for seeding used from 1968 through 1970. Table L-1 shows the number of occurrences of hurricanes eligible for STORMFURY experiments during the months of August, September, and October from 1954 through 1970 using the "18-hour after seeding" eligibility rule. The addition of the storms which became eligible under the change from the "24-hour" to "18-hour" rule adds three storms to the Atlantic, two to the Gulf of Mexico, and one to the Caribbean. These additions increased the expected opportunities per year from an average of approximately 2 to 2.35 hurricanes per year eligible for seeding under the current seeding eligibility rules regarding position of the storm.

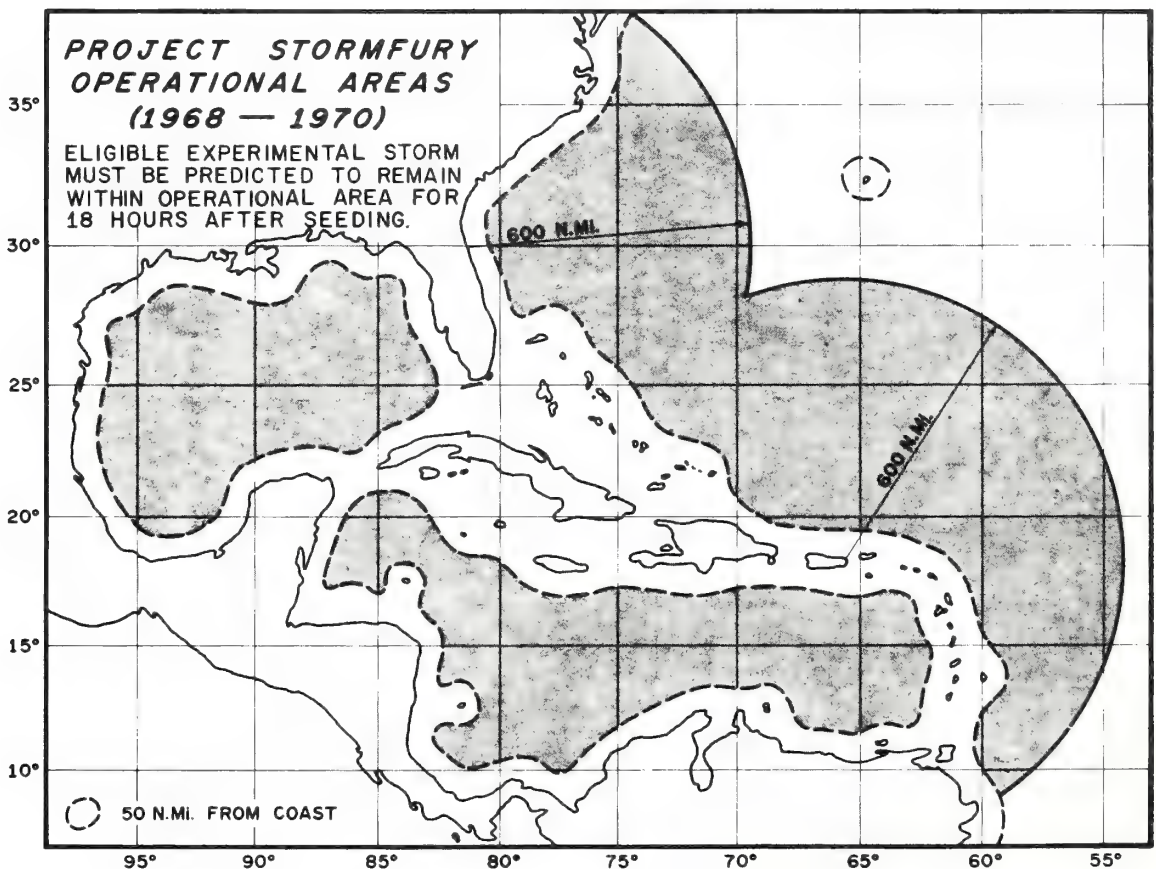


Figure L-1. Project STORMFURY operational areas (1968-1970). Eligible experimental storm must be predicted to remain within operational area for 18 hours after seeding.

Table L-1. Annual Frequency of Hurricanes Eligible for Seeding Between 1 August and 31 October Under Forecasting Techniques Criteria Approved for STORMFURY Operations Subsequent to 1970.

Year	Atlantic	Gulf of Mexico	Caribbean Sea	Total
1954	2	0	1	3
1955	4	0	1	5
1956	1	0	0	1
1957	1	0	0	1
1958	5	0	0	5
1959	2	0	0	2
1960	2	0	1	3
1961	2	1	0	3
1962	2	0	0	2
1963	3	0	1	4
1964	4	1	0	5
1965	2	0	0	2
1966	1	0	0	1
1967	0	0	0	0
1968	0	0	0	0
1969	2	1	0	3
1970	0	0	0	0
TOTAL	33	3	4	40

This number is misleading on the high side because some of these storms either had structure considered unsuitable for experimentation or were changing rapidly in intensity at the time and might not have been used for experiments even though they fell within the criteria established for area seeding eligibility. In addition, some of the storms considered eligible in the Gulf of Mexico and Caribbean Sea might not have been seeded for political reasons.

WESTERN NORTH PACIFIC

Figure L-2 shows the proposed operational areas if experiments are to be conducted from Guam and Okinawa. The eligibility rules considered in this study for the Western Pacific are: (1) The typhoon must be within 600 miles of the operations base for a minimum of 12 daylight hours, (2) maximum winds must be at least 65 knots, and (3) the predicted movement of the typhoon must indicate that it will not be within 50 n miles of a populated land area within 24 hours after seeding.

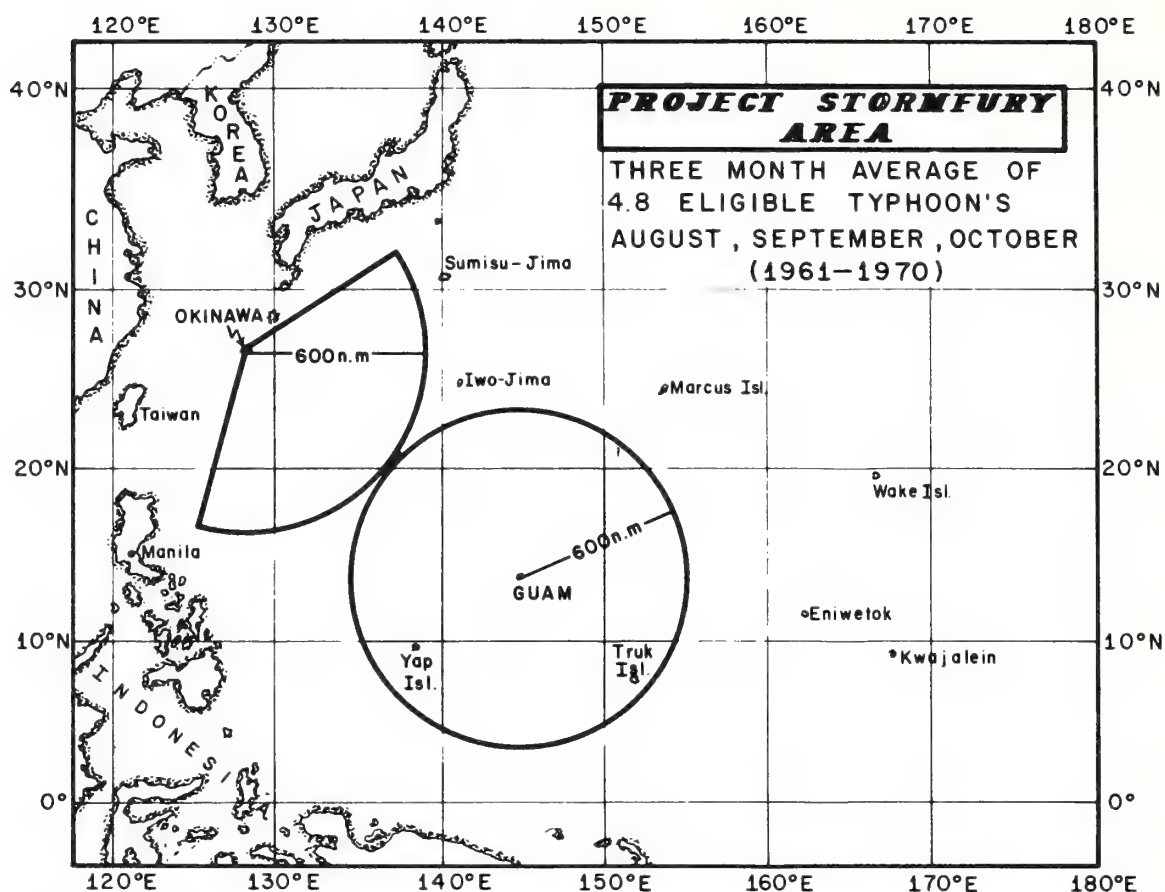


Figure L-2. Project STORMFURY area in the Western Pacific.

The list of Western Pacific typhoons eligible for seeding was updated to include 1970 tropical cyclones and was divided into two categories: (1) those that could be used for STORMFURY experiments with forces limited to operations from Guam only, and (2) those which permitted free use of either *Guam* or *Okinawa* from which to launch experiments (see table L-2).

Two of the 24 "Guam only" opportunities would have required such rapid reaction in order to mount a seeding experiment that they would probably have been missed. These storms formed within the 600 n mile radius of Guam and rapidly deepened while they continued to move out of the area. If a 48-hour notice to alert, deploy, and brief the participants in the experiment were required, both storms would definitely have been missed. A WP-3 or C-130 type aircraft might be used as a seeder in such cases when time does not permit the deployment of jet seeders to the operating base. If this is not feasible, STORMFURY monitoring missions without seeding might be conducted on shorter notice in these storms.

Table L-2. Western Pacific Typhoons Eligible for STORMFURY Experiments - August, September, and October (1961-1970).

Year	Guam Only	Combined use of Guam and Okinawa
1961	2	6
1962	3	7
1963	2	6
1964	1	2
1965	3	7
1966	1	3
1967	3	4
1968	5	8
1969	2	2
1970	2	3
TOTAL	24 (2.4 ¹)	48 (4.8 ¹)

¹ Number of storms per year

Seven of the 24 "Guam only" typhoons were also eligible later in their lives if forces operated from Okinawa. Several of these storms would have been eligible for seeding both from Guam and later from Okinawa, permitting two experiments on the same storm. It is also possible that a storm could be subjected to two experiments from either Guam or Okinawa although this opportunity occurs infrequently.

The free use of both Guam and Okinawa as STORMFURY bases of operation is essential to obtaining a suitable number of experiments during the 3-month period. Safety of personnel and aircraft is paramount and will require a multitude of decisions concerning the best and safest use of the STORMFURY forces. Examples of this are as follows: (1) A storm or typhoon approaching Guam from the east which, while eligible for experimentation, would not be seeded because forces would have to execute a typhoon evacuation (aircraft flyaway) for safety reasons. If these aircraft could be deployed to Okinawa for their evacuation, when the storm had passed Guam a mission could be mounted from Okinawa and terminated in Guam. Some changes in operational plans and techniques will be required to execute this type of experiment. (2) A typhoon that develops while approaching the 600 n mile radius to the west of Guam would be eligible in many cases if Project aircraft could terminate their missions in Okinawa. This also will require modified STORMFURY flight plans and schedules in order to accomplish the experiment.

If the flexibility of using both Guam and Okinawa as STORMFURY operational bases is not possible, opportunities to seed some of the storms would be lost because Project aircraft might have to fly away from Guam until an approaching typhoon had safely passed. Upon return of the forces to Guam and after mission preparations, the typhoon would have approached or exceeded the maximum operating range of STORMFURY forces.

The study was further expanded to examine the number of calendar days during which a large number of tropical cyclones exists in the Western Pacific to determine the effect that this factor would have on the availability and participation of reconnaissance aircraft for STORMFURY operations. Cyclone activity (tropical depressions, tropical storms, and typhoons) during the 3-month period of August, September, and October is listed by the number and percentage of days occurrence in table L-3.

During the months of August, September, and October tropical cyclones occur somewhere in the western North Pacific Ocean 84 percent of the time or an average of 77 days out of the 92. Three or more tropical cyclones occur simultaneously during an average of about 9 of these 77 days. Fortunately, during some of these periods, because of their location and strength, the tropical cyclones did not all require full reconnaissance coverage. Reconnaissance forces may be hard

Table L-3. Tropical Cyclone Days in Western North Pacific - August, September, October.

Year	Number of Days with 0 to 5 Cyclones					
	0	1	2	3	4	5
1960	8	41	22	14	4	3
1961	7	38	39	8	0	0
1962	15	23	39	15	0	0
1963	23	40	25	4	0	0
1964	10	42	29	11	0	0
1965	24	35	24	9	0	0
1966	11	40	25	16	0	0
1967	9	39	30	8	6	0
1968	15	31	37	9	0	0
1969	32	48	11	1	0	0
1970	8	60	23	1	0	0
TOTAL DAYS	162	437	304	96	10	3
AVERAGE DAYS	14.8	39.7	27.6	8.7	0.9	0.3
% OF DAYS	16.1	43.1	30.0	9.5	1.0	0.3
% of tropical cyclone days with one or two cyclones -						87.2
% of tropical cyclone days with three or more cyclones-						12.8

pressed at times to participate in full scale Project STORM-FURY experiments during periods when there are three or more active cyclones, but should be able to provide reconnaissance on one cyclone while participating in Project STORMFURY operations on another. There are exceptions to these assumptions; but, in general, sufficient forces to conduct experiments should be available during 68 of the 77 cyclone days. When, because of other commitments, DOD reconnaissance and seeder aircraft are not available to mount a full seeding experiment, the remaining available Project aircraft can be utilized to gather data on the natural variability within typhoons.

CONCLUSIONS AND RECOMMENDATIONS

(1) Conducting operations in the Western Pacific is worthwhile and should increase the number of experimental opportunities per average season by a factor of 2-3 over those experienced in the Atlantic regions provided that *both Guam and Okinawa* are available for use by STORMFURY forces. Addition of a base in the Philippines and in other locations in the Pacific adds a few opportunities per 10 years, but most of the eligible storms can be worked from either Guam or Okinawa. If Guam is available, but Okinawa is not, the desirability of moving the project to the Pacific should be reconsidered because of the limited increase in the number of expected opportunities over those in the Atlantic operating areas.

(2) During periods when there are three or more tropical cyclones occurring simultaneously (13 percent of the cyclone active periods during August, September, and October), monitoring missions could be conducted on suitable storms using fewer forces and without actual seeding.

(3) Some additional experiments could be conducted on tropical storms and tropical depressions during periods when no eligible typhoon activity was occurring.

U.S. DEPARTMENT OF COMMERCE
National Oceanic and Atmospheric Administration
Environmental Research Laboratories

NOAA Technical Memorandum ERL NHRL-93

HORIZONTAL ASYMMETRIES
IN A NUMERICAL MODEL OF A HURRICANE

James W. Trout
Richard A. Anthes

National Hurricane Research Laboratory
Coral Gables, Florida
November 1971



TABLE OF CONTENTS

	Page
ABSTRACT	1
1. INTRODUCTION	1
2. SUMMARY OF THE MODEL	2
3. COMPUTATIONAL PROCEDURE.	4
3.1 The Polar Grid.	5
3.2 Interpolation Schemes to the Polar Grid	5
4. THE ASYMMETRIC STAGE	7
4.1 Time Variations of Azimuthal Standard Deviations. .	9
4.2 Harmonic Analysis of the Momentum and Temperature Fields.	13
5. EDDY FLOW RELATED TO THE MATURE VORTEX	17
5.1 Asymmetries in the Outflow Layer.	20
5.2 Asymmetries in the Inflow Layer	25
6. HORIZONTAL TRANSPORT MECHANISM	27
6.1 Flux of Absolute Vorticity.	28
6.2 Flux of Angular Momentum.	30
6.3 Vertical Flux of Relative Angular Momentum.	32
7. SUMMARY AND CONCLUSIONS.	33
8. REFERENCES	36

HORIZONTAL ASYMMETRIES IN A NUMERICAL MODEL OF A HURRICANE

James W. Trout and Richard A. Anthes

Statistical techniques are employed to investigate the development and structure of horizontal asymmetries in the numerical model of a hurricane developed by Anthes et al. (1971a). Strong asymmetries in the momentum and temperature fields develop in the outflow layer at approximately 120 hours. Weaker asymmetries also develop in the inflow layer at this time. Harmonic analyses are used to determine the predominant scale of asymmetries. Detailed spatial analyses are carried out for the momentum and temperature fields in the mature asymmetric stage of the model. The analyses are compared to observational data compiled by Black and Anthes (1971). The results show that the model reproduces many observed features of a three-dimensional tropical cyclone.

1. INTRODUCTION

Recent experiments conducted with an asymmetric hurricane model (Anthes et al., 1971a) dramatically illustrate certain asymmetric properties of the horizontal and vertical motion fields. Examples of these are horizontal eddies in the upper tropospheric outflow layer, rainbands, and meandering of the hurricane eye. Two distinct stages are observed in a typical experiment. During the early stages, the storm circulation is quite symmetric about the vertical axis of rotation. In the second stage, the storm acquires marked asymmetric characteristics in the outflow layer, and the vertical motion patterns form spiral bands which resemble hurricane rainbands.

The purpose of this paper is to report the quantitative investigation of the nature and importance of the asymmetric character of the model storm. Various statistical measures are employed to show the

time-dependent development and locations of the asymmetries. Harmonic analysis of the radial and tangential wind components determines the predominant scale of the asymmetries. Computations of fluxes of angular momentum and absolute vorticity show the importance of asymmetries as horizontal transport mechanisms. The asymmetries in the model outflow layer are compared with the asymmetric features of real storms (Black and Anthes, 1971).

2. SUMMARY OF THE MODEL

The equations are written in σ -coordinates (Phillips, 1957) on an f -plane. The equations of motion and the continuity, thermodynamic, and hydrostatic equations are identical to those utilized by Smagorinsky et al. (1965) for general circulation studies. The basic equations are given in Anthes et al. (1971a). The vertical structure of the model consists of an upper layer and a lower layer of equal pressure depth and a thinner Ekman boundary layer. The information levels for the dynamic and thermodynamic variables are staggered according to the method used by Kurihara and Holloway (1967).

For computational economy, the horizontal mesh has been limited to a square grid with a uniform spacing of 30 km. The lateral boundary points approximate a circle, and all points are contained between radii of 435 and 450 km. The thermodynamic grid points are staggered from the velocity component grid points on the σ -surfaces. A comprehensive summary of the mathematical details is given elsewhere (Anthes, 1972) and need not be repeated here.

The Matsuno (1966) simulated forward-backward scheme is utilized in the model for the time integration scheme. The Matsuno scheme has the property of dampening the very high temporal frequencies associated with internal and external gravity waves. The lateral boundary conditions consist of a steady-state pressure and temperature on the boundary and a variable momentum based on extrapolation outward from the interior of the domain. The cumulus scale convective processes are parameterized similarly to the version of Rosenthal's (1970b) symmetric model. The current model also contains an explicit water vapor cycle. For further details refer to Anthes (1972). The initial conditions consist of an axisymmetric vortex in gradient balance. The minimum pressure is 1011 mb, and the environmental pressure on the lateral boundary is 1015 mb, yielding a maximum gradient wind of 18 m sec^{-1} at a radius of 240 km. With these initial conditions and utilizing a time step of 45 seconds, the experiment has been executed for 192 hours.

With symmetric initial and boundary conditions, the solutions to the differential equations must remain symmetric for all time. However, truncation and roundoff errors in the finite difference equations, as well as the lack of complete circular symmetry in boundary conditions, produce extremely weak asymmetries after the first time step. Although objections might be raised concerning the desirability of allowing the initial asymmetries to be generated by truncation, later experiments in which asymmetries were deliberately introduced in a random fashion yield essentially the same results during the asymmetric stage (Anthes, 1972).

Thus, it appears that the actual source of the initial asymmetries is unimportant in the mature asymmetric stage.

3. COMPUTATIONAL PROCEDURE

During the asymmetric stage an interesting anticyclonic looping of the eye is observed. This looping appears to be related to the asymmetric outflow and is discussed by Anthes (1972). The center of the grid is depicted as zero (fig. 1), with north-south, east-west deviations from the center plotted in kilometers.

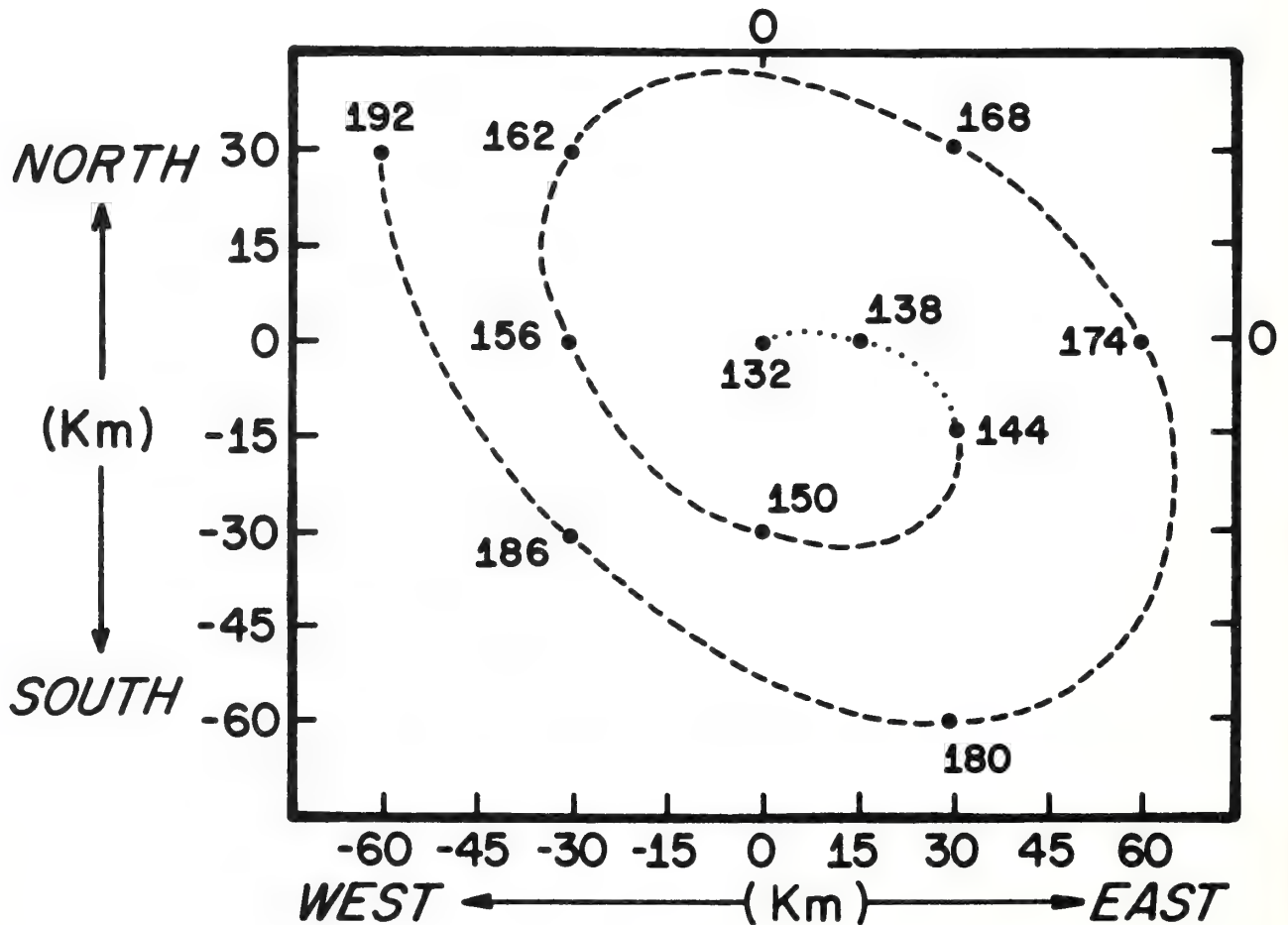


Figure 1: Model vortex motion. Positions are labeled in hours.

3.1 The Polar Grid

The computation of circular averages and mean and eddy fluxes of vorticity and momentum requires interpolation from the cartesian grid system to a polar grid system whose origin is coincident with the looping vortex center. The rectangular (u) and (v) wind components are converted into tangential (V_λ) and radial (V_r) wind components by use of:

$$V_\lambda = (vX - uY)/R \quad (1)$$

and

$$V_r = (uX + vY)/R \quad (2)$$

where X and Y are the distances along the x and y axis between the vortex center and a given grid point;

and
$$R = (X^2 + Y^2)^{\frac{1}{2}}. \quad (3)$$

The cartesian arrays are interpolated to a polar coordinate grid consisting of 15 radial increments of 30 km ($r = 15, 45, 75 \dots$) and 16 azimuthal increments of 22.5 degrees. The calculation extends to a radius of 435 km when the storm center is located on the center of the cartesian grid. When the storm center is located away from the grid center, the maximum radius of the polar grid is reduced.

3.2 Interpolation Schemes to the Polar Grid

The accuracy of two interpolation formulae is tested. The first of these is a bilinear interpolation formula:

$$\begin{aligned} \frac{1}{S} = & S_{I,J} + h[S_{I,J+1} - S_{I,J}] + K[(S_{I+1,J} - S_{I,J}) (1-h) \\ & + (S_{I+1,J+1} - S_{I,J+1})h]. \end{aligned} \quad (4)$$

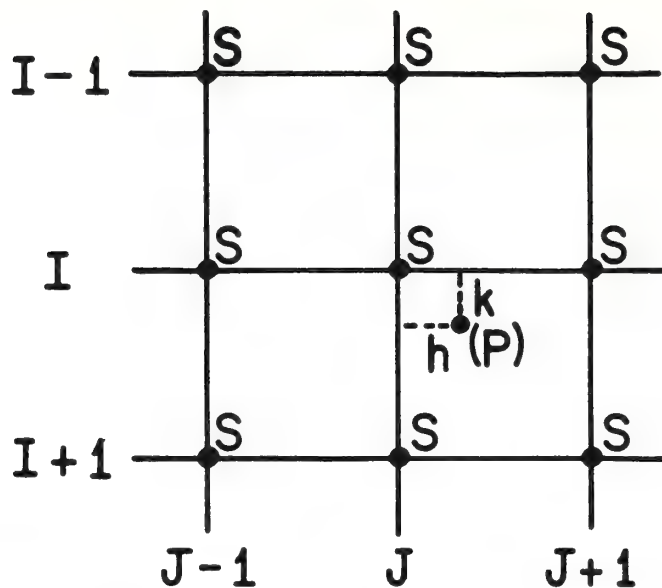


Figure 2: Interpolation to polar grid point (P).

Here the interpolated value of S , at the location of the polar point (fig. 2), is denoted by P . In (4), (I, J) is the grid point (row, column) index in the usual matrix sense; h and K are the coordinate distances from point P to grid point (I, J) . Satisfactory results are obtainable with (4) at large radii. However, at smaller radii the curvature in the variables associated with the hurricane vortex is too extreme for linear interpolation. The second method is a nine point interpolation function. The formula is a finite difference form of the truncated Taylor's expansion of a function of two independent variables.

$$\begin{aligned}
 \frac{2}{S} = & S_{I,J} + .5h(S_{I,J+1} - S_{I,J-1}) + .5K(S_{I-1,J} - S_{I+1,J}) \\
 & + .5h^2(S_{I,J+1} + S_{I,J-1} - 2S_{I,J}) + .5K^2(S_{I-1,J} + S_{I+1,J} - 2S_{I,J}) \\
 & + .25hK(S_{I-1,J+1} - S_{I-1,J-1} - S_{I+1,J+1} + S_{I+1,J-1}).
 \end{aligned} \tag{5}$$

For all interpolations the base point (I, J) is selected so that h and K are not greater than one-half a grid increment.

Both interpolation formulae are applied to the function,

$$f(r) = (r+15)/30 \quad (r \text{ in km}). \quad (6)$$

With the vortex center coincident with the grid center, (6) yields integer values increasing from 1 at $r = 15$ km to 15 at $r = 435$ km at all azimuth angles. Table 1 shows circular averages, for the first five radii, computed from data obtained by use of (4) and (5).

Table 1: Circular Averages Computed from Interpolation
Scheme (4) and (5)

Radius (km)	Bilinear Interpolation Eqn. (4)	9-Point Interpolation Eqn. (5)
15	1.2071	1.0969
45	2.0529	2.0137
75	3.0447	2.9920
90	4.0211	4.0022
105	5.0230	5.0008

Table 1 clearly shows the superiority of the 9-Point Interpolation formula at small radii. Hence, interpolation formula (5) is utilized throughout this paper.

4. THE ASYMMETRIC STAGE

Notable asymmetries of the cyclone circulation include large horizontal eddies in the upper tropospheric outflow region. Figure 3 shows the trajectories of 10 particles which are released in the lower levels of the cyclone and provides a qualitative view of the asymmetric circulation over the life cycle of a typical experiment. The trajectories are

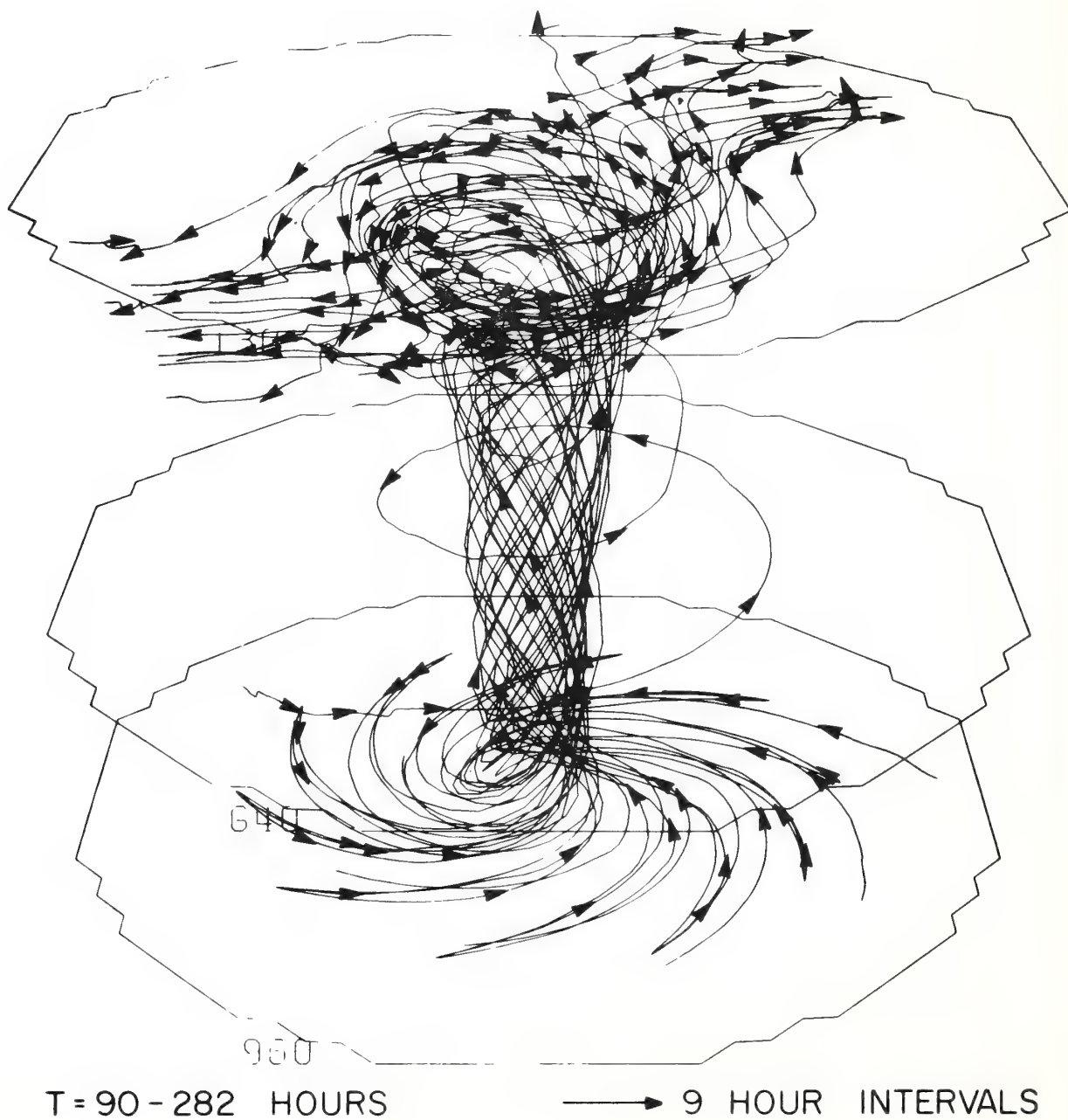


Figure 3: Ten trajectories of parcels released in the boundary layer over an 8-day period.

computed over an 8-day period from the forecast velocity components. For additional illustrations and computational procedure refer to Anthes et al. (1971c). The figure greatly exaggerates the vertical dimension of the storm but clearly illustrates the asymmetric outflow characteristics. Particles, upon reaching the upper levels of the model, are carried outward from the vortex center, mainly in the northeast and southwest quadrants. This should be contrasted to the nearly symmetric inflow depicted in the lower layers. The preferred quadrants of outflow reflect the asymmetric circulation around upper level horizontal eddies that are present during the 8-day period.

4.1 Time Variations of Azimuthal Standard Deviations

The principal measure of asymmetry employed here is the standard deviations (SD) from the azimuthal averages of momentum and temperature. Figure 4 and figure 5 are plots of SD versus time for the radial winds, tangential winds and temperature at selected radii in the inflow and outflow layers.

Large SD are computed at very small radii (not plotted), where the interpolation error due to the relatively few cartesian grid point values is the greatest. However, the asymmetries are relatively small compared to the azimuthal means. The inflow asymmetries diminish rapidly with increasing radius. The outflow asymmetries, on the other hand, appear to be greatest near the 165 km radius (fig. 4). The ratio of the standard deviation to the mean at all radii is larger in the outflow layer.

Three distinct development phases of the model can be defined from the time variation of the SD. First, there is an "organizational phase,"

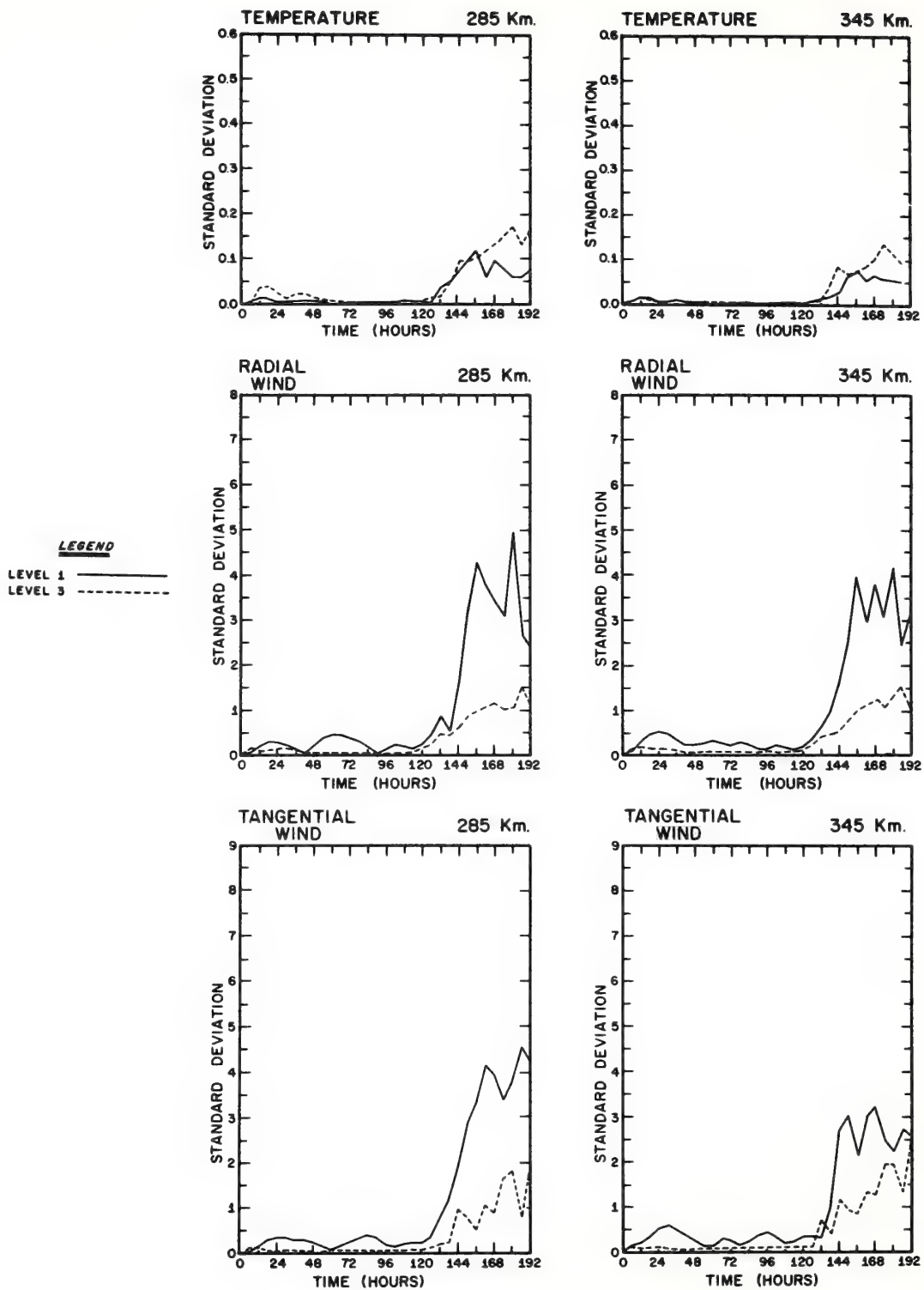


Figure 4: Time variations of the standard deviations for temperatures, radial winds, and tangential winds at inner radii.

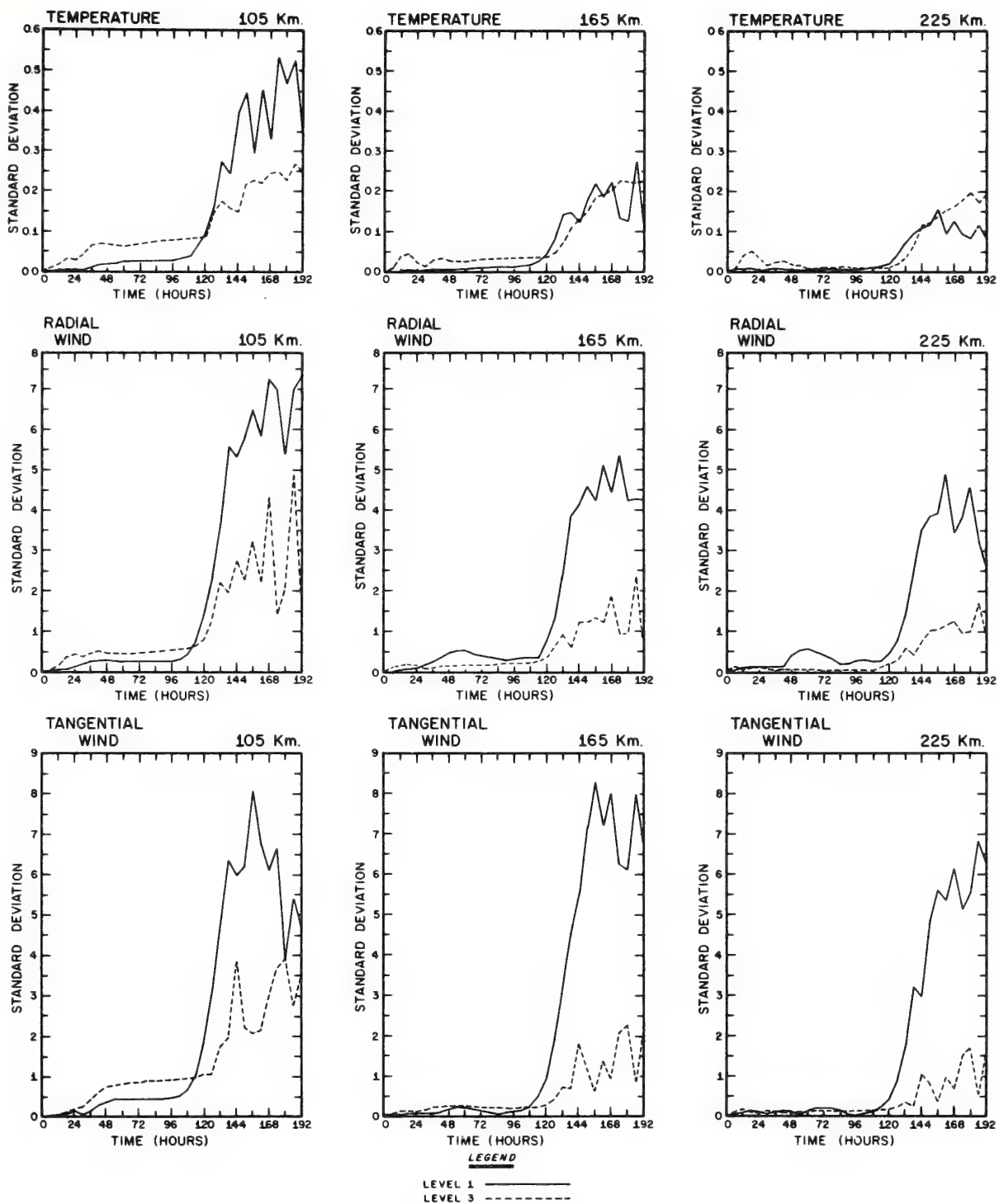


Figure 5: Time variations of the standard deviations for temperatures, radial winds, and tangential winds at outer radii.

exhibited initially by the lack of asymmetries. Standard deviations of 0.5 m sec^{-1} or less are computed for both the radial and tangential winds during this phase. Increasing deviations first appear in the inflow layer and this is closely followed by the development of small asymmetries in the outflow layer. A period (symmetric phase) in which the SD's are small and relatively steady follows. Finally, an asymmetric phase begins at approximately 120 hours. This is characterized by the development of large scale asymmetries in the outflow layer and spiral bands of convection in the lower layer. At small radii, the SD of the tangential winds increases to 8 m sec^{-1} in the outflow layer. The asymmetries in the outflow layer radial wind field also experience rapid growth, but the magnitude of the SD is somewhat smaller than that of the tangential winds. The magnitude of the asymmetries of the two components is comparable in the inflow layer as are the circular means.

At the larger radii, both the inflow and outflow asymmetries decrease with increasing radius (figs. 4 and 5). However, at a radius of 350 km from the vortex center, the asymmetries are still well defined and contain SD approximately equal to the magnitude of the mean radial and tangential flow. The lateral boundary conditions require the boundary velocity components to vanish at inflow points, and thus contribute to decreased SD's at large radii in the inflow layer.

The plots of temperature SD versus time also distinctly illustrate the three phases of the development of the model. However, the temperature field is much more symmetric than the momentum field, as indicated by the small standard deviations of temperature. The decrease of SD with

increasing radius is due to the boundary conditions of a steady symmetric temperature.

4.2 Harmonic Analysis of the Momentum and Temperature Fields

The previous section established the rapid development of asymmetries at model time equal to 120 hours. In this section harmonic analysis establishes the predominant scale of the asymmetries for both the inflow and outflow levels. Figures 6, 7, and 8 show the time variation of the scale of the percent variance accounted for by harmonic 1, 2, 3, 4, and 8 at a typical inner (45 km) and outer (285 km) radius of the vortex.

An important feature revealed by the harmonic analysis is the predominance of wave numbers 4 and 8 during the organizational and symmetric stages of the vortex development. The grid boundary is an 8-sided figure comprised of 4 regular sides and 4 irregular sides. Wave number 8 is, therefore, probably a manifestation of the octagon shaped boundary of the grid. Wave number 4 is apparently a manifestation of the 4 irregular corners of the grid. Both wave patterns are also affected by errors associated with the numerical differencing scheme, especially in corner regions of the grid where the lateral boundary conditions may cause different truncation errors. Recent investigations by Koss (1971) show that the numerical differencing utilized in an asymmetric vortex model can also induce error patterns that persist with time in the form of wave number 4. Caution must be exercised in interpreting figures 6, 7, and 8. During the early stages of the experiment, the percent of variance contained by wave number 4 is very high (70% to 95%); however, the total

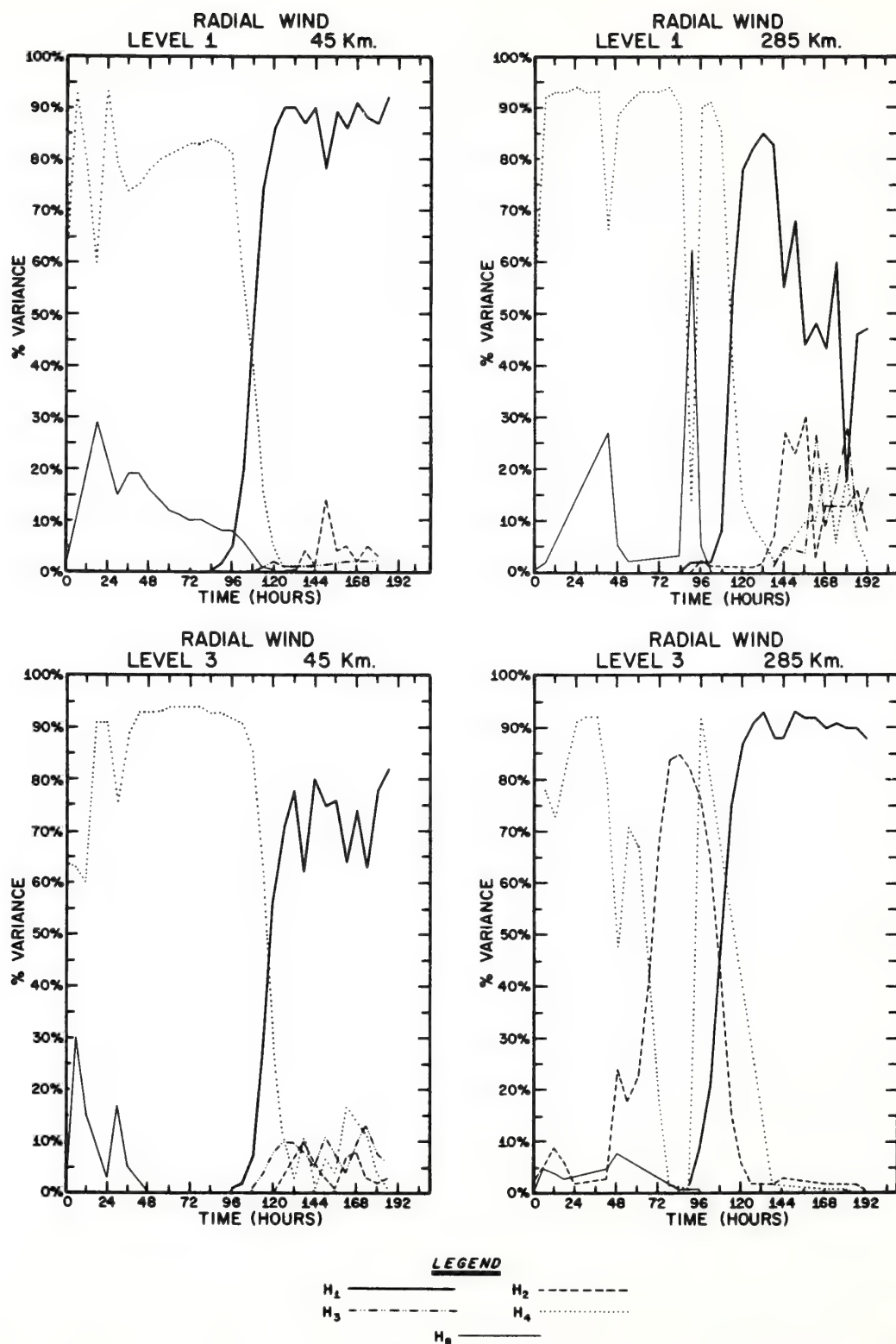


Figure 6: Harmonic analysis of the model outflow layer and inflow layer radial wind component. Wave numbers 1, 2, 3, 4, and 8 are illustrated at an inner and outer radius.

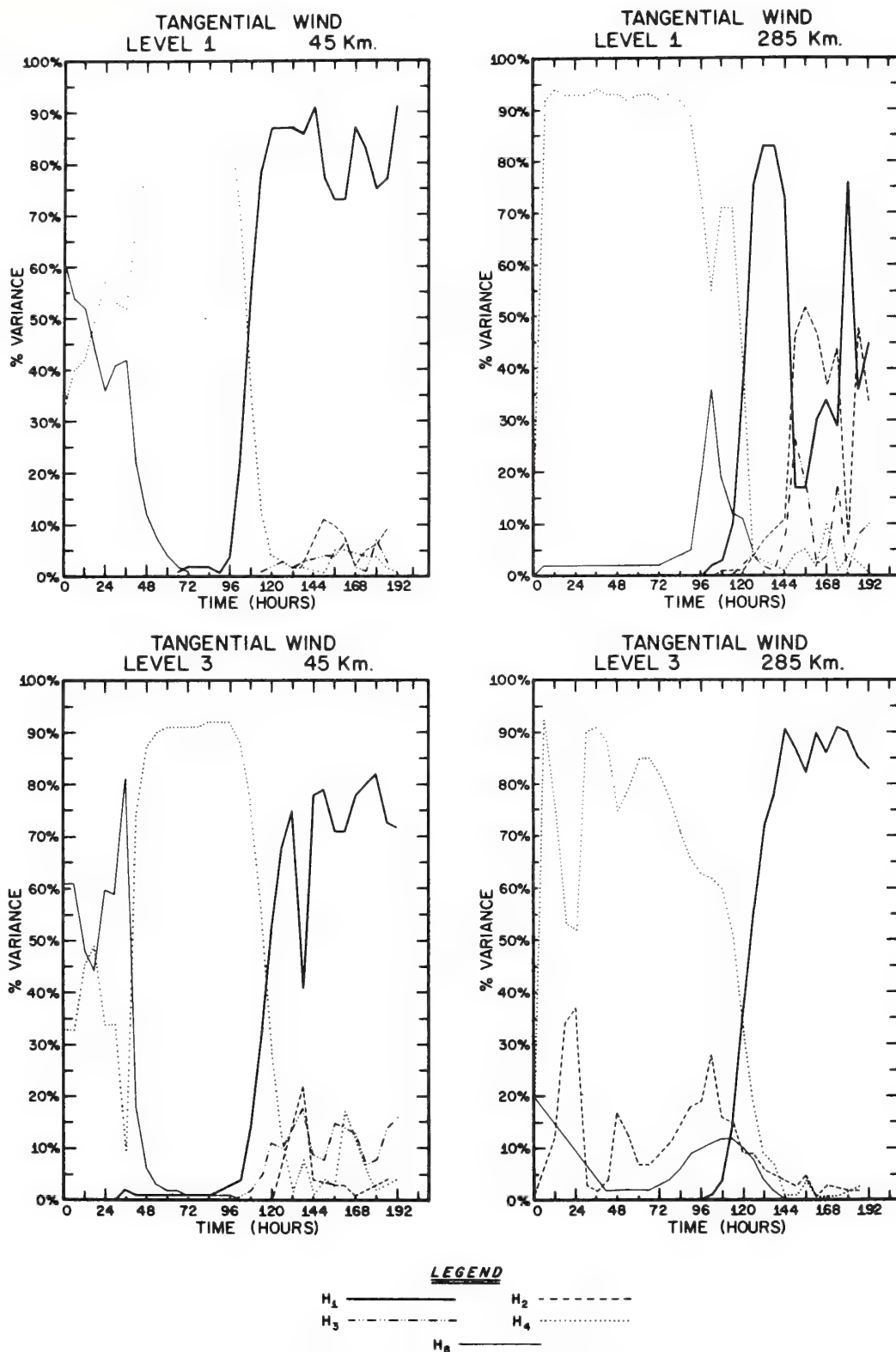


Figure 7: Harmonic analysis of the model outflow layer and inflow layer tangential wind component. Wave numbers 1, 2, 3, 4, and 8 are illustrated at an inner and outer radius.

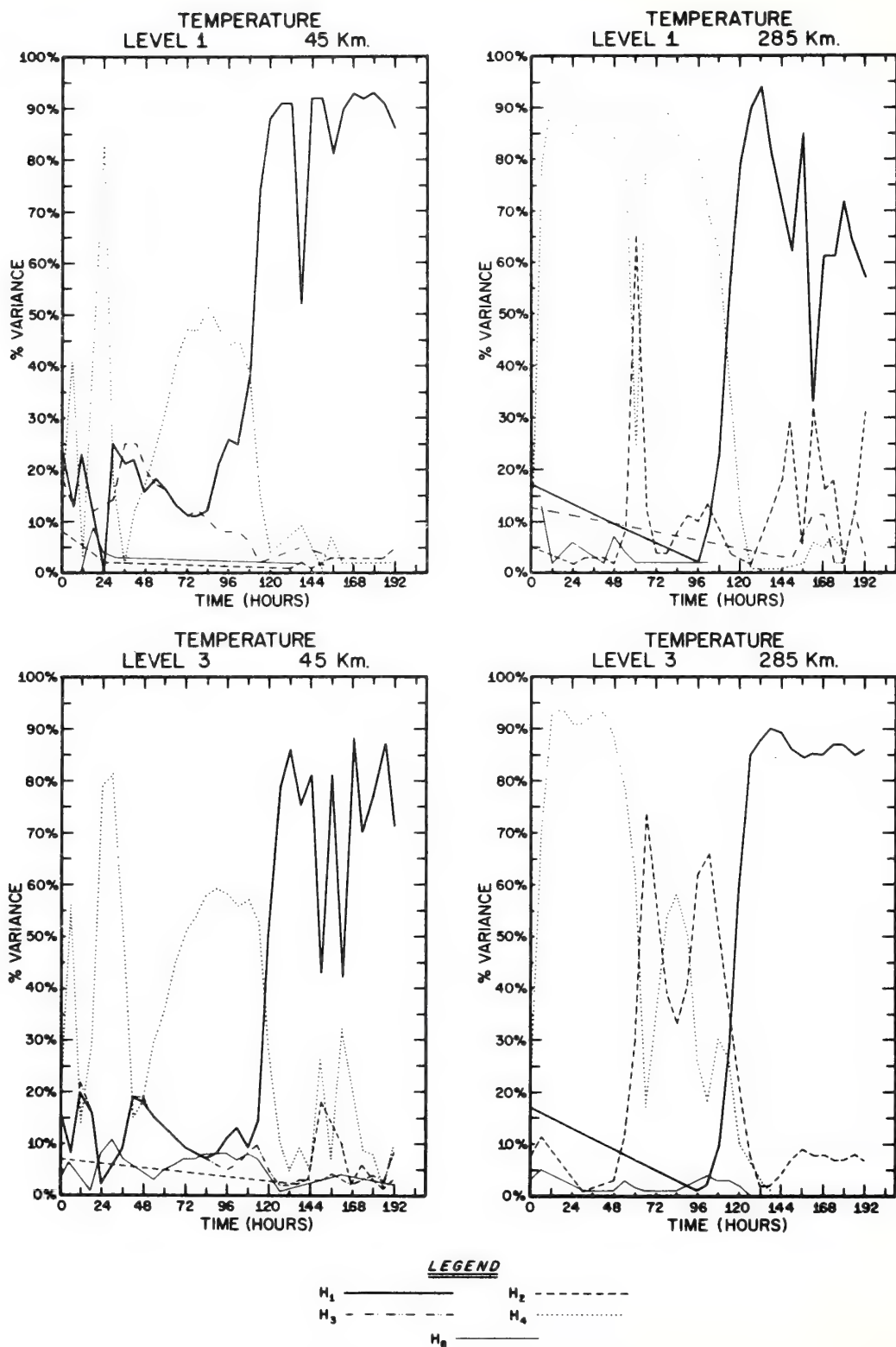


Figure 8: Harmonic analysis of the model outflow layer and inflow layer temperatures. Wave numbers 1, 2, 3, 4, and 8 are illustrated at an inner and outer radius.

variance is very small. The SD of the tangential wind, for example, is only about 0.5 m sec^{-1} contrasted with the mean flow of about 10 m sec in the outflow and 30 m sec^{-1} in the inflow layers.

The boundary induced wave numbers 4 and 8 are rapidly obscured by the presumably meteorological waves, 1, 2 and 3 with the onset of the asymmetric stages of the model. Figures 6, 7, and 8 all show the wave 4 trace and wave 1 trace intersecting at a time slightly less than 120 hours. Thereafter, the predominant wave is clearly wave 1 for both inflow and outflow layers. Recent results (Anthes, 1972) show the growth of asymmetries in the outflow layer to be a result of barotropic instability in which the energy source of the eddies is the kinetic energy of the mean flow. The temperature harmonic analysis shows essentially the same behavior as the momentum analysis, with wave number 1 becoming predominant during the asymmetric stage. In summary it should be reemphasized that the total variance in the inflow layer is small and that the temperature variance is small at both levels.

5. EDDY FLOW RELATED TO THE MATURE VORTEX

This section presents a detailed analysis of the eddy flow in both the inflow and outflow levels during the mature stage of the vortex (174 hours). Figures 9 and 10 are the streamline and isotach analysis for the outflow and inflow levels, respectively. The asymmetric circulation in the outflow layer, the displacement of the vortex center from the grid center, and the relative symmetry of the inflow level, discussed earlier, are again illustrated by these figures. The isotach analysis shows that

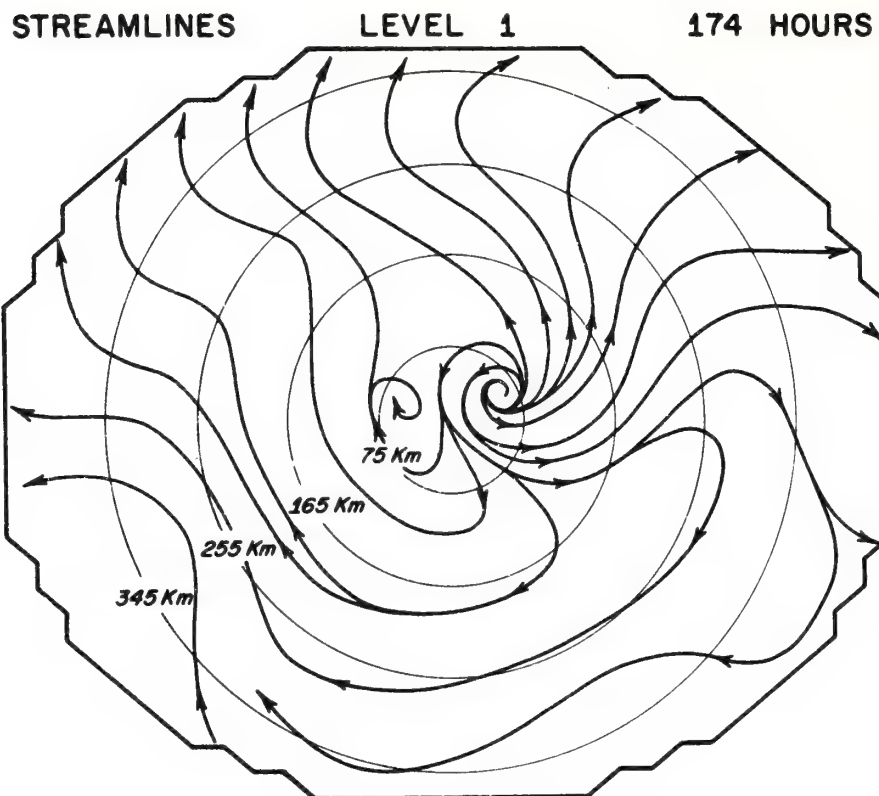


Figure 9A: Streamlines - Level 1 - 174 hours.

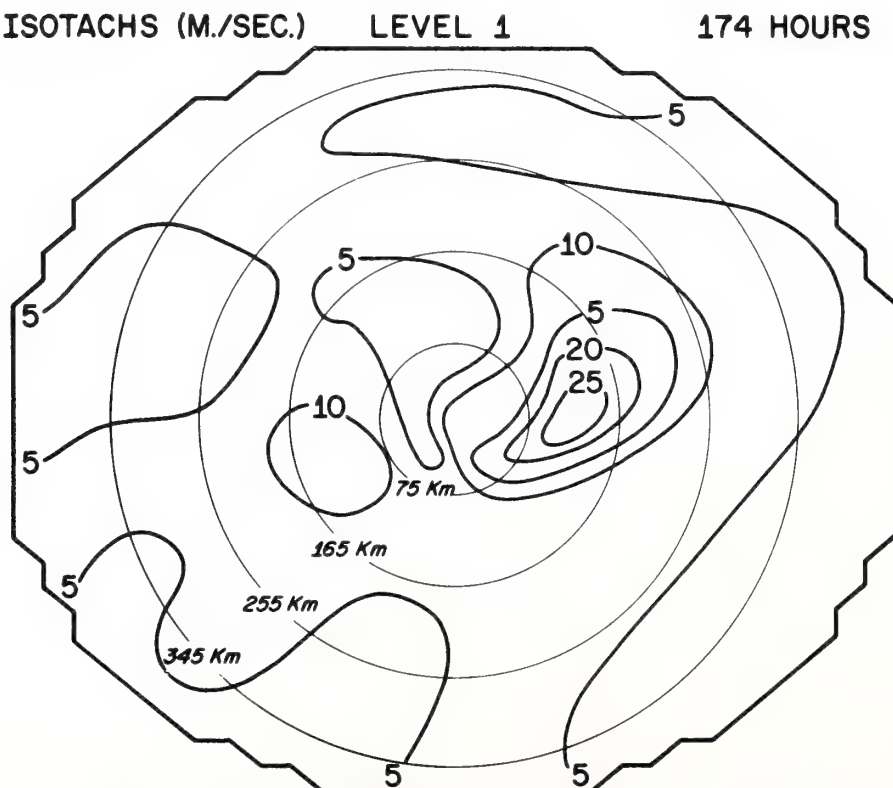


Figure 9B: Isotachs (m./sec.) - Level 1 - 174 hours.

STREAMLINES

LEVEL 3

174 HOURS

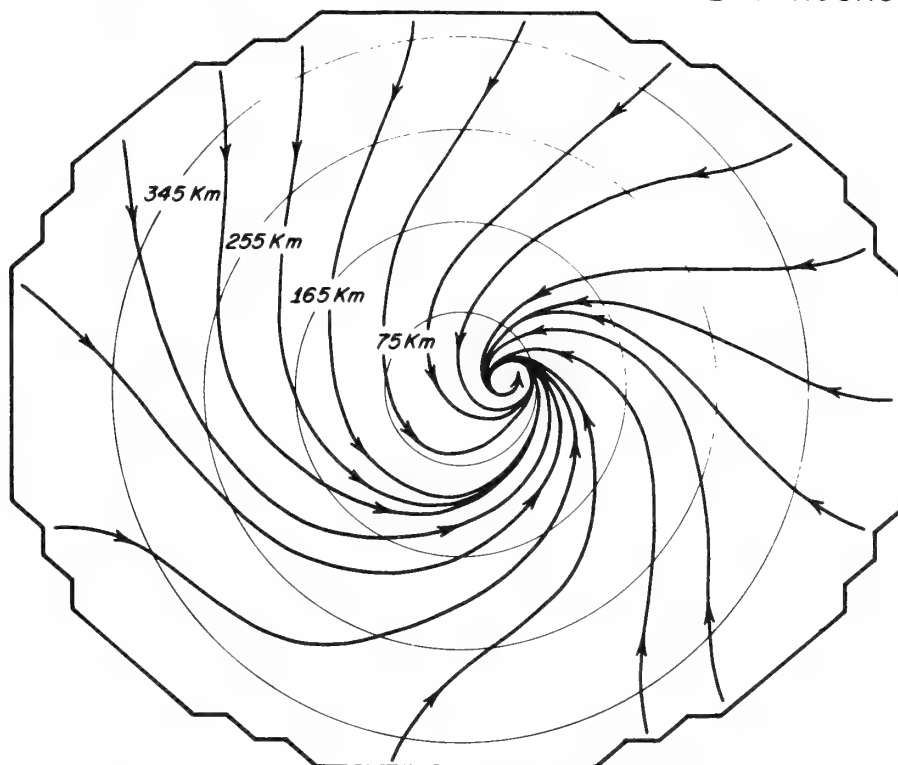


Figure 10A: Streamlines - Level 3 - 174 hours.

ISOTACHS (M./SEC.)

LEVEL 3

174 HOURS

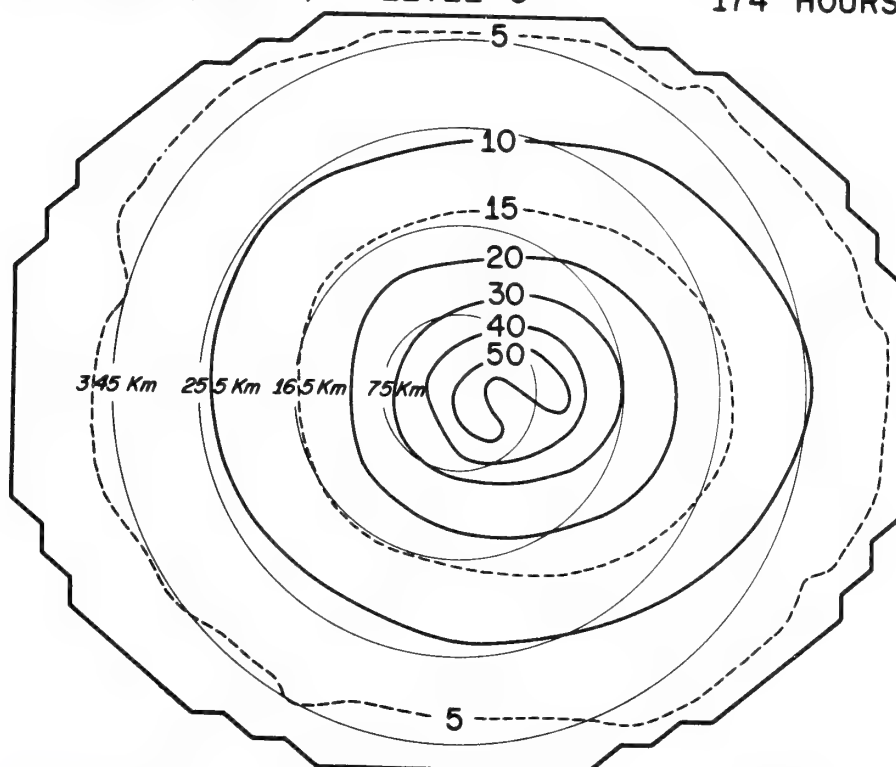


Figure 10B: Isotachs (m./sec.) - Level 3 - 174 hours.

at least one or two maxima and minima can be located about the storm's center in the outflow layer.

5.1 Asymmetries in the Outflow Layer

Figure 11 shows the azimuthal means and SD for the upper level wind components at 174 hours. The radial component is characterized by outflow at all radii, with a maximum value of 7 m sec^{-1} at 75 km. The outflow velocities decrease with increasing radii to a value of 2 m sec^{-1} at 435 km, the edge of the domain. The tangential component is characterized by a strong band of cyclonic winds near the center, with a maximum of 14 m sec^{-1} at 45 km. The mean tangential winds become anticyclonic at a radius of 135 km and remain anticyclonic with increasing radii.

Black and Anthes (1971) used cirrus band motions, radiosonde winds, and limited aircraft data to construct similar figures for six individual Atlantic storms. They also presented data from Miller's (1958) mean Atlantic storm and Izawa's (1964) mean Pacific storm. However, their calculations begin at approximately 105 km from the center and extend well beyond 435 km. Two limitations exist in comparing the real storm data to the model storm data. First, the isolated nature of the vortex implies that the asymmetries and the mean flow diminish as the boundary is approached. In contrast, in the real atmosphere, the flow patterns at large radii interact with other atmospheric systems which produce additional asymmetries. Second, near the center of the storms, Black and Anthes' data are compiled utilizing a coarse grid of 111 km as compared to the 30 km model grid. With these limitations in mind, a comparison between the model figures and the actual storm data shows:

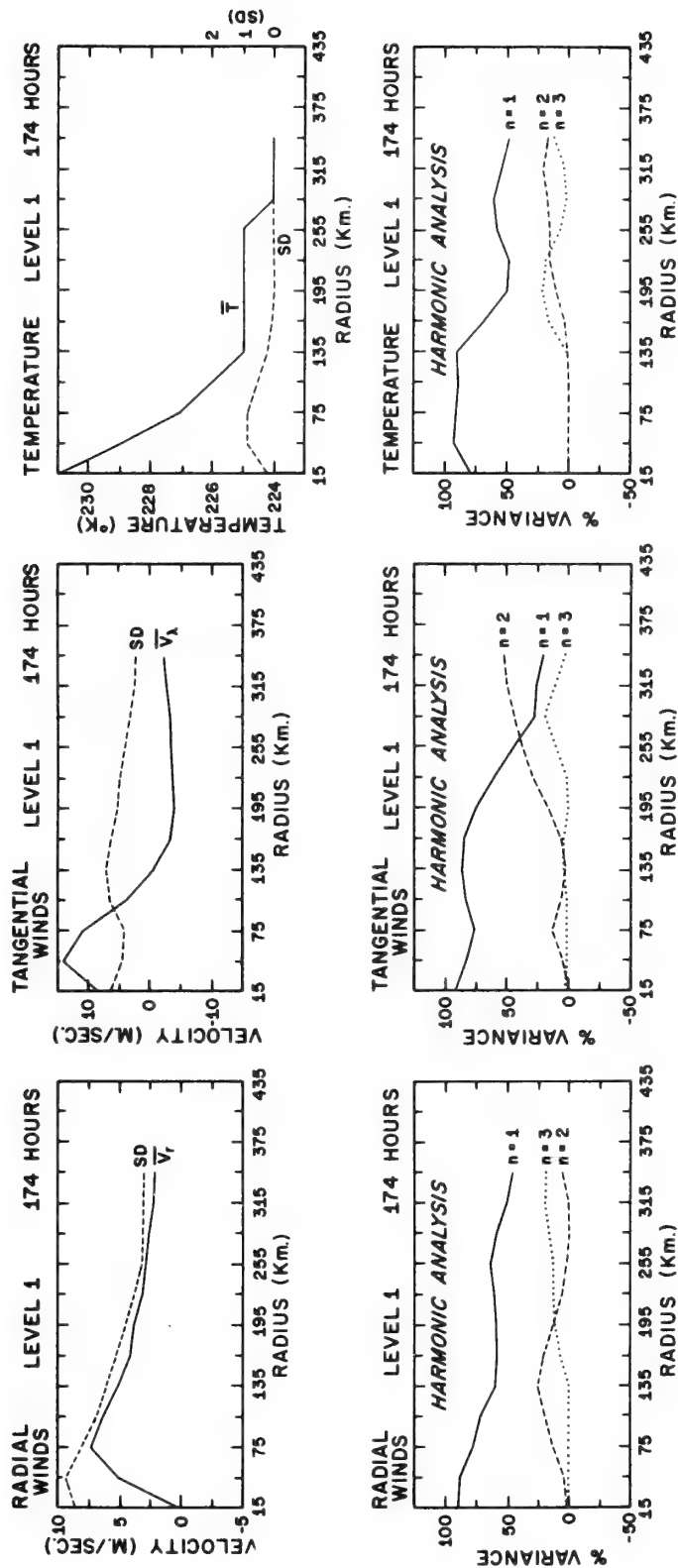


Figure 11: Standard deviations (SD), azimuthal means (-), and percent variance accounted for by wave numbers 1-4 for the mature outflow layer.

1. There is favorable agreement between the magnitude of the model mean radial wind component (V_r) compared with the six Atlantic storms. However, the magnitude of V_r is larger than either the Pacific or Atlantic mean profiles. Defining symmetry as a high ratio of the mean to the SD, the following comparisons of real and model outflow can be made:

- (a) The SD approaches the magnitude of the mean radial wind in both the model and actual storm data.
- (b) The magnitude of \overline{V}_r falls within the range of the magnitude of the real storm's radial winds.
- (c) At large radii, the real storm tends to be more asymmetric than the model storm because the latter diminishes in intensity with increasing radius and the former merges with other large scale circulations.
- (d) The magnitude of the asymmetries compares favorably with that of the mean Atlantic and Pacific storm's radial winds.

The harmonic analyses reveal the dominance of wave number 1 for both the model and the actual storm outflow. The percent of variance accounted for by the higher order wave numbers at increasing radii indicates the presence of more than one eddy in the outflow layer far from the model vortex center.

2. There is also favorable agreement between the magnitude of the model mean tangential wind component (\overline{V}_λ) compared with the actual storm data, although again the model storm circulation is somewhat smaller in radial extent than the real storm circulation. Specifically, the model storm and the real storm show:

- (a) a low ratio of the SD to the mean at inner radii, indicating symmetry;
- (b) a higher ratio of the SD to the mean at the outer radii, indicating asymmetry;
- (c) standard deviations for both tangential and radial wind components of about the same order of magnitude.

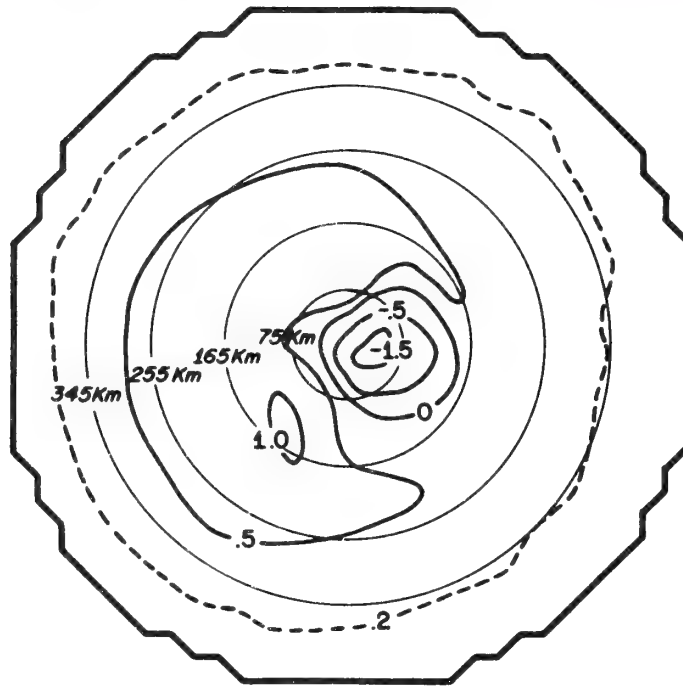
The harmonic analysis again shows a predominance of wave number 1 associated with the \bar{V}_λ . Higher wave numbers appear at radii greater than 200 km and account for a larger percent of the variance than the higher wave numbers associated with V_r .

Figure 12 shows the temperature departures from the mean tropical sounding (Herbert and Jordan, 1959) for both the inflow and outflow levels. The maximum departure of 7 degrees occurs to the east of the vortex center with smaller departures occurring to the west of the center. The SD are small (less than 1°C) at all radii and approach zero with increasing radius, reflecting the steady state, uniform boundary conditions imposed on the temperature fields. The symmetry ratio of the mean to the SD is large, indicating that the temperature is nearly symmetric. The harmonic analysis shows a large percentage of the variance to be contained in harmonic one, with higher harmonics becoming more important at large radii.

In summary, the model outflow momentum components are quite asymmetric, in agreement with the outflow asymmetries of the wind fields found in real storms. The temperature field is considerably more symmetric than the corresponding wind fields.

TEMPERATURE DEPARTURES 174 HOURS

LEVEL 3



LEVEL 1

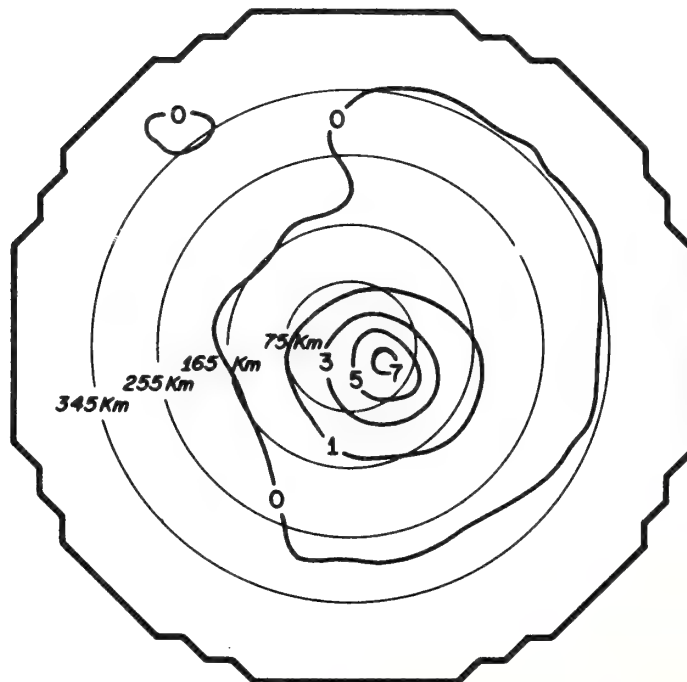


Figure 12: Temperature departures - 174 hours.

5.2 Asymmetries in the Inflow Layer

Figure 13 exhibits the inflow level mean radial profiles and harmonic analysis for the model momentum and temperature fields at time equal to 174 hours. Real storm data for a direct comparison are difficult to obtain since most low-level studies have been performed at elevations considerably above the boundary layer.

The radial wind component is characterized by an inflow maximum of 28 m sec^{-1} occurring at a radius of 75 km (same radius as the maximum outflow component). The inflow maximum rapidly diminishes to a value of approximately 1 m sec^{-1} at R_{max} (435 km). The small ratio of the SD to the mean indicates some minor asymmetry at the outer radii. These features are within observable limits, but they are difficult to substantiate. This ratio is much smaller in the inflow layer than in the outflow layer, indicating a closer approximation to axial symmetry in the low levels.

The radial wind harmonic analysis shows that wave number 1 explains approximately 80-90 percent of the variance from 135 km outward. A possible verification of the dominance of wave 1 in the boundary level could be the track of low-level actual storm radar echoes as reported by Black (1971). By tracking and plotting the variations of echo velocities about an actual hurricane, Black found patterns which reproduced a nearly sinusoidal wave--hence, wave number 1.

Inward from 135 km, wave number 4 is large in the model storm. Additional data (not presented) show wave number 4 to be a persistent feature of the model during its life history before and after 174 hours.

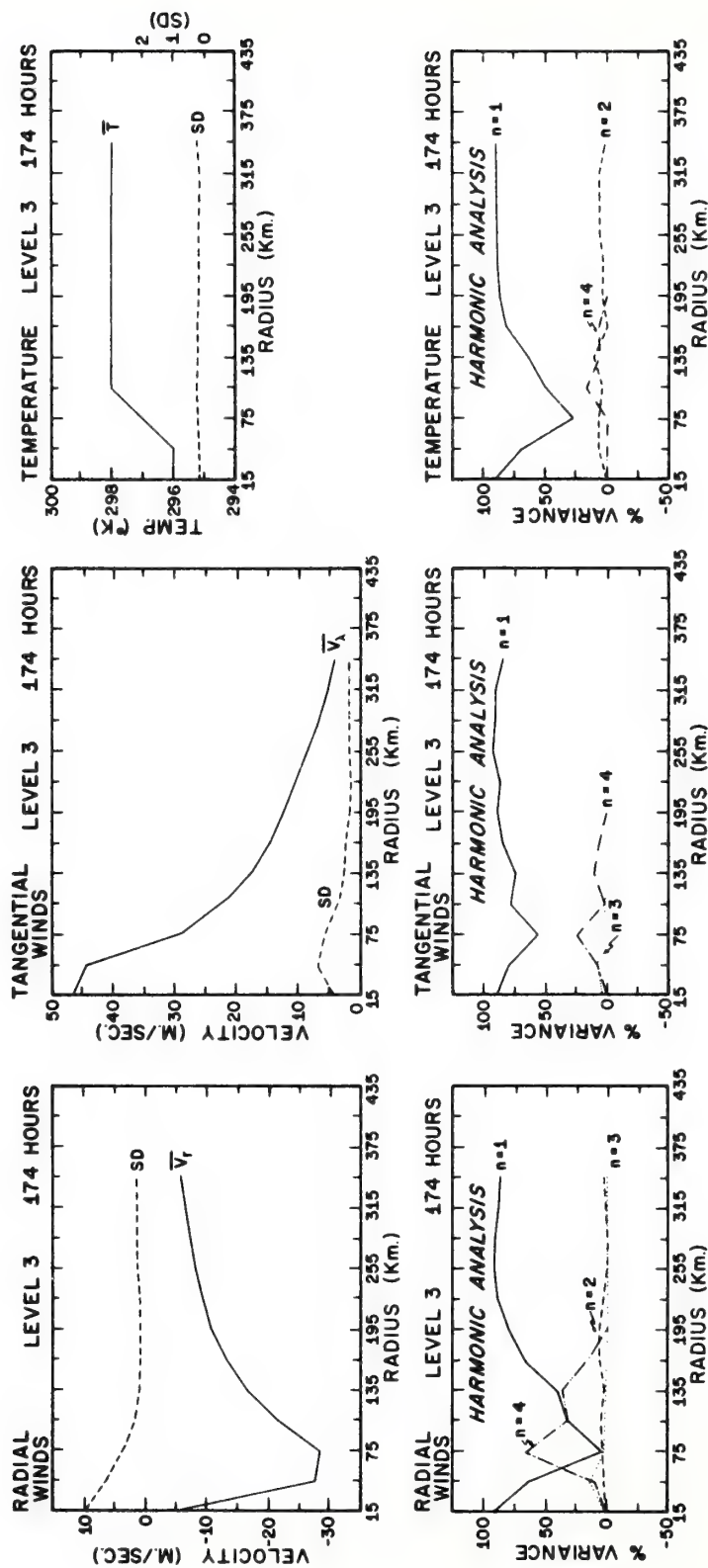


Figure 13: Standard deviations, azimuthal means, and harmonic analysis for the mature inflow layer.

This condition is probably artificial and is a manifestation of the initialization error due to the finite differencing scheme and boundary conditions. The standing wave number 4 does not occur in the upper outflow layer which is upstream from the lateral boundary.

The mean tangential wind component is characterized by a maximum cyclonic circulation of 47 m sec^{-1} at a radius of 15 km (fig. 13) which gradually diminishes to a value of 4 m sec^{-1} at R_{max} . For all radii, the SD remains small with a maximum of 7 m sec^{-1} at 45 km. The harmonic analysis shows that the greatest percent of the variance is contained in wave number 1. In summary, the small ratio of the SD to the mean indicates that the asymmetries in the boundary layer are much smaller than the asymmetries in the outflow layer.

The low-level temperature analysis (fig. 12) shows a maximum temperature deficit of 1.5°C . The deficit occurs at the vortex center with the remaining field characterized by flat gradients. Figure 13 displays the small SD found in the azimuthal mean temperatures and the strong boundary effects. Wave number 1 and 2 explain over 90% of the variance. Wave number 4 accounts for a smaller percent of the variance of temperature than of momentum.

6. HORIZONTAL TRANSPORT MECHANISMS

The time variations and the scale of the boundary and outflow layer asymmetries have been discussed in previous sections. This section investigates the importance of asymmetries as horizontal transport mechanisms. Computations of radially averaged horizontal and vertical fluxes of absolute vorticity and angular momentum are presented, with the greatest emphasis placed on the horizontal transports.

6.1 Flux of Absolute Vorticity

The mean and eddy transports of absolute vorticity, $\overline{v_r^\lambda \zeta_a^\lambda}$ and $\overline{v_r' \zeta_a'^\lambda}$, for both the inflow and outflow levels of the model are presented in figure 14. The circularly averaged absolute vorticity, ζ_a , is given by

$$\overline{\zeta}^\lambda = \frac{\overline{\partial_r v_r^\lambda}}{r \partial_r} + f \quad (7)$$

where f is the coriolis parameter. The operator $\overline{(\quad)}^\lambda$ refers to the azimuthal mean at a given radius and $(\quad)'$ refers to the departure from the mean. The outflow level flux of absolute vorticity shows that the eddy transports oppose the mean flux beyond 75 km. From 75 km to 165 km the eddy transport of vorticity is positive (outward) and dominant over the negative mean flux. Beyond 165 km, the mean flux becomes positive and is opposed by a negative eddy transport of vorticity of comparable magnitude. At the inner radii the mean and eddy transports are both positive with the mean flux much larger than the eddy flux.

The mean and eddy profiles of vorticity flux computed from the model experiment may be compared to similar profiles computed by Black and Anthes (1971) for real storms. Both model and real storms exhibit a radial annulus of substantial area in which the eddy transport of vorticity is negative and nearly balances the mean. This annular ring appears to be somewhat smaller in the model storm, a consequence perhaps of the overall small size of the model circulation. Comparisons near the center of the storm are difficult, because Black and Anthes' data begin at 111 km from the storm center, and the errors associated with their

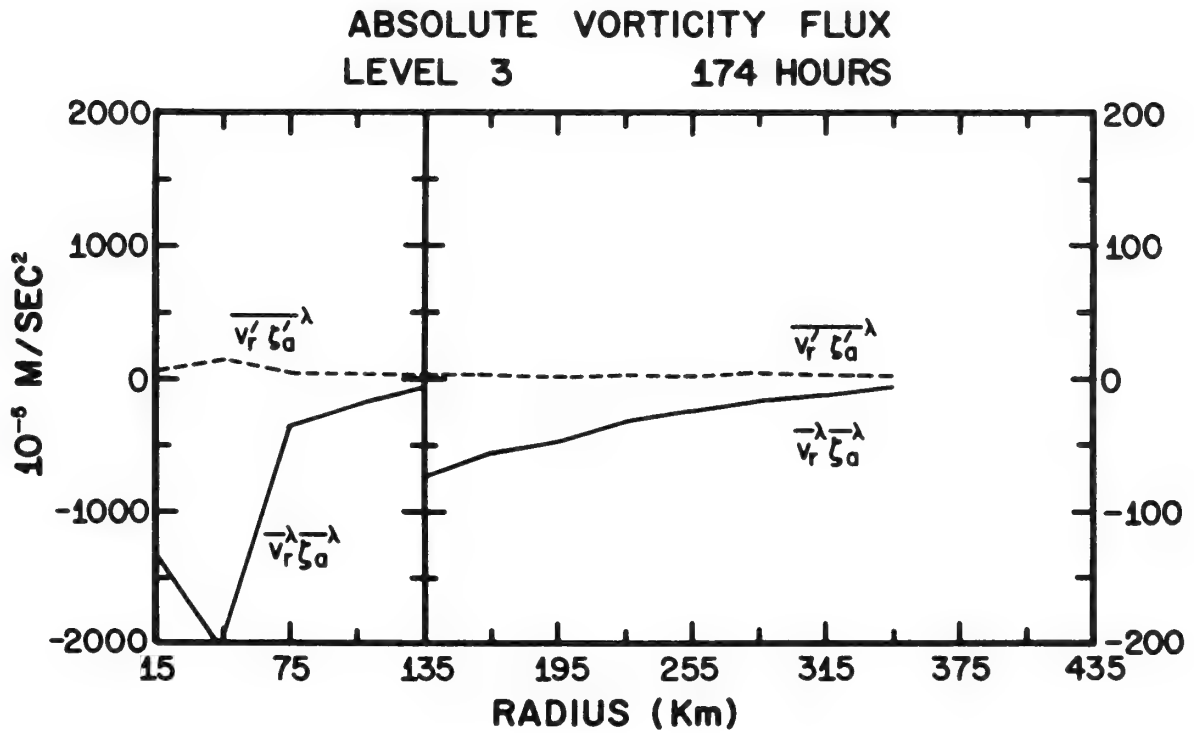
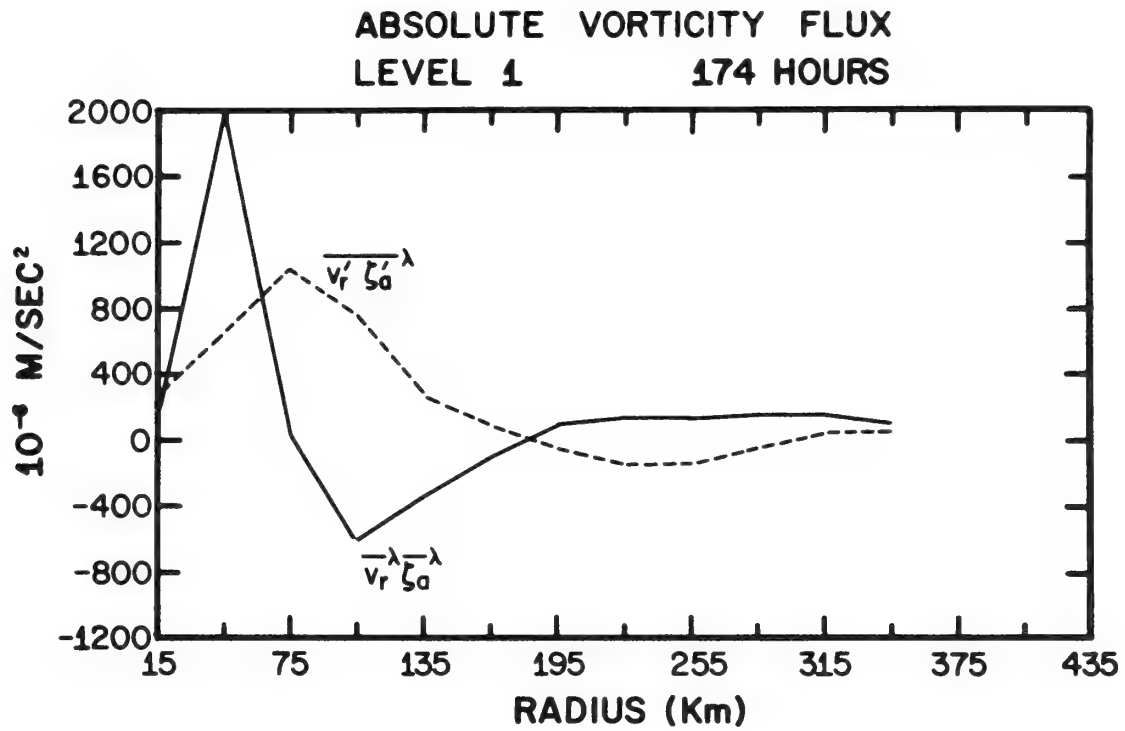


Figure 14: Profiles of mean and eddy transports of absolute vorticity for the model outflow and inflow levels.

measurements are maximum in this region. At the outer radii ($r \geq 195$ km) the model transports agree in sign and magnitude with observations.

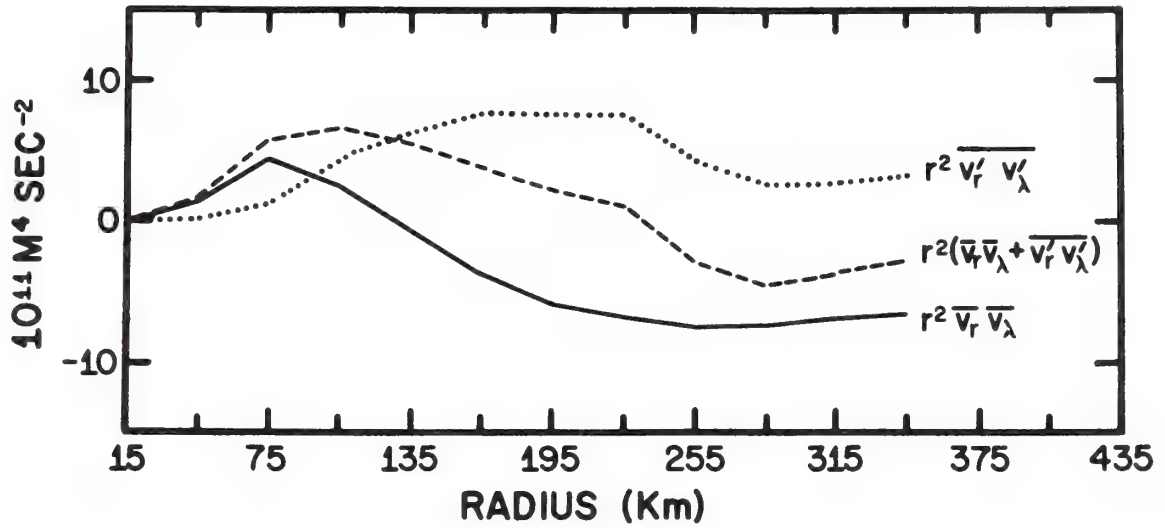
In summary, the eddies in the outflow layer (at moderate distances from the storm center) convey absolute vorticity inward toward the storm center and oppose the outward vorticity flux by the mean flow in both the real and model storm.

The boundary layer flux of absolute vorticity (fig. 14) shows small positive eddy transports of vorticity at all radii in agreement with previous theoretical estimates (Anthes, 1970). The mean flux is strongly negative (inward) at all radii. Values range over two orders of magnitude. Therefore, vorticity is conveyed inward by the mean flow and completely dominates the eddy flow. This again emphasizes the basic symmetry in the inflow layer.

6.2 Flux of Angular Momentum

The mean, the eddy and the total transports of relative angular momentum, (weighted by radial distance), for both the outflow and inflow levels of the model are presented in figure 15. In the outflow layer, the mean flow transports negative momentum outward, while the eddies oppose the mean flow by transporting positive angular momentum outward. The mean and eddy terms are the same order of magnitude and tend to compensate for each other. In contrast, actual storm data of Black and Anthes (1971) show both components to have a net outward transport of negative relative angular momentum. However, the radial extent of the model is only half of that of the actual storm data and does not extend to the outer radii where the larger negative angular momentum fluxes are

ANGULAR MOMENTUM FLUX
LEVEL 1 174 HOURS



ANGULAR MOMENTUM FLUX
LEVEL 3 174 HOURS

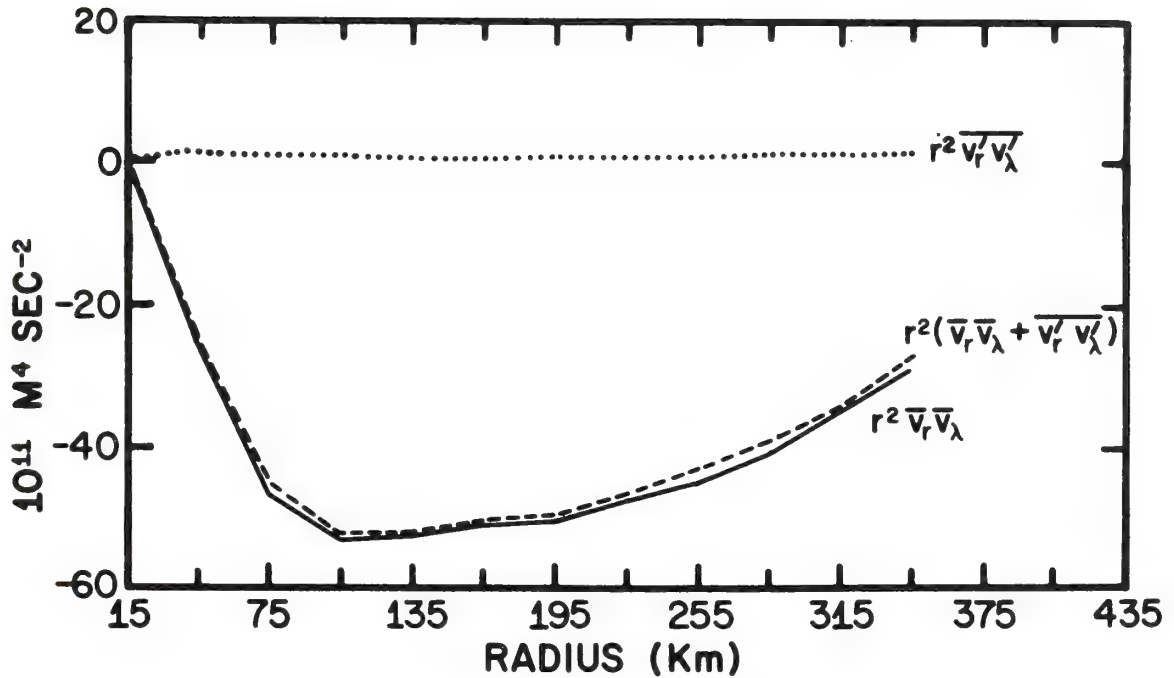


Figure 15: Profiles of mean ($r^2 \bar{v}_r \bar{v}_\lambda$), eddy ($r^2 \overline{v'_r v'_\lambda}$), and total ($r^2(\bar{v}_r \bar{v}_\lambda + \overline{v'_r v'_\lambda})$) transports of angular momentum for the model outflow and inflow levels.

found (Palmén and Riehl, 1957). In general, the magnitudes of the eddy momentum flux associated with the model and real storms are small inside 400 km. The model flux tends to be positive, and the flux associated with real storms tends to be negative.

The boundary layer flux of relative angular momentum (fig. 15) shows a very small outward eddy flux of positive angular momentum. The mean transport shows a strong inward flux of positive angular momentum. The mean completely dominates the eddy transport at all radii. This result is in agreement with Riehl and Malkus (1958), who found the eddy transports of momentum to be either negligible or outward in the inflow layer of hurricane Daisy. These results also agree with Pfeffer (1958) who found that within a few hundred kilometers from the vortex center the horizontal-eddy processes are of the wrong sign to account for the inward transport of angular momentum in the inflow layer of hurricane Connie, 1955.

In summary, the eddy transport of angular momentum in the model outflow layer is slightly positive; while in contrast, the eddy flux in real storms appears to be slightly negative. There is good agreement between the model and observations in the mean flux, however. In the inflow layer, the mean flux is dominant and is directed inward. The eddy flux is small, but directed outward, in good agreement with observations.

6.3 Vertical Flux of Relative Angular Momentum

It is of considerable importance to the overall dynamics of the model to determine the origin of the asymmetries in the outflow layer. As previously established, the outflow level is characterized by two

preferred quadrants of outflow (fig. 3). It is conceivable that azimuthal variation in the vertical flux of relative angular momentum could be responsible for the two streams of outflow.

Figure 16 shows azimuthal mean radial profiles of the mean vertical transport and eddy vertical transport of relative angular momentum, $(r \overline{v_{\lambda}^{\sigma}})$, $(r \overline{v_{\lambda}^{\sigma'}})$, where σ is the "vertical velocity" in the σ -system. The σ information levels are staggered in the vertical from the dynamic variables, necessitating the interpolation of the wind components to the σ levels. The radial profiles clearly show that the vertical flux of momentum is predominantly from the mean current. Although the outflow occurs in two quadrants the vertical motion is bringing momentum to the outflow level in a symmetric fashion. Thus the asymmetries are developing after the air reaches the outflow layer. This result is consistent with Anthes' (1972) findings that the asymmetries are a result of dynamic instability in the horizontal flow, with the eddies growing at the expense of the mean horizontal flow.

7. SUMMARY AND CONCLUSIONS

Conventional statistical techniques have been utilized to show the formation and structure of horizontal asymmetries in the outflow and inflow levels of a numerical hurricane model. The outflow layer is highly asymmetric, especially at the outer radii. The inflow layer contains relatively small asymmetries, and the approximation to axial symmetry is very good in the low levels. These results agree well with observations.

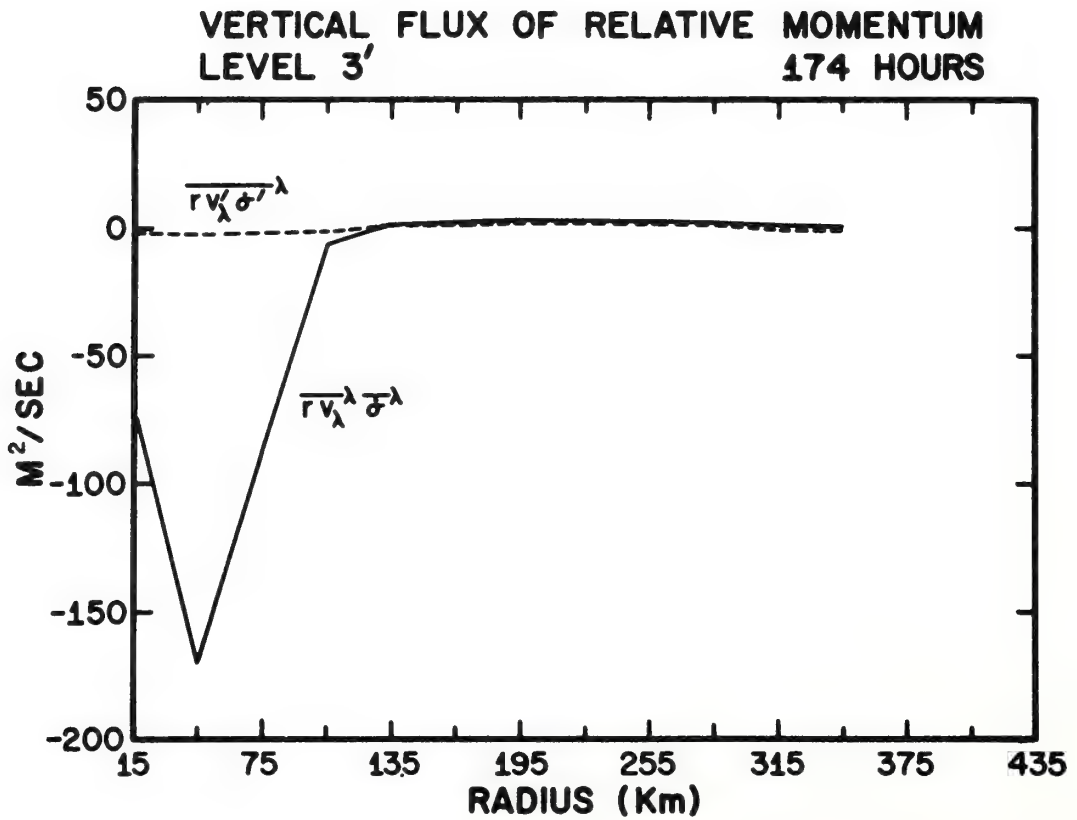
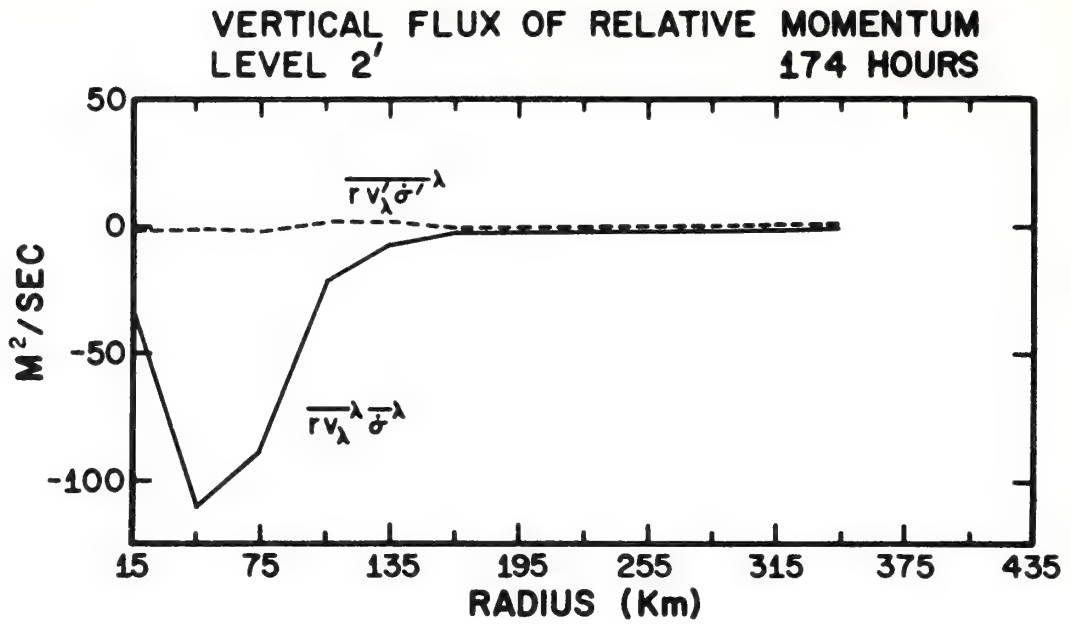


Figure 16: Profiles of mean and eddy vertical transports of relative momentum for the model outflow and inflow levels.

A comparison with real storms reveals that the model is capable of reproducing many observed features of the mature three-dimensional tropical cyclone. Slight differences between the observed and model vortices are attributed to the limited lateral extent of the model as the errors associated with the irregular boundary.

The mean transport of absolute vorticity beyond 200 km in the outflow layer is outward from the storm center and is opposed by the eddy flux of absolute vorticity in both the real and model vortices. The mean flux of absolute vorticity in the model inflow layer is strongly inward and completely dominates the small eddy flow, in agreement with real storms. Beyond 135 km, the mean transport of relative angular momentum in the outflow layer is negative; the eddy flux of angular momentum is positive. Radial profiles of the vertical flux of momentum show that the vertical transport of momentum is dominated by the mean current, indicating that vertical eddies play no important role in the formation of the eddies in the outflow layer.

8. REFERENCES

- Anthes, R. A. (1972), The development of asymmetries in a three-dimensional numerical model of a tropical cyclone, *Monthly Weather Review*, (in press).
- Anthes, R. A. (1970), The role of large-scale asymmetries and internal mixing in computing meridional circulations associated with the steady-state hurricane, *Monthly Weather Review*, 98, No. 7, July, 521-528.
- Anthes, R. A., S. L. Rosenthal, and J. W. Trout (1971a), Preliminary results from an asymmetric model of the tropical cyclone, *Monthly Weather Review*, (in press).
- Anthes, R. A., J. W. Trout, and S. S. Ostlund (1971b), Three dimensional particle trajectories in a model hurricane, *Weatherwise*, (in press).
- Anthes, R. A., J. W. Trout, and S. L. Rosenthal (1971c), Comparisons of tropical cyclone simulations with and without the assumption of circular symmetry, *Monthly Weather Review*, (in press).
- Black, P. G. and R. A. Anthes (1971), On the asymmetric structure of the tropical cyclone outflow layer, *Journal of the Atmospheric Sciences*, (in press).
- Black, P. G. (1971), Use of echo velocities to evaluate hurricane modification experiments, Project STORMFURY Annual Report 1970, U. S. Department of the Navy and U. S. Department of Commerce, Appendix J, J-1 - J-20.
- Gray, W. M. (1967), The mutual variation of wind, shear and baroclinicity in the cumulus convective atmosphere of the hurricane, *Monthly Weather Review*, 95, No. 2, February, 55-73.
- Izawa, T. (1964), On the mean wind structure of typhoons, Typhoon Research Laboratory, Technical Note N . 2, Meteorological Research Institute, Tokyo, Japan.
- Koss, W. J. (1971), Numerical integration experiments with variable resolution two-dimensional cartesian grids using the box method, *Monthly Weather Review*, (in press).
- Kurihara, Y. and J. L. Holloway (1967), Numerical integrations of a nine-level global primitive equation model formulated by the box method, *Monthly Weather Review*, 95, No. 8, August, 509-530.

- Matsuno, T. (1966), Numerical integrations of the primitive equations by a simulated backward difference method, *Journal of the Meteorological Society of Japan*, 44, February, 76-83.
- Miller, B. I. (1958), The three-dimensional wind structure around a tropical cyclone, National Hurricane Research Project Report 15, U. S. Department of Commerce, National Hurricane Research Laboratory, Miami, Florida, January, 41 pp.
- Palmén, E. and H. Riehl (1957), Budget of angular momentum and energy in tropical cyclones, *Journal of Meteorology*, 14, 150-159.
- Pfeffer, R. L. (1958), Concerning the mechanics of hurricanes, *Journal of Meteorology*, 15, 113-119.
- Phillips, N. A. (1957), A coordinate system having some special advantages for numerical forecasting, *Journal of Meteorology*, 14, April, 184-185.
- Riehl, H. and J. S. Malkus (1958), Some aspects of hurricane Daisy, *Tellus*, 13, 181-213.
- Rosenthal, S. L. (1971), A circularly symmetric primitive equation model of tropical cyclones and its response to artificial enhancement of the convective heating functions, *Monthly Weather Review*, 99, No. 5, May, 414-426.
- Rosenthal, S. L. (1970a), Experiments with a numerical model of tropical cyclone development--some effects of radial resolution, *Monthly Weather Review*, 98, No. 2, February, 106-120.
- Rosenthal, S. L. (1970b), A circularly symmetric primitive equation model of tropical cyclone development containing an explicit water vapor cycle, *Monthly Weather Review*, 98, Vol. 9, September, 643-663.
- Rosenthal, S. L. (1969), Numerical experiments with a multilevel primitive equation model designed to simulate the development of tropical cyclones: experiment I, ESSA Technical Memorandum ERLTM-NHRL 82, U. S. Department of Commerce, National Hurricane Research Laboratory, Miami, Florida, 36 pp.
- Smagorinsky, J., S. Manabe, and J. L. Holloway (1965), Numerical results from a nine-level general circulation model of the atmosphere, *Monthly Weather Review*, 93, No. 12, December, 727-768.

U.S. DEPARTMENT OF COMMERCE
National Oceanic and Atmospheric Administration
Environmental Research Laboratories

NOAA Technical Memorandum ERL AOML-14

FREE-AIR GRAVITY ANOMALIES
SOUTH OF PANAMA AND COSTA RICA
(NOAA SHIP OCEANOGRAPHER - AUGUST 1969)

Robert J. Barday
Marine Geology and Geophysics Laboratory

Atlantic Oceanographic and Meteorological Laboratories
Miami, Florida
September 1971



TABLE OF CONTENTS

	PAGE
1. INTRODUCTION	1
2. DATA ACQUISITION AND REDUCTION	2
2.1 Zeroed Meter Gravity	2
2.2 Gravity Meter Reading	3
2.3 Eötvös Correction	3
2.4 Drift Correction	8
3. DATA QUALITY	12
4. DATA PRESENTATION	12
5. DISCUSSION	14
6. ACKNOWLEDGEMENTS	18
7. REFERENCES	19
APPENDIX: Profiles	21

ILLUSTRATIONS

	PAGE
Figure 1	6
Figure 2	9
Figure 3	11
Figure 4	13
Plate 1	(in pocket)

FREE-AIR GRAVITY ANOMALIES SOUTH OF PANAMA AND COSTA RICA

(NOAA SHIP OCEANOGRAPHER - August 1969)

Robert J. Barday

Free-air anomaly profiles from a geophysical investigation centered on the Panama Fracture Zone are presented with their corresponding bathymetric profiles. The quality of these profiles is indicated by a mean free-air anomaly discrepancy of 3.48 milligals with a standard deviation of 3.28 milligals for 99 crossings of the ship's track. These data support the existence of a deep, sediment-filled depression at the northern end of the Panama Fracture Zone, the presence of a sediment-filled marginal trough east of the Coiba Ridge, and the accumulation of thick sedimentary deposits on the eastern flanks of both the Cocos and Coiba Ridges. The gravity data also suggest that there is no large-scale change in crustal structure across the Panama Fracture Zone, and the entire survey area may be slightly out of isostatic adjustment.

1. INTRODUCTION

In August 1969 a geophysical investigation of the Panama Fracture Zone was conducted by the National Oceanic and Atmospheric Administration Ship OCEANOGRAPHER. Depth, total magnetic intensity, and gravity meter readings were recorded continuously over approximately 11,200 km of track-line controlled by satellite navigation. This report presents free-air anomaly profiles and discusses certain

geological conclusions that are consistent with the observed gravity data.

2. DATA ACQUISITION AND REDUCTION

By definition, the free-air anomaly can be expressed as

$$FA = g_O - \gamma_O \quad (1)$$

where $\gamma_O = 978.049(1 + 0.0052884\sin^2\phi - 0.0000059\sin^2 2\phi)$ is the theoretical sea level gravity given by the 1930 international gravity formula, and g_O is the observed gravity reduced to sea level. For sea level gravity observations

$$g_O = ZMG + R + E_C + D_C \quad (2)$$

where ZMG (zeroed meter gravity) is a value equivalent to a gravity meter reading of zero, R is the meter reading (in milligals), E_C is the Eötvös correction, and D_C is the drift correction.

Both data acquisition and reduction can most easily be discussed from a term-by-term consideration of (2).

2.1 Zeroed Meter Gravity

The ZMG was obtained from a land tie at Rodman Naval Station, Canal Zone, immediately before the survey. [The details of the ZMG computation have been discussed by Orlin and Sibila (1966).] The base station is described by Woollard and Rose (1963) as follows:

WH 1015. Rodman Naval Base, at shore end of center of three piers next to large valve block painted black and yellow, Lamont No. BE 1-1.

2.2 Gravity Meter Reading

The gravity meter used for this survey was Askania "Sea Gravimeter Gss2 after Graf", Model C, No. 22 (Graf and Schulze, 1961; Schulze, 1962) mounted on an electrically erected Anschütz Gyrotable. The gravity meter dial reading, R_d ($R_d = R/K_d$ where K_d is a constant necessary to convert dial divisions into milligals), was recorded both digitally and on analog strip chart.

All digitized dial readings were plotted against time, and the values appearing to be inconsistent were checked against the analog strip chart. If discrepancies were found, the digitized values were adjusted. If the inconsistencies persisted, the values in question were deleted unless they could be related to any changes in speed or changes in course less than 90° .

2.3 Eötvös Correction

Accurate navigation is critical to marine gravity observations. At 5°N , the mean latitude of this survey, and at 27 km/hr, the average speed of this survey, the rates at

which the Eötvös correction changes with respect to course and speed are 2.1 milligals/ $^{\circ}$ (for a N-S trackline) and 3.7 milligals/km/hr (for an E-W trackline). If the free-air anomaly is to be determined to an accuracy of 1 milligal (the accuracy to which R was measured), the course and speed must be known within 0.5° and 0.2 km/hr, respectively.

Because the course and speed are computed from the smooth plotted track, their accuracy depends upon the accuracy of the fixes, the elapsed time between fixes, and the interpolation method used to determine the ship's track between fixes.

This survey was controlled by the Navy's satellite navigation system with the AN/SRN-9 equipment (Guier, 1966). The accuracy of this system is largely influenced by uncertainty in the ship's velocity. As a first approximation, a 1.8-km/hr error in the ship's velocity results in a 0.45-km error in the computed satellite fix (Stansell, 1970). If the velocity is estimated from sea trial data or the speed made good between previous fixes, as in the case of this survey, then the computed fixes may be in error by as much as 2 km.

The average time interval between fixes was 2 hr. At this interval an error of 45 km in the satellite fixes would result in a one-milligal error in the computed Eötvös

correction. However, the elapsed time between fixes ranged downward to 22 minutes implying a possible error in the Eötvös correction of 10 milligals or more.

The interpolation method used to determine the smooth plotted track was based on the assumption that the course and speed made good are constant between navigation points. (Navigation point is used here to mean a point where there is a satellite fix or a change in course and/or speed.) The computed Eötvös correction was, therefore, a discontinuous step function rather than a continuous function between course and speed changes.

To remove these artificial discontinuities and minimize error in the Eötvös correction, the following technique was used (refer to fig. 1):

- (1) For all but E-W lines both the speed made good, SMG (B, fig. 1), and the difference between the course made good and the course steered, CMG-CST (A, fig. 1), were plotted against time. Both plots were then approximated by piecewise continuous curves in which discontinuities occurred at any changes in speed and at changes in course greater than 10° .
- (2) For E-W lines the Eötvös correction (C, fig. 1), rather than SMG and CMG-CST, was similarly treated.
- (3) These piecewise continuous curves were, in turn, approximated by straight line segments.

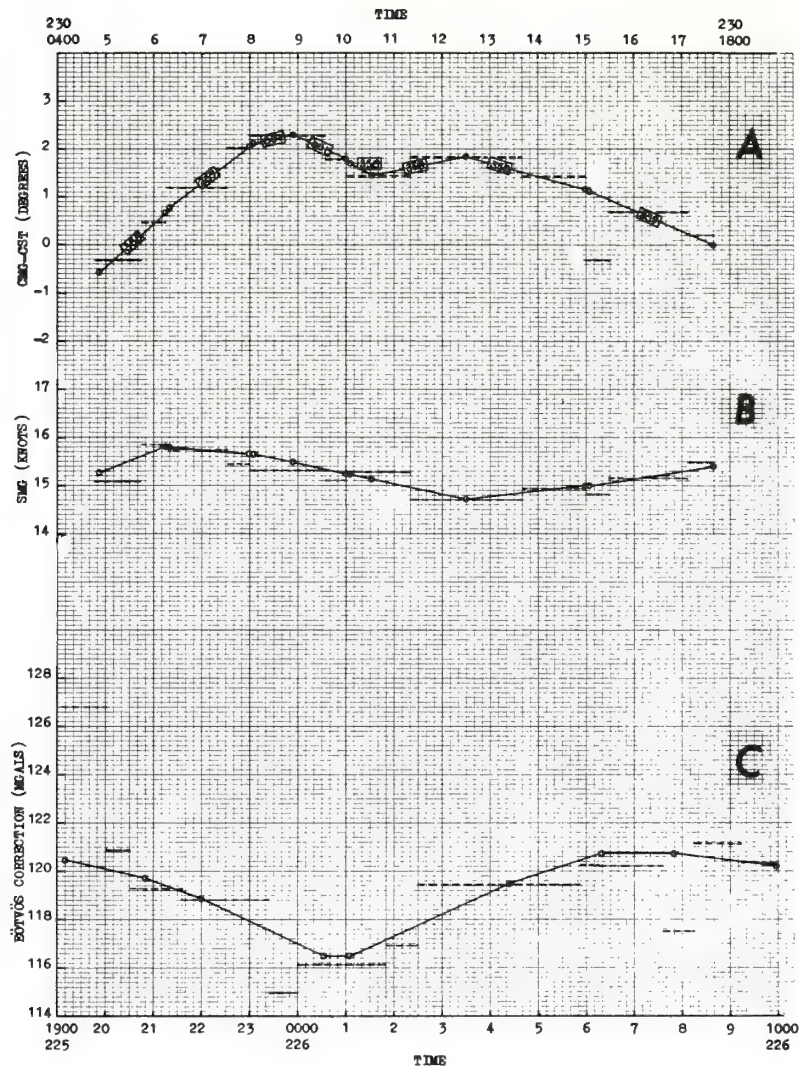


Figure 1. Based on the assumption that the course and speed made good are constant between navigation points, the difference between the course made good and the course steered (CMG-CST), the speed made good (SMG), and the Eötvös correction become piecewise continuous step functions of time [dashed curves (---)]. The solid curves (—) illustrate a technique whereby these parameters can be made to more closely approximate continuous functions of time (not shown for clarity). Curves A and B are from a N-S profile (No. 14) and curve C is from an E-W profile (No. 3). The numbers enclosed in boxes (359) signify the course steered for each segment of the CMG-CST curve bounded by circles (o). The Eötvös correction used to compute the free-air anomaly is determined from a linear time interpolation of the circled values.

(4) The time, course, and speed or the time and Eötvös correction at each break in slope were entered into a computer program that obtained the free-air anomaly at each data point using the Eötvös correction computed from a linear time interpolation of these parameters. For all but E-W lines the program also requires course and speed values immediately before and after each change in course steered.

This technique is based on the assumption that the difference between the course and speed made good and the ordered course and speed is the result of the current acting on the ship. Although current in this sense of the word includes many factors in addition to horizontal movement of the water, its effect on the ship should vary smoothly between large changes in course and speed. Therefore, the speed made good and the difference between the course made good and the course steered should be continuous functions of time between speed changes and large changes in course steered. Because the Eötvös correction computed for E-W lines is insensitive to small changes in course, it must likewise be continuous.

2.4 Drift Correction

Because of instrumentation failure it was impossible to complete a land tie at the conclusion of this survey. The drift, D [$D = -D_o / (t - t_o)$ where t is the time of observation and t_o is the time of ZMG determination], was determined as follows:

- (1) The free-air anomaly was computed without a drift correction.
- (2) The differences ΔFA_{ij} and Δt_{ij} where $i < j$ were determined for each trackline intersection; $\Delta FA_{ij} = FA_{ji} - FA_{ij}$ and $\Delta t_{ij} = t_{ji} - t_{ij}$ where FA_{ji} is the free-air anomaly and t_{ji} is the time of profile j at its intersection with profile i .
- (3) The drift was computed by a least squares fit of the function $\Delta FA = D \times \Delta t$ to the pairs $\Delta FA_{ij}, \Delta t_{ij}$.

Illustrated in figure 2, this procedure follows from the identities $FAN_{ij} \equiv FA_{ij} - D \times (t_{ij} - t_o)$ and $FAN_{ji} \equiv FA_{ji} - D \times (t_{ji} - t_o)$ where FAN_{ji} is the drift-corrected free-air anomaly of profile j at its intersection with profile i . Therefore,

$$\begin{aligned}\Delta FAN_{ij} &= FAN_{ji} - FAN_{ij} \\ &= FA_{ji} - D \times (t_{ji} - t_o) - FA_{ij} + D \times (t_{ij} - t_o) \\ &= FA_{ji} - FA_{ij} - D \times (t_{ji} - t_{ij}) \\ &= \Delta FA_{ij} - D \times \Delta t_{ij}.\end{aligned}$$

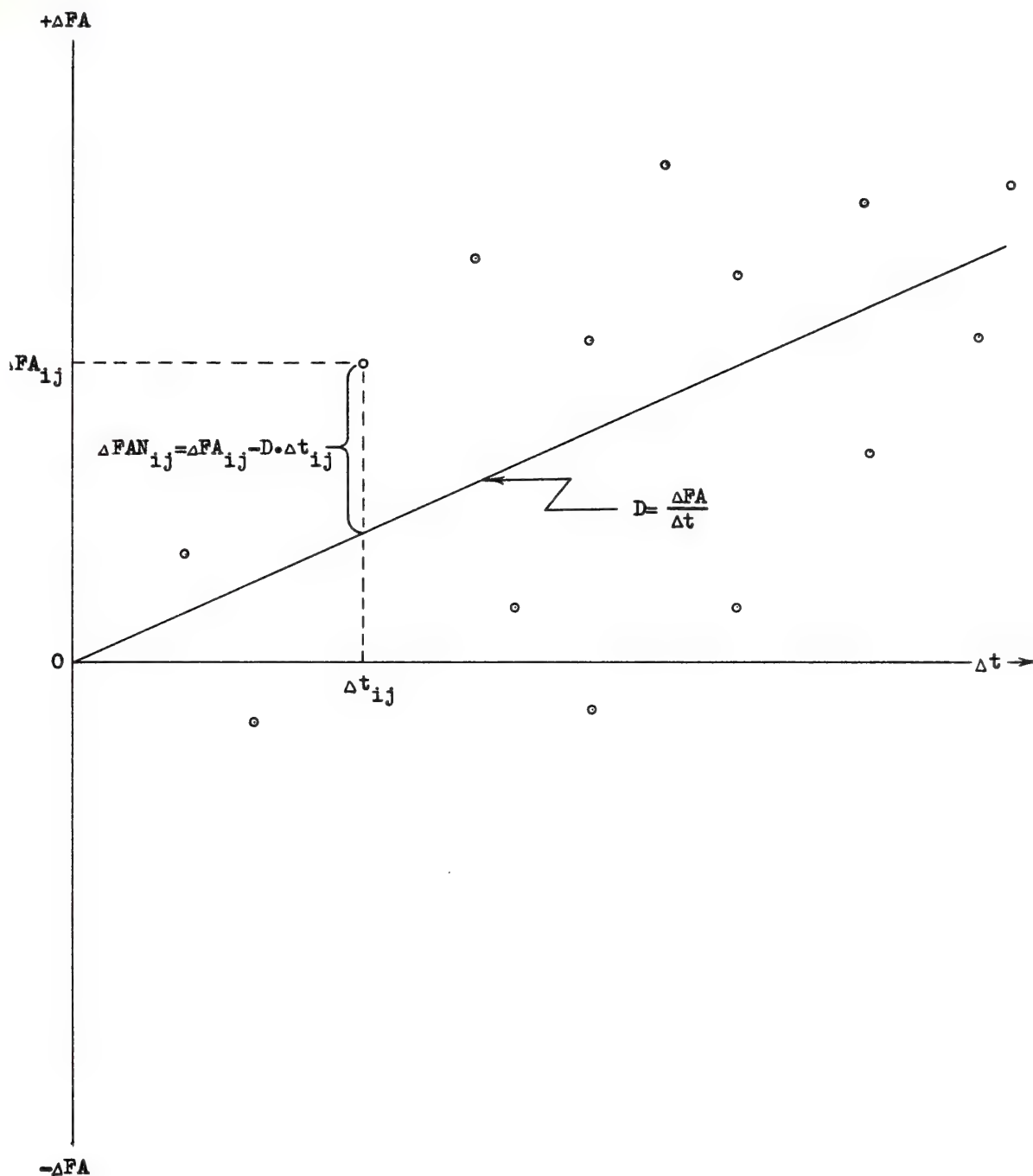


Figure 2. A statistical method for determining drift. The free-air anomaly difference for each crossing of the ship's track is plotted against the corresponding time difference. The drift, D , is the slope of the straight line through the origin which (in a least squares sense) most closely fits all the points $(\Delta FA_{ij}, \Delta t_{ij})$.

Assuming that the correct drift would minimize the crossing errors,

$$\frac{\partial}{\partial D} \left[\sum_{i,j=1}^N a_{ij} \times (\Delta FAN_{ij})^2 \right] = 0$$

$$-2 \times \sum_{i,j=1}^N a_{ij} \times (\Delta FA_{ij} - D \times \Delta t_{ij}) \times \Delta t_{ij} = 0$$

$$\sum_{i,j=1}^N (a_{ij} \times FA_{ij} \times \Delta t_{ij}) - D \times \sum_{i,j=1}^N a_{ij} \times (\Delta t_{ij})^2 = 0$$

$$D = \frac{\sum_{i,j=1}^N a_{ij} \times FA_{ij} \times \Delta t_{ij}}{\sum_{i,j=1}^N a_{ij} \times (\Delta t_{ij})^2}$$

where N=the number of tracklines and $a_{ij}=1$ if $i < j$, or $a_{ij}=0$ if $i > j$.

The method outlined above is valid if a statistically significant number of crossings are available. For this survey (fig. 3), 99 crossings were used, and the computed drift of 0.17 milligals per day is consistent with the gravimeter's drift history.

In the final stages of data processing, time profiles of the free-air anomaly were plotted on an automatic X-Y plotter. Residual discontinuities at course and speed

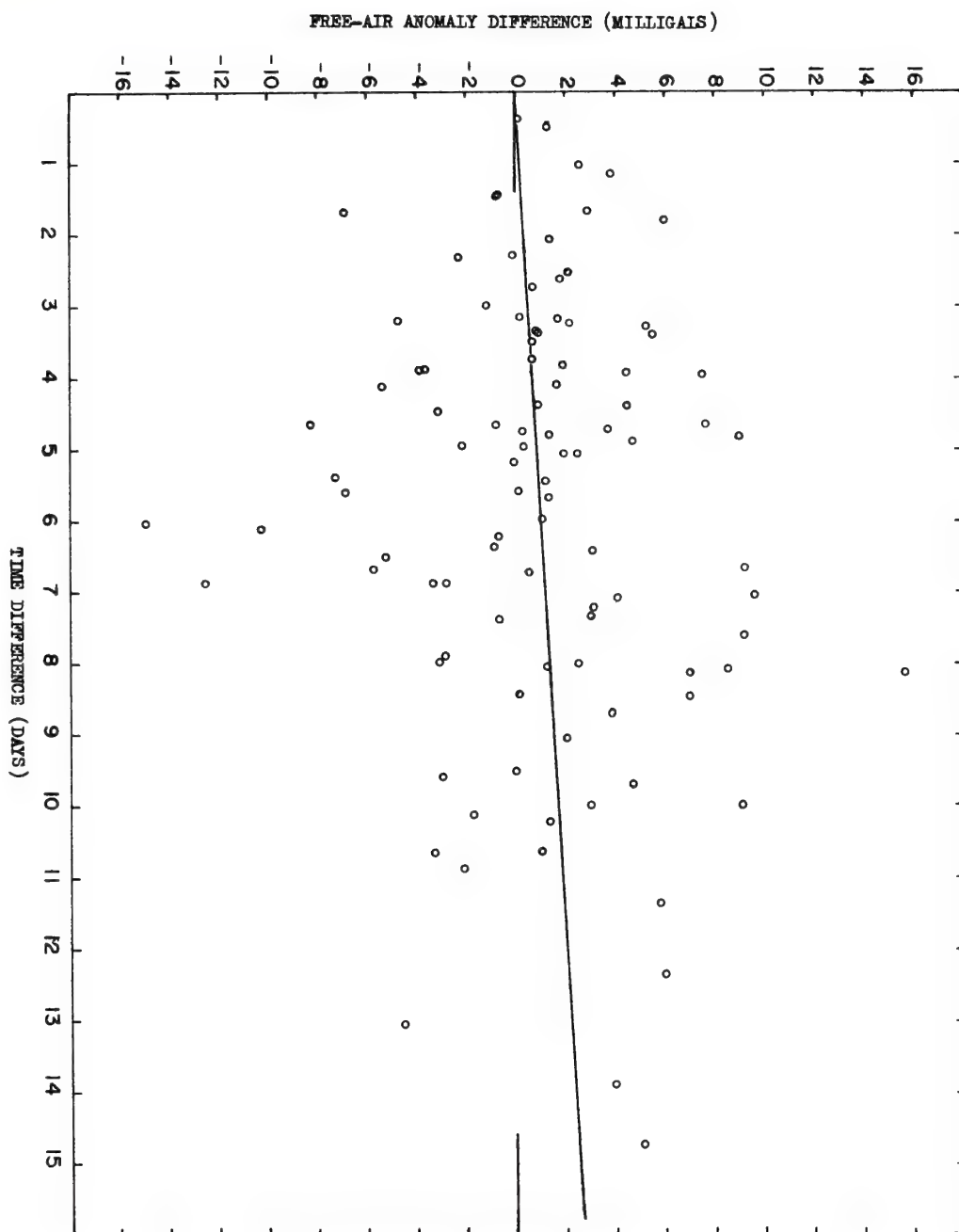


Figure 3. The free-air anomaly differences plotted against the corresponding time differences for 99 crossings of the ship's track. The slope of the solid line through the origin (0.17 milligals per day) is the drift of the gravimeter during this survey.

changes were smoothed out by eye or deleted, and appropriate corrections were applied to the raw data tape.

3. DATA QUALITY

Figure 4 is a histogram of free-air anomaly discrepancies [free-air anomaly discrepancy is defined here as the absolute value of the free-air anomaly difference, ΔFA_{ij} (sect. 2.4)] at crossings of the ship's track. For 99 usable crossings the mean free-air anomaly discrepancy is 3.48 milligals with a standard deviation of 3.28 milligals. Free-air anomaly discrepancies larger than 10 milligals are without exception from regions of very steep gravitational gradient.

In regions of gentle gravitational gradient the free-air anomalies compare within 10 milligals to those furnished by Oregon State University and Lamont-Doherty Geological Observatory.

Satellite navigation contributed immeasurably to the data quality, and the calm seas (sea state 3 or less) encountered throughout the survey kept the cross-coupling and off-leveling errors to a minimum.

4. DATA PRESENTATION

The data are presented in profile form with the free-air anomaly plotted above the corresponding bathymetry. All

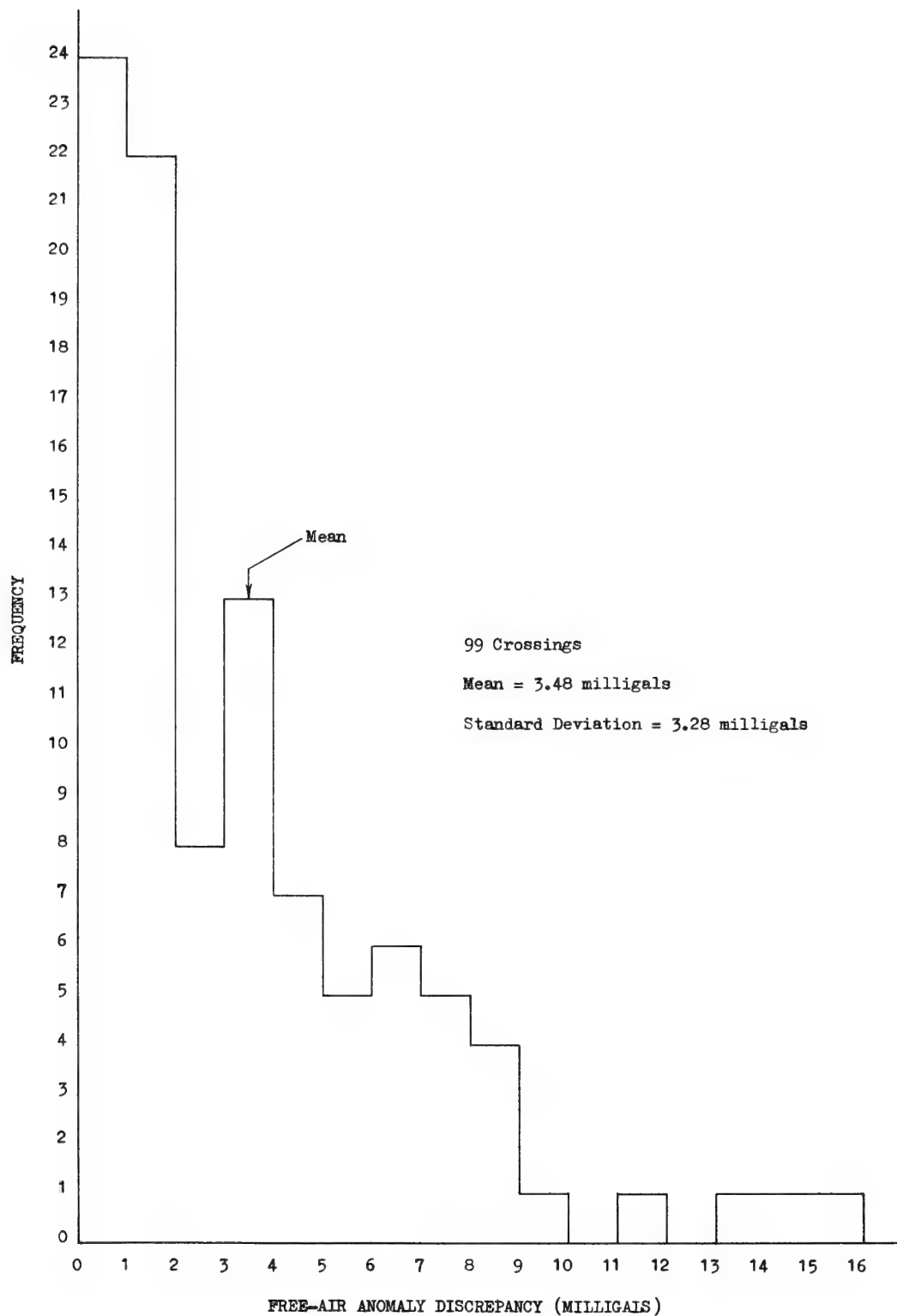


Figure 4. Histogram of free-air anomaly discrepancies at crossings of the ship's track.

profiles are numbered and keyed to an index map (see Appendix and Plate 1). The free-air anomaly profiles are plotted with a vertical scale labeled in milligals and selected to give them a "relief" comparable with the accompanying bathymetric profiles. Depths (after Grim, 1970a) are plotted in meters with a vertical exaggeration of 50:1. Those profiles from trackline segments that are essentially N-S or E-W are plotted against latitude or longitude, respectively. All other profiles are plotted against distance.

The profiles are in three groups. The first includes all E-W profiles south of 7°N. Generally these profiles are arranged according to decreasing latitude. Included in the second group and arranged according to decreasing longitude are all the N-S profiles south of 7°N. The third group includes the relatively short profiles north of 7°N and those profiles that are oblique to meridians and parallels of latitude.

The profiles presented were produced by an off line CalComp plotter with a computer program written by Grim (1970b).

5. DISCUSSION

If the vertical exaggeration of the free-air anomaly profiles is selected to give them about the same "relief" as the bathymetric profiles, then they should look like

filtered versions of the bottom topography. Departures from this relationship are attributable to lateral variations in the subsurface density.

The most striking departure of the free-air anomaly profiles from their corresponding bathymetric profiles is a negative anomaly, shown in profiles 33, 36, 38, 53, 54, and 55, associated with the northern extension of the Panama Fracture Zone. North of 7°N the western trough of the Panama Fracture Zone bends slightly to the west and develops an asymmetric V-shaped profile (profiles 38 and 55). Whereas the western flank of this trough is very steep, the nearshore, eastern flank has a gentle slope with a characteristically rugged appearance. The free-air anomaly associated with the western flank follows the bathymetry quite closely, decreasing sharply from +25 milligals or more to less than -25 milligals. The eastern flank free-air anomaly, however, departs radically from the bottom profile; whereas the bottom profile slopes toward the trough, the free-air anomaly in most cases slopes away from the trough. Furthermore, the free-air anomaly shoreward of the trough is considerably more negative than would be expected from the bathymetry.

In profile 55 the trough is marked only by an inflexion in the free-air anomaly. A -68-milligal low in the free-air anomaly profile lies about 40 km shoreward of the trough.

Similarly, the -62-milligal low of profile 36 is displaced about 20 km east of the trough. The free-air anomaly of profile 38, on the other hand, apparently does not continue to decrease east of the trough. Profiles 33, 53, and the extreme eastern end of profile 54 show an inverse relationship between the slopes of the free-air anomaly and the characteristically rugged bathymetry.

These observations are consistent with the occurrence of a deep, sediment-filled depression that van Andel et al. (1971) have proposed to exist between the Cocos and Coiba Ridges.

Another similar departure of the free-air anomaly from the bathymetry is the negative anomaly associated with a gentle bathymetric depression extending from the eastern edge of the survey area (80°W) to about $81^{\circ}40'\text{W}$ on the eastern flank of the Coiba Ridge. Although the axis of this depression is not crossed by any of the survey lines, it appears to be nearly coincident with profile 31. The free-air anomaly, on the other hand, continues to decrease at least as far north as profile 1.

It is evident that this free-air anomaly pattern is a continuation of the negative anomaly belt (Hayes, 1966) that extends around the Gulf of Panama from the Peru-Chile Trench. Hayes suggested that the most significant contribution to this negative anomaly belt may be the "edge effect" (Worzel,

1965) of a steep continental slope. However, the observation that west of 80°W the axis of this negative anomaly belt lies well shoreward of the bathymetric depression axis is better explained by the sequence of deep, sediment-filled marginal troughs proposed by van Andel et al. (1971).

Especially evident in profile 3 is the departure of the free-air anomaly from the bathymetry on the eastern flanks of the Cocos and Coiba Ridges. West of the Panama Fracture Zone the eastern flank of the Cocos Ridge rises rather uniformly while the free-air anomaly levels off west of $83^{\circ}40'\text{W}$. The free-air anomaly centered over the crest of the Coiba Ridge falls off more rapidly to the east than might be expected from the bathymetry. These deviations of the free-air anomaly from the bottom topography are the reflection of thick accumulations of sediment on the eastern flanks of both ridges (van Andel et al., 1971, figs. 5B and 11G). This profile also suggests that there is no large-scale change in crustal structure across the Panama Fracture Zone.

The entire survey area may be slightly out of isostatic adjustment, as indicated by an average free-air anomaly of between +10 and +20 milligals.

6. ACKNOWLEDGEMENTS

I thank the officers and crew of the National Oceanic and Atmospheric Administration Ship OCEANOGRAPHER who made this study possible. Paul Grim furnished the data presented in this report. He also supplied most of the computer programs used and assisted in many ways throughout this study. Additional gravity data were provided by Dr. Richard Couch, Oregon State University, and Manik Talwani, Lamont-Doherty Geological Observatory. R. K. Lattimore, Paul Grim, and Dr. George Peter assisted by reviewing the manuscript.

7. REFERENCES

- Graf, A. and R. Schulze (1961), Improvements in the sea gravimeter Gss2, J. Geophys. Res. 66, 1811-1821.
- Grim, P. J. (1970a), Bathymetric and magnetic anomaly profiles from a survey south of Panama and Costa Rica, (unpublished report) ESSA Tech. Memo, ERLTM-AOML 9. (Environmental Research Laboratories, Boulder, Colorado 80302).
- Grim, P. J. (1970b), Computer program for automatic plotting of bathymetric and magnetic anomaly profiles, (unpublished report) ESSA Tech. Memo, ERLTM-AOML 8. (Environmental Research Laboratories, Boulder, Colorado 80302).
- Guier, W. H. (1966), Satellite navigation using integral Doppler data -- the AN/SRN-9 equipment, J. Geophys. Res. 71, 5903-5910.
- Hayes, D. E. (1966), A geophysical investigation of the Peru-Chile trench, Marine Geology 4, 309-351.
- Orlin, H. and D. V. Sibila (1966), General instructions, gravity observations at sea, part II: askania stable platform mounted seagravimeter, U. S. Department of Commerce, ESSA, Coast and Geodetic Survey.
- Schulze, R (1962), Automation of the sea gravimeter Gss2, J. Geophys. Res. 67, 3397-3401.

- Stansell, P. A., Jr. (1970), The Navy navigation satellite system: description and status, The International Hydrographic Review, XLVII, 51-70.
- van Andel, T. H., G. R. Heath, B. T. Malfait, D. F. Heinrichs, and J. I. Ewing (1971), Tectonics of the Panama Basin, eastern equatorial Pacific, Geol. Soc. Amer. Bull. 82, 1489-1508.
- Woollard, G. P. and J. C. Rose (1963), International Gravity Measurements, Society of Exploration Geophysicists, Tulsa, Oklahoma, 518 p.
- Worzel, J. L. (1965), Deep structure of continental margins and mid-ocean ridges, In: W. F. Whittard and R. Bradshaw (Editors), Submarine Geology and Geophysics -- Colston Papers, Butterworth, Washington, D.C., 335-359.

APPENDIX

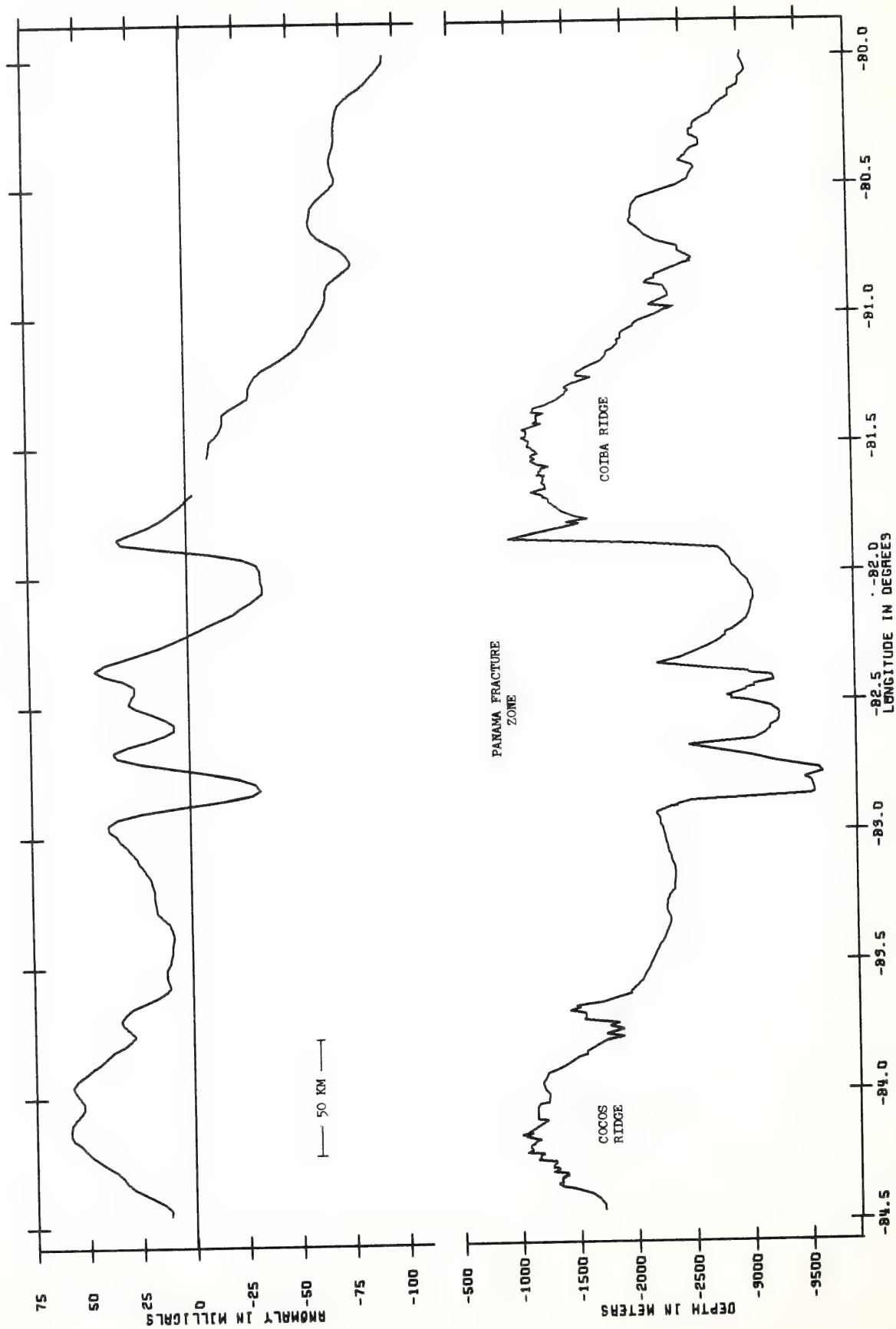
Profiles

The following pages display the computer-produced profiles from the survey area

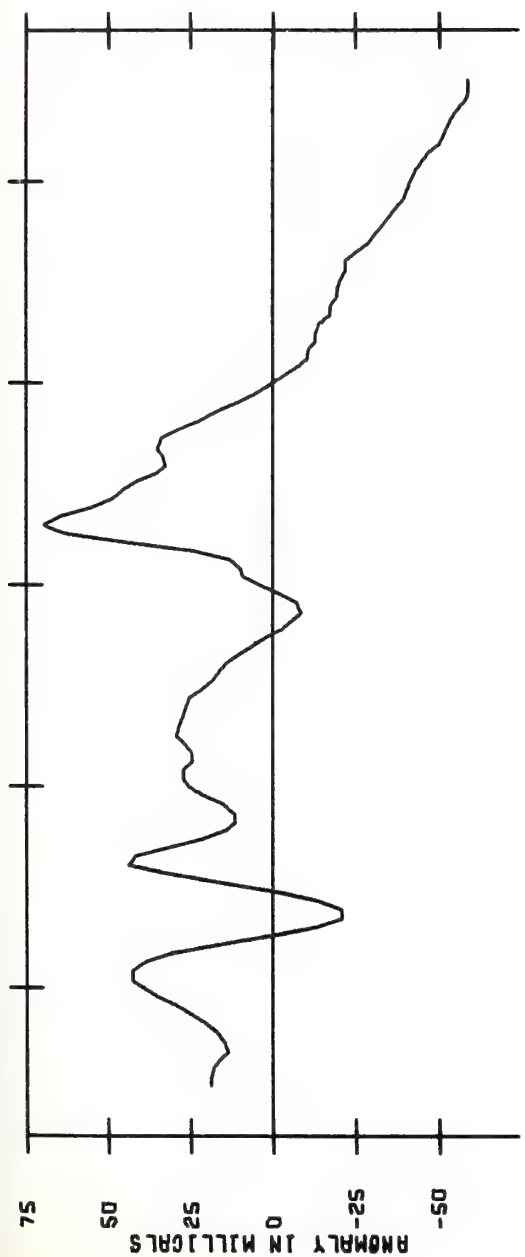
Profile Page	Profile Page	Profile Page	Profile Page
1 22	14 35	27 23	42 27
3 24	15 49	28 44	43 37
4 40	16 36	29 51	44 29
5 26	17 25	30 44	45 43
6 37	18 39	31 23	46 31
7 28	19 49	32 48	47 38
8 42	20 40	33 48	48 29
9 30	21 27	34 46	49 38
10 34	22 41	36 46	50 31
11 32	23 49	38 47	51 34
12 51	24 42	39 37	52 50
13A 33	25 51	40 25	53 48
13B 33	26 43	41 43	54 47
			55 45
			62 45

Table 1. Index of Profiles

PROFILE 1

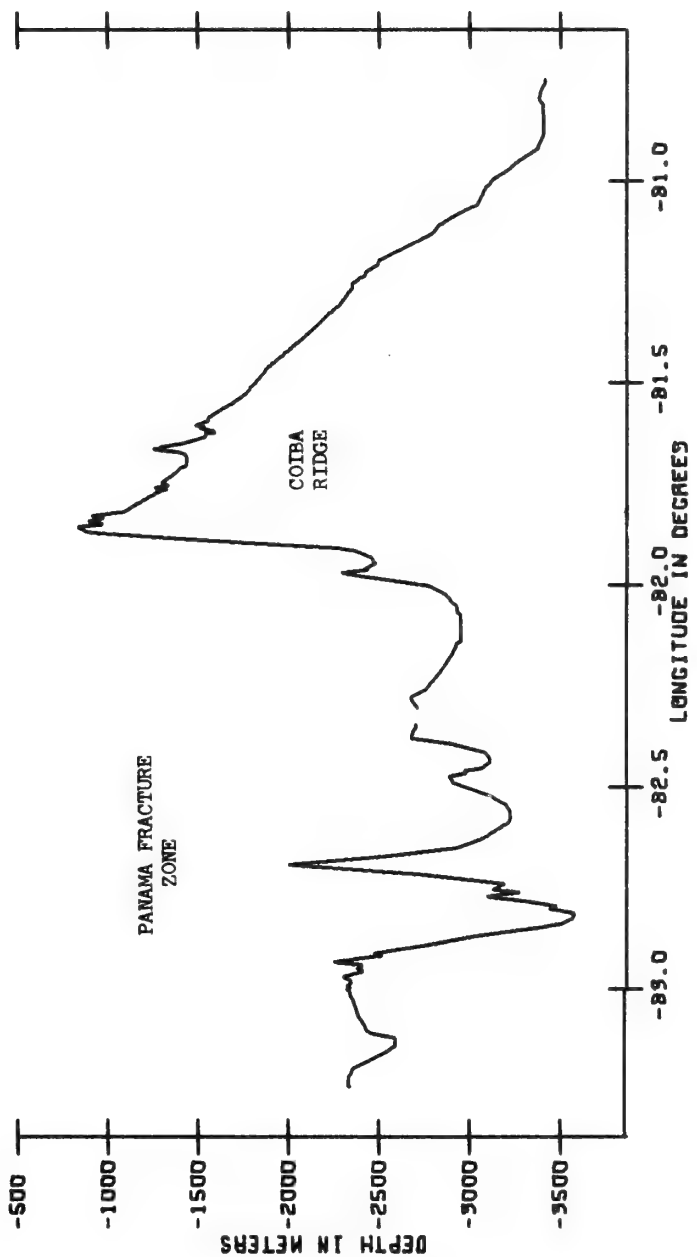
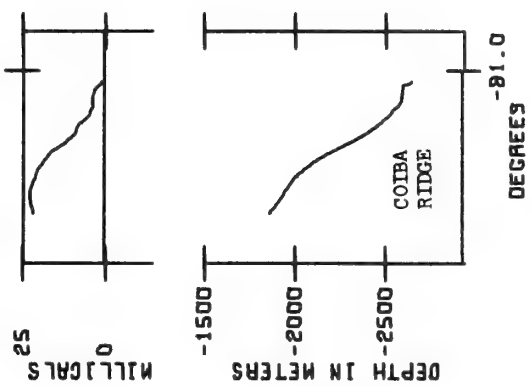


PROFILE 31

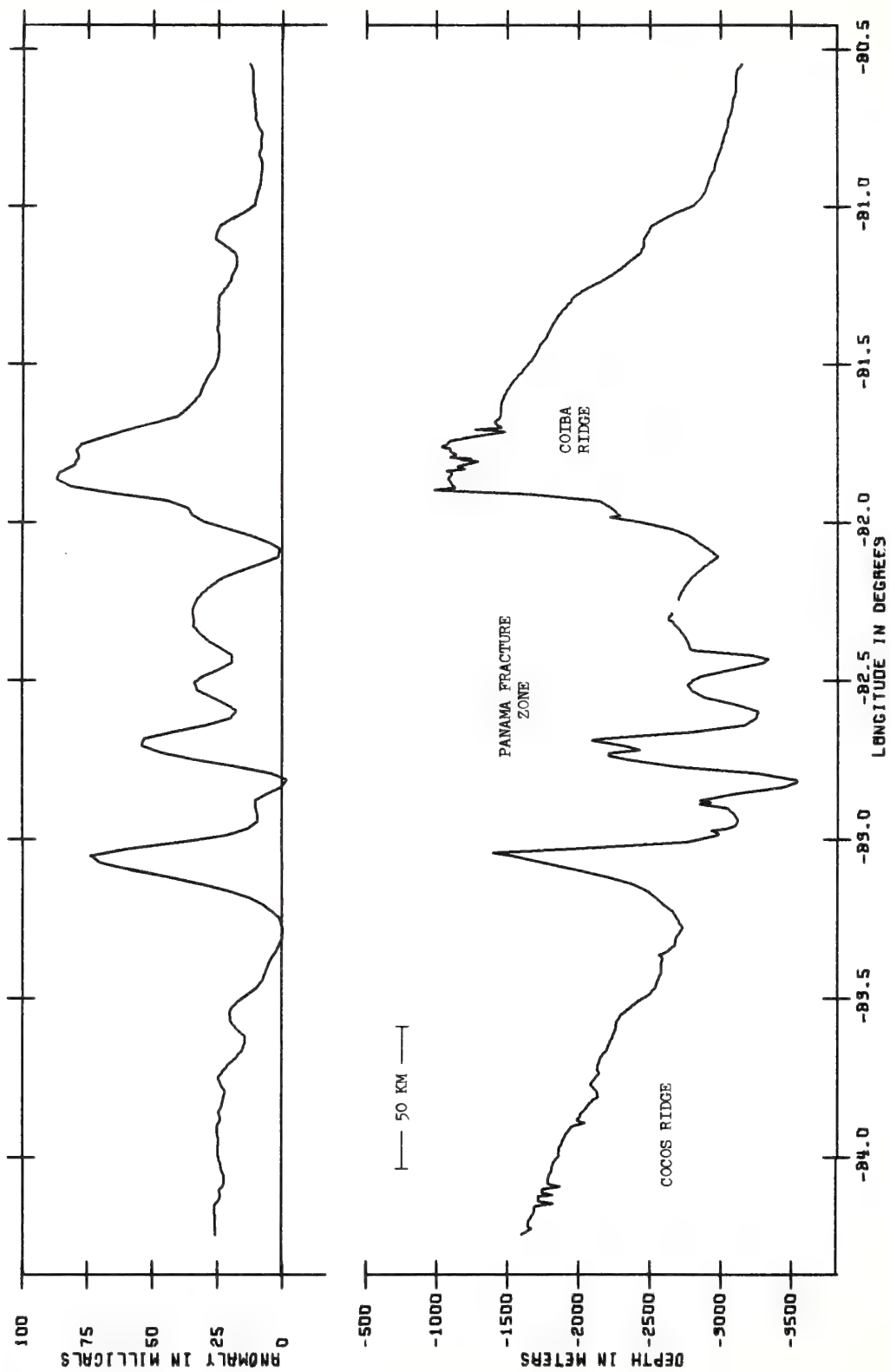


50 KM

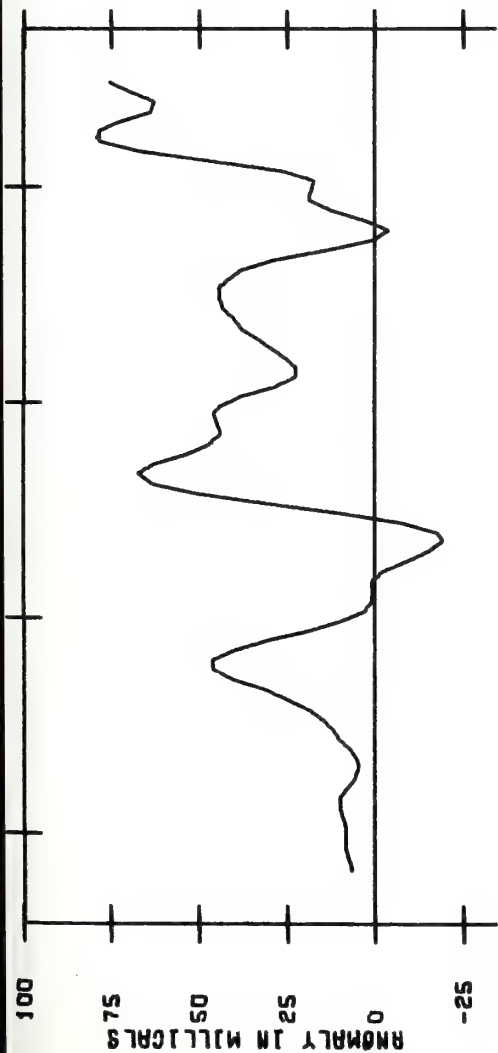
PROFILE 27



PROFILE 3



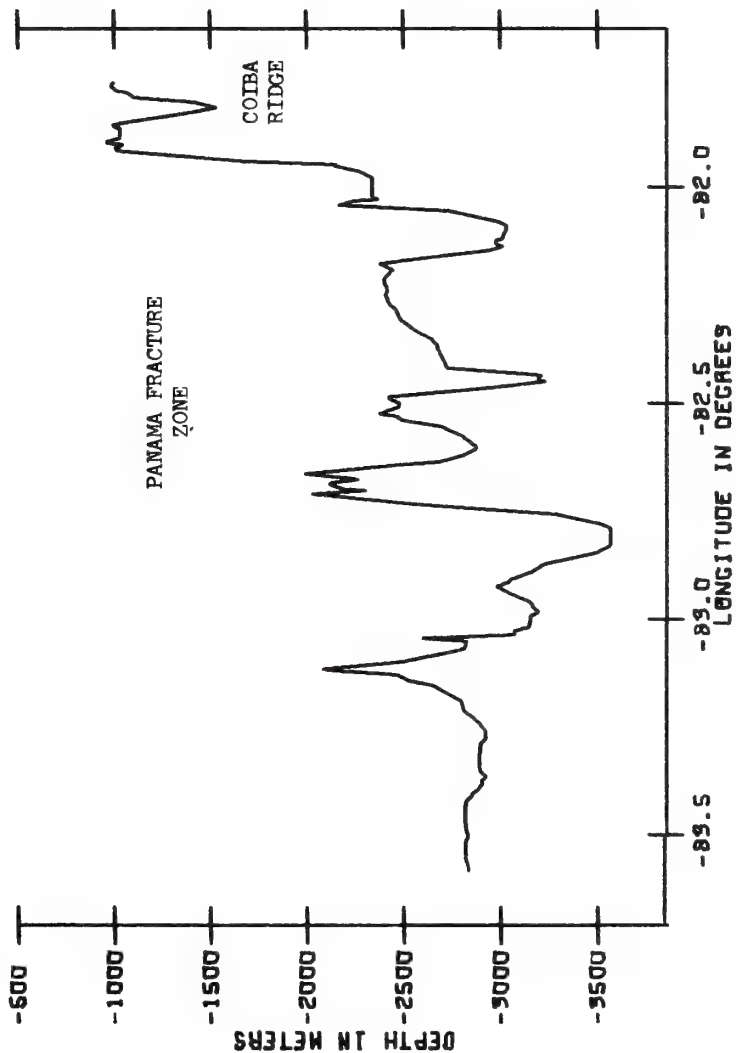
PROFILE 40



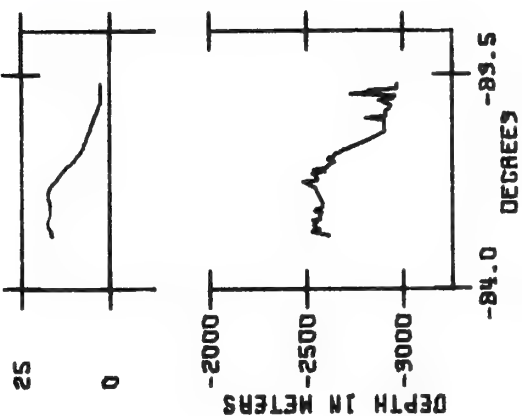
50 KM

PANAMA FRACTURE
ZONE

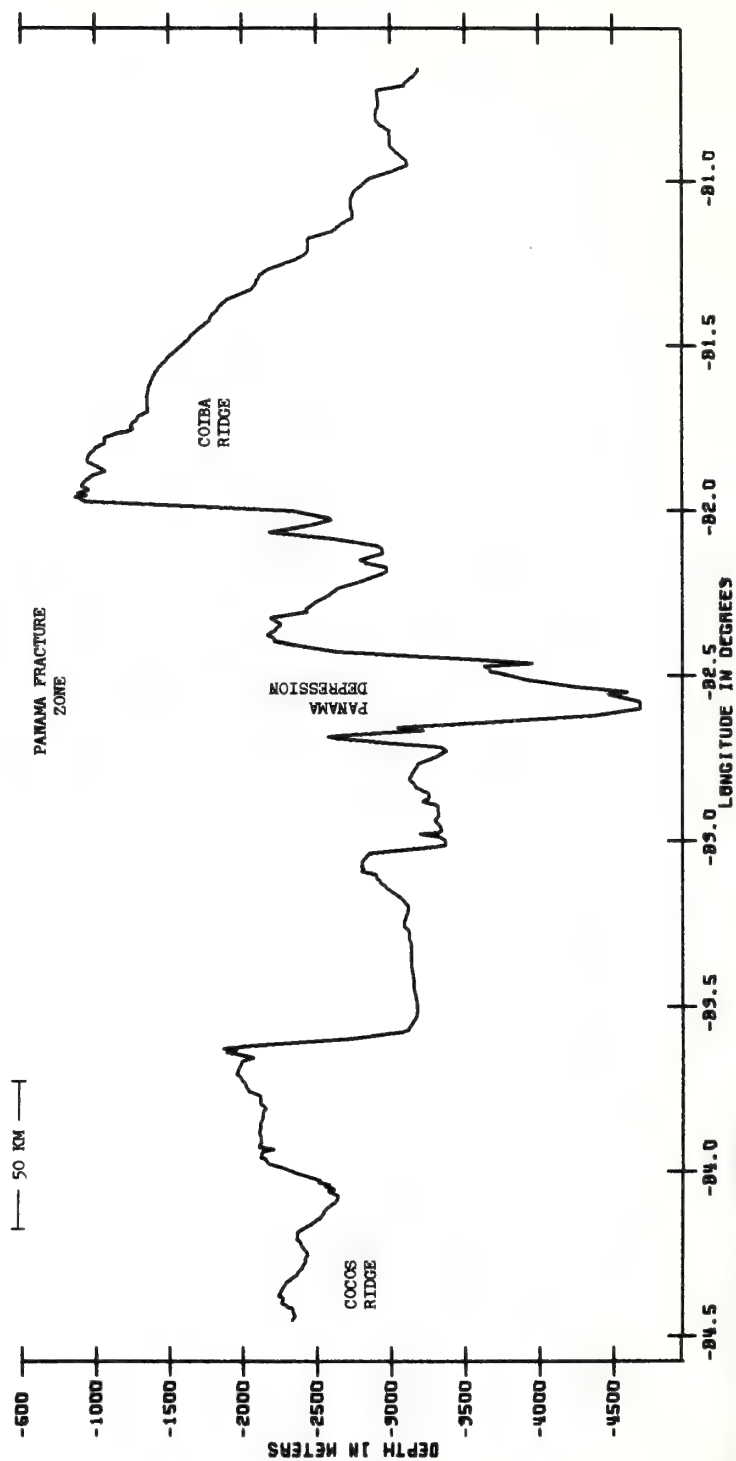
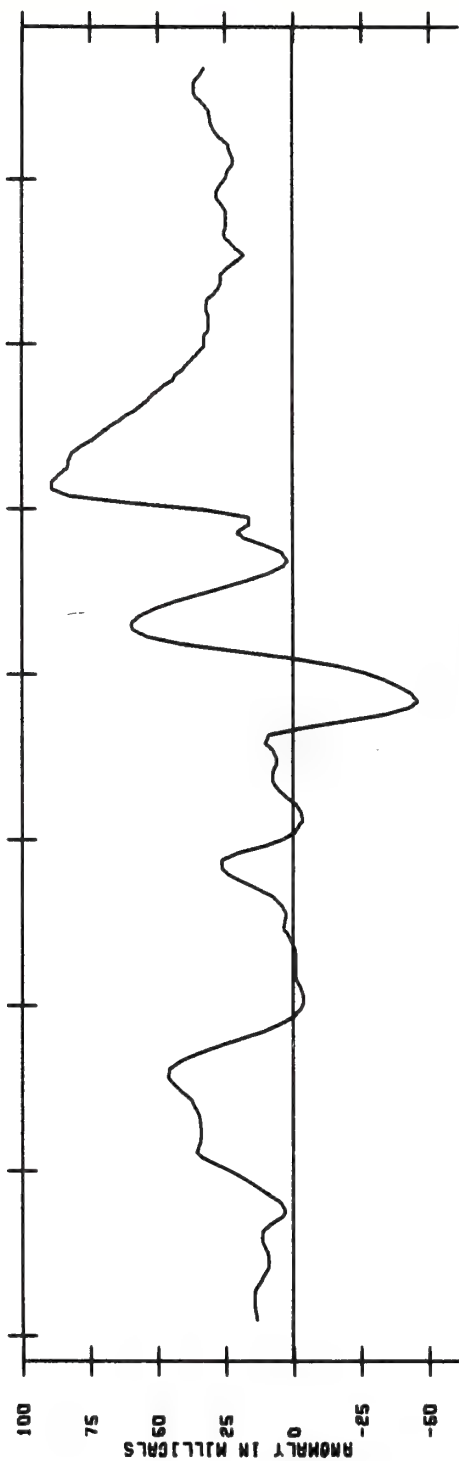
COIBA
RIDGE



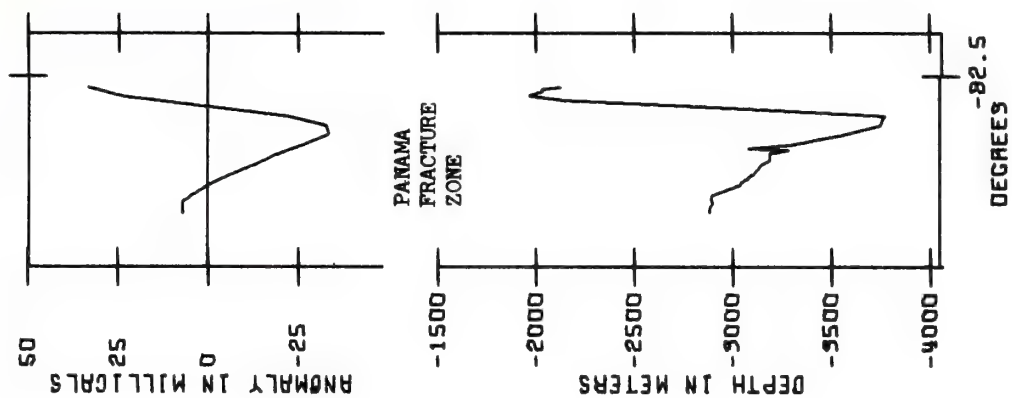
PROFILE 17



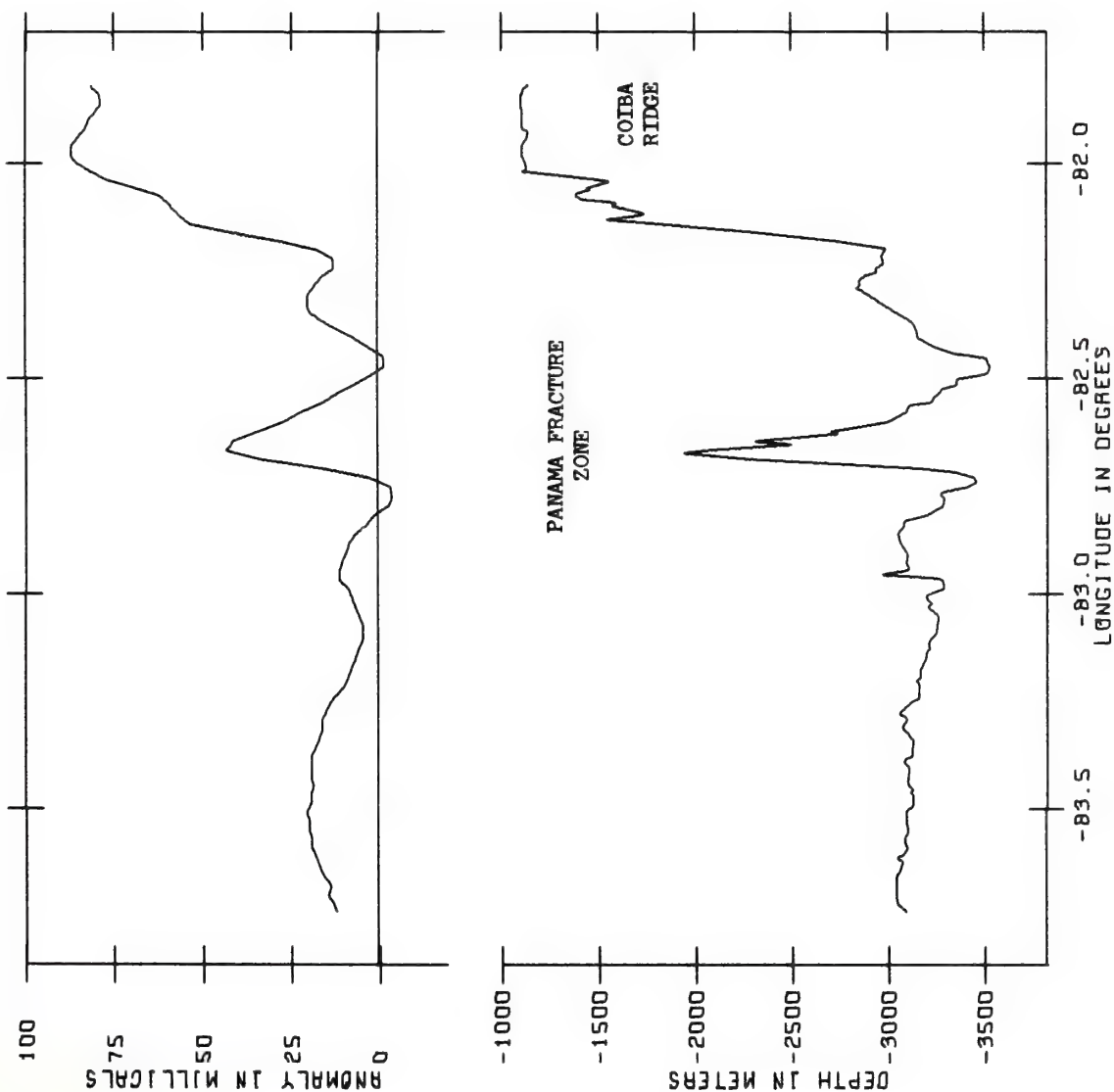
PROFILE 5



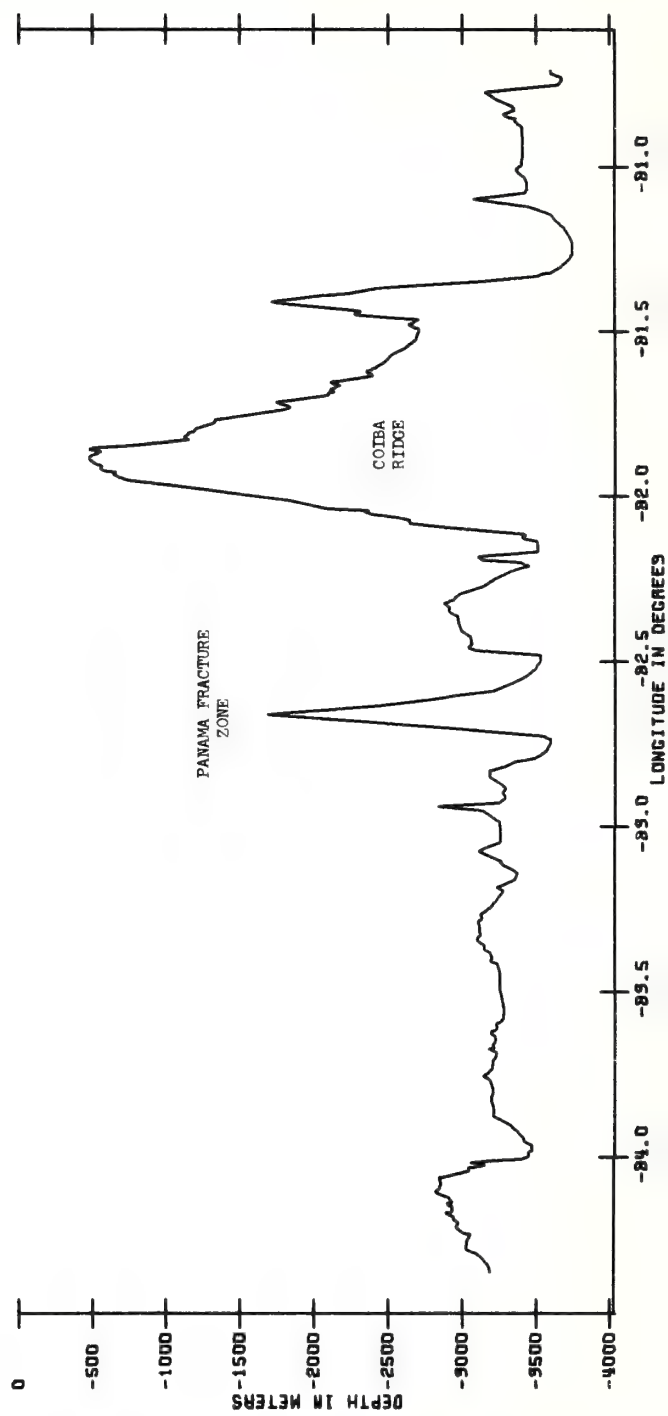
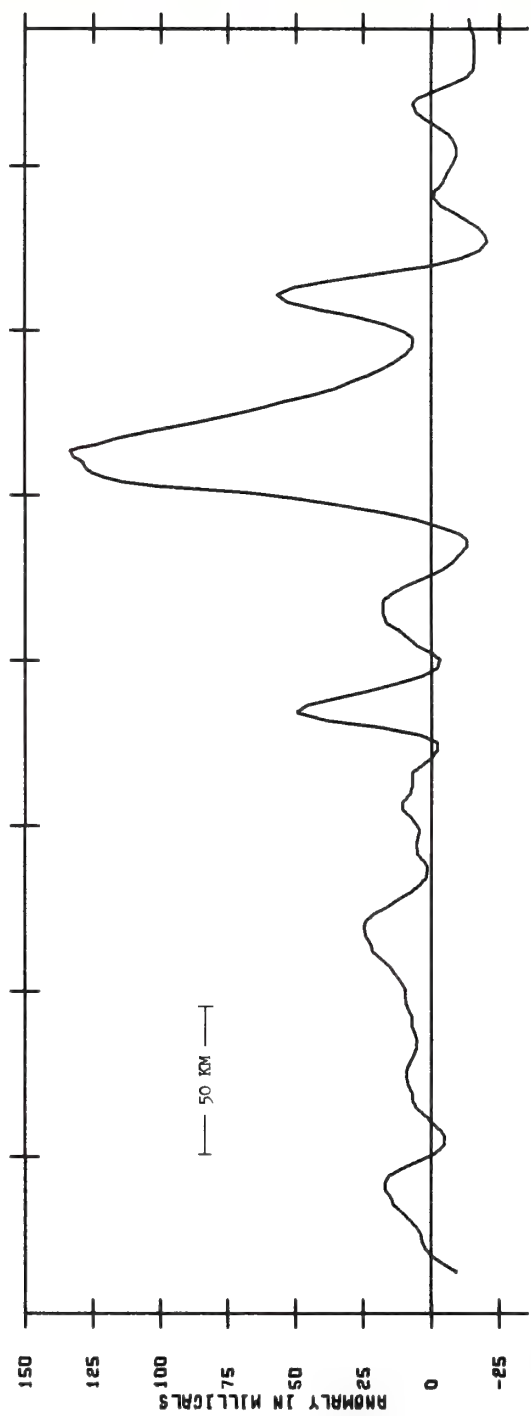
PROFILE 21



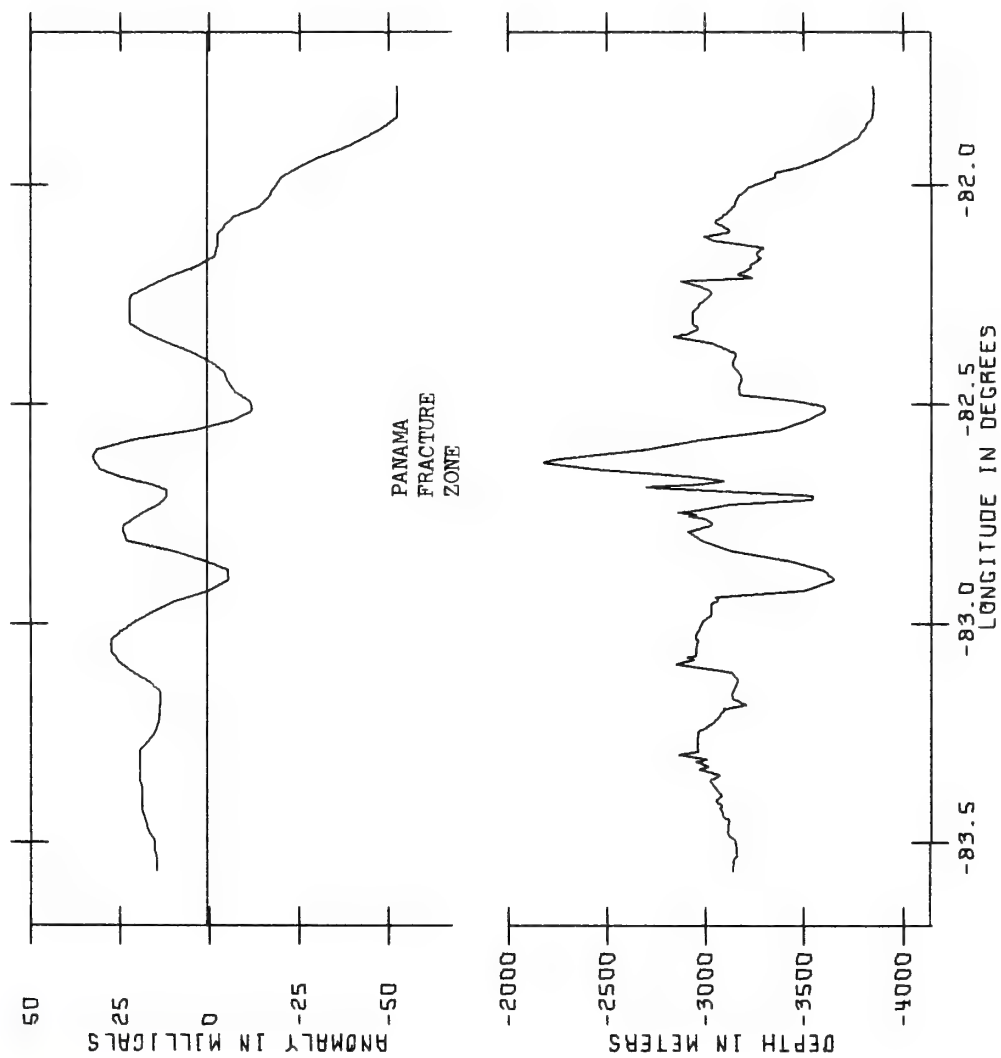
PROFILE 42



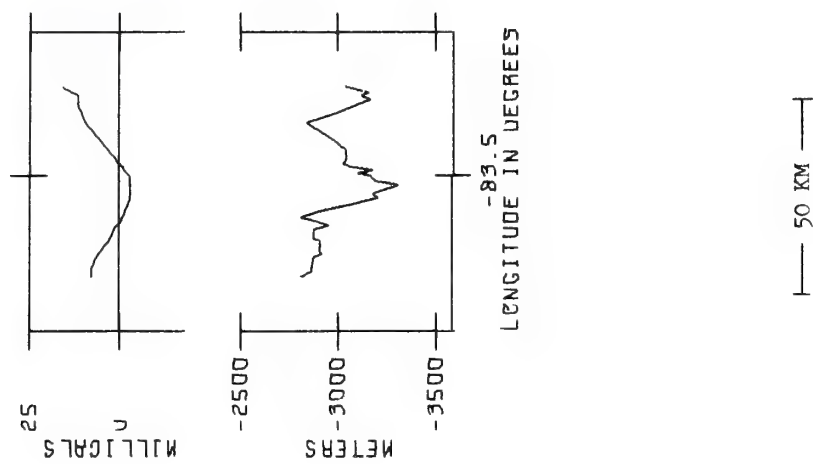
PROFILE 7



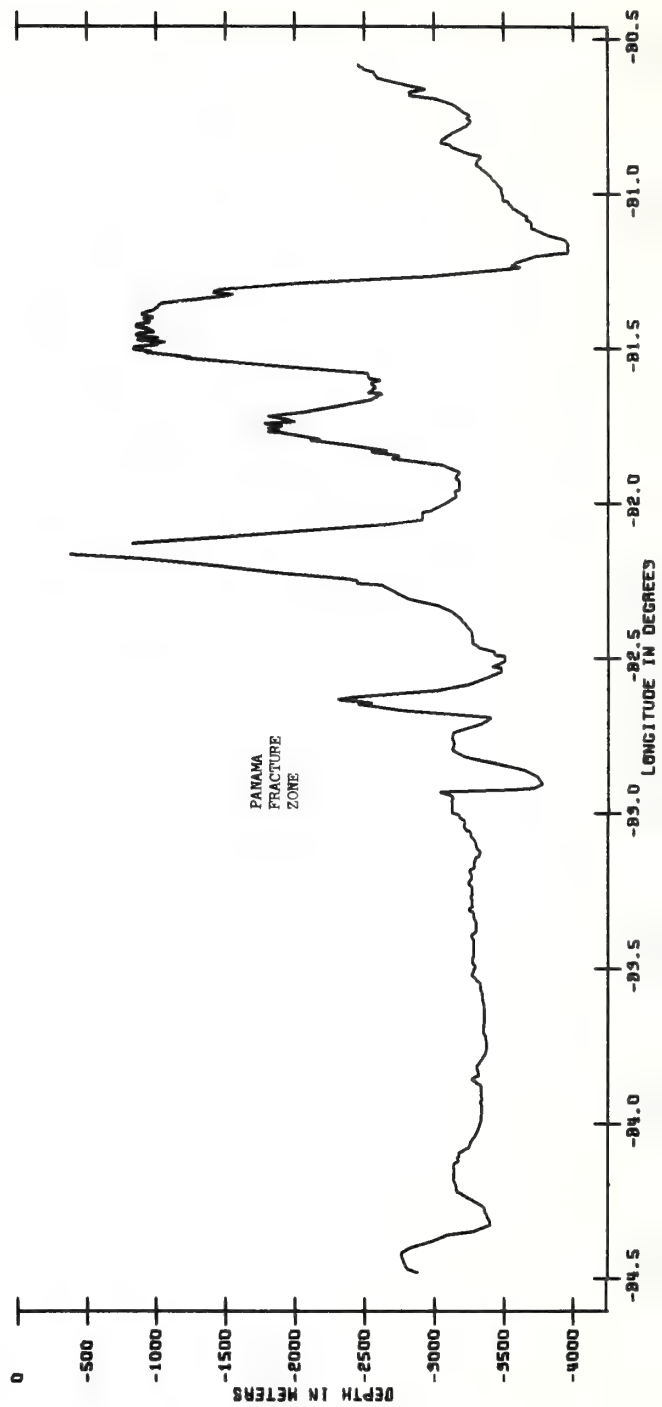
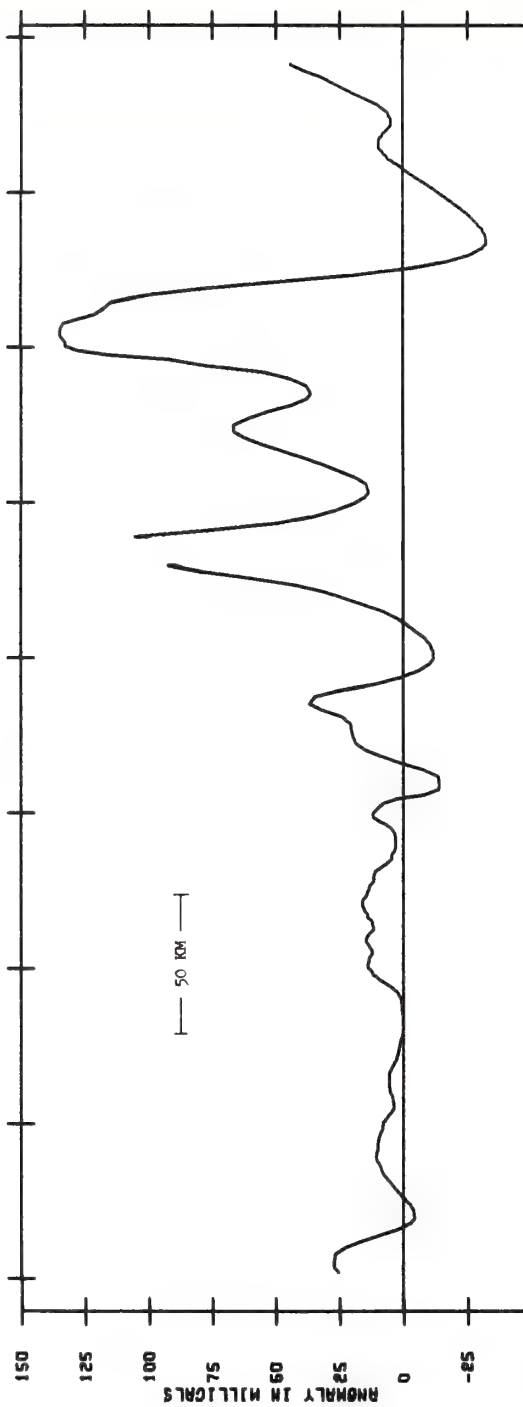
PROFILE 44



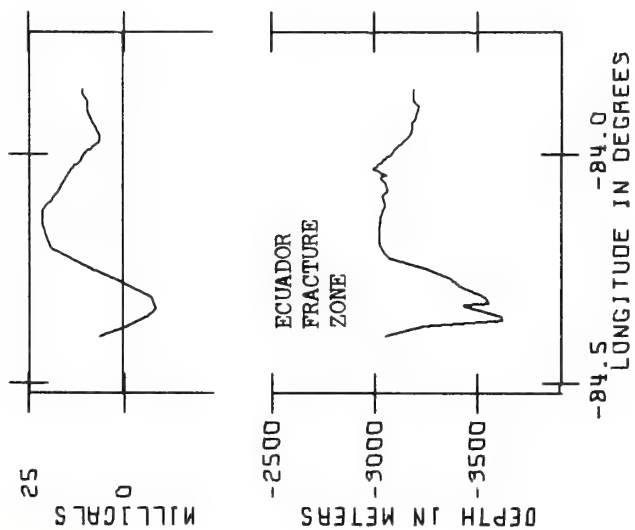
PROFILE 48



PROFILE 9

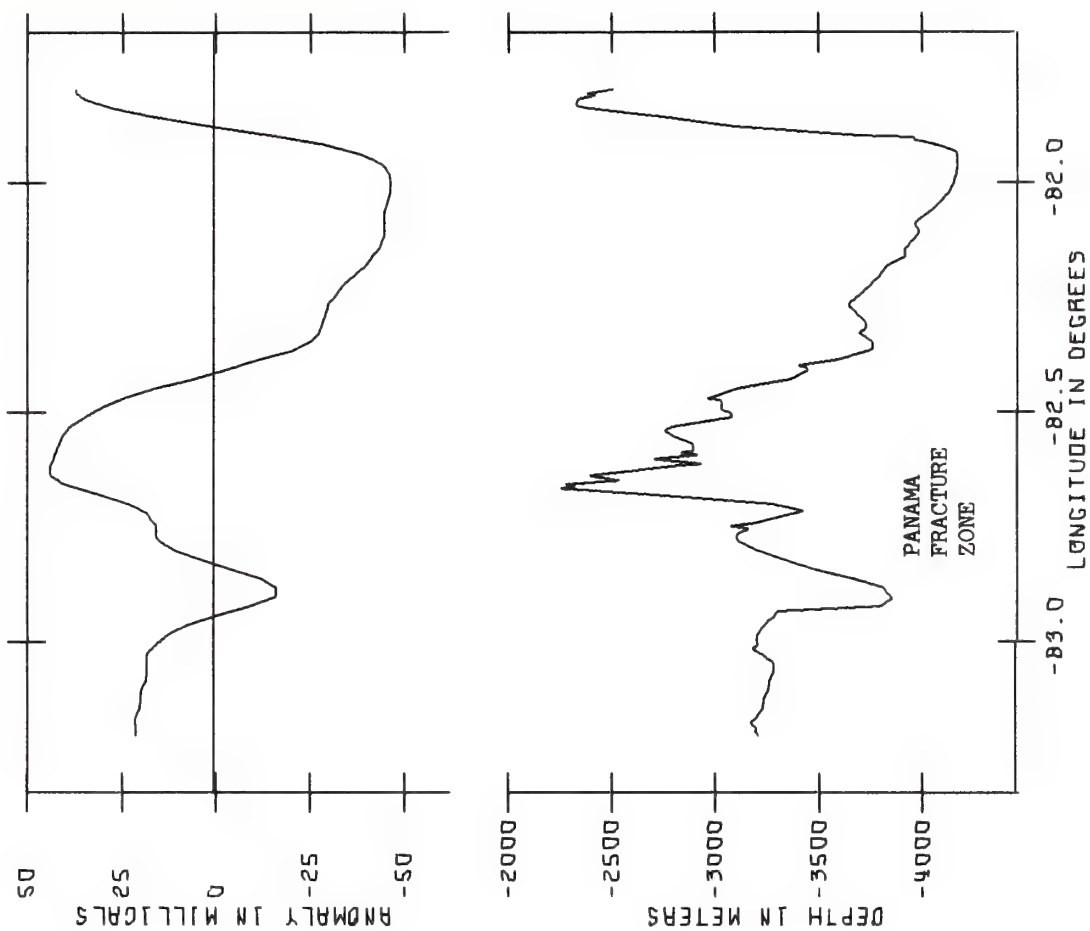


PROFILE 50

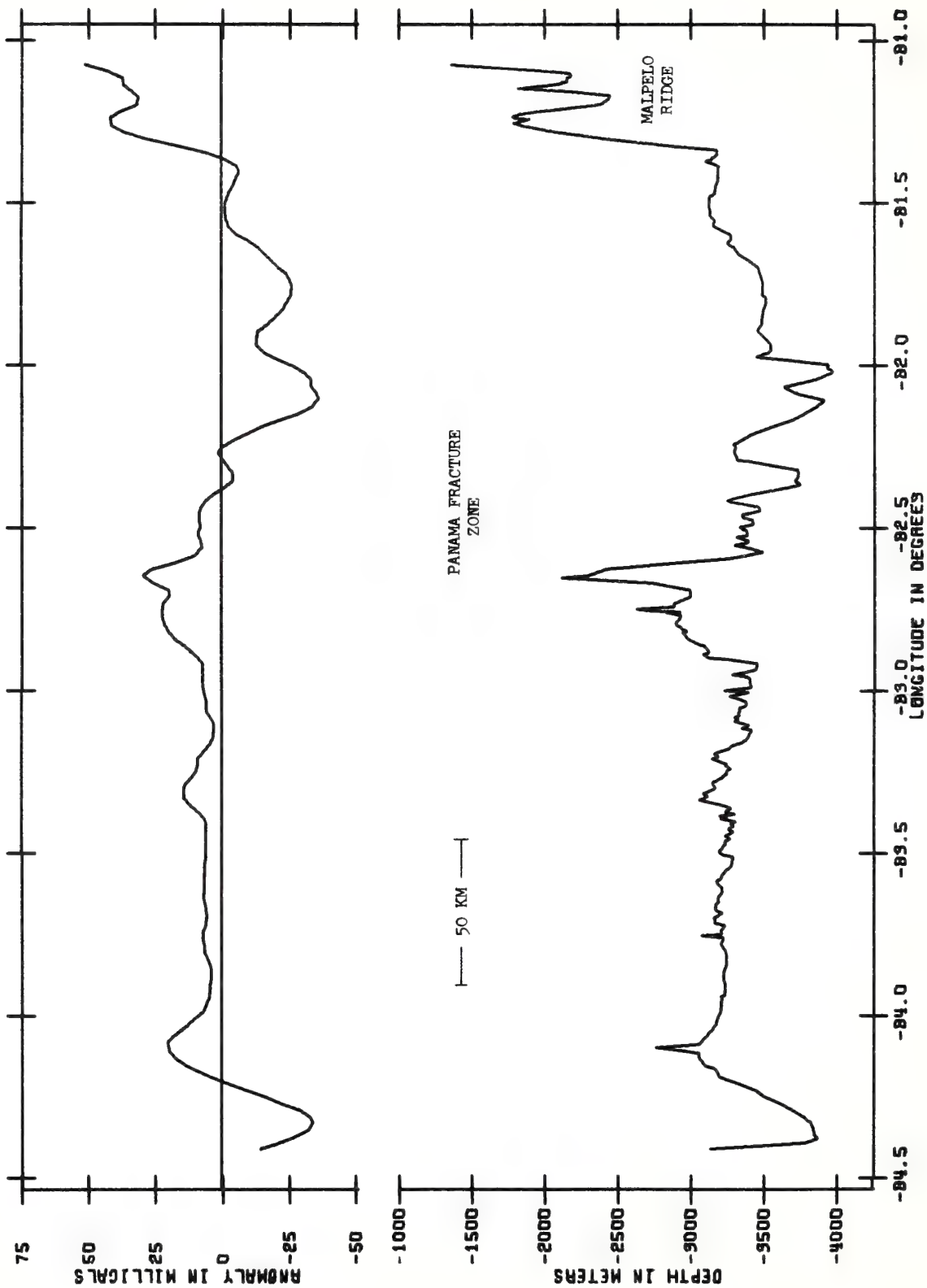


— 50 KM —

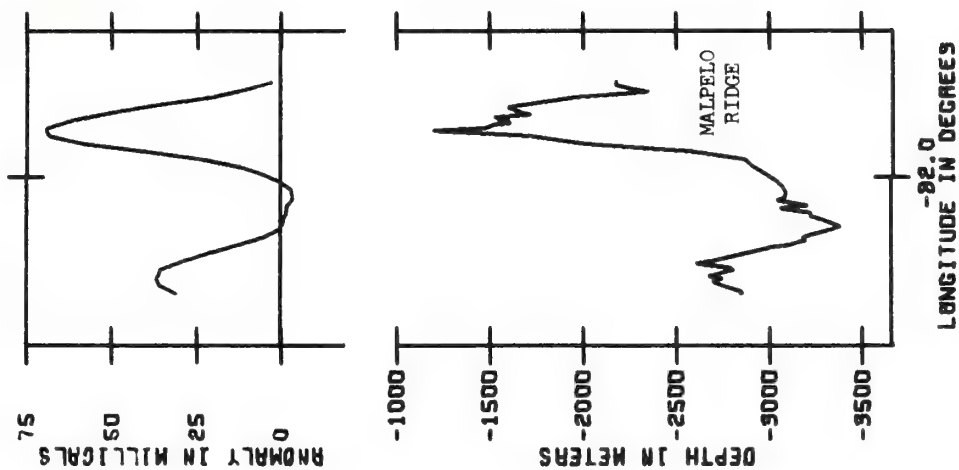
PROFILE 46



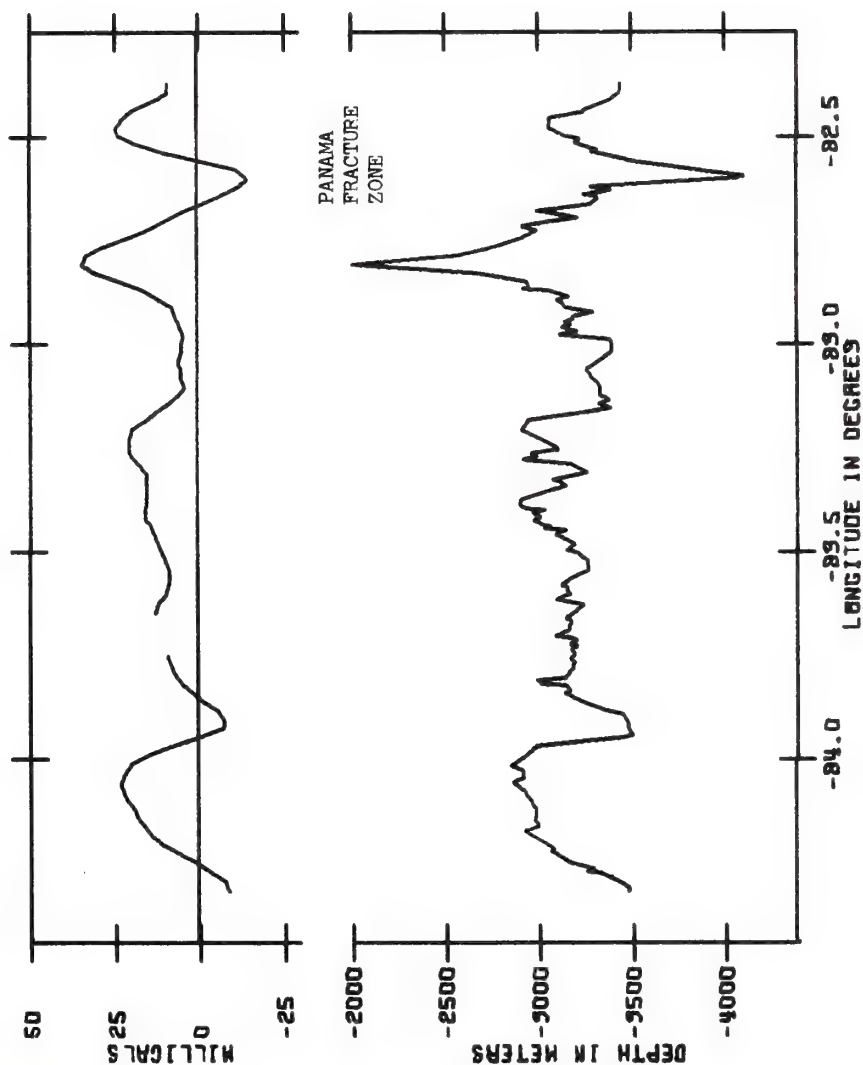
PROFILE 11



PROFILE 13A

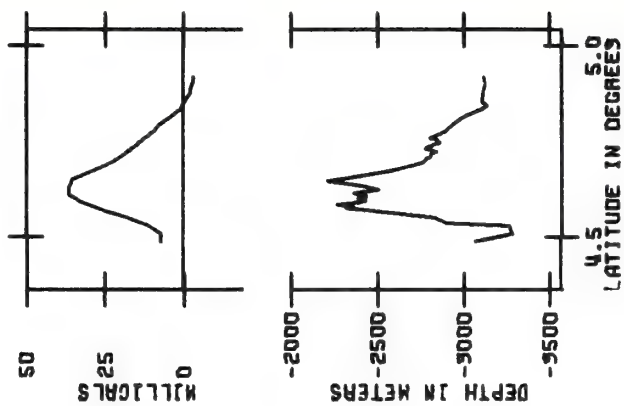


PROFILE 13B

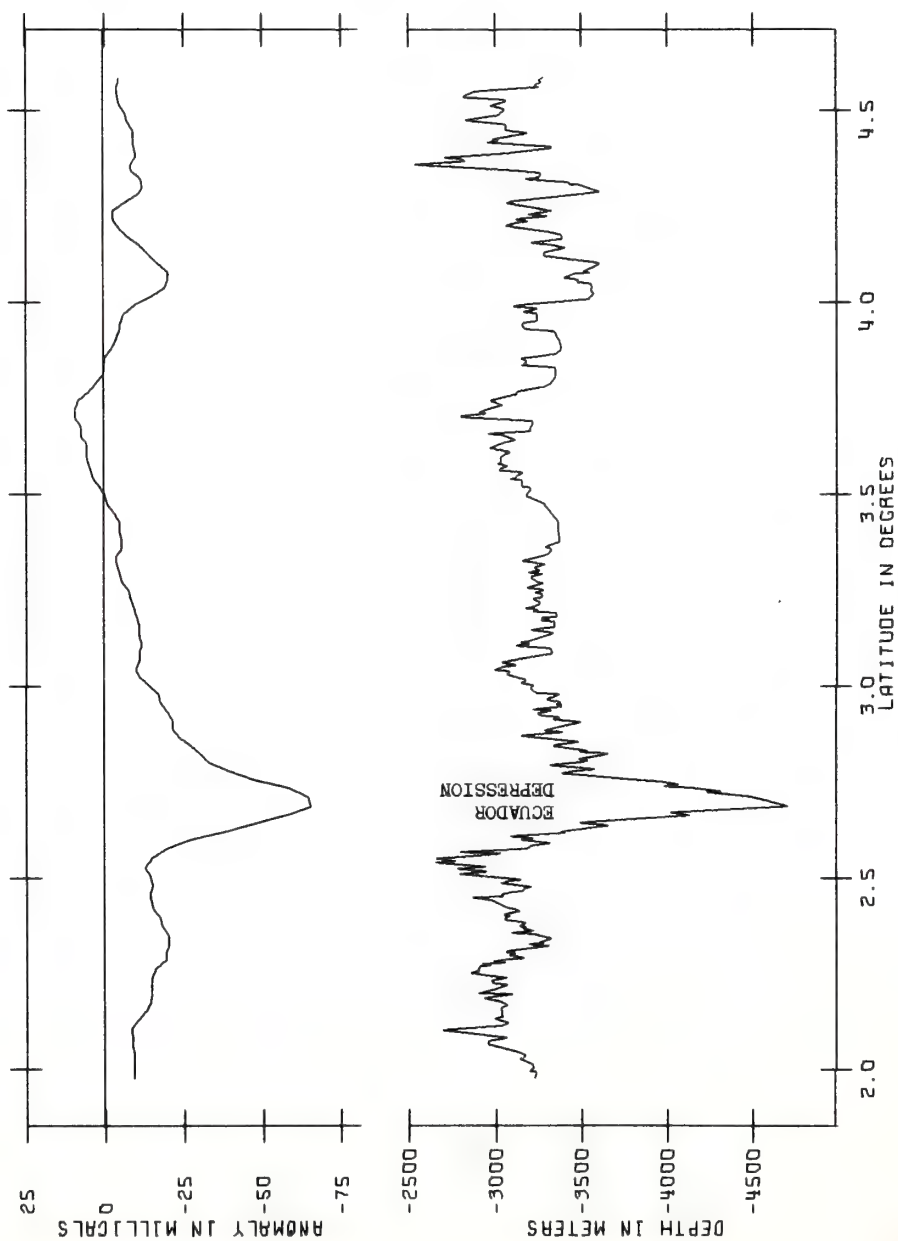


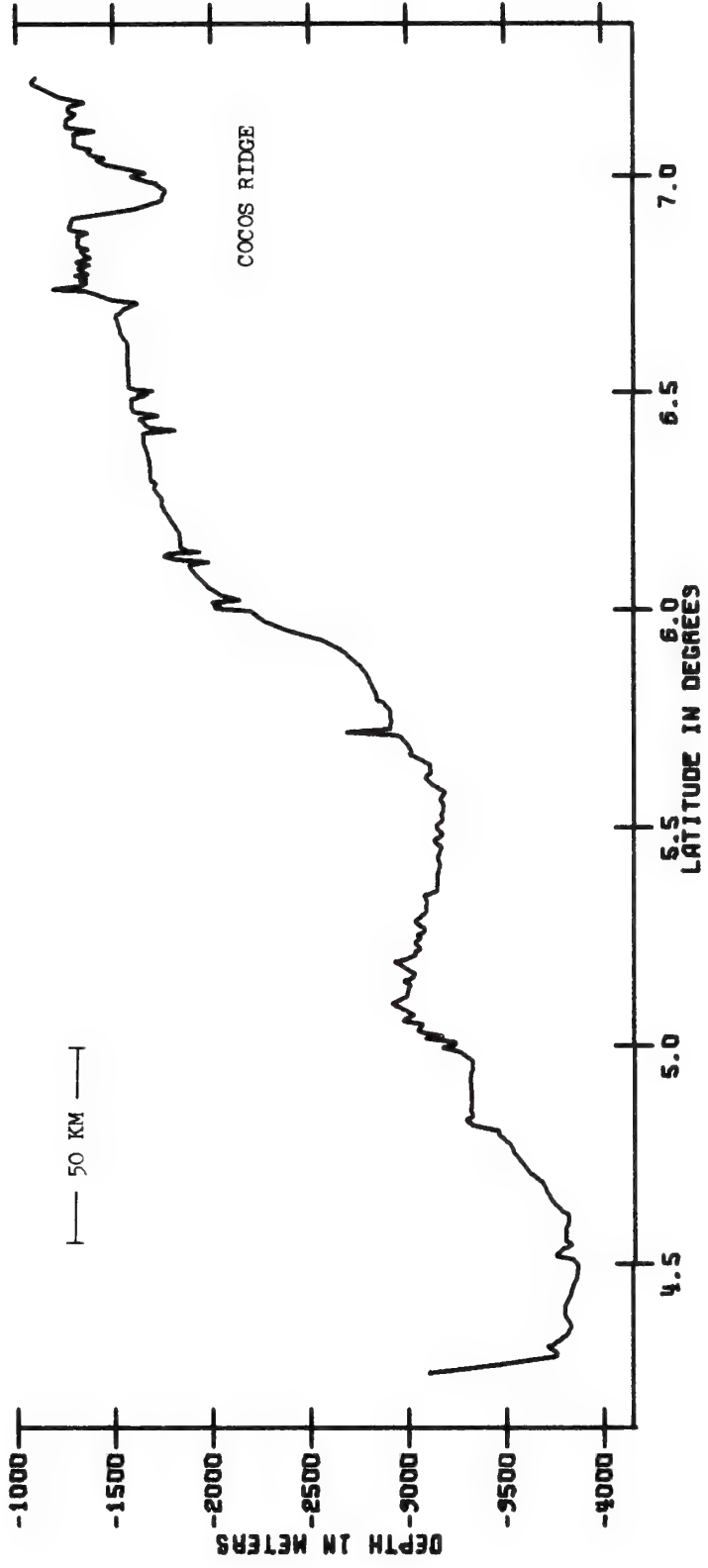
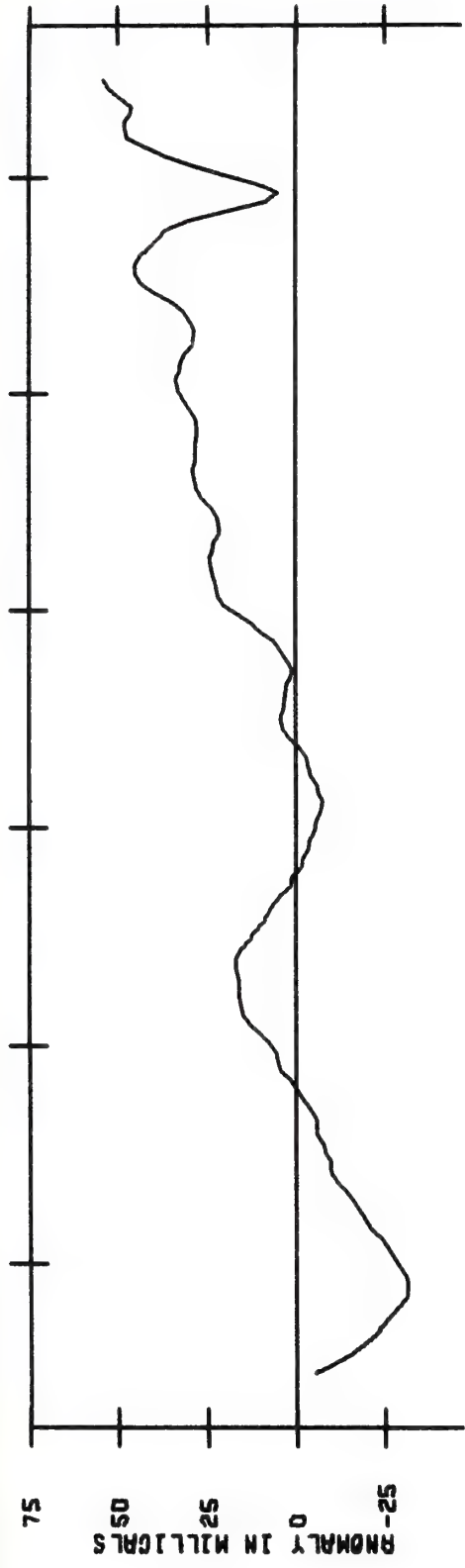
— 50 KM —

PROFILE 10

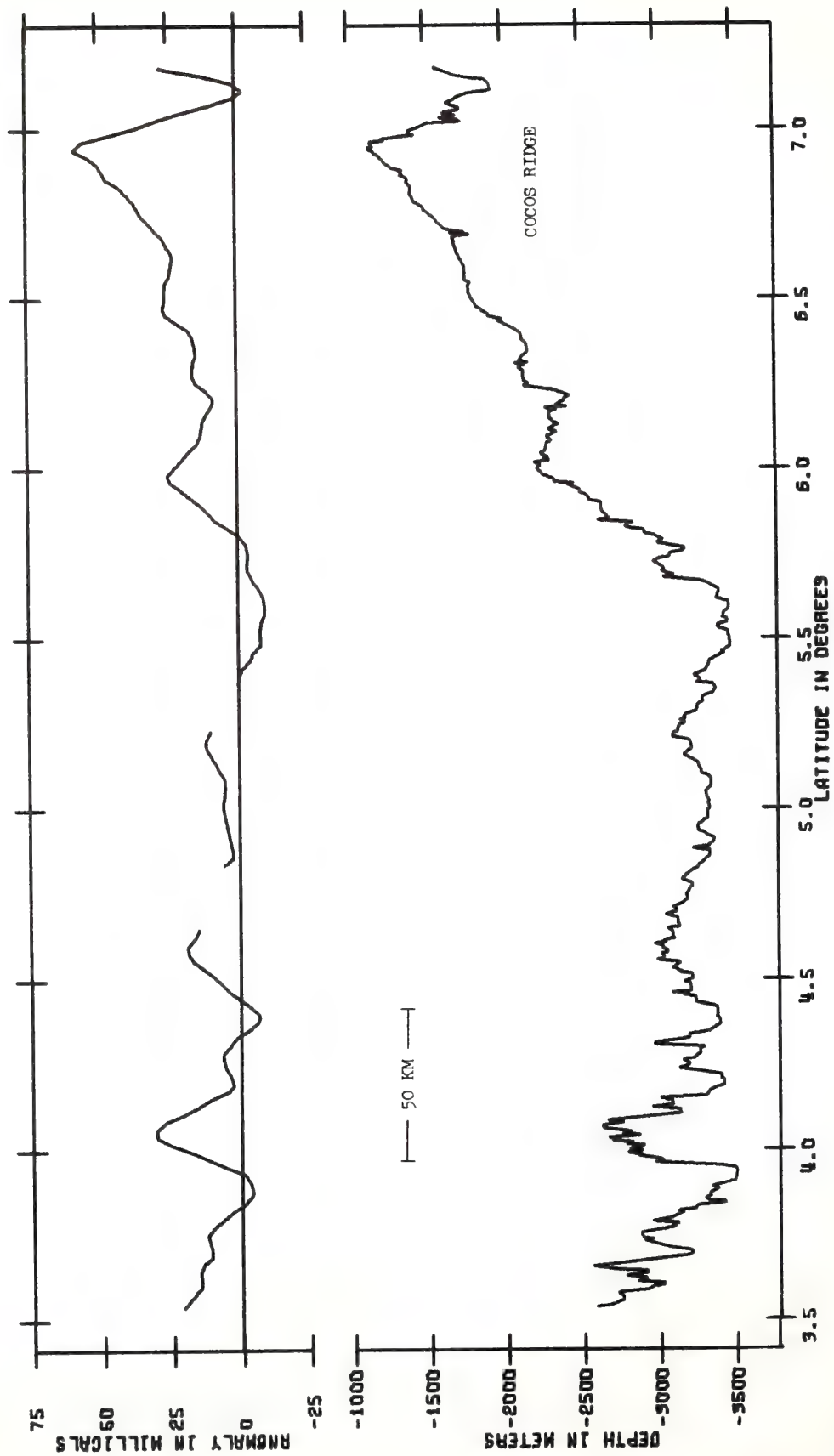


PROFILE 51

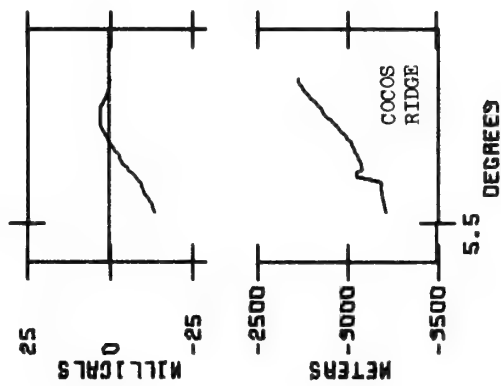




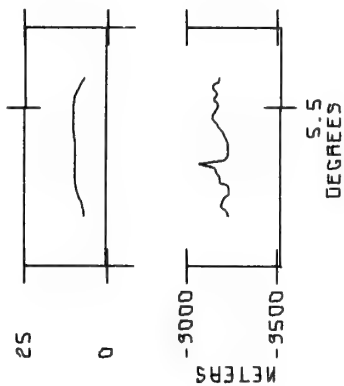
PROFILE 16



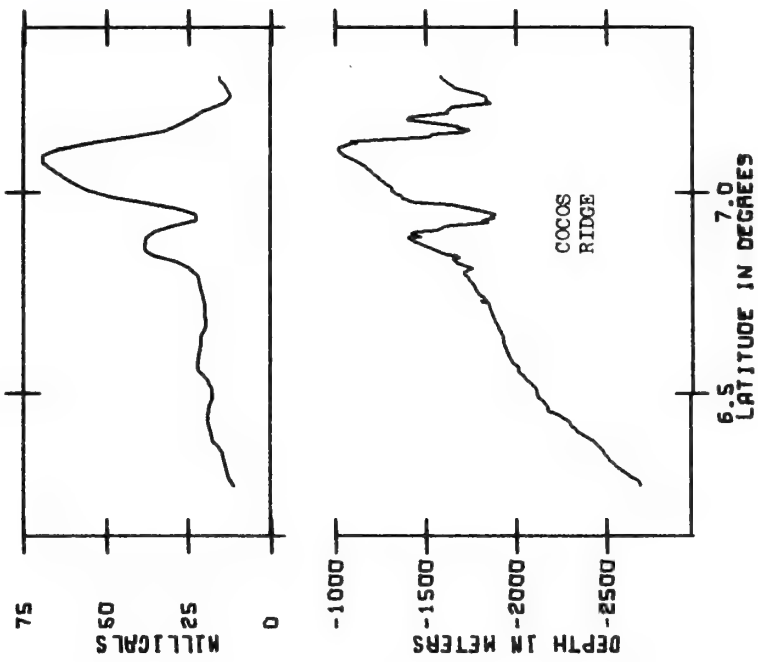
PROFILE 6



PROFILE 43

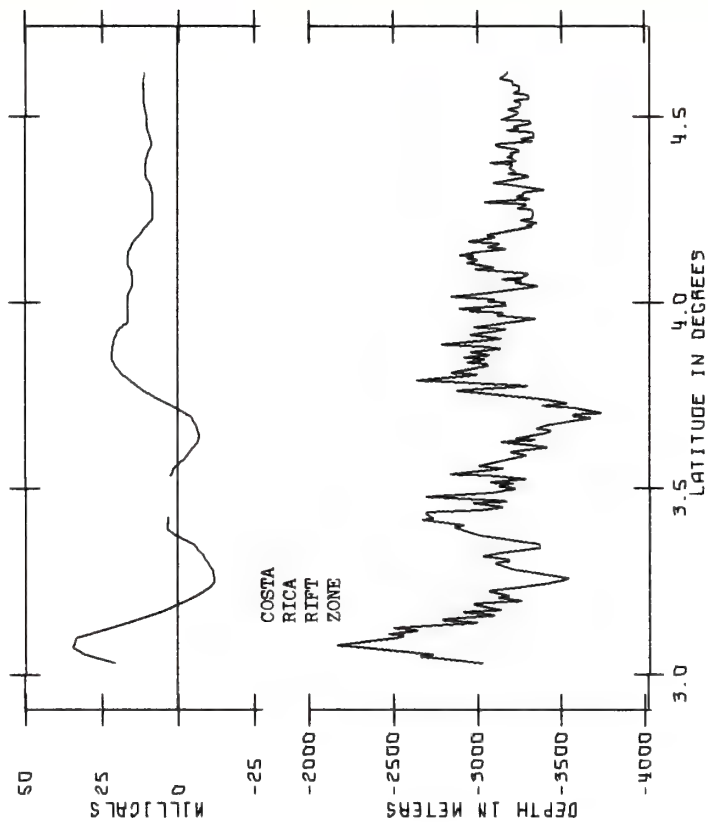


PROFILE 39

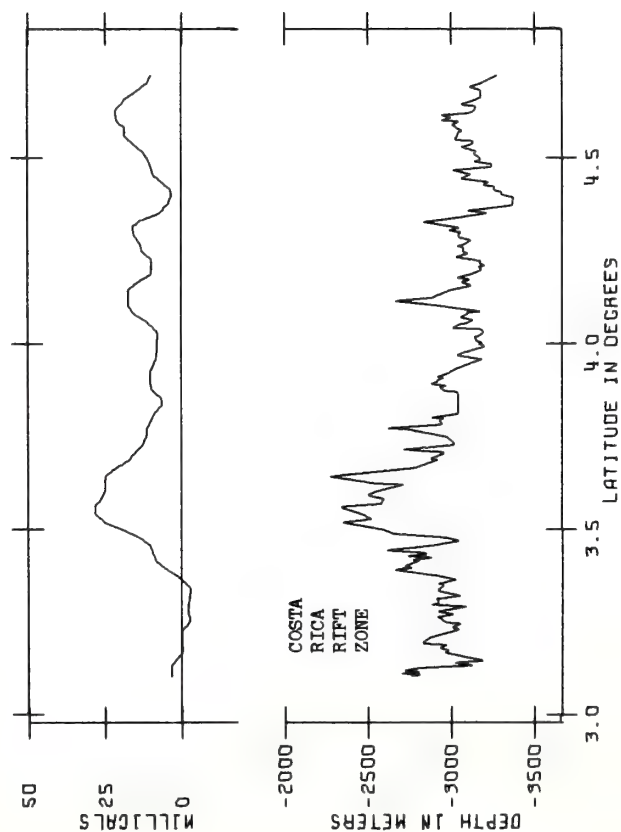


50 KM

PROFILE 47

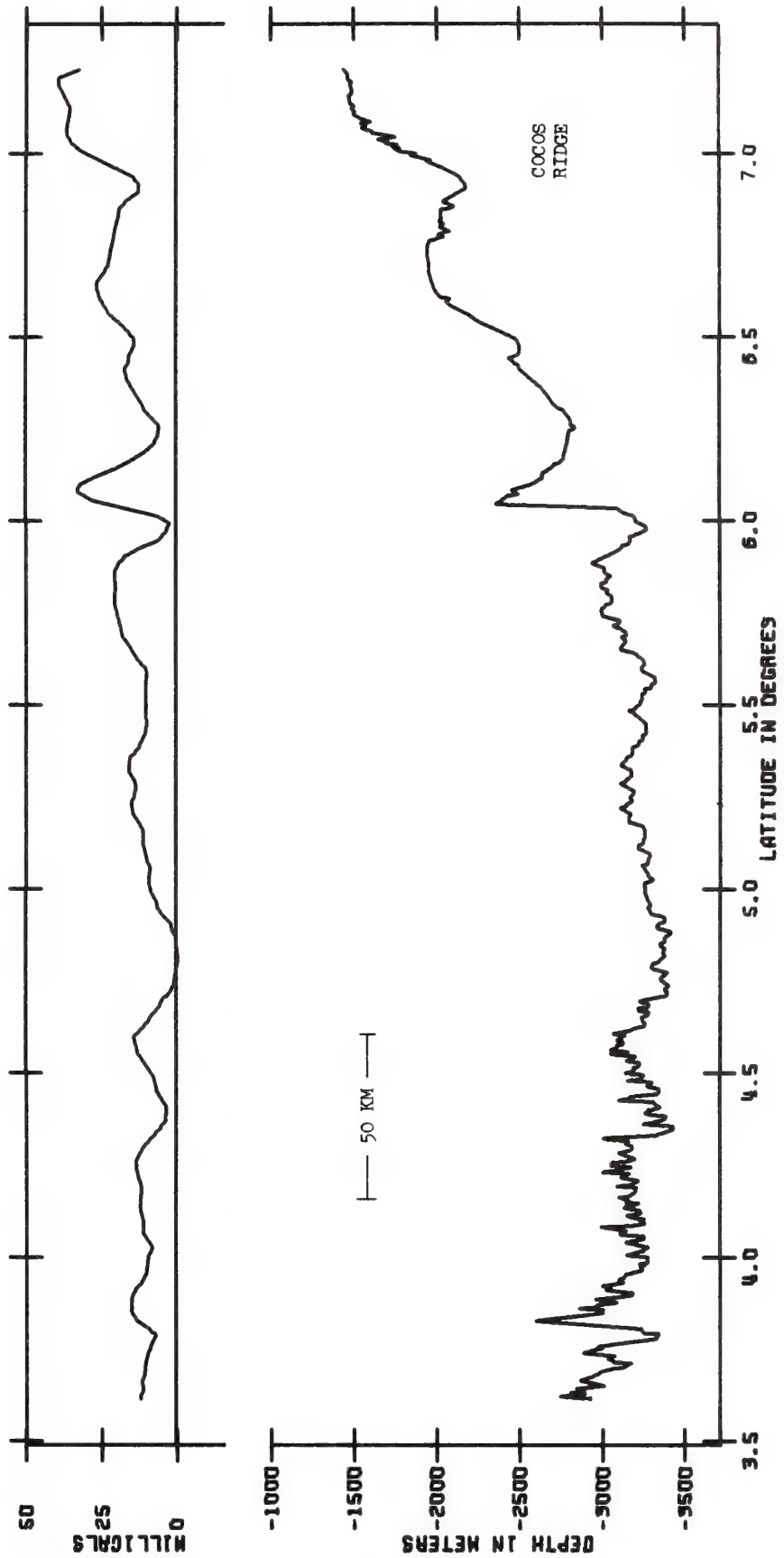


PROFILE 49

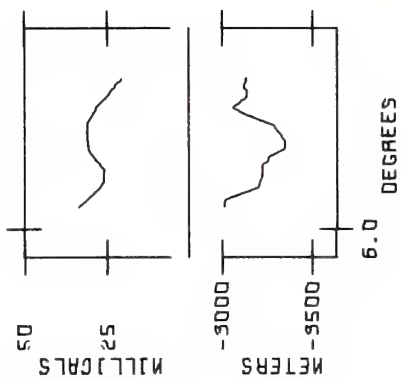


— 50 KM —

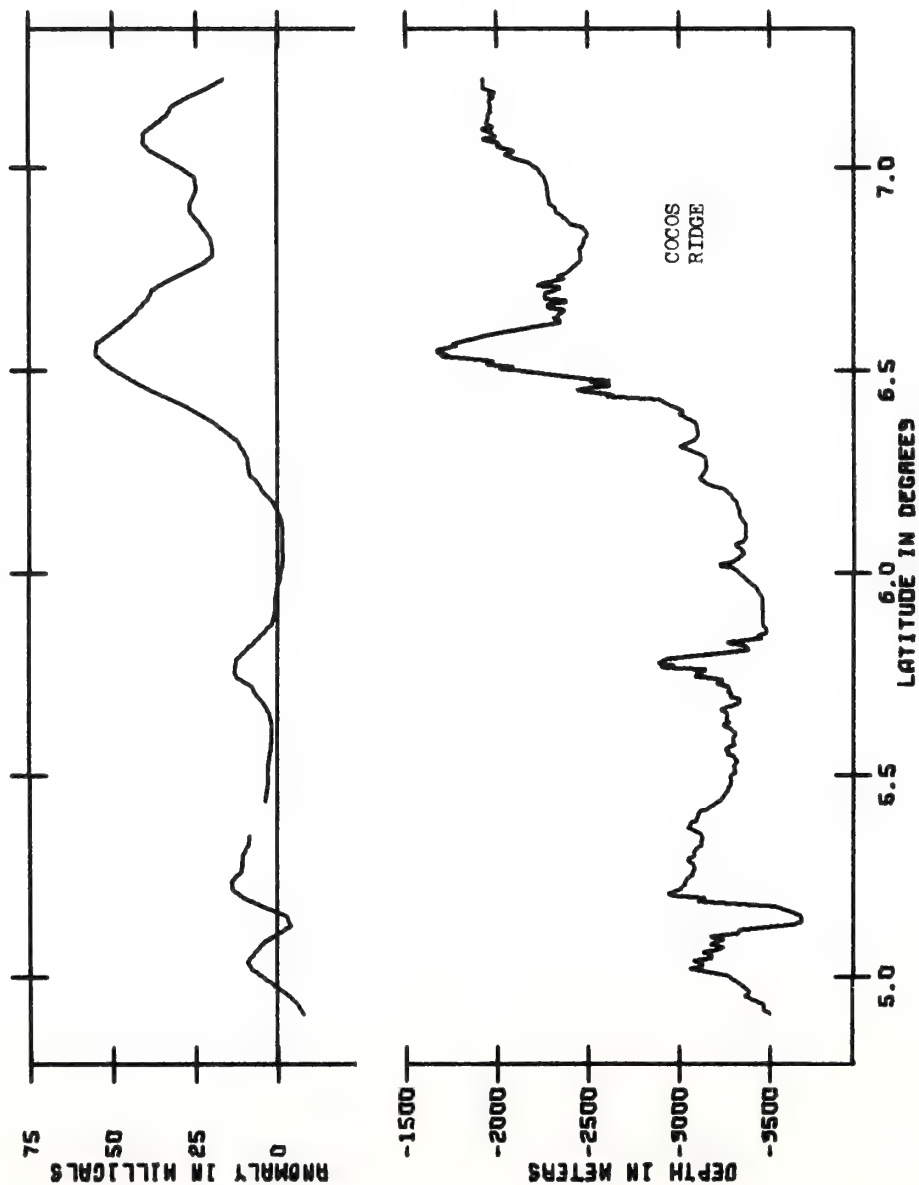
PROFILE 18



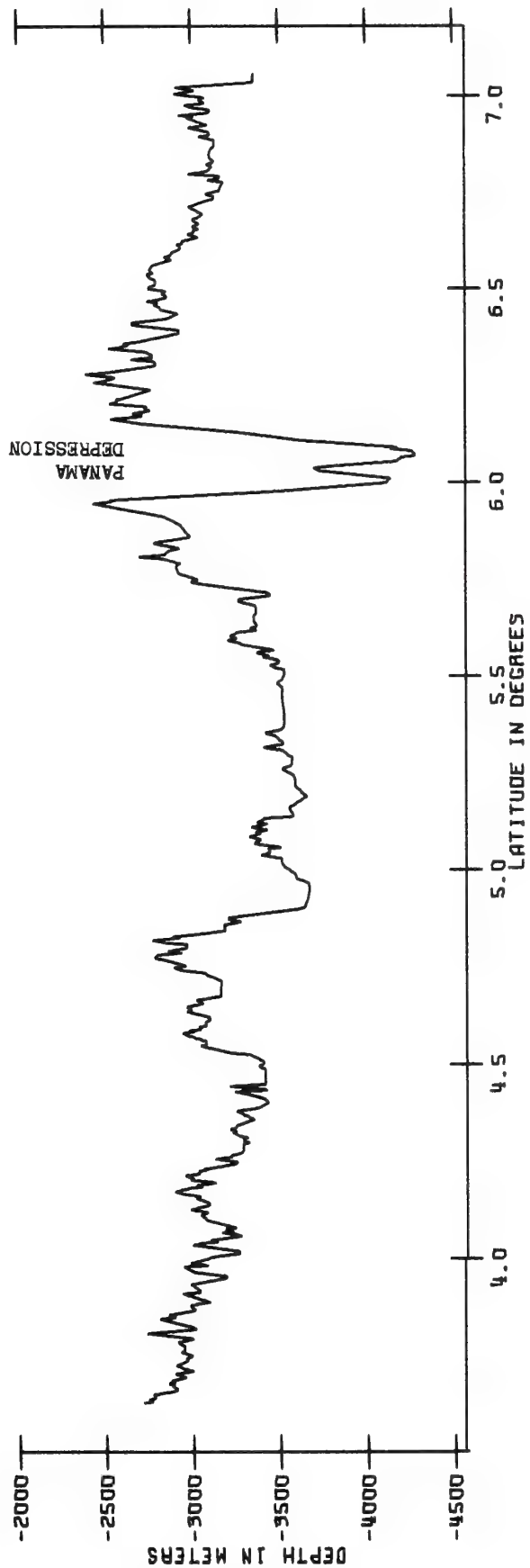
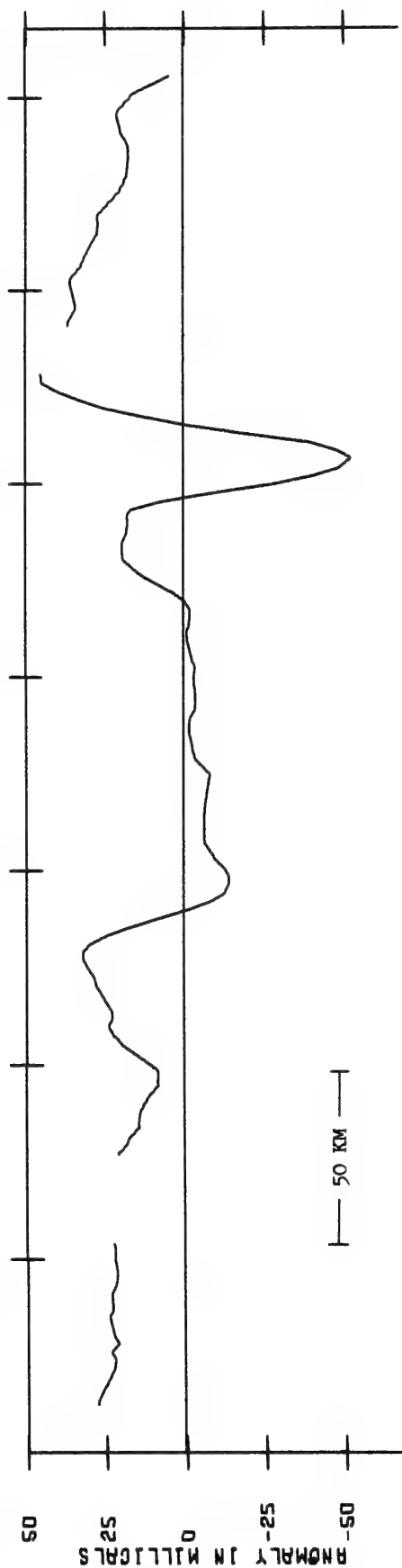
PROFILE 4

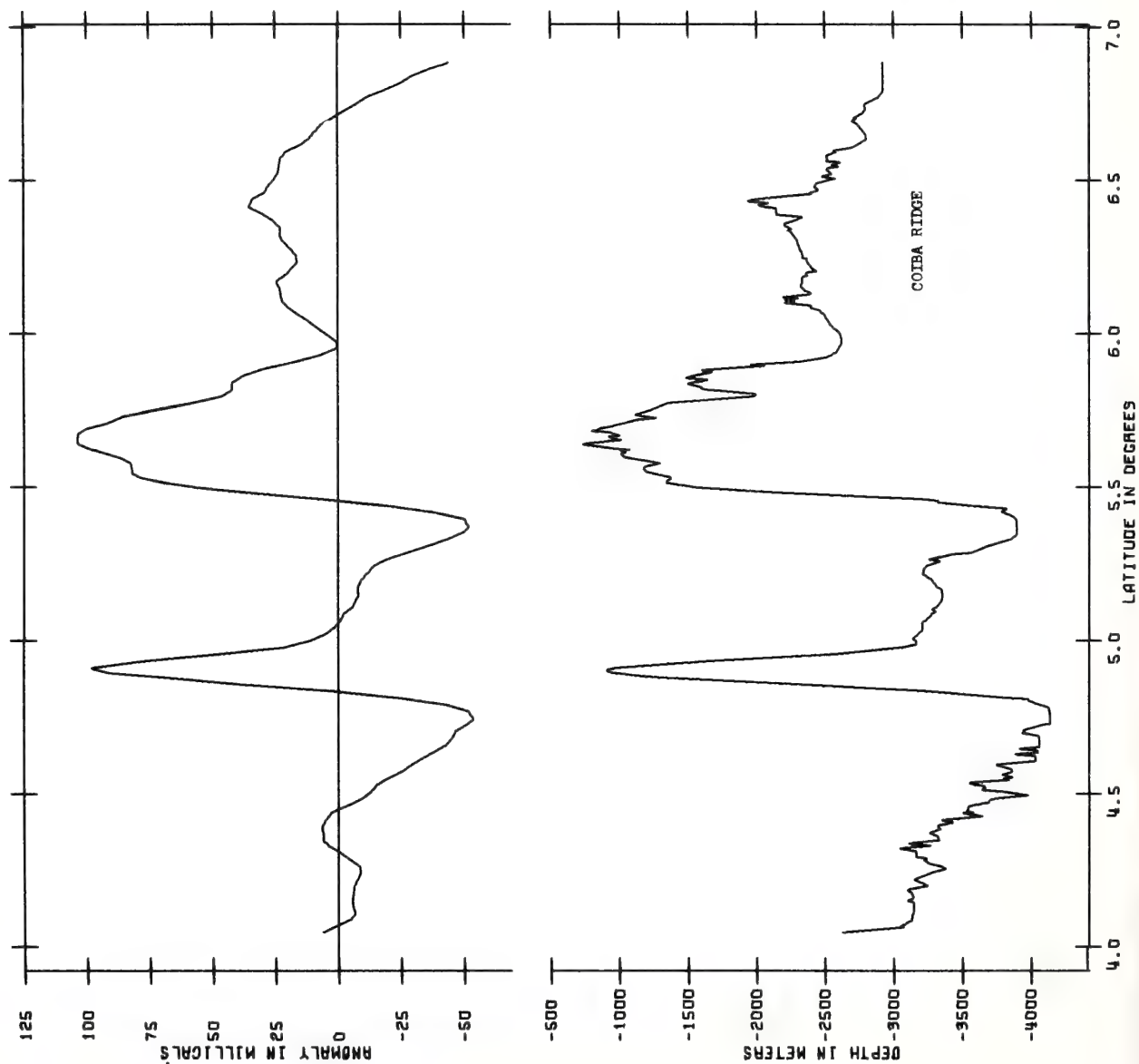


PROFILE 20



PROFILE 22

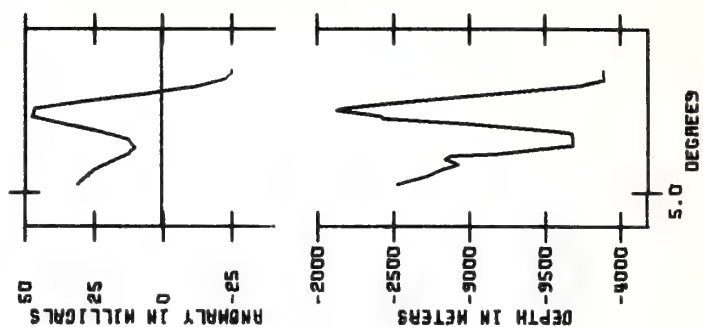


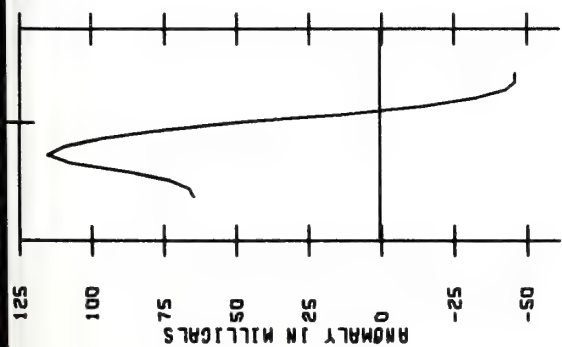


PROFILE 24

— 50 KM —

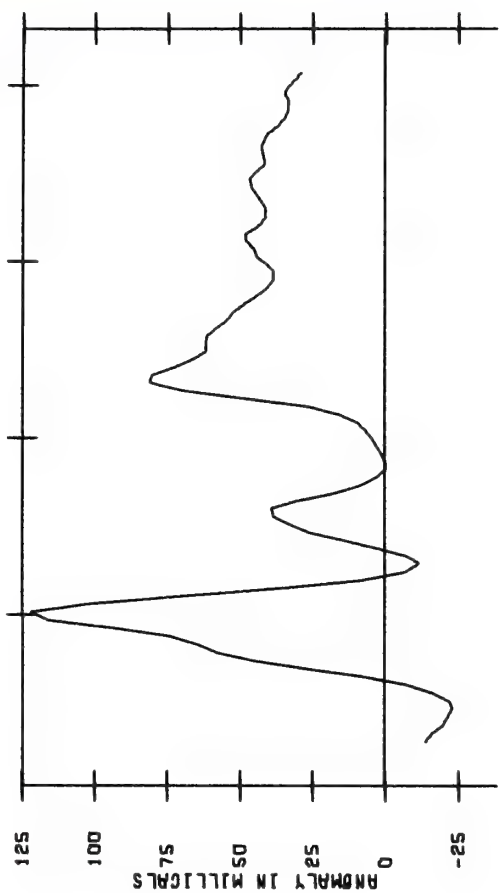
PROFILE 8



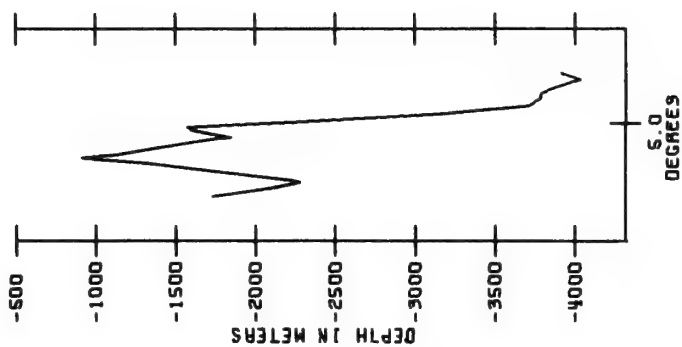


PROFILE 45

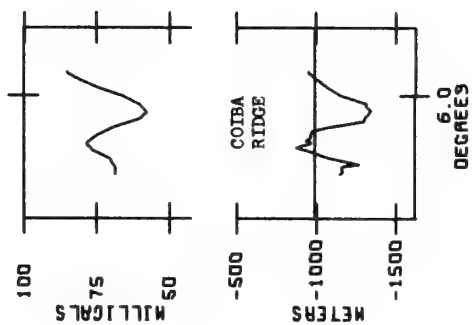
PROFILE 26

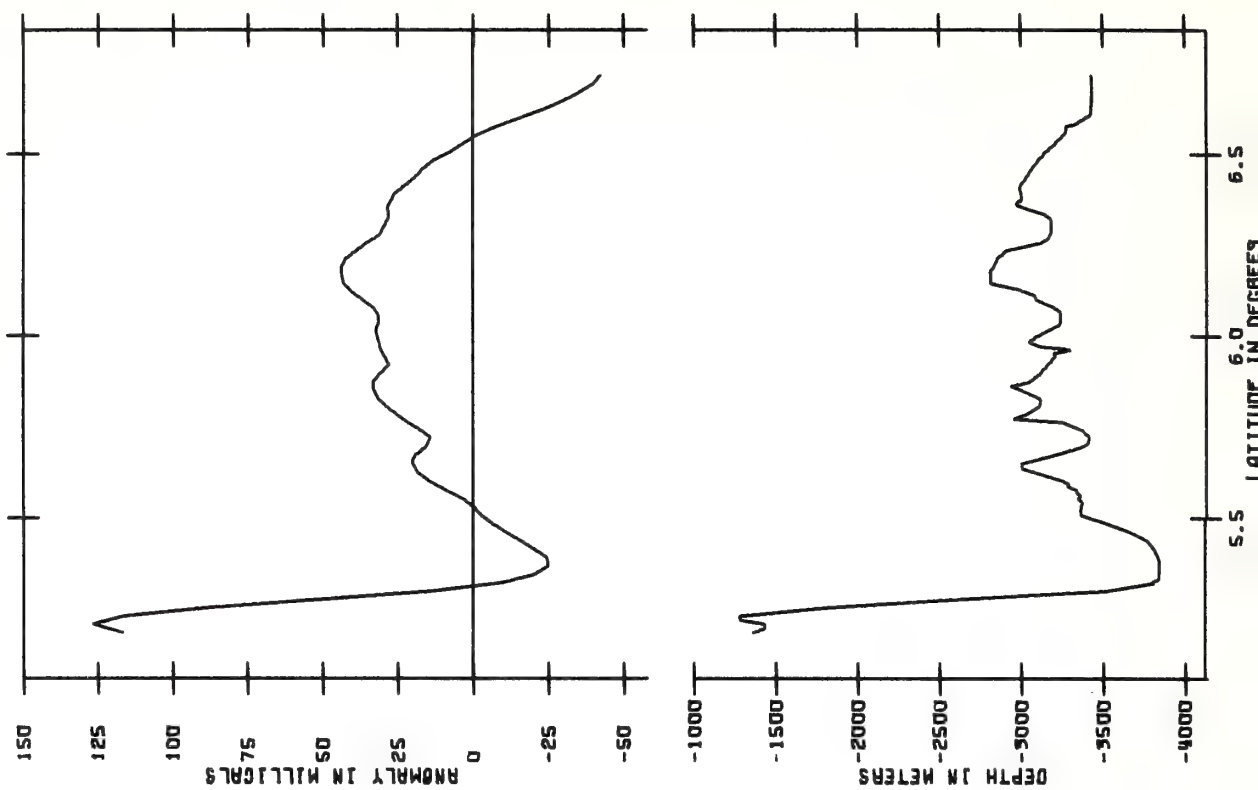


50 KM



PROFILE 41

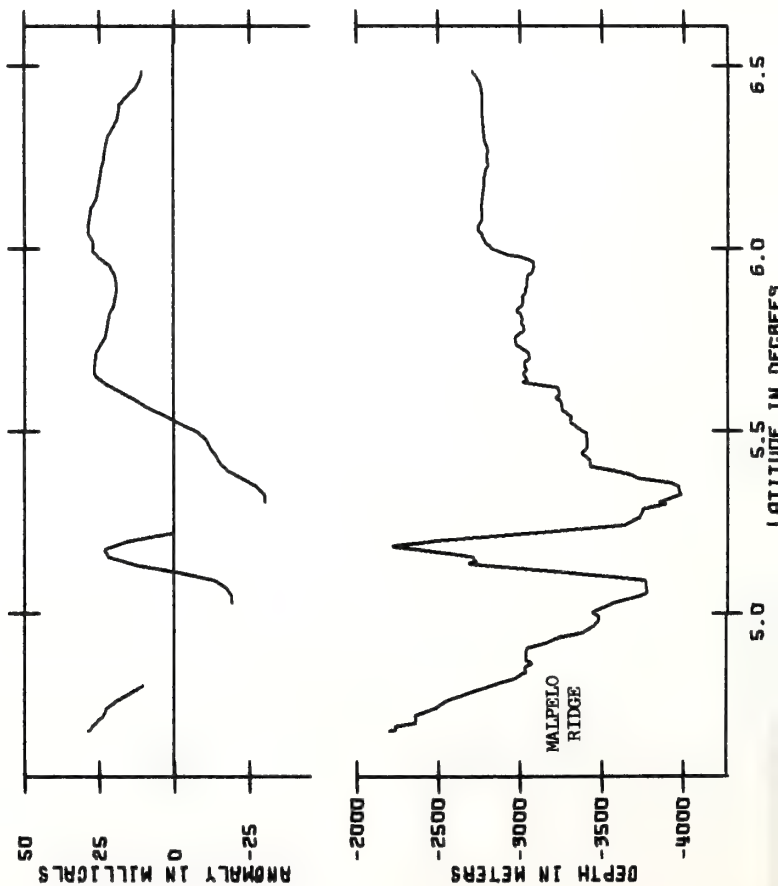


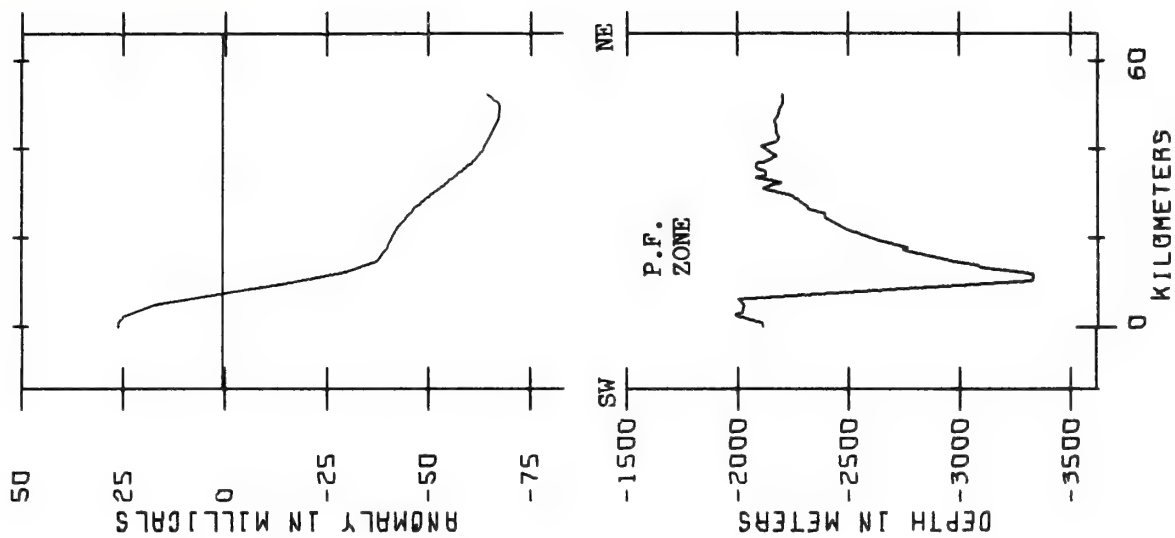
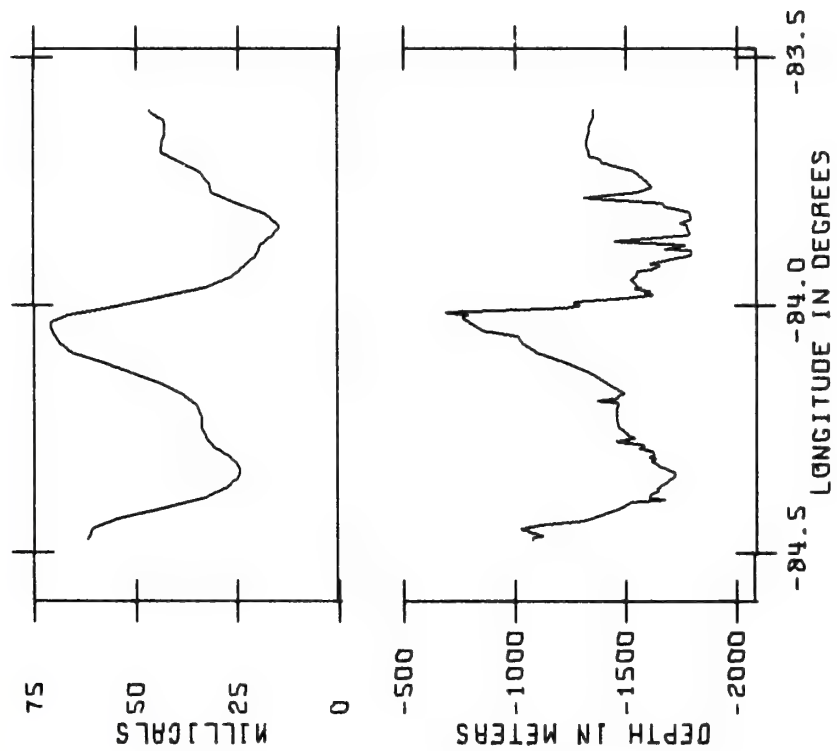


PROFILE 30

— 50 KM —

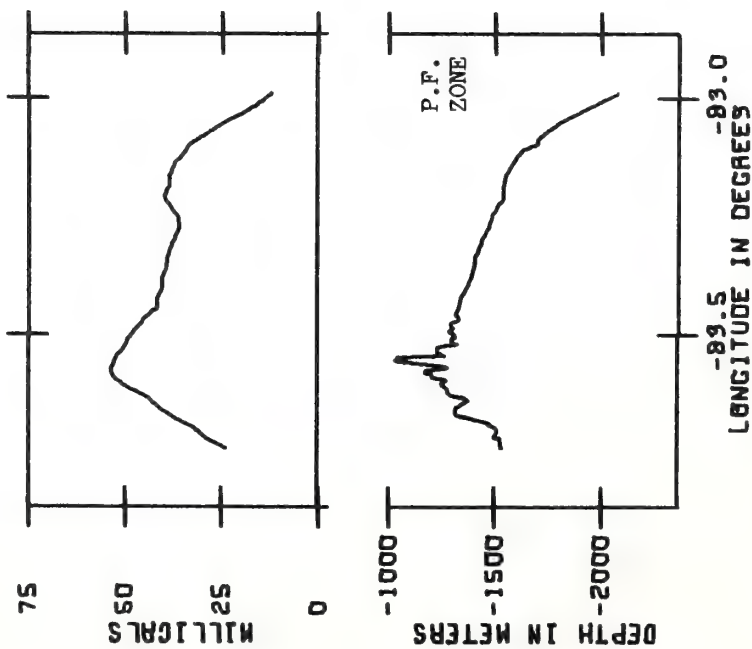
PROFILE 28



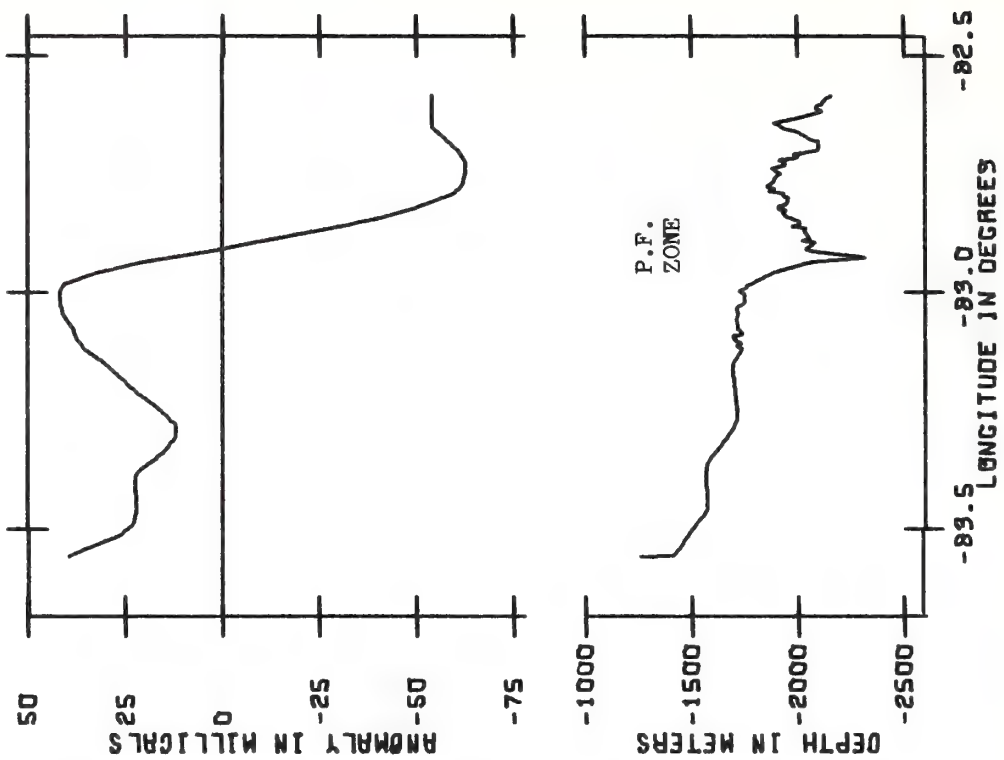


50 KM

PROFILE 34

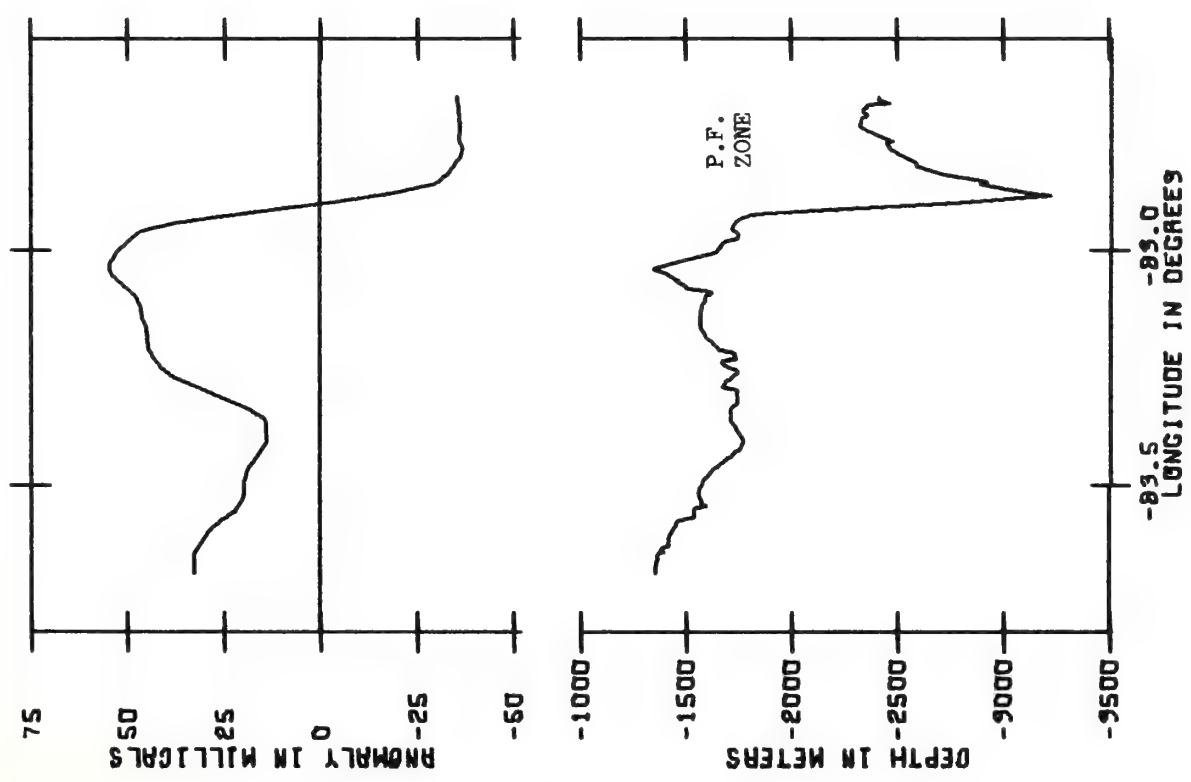


PROFILE 36

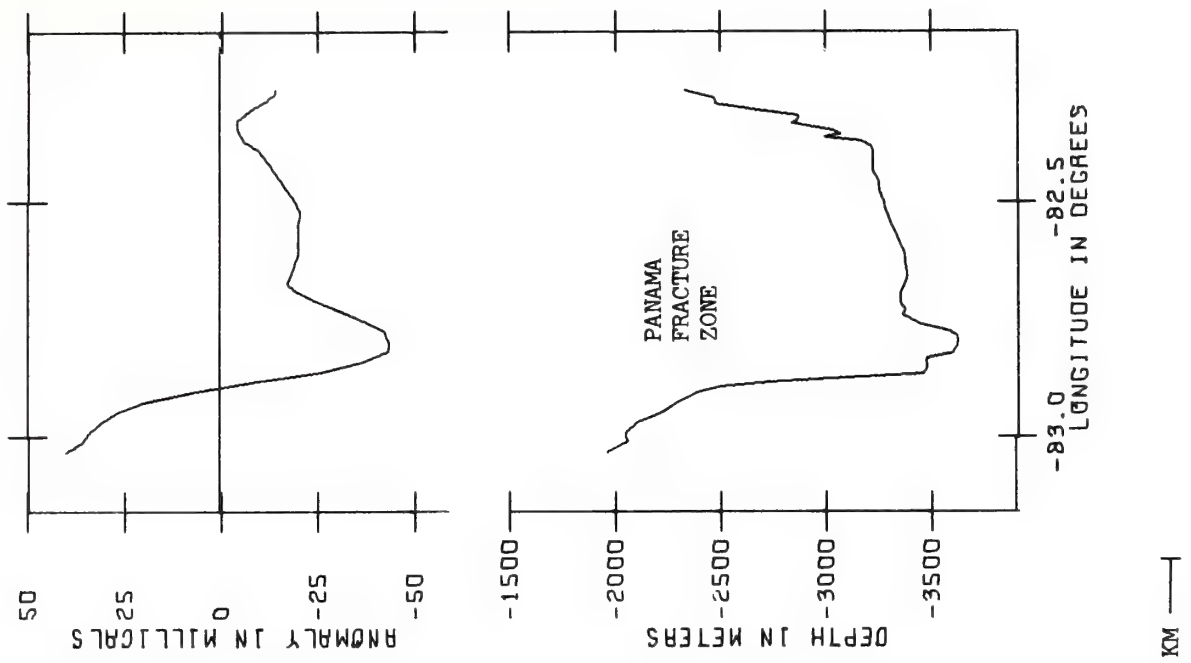


— 50 KM —

PROFILE 38

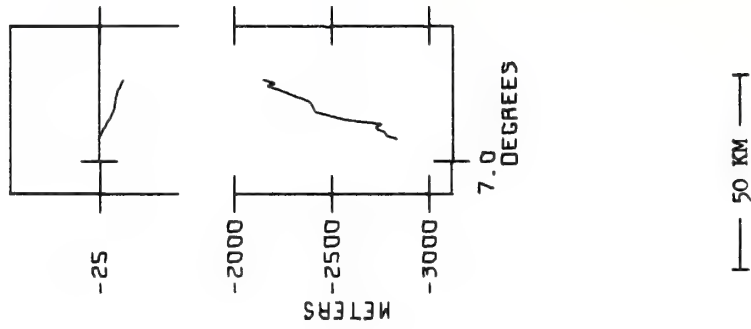


PROFILE 54

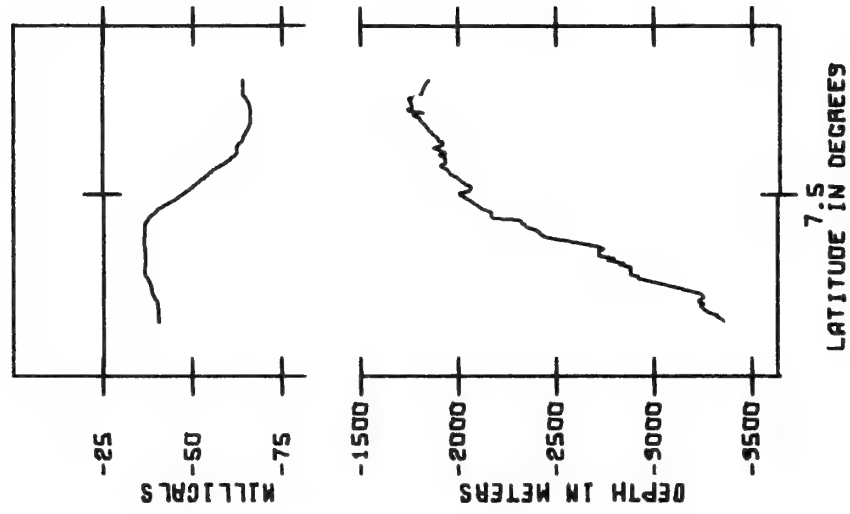


— 50 KM —

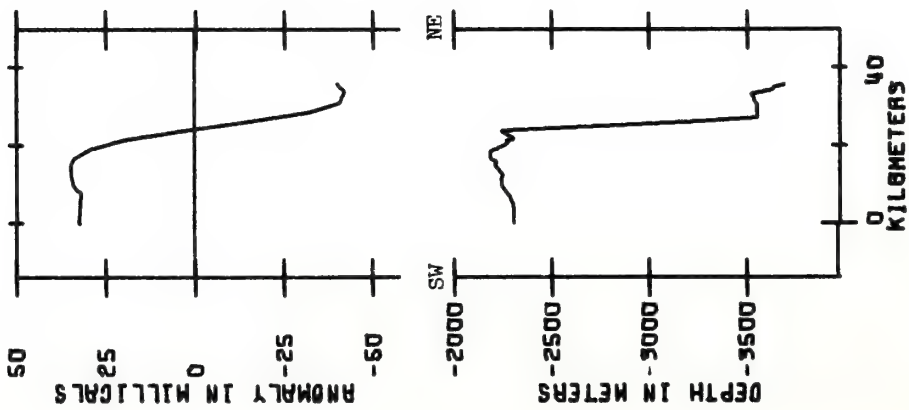
PROFILE 53



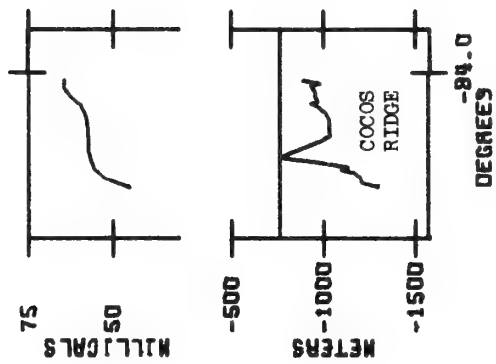
PROFILE 33



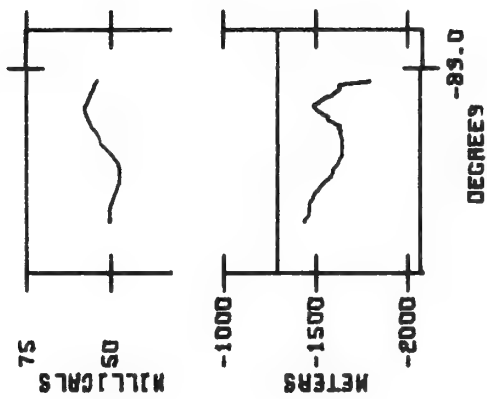
PROFILE 32



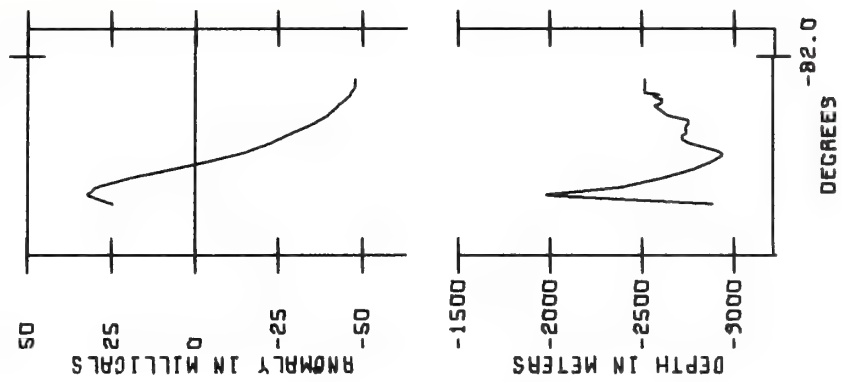
PROFILE 15



PROFILE 19

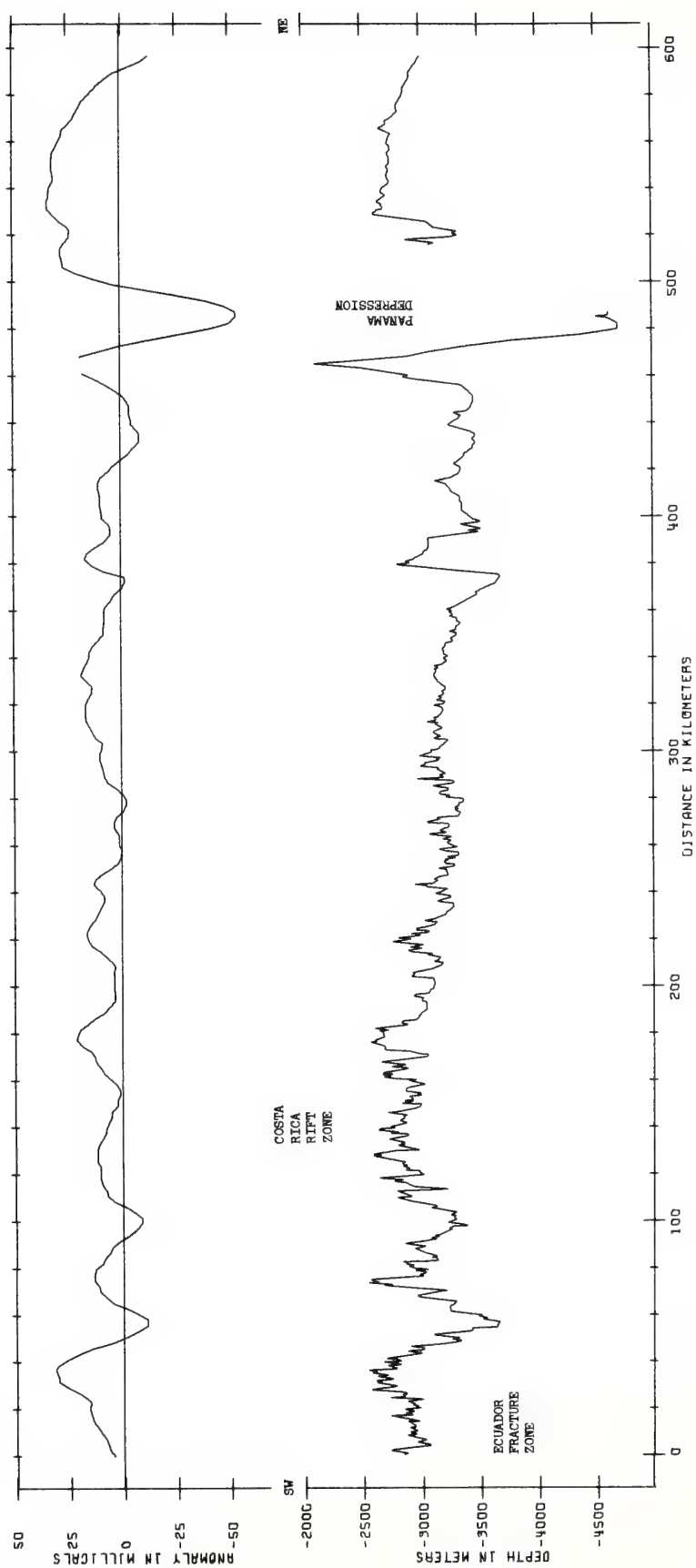


PROFILE 23

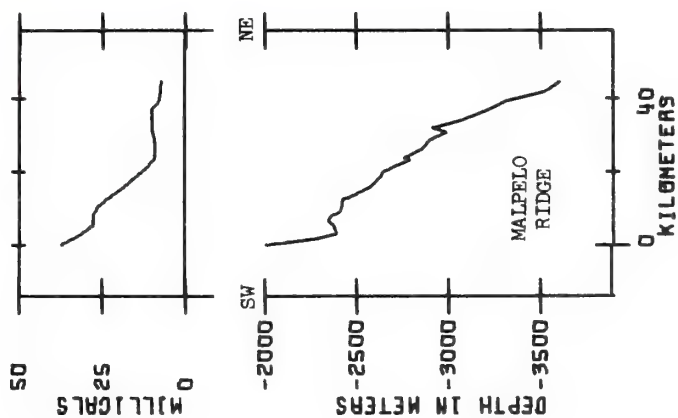


50 KM

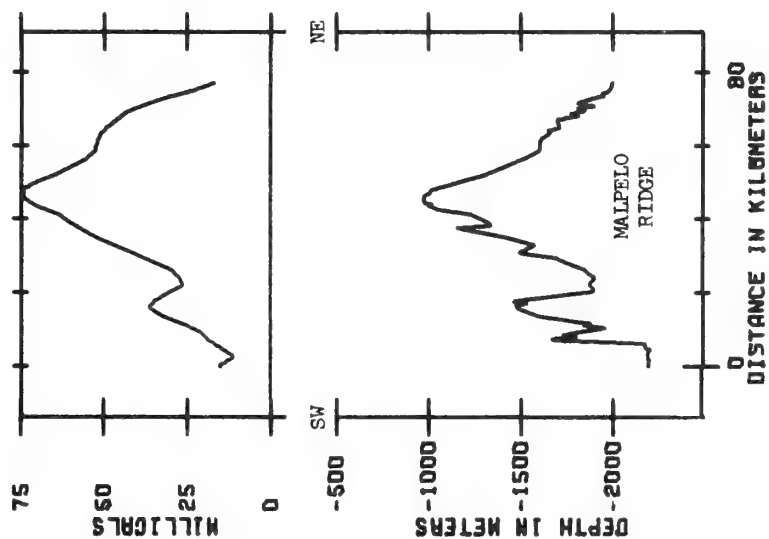
PROFILE 52



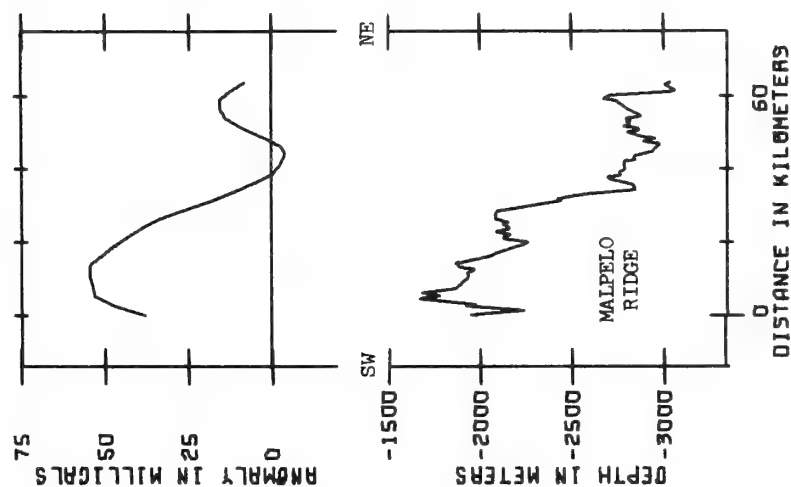
PROFILE 29



PROFILE 12



PROFILE 25



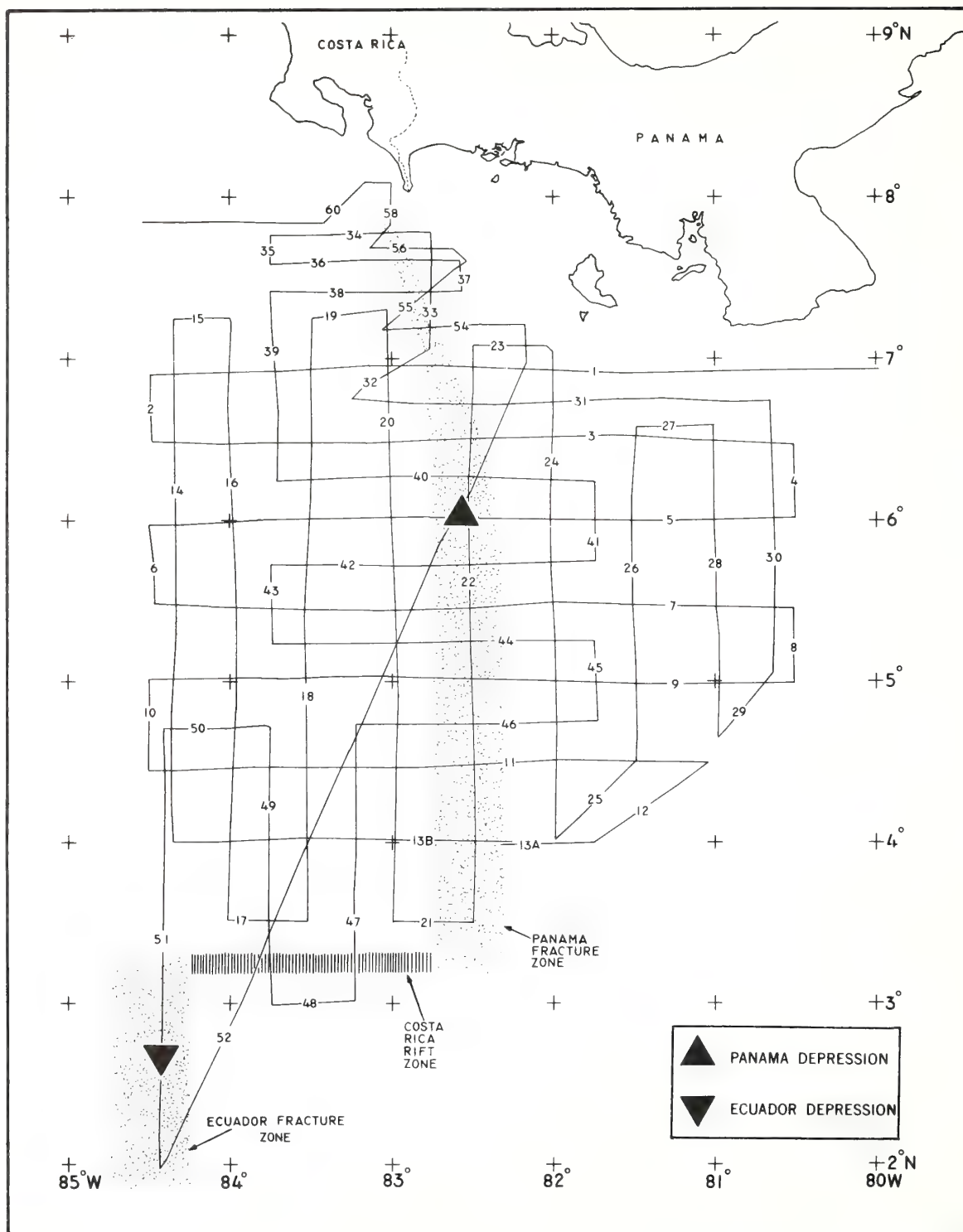


PLATE 1

Reprinted from *The American Association of Petroleum Geologists Bulletin* 55, No. 10, 1730-1740.

Marine Geophysical Study Northeast of Trinidad-Tobago¹

B. G. BASSINGER,² R. N. HARBISON,² and L. AUSTIN WEEKS³

Miami, Florida 33130, 33158

Abstract Marine geophysical measurements off Trinidad-Tobago delineate prominent structural trends revealed in the shallow sedimentary strata. Pilar block is one of the prominent structures along the boundary between the South American continent and Caribbean plate. The block is a narrow horst bounded on the north and south by major fault zones, which apparently continue from the Araya Peninsula of Venezuela eastward to about 58°50'W. Structural features north and south of the Pilar block either die out at the block or veer subparallel with it. North of the block, the Barbados Ridge is an anticlinorium which shows evidence of folding and fracturing apparently as a single tectonic unit. Long-period, high-amplitude magnetic anomalies, forming a zone somewhat parallel with the Lesser Antilles arcuate trend, suggest that the prominent trends of the anticlinorium extend across the continental shelf to the Pilar block. Within the study area, the geophysical data show no evidence for extensive translation between the South American continent and the Caribbean plate in comparatively recent time.

INTRODUCTION

During the summers of 1968 and 1969, the USC&GS ship *Discoverer* conducted reconnaissance marine geophysical investigations in the area off northern Venezuela and Trinidad and around the southern end of the Lesser Antilles arc. Ship's traverses for this study covered the area south of 12°30'N between the Tobago Trough and Trinidad to 58°30'W (Fig. 1). The investigation was designed to study the eastward extension of the predominantly east-west-trending structures of northern Venezuela and Trinidad, and their structural relation to the island of Tobago and the Barbados Ridge on the north. Data collected west of the study

area are presented by Lattimore *et al.* (1971). Regional implications of both studies are discussed by Weeks *et al.* (1971).

Seismic reflection profiles (SRP) were made only on traverses across postulated major structural trends. Continuous gravity, magnetic, and bathymetric observations were recorded on all traverses. Within the study area of this paper, geophysical data were obtained along approximately 3,430 km (1,850 n. mi) of ship's track with SRP records made over about 2,410 km (1,300 n. mi) of the area traversed. The sound source for the SRP system was a 164-cc (10 cu in.) pneumatic gun. Gravity and magnetic observations were made with an Askania seagravimeter and a Varian nuclear resonance magnetometer respectively. Position control was determined by the best source available—dead reckoning, land ties by visual fixes and radar, Loran A and C, and Omega. These data were collected by methods described in Lattimore *et al.* (1971).

The track-line pattern and bathymetry in the study area are shown in Figure 1 of Weeks *et al.* (1971). Line drawings of representative SRP records correlated with gravity and magnetic observations are presented in Figure 2. Parts of original SRP traverses are reproduced in Figures 3-7. In the interpretation of the SRP records, the reflector generally referred to as basement is the deepest observed reverberant reflector beyond which no penetration is obtained within the resolution of the equipment. This reflector, varying in acoustic character over the study area, corresponds in depth to the 3.97 km/sec (13,000 ft/sec) or higher velocity material reported by Ewing *et al.* (1957).

PREVIOUS INVESTIGATIONS

Geologic structures of the islands of Trinidad-Tobago and surrounding area have been described by numerous investigators. Some of the results have been presented by Schuchert (1935), Maxwell (1948), and Suter (1960). In the study area, near-surface, shallow-water sedimentation and geologic structure were studied by Koldewijn (1958), van Andel and Sachs (1964), and van Andel (1967). Deep crustal studies based on seismic refraction results in

¹ Manuscript received, August 24, 1970; accepted, December 3, 1970.

² National Oceanic and Atmospheric Administration (NOAA), Atlantic Oceanographic and Meteorological Laboratories.

³ Consultant; formerly, Environmental Science Services Administration.

The writers are grateful to the officers and men of the USC&GS (NOAA) ship *Discoverer* and the AOML personnel who participated in the project. We are particularly indebted to G. A. Lapiene, Jr., and L. W. Mordock (USESSA) for their assistance in conducting the field work and to Sue O'Brien and George Merrill for drafting the figures. L. W. Butler and G. H. Keller critically reviewed the paper.

© 1971. The American Association of Petroleum Geologists. All rights reserved.

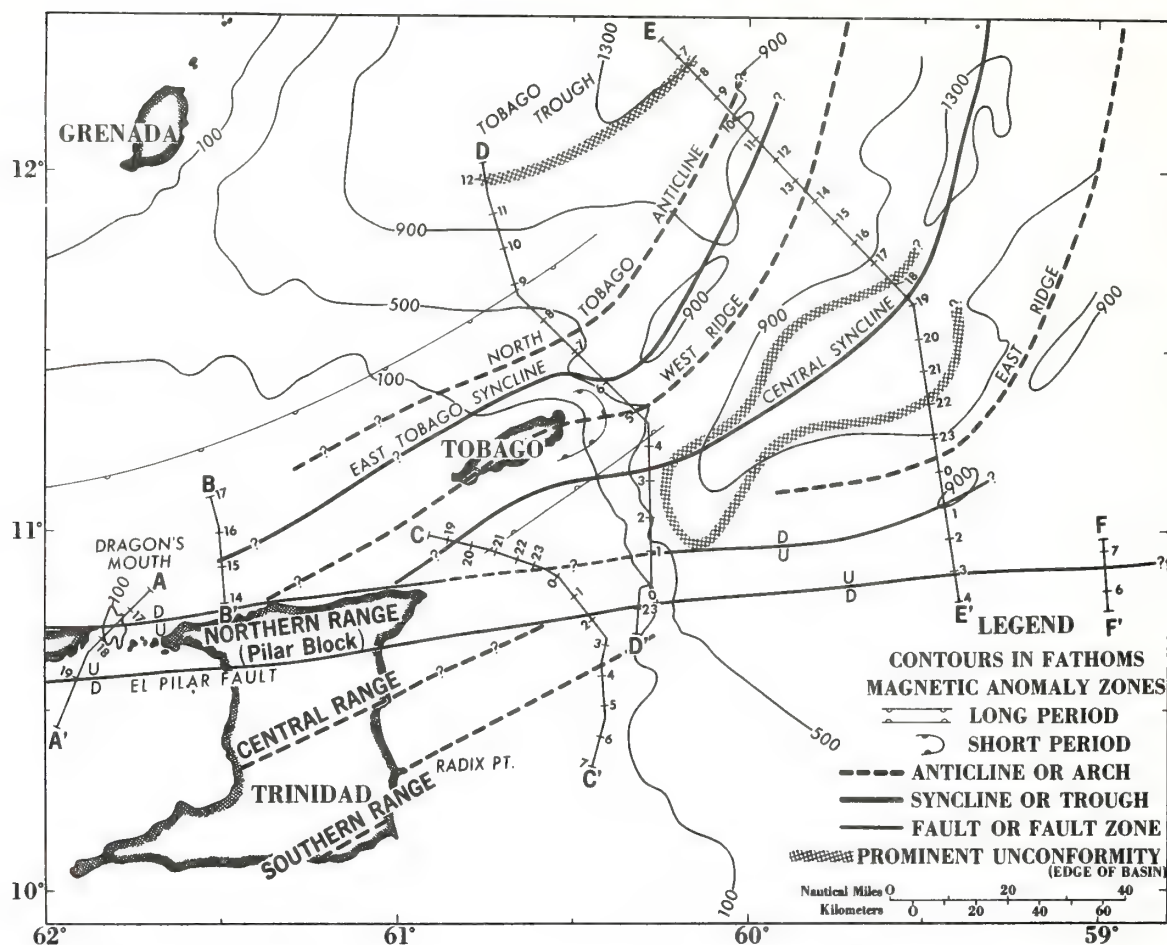


FIG. 1.—Major structural trends and location of representative traverses. Barbados anticlinorium is complex of structures lying east of Tobago Trough through East ridge.

the Caribbean, across the Lesser Antilles island arc, and in the Atlantic were summarized by Officer *et al.* (1959). Some of these velocity data were analyzed by Ewing *et al.* (1957) and later utilized in presenting a summary of the crustal section of the Caribbean area (Edgar, 1968). Higgins (1959) compared the offshore velocity data with similar velocities from geologic structures on Trinidad. Recently, Sykes and Ewing (1965) discussed the seismicity of the Caribbean for the period 1950–1964 and related its occurrence to boundaries between prominent structures.

The Caribbean plate and adjacent South American continent have been described as contrasting crustal blocks with great horizontal movements along major boundary faults. Di-

verse interpretations were made concerning the interaction between these crustal blocks and the boundary fault systems. Hess (1938) suggested that the Caribbean block was translated eastward 80–160 km (50–100 mi). However, Eardley (1954) summarized the earlier hypotheses and presented an argument for subsidence of the Caribbean basin. On the contrary, Rod (1956) implied that the overall displacement within the Caribbean area of more than 100 km (62 mi) was not unreasonable, based on an analysis of the supposed strike-slip fault system along northern Venezuela. In further support of strike-slip movement, Alberding (1957), applying the principle of wrench-fault tectonics of Moody and Hill (1956) to northern South America, concluded that during the Cre-

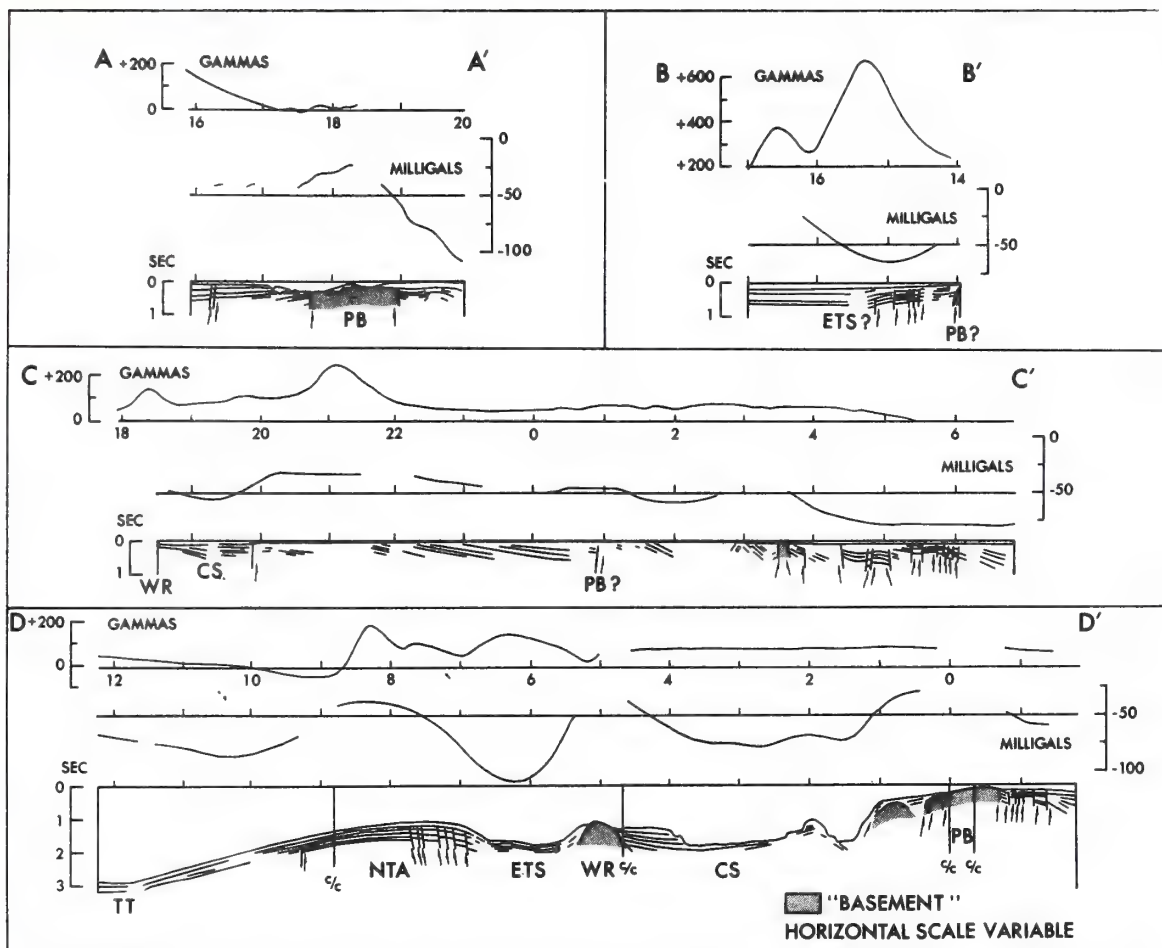


FIG. 2.—Residual magnetic field intensity (regional field removed by inspection), free-air gravity anomaly, and seismic reflection profiles. Vertical scale of seismic records is two-way time. Position numbers are hours. CS, Central syncline; ER, East ridge; ETS, East Tobago syncline; NTA, North Tobago anticline; PB, Pilar block; TT, Tobago Trough; and WR, West ridge.

taceous the Araya and Paria Peninsulas of Venezuela and the Northern Range of Trinidad formerly were 475 km (295 n. mi) west. A study of the pre-Tertiary rocks along one of the several prominent east-west-trending faults across northern Venezuela suggested no more than 10–15 km (6–9 n. mi) of strike-slip movement along the El Pilar fault (Metz, 1964). However, recent field mapping in the Northern Range of Trinidad (Potter, 1968) revealed only vertical displacement of up to 1.8 km (6,000 ft). In addition, seismic-reflection profiling and sediment coring indicated that the tectonics of the margins of the Caribbean ba-

sins show vertical rather than horizontal displacements (Ewing *et al.*, 1967).

RESULTS AND DISCUSSION

The geophysical data suggest a division of the study area into three prominent structural features: (1) Pilar block, (2) Barbados anticlinorium, and (3) Tobago Trough. Pilar block is defined as the tectonically positive element bounded on the north and south by faults of major displacement. The block consists of the Araya and Paria Peninsulas of Venezuela and their continuation through the Northern Range of Trinidad. Barbados anticlinorium is the

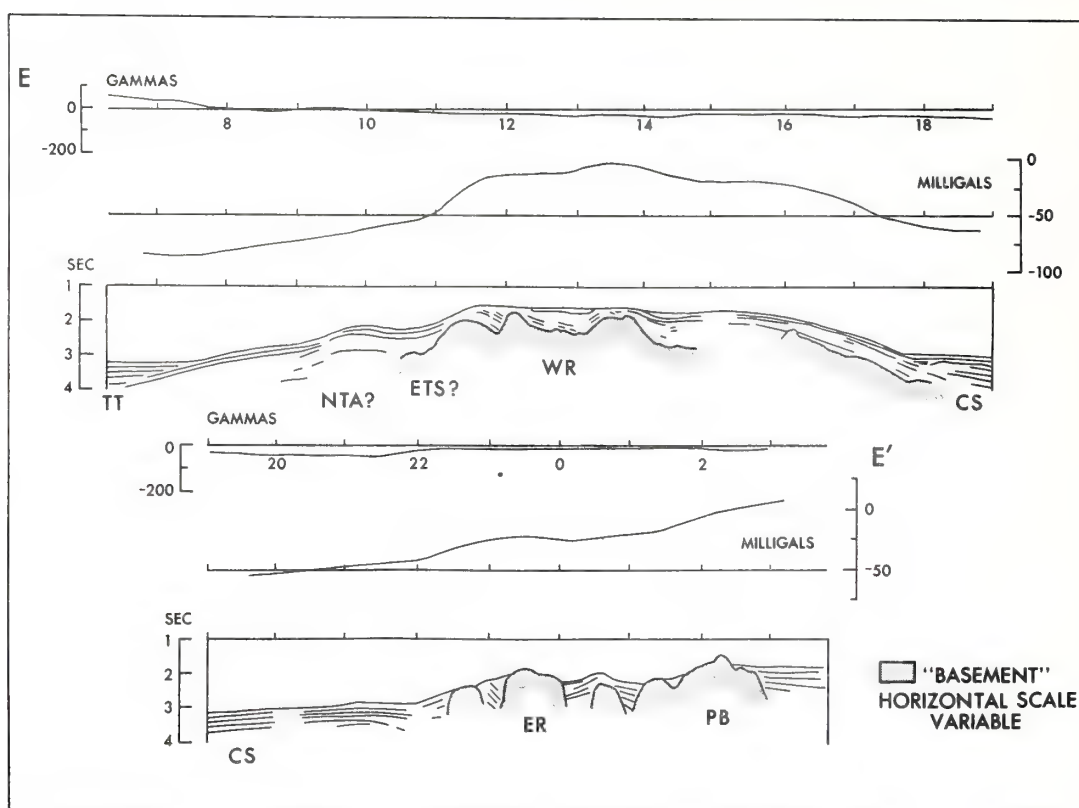


FIG. 2 (Continued)

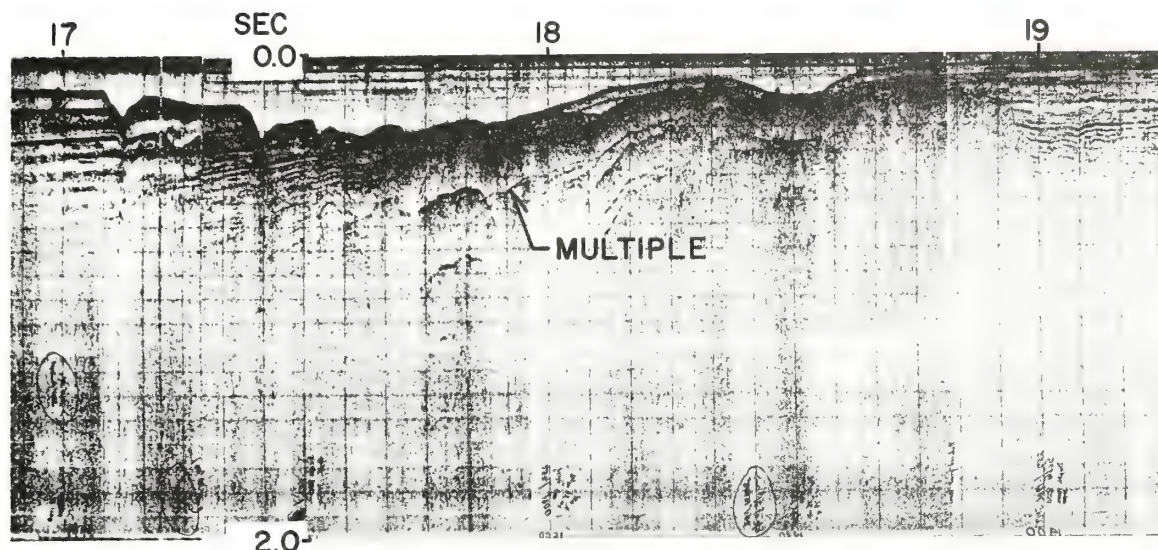
complex of structures lying between the Tobago Trough and the Atlantic basin, and is divided into two separate tectonically positive structures separated by a medial syncline (Weeks *et al.*, 1969). These structures are: West ridge, Central syncline, and East ridge. North Tobago anticline and East Tobago syncline are two subsidiary structures west of the West ridge. Tobago Trough is the tectonically negative element separating the Lesser Antilles from the Barbados anticlinorium (Fig. 1).

Pilar Block

A correlation of earthquake epicenter locations with structural units in the Paria Peninsula region of Venezuela seems to indicate two sequences of tectonic events (Sykes and Ewing, 1965). According to that study, one series of events north and another south of $10^{\circ}36'N$ may suggest movements along two major fault

zones. Although the epicenter locations are confined to a small area of the Paria Peninsula, our data farther east support their conclusion. Within the study area, the Pilar block is a distinct structural unit, bounded on the north and south by prominent fault zones which apparently continue eastward to about $58^{\circ}50'W$ (Fig. 1).

The traverse through the Dragon's Mouth (profile A-A', Figs. 2, 3) shows the Pilar block as a partly buried horst flanked by sedimentary strata. Presumably, this basement block is the lateral continuation of pre-Late Jurassic to Late Cretaceous metamorphic rocks of the Northern Range and Paria Peninsula mapped by Kugler (1961). Small down-to-the-north growth faults are present near the north end of the profile. The southern half of the profile shows a shallow zone of relatively transparent sediments apparently transgressing the block from the south.



PILAR BLOCK

FIG. 3.—North-south seismic reflection profile through Dragon's Mouth (profile A-A', Fig. 1) showing Pilar block adjacent to thick sedimentary sequences. Vertical scale is two-way time.

In the same area the free-air gravity gradient of 90 mgals is consistent with a thick accumulation of sediments in the Gulf of Paria on the south, but is also in part a reflection of the regional gradient. This regional gravity trend is the northern flank of an arcuate gravity low paralleling the Lesser Antilles (Bush and Bush, 1969), which is coincident with a negative Bouguer anomaly along the Barbados Ridge. This negative anomaly is apparently the result of intermediate velocity material that lies in downwarped high-velocity layers (Officer *et al.*, 1959). In addition to the regional field, local anomalies of a few milligals are related to the block and to the near-surface arched structure observed in the SRP records near location 19.5. The suggestion of major tectonic activity is confirmed further by a change from a high-amplitude, long-period to a low-amplitude, short period magnetic trace near the northern margin of the block. These short-period variations of up to 10 γ may be caused by lithologic changes in the observed part of the Pilar block similar to those found in exposed rocks of the Paria Peninsula and Northern Range.

The SRP record off the north coast of Trinidad suggests a basement complex that is most probably an eastward continuation of the Pilar block (profile B-B', Fig. 2). North of the basement block, a zone of normal down-to-the-north

growth faulting correlates well with similar features on the west in profile A-A'. These occurrences, which coincide with an increase in gravity also suggest a rise in the basement complex.

A seismic refraction traverse (line 24 of Ewing *et al.*, 1957) crosses the northern ends of profile A-A' and B-B'. It shows relatively flat-lying sedimentary sequences with velocities of 1.66–1.93 km/sec (5,500–6,300 ft/sec) underlain by north-dipping velocity sequences of 2.75–4.80 km/sec (9,000–15,800 ft/sec). A comparison of these velocities with those recorded in south and central Trinidad suggests that the uppermost sedimentary layers above the 2.75 km/sec (9,000 ft/sec) layer are post-Pliocene material (Higgins, 1959). The upper half of the 1.93 km/sec (6,300 ft/sec) sediment sequence, showing evidence of down-to-the-north normal growth faults, can be traced close to the surface near the southern end of the profile adjacent to a basement complex (Profile B-B', Fig. 2).

Near the north end of profile A-A' (Fig. 2), Ewing *et al.* (1957) obtained a depth of 3.1 km (10,200 ft) to the top of the 4.8 km/sec (15,800 ft/sec) layer and related it to the north flank of the Northern Range. In support of that conclusion, Higgins (1959), correlating these velocities with those recorded in Trinidad, suggested that material with the same velocity

may be related to the Northern Range metamorphic rocks. If the top of the 4.8 km/sec (15,800 ft/sec) interface is projected to the northern margin of the exposed Pilar block and if one assumes that the exposed block in the Dragon's Mouth is comparable material, a minimum vertical displacement of 2.3 km (7,800 ft) is indicated along the north boundary fault system of Trinidad. This displacement is comparable with, but somewhat greater than, the 1.8 km (6,000 ft) uplift reported by Potter (1968) for the Northern Range along the El Pilar fault system.

The impression conveyed by the structural cross sections through Trinidad (Kugler, 1961) is that the Pilar block becomes less pronounced toward the east. Our geophysical information is in agreement with that conclusion. From location 20 (profile C-C', Fig. 2) off the northern coast of Trinidad to midway between the off-shore projection of the Pilar block, the SRP records show well-stratified, shallow sedimentary strata of up to 1.0-sec penetration in an area where, according to Koldewijn (1958), only a few centimeters of recent sediments have been found above older deposits. These relatively undeformed sediments are a strong indication of a lack of postdepositional tectonic activity in the vicinity of the northern boundary fault system of Trinidad.

The stratigraphic section south of the projected El Pilar fault system contrasts markedly with that on the north (profile C-C', Fig. 2). Off the east coast of Trinidad, the shallow sedimentary strata are faulted, folded, and broadly arched, and thus resemble the structures of southern Trinidad shown by Kugler (1961).

The basement complex centered around location 3.7 can be traced across the shelf through shoals and banks to Radix Point. These occurrences seem to indicate that the northeast-southwest-striking tectonic belts of Trinidad continue across the continental shelf—a conclusion in general agreement with Koldewijn's (1958) structural trend map.

Gravity observations in the area of the off-shore projection of the Pilar block (profile C-C', Fig. 2) show no large density contrast at any depth within the crust as found in the Dragon's Mouth profile (profile A-A', Fig. 2). However, the only positive suggestion of the continuation of an uplifted feature across the shelf is revealed by a minor gravity anomaly of less than 8 mgal between locations 0.2 and 1.5. This anomaly coincides with low-amplitude magnetic signatures of approximately 10 γ , which may be the result of faulting with subsequent intrusion or local susceptibility contrasts.

Off the east coast of Trinidad, the Pilar block is easily identified in the vicinity of location 23.8 (profile D-D', Figs. 2, 4) as an exposed basement complex showing evidence of planation. On six successive crossings to 58°50' W, the El Pilar fault is characterized by a basement-sediment contact, but the northern boundary fault is less obvious (profile E-E', Figs. 2, 5, 6). These observations confirm the interpretation of Collette *et al.* (1969), that the block apparently acts as a barrier preventing the northward flow of sediments.

Barbados Anticlinorium

The East ridge could not be traced west of 60°W, just off the Trinidad shelf. In that area,

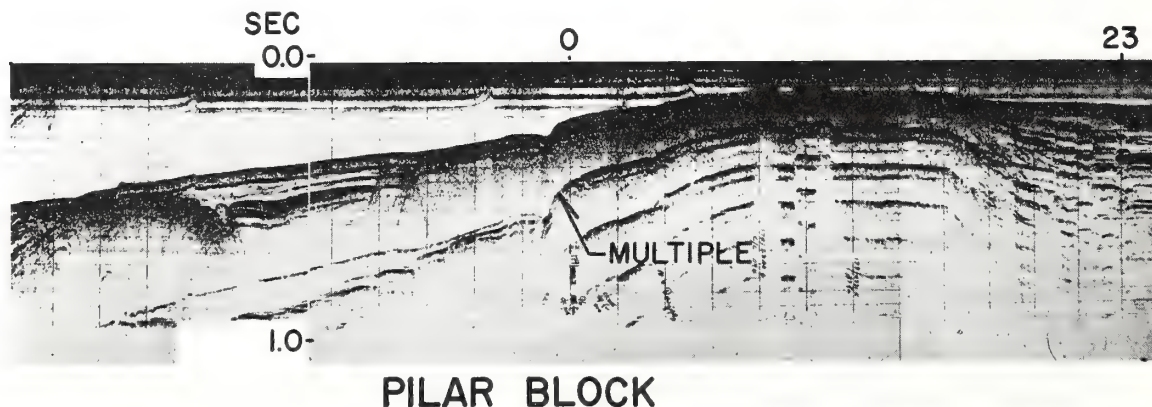


FIG. 4.—Part of north-south seismic reflection profile D-D' (Fig. 1) showing Pilar block near shelf edge. Vertical scale is two-way time.

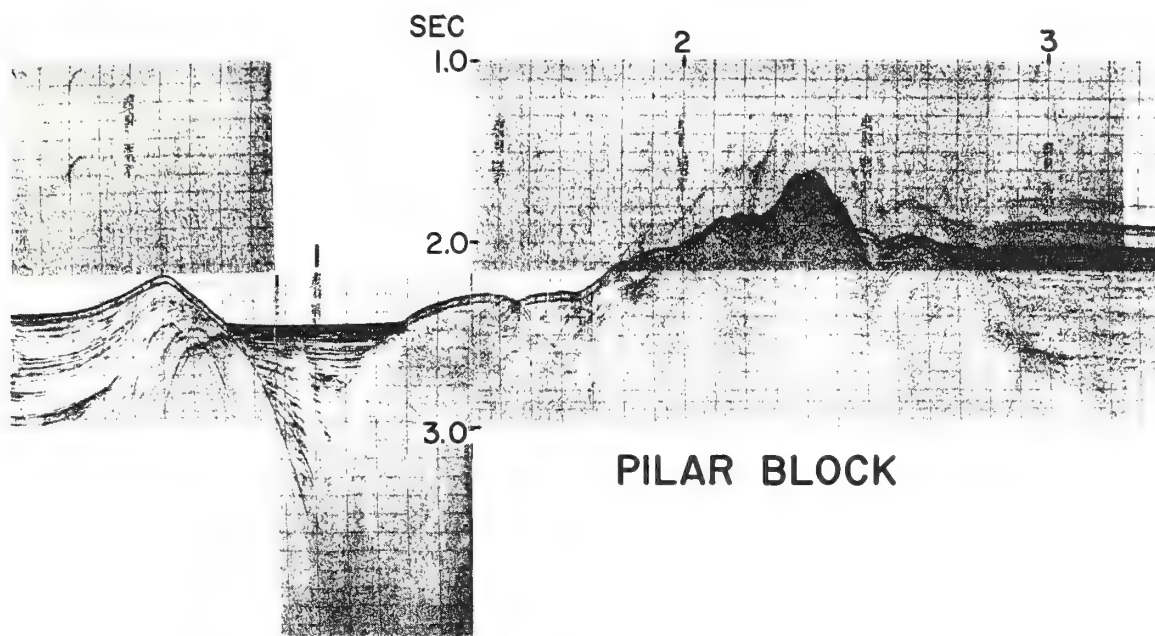


FIG. 5.—Part of north-south seismic reflection profile E-E' (Fig. 1) showing Pilar block adjacent to level sedimentary sequences of different depths. Vertical scale is two-way time.

the ridge apparently either dies out or plunges below the flat-lying sediments of the Central syncline (Fig. 1). Its northward projection east of $59^{\circ}10'$ is based primarily on bathymetry (Fig. 1 of Weeks *et al.*, 1971). Near the Pilar block, much of the trend is characterized by three basement highs, with intervening strata whose sedimentary layers seem to exhibit a progressive increase in dip with increasing depth (profile E-E', Figs. 2, 5). This deformation and the apparent termination of the East ridge below the Central syncline imply that the process which formed the ridge has been primarily vertical and persistently active during the period of sedimentation.

The Central syncline separates the West and East ridges and extends from near the Pilar block between Trinidad and Tobago to the northeast limit of the study area. Within the shelf area north of Trinidad, the syncline occupies a topographic depression with somewhat conformable sedimentary reflectors (profile C-C', Fig. 2), probably reflecting a continuation of a linear bathymetric low southeast of Tobago (Fig. 1 of Weeks *et al.*, 1971). Along the line of track, the feature is bounded on the southeast by a fault that extends to the surface. There, the gravity anomaly is produced in part by an accumulation of lower density sediments

and in part by a density differential resulting from faulting at depth. Off the shelf edge the syncline is defined more clearly by relatively undeformed, gently downfolded reflectors which continue under a layered sequence (profile D-D', Figs. 2, 7).

Off the continental shelf the prominent flanking unconformities of the Central syncline generally die out toward the northeast (Fig. 1). The older folded sediments of the West and East ridges plunge under the syncline beneath a younger unconformable wedge of well-stratified, almost horizontal sediments (profile E-E', Fig. 2).

The West ridge is a continuous element of the Barbados anticlinorium that extends from north of Barbados, across the study area through Tobago, and well into the shelf area off Trinidad. First indications of this feature are thinning sedimentary sequences below the apparently flat shelf at the beginning of profile C-C' (Fig. 2). However, the rise is more apparent on seismic reflection profiles about $10^{\circ}55'N$ (Lowrie and Escowitz, 1969). In this area of the shelf, an arched sedimentary zone is marked by a change of sedimentary environment with distinctive patterns of reflectors. The characteristic pattern of reflectors, presumably post-Pliocene material, occupies the near-surface area be-

tween the Dragon's Mouth and the West ridge axis. The suggestion of an arched zone is confirmed further by an increase in gravity and a small isolated magnetic anomaly that may reflect a shallowing of the basement surface.

Near the shelf edge the West ridge is expressed as an exposed basement complex (profile D-D', Figs. 2, 7). Northeastward the ridge is marked by an irregular surface that widens rapidly and plunges well below thick sedimentary sequences (profile E-E', Fig. 2). Although the reflected basement surface has different acoustic characteristics across the traverse, near location 13 it corresponds in depth to the 3.97 km/sec (13,000 ft/sec) material reported by Ewing *et al.* (1957). On the margins of the ridge, the basement surface and its sediment overburden plunge well below the seismic penetration limit in both the Central syncline and Tobago Trough.

North Tobago anticline and East Tobago syncline are separate tectonic elements within the Barbados anticlinorium. In the Tobago area the North Tobago anticline shows well-defined reflectors cut by small, normal down-to-the-

south faults, principally south of the crest of the anticline (profile D-D', Fig. 2). These strata belong to the pre-unconformity suite of rocks, for they plunge under the younger beds of the Tobago Trough (profile E-E', Fig. 2). Over this general area, the magnitude of the gravity anomaly (in part reflecting sea-floor topography) compared to the surrounding area and the disruption of the regional magnetic field suggest deeper structural implications as a result of the development of the structures near Tobago. A definite correlation exists between the magnetic anomalies in this area and the magnetic anomaly zone traced across the shelf by Lattimore *et al.* (1971). Even though the amplitudes of the anomalies are considerably less than those identified farther southwest, the overall disruption of the magnetic field is comparable in extent.

The close double-anomaly (two source) pattern observed on profile B-B' (Fig. 2) is helpful in making a reasonable correlation within the study area (Fig. 1). These anomalies appear to be part of a large arcuate magnetic anomaly zone, occupying an area approxi-

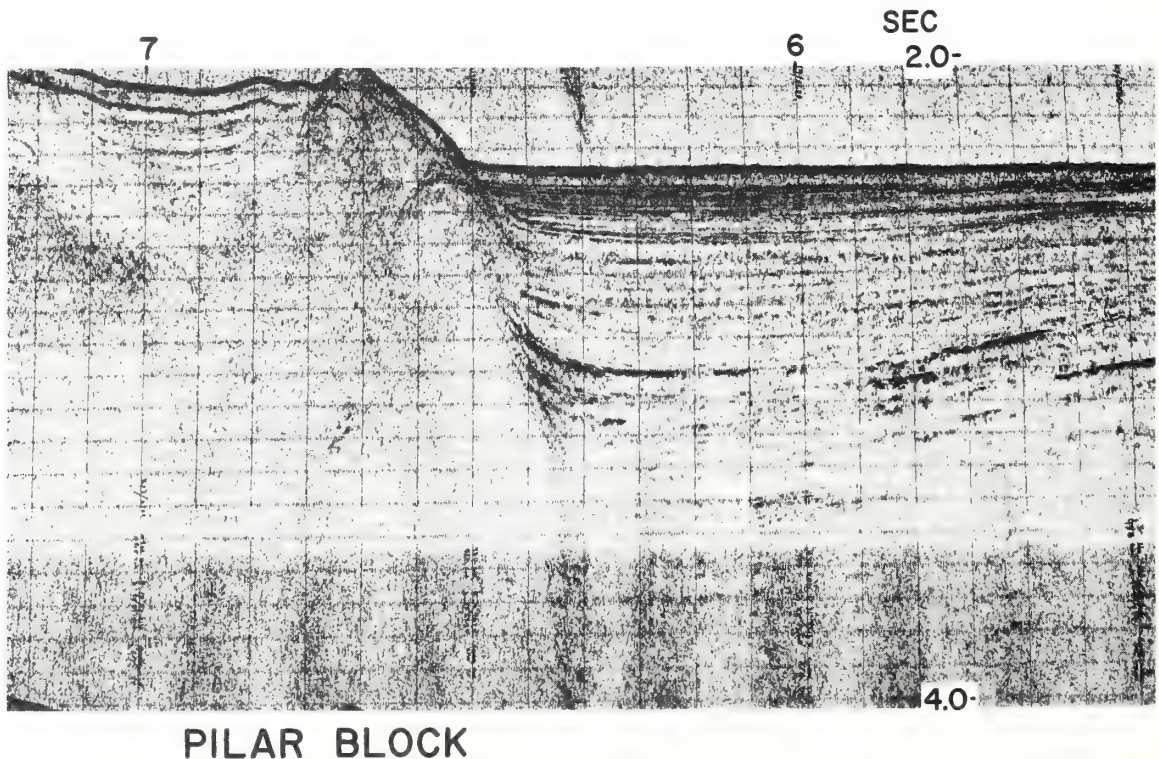


FIG. 6.—North-south seismic reflection profile F-F' (Fig. 1) showing Pilar block (on south) adjacent to thick sedimentary sequence near 59°W. Vertical scale is two-way time.

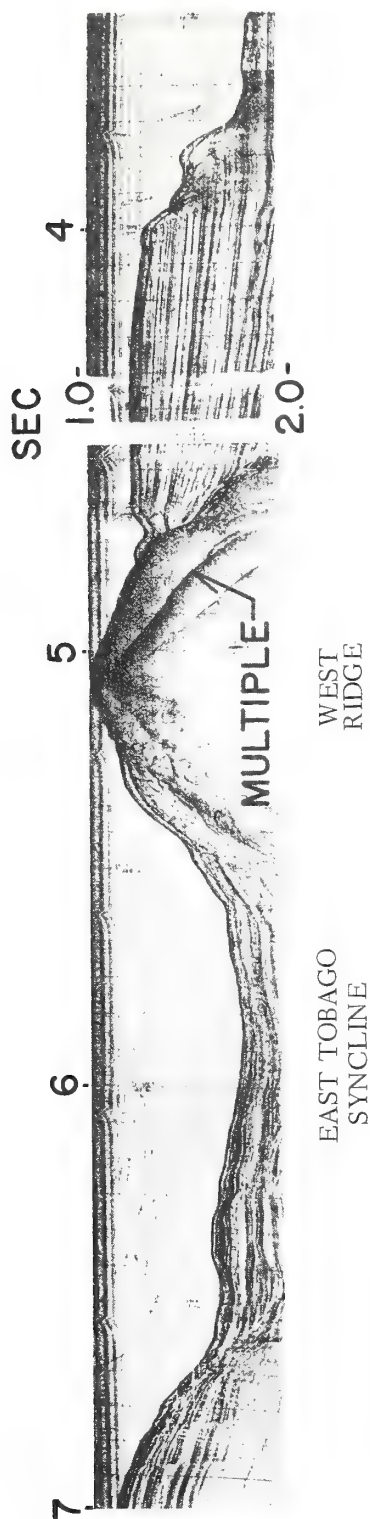


FIG. 7.—Part of north-south seismic reflection profile D-D' (Fig. 1) showing basement complex of West ridge adjacent to thick sedimentary sequence that crops out at erosional surface on south (right). Vertical scale is two-way time.

mately 60 km (35 n. mi) wide that extends across the shelf somewhat parallel with the island arc system. They continue across the shelf in a northeast direction, disrupting the magnetic field as multiple source anomalies off Tobago (profile D-D', Fig. 2) and terminating before profile E-E' (Fig. 2). On the south the anomalies appear to terminate abruptly at the Pilar block (profile A-A', Fig. 2). These prominent features can be attributed only to deep-seated structures related to the island arc system.

Peters' method (Peters, 1949) of depth determination applied to the magnetic anomaly observed near $11^{\circ}17'N$ and $61^{\circ}19'W$ reveals a depth to source of approximately 3.7 km (12,000 ft). The depth reliability of such determinations, however, depends on the absence of disturbing effects from other magnetic bodies, and assumes that polarization of the body is uniform and essentially vertical. In this general area, seismic refraction data indicate a depth of 3.2 km (10,500 ft) to the top of the 4.85 km/sec (15,900 ft/sec) layer, which Ewing *et al.* (1957) considered to be the north flank of the Northern Range metamorphic rocks. Consequently, the material causing the magnetic anomaly apparently would be emplaced near the top of the material having comparable velocity to that of the metamorphic rocks of the Northern Range.

Off the northeast coast of Tobago between $11^{\circ}12'N$ and $11^{\circ}23'N$ to $60^{\circ}25'W$, a distinctive magnetic pattern of short-period, high-amplitude anomalies is in sharp contrast to the high-amplitude, long-period anomalies of the surrounding area (Fig. 1). These high-frequency observations are attributed to shallow variations in the magnetic susceptibility, probably caused by near-surface intrusive activity. This zone is considered to be related to a tectonic unit of high magnetic susceptibility that is useful in delineating the near-surface eastern limit of the volcanic rocks similar to those mapped on Tobago by Maxwell (1948).

SUMMARY AND CONCLUSIONS

The Pilar block is a distinct structural unit expressed as a relatively narrow horst, bounded both north and south by prominent fault zones. From the Dragon's Mouth to about $61^{\circ}12'W$, the block appears to be flanked on the north by moderately deformed sediments of presumably post-Pliocene age. In this general area, refraction data indicate an overall displacement of at least 2.3 km (7,800 ft), which is comparable to

an earlier estimate of 1.8 km (6,000 ft) of uplift along the El Pilar fault. The block is a rigid unit traceable from the Araya Peninsula of Venezuela to 59°50'W however, it is not immune to extensional collapse features, such as the Dragon's Mouth. Outside the shelf edge the El Pilar fault system is characterized by its sediment-basement contact. In this area the block apparently acts as a barrier preventing the northward flow of sediments. As a result, sedimentary accumulations equivalent to more than 2.0 sec of penetration are found south of the fault near 59°W. Prominent structures on the north and south either die out or change trend to subparallel with the Pilar block. South of the block, structures apparently continue across the various shoals and banks of the shelf and terminate at the block. In this area, structures revealed by the SRP records near the shelf edge are similar to those in structural cross sections of eastern Trinidad.

Barbados anticlinorium is folded and faulted apparently as a tectonic unit. The observed basement complex plunges to depths beneath the sediments of the shelf beyond the limit of penetration of the SRP equipment. Much of the trend of the anticlinorium within the study area is occupied by magnetic anomalies of varied characteristics. A zone approximately 60 km (35 n. mi) wide, approximately parallel with the principal arcuate trend of the island arc system, contains high-amplitude, long-period magnetic anomalies. This zone continues across the shelf and through Tobago but does not extend east of about 60°W. Depth computations on one of these anomalies reveals a depth to source of about 3.7 km (12,000 ft), implying that the source is emplaced near the surface of the 4.85 km/sec (15,900 ft/sec) velocity material, which is believed to be comparable with the Northern Range metamorphic rocks. If these are in fact related, a sedimentary accumulation of 3.2 km (10,500 ft) as revealed by refraction data is expected in the area off northern Trinidad. In sharp contrast to these prominent magnetic anomalies, but perhaps originating from the same source, high-amplitude, short-period anomalies indicative of a near-surface source occupy an area 11 km (6 n. mi) northeast of Tobago. These anomalies are apparently related to the igneous rocks exposed in Tobago.

Off the shelf the Barbados anticlinorium is characterized by a basement complex of 3.97 km/sec (13,000 ft/sec) velocity material with a sedimentary overburden. These older

sediments plunge under the flat-lying deposits of the Tobago Trough and Central syncline. The younger, relatively undeformed, sediments to 1.0-sec penetration have not been affected by any significant tectonic activity since their deposition.

If the Caribbean plate and the adjacent South American continent are contrasting crustal blocks with great horizontal movements along major boundary faults, a condition required by "new global tectonics," some evidence of transform faulting should be observed near the shelf edge, along the north boundary fault zone of Trinidad, or along the El Pilar fault zone. The following points lend little support to extensive translation of such plates.

1. The observation that the deeper trends of the Barbados anticlinorium continue well into the shelf area implies that there is no major translation near the shelf edge. This conclusion is supported also by the continuation of the deeper structural trends of the volcanic island arc across the shelf and through Los Testigos Islands.

2. The north boundary fault zone of Trinidad apparently terminates or plunges under at least 1.0 sec penetration of relatively undeformed sedimentary strata in an area where the recent depositional rate is low. Consequently, the north-bounding fault system shows no evidence of relatively recent movement.

3. The lack of an obvious gouge zone along the El Pilar fault system, as might be expected in wrench faulting, and the absence of a measurable offset in the continental slope near the continuation of the fault system do not support extensive translation in comparatively recent time.

REFERENCES CITED

- Alberding, H., 1957, Application of principles of wrench-fault tectonics of Moody and Hill to northern South America: *Geol. Soc. America Bull.*, v. 68, p. 785-790.
- Bush, S. A., and P. A. Bush, 1969, Isostatic gravity map of the eastern Caribbean region: *Gulf Coast Assoc. Geol. Soc. Trans.*, v. 19, p. 281-285.
- Collette, B. J., J. I. Ewing, R. A. Lagaay, and M. Truchan, 1969, Sediment distribution in the oceans—the Atlantic between 10° and 19°N: *Marine Geology*, v. 7, p. 279-347.
- Eardley, A. J., 1954, Tectonic relations of North and South America: *Am. Assoc. Petroleum Geologists Bull.*, v. 38, no. 5, p. 707-773.
- Edgar, N. T., 1968, Seismic refraction and reflection in the Caribbean Sea: Ph.D. dissert., Columbia Univ., 163 p.
- Ewing, J. I., C. B. Officer, H. R. Johnson, and R. S. Edwards, 1957, Geophysical investigations in the eastern Caribbean—Trinidad shelf, Tobago Trough,

- Barbados ridge, Atlantic Ocean: *Geol. Soc. America Bull.*, v. 68, p. 897-912.
- M. Talwani, M. Ewing, and T. Edgar, 1967, Sediments of the Caribbean: *Internat. Conf. Tropical Oceanography Proc.*, Miami Univ., 1965, p. 88-102.
- Hess, H. H., 1938, Gravity anomalies and island arc structure with particular reference to the West Indies: *Am. Philos. Soc. Proc.*, v. 79, p. 71-96.
- Higgins, G. E., 1959, Seismic velocity data from Trinidad, B. W. I., and comparison with the Caribbean area: *Geophysics*, v. 24, p. 580-597.
- Koldewijn, B. W., 1958, Sediments of the Paria-Trinidad shelf, v. 3 of *Reports of the Orinoco Shelf expedition*: The Hague, Mouton and Co., 109 p.
- Kugler, H. K., 1961, Geological map of Trinidad and geological sections through Trinidad: pub. for Petroleum Assoc. Trinidad; Zurich, Orell Fussli, and London, E. Strand.
- Lattimore, R. K., L. A. Weeks, and L. W. Mordock, 1971, Marine geophysical reconnaissance of continental margin north of Paria Peninsula, Venezuela: *Am. Assoc. Petroleum Geologists Bull.*, v. 55, no. 10, p. 1719-1729.
- Lowrie, A., and E. Escowitz, 1969, Global ocean floor analysis and research data series, v. 1: U. S. Naval Oceanog. Office, p. 971.
- Maxwell, J. C., 1948, Geology of Tobago, B. W. I.: *Geol. Soc. America Bull.*, v. 59, p. 801-854.
- Metz, H. L., 1964, Geology of the El Pilar fault zone, state of Sucre, Venezuela: Ph.D. thesis, Princeton Univ., 102 p.
- Moody, J. D., and M. J. Hill, 1956, Wrench-fault tectonics: *Geol. Soc. America Bull.*, v. 67, p. 1207-1246.
- Officer, C. B., J. I. Ewing, J. F. Hennion, D. G. Harkrider, and D. E. Miller, 1959, Geophysical investigations in the eastern Caribbean: summary of 1955 and 1956 cruises, in L. H. Ahrens *et al.*, eds., *Physics and chemistry of the earth*, v. 3: New York, Pergamon Press, p. 17-109.
- Peters, L. J., 1949, The direct approach to magnetic interpretation and its practical applications: *Geophysics*, v. 14, p. 290-320.
- Potter, H. C., 1968, Faulting in the Northern Range of Trinidad (abs.): 23d *Internat. Geol. Cong. Rept.*, Prague, p. 95.
- Rod, E., 1956, Strike-slip faults of northern Venezuela: *Am. Assoc. Petroleum Geologists Bull.*, v. 40, no. 3, p. 457-476.
- Schuchert, C., 1935 (1968 Reprint), *Historical geology of the Antillean-Caribbean region*: New York and London, Hafner Pub. Co., 811 p.
- Suter, H. H., 1960, The general and economic geology of Trinidad, B.W.I.: London, Her Majesty's Stationery Office, 145 p.
- Sykes, L. R., and M. Ewing, 1965, The seismicity of the Caribbean region: *Jour. Geophys. Research*, v. 70, p. 5065-5074.
- van Andel, Tj. H., 1967, The Orinoco delta: *Jour. Sed. Petrology*, v. 37, no. 2, p. 297-310.
- and P. L. Sachs, 1964, Sedimentation in the Gulf of Paria during the Holocene transgressions—a subsurface acoustic reflection study: *Jour. Marine Research*, v. 22, p. 30-50.
- Weeks, L. A., R. K. Lattimore, R. N. Harbison, B. G. Bassinger, and G. F. Merrill, 1969, Structural relationships between Lesser Antilles, Venezuela, and Trinidad-Tobago (abs.): *Gulf Coast Assoc. Geol. Socs. Trans.*, v. 19, p. 321.
- and ——— 1971, Structural relations among Lesser Antilles, Venezuela, and Trinidad-Tobago: *Am. Assoc. Petroleum Geologists Bull.*, v. 55, no. 10, p. 1741-1752.

RAPID AND RELIABLE TECHNIQUE FOR DETERMINING UNIT WEIGHT AND POROSITY OF DEEP-SEA SEDIMENTS

RICHARD H. BENNETT AND DOUGLAS N. LAMBERT

National Oceanic and Atmospheric Administration, Atlantic Oceanographic and Meteorological Laboratories, Marine Geology and Geophysics Laboratory, Miami, Fla. (U.S.A.)

(Received March 10, 1971)

ABSTRACT

BENNETT, R. H. and LAMBERT, D. N., 1971. Rapid and reliable technique for determining unit weight and porosity of deep-sea sediments. *Marine Geol.*, 11: 201-207.

A rapid and reliable technique is explained for determining unit weight and porosity of deep-sea sediment from water content and average grain density measurements. Comparisons are made between this method and the standard tube method (volumetric), with 77 samples. The correlation coefficient is found to be 0.994 with a standard deviation between the methods of ± 0.01 g/cm³. The two techniques used to determine porosity are found to have a correlation coefficient of 0.998 with a standard deviation of 0.42%.

A nomographic chart is shown which permits rapid determination of unit weight using water content and average grain density.

INTRODUCTION

Unit weight of submarine sediments, also referred to as wet bulk density or saturated unit weight, is a function of the grain specific gravity and water content. By definition, unit weight is the weight per unit of volume regardless of the degree of saturation (A.S.T.M., 1967). However, submarine sediments, especially deep-sea sediments, are usually totally saturated.

A common technique for measuring unit weight is by inserting a tube of known volume into a sediment mass, such as a core, extracting the tube and sediment and determining the sediment weight. This gives a measure of the mass in grams per unit of volume. Difficulty in eliminating small voids between the cylinder wall and the sample as well as the influence of gases which may be present in the interstitial water due to the change from high hydrostatic pressure to atmospheric pressure could affect the unit weight as measured in the laboratory. In an undisturbed sediment sample the relative proportions of water to solids are not destroyed and at 100% saturation, unit weight is at a maximum. BENNETT et al. (1970) consider $\pm 1\%$ of the observed value to be a reasonable estimate of the reproducibility of the tube method.

Porosity (n), defined as the ratio of the volume of the voids to the total volume of the sediment mass, is usually computed from unit weight, average grain

density, water content and an assumed interstitial water density. It is sometimes determined from the void ratio by the relationship $n = e/(1 + e)$. Void ratio (e) is defined as the ratio of the volume of the voids to the volume of the solids.

The purpose of this study is to describe a rapid and reliable technique for determining unit weight and porosity of deep-sea sediment with an evaluation of the method using various sediment types. Carbonate content of the sediments ranged from less than 10% to greater than 98%, and textures ranged from less than 1% to greater than 66% sand-size particles.

TECHNIQUES AND BASIC PRINCIPLES

An advantage of the technique employed here for determining unit weight and porosity is that raw data from water content and grain density measurements are used. These data are frequently studied by the marine geologist and ocean engineer concerned with mass physical properties of submarine sediments and are usually numerous and readily available from laboratory reports.

Water content measurements are determined from approximately 10–20 g samples of sediment taken from the center of a core. The sample is immediately weighed and dried for about 24 h at 110°C and then reweighed to determine water loss. Average grain density is usually found by volumetric displacement of distilled water by the solids in a calibrated flask (LAMBE, 1951). From these three measurements, weight of dry solids, weight of water driven off during drying, and the average grain density, the unit weight (γ) can be easily determined by the following relationships:

$$\gamma = \frac{W_t}{\frac{W_d}{D_g} + W_w} = \frac{W_t D_g}{W_d + W_w D_g} \quad (1)$$

where $W_t = W_w + W_d$; W_w = weight of the water = approximately the volume of water; W_d = weight of dry solids including salts; D_g = average grain density.

The total weight (W_t) of the sample taken for water content determination is equal to the weight of the water lost during oven drying (W_w) plus the weight of the dry solids (W_d). For practical purposes W_w is equivalent to the volume of water in the cgs system. The weight of the solids divided by the average grain density (W_d/D_g) is the volume of the dry solids. The weight of the dry solids contains the weight of the salt. However, this increase in the volume of the solids, due to the presence of salts, closely approximates the slight deficit in the volume of the water (W_w) owing to the dissolved salts in the interstitial water. Therefore, by definition, the unit weight of the sample is equal to the total weight divided by the total volume. Similar expressions may be equated with eq.1 in text books on soil mechanics such as TERZAGHI and PECK (1967), SCOTT (1963) and WU (1966) and

are usually intended to show the relationships among density, porosity, and void ratio for a given sediment mass.

Porosity (n), expressed in percent, is the ratio of the volume of the voids to the total volume of the sediment mass and can be determined by the relationship:

$$n = \frac{V_w + V_{ss}}{\frac{W_d}{D_g} + W_w} \times 100 \quad (2)$$

V_{ss} is the volume of the salts in solution. Again, V_w is equal to the volume of the water and approximately equal to the weight of the water in grams. If V_{ss} is neglected or considered negligible the equation then becomes:

$$n = \frac{W_w}{\frac{W_d}{D_g} + W_w} \times 100 \quad (3)$$

V_{ss} is very close to 1.2% of V_w for concentrations of dissolved salts of 35‰.

RELIABILITY

As a measure of the reliability of the above technique expressed by eq.1, 77 unit weight measurements were determined using this method and compared with unit weight determinations using the tube method. In addition, porosity was determined using eq.3 from the same raw data used to obtain unit weight. These values were compared with porosities calculated from unit weight measurements determined by the tube method, average grain density and water content values with no corrections for salt content. Correlation coefficients were determined for unit weight and porosity. A linear correlation coefficient of +0.994 was found between the two unit weight techniques with 67% of all measured values falling within $\pm 0.01 \text{ g/cm}^3$ of each other. A linear correlation coefficient of +0.998 was found between the two porosity methods with 67% of all measured values falling within $\pm 0.42\%$ of each other. The significance of these data shows that for all practical purposes, the correlation between the techniques is nearly perfect and that either method for determining unit weight and porosity is as good as the other.

RELATIONSHIPS

The effect of large differences in drying temperatures has been found to be not as critical as might be expected. Using eq.1 and data from LAMBE (1951), differences in drying temperatures from 90°C to 190°C increase the unit weight measurement by only 0.002–0.004 g/cm³. Porosity values determined by eq.3 however, show differences ranging between 1% and 3% when drying temperature varies from 90°C to 190°C. Usually consistent techniques and control of tem-

perature within reasonable limits are well within the means of most soils laboratories.

Examination of eq.1 reveals that large changes in average grain density are necessary to appreciably affect the unit weight measurement. Clearly, the higher the water content the less average grain density variation influences those determinations. For example, with a water content of 50% an increase in average grain density from 2.75 to 2.80 increases the unit weight from 1.736 to 1.750. However, at a water content of 100% a change in the grain density of 0.05 changes the unit weight by only 0.007 g/cm³. The other parameters W_t , W_w and W_d depend upon the accuracy of the balance which is usually well within the reproducibility of the technique described here.

Due to the above relationships, difficulty in determining unit weight and porosity of relatively clean sands by the proposed method might be encountered because such sediments are usually characterized by low water contents. Obtaining a true water content for this sediment type may be difficult. However, accurate unit weight and porosity values of a relatively clean sand are also difficult to obtain with the tube method because of possible loss of pore water in inserting the tube into the sediment and its subsequent handling.

DISCUSSION

Several advantages of the technique expressed in eq.1 for determining unit weight are apparent. If gas is present it does not affect the measurement, and values of unit weight for 100% saturation at a given water content are obtained. This is considered by the authors to be a closer approximation of the actual unit weight, in situ, than values obtained by the tube method (volumetric), especially for sediment that includes gas. In addition, unit weight and porosity can be determined for relatively thin stratified sediment with a minimum amount of material and for small irregularly shaped pieces of cohesive sediment not amenable to the tube method. Volumetric errors introduced in the tube method include error resulting in the incomplete filling of the tube with sediment and inaccurate measurement of the radius of the tube (any error in the radius is squared).

Unit weight and porosity, using the relationships of eq.1 and 3, are determined from measured parameters which consequently avoids the use of any assumed values such as the density of interstitial water and average grain density. However, relatively large variations in the average grain density are required to appreciably influence the unit weight determination by eq.1. Large changes in the drying temperatures such as 90°–190°C usually have small effects on the unit weight determination; however, porosity by eq.3 is more responsive to these temperature differences. Control of temperature is important when porosity values are critical and comparable to within 1% of the observed values.

Fig.1 was constructed using eq.1 with a range of average grain density

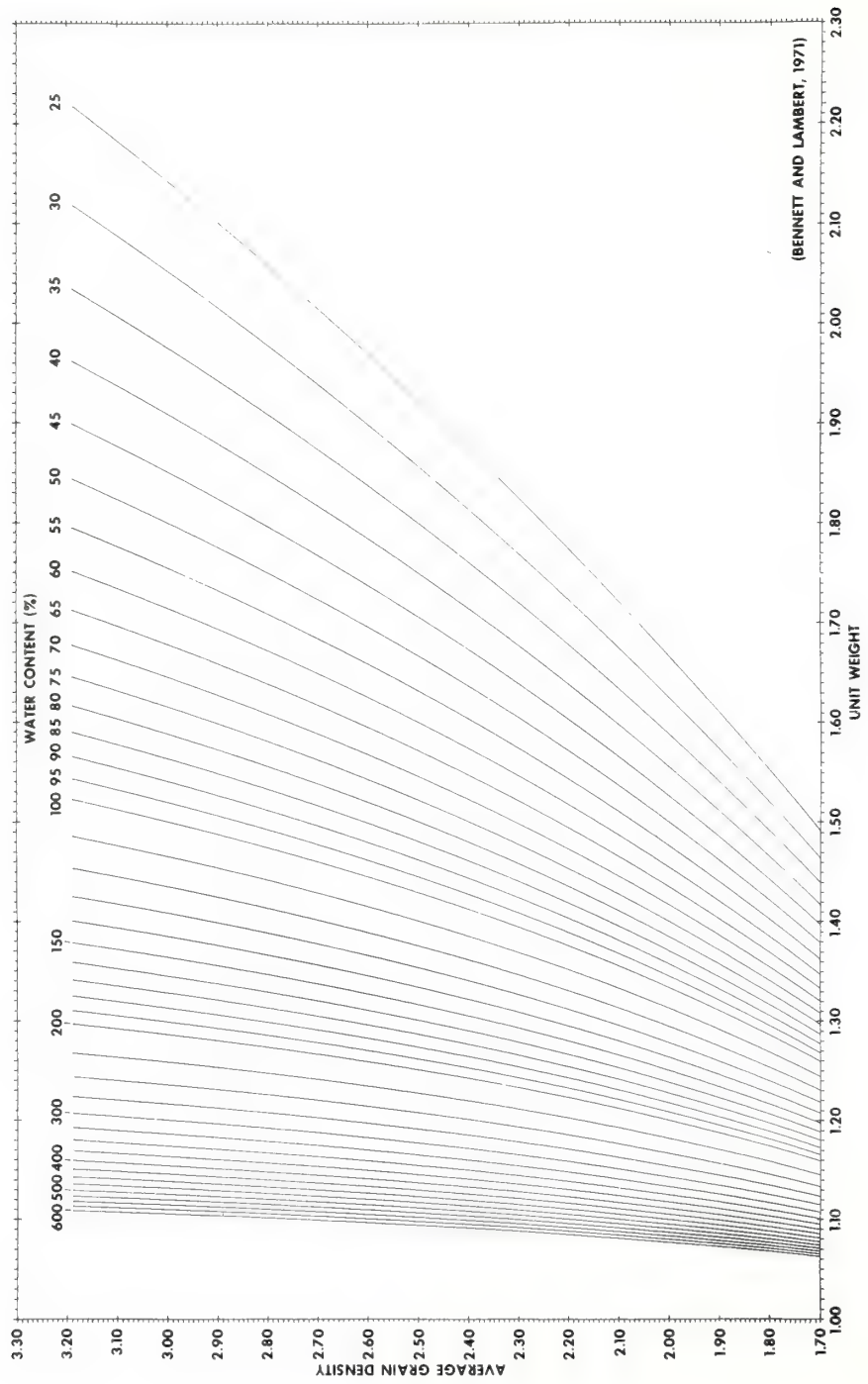


Fig.1. Nomographic chart for determining unit weight from grain density and water content.

values from 1.70 to 3.19 and a number of selected weights of dry solids (W_d) and water (W_w). This nomographic chart shows average grain density plotted against unit weight with isolines for water content (used here as $W_w/W_d \times 100$) ranging between 25% and 600%. Clearly, the relationship is non-linear and the isolines (delineating water content) would ultimately converge at a value of 1.00. The relationships among porosity, unit weight, and grain density have been clearly depicted by RICHARDS (1962). The advantage of this chart is that, given values of average grain density and water content, values for unit weight can be readily determined. The chart covers values for average grain density and water content most commonly found in submarine sediments (KELLER and BENNETT, 1970). Detailed tables for determining unit weight from water content and average grain density have been compiled and will form the bulk of a N.O.A.A. Technical Memorandum (BENNETT and LAMBERT, in preparation).

In deep-sea sediments, unit weight as measured in the laboratory, may be lower than in situ unit weight owing to the increase in the density of interstitial water at high hydrostatic pressures. This effect has been shown by HAMILTON (1969) to be significant, especially for deep-sea sediments with high porosities (75%–85%). At these porosities, such as in the deep Central Pacific (5,000 m), the increase in unit weight can be 0.02 g/cm^3 .

Sediments high in organic carbon content may significantly influence measurement of average grain density, therefore caution should be exercised when dealing with such materials.

ACKNOWLEDGEMENTS

The authors express their sincere appreciation to Drs. George H. Keller, Edwin L. Hamilton, Peter A. Rona, Louis W. Butler and Adrian F. Richards for their critical review of the manuscript. Many thanks are due to Paul J. Grim and Alan Herman for their competent computer programming of the nomographic chart and statistical parameters. The helpful discussions with John W. van Lanningham are appreciated.

REFERENCES

- AMERICAN SOCIETY FOR TESTING MATERIALS, 1967. *1967 Book of A.S.T.M. Standards, Part II*. A.S.T.M., Philadelphia, Pa., pp. 285–302.
- BENNETT, R. H., LAMBERT, D. N. and GRIM, P. J., in preparation. Tables for determining unit weight of deep-sea sediments using water content and average grain density. *Natl. Oceanic Atmospheric Admin., Tech. Mem.*, ERL TM-AOML.
- BENNETT, R. H., KELLER, G. H. and BUSBY, R. F., 1970. Mass property variability in three closely spaced deep-sea sediment cores. *J. Sediment. Petrol.*, 40: 1038–1043.
- HAMILTON, E. L., 1969. Sound velocity, elasticity, and related properties of marine sediments, North Pacific III. Prediction of in situ properties. *Naval Undersea Res., Develop. Center*, NUC TP: 145 pp.

- KELLER, G. H. and BENNETT, R. H., 1970. Variations in the mass physical properties of selected submarine sediments. *Marine Geol.*, 9: 215–223.
- LAMBE, T. W., 1951. *Soil Testing for Engineers*. Wiley, New York, N.Y., 165 pp.
- RICHARDS, A. F., 1962. Investigations of deep-sea sediment cores, II. Mass physical properties. *U.S. Navy Hydrograph. Office, Tech. Rept.*, TR-106: 146 pp.
- SCOTT, R. F., 1963. *Principles of Soil Mechanics*. Addison-Wesley, Reading, Mass., 550 pp.
- TERZAGHI, K. and PECK, R., 1967. *Soil Mechanics in Engineering Practice*. Wiley, New York, N.Y., 2nd ed., 729 pp.
- WU, T. H., 1966. *Soil Mechanics*. Allyn and Bacon, Boston, Mass., 431 pp.

U.S. DEPARTMENT OF COMMERCE
National Oceanic and Atmospheric Administration
Environmental Research Laboratories

NOAA Technical Memorandum ERL AOML-13

TABLES FOR DETERMINING UNIT WEIGHT
OF DEEP-SEA SEDIMENTS FROM WATER CONTENT
AND AVERAGE GRAIN DENSITY MEASUREMENTS

Richard H. Bennett
Douglas N. Lambert
Paul J. Grim

Marine Geology and Geophysics Laboratory

Atlantic Oceanographic and Meteorological Laboratories
Miami, Florida
August 1971



TABLE OF CONTENTS

	PAGE
1. INTRODUCTION	1
2. MEASUREMENTS AND PROCEDURES	2
3. TABULAR RESULTS	3
4. SUMMARY AND CONCLUSIONS	5
5. REFERENCES	5
FIGURE	7
TABLES	8-56

TABLES FOR DETERMINING UNIT WEIGHT OF DEEP-SEA SEDIMENTS FROM WATER CONTENT AND AVERAGE GRAIN DENSITY MEASUREMENTS

Richard H. Bennett, Douglas N. Lambert and Paul J. Grim

An expedient and reliable method is shown for determining unit weight of deep-sea sediment using water content and average grain density measurements. Tables form the bulk of this report with water contents ranging from 25 percent to 700 percent and average grain densities ranging from 1.70 to 3.10. A nomographic chart is included to supplement the tables.

1. INTRODUCTION

Unit weight of submarine sediments, also referred to as mass unit weight, is a function of the grain specific gravity and water content. By definition, unit weight is the weight (solids plus water) per unit of total volume of a sediment mass, regardless of the degree of saturation (ASTM, 1967). Bennett and Lambert (in press) have presented a rapid and reliable technique, using the above relationships, to determine unit weight (γ) for laboratory measured values of water content ($W_w/W_d \times 100$, the weight of the water to the weight of the dried solids) and average grain density (DG). This relationship is expressed as

$$\gamma = \frac{W_t}{V_t} = \frac{\frac{W_t}{\frac{W_d}{DG} + W_w}}{1} = \frac{W_t DG}{W_d + W_w DG},$$

where total weight (W_t) of a sediment sample equals the weight of water (W_w), approximately equal to the volume of water, plus the weight of the dry solids (W_d) including salts. The total volume is the dry solids (W_d/DG) plus the volume of the water.

2. MEASUREMENTS AND PROCEDURES

As a measure of the reliability of the above technique, 77 unit weights were determined using this method and compared with analyses by the standard tube method (volumetric) (Richards, 1962). A linear correlation coefficient of +0.994 was found between the two unit weight techniques with 67 percent of all measured values falling within ± 0.01 g/cc of each other. These data show that for all practical purposes, correlation between the techniques is nearly perfect and that either method for determining unit weight is equally useable.

Several advantages of the technique expressed in the above equation are apparent. If gas is present it does not affect the measurement, and values of unit weight for 100 percent saturation at a given water content are obtained.

This is considered by the authors to be a closer approximation of the actual in situ unit weight, of deep-sea sediment, than values obtained by the tube method (volumetric), especially for sediment that includes gas. In addition, unit weight can be determined for relatively thin stratified sediment with a minimum amount of material and for small irregularly shaped pieces of cohesive sediment not amenable to the tube method. Volumetric errors introduced in the tube method include error resulting in the incomplete filling of the tube with sediment and inaccurate measurement of the radius of the tube (any error in the radius is squared).

3. TABULAR RESULTS

The bulk of this report consists of tables for determining unit weight using the given equation. These tables include the range of values for water content and average grain density commonly found in submarine sediments (Keller and Bennett, 1970). The respective tables are established for water contents at one-percent intervals from 25 to 100 percent, five-percent intervals from 100 to 200 percent and at ten-percent intervals from 200 to 700 percent. Water content is given at the heading of each table, and the left-hand column (DG) shows the range of average grain densities (1.70 to 3.10). To find the unit weight of a particular

sediment sample, select the table which nearly approximates or equals the water content for that sample and then locate the grain density of the sample to the first decimal place in the lefthand column. Move across the row to the appropriate column (numbered zero through nine at the top of each column) for the second decimal place of the average grain density. The number given in this column is the unit weight for that particular sample given to the third decimal place.

Also included in this report is a nomographic chart (fig. 1) constructed using the above equation with a range of average grain density values from 1.70 to 3.19 and a number of selected weights of dry solids (W_d) and water (W_w). The chart shows average grain density plotted against unit weight with isolines for water content (used here as $W_w/W_d \times 100$) ranging between 25 and 600 percent. Clearly the relationship is non-linear and the isolines (delineating water content) would ultimately converge at a value of 1.00. The advantage of this chart is that, given values of average grain density and water content, reliable values for wet unit weight are readily determined. For more detailed values of unit weight the authors recommend the use of the included tables.

4. SUMMARY AND CONCLUSIONS

Laboratory measurement of water content and average grain density is particularly useful for determining unit weight of deep-sea sediment especially for samples not amenable to the tube (volumetric) method. Data show that for all practical purposes, correlation between techniques is nearly perfect. Use of the tables or nomographic chart is expedient and reliable.

5. REFERENCES

- American Society for Testing Materials, 1967, 1967 Book of ASTM Standards, Part II. Philadelphia, Pa., p. 285-302.
- Bennett, Richard H. and Douglas N. Lambert, 1971, Rapid and Reliable Technique for Determining Unit Weight and Porosity of Deep-Sea sediments, Vol. 11 (in press Marine Geology).
- Keller, G. H. and R. H. Bennett, 1970, Variations in the mass physical properties of selected submarine sediments, Marine Geology, 9: p. 215-223.
- Richards, A. F., 1962, Investigations of deep-sea sediment cores, II. Mass Physical Properties: Tech. Rept., TR-106 U.S. Navy Hydrographic Office, Washington, D.C.: 146 p.

NOMOGRAPHIC CHART FOR DETERMINING UNIT WEIGHT FROM GRAIN DENSITY AND WATER CONTENT

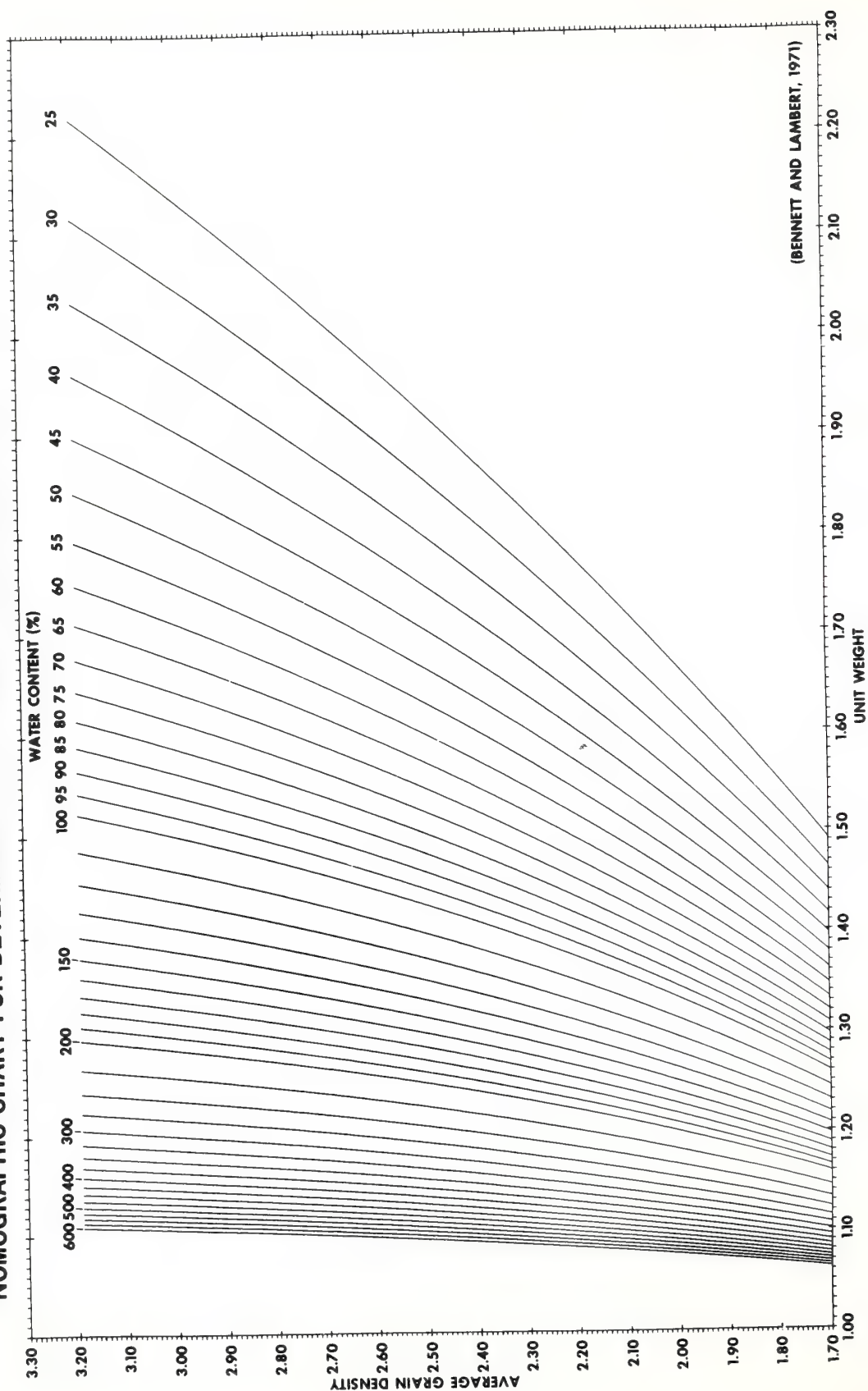


Figure 1

TABLE 1—Unit weight as a function of average grain density and water content

Unit Weights

WATER CONTENT 25 PERCENT

DG	0	1	2	3	4	5	6	7	8	9
1.70	1.491	1.497	1.503	1.510	1.516	1.522	1.528	1.534	1.540	1.546
1.80	1.552	1.558	1.564	1.569	1.575	1.581	1.587	1.593	1.599	1.604
1.90	1.610	1.616	1.622	1.627	1.633	1.639	1.644	1.650	1.656	1.661
2.00	1.667	1.672	1.678	1.683	1.689	1.694	1.700	1.705	1.711	1.716
2.10	1.721	1.727	1.732	1.737	1.743	1.748	1.753	1.759	1.764	1.769
2.20	1.774	1.779	1.785	1.790	1.795	1.800	1.805	1.810	1.815	1.820
2.30	1.825	1.830	1.835	1.840	1.845	1.850	1.855	1.860	1.865	1.870
2.40	1.875	1.880	1.885	1.890	1.894	1.899	1.904	1.909	1.914	1.918
2.50	1.923	1.928	1.933	1.937	1.942	1.947	1.951	1.956	1.960	1.965
2.60	1.970	1.974	1.979	1.983	1.988	1.992	1.997	2.001	2.006	2.010
2.70	2.015	2.019	2.024	2.028	2.033	2.037	2.041	2.046	2.050	2.054
2.80	2.059	2.063	2.067	2.072	2.076	2.080	2.085	2.089	2.093	2.097
2.90	2.101	2.106	2.110	2.114	2.118	2.122	2.126	2.131	2.135	2.139
3.00	2.143	2.147	2.151	2.155	2.159	2.163	2.167	2.171	2.175	2.179
3.10	2.183	2.187	2.191	2.195	2.199	2.203	2.207	2.211	2.214	2.218

WATER CONTENT 26 PERCENT

DG	0	1	2	3	4	5	6	7	8	9
1.70	1.485	1.491	1.498	1.504	1.510	1.515	1.521	1.527	1.533	1.539
1.80	1.545	1.551	1.557	1.562	1.568	1.574	1.580	1.585	1.591	1.597
1.90	1.602	1.608	1.614	1.619	1.625	1.630	1.636	1.641	1.647	1.652
2.00	1.658	1.663	1.669	1.674	1.680	1.685	1.690	1.696	1.701	1.706
2.10	1.712	1.717	1.722	1.727	1.732	1.738	1.743	1.748	1.753	1.758
2.20	1.763	1.768	1.774	1.779	1.784	1.789	1.794	1.799	1.804	1.809
2.30	1.814	1.818	1.823	1.828	1.833	1.838	1.843	1.848	1.852	1.857
2.40	1.862	1.867	1.872	1.876	1.881	1.886	1.890	1.895	1.900	1.904
2.50	1.909	1.914	1.918	1.923	1.927	1.932	1.937	1.941	1.946	1.950
2.60	1.955	1.959	1.964	1.968	1.972	1.977	1.981	1.986	1.990	1.994
2.70	1.999	2.003	2.007	2.012	2.016	2.020	2.025	2.029	2.033	2.037
2.80	2.042	2.046	2.050	2.054	2.058	2.063	2.067	2.071	2.075	2.079
2.90	2.083	2.087	2.091	2.095	2.100	2.104	2.108	2.112	2.116	2.120
3.00	2.124	2.128	2.132	2.135	2.139	2.143	2.147	2.151	2.155	2.159
3.10	2.163	2.167	2.170	2.174	2.178	2.182	2.186	2.190	2.193	2.197

WATER CONTENT 27 PERCENT

DG	0	1	2	3	4	5	6	7	8	9
1.70	1.480	1.486	1.492	1.498	1.503	1.509	1.515	1.521	1.527	1.533
1.80	1.538	1.544	1.550	1.556	1.561	1.567	1.572	1.578	1.584	1.589
1.90	1.595	1.600	1.606	1.611	1.617	1.622	1.628	1.633	1.639	1.644
2.00	1.649	1.655	1.660	1.665	1.671	1.676	1.681	1.686	1.692	1.697
2.10	1.702	1.707	1.712	1.717	1.723	1.728	1.733	1.738	1.743	1.748
2.20	1.753	1.758	1.763	1.768	1.773	1.778	1.783	1.787	1.792	1.797
2.30	1.802	1.807	1.812	1.816	1.821	1.826	1.831	1.835	1.840	1.845
2.40	1.850	1.854	1.859	1.863	1.868	1.873	1.877	1.882	1.886	1.891
2.50	1.896	1.900	1.905	1.909	1.914	1.918	1.922	1.927	1.931	1.936
2.60	1.940	1.944	1.949	1.953	1.957	1.962	1.966	1.970	1.975	1.979
2.70	1.983	1.987	1.992	1.996	2.000	2.004	2.008	2.013	2.017	2.021
2.80	2.025	2.029	2.033	2.037	2.041	2.045	2.050	2.054	2.058	2.062
2.90	2.066	2.070	2.074	2.078	2.081	2.085	2.089	2.093	2.097	2.101
3.00	2.105	2.109	2.113	2.117	2.120	2.124	2.128	2.132	2.136	2.139
3.10	2.143	2.147	2.151	2.154	2.158	2.162	2.166	2.169	2.173	2.177

AVERAGE GRAIN DENSITY

WATER CONTENT 28 PERCENT

DG	0	1	2	3	4	5	6	7	8	9
1.70	1.474	1.480	1.486	1.492	1.498	1.503	1.509	1.515	1.521	1.526
1.80	1.532	1.538	1.543	1.549	1.554	1.560	1.565	1.571	1.577	1.582
1.90	1.587	1.593	1.598	1.604	1.609	1.614	1.620	1.625	1.630	1.636
2.00	1.641	1.646	1.652	1.657	1.662	1.667	1.672	1.677	1.683	1.688
2.10	1.693	1.698	1.703	1.708	1.713	1.718	1.723	1.728	1.733	1.738
2.20	1.743	1.747	1.752	1.757	1.762	1.767	1.772	1.776	1.781	1.786
2.30	1.791	1.795	1.800	1.805	1.810	1.814	1.819	1.824	1.828	1.833
2.40	1.837	1.842	1.846	1.851	1.856	1.860	1.865	1.869	1.873	1.878
2.50	1.882	1.887	1.891	1.896	1.900	1.904	1.909	1.913	1.917	1.922
2.60	1.926	1.930	1.934	1.939	1.943	1.947	1.951	1.956	1.960	1.964
2.70	1.968	1.972	1.976	1.981	1.985	1.989	1.993	1.997	2.001	2.005
2.80	2.009	2.013	2.017	2.021	2.025	2.029	2.033	2.037	2.041	2.045
2.90	2.049	2.052	2.056	2.060	2.064	2.068	2.072	2.076	2.079	2.083
3.00	2.087	2.091	2.094	2.098	2.102	2.106	2.109	2.113	2.117	2.121
3.10	2.124	2.128	2.132	2.135	2.139	2.142	2.146	2.150	2.153	2.157

WATER CONTENT 29 PERCENT

DG	0	1	2	3	4	5	6	7	8	9
1.70	1.469	1.475	1.480	1.486	1.492	1.498	1.503	1.509	1.514	1.520
1.80	1.526	1.531	1.537	1.542	1.548	1.553	1.559	1.564	1.570	1.575
1.90	1.580	1.586	1.591	1.596	1.602	1.607	1.612	1.617	1.623	1.628
2.00	1.633	1.638	1.643	1.648	1.653	1.659	1.664	1.669	1.674	1.679
2.10	1.684	1.689	1.694	1.699	1.703	1.708	1.713	1.718	1.723	1.728
2.20	1.733	1.737	1.742	1.747	1.752	1.756	1.761	1.766	1.771	1.775
2.30	1.780	1.784	1.789	1.794	1.798	1.803	1.807	1.812	1.816	1.821
2.40	1.825	1.830	1.834	1.839	1.843	1.848	1.852	1.856	1.861	1.865
2.50	1.870	1.874	1.878	1.883	1.887	1.891	1.895	1.900	1.904	1.908
2.60	1.912	1.916	1.921	1.925	1.929	1.933	1.937	1.941	1.945	1.949
2.70	1.953	1.957	1.962	1.966	1.970	1.974	1.978	1.982	1.985	1.989
2.80	1.993	1.997	2.001	2.005	2.009	2.013	2.017	2.021	2.024	2.028
2.90	2.032	2.036	2.040	2.043	2.047	2.051	2.055	2.058	2.062	2.066
3.00	2.070	2.073	2.077	2.081	2.084	2.088	2.091	2.095	2.099	2.102
3.10	2.106	2.109	2.113	2.117	2.120	2.124	2.127	2.131	2.134	2.138

WATER CONTENT 30 PERCENT

DG	0	1	2	3	4	5	6	7	8	9
1.70	1.464	1.469	1.475	1.481	1.486	1.492	1.497	1.503	1.508	1.514
1.80	1.519	1.525	1.530	1.536	1.541	1.547	1.552	1.557	1.563	1.568
1.90	1.573	1.579	1.584	1.589	1.594	1.599	1.605	1.610	1.615	1.620
2.00	1.625	1.630	1.635	1.640	1.645	1.650	1.655	1.660	1.665	1.670
2.10	1.675	1.680	1.685	1.689	1.694	1.699	1.704	1.709	1.713	1.718
2.20	1.723	1.728	1.732	1.737	1.742	1.746	1.751	1.756	1.760	1.765
2.30	1.769	1.774	1.778	1.783	1.787	1.792	1.796	1.801	1.805	1.810
2.40	1.814	1.818	1.823	1.827	1.831	1.836	1.840	1.844	1.849	1.853
2.50	1.857	1.861	1.866	1.870	1.874	1.878	1.882	1.887	1.891	1.895
2.60	1.899	1.903	1.907	1.911	1.915	1.919	1.923	1.927	1.931	1.935
2.70	1.939	1.943	1.947	1.951	1.955	1.959	1.963	1.967	1.971	1.974
2.80	1.978	1.982	1.986	1.990	1.994	1.997	2.001	2.005	2.009	2.012
2.90	2.016	2.020	2.023	2.027	2.031	2.034	2.038	2.042	2.045	2.049
3.00	2.053	2.056	2.060	2.063	2.067	2.070	2.074	2.078	2.081	2.085
3.10	2.088	2.092	2.095	2.098	2.102	2.105	2.109	2.112	2.116	2.119

WATER CONTENT 31 PERCENT

DG	0	1	2	3	4	5	6	7	8	9
1.70	1.458	1.464	1.470	1.475	1.481	1.486	1.492	1.497	1.503	1.508
1.80	1.513	1.519	1.524	1.530	1.535	1.540	1.545	1.551	1.556	1.561
1.90	1.566	1.572	1.577	1.582	1.587	1.592	1.597	1.602	1.607	1.612
2.00	1.617	1.622	1.627	1.632	1.637	1.642	1.647	1.652	1.657	1.661
2.10	1.666	1.671	1.676	1.681	1.685	1.690	1.695	1.699	1.704	1.709
2.20	1.713	1.719	1.723	1.727	1.732	1.736	1.741	1.745	1.750	1.754
2.30	1.759	1.763	1.768	1.772	1.777	1.781	1.785	1.790	1.794	1.798
2.40	1.803	1.807	1.811	1.816	1.820	1.824	1.828	1.833	1.837	1.841
2.50	1.845	1.849	1.853	1.857	1.862	1.866	1.870	1.874	1.878	1.882
2.60	1.886	1.890	1.894	1.898	1.902	1.906	1.910	1.914	1.918	1.922
2.70	1.925	1.929	1.933	1.937	1.941	1.945	1.948	1.952	1.956	1.960
2.80	1.964	1.967	1.971	1.975	1.979	1.982	1.986	1.990	1.993	1.997
2.90	2.001	2.004	2.008	2.011	2.015	2.019	2.022	2.026	2.029	2.033
3.00	2.036	2.040	2.043	2.047	2.050	2.054	2.057	2.061	2.064	2.067
3.10	2.071	2.074	2.078	2.081	2.084	2.088	2.091	2.094	2.098	2.101

WATER CONTENT 32 PERCENT

DG	0	1	2	3	4	5	6	7	8	9
1.70	1.453	1.459	1.464	1.470	1.475	1.481	1.486	1.492	1.497	1.502
1.80	1.508	1.513	1.518	1.523	1.529	1.534	1.539	1.544	1.549	1.555
1.90	1.560	1.565	1.570	1.575	1.580	1.585	1.590	1.595	1.600	1.605
2.00	1.610	1.615	1.620	1.624	1.629	1.634	1.639	1.644	1.648	1.653
2.10	1.658	1.663	1.667	1.672	1.677	1.681	1.686	1.691	1.695	1.700
2.20	1.704	1.709	1.713	1.718	1.722	1.727	1.731	1.736	1.740	1.744
2.30	1.749	1.753	1.758	1.762	1.766	1.771	1.775	1.779	1.783	1.788
2.40	1.792	1.796	1.800	1.804	1.809	1.813	1.817	1.821	1.825	1.829
2.50	1.833	1.837	1.841	1.845	1.850	1.854	1.858	1.862	1.865	1.869
2.60	1.873	1.877	1.881	1.885	1.889	1.893	1.897	1.901	1.904	1.908
2.70	1.912	1.916	1.920	1.923	1.927	1.931	1.935	1.938	1.942	1.946
2.80	1.949	1.953	1.957	1.960	1.964	1.968	1.971	1.975	1.978	1.982
2.90	1.985	1.989	1.993	1.996	2.000	2.003	2.007	2.010	2.014	2.017
3.00	2.020	2.024	2.027	2.031	2.034	2.037	2.041	2.044	2.048	2.051
3.10	2.054	2.058	2.061	2.064	2.067	2.071	2.074	2.077	2.080	2.084

WATER CONTENT 33 PERCENT

DG	0	1	2	3	4	5	6	7	8	9
1.70	1.448	1.454	1.459	1.465	1.470	1.475	1.481	1.486	1.491	1.497
1.80	1.502	1.507	1.512	1.517	1.523	1.528	1.533	1.538	1.543	1.548
1.90	1.553	1.558	1.563	1.568	1.573	1.578	1.583	1.588	1.593	1.598
2.00	1.602	1.607	1.612	1.617	1.622	1.626	1.631	1.636	1.640	1.645
2.10	1.650	1.654	1.659	1.664	1.668	1.673	1.677	1.682	1.686	1.691
2.20	1.695	1.700	1.704	1.709	1.713	1.717	1.722	1.726	1.730	1.735
2.30	1.739	1.743	1.748	1.752	1.756	1.760	1.765	1.769	1.773	1.777
2.40	1.781	1.785	1.790	1.794	1.798	1.802	1.806	1.810	1.814	1.818
2.50	1.822	1.826	1.830	1.834	1.838	1.842	1.846	1.850	1.853	1.857
2.60	1.861	1.865	1.869	1.873	1.876	1.880	1.884	1.888	1.892	1.895
2.70	1.899	1.903	1.906	1.910	1.914	1.917	1.921	1.925	1.928	1.932
2.80	1.936	1.939	1.943	1.946	1.950	1.953	1.957	1.960	1.964	1.967
2.90	1.971	1.974	1.978	1.981	1.985	1.988	1.991	1.995	1.998	2.002
3.00	2.005	2.008	2.012	2.015	2.018	2.022	2.025	2.028	2.032	2.035
3.10	2.038	2.041	2.045	2.048	2.051	2.054	2.057	2.061	2.064	2.067

WATER CONTENT 34 PERCENT

DG	0	1	2	3	4	5	6	7	8	9
1.70	1.444	1.449	1.454	1.460	1.465	1.470	1.475	1.481	1.486	1.491
1.80	1.496	1.501	1.507	1.512	1.517	1.522	1.527	1.532	1.537	1.542
1.90	1.547	1.552	1.557	1.562	1.566	1.571	1.576	1.581	1.586	1.590
2.00	1.595	1.600	1.605	1.609	1.614	1.619	1.623	1.628	1.633	1.637
2.10	1.642	1.646	1.651	1.655	1.660	1.664	1.669	1.673	1.678	1.682
2.20	1.686	1.691	1.695	1.700	1.704	1.708	1.713	1.717	1.721	1.725
2.30	1.730	1.734	1.738	1.742	1.746	1.750	1.755	1.759	1.763	1.767
2.40	1.771	1.775	1.779	1.783	1.787	1.791	1.795	1.799	1.803	1.807
2.50	1.811	1.815	1.819	1.822	1.826	1.830	1.834	1.838	1.842	1.845
2.60	1.849	1.853	1.857	1.861	1.864	1.868	1.872	1.875	1.879	1.883
2.70	1.886	1.890	1.894	1.897	1.901	1.904	1.908	1.912	1.915	1.919
2.80	1.922	1.926	1.929	1.933	1.936	1.940	1.943	1.946	1.950	1.953
2.90	1.957	1.960	1.963	1.967	1.970	1.974	1.977	1.980	1.984	1.987
3.00	1.990	1.993	1.997	2.000	2.003	2.006	2.010	2.013	2.016	2.019
3.10	2.022	2.026	2.029	2.032	2.035	2.038	2.041	2.044	2.047	2.051

WATER CONTENT 35 PERCENT

DG	0	1	2	3	4	5	6	7	8	9
1.70	1.439	1.444	1.449	1.455	1.460	1.465	1.470	1.475	1.481	1.486
1.80	1.491	1.496	1.501	1.506	1.511	1.516	1.521	1.526	1.531	1.536
1.90	1.541	1.545	1.550	1.555	1.560	1.565	1.569	1.574	1.579	1.584
2.00	1.588	1.593	1.598	1.602	1.607	1.611	1.616	1.620	1.625	1.630
2.10	1.634	1.638	1.643	1.647	1.652	1.656	1.661	1.665	1.669	1.674
2.20	1.678	1.682	1.687	1.691	1.695	1.699	1.704	1.708	1.712	1.716
2.30	1.720	1.724	1.728	1.733	1.737	1.741	1.745	1.749	1.753	1.757
2.40	1.761	1.765	1.769	1.773	1.777	1.781	1.785	1.788	1.792	1.796
2.50	1.800	1.804	1.808	1.811	1.815	1.819	1.823	1.827	1.830	1.834
2.60	1.838	1.841	1.845	1.849	1.852	1.856	1.860	1.863	1.867	1.870
2.70	1.874	1.878	1.881	1.885	1.888	1.892	1.895	1.899	1.902	1.906
2.80	1.909	1.913	1.916	1.919	1.923	1.926	1.930	1.933	1.936	1.940
2.90	1.943	1.946	1.950	1.953	1.956	1.959	1.963	1.966	1.969	1.972
3.00	1.976	1.979	1.982	1.985	1.988	1.992	1.995	1.998	2.001	2.004
3.10	2.007	2.010	2.013	2.016	2.020	2.023	2.026	2.029	2.032	2.035

WATER CONTENT 36 PERCENT

DG	0	1	2	3	4	5	6	7	8	9
1.70	1.434	1.439	1.445	1.450	1.455	1.460	1.465	1.470	1.475	1.480
1.80	1.485	1.490	1.495	1.500	1.505	1.510	1.515	1.520	1.525	1.530
1.90	1.534	1.539	1.544	1.549	1.553	1.558	1.563	1.568	1.572	1.577
2.00	1.581	1.586	1.591	1.595	1.600	1.604	1.609	1.613	1.618	1.622
2.10	1.626	1.631	1.635	1.640	1.644	1.648	1.653	1.657	1.661	1.665
2.20	1.670	1.674	1.678	1.682	1.686	1.691	1.695	1.699	1.703	1.707
2.30	1.711	1.715	1.719	1.723	1.727	1.731	1.735	1.739	1.743	1.747
2.40	1.751	1.755	1.759	1.763	1.767	1.770	1.774	1.778	1.782	1.786
2.50	1.789	1.793	1.797	1.801	1.804	1.808	1.812	1.815	1.819	1.823
2.60	1.826	1.830	1.834	1.837	1.841	1.844	1.848	1.852	1.855	1.859
2.70	1.862	1.866	1.869	1.873	1.876	1.879	1.883	1.886	1.890	1.893
2.80	1.896	1.900	1.903	1.906	1.910	1.913	1.916	1.920	1.923	1.926
2.90	1.930	1.933	1.936	1.939	1.942	1.946	1.949	1.952	1.955	1.958
3.00	1.962	1.965	1.968	1.971	1.974	1.977	1.980	1.983	1.986	1.989
3.10	1.992	1.995	1.998	2.001	2.004	2.007	2.010	2.013	2.016	2.019

WATER CONTENT 37 PERCENT

DG	0	1	2	3	4	5	6	7	8	9
1.70	1.430	1.435	1.440	1.445	1.450	1.455	1.460	1.465	1.470	1.475
1.80	1.480	1.485	1.490	1.495	1.500	1.505	1.509	1.514	1.519	1.524
1.90	1.528	1.533	1.538	1.543	1.547	1.552	1.556	1.561	1.566	1.570
2.00	1.575	1.579	1.584	1.588	1.593	1.597	1.602	1.606	1.610	1.615
2.10	1.619	1.623	1.628	1.632	1.636	1.640	1.645	1.649	1.653	1.657
2.20	1.662	1.666	1.670	1.674	1.678	1.682	1.686	1.690	1.694	1.698
2.30	1.702	1.706	1.710	1.714	1.718	1.722	1.726	1.730	1.734	1.738
2.40	1.742	1.745	1.749	1.753	1.757	1.761	1.764	1.768	1.772	1.776
2.50	1.779	1.783	1.787	1.790	1.794	1.798	1.801	1.805	1.808	1.812
2.60	1.815	1.819	1.823	1.826	1.830	1.833	1.837	1.840	1.844	1.847
2.70	1.850	1.854	1.857	1.861	1.864	1.867	1.871	1.874	1.877	1.881
2.80	1.884	1.887	1.891	1.894	1.897	1.900	1.904	1.907	1.910	1.913
2.90	1.917	1.920	1.923	1.926	1.929	1.932	1.935	1.939	1.942	1.945
3.00	1.948	1.951	1.954	1.957	1.960	1.963	1.966	1.969	1.972	1.975
3.10	1.978	1.981	1.984	1.987	1.990	1.993	1.996	1.999	2.002	2.004

WATER CONTENT 38 PERCENT

DG	0	1	2	3	4	5	6	7	8	9
1.70	1.425	1.430	1.435	1.440	1.445	1.450	1.455	1.460	1.465	1.470
1.80	1.475	1.480	1.485	1.490	1.494	1.499	1.504	1.509	1.513	1.518
1.90	1.523	1.527	1.532	1.537	1.541	1.546	1.550	1.555	1.559	1.564
2.00	1.568	1.573	1.577	1.581	1.586	1.590	1.595	1.599	1.603	1.608
2.10	1.612	1.616	1.620	1.625	1.629	1.633	1.637	1.641	1.645	1.649
2.20	1.654	1.658	1.662	1.666	1.670	1.674	1.678	1.682	1.686	1.690
2.30	1.694	1.698	1.702	1.705	1.709	1.713	1.717	1.721	1.725	1.728
2.40	1.732	1.736	1.740	1.743	1.747	1.751	1.755	1.758	1.762	1.766
2.50	1.769	1.773	1.776	1.780	1.784	1.787	1.791	1.794	1.798	1.801
2.60	1.805	1.808	1.812	1.815	1.819	1.822	1.826	1.829	1.832	1.836
2.70	1.839	1.842	1.846	1.849	1.852	1.856	1.859	1.862	1.866	1.869
2.80	1.872	1.875	1.879	1.882	1.885	1.888	1.891	1.894	1.898	1.901
2.90	1.904	1.907	1.910	1.913	1.916	1.919	1.922	1.925	1.929	1.932
3.00	1.935	1.938	1.941	1.944	1.947	1.950	1.952	1.955	1.958	1.961
3.10	1.964	1.967	1.970	1.973	1.976	1.979	1.981	1.984	1.987	1.990

WATER CONTENT 39 PERCENT

DG	0	1	2	3	4	5	6	7	8	9
1.70	1.421	1.426	1.431	1.436	1.441	1.446	1.451	1.456	1.460	1.465
1.80	1.470	1.475	1.480	1.484	1.489	1.494	1.498	1.503	1.508	1.512
1.90	1.517	1.522	1.526	1.531	1.535	1.540	1.544	1.549	1.553	1.557
2.00	1.562	1.566	1.571	1.575	1.579	1.583	1.588	1.592	1.596	1.601
2.10	1.605	1.609	1.613	1.617	1.621	1.626	1.630	1.634	1.638	1.642
2.20	1.646	1.650	1.654	1.658	1.662	1.666	1.670	1.674	1.678	1.681
2.30	1.685	1.689	1.693	1.697	1.701	1.704	1.708	1.712	1.716	1.719
2.40	1.723	1.727	1.731	1.734	1.738	1.741	1.745	1.749	1.752	1.756
2.50	1.759	1.763	1.767	1.770	1.774	1.777	1.781	1.784	1.788	1.791
2.60	1.794	1.798	1.801	1.805	1.808	1.811	1.815	1.818	1.821	1.825
2.70	1.828	1.831	1.835	1.838	1.841	1.844	1.848	1.851	1.854	1.857
2.80	1.860	1.864	1.867	1.870	1.873	1.876	1.879	1.882	1.885	1.889
2.90	1.892	1.895	1.898	1.901	1.904	1.907	1.910	1.913	1.916	1.919
3.00	1.922	1.925	1.928	1.930	1.933	1.936	1.939	1.942	1.945	1.948
3.10	1.951	1.953	1.956	1.959	1.962	1.965	1.968	1.970	1.973	1.976

WATER CONTENT 40 PERCENT

DG	0	1	2	3	4	5	6	7	8	9
1.70	1.417	1.422	1.427	1.431	1.436	1.441	1.446	1.451	1.456	1.460
1.80	1.465	1.470	1.475	1.479	1.484	1.489	1.493	1.498	1.502	1.507
1.90	1.511	1.516	1.520	1.525	1.529	1.534	1.538	1.543	1.547	1.551
2.00	1.556	1.560	1.564	1.568	1.573	1.577	1.581	1.585	1.590	1.594
2.10	1.598	1.602	1.606	1.610	1.614	1.618	1.622	1.626	1.630	1.634
2.20	1.638	1.642	1.646	1.650	1.654	1.658	1.662	1.666	1.669	1.673
2.30	1.677	1.681	1.685	1.688	1.692	1.696	1.700	1.703	1.707	1.711
2.40	1.714	1.718	1.722	1.725	1.729	1.732	1.736	1.739	1.743	1.746
2.50	1.750	1.753	1.757	1.760	1.764	1.767	1.771	1.774	1.778	1.781
2.60	1.784	1.788	1.791	1.794	1.798	1.801	1.804	1.808	1.811	1.814
2.70	1.817	1.821	1.824	1.827	1.830	1.833	1.837	1.840	1.843	1.846
2.80	1.849	1.852	1.855	1.858	1.861	1.864	1.868	1.871	1.874	1.877
2.90	1.880	1.883	1.886	1.889	1.892	1.894	1.897	1.900	1.903	1.906
3.00	1.909	1.912	1.915	1.918	1.921	1.923	1.926	1.929	1.932	1.935
3.10	1.937	1.940	1.943	1.946	1.949	1.951	1.954	1.957	1.959	1.962

WATER CONTENT 41 PERCENT

DG	0	1	2	3	4	5	6	7	8	9
1.70	1.412	1.417	1.422	1.427	1.432	1.437	1.441	1.446	1.451	1.456
1.80	1.460	1.465	1.470	1.474	1.479	1.483	1.488	1.492	1.497	1.501
1.90	1.506	1.510	1.515	1.519	1.524	1.528	1.532	1.537	1.541	1.545
2.00	1.549	1.554	1.558	1.562	1.566	1.570	1.575	1.579	1.583	1.587
2.10	1.591	1.595	1.599	1.603	1.607	1.611	1.615	1.619	1.623	1.627
2.20	1.631	1.635	1.639	1.643	1.646	1.650	1.654	1.658	1.662	1.665
2.30	1.669	1.673	1.677	1.680	1.684	1.688	1.691	1.695	1.698	1.702
2.40	1.706	1.709	1.713	1.716	1.720	1.723	1.727	1.730	1.734	1.737
2.50	1.741	1.744	1.748	1.751	1.754	1.758	1.761	1.764	1.768	1.771
2.60	1.774	1.778	1.781	1.784	1.788	1.791	1.794	1.797	1.800	1.804
2.70	1.807	1.810	1.813	1.816	1.819	1.823	1.826	1.829	1.832	1.835
2.80	1.838	1.841	1.844	1.847	1.850	1.853	1.856	1.859	1.862	1.865
2.90	1.868	1.871	1.874	1.877	1.880	1.883	1.885	1.888	1.891	1.894
3.00	1.897	1.900	1.903	1.905	1.908	1.911	1.914	1.916	1.919	1.922
3.10	1.925	1.927	1.930	1.933	1.936	1.938	1.941	1.944	1.946	1.949

WATER CONTENT 42 PERCENT

DG	0	1	2	3	4	5	6	7	8	9
1.70	1.408	1.413	1.418	1.423	1.428	1.432	1.437	1.442	1.446	1.451
1.80	1.456	1.460	1.465	1.469	1.474	1.478	1.483	1.487	1.492	1.496
1.90	1.501	1.505	1.509	1.514	1.518	1.522	1.527	1.531	1.535	1.539
2.00	1.543	1.548	1.552	1.556	1.560	1.564	1.568	1.572	1.576	1.580
2.10	1.584	1.588	1.592	1.596	1.600	1.604	1.608	1.612	1.616	1.620
2.20	1.624	1.629	1.631	1.635	1.639	1.643	1.646	1.650	1.654	1.658
2.30	1.661	1.665	1.669	1.672	1.676	1.679	1.683	1.687	1.690	1.694
2.40	1.697	1.701	1.704	1.708	1.711	1.715	1.718	1.722	1.725	1.728
2.50	1.732	1.735	1.738	1.742	1.745	1.748	1.752	1.755	1.758	1.762
2.60	1.765	1.768	1.771	1.774	1.778	1.781	1.784	1.787	1.790	1.794
2.70	1.797	1.800	1.803	1.806	1.809	1.812	1.815	1.818	1.821	1.824
2.80	1.827	1.830	1.833	1.836	1.839	1.842	1.845	1.848	1.851	1.854
2.90	1.857	1.860	1.862	1.865	1.868	1.871	1.874	1.877	1.879	1.882
3.00	1.885	1.888	1.890	1.893	1.896	1.899	1.901	1.904	1.907	1.910
3.10	1.912	1.915	1.918	1.920	1.923	1.926	1.928	1.931	1.933	1.936

WATER CONTENT 43 PERCENT

DG	0	1	2	3	4	5	6	7	8	9
1.70	1.404	1.409	1.414	1.419	1.423	1.428	1.433	1.437	1.442	1.446
1.80	1.451	1.455	1.460	1.464	1.469	1.473	1.478	1.482	1.487	1.491
1.90	1.495	1.500	1.504	1.508	1.512	1.517	1.521	1.525	1.529	1.533
2.00	1.538	1.542	1.546	1.550	1.554	1.558	1.562	1.566	1.570	1.574
2.10	1.578	1.582	1.586	1.590	1.594	1.598	1.601	1.605	1.609	1.613
2.20	1.617	1.620	1.624	1.628	1.632	1.635	1.639	1.643	1.646	1.650
2.30	1.654	1.657	1.661	1.664	1.668	1.671	1.675	1.679	1.682	1.686
2.40	1.689	1.692	1.696	1.699	1.703	1.706	1.709	1.713	1.716	1.720
2.50	1.723	1.726	1.730	1.733	1.736	1.739	1.743	1.746	1.749	1.752
2.60	1.755	1.759	1.762	1.765	1.768	1.771	1.774	1.777	1.781	1.784
2.70	1.787	1.790	1.793	1.796	1.799	1.802	1.805	1.808	1.811	1.814
2.80	1.817	1.820	1.823	1.825	1.828	1.831	1.834	1.837	1.840	1.843
2.90	1.846	1.848	1.851	1.854	1.857	1.860	1.862	1.865	1.868	1.871
3.00	1.873	1.876	1.879	1.881	1.884	1.887	1.890	1.892	1.895	1.897
3.10	1.900	1.903	1.905	1.908	1.911	1.913	1.916	1.918	1.921	1.923

WATER CONTENT 44 PERCENT

DG	0	1	2	3	4	5	6	7	8	9
1.70	1.400	1.405	1.410	1.414	1.419	1.424	1.428	1.433	1.437	1.442
1.80	1.446	1.451	1.455	1.460	1.464	1.469	1.473	1.477	1.482	1.486
1.90	1.490	1.494	1.499	1.503	1.507	1.511	1.515	1.520	1.524	1.528
2.00	1.532	1.536	1.540	1.544	1.548	1.552	1.556	1.560	1.564	1.568
2.10	1.572	1.576	1.579	1.583	1.587	1.591	1.595	1.599	1.602	1.606
2.20	1.610	1.613	1.617	1.621	1.624	1.628	1.632	1.635	1.639	1.643
2.30	1.646	1.650	1.653	1.657	1.660	1.664	1.667	1.671	1.674	1.678
2.40	1.681	1.684	1.688	1.691	1.694	1.698	1.701	1.704	1.708	1.711
2.50	1.714	1.718	1.721	1.724	1.727	1.730	1.734	1.737	1.740	1.743
2.60	1.746	1.749	1.753	1.756	1.759	1.762	1.765	1.768	1.771	1.774
2.70	1.777	1.780	1.783	1.786	1.789	1.792	1.795	1.798	1.801	1.804
2.80	1.806	1.809	1.812	1.815	1.818	1.821	1.824	1.826	1.829	1.832
2.90	1.835	1.838	1.840	1.843	1.846	1.849	1.851	1.854	1.857	1.859
3.00	1.862	1.865	1.867	1.870	1.873	1.875	1.878	1.881	1.883	1.886
3.10	1.888	1.891	1.893	1.896	1.899	1.901	1.904	1.906	1.909	1.911

WATER CONTENT 45 PERCENT

DG	0	1	2	3	4	5	6	7	8	9
1.70	1.397	1.401	1.406	1.410	1.415	1.420	1.424	1.429	1.433	1.438
1.80	1.442	1.446	1.451	1.455	1.460	1.464	1.468	1.472	1.477	1.481
1.90	1.485	1.489	1.494	1.498	1.502	1.506	1.510	1.514	1.518	1.522
2.00	1.526	1.530	1.534	1.538	1.542	1.546	1.550	1.554	1.558	1.562
2.10	1.566	1.569	1.573	1.577	1.581	1.584	1.588	1.592	1.596	1.599
2.20	1.603	1.607	1.610	1.614	1.618	1.621	1.625	1.628	1.632	1.635
2.30	1.639	1.642	1.646	1.649	1.653	1.656	1.660	1.663	1.666	1.670
2.40	1.673	1.676	1.680	1.683	1.686	1.690	1.693	1.696	1.699	1.703
2.50	1.706	1.709	1.712	1.715	1.719	1.722	1.725	1.728	1.731	1.734
2.60	1.737	1.740	1.743	1.747	1.750	1.753	1.756	1.759	1.762	1.765
2.70	1.767	1.770	1.773	1.776	1.779	1.782	1.785	1.788	1.791	1.794
2.80	1.796	1.799	1.802	1.805	1.808	1.811	1.813	1.816	1.819	1.822
2.90	1.824	1.827	1.830	1.832	1.835	1.838	1.840	1.843	1.846	1.848
3.00	1.851	1.854	1.856	1.859	1.861	1.864	1.867	1.869	1.872	1.874
3.10	1.877	1.879	1.882	1.884	1.887	1.889	1.892	1.894	1.897	1.899

WATER CONTENT 46 PERCENT

DG	0	1	2	3	4	5	6	7	8	9
1.70	1.393	1.397	1.402	1.407	1.411	1.416	1.420	1.424	1.429	1.433
1.80	1.438	1.442	1.446	1.451	1.455	1.459	1.463	1.468	1.472	1.476
1.90	1.480	1.484	1.489	1.493	1.497	1.501	1.505	1.509	1.513	1.517
2.00	1.521	1.525	1.529	1.533	1.537	1.540	1.544	1.548	1.552	1.556
2.10	1.560	1.563	1.567	1.571	1.574	1.578	1.582	1.586	1.589	1.593
2.20	1.596	1.600	1.604	1.607	1.611	1.614	1.618	1.621	1.625	1.628
2.30	1.632	1.635	1.639	1.642	1.645	1.649	1.652	1.655	1.659	1.662
2.40	1.665	1.669	1.672	1.675	1.678	1.682	1.685	1.688	1.691	1.695
2.50	1.698	1.701	1.704	1.707	1.710	1.713	1.716	1.719	1.723	1.726
2.60	1.729	1.732	1.735	1.738	1.741	1.744	1.747	1.749	1.752	1.755
2.70	1.758	1.761	1.764	1.767	1.770	1.773	1.775	1.778	1.781	1.784
2.80	1.787	1.789	1.792	1.795	1.798	1.801	1.803	1.806	1.809	1.811
2.90	1.814	1.817	1.819	1.822	1.825	1.827	1.830	1.833	1.835	1.838
3.00	1.840	1.843	1.845	1.848	1.851	1.853	1.856	1.858	1.861	1.863
3.10	1.866	1.868	1.871	1.873	1.875	1.878	1.880	1.883	1.885	1.888

WATER CONTENT 47 PERCENT

DG	0	1	2	3	4	5	6	7	8	9
1.70	1.389	1.394	1.398	1.403	1.407	1.412	1.416	1.420	1.425	1.429
1.80	1.433	1.438	1.442	1.446	1.450	1.455	1.459	1.463	1.467	1.471
1.90	1.475	1.480	1.484	1.488	1.492	1.496	1.500	1.504	1.508	1.512
2.00	1.515	1.519	1.523	1.527	1.531	1.535	1.539	1.542	1.546	1.550
2.10	1.554	1.557	1.561	1.565	1.568	1.572	1.576	1.579	1.583	1.586
2.20	1.590	1.594	1.597	1.601	1.604	1.608	1.611	1.614	1.618	1.621
2.30	1.625	1.628	1.631	1.635	1.638	1.641	1.645	1.648	1.651	1.655
2.40	1.658	1.661	1.664	1.668	1.671	1.674	1.677	1.680	1.683	1.687
2.50	1.690	1.693	1.696	1.699	1.702	1.705	1.708	1.711	1.714	1.717
2.60	1.720	1.723	1.726	1.729	1.732	1.735	1.738	1.741	1.743	1.746
2.70	1.749	1.752	1.755	1.758	1.761	1.763	1.766	1.769	1.772	1.774
2.80	1.777	1.780	1.783	1.785	1.788	1.791	1.793	1.796	1.799	1.801
2.90	1.804	1.807	1.809	1.812	1.815	1.817	1.820	1.822	1.825	1.827
3.00	1.830	1.832	1.835	1.837	1.840	1.842	1.845	1.847	1.850	1.852
3.10	1.855	1.857	1.860	1.862	1.864	1.867	1.869	1.872	1.874	1.876

WATER CONTENT 48 PERCENT

DG	0	1	2	3	4	5	6	7	8	9
1.70	1.385	1.390	1.394	1.399	1.403	1.408	1.412	1.416	1.421	1.425
1.80	1.429	1.433	1.438	1.442	1.446	1.450	1.454	1.458	1.463	1.467
1.90	1.471	1.475	1.479	1.483	1.487	1.491	1.495	1.499	1.502	1.506
2.00	1.510	1.514	1.518	1.522	1.525	1.529	1.533	1.537	1.540	1.544
2.10	1.548	1.551	1.555	1.559	1.562	1.566	1.570	1.573	1.577	1.580
2.20	1.584	1.587	1.591	1.594	1.598	1.601	1.604	1.608	1.611	1.615
2.30	1.618	1.621	1.625	1.628	1.631	1.634	1.638	1.641	1.644	1.647
2.40	1.651	1.654	1.657	1.660	1.663	1.666	1.669	1.673	1.676	1.679
2.50	1.682	1.685	1.688	1.691	1.694	1.697	1.700	1.703	1.706	1.709
2.60	1.712	1.715	1.718	1.720	1.723	1.726	1.729	1.732	1.735	1.738
2.70	1.740	1.743	1.746	1.749	1.752	1.754	1.757	1.760	1.763	1.765
2.80	1.768	1.771	1.773	1.776	1.779	1.781	1.784	1.787	1.789	1.792
2.90	1.794	1.797	1.799	1.802	1.805	1.807	1.810	1.812	1.815	1.817
3.00	1.820	1.822	1.825	1.827	1.830	1.832	1.834	1.837	1.839	1.842
3.10	1.844	1.846	1.849	1.851	1.854	1.856	1.858	1.861	1.863	1.865

WATER CONTENT 49 PERCENT

DG	0	1	2	3	4	5	6	7	8	9
1.70	1.382	1.386	1.391	1.395	1.399	1.404	1.408	1.412	1.417	1.421
1.80	1.425	1.429	1.433	1.438	1.442	1.446	1.450	1.454	1.458	1.462
1.90	1.466	1.470	1.474	1.478	1.482	1.486	1.490	1.494	1.497	1.501
2.00	1.505	1.509	1.513	1.516	1.520	1.524	1.528	1.531	1.535	1.539
2.10	1.542	1.546	1.549	1.553	1.556	1.560	1.564	1.567	1.571	1.574
2.20	1.577	1.581	1.584	1.588	1.591	1.595	1.598	1.601	1.605	1.608
2.30	1.611	1.614	1.618	1.621	1.624	1.627	1.631	1.634	1.637	1.640
2.40	1.643	1.647	1.650	1.653	1.656	1.659	1.662	1.665	1.668	1.671
2.50	1.674	1.677	1.680	1.683	1.686	1.689	1.692	1.695	1.698	1.701
2.60	1.704	1.706	1.709	1.712	1.715	1.718	1.721	1.723	1.726	1.729
2.70	1.732	1.735	1.737	1.740	1.743	1.745	1.748	1.751	1.754	1.756
2.80	1.759	1.761	1.764	1.767	1.769	1.772	1.775	1.777	1.780	1.782
2.90	1.785	1.787	1.790	1.792	1.795	1.797	1.800	1.802	1.805	1.807
3.00	1.810	1.812	1.815	1.817	1.819	1.822	1.824	1.827	1.829	1.831
3.10	1.834	1.836	1.838	1.841	1.843	1.845	1.848	1.850	1.852	1.854

WATER CONTENT 50 PERCENT

DG	0	1	2	3	4	5	6	7	8	9
1.70	1.378	1.383	1.387	1.391	1.396	1.400	1.404	1.408	1.413	1.417
1.80	1.421	1.425	1.429	1.433	1.437	1.442	1.446	1.450	1.454	1.458
1.90	1.462	1.465	1.469	1.473	1.477	1.481	1.485	1.489	1.492	1.496
2.00	1.500	1.504	1.507	1.511	1.515	1.519	1.522	1.526	1.529	1.533
2.10	1.537	1.540	1.544	1.547	1.551	1.554	1.558	1.561	1.565	1.568
2.20	1.571	1.575	1.578	1.582	1.585	1.588	1.592	1.595	1.598	1.601
2.30	1.605	1.608	1.611	1.614	1.618	1.621	1.624	1.627	1.630	1.633
2.40	1.636	1.639	1.643	1.646	1.649	1.652	1.655	1.658	1.661	1.664
2.50	1.667	1.670	1.673	1.675	1.678	1.681	1.684	1.687	1.690	1.693
2.60	1.696	1.698	1.701	1.704	1.707	1.710	1.712	1.715	1.718	1.721
2.70	1.723	1.726	1.729	1.732	1.734	1.737	1.739	1.742	1.745	1.747
2.80	1.750	1.753	1.755	1.758	1.760	1.763	1.765	1.768	1.770	1.773
2.90	1.776	1.778	1.780	1.783	1.785	1.788	1.790	1.793	1.795	1.798
3.00	1.800	1.802	1.805	1.807	1.810	1.812	1.814	1.817	1.819	1.821
3.10	1.824	1.826	1.828	1.830	1.833	1.835	1.837	1.839	1.842	1.844

WATER CONTENT 51 PERCENT

DG	0	1	2	3	4	5	6	7	8	9
1.70	1.375	1.379	1.384	1.388	1.392	1.396	1.401	1.405	1.409	1.413
1.80	1.417	1.421	1.425	1.429	1.433	1.437	1.441	1.445	1.449	1.453
1.90	1.457	1.461	1.465	1.469	1.473	1.476	1.480	1.484	1.488	1.491
2.00	1.495	1.499	1.502	1.506	1.510	1.513	1.517	1.521	1.524	1.528
2.10	1.531	1.535	1.538	1.542	1.545	1.549	1.552	1.555	1.559	1.562
2.20	1.566	1.569	1.572	1.575	1.579	1.582	1.585	1.589	1.592	1.595
2.30	1.598	1.601	1.605	1.608	1.611	1.614	1.617	1.620	1.623	1.626
2.40	1.629	1.633	1.636	1.639	1.642	1.645	1.648	1.651	1.653	1.656
2.50	1.659	1.662	1.665	1.668	1.671	1.674	1.677	1.679	1.682	1.685
2.60	1.688	1.691	1.693	1.696	1.699	1.702	1.704	1.707	1.710	1.713
2.70	1.715	1.718	1.721	1.723	1.726	1.728	1.731	1.734	1.736	1.739
2.80	1.741	1.744	1.746	1.749	1.752	1.754	1.757	1.759	1.762	1.764
2.90	1.766	1.769	1.771	1.774	1.776	1.779	1.781	1.783	1.786	1.788
3.00	1.791	1.793	1.795	1.798	1.800	1.802	1.804	1.807	1.809	1.811
3.10	1.814	1.816	1.818	1.820	1.823	1.825	1.827	1.829	1.831	1.834

WATER CONTENT 52 PERCENT

DG	0	1	2	3	4	5	6	7	8	9
1.70	1.372	1.376	1.380	1.384	1.388	1.393	1.397	1.401	1.405	1.409
1.80	1.413	1.417	1.421	1.425	1.429	1.433	1.437	1.441	1.445	1.449
1.90	1.453	1.457	1.460	1.464	1.468	1.472	1.475	1.479	1.483	1.487
2.00	1.490	1.494	1.497	1.501	1.505	1.508	1.512	1.515	1.519	1.522
2.10	1.526	1.529	1.533	1.536	1.540	1.543	1.546	1.550	1.553	1.556
2.20	1.560	1.563	1.566	1.570	1.573	1.576	1.579	1.582	1.586	1.589
2.30	1.592	1.595	1.598	1.601	1.604	1.608	1.611	1.614	1.617	1.620
2.40	1.623	1.626	1.629	1.632	1.635	1.638	1.641	1.643	1.646	1.649
2.50	1.652	1.655	1.658	1.661	1.664	1.666	1.669	1.672	1.675	1.678
2.60	1.680	1.683	1.686	1.688	1.691	1.694	1.697	1.699	1.702	1.705
2.70	1.707	1.710	1.712	1.715	1.718	1.720	1.723	1.725	1.728	1.730
2.80	1.733	1.735	1.738	1.740	1.743	1.745	1.748	1.750	1.753	1.755
2.90	1.758	1.760	1.762	1.765	1.767	1.770	1.772	1.774	1.777	1.779
3.00	1.781	1.784	1.786	1.788	1.790	1.793	1.795	1.797	1.800	1.802
3.10	1.804	1.806	1.808	1.811	1.813	1.815	1.817	1.819	1.822	1.824

WATER CONTENT 53 PERCENT

DG	0	1	2	3	4	5	6	7	8	9
1.70	1.368	1.372	1.377	1.381	1.385	1.389	1.393	1.397	1.401	1.405
1.80	1.409	1.413	1.417	1.421	1.425	1.429	1.433	1.437	1.441	1.445
1.90	1.448	1.452	1.456	1.460	1.463	1.467	1.471	1.475	1.478	1.482
2.00	1.485	1.489	1.493	1.496	1.500	1.503	1.507	1.510	1.514	1.517
2.10	1.521	1.524	1.527	1.531	1.534	1.538	1.541	1.544	1.547	1.551
2.20	1.554	1.557	1.561	1.564	1.567	1.570	1.573	1.576	1.580	1.583
2.30	1.586	1.589	1.592	1.595	1.598	1.601	1.604	1.607	1.610	1.613
2.40	1.616	1.619	1.622	1.625	1.628	1.631	1.634	1.637	1.639	1.642
2.50	1.645	1.648	1.651	1.654	1.656	1.659	1.662	1.665	1.667	1.670
2.60	1.673	1.676	1.678	1.681	1.684	1.686	1.689	1.691	1.694	1.697
2.70	1.699	1.702	1.704	1.707	1.710	1.712	1.715	1.717	1.720	1.722
2.80	1.725	1.727	1.730	1.732	1.734	1.737	1.739	1.742	1.744	1.747
2.90	1.749	1.751	1.754	1.756	1.758	1.761	1.763	1.765	1.768	1.770
3.00	1.772	1.774	1.777	1.779	1.781	1.783	1.786	1.788	1.790	1.792
3.10	1.795	1.797	1.799	1.801	1.803	1.805	1.808	1.810	1.812	1.814

WATER CONTENT 54 PERCENT

DG	0	1	2	3	4	5	6	7	8	9
1.70	1.365	1.369	1.373	1.377	1.382	1.386	1.390	1.394	1.398	1.402
1.80	1.406	1.410	1.414	1.417	1.421	1.425	1.429	1.433	1.437	1.440
1.90	1.444	1.448	1.452	1.455	1.459	1.463	1.466	1.470	1.474	1.477
2.00	1.481	1.484	1.488	1.491	1.495	1.498	1.502	1.505	1.509	1.512
2.10	1.515	1.519	1.522	1.526	1.529	1.532	1.535	1.539	1.542	1.545
2.20	1.548	1.552	1.555	1.558	1.561	1.564	1.567	1.571	1.574	1.577
2.30	1.580	1.583	1.586	1.589	1.592	1.595	1.598	1.601	1.604	1.607
2.40	1.610	1.613	1.616	1.618	1.621	1.624	1.627	1.630	1.633	1.636
2.50	1.638	1.641	1.644	1.647	1.649	1.652	1.655	1.658	1.660	1.663
2.60	1.666	1.668	1.671	1.673	1.676	1.679	1.681	1.684	1.686	1.689
2.70	1.692	1.694	1.697	1.699	1.702	1.704	1.707	1.709	1.712	1.714
2.80	1.717	1.719	1.721	1.724	1.726	1.729	1.731	1.733	1.736	1.738
2.90	1.740	1.743	1.745	1.747	1.750	1.752	1.754	1.757	1.759	1.761
3.00	1.763	1.766	1.768	1.770	1.772	1.774	1.777	1.779	1.781	1.783
3.10	1.785	1.787	1.790	1.792	1.794	1.796	1.798	1.800	1.802	1.804

WATER CONTENT 55 PERCENT

DG	0	1	2	3	4	5	6	7	8	9
1.70	1.362	1.366	1.370	1.374	1.378	1.382	1.386	1.390	1.394	1.398
1.80	1.402	1.406	1.410	1.414	1.417	1.421	1.425	1.429	1.433	1.436
1.90	1.440	1.444	1.447	1.451	1.455	1.458	1.462	1.466	1.469	1.473
2.00	1.476	1.480	1.483	1.487	1.490	1.494	1.497	1.500	1.504	1.507
2.10	1.510	1.514	1.517	1.520	1.524	1.527	1.530	1.533	1.537	1.540
2.20	1.543	1.546	1.549	1.552	1.556	1.559	1.562	1.565	1.568	1.571
2.30	1.574	1.577	1.580	1.583	1.586	1.589	1.592	1.595	1.598	1.601
2.40	1.603	1.606	1.609	1.612	1.615	1.618	1.620	1.623	1.626	1.629
2.50	1.632	1.634	1.637	1.640	1.642	1.645	1.648	1.651	1.653	1.656
2.60	1.658	1.661	1.664	1.666	1.669	1.671	1.674	1.677	1.679	1.682
2.70	1.684	1.687	1.689	1.692	1.694	1.697	1.699	1.701	1.704	1.706
2.80	1.709	1.711	1.713	1.716	1.718	1.721	1.723	1.725	1.728	1.730
2.90	1.732	1.734	1.737	1.739	1.741	1.744	1.746	1.748	1.750	1.753
3.00	1.755	1.757	1.759	1.761	1.763	1.766	1.768	1.770	1.772	1.774
3.10	1.776	1.778	1.781	1.783	1.785	1.787	1.789	1.791	1.793	1.795

WATER CONTENT 56 PERCENT

DG	0	1	2	3	4	5	6	7	8	9
1.70	1.359	1.363	1.367	1.371	1.375	1.379	1.383	1.387	1.391	1.395
1.80	1.398	1.402	1.406	1.410	1.414	1.417	1.421	1.425	1.429	1.432
1.90	1.436	1.440	1.443	1.447	1.451	1.454	1.458	1.461	1.465	1.468
2.00	1.472	1.475	1.479	1.482	1.485	1.489	1.492	1.496	1.499	1.502
2.10	1.506	1.509	1.512	1.515	1.519	1.522	1.525	1.528	1.531	1.534
2.20	1.538	1.541	1.544	1.547	1.550	1.553	1.556	1.559	1.562	1.565
2.30	1.568	1.571	1.574	1.577	1.580	1.583	1.586	1.589	1.592	1.594
2.40	1.597	1.600	1.603	1.606	1.609	1.611	1.614	1.617	1.620	1.622
2.50	1.625	1.628	1.630	1.633	1.636	1.638	1.641	1.644	1.646	1.649
2.60	1.651	1.654	1.657	1.659	1.662	1.664	1.667	1.669	1.672	1.674
2.70	1.677	1.679	1.682	1.684	1.687	1.689	1.691	1.694	1.696	1.699
2.80	1.701	1.703	1.706	1.708	1.710	1.713	1.715	1.717	1.720	1.722
2.90	1.724	1.726	1.729	1.731	1.733	1.735	1.738	1.740	1.742	1.744
3.00	1.746	1.748	1.751	1.753	1.755	1.757	1.759	1.761	1.763	1.765
3.10	1.768	1.770	1.772	1.774	1.776	1.778	1.780	1.782	1.784	1.786

WATER CONTENT 57 PERCENT

DG	0	1	2	3	4	5	6	7	8	9
1.70	1.356	1.360	1.364	1.368	1.372	1.375	1.379	1.383	1.387	1.391
1.80	1.395	1.399	1.402	1.406	1.410	1.414	1.417	1.421	1.425	1.428
1.90	1.432	1.436	1.439	1.443	1.446	1.450	1.453	1.457	1.460	1.464
2.00	1.467	1.471	1.474	1.477	1.481	1.484	1.488	1.491	1.494	1.497
2.10	1.501	1.504	1.507	1.510	1.514	1.517	1.520	1.523	1.526	1.529
2.20	1.532	1.535	1.539	1.542	1.545	1.548	1.551	1.554	1.557	1.560
2.30	1.563	1.565	1.568	1.571	1.574	1.577	1.580	1.583	1.586	1.588
2.40	1.591	1.594	1.597	1.600	1.602	1.605	1.608	1.610	1.613	1.616
2.50	1.619	1.621	1.624	1.627	1.629	1.632	1.634	1.637	1.640	1.642
2.60	1.645	1.647	1.650	1.652	1.655	1.657	1.660	1.662	1.665	1.667
2.70	1.670	1.672	1.674	1.677	1.679	1.682	1.684	1.686	1.689	1.691
2.80	1.693	1.696	1.698	1.700	1.703	1.705	1.707	1.709	1.712	1.714
2.90	1.716	1.718	1.721	1.723	1.725	1.727	1.729	1.732	1.734	1.736
3.00	1.738	1.740	1.742	1.744	1.746	1.749	1.751	1.753	1.755	1.757
3.10	1.759	1.761	1.763	1.765	1.767	1.769	1.771	1.773	1.775	1.777

WATER CONTENT 58 PERCENT

DG	0	1	2	3	4	5	6	7	8	9
1.70	1.352	1.356	1.360	1.364	1.368	1.372	1.376	1.380	1.384	1.388
1.80	1.391	1.395	1.399	1.403	1.406	1.410	1.414	1.417	1.421	1.425
1.90	1.428	1.432	1.435	1.439	1.442	1.446	1.449	1.453	1.456	1.460
2.00	1.463	1.466	1.470	1.473	1.476	1.480	1.483	1.486	1.489	1.493
2.10	1.496	1.499	1.502	1.506	1.509	1.512	1.515	1.518	1.521	1.524
2.20	1.527	1.530	1.533	1.536	1.539	1.542	1.545	1.548	1.551	1.554
2.30	1.557	1.560	1.563	1.566	1.568	1.571	1.574	1.577	1.580	1.583
2.40	1.585	1.588	1.591	1.594	1.596	1.599	1.602	1.604	1.607	1.610
2.50	1.612	1.615	1.617	1.620	1.623	1.625	1.628	1.630	1.633	1.635
2.60	1.638	1.640	1.643	1.645	1.648	1.650	1.653	1.655	1.658	1.660
2.70	1.663	1.665	1.667	1.670	1.672	1.674	1.677	1.679	1.681	1.684
2.80	1.686	1.688	1.691	1.693	1.695	1.697	1.700	1.702	1.704	1.706
2.90	1.708	1.711	1.713	1.715	1.717	1.719	1.721	1.724	1.726	1.728
3.00	1.730	1.732	1.734	1.736	1.738	1.740	1.742	1.744	1.746	1.749
3.10	1.751	1.753	1.755	1.757	1.759	1.761	1.762	1.764	1.766	1.768

WATER CONTENT 59 PERCENT

DG	0	1	2	3	4	5	6	7	8	9
1.70	1.349	1.353	1.357	1.361	1.365	1.369	1.373	1.377	1.380	1.384
1.80	1.388	1.392	1.395	1.399	1.403	1.406	1.410	1.414	1.417	1.421
1.90	1.424	1.428	1.431	1.435	1.438	1.442	1.445	1.449	1.452	1.455
2.00	1.459	1.462	1.465	1.469	1.472	1.475	1.478	1.482	1.485	1.488
2.10	1.491	1.494	1.498	1.501	1.504	1.507	1.510	1.513	1.516	1.519
2.20	1.522	1.525	1.528	1.531	1.534	1.537	1.540	1.543	1.546	1.549
2.30	1.552	1.554	1.557	1.560	1.563	1.566	1.568	1.571	1.574	1.577
2.40	1.579	1.582	1.585	1.588	1.590	1.593	1.596	1.598	1.601	1.603
2.50	1.606	1.609	1.611	1.614	1.616	1.619	1.621	1.624	1.626	1.629
2.60	1.631	1.634	1.636	1.639	1.641	1.644	1.646	1.648	1.651	1.653
2.70	1.656	1.658	1.660	1.663	1.665	1.667	1.670	1.672	1.674	1.676
2.80	1.679	1.681	1.683	1.685	1.688	1.690	1.692	1.694	1.697	1.699
2.90	1.701	1.703	1.705	1.707	1.709	1.712	1.714	1.716	1.718	1.720
3.00	1.722	1.724	1.726	1.728	1.730	1.732	1.734	1.736	1.738	1.740
3.10	1.742	1.744	1.746	1.748	1.750	1.752	1.754	1.756	1.758	1.760

WATER CONTENT 60 PERCENT

DG	0	1	2	3	4	5	6	7	8	9
1.70	1.347	1.350	1.354	1.358	1.362	1.366	1.370	1.373	1.377	1.381
1.80	1.385	1.388	1.392	1.396	1.399	1.403	1.406	1.410	1.414	1.417
1.90	1.421	1.424	1.428	1.431	1.434	1.438	1.441	1.445	1.448	1.451
2.00	1.455	1.458	1.461	1.464	1.468	1.471	1.474	1.477	1.480	1.484
2.10	1.487	1.490	1.493	1.496	1.499	1.502	1.505	1.508	1.511	1.514
2.20	1.517	1.520	1.523	1.526	1.529	1.532	1.535	1.538	1.541	1.543
2.30	1.546	1.549	1.552	1.555	1.557	1.560	1.563	1.566	1.568	1.571
2.40	1.574	1.576	1.579	1.582	1.584	1.587	1.590	1.592	1.595	1.597
2.50	1.600	1.603	1.605	1.608	1.610	1.613	1.615	1.618	1.620	1.623
2.60	1.625	1.627	1.630	1.632	1.635	1.637	1.639	1.642	1.644	1.647
2.70	1.649	1.651	1.653	1.656	1.658	1.660	1.663	1.665	1.667	1.669
2.80	1.672	1.674	1.676	1.678	1.680	1.683	1.685	1.687	1.689	1.691
2.90	1.693	1.696	1.698	1.700	1.702	1.704	1.706	1.708	1.710	1.712
3.00	1.714	1.716	1.718	1.720	1.722	1.724	1.726	1.728	1.730	1.732
3.10	1.734	1.736	1.738	1.740	1.742	1.744	1.746	1.748	1.750	1.752

WATER CONTENT 61 PERCENT

DG	0	1	2	3	4	5	6	7	8	9
1.70	1.344	1.348	1.351	1.355	1.359	1.363	1.367	1.370	1.374	1.378
1.80	1.381	1.385	1.389	1.392	1.396	1.399	1.403	1.406	1.410	1.413
1.90	1.417	1.420	1.424	1.427	1.431	1.434	1.437	1.441	1.444	1.447
2.00	1.450	1.454	1.457	1.460	1.463	1.467	1.470	1.473	1.476	1.479
2.10	1.482	1.485	1.488	1.491	1.494	1.498	1.501	1.504	1.506	1.509
2.20	1.512	1.515	1.518	1.521	1.524	1.527	1.530	1.533	1.535	1.538
2.30	1.541	1.544	1.547	1.549	1.552	1.555	1.557	1.560	1.563	1.566
2.40	1.568	1.571	1.573	1.576	1.579	1.581	1.584	1.586	1.589	1.592
2.50	1.594	1.597	1.599	1.602	1.604	1.607	1.609	1.611	1.614	1.616
2.60	1.619	1.621	1.624	1.626	1.628	1.631	1.633	1.635	1.638	1.640
2.70	1.642	1.645	1.647	1.649	1.651	1.654	1.656	1.658	1.660	1.662
2.80	1.665	1.667	1.669	1.671	1.673	1.676	1.678	1.680	1.682	1.684
2.90	1.686	1.688	1.690	1.692	1.694	1.697	1.699	1.701	1.703	1.705
3.00	1.707	1.709	1.711	1.713	1.715	1.717	1.719	1.721	1.723	1.724
3.10	1.726	1.728	1.730	1.732	1.734	1.736	1.738	1.740	1.742	1.743

WATER CONTENT 62 PERCENT

DG	0	1	2	3	4	5	6	7	8	9
1.70	1.341	1.345	1.348	1.352	1.356	1.360	1.363	1.367	1.371	1.374
1.80	1.378	1.382	1.385	1.389	1.392	1.396	1.399	1.403	1.406	1.410
1.90	1.413	1.417	1.420	1.423	1.427	1.430	1.433	1.437	1.440	1.443
2.00	1.446	1.450	1.453	1.456	1.459	1.462	1.465	1.469	1.472	1.475
2.10	1.478	1.481	1.484	1.487	1.490	1.493	1.496	1.499	1.502	1.505
2.20	1.508	1.511	1.513	1.516	1.519	1.522	1.525	1.528	1.530	1.533
2.30	1.536	1.539	1.541	1.544	1.547	1.549	1.552	1.555	1.557	1.560
2.40	1.563	1.565	1.568	1.570	1.573	1.576	1.578	1.581	1.583	1.586
2.50	1.588	1.591	1.593	1.596	1.598	1.601	1.603	1.605	1.608	1.610
2.60	1.613	1.615	1.617	1.620	1.622	1.624	1.627	1.629	1.631	1.633
2.70	1.636	1.638	1.640	1.643	1.645	1.647	1.649	1.651	1.654	1.656
2.80	1.658	1.660	1.662	1.664	1.666	1.669	1.671	1.673	1.675	1.677
2.90	1.679	1.681	1.683	1.685	1.687	1.689	1.691	1.693	1.695	1.697
3.00	1.699	1.701	1.703	1.705	1.707	1.709	1.711	1.713	1.715	1.717
3.10	1.719	1.721	1.722	1.724	1.726	1.728	1.730	1.732	1.734	1.735

WATER CONTENT 63 PERCENT

DG	0	1	2	3	4	5	6	7	8	9
1.70	1.338	1.342	1.346	1.349	1.353	1.357	1.360	1.364	1.368	1.371
1.80	1.375	1.378	1.382	1.386	1.389	1.393	1.396	1.399	1.403	1.406
1.90	1.410	1.413	1.416	1.420	1.423	1.426	1.430	1.433	1.436	1.439
2.00	1.442	1.446	1.449	1.452	1.455	1.458	1.461	1.464	1.467	1.470
2.10	1.474	1.477	1.480	1.483	1.485	1.488	1.491	1.494	1.497	1.500
2.20	1.503	1.506	1.509	1.511	1.514	1.517	1.520	1.523	1.525	1.528
2.30	1.531	1.534	1.536	1.539	1.542	1.544	1.547	1.550	1.552	1.555
2.40	1.557	1.560	1.562	1.565	1.568	1.570	1.573	1.575	1.578	1.580
2.50	1.583	1.585	1.587	1.590	1.592	1.595	1.597	1.599	1.602	1.604
2.60	1.607	1.609	1.611	1.613	1.616	1.618	1.620	1.623	1.625	1.627
2.70	1.629	1.632	1.634	1.636	1.638	1.640	1.643	1.645	1.647	1.649
2.80	1.651	1.653	1.655	1.658	1.660	1.662	1.664	1.666	1.668	1.670
2.90	1.672	1.674	1.676	1.678	1.680	1.682	1.684	1.686	1.688	1.690
3.00	1.692	1.694	1.696	1.698	1.700	1.702	1.704	1.705	1.707	1.709
3.10	1.711	1.713	1.715	1.717	1.719	1.720	1.722	1.724	1.726	1.728

WATER CONTENT 64 PERCENT

DG	0	1	2	3	4	5	6	7	8	9
1.70	1.335	1.339	1.343	1.346	1.350	1.354	1.357	1.361	1.365	1.368
1.80	1.372	1.375	1.379	1.382	1.386	1.389	1.393	1.396	1.399	1.403
1.90	1.406	1.409	1.413	1.416	1.419	1.423	1.426	1.429	1.432	1.435
2.00	1.439	1.442	1.445	1.448	1.451	1.454	1.457	1.460	1.463	1.466
2.10	1.469	1.472	1.475	1.478	1.481	1.484	1.487	1.490	1.493	1.496
2.20	1.498	1.501	1.504	1.507	1.510	1.512	1.515	1.518	1.520	1.523
2.30	1.526	1.529	1.531	1.534	1.537	1.539	1.542	1.544	1.547	1.549
2.40	1.552	1.555	1.557	1.560	1.562	1.565	1.567	1.570	1.572	1.574
2.50	1.577	1.579	1.582	1.584	1.587	1.589	1.591	1.594	1.596	1.598
2.60	1.601	1.603	1.605	1.607	1.610	1.612	1.614	1.617	1.619	1.621
2.70	1.623	1.625	1.628	1.630	1.632	1.634	1.636	1.638	1.640	1.643
2.80	1.645	1.647	1.649	1.651	1.653	1.655	1.657	1.659	1.661	1.663
2.90	1.665	1.667	1.669	1.671	1.673	1.675	1.677	1.679	1.681	1.683
3.00	1.685	1.687	1.689	1.691	1.693	1.694	1.696	1.698	1.700	1.702
3.10	1.704	1.706	1.707	1.709	1.711	1.713	1.715	1.716	1.718	1.720

WATER CONTENT 65 PERCENT

DG	0	1	2	3	4	5	6	7	8	9
1.70	1.333	1.336	1.340	1.344	1.347	1.351	1.354	1.358	1.362	1.365
1.80	1.369	1.372	1.376	1.379	1.383	1.386	1.389	1.393	1.396	1.399
1.90	1.403	1.406	1.409	1.413	1.416	1.419	1.422	1.425	1.429	1.432
2.00	1.435	1.438	1.441	1.444	1.447	1.450	1.453	1.456	1.459	1.462
2.10	1.465	1.468	1.471	1.474	1.477	1.480	1.483	1.485	1.488	1.491
2.20	1.494	1.497	1.499	1.502	1.505	1.508	1.510	1.513	1.516	1.518
2.30	1.521	1.524	1.526	1.529	1.532	1.534	1.537	1.539	1.542	1.544
2.40	1.547	1.549	1.552	1.554	1.557	1.559	1.562	1.564	1.567	1.569
2.50	1.571	1.574	1.576	1.579	1.581	1.583	1.586	1.588	1.590	1.593
2.60	1.595	1.597	1.599	1.602	1.604	1.606	1.608	1.610	1.613	1.615
2.70	1.617	1.619	1.621	1.624	1.626	1.628	1.630	1.632	1.634	1.636
2.80	1.638	1.640	1.642	1.644	1.647	1.649	1.651	1.653	1.655	1.657
2.90	1.659	1.661	1.663	1.664	1.666	1.668	1.670	1.672	1.674	1.676
3.00	1.678	1.680	1.682	1.684	1.685	1.687	1.689	1.691	1.693	1.695
3.10	1.697	1.698	1.700	1.702	1.704	1.705	1.707	1.709	1.711	1.713

WATER CONTENT 66 PERCENT

DG	0	1	2	3	4	5	6	7	8	9
1.70	1.330	1.334	1.337	1.341	1.344	1.348	1.352	1.355	1.359	1.362
1.80	1.366	1.369	1.373	1.376	1.379	1.383	1.386	1.389	1.393	1.396
1.90	1.399	1.403	1.406	1.409	1.412	1.415	1.419	1.422	1.425	1.428
2.00	1.431	1.434	1.437	1.440	1.443	1.446	1.449	1.452	1.455	1.458
2.10	1.461	1.464	1.467	1.470	1.473	1.475	1.478	1.481	1.484	1.487
2.20	1.489	1.492	1.495	1.498	1.500	1.503	1.506	1.508	1.511	1.514
2.30	1.516	1.519	1.521	1.524	1.527	1.529	1.532	1.534	1.537	1.539
2.40	1.542	1.544	1.547	1.549	1.552	1.554	1.556	1.559	1.561	1.564
2.50	1.566	1.568	1.571	1.573	1.575	1.578	1.580	1.582	1.585	1.587
2.60	1.589	1.591	1.594	1.596	1.598	1.600	1.602	1.605	1.607	1.609
2.70	1.611	1.613	1.615	1.617	1.620	1.622	1.624	1.626	1.628	1.630
2.80	1.632	1.634	1.636	1.638	1.640	1.642	1.644	1.646	1.648	1.650
2.90	1.652	1.654	1.656	1.658	1.660	1.662	1.664	1.665	1.667	1.669
3.00	1.671	1.673	1.675	1.677	1.679	1.680	1.682	1.684	1.686	1.688
3.10	1.689	1.691	1.693	1.695	1.697	1.698	1.700	1.702	1.703	1.705

WATER CONTENT 67 PERCENT

DG	0	1	2	3	4	5	6	7	8	9
1.70	1.327	1.331	1.335	1.338	1.342	1.345	1.349	1.352	1.356	1.359
1.80	1.363	1.366	1.369	1.373	1.376	1.380	1.383	1.386	1.389	1.393
1.90	1.396	1.399	1.402	1.406	1.409	1.412	1.415	1.418	1.421	1.424
2.00	1.427	1.430	1.433	1.436	1.439	1.442	1.445	1.448	1.451	1.454
2.10	1.457	1.460	1.463	1.466	1.468	1.471	1.474	1.477	1.480	1.482
2.20	1.485	1.488	1.490	1.493	1.496	1.499	1.501	1.504	1.506	1.509
2.30	1.512	1.514	1.517	1.519	1.522	1.524	1.527	1.529	1.532	1.534
2.40	1.537	1.539	1.542	1.544	1.547	1.549	1.551	1.554	1.556	1.558
2.50	1.561	1.563	1.565	1.568	1.570	1.572	1.575	1.577	1.579	1.581
2.60	1.584	1.586	1.588	1.590	1.592	1.594	1.597	1.599	1.601	1.603
2.70	1.605	1.607	1.609	1.612	1.614	1.616	1.618	1.620	1.622	1.624
2.80	1.626	1.628	1.630	1.632	1.634	1.636	1.638	1.640	1.642	1.644
2.90	1.646	1.648	1.649	1.651	1.653	1.655	1.657	1.659	1.661	1.663
3.00	1.664	1.666	1.668	1.670	1.672	1.674	1.675	1.677	1.679	1.681
3.10	1.682	1.684	1.686	1.688	1.689	1.691	1.693	1.695	1.696	1.698

WATER CONTENT 68 PERCENT

DG	0	1	2	3	4	5	6	7	8	9
1.70	1.325	1.328	1.332	1.335	1.339	1.342	1.346	1.349	1.353	1.356
1.80	1.360	1.363	1.366	1.370	1.373	1.376	1.380	1.383	1.386	1.389
1.90	1.393	1.396	1.399	1.402	1.405	1.408	1.412	1.415	1.418	1.421
2.00	1.424	1.427	1.430	1.433	1.436	1.439	1.442	1.444	1.447	1.450
2.10	1.453	1.456	1.459	1.462	1.464	1.467	1.470	1.473	1.475	1.478
2.20	1.481	1.483	1.486	1.489	1.491	1.494	1.497	1.499	1.502	1.504
2.30	1.507	1.510	1.512	1.515	1.517	1.520	1.522	1.525	1.527	1.529
2.40	1.532	1.534	1.537	1.539	1.542	1.544	1.546	1.549	1.551	1.553
2.50	1.556	1.558	1.560	1.562	1.565	1.567	1.569	1.571	1.574	1.576
2.60	1.578	1.580	1.582	1.585	1.587	1.589	1.591	1.593	1.595	1.597
2.70	1.599	1.602	1.604	1.606	1.608	1.610	1.612	1.614	1.616	1.618
2.80	1.620	1.622	1.624	1.626	1.628	1.630	1.632	1.634	1.635	1.637
2.90	1.639	1.641	1.643	1.645	1.647	1.649	1.651	1.652	1.654	1.656
3.00	1.658	1.660	1.662	1.663	1.665	1.667	1.669	1.670	1.672	1.674
3.10	1.676	1.677	1.679	1.681	1.683	1.684	1.686	1.688	1.689	1.691

WATER CONTENT 69 PERCENT

DG	0	1	2	3	4	5	6	7	8	9
1.70	1.322	1.326	1.329	1.333	1.336	1.340	1.343	1.347	1.350	1.353
1.80	1.357	1.360	1.364	1.367	1.370	1.373	1.377	1.380	1.383	1.386
1.90	1.389	1.393	1.396	1.399	1.402	1.405	1.408	1.411	1.414	1.417
2.00	1.420	1.423	1.426	1.429	1.432	1.435	1.438	1.441	1.443	1.446
2.10	1.449	1.452	1.455	1.458	1.460	1.463	1.466	1.469	1.471	1.474
2.20	1.477	1.479	1.482	1.484	1.487	1.490	1.492	1.495	1.497	1.500
2.30	1.503	1.505	1.508	1.510	1.513	1.515	1.517	1.520	1.522	1.525
2.40	1.527	1.529	1.532	1.534	1.537	1.539	1.541	1.544	1.546	1.548
2.50	1.550	1.553	1.555	1.557	1.559	1.562	1.564	1.566	1.568	1.570
2.60	1.573	1.575	1.577	1.579	1.581	1.583	1.585	1.588	1.590	1.592
2.70	1.594	1.596	1.598	1.600	1.602	1.604	1.606	1.608	1.610	1.612
2.80	1.614	1.616	1.618	1.620	1.622	1.624	1.626	1.627	1.629	1.631
2.90	1.633	1.635	1.637	1.639	1.641	1.642	1.644	1.646	1.648	1.650
3.00	1.651	1.653	1.655	1.657	1.659	1.660	1.662	1.664	1.666	1.667
3.10	1.669	1.671	1.672	1.674	1.676	1.677	1.679	1.681	1.682	1.684

WATER CONTENT 70 PERCENT

DG	0	1	2	3	4	5	6	7	8	9
1.70	1.320	1.323	1.327	1.330	1.334	1.337	1.341	1.344	1.347	1.351
1.80	1.354	1.357	1.361	1.364	1.367	1.370	1.374	1.377	1.380	1.383
1.90	1.386	1.389	1.392	1.396	1.399	1.402	1.405	1.408	1.411	1.414
2.00	1.417	1.420	1.423	1.425	1.428	1.431	1.434	1.437	1.440	1.443
2.10	1.445	1.448	1.451	1.454	1.456	1.459	1.462	1.464	1.467	1.470
2.20	1.472	1.475	1.478	1.480	1.483	1.485	1.488	1.491	1.493	1.496
2.30	1.498	1.501	1.503	1.506	1.508	1.510	1.513	1.515	1.518	1.520
2.40	1.522	1.525	1.527	1.529	1.532	1.534	1.536	1.539	1.541	1.543
2.50	1.545	1.548	1.550	1.552	1.554	1.557	1.559	1.561	1.563	1.565
2.60	1.567	1.570	1.572	1.574	1.576	1.578	1.580	1.582	1.584	1.586
2.70	1.588	1.590	1.592	1.594	1.596	1.598	1.600	1.602	1.604	1.606
2.80	1.608	1.610	1.612	1.614	1.616	1.618	1.620	1.621	1.623	1.625
2.90	1.627	1.629	1.631	1.633	1.634	1.636	1.638	1.640	1.642	1.643
3.00	1.645	1.647	1.649	1.650	1.652	1.654	1.656	1.657	1.659	1.661
3.10	1.662	1.664	1.666	1.667	1.669	1.671	1.672	1.674	1.676	1.677

WATER CONTENT 71 PERCENT

DG	0	1	2	3	4	5	6	7	8	9
1.70	1.317	1.321	1.324	1.328	1.331	1.334	1.338	1.341	1.345	1.348
1.80	1.351	1.354	1.358	1.361	1.364	1.367	1.371	1.374	1.377	1.380
1.90	1.383	1.386	1.389	1.392	1.395	1.398	1.401	1.404	1.407	1.410
2.00	1.413	1.416	1.419	1.422	1.425	1.428	1.430	1.433	1.436	1.439
2.10	1.442	1.444	1.447	1.450	1.452	1.455	1.458	1.461	1.463	1.466
2.20	1.468	1.471	1.474	1.476	1.479	1.481	1.484	1.486	1.489	1.491
2.30	1.494	1.496	1.499	1.501	1.503	1.506	1.508	1.511	1.513	1.515
2.40	1.518	1.520	1.522	1.525	1.527	1.529	1.532	1.534	1.536	1.538
2.50	1.541	1.543	1.545	1.547	1.549	1.552	1.554	1.556	1.558	1.560
2.60	1.562	1.564	1.566	1.568	1.571	1.573	1.575	1.577	1.579	1.581
2.70	1.583	1.585	1.587	1.589	1.591	1.593	1.595	1.597	1.599	1.600
2.80	1.602	1.604	1.606	1.608	1.610	1.612	1.614	1.616	1.617	1.619
2.90	1.621	1.623	1.625	1.627	1.628	1.630	1.632	1.634	1.635	1.637
3.00	1.639	1.641	1.642	1.644	1.646	1.648	1.649	1.651	1.653	1.654
3.10	1.656	1.658	1.659	1.661	1.663	1.664	1.666	1.668	1.669	1.671

WATER CONTENT 72 PERCENT

DG	0	1	2	3	4	5	6	7	8	9
1.70	1.315	1.318	1.322	1.325	1.328	1.332	1.335	1.339	1.342	1.345
1.80	1.348	1.352	1.355	1.358	1.361	1.364	1.368	1.371	1.374	1.377
1.90	1.380	1.383	1.386	1.389	1.392	1.395	1.398	1.401	1.404	1.407
2.00	1.410	1.413	1.416	1.418	1.421	1.424	1.427	1.430	1.432	1.435
2.10	1.438	1.441	1.443	1.446	1.449	1.451	1.454	1.457	1.459	1.462
2.20	1.464	1.467	1.470	1.472	1.475	1.477	1.480	1.482	1.485	1.487
2.30	1.489	1.492	1.494	1.497	1.499	1.501	1.504	1.506	1.509	1.511
2.40	1.513	1.516	1.518	1.520	1.522	1.525	1.527	1.529	1.531	1.534
2.50	1.536	1.538	1.540	1.542	1.544	1.547	1.549	1.551	1.553	1.555
2.60	1.557	1.559	1.561	1.563	1.565	1.567	1.569	1.571	1.573	1.575
2.70	1.577	1.579	1.581	1.583	1.585	1.587	1.589	1.591	1.593	1.595
2.80	1.597	1.599	1.601	1.602	1.604	1.606	1.608	1.610	1.612	1.613
2.90	1.615	1.617	1.619	1.621	1.622	1.624	1.626	1.628	1.629	1.631
3.00	1.633	1.635	1.636	1.638	1.640	1.641	1.643	1.645	1.646	1.648
3.10	1.650	1.651	1.653	1.655	1.656	1.658	1.659	1.661	1.663	1.664

WATER CONTENT 73 PERCENT

DG	0	1	2	3	4	5	6	7	8	9
1.70	1.312	1.316	1.319	1.323	1.326	1.329	1.333	1.336	1.339	1.342
1.80	1.346	1.349	1.352	1.355	1.358	1.362	1.365	1.368	1.371	1.374
1.90	1.377	1.380	1.383	1.386	1.389	1.392	1.395	1.398	1.401	1.404
2.00	1.407	1.409	1.412	1.415	1.418	1.421	1.423	1.426	1.429	1.432
2.10	1.434	1.437	1.440	1.442	1.445	1.448	1.450	1.453	1.455	1.458
2.20	1.460	1.463	1.466	1.468	1.471	1.473	1.476	1.478	1.480	1.483
2.30	1.485	1.488	1.490	1.492	1.495	1.497	1.499	1.502	1.504	1.506
2.40	1.509	1.511	1.513	1.516	1.518	1.520	1.522	1.524	1.527	1.529
2.50	1.531	1.533	1.535	1.537	1.540	1.542	1.544	1.546	1.548	1.550
2.60	1.552	1.554	1.556	1.558	1.560	1.562	1.564	1.566	1.568	1.570
2.70	1.572	1.574	1.576	1.578	1.580	1.582	1.584	1.586	1.588	1.589
2.80	1.591	1.593	1.595	1.597	1.599	1.601	1.602	1.604	1.606	1.608
2.90	1.610	1.611	1.613	1.615	1.617	1.618	1.620	1.622	1.624	1.625
3.00	1.627	1.629	1.630	1.632	1.634	1.635	1.637	1.639	1.640	1.642
3.10	1.644	1.645	1.647	1.648	1.650	1.652	1.653	1.655	1.656	1.658

WATER CONTENT 74 PERCENT

DG	0	1	2	3	4	5	6	7	8	9
1.70	1.310	1.313	1.317	1.320	1.323	1.327	1.330	1.333	1.337	1.340
1.80	1.343	1.346	1.349	1.353	1.356	1.359	1.362	1.365	1.368	1.371
1.90	1.374	1.377	1.380	1.383	1.386	1.389	1.392	1.395	1.398	1.400
2.00	1.403	1.406	1.409	1.412	1.414	1.417	1.420	1.423	1.425	1.428
2.10	1.431	1.433	1.436	1.439	1.441	1.444	1.446	1.449	1.452	1.454
2.20	1.457	1.459	1.462	1.464	1.467	1.469	1.471	1.474	1.476	1.479
2.30	1.481	1.484	1.486	1.488	1.491	1.493	1.495	1.497	1.500	1.502
2.40	1.504	1.507	1.509	1.511	1.513	1.515	1.518	1.520	1.522	1.524
2.50	1.526	1.528	1.531	1.533	1.535	1.537	1.539	1.541	1.543	1.545
2.60	1.547	1.549	1.551	1.553	1.555	1.557	1.559	1.561	1.563	1.565
2.70	1.567	1.569	1.571	1.573	1.575	1.577	1.578	1.580	1.582	1.584
2.80	1.586	1.588	1.590	1.591	1.593	1.595	1.597	1.599	1.600	1.602
2.90	1.604	1.606	1.607	1.609	1.611	1.613	1.614	1.616	1.618	1.619
3.00	1.621	1.623	1.624	1.626	1.628	1.629	1.631	1.633	1.634	1.636
3.10	1.638	1.639	1.641	1.642	1.644	1.645	1.647	1.649	1.650	1.652

WATER CONTENT 75 PERCENT

DG	0	1	2	3	4	5	6	7	8	9
1.70	1.308	1.311	1.314	1.318	1.321	1.324	1.328	1.331	1.334	1.337
1.80	1.340	1.344	1.347	1.350	1.353	1.356	1.359	1.362	1.365	1.368
1.90	1.371	1.374	1.377	1.380	1.383	1.386	1.389	1.392	1.394	1.397
2.00	1.400	1.403	1.406	1.408	1.411	1.414	1.417	1.419	1.422	1.425
2.10	1.427	1.430	1.432	1.435	1.438	1.440	1.443	1.445	1.448	1.450
2.20	1.453	1.455	1.458	1.460	1.463	1.465	1.468	1.470	1.472	1.475
2.30	1.477	1.479	1.482	1.484	1.486	1.489	1.491	1.493	1.496	1.498
2.40	1.500	1.502	1.504	1.507	1.509	1.511	1.513	1.515	1.517	1.520
2.50	1.522	1.524	1.526	1.528	1.530	1.532	1.534	1.536	1.538	1.540
2.60	1.542	1.544	1.546	1.548	1.550	1.552	1.554	1.556	1.558	1.560
2.70	1.562	1.564	1.566	1.568	1.570	1.571	1.573	1.575	1.577	1.579
2.80	1.581	1.582	1.584	1.586	1.588	1.590	1.591	1.593	1.595	1.597
2.90	1.598	1.600	1.602	1.604	1.605	1.607	1.609	1.610	1.612	1.614
3.00	1.615	1.617	1.619	1.620	1.622	1.624	1.625	1.627	1.628	1.630
3.10	1.632	1.633	1.635	1.636	1.638	1.639	1.641	1.642	1.644	1.646

WATER CONTENT 76 PERCENT

DG	0	1	2	3	4	5	6	7	8	9
1.70	1.305	1.309	1.312	1.315	1.319	1.322	1.325	1.328	1.332	1.335
1.80	1.338	1.341	1.344	1.347	1.350	1.353	1.356	1.359	1.362	1.365
1.90	1.368	1.371	1.374	1.377	1.380	1.383	1.386	1.388	1.391	1.394
2.00	1.397	1.400	1.402	1.405	1.408	1.410	1.413	1.416	1.418	1.421
2.10	1.424	1.426	1.429	1.431	1.434	1.437	1.439	1.442	1.444	1.447
2.20	1.449	1.452	1.454	1.456	1.459	1.461	1.464	1.466	1.468	1.471
2.30	1.473	1.475	1.478	1.480	1.482	1.485	1.487	1.489	1.491	1.494
2.40	1.496	1.498	1.500	1.502	1.504	1.507	1.509	1.511	1.513	1.515
2.50	1.517	1.519	1.521	1.523	1.526	1.528	1.530	1.532	1.534	1.536
2.60	1.538	1.540	1.542	1.544	1.546	1.547	1.549	1.551	1.553	1.555
2.70	1.557	1.559	1.561	1.563	1.564	1.566	1.568	1.570	1.572	1.574
2.80	1.575	1.577	1.579	1.581	1.583	1.584	1.586	1.588	1.590	1.591
2.90	1.593	1.595	1.596	1.598	1.600	1.601	1.603	1.605	1.606	1.608
3.00	1.610	1.611	1.613	1.615	1.616	1.618	1.619	1.621	1.623	1.624
3.10	1.626	1.627	1.629	1.630	1.632	1.633	1.635	1.637	1.638	1.640

WATER CONTENT 77 PERCENT

DG	0	1	2	3	4	5	6	7	8	9
1.70	1.303	1.306	1.310	1.313	1.316	1.319	1.323	1.326	1.329	1.332
1.80	1.335	1.338	1.341	1.345	1.348	1.351	1.354	1.357	1.360	1.362
1.90	1.365	1.368	1.371	1.374	1.377	1.380	1.383	1.385	1.388	1.391
2.00	1.394	1.396	1.399	1.402	1.405	1.407	1.410	1.413	1.415	1.418
2.10	1.420	1.423	1.425	1.428	1.431	1.433	1.436	1.438	1.441	1.443
2.20	1.445	1.448	1.450	1.453	1.455	1.457	1.460	1.462	1.465	1.467
2.30	1.469	1.471	1.474	1.476	1.478	1.481	1.483	1.485	1.487	1.489
2.40	1.492	1.494	1.496	1.498	1.500	1.502	1.504	1.507	1.509	1.511
2.50	1.513	1.515	1.517	1.519	1.521	1.523	1.525	1.527	1.529	1.531
2.60	1.533	1.535	1.537	1.539	1.541	1.543	1.545	1.546	1.548	1.550
2.70	1.552	1.554	1.556	1.558	1.560	1.561	1.563	1.565	1.567	1.569
2.80	1.570	1.572	1.574	1.576	1.577	1.579	1.581	1.583	1.584	1.586
2.90	1.588	1.589	1.591	1.593	1.594	1.596	1.598	1.599	1.601	1.603
3.00	1.604	1.606	1.607	1.609	1.611	1.612	1.614	1.615	1.617	1.618
3.10	1.620	1.622	1.623	1.625	1.626	1.628	1.629	1.631	1.632	1.634

WATER CONTENT 78 PERCENT

DG	0	1	2	3	4	5	6	7	8	9
1.70	1.301	1.304	1.307	1.311	1.314	1.317	1.320	1.323	1.327	1.330
1.80	1.333	1.336	1.339	1.342	1.345	1.348	1.351	1.354	1.357	1.360
1.90	1.363	1.365	1.368	1.371	1.374	1.377	1.380	1.382	1.385	1.388
2.00	1.391	1.393	1.396	1.399	1.401	1.404	1.407	1.409	1.412	1.414
2.10	1.417	1.420	1.422	1.425	1.427	1.430	1.432	1.435	1.437	1.439
2.20	1.442	1.444	1.447	1.449	1.451	1.454	1.456	1.458	1.461	1.463
2.30	1.465	1.468	1.470	1.472	1.474	1.477	1.479	1.481	1.483	1.485
2.40	1.487	1.490	1.492	1.494	1.496	1.498	1.500	1.502	1.504	1.506
2.50	1.508	1.511	1.513	1.515	1.517	1.519	1.521	1.523	1.524	1.526
2.60	1.528	1.530	1.532	1.534	1.536	1.538	1.540	1.542	1.544	1.545
2.70	1.547	1.549	1.551	1.553	1.555	1.556	1.558	1.560	1.562	1.564
2.80	1.565	1.567	1.569	1.571	1.572	1.574	1.576	1.577	1.579	1.581
2.90	1.582	1.584	1.586	1.587	1.589	1.591	1.592	1.594	1.596	1.597
3.00	1.599	1.600	1.602	1.604	1.605	1.607	1.608	1.610	1.611	1.613
3.10	1.614	1.616	1.617	1.619	1.620	1.622	1.623	1.625	1.626	1.628

WATER CONTENT 79 PERCENT

DG	0	1	2	3	4	5	6	7	8	9
1.70	1.299	1.302	1.305	1.308	1.312	1.315	1.318	1.321	1.324	1.327
1.80	1.330	1.333	1.336	1.339	1.342	1.345	1.348	1.351	1.354	1.357
1.90	1.360	1.363	1.366	1.368	1.371	1.374	1.377	1.379	1.382	1.385
2.00	1.388	1.390	1.393	1.396	1.398	1.401	1.403	1.406	1.409	1.411
2.10	1.414	1.416	1.419	1.421	1.424	1.426	1.429	1.431	1.433	1.436
2.20	1.438	1.441	1.443	1.445	1.448	1.450	1.452	1.455	1.457	1.459
2.30	1.461	1.464	1.466	1.468	1.470	1.473	1.475	1.477	1.479	1.481
2.40	1.483	1.486	1.488	1.490	1.492	1.494	1.496	1.498	1.500	1.502
2.50	1.504	1.506	1.508	1.510	1.512	1.514	1.516	1.518	1.520	1.522
2.60	1.524	1.526	1.528	1.530	1.532	1.533	1.535	1.537	1.539	1.541
2.70	1.543	1.544	1.546	1.548	1.550	1.552	1.553	1.555	1.557	1.559
2.80	1.560	1.562	1.564	1.566	1.567	1.569	1.571	1.572	1.574	1.576
2.90	1.577	1.579	1.581	1.582	1.584	1.585	1.587	1.589	1.590	1.592
3.00	1.593	1.595	1.597	1.598	1.600	1.601	1.603	1.604	1.606	1.607
3.10	1.609	1.610	1.612	1.613	1.615	1.616	1.618	1.619	1.621	1.622

WATER CONTENT 80 PERCENT

DG	0	1	2	3	4	5	6	7	8	9
1.70	1.297	1.300	1.303	1.306	1.309	1.312	1.316	1.319	1.322	1.325
1.80	1.328	1.331	1.334	1.337	1.340	1.343	1.346	1.349	1.351	1.354
1.90	1.357	1.360	1.363	1.366	1.368	1.371	1.374	1.377	1.379	1.382
2.00	1.385	1.387	1.390	1.393	1.395	1.398	1.400	1.403	1.405	1.408
2.10	1.410	1.413	1.415	1.418	1.420	1.423	1.425	1.428	1.430	1.432
2.20	1.435	1.437	1.439	1.442	1.444	1.446	1.449	1.451	1.453	1.456
2.30	1.458	1.460	1.462	1.464	1.467	1.469	1.471	1.473	1.475	1.477
2.40	1.479	1.482	1.484	1.486	1.488	1.490	1.492	1.494	1.496	1.498
2.50	1.500	1.502	1.504	1.506	1.508	1.510	1.512	1.514	1.516	1.518
2.60	1.519	1.521	1.523	1.525	1.527	1.529	1.531	1.533	1.534	1.536
2.70	1.538	1.540	1.542	1.543	1.545	1.547	1.549	1.550	1.552	1.554
2.80	1.556	1.557	1.559	1.561	1.562	1.564	1.566	1.567	1.569	1.571
2.90	1.572	1.574	1.576	1.577	1.579	1.580	1.582	1.584	1.585	1.587
3.00	1.588	1.590	1.591	1.593	1.594	1.596	1.597	1.599	1.600	1.602
3.10	1.603	1.605	1.606	1.608	1.609	1.611	1.612	1.614	1.615	1.617

WATER CONTENT 81 PERCENT

DG	0	1	2	3	4	5	6	7	8	9
1.70	1.294	1.298	1.301	1.304	1.307	1.310	1.313	1.316	1.319	1.322
1.80	1.325	1.328	1.331	1.334	1.337	1.340	1.343	1.346	1.349	1.352
1.90	1.354	1.357	1.360	1.363	1.366	1.368	1.371	1.374	1.376	1.379
2.00	1.382	1.384	1.387	1.390	1.392	1.395	1.397	1.400	1.402	1.405
2.10	1.407	1.410	1.412	1.415	1.417	1.419	1.422	1.424	1.427	1.429
2.20	1.431	1.434	1.436	1.438	1.441	1.443	1.445	1.447	1.450	1.452
2.30	1.454	1.456	1.458	1.461	1.463	1.465	1.467	1.469	1.471	1.473
2.40	1.476	1.478	1.480	1.482	1.484	1.486	1.488	1.490	1.492	1.494
2.50	1.496	1.498	1.500	1.502	1.504	1.506	1.508	1.509	1.511	1.513
2.60	1.515	1.517	1.519	1.521	1.523	1.524	1.526	1.528	1.530	1.532
2.70	1.533	1.535	1.537	1.539	1.540	1.542	1.544	1.546	1.547	1.549
2.80	1.551	1.552	1.554	1.556	1.558	1.559	1.561	1.562	1.564	1.566
2.90	1.567	1.569	1.571	1.572	1.574	1.575	1.577	1.578	1.580	1.582
3.00	1.583	1.585	1.586	1.588	1.589	1.591	1.592	1.594	1.595	1.597
3.10	1.598	1.600	1.601	1.602	1.604	1.605	1.607	1.608	1.610	1.611

WATER CONTENT 82 PERCENT

DG	0	1	2	3	4	5	6	7	8	9
1.70	1.292	1.296	1.299	1.302	1.305	1.308	1.311	1.314	1.317	1.320
1.80	1.323	1.326	1.329	1.332	1.335	1.338	1.341	1.343	1.346	1.349
1.90	1.352	1.355	1.357	1.360	1.363	1.366	1.368	1.371	1.374	1.376
2.00	1.379	1.381	1.384	1.387	1.389	1.392	1.394	1.397	1.399	1.402
2.10	1.404	1.407	1.409	1.411	1.414	1.416	1.419	1.421	1.423	1.426
2.20	1.428	1.430	1.433	1.435	1.437	1.439	1.442	1.444	1.446	1.448
2.30	1.450	1.453	1.455	1.457	1.459	1.461	1.463	1.465	1.468	1.470
2.40	1.472	1.474	1.476	1.478	1.480	1.482	1.484	1.486	1.488	1.490
2.50	1.492	1.494	1.496	1.498	1.500	1.501	1.503	1.505	1.507	1.509
2.60	1.511	1.513	1.515	1.516	1.518	1.520	1.522	1.524	1.525	1.527
2.70	1.529	1.531	1.532	1.534	1.536	1.538	1.539	1.541	1.543	1.544
2.80	1.546	1.548	1.549	1.551	1.553	1.554	1.556	1.558	1.559	1.561
2.90	1.562	1.564	1.566	1.567	1.569	1.570	1.572	1.573	1.575	1.577
3.00	1.578	1.580	1.581	1.583	1.584	1.586	1.587	1.589	1.590	1.591
3.10	1.593	1.594	1.596	1.597	1.599	1.600	1.601	1.603	1.604	1.606

WATER CONTENT 83 PERCENT

DG	0	1	2	3	4	5	6	7	8	9
1.70	1.290	1.293	1.297	1.300	1.303	1.306	1.309	1.312	1.315	1.318
1.80	1.321	1.324	1.327	1.330	1.332	1.335	1.338	1.341	1.344	1.346
1.90	1.349	1.352	1.355	1.357	1.360	1.363	1.365	1.368	1.371	1.373
2.00	1.376	1.379	1.381	1.384	1.386	1.389	1.391	1.394	1.396	1.399
2.10	1.401	1.403	1.406	1.408	1.411	1.413	1.415	1.418	1.420	1.422
2.20	1.425	1.427	1.429	1.431	1.434	1.436	1.438	1.440	1.443	1.445
2.30	1.447	1.449	1.451	1.453	1.455	1.458	1.460	1.462	1.464	1.466
2.40	1.468	1.470	1.472	1.474	1.476	1.478	1.480	1.482	1.484	1.486
2.50	1.488	1.490	1.492	1.494	1.495	1.497	1.499	1.501	1.503	1.505
2.60	1.507	1.508	1.510	1.512	1.514	1.516	1.517	1.519	1.521	1.523
2.70	1.525	1.526	1.528	1.530	1.531	1.533	1.535	1.537	1.538	1.540
2.80	1.542	1.543	1.545	1.546	1.548	1.550	1.551	1.553	1.555	1.556
2.90	1.558	1.559	1.561	1.562	1.564	1.565	1.567	1.569	1.570	1.572
3.00	1.573	1.575	1.576	1.578	1.579	1.580	1.582	1.583	1.585	1.586
3.10	1.588	1.589	1.591	1.592	1.593	1.595	1.596	1.598	1.599	1.600

WATER CONTENT 84 PERCENT

DG	0	1	2	3	4	5	6	7	8	9
1.70	1.288	1.291	1.295	1.298	1.301	1.304	1.307	1.310	1.313	1.316
1.80	1.318	1.321	1.324	1.327	1.330	1.333	1.336	1.338	1.341	1.344
1.90	1.347	1.349	1.352	1.355	1.357	1.360	1.363	1.365	1.368	1.371
2.00	1.373	1.376	1.378	1.381	1.383	1.386	1.388	1.391	1.393	1.396
2.10	1.398	1.400	1.403	1.405	1.407	1.410	1.412	1.414	1.417	1.419
2.20	1.421	1.424	1.426	1.428	1.430	1.433	1.435	1.437	1.439	1.441
2.30	1.443	1.446	1.448	1.450	1.452	1.454	1.456	1.458	1.460	1.462
2.40	1.464	1.466	1.468	1.470	1.472	1.474	1.476	1.478	1.480	1.482
2.50	1.484	1.486	1.488	1.490	1.491	1.493	1.495	1.497	1.499	1.501
2.60	1.503	1.504	1.506	1.508	1.510	1.511	1.513	1.515	1.517	1.518
2.70	1.520	1.522	1.524	1.525	1.527	1.529	1.530	1.532	1.534	1.535
2.80	1.537	1.539	1.540	1.542	1.543	1.545	1.547	1.548	1.550	1.551
2.90	1.553	1.555	1.556	1.558	1.559	1.561	1.562	1.564	1.565	1.567
3.00	1.568	1.570	1.571	1.573	1.574	1.576	1.577	1.578	1.580	1.581
3.10	1.583	1.584	1.586	1.587	1.588	1.590	1.591	1.592	1.594	1.595

WATER CONTENT 85 PERCENT

DG	0	1	2	3	4	5	6	7	8	9
1.70	1.286	1.289	1.292	1.295	1.299	1.302	1.304	1.307	1.310	1.313
1.80	1.316	1.319	1.322	1.325	1.328	1.330	1.333	1.336	1.339	1.341
1.90	1.344	1.347	1.350	1.352	1.355	1.357	1.360	1.363	1.365	1.368
2.00	1.370	1.373	1.375	1.378	1.380	1.383	1.385	1.388	1.390	1.393
2.10	1.395	1.397	1.400	1.402	1.404	1.407	1.409	1.411	1.414	1.416
2.20	1.418	1.420	1.423	1.425	1.427	1.429	1.431	1.434	1.436	1.438
2.30	1.440	1.442	1.444	1.446	1.448	1.450	1.452	1.454	1.457	1.459
2.40	1.461	1.463	1.465	1.466	1.468	1.470	1.472	1.474	1.476	1.478
2.50	1.480	1.482	1.484	1.486	1.487	1.489	1.491	1.493	1.495	1.497
2.60	1.498	1.500	1.502	1.504	1.506	1.507	1.509	1.511	1.513	1.514
2.70	1.516	1.518	1.519	1.521	1.523	1.524	1.526	1.528	1.529	1.531
2.80	1.533	1.534	1.536	1.537	1.539	1.541	1.542	1.544	1.545	1.547
2.90	1.548	1.550	1.551	1.553	1.554	1.556	1.557	1.559	1.560	1.562
3.00	1.563	1.565	1.566	1.568	1.569	1.571	1.572	1.573	1.575	1.576
3.10	1.578	1.579	1.581	1.582	1.583	1.585	1.586	1.587	1.589	1.590

WATER CONTENT 86 PERCENT

DG	0	1	2	3	4	5	6	7	8	9
1.70	1.284	1.287	1.290	1.293	1.296	1.299	1.302	1.305	1.308	1.311
1.80	1.314	1.317	1.320	1.322	1.325	1.328	1.331	1.334	1.336	1.339
1.90	1.342	1.344	1.347	1.350	1.352	1.355	1.357	1.360	1.363	1.365
2.00	1.368	1.370	1.373	1.375	1.378	1.380	1.382	1.385	1.387	1.390
2.10	1.392	1.394	1.397	1.399	1.401	1.404	1.406	1.408	1.410	1.413
2.20	1.415	1.417	1.419	1.422	1.424	1.426	1.428	1.430	1.432	1.434
2.30	1.437	1.439	1.441	1.443	1.445	1.447	1.449	1.451	1.453	1.455
2.40	1.457	1.459	1.461	1.463	1.465	1.467	1.469	1.471	1.472	1.474
2.50	1.476	1.478	1.480	1.482	1.484	1.485	1.487	1.489	1.491	1.493
2.60	1.494	1.496	1.498	1.500	1.501	1.503	1.505	1.507	1.508	1.510
2.70	1.512	1.513	1.515	1.517	1.518	1.520	1.522	1.523	1.525	1.527
2.80	1.528	1.530	1.531	1.533	1.535	1.536	1.538	1.539	1.541	1.542
2.90	1.544	1.545	1.547	1.548	1.550	1.551	1.553	1.554	1.556	1.557
3.00	1.559	1.560	1.562	1.563	1.564	1.566	1.567	1.569	1.570	1.571
3.10	1.573	1.574	1.576	1.577	1.578	1.580	1.581	1.582	1.584	1.585

WATER CONTENT 87 PERCENT

DG	0	1	2	3	4	5	6	7	8	9
1.70	1.282	1.285	1.288	1.291	1.294	1.297	1.300	1.303	1.306	1.309
1.80	1.312	1.315	1.317	1.320	1.323	1.326	1.328	1.331	1.334	1.337
1.90	1.339	1.342	1.345	1.347	1.350	1.352	1.355	1.357	1.360	1.362
2.00	1.365	1.367	1.370	1.372	1.375	1.377	1.380	1.382	1.384	1.387
2.10	1.389	1.391	1.394	1.396	1.398	1.401	1.403	1.405	1.407	1.410
2.20	1.412	1.414	1.416	1.418	1.421	1.423	1.425	1.427	1.429	1.431
2.30	1.433	1.435	1.437	1.439	1.441	1.443	1.445	1.447	1.449	1.451
2.40	1.453	1.455	1.457	1.459	1.461	1.463	1.465	1.467	1.469	1.471
2.50	1.472	1.474	1.476	1.478	1.480	1.482	1.483	1.485	1.487	1.489
2.60	1.490	1.492	1.494	1.496	1.497	1.499	1.501	1.503	1.504	1.506
2.70	1.508	1.509	1.511	1.513	1.514	1.516	1.517	1.519	1.521	1.522
2.80	1.524	1.525	1.527	1.529	1.530	1.532	1.533	1.535	1.536	1.538
2.90	1.539	1.541	1.542	1.544	1.545	1.547	1.548	1.550	1.551	1.553
3.00	1.554	1.555	1.557	1.558	1.560	1.561	1.563	1.564	1.565	1.567
3.10	1.568	1.569	1.571	1.572	1.573	1.575	1.576	1.577	1.579	1.580

WATER CONTENT 88 PERCENT

DG	0	1	2	3	4	5	6	7	8	9
1.70	1.280	1.283	1.286	1.289	1.292	1.295	1.298	1.301	1.304	1.307
1.80	1.310	1.312	1.315	1.318	1.321	1.323	1.326	1.329	1.332	1.334
1.90	1.337	1.339	1.342	1.345	1.347	1.350	1.352	1.355	1.357	1.360
2.00	1.362	1.365	1.367	1.370	1.372	1.374	1.377	1.379	1.382	1.384
2.10	1.386	1.389	1.391	1.393	1.395	1.398	1.400	1.402	1.404	1.407
2.20	1.409	1.411	1.413	1.415	1.417	1.419	1.422	1.424	1.426	1.428
2.30	1.430	1.432	1.434	1.436	1.438	1.440	1.442	1.444	1.446	1.448
2.40	1.450	1.452	1.454	1.456	1.458	1.459	1.461	1.463	1.465	1.467
2.50	1.469	1.471	1.472	1.474	1.476	1.478	1.480	1.481	1.483	1.485
2.60	1.487	1.488	1.490	1.492	1.494	1.495	1.497	1.499	1.500	1.502
2.70	1.504	1.505	1.507	1.508	1.510	1.512	1.513	1.515	1.516	1.518
2.80	1.520	1.521	1.523	1.524	1.526	1.527	1.529	1.530	1.532	1.533
2.90	1.535	1.536	1.538	1.539	1.541	1.542	1.544	1.545	1.547	1.548
3.00	1.549	1.551	1.552	1.554	1.555	1.556	1.558	1.559	1.561	1.562
3.10	1.563	1.565	1.566	1.567	1.569	1.570	1.571	1.573	1.574	1.575

WATER CONTENT 89 PERCENT

DG	0	1	2	3	4	5	6	7	8	9
1.70	1.279	1.282	1.284	1.287	1.290	1.293	1.296	1.299	1.302	1.305
1.80	1.307	1.310	1.313	1.316	1.318	1.321	1.324	1.327	1.329	1.332
1.90	1.334	1.337	1.340	1.342	1.345	1.347	1.350	1.352	1.355	1.357
2.00	1.360	1.362	1.365	1.367	1.369	1.372	1.374	1.376	1.379	1.381
2.10	1.383	1.386	1.388	1.390	1.392	1.395	1.397	1.399	1.401	1.404
2.20	1.406	1.408	1.410	1.412	1.414	1.416	1.418	1.420	1.423	1.425
2.30	1.427	1.429	1.431	1.433	1.435	1.437	1.439	1.441	1.443	1.445
2.40	1.446	1.448	1.450	1.452	1.454	1.456	1.458	1.460	1.461	1.463
2.50	1.465	1.467	1.469	1.471	1.472	1.474	1.476	1.478	1.479	1.481
2.60	1.483	1.485	1.486	1.488	1.490	1.491	1.493	1.495	1.496	1.498
2.70	1.500	1.501	1.503	1.504	1.506	1.508	1.509	1.511	1.512	1.514
2.80	1.515	1.517	1.519	1.520	1.522	1.523	1.525	1.526	1.528	1.529
2.90	1.531	1.532	1.534	1.535	1.536	1.538	1.539	1.541	1.542	1.544
3.00	1.545	1.546	1.548	1.549	1.551	1.552	1.553	1.555	1.556	1.557
3.10	1.559	1.560	1.561	1.563	1.564	1.565	1.567	1.568	1.569	1.570

WATER CONTENT 90 PERCENT

DG	0	1	2	3	4	5	6	7	8	9
1.70	1.277	1.280	1.283	1.285	1.288	1.291	1.294	1.297	1.300	1.303
1.80	1.305	1.308	1.311	1.314	1.316	1.319	1.322	1.324	1.327	1.330
1.90	1.332	1.335	1.337	1.340	1.342	1.345	1.347	1.350	1.352	1.355
2.00	1.357	1.360	1.362	1.364	1.367	1.369	1.371	1.374	1.376	1.378
2.10	1.381	1.383	1.385	1.387	1.390	1.392	1.394	1.396	1.398	1.401
2.20	1.403	1.405	1.407	1.409	1.411	1.413	1.415	1.417	1.419	1.421
2.30	1.423	1.425	1.427	1.429	1.431	1.433	1.435	1.437	1.439	1.441
2.40	1.443	1.445	1.447	1.449	1.451	1.452	1.454	1.456	1.458	1.460
2.50	1.462	1.463	1.465	1.467	1.469	1.470	1.472	1.474	1.476	1.477
2.60	1.479	1.481	1.482	1.484	1.486	1.487	1.489	1.491	1.492	1.494
2.70	1.496	1.497	1.499	1.500	1.502	1.504	1.505	1.507	1.508	1.510
2.80	1.511	1.513	1.514	1.516	1.517	1.519	1.520	1.522	1.523	1.525
2.90	1.526	1.528	1.529	1.531	1.532	1.534	1.535	1.536	1.538	1.539
3.00	1.541	1.542	1.543	1.545	1.546	1.547	1.549	1.550	1.551	1.553
3.10	1.554	1.555	1.557	1.558	1.559	1.561	1.562	1.563	1.564	1.566

WATER CONTENT 91 PERCENT

DG	0	1	2	3	4	5	6	7	8	9
1.70	1.275	1.278	1.281	1.284	1.286	1.289	1.292	1.295	1.298	1.301
1.80	1.303	1.306	1.309	1.311	1.314	1.317	1.319	1.322	1.325	1.327
1.90	1.330	1.332	1.335	1.337	1.340	1.342	1.345	1.347	1.350	1.352
2.00	1.355	1.357	1.359	1.362	1.364	1.366	1.369	1.371	1.373	1.376
2.10	1.378	1.380	1.382	1.385	1.387	1.389	1.391	1.393	1.395	1.398
2.20	1.400	1.402	1.404	1.406	1.408	1.410	1.412	1.414	1.416	1.418
2.30	1.420	1.422	1.424	1.426	1.428	1.430	1.432	1.434	1.436	1.438
2.40	1.440	1.442	1.443	1.445	1.447	1.449	1.451	1.453	1.454	1.456
2.50	1.458	1.460	1.462	1.463	1.465	1.467	1.469	1.470	1.472	1.474
2.60	1.475	1.477	1.479	1.480	1.482	1.484	1.485	1.487	1.489	1.490
2.70	1.492	1.493	1.495	1.497	1.498	1.500	1.501	1.503	1.504	1.506
2.80	1.507	1.509	1.510	1.512	1.513	1.515	1.516	1.518	1.519	1.521
2.90	1.522	1.524	1.525	1.526	1.528	1.529	1.531	1.532	1.533	1.535
3.00	1.536	1.538	1.539	1.540	1.542	1.543	1.544	1.546	1.547	1.548
3.10	1.550	1.551	1.552	1.553	1.555	1.556	1.557	1.559	1.560	1.561

WATER CONTENT 92 PERCENT

DG	0	1	2	3	4	5	6	7	8	9
1.70	1.273	1.276	1.279	1.282	1.285	1.287	1.290	1.293	1.296	1.298
1.80	1.301	1.304	1.307	1.309	1.312	1.315	1.317	1.320	1.322	1.325
1.90	1.328	1.330	1.333	1.335	1.338	1.340	1.342	1.345	1.347	1.350
2.00	1.352	1.354	1.357	1.359	1.362	1.364	1.366	1.368	1.371	1.373
2.10	1.375	1.377	1.380	1.382	1.384	1.386	1.388	1.390	1.393	1.395
2.20	1.397	1.399	1.401	1.403	1.405	1.407	1.409	1.411	1.413	1.415
2.30	1.417	1.419	1.421	1.423	1.425	1.427	1.429	1.431	1.433	1.435
2.40	1.436	1.438	1.440	1.442	1.444	1.446	1.447	1.449	1.451	1.453
2.50	1.455	1.456	1.458	1.460	1.462	1.463	1.465	1.467	1.468	1.470
2.60	1.472	1.473	1.475	1.477	1.478	1.480	1.482	1.483	1.485	1.486
2.70	1.488	1.490	1.491	1.493	1.494	1.496	1.497	1.499	1.500	1.502
2.80	1.503	1.505	1.506	1.508	1.509	1.511	1.512	1.514	1.515	1.517
2.90	1.518	1.519	1.521	1.522	1.524	1.525	1.526	1.528	1.529	1.531
3.00	1.532	1.533	1.535	1.536	1.537	1.539	1.540	1.541	1.543	1.544
3.10	1.545	1.546	1.548	1.549	1.550	1.552	1.553	1.554	1.555	1.557

WATER CONTENT 93 PERCENT

DG	0	1	2	3	4	5	6	7	8	9
1.70	1.271	1.274	1.277	1.280	1.283	1.285	1.288	1.291	1.294	1.296
1.80	1.299	1.302	1.305	1.307	1.310	1.312	1.315	1.318	1.320	1.323
1.90	1.325	1.328	1.330	1.333	1.335	1.338	1.340	1.343	1.345	1.347
2.00	1.350	1.352	1.354	1.357	1.359	1.361	1.364	1.366	1.368	1.370
2.10	1.373	1.375	1.377	1.379	1.381	1.383	1.386	1.388	1.390	1.392
2.20	1.394	1.396	1.398	1.400	1.402	1.404	1.406	1.408	1.410	1.412
2.30	1.414	1.416	1.418	1.420	1.422	1.424	1.426	1.428	1.429	1.431
2.40	1.433	1.435	1.437	1.439	1.440	1.442	1.444	1.446	1.448	1.449
2.50	1.451	1.453	1.455	1.456	1.458	1.460	1.461	1.463	1.465	1.466
2.60	1.468	1.470	1.471	1.473	1.475	1.476	1.478	1.479	1.481	1.483
2.70	1.484	1.486	1.487	1.489	1.490	1.492	1.493	1.495	1.496	1.498
2.80	1.499	1.501	1.502	1.504	1.505	1.507	1.508	1.510	1.511	1.513
2.90	1.514	1.515	1.517	1.518	1.520	1.521	1.522	1.524	1.525	1.526
3.00	1.528	1.529	1.530	1.532	1.533	1.534	1.536	1.537	1.538	1.540
3.10	1.541	1.542	1.543	1.545	1.546	1.547	1.548	1.550	1.551	1.552

WATER CONTENT 94 PERCENT

DG	0	1	2	3	4	5	6	7	8	9
1.70	1.269	1.272	1.275	1.278	1.281	1.284	1.286	1.289	1.292	1.294
1.80	1.297	1.300	1.302	1.305	1.308	1.310	1.313	1.315	1.318	1.321
1.90	1.323	1.326	1.328	1.330	1.333	1.335	1.338	1.340	1.343	1.345
2.00	1.347	1.350	1.352	1.354	1.356	1.359	1.361	1.363	1.365	1.368
2.10	1.370	1.372	1.374	1.376	1.379	1.381	1.383	1.385	1.387	1.389
2.20	1.391	1.393	1.395	1.397	1.399	1.401	1.403	1.405	1.407	1.409
2.30	1.411	1.413	1.415	1.417	1.419	1.421	1.423	1.424	1.426	1.428
2.40	1.430	1.432	1.434	1.435	1.437	1.439	1.441	1.443	1.444	1.446
2.50	1.448	1.449	1.451	1.453	1.455	1.456	1.458	1.460	1.461	1.463
2.60	1.465	1.466	1.468	1.469	1.471	1.473	1.474	1.476	1.477	1.479
2.70	1.480	1.482	1.484	1.485	1.487	1.488	1.490	1.491	1.493	1.494
2.80	1.496	1.497	1.499	1.500	1.501	1.503	1.504	1.506	1.507	1.509
2.90	1.510	1.511	1.513	1.514	1.515	1.517	1.518	1.520	1.521	1.522
3.00	1.524	1.525	1.526	1.528	1.529	1.530	1.531	1.533	1.534	1.535
3.10	1.537	1.538	1.539	1.540	1.542	1.543	1.544	1.545	1.546	1.548

WATER CONTENT 95 PERCENT

DG	0	1	2	3	4	5	6	7	8	9
1.70	1.268	1.271	1.273	1.276	1.279	1.282	1.284	1.287	1.290	1.293
1.80	1.295	1.298	1.300	1.303	1.306	1.308	1.311	1.313	1.316	1.318
1.90	1.321	1.323	1.326	1.328	1.331	1.333	1.335	1.338	1.340	1.343
2.00	1.345	1.347	1.349	1.352	1.354	1.356	1.358	1.361	1.363	1.365
2.10	1.367	1.369	1.372	1.374	1.376	1.378	1.380	1.382	1.384	1.386
2.20	1.388	1.390	1.392	1.394	1.396	1.398	1.400	1.402	1.404	1.406
2.30	1.408	1.410	1.412	1.414	1.416	1.418	1.419	1.421	1.423	1.425
2.40	1.427	1.429	1.430	1.432	1.434	1.436	1.438	1.439	1.441	1.443
2.50	1.444	1.446	1.448	1.450	1.451	1.453	1.455	1.456	1.458	1.459
2.60	1.461	1.463	1.464	1.466	1.468	1.469	1.471	1.472	1.474	1.475
2.70	1.477	1.478	1.480	1.481	1.483	1.484	1.486	1.487	1.489	1.490
2.80	1.492	1.493	1.495	1.496	1.498	1.499	1.500	1.502	1.503	1.505
2.90	1.506	1.507	1.509	1.510	1.511	1.513	1.514	1.516	1.517	1.518
3.00	1.519	1.521	1.522	1.523	1.525	1.526	1.527	1.529	1.530	1.531
3.10	1.532	1.534	1.535	1.536	1.537	1.539	1.540	1.541	1.542	1.543

WATER CONTENT 96 PERCENT

DG	0	1	2	3	4	5	6	7	8	9
1.70	1.266	1.269	1.272	1.274	1.277	1.280	1.283	1.285	1.288	1.291
1.80	1.293	1.296	1.298	1.301	1.304	1.306	1.309	1.311	1.314	1.316
1.90	1.319	1.321	1.324	1.326	1.328	1.331	1.333	1.335	1.338	1.340
2.00	1.342	1.345	1.347	1.349	1.352	1.354	1.356	1.358	1.360	1.363
2.10	1.365	1.367	1.369	1.371	1.373	1.375	1.377	1.379	1.382	1.384
2.20	1.386	1.388	1.390	1.392	1.394	1.396	1.398	1.399	1.401	1.403
2.30	1.405	1.407	1.409	1.411	1.413	1.415	1.416	1.418	1.420	1.422
2.40	1.424	1.426	1.427	1.429	1.431	1.433	1.434	1.436	1.438	1.439
2.50	1.441	1.443	1.445	1.446	1.448	1.450	1.451	1.453	1.454	1.456
2.60	1.458	1.459	1.461	1.462	1.464	1.466	1.467	1.469	1.470	1.472
2.70	1.473	1.475	1.476	1.478	1.479	1.481	1.482	1.484	1.485	1.487
2.80	1.488	1.490	1.491	1.492	1.494	1.495	1.497	1.498	1.499	1.501
2.90	1.502	1.503	1.505	1.506	1.508	1.509	1.510	1.512	1.513	1.514
3.00	1.515	1.517	1.518	1.519	1.521	1.522	1.523	1.524	1.526	1.527
3.10	1.528	1.529	1.531	1.532	1.533	1.534	1.535	1.537	1.538	1.539

WATER CONTENT 97 PERCENT

DG	0	1	2	3	4	5	6	7	8	9
1.70	1.264	1.267	1.270	1.273	1.275	1.278	1.281	1.283	1.286	1.289
1.80	1.291	1.294	1.297	1.299	1.302	1.304	1.307	1.309	1.312	1.314
1.90	1.317	1.319	1.321	1.324	1.326	1.329	1.331	1.333	1.336	1.338
2.00	1.340	1.342	1.345	1.347	1.349	1.351	1.354	1.356	1.358	1.360
2.10	1.362	1.364	1.366	1.369	1.371	1.373	1.375	1.377	1.379	1.381
2.20	1.383	1.385	1.387	1.389	1.391	1.393	1.395	1.397	1.399	1.400
2.30	1.402	1.404	1.406	1.408	1.410	1.412	1.413	1.415	1.417	1.419
2.40	1.421	1.422	1.424	1.426	1.428	1.429	1.431	1.433	1.435	1.436
2.50	1.438	1.440	1.441	1.443	1.445	1.446	1.448	1.449	1.451	1.453
2.60	1.454	1.456	1.457	1.459	1.461	1.462	1.464	1.465	1.467	1.468
2.70	1.470	1.471	1.473	1.474	1.476	1.477	1.479	1.480	1.482	1.483
2.80	1.484	1.486	1.487	1.489	1.490	1.491	1.493	1.494	1.496	1.497
2.90	1.498	1.500	1.501	1.502	1.504	1.505	1.506	1.508	1.509	1.510
3.00	1.512	1.513	1.514	1.515	1.517	1.518	1.519	1.520	1.522	1.523
3.10	1.524	1.525	1.527	1.528	1.529	1.530	1.531	1.533	1.534	1.535

WATER CONTENT 98 PERCENT

DG	0	1	2	3	4	5	6	7	8	9
1.70	1.263	1.265	1.268	1.271	1.274	1.276	1.279	1.282	1.284	1.287
1.80	1.289	1.292	1.295	1.297	1.300	1.302	1.305	1.307	1.310	1.312
1.90	1.314	1.317	1.319	1.322	1.324	1.326	1.329	1.331	1.333	1.336
2.00	1.338	1.340	1.342	1.345	1.347	1.349	1.351	1.353	1.355	1.358
2.10	1.360	1.362	1.364	1.366	1.368	1.370	1.372	1.374	1.376	1.378
2.20	1.380	1.382	1.384	1.386	1.388	1.390	1.392	1.394	1.396	1.398
2.30	1.400	1.401	1.403	1.405	1.407	1.409	1.411	1.412	1.414	1.416
2.40	1.418	1.419	1.421	1.423	1.425	1.426	1.428	1.430	1.431	1.433
2.50	1.435	1.436	1.438	1.440	1.441	1.443	1.445	1.446	1.448	1.449
2.60	1.451	1.453	1.454	1.456	1.457	1.459	1.460	1.462	1.463	1.465
2.70	1.466	1.468	1.469	1.471	1.472	1.474	1.475	1.476	1.478	1.479
2.80	1.481	1.482	1.484	1.485	1.486	1.488	1.489	1.490	1.492	1.493
2.90	1.495	1.496	1.497	1.499	1.500	1.501	1.502	1.504	1.505	1.506
3.00	1.508	1.509	1.510	1.511	1.513	1.514	1.515	1.516	1.518	1.519
3.10	1.520	1.521	1.522	1.524	1.525	1.526	1.527	1.528	1.530	1.531

WATER CONTENT 99 PERCENT

DG	0	1	2	3	4	5	6	7	8	9
1.70	1.261	1.264	1.266	1.269	1.272	1.274	1.277	1.280	1.282	1.285
1.80	1.288	1.290	1.293	1.295	1.298	1.300	1.303	1.305	1.308	1.310
1.90	1.312	1.315	1.317	1.320	1.322	1.324	1.326	1.329	1.331	1.333
2.00	1.336	1.338	1.340	1.342	1.344	1.347	1.349	1.351	1.353	1.355
2.10	1.357	1.359	1.361	1.363	1.366	1.368	1.370	1.372	1.374	1.376
2.20	1.378	1.380	1.382	1.383	1.385	1.387	1.389	1.391	1.393	1.395
2.30	1.397	1.399	1.400	1.402	1.404	1.406	1.408	1.409	1.411	1.413
2.40	1.415	1.416	1.418	1.420	1.422	1.423	1.425	1.427	1.428	1.430
2.50	1.432	1.433	1.435	1.437	1.438	1.440	1.441	1.443	1.445	1.446
2.60	1.448	1.449	1.451	1.452	1.454	1.455	1.457	1.458	1.460	1.461
2.70	1.463	1.464	1.466	1.467	1.469	1.470	1.472	1.473	1.474	1.476
2.80	1.477	1.479	1.480	1.481	1.483	1.484	1.485	1.487	1.488	1.489
2.90	1.491	1.492	1.493	1.495	1.496	1.497	1.499	1.500	1.501	1.503
3.00	1.504	1.505	1.506	1.508	1.509	1.510	1.511	1.512	1.514	1.515
3.10	1.516	1.517	1.518	1.520	1.521	1.522	1.523	1.524	1.526	1.527

WATER CONTENT 100 PERCENT

DG	0	1	2	3	4	5	6	7	8	9
1.70	1.259	1.262	1.265	1.267	1.270	1.273	1.275	1.278	1.281	1.283
1.80	1.286	1.288	1.291	1.293	1.296	1.298	1.301	1.303	1.306	1.308
1.90	1.310	1.313	1.315	1.317	1.320	1.322	1.324	1.327	1.329	1.331
2.00	1.333	1.336	1.338	1.340	1.342	1.344	1.346	1.349	1.351	1.353
2.10	1.355	1.357	1.359	1.361	1.363	1.365	1.367	1.369	1.371	1.373
2.20	1.375	1.377	1.379	1.381	1.383	1.385	1.387	1.388	1.390	1.392
2.30	1.394	1.396	1.398	1.399	1.401	1.403	1.405	1.407	1.408	1.410
2.40	1.412	1.413	1.415	1.417	1.419	1.420	1.422	1.424	1.425	1.427
2.50	1.429	1.430	1.432	1.433	1.435	1.437	1.438	1.440	1.441	1.443
2.60	1.444	1.446	1.448	1.449	1.451	1.452	1.454	1.455	1.457	1.458
2.70	1.459	1.461	1.462	1.464	1.465	1.467	1.468	1.469	1.471	1.472
2.80	1.474	1.475	1.476	1.478	1.479	1.481	1.482	1.483	1.485	1.486
2.90	1.487	1.488	1.490	1.491	1.492	1.494	1.495	1.496	1.497	1.499
3.00	1.500	1.501	1.502	1.504	1.505	1.506	1.507	1.509	1.510	1.511
3.10	1.512	1.513	1.515	1.516	1.517	1.518	1.519	1.520	1.522	1.523

WATER CONTENT 105 PERCENT

DG	0	1	2	3	4	5	6	7	8	9
1.70	1.251	1.254	1.257	1.259	1.262	1.264	1.267	1.269	1.272	1.274
1.80	1.277	1.279	1.282	1.284	1.286	1.289	1.291	1.294	1.296	1.298
1.90	1.301	1.303	1.305	1.307	1.310	1.312	1.314	1.316	1.318	1.320
2.00	1.323	1.325	1.327	1.329	1.331	1.333	1.335	1.337	1.339	1.341
2.10	1.343	1.345	1.347	1.349	1.351	1.353	1.355	1.357	1.359	1.361
2.20	1.363	1.364	1.366	1.368	1.370	1.372	1.374	1.375	1.377	1.379
2.30	1.381	1.382	1.384	1.386	1.388	1.389	1.391	1.393	1.394	1.396
2.40	1.398	1.399	1.401	1.403	1.404	1.406	1.407	1.409	1.411	1.412
2.50	1.414	1.415	1.417	1.418	1.420	1.421	1.423	1.424	1.426	1.427
2.60	1.429	1.430	1.432	1.433	1.435	1.436	1.438	1.439	1.440	1.442
2.70	1.443	1.445	1.446	1.447	1.449	1.450	1.452	1.453	1.454	1.456
2.80	1.457	1.458	1.459	1.461	1.462	1.463	1.465	1.466	1.467	1.468
2.90	1.470	1.471	1.472	1.473	1.475	1.476	1.477	1.478	1.480	1.481
3.00	1.482	1.483	1.484	1.485	1.487	1.488	1.489	1.490	1.491	1.492
3.10	1.494	1.495	1.496	1.497	1.498	1.499	1.500	1.501	1.502	1.504

WATER CONTENT 110 PERCENT

DG	0	1	2	3	4	5	6	7	8	9
1.70	1.244	1.246	1.249	1.251	1.254	1.256	1.259	1.261	1.264	1.266
1.80	1.268	1.271	1.273	1.275	1.278	1.280	1.282	1.285	1.287	1.289
1.90	1.291	1.293	1.296	1.298	1.300	1.302	1.304	1.306	1.308	1.310
2.00	1.312	1.315	1.317	1.319	1.321	1.323	1.325	1.327	1.328	1.330
2.10	1.332	1.334	1.336	1.338	1.340	1.342	1.344	1.345	1.347	1.349
2.20	1.351	1.353	1.354	1.356	1.358	1.360	1.361	1.363	1.365	1.367
2.30	1.368	1.370	1.372	1.373	1.375	1.377	1.378	1.380	1.381	1.383
2.40	1.385	1.386	1.388	1.389	1.391	1.392	1.394	1.395	1.397	1.399
2.50	1.400	1.401	1.403	1.404	1.406	1.407	1.409	1.410	1.412	1.413
2.60	1.415	1.416	1.417	1.419	1.420	1.421	1.423	1.424	1.426	1.427
2.70	1.428	1.430	1.431	1.432	1.433	1.435	1.436	1.437	1.439	1.440
2.80	1.441	1.442	1.444	1.445	1.446	1.447	1.449	1.450	1.451	1.452
2.90	1.453	1.455	1.456	1.457	1.458	1.459	1.461	1.462	1.463	1.464
3.00	1.465	1.466	1.467	1.468	1.470	1.471	1.472	1.473	1.474	1.475
3.10	1.476	1.477	1.478	1.479	1.480	1.482	1.483	1.484	1.485	1.486

WATER CONTENT 115 PERCENT

DG	0	1	2	3	4	5	6	7	8	9
1.70	1.237	1.239	1.242	1.244	1.247	1.249	1.251	1.254	1.256	1.258
1.80	1.261	1.263	1.265	1.267	1.270	1.272	1.274	1.276	1.278	1.280
1.90	1.283	1.285	1.287	1.289	1.291	1.293	1.295	1.297	1.299	1.301
2.00	1.303	1.305	1.307	1.309	1.311	1.313	1.315	1.317	1.318	1.320
2.10	1.322	1.324	1.326	1.328	1.329	1.331	1.333	1.335	1.336	1.338
2.20	1.340	1.342	1.343	1.345	1.347	1.348	1.350	1.352	1.353	1.355
2.30	1.357	1.358	1.360	1.361	1.363	1.365	1.366	1.368	1.369	1.371
2.40	1.372	1.374	1.375	1.377	1.378	1.380	1.381	1.383	1.384	1.386
2.50	1.387	1.389	1.390	1.391	1.393	1.394	1.396	1.397	1.398	1.400
2.60	1.401	1.402	1.404	1.405	1.406	1.408	1.409	1.410	1.412	1.413
2.70	1.414	1.415	1.417	1.418	1.419	1.420	1.422	1.423	1.424	1.425
2.80	1.427	1.428	1.429	1.430	1.431	1.432	1.434	1.435	1.436	1.437
2.90	1.438	1.439	1.441	1.442	1.443	1.444	1.445	1.446	1.447	1.448
3.00	1.449	1.451	1.452	1.453	1.454	1.455	1.456	1.457	1.458	1.459
3.10	1.460	1.461	1.462	1.463	1.464	1.465	1.466	1.467	1.468	1.469

WATER CONTENT 120 PERCENT

DG	0	1	2	3	4	5	6	7	8	9
1.70	1.230	1.233	1.235	1.237	1.240	1.242	1.244	1.246	1.249	1.251
1.80	1.253	1.255	1.258	1.260	1.262	1.264	1.266	1.268	1.270	1.272
1.90	1.274	1.276	1.278	1.280	1.282	1.284	1.286	1.288	1.290	1.292
2.00	1.294	1.296	1.298	1.300	1.302	1.303	1.305	1.307	1.309	1.311
2.10	1.313	1.314	1.316	1.318	1.320	1.321	1.323	1.325	1.326	1.328
2.20	1.330	1.331	1.333	1.335	1.336	1.338	1.339	1.341	1.343	1.344
2.30	1.346	1.347	1.349	1.350	1.352	1.353	1.355	1.356	1.358	1.359
2.40	1.361	1.362	1.364	1.365	1.367	1.368	1.369	1.371	1.372	1.374
2.50	1.375	1.376	1.378	1.379	1.380	1.382	1.383	1.384	1.386	1.387
2.60	1.388	1.390	1.391	1.392	1.393	1.395	1.396	1.397	1.398	1.400
2.70	1.401	1.402	1.403	1.405	1.406	1.407	1.408	1.409	1.411	1.412
2.80	1.413	1.414	1.415	1.416	1.417	1.419	1.420	1.421	1.422	1.423
2.90	1.424	1.425	1.426	1.427	1.428	1.430	1.431	1.432	1.433	1.434
3.00	1.435	1.436	1.437	1.438	1.439	1.440	1.441	1.442	1.443	1.444
3.10	1.445	1.446	1.447	1.448	1.449	1.450	1.451	1.452	1.453	1.454

WATER CONTENT 125 PERCENT

DG	0	1	2	3	4	5	6	7	8	9
1.70	1.224	1.226	1.229	1.231	1.233	1.235	1.237	1.240	1.242	1.244
1.80	1.246	1.248	1.250	1.252	1.255	1.257	1.259	1.261	1.263	1.265
1.90	1.267	1.269	1.271	1.273	1.274	1.276	1.278	1.280	1.282	1.284
2.00	1.286	1.288	1.289	1.291	1.293	1.295	1.297	1.298	1.300	1.302
2.10	1.303	1.305	1.307	1.309	1.310	1.312	1.314	1.315	1.317	1.318
2.20	1.320	1.322	1.323	1.325	1.326	1.328	1.329	1.331	1.332	1.334
2.30	1.335	1.337	1.338	1.340	1.341	1.343	1.344	1.346	1.347	1.349
2.40	1.350	1.351	1.353	1.354	1.356	1.357	1.358	1.360	1.361	1.362
2.50	1.364	1.365	1.366	1.368	1.369	1.370	1.371	1.373	1.374	1.375
2.60	1.376	1.378	1.379	1.380	1.381	1.383	1.384	1.385	1.386	1.387
2.70	1.389	1.390	1.391	1.392	1.393	1.394	1.396	1.397	1.398	1.399
2.80	1.400	1.401	1.402	1.403	1.404	1.405	1.407	1.408	1.409	1.410
2.90	1.411	1.412	1.413	1.414	1.415	1.416	1.417	1.418	1.419	1.420
3.00	1.421	1.422	1.423	1.424	1.425	1.426	1.427	1.428	1.429	1.430
3.10	1.431	1.432	1.433	1.434	1.435	1.435	1.436	1.437	1.438	1.439

WATER CONTENT 130 PERCENT

DG	0	1	2	3	4	5	6	7	8	9
1.70	1.218	1.220	1.222	1.225	1.227	1.229	1.231	1.233	1.235	1.237
1.80	1.240	1.242	1.244	1.246	1.248	1.250	1.252	1.254	1.256	1.257
1.90	1.259	1.261	1.263	1.265	1.267	1.269	1.271	1.272	1.274	1.276
2.00	1.278	1.280	1.281	1.283	1.285	1.286	1.288	1.290	1.292	1.293
2.10	1.295	1.297	1.298	1.300	1.301	1.303	1.305	1.306	1.308	1.309
2.20	1.311	1.312	1.314	1.315	1.317	1.318	1.320	1.321	1.323	1.324
2.30	1.326	1.327	1.329	1.330	1.332	1.333	1.334	1.336	1.337	1.338
2.40	1.340	1.341	1.342	1.344	1.345	1.346	1.348	1.349	1.350	1.352
2.50	1.353	1.354	1.355	1.357	1.358	1.359	1.360	1.362	1.363	1.364
2.60	1.365	1.366	1.368	1.369	1.370	1.371	1.372	1.374	1.375	1.376
2.70	1.377	1.378	1.379	1.380	1.381	1.383	1.384	1.385	1.386	1.387
2.80	1.388	1.389	1.390	1.391	1.392	1.393	1.394	1.395	1.396	1.397
2.90	1.398	1.399	1.400	1.401	1.402	1.403	1.404	1.405	1.406	1.407
3.00	1.408	1.409	1.410	1.411	1.412	1.413	1.414	1.415	1.416	1.417
3.10	1.417	1.418	1.419	1.420	1.421	1.422	1.423	1.424	1.425	1.425

WATER CONTENT 135 PERCENT

DG	0	1	2	3	4	5	6	7	8	9
1.70	1.212	1.215	1.217	1.219	1.221	1.223	1.225	1.227	1.229	1.231
1.80	1.233	1.235	1.237	1.239	1.241	1.243	1.245	1.247	1.249	1.251
1.90	1.252	1.254	1.256	1.258	1.260	1.262	1.263	1.265	1.267	1.269
2.00	1.270	1.272	1.274	1.275	1.277	1.279	1.280	1.282	1.284	1.285
2.10	1.287	1.288	1.290	1.292	1.293	1.295	1.296	1.298	1.299	1.301
2.20	1.302	1.304	1.305	1.307	1.308	1.310	1.311	1.312	1.314	1.315
2.30	1.317	1.318	1.319	1.321	1.322	1.324	1.325	1.326	1.328	1.329
2.40	1.330	1.331	1.333	1.334	1.335	1.337	1.338	1.339	1.340	1.342
2.50	1.343	1.344	1.345	1.347	1.348	1.349	1.350	1.351	1.352	1.354
2.60	1.355	1.356	1.357	1.358	1.359	1.360	1.362	1.363	1.364	1.365
2.70	1.366	1.367	1.368	1.369	1.370	1.371	1.372	1.373	1.374	1.376
2.80	1.377	1.378	1.379	1.380	1.381	1.382	1.383	1.384	1.385	1.386
2.90	1.387	1.388	1.389	1.389	1.390	1.391	1.392	1.393	1.394	1.395
3.00	1.396	1.397	1.398	1.399	1.400	1.401	1.401	1.402	1.403	1.404
3.10	1.405	1.406	1.407	1.408	1.408	1.409	1.410	1.411	1.412	1.413

WATER CONTENT 140 PERCENT

DG	0	1	2	3	4	5	6	7	8	9
1.70	1.207	1.209	1.211	1.213	1.215	1.217	1.219	1.221	1.223	1.225
1.80	1.227	1.229	1.231	1.233	1.235	1.237	1.239	1.240	1.242	1.244
1.90	1.246	1.248	1.249	1.251	1.253	1.255	1.256	1.258	1.260	1.261
2.00	1.263	1.265	1.266	1.268	1.270	1.271	1.273	1.274	1.276	1.278
2.10	1.279	1.281	1.282	1.284	1.285	1.287	1.288	1.290	1.291	1.293
2.20	1.294	1.296	1.297	1.298	1.300	1.301	1.303	1.304	1.305	1.307
2.30	1.308	1.309	1.311	1.312	1.313	1.315	1.316	1.317	1.319	1.320
2.40	1.321	1.322	1.324	1.325	1.326	1.327	1.329	1.330	1.331	1.332
2.50	1.333	1.335	1.336	1.337	1.338	1.339	1.340	1.341	1.343	1.344
2.60	1.345	1.346	1.347	1.348	1.349	1.350	1.351	1.352	1.354	1.355
2.70	1.356	1.357	1.358	1.359	1.360	1.361	1.362	1.363	1.364	1.365
2.80	1.366	1.367	1.368	1.369	1.370	1.371	1.372	1.373	1.374	1.375
2.90	1.375	1.376	1.377	1.378	1.379	1.380	1.381	1.382	1.383	1.384
3.00	1.385	1.385	1.386	1.387	1.388	1.389	1.390	1.391	1.392	1.392
3.10	1.393	1.394	1.395	1.396	1.397	1.397	1.398	1.399	1.400	1.401

WATER CONTENT 145 PERCENT

DG	0	1	2	3	4	5	6	7	8	9
1.70	1.202	1.204	1.206	1.208	1.210	1.212	1.214	1.216	1.218	1.220
1.80	1.222	1.223	1.225	1.227	1.229	1.231	1.233	1.234	1.236	1.238
1.90	1.240	1.241	1.243	1.245	1.247	1.248	1.250	1.252	1.253	1.255
2.00	1.256	1.258	1.260	1.261	1.263	1.264	1.266	1.267	1.269	1.270
2.10	1.272	1.273	1.275	1.276	1.278	1.279	1.281	1.282	1.284	1.285
2.20	1.286	1.288	1.289	1.291	1.292	1.293	1.295	1.296	1.297	1.299
2.30	1.300	1.301	1.302	1.304	1.305	1.306	1.308	1.309	1.310	1.311
2.40	1.312	1.314	1.315	1.316	1.317	1.319	1.320	1.321	1.322	1.323
2.50	1.324	1.325	1.327	1.328	1.329	1.330	1.331	1.332	1.333	1.334
2.60	1.335	1.337	1.338	1.339	1.340	1.341	1.342	1.343	1.344	1.345
2.70	1.346	1.347	1.348	1.349	1.350	1.351	1.352	1.353	1.354	1.355
2.80	1.356	1.357	1.358	1.359	1.360	1.360	1.361	1.362	1.363	1.364
2.90	1.365	1.366	1.367	1.368	1.369	1.369	1.370	1.371	1.372	1.373
3.00	1.374	1.375	1.376	1.376	1.377	1.378	1.379	1.380	1.381	1.381
3.10	1.382	1.383	1.384	1.385	1.385	1.386	1.387	1.388	1.389	1.389

WATER CONTENT 150 PERCENT

DG	0	1	2	3	4	5	6	7	8	9
1.70	1.197	1.199	1.201	1.203	1.205	1.207	1.209	1.211	1.213	1.214
1.80	1.216	1.218	1.220	1.222	1.223	1.225	1.227	1.229	1.230	1.232
1.90	1.234	1.235	1.237	1.239	1.240	1.242	1.244	1.245	1.247	1.248
2.00	1.250	1.252	1.253	1.255	1.256	1.258	1.259	1.261	1.262	1.264
2.10	1.265	1.267	1.268	1.269	1.271	1.272	1.274	1.275	1.276	1.278
2.20	1.279	1.280	1.282	1.283	1.284	1.286	1.287	1.288	1.290	1.291
2.30	1.292	1.293	1.295	1.296	1.297	1.298	1.300	1.301	1.302	1.303
2.40	1.304	1.306	1.307	1.308	1.309	1.310	1.311	1.312	1.314	1.315
2.50	1.316	1.317	1.318	1.319	1.320	1.321	1.322	1.323	1.324	1.325
2.60	1.327	1.328	1.329	1.330	1.331	1.332	1.333	1.334	1.335	1.336
2.70	1.337	1.338	1.339	1.340	1.341	1.341	1.342	1.343	1.344	1.345
2.80	1.346	1.347	1.348	1.349	1.350	1.351	1.352	1.352	1.353	1.354
2.90	1.355	1.356	1.357	1.358	1.359	1.359	1.360	1.361	1.362	1.363
3.00	1.364	1.364	1.365	1.366	1.367	1.368	1.369	1.369	1.370	1.371
3.10	1.372	1.372	1.373	1.374	1.375	1.376	1.376	1.377	1.378	1.379

WATER CONTENT 155 PERCENT

DG	0	1	2	3	4	5	6	7	8	9
1.70	1.193	1.194	1.196	1.198	1.200	1.202	1.204	1.206	1.208	1.209
1.80	1.211	1.213	1.215	1.216	1.218	1.220	1.221	1.223	1.225	1.226
1.90	1.228	1.230	1.231	1.233	1.235	1.236	1.238	1.239	1.241	1.242
2.00	1.244	1.245	1.247	1.248	1.250	1.251	1.253	1.254	1.256	1.257
2.10	1.259	1.260	1.261	1.263	1.264	1.265	1.267	1.268	1.269	1.271
2.20	1.272	1.273	1.275	1.276	1.277	1.279	1.280	1.281	1.282	1.284
2.30	1.285	1.286	1.287	1.288	1.290	1.291	1.292	1.293	1.294	1.295
2.40	1.297	1.298	1.299	1.300	1.301	1.302	1.303	1.304	1.306	1.307
2.50	1.308	1.309	1.310	1.311	1.312	1.313	1.314	1.315	1.316	1.317
2.60	1.318	1.319	1.320	1.321	1.322	1.323	1.324	1.325	1.326	1.327
2.70	1.328	1.329	1.330	1.331	1.332	1.333	1.333	1.334	1.335	1.336
2.80	1.337	1.338	1.339	1.340	1.341	1.341	1.342	1.343	1.344	1.345
2.90	1.346	1.347	1.347	1.348	1.349	1.350	1.351	1.352	1.352	1.353
3.00	1.354	1.355	1.356	1.356	1.357	1.358	1.359	1.359	1.360	1.361
3.10	1.362	1.363	1.363	1.364	1.365	1.365	1.366	1.367	1.368	1.368

WATER CONTENT 160 PERCENT

DG	0	1	2	3	4	5	6	7	8	9
1.70	1.188	1.190	1.192	1.194	1.196	1.197	1.199	1.201	1.203	1.204
1.80	1.206	1.208	1.210	1.211	1.213	1.215	1.216	1.218	1.220	1.221
1.90	1.223	1.224	1.226	1.227	1.229	1.231	1.232	1.234	1.235	1.237
2.00	1.238	1.240	1.241	1.242	1.244	1.245	1.247	1.248	1.250	1.251
2.10	1.252	1.254	1.255	1.256	1.258	1.259	1.260	1.262	1.263	1.264
2.20	1.265	1.267	1.268	1.269	1.271	1.272	1.273	1.274	1.275	1.277
2.30	1.278	1.279	1.280	1.281	1.282	1.284	1.285	1.286	1.287	1.288
2.40	1.289	1.290	1.291	1.293	1.294	1.295	1.296	1.297	1.298	1.299
2.50	1.300	1.301	1.302	1.303	1.304	1.305	1.306	1.307	1.308	1.309
2.60	1.310	1.311	1.312	1.313	1.314	1.315	1.316	1.317	1.318	1.319
2.70	1.320	1.320	1.321	1.322	1.323	1.324	1.325	1.326	1.327	1.328
2.80	1.328	1.329	1.330	1.331	1.332	1.333	1.334	1.334	1.335	1.336
2.90	1.337	1.338	1.339	1.339	1.340	1.341	1.342	1.342	1.343	1.344
3.00	1.345	1.346	1.346	1.347	1.348	1.349	1.349	1.350	1.351	1.352
3.10	1.352	1.353	1.354	1.355	1.355	1.356	1.357	1.357	1.358	1.359

WATER CONTENT 165 PERCENT

DG	0	1	2	3	4	5	6	7	8	9
1.70	1.184	1.186	1.188	1.189	1.191	1.193	1.195	1.196	1.198	1.200
1.80	1.202	1.203	1.205	1.206	1.208	1.210	1.211	1.213	1.215	1.216
1.90	1.218	1.219	1.221	1.222	1.224	1.225	1.227	1.228	1.230	1.231
2.00	1.233	1.234	1.235	1.237	1.238	1.240	1.241	1.242	1.244	1.245
2.10	1.246	1.248	1.249	1.250	1.252	1.253	1.254	1.255	1.257	1.258
2.20	1.259	1.260	1.262	1.263	1.264	1.265	1.266	1.268	1.269	1.270
2.30	1.271	1.272	1.273	1.275	1.276	1.277	1.278	1.279	1.280	1.281
2.40	1.282	1.283	1.284	1.285	1.287	1.288	1.289	1.290	1.291	1.292
2.50	1.293	1.294	1.295	1.296	1.297	1.298	1.299	1.300	1.301	1.302
2.60	1.302	1.303	1.304	1.305	1.306	1.307	1.308	1.309	1.310	1.311
2.70	1.312	1.313	1.313	1.314	1.315	1.316	1.317	1.318	1.319	1.319
2.80	1.320	1.321	1.322	1.323	1.324	1.324	1.325	1.326	1.327	1.328
2.90	1.328	1.329	1.330	1.331	1.332	1.332	1.333	1.334	1.335	1.335
3.00	1.336	1.337	1.338	1.338	1.339	1.340	1.341	1.341	1.342	1.343
3.10	1.343	1.344	1.345	1.346	1.346	1.347	1.348	1.348	1.349	1.350

WATER CONTENT 170 PERCENT

DG	0	1	2	3	4	5	6	7	8	9
1.70	1.180	1.182	1.183	1.185	1.187	1.189	1.190	1.192	1.194	1.195
1.80	1.197	1.199	1.200	1.202	1.203	1.205	1.207	1.208	1.210	1.211
1.90	1.213	1.214	1.216	1.217	1.219	1.220	1.222	1.223	1.224	1.226
2.00	1.227	1.229	1.230	1.231	1.233	1.234	1.235	1.237	1.238	1.239
2.10	1.241	1.242	1.243	1.245	1.246	1.247	1.248	1.250	1.251	1.252
2.20	1.253	1.254	1.256	1.257	1.258	1.259	1.260	1.261	1.263	1.264
2.30	1.265	1.266	1.267	1.268	1.269	1.270	1.271	1.272	1.273	1.275
2.40	1.276	1.277	1.278	1.279	1.280	1.281	1.282	1.283	1.284	1.285
2.50	1.286	1.287	1.288	1.289	1.290	1.291	1.291	1.292	1.293	1.294
2.60	1.295	1.296	1.297	1.298	1.299	1.300	1.301	1.301	1.302	1.303
2.70	1.304	1.305	1.306	1.307	1.308	1.308	1.309	1.310	1.311	1.312
2.80	1.312	1.313	1.314	1.315	1.316	1.317	1.317	1.318	1.319	1.320
2.90	1.320	1.321	1.322	1.323	1.323	1.324	1.325	1.326	1.326	1.327
3.00	1.328	1.329	1.329	1.330	1.331	1.331	1.332	1.333	1.334	1.334
3.10	1.335	1.336	1.336	1.337	1.338	1.338	1.339	1.340	1.340	1.341

WATER CONTENT 175 PERCENT

DG	0	1	2	3	4	5	6	7	8	9
1.70	1.176	1.178	1.180	1.181	1.183	1.185	1.186	1.188	1.190	1.191
1.80	1.193	1.194	1.196	1.198	1.199	1.201	1.202	1.204	1.205	1.207
1.90	1.208	1.210	1.211	1.212	1.214	1.215	1.217	1.218	1.219	1.221
2.00	1.222	1.224	1.225	1.226	1.228	1.229	1.230	1.231	1.233	1.234
2.10	1.235	1.237	1.238	1.239	1.240	1.241	1.243	1.244	1.245	1.246
2.20	1.247	1.249	1.250	1.251	1.252	1.253	1.254	1.255	1.257	1.258
2.30	1.259	1.260	1.261	1.262	1.263	1.264	1.265	1.266	1.267	1.268
2.40	1.269	1.270	1.271	1.272	1.273	1.274	1.275	1.276	1.277	1.278
2.50	1.279	1.280	1.281	1.282	1.283	1.284	1.285	1.286	1.286	1.287
2.60	1.288	1.289	1.290	1.291	1.292	1.293	1.294	1.294	1.295	1.296
2.70	1.297	1.298	1.299	1.299	1.300	1.301	1.302	1.303	1.303	1.304
2.80	1.305	1.306	1.307	1.307	1.308	1.309	1.310	1.311	1.311	1.312
2.90	1.313	1.313	1.314	1.315	1.316	1.316	1.317	1.318	1.319	1.319
3.00	1.320	1.321	1.321	1.322	1.323	1.323	1.324	1.325	1.326	1.326
3.10	1.327	1.328	1.328	1.329	1.329	1.330	1.331	1.331	1.332	1.333

WATER CONTENT 180 PERCENT

DG	0	1	2	3	4	5	6	7	8	9
1.70	1.172	1.174	1.176	1.177	1.179	1.181	1.182	1.184	1.186	1.187
1.80	1.189	1.190	1.192	1.193	1.195	1.196	1.198	1.199	1.201	1.202
1.90	1.204	1.205	1.206	1.208	1.209	1.211	1.212	1.213	1.215	1.216
2.00	1.217	1.219	1.220	1.221	1.223	1.224	1.225	1.226	1.228	1.229
2.10	1.230	1.231	1.233	1.234	1.235	1.236	1.237	1.238	1.240	1.241
2.20	1.242	1.243	1.244	1.245	1.246	1.248	1.249	1.250	1.251	1.252
2.30	1.253	1.254	1.255	1.256	1.257	1.258	1.259	1.260	1.261	1.262
2.40	1.263	1.264	1.265	1.266	1.267	1.268	1.269	1.270	1.271	1.272
2.50	1.273	1.274	1.275	1.275	1.276	1.277	1.278	1.279	1.280	1.281
2.60	1.282	1.283	1.283	1.284	1.285	1.286	1.287	1.288	1.288	1.289
2.70	1.290	1.291	1.292	1.293	1.293	1.294	1.295	1.296	1.296	1.297
2.80	1.298	1.299	1.300	1.300	1.301	1.302	1.303	1.303	1.304	1.305
2.90	1.305	1.306	1.307	1.308	1.308	1.309	1.310	1.310	1.311	1.312
3.00	1.312	1.313	1.314	1.315	1.315	1.316	1.317	1.317	1.318	1.318
3.10	1.319	1.320	1.320	1.321	1.322	1.322	1.323	1.324	1.324	1.325

WATER CONTENT 185 PERCENT

DG	0	1	2	3	4	5	6	7	8	9
1.70	1.169	1.171	1.172	1.174	1.175	1.177	1.179	1.180	1.182	1.183
1.80	1.185	1.186	1.188	1.189	1.191	1.192	1.194	1.195	1.197	1.198
1.90	1.199	1.201	1.202	1.203	1.205	1.206	1.208	1.209	1.210	1.211
2.00	1.213	1.214	1.215	1.217	1.218	1.219	1.220	1.222	1.223	1.224
2.10	1.225	1.226	1.228	1.229	1.230	1.231	1.232	1.233	1.234	1.236
2.20	1.237	1.238	1.239	1.240	1.241	1.242	1.243	1.244	1.245	1.246
2.30	1.247	1.248	1.249	1.250	1.251	1.252	1.253	1.254	1.255	1.256
2.40	1.257	1.258	1.259	1.260	1.261	1.262	1.263	1.264	1.265	1.266
2.50	1.267	1.268	1.268	1.269	1.270	1.271	1.272	1.273	1.274	1.275
2.60	1.275	1.276	1.277	1.278	1.279	1.280	1.280	1.281	1.282	1.283
2.70	1.284	1.284	1.285	1.286	1.287	1.287	1.288	1.289	1.290	1.291
2.80	1.291	1.292	1.293	1.293	1.294	1.295	1.296	1.296	1.297	1.298
2.90	1.299	1.299	1.300	1.301	1.301	1.302	1.303	1.303	1.304	1.305
3.00	1.305	1.306	1.307	1.307	1.308	1.309	1.309	1.310	1.311	1.311
3.10	1.312	1.312	1.313	1.314	1.314	1.315	1.316	1.316	1.317	1.317

WATER CONTENT 190 PERCENT

DG	0	1	2	3	4	5	6	7	8	9
1.70	1.165	1.167	1.169	1.170	1.172	1.173	1.175	1.176	1.178	1.180
1.80	1.181	1.182	1.184	1.185	1.187	1.188	1.190	1.191	1.192	1.194
1.90	1.195	1.197	1.198	1.199	1.201	1.202	1.203	1.205	1.206	1.207
2.00	1.208	1.210	1.211	1.212	1.213	1.215	1.216	1.217	1.218	1.219
2.10	1.220	1.222	1.223	1.224	1.225	1.226	1.227	1.228	1.229	1.231
2.20	1.232	1.233	1.234	1.235	1.236	1.237	1.238	1.239	1.240	1.241
2.30	1.242	1.243	1.244	1.245	1.246	1.247	1.248	1.249	1.250	1.251
2.40	1.252	1.253	1.254	1.255	1.255	1.256	1.257	1.258	1.259	1.260
2.50	1.261	1.262	1.263	1.263	1.264	1.265	1.266	1.267	1.268	1.269
2.60	1.269	1.270	1.271	1.272	1.273	1.273	1.274	1.275	1.276	1.277
2.70	1.277	1.278	1.279	1.280	1.280	1.281	1.282	1.283	1.283	1.284
2.80	1.285	1.286	1.286	1.287	1.288	1.288	1.289	1.290	1.290	1.291
2.90	1.292	1.293	1.293	1.294	1.295	1.295	1.296	1.297	1.297	1.298
3.00	1.299	1.299	1.300	1.300	1.301	1.302	1.302	1.303	1.304	1.304
3.10	1.305	1.305	1.306	1.307	1.307	1.308	1.308	1.309	1.310	1.310

WATER CONTENT 195 PERCENT

DG	0	1	2	3	4	5	6	7	8	9
1.70	1.162	1.164	1.165	1.167	1.168	1.170	1.171	1.173	1.174	1.176
1.80	1.177	1.179	1.180	1.182	1.183	1.184	1.186	1.187	1.189	1.190
1.90	1.191	1.193	1.194	1.195	1.197	1.198	1.199	1.200	1.202	1.203
2.00	1.204	1.205	1.207	1.208	1.209	1.210	1.211	1.212	1.214	1.215
2.10	1.216	1.217	1.218	1.219	1.220	1.221	1.223	1.224	1.225	1.226
2.20	1.227	1.228	1.229	1.230	1.231	1.232	1.233	1.234	1.235	1.236
2.30	1.237	1.238	1.239	1.240	1.241	1.242	1.243	1.244	1.245	1.246
2.40	1.246	1.247	1.248	1.249	1.250	1.251	1.252	1.253	1.254	1.254
2.50	1.255	1.256	1.257	1.258	1.259	1.260	1.260	1.261	1.262	1.263
2.60	1.264	1.264	1.265	1.266	1.267	1.268	1.268	1.269	1.270	1.271
2.70	1.271	1.272	1.273	1.274	1.274	1.275	1.276	1.276	1.277	1.278
2.80	1.279	1.279	1.280	1.281	1.281	1.282	1.283	1.283	1.284	1.285
2.90	1.285	1.286	1.287	1.287	1.288	1.289	1.289	1.290	1.291	1.291
3.00	1.292	1.293	1.293	1.294	1.294	1.295	1.296	1.296	1.297	1.297
3.10	1.298	1.299	1.299	1.300	1.300	1.301	1.302	1.302	1.303	1.303

WATER CONTENT 200 PERCENT

DG	0	1	2	3	4	5	6	7	8	9
1.70	1.159	1.161	1.162	1.164	1.165	1.167	1.168	1.170	1.171	1.172
1.80	1.174	1.175	1.177	1.178	1.179	1.181	1.182	1.184	1.185	1.186
1.90	1.188	1.189	1.190	1.191	1.193	1.194	1.195	1.196	1.198	1.199
2.00	1.200	1.201	1.202	1.204	1.205	1.206	1.207	1.208	1.209	1.210
2.10	1.212	1.213	1.214	1.215	1.216	1.217	1.218	1.219	1.220	1.221
2.20	1.222	1.223	1.224	1.225	1.226	1.227	1.228	1.229	1.230	1.231
2.30	1.232	1.233	1.234	1.235	1.236	1.237	1.238	1.239	1.240	1.240
2.40	1.241	1.242	1.243	1.244	1.245	1.246	1.247	1.247	1.248	1.249
2.50	1.250	1.251	1.252	1.252	1.253	1.254	1.255	1.256	1.256	1.257
2.60	1.258	1.259	1.260	1.260	1.261	1.262	1.263	1.263	1.264	1.265
2.70	1.266	1.266	1.267	1.268	1.269	1.269	1.270	1.271	1.271	1.272
2.80	1.273	1.273	1.274	1.275	1.275	1.276	1.277	1.277	1.278	1.279
2.90	1.279	1.280	1.281	1.281	1.282	1.283	1.283	1.284	1.284	1.285
3.00	1.286	1.286	1.287	1.288	1.288	1.289	1.289	1.290	1.291	1.291
3.10	1.292	1.292	1.293	1.293	1.294	1.295	1.295	1.296	1.296	1.297

WATER CONTENT 210 PERCENT

DG	0	1	2	3	4	5	6	7	8	9
1.70	1.153	1.155	1.156	1.158	1.159	1.160	1.162	1.163	1.165	1.166
1.80	1.167	1.169	1.170	1.171	1.173	1.174	1.175	1.177	1.178	1.179
1.90	1.180	1.182	1.183	1.184	1.185	1.186	1.188	1.189	1.190	1.191
2.00	1.192	1.193	1.195	1.196	1.197	1.198	1.199	1.200	1.201	1.202
2.10	1.203	1.204	1.205	1.206	1.207	1.209	1.210	1.211	1.212	1.213
2.20	1.214	1.215	1.215	1.216	1.217	1.218	1.219	1.220	1.221	1.222
2.30	1.223	1.224	1.225	1.226	1.227	1.227	1.228	1.229	1.230	1.231
2.40	1.232	1.233	1.233	1.234	1.235	1.236	1.237	1.238	1.238	1.239
2.50	1.240	1.241	1.242	1.242	1.243	1.244	1.245	1.245	1.246	1.247
2.60	1.248	1.248	1.249	1.250	1.251	1.251	1.252	1.253	1.253	1.254
2.70	1.255	1.256	1.256	1.257	1.258	1.258	1.259	1.260	1.260	1.261
2.80	1.262	1.262	1.263	1.264	1.264	1.265	1.265	1.266	1.267	1.267
2.90	1.268	1.269	1.269	1.270	1.270	1.271	1.272	1.272	1.273	1.273
3.00	1.274	1.275	1.275	1.276	1.276	1.277	1.277	1.278	1.279	1.279
3.10	1.280	1.280	1.281	1.281	1.282	1.282	1.283	1.283	1.284	1.284

WATER CONTENT 220 PERCENT

DG	0	1	2	3	4	5	6	7	8	9
1.70	1.148	1.149	1.151	1.152	1.153	1.155	1.156	1.157	1.159	1.160
1.80	1.161	1.163	1.164	1.165	1.166	1.168	1.169	1.170	1.171	1.173
1.90	1.174	1.175	1.176	1.177	1.178	1.180	1.181	1.182	1.183	1.184
2.00	1.185	1.186	1.187	1.188	1.190	1.191	1.192	1.193	1.194	1.195
2.10	1.196	1.197	1.198	1.199	1.200	1.201	1.202	1.203	1.204	1.205
2.20	1.205	1.206	1.207	1.208	1.209	1.210	1.211	1.212	1.213	1.214
2.30	1.215	1.215	1.216	1.217	1.218	1.219	1.220	1.220	1.221	1.222
2.40	1.223	1.224	1.225	1.225	1.226	1.227	1.228	1.228	1.229	1.230
2.50	1.231	1.232	1.232	1.233	1.234	1.234	1.235	1.236	1.237	1.237
2.60	1.238	1.239	1.240	1.240	1.241	1.242	1.242	1.243	1.244	1.244
2.70	1.245	1.246	1.246	1.247	1.248	1.248	1.249	1.250	1.250	1.251
2.80	1.251	1.252	1.253	1.253	1.254	1.254	1.255	1.256	1.256	1.257
2.90	1.257	1.258	1.259	1.259	1.260	1.260	1.261	1.261	1.262	1.263
3.00	1.263	1.264	1.264	1.265	1.265	1.266	1.266	1.267	1.267	1.268
3.10	1.269	1.269	1.270	1.270	1.271	1.271	1.272	1.272	1.273	1.273

WATER CONTENT 230 PERCENT

DG	0	1	2	3	4	5	6	7	8	9
1.70	1.143	1.144	1.145	1.147	1.148	1.149	1.151	1.152	1.153	1.154
1.80	1.156	1.157	1.158	1.159	1.161	1.162	1.163	1.164	1.165	1.166
1.90	1.168	1.169	1.170	1.171	1.172	1.173	1.174	1.175	1.176	1.178
2.00	1.179	1.180	1.181	1.182	1.183	1.184	1.185	1.186	1.187	1.188
2.10	1.189	1.190	1.191	1.192	1.193	1.193	1.194	1.195	1.196	1.197
2.20	1.198	1.199	1.200	1.201	1.202	1.202	1.203	1.204	1.205	1.206
2.30	1.207	1.208	1.208	1.209	1.210	1.211	1.212	1.212	1.213	1.214
2.40	1.215	1.215	1.216	1.217	1.218	1.219	1.219	1.220	1.221	1.221
2.50	1.222	1.223	1.224	1.224	1.225	1.226	1.226	1.227	1.228	1.229
2.60	1.229	1.230	1.231	1.231	1.232	1.233	1.233	1.234	1.235	1.235
2.70	1.236	1.236	1.237	1.238	1.238	1.239	1.240	1.240	1.241	1.241
2.80	1.242	1.243	1.243	1.244	1.244	1.245	1.245	1.246	1.247	1.247
2.90	1.248	1.248	1.249	1.249	1.250	1.250	1.251	1.252	1.252	1.253
3.00	1.253	1.254	1.254	1.255	1.255	1.256	1.256	1.257	1.257	1.258
3.10	1.258	1.259	1.259	1.260	1.260	1.261	1.261	1.262	1.262	1.263

WATER CONTENT 240 PERCENT

DG	0	1	2	3	4	5	6	7	8	9
1.70	1.138	1.139	1.140	1.142	1.143	1.144	1.145	1.147	1.148	1.149
1.80	1.150	1.152	1.153	1.154	1.155	1.156	1.157	1.159	1.160	1.161
1.90	1.162	1.163	1.164	1.165	1.166	1.167	1.168	1.169	1.170	1.171
2.00	1.172	1.173	1.174	1.175	1.176	1.177	1.178	1.179	1.180	1.181
2.10	1.182	1.183	1.184	1.185	1.186	1.187	1.188	1.188	1.189	1.190
2.20	1.191	1.192	1.193	1.194	1.194	1.195	1.196	1.197	1.198	1.199
2.30	1.199	1.200	1.201	1.202	1.203	1.203	1.204	1.205	1.206	1.206
2.40	1.207	1.208	1.209	1.209	1.210	1.211	1.211	1.212	1.213	1.214
2.50	1.214	1.215	1.216	1.216	1.217	1.218	1.218	1.219	1.220	1.220
2.60	1.221	1.222	1.222	1.223	1.224	1.224	1.225	1.225	1.226	1.227
2.70	1.227	1.228	1.228	1.229	1.230	1.230	1.231	1.231	1.232	1.233
2.80	1.233	1.234	1.234	1.235	1.235	1.236	1.237	1.237	1.238	1.238
2.90	1.239	1.239	1.240	1.240	1.241	1.241	1.242	1.242	1.243	1.243
3.00	1.244	1.244	1.245	1.245	1.246	1.246	1.247	1.247	1.248	1.248
3.10	1.249	1.249	1.250	1.250	1.251	1.251	1.252	1.252	1.253	1.253

WATER CONTENT 250 PERCENT

DG	0	1	2	3	4	5	6	7	8	9
1.70	1.133	1.135	1.136	1.137	1.138	1.140	1.141	1.142	1.143	1.144
1.80	1.145	1.147	1.148	1.149	1.150	1.151	1.152	1.153	1.154	1.155
1.90	1.157	1.158	1.159	1.160	1.161	1.162	1.163	1.164	1.165	1.166
2.00	1.167	1.168	1.169	1.170	1.170	1.171	1.172	1.173	1.174	1.175
2.10	1.176	1.177	1.178	1.179	1.180	1.180	1.181	1.182	1.183	1.184
2.20	1.185	1.185	1.186	1.187	1.188	1.189	1.189	1.190	1.191	1.192
2.30	1.193	1.193	1.194	1.195	1.196	1.196	1.197	1.198	1.199	1.199
2.40	1.200	1.201	1.201	1.202	1.203	1.204	1.204	1.205	1.206	1.206
2.50	1.207	1.208	1.208	1.209	1.210	1.210	1.211	1.211	1.212	1.213
2.60	1.213	1.214	1.215	1.215	1.216	1.216	1.217	1.218	1.218	1.219
2.70	1.219	1.220	1.221	1.221	1.222	1.222	1.223	1.223	1.224	1.224
2.80	1.225	1.226	1.226	1.227	1.227	1.228	1.228	1.229	1.229	1.230
2.90	1.230	1.231	1.231	1.232	1.232	1.233	1.233	1.234	1.234	1.235
3.00	1.235	1.236	1.236	1.237	1.237	1.238	1.238	1.239	1.239	1.240
3.10	1.240	1.240	1.241	1.241	1.242	1.242	1.243	1.243	1.244	1.244

WATER CONTENT 260 PERCENT

DG	0	1	2	3	4	5	6	7	8	9
1.70	1.129	1.130	1.132	1.133	1.134	1.135	1.136	1.137	1.139	1.140
1.80	1.141	1.142	1.143	1.144	1.145	1.146	1.147	1.148	1.149	1.150
1.90	1.152	1.153	1.154	1.155	1.156	1.157	1.157	1.158	1.159	1.160
2.00	1.161	1.162	1.163	1.164	1.165	1.166	1.167	1.168	1.169	1.169
2.10	1.170	1.171	1.172	1.173	1.174	1.175	1.175	1.176	1.177	1.178
2.20	1.179	1.179	1.180	1.181	1.182	1.182	1.183	1.184	1.185	1.186
2.30	1.186	1.187	1.188	1.188	1.189	1.190	1.191	1.191	1.192	1.193
2.40	1.193	1.194	1.195	1.195	1.196	1.197	1.197	1.198	1.199	1.199
2.50	1.200	1.201	1.201	1.202	1.203	1.203	1.204	1.204	1.205	1.206
2.60	1.206	1.207	1.207	1.208	1.209	1.209	1.210	1.210	1.211	1.211
2.70	1.212	1.213	1.213	1.214	1.214	1.215	1.215	1.216	1.216	1.217
2.80	1.217	1.218	1.218	1.219	1.219	1.220	1.220	1.221	1.221	1.222
2.90	1.222	1.223	1.223	1.224	1.224	1.225	1.225	1.226	1.226	1.227
3.00	1.227	1.228	1.228	1.229	1.229	1.230	1.230	1.230	1.231	1.231
3.10	1.232	1.232	1.233	1.233	1.234	1.234	1.234	1.235	1.235	1.236

WATER CONTENT 270 PERCENT

DG	0	1	2	3	4	5	6	7	8	9
1.70	1.125	1.126	1.128	1.129	1.130	1.131	1.132	1.133	1.134	1.135
1.80	1.137	1.138	1.139	1.140	1.141	1.142	1.143	1.144	1.145	1.146
1.90	1.147	1.148	1.149	1.150	1.151	1.152	1.153	1.154	1.154	1.155
2.00	1.156	1.157	1.158	1.159	1.160	1.161	1.162	1.162	1.163	1.164
2.10	1.165	1.166	1.167	1.167	1.168	1.169	1.170	1.171	1.171	1.172
2.20	1.173	1.174	1.174	1.175	1.176	1.177	1.177	1.178	1.179	1.180
2.30	1.180	1.181	1.182	1.182	1.183	1.184	1.184	1.185	1.186	1.187
2.40	1.187	1.188	1.188	1.189	1.190	1.190	1.191	1.192	1.192	1.193
2.50	1.194	1.194	1.195	1.195	1.196	1.197	1.197	1.198	1.198	1.199
2.60	1.200	1.200	1.201	1.201	1.202	1.202	1.203	1.203	1.204	1.205
2.70	1.205	1.206	1.206	1.207	1.207	1.208	1.208	1.209	1.209	1.210
2.80	1.210	1.211	1.211	1.212	1.212	1.213	1.213	1.214	1.214	1.215
2.90	1.215	1.216	1.216	1.217	1.217	1.218	1.218	1.218	1.219	1.219
3.00	1.220	1.220	1.221	1.221	1.222	1.222	1.222	1.223	1.223	1.224
3.10	1.224	1.225	1.225	1.225	1.226	1.226	1.227	1.227	1.227	1.228

WATER CONTENT 280 PERCENT

DG	0	1	2	3	4	5	6	7	8	9
1.70	1.122	1.123	1.124	1.125	1.126	1.127	1.128	1.129	1.130	1.131
1.80	1.132	1.133	1.135	1.136	1.137	1.138	1.139	1.140	1.140	1.141
1.90	1.142	1.143	1.144	1.145	1.146	1.147	1.148	1.149	1.150	1.151
2.00	1.152	1.152	1.153	1.154	1.155	1.156	1.157	1.157	1.158	1.159
2.10	1.160	1.161	1.161	1.162	1.163	1.164	1.165	1.165	1.166	1.167
2.20	1.168	1.168	1.169	1.170	1.171	1.171	1.172	1.173	1.173	1.174
2.30	1.175	1.175	1.176	1.177	1.177	1.178	1.179	1.179	1.180	1.181
2.40	1.181	1.182	1.183	1.183	1.184	1.184	1.185	1.186	1.186	1.187
2.50	1.187	1.188	1.189	1.189	1.190	1.190	1.191	1.192	1.192	1.193
2.60	1.193	1.194	1.194	1.195	1.195	1.196	1.196	1.197	1.198	1.198
2.70	1.199	1.199	1.200	1.200	1.201	1.201	1.202	1.202	1.203	1.203
2.80	1.204	1.204	1.205	1.205	1.206	1.206	1.206	1.207	1.207	1.208
2.90	1.208	1.209	1.209	1.210	1.210	1.211	1.211	1.211	1.212	1.212
3.00	1.213	1.213	1.214	1.214	1.214	1.215	1.215	1.216	1.216	1.217
3.10	1.217	1.217	1.218	1.218	1.219	1.219	1.219	1.220	1.220	1.220

WATER CONTENT 290 PERCENT

DG	0	1	2	3	4	5	6	7	8	9
1.70	1.118	1.119	1.120	1.121	1.122	1.123	1.125	1.126	1.127	1.128
1.80	1.129	1.130	1.131	1.132	1.133	1.134	1.135	1.135	1.136	1.137
1.90	1.138	1.139	1.140	1.141	1.142	1.143	1.144	1.144	1.145	1.146
2.00	1.147	1.148	1.149	1.150	1.150	1.151	1.152	1.153	1.154	1.154
2.10	1.155	1.156	1.157	1.157	1.158	1.159	1.160	1.160	1.161	1.162
2.20	1.163	1.163	1.164	1.165	1.165	1.166	1.167	1.167	1.168	1.169
2.30	1.169	1.170	1.171	1.171	1.172	1.173	1.173	1.174	1.175	1.175
2.40	1.176	1.176	1.177	1.178	1.178	1.179	1.179	1.180	1.181	1.181
2.50	1.182	1.182	1.183	1.184	1.184	1.185	1.185	1.186	1.186	1.187
2.60	1.187	1.188	1.188	1.189	1.189	1.190	1.190	1.191	1.192	1.192
2.70	1.193	1.193	1.194	1.194	1.194	1.195	1.195	1.196	1.196	1.197
2.80	1.197	1.198	1.198	1.199	1.199	1.200	1.200	1.201	1.201	1.201
2.90	1.202	1.202	1.203	1.203	1.204	1.204	1.205	1.205	1.205	1.206
3.00	1.206	1.207	1.207	1.207	1.208	1.208	1.209	1.209	1.209	1.210
3.10	1.210	1.211	1.211	1.211	1.212	1.212	1.213	1.213	1.213	1.214

WATER CONTENT 300 PERCENT

DG	0	1	2	3	4	5	6	7	8	9
1.70	1.115	1.116	1.117	1.118	1.119	1.120	1.121	1.122	1.123	1.124
1.80	1.125	1.126	1.127	1.128	1.129	1.130	1.131	1.132	1.133	1.133
1.90	1.134	1.135	1.136	1.137	1.138	1.139	1.140	1.140	1.141	1.142
2.00	1.143	1.144	1.144	1.145	1.146	1.147	1.148	1.148	1.149	1.150
2.10	1.151	1.151	1.152	1.153	1.154	1.154	1.155	1.156	1.156	1.157
2.20	1.158	1.159	1.159	1.160	1.161	1.161	1.162	1.163	1.163	1.164
2.30	1.165	1.165	1.166	1.166	1.167	1.168	1.168	1.169	1.170	1.170
2.40	1.171	1.171	1.172	1.172	1.173	1.174	1.174	1.175	1.175	1.176
2.50	1.176	1.177	1.178	1.178	1.179	1.179	1.180	1.180	1.181	1.181
2.60	1.182	1.182	1.183	1.183	1.184	1.184	1.185	1.185	1.186	1.186
2.70	1.187	1.187	1.188	1.188	1.189	1.189	1.190	1.190	1.191	1.191
2.80	1.191	1.192	1.192	1.193	1.193	1.194	1.194	1.195	1.195	1.195
2.90	1.196	1.196	1.197	1.197	1.198	1.198	1.198	1.199	1.199	1.200
3.00	1.200	1.200	1.201	1.201	1.202	1.202	1.202	1.203	1.203	1.204
3.10	1.204	1.204	1.205	1.205	1.205	1.206	1.206	1.206	1.207	1.207

WATER CONTENT 310 PERCENT

DG	0	1	2	3	4	5	6	7	8	9
1.70	1.112	1.113	1.114	1.115	1.116	1.117	1.118	1.119	1.120	1.121
1.80	1.122	1.123	1.123	1.124	1.125	1.126	1.127	1.128	1.129	1.130
1.90	1.131	1.131	1.132	1.133	1.134	1.135	1.136	1.136	1.137	1.138
2.00	1.139	1.140	1.140	1.141	1.142	1.143	1.144	1.144	1.145	1.146
2.10	1.146	1.147	1.148	1.149	1.149	1.150	1.151	1.151	1.152	1.153
2.20	1.153	1.154	1.155	1.155	1.156	1.157	1.157	1.158	1.159	1.159
2.30	1.160	1.161	1.161	1.162	1.162	1.163	1.164	1.164	1.165	1.165
2.40	1.166	1.166	1.167	1.168	1.168	1.169	1.169	1.170	1.170	1.171
2.50	1.171	1.172	1.172	1.173	1.174	1.174	1.175	1.175	1.176	1.176
2.60	1.177	1.177	1.178	1.178	1.179	1.179	1.180	1.180	1.180	1.181
2.70	1.181	1.182	1.182	1.183	1.183	1.184	1.184	1.185	1.185	1.186
2.80	1.186	1.186	1.187	1.187	1.188	1.188	1.189	1.189	1.189	1.190
2.90	1.190	1.191	1.191	1.191	1.192	1.192	1.193	1.193	1.193	1.194
3.00	1.194	1.195	1.195	1.195	1.196	1.196	1.196	1.197	1.197	1.198
3.10	1.198	1.198	1.199	1.199	1.199	1.200	1.200	1.200	1.201	1.201

WATER CONTENT 320 PERCENT

DG	0	1	2	3	4	5	6	7	8	9
1.70	1.109	1.110	1.111	1.112	1.113	1.114	1.115	1.116	1.116	1.117
1.80	1.118	1.119	1.120	1.121	1.122	1.123	1.124	1.125	1.125	1.126
1.90	1.127	1.128	1.129	1.130	1.130	1.131	1.132	1.133	1.134	1.134
2.00	1.135	1.136	1.137	1.137	1.138	1.139	1.140	1.140	1.141	1.142
2.10	1.142	1.143	1.144	1.145	1.145	1.146	1.147	1.147	1.148	1.149
2.20	1.149	1.150	1.151	1.151	1.152	1.152	1.153	1.154	1.154	1.155
2.30	1.156	1.156	1.157	1.157	1.158	1.158	1.159	1.160	1.160	1.161
2.40	1.161	1.162	1.162	1.163	1.163	1.164	1.165	1.165	1.166	1.166
2.50	1.167	1.167	1.168	1.168	1.169	1.169	1.170	1.170	1.171	1.171
2.60	1.172	1.172	1.173	1.173	1.174	1.174	1.175	1.175	1.175	1.176
2.70	1.176	1.177	1.177	1.178	1.178	1.179	1.179	1.179	1.180	1.180
2.80	1.181	1.181	1.182	1.182	1.182	1.183	1.183	1.184	1.184	1.184
2.90	1.185	1.185	1.186	1.186	1.186	1.187	1.187	1.188	1.188	1.188
3.00	1.189	1.189	1.189	1.190	1.190	1.191	1.191	1.191	1.192	1.192
3.10	1.192	1.193	1.193	1.193	1.194	1.194	1.194	1.195	1.195	1.195

WATER CONTENT 330 PERCENT

DG	0	1	2	3	4	5	6	7	8	9
1.70	1.106	1.107	1.108	1.109	1.110	1.111	1.112	1.113	1.113	1.114
1.80	1.115	1.116	1.117	1.118	1.119	1.120	1.120	1.121	1.122	1.123
1.90	1.124	1.125	1.125	1.126	1.127	1.128	1.129	1.129	1.130	1.131
2.00	1.132	1.132	1.133	1.134	1.135	1.135	1.136	1.137	1.137	1.138
2.10	1.139	1.139	1.140	1.141	1.141	1.142	1.143	1.143	1.144	1.145
2.20	1.145	1.146	1.147	1.147	1.148	1.148	1.149	1.150	1.150	1.151
2.30	1.151	1.152	1.152	1.153	1.154	1.154	1.155	1.155	1.156	1.156
2.40	1.157	1.157	1.158	1.159	1.159	1.160	1.160	1.161	1.161	1.162
2.50	1.162	1.163	1.163	1.164	1.164	1.165	1.165	1.166	1.166	1.167
2.60	1.167	1.167	1.168	1.168	1.169	1.169	1.170	1.170	1.171	1.171
2.70	1.172	1.172	1.172	1.173	1.173	1.174	1.174	1.175	1.175	1.175
2.80	1.176	1.176	1.177	1.177	1.177	1.178	1.178	1.179	1.179	1.179
2.90	1.180	1.180	1.181	1.181	1.181	1.182	1.182	1.182	1.183	1.183
3.00	1.183	1.184	1.184	1.185	1.185	1.185	1.186	1.186	1.186	1.187
3.10	1.187	1.187	1.188	1.188	1.188	1.189	1.189	1.189	1.190	1.190

WATER CONTENT 340 PERCENT

DG	0	1	2	3	4	5	6	7	8	9
1.70	1.103	1.104	1.105	1.106	1.107	1.108	1.109	1.110	1.111	1.111
1.80	1.112	1.113	1.114	1.115	1.116	1.117	1.117	1.118	1.119	1.120
1.90	1.121	1.121	1.122	1.123	1.124	1.125	1.125	1.126	1.127	1.127
2.00	1.128	1.129	1.130	1.130	1.131	1.132	1.132	1.133	1.134	1.134
2.10	1.135	1.136	1.136	1.137	1.138	1.138	1.139	1.140	1.140	1.141
2.20	1.142	1.142	1.143	1.143	1.144	1.145	1.145	1.146	1.146	1.147
2.30	1.147	1.148	1.149	1.149	1.150	1.150	1.151	1.151	1.152	1.152
2.40	1.153	1.153	1.154	1.154	1.155	1.155	1.156	1.156	1.157	1.157
2.50	1.158	1.158	1.159	1.159	1.160	1.160	1.161	1.161	1.162	1.162
2.60	1.163	1.163	1.164	1.164	1.164	1.165	1.165	1.166	1.166	1.167
2.70	1.167	1.167	1.168	1.168	1.169	1.169	1.169	1.170	1.170	1.171
2.80	1.171	1.171	1.172	1.172	1.173	1.173	1.173	1.174	1.174	1.175
2.90	1.175	1.175	1.176	1.176	1.176	1.177	1.177	1.178	1.178	1.178
3.00	1.179	1.179	1.179	1.180	1.180	1.180	1.181	1.181	1.181	1.182
3.10	1.182	1.182	1.183	1.183	1.183	1.184	1.184	1.184	1.185	1.185

WATER CONTENT 350 PERCENT

DG	0	1	2	3	4	5	6	7	8	9
1.70	1.101	1.102	1.103	1.103	1.104	1.105	1.106	1.107	1.108	1.109
1.80	1.110	1.110	1.111	1.112	1.113	1.114	1.115	1.115	1.116	1.117
1.90	1.118	1.118	1.119	1.120	1.121	1.121	1.122	1.123	1.124	1.124
2.00	1.125	1.126	1.126	1.127	1.128	1.128	1.129	1.130	1.130	1.131
2.10	1.132	1.132	1.133	1.134	1.134	1.135	1.136	1.136	1.137	1.137
2.20	1.138	1.139	1.139	1.140	1.140	1.141	1.141	1.142	1.143	1.143
2.30	1.144	1.144	1.145	1.145	1.146	1.146	1.147	1.147	1.148	1.148
2.40	1.149	1.149	1.150	1.150	1.151	1.151	1.152	1.152	1.153	1.153
2.50	1.154	1.154	1.155	1.155	1.156	1.156	1.157	1.157	1.158	1.158
2.60	1.158	1.159	1.159	1.160	1.160	1.161	1.161	1.161	1.162	1.162
2.70	1.163	1.163	1.163	1.164	1.164	1.165	1.165	1.165	1.166	1.166
2.80	1.167	1.167	1.167	1.168	1.168	1.169	1.169	1.169	1.170	1.170
2.90	1.170	1.171	1.171	1.171	1.172	1.172	1.173	1.173	1.173	1.174
3.00	1.174	1.174	1.175	1.175	1.175	1.176	1.176	1.176	1.177	1.177
3.10	1.177	1.178	1.178	1.178	1.178	1.179	1.179	1.179	1.180	1.180

WATER CONTENT 360 PERCENT

DG	0	1	2	3	4	5	6	7	8	9
1.70	1.098	1.099	1.100	1.101	1.102	1.103	1.104	1.104	1.105	1.106
1.80	1.107	1.108	1.109	1.109	1.110	1.111	1.112	1.113	1.113	1.114
1.90	1.115	1.116	1.116	1.117	1.118	1.118	1.119	1.120	1.121	1.121
2.00	1.122	1.123	1.123	1.124	1.125	1.125	1.126	1.127	1.127	1.128
2.10	1.129	1.129	1.130	1.130	1.131	1.132	1.132	1.133	1.133	1.134
2.20	1.135	1.135	1.136	1.136	1.137	1.137	1.138	1.138	1.139	1.140
2.30	1.140	1.141	1.141	1.142	1.142	1.143	1.143	1.144	1.144	1.145
2.40	1.145	1.146	1.146	1.147	1.147	1.148	1.148	1.149	1.149	1.150
2.50	1.150	1.150	1.151	1.151	1.152	1.152	1.153	1.153	1.154	1.154
2.60	1.154	1.155	1.155	1.156	1.156	1.157	1.157	1.157	1.158	1.158
2.70	1.159	1.159	1.159	1.160	1.160	1.161	1.161	1.161	1.162	1.162
2.80	1.162	1.163	1.163	1.164	1.164	1.164	1.165	1.165	1.165	1.166
2.90	1.166	1.166	1.167	1.167	1.167	1.168	1.168	1.168	1.169	1.169
3.00	1.169	1.170	1.170	1.170	1.171	1.171	1.171	1.172	1.172	1.172
3.10	1.173	1.173	1.173	1.174	1.174	1.174	1.175	1.175	1.175	1.175

WATER CONTENT 370 PERCENT

DG	0	1	2	3	4	5	6	7	8	9
1.70	1.096	1.097	1.098	1.099	1.099	1.100	1.101	1.102	1.103	1.104
1.80	1.104	1.105	1.106	1.107	1.108	1.108	1.109	1.110	1.111	1.111
1.90	1.112	1.113	1.114	1.114	1.115	1.116	1.116	1.117	1.118	1.118
2.00	1.119	1.120	1.120	1.121	1.122	1.122	1.123	1.124	1.124	1.125
2.10	1.125	1.126	1.127	1.127	1.128	1.128	1.129	1.130	1.130	1.131
2.20	1.131	1.132	1.132	1.133	1.134	1.134	1.135	1.135	1.136	1.136
2.30	1.137	1.137	1.138	1.138	1.139	1.139	1.140	1.140	1.141	1.141
2.40	1.142	1.142	1.143	1.143	1.144	1.144	1.145	1.145	1.145	1.146
2.50	1.146	1.147	1.147	1.148	1.148	1.149	1.149	1.149	1.150	1.150
2.60	1.151	1.151	1.151	1.152	1.152	1.153	1.153	1.154	1.154	1.154
2.70	1.155	1.155	1.155	1.156	1.156	1.157	1.157	1.157	1.158	1.158
2.80	1.158	1.159	1.159	1.160	1.160	1.160	1.161	1.161	1.161	1.162
2.90	1.162	1.162	1.163	1.163	1.163	1.164	1.164	1.164	1.165	1.165
3.00	1.165	1.166	1.166	1.166	1.167	1.167	1.167	1.167	1.168	1.168
3.10	1.168	1.169	1.169	1.169	1.170	1.170	1.170	1.170	1.171	1.171

WATER CONTENT 380 PERCENT

DG	0	1	2	3	4	5	6	7	8	9
1.70	1.094	1.095	1.096	1.096	1.097	1.098	1.099	1.100	1.100	1.101
1.80	1.102	1.103	1.104	1.104	1.105	1.106	1.107	1.107	1.108	1.109
1.90	1.109	1.110	1.111	1.112	1.112	1.113	1.114	1.114	1.115	1.116
2.00	1.116	1.117	1.118	1.118	1.119	1.119	1.120	1.121	1.121	1.122
2.10	1.122	1.123	1.124	1.124	1.125	1.125	1.126	1.127	1.127	1.128
2.20	1.128	1.129	1.129	1.130	1.130	1.131	1.131	1.132	1.132	1.133
2.30	1.133	1.134	1.134	1.135	1.135	1.136	1.136	1.137	1.137	1.138
2.40	1.138	1.139	1.139	1.140	1.140	1.141	1.141	1.142	1.142	1.142
2.50	1.143	1.143	1.144	1.144	1.145	1.145	1.145	1.146	1.146	1.147
2.60	1.147	1.147	1.148	1.148	1.149	1.149	1.149	1.150	1.150	1.151
2.70	1.151	1.151	1.152	1.152	1.152	1.153	1.153	1.154	1.154	1.154
2.80	1.155	1.155	1.155	1.156	1.156	1.156	1.157	1.157	1.157	1.158
2.90	1.158	1.158	1.159	1.159	1.159	1.160	1.160	1.160	1.161	1.161
3.00	1.161	1.162	1.162	1.162	1.163	1.163	1.163	1.163	1.164	1.164
3.10	1.164	1.165	1.165	1.165	1.165	1.166	1.166	1.166	1.167	1.167

WATER CONTENT 390 PERCENT

DG	0	1	2	3	4	5	6	7	8	9
1.70	1.092	1.093	1.093	1.094	1.095	1.096	1.097	1.097	1.098	1.099
1.80	1.100	1.101	1.101	1.102	1.103	1.103	1.104	1.105	1.106	1.106
1.90	1.107	1.108	1.108	1.109	1.110	1.110	1.111	1.112	1.112	1.113
2.00	1.114	1.114	1.115	1.116	1.116	1.117	1.117	1.118	1.119	1.119
2.10	1.120	1.120	1.121	1.121	1.122	1.123	1.123	1.124	1.124	1.125
2.20	1.125	1.126	1.126	1.127	1.127	1.128	1.128	1.129	1.129	1.130
2.30	1.130	1.131	1.131	1.132	1.132	1.133	1.133	1.134	1.134	1.135
2.40	1.135	1.136	1.136	1.136	1.137	1.137	1.138	1.138	1.139	1.139
2.50	1.140	1.140	1.140	1.141	1.141	1.142	1.142	1.142	1.143	1.143
2.60	1.144	1.144	1.144	1.145	1.145	1.146	1.146	1.146	1.147	1.147
2.70	1.147	1.148	1.148	1.149	1.149	1.149	1.150	1.150	1.150	1.151
2.80	1.151	1.151	1.152	1.152	1.152	1.153	1.153	1.153	1.154	1.154
2.90	1.154	1.155	1.155	1.155	1.156	1.156	1.156	1.157	1.157	1.157
3.00	1.157	1.158	1.158	1.158	1.159	1.159	1.159	1.160	1.160	1.160
3.10	1.160	1.161	1.161	1.161	1.162	1.162	1.162	1.162	1.163	1.163

WATER CONTENT 400 PERCENT

DG	0	1	2	3	4	5	6	7	8	9
1.70	1.090	1.091	1.091	1.092	1.093	1.094	1.095	1.095	1.096	1.097
1.80	1.098	1.098	1.099	1.100	1.100	1.101	1.102	1.103	1.103	1.104
1.90	1.105	1.105	1.106	1.107	1.107	1.108	1.109	1.109	1.110	1.110
2.00	1.111	1.112	1.112	1.113	1.114	1.114	1.115	1.115	1.116	1.116
2.10	1.117	1.118	1.118	1.119	1.119	1.120	1.120	1.121	1.121	1.122
2.20	1.122	1.123	1.123	1.124	1.124	1.125	1.125	1.126	1.126	1.127
2.30	1.127	1.128	1.128	1.129	1.129	1.130	1.130	1.131	1.131	1.132
2.40	1.132	1.133	1.133	1.133	1.134	1.134	1.135	1.135	1.136	1.136
2.50	1.136	1.137	1.137	1.138	1.138	1.138	1.139	1.139	1.140	1.140
2.60	1.140	1.141	1.141	1.141	1.142	1.142	1.143	1.143	1.143	1.144
2.70	1.144	1.144	1.145	1.145	1.145	1.146	1.146	1.147	1.147	1.147
2.80	1.148	1.148	1.148	1.149	1.149	1.149	1.150	1.150	1.150	1.150
2.90	1.151	1.151	1.151	1.152	1.152	1.152	1.153	1.153	1.153	1.154
3.00	1.154	1.154	1.154	1.155	1.155	1.155	1.156	1.156	1.156	1.156
3.10	1.157	1.157	1.157	1.158	1.158	1.158	1.158	1.159	1.159	1.159

WATER CONTENT 410 PERCENT

DG	0	1	2	3	4	5	6	7	8	9
1.70	1.088	1.089	1.089	1.090	1.091	1.092	1.093	1.093	1.094	1.095
1.80	1.095	1.096	1.097	1.098	1.098	1.099	1.100	1.100	1.101	1.102
1.90	1.102	1.103	1.104	1.104	1.105	1.106	1.106	1.107	1.107	1.108
2.00	1.109	1.109	1.110	1.110	1.111	1.112	1.112	1.113	1.113	1.114
2.10	1.114	1.115	1.116	1.116	1.117	1.117	1.118	1.118	1.119	1.119
2.20	1.120	1.120	1.121	1.121	1.122	1.122	1.123	1.123	1.124	1.124
2.30	1.125	1.125	1.126	1.126	1.126	1.127	1.127	1.128	1.128	1.129
2.40	1.129	1.130	1.130	1.130	1.131	1.131	1.132	1.132	1.133	1.133
2.50	1.133	1.134	1.134	1.135	1.135	1.135	1.136	1.136	1.136	1.137
2.60	1.137	1.138	1.138	1.138	1.139	1.139	1.139	1.140	1.140	1.140
2.70	1.141	1.141	1.142	1.142	1.142	1.143	1.143	1.143	1.144	1.144
2.80	1.144	1.145	1.145	1.145	1.146	1.146	1.146	1.146	1.147	1.147
2.90	1.147	1.148	1.148	1.148	1.149	1.149	1.149	1.150	1.150	1.150
3.00	1.150	1.151	1.151	1.151	1.152	1.152	1.152	1.152	1.153	1.153
3.10	1.153	1.153	1.154	1.154	1.154	1.155	1.155	1.155	1.155	1.156

WATER CONTENT 420 PERCENT

DG	0	1	2	3	4	5	6	7	8	9
1.70	1.086	1.087	1.088	1.088	1.089	1.090	1.091	1.091	1.092	1.093
1.80	1.093	1.094	1.095	1.096	1.096	1.097	1.098	1.098	1.099	1.100
1.90	1.100	1.101	1.101	1.102	1.103	1.103	1.104	1.105	1.105	1.106
2.00	1.106	1.107	1.108	1.108	1.109	1.109	1.110	1.110	1.111	1.111
2.10	1.112	1.113	1.113	1.114	1.114	1.115	1.115	1.116	1.116	1.117
2.20	1.117	1.118	1.118	1.119	1.119	1.120	1.120	1.121	1.121	1.121
2.30	1.122	1.122	1.123	1.123	1.124	1.124	1.125	1.125	1.125	1.126
2.40	1.126	1.127	1.127	1.128	1.128	1.128	1.129	1.129	1.130	1.130
2.50	1.130	1.131	1.131	1.132	1.132	1.132	1.133	1.133	1.133	1.134
2.60	1.134	1.135	1.135	1.135	1.136	1.136	1.136	1.137	1.137	1.137
2.70	1.138	1.138	1.138	1.139	1.139	1.139	1.140	1.140	1.140	1.141
2.80	1.141	1.141	1.142	1.142	1.142	1.143	1.143	1.143	1.144	1.144
2.90	1.144	1.144	1.145	1.145	1.145	1.146	1.146	1.146	1.146	1.147
3.00	1.147	1.147	1.148	1.148	1.148	1.148	1.149	1.149	1.149	1.150
3.10	1.150	1.150	1.150	1.151	1.151	1.151	1.151	1.152	1.152	1.152

WATER CONTENT 430 PERCENT

DG	0	1	2	3	4	5	6	7	8	9
1.70	1.084	1.085	1.086	1.087	1.087	1.088	1.089	1.089	1.090	1.091
1.80	1.092	1.092	1.093	1.094	1.094	1.095	1.096	1.096	1.097	1.098
1.90	1.098	1.099	1.099	1.100	1.101	1.101	1.102	1.102	1.103	1.104
2.00	1.104	1.105	1.105	1.106	1.106	1.107	1.108	1.108	1.109	1.109
2.10	1.110	1.110	1.111	1.111	1.112	1.112	1.113	1.113	1.114	1.114
2.20	1.115	1.115	1.116	1.116	1.117	1.117	1.118	1.118	1.118	1.119
2.30	1.119	1.120	1.120	1.121	1.121	1.122	1.122	1.122	1.123	1.123
2.40	1.124	1.124	1.124	1.125	1.125	1.126	1.126	1.126	1.127	1.127
2.50	1.128	1.128	1.128	1.129	1.129	1.130	1.130	1.130	1.131	1.131
2.60	1.131	1.132	1.132	1.132	1.133	1.133	1.133	1.134	1.134	1.134
2.70	1.135	1.135	1.135	1.136	1.136	1.136	1.137	1.137	1.137	1.138
2.80	1.138	1.138	1.139	1.139	1.139	1.140	1.140	1.140	1.140	1.141
2.90	1.141	1.141	1.142	1.142	1.142	1.142	1.143	1.143	1.143	1.144
3.00	1.144	1.144	1.144	1.145	1.145	1.145	1.145	1.146	1.146	1.146
3.10	1.147	1.147	1.147	1.147	1.148	1.148	1.148	1.148	1.149	1.149

WATER CONTENT 440 PERCENT

DG	0	1	2	3	4	5	6	7	8	9
1.70	1.083	1.083	1.084	1.085	1.085	1.086	1.087	1.088	1.088	1.089
1.80	1.090	1.090	1.091	1.092	1.092	1.093	1.094	1.094	1.095	1.096
1.90	1.096	1.097	1.097	1.098	1.099	1.099	1.100	1.100	1.101	1.101
2.00	1.102	1.103	1.103	1.104	1.104	1.105	1.105	1.106	1.106	1.107
2.10	1.107	1.108	1.108	1.109	1.109	1.110	1.110	1.111	1.111	1.112
2.20	1.112	1.113	1.113	1.114	1.114	1.115	1.115	1.116	1.116	1.116
2.30	1.117	1.117	1.118	1.118	1.119	1.119	1.119	1.120	1.120	1.121
2.40	1.121	1.122	1.122	1.122	1.123	1.123	1.123	1.124	1.124	1.125
2.50	1.125	1.125	1.126	1.126	1.126	1.127	1.127	1.128	1.128	1.128
2.60	1.129	1.129	1.129	1.130	1.130	1.130	1.131	1.131	1.131	1.132
2.70	1.132	1.132	1.133	1.133	1.133	1.134	1.134	1.134	1.135	1.135
2.80	1.135	1.135	1.136	1.136	1.136	1.137	1.137	1.137	1.138	1.138
2.90	1.138	1.138	1.139	1.139	1.139	1.139	1.140	1.140	1.140	1.141
3.00	1.141	1.141	1.141	1.142	1.142	1.142	1.142	1.143	1.143	1.143
3.10	1.143	1.144	1.144	1.144	1.144	1.145	1.145	1.145	1.145	1.146

WATER CONTENT 450 PERCENT

DG	0	1	2	3	4	5	6	7	8	9
1.70	1.081	1.082	1.082	1.083	1.084	1.085	1.085	1.086	1.087	1.087
1.80	1.088	1.089	1.089	1.090	1.091	1.091	1.092	1.092	1.093	1.094
1.90	1.094	1.095	1.095	1.096	1.097	1.097	1.098	1.098	1.099	1.099
2.00	1.100	1.101	1.101	1.102	1.102	1.103	1.103	1.104	1.104	1.105
2.10	1.105	1.106	1.106	1.107	1.107	1.108	1.108	1.109	1.109	1.110
2.20	1.110	1.111	1.111	1.111	1.112	1.112	1.113	1.113	1.114	1.114
2.30	1.115	1.115	1.115	1.116	1.116	1.117	1.117	1.117	1.118	1.118
2.40	1.119	1.119	1.119	1.120	1.120	1.121	1.121	1.121	1.122	1.122
2.50	1.122	1.123	1.123	1.124	1.124	1.124	1.125	1.125	1.125	1.126
2.60	1.126	1.126	1.127	1.127	1.127	1.128	1.128	1.128	1.129	1.129
2.70	1.129	1.130	1.130	1.130	1.131	1.131	1.131	1.131	1.132	1.132
2.80	1.132	1.133	1.133	1.133	1.134	1.134	1.134	1.134	1.135	1.135
2.90	1.135	1.136	1.136	1.136	1.136	1.137	1.137	1.137	1.137	1.138
3.00	1.138	1.138	1.138	1.139	1.139	1.139	1.139	1.140	1.140	1.140
3.10	1.140	1.141	1.141	1.141	1.141	1.142	1.142	1.142	1.142	1.143

WATER CONTENT 460 PERCENT

DG	0	1	2	3	4	5	6	7	8	9
1.70	1.079	1.080	1.081	1.081	1.082	1.083	1.084	1.084	1.085	1.086
1.80	1.086	1.087	1.087	1.088	1.089	1.089	1.090	1.091	1.091	1.092
1.90	1.092	1.093	1.094	1.094	1.095	1.095	1.096	1.096	1.097	1.097
2.00	1.098	1.099	1.099	1.100	1.100	1.101	1.101	1.102	1.102	1.103
2.10	1.103	1.104	1.104	1.105	1.105	1.106	1.106	1.107	1.107	1.107
2.20	1.108	1.108	1.109	1.109	1.110	1.110	1.111	1.111	1.111	1.112
2.30	1.112	1.113	1.113	1.113	1.114	1.114	1.115	1.115	1.116	1.116
2.40	1.116	1.117	1.117	1.117	1.118	1.118	1.119	1.119	1.119	1.120
2.50	1.120	1.120	1.121	1.121	1.121	1.122	1.122	1.122	1.123	1.123
2.60	1.123	1.124	1.124	1.124	1.125	1.125	1.125	1.126	1.126	1.126
2.70	1.127	1.127	1.127	1.128	1.128	1.128	1.129	1.129	1.129	1.129
2.80	1.130	1.130	1.130	1.131	1.131	1.131	1.131	1.132	1.132	1.132
2.90	1.132	1.133	1.133	1.133	1.134	1.134	1.134	1.134	1.135	1.135
3.00	1.135	1.135	1.136	1.136	1.136	1.136	1.137	1.137	1.137	1.137
3.10	1.138	1.138	1.138	1.138	1.139	1.139	1.139	1.139	1.139	1.140

WATER CONTENT 470 PERCENT

DG	0	1	2	3	4	5	6	7	8	9
1.70	1.078	1.079	1.079	1.080	1.081	1.081	1.082	1.083	1.083	1.084
1.80	1.085	1.085	1.086	1.086	1.087	1.088	1.088	1.089	1.089	1.090
1.90	1.091	1.091	1.092	1.092	1.093	1.093	1.094	1.095	1.095	1.096
2.00	1.096	1.097	1.097	1.098	1.098	1.099	1.099	1.100	1.100	1.101
2.10	1.101	1.102	1.102	1.103	1.103	1.104	1.104	1.104	1.105	1.105
2.20	1.106	1.106	1.107	1.107	1.108	1.108	1.108	1.109	1.109	1.110
2.30	1.110	1.110	1.111	1.111	1.112	1.112	1.112	1.113	1.113	1.114
2.40	1.114	1.114	1.115	1.115	1.115	1.116	1.116	1.117	1.117	1.117
2.50	1.118	1.118	1.118	1.119	1.119	1.119	1.120	1.120	1.120	1.121
2.60	1.121	1.121	1.122	1.122	1.122	1.123	1.123	1.123	1.124	1.124
2.70	1.124	1.124	1.125	1.125	1.125	1.126	1.126	1.126	1.127	1.127
2.80	1.127	1.127	1.128	1.128	1.128	1.129	1.129	1.129	1.129	1.130
2.90	1.130	1.130	1.130	1.131	1.131	1.131	1.131	1.132	1.132	1.132
3.00	1.132	1.133	1.133	1.133	1.133	1.134	1.134	1.134	1.134	1.135
3.10	1.135	1.135	1.135	1.136	1.136	1.136	1.136	1.136	1.137	1.137

WATER CONTENT 480 PERCENT

DG	0	1	2	3	4	5	6	7	8	9
1.70	1.076	1.077	1.078	1.078	1.079	1.080	1.080	1.081	1.082	1.082
1.80	1.083	1.084	1.084	1.085	1.085	1.086	1.087	1.087	1.088	1.088
1.90	1.089	1.089	1.090	1.091	1.091	1.092	1.092	1.093	1.093	1.094
2.00	1.094	1.095	1.095	1.096	1.096	1.097	1.097	1.098	1.098	1.099
2.10	1.099	1.100	1.100	1.101	1.101	1.102	1.102	1.102	1.103	1.103
2.20	1.104	1.104	1.105	1.105	1.106	1.106	1.106	1.107	1.107	1.108
2.30	1.108	1.108	1.109	1.109	1.110	1.110	1.110	1.111	1.111	1.111
2.40	1.112	1.112	1.113	1.113	1.113	1.114	1.114	1.114	1.115	1.115
2.50	1.115	1.116	1.116	1.116	1.117	1.117	1.117	1.118	1.118	1.118
2.60	1.119	1.119	1.119	1.120	1.120	1.120	1.121	1.121	1.121	1.121
2.70	1.122	1.122	1.122	1.123	1.123	1.123	1.124	1.124	1.124	1.124
2.80	1.125	1.125	1.125	1.125	1.126	1.126	1.126	1.127	1.127	1.127
2.90	1.127	1.128	1.128	1.128	1.128	1.129	1.129	1.129	1.129	1.130
3.00	1.130	1.130	1.130	1.131	1.131	1.131	1.131	1.132	1.132	1.132
3.10	1.132	1.132	1.133	1.133	1.133	1.133	1.134	1.134	1.134	1.134

WATER CONTENT 490 PERCENT

DG	0	1	2	3	4	5	6	7	8	9
1.70	1.075	1.076	1.076	1.077	1.078	1.078	1.079	1.080	1.080	1.081
1.80	1.081	1.082	1.083	1.083	1.084	1.084	1.085	1.086	1.086	1.087
1.90	1.087	1.088	1.088	1.089	1.089	1.090	1.091	1.091	1.092	1.092
2.00	1.093	1.093	1.094	1.094	1.095	1.095	1.096	1.096	1.096	1.097
2.10	1.097	1.098	1.098	1.099	1.099	1.100	1.100	1.101	1.101	1.101
2.20	1.102	1.102	1.103	1.103	1.104	1.104	1.104	1.105	1.105	1.106
2.30	1.106	1.106	1.107	1.107	1.107	1.108	1.108	1.109	1.109	1.109
2.40	1.110	1.110	1.110	1.111	1.111	1.111	1.112	1.112	1.113	1.113
2.50	1.113	1.114	1.114	1.114	1.115	1.115	1.115	1.116	1.116	1.116
2.60	1.116	1.117	1.117	1.117	1.118	1.118	1.118	1.119	1.119	1.119
2.70	1.119	1.120	1.120	1.120	1.121	1.121	1.121	1.121	1.122	1.122
2.80	1.122	1.123	1.123	1.123	1.123	1.124	1.124	1.124	1.124	1.125
2.90	1.125	1.125	1.125	1.126	1.126	1.126	1.126	1.127	1.127	1.127
3.00	1.127	1.128	1.128	1.128	1.128	1.129	1.129	1.129	1.129	1.129
3.10	1.130	1.130	1.130	1.130	1.131	1.131	1.131	1.131	1.131	1.132

WATER CONTENT 500 PERCENT

DG	0	1	2	3	4	5	6	7	8	9
1.70	1.074	1.074	1.075	1.076	1.076	1.077	1.078	1.078	1.079	1.079
1.80	1.080	1.081	1.081	1.082	1.082	1.083	1.083	1.084	1.085	1.085
1.90	1.086	1.086	1.087	1.087	1.088	1.088	1.089	1.089	1.090	1.090
2.00	1.091	1.091	1.092	1.092	1.093	1.093	1.094	1.094	1.095	1.095
2.10	1.096	1.096	1.097	1.097	1.097	1.098	1.098	1.099	1.099	1.100
2.20	1.100	1.100	1.101	1.101	1.102	1.102	1.102	1.103	1.103	1.104
2.30	1.104	1.104	1.105	1.105	1.106	1.106	1.106	1.107	1.107	1.107
2.40	1.108	1.108	1.108	1.109	1.109	1.109	1.110	1.110	1.110	1.111
2.50	1.111	1.111	1.112	1.112	1.112	1.113	1.113	1.113	1.114	1.114
2.60	1.114	1.115	1.115	1.115	1.115	1.116	1.116	1.116	1.117	1.117
2.70	1.117	1.118	1.118	1.118	1.118	1.119	1.119	1.119	1.119	1.120
2.80	1.120	1.120	1.121	1.121	1.121	1.121	1.122	1.122	1.122	1.122
2.90	1.123	1.123	1.123	1.123	1.124	1.124	1.124	1.124	1.125	1.125
3.00	1.125	1.125	1.125	1.126	1.126	1.126	1.126	1.127	1.127	1.127
3.10	1.127	1.127	1.128	1.128	1.128	1.128	1.129	1.129	1.129	1.129

WATER CONTENT 510 PERCENT

DG	0	1	2	3	4	5	6	7	8	9
1.70	1.072	1.073	1.074	1.074	1.075	1.076	1.076	1.077	1.077	1.078
1.80	1.079	1.079	1.080	1.080	1.081	1.081	1.082	1.083	1.083	1.084
1.90	1.084	1.085	1.085	1.086	1.086	1.087	1.087	1.088	1.088	1.089
2.00	1.089	1.090	1.090	1.091	1.091	1.092	1.092	1.093	1.093	1.093
2.10	1.094	1.094	1.095	1.095	1.096	1.096	1.097	1.097	1.097	1.098
2.20	1.098	1.099	1.099	1.099	1.100	1.100	1.101	1.101	1.101	1.102
2.30	1.102	1.102	1.103	1.103	1.104	1.104	1.104	1.105	1.105	1.105
2.40	1.106	1.106	1.106	1.107	1.107	1.107	1.108	1.108	1.108	1.109
2.50	1.109	1.109	1.110	1.110	1.110	1.111	1.111	1.111	1.112	1.112
2.60	1.112	1.113	1.113	1.113	1.113	1.114	1.114	1.114	1.115	1.115
2.70	1.115	1.115	1.116	1.116	1.116	1.116	1.117	1.117	1.117	1.118
2.80	1.118	1.118	1.118	1.119	1.119	1.119	1.119	1.120	1.120	1.120
2.90	1.120	1.121	1.121	1.121	1.121	1.122	1.122	1.122	1.122	1.122
3.00	1.123	1.123	1.123	1.123	1.124	1.124	1.124	1.124	1.124	1.125
3.10	1.125	1.125	1.125	1.126	1.126	1.126	1.126	1.126	1.127	1.127

WATER CONTENT 520 PERCENT

DG	0	1	2	3	4	5	6	7	8	9
1.70	1.071	1.072	1.072	1.073	1.074	1.074	1.075	1.075	1.076	1.077
1.80	1.077	1.078	1.078	1.079	1.079	1.080	1.081	1.081	1.082	1.082
1.90	1.083	1.083	1.084	1.084	1.085	1.085	1.086	1.086	1.087	1.087
2.00	1.088	1.088	1.089	1.089	1.090	1.090	1.091	1.091	1.091	1.092
2.10	1.092	1.093	1.093	1.094	1.094	1.094	1.095	1.095	1.096	1.096
2.20	1.096	1.097	1.097	1.098	1.098	1.098	1.099	1.099	1.100	1.100
2.30	1.100	1.101	1.101	1.101	1.102	1.102	1.102	1.103	1.103	1.104
2.40	1.104	1.104	1.105	1.105	1.105	1.106	1.106	1.106	1.107	1.107
2.50	1.107	1.107	1.108	1.108	1.108	1.109	1.109	1.109	1.110	1.110
2.60	1.110	1.110	1.111	1.111	1.111	1.112	1.112	1.112	1.112	1.113
2.70	1.113	1.113	1.114	1.114	1.114	1.114	1.115	1.115	1.115	1.115
2.80	1.116	1.116	1.116	1.116	1.117	1.117	1.117	1.117	1.118	1.118
2.90	1.118	1.118	1.119	1.119	1.119	1.119	1.120	1.120	1.120	1.120
3.00	1.120	1.121	1.121	1.121	1.121	1.122	1.122	1.122	1.122	1.122
3.10	1.123	1.123	1.123	1.123	1.123	1.124	1.124	1.124	1.124	1.125

WATER CONTENT 530 PERCENT

DG	0	1	2	3	4	5	6	7	8	9
1.70	1.070	1.071	1.071	1.072	1.072	1.073	1.074	1.074	1.075	1.075
1.80	1.076	1.076	1.077	1.078	1.078	1.079	1.079	1.080	1.080	1.081
1.90	1.081	1.082	1.082	1.083	1.083	1.084	1.084	1.085	1.085	1.086
2.00	1.086	1.087	1.087	1.088	1.088	1.088	1.089	1.089	1.090	1.090
2.10	1.091	1.091	1.092	1.092	1.092	1.093	1.093	1.094	1.094	1.094
2.20	1.095	1.095	1.096	1.096	1.096	1.097	1.097	1.097	1.098	1.098
2.30	1.099	1.099	1.099	1.100	1.100	1.100	1.101	1.101	1.101	1.102
2.40	1.102	1.102	1.103	1.103	1.103	1.104	1.104	1.104	1.105	1.105
2.50	1.105	1.106	1.106	1.106	1.106	1.107	1.107	1.107	1.108	1.108
2.60	1.108	1.109	1.109	1.109	1.109	1.110	1.110	1.110	1.110	1.111
2.70	1.111	1.111	1.112	1.112	1.112	1.112	1.113	1.113	1.113	1.113
2.80	1.114	1.114	1.114	1.114	1.115	1.115	1.115	1.115	1.116	1.116
2.90	1.116	1.116	1.117	1.117	1.117	1.117	1.117	1.118	1.118	1.118
3.00	1.118	1.119	1.119	1.119	1.119	1.119	1.120	1.120	1.120	1.120
3.10	1.120	1.121	1.121	1.121	1.121	1.122	1.122	1.122	1.122	1.122

WATER CONTENT 540 PERCENT

DG	0	1	2	3	4	5	6	7	8	9
1.70	1.069	1.069	1.070	1.071	1.071	1.072	1.072	1.073	1.074	1.074
1.80	1.075	1.075	1.076	1.076	1.077	1.077	1.078	1.078	1.079	1.079
1.90	1.080	1.080	1.081	1.081	1.082	1.082	1.083	1.083	1.084	1.084
2.00	1.085	1.085	1.086	1.086	1.087	1.087	1.087	1.088	1.088	1.089
2.10	1.089	1.090	1.090	1.090	1.091	1.091	1.092	1.092	1.092	1.093
2.20	1.093	1.094	1.094	1.094	1.095	1.095	1.095	1.096	1.096	1.097
2.30	1.097	1.097	1.098	1.098	1.098	1.099	1.099	1.099	1.100	1.100
2.40	1.100	1.101	1.101	1.101	1.102	1.102	1.102	1.103	1.103	1.103
2.50	1.103	1.104	1.104	1.104	1.105	1.105	1.105	1.106	1.106	1.106
2.60	1.106	1.107	1.107	1.107	1.107	1.108	1.108	1.108	1.109	1.109
2.70	1.109	1.109	1.110	1.110	1.110	1.110	1.111	1.111	1.111	1.111
2.80	1.112	1.112	1.112	1.112	1.113	1.113	1.113	1.113	1.114	1.114
2.90	1.114	1.114	1.115	1.115	1.115	1.115	1.115	1.116	1.116	1.116
3.00	1.116	1.116	1.117	1.117	1.117	1.117	1.118	1.118	1.118	1.118
3.10	1.118	1.119	1.119	1.119	1.119	1.119	1.120	1.120	1.120	1.120

WATER CONTENT 550 PERCENT

DG	0	1	2	3	4	5	6	7	8	9
1.70	1.068	1.068	1.069	1.069	1.070	1.071	1.071	1.072	1.072	1.073
1.80	1.073	1.074	1.074	1.075	1.076	1.076	1.077	1.077	1.078	1.078
1.90	1.079	1.079	1.080	1.080	1.081	1.081	1.081	1.082	1.082	1.083
2.00	1.083	1.084	1.084	1.085	1.085	1.086	1.086	1.086	1.087	1.087
2.10	1.088	1.088	1.088	1.089	1.089	1.090	1.090	1.090	1.091	1.091
2.20	1.092	1.092	1.092	1.093	1.093	1.093	1.094	1.094	1.095	1.095
2.30	1.095	1.096	1.096	1.096	1.097	1.097	1.097	1.098	1.098	1.098
2.40	1.099	1.099	1.099	1.100	1.100	1.100	1.100	1.101	1.101	1.101
2.50	1.102	1.102	1.102	1.103	1.103	1.103	1.103	1.104	1.104	1.104
2.60	1.105	1.105	1.105	1.105	1.106	1.106	1.106	1.106	1.107	1.107
2.70	1.107	1.108	1.108	1.108	1.108	1.109	1.109	1.109	1.109	1.110
2.80	1.110	1.110	1.110	1.110	1.111	1.111	1.111	1.111	1.112	1.112
2.90	1.112	1.112	1.113	1.113	1.113	1.113	1.113	1.114	1.114	1.114
3.00	1.114	1.114	1.115	1.115	1.115	1.115	1.116	1.116	1.116	1.116
3.10	1.116	1.117	1.117	1.117	1.117	1.117	1.118	1.118	1.118	1.118

WATER CONTENT 560 PERCENT

DG	0	1	2	3	4	5	6	7	8	9
1.70	1.067	1.067	1.068	1.068	1.069	1.069	1.070	1.071	1.071	1.072
1.80	1.072	1.073	1.073	1.074	1.074	1.075	1.075	1.076	1.076	1.077
1.90	1.077	1.078	1.078	1.079	1.079	1.080	1.080	1.081	1.081	1.082
2.00	1.082	1.082	1.083	1.083	1.084	1.084	1.085	1.085	1.085	1.086
2.10	1.086	1.087	1.087	1.087	1.088	1.088	1.089	1.089	1.089	1.090
2.20	1.090	1.090	1.091	1.091	1.092	1.092	1.092	1.093	1.093	1.093
2.30	1.094	1.094	1.094	1.095	1.095	1.095	1.096	1.096	1.096	1.097
2.40	1.097	1.097	1.098	1.098	1.098	1.099	1.099	1.099	1.099	1.100
2.50	1.100	1.100	1.101	1.101	1.101	1.101	1.102	1.102	1.102	1.103
2.60	1.103	1.103	1.103	1.104	1.104	1.104	1.104	1.105	1.105	1.105
2.70	1.105	1.106	1.106	1.106	1.106	1.107	1.107	1.107	1.107	1.108
2.80	1.108	1.108	1.108	1.109	1.109	1.109	1.109	1.110	1.110	1.110
2.90	1.110	1.110	1.111	1.111	1.111	1.111	1.112	1.112	1.112	1.112
3.00	1.112	1.113	1.113	1.113	1.113	1.113	1.114	1.114	1.114	1.114
3.10	1.114	1.115	1.115	1.115	1.115	1.115	1.116	1.116	1.116	1.116

WATER CONTENT 570 PERCENT

DG	0	1	2	3	4	5	6	7	8	9
1.70	1.065	1.066	1.067	1.067	1.068	1.068	1.069	1.069	1.070	1.071
1.80	1.071	1.072	1.072	1.073	1.073	1.074	1.074	1.075	1.075	1.076
1.90	1.076	1.077	1.077	1.077	1.078	1.078	1.079	1.079	1.080	1.080
2.00	1.081	1.081	1.082	1.082	1.082	1.083	1.083	1.084	1.084	1.084
2.10	1.085	1.085	1.086	1.086	1.086	1.087	1.087	1.088	1.088	1.088
2.20	1.089	1.089	1.089	1.090	1.090	1.090	1.091	1.091	1.091	1.092
2.30	1.092	1.092	1.093	1.093	1.093	1.094	1.094	1.094	1.095	1.095
2.40	1.095	1.096	1.096	1.096	1.097	1.097	1.097	1.097	1.098	1.098
2.50	1.098	1.099	1.099	1.099	1.099	1.100	1.100	1.100	1.101	1.101
2.60	1.101	1.101	1.102	1.102	1.102	1.102	1.103	1.103	1.103	1.103
2.70	1.104	1.104	1.104	1.104	1.105	1.105	1.105	1.105	1.106	1.106
2.80	1.106	1.106	1.107	1.107	1.107	1.107	1.108	1.108	1.108	1.108
2.90	1.108	1.109	1.109	1.109	1.109	1.109	1.110	1.110	1.110	1.110
3.00	1.110	1.111	1.111	1.111	1.111	1.112	1.112	1.112	1.112	1.112
3.10	1.112	1.113	1.113	1.113	1.113	1.113	1.114	1.114	1.114	1.114

WATER CONTENT 580 PERCENT

DG	0	1	2	3	4	5	6	7	8	9
1.70	1.064	1.065	1.066	1.066	1.067	1.067	1.068	1.068	1.069	1.069
1.80	1.070	1.070	1.071	1.071	1.072	1.072	1.073	1.073	1.074	1.074
1.90	1.075	1.075	1.076	1.076	1.077	1.077	1.078	1.078	1.078	1.079
2.00	1.079	1.080	1.080	1.081	1.081	1.081	1.082	1.082	1.083	1.083
2.10	1.083	1.084	1.084	1.085	1.085	1.085	1.086	1.086	1.086	1.087
2.20	1.087	1.088	1.088	1.088	1.089	1.089	1.089	1.090	1.090	1.090
2.30	1.091	1.091	1.091	1.092	1.092	1.092	1.093	1.093	1.093	1.094
2.40	1.094	1.094	1.094	1.095	1.095	1.095	1.096	1.096	1.096	1.096
2.50	1.097	1.097	1.097	1.098	1.098	1.098	1.098	1.099	1.099	1.099
2.60	1.100	1.100	1.100	1.100	1.101	1.101	1.101	1.101	1.102	1.102
2.70	1.102	1.102	1.103	1.103	1.103	1.103	1.103	1.104	1.104	1.104
2.80	1.104	1.105	1.105	1.105	1.105	1.106	1.106	1.106	1.106	1.106
2.90	1.107	1.107	1.107	1.107	1.107	1.108	1.108	1.108	1.108	1.108
3.00	1.109	1.109	1.109	1.109	1.109	1.110	1.110	1.110	1.110	1.110
3.10	1.111	1.111	1.111	1.111	1.111	1.112	1.112	1.112	1.112	1.112

WATER CONTENT 590 PERCENT

DG	0	1	2	3	4	5	6	7	8	9
1.70	1.063	1.064	1.065	1.065	1.066	1.066	1.067	1.067	1.068	1.068
1.80	1.069	1.069	1.070	1.070	1.071	1.071	1.072	1.072	1.073	1.073
1.90	1.074	1.074	1.075	1.075	1.076	1.076	1.076	1.077	1.077	1.078
2.00	1.078	1.079	1.079	1.079	1.080	1.080	1.081	1.081	1.081	1.082
2.10	1.082	1.083	1.083	1.083	1.084	1.084	1.084	1.085	1.085	1.085
2.20	1.086	1.086	1.087	1.087	1.087	1.088	1.088	1.088	1.089	1.089
2.30	1.089	1.090	1.090	1.090	1.091	1.091	1.091	1.091	1.092	1.092
2.40	1.092	1.093	1.093	1.093	1.094	1.094	1.094	1.094	1.095	1.095
2.50	1.095	1.096	1.096	1.096	1.096	1.097	1.097	1.097	1.097	1.098
2.60	1.098	1.098	1.098	1.099	1.099	1.099	1.099	1.100	1.100	1.100
2.70	1.100	1.101	1.101	1.101	1.101	1.102	1.102	1.102	1.102	1.103
2.80	1.103	1.103	1.103	1.103	1.104	1.104	1.104	1.104	1.104	1.105
2.90	1.105	1.105	1.105	1.106	1.106	1.106	1.106	1.106	1.107	1.107
3.00	1.107	1.107	1.107	1.108	1.108	1.108	1.108	1.108	1.108	1.109
3.10	1.109	1.109	1.109	1.109	1.110	1.110	1.110	1.110	1.110	1.110

WATER CONTENT 600 PERCENT

DG	0	1	2	3	4	5	6	7	8	9
1.70	1.063	1.063	1.064	1.064	1.065	1.065	1.066	1.066	1.067	1.067
1.80	1.068	1.068	1.069	1.069	1.070	1.070	1.071	1.071	1.072	1.072
1.90	1.073	1.073	1.073	1.074	1.074	1.075	1.075	1.076	1.076	1.077
2.00	1.077	1.077	1.078	1.078	1.079	1.079	1.079	1.080	1.080	1.081
2.10	1.081	1.081	1.082	1.082	1.082	1.083	1.083	1.083	1.084	1.084
2.20	1.085	1.085	1.085	1.086	1.086	1.086	1.087	1.087	1.087	1.088
2.30	1.088	1.088	1.088	1.089	1.089	1.089	1.090	1.090	1.090	1.091
2.40	1.091	1.091	1.091	1.092	1.092	1.092	1.093	1.093	1.093	1.093
2.50	1.094	1.094	1.094	1.095	1.095	1.095	1.095	1.096	1.096	1.096
2.60	1.096	1.097	1.097	1.097	1.097	1.098	1.098	1.098	1.098	1.099
2.70	1.099	1.099	1.099	1.100	1.100	1.100	1.100	1.100	1.101	1.101
2.80	1.101	1.101	1.102	1.102	1.102	1.102	1.102	1.103	1.103	1.103
2.90	1.103	1.103	1.104	1.104	1.104	1.104	1.104	1.105	1.105	1.105
3.00	1.105	1.105	1.106	1.106	1.106	1.106	1.106	1.107	1.107	1.107
3.10	1.107	1.107	1.108	1.108	1.108	1.108	1.108	1.108	1.109	1.109

WATER CONTENT 610 PERCENT

DG	0	1	2	3	4	5	6	7	8	9
1.70	1.062	1.062	1.063	1.063	1.064	1.064	1.065	1.065	1.066	1.066
1.80	1.067	1.067	1.068	1.068	1.069	1.069	1.070	1.070	1.071	1.071
1.90	1.071	1.072	1.072	1.073	1.073	1.074	1.074	1.075	1.075	1.075
2.00	1.076	1.076	1.077	1.077	1.077	1.078	1.078	1.079	1.079	1.079
2.10	1.080	1.080	1.080	1.081	1.081	1.081	1.082	1.082	1.083	1.083
2.20	1.083	1.084	1.084	1.084	1.085	1.085	1.085	1.086	1.086	1.086
2.30	1.086	1.087	1.087	1.087	1.088	1.088	1.088	1.089	1.089	1.089
2.40	1.090	1.090	1.090	1.090	1.091	1.091	1.091	1.091	1.092	1.092
2.50	1.092	1.093	1.093	1.093	1.093	1.094	1.094	1.094	1.094	1.095
2.60	1.095	1.095	1.095	1.096	1.096	1.096	1.096	1.097	1.097	1.097
2.70	1.097	1.098	1.098	1.098	1.098	1.098	1.099	1.099	1.099	1.099
2.80	1.100	1.100	1.100	1.100	1.100	1.101	1.101	1.101	1.101	1.101
2.90	1.102	1.102	1.102	1.102	1.102	1.103	1.103	1.103	1.103	1.103
3.00	1.104	1.104	1.104	1.104	1.104	1.105	1.105	1.105	1.105	1.105
3.10	1.105	1.106	1.106	1.106	1.106	1.106	1.107	1.107	1.107	1.107

WATER CONTENT 620 PERCENT

DG	0	1	2	3	4	5	6	7	8	9
1.70	1.061	1.061	1.062	1.062	1.063	1.063	1.064	1.064	1.065	1.065
1.80	1.066	1.066	1.067	1.067	1.068	1.068	1.069	1.069	1.070	1.070
1.90	1.070	1.071	1.071	1.072	1.072	1.073	1.073	1.073	1.074	1.074
2.00	1.075	1.075	1.075	1.076	1.076	1.077	1.077	1.077	1.078	1.078
2.10	1.078	1.079	1.079	1.080	1.080	1.080	1.081	1.081	1.081	1.082
2.20	1.082	1.082	1.083	1.083	1.083	1.084	1.084	1.084	1.085	1.085
2.30	1.085	1.085	1.086	1.086	1.086	1.087	1.087	1.087	1.088	1.088
2.40	1.088	1.088	1.089	1.089	1.089	1.090	1.090	1.090	1.090	1.091
2.50	1.091	1.091	1.091	1.092	1.092	1.092	1.092	1.093	1.093	1.093
2.60	1.093	1.094	1.094	1.094	1.094	1.095	1.095	1.095	1.095	1.096
2.70	1.096	1.096	1.096	1.097	1.097	1.097	1.097	1.097	1.098	1.098
2.80	1.098	1.098	1.098	1.099	1.099	1.099	1.099	1.099	1.100	1.100
2.90	1.100	1.100	1.101	1.101	1.101	1.101	1.101	1.101	1.102	1.102
3.00	1.102	1.102	1.102	1.103	1.103	1.103	1.103	1.103	1.104	1.104
3.10	1.104	1.104	1.104	1.104	1.105	1.105	1.105	1.105	1.105	1.105

WATER CONTENT 630 PERCENT

DG	0	1	2	3	4	5	6	7	8	9
1.70	1.060	1.060	1.061	1.061	1.062	1.062	1.063	1.063	1.064	1.064
1.80	1.065	1.065	1.066	1.066	1.067	1.067	1.068	1.068	1.069	1.069
1.90	1.069	1.070	1.070	1.071	1.071	1.072	1.072	1.072	1.073	1.073
2.00	1.074	1.074	1.074	1.075	1.075	1.075	1.076	1.076	1.077	1.077
2.10	1.077	1.078	1.078	1.078	1.079	1.079	1.079	1.080	1.080	1.080
2.20	1.081	1.081	1.081	1.082	1.082	1.082	1.083	1.083	1.083	1.084
2.30	1.084	1.084	1.085	1.085	1.085	1.085	1.086	1.086	1.086	1.087
2.40	1.087	1.087	1.087	1.088	1.088	1.088	1.088	1.089	1.089	1.089
2.50	1.090	1.090	1.090	1.090	1.091	1.091	1.091	1.091	1.092	1.092
2.60	1.092	1.092	1.093	1.093	1.093	1.093	1.093	1.094	1.094	1.094
2.70	1.094	1.095	1.095	1.095	1.095	1.095	1.096	1.096	1.096	1.096
2.80	1.097	1.097	1.097	1.097	1.097	1.098	1.098	1.098	1.098	1.098
2.90	1.099	1.099	1.099	1.099	1.099	1.100	1.100	1.100	1.100	1.100
3.00	1.101	1.101	1.101	1.101	1.101	1.101	1.102	1.102	1.102	1.102
3.10	1.102	1.102	1.103	1.103	1.103	1.103	1.103	1.103	1.104	1.104

WATER CONTENT 640 PERCENT

DG	0	1	2	3	4	5	6	7	8	9
1.70	1.059	1.059	1.060	1.060	1.061	1.061	1.062	1.062	1.063	1.063
1.80	1.064	1.064	1.065	1.065	1.066	1.066	1.067	1.067	1.068	1.068
1.90	1.068	1.069	1.069	1.070	1.070	1.070	1.071	1.071	1.072	1.072
2.00	1.072	1.073	1.073	1.074	1.074	1.074	1.075	1.075	1.075	1.076
2.10	1.076	1.077	1.077	1.077	1.078	1.078	1.078	1.079	1.079	1.079
2.20	1.080	1.080	1.080	1.081	1.081	1.081	1.081	1.082	1.082	1.082
2.30	1.083	1.083	1.083	1.084	1.084	1.084	1.084	1.085	1.085	1.085
2.40	1.086	1.086	1.086	1.086	1.087	1.087	1.087	1.087	1.088	1.088
2.50	1.088	1.088	1.089	1.089	1.089	1.089	1.090	1.090	1.090	1.090
2.60	1.091	1.091	1.091	1.091	1.092	1.092	1.092	1.092	1.093	1.093
2.70	1.093	1.093	1.093	1.094	1.094	1.094	1.094	1.095	1.095	1.095
2.80	1.095	1.095	1.096	1.096	1.096	1.096	1.096	1.097	1.097	1.097
2.90	1.097	1.097	1.098	1.098	1.098	1.098	1.098	1.098	1.099	1.099
3.00	1.099	1.099	1.099	1.100	1.100	1.100	1.100	1.100	1.100	1.101
3.10	1.101	1.101	1.101	1.101	1.101	1.102	1.102	1.102	1.102	1.102

WATER CONTENT 650 PERCENT

DG	0	1	2	3	4	5	6	7	8	9
1.70	1.058	1.059	1.059	1.060	1.060	1.061	1.061	1.062	1.062	1.063
1.80	1.063	1.063	1.064	1.064	1.065	1.065	1.066	1.066	1.067	1.067
1.90	1.067	1.068	1.068	1.069	1.069	1.069	1.070	1.070	1.071	1.071
2.00	1.071	1.072	1.072	1.073	1.073	1.073	1.074	1.074	1.074	1.075
2.10	1.075	1.075	1.076	1.076	1.076	1.077	1.077	1.077	1.078	1.078
2.20	1.078	1.079	1.079	1.079	1.080	1.080	1.080	1.081	1.081	1.081
2.30	1.082	1.082	1.082	1.082	1.083	1.083	1.083	1.084	1.084	1.084
2.40	1.084	1.085	1.085	1.085	1.085	1.086	1.086	1.086	1.086	1.087
2.50	1.087	1.087	1.087	1.088	1.088	1.088	1.088	1.089	1.089	1.089
2.60	1.089	1.090	1.090	1.090	1.090	1.091	1.091	1.091	1.091	1.091
2.70	1.092	1.092	1.092	1.092	1.093	1.093	1.093	1.093	1.093	1.094
2.80	1.094	1.094	1.094	1.094	1.095	1.095	1.095	1.095	1.095	1.096
2.90	1.096	1.096	1.096	1.096	1.096	1.097	1.097	1.097	1.097	1.097
3.00	1.098	1.098	1.098	1.098	1.098	1.098	1.099	1.099	1.099	1.099
3.10	1.099	1.099	1.100	1.100	1.100	1.100	1.100	1.100	1.101	1.101

WATER CONTENT 660 PERCENT

DG	0	1	2	3	4	5	6	7	8	9
1.70	1.057	1.058	1.058	1.059	1.059	1.060	1.060	1.061	1.061	1.062
1.80	1.062	1.063	1.063	1.063	1.064	1.064	1.065	1.065	1.066	1.066
1.90	1.066	1.067	1.067	1.068	1.068	1.068	1.069	1.069	1.070	1.070
2.00	1.070	1.071	1.071	1.072	1.072	1.072	1.073	1.073	1.073	1.074
2.10	1.074	1.074	1.075	1.075	1.075	1.076	1.076	1.076	1.077	1.077
2.20	1.077	1.078	1.078	1.078	1.079	1.079	1.079	1.079	1.080	1.080
2.30	1.080	1.081	1.081	1.081	1.081	1.082	1.082	1.082	1.083	1.083
2.40	1.083	1.083	1.084	1.084	1.084	1.084	1.085	1.085	1.085	1.085
2.50	1.086	1.086	1.086	1.086	1.087	1.087	1.087	1.087	1.088	1.088
2.60	1.088	1.088	1.089	1.089	1.089	1.089	1.089	1.090	1.090	1.090
2.70	1.090	1.091	1.091	1.091	1.091	1.091	1.092	1.092	1.092	1.092
2.80	1.092	1.093	1.093	1.093	1.093	1.093	1.094	1.094	1.094	1.094
2.90	1.094	1.095	1.095	1.095	1.095	1.095	1.095	1.096	1.096	1.096
3.00	1.096	1.096	1.097	1.097	1.097	1.097	1.097	1.097	1.098	1.098
3.10	1.098	1.098	1.098	1.098	1.099	1.099	1.099	1.099	1.099	1.099

WATER CONTENT 670 PERCENT

DG	0	1	2	3	4	5	6	7	8	9
1.70	1.056	1.057	1.057	1.058	1.058	1.059	1.059	1.060	1.060	1.061
1.80	1.061	1.062	1.062	1.063	1.063	1.063	1.064	1.064	1.065	1.065
1.90	1.066	1.066	1.066	1.067	1.067	1.068	1.068	1.068	1.069	1.069
2.00	1.069	1.070	1.070	1.071	1.071	1.071	1.072	1.072	1.072	1.073
2.10	1.073	1.073	1.074	1.074	1.074	1.075	1.075	1.075	1.076	1.076
2.20	1.076	1.077	1.077	1.077	1.077	1.078	1.078	1.078	1.079	1.079
2.30	1.079	1.080	1.080	1.080	1.080	1.081	1.081	1.081	1.081	1.082
2.40	1.082	1.082	1.082	1.083	1.083	1.083	1.084	1.084	1.084	1.084
2.50	1.085	1.085	1.085	1.085	1.085	1.086	1.086	1.086	1.086	1.087
2.60	1.087	1.087	1.087	1.088	1.088	1.088	1.088	1.088	1.089	1.089
2.70	1.089	1.089	1.089	1.090	1.090	1.090	1.090	1.090	1.091	1.091
2.80	1.091	1.091	1.091	1.092	1.092	1.092	1.092	1.092	1.093	1.093
2.90	1.093	1.093	1.093	1.094	1.094	1.094	1.094	1.094	1.094	1.095
3.00	1.095	1.095	1.095	1.095	1.095	1.096	1.096	1.096	1.096	1.096
3.10	1.096	1.097	1.097	1.097	1.097	1.097	1.097	1.098	1.098	1.098

WATER CONTENT 680 PERCENT

DG	0	1	2	3	4	5	6	7	8	9
1.70	1.056	1.056	1.057	1.057	1.058	1.058	1.059	1.059	1.060	1.060
1.80	1.060	1.061	1.061	1.062	1.062	1.063	1.063	1.063	1.064	1.064
1.90	1.065	1.065	1.065	1.066	1.066	1.067	1.067	1.067	1.068	1.068
2.00	1.068	1.069	1.069	1.070	1.070	1.070	1.071	1.071	1.071	1.072
2.10	1.072	1.072	1.073	1.073	1.073	1.074	1.074	1.074	1.075	1.075
2.20	1.075	1.075	1.076	1.076	1.076	1.077	1.077	1.077	1.078	1.078
2.30	1.078	1.078	1.079	1.079	1.079	1.080	1.080	1.080	1.080	1.081
2.40	1.081	1.081	1.081	1.082	1.082	1.082	1.082	1.083	1.083	1.083
2.50	1.083	1.084	1.084	1.084	1.084	1.085	1.085	1.085	1.085	1.085
2.60	1.086	1.086	1.086	1.086	1.087	1.087	1.087	1.087	1.087	1.088
2.70	1.088	1.088	1.088	1.088	1.089	1.089	1.089	1.089	1.089	1.090
2.80	1.090	1.090	1.090	1.090	1.091	1.091	1.091	1.091	1.091	1.092
2.90	1.092	1.092	1.092	1.092	1.092	1.093	1.093	1.093	1.093	1.093
3.00	1.093	1.094	1.094	1.094	1.094	1.094	1.094	1.095	1.095	1.095
3.10	1.095	1.095	1.095	1.096	1.096	1.096	1.096	1.096	1.096	1.097

WATER CONTENT 690 PERCENT

DG	0	1	2	3	4	5	6	7	8	9
1.70	1.055	1.055	1.056	1.056	1.057	1.057	1.058	1.058	1.059	1.059
1.80	1.060	1.060	1.060	1.061	1.061	1.062	1.062	1.063	1.063	1.063
1.90	1.064	1.064	1.065	1.065	1.065	1.066	1.066	1.066	1.067	1.067
2.00	1.068	1.068	1.068	1.069	1.069	1.069	1.070	1.070	1.070	1.071
2.10	1.071	1.071	1.072	1.072	1.072	1.073	1.073	1.073	1.074	1.074
2.20	1.074	1.074	1.075	1.075	1.075	1.076	1.076	1.076	1.076	1.077
2.30	1.077	1.077	1.078	1.078	1.078	1.078	1.079	1.079	1.079	1.079
2.40	1.080	1.080	1.080	1.080	1.081	1.081	1.081	1.081	1.082	1.082
2.50	1.082	1.082	1.083	1.083	1.083	1.083	1.084	1.084	1.084	1.084
2.60	1.084	1.085	1.085	1.085	1.085	1.086	1.086	1.086	1.086	1.086
2.70	1.087	1.087	1.087	1.087	1.087	1.088	1.088	1.088	1.088	1.088
2.80	1.089	1.089	1.089	1.089	1.089	1.090	1.090	1.090	1.090	1.090
2.90	1.090	1.091	1.091	1.091	1.091	1.091	1.091	1.092	1.092	1.092
3.00	1.092	1.092	1.092	1.093	1.093	1.093	1.093	1.093	1.093	1.094
3.10	1.094	1.094	1.094	1.094	1.094	1.095	1.095	1.095	1.095	1.095

WATER CONTENT 700 PERCENT

DG	0	1	2	3	4	5	6	7	8	9
1.70	1.054	1.055	1.055	1.056	1.056	1.057	1.057	1.058	1.058	1.058
1.80	1.059	1.059	1.060	1.060	1.061	1.061	1.061	1.062	1.062	1.063
1.90	1.063	1.063	1.064	1.064	1.064	1.065	1.065	1.066	1.066	1.066
2.00	1.067	1.067	1.067	1.068	1.068	1.068	1.069	1.069	1.069	1.070
2.10	1.070	1.070	1.071	1.071	1.071	1.072	1.072	1.072	1.073	1.073
2.20	1.073	1.073	1.074	1.074	1.074	1.075	1.075	1.075	1.075	1.076
2.30	1.076	1.076	1.077	1.077	1.077	1.077	1.078	1.078	1.078	1.078
2.40	1.079	1.079	1.079	1.079	1.080	1.080	1.080	1.080	1.081	1.081
2.50	1.081	1.081	1.082	1.082	1.082	1.082	1.082	1.083	1.083	1.083
2.60	1.083	1.084	1.084	1.084	1.084	1.084	1.085	1.085	1.085	1.085
2.70	1.085	1.086	1.086	1.086	1.086	1.086	1.087	1.087	1.087	1.087
2.80	1.087	1.088	1.088	1.088	1.088	1.088	1.088	1.089	1.089	1.089
2.90	1.089	1.089	1.090	1.090	1.090	1.090	1.090	1.090	1.091	1.091
3.00	1.091	1.091	1.091	1.091	1.092	1.092	1.092	1.092	1.092	1.092
3.10	1.093	1.093	1.093	1.093	1.093	1.093	1.093	1.094	1.094	1.094

**NORTH ATLANTIC – GEOLOGY AND CONTINENTAL
DRIFT (*A Symposium*)**

Edited by *Marshall Kay*

Published by AAPG Press, Tulsa, Okla. 1081 pp; \$32.00.

Reviewed by: *Robert S. Dietz*, National Oceanic &
Atmospheric Adm., Atlantic Oceanographic and Meteorological Lab. 901 S. Miami Ave., Miami, Fla. 33130

This weighty tome is a collection of 66 papers which examines in depth the stratigraphic and structural evidence that the far north Atlantic Ocean has been opened by continental drift. The papers were originally presented in August 1967 at the Gander Conference on "Stratigraphy and Structure Bearing on the Origin of the North Atlantic Ocean." Emphasis is placed upon paleontologic and orogenic-style comparisons between Appalachian foldbelt and presumably formerly contiguous foldbelts in Ireland and Great Britain but which now strike into the Atlantic discordantly. The book contains little information bearing upon marine geology except for a review paper by J.E. Nafe and C.L. Drake on the "Floor of the North Atlantic – A Summary of Geophysical Data."

The volume contains the most comprehensive stratigraphic and structural comparison between Newfoundland and the British Isles ever published. It is divided into the following principle topics: – (1) introductory papers, (2) the southeastern border of the orogenic belt, (3) the central orogenic belt, (4) the northwestern border of the orogenic belt, (5) late orogenic stratigraphy and structure, (6) arctic regions, and (7) interpretations of drift.

W.H. Harland's proposal for the opening of the far north Atlantic based mainly on studies in Spitzbergen is especially interesting. He advocates an ancestral Atlantic Ocean which closed in the Precambrian or early Paleozoic. The present blocking out of Greenland and the separation of Europe from North America then began in late Cretaceous. His arguments are supported by a series of palinspastic maps.

The scholarly treatise replete with its massive array of references is not easy reading, but it will interest the serious students of land geology and is an excellent source book which any good technical library should hold. With but few exceptions the authors appear to accept the probable validity of continental drift controlled by the process of sea floor spreading.

SHATTER CONES (SHOCK FRACTURES) IN ASTROBLEMES

Robert S. Dietz

*NOAA, Atlantic Oceanographic and Meteorological Laboratories,
Miami, Florida 33130*

Shatter cones, conical shock fractures, are known from more than a score of cryptotoexplosion structures, presumed to be astroblemes (ancient meteorite or comet-head impact scars) around the world. These structures include: Steinheim Basin and Ries Basin in Germany; Vredefort Ring in South Africa; Gosses Bluff in Australia; Rochechouart in France; Kentland, Wells Creek Basin, Crooked Creek, Serpent Mound, Flynn Creek, Sierra Madera, Decaturville, and Middlesboro in the U.S.A., and at Sudbury, Manicouagan, Nicholson Lake, Carswell Lake, Clearwater Lake West, Lake Mistastin, and Charlevoix in Canada. In addition, they occur at Kaaliyarv and Lake Bosumtwi, modern meteorite craters. In addition to indicating shock overloading in excess of that which can be created by any endogenic explosion (e.g., cryptovolcanism), they permit vectoring of the force field since their formation precedes disruption and the cones point toward the oncoming shock wave. At several locations (Vredefort, Sudbury, Decaturville, Wells Creek, Sierra Madera, Kentland, Gosses Bluff and Charlevoix) they indicate that the explosion focus (ground zero) was either from above and/or inward toward the center of the structure. At Charlevoix, the finding of shatter cones by Rondot led to the discovery of the cryptotoexplosion structure. Shatter cones are an especially useful criterion of shock in carbonate terranes, where shock metamorphic effects commonly are absent. Recently, Alexander and Hawk have used shatter cone distribution at Wells Creek Basin and Vredefort to compute the total energy of impact. Other aspects of the shatter cone criterion for astroblemes are reviewed. There remains little doubt but that, when shatter cones can be identified with certainty, they are a valid and definitive criterion for an astrobleme.

SUDBURY ASTROBLEME: A REVIEW

Robert S. Dietz

*NOAA, Atlantic Oceanographic and Meteorological Laboratories
Miami, Florida 33130*

The Sudbury Basin in Ontario, Canada, is a now widely accepted astrobleme, or meteorite impact scar, created about 1700 m.y. ago. Evidence is provided by shatter coning, shock metamorphic effects, the Sudbury breccia, "geologic overkill," etc. A thick deposit of impact microbreccia (Onaping suevite) also was laid down in the crater. This astrobleme is of unusual interest not only because of its economic importance (dominating the world's nickel production), but also because extensive magmatism was associated with the impact, creating an extrusive lopolith. The origin of the so-called sublayer is now of critical importance in understanding the Sudbury event. The sublayer, composed of "quartz diorite," breccia and sulfides, forms a liner to the crater and invades the surrounding country rock as a spokelike injection extending 10 km or more. The sublayer appears to be the product of splash emplacement, a mixture of bolide and target rock injected just prior to the extrusion of the lopolith. It seems possible that the sulfide ores may be, at least in part, cosmogenic, derived from the substance of the bolide. The history of the Sudbury Basin as an astrobleme is also reviewed. The significance of shatter coning as evidence of shock, for reconstructing the force vector field, and for unraveling the timing of the event is also emphasized.

MAXWELL, Arthur E., ed. *The Sea: Ideas and Observations on Progress in the Study of the Seas*. Vol. 4: *New Concepts of Sea Floor Evolution*. Part 1: 791 pp. Part 2: 664 pp. Wiley-Interscience, 1970. \$32.50 each.

This weighty and comprehensive volume of invited papers by 77 authors covering recent advances in our understanding of the ocean floor marks a major milestone. Its contents emphasize that a modern scientific revolution has been wrought by the new model of the earth based on plate tectonics and sea floor spreading. The ocean basins are young; they are born, expand, contract, and die while the continents live on. The authors have been carefully chosen for their eminence, and the contents reveal that marine geology and geophysics is dominated by American scientists. Some papers jointly offered by American and Russian authors indicate a new level of workable collaboration between the East and the West.

Volume 4 is subdivided into two tomes: the first, which concerns general observations, contains 20 articles that treat the ocean floor worldwide on a discipline basis. Included are papers on marine geodesy; acidic, basic, and ultramafic rocks of the ocean floor; gravity; magnetic reversal anomalies; seismic reflection and refraction; paleomagnetism; seamount magnetism; gravity; heat flow; earthquakes and tectonics; pre-Quaternary microfossil distribution; etc.

The second tome describes the ocean floor regionally. Among its 14 articles are 5 on the Pacific floor, while the others cover most of the other oceans of the world. Two thorough papers on the structure of the little-known Indian Ocean and the Mediterranean basin are especially welcome. A final part, which offers new concepts, contains a paper on sea floor spreading, by Fred Vine and the late Harry Hess, and one by J. Tuzo Wilson on transform faults.

Shortcomings are few in this excellent volume, but some may be noted. (1) In these times of voluminous literature, abstracts seem essential, but there are none. (2) The lack of any treatment of the Atlantic basin leaves a gap in an otherwise balanced regional coverage of the ocean floors of the world. (3) The high price places the volume beyond the grasp of most individual researchers, let alone the impecunious student. Thus, this series will serve only as a library source book and not as a replacement for the classic textbook *The Oceans*, an avowed original intention. (4) The long delay between receipt of manuscripts (2-3 years) and the availability of the book means that the papers are somewhat out of date. (The volume is dated 1970, but actually was not available until spring 1971.) Fortunately, the papers were prepared after the 1967 sweeping conversion of marine geologists to sea floor spreading and plate tectonics. There is, however, no impact of the JOIDES (deep-sea drilling program) results. (5) Typographical errors are rather numerous.—Robert S. Dietz, *Environmental Science Services, U. S. Department of Commerce*

Those Shifty Continents

By ROBERT S. DIETZ

NOAA, Atlantic Oceanographic and Meteorological Laboratories
Miami, Florida

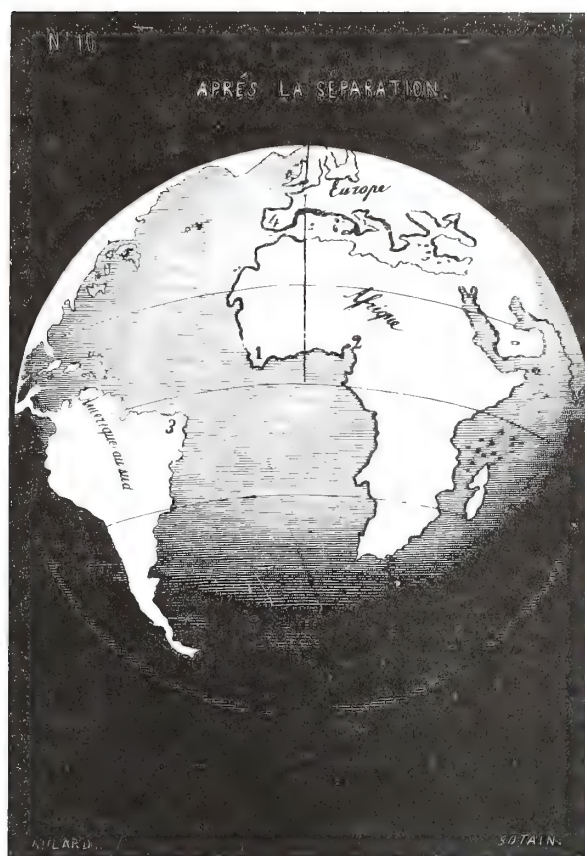
DURING THE PAST DECADE, the concept of continental drift has undergone a remarkable transformation from an outrageous hypothesis, through a period of nagging reappraisal and finally to verification. The reality of drift is no longer questioned by the large majority of earth scientists but many problems remain unresolved. Most importantly, when did this drift begin and where were the continents in the beginning? In short, we need to understand the pattern of the continental breakup and dispersion in space and time.

In modern context, continental drift is simply a necessary consequence of the even grander theory of *plate tectonics*. The term *tectonics* refers to the slow geological motions of the earth crust (up, down or sideways) and also to compressional folding and extensional rifting. This concept holds that the earth's outer crust is divided into about nine major rigid plates, or spherical caps, separated by seams

something like the segments on a turtle's carapace. These 60-mile-thick plates are in slow but inexorable motion and they interact along their boundaries, causing earthquakes among other things, in the process. The 22-mile-thick continents are granitic "plateaus" embedded within the plate. With the exception of the Pacific plate, each plate contains a continent, if India is included as a subcontinent. As the plates move so must the continents that ride piggyback upon them.

A Humpty-Dumpty Problem

We now believe that about 200 million years ago the continents were all joined together, forming the supercontinent of Pangaea, meaning "all earth." Although the solution is not straightforward, we can in principle solve this jigsaw reconstruction or "Humpty-Dumpty" problem, and fit all of the continents back together again. We cannot do this for the plates since they change their size and shape.



THE CONTINENTAL DRIFT CONCEPT is not new. Reproduced here in lithograph is the first depiction of the drift opening of the Atlantic Ocean in *The Creation and its Mysteries Explained: A Treatise...which Explains the Origin of America and its Primitive Inhabitants*, by A. Snider, published in Paris in 1859. Snider supposed that the Atlantic Ocean did not exist prior to the biblical flood. During the Deluge great volcanoes erupted which split off the Americas along with the island of Atlantis both of which drifted westward. Snider argued, by a series of farfetched assumptions, that the Americas somehow escaped the Deluge and were not covered with water. The antediluvian population therefore escaped the catastrophe and eventually evolved into the indigenes found by the European explorers. Snider concluded that "L'Amérique est réellement l'ancienne Atlantide de l'époque antédiluvienne," or "America is really the ancient Atlantis of antediluvian times."

They can grow either larger or smaller by adding new crust or resorbing old crust. The growth occurs at the so-called mid-ocean ridges, where the plates are pulled apart and new lava from the earth's mantle rises into the crack. The process may be likened to the freezing of newly exposed water as ice floes drift apart.

Where the Crust is Sucked In

Resorption of crust occurs in trenches or subduction (lead down) zones, those areas where the crustal plate dives steeply into the earth's mantle. Those rock components that are fusible in the earth's hot mantle rise again, causing volcanic activity, granitic intrusions and mountain building. These subduction zones are found in the Pacific trenches and a line of filled trenches extending from Gibraltar through the Himalayas to New Guinea—known as the great Tethys subduction zone.

We may visualize the ideal crustal plate as being rectangular with a rift (a mid-ocean ridge) and a trench forming one pair of opposing margins. The other two opposing sides would be great shear zones, called transform faults, which are regions of slippage, along which crust is neither made nor destroyed, but rather conserved. An example well known to Americans is the San Andreas fault, which strikes through California and is a portion of the margin of the Pacific plate. Slippage along this plate boundary was responsible for the disastrous San Francisco earthquake of 1906.

This remarkable new understanding of the earth, as important to geology

(Continued on page 210)

CONTINENTAL DRIFT as envisioned by Alfred Wegener, in his book Origin of Continents and Ocean Basins. This volume was published in 1929, just prior to his death on the Greenland ice cap, where he had gone to prove by precise geodetic measurements that this subcontinent was drifting westward. Wegener first formalized the concept of drifting continents and is regarded the founder of the drift hypothesis. Considering its vintage, Wegener's idea that the world's land masses emerged from the single continent of Pangaea (a name he coined) was remarkably precocious.

Wegener's interest in drift was triggered by "the direct impression produced by the congruency of the coastlines on either side of the Atlantic." Accordingly he fitted the continents together as in a jigsaw puzzle, but he distorted their outlines. The enlargement of India is a good example. He also considered India as always being an integral part of Asia. The stippled areas in the lowest diagram are modern continental shelves.

Wegener's timing of the initial breakup of Pangaea (Upper Carboniferous, or 300 million years ago) is somewhat earlier than the late Triassic breakup (200 million years ago) proposed by modern theorists. Wegener also erroneously supposed that much of the drifting occurred late in geologic time with Europe remaining attached to Greenland until about 1 million years ago. He also considered Africa and Eurasia to be fixed in position and used an arbitrary map grid. He accommodated the northward motion of India simply by the distortion of Eurasia.

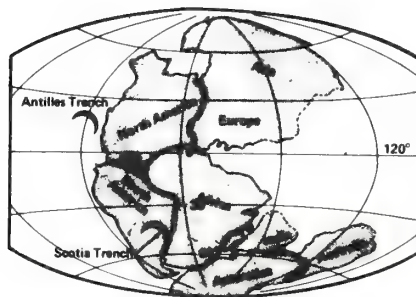
UPPER CARBONIFEROUS



EOCENE

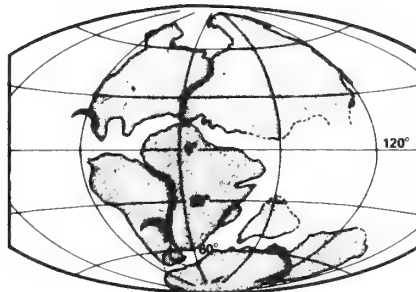


LOWER QUATERNARY

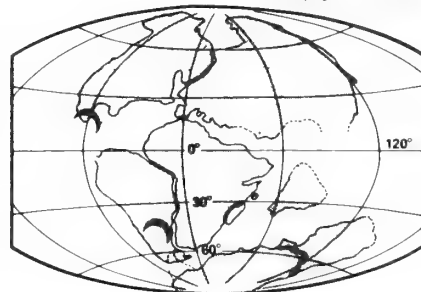


1: End of Permian, 225 million years ago

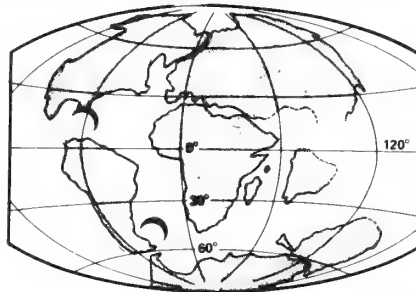
Maps adapted from Journal of
Geophysical Research



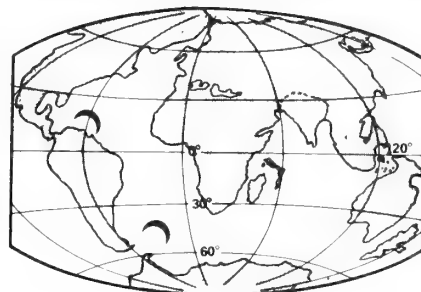
2: End of Triassic, 190 million years ago



3: End of Jurassic, 135 million years ago



4: End of Cretaceous, 65 million years ago



5: Today

A MUCH SIMPLIFIED SERIES of drawings which depict the breakup of Pangaea according to R. S. Dietz and John C. Holden, adapted from the original presentation in *J. Geophysical Research* (1970:75: p. 4939). The universal landmass is believed to have undergone initial separation into the supercontinents of Laurasia (northern group) and Gondwana (southern group) in the late Triassic, 200 million years ago. An east-west rift near the equator opened the proto-North Atlantic Ocean. Simultaneously the Indian Ocean commenced forming as well. In general, the new world has drifted westward while the continents surrounding the Indian Ocean (Africa, India and Australia) moved northward. Although his mechanisms for drift are no longer accepted, Wegener interestingly proposed a "westward wandering" and a "flight from the poles." These maps confirm this westward drift but Wegener's flight from the poles is replaced as a drift from the south pole only.

This time-sequence map series is the first attempt ever to show the past positions of continents in absolute geographic coordinates. To achieve this absolute tracking of the continents, Dietz and Holden used as fix markers lavas thought to be derived in ascending plumes from the earth's deep mantle. Unlike earlier reconstructions none of the continents remain anchored in position, although Antarctica has moved relatively little. India and Australia have undergone exceedingly fast drift rates of more than 4 inches per year. Although moving at a slower rate of about 1 inch per year, North America has nevertheless drifted northwestward for 5,000 miles. (This drift rate is about equivalent to the length of a human body in a lifetime.) New York, now at 40°N latitude, originally was near the equator. The last major event was the detachment of Australia from Antarctica only 45 million years ago. The Himalaya Mountains were pushed up when India struck the underbelly of Asia about 25 million years ago.

The Atlantic Ocean is wholly new with the central North Atlantic opening first, the South Atlantic opening second, and finally, with the detachment of Greenland from Europe, the far North Atlantic opened and created a passage into the Arctic Ocean. The Indian Ocean is a complex basin created by the repositioning of landmasses associated with the closing of the Tethys Sea—a huge embayment which once extended westward from the ancestral Pacific Ocean. Although still covering nearly a full hemisphere, the Pacific is growing ever smaller. Drift theorists call the ancestral Pacific *Panthalassa*, meaning universal sea.

To help clarify the breakup of Pangaea, two well-known oceanic landmarks, the Antilles and the Scotia arcs, are placed in their modern position on all of the charts. Also, for best centering of the landmasses, the vertical center line of the projection is the 20°E longitude meridian rather than Greenwich.

as the theory of evolution was to biology, was preceded by two developments in the study of terrestrial magnetism. The first involves detecting the changes in the position of the earth's magnetic pole (the polar method), and the other, reversals of the earth's magnetic field (the reversal method). These were critical to the ultimate proof of continental drift.

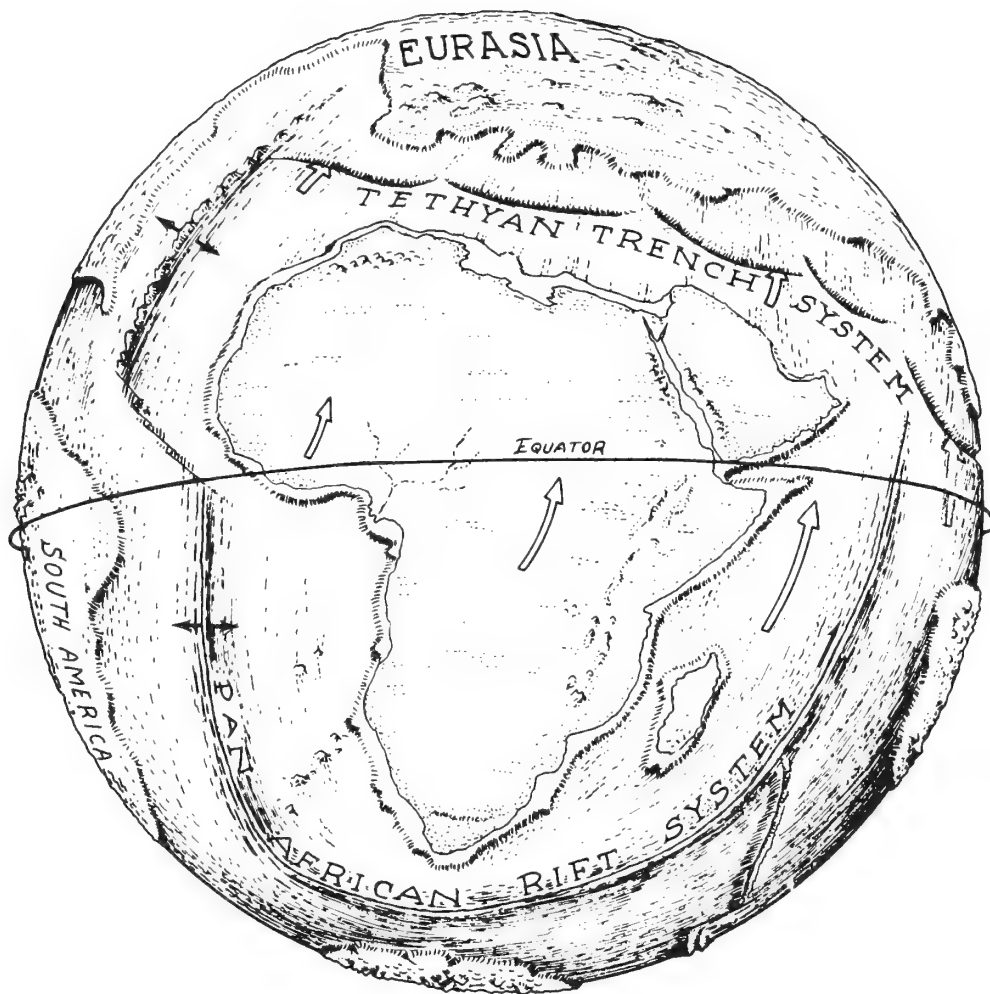
Where Did the North Pole Go?

In the late 1940's, scientists recognized that certain rocks, especially ancient lavas, are in effect "fossil compasses." As freshly extruded lava cools through the Curie point at about 575° C., an imprint of the earth's magnetic field, as it existed at that point in time, is "frozen in." By collecting oriented samples of ancient lavas, specialists in paleomagnetism have clearly shown that these "fossil compasses" generally give a different solution for both the direction and the dip of the North Magnetic Pole than does a modern compass needle placed on the point from which the lava sample was taken. Some of these differences (but not all), established through thousands of measurements, could only be explained if continents had drifted.

As with many scientific techniques, there are significant limitations. The earth's surface is curved, so that three coordinates are needed to establish a fix on the globe. The "fossil compasses" of paleomagnetism can only provide orientation and magnetic latitude; longitude remains forever indeterminate. In the same way the navigator at sea with only a dip compass can, in principle, roughly determine his orientation with respect to the geographic

grid as well as his magnetic latitude—but not his longitude. Unfortunately, using paleomagnetism no one has discovered as yet the equivalent of the chronometer, which makes the determination of a ship's longitude possible. Because of this restriction, many scientists remained skeptical of the paleopole position evidence for continental drift.

Fortunately, an even more powerful method—magnetic reversal—was discovered within the past decade. In the late fifties, extensive regions of the ocean floor were first found to be characterized by strong magnetic anomalies, or departures from the earth's normal ambient magnetic field. These were disposed in horizontal patterns like zebra stripes. British workers soon realized that these could be explained as growth increments of new ocean crust being added as the crustal plates spread apart at the mid-ocean ridges. There also was good evidence to show that the earth's magnetic poles flipped, with the North Magnetic Pole becoming the South Magnetic Pole and vice versa, every million years or so. This flipping is related to circulation patterns within the earth's nickel-iron core and not to any geographic tipping of the earth. With each flip a new anomaly is added to the pattern of a spreading ocean floor so that large regions of the ocean floor acted like a magnetic tape recorder. It soon became possible to measure quite precisely the horizontal shifts of the plates—a new dimension to which terrestrial geology was blind. We now have a magnetic chronology, rather analogous to the method of aging trees by ring counting, which extends 80 million years back in time.



THE AFRICAN CRUSTAL PLATE, upon which the continent of Africa is superimposed, is depicted in this diagram. Throughout its history the African plate has drifted northward and rotated counterclockwise. The plate is bordered on three sides by the Pan-African rift system, which has acted at various times as both a shear zone (especially on the Indian Ocean side) for accommodating the shifting of the plate, and a zone of sea floor spreading (especially on the Atlantic side) where new ocean floor has been extruded. The northward drift of the African plate is accommodated by a descent and resorption of the outer crust of the earth into the Tethyan trench system, a remnant of which now lies beneath the Mediterranean Sea. (Drawing by John C. Holden)

Thus it is now known that the earth's crust not only goes up and down but also moves sideways. The horizontal velocities of a few centimeters per year are slow by human standards, but they are ten, one hundred or a thousand times faster than other grand geologic processes like the rising of mountains, subsidence of land masses or the erosion of continents. It has long been known that Florida and the adjacent Bahama platform reveal a long history of continued subsidence of a few miles over the past 150 million years. But geologists have only recently realized that during this same interval these crustal blocks have drifted northwestward for more than 3,000 miles. When added to the vertical displacements and time—the substance of classical geology—this new horizontal drift gives earth history a fourth dimension and increases its complexity.

Rewrite the Texts

The textbooks are now being rewritten to incorporate this new mobilistic philosophy, and an exciting era has come to the earth sciences. Practi-

cal benefits may ensue, once we understand the plate motions in detail. For example, it should then be possible to predict earthquakes with some precision. A step in this direction was made recently by Robert Wallace of the United States Geological Survey. By analyzing the motions along California's San Andreas fault, he predicts that there will be an important earthquake every five years and a large earthquake every 15 years. A really disastrous quake, like that which shook San Francisco in 1906, will occur once each century.

ADDITIONAL READING

Other articles on continental drift that have appeared in *Sea Frontiers*:

POTHIER, R. J. "Deep Sea Drilling Record," Vol. 14, No. 6, page 322.

DIETZ, R. S. "More About Continental Drift," Vol. 13, No. 2, page 66.

RUNCORN, S. K. "Corals and the History of the Earth's Rotation," Vol. 13, No. 1, page 4.

CREER, K. M. "Continents on the Move," Vol. 12, No. 3, page 148.



PORTRAIT
OF A SCIENTIST

*FRANCIS
SHEPARD*

ROBERT S. DIETZ¹
and K.O. EMERY²

Where Alph, the sacred river ran/ Through caverns measureless to man/ Down to the sunless sea, . . .
Coleridge

Geology has undergone a revolution during the past decade paced by discoveries about the ocean floor — and this is where the geologic action is. To a significant degree, this revolution can be traced to one man, Francis Parker Shepard. His researches and those of his many students, numbering more than threescore, have left an indelible imprint on marine geology.

Francis P. Shepard (now Professor Emeritus of Submarine Geology at Scripps Institution of Oceanography of the University of California at San Diego), a native of Brookline, Massachusetts, received his AB from Harvard University in 1920 and his PhD in 1922 from the University of Chicago. From 1923 to 1937 he was a faculty member of the University of Illinois, but his growing commitment to submarine geology drew him to the Scripps Institution of Oceanography at La Jolla, California — firstly part time, and then full time after World War II. During the war years he served with the University of California Division of War Research, making sediment studies to help understand the behavior of under-

¹National Oceanic and Atmospheric Administration, Atlantic Oceanographic and Meteorological Laboratories, Miami, Florida.

²Woods Hole Oceanographic Institution, Woods Hole, Massachusetts

water sound in relation to submarine detection, and compiling shelf sediment charts of foreign areas to support military operations. With the termination of hostilities, he returned to Scripps Institution where he has remained even after his retirement in 1966, and where he now continues to actively pursue his interests in marine geology.

A PROFILIC WRITER

Shepard's eminence derives from his cascade of scientific papers numbering nearly 200, plus several books. This output reflects his boundless energy and enthusiasm. *Submarine Geology* (Harper and Row) now is the standard text in the field. It was first published in 1948, went into a completely rewritten second edition in 1963, and a third edition is now under preparation. He also authored the popular book, *The Earth Beneath the Sea* (Johns Hopkins Press) in 1959, which has recently been reissued. In 1966 he published *Submarine Canyons and Other Sea Valleys* with Robert F. Dill as co-author. Earlier he also edited the monograph, *Sediments of the Northwest Gulf of Mexico*, published by the American Association of Petroleum Geologists. This was a byproduct of the American Petroleum Institute's Project 51, which he directed from 1951 to 1957, on the paralic and deltaic sedimentation along the Gulf coast¹. Currently in press is *Our Changing Coastlines*, written with the late Harold R. Wanless. This book examines the coastline changes around the United States, including Alaska and the Hawaiian Islands, by comparing early charts and aerial photographs with their modern counterparts. It is a final chapter in a theme which Shepard has pursued throughout his life — the geomorphology and classification of shorelines. Early in his career he led the breakaway from the then widely accepted genetic shoreline classification of Douglas Johnson after William Morris Davis' philosophy of historical sequences.

ORIGINAL IDEAS

Among the many original ideas which can be ascribed to Shepard are the following: (1) troughs and fjords of shelves in high latitudes resulted primarily from glacial erosion and not from faulting; (2) the pattern of shelf sedimentation is complex, and beyond the surf zone there is no general gradation of sediments from coarse to fine across continental shelves; (3) submarine canyons are maintained by periodic and sudden removal of clogging sediments; (4) the shelf-edge topographic highs and much of the slope relief of the continental margin off Texas are related to salt intrusions; (5) undertow is largely a myth, and rip currents are responsible, instead, for numerous drownings; (6) tsunamis are mostly the direct result of fault displacements rather than of landslides; and (7) there has been no high stand of sea level associated with a climatic optimum during the Holocene.

To Shepard, geology is an observational and descriptive science. He is skeptical of highly sophisticated theoretical analysis and is impatient with oblique contemplation of the sea from ivory towers. He prefers to overwhelm a problem by an extensive collection of data. Utilizing T.C. Chamberlain's principle of multiple working hypotheses, Shepard, in turn, likes to set up "truth tables," listing the points for or against any idea. His predilection is to jump on his horse (or, rather, ship) and go and see. He develops his views in the field rather than accepting answers recorded in authoritative books, thus "counting the lion's teeth instead of consulting Aristotle."

Of iconoclastic bent, many of Shepard's early writings were directed towards proving that some accepted principle of geology (such as periodic diastrophism) is wrong. His doctoral dissertation on the structural geology of the Rocky Mountain trench proposed that this feature was not a graben, as previously supposed, but even in one place a horst. R.A. Daly and R.T. Chamberlain, his early mentors at Harvard and Chicago respectively, were among those with whom Shepard quickly found reason to disagree. An interesting footnote to this background is that Shepard in 1966 followed Daly as the next American

recipient of the coveted Wollaston Medal of the Geological Society of London. It had been bestowed on Daly in 1942.

SHIPBOARD OBSERVATIONS

Shepard's focus on shipboard observations beginning in the early thirties marked a change of method in marine geology. He had developed an early love for the sea aboard his father's yacht out of Marblehead, Massachusetts. The spark that propelled him into marine geology was his observation that the sediment samples he collected with the yacht off the New England coast strikingly disagreed with the classical dogma that they would become finer grained offshore and toward a "wave base" marked by the shelf break. Once bitten by the taste of the sea, Shepard never returned to classical geology. He kept ties to the land, however, for he became a "green-water" marine geologist, confining his interests largely to the shoreline, the shelf and slope, and especially the precipitous canyons which incised the continental slope. He became a marine geologist and not a geological oceanographer and has treated marine geology as an extension of land geology.

Shepard's canyon studies had modest beginnings — a rowboat, a sounding line, and a sextant. With these simple tools, he made repetitive surveys in the nineteen-thirties of several canyon heads along the California coast. His report that some canyon heads had deepened or shoaled within a six-month interval was at first dismissed with a smile. Were they not due to surveying inaccuracies?² Shepard's findings subsequently have been fully verified. Some of the canyon heads gradually fill with sand and then are periodically cleaned out by some process which still is not fully understood.

Shepard has never been a man with a "greasy thumb" and has little patience with complex mechanical gadgets, let alone electronic black boxes. He likes to rely solely upon simple devices which are foolproof and have stood the test of shipboard use. One master-stroke of simple instrumentation was dispatching 2m-high Roger Revelle (later Director

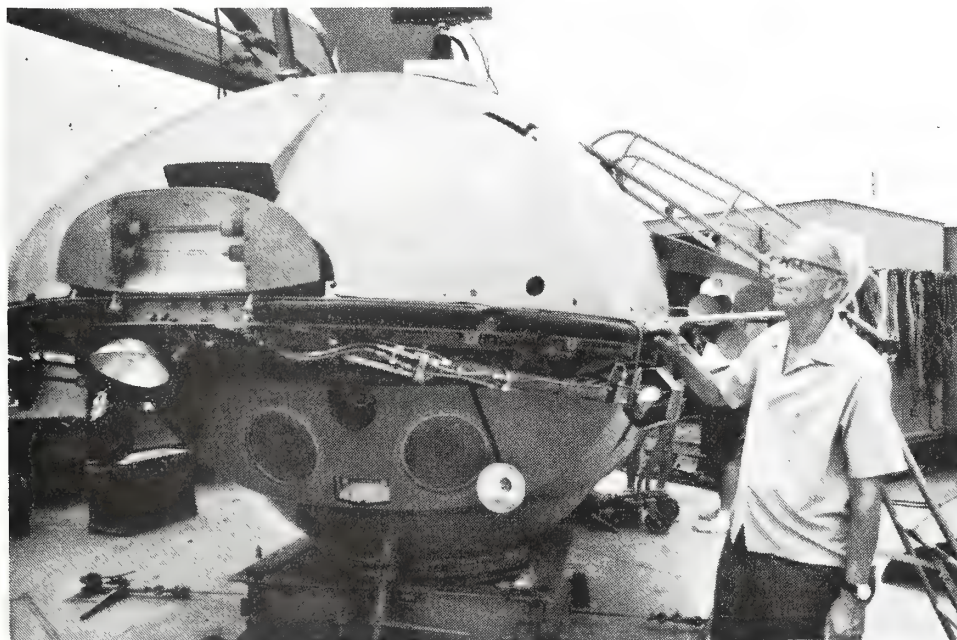


Fig. 2. Francis Shepard inspecting the Westinghouse Deepstar 4000, a deep-research vehicle, just prior to a dive into Mississippi Submarine Trough. Commencing with dives in Cousteau's Diving Saucer in 1964, Shepard has carried out a program of visual studies of submarine canyons. (Photo by Ron Church.)

of Scripps Institution of Oceanography) into the surf zone to act as a calibrated wave staff. This interest in simplicity probably in part stems from his involvement in attempting to develop, in the mid-nineteen-thirties a highly touted hydrostatic corer which would utilize the ambient pressure of the deep ocean to drive a core barrel into the bottom. On its first deep trial off California, this device imploded, and all that was recovered was the cable's frayed bitter end. This loss virtually wiped out the instrumentation funds in Shepard's grant for studying canyons off the California coast.

Over the years, the techniques of marine geology have, of course, become ever more sophisticated. By 1966 it was even possible for Shepard to break away from remote sensing and directly inspect the La Jolla Submarine Canyon off California through the portholes of the Cousteau diving saucer. He describes this as "a thrilling experience and the greatest day in my life."

A TURNING POINT IN MARINE GEOLOGY

A turning point in Shepard's career was a \$10,000 grant in 1936 from the Penrose Fund of the Geological Society of America for investigating the submarine canyons off California. This was a large grant for those years and the largest ever granted to that date by the G.S.A. With these funds, Shepard was able to use the oceanographic research ship, "E.W. Scripps", for six months, support two student assistants (the authors of this article), and supply the equipment needed. Along with H.C. Stetson's studies during the same period at Woods Hole Oceanographic Institution, this effort founded sea-going marine geology in the United States. A spate of papers resulted from this research, including the monograph, *Submarine Topography off the California Coast: Canyons and Tectonic Interpretation* (GSA Special Paper No. 31, with K.O. Emery). With a follow-on G.S.A. grant, Shepard in 1940 did extensive work in the Gulf of California.

Shepard is perhaps best known for his vigorous espousal of the belief that submarine canyons resulted from river cutting when the continental slopes were exposed due to lowering of sea level as much as 2000m during the Pleistocene. Many sharp exchanges of opinion were published by Shepard and his antagonists, who included Daly and D.W. Johnson, but eventually the turbidity-current origin won the dominating role in the origin of these canyons. To err is human, and Shepard retracted his hypothesis once sufficient data accumulated to show that it was not tenable. He now believes that a highly complex set of processes have been at work in submarine canyons, including not only modest sea level lowering and turbidity currents, but also many other types of water currents and mass movements. His recent work has been directed toward learning more about the transportation of sands from shallow to deep water, on cable breaks associated with turbidity currents, and on the scouring of canyon walls by creeping sand masses. In his treatise on submarine canyons, he has modestly written, "The book. . . should be considered only an installment in a continued story."

In association with Hans Suess, Shepard in 1956 made a classic study of the post-glacial rise of sea level using radiocarbon dating. Recently he led a large team investigation to the coral reefs of the west Pacific Ocean, Daly's type locality for his plus-two-meter Holocene high sea level during the so-called Climatic Optimum: This team found no supporting evidence of any such high stand as advocated in recent years by Rhodes Fairbridge and others.

PROFOUND LOVE OF THE SEA

When not actually at sea, Shepard prefers to work within the sight and sound of the surf. This attachment for the sea cost Shepard the first draft of his textbook on submarine geology and nearly his life, as well. In 1946 while writing the manuscript, he was living in a small cottage on the north coast of Hawaii. When the April 1 tsunami, triggered

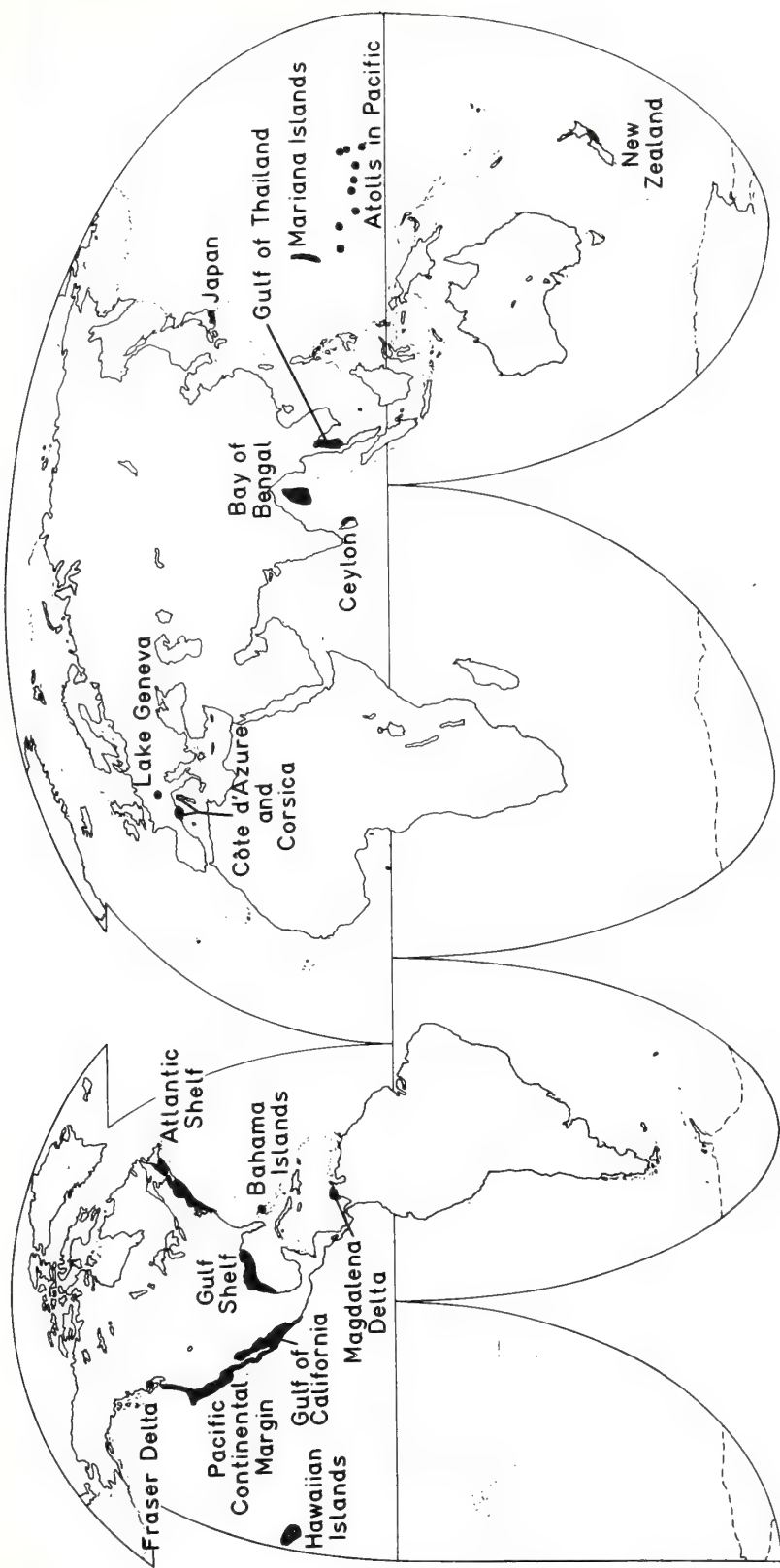


Fig. 3. Localities where Francis Shepard has made marine geologic researches.

by an earthquake in the Aleutian trench, struck, his wife, Elizabeth, quickly retreated to high ground. Shepard himself incautiously remained behind to observe and photograph this rare natural phenomenon. The cottage was completely demolished, the manuscript was washed away, and only by climbing a tree was he able to avoid being washed away by the inundating eighth wave. With characteristic energy and enthusiasm, Shepard (with D.C. Cox and G.A. MacDonald) immediately initiated a now-classic investigation of the coastal effects of that tsunami on the Hawaiian Islands.



Fig. 4. F.P. Shepard as a Navy cadet at Harvard with his future bride, Elizabeth Buchner. World War I ended before Shepard was called to duty overseas.

Surely we can identify Shepard as the first American marine geologist³. During the late nineteen-thirties, when the submarine-canyon controversy was raging, Shepard was the only participant who had actually ever sounded and sampled a submarine canyon. Shepard's approach has always been direct as he quickly moved to the ocean's edge and grappled intimately with his chosen subject. His overall time at sea must run about five years and there probably are few oceanographers who have spent any more than this on a rolling deck. His wife, Elizabeth, has accompanied him on many of these cruises, especially in recent years, in a supporting role such as monitoring the echo sounder.

HONORS AND RECOGNITION

In 1964 Shepard's students presented him with a book of their papers in his honor entitled *Papers in Marine Geology: Shepard Commemorative Volume* (Macmillan).⁴ To keep this effort a secret until published it was given the code name "Project Sextant" in recognition of Shepard's numerous hydrographic surveys in which he utilized this instrument. Shepard has received many other honors including an honorary DSc from Beloit College in 1968. In 1968 he was also selected as the San Diego Man of Distinction in recognition of his scientific achievements. From 1958 to 1963 he was President of the International Association of Sedimentologists and presided over the Association's general meetings at Copenhagen in 1960 and at Amsterdam in 1963. He is a member or fellow of many scientific societies which are too numerous to list here.

A signal honor and token of high regard by his colleagues was the recent establishment of an award in his name by the Society of Economic Geologists. The SEPM has designated it as the *Francis P. Shepard Award for Excellence in Marine Geology*. It is presented usually annually to an outstanding marine geologist, based on "excellence in marine geology, with primary consideration for excellence in those fields for which Professor Shepard has become well known. These fields are the distribution and characteristics of sediments, marine geomorphology, and structure of the continental margins of the world".

Shepard's accomplishments of the past are part of a continuing series. Retirement means little other than providing more unfettered time for marine studies. Judging from the longevity of his parents, Shepard has yet several decades of productivity. We look forward to reading the results of this work.

REFERENCES AND NOTES

1. (see page A10) During this period, one of his students, Harris B. Stewart, composed a poem entitled "An Ode to F.P. Shepard's 100th Reprint* — or, One Sansicle, Please, and No Mud."

We had drinks and hors d'oeuvres from the platter / The Department was there to a man
It was during a lull in the chatter / That Shepard put forth his new plan.
"If clay and silt are contiguous, / And next to the silt is the sand,
Then 'mud' as a term is ambiguous, / And in consequence should be banned.
If a triangle's used in the riddle, / And sand, silt, and clay juxtaposed,
For the triangle left in the middle, / The term 'sansicle' is proposed."

*(We can excuse this inaccuracy as poetic licence, but in the interest of precise reporting we must point out that the paper in question (Nomenclature based on sand-silt-clay ratios. *J. Sediment. Petrol.*, 24(3): 151–158, 1954) was actually his 112th.)

2. (see page A11) As Shepard's student assistants in these early surveys, the authors of this article must now admit nagging doubts about the validity of these surveys. But, after all, are not apprentice scientists supposed to be skeptics?

3. (see page A14) We have hesitated in referring to Shepard as the "father of marine geology." However, the venerable Madame Klenova of the U.S.S.R. Institute of Oceanology did so upon the occasion of the International Geological Congress in Mexico City in 1956, when the cold war first had thawed sufficiently for Russian scientists to attend such functions. As they met for the first time, Mme. Klenova warmly remarked, "You are the father of marine geology and I am the mother of marine geology." To this, Elizabeth Shepard replied, "And that, in turn, must make me the concubine."

4. (see page A15) In addition to its 24 papers by his students, this volume contains a biographical foreward about Francis P. Shepard, a "Vita," and a listing of his 141 publications to 1961.

Pre-Mesozoic Oceanic Crust in the Eastern Indian Ocean (Wharton Basin)?

by

ROBERT S. DIETZ & JOHN C. HOLDEN

ESSA, Atlantic Oceanographic and Meteorological Laboratories, 901 South Miami Avenue, Miami, Florida 33130

A search for ocean basins underlain by old crust has suggested that the Wharton Basin would be a likely place to investigate.

THERE IS NOW great interest in the search for old Earth's crust, not only for the sake of a better understanding of ocean floor evolution but also because such material would be more highly mineralized and the thick cover of sediments would offer enticing prospects for petroleum. In what follows, by "old crust" we mean merely pre-Mesozoic crust, older than 225 m.y. Even this modest antiquity would, however, antedate the great sequence of events beginning with the breakup and dispersion of Pangaea, which probably commenced in mid-Triassic, 200 m.y. ago¹.

The half spreading rates associated with seafloor spreading (that is, the spreading on each limb of a spreading mid-ocean rift) of 1-6 cm per year are suggested by the magnetic anomaly growth lines reaching back over the past 4 m.y. If these rates can be extrapolated linearly back in time to anomaly 32 of Heirtzler *et al.*², about half of the ocean floor is of Cainozoic age (less than 65 m.y.)³ except in special situations; nearly all the remainder must be Mesozoic.

The scientific staff on JOIDES (Deep Sea Drilling Project) leg 6 concluded that the North-west Pacific basin was the oldest part of the oldest ocean⁴. Upper Jurassic sediments (Tithonian, 140 m.y.) were encountered in two cores but, by inference, Lower Jurassic or even Triassic ocean floor might be present closer to the Marianas subduction zone. The Philippine Sea, which lies behind the Japan-Marianas-Palau trench system, was found to be young, probably not older than early Cainozoic. (In deep sea drilling, the assumption is made that the age of the sediments immediately overlying basement basalts, as indicated by seismic reflexion profiling, is the age of the oceanic crust. This interpretation is reasonable if the crust was emplaced according to the seafloor spreading concept.)

The search for Palaeozoic crust was also a primary aim of the recent JOIDES leg 11 off the eastern United States⁵. Only mid-Jurassic (about 160 m.y.) strata were found, but this is the oldest rock so far recovered from any ocean basin. This makes it unlikely that the Atlantic commenced opening at the beginning of the Permian and that the peripheral quiet magnetic zone of the Central North Atlantic represents crust emplaced in the 50 m.y. long Kiaman interval of constantly reversed magnetic polarity essentially during the Permian^{6,7}. We agree with Vogt *et al.*⁸ that the magnetic quiet zone represents crustal emplacement during the Triassic. The South Atlantic is clearly younger than the North Atlantic, and so this entire rift ocean (excluding subplates) is unlikely to contain Palaeozoic ocean crust.

It is possible, but perhaps unlikely, that the Arctic Ocean contains old crust. Apparently there was an ancestral Arctic basin within the framework of Pangaea, which we have named *Sinus Borealis* (Latin for northern embayment)⁹. The Eurasian Basin, between the Lomonosov Ridge and Eurasia, must be neo-oceanic, for it contains a central spreading rift, an extension of the mid-Atlantic ridge¹⁰. Perhaps the Canadian Basin

contains old crust. But a likely history for the Arctic Ocean is that the Alpha Ridge in the Canadian Basin is a "fossil" but now abandoned spreading rift. This old rift then "jumped" to its present location, splitting off a sector of the Eurasian craton (the Lomonosov Ridge) in the process¹¹. This would infer that the oceanic crust of the Canadian Basin is not very old, at least in its northern portion. On the other hand, Churkin's¹² interpretation, based on the marginal lower Palaeozoic geosynclines of Alaska and Canada, may be correct. He believes that the oceanic crust of the Canadian Basin must be early Palaeozoic or even Pre-Cambrian.

Seafloor marginal to Antarctica also seems at first to contain sectors of Palaeozoic crust for the following reasons. This continent is surrounded by a rift-megashear system (the pan-Antarctic rift) bounding the Antarctic crustal plate. No trenches are associated with this plate, into which ocean crust is being subducted. It is unique in this respect, for the other major crustal plates—North American, South American, Eurasian, African, Indian, Australian, main Pacific and East Pacific plates—include a subduction zone. Clearly the Antarctic crustal plate has evolved by the outward migration of the pan-Antarctic rift with time. Inside those sectors, where the rift did not initially block out Antarctica's continental slope, areas of old seafloor might be stranded and preserved. The broad sector of West Antarctica which faces the Pacific Ocean seems to offer such a possibility, for this is obviously not a rift margin. A Mesozoic foldbelt, however, a portion of the circum-Pacific orogenic girdle, makes up the periphery of West Antarctica, suggesting that seafloor was once subducted along this margin even if not now. Although volcanic zone extends along the Pacific margin of East Antarctica, the volcanoes are alkaline, not calc-alkaline, and provide no evidence for crustal subduction today. Future seismic profiling, however, will probably indicate the former presence of a trench zone there.

Pursuing the question of old crust, attention is drawn to the so-called subplates. The small ocean basins, such as the Sea of Japan, seem to be of prime interest, for they lie isolated and "protected" behind the subduction zones (trenches) where a descending lithospheric plate is being consumed. Geological and heat flow studies, however, suggest that the Japan Sea is also neo-oceanic¹³. There are Asiatic strata along the inner margin of the Honshu arc, suggesting that Japan was once attached to Asia, but that the Japanese arc subsequently moved outward. Apparently a mid-ocean rift is not a necessity for the emplacement of new oceanic crust, for there are no linear magnetic anomalies in the Japan Sea. The Fuji Basin, behind the Tonga-Kermadec trench, also has been inferred to have young crust¹⁴. It seems likely that the small ocean basins of the Pacific which form subplates are generally neo-oceanic.

The Caribbean is another type of isolated subplate which is protected by a subduction zone—the east by the Antilles trench and the west by the Central American trench. The crust, however, is probably Mesozoic, not Palaeozoic. It was probably created with extension associated with the initial breakup of Pangaea into North America/Eurasia and South America/Africa in the mid-Triassic¹. There is only a small chance that old Pacific floor is trapped within the Caribbean region.

The history of the Gulf of Mexico is an open question

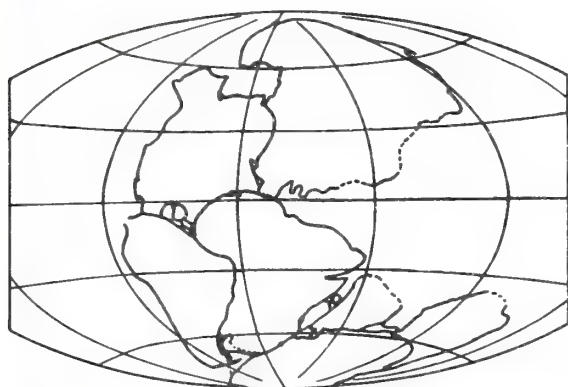


Fig. 1 Reconstruction of the continents into Pangaea before 200 m.y. ago (adapted from Dietz and Holden¹).

depending largely on whether it was an arm of the world ocean (Panthalassa), a *sinus occidentalis*, or was created, like the Caribbean, with the initial breakup of Pangaea. Results from JOIDES leg 10 indicate that the central Gulf of Mexico was already deep water in the late Cretaceous (Santonian, -80 m.y.) and the south-east part since Cainomanian time (-100 m.y.)¹⁵. If the Luann salt is a deep water salt laid down with the initial formation of the Gulf of Mexico, its age would be late Triassic or early Jurassic. It seems most likely that the Gulf of Mexico is neo-oceanic, forming in mid-Triassic with the clockwise rotation of the Honduras and Yucatan blocks which rotated outward to form Central America.

Generally regarded as a rift ocean like the Atlantic, the Indian Ocean would seem at first thought to offer little prospect of containing old ocean floor, but its history is much more

complex than the Atlantic. It differs markedly from the Atlantic Ocean in that there was an ancestral Indian Ocean—namely, the eastern reaches of Tethys. As well as being a rift ocean, it is of the Pacific type, its northern boundary being margined by a subduction zone—the Himalayan–Java trench system. We suggest that the eastern Indian Ocean floor, or the Wharton Basin in the broad sense (as defined by the Ninetyeast ridge, the Java trench, the western Australian margin, and the Diamantina fracture zone), is underlain by pre-Mesozoic crust, for the following reasons.

A generalized reconstruction of Pangaea, adapted from an earlier publication of ours (Fig. 1), shows that the Tethys Sea occupied the region of the Indian Ocean. The region between India and Australia is occupied by a bay of Tethys which we have termed Sinus Australis. A more detailed and precise reconstruction of the continents around Antarctica is shown in Fig. 2, which is quite similar to the assembly offered by Smith and Hallam¹⁶. We believe that this reconstruction is essentially correct and provides a basis on which the subsequent history of breakup and continental drift dispersion in terms of plate tectonics can be reasonably determined and schematized (Fig. 3).

Fig. 3A (a Hammer transverse elliptical projection centred on 90° E longitude and 70° S latitude) shows the probable assembly of the continents around the Indian Ocean before continental drift breakup. Regions to the east of Australia and to the west of India are not considered. India and Australia are joined to Antarctica within the framework of the universal continent of Pangaea before the mid-Triassic, or -200 m.y. In Fig. 3A Antarctica is fixed in position and the geographical coordinates are drawn relative to modern coordinates. This is not entirely gratuitous, for Antarctica probably has remained almost fixed with the other continents doing most of the drifting¹¹.

Fig. 3B shows the situation in the early Cainozoic or about -45 m.y., just before the detachment of Australia from

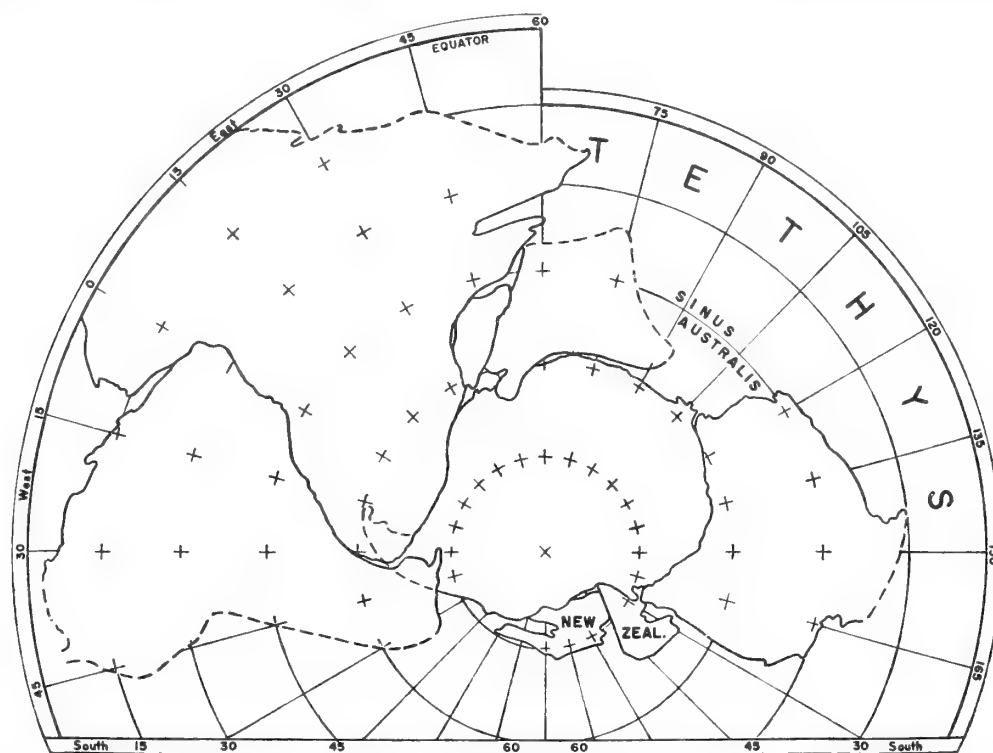
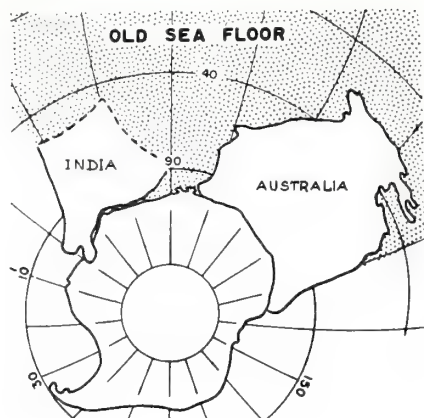
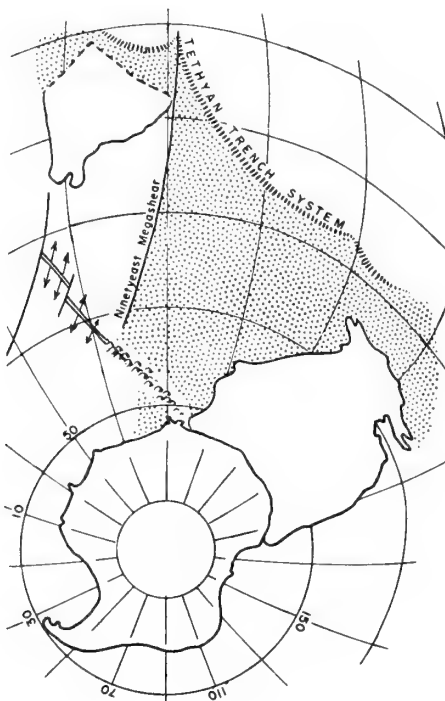


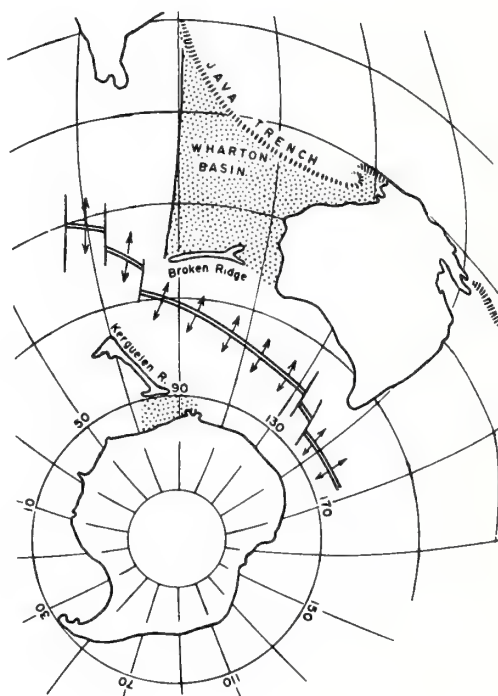
Fig. 2 Detailed depiction showing the reconstruction of continents around Antarctica before 200 m.y. ago. New Zealand has been broken into two parts along the Alpine fault.



A



B



C

Fig. 3 Time sequence diagram showing the breakup and drift dispersion of India and Australia from Antarctica and consequent preservation of old crust in the Wharton Basin.

Antarctica. India had previously been detached from Antarctica, drifted far northward and almost reached the Tethyan subduction zone (Himalaya "trench"). The Indian plate was bounded on the west by the Chagos-Laccodive megashear and on the east by the Ninetyeast megashear (rift-trench strike-slip transform faults) and on the south by a rift. Old ocean floor was subducted into the Tethyan trench while new ocean crust was emplaced by seafloor spreading in the "wake" of India on both limbs of a northward migrating rift ("mid-ocean ridge"). Thus a broad swath of Tethys was "repaved". An undersea plateau (possibly a partially differentiated outpouring of lava of semi-simatic composition) is shown as having come into existence—the ancestral Kerguelen Plateau—Broken Ridge highground. It had been incipiently split into two parts by the penetration of the India rift.

Fig. 3C shows the position of the continents and the disposition of the crustal plates today. According to the magnetic

reversal chronology impressed on the oceanic crust between Australia and Antarctica, these two continents were not detached until the early Cainozoic, for no anomalies older than anomaly 18 (Eocene, -45 m.y.) are present¹⁷. Consequently the old Tethyan seafloor, especially Sinus Australis, forming the western part of the Australian plate remains undisturbed. This plate later underwent subduction into the Java trench, but the Wharton Basin remains as unconsumed old crust while new ocean floor is being emplaced between Antarctica and Australia. Also, as we have depicted the drift dispersion of continents in this region, a small sector of old crust has been trapped along the margin of Antarctica near 90° E longitude. The reality of such details of this interpretation depends, of course, on the exact timing and geometry of the breakup.

This treatment considers that both Broken Ridge and the Kerguelen Plateau are of simatic composition. If either or both of these features should be identified as microcontinents

there is some evidence that Broken Ridge may be so¹⁸—our proposed history would have to be modified. For example, if Kerguelen proves to be young while Broken Ridge is old sial, it would most likely have been detached from Antarctica by the rift shown in Fig. 3B and little, if any, pre-Mesozoic crust would remain stranded adjacent to Antarctica.

We have not treated that portion of the Australian plate in the Pacific Ocean to the east of Australia. However, if the New Zealand subcontinent (a reasonable term as the area of the New Zealand platform is almost as large as India) was once attached to Australia, as seems probable, spreading has occurred between these two sialic platforms such that most of the ocean floor in between must be new.

(An alternative solution to closing the Indian Ocean by our continental drift reconstruction is to place India's east coast against Australia. Such a reconstruction leaves a large triangular mediterranean sea within Gondwana, margined by western India, Africa/Madagascar and Central East Antarctica. We suggest that this inland small ocean basin, if it existed (and we are inclined to doubt it) be termed *Mare Gondwanis* (Latin for sea of Gondwana). The breakup of this assembly would then involve the insertion of a spreading rift into the centre of this mediterranean and, in turn, would imply that old ocean floor would now be stranded marginal to parts of India, Africa and Antarctica (from 40°–80° E longitude), the exact sectors involved depending on how the spreading rift was initially inserted. We believe, however, that such a breakup and dispersion history for the Indian Ocean continents is unlikely.)

There is some suggestive evidence that the Wharton Basin is at least of modest antiquity, and its unusual topography supports this interpretation. There are numerous large ridges, marginal plateaus, and blocky highs quite unlike ocean floors elsewhere. This is strikingly revealed by the National Geographic Society's 1967 map of the Indian Ocean floor based on the bathymetric studies of B. C. Heezen and M. Tharp. Sixty million year old basalt has been dredged from Ninety-

east ridge, so that this feature is not young¹⁹. Upper Cretaceous (Turonian) ooze has been cored on the Naturaliste plateau²⁰ and Cretaceous ooze has been recovered from the centre of this basin²¹. Our interpretation awaits testing by seismic reflexion profiling, dredging, coring and, we hope, drilling by the Deep Sea Sampling Project. If our view is correct, the Wharton Basin is the only broad expanse of pre-Mesozoic seafloor in the world.

Received October 20, 1970.

- ¹ Dietz, R. S., and Holden, J. C., *J. Geophys. Res.*, **75**, 26, 4939 (1970).
- ² Heirtzler, J., Dickson, G., Herron, E., Pitman, W., and Le Pichon, X., *J. Geophys. Res.*, **73**, 6, 2119 (1968).
- ³ Vine, F. J., *J. Geol. Education*, **18**, 2, 87 (1970).
- ⁴ *Geotimes*, **14**, 8, 13 (1969).
- ⁵ *Geotimes*, **15**, 7, 14 (1970).
- ⁶ Heirtzler, J. R., and Hayes, D. E., *Science*, **157**, 185 (1967).
- ⁷ Emery, K. O., Uchupi, E., Phillips, J., Bowin, C., Bunce, E., and Knott, S., *Amer. Assoc. Petrol. Geol. Bull.*, **54**, 1, 44 (1970).
- ⁸ Vogt, P., Anderson, C., Bracey, D., and Schneider, E., *J. Geophys. Res.*, **75**, 20, 3955 (1970).
- ⁹ Dietz, R. S., and Holden, J. C., *Sci. Amer.*, **223**, 4, 30 (1970).
- ¹⁰ Dement'skaya, R., and Karasik, A., *Tectonophysics*, **8**, 345 (1969).
- ¹¹ Ostenso, N. A., and Wold, K. L., *Intern. Assoc. Geomag. Aeron. Bull.*, **24**, 67 (1967).
- ¹² Churkin, H., *Science*, **165**, 549 (1969).
- ¹³ Fujii, N., *Intern. Symp. Mechanical Properties and Processes in the Mantle*, Flagstaff, abstract (1970).
- ¹⁴ Karig, D., *J. Geophys. Res.*, **75**, 2, 239 (1970).
- ¹⁵ *Geotimes*, **15**, 6, 11 (1970).
- ¹⁶ Smith, A. G., and Hallam, A., *Nature*, **225**, 139 (1970).
- ¹⁷ Le Pichon, X., and Heirtz, J. R., *J. Geophys. Res.*, **72**, 6, 2101 (1968).
- ¹⁸ Francis, T., and Raitt, R., *J. Geophys. Res.*, **72**, 12, 3015 (1967).
- ¹⁹ Bezrukov, P., Krylov, A., and Cernishev, V., *Oceanologia*, **6**, 261 (1966).
- ²⁰ Burkle, L., Saito, T., and Ewing, M., *Deep-Sea Res.*, **14**, 4, 421 (1967).
- ²¹ Saito, T., *Symp. Micropaleontology of Marine Bottom Sediments* (Special Committee on Oceanic Research, 19, 1967).

ROBERT S. DIETZ }
JOHN C. HOLDEN } NOAA, Atlantic Oceanographic and Meteorological Laboratories, 901 South
WALTER P. SPROLL } Miami Ave., Miami, Florida 33130

Geotectonic Evolution and Subsidence of Bahama Platform: Reply

The preceding discussion by Sheridan of our paper provides a welcome chance to clarify and amplify certain aspects of our views on the evolution of the Bahama platform (Dietz and others, 1970).

We agree with Sheridan that our crustal model for the Bahamas is a liberation from the standard concept that all continental regions (defined here as those at or near sea level) need not be necessarily underlain by "mountain roots"—a sialic basement complex. In particular, we suppose that other marginal plateaus formed at former Y-junctions of crustal plates may be thick sedimentary accumulations emplaced directly on oceanic crust (such as Demerara marginal plateau) or volcanic accumulations (such as Afar triangle). We are inclined to doubt, however, Sheridan's speculation that the Jurassic Luann salt of the Gulf of Mexico is a shallow-water deposit. More likely it was deposited as a deep-water salt. The recent finding by oil companies that there is 3000 to 4000 m of Miocene salt beneath the Red Sea, without associated marginal facies characteristic of evaporites (gypsum and limestone), provides a strong case for deep-sea deposition of halite.

We agree that our presumed crustal section beneath the Bahama platform may be unrealistic in that the density chosen for the oceanic crust is too low. Sheridan's proposal for a more probable crustal section, in which he infers the existence of a thick intermediate layer between the normal oceanic crust and the Moho, is certainly an improvement. The problem to be faced, of course, is to somehow fill up with sediments a small ocean basin, or quasi-ocean basin, to sea level without grossly violating isostasy so that algal-coral carbonate deposition can gain a foothold. We are open to any suggestions for accomplishing this solution.

Sheridan (1969) believes that the deep Atlantic (Blake-Bahama basin) to the east of the Bahama platform was once much shallower than now. Results from JOIDES Leg 11 seem to support this point of view to some degree. For example, the Tithonian limestones penetrated in Hole 99 just east of San Salvador Island "probably indicate deposition in a relatively shallow pelagic environment," and from Hole 100 nearby, "The nature of these sediments and character of the microfauna suggest a neritic-upper bathyal environment during their deposition" (Scientific staff, 1970). By the sea-floor-spreading concept, *all* of the floor in a rift ocean was originally generated at the rifted crest of a mid-ocean ridge. Subsequently, these mid-ocean ridges subside, and the original floor is further isostatically depressed by sedimentary loading. The subsidence of the basal sedimentary layers would be the expected history with depression of basal carbonate layers below the modern lysocline (carbonate compensation depth).

We regard as unlikely, however, Sheridan's supposition that the adjacent deep Atlantic has taken part in the full subsidence of the Bahama platform of about 5 km, which would mean that the Blake-Bahama basin was once almost at sea level. We know of no evidence that the Bahama carbonate section monoclinaly dips toward the shelf edge, as do those sections of the Atlantic continental shelf. This dip suggests a coupling between the craton and the ocean floor and suggests regional isostatic compensation. If the Bahama carbonates are really flat lying, the presence of a fault along the platform boundary remains probable. Because ocean-floor sedimentary layers are incompetent, we would not expect seismic profiler records to indicate any marked disturbance or drag effect such as would make the fault evident.

We caution also that deep-ocean sediments do not record large vertical displacement with clarity, and displaced shallow-water sediments create much confusion. Rather remarkably, with the new chronology of magnetic reversal anomalies, we can for the first time identify large horizontal shifts of the ocean floor. This stands in sharp contrast to continental geology which is largely blind to horizontal shifts while clearly recording vertical shifts, especially those which penetrate the plane of sea level.

Although the Bahama platform is an aseismic region, this cannot be taken to prove that a normal fault does not exist along the platform margin. Faulting of this type may occur in small increments with little buildup of stress and, as such, would not produce measurable seisms. Also, most of the subsidence of the Bahamas occurred in the Mesozoic when the platform was young, with only a small amount of sinking subsequent to the Eocene.

The dredging of a limestone block with slickensides parallel to bedding from Abaco Canyon by Sheridan, Elliott, and Oostdam (in press) and Sheridan, Berman, and Corman (1971) is most interesting and suggestive, but it does not really constitute a weighty argument favoring an important role for strike-slip tectonics in the Bahama region. The development of this carbonate platform is doubtless complex and defies any simple or single interpretation. Our thoughts on the environmental development of the curious indentations (such as Tongue of the Ocean) was incidental to the main theme. Nevertheless, it seemed worthwhile to emphasize an aspect of carbonate bank evolution that previously had been overlooked in favor of these re-entrants that were either tectonic or inherited features. We note that "textbook" atolls, whose perfect circularity reflects the circularity of subsided seamount tops, are rare. Atolls become more irregular with increasing size—and more and more reflect environmental factors. The Bahama platform is positioned in a strongly asymmetrical part of the Atlantic with respect to planetary currents and tradewinds. The Bahamian islands themselves have marked environmental disposition; nearly all are located on the windward side of deep-water passes. We suspect that environmental factors are important and even may dominate in account-

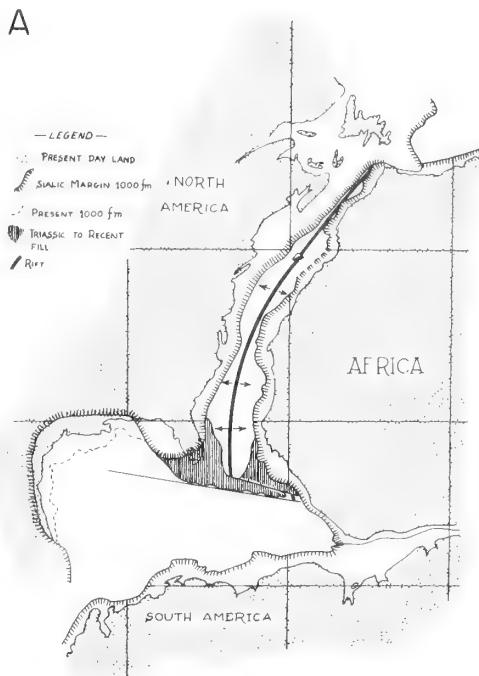
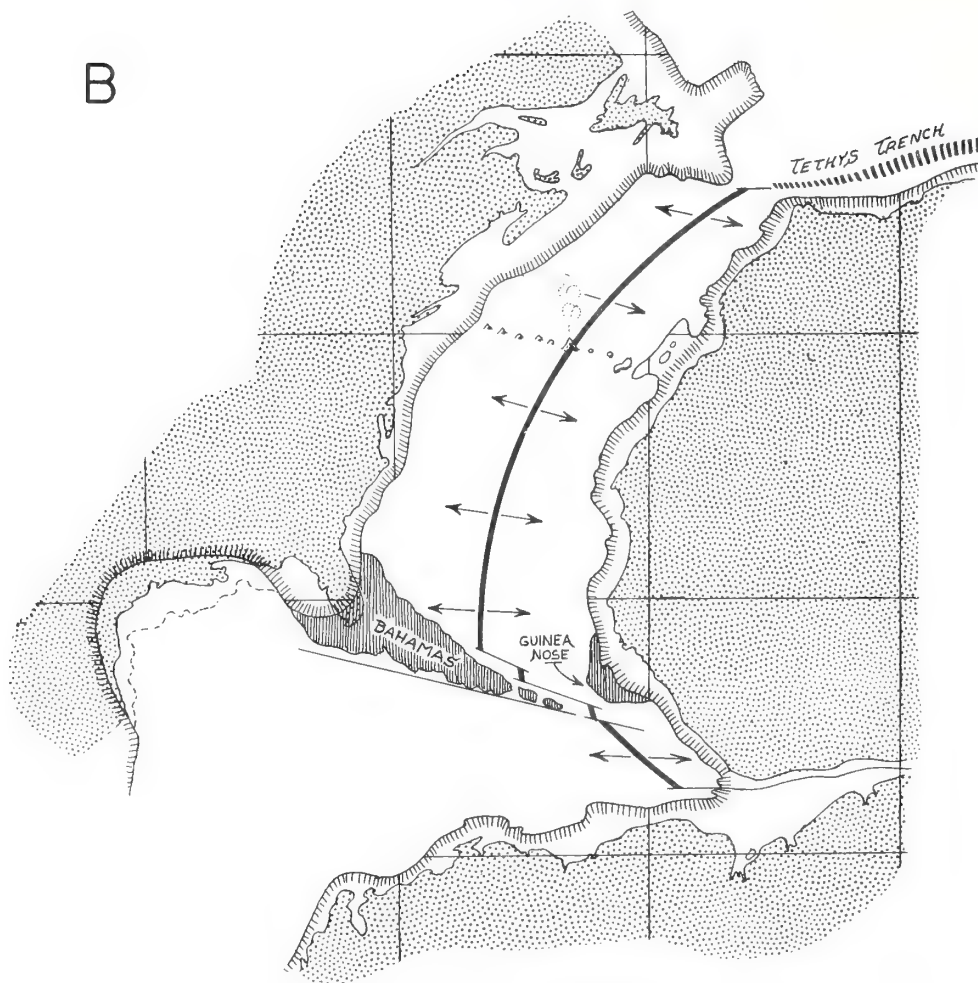


Figure 1. Formation of the Bahama platform following the mid-Triassic opening of the central North Atlantic. Events in the Gulf of Mexico and the Caribbean are left unspecified. Most likely, the region was closed with cratonic blocks which later became Honduras, Yucatan, and the Antilles islands. A. Shortly after rifting, late Triassic. B. After further opening, as of mid-Jurassic.

ing for the irregularities of the Bahama platform.

We were aware of the view of Sheridan and others (1969), that the "Guinea Nose" (a marginal plateau) is underlain by an extension in basement structural arch and, thus, is an integral part of the African craton, but there is conflicting evidence. On one hand, this interpretation accords with that of Sougy (1962), who extrapolates his Paleozoic Mauritanides foldbelt across the Guinea Nose. On the other hand, from recent oil company surveys Templeton (in press) believes that this foldbelt bifurcates well inshore of the Guinea Nose and that a syncline lies athwart Sougy's trend and yet is inshore of the Guinea Nose. Templeton shows the pre-Mesozoic



surface to be 3000 to 5000 m deep over the Guinea Nose. From their magnetic survey, McMaster and others (1970, p. 161) also specifically question the existence of a west-southwest-trending "Guinea Arch" underlying the Guinea Nose as proposed by Sheridan. It should be borne in mind, however, that Sheridan, using the seismic refraction method, may have measured Paleozoic structure in sedimentary strata, while McMaster and others measured Precambrian basement effects. We suppose that the possibility remains that the Guinea marginal plateau is a postdrift deposition excrecence to the African craton and so, in a small way, a mirror counterpart of the Bahama platform.

We would like to offer a novel way in which

one might determine whether or not the Guinea Nose is old craton or postdrift excrecence ("new ground"). The ghost outline of the African margin is rather faithfully reproduced in the mid-ocean rift. Probably the Guinea Nose is sufficiently large to be reflected thus, if it, in fact, was present at the time of breakup (≈ 200 m.y. ago). We have examined the shape of the rift zone where it is intersected by what appears to be the Guinea fracture zone. It appears to resemble more closely the African margin with the Guinea Nose subtracted rather than added, which supports the idea that it is "new ground." However, detailed survey of the mid-ocean rift is necessary before much credence can be placed in this evaluation.

Some new evidence, that the Bahamas are a postrift excrement to North America, follows from the finding of Vogt (written commun., 1970). Magnetic reversal anomalies created by sea-floor spreading should, and in fact do, generally parallel the margins of North America and Africa. However, the J-series anomalies identified by the Gofar Project of the Naval Oceanographic Office parallel the Atlantic coast, but strike abruptly into the north margin of the Bahama platform. Therefore, these spreading anomalies originally may have underlain the Bahama platform and subsequently have been covered by the growth of that platform.

It is also worth noting that the results of JOIDES Leg 11, which drilled in the deep Atlantic off the Bahamas, is consistent with our interpretation (Scientific staff, 1970). The oldest rocks yet found in the Atlantic were recovered just east of San Salvador Island and are estimated to be 160 m.y. old. This observation supports our suggestion that the clastic sediments of the inferred Bahama cryptobasin, underlying the carbonate cap, must be Late Triassic or Early Jurassic.

REFERENCES CITED

- Dietz, R. S.; Holden, J. C.; and Sproll, W. P. Geotectonic evolution and subsidence of Bahama platform: *Geol. Soc. Amer., Bull.*, Vol. 81, p. 1915-1928, 1970.
- McMaster, R. L.; De Boer, J.; and Ashraf, A. Magnetic and seismic reflection studies on continental shelf off Portuguese Guinea, Guinea, and Sierra Leone, West Africa: *Amer. Ass. Petrol. Geol., Bull.*, Vol. 54, No. 1, p. 158-167, 1970.
- Scientific staff. Deep sea drilling project: Leg 11: *Geotimes*, Vol. 15, No. 7, p. 14-16, 1970.
- Sheridan, R. E. Subsidence of continental margins: *Tectonophys.*, Vol. 7, p. 219-229, 1969.
- Sheridan, R. E.; Berman, R.; and Corman, D. Faulted limestone block dredged from Blake escarpment: *Geol. Soc. Amer., Bull.*, Vol. 82, No. 1, p. 199-206, 1971.
- Sheridan, R. E.; Elliott, G. K.; and Oostdam, B. L. Seismic-reflection profile across Blake escarpment near Great Abaco Canyon: *Amer. Ass. Petrol. Geol., Bull.*, in press.
- Sheridan, R. E.; Houtz, R. E.; Drake, C. L.; and Ewing, M. Structure of continental margin off Sierra Leone, West Africa: *J. Geophys. Res.*, Vol. 74, p. 2512-2530, 1969.
- Sougy, J. West Africa fold belt: *Geol. Soc. Amer., Bull.*, Vol. 73, p. 871-876, 1962.
- Templeton, R. Geology of the continental margin between Dakar and Cape Palmas: SCOR symposium on Geology of the East Atlantic continental margin, Cambridge, England, March 1970, H.M.S. Stationery Office, London, in press.

MANUSCRIPT RECEIVED BY THE SOCIETY
NOVEMBER 9, 1970

SHORTER CONTRIBUTION

Trou sans Fond submarine canyon: Ivory Coast, Africa

ROBERT S. DIETZ* and HARLEY J. KNEBEL†

(Received 10 June 1970; in revised form 16 November 1970; accepted 18 November 1970)

Abstract—A bathymetric chart of the Trou sans Fond (Bottomless Hole) submarine canyon off the Ivory Coast, Africa, is presented, based upon a 1400-km survey in 1968 by the O.S.S. *Discoverer*. The canyon originates with a double head just off the beach and cuts a deep V-shaped furrow across the 30-km-wide shelf, attaining a maximum relief of 450 fm (823 m) near the shelf break. The canyon has a slightly sinuous and rugged relief down the continental slope, indicating an active erosional regime. At 1500 fm (2745 m) where the continental rise commences, the canyon is abruptly offset 20 km to the west, suggesting that the present outer fan valley is a newly developed channel. On the continental rise a depositional regime is indicated by well developed natural levees which have a cross-sectional area 60 times that of the Mississippi in the delta region. The Trou sans Fond appears to be the only canyon which taps the paralic zone between the Cayar Canyon to the north and the Congo Canyon to the south.

INTRODUCTION

IN FEBRUARY 1968 the O.S.S. *Discoverer*, a research ship operated by the National Ocean Survey of the National Oceanic and Atmospheric Administration, surveyed the Trou sans Fond (Bottomless Hole) submarine canyon which lies off the Ivory Coast. Its existence has been known since at least 1846 when it first appeared on a chart published by the French engineer, Bellin. More recently the canyon head has been studied by French engineers for harbor entrance purposes, but its over-all bathymetry remained little known. No mention of it was made, for example, in the excellent monograph on the world's submarine canyons by SHEPARD and DILL (1964). This survey provides for the first time a detailed chart showing its bathymetry to 100 nautical miles offshore. Canyons such as the Trou sans Fond which tap the paralic zone are of unusual geologic interest, as they funnel neritic sediments to the deep ocean floor. By incising the continental shelf almost to the shore, they partially intercept the longshore 'river of sand' and thus may be called 'sand-eating' canyons.

The Trou sans Fond is of unusual economic significance in that it provides an access route for deep draft ships to nearshore. Taking advantage of the naturally deep water, the artificial Vridi ship channel was cut in 1952 through the longshore bar to an interior lagoon, making a major regional port and, in turn, creating the practically new city of Abidjan. Presumably owing to flushing of sand into the canyon head, silting-up of the canal entrance has not been a problem; on the contrary, a deepening has occurred over the past 15 years. The canyon head was also the site of an abortive attempt by Georges Claude in the 1930's to create a novel type of power plant which would have utilized the thermal contrast between the cold, deep canyon head waters and the hot lagoonal waters to create a thermal engine. An excellent recent account of the general marine geology of the Ivory Coast continental shelf and the inner portion of the Trou sans Fond was published by MARTIN (1969). Aspects of physical oceanography and shoreline dynamics have been treated by VARLET (1958).

*National Oceanic and Atmospheric Administration, Atlantic Oceanographic and Meteorological Laboratories, 901 South Miami Ave., Miami, Florida 33130.

†Now at Department of Oceanography, University of Washington, Seattle, Wash.

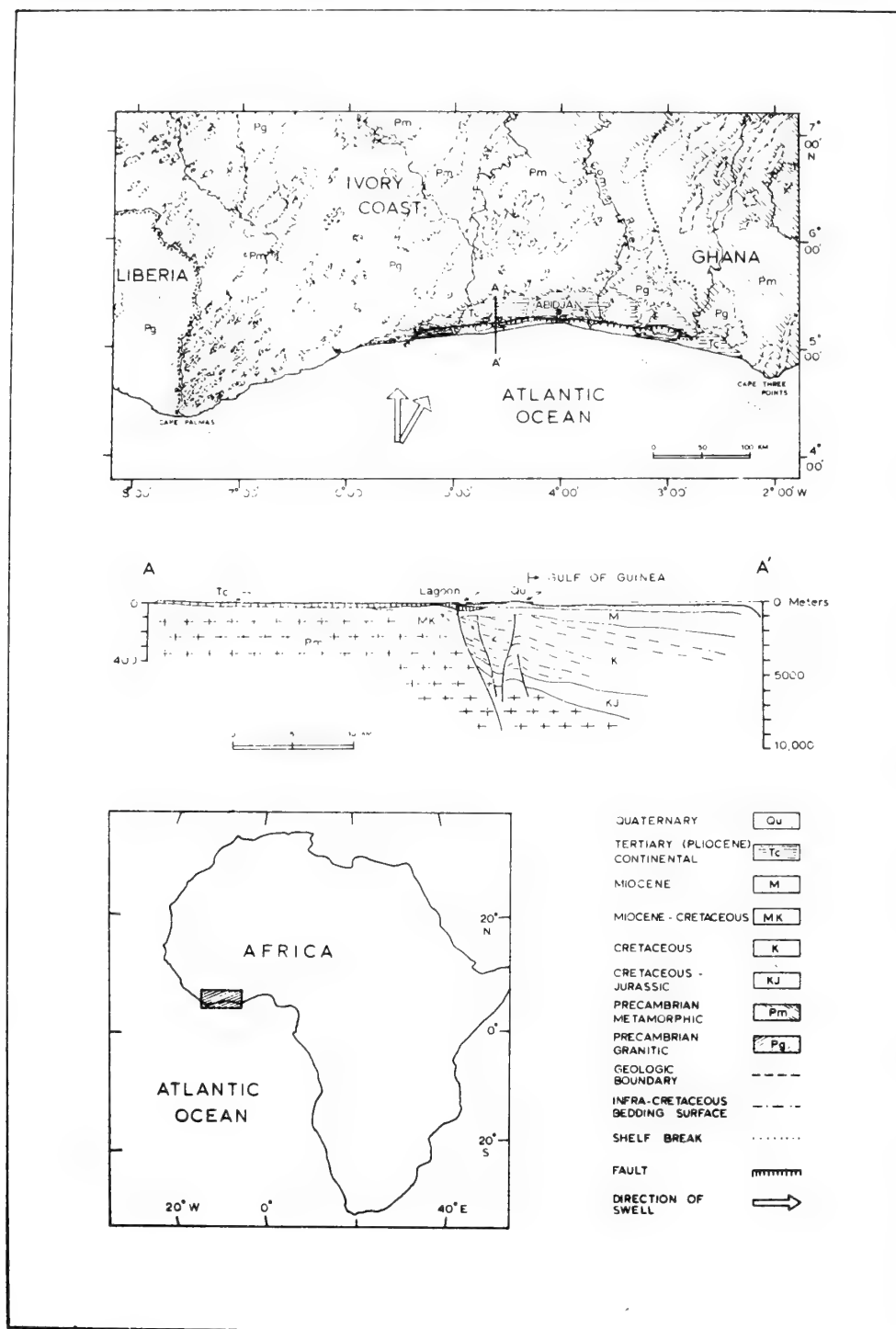


Fig. 1. Regional geologic setting of the Trou sans Fond canyon. Adapted from SPENGLER and DETEIL (1966).

REGIONAL SETTING

The regional setting of the Trou sans Fond is sketched in Fig. 1. The canyon is cut into a narrow continental shelf about 30-km-wide near the midpoint of a 600-km-wide shallow bight in the African margin extending from Cape Palmas in Liberia to Cape Three Points in Ghana. Although most of the Ivory Coast is a peneplained, early mid-Precambrian shield, a late Mesozoic–Cenozoic basin is present along the shoreline and on the central shelf of the Ivory Coast. Its inner margin is marked by large, down-to-the-basin normal faults. The filling is mostly Cretaceous sediments probably in excess of 5 km thick (SPENGLER and DETEIL, 1966). The creation of this basin is probably related to the shearing and taphrogenesis associated with the continental drift rifting of South America from Africa probably near the end of the Jurassic (DIETZ and HOLDEN, 1970).

Some submarine canyons are found off large rivers, but this is not true for the Trou sans Fond, at least today. There are four rivers of moderate size along the Ivory Coast, but they enter estuaries or lagoons, as this is a ria coastline owing to the post-glacial sea level rise. None now reach the strand line, but apparently the Comoé River did so until recently (MARTIN, 1969). This river is the nearest one to the canyon head, lying 30 km east.

BATHYMETRIC SURVEY

Echograms from 760 nautical miles (1400 km) of trackline were obtained from aboard the O.S.S. *Discoverer* during February 1968. A Precision Depth Recorder coupled with an Edo transducer was used throughout the survey. This echo sounder is calibrated for an assumed velocity of 800 fm/sec (1463 m/sec), but the soundings were later corrected for velocity variations in the water column due to temperature and salinity. Navigation control was obtained nearshore by visual and radar bearings. Further offshore, positions were maintained by dead reckoning with respect to land ties and celestial fixes, and a constant drift set was assumed. The positional accuracy for the nearshore areas is probably within one nautical mile, while that offshore may be as much as two or three miles, because strong and confusing east-setting currents of the Guinea Current were encountered.

A bathymetric chart contoured at 100-fm intervals is presented as Fig. 2. The canyon commences at the shoreline in an amphitheater-shaped double head, but quickly assumes a deep V-shaped cross section as it incises the continental shelf. It cuts deeply into both the shelf and upper continental slope, attaining a maximum relief near the shelf break of 450 fm (823 m). The sidewall slopes in the steeper portions of the canyon generally average about 15°.

The canyon cuts through four physiographic provinces: the continental shelf, the steep upper continental slope to 1000 fm (1830 m), the more gentle lower continental slope to 1500 fm (2740 m), and the continental rise from 1500 fm to the limit of the survey at 2200 fm. The survey extended for 100 nautical miles offshore, but it is likely that the canyon extends for another 120 nautical miles until it reaches the Guinea abyssal plain at a depth of 2760 fm (5038 m). The long profile of the canyon is concave and is cut normal to the regional slope. At the canyon head, the thalweg declivity attains 12% but quickly decreases to 3%. A steepening occurs near the shelf break to 8%, then decreases to 3.5% across the upper continental slope. The thalweg slope then slowly decreases seaward, being about 1% in the lower reaches of the continental rise. This canyon has no well developed abyssal cone, but rather cuts across an abyssal fan which forms the upper continental rise. Although clearly erosional across the shelf and upper continental slope, the canyon appears to be dominantly depositional on the continental rise and has developed large natural levees.

Between 1500 and 1900 fm (2745–3477 m), the canyon axis is sharply offset 20 km to the west. This may represent a relatively new course selected by the canyon in seeking a steeper gradient. The former course of the canyon across the continental rise may be marked by a broad channel which lies more exactly along the extended strike of the upper portion of the Trou sans Fond Canyon. Its subdued outline may be due to blanketing pelagic sedimentation since it became inactive.

The stratigraphy of the canyon head probably can be inferred from a deep well drilled in 1959, on shore at Port Bouet but near the canyon, by the Société Africaine des Pétroles (MARTIN, 1969). This well revealed the following section: 0–71 m, Quaternary, coarse sand; 71–123 m, Miocene, fine sand; 123–706 m, marine Miocene, plastic clay; 706–757 m, Senonian, slightly sandy clay with shell debris; 757–1037 m, Turonian, calcareous sands with sand and clay; 1037–1408 m, Cenomanian, conglomerates, sandstones, calcareous sands, clays with gypsum; 1408–3938 m, Albo-Aptian, fossiliferous clays, sandstones and gravels, also limestones and arkoses, some lignite. It appears likely that

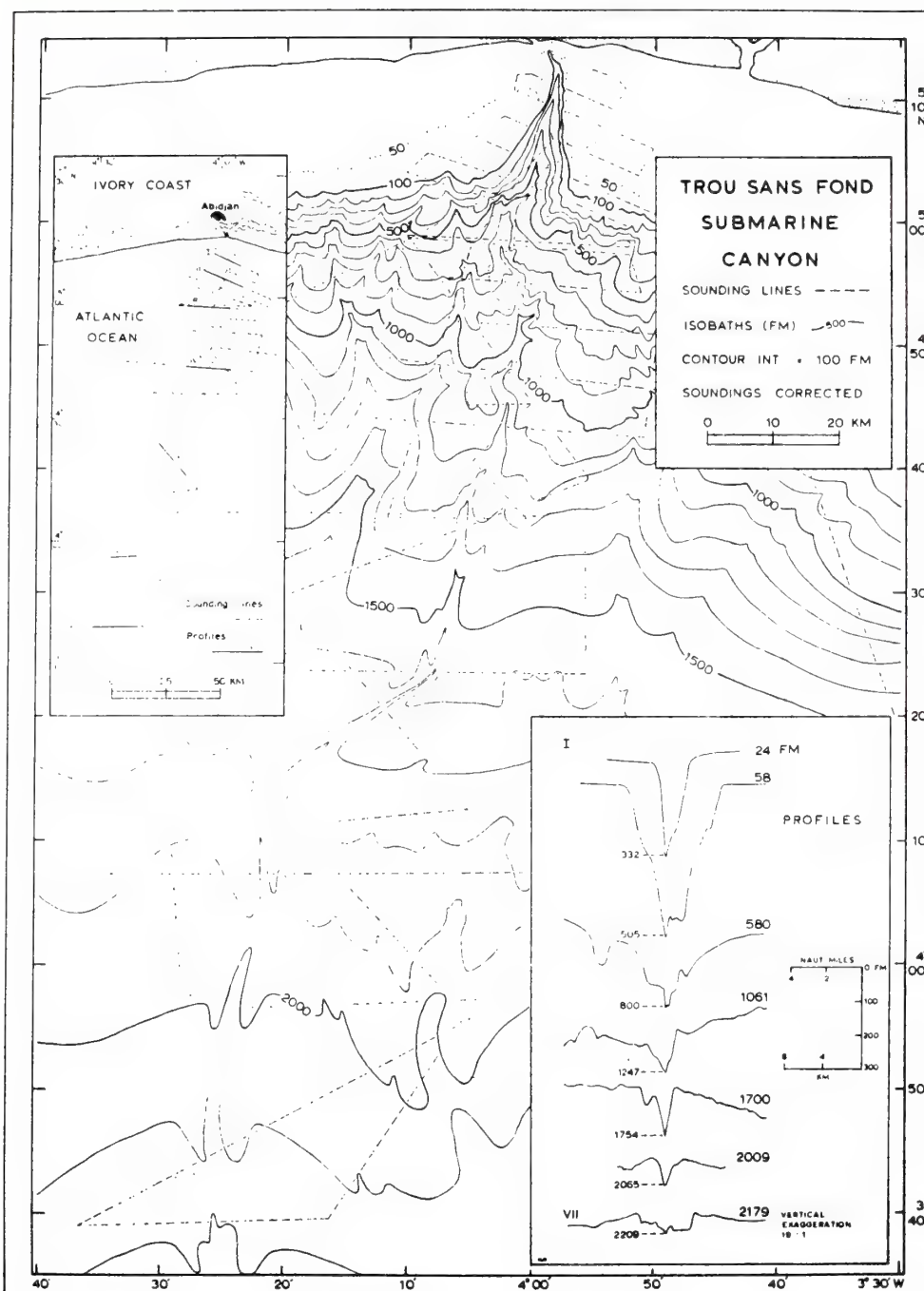


Fig. 2. Bathymetric chart of the Trou sans Fond submarine canyon, Ivory Coast, Africa. Based on 1968 survey by O.S.S. *Discoverer*, of the National Oceanic and Atmospheric Administration.

the upper portion of the Trou sans Fond Canyon is cut entirely in soft sedimentary rocks of Cretaceous and Cenozoic age.

Our attempt to sample the thalweg of the canyon failed, but suggested firm bottom presumably well swept by turbidity currents. A dredge haul up the west face of the canyon head produced only large blocks of slightly indurated, non-fossiliferous green clay which, from the above stratigraphy, was inferred to be marine Miocene. MARTIN (1969) also reports only soft sedimentary rocks comprising the canyon wall and an axis of hard sand and gravel. The continental shelf fringing the Trou sans Fond was found to be covered with green mud and silt rich in glauconitized ovoid coprolitic pellets. The shelf is generally smooth and featureless, but interrupted to the west by patches of irregular and hummocky bottom. The high acoustic reflectivity of these patches suggests they contain rocky reefs.

DISCUSSION

Inspection of existing bathymetric charts reveals that Trou sans Fond probably is the only canyon tapping the paralic zone between the Cayar Canyon north of Dakar in Senegal and the Congo Canyon off the Congo River in the Congo. For the sector between the Trou sans Fond and Dakar, this was further established by our own reconnaissance survey of that continental margin. This emphasizes the importance of this canyon as a conduit for funneling neritic sediments onto the abyssal floor. On the other hand, our survey identified numerous large canyons which were either entirely confined to the continental slope or incised the shelf break at the edge of the continental shelf for only a few miles.

A comparison of the Trou sans Fond with the Congo Canyon (HEEZEN *et al.*, 1964) and the Cayar Canyon (DIETZ *et al.*, 1968) is interesting. Both of them are located at the classical positions for submarine canyons which tap the shoreline, the former off a river mouth and the latter upcurrent of a headland. The Congo Canyon enters the estuary of the Congo River, which is second in the world only to the Amazon River in terms of total water flow. A direct relationship between a river mouth and a submarine canyon is nowhere more evident. The principal role of the river presumably has been to supply sediments for turbidity currents rather than for cutting this canyon during lower sea level stands. The Cayar Canyon is positioned north of the prominent headland of Cap Verde, the westernmost salient of Africa, toward which sand is transported by strong south-setting longshore currents. The ultimate source of much of this sediment is the Sahara Desert, from which sand has been blown onto the beaches of Mauritania and Senegal by the prevailing northeasterly winds.

We surmise that the Trou sans Fond canyon head has also been cut in response to an abundant supply of sand, although a strong case cannot be made. The Trou sans Fond is located near the center of a broad concavity in the continental margin of Africa, an indentation which pertains to the continental slope as well as the shoreline. It undergoes an abrupt 18° flexure at the canyon head. This shoreline is a region of large waves and plunging breakers creating a high energy regime. Sand transport is largely toward the east, owing to the prevailing swell direction and the east-setting Guinea Current, but this direction at times may reverse nearshore, especially in the subsurface. Under these conditions, sand may tend to accumulate in the center of the bight. The eastward offset of the canyon head from the exact center of this bight may represent a skewness impressed by the prevailing swell direction plus the usual set of the Guinea current (Fig. 1). One may suppose that, were it not for canyon head funneling sand into the deep ocean, the usual shoreline straightening processes would tend to fill in this bight or even create a cusped foreland at the site of the canyon head. Possibly other factors have played a role as well in localizing the canyon head, such as an easily eroded fault zone, but any such fault remains to be identified.

The Trou sans Fond may be said, in a sense, to extend above sea level because the beach inside the canyon head has an abrupt foreshore, considerably steeper than is normal for the region. A narrow shallow bench, however, separates the brink of the canyon head proper from the beach. Presumably, this is a sand embankment formed in response to the vigorous surf regime.

In the early twentieth century two slumps which carried large volumes of sediment into the canyon head occurred along this shoreline. In 1905 a slump lasting 35 min slowly swallowed a wharf 70 m long upon which were a hundred barrels of cement and a warehouse. The shoreline receded 70 m and formed a small bight 280 m wide and an area formerly 5 m deep deepened to 25 m. Subsequently the strand line was rapidly reshaped by longshore processes. Sand budget surveys prior to modification of the beach environment by the Vridi Canal jetties showed 800,000 m³ of sand moving from the west

into the canyon head region of the shoreline but only 400,000 m³ continuing on to the east, indicating a loss of 400,000 m³ of sand to the canyon head (VARLET, 1958).

There is another argument which favors active erosion within the Trou sans Fond canyon head. The abruptness of the shelf break around the world is now generally regarded as having been sharpened by erosional bevelling during the last glacial eustatic lowering of sea level to a depth of about 65 fm (120 m) (DIETZ and MENARD, 1951). Hence, if a canyon head has not experienced considerable side-wall erosion, a terrace should be etched into the canyon mouth at the shelf break depth, which lies at about 60 fm (110 m) for the Trou sans Fond. No such bench is now present, indicating that it must have been removed by erosion subsequent to the post-glacial rise of sea level.

Canyons which tap the paralic zone, as distinct from those incising the continental slope only, are distinguished by large natural levees on the continental rise. Upon approaching the survey region aboard the *Discoverer* while still in deep water, the Trou sans Fond was readily detected amongst a wealth of other bottom irregularities by its prominent levees. These levees and the underlying delta fans have a sedimentary volume clearly much larger than can be accounted for by the volume of material eroded from the upper erosional portion of the canyon. This emphasizes the important role of such canyons in conveying shelf and shoreline sediments to the deep ocean floor.

The large size of the undersea leveed fan valleys associated with the lower reaches of submarine canyons is not generally appreciated. For example, profile VII (Fig. 2) across the leveed outer channel of the Trou sans Fond shows a width of 6 km and a depth of 100 m, for a cross-sectional area of 600,000 m². This is 60 times as large as the cross-sectional area of the Mississippi River below its natural levees in the delta region. Huge volumes of water are needed to overflow such giant channels and create the natural levee system. It would appear that such flows must only be triggered at infrequent intervals. Perhaps low-volume, high-density turbidity currents are first generated in the canyon heads and then through turbulent mixing are transformed into flows only slightly more dense than the ambient sea water, but of sufficient volume to overflow, and promote the growth of, the levees. The mode of triggering turbidity flows in a canyon head is largely unknown, but instrumented observations over several years by INMAN (1970) in the Scripps submarine canyon off California indicate the existence of current sufficient to initiate strong sand transport.

Little can be said with assurance about the age of the Trou sans Fond Canyon. Its present head, however, must be younger than the Miocene marine claystone through which it is apparently cut and which is not of an open shelf facies. On the other hand, the great scale of the canyon indicates at least moderate geologic antiquity. Some students regard submarine canyon cutting as a Pleistocene process, but it seems more reasonable that ice age low stands of sea level only enhanced the vigor of turbidity currents. The basic processes involved in canyon cutting must have been active since the continental slope was created which, in this particular case, would have commenced with the breakup of the South America-Africa supercontinent in the mid-Mesozoic. Doubtless, the history of this canyon is complex and involves the switching of channels, the filling of old canyon heads, and the cutting of new ones.

Acknowledgements—We thank Captain LORNE TAYLOR, the officers and crew of the O.S.S. *Discoverer* for performing this survey. J. P. PINOT and J. R. VANNEY of the Institut de Géographie, University of Paris, assisted in preparing the bathymetric map of the canyon. Also contributing to the survey were geologists PHILIPPE BOUYASSE, CARLOS URIEN, DON HAWKES and LEE SOMERS.

REFERENCES

- DIETZ R. and H. MENARD (1951) Origin of the abrupt change of slope at the continental shelf margin. *Bull. Am. Ass. Petrol. Geol.*, **35**, 1994–2016.
- DIETZ R., H. KNEBEL and L. SOMERS (1968) Cayar submarine canyon. *Geol. Soc. Am. Bull.*, **79**, 1821–1828.
- DIETZ R. and J. HOLDEN (1970) Reconstruction of Pangaea: breakup and dispersion of continents, Permian to Present. *J. Geophys. Res.*, **75**, (26) 4939–4956.
- HEEZEN B., R. MENZIES, E. SCHNEIDER, W. EWING and N. GRANELLI (1964) Congo submarine canyon. *Am. Ass. Petrol. Geol. Bull.*, **48**, 1126–1149.
- INMAN D. (1970) Strong currents in submarine canyons. *Eos*, **51** (4) 319 (abs).

-
- MARTIN L. (1969) *Introduction a l'étude géologique du plateau continental ivoirien: premiers résultats*. Ivory Coast Center for Oceanographic Research (ORSTOM), No. 034, 163 pp.
- SHEPARD F. and R. DILL (1966) *Submarine Canyons and other Sea Valleys*. Rand McNally Co., 381 pp.
- SPENGLER A. and J. DETEIL (1966) Le bassin secondaire-tertiare de Cote d'Ivoire. In D. REYRE, editor, *Sedimentary basins of the African coasts. Ass. African Geol. Surv.*, Paris, 108-112.
- VARLET F. (1958) *Le régime de l'Atlantique près Abijan*. Inst. Francaise Afrique Noire, Études Ébur-néennes, No. 7, 97-222.

Plate Tectonic Evolution of Caribbean-Gulf of Mexico Region

GEORGE L. FREELAND & ROBERT S. DIETZ

National Oceanic and Atmospheric Administration, Atlantic Oceanographic and Meteorological Laboratories,
901 South Miami Avenue, Miami, Florida 33130

A geotectonic history of the American Mediterranean is presented in terms of plate tectonics. The development of this region is presented as seven time sequence reconstructions from past Palaeozoic to present times.

PREVIOUS attempts to write a geotectonic history of the American Mediterranean (Caribbean-Gulf of Mexico area) based on continental drift models¹⁻³ or, more classically, the foundering of a Palaeozoic landmass⁴ need revision because of the success of plate tectonics. New data are available from recent land field work⁵⁻¹¹ and marine surveys¹²⁻²¹. Apparently, the evolution of this region is related to former plate junctions between North America, South America, and Africa and to strike-slip, extensional, and compressional motions as the new world drifted westward²². This is the theme of the synthesis presented in this article.

The geotectonic evolution of the American Mediterranean is presented as seven time sequence reconstructions which are azimuthal equidistant projections.

Reconstruction of Drift

Pre-drift reconstruction: The closure of the Atlantic Ocean at the end of the Palaeozoic according to Bullard *et al.*²³ is modified by us (Fig. 1) to show the overlaps (in dashed lines) of the Bahama platform, southern Mexico, and Central America on to Africa and South America. In our reconstruction, we have eliminated the overlaps and the oceanic areas by rotations of these cratons (Fig. 2). Three of these, Yucatan²⁴, Honduras-Nicaragua²⁵, and Oaxaca (southern Mexico)⁹, are underlain by pre-Mesozoic basement. The isthmus of Panama and the Antilles are thought to be neo-cratons ("new ground"), created in Mesozoic-Cenozoic time, and are omitted.

The Bahama platform (more exactly, the Blake-Florida-Bahama platform) is a crescent-shaped craton with a 3-5 km post-Triassic carbonate capping²⁶. Although the nature of the basement remains unknown, we assume here that it is pre-Mesozoic, thus differing from the neo-cratonic origin of Dietz *et al.*²⁷. We propose that the south-eastern Bahamas spur moved eastward to its modern position along a shear now marked by

the Straits of Florida and the North-east Providence (Bahamas) Channel. This spur would then have originally filled the V-shaped gap between Africa and South America.

Our fit of the Oaxaca craton along western Mexico is speculative, but not unreasonable. In the Bullard fit, southern Mexico south of the Trans-Mexican Volcanic Belt (clearly "old ground")⁹ overlaps onto South America. The overlapped portion (mostly the Andean foldbelt of north-western Colombia) may be partly a marginal Mesozoic accretionary belt²⁸, but the gap created would still be too small to accommodate the Oaxaca craton.

We identify the initial suture of the Gulf of Mexico by the margin of the mid-Jurassic (Collovian-Oxfordian) basin. Starting from DeSoto submarine canyon, it trends north-westward through southern Alabama and central Mississippi, westward along the Arkansas-Louisiana state line, south-westward around the East Texas Basin, and southward into Mexico²⁹⁻³¹. This model is supported by subsurface Triassic redbeds, located by drilling, which lie just inland from the basin margin³². These presumably represent taphrogenic basins associated with detachment of the Yucatan-Nicaraguan craton.

Although Fig. 2 shows some gaps, the area probably was fully closed originally. Part of the central gap may be inter-

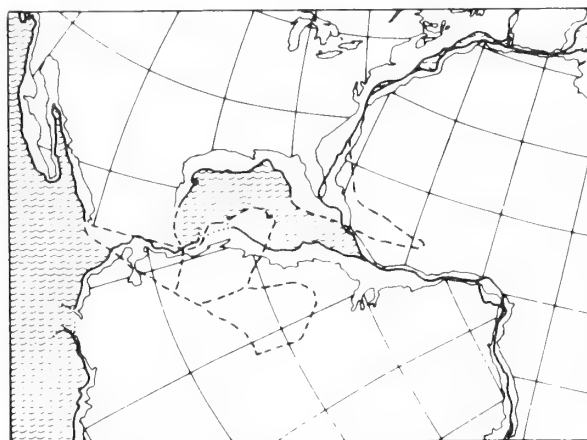


Fig. 1 The Bullard continental drift closure of the Atlantic Ocean, modified by adding areas of cratonic overlap shown in dashed lines. The fit is made at the 500-fm isobath.

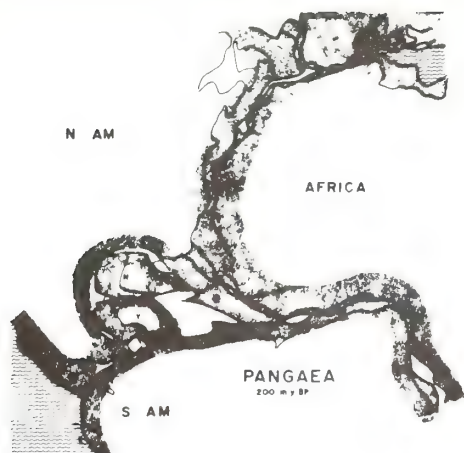


Fig. 2 Closure of the Atlantic Ocean and American Mediterranean in late Triassic (about 200 m.y. BP) according to this article. Microcontinents which are later translated are O, Oaxaca; Y, Yucatan; N, Nicaragua-Honduras; and B, south-eastern Bahama platform. The northern Bahamas-Blake Plateau area is accommodated by subtracting the neo-cratonic, western Senegal Basin. Continental margins are drawn to the 1,000-fm isobath, except where dashed.

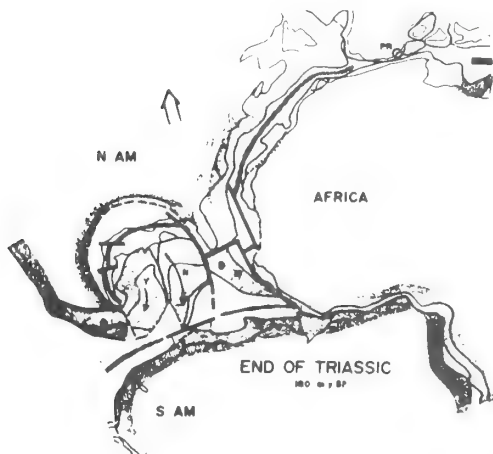


Fig. 3 Initial rifting and breakup at the end of the Triassic, 180 m.y. BP. Initial movement was rapid. Arrows are vectors showing drift relative to Africa-South America, which is arbitrarily held fixed. Dotted bands are where new oceanic crust is implaced; the dashed lines are transform faults and/or shear zones. Dotted lines on the continents outline Triassic taphrogenic basins. PR is the pole of rotation for the North American plate.

mediate crust which has been incorporated, after tectonization, into the neo-cratons of the Greater Antilles. The western part was squeezed into the Guatemala foldbelt. We would not expect a solution in the form of a simple jigsaw-fit due to the complexity of the problem.

Initial breakup. Fig. 3 shows the initial opening of the proto-North Atlantic Ocean and the pull-apart of North and South America. This is dated at or after 200 m.y. BP (late Triassic¹⁴) by basalts presumably associated with this rifting¹⁵.

The rotation pole of Dietz and Holden¹² near south-eastern Spain for the opening of the North Atlantic is used with an

initial clockwise rotation of North America of 10°. South America and Africa remained joined. The split between North and South America was accomplished mostly by the opening of the Gulf of Mexico, with the Yucatan and Honduras-Nicaragua blocks rotating as a single unit about a point near the Isthmus of Tehuantepec. Sinistral shear occurred along northern South America (the El Pilar or South Caribbean shear zone). The Bahama block also started moving north-eastward.

Early Jurassic: Fig. 4 shows the plate positions at early Jurassic time (170 m.y. BP). Laurasia drifted south-westward, accommodated by sinistral shear along the Tethys seaway and the El Pilar fault zone of northern South America. Opening continued in the Gulf of Mexico. The Yucatan-Nicaraguan craton was split, creating the Gulf of Honduras sphenochasm. The Bahama craton lagged behind North America with respect to Africa and thus continued moving north-eastward. As the Gulf of Mexico, Caribbean Sea, and North Atlantic Ocean were small ocean basins at this time, lacking open circulation with the world ocean, deep-water evaporites such as the Louann were laid down.

Mid-Jurassic: Fig. 5 shows the plate positions at the end of mid-Jurassic (150 m.y. BP). As North America rotated north-westward, Newfoundland separated from Spain. Continued left-lateral shear occurred along the Tethys and El Pilar zones. The Gulf of Mexico, Caribbean, and North Atlantic remained as intracratonic ocean basins with continued salt deposition.

During the initial Atlantic opening the lack of reversals in the Earth's magnetic field is reflected in the magnetic quiet zone (MQZ). Starting at about 155 m.y. BP, however, reversals created the magnetic anomalies seen in the North Atlantic floor³⁵. The absence of anomalies in the Gulf of Mexico is mostly due to opening during the magnetic quiet time. During the last stages of opening, rapid sedimentation into the rift zone probably prevented rapid chilling of the pillow lavas which record the polarity of the magnetic field.

As the Gulf of Honduras sphenochasm completed its opening, the Yucatan and Nicaraguan cratons assumed their modern positions relative to North America. West of the sphenochasm hinge, the east-west Guatemalan foldbelt was formed, accompanied by the emplacement of serpentine bodies. Highlands produced by this orogenesis shed a thick sequence of continental and marine Jurassic sediments in Central America²⁵. We propose that this deposition extended the eastern continental margin of the Nicaragua craton and filled the western end of the Gulf of Honduras. This sedimentary wedge would later form the nucleus of the Greater Antilles.

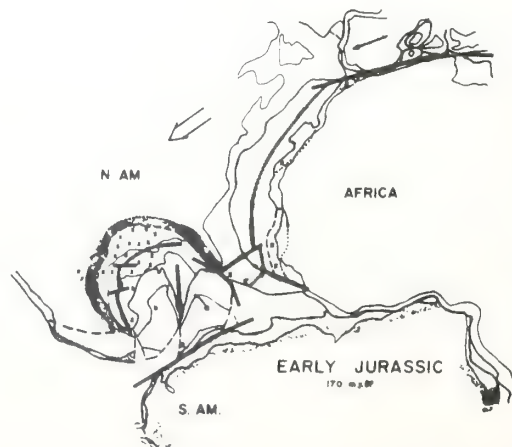


Fig. 4 Blocking out of the American Mediterranean 30 m.y. after commencement of drift. X indicates salt deposits; other symbols as in Fig. 3.

The formation of the Gulf of Mexico was complete at this stage; the Nicaraguan block had rotated about 2,500 km over 50 m.y., an opening rate of 5.0 cm/yr.

Lower Cretaceous: Fig. 6 shows the plate positions at the end of the Lower Cretaceous (100 m.y. BP). South America separated from Africa at about 135 m.y. BP and became a new plate. Both the North and South American plates encountered subduction zones (trenches) along their western margins which probably had west-dipping Benioff zones. On impingement with the continents, the zones flipped to east-dipping. Marginal orogeny with attendant volcanism ensued.

Soon after South America separated from Africa, Nicaragua separated from South America as a result of the more northerly motion of the North American plate. An open connexion to the Pacific Ocean was established. The Caribbean Sea, thus created, opened wider than it is today. Towards the end of the Lower Cretaceous, the South American plate shifted to a more northerly motion. This resulted in cessation of strike-slip motion along the El Pilar zone and the initiation of subduction, compression, and orogeny along northern Venezuela³⁶.

We propose that the Jurassic sedimentary accretionary wedge within the Gulf of Honduras (the proto-Cayman trench) and under the eastern edge of the Nicaraguan block split away from the Nicaraguan craton on both sides of the proto-Cayman trough to form the nucleus of proto-Cuba and proto-Hispaniola. As North America drifted westward, these blocks lagged behind, drifting north-eastward with respect to North America. Subduction zones formed along their northern margins causing orogeny, metamorphism of the Jurassic sediments, and volcanism. Rocks from the central gap in the original fit (Fig. 2) were also incorporated. Later, platform sediments were deposited along the northern edge of Cuba, completing the geosynclinal sequence there.

The Lesser Antilles arc was also initiated as a subduction zone, reflecting the faster rate of westward drift of the North American plate. We suggest that the Aves Ridge, located 250 km west of the modern Lesser Antilles, was the initial arc which was later abandoned by eastward migration of the Benioff zone. The plate boundary between the North and South American plates in the Atlantic Ocean is thought to be marked by several shear zones extending eastward from the Lesser Antilles¹.

Mid-Eocene: The Caribbean region attained essentially its modern aspect by the end of the Middle Eocene (45 m.y. BP)

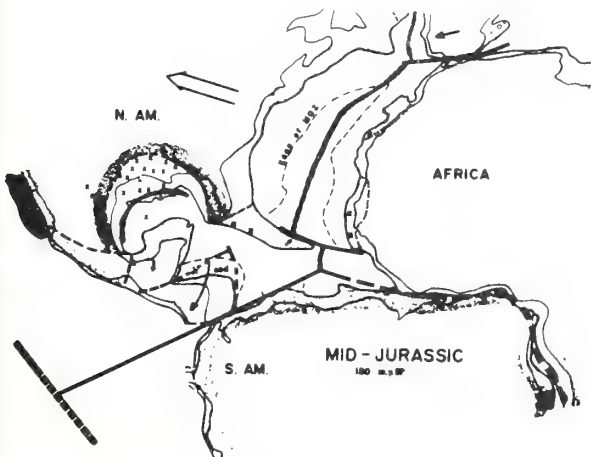


Fig. 5 The Gulf of Mexico/Caribbean near the end of the mid-Jurassic (150 m.y. BP). Note area of Jurassic sediments along the Nicaraguan craton. MQZ is the Magnetic Quiet Zone. Yucatan, Nicaragua, and the south-eastern Bahamas have reached their present position relative to North America. Heavy dashed line west of South America is a trench zone.

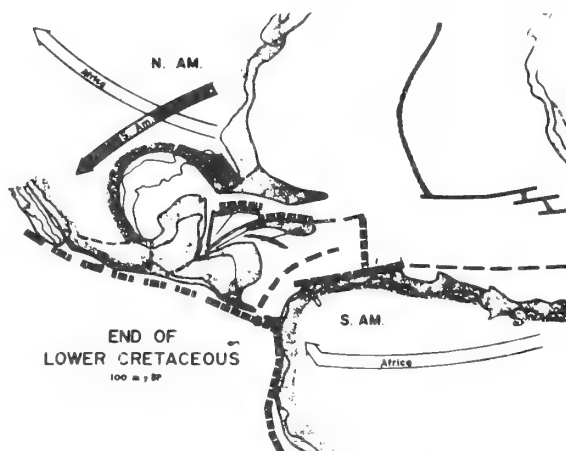


Fig. 6 Positions at the end of the Lower Cretaceous after 100 m.y. of drift. Hatched arrow on North American plate shows the relative motion between the North and South American plates; open arrows show motion relative to Africa as in previous diagrams. Heavy dashed lines are subduction (trench or compression) zones. The Jurassic sediment wedge from Fig. 5 has split off into two parts to form the nucleus of the Greater Antilles. The Lesser Antilles subduction zone is at the Aves Ridge. The Caribbean Sea is seen to be wider than it is today. Venezuelan orogenesis starts.

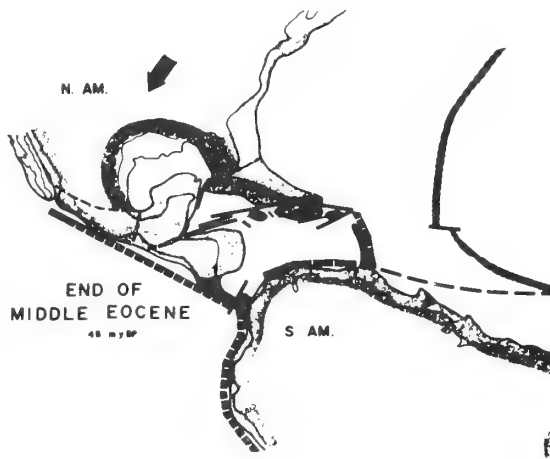


Fig. 7 The end of the mid-Eocene. The plates are essentially in their present position. The Panama twist is formed due to differential motion between the North and South American plates.

(Fig. 7). Cuba and Hispaniola completed their north-eastward relative motion. Additional spreading centres south of the Cayman trough are postulated to have split proto-Hispaniola into further numerous sub-blocks—that is, Jamaica, Hispaniola, Puerto Rico, the Virgin Islands and so on—whose edges are reflected by intermediate depths. The Beata Ridge may also be one of these. Interaction along the leading plate boundaries and within the Caribbean blocks continued orogeny throughout the Tertiary^{10,37-39}. Active subduction beneath the Lesser Antilles arc moved eastward to its modern position during the Eocene. As North America drifted faster than South America, the Caribbean region closed slightly. Continued compression along northern Venezuela and distortion of the Panamanian region resulted. Volcanism slowly closed the Isthmus land gap.

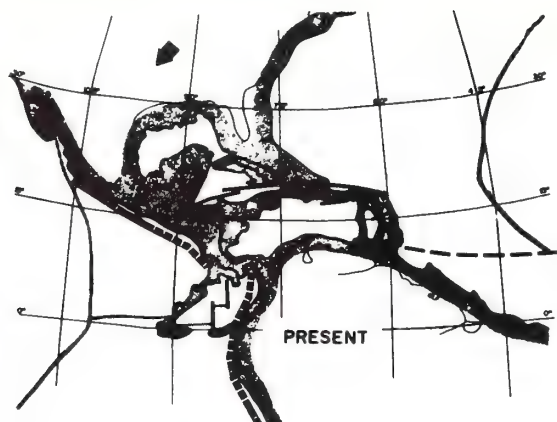


Fig. 8 Present situation. Continued motion between the North and South American plates is accommodated mainly by the Cayman-Puerto Rico shear zones, the Lesser Antilles subduction zone (which has migrated eastward), and a poorly defined shear zone extending eastward from the Lesser Antilles.

Orogeny also continued along the Pacific plate margins, responding to this subduction zone which was pushed westward along the leading continental edge.

Present: Throughout the remainder of the Cenozoic to the Present there was and is continued differential motion, interaction and closure between the two American plates (Fig. 8). We regard these two plates as distinct entities separated mainly by the Cayman-Puerto Rico megashear. Thus, the east-west plate boundary has shifted from the northern margin of South America to the Cayman-Puerto Rican shear zone. The Gulf of Mexico is part of the North American plate, while the Caribbean region is part of the South American plate. The El Pilar zone is mostly inactive today⁴⁰.

In the Neogene interaction of the North American plate with part of the East Pacific Rise caused separation and northward slippage of Baja California. The Galapagos-Panama ridge-fracture system was created within the East Pacific plate during the last 10 m.y.⁴¹.

Consequences of the Model

The foregoing is an attempt to formulate a reasonable plate tectonic history of the Gulf of Mexico/Caribbean region within the context of known geology. Some consequences of our model are as follows.

(1) The age of the sea floor crust of the region would be largely early drift—that is, early Jurassic for the Gulf of Mexico and mostly Lower Cretaceous for the Caribbean. There was a large amount of early extension and emplacement of new crust, followed by slight closure during the Tertiary. No Palaeozoic oceanic crust would be present.

(2) The Yucatan and Nicaraguan blocks are clearly old cratons which, by their movement, formed the Gulf of Mexico before the mid-Jurassic period. Movement of these blocks was completed before South America separated from Africa at about 135 m.y. BP. The Caribbean Sea attained a modern aspect by Upper Cretaceous time at 100 m.y. BP.

(3) Both the Greater and Lesser Antilles are regarded as primarily neocratonic (that is, post-breakup in origin). Metamorphism has obscured the central pre-drift "gap" material which, if present, was incorporated into the eugeosynclinal belts of the Greater Antilles.

(4) The Caribbean area is a subplate presently attached to the South American plate, with little or no movement between them at this time. It is protected from destruction by inward-dipping subduction zones on both east and west. The Gulf of

Mexico, Yucatan, Cuba, and Bahama areas are parts of the North American plate.

(5) The early differential motion between the North and South American plates was accommodated by a shear zone along the northern margin of South America. The present differential motion is accommodated by shear along the northern Caribbean margin (the Cayman-Puerto Rico trench system), and is much less than during the initial stages of movement.

(6) Unlike the solution from Bullard's fit, the region was fully closed before 200 m.y. BP so that there was no "Mare Occidentalis"—western bay indenting Pangaea.

Received March 23; revised May 24, 1971.

- ¹ Ball, M. M., and Harrison, C. G. A., *Trans. Gulf Coast Assoc. Geol. Soc.*, 287 (1969).
- ² Carey, S. W., in *A Symposium on Continental Drift*, 177 (Univ. Tasmania, Hobart, 1958).
- ³ MacGillivray, H. J., *Proc. Kon. Neder. Akad. van Wet.*, B, 73, 64 (1970).
- ⁴ Meyerhoff, A. A., *Trans. Gulf Coast Assoc. Geol. Soc.*, 217 (1967).
- ⁵ Almy, jun., C. C., *Trans. Gulf Coast Assoc. Geol. Soc.*, 269 (1969).
- ⁶ Bass, M. N., in *Tectonic Relations of North Central America and the Western Caribbean*, 283 (AAPG Mem. 11, 1969).
- ⁷ Dengo, G., and Bohnenberger, O., in *Backbone of the Americas*, 203 (AAPG Mem. 11, 1969).
- ⁸ Hess, H. H., in *Caribbean Geological Investigations*, 1 (Geol. Soc. Amer. Mem. 98, 1966).
- ⁹ Kesler, S. E., and Heath, S. A., *Bull. Geol. Soc. Amer.*, 81, 2471 (1970).
- ¹⁰ Khudoley, K. M., *Amer. Assoc. Petrol. Geol. Bull.*, 51, 668 (1967).
- ¹¹ McBirney, A. R., and Bass, M. N., in *Tectonic Relations of North Central America and the Western Caribbean*, 203 and 269 (AAPG Mem. 11, 1969).
- ¹² Bowin, C. O., *J. Geophys. Res.*, 73, 5159 (1968).
- ¹³ Bracey, D. R., *Geophysics*, 33, 950 (1968).
- ¹⁴ Bush, S. A., and Bush, P., *Trans. Gulf Coast Assoc. Geol. Soc.*, 281 (1969).
- ¹⁵ Chase, R. L., and Bunce, E. T., *J. Geophys. Res.*, 74, 1413 (1969).
- ¹⁶ Malloy, R. J., and Hurley, R. J., *Geol. Soc. Amer. Bull.*, 81, 1947 (1970).
- ¹⁷ Molnar, P., and Sykes, L. R., *Geol. Soc. Amer. Bull.*, 80, 1639 (1969).
- ¹⁸ Rona, P. A., *Nature*, 224, 141 (1969).
- ¹⁹ Uchupi, E., and Emery, K. O., *Amer. Assoc. Petrol. Geol. Bull.*, 51, 223 (1967).
- ²⁰ Uchupi, E., and Emery, K. O., *Amer. Assoc. Petrol. Geol. Bull.*, 52, 1162 (1968).
- ²¹ Uchupi, E., and Emery, K. O., *Woods Hole Oceanog. Inst. Contrib.*, 2525 (1970).
- ²² Dietz, R. S., and Holden, J. C., *J. Geophys. Res.*, 75, 4939 (1970).
- ²³ Bullard, E., Everett, J. E., and Smith, G. E., in *A Symposium on Continental Drift*, 41 (Royal Soc., London, Philos. Trans., 1965).
- ²⁴ Dengo, G., *Trans. Gulf Coast Assoc. Geol. Soc.*, 311 (1969).
- ²⁵ Mills, R. A., Hugh, K. E., Feray, D. E., and Swolfs, H. C., *Amer. Assoc. Petrol. Geol. Bull.*, 51, 1711 (1967).
- ²⁶ Sheridan, R. E., Drake, C. L., Nafe, J. E., and Hennion, J., *Amer. Assoc. Petrol. Geol. Bull.*, 50, 1972 (1966).
- ²⁷ Dietz, R. S., Holden, J. C., and Sproll, W. P., *Geol. Soc. Amer. Bull.*, 81, 1915 (1970).
- ²⁸ Jacobs, C., Burgl, H., and Daniel, L. C., in *Backbone of the Americas*, 62 (AAPG Mem. 2, 1963).
- ²⁹ Bayley, R. W., and Muehlberger, W. R., *Basement Map of the US* (US Geol. Surv., 1968).
- ³⁰ deCserna, Z., *Bol. Soc. Geol. Mexico*, 30, 159 (1969).
- ³¹ Flawn, P., *The Ouachita System* (Univ. Texas Pub. 6120, 1961).
- ³² Scott, K. R., Hayes, W. E., and Fietz, R. P., *Trans. Gulf Coast Assoc. Geol. Soc.*, 11, 1 (1961).
- ³³ deBoer, J., *Geol. Soc. Amer. Bull.*, 79, 609 (1968).
- ³⁴ *Geol. Soc. Phanerozoic Time Scale: Quart. J. Geol. Soc. London*, 120S, 260 (1964).
- ³⁵ Talwani, M., Windisch, C. G., and Langseth, jun., M. G., *J. Geophys. Res.*, 76, 473 (1971).
- ³⁶ Mencher, E., Fichter, H. J., Renz, H. H., Wallis, W. E., Patterson, J. M., and Robie, R. H., *Amer. Assoc. Petrol. Geol. Bull.*, 37, 690 (1953).
- ³⁷ Bowin, C. O., in *Caribbean Geological Investigations*, 11 (Geol. Soc. Amer. Mem. 98, 1966).
- ³⁸ Mattson, P. H., in *Continental Margins and Island Arcs* (edit. by Poole, W. H.), 124 (Geol. Surv. Canada, 1966).
- ³⁹ Whetten, J. T., in *Caribbean Geological Investigations*, 177 (Geol. Soc. Amer. Mem. 98, 1966).
- ⁴⁰ Metz, H. L., *Proc. IV Caribbean Geol. Conf.*, 293 (1965).
- ⁴¹ Grim, P. J., *Marine Geophys. Res.*, 1, 85 (1970).

Engineering Properties of North Atlantic Deep-Sea Sediments

George H. Keller, National Oceanic and Atmospheric Administration, Atlantic Oceanographic and Meteorological Laboratories, Miami, Florida, USA

Abstract

The engineering characteristics of river, harbor and certain coastal sediments have been investigated since man found it necessary to construct structures such as wharves, jetties and various pile supported platforms. Only during the past decade has some attention been devoted to the engineering properties of deeper coastal water deposits and even more recently to the similar aspects of deep-sea sediments. Initial studies of North Atlantic deposits (upper 10 to 20 m [33 to 66 ft.]) for such properties as shear strength, unit weight, water content, and porosity reveal considerable variation, yet in some areas there exists a definite correlation between these properties and sediment type, current flow and sea floor topography. With the advent of the U. S. Deep Sea Drilling Project, our knowledge of the sediment blanket covering the ocean basins has been advanced appreciably. Among the many analyses made on the Deep Sea Drilling Project cores are those for water content, unit weight (bulk density) and porosity to depths of 1070 m (3510 ft.) below the sea floor. This program has provided a significant insight into range and variation of these properties to depths greater than has been possible to reach by conventional deep-sea coring techniques. Although some generalizations can be made about the areal distribution and range of certain engineering properties within the surface layers of deep-sea deposits, local lateral variation may be considerable, in some cases exhibiting coefficients of variation as high as 147 percent and more frequently on the order of 30 to 50 percent. To date, we have but little insight into the engineering properties of deep-sea sediments. Before significant data is available to deal with the stability of sea floor deposits both in regard to their foundation characteristics as well as their mass movement, much more regional and detailed sampling is required.

Introduction

Relatively little is known about the engineering properties of deep-sea sediments and as yet only broad generalizations can be made concerning these properties within the upper few meters of the sea floor. An untold number of engineering investigations have been made in river and coastal waters for various projects such as the construction of wharves and jetties or the installation of submarine pipelines. Since about 1950 an increasing number of foundation studies have been carried out on the continental shelves in conjunction with the erection of offshore drilling platforms. To date, the majority of the engineering studies conducted on deep-sea deposits have been made by marine geologists investigating different aspects of the deep ocean environment (Richards, 1961, 1962). A number of these studies have dealt with specific relationships such as sound velocity and mass properties (Hamilton, 1956; Buchan et al., 1967), density variation with depth (Igelman and Hamilton, 1963), consolidation characteristics and depositional history (Bryant et al., 1967; Richards and Hamilton, 1967) or have discussed the engineering properties of a local area (Moore and Shumway, 1959; Harrison et al., 1964). Utilizing data from approximately 500 sediment cores (Atlantik - 300, Pacific - 200), Keller (1968) provided the first

regional generalization of the distribution of selected engineering properties in the North Atlantic and North Pacific basins.

Commencing with the U. S. Deep Sea Drilling Project in 1968 an entirely new aspect of these studies has been made possible. This program has provided deep-sea cores from depths as great as 1070 m (3510 ft.) below the sea floor on which engineering tests have been made for unit weight (bulk density), water content, porosity and relative strength. A discussion of some of these data follow in a later section.

This paper is a discussion of the available engineering properties data for the North Atlantic basin deposits. In addition to presenting the areal distribution of selected properties, it also includes a section dealing with ultimate bearing capacity of surface materials and the consolidation characteristics of deep-sea sediments. Local variation of engineering properties both laterally and vertically proves to be significant in contrast to some early speculations that deep-sea deposits are homogeneous. These findings, in conjunction with presentation of data from one of the deepest holes yet drilled in the North Atlantic are discussed herein.

Areal Distribution of Engineering Properties

Sediment Types

To set the stage for later discussions it is important to visualize the overall types of sediment that occur in the North Atlantic basin. The distribution pattern of bottom sediments as it is known today has been presented in various publications (U. S. Naval Oceanographic Office, 1965; Keller and Bennett, 1968; and Interdepartmental Geophysical Committee of the Academy of Sciences, USSR, 1969). Using the classification of Keller and Bennett (1968) it is seen that much of the North Atlantic is blanketed by calcareous ooze, Fig. 1, which, as used here, is a sediment consisting of at least 30 percent calcium carbonate in the form of skeletal material from various planktonic animals and plants. Deposits of terrestrial origin, later reworked by the sea, constitute the major sediment type (fluvial marine) along the margin of the basin. These deposits are relatively widespread and extend considerable distances into the basin revealing the strong influence terrestrial drainage has on the sediments of the North Atlantic. Unlike the Pacific basin, the occurrence of "red clay" is not very extensive. Unique deposits of calcareous sand and silt (commonly shell fragments and coralline debris) occur in the area of the Bahama Islands and the Straits of Florida. Although the distribution pattern shown in Fig. 1 is relatively simple, it is highly probable that it will increase in complexity as more samples become available. The reader is referred to the study by Keller and Bennett (1968) for a more detailed discussion of the classification used here.

Shear Strength

Shear strength measurements were made on samples consisting primarily of fine grained cohesive material (silty clay and clayey silt) with an occasional stringer of fine sand occurring in some of the cores. Shear strength of this sediment type is a function of

cohesion, the angle of internal friction of the material and the effective stress normal to the shear plane, commonly expressed as:

$$\tau_f = c + \bar{\sigma} \tan \phi$$

where c is cohesion, $\bar{\sigma}$ the effective stress and ϕ the angle of internal friction. Cohesive, saturated sediments stressed without loss of pore water behave with respect to the applied load as if they were materials without any angle of internal friction ($\phi=0$). In which case, shear strength is equal to the cohesion ($\tau_f = c$). A more detailed discussion of shear strength can be found in soil mechanics texts such as *Taylor (1948)* and *Scott (1963)*.

Shear strength measurements were made by either of two methods: unconfined compression test or laboratory vane shear. Testing procedures used to accommodate the relatively weak submarine sediments have been discussed by *Richards (1961)*. In the case of the unconfined test, the sediments were considered to be clays or materials behaving like clays and the shear strength was taken as one-half the unconfined compressive strength.

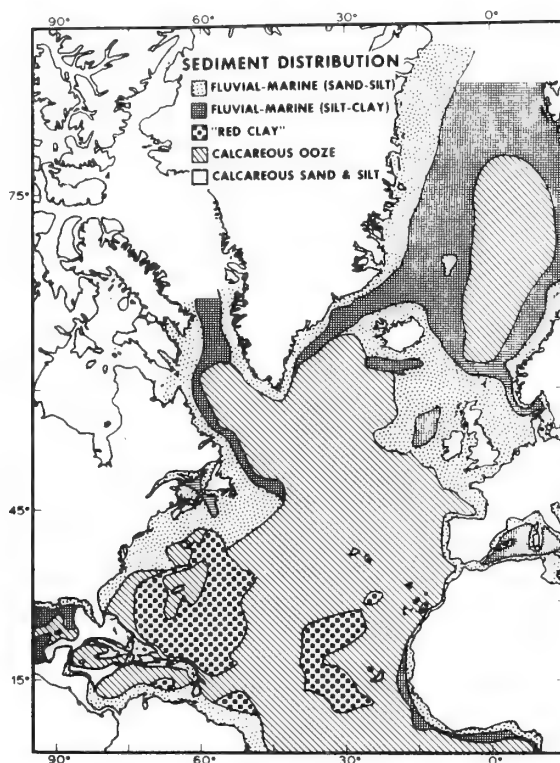


Figure 1. Sediment distribution in the North Atlantic

Sediment cores used in this study vary from 30 cm (12 in.) to approximately 7 m (23 ft.) in length. Values of shear strength and water content shown in Fig. 2 and 3 respectively, represent averages of the measured parameter over the entire length of each core. As a rule of thumb, these data can be considered as representing average values for the upper 2.5 m (8 ft.) of the sea floor.

Shear strengths in the upper few meters of the sea floor are found to vary from 0.5 to 2.0 psi (35 to 141 g/cm²). As shown in Fig. 2, much of the basin consists of deposits possessing average shear strengths of 0.5 to 1.0 psi (35 to 70 g/cm²). Strengths of less than 0.5 psi (35 g/cm²) are often observed in coastal areas where local drainage or current conditions result in the deposition of relatively weak deposits. Other areas of low shear strength are found associated with the "red clay" deposits and in isolated patches

along the Mid-Atlantic Ridge. Available data indicates that a band of low shear strength material may extend in an east-west direction across the Atlantic at approximately 15°N. A definite explanation for this occurrence is not readily available without additional data. However, the westward flow of the Equatorial Currents across this portion of the basin may in some way account for the distribution of these relatively low strength sediments. Sediments along this band tend also to possess low unit weights and high water contents.

Sediments east of Greenland display unique properties relative to most of the North Atlantic deposits. Here, shear strengths are some of the lowest yet reported for the North Atlantic and possibly may be attributed to the influx of sediment from Greenland and the Arctic as well as reflecting the general current circulation pattern for this area (*Keller and Bennett, 1968*). The highest average shear strengths (1.5 to 2.0 psi [105 to 141 g/cm²]) yet found in the Atlantic are those associated with the calcareous

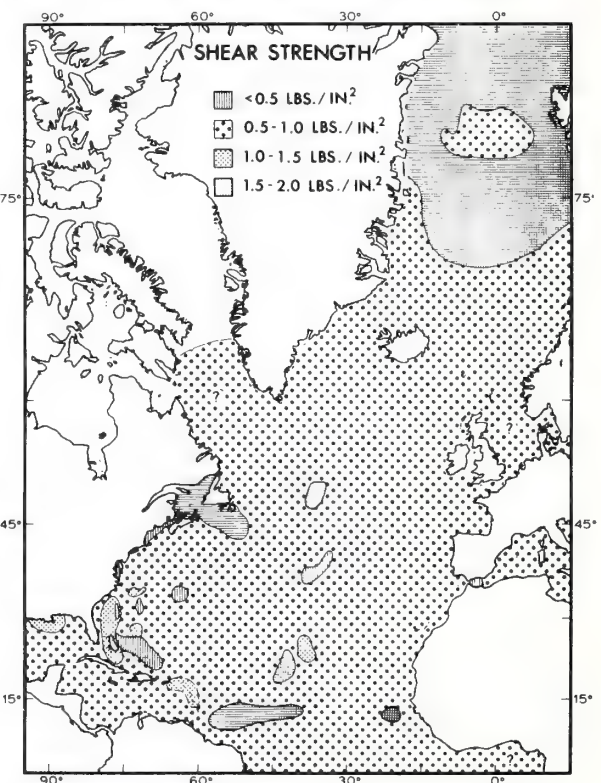


Figure 2. Distribution of average shear strength in the North Atlantic

deposits surrounding the Bahama Islands and on the Blake Plateau off the southeast coast of the United States.

Water Content

Water content is expressed as a percent of the ratio: weight of water to the weight of oven dried solids in a given sediment mass. Laboratory techniques for this determination can be found in most texts dealing with soil mechanics and are not discussed here.

Average sediment water contents for the North Atlantic range from 30 to 175 percent, but more commonly are between 50 and 100 percent (*Keller and Bennett, 1968*) (Fig. 3). Higher water contents are found in areas influenced by major drainage systems such as off the Mississippi and St. Lawrence rivers. A sizable area of relatively high water content extends from Africa westward to

the Caribbean and may, as noted earlier, possibly be attributed to the general current pattern in this part of the basin. The isolated patches of high and low water content sediments found in the basin may be related to topographic irregularities, which by influencing current conditions have altered the depositional environment on a local basis (*Keller and Bennett, 1968*). As observed in the case of shear strength, the sediments east of Greenland display anomalous water contents relative to those of other portions of the basin. Water contents of less than 50 percent predominate throughout much of the Greenland Sea area.

Unit Weight and Porosity

The distribution of average sediment unit weight (bulk density) and porosity for the North Atlantic has been discussed by *Keller and Bennett (1968)* and will only be summarized here. Unit weights range from 80 to 125 pcf (1,3 to 2,0 g/cc), with the majority of the basin deposits exhibiting values between 95 and

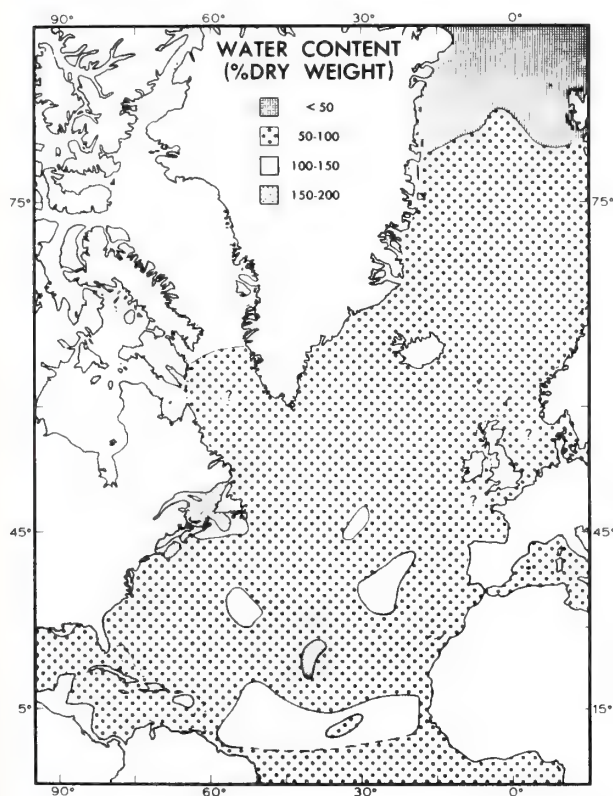


Figure 3. Distribution of average water content in North Atlantic sediments

110 pcf (1,5 to 1,8 g/cc). Offshore from large drainage systems (Mississippi and St. Lawrence rivers) densities are commonly below 95 pcf (1,5 g/cc). A prominent feature in the regional distribution of bulk density is a band of relatively low density (78 to 94 pcf [1,2 to 1,5 g/cc]) material characterizing a 350 mile (563 km) wide portion of the sea floor between Africa and the Caribbean in the vicinity of latitude 15°N.

Average sediment porosities for most of the North Atlantic seldom exceed 70 percent and more commonly range between 60 and 65 percent. Only in small isolated portions of the basin and in the area influenced by the St. Lawrence River are porosities greater than 80 percent found (*Keller and Bennett, 1968*). Average porosities of less than 50 percent are relatively rare in the North Atlantic.

Ultimate Bearing Capacity

For the engineer concerned with the placement of an installation on the sea floor, the bearing capacity and consolidation characteristics of the foundation material must be ascertained. If the load is relatively small, it may only be necessary to determine the bearing capacity in order to know the depth to which a structure or piece of hardware will penetrate the sea floor during the initial installation.

Ultimate bearing capacity is the average load per unit area required to provide failure by rupture of a supporting sediment mass. It is a function of the product of the shear strength and one or more factors, which are dependent on the size and shape of the load as well as the depth of loading. For the purpose of this discussion, a formula for the ultimate bearing capacity of sediment under a strip load (load infinitely long relative to width) at the surface is used for the determination of the values shown in Fig. 4. The general bearing capacity formula for a shallow strip foundation developed by *Prandtl (1920)* and later modified by *Terzaghi (1943)* is:

$$Q_c = cN_c + \gamma DN_q + \frac{\gamma BN\gamma}{2} \quad (1)$$

when Q_c is the ultimate bearing capacity, γ the sediment unit weight, B the width of the load, D the depth of the load below the surface, and N_c , N_q , and N_γ are dimensionless factors dependent on the angle of internal friction, depth and shape of the foundation and roughness of the base. For the case of a surface load and zero angle of internal friction, the factors N_q and N_γ are equal to unity and zero respectively and equation (1) is simplified to:

$$Q_c = cN_c \quad (2)$$

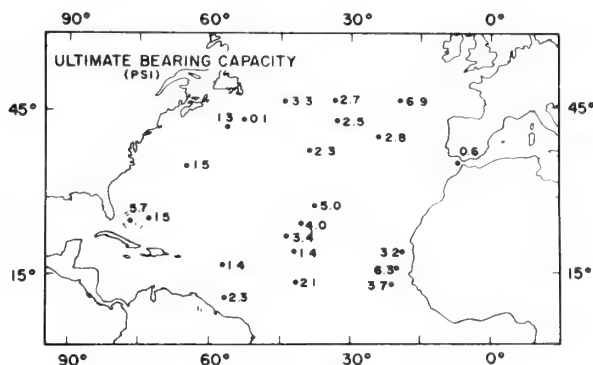


Figure 4. Ultimate bearing capacity values at the sea-floor surface for a strip load

where N_c equals 5,14 according to *Prandtl*. Other values for N_c are found to be in use by various investigators. Using equation (2) and a selected number of essentially surface (0–5 cm [0–2 in.]) shear strength values, ultimate bearing capacities have been determined for portions of the North Atlantic (Fig. 4).

An example comparing values shown in Fig. 4 with a calculated load will serve to illustrate the significance of these bearing capacity values. If a strip load whose buoyed weight is 1,000 pounds (454 kg) and has a surface area of 400 in² (2581 cm²), is placed on the sea floor without impact, the resulting stress on the sediment will be 2,5 psi (176 g/cm²). An ultimate bearing capacity of at least this amount is necessary to prevent a shear failure. As can be seen from Fig. 4, such a load would not cause a shear failure at most of the core sites. This assumes no safety factor is used, which

generally is never the case in actual practice. Depending on the safety factor used, much of the North Atlantic deposits would not be considered capable of supporting the strip load used in this example.

Consolidation Characteristics

Consolidation in the engineering sense refers to the gradual decrease in volume of a sediment under an imposed load. Consolidation characteristics are rather important since they indicate the depth to which a structure or some load will settle into a sediment, and, in conjunction with studies of overburden pressures, they may result in geological conclusions as to the volume of original sediment and the vertical variations of density and porosity in the sedimentary deposit. Based on the consolidation test, sediments are usually classified as normally consolidated, underconsolidated or overconsolidated. They are classed as normally consolidated if the present effective overburden pressure is the greatest yet imposed on the deposit; they are said to be overconsolidated if the test indicates that the deposit has been subjected to pressures greater than those presently effective. If a deposit has not yet been consolidated under the present pressure, it is considered to be underconsolidated.

A majority of the deep-sea sediments that have been tested for their consolidation characteristics reveal they are slightly overconsolidated (Hamilton, 1964; Bryant et al., 1967; and Richards and Hamilton, 1967). Although there is little doubt about the validity of the consolidation tests, it is obvious that the deposits have not been subjected to loads greater than their present overburden pressure nor have they been desiccated. Factual data are not yet available, but a number of investigators have proposed that this unique overconsolidation condition may result from very slow rates of deposition, and "chemical cementation" by interparticle or ionic bonding (Rittenberg et al., 1963; Hamilton, 1964). This unique property of deep-sea sediments would indicate that they can support greater loads than might have been anticipated.

Lateral Variations of Engineering Properties

The earlier figures displaying regional distribution of shear strength and water content may be deceiving in that they suggest that sediments possessing relatively uniform properties extend over large areas of the North Atlantic. In reviewing the available engineering data for deep-sea sediments within the upper 7 m (23 ft.) of the sea floor, Keller and Bennett (1970) reported on the variations of selected properties both for the North Atlantic as a whole as well as for specific sediment types found in the basin, Table 1. These data clearly point out some of the large variations that can be anticipated in this environment.

Variation of engineering properties within a local area have recently been examined by Bennett et al. (1970). Their study consisted of determining certain engineering properties in three sediment cores collected from an area of 400 cm² (6.2 in.²) in a basin approximately 2000 m (6560 ft.) deep off the island of Puerto Rico. Tests were carried out on three corresponding horizons in each core and a comparison made of the variation among the measured parameters in these horizons using the statistical expression, "coefficient of variation". As shown in Table 2, a considerable degree of variation exists in even such a small area. The greatest variations occurred among such properties as sensitivity (ratio of natural to remolded strength), shear strength and texture, whereas unit weight and grain specific gravity displayed relatively little change. This same discussion included a comparison of data taken from a study by Richards (1964) on four cores collected from an area approximately 0.2 km² (0.08 mile²) in the northwest

Table 1. Variation of Engineering Properties for the North Atlantic as a whole (modified from Keller and Bennett, 1970)

	γ (pcf)	w (%)	η (%)	τ_f (psi)	St	G	w _L	w _p
Max.	165	207	85	12.9	88	2.86	109	38
Min.	78	15	32	.01	1	2.45	47	20
Ave.	95	86	66	0.7	4	2.73	65	27

Variation of Engineering Properties for Selected Sediment Types in the North Atlantic Basin								
Carbonates								
	γ (pcf)	w (%)	η (%)	τ_f (psi)	St	G	w _L	w _p
Max.	119	132	78	12.9	88	2.86	109	30
Min.	84	15	45	0.1	1	2.63	77	26
Ave.	94	96	72	1.1	10	2.71	101	29
Fluvial Marine								
Max.	165	188	80	10.1	57	2.81	101	38
Min.	80	28	44	.01	1	2.45	47	20
Ave.	91	112	73	0.9	4	2.67	85	29
"Red Clay"								
Max.	127	207	85	3.3	25	2.84	107	—
Min.	78	23	32	.01	1	2.46	102	—
Ave.	90	159	74	0.6	9	2.54	105	—

γ	unit weight of soil	St	sensitivity
w	water content (% dry wt.)	G	grain specific gravity
η	porosity	w _L	liquid limit
τ_f	shear strength	w _p	plastic limit

Atlantic. Although covering a much larger area and a different sediment type than that represented by the three cores, the relative degrees of variation were much the same among all seven cores.

Vertical Variation of Engineering Properties

Until recently, sediment cores collected from the deep-sea floor seldom reached lengths greater than 20 m (66 ft.). As a result, very little is yet known about the variation of engineering properties to any great depth below the sea floor. Certain changes with depth such as increasing shear strength and unit weight and decreasing water content might be anticipated, based on terrestrial studies. Care must be used, however, in applying such generalizations to deep-sea deposits. Detailed studies on the upper few meters of

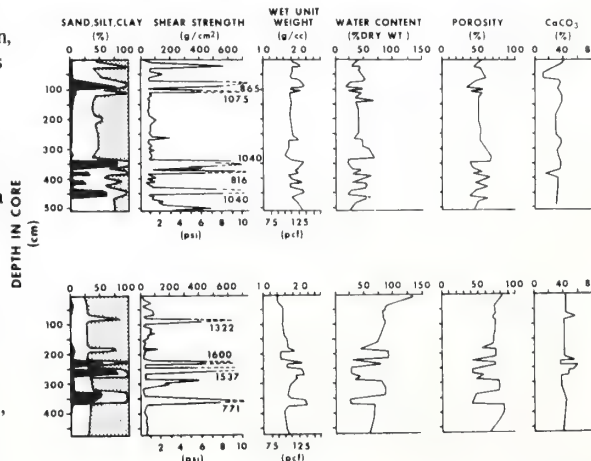


Figure 5. Variation of selected mass properties with depth in two turbidite sequences

Table 2. Mass Physical Properties and Coefficients of Variation (V*) of three Whiting Basin Cores (modified from *Bennet, Keller and Busby, 1970*)

Horizon	Sampling Interval (cm)			Water Content (% dry weight)				Unit Weight (pcf)											
	Core 1	Core 2	Core 3	1	2	3	V	1	2	3	V								
A	0-8	0-7	0-9	75	66	78	17	97.3	98.0	96.7	1.3								
B	8-15	10-17	10-17	67	60	65	11	100.5	102.3	101.1	1.8								
C	17-25	17-25	17-26	59	57	63	10	103.0	104.2	101.1	3.0								
Grain Specific Gravity				Shear Strength (psi)				Sensitivity				Liquid Limit (%)							
1	2	3	V	1	2	3	V	1	2	3	V	1	2	3	V				
2.78	2.77	2.78	0.4	0.3	0.3	0.2	37	3.2	2.7	2.5	25	34	35	35	3				
2.79	2.78	2.78	0.4	0.7	0.6	0.5	33	3.3	5.4	2.8	63	41	39	37	10				
2.78	2.80	2.79	0.7	1.1	2.1	0.8	100	6.2	40.7	7.4	147	35	34	38	11				
Plastic Limit (%)				Porosity (%)				Sand (%)				Silt (%)				Clay (%)			
1	2	3	V	1	2	3	V	1	2	3	V	1	2	3	V	1	2	3	V
29	29	28	3	67.8	65.9	68.6	4	42	36	41	15	35	40	37	13	23	24	22	9
29	31	31	7	65.6	63.1	64.7	5	29	22	36	48	42	46	40	14	29	32	24	29
28	25	31	21	62.6	62.1	64.4	3	29	40	25	46	43	39	45	14	28	21	30	35

*) coefficient of variation represents a measure of the range of values expressed as a percent of the median value (*Balsley, 1964*)

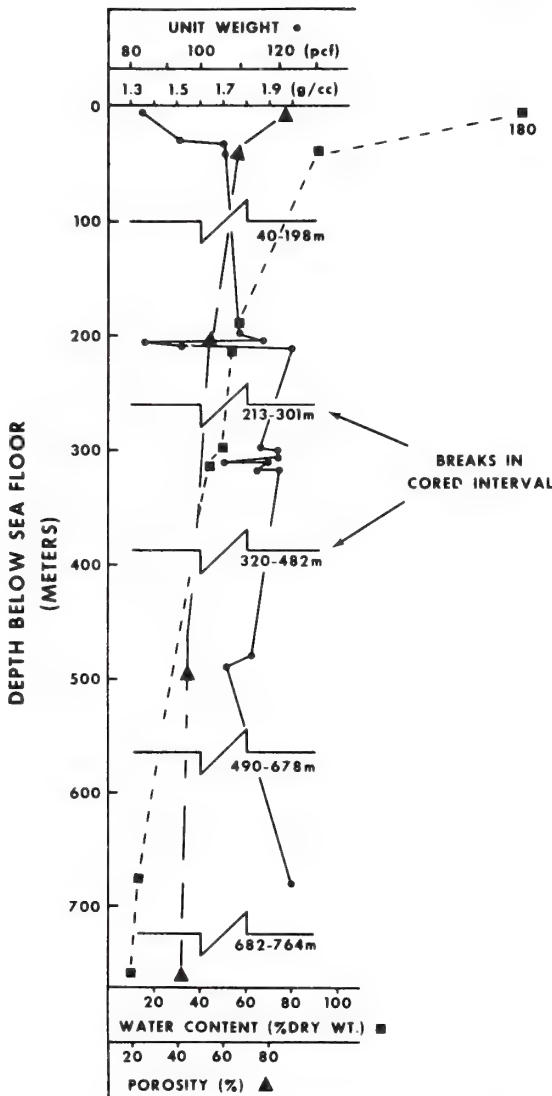


Figure 6. Variation of unit weight, water content and porosity with depth at Site 9 (32° 37' N, 59° 10' W) of the Deep Sea Drilling Project

the sea floor indicated that some portions of the ocean basins contain sediments exhibiting considerable degrees of variation with depth (*Richards, 1961*).

Turbidite sequences (layers of relatively coarse material interlaid with fine sediments) are common to many portions of the deep-sea and possess extreme variations among their mass properties within relatively short intervals. Analyses of cored samples from two such deposits clearly attest to this distinctive characteristic, Fig. 5. *Richards and Keller (1962)* found in their detailed study of a sediment core from off Nova Scotia, that within the upper 180 cm (71 in.) of the sea floor, water contents varied from 27 to 100 percent.

It was not until 1961, during the United States MOHOLE project, that sediment cores longer than 25 m (82 ft.) were obtained from the sea floor. More recently the U. S. Deep Sea Drilling Project has provided sediment cores from as deep as 1070 m (3510 ft.) below the ocean floor. Although these samples are disturbed to some degree, it has been possible to make tests for certain engineering properties of these cores.

The 1961 MOHOLE drilling off Guadalupe Island in the Pacific (28° 59' N, 117° 30' W) obtained cores through the 170 m (558 ft.) of sediment overlying the basaltic basement. At this site water contents ranged from 110 percent at the surface to 40 percent at a depth of 170 m (558 ft.) (*Rittenberg et al., 1963*). There was not, however, a continual decrease in water content with depth. Within the interval 100 to 140 m (328 to 459 ft.) values as high as 120 percent were reported. *Hamilton (1964)* reported the somewhat surprising finding, that porosity varied little (5 percent) within the 170 m (558 ft.) interval.

Recent deep-sea drilling in the North Atlantic has contributed significant data on deposits as much as 834.5 m (2737 ft.) below the sea floor (*Peterson et al., 1970*). Site 9 (32° 37' N, 59° 10' W) of the Deep Sea Drilling Project provides the deepest cored interval in the North Atlantic basin yet obtained. Although the hole was not cored continuously, these samples are of the utmost value in any study pertaining to deep-sea sedimentation. Variations with depth of porosity, unit weight and water content have been plotted, Fig. 6, based on the report of *Peterson et al. (1970)*. Surface values were obtained from unpublished data obtained from short cores collected in the vicinity of Site 9. Porosity and water content tend to decrease with depth. Contrary to the findings of *Hamilton (1964)* at the Guadalupe site, porosity decreases signifi-

cantly from approximately 82 percent at the surface to 43 percent at a depth of 764 m (2506 ft.). It should be noted, however, that there is very little change in porosity below 450 m (1476 ft.). Unit weight (bulk density) increases gradually with depth, ranging from 1,5 g/cc (94 pcf) at the surface to 2,0 g/cc (125 pcf) at a depth of 682 m (2237 ft.). An anomalous interval between 204 and 213 m (669 to 699 ft.) is attributed to the interbedding of clay and foraminiferal ooze.

Summary

Investigation of the engineering properties of deep-sea sediments has only received serious consideration in the past ten to fifteen years, and as yet, relatively little has been learned in this area of study. To date, most of the studies have been carried out by marine geologists, who, by applying certain aspects of soil mechanics, have and are attempting to investigate the various sedimentological and environmental characteristics of the unconsolidated deposits blanketing much of the sea floor. Thousands of sediment cores have been collected from the North Atlantic, however, relatively few (400 to 500) were obtained for the specific purpose of investigating the engineering properties of submarine sediments. Although 400 to 500 cores from an area of approximately $41 \times 10^6 \text{ km}^2$ ($15,8 \times 10^6 \text{ miles}^2$) do not provide representative samples of all the North Atlantic deposits, some generalizations are possible based on these few data:

(a) Calcareous oozes constitute the greatest single sediment type blanketing the North Atlantic basin. Fluvial-marine deposits are the second most abundant sediment type, occurring primarily along the basin margins and in the area between Greenland and Europe.

Although "red clays" are present, they make up only a small percentage of the sediment types found in the North Atlantic.

(b) Average shear strength values for the upper few meters of the sea floor vary from less than 0,5 psi (35 g/cm²) to 2 psi (140 g/cm²), but more commonly are found to range from 0,5 to 1 psi (35 to 70 g/cm²) over most of the North Atlantic. The highest values yet observed are found in association with the almost pure carbonate deposits of the Bahamas.

(c) Average water contents within the upper 9 to 10 m (30 to 33 ft.) of deep-sea sediments range from slightly less than 50 percent to about 175 percent by dry weight. The majority of the North Atlantic deposits exhibit water contents on the order of 50 to 100 percent.

(d) Unit weight (bulk density) varies from 80 to 125 pcf (1,3 to 2,0 g/cc), but more frequently from 95 to 109 pcf (1,5 to 1,8 g/cc) for the majority of the sediments yet investigated in this basin. Lower densities are commonly found in areas influenced by the debouching of large drainage systems such as the Mississippi and St. Lawrence rivers. Sediment porosities seldom exceed 70 percent, but do reach as high as 85 percent in a limited number of areas. More commonly, average porosities are on the order of 60 to 65 percent over most of the basin.

(e) Using the bearing capacity equation for surface loading of a strip load, ultimate bearing capacities were calculated for 22 sites in the North Atlantic. These values ranged from 0,1 to 6,9 psi (7 to 485 g/cm²), with the majority being 1,5 psi (105 g/cm²) or higher.

Deep-sea sediments are commonly found to exhibit consolidation characteristics similar to those terrestrial deposits classed as slightly overconsolidated. This property is undoubtedly not due to previous loading or desiccation, but may be a result of the very slow rate of deposition taking place in the deep-sea along with possible "cementation" from interparticle or ionic bonding forces.

A few studies of the degree of lateral variation of engineering properties within a local area indicate that rapid changes of these properties often occur over short distances. In one such study of a 400 cm² (6,2 in.²) area, coefficients of variation (degree of dispersion) were found to be as great as 147 percent and 100 percent for sensitivity and shear strength respectively.

Not only are lateral variations important in some areas, but as might be expected, vertical changes in engineering properties can be quite significant even within the upper few meters of the sea floor. Turbidity current deposits, which are found to varying degrees over most of the North Atlantic, exhibit some of the severest variations in mass properties over intervals as small as a few centimeters. Not until the advent of the U. S. Deep Sea Drilling Project have sediment cores longer than 25 m (82 ft.) been collected from the deep sea. Analysis of cored sediments collected during this project to a depth of 834,5 m (2737 ft.) in the North Atlantic has provided an insight into the changes of such properties as unit weight, water content, and porosity to this relatively great depth. At drilling Site 9, the most drastic changes in these properties occurred within the upper 40 m (131 ft.) of the sea floor. Water content and porosity decreased considerably as unit weight increased significantly. Below this depth water content decreased continually throughout the cored interval, whereas below a depth of 400 m (1312 ft.) no significant change in porosity was observed. Unit weight increased gradually with depth except in a few intervals where relatively thin layers of contrasting sediments such as foraminiferal ooze caused notable decrease in the unit weight.

The distribution and range of values presented here for selected engineering properties is indeed an over simplification as to the characteristics of deep-sea sediments. We have only begun to study these properties and as with any new investigation there will be continued revisions as more information becomes available.

Acknowledgements

I express my sincere appreciation to *Joseph Kravitz* of the U. S. Naval Oceanographic Office and *Suzanne Bershad* of the National Oceanographic Data Center for providing much of the basic data used in this study. Critical review of the manuscript by *Louis Butler* is gratefully acknowledged.

References

- Baisley, H.L.*: Introduction to statistical method. Littlefield, Adams & Co., Paterson, New Jersey 1964, 347 p.
- Bennett, R.H., G.H. Keller and R.F. Busby*: Mass property variability in three closely spaced deep-sea sediment cores. *J. Sedimentary Petrology* (in press), (1970).
- Bryant, W.R., P. Cernock and J. Morelock Jr.*: Shear strength and consolidation characteristics of marine sediments from the western Gulf of Mexico. pp. 41–62, in: *Richards, A.F.* (ed.) *Marine Geotechnique*, Univ. Ill. Press, Urbana, Ill., 1967, 327 p.
- Buchan, S., F.C.D. Dewes, D.M. McCann and D. Taylor Smith*: Measurements of the acoustic and geotechnical properties of marine sediment cores. pp. 65–92, in: *Richards, A.F.* (ed.) *Marine Geotechnique*, Univ. Ill. Press, Urbana, Ill., 1967, 327 p.
- Hamilton, E.L.*: Low sound velocities in high porosity sediments. *J. Acoustical Soc. America*, v. 28 (1956) pp. 16/19.
- Hamilton, E.L.*: Consolidation characteristics and related properties of sediments from experimental Mohole (Guadalupe site). *J. Geophysical Research* v. 69 (1964) pp. 4257/269.
- Harrison, W., M.P. Lynch and A.G. Altschaeffl*: Sediments of lower Chesapeake Bay, with emphasis on mass properties. *J. Sedimentary Petrology*, v. 34 (1964) pp. 727/55.
- Igelman, K.R. and E.L. Hamilton*: Bulk densities of mineral grains from Mohole samples (Guadalupe site). *J. Sedimentary Petrology*, v. 33 (1963), pp. 474/78.
- Interdepartmental Geophysical Committee of the Academy of Sciences, USSR: Bottom sediment chart. Main Administration for Geodesy and Cartography, Moscow, USSR, 1969.

- Keller, G.H.*: Shear strength and other physical properties of sediments from some ocean basins. pp. 391–417 in: *Proceedings, Civil Engineering in the Oceans*. American Society of Civil Engineering, 1968, 926 p.
- Keller, G.H.* and *R.H. Bennett*: Mass physical properties of submarine sediments in the Atlantic and Pacific basins. pp. 33–50, in: *Proceedings, XXIII International Geological Congress*, Sec. 8, 1968, 321 p.
- Keller, G.H.* and *R.H. Bennett*: Variations in the mass physical properties of selected submarine sediments. *Marine Geology* (in press), 1970.
- Moore, D.G.* and *G. Shumway*: Sediment thickness and physical properties: Pigeon Point Shelf, California. *J. Geophysical Research*, v. 64 (1959), pp. 367/74.
- Peterson, M.N.A., N.T. Edgar, M. Cita, S. Gartner Jr., R. Goll, C. Nigrini, C. von der Borch*: Initial reports of the Deep Sea Drilling Project, v. II. Washington, D. C., 1970, 501 p.
- Prandtl, L.*: Über die Härte plastischer Körper. *Königliche Gesellschaft der Wissenschaften zu Göttingen, Mathematisch-physikalische Klasse*, 1920, p. 74/85.
- Richards, A.F.*: Investigations of deep-sea sediment cores, I. Shear strength, bearing capacity, and consolidation. U. S. Navy Hydrographic Office, Tech. Rept. 63, 1961, 70 p.
- Richards, A.F.*: Investigations of deep-sea sediment cores, II. Mass physical properties. U. S. Navy Hydrographic Office, Tech. Rept. 106, 1962, 146 p.
- Richards, A.F.*: Local sediment shear strength and water content. pp. 474–487, in: *Miller, R.L.* (ed.) *Papers in Marine Geology*, Shepard Commemorative Volume. MacMillan Co., New York, 1964, 531 p.
- Richards, A.F.* and *G.H. Keller*: Water content variability in a silty clay core from off Nova Scotia. *J. Limnology & Oceanography*, v. 7, (1962), pp. 426/27.
- Richards, A.F.* and *E.L. Hamilton*: Investigations of deep-sea sediment cores, III Consolidation. pp. 93–117, in: *Richards, A.F.* (ed.) *Marine Geotechnique*, Univ. Ill. Press, Urbana, Ill., 1967, 327 p.
- Rittenberg, S.C., K.O. Emery, J. Hülseman, E.T. Degens, R.C. Fay, J.H. Reuter, J.R. Grady, S.H. Richardson and E.E. Bray*: Biochemistry of sediments in experimental Mohole. *J. Sedimentary Petrology*, v. 33 (1963), pp. 140/72.
- Scott, R.F.*: Principles of soil mechanics. Addison-Wesley Pub. Co., Inc., Reading, Massachusetts, 1963, 550 p.
- Taylor, D.W.*: Fundamentals of soil mechanics. New York: John Wiley & Sons, Inc., 1948, 700 p.
- Terzaghi, K.*: Theoretical soil mechanics. New York: John Wiley & Sons, Inc., 1943, 510 p.
- U. S. Naval Oceanographic Office: Oceanographic atlas of the North Atlantic Ocean. Section V. Marine Geology, Pub. 700, 1965, 71 p.

MASS PROPERTIES OF THE SEA FLOOR IN A SELECTED
DEPOSITIONAL ENVIRONMENT

by

GEORGE H. KELLER¹

INTRODUCTION

Man has only begun in the last twenty years to give serious thought to exploiting the sea floor and subsea floor. These interests have progressed gradually from the shoreline to the continental shelf and now, in a few specific areas such as sea-floor mining, into the deep sea. As a result of rapid advances in science and technology, along with man's increasing desire to understand and utilize the marine environment, the new field of ocean engineering has evolved and is fast taking its place beside the other areas of engineering. At this early stage, much of the effort in this field consists of adapting already established engineering principles to the marine environment. This approach has worked reasonably well for the civil engineer concerned with the soil mechanics or foundation aspects of the sea floor in the relatively shallow waters of the continental shelf. Investigation of the engineering properties of deep-sea deposits has been limited to a small number of studies, generally by marine geologists interested in the depositional processes taking place in the ocean basins.

In contrast to the wealth of soil mechanics data available for terrestrial soils, very little is known about the engineering properties of deep-sea sediments and even less is understood about the influence this unique environment may have on these properties. As might be expected, a number of these properties, particularly in the upper few meters of the ocean floor, differ considerably from those reported for terrestrial deposits.

This study was undertaken to investigate the engineering properties of deposits occurring in a somewhat unique deep-sea environment, specifically one consisting of a volcanic cone (seamount) surrounded by the abyssal plain. By examining a number of sediment cores from a small area it was anticipated that not only could the engineering properties be determined, but also ascertain the variation and possible relationship of these properties to the contrasting topography found at the site. A detailed analysis was made of selected mass properties (cohesion, water content, wet bulk density, texture, porosity, and calcium carbonate content) in order to determine their lateral and vertical variability within the confines of the study area

¹ESSA, Atlantic Oceanographic and Meteorological Laboratories, Miami, Florida 33130

PREVIOUS INVESTIGATIONS

It is estimated that on the order of 1500 to 2000 sediment cores have been collected from the deep sea for the purpose of studying the engineering properties of sea-floor deposits. Considering the extent to which the sea covers the earth (70 percent), this sampling density clearly points out our lack of information in this environment.

Very few data are available that can be related to the deeper foundation characteristics of the sea floor. This primarily stems from limitations of the sampling techniques presently used by marine geologists to collect deep-sea sediments. Core samples suitable for engineering studies seldom exceed 7m (21 ft.) in length. Studies conducted to date, can only be related to the upper few meters of the sea floor.

The first report on wet unit weight, water content, and shear strength of deep-sea sediments was made by Arrhenius (1952) from his study of a number of Pacific cores collected during the 1947-48 Swedish Deep-Sea Expedition. Shear strength was determined with a fall cone and only relative strengths reported. These values have since been converted to conventional units (Moore and Richards, 1962). Later interest in the engineering properties of submarine sediments stem from the requirements of various military programs for an increased knowledge of the sea-floor environment (Hamilton, 1956; Hamilton, et al., 1956; and Keller, 1964).

In their efforts to investigate depositional processes or specific characteristics of deep-sea sediments, scientists have conducted a number of studies either on specific relationships such as sound velocity and mass properties (Buchan, et al., 1967), density and depth of burial (Igelman and Hamilton, 1963), consolidation and depositional history (Hamilton, 1964; Richards and Hamilton, 1967) or they have studied the mass properties of a local area (Moore and Shumway, 1959; Richards, 1964; and Almagor, 1967).

One of the early comprehensive studies on the mass physical properties of deep-sea sediments was that by Richards (1961, 1962) which reported in detail on the testing and analysis of 35 sediment cores collected from the north Atlantic, western Mediterranean and north Pacific. This work has provided the basis and impetus for many recent investigations in this field, now referred to as "Marine Geotechnique" (Richards, 1967). As more data have

become available, larger scale studies have provided basic engineering properties data on a regional basis, for example, the work of Moore (1962) in the north Pacific, Einsele (1967) in the Red Sea, Bryant and Wallin (1968) in the Gulf of Mexico, and that of Keller and Bennett (1968) who compiled data from approximately 800 cores from the north Pacific and north Atlantic.

Although there is little doubt that considerable instability of the sea floor exists as shown by the occurrence of numerous slump features and turbidites (graded beds indicative of turbidity flows), only limited information is available as to the stability of submarine slopes. Terzaghi (1956) presented a lengthy discussion on the various types of failures in submarine slopes, but dealt primarily with the nearshore zone. Moore (1961) investigated the shear strength of a number of cores collected from the continental shelf off California. From this study he concluded that submarine sediments were essentially in a stable state on most slopes, except in specialized environments where the rate of sedimentation was rapid, e.g., deltas and submarine canyons.

An after the fact study of the gullied portion of the San Diego trough by Inderbitzen (1965) presented the characteristic properties of what were reported to be slump deposits. Most recently, Morgenstein (1967) has brought together much of the available information on submarine slumping and has presented a detailed discussion of the mechanics of slumping and the transformation of some such slumps into high density turbidity flows.

STUDY SITE

The setting for this study is 370 km (230 mi.) southwest of San Diego, California in a tectonically active area referred to as the Baja California Seamount province. An abundance of volcanic cones (seamounts) and a micro-relief (40 to 100 m [132 to 330 ft.]) of the abyssal sea floor, too rough to permit a generalization regarding depth, characterized this province (Fig. 1). The irregular micro-topography results from tectonic activity, but the specific mechanism such as volcanism or faulting, is not clearly defined. A clear indication of the wide spread volcanism in this area was revealed from a 1,400,000 km² (538,000 mi.²) survey of the province by Menard (1959) in which the presence of 1000 seamounts was reported. The eastern margin

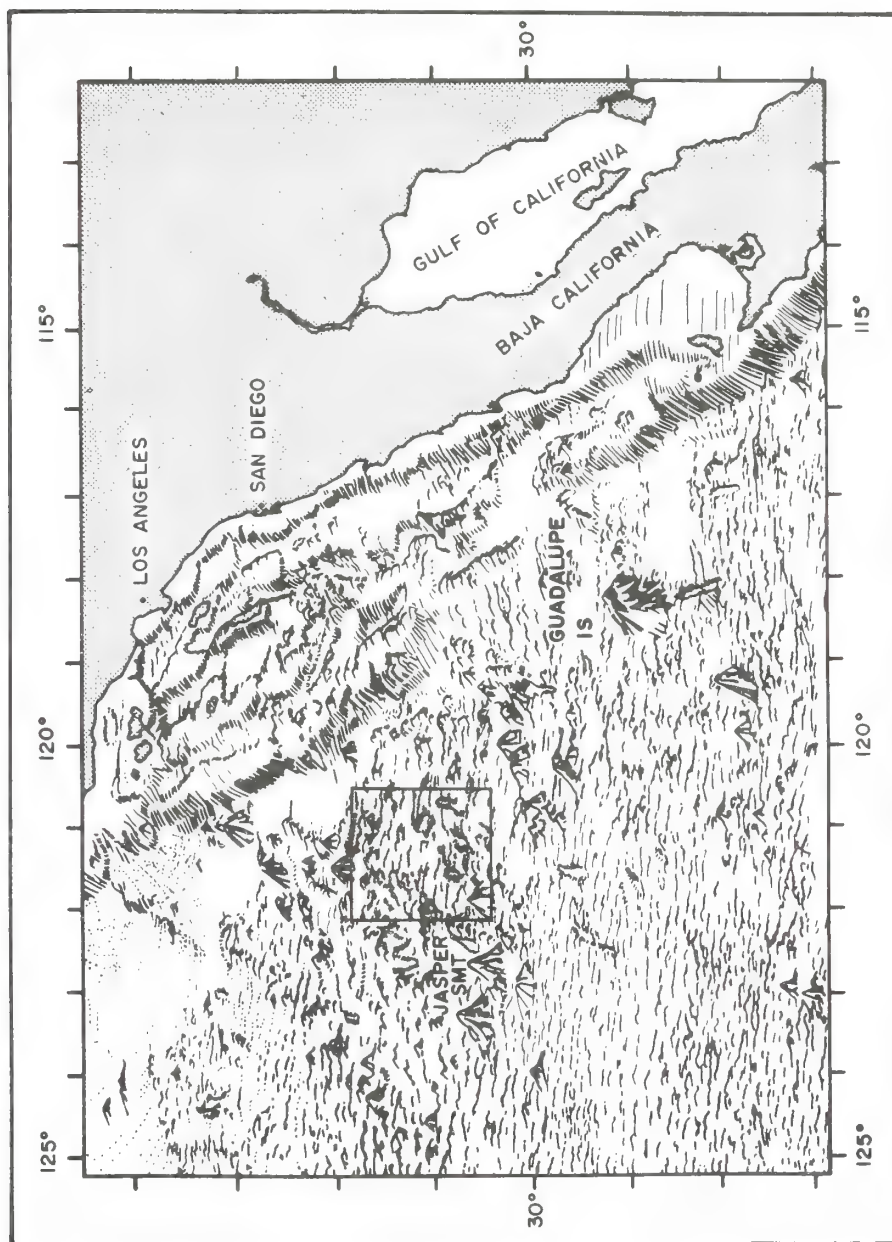


FIGURE 1. STUDY AREA (SHADED) AND THE SURROUNDING PHYSIOGRAPHY.

of this province is bordered by a number of basins and troughs (southern continuation of the continental borderland) which appear to trap sediment being eroded from Baja California (Menard, 1955). Lack of an extensive smooth sediment blanket covering the sea floor, as is found north and south of the province, indicates that little sediment actually bypasses these traps.

Near-bottom currents in the vicinity of the study area trend in a southeast direction at velocities of 2.4 to 4.10 cm/sec (.08 to 0.14 ft./sec) (Isaacs, et al., 1966). These investigators also reported similar velocities from the flank of a seamount approximately 48 km (30 mi.) west of the study site. Although their data did not show stronger currents in the vicinity of the seamount they did find, using bottom photographs, that the sea floor was a pavement of pillow lava swept clean of sediment. The occurrence of stronger currents is highly possible since the reported measurements were only for periods of 23.5 to 80.5 hours and during one time of the year.

The actual study area extends over 23,640 km² (7,200 mi.²) and consists of a prominent seamount rising 2960 m (9768 ft.) above an abyssal plain characterized by a rough micro-relief (Fig. 2). Lack of sufficient bathymetric data precludes the display of this micro-topography. The gentle westerly slope of the sea floor is common to much of the province.

SAMPLING

Twenty sediment cores varying in length from 128 to 320 cm (50 to 128 in.) were collected by the U. S. Naval Oceanographic Office from a small area incorporating a portion of the Pacific abyssal plain and a prominent seamount (Fig. 2). Modified Ewing and Kullenberg corers were used, providing samples 6.05 and 4.76 cm (2.38 and 1.88 in.) in diameter respectively (U. S. Navy Hydrographic Office, 1955). The characteristics of these samplers are not ideal for obtaining "undisturbed" material (Richards and Keller, 1961), however, no visible disturbance of the tested portions of the cores was noted and the samples were considered on a par with others reported in the literature.

Inert plastic (cellulose acetate butyrate) liners were used in the corers in an effort to reduce chemical reactions between the sediment and the steel barrel and to provide a container in which to transport the sample to the laboratory.

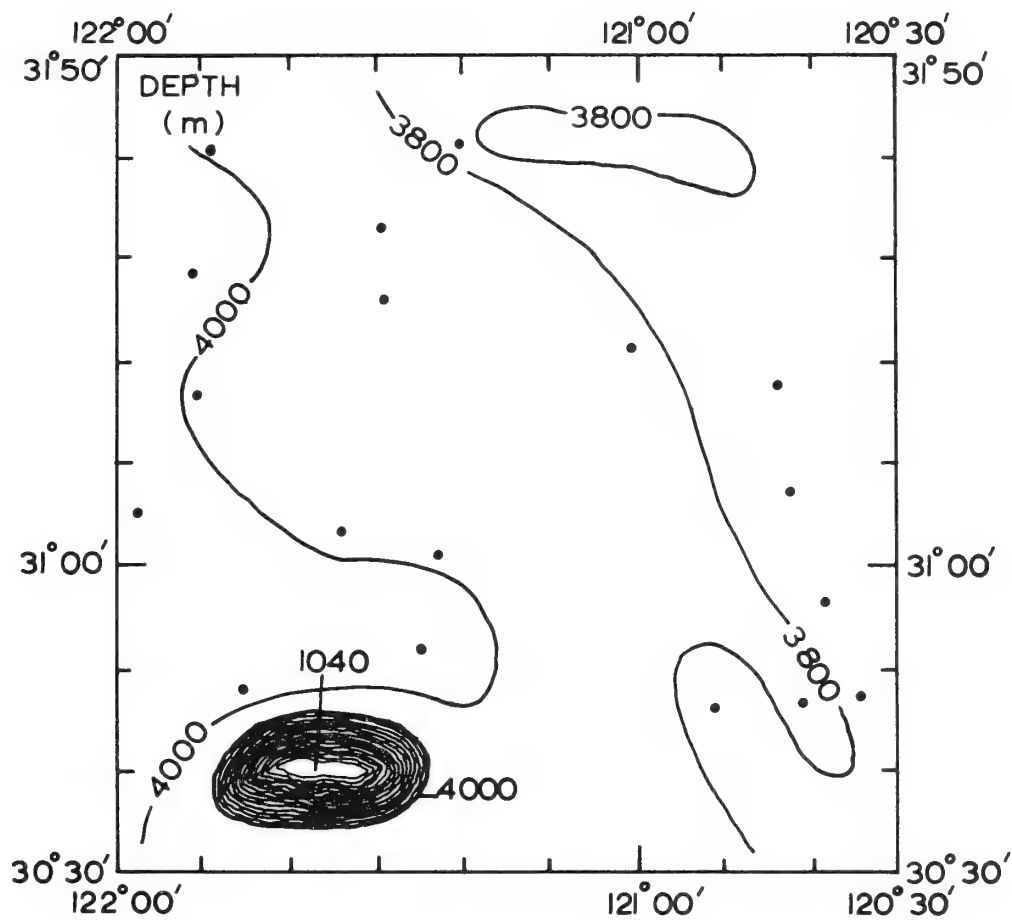


FIGURE 2. BATHYMETRIC MAP AND SAMPLE LOCATIONS.

Since water loss through such a liner can be appreciable (Keller, et al., 1961), each liner was coated with a micro-crystalline wax after the sample was retrieved.

LABORATORY TESTS

A total of 365 subsamples was tested for selected engineering properties (cohesion, water content, wet bulk density, and grain specific gravity), of these, 207 samples were also analysed for their textural characteristics and calcium carbonate content. Testing procedures for the engineering properties are essentially the same as those established by the American Society for Testing Materials (1958) and have been discussed specifically in regard to submarine sediments by Richards (1961). Because of the characteristics of this sediment (low cohesion and relatively high water content) the standard tests for shear strength were scaled down, but otherwise not altered. The majority of the tests were made with a laboratory-vane shear apparatus (Evans and Sherratt, 1948) and only in a few instances could a modified unconfined compression apparatus be used (Richards, 1961). Undrained shear strength tests were conducted on totally saturated, unconsolidated sediments. Under these special conditions, shear strength is equal to cohesion, and the strength measured by these tests is a measure of cohesion and is so used here. No corrections have been made for the salt content of the sediment.

Textural determinations were made by the sieving and pipette technique and the analyses for calcium carbonate by the insoluble residue method (Krumbein and Pettijohn, 1938).

Some degree of desiccation or slight disturbance was observed at the ends of almost all the cores. For this reason only those data obtained from the middle portion of the cored interval have been used in this study. The values reported herein are the averages of the respective parameters over the tested portion of the core.

DISCUSSION

The study area consists primarily of an abyssal plain environment with water depths varying from 3712 to 4133 m (12,175 to 13,556 ft.). For the purpose of this study, the abyssal plain is considered to be a relatively flat

surface sloping gently to the west, although a micro-topography exists in this area as noted earlier. The sea floor is interrupted in the southwest sector of the study area by a seamount displaying 2960 m (9768 ft.) of relief.

The depositional environment of the site is that of the deep-sea "red clay" deposits, indicating a slow and somewhat uniform rate of sedimentation (few mm per 1000 years). These deposits are terrestrial in origin and are primarily carried in suspension out from the land. Abyssal plain deposits in the study area are texturally quite uniform and exhibit only very minor variation both laterally and with depth (Fig. 3). In 194 out of the 207 subsamples examined, the median diameter ranged from 1 to 5μ with an average of 2μ . As is commonly found in association with "red clays", a silty clay texture predominates in the study area.

Only in those samples taken from the flank of the seamount was any noticeable difference observed in the textural characteristics. These sediments were notably coarser than the abyssal plain deposits and were characterized by a median diameter of 17μ and a clayey silt texture. The coarser texture is attributed to the winnowing out of a portion of the finer material by currents, along with an increased concentration of calcareous foraminiferal tests which comprise most of the fine sand- and silt-size particles. Although the tests were present in the abyssal plain sediments the relative concentration is considerably higher at the shallow depths of the seamount owing to the lower rate of calcium carbonate solution.

Calcium carbonate content of the surface sediments was low in the abyssal "red clays", averaging about 7 percent, but considerably higher (17 percent) on the flank of the seamount (Fig. 4). Microfaunal tests constitute the bulk of the carbonate material, thus the coarser deposits on the seamount correspond to the areas of higher calcium carbonate. A slight decrease in carbonate content is observed from east to west on the abyssal plain which may reflect the corresponding gradual increase in water depth in the same direction. The effects of solution at the deeper depths was observed on a number of tests.

Organic carbon analyses of the upper few centimeters of each core revealed an overall average of 0.74 percent for the "red clay" and 0.17 percent for the coarser seamount sediments. As a general rule, all other things being equal, organic carbon content is directly proportional to

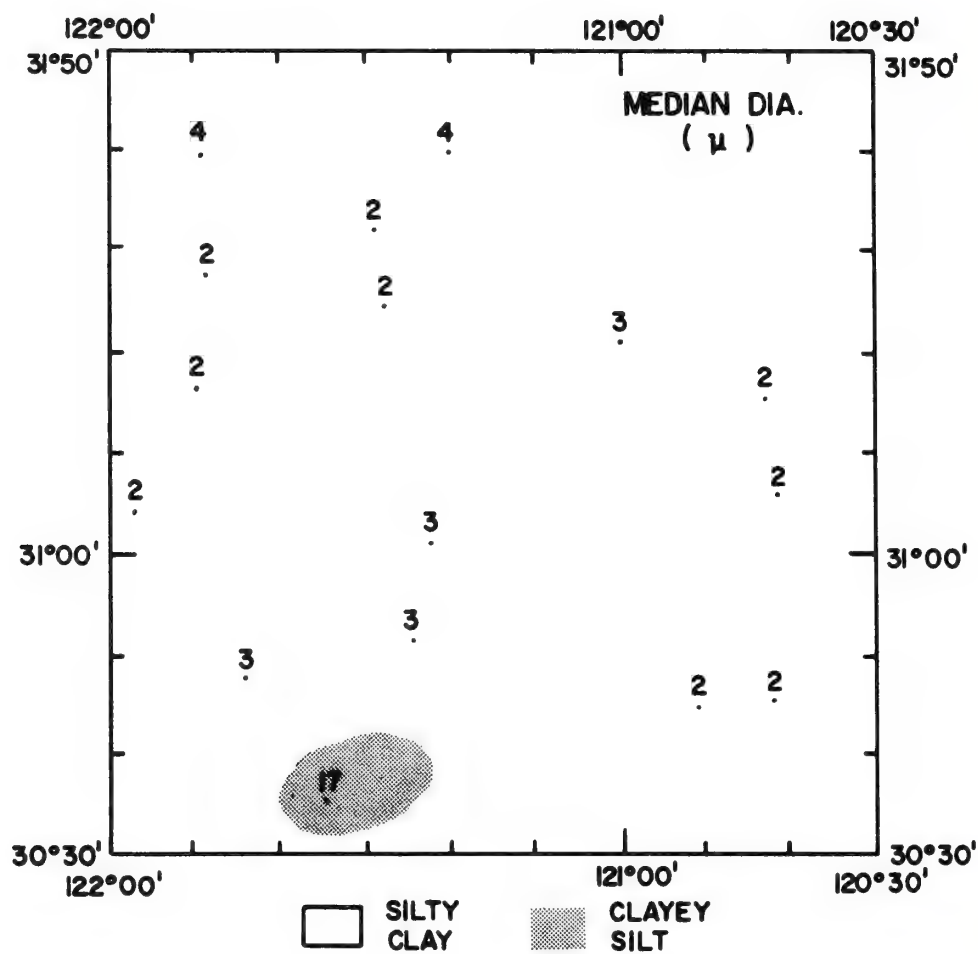


FIGURE 3. MEDIAN DIAMETER AND TEXTURAL DISTRIBUTION.
 TEXTURE BASED ON SHEPARD'S (1954) NOMENCLATURE.

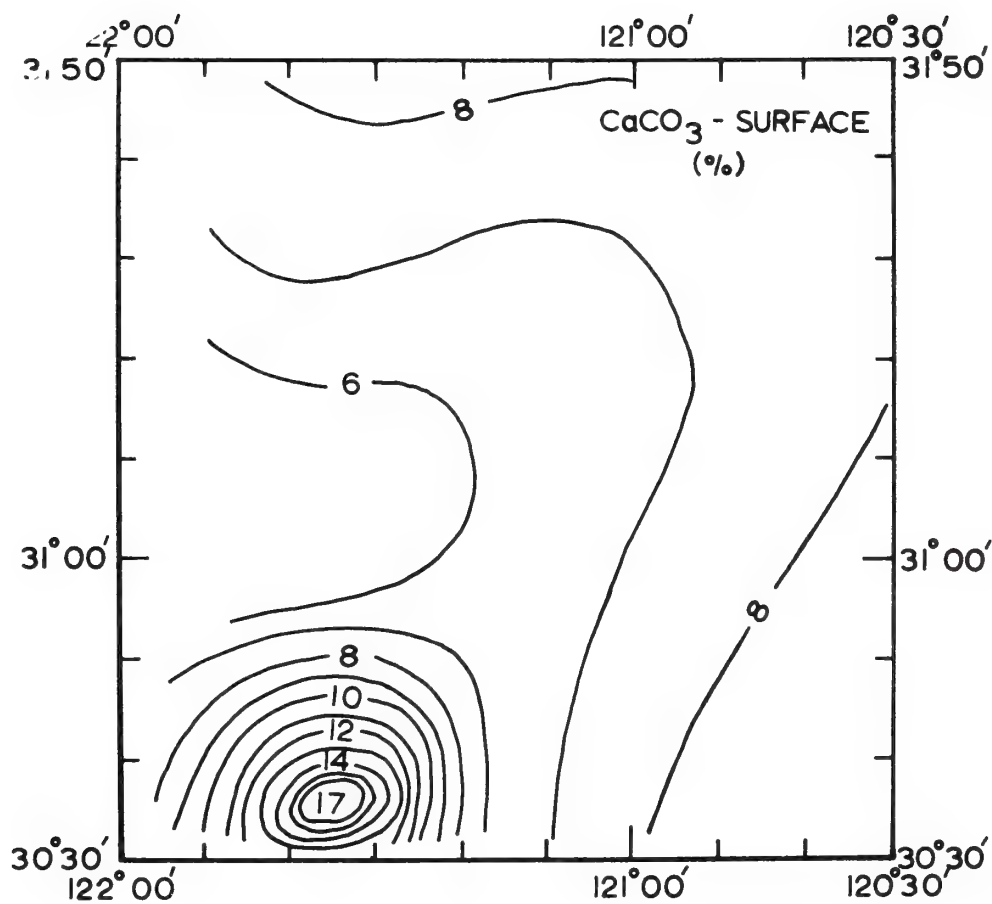


FIGURE 4. CALCIUM CARBONATE CONTENT OF SURFACE SEDIMENTS.

the concentration of finer particles. It is also found in some instances to have a definite correlation with such properties as cohesion and sensitivity of sediments (Jerbo, 1966).

Specific gravity of the solids varies only slightly in this area, as might be expected for deposits which are not influenced by a number of different source areas. Average values determined for each core range from 2.68 to 2.73. An occasional value as high as 2.93 was found in conjunction with a few thin layers of coarse material (volcanic debris).

Variations in wet bulk density in the area of the abyssal plain are relatively minor and reflect the uniform sediment type comprising most of this portion of the Pacific sea floor. Values range from 1.36 to 1.42 g/cm³ (84.9 to 88.6 pcf), which are reasonably close to an average value of 1.44 g/cm³ (89.9 pcf) reported by Keller and Bennett (1970) for "red clay" deposits. Bulk density values were noticeably higher on the flank of the seamount, varying from 1.57 to 1.70 g/cm³ (98 to 106 pcf) with an average of 1.65 g/cm³ (103 pcf). These higher values are attributed to the effects of currents acting on the seamount. Winnowing by currents apparently results in the removal of softer (less dense) material and leaving both coarser and denser sediments behind. The distribution pattern shown in Figure 5 clearly reflects the influence pronounced changes in relief have on bulk density.

Water content (percent dry weight) of the deep-sea sediments reveals a gradual increase away from the seamount (Fig. 6). Water contents of the abyssal-plain deposits vary from 119 to 141 percent and do not appear to be influenced by the minor regional changes in topography. The lowest water content values observed (68 percent) occur on the flanks of the seamount, correlating with the coarser and denser sediments also found there.

Although porosity is a calculated value (Terzaghi and Peck, 1948) based on other parameters (water content, bulk density and grain specific gravity) it has been included here because of its importance to those investigating the acoustic properties of the sea floor. Porosity was essentially uniform throughout the abyssal plain deposits, varying only 4 percentage points within the study area (Fig. 7). In contrast, the porosity of the seamount sediments was considerably lower (12 to 13 percentage points) than that of the surrounding sea floor.

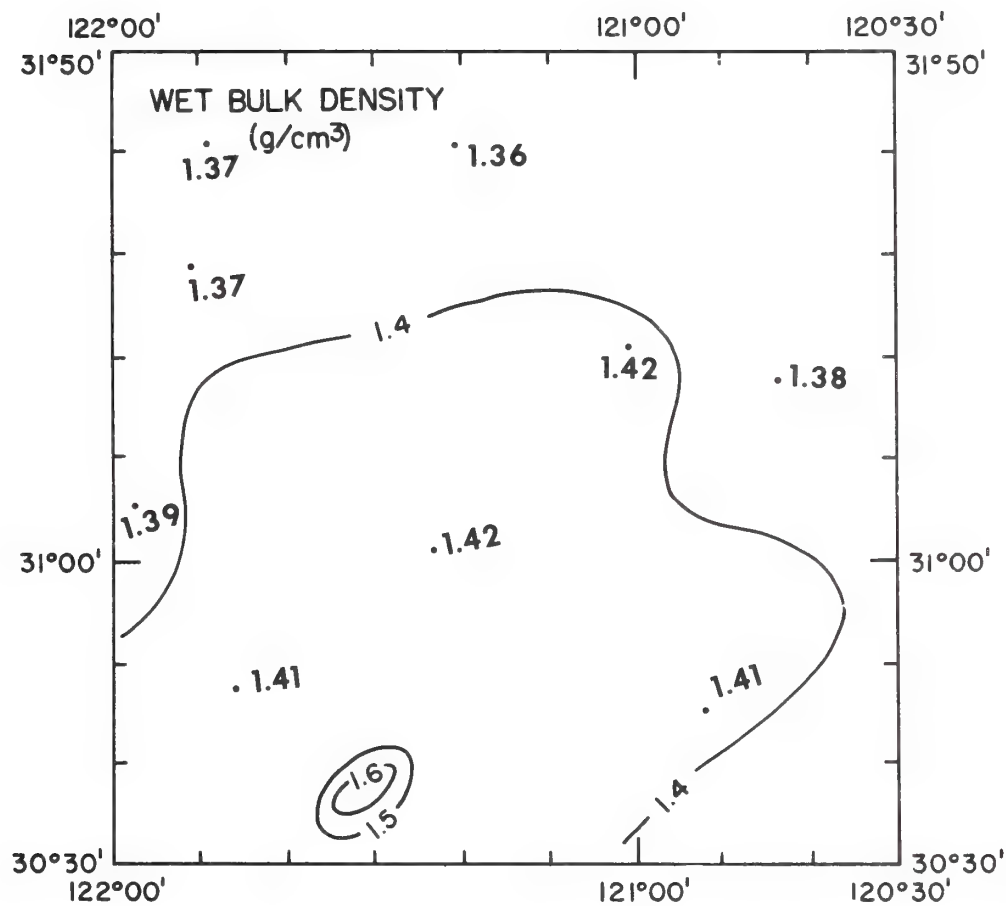


FIGURE 5. AVERAGE WET BULK DENSITY OF THE MIDDLE SEGMENT OF THE CORED INTERVAL.

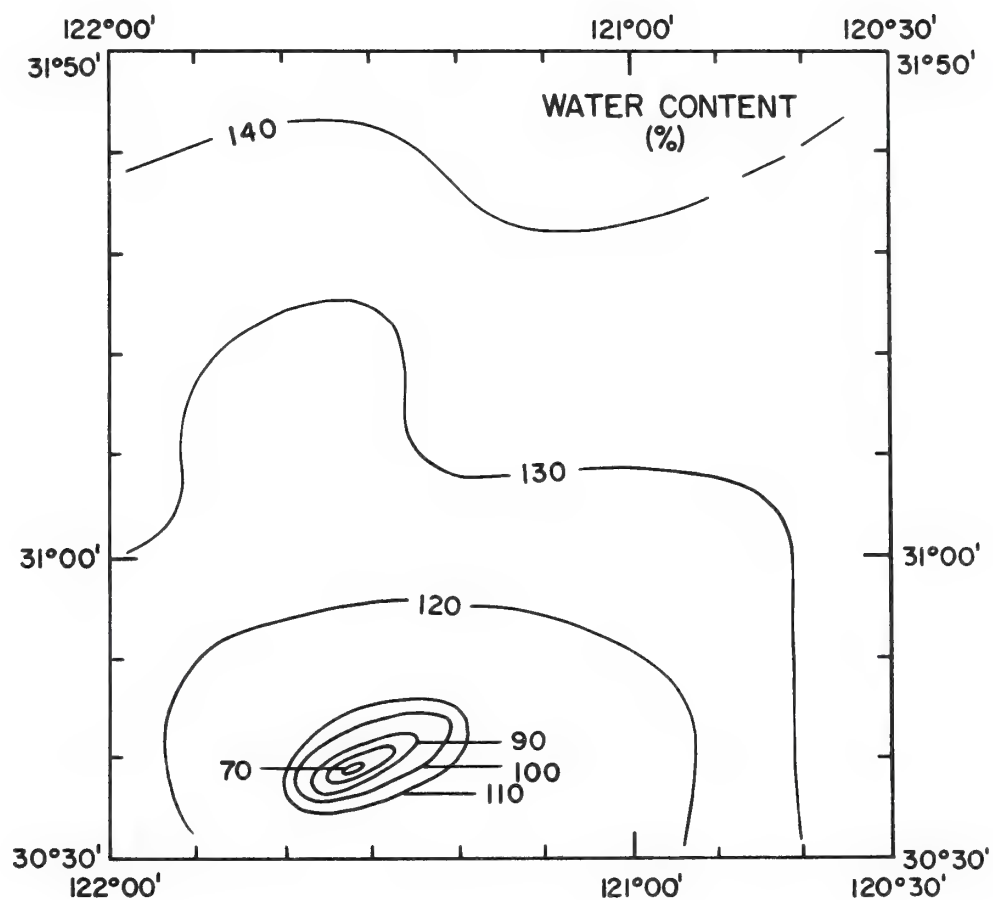


FIGURE 6. AVERAGE WATER CONTENT OF THE MIDDLE SEGMENT OF THE CORED INTERVAL.

The distribution pattern for cohesion is not as simple as that shown by the other parameters (Fig. 8), however, a clear distinction exists between the cohesion of abyssal plain sediments and that of the seamount just as has been found for the other properties. Although the other measured parameters appear to show very little variation in the abyssal plain sediments, a noticeable contrast in cohesion is found within these deposits. Much of the area exhibits a cohesion of 60 to 70 g/cm² (.85 to 1.0 psi) which approximates an average value of 45 g/cm² (.64 psi) reported for "red clay" (Keller and Bennett, 1970). A prominent portion of the sea floor north of the seamount, however, possesses a relatively high cohesion which does not appear to correlate with variations in any of the other measured properties. Sediments on the seamount clearly possess higher cohesion as would be anticipated in conjunction with the lower water content and higher bulk densities found there.

CONCLUSIONS

Abyssal plain deposits commonly display rather uniform mass physical properties as has been shown for a large portion of the north Pacific (Keller and Bennett, 1968). During this study a similar uniformity was observed for the overall sea floor indicating a normal abyssal plain environment. Only in the case of cohesion were anomalous areas of high values observed. Since the other properties measured in this area exhibit no distinct contrast to other portions of the abyssal plain, it is assumed that some other factor has contributed to the zone of higher cohesion. The presence of micro-relief may in some way have affected cohesion yet not have been significant enough to influence the other measured properties. Another possible source for increased cohesion could be local cementation or bonding as a result of pore-water migration. Without considerably more data, a clear explanation for this occurrence is not readily available.

The distribution of the various mass properties is clearly affected by the presence of a volcanic peak rising 2960 m (9768 ft.) above the relatively flat sea floor. As in any dynamic environment a projection above a plain serves to concentrate whatever forces are active in the environment, ocean currents in this case. Samples taken from the flanks of the seamount possess distinctly different characteristics than those of the abyssal plain.

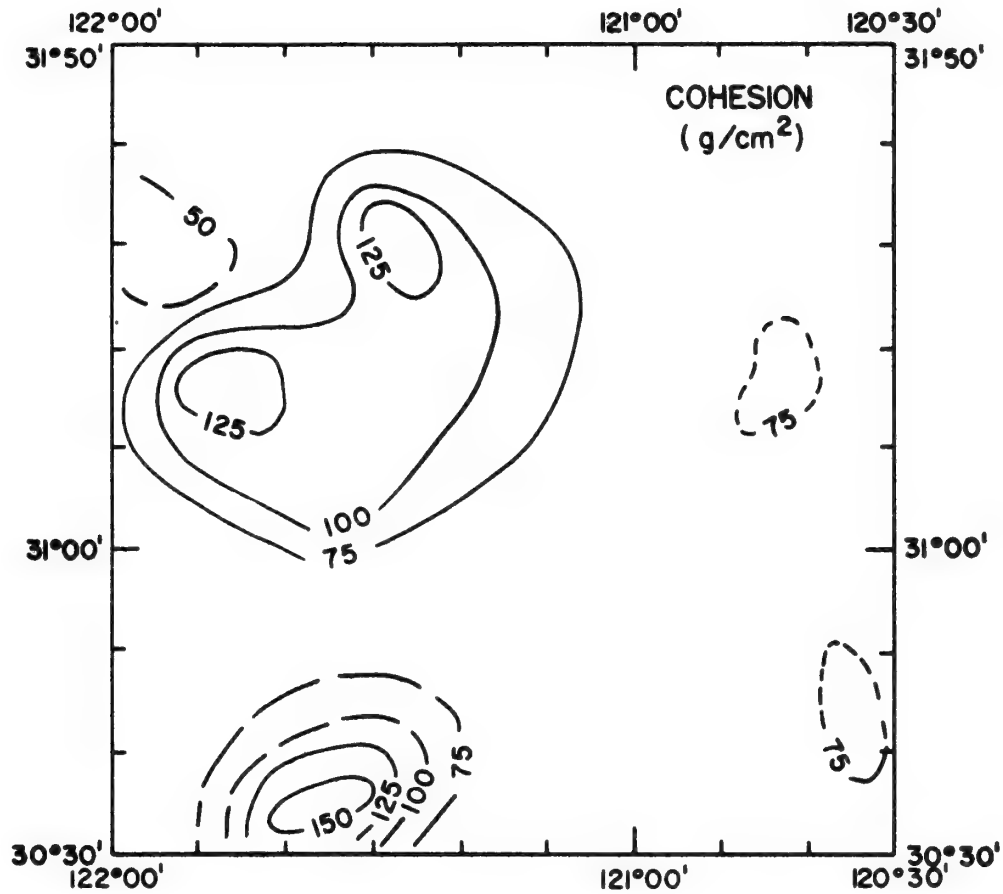


FIGURE 8. AVERAGE COHESION OF THE MIDDLE SEGMENT OF THE CORED INTERVAL.

In viewing the distribution patterns of the various parameters, there is basically little difference found among them. Values tend to increase (grain size, bulk density and cohesion) or decrease (water content and porosity) in a radial pattern away from the seamount. Such a pattern would be expected in an area where current velocities are lower away from a topographic high. Relatively higher current velocities acting on the seamount would tend to winnow out much of the finer particles and leave behind both a coarser and denser deposit.

Although micro-relief of 40-100 m (132 - 330 ft.) exists on the abyssal plain, this scale of relief did not appear to effect the properties of these deposits. This study clearly reveals that a pronounced relationship does exist between the sediment mass physical properties and abrupt changes in relief such as the presence of a seamount on a relatively flat portion of the sea floor.

REFERENCES

- Almagor, G., (1967): Interpretation of strength and consolidation data from some bottom cores off Tel-Aviv —Palmakhim Coast, Israel: in Marine Geotechnique, Richards, A. F., Ed., Univ. Ill. press, pp. 131-153.
- American Society for Testing Materials, (1958): 1958 book of ASTM standards including tentatives, part 4. Philadelphia, Pa., 1426 pages.
- Arrhenius, G., (1952): Sediment cores from the East Pacific: Reports of the Swedish Deep-Sea Expedition 1947-1948, V. 5, No. 1, 227 pages.
- Bryant, W. R., and C. S. Wallin, (1968): Stability and geotechnical characteristics of marine sediments, Gulf of Mexico: Trans. 18th Ann. meeting, Gulf Coast Assoc. Geol. Societies, pp. 334-356.
- Buchan, S., F. C. D. Dewes, D. M. McCann, and D. Taylor Smith, (1967): Measurements of the acoustic and geotechnical properties of marine sediment cores: in Marine Geotechnique, Richards, A. F., Ed., Univ. Ill. press, pp. 65-92.
- Einsele, G., (1967): Sedimentary processes and physical properties of cores from the Red Sea, Gulf of Aden, and off the Nile delta: in Marine Geotechnique, Richards, A. F., Ed., Univ. Ill. press, pp. 154-169.
- Evans, I., and G. G. Sherratt, (1948): A simple and convenient instrument for measuring the shearing resistance of clay soils: Jour. Sci. Instruments - Physics in Industry, V. 25, pp. 411-414.
- Hamilton, E. L., (1956): Low sound velocities in high porosity sediments: Jour. Acoustical Soc. America, V. 28, pp. 16-19.
- Hamilton, E. L., (1964): Consolidation characteristics and related properties of sediments for experimental Mohole (Guadalupe site): Jour. Geoph. Research, V. 69, pp. 4257-4269.
- Hamilton, E. L., G. Shumway, H. W. Menard, and C. J. Shipek, (1956): Acoustic and other physical properties of shallow water sediments off San Diego: Jour. Acoustical Soc. America, V. 28, pp. 1-15.

- Igelman, K. R., and E. L. Hamilton, (1963): Bulk densities of mineral grains from Mohole samples (Guadalupe site): Jour. Sed. Petrology, V. 33, pp. 474-478.
- Inderbitzen, A. L., (1965): An investigation of submarine slope stability: Trans. Conf. on Ocean Science and Ocean Eng. 1965, Marine Tech. Soc., and Amer. Soc. Limn. and Oceanography, V. 2, pp. 1309-1344.
- Isaac, J. D., J. L. Reid, Jr., G. B. Schick, and R. A. Schwartzlose, (1966): Near-bottom currents measured in 4 kilometers depth off the Baja California coast: Jour. Geoph. Research, V. 71, pp. 4297-4303.
- Jerbo, A., (1966): Bothnian Clay Sediments - a geological-geotechnical survey: Stockholm, Geotechnical Dept., Swedish State Railways, Bull. 11, 159 pages.
- Keller, G. H., (1964): Investigation of the application of standard soil mechanics techniques and principles to bay sediments: Proc. 1st U. S. Navy Symposium on Military Oceanography, pp. 329-360.
- Keller, G. H., A. F. Richards, and J. H. Recknagel, (1961): Prevention of water loss through CAB plastic sediment core liners: Deep-Sea Res., V. 8, pp. 148-151.
- Keller, G. H., and R. H. Bennett, (1968): Mass physical properties of submarine sediments in the Atlantic and Pacific basins: Proc. XXIII Internat'l Geol. Congress, Sect. 8, pp. 33-50.
- Keller, G. H., and R. H. Bennett, (1970): Variations in the mass physical properties of submarine sediments: Marine Geology, (in press).
- Krumbein, W. C., and F. J. Pettijohn, (1938): Manual of Sedimentary Petrography: New York, Appleton-Century-Crofts, Inc., 549 pages.
- Menard, H. W., (1955): Deformation of the northeastern Pacific basin and the west coast of North America: Geol. Soc. America Bull., V. 66, pp. 1149-1198.
- Menard, H. W., (1959): Geology of the Pacific sea floor: Experientia, V. 15, pp. 205-213.
- Moore, D. G., (1961): Submarine slumps: Jour. Sed. Petrology, V. 31, pp. 343-357.

- Moore, D. G., (1962): Bearing strength and other physical properties of some shallow and deep-sea sediments from the North Pacific: Geol. Soc. America Bull., V. 73, pp. 1163-1166.
- Moore, D. G., and G. Shumway, (1959): Sediment thickness and physical properties: Pigeon Point Shelf, California: Jour. Geoph. Research, V. 64, pp. 367-374.
- Moore, D. G., and A. F. Richards, (1962): Conversion of "relative shear strength" measurements by Arrhenius on East Pacific cores to conventional units of shear stress: Geotechnique, V. 11, pp. 55-59.
- Morgenstein, N. R., (1967): Submarine slumping and the initiation of turbidity currents: in Marine Geotechnique, Richards, A. F., Ed., Univ. Ill. press, pp. 189-220.
- Richards, A. F., (1961): Investigations of deep-sea sediment cores, I. Shear strength, bearing capacity, and consolidation: U. S. Navy Hydrographic Office Tech. Rept. 63, 70 pages.
- Richards, A. F., (1962): Investigations of deep-sea sediment cores, II. Mass physical properties: U. S. Navy Hydrographic Office, Tech. Rept. 106, 146 pages.
- Richards, A. F., (1964): Local sediment shear strength and water content: in Papers in Marine Geology, Shepard Commemorative Volume, Miller, R. L., Ed., The Macmillan Co., New York, pp. 474-487.
- Richards, A. F., (1967): Marine Geotechnique: Univ. Ill. press, 327 pages.
- Richards, A. F., and G. H. Keller, (1961): A plastic-barrell sediment corer: Deep-Sea Res., V. 8, pp. 306-312.
- Richards, A. F., and E. L. Hamilton, (1967): Investigation of deep-sea sediment cores, III. Consolidation: in Marine Geotechnique, Richards, A. F., Ed., Univ. Ill. press, pp. 93-117.
- Shepard, F. P., (1954): Nomenclature based on sand-silt-clay ratios: Jour. Sed. Petrology, V. 24, pp. 151-158.
- Terzaghi, K., (1956): Varieties of submarine slope failures: Proc. 8th Texas Conf. on Soil Mech. and Found. Eng. Spec. Pub. No. 29, Univ. Texas, Austin, Texas, 42 pages.

Terzaghi, K., and R. B. Peck, (1948): Soil mechanics in engineering practice: John A. Wiley & Sons, New York, 566 pages.

U. S. Navy Hydrographic Office, (1955): Instruction manual for oceanographic observations: U. S. Navy Hydrographic Office Pub. No. 607, Washington, 210 pages.

Marine Geophysical Reconnaissance of Continental Margin North of Paria Peninsula, Venezuela¹

R. K. LATTIMORE,² L. AUSTIN WEEKS,³ and L. W. MORDOCK⁴
Miami, Florida 33130, 33158, and Seattle, Washington 98102

Abstract Marine geophysical observations north of the Paria (Venezuela) Peninsula and westernmost Trinidad have delineated three features that dominate the shallow structural pattern of the shelf: (1) Carupano Sea Valley, which extends eastward along the Paria-Araya shoreline and occupies a structural depression bounded on the south by a major fault system; (2) Cumberland Rise, a locally complex structural and topographic high north of the sea valley; and (3) Tobago Trough, which appears to extend southwest across the shelf almost to the Paria-Trinidad coast. The orientation of the positive elements of Cumberland Rise and the trend of magnetic anomalies that seem to be associated with the Carupano depression suggest that both features may be related to the Lesser Antilles arc. Detritus eroded from the Paria-Araya Peninsulas is inferred to have been transported eastward through Carupano Sea Valley into Tobago Trough; the Paria shelf has been built upward and northward by sediments which bypassed the valley and were carried directly offshore, over the Cumberland Rise, to be deposited as foreset beds on an old erosion surface.

The extension of the Lesser Antilles arc southwest into the Paria-Araya shelf is marked by a +60 to +100 mgal free-air gravity anomaly. A shallow igneous intrusive extends from Los Testigos Islands northeast along the trend of this anomaly to the upper continental slope, where the intrusive is truncated by a northwest-southeast fault. The fact that the trends of the arc can be traced well into the Paria shelf militates against the presence of an east-west transcurrent fault between Carupano Sea Valley and the Grenada platform.

INTRODUCTION

As part of an Environmental Science Services Administration program for the investigation of the structure of ocean basins and their margins, marine geophysical observations have been made in an extensive area of the Caribbean Sea and Atlantic Ocean adjacent to the Paria-Araya Peninsulas of Venezuela, and surrounding the islands of Trinidad, Tobago, and Grenada. The results of reconnaissance seismic-reflection, bathymetric, gravimetric, and magnetic observations made by USC&GS *Discoverer* in the summers of 1968 and 1969 will be presented in a series of reports, the first of which are three papers in this issue of the *Bulletin*. Our study, which covers measurements made over the Paria-Trinidad shelf and Grenada platform between 61°30'W and 63°00'W (Fig. 1), is addressed to two specific objectives: (1) determination of the structure of the Paria-Trinidad shelf and its relation to

the Lesser Antilles island arc and the South American continent; and (2) location of the transcurrent or transform fault which, according to the hypotheses of the "new global tectonics" (Isacks *et al.*, 1968), must separate the Caribbean "plate" from the South American continent.

PREVIOUS STUDY

The earliest marine geophysical observations in the southeast Caribbean were isolated submarine gravity measurements made in 1936-1937 (M. Ewing *et al.*, 1957). In 1947, additional gravity measurements were made along a northwest-southeast traverse of the Paria shelf (M. Ewing *et al.*, 1957). The first detailed bathymetric map of the Paria and Trinidad shelves was published by Koldewijn (1958) as part of a study of the near-surface sediments. Seismic-refraction investigations of the shelf, Tobago Trough, and adjacent parts of the Lesser Antilles arc, conducted by Lamont Geological Observatory in 1955, were reported by J. Ewing *et al.* (1957) and Officer *et al.* (1959). This and subsequent work have been summarized and reviewed by Edgar (1968) and J. Ewing *et al.* (in press).

¹ Manuscript received, August 24, 1970; accepted, December 3, 1970.

² National Oceanic and Atmospheric Administration (NOAA), Atlantic Oceanographic and Meteorological Laboratories.

³ Consultant; formerly, Environmental Science Services Administration.

⁴ NOAA, National Ocean Survey, Pacific Marine Center; formerly, seismic-profile officer, USC&GS ship *Discoverer*.

The writers thank the officers and crew of USC&GS (now NOAA) ship *Discoverer*, W. W. Doeringsfeld, Jr., William Everard, G. A. Lapiene, Jr., N. J. Maloney, Wendell Mickey, and Paul Miller, for their support and cooperation in conducting the field work. G. H. Keller served as chief scientist during part of the survey. Geophysical data were reduced and plotted using programs developed by Paul Grim and Bobby Basinger. Sue O'Brien drafted the figures. The paper was reviewed critically by L. W. Butler and B. J. Szenk.

© 1971. The American Association of Petroleum Geologists. All rights reserved.

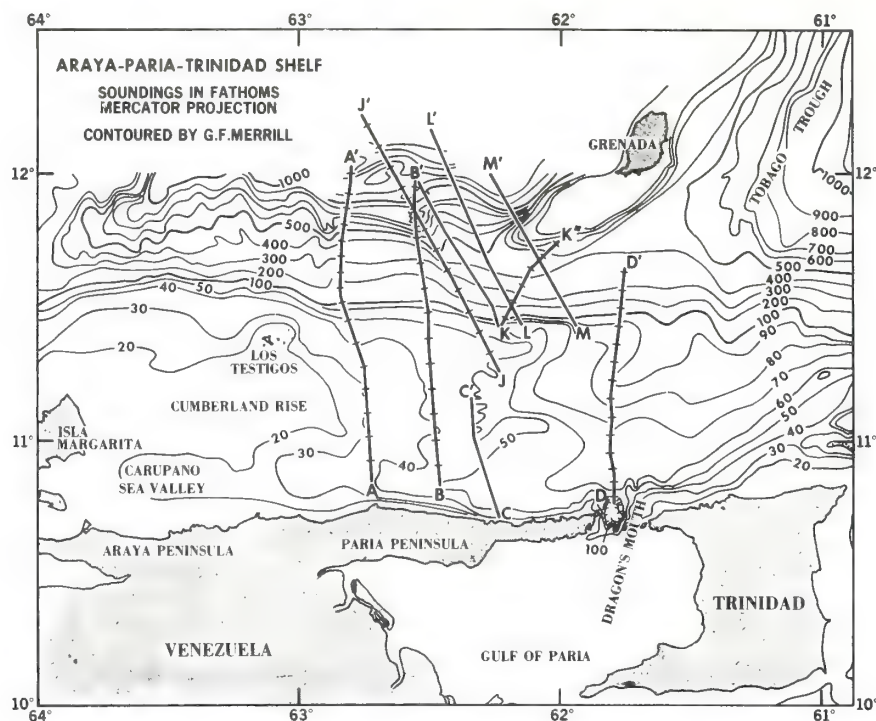


FIG. 1.—Track-line index and bathymetric map, Araya-Paria-Trinidad shelf and Grenada platform. (Sound-velocity corrections were not applied to soundings.)

METHODS

Continuous underway seismic-reflection, bathymetric, gravimetric, and magnetic observations were made along the ship's tracks shown on the bathymetric map (Fig. 1). The profiles were run at a nominal speed of 5 knots (9 km/hr); as a result of sea conditions and equipment testing, actual speeds varied from 2 to 9 knots (3.7 to 17 km/hr). Navigational control was by radar range and bearing, visual bearings, and astronomical fixes. The estimated probable error in any ship's position is ± 2 n.mi (± 3.7 km).

The seismic reflection profiles were made with a Bolt Associates, Inc., 10-cu in. (164 cc) air gun system with a 25-ft (7.6 m) array of 10 variable reluctance hydrophones. The sound source was fired at 2- or 4-second intervals; the return signal was subjected to a 39-320 Hz bandpass filter and recorded on an Alpine-Muirhead recorder. Interpretative line drawings of representative seismic profiles are presented in Figure 2.

In water depths greater than 100 fm (183 m), soundings were taken with a General In-

strument Corporation "narrow-beam echosounding system" which utilizes an electronically-stabilized beam having an effective cone-width of $2\frac{3}{4}^\circ$. Shallow-water soundings were obtained with Raytheon DE-723 fathometer. Soundings are considered accurate to ± 1 percent (L. G. Taylor, personal commun.). The bathymetric map (Fig. 1) was prepared from published and unpublished data collected by the U.S. Navy and other sources, in addition to our own profiles.

Underway gravity measurements were made with an Askania-Graf seagravimeter mounted on an Anschütz gyro-stabilized platform. The data, corrected for instrumental drift and Eötvös effect⁵, are presented in the form of free-air anomaly profiles in Figure 3. Although gravity values at track intersections consistently were within 10 mgal of each other, discrepancies with older data (e.g., M. Ewing *et al.*, 1957) range up to ± 20 mgal.

Continuous profiles of earth's total magnetic field were obtained with a Varian Associates,

⁵ Observed gravity values are relative to Barbados: Seawell Airport $\bar{g} = 978.2997$.

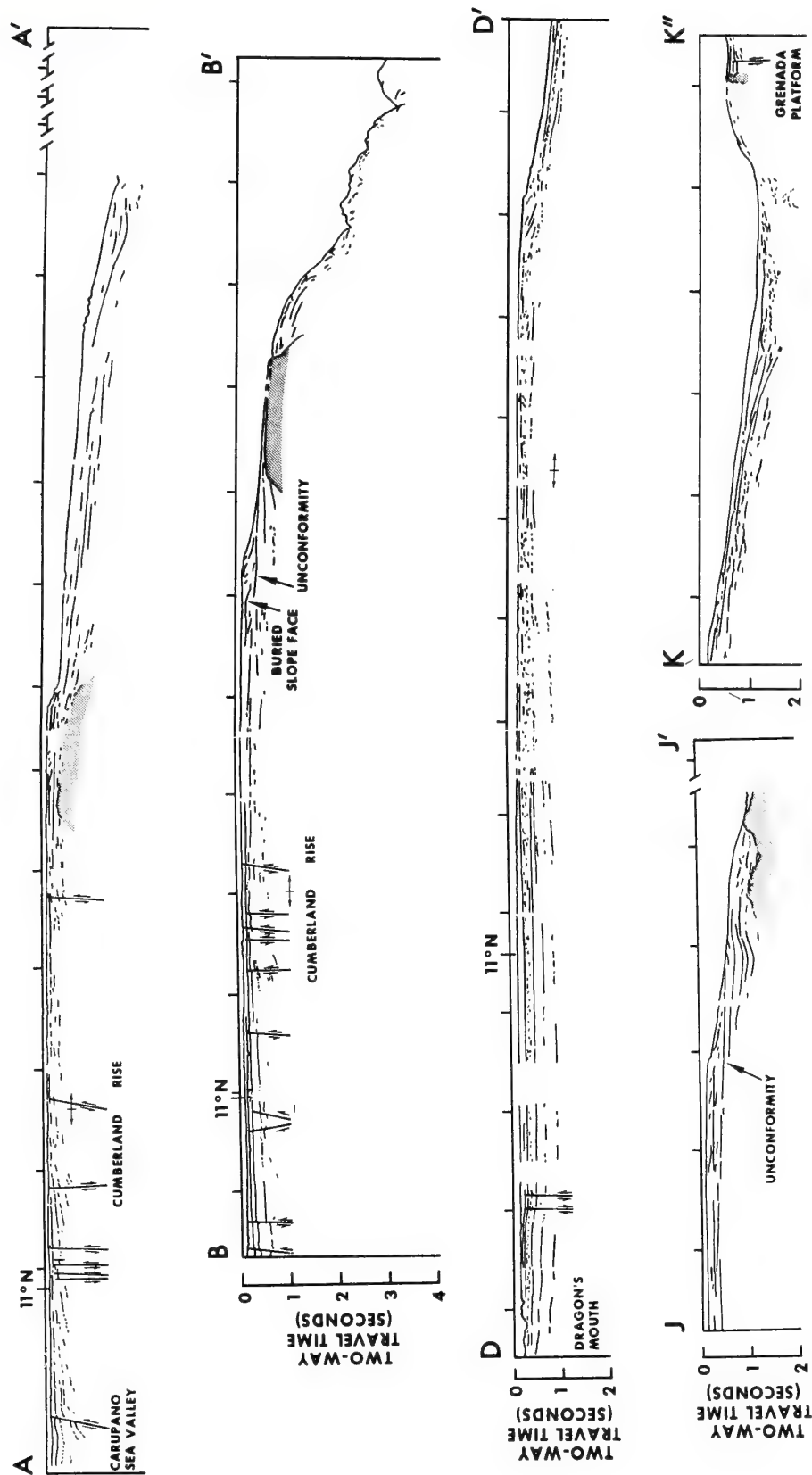


Fig. 2.—Interpretative line drawings of representative seismic-reflection profiles, Paria shelf (AA', BB', and DD') and Grenada platform (JJ', KK'). Fiducial marks on zero ordinate correspond with those on track line, Figure 1.

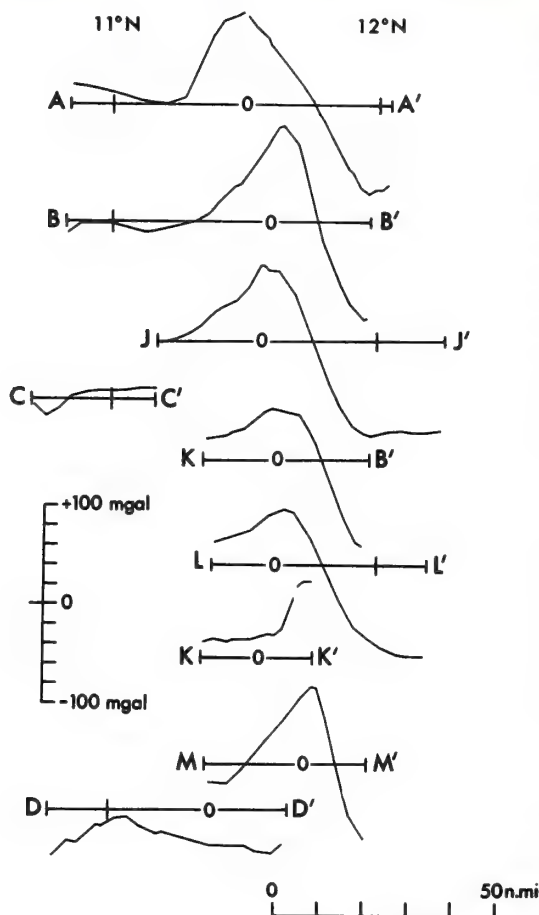


FIG. 3.—Free-air gravity anomaly profiles, Paria shelf (AA'–DD') and Grenada platform (JJ'–MM'). From top to bottom, the profiles are arranged from west to east.

Inc., direct-reading proton precession magnetometer. Critical values were scaled from the graphic record and reduced to residual anomalies by using the parameters of the International Geomagnetic Reference Field. The magnetic-anomaly profiles (Fig. 4) are considered to be internally consistent to $\pm 20 \gamma$.

REGIONAL SETTING

A nearly flat continental shelf, 40–60 n.mi (75–110 km) across, lies where the trends of the Lesser Antilles arc intersect the margin of the South American continent (Fig. 1). This shelf extends from the island of Tobago westward beyond 64°W ; it is bounded on the south by the rugged coast ranges of Trinidad and the

Paria-Araya Peninsulas of Venezuela. The coast ranges are breached at Dragon's Mouth, where depths greater than 120 fm (220 m) were measured.

West of Dragon's Mouth, the southernmost part of the shelf is occupied by a shallow valley which Maloney (1967) named the Carupano Sea Valley (Fig. 1). This valley extends from southeast of Isla Margarita due east to about 62°W , where it opens into a north- to north-east-trending embayment that is considered to be an extension of Tobago Trough (Edgar, 1968). North of the sea valley a broad, very gentle swell can be traced for about 70 n.mi (130 km) east from Isla Margarita; shoals of 10 fm (18 m) or less occur on this swell south of Los Testigos Islands. We propose the name "Cumberland Rise," for this feature.

The nearly flat part of the Paria shelf terminates in a scarp of 50–80 fm (90–150 m) relief, which extends east along $11^\circ 30'\text{N}$ from 63°W to approximately $61^\circ 40'\text{W}$. North of this scarp, a gradient of 1:100 or less persists to depths of approximately 400 fm (730 m), where the slope increases by a factor of two or more. Below 700–800 fm (1,280–1,460 m) the smooth slope gives way to a zone of rough, rolling topography.

A platform extends southwest of the island of Grenada to approximately 62°W , where the sea floor dips abruptly to depths of 300–500 fm (550–910 m; Fig. 1). This platform is separated from the Paria shelf by a broad, asymmetric trough or basin in which depths do not exceed 500 fm (910 m). The floor of this basin generally is smooth and undissected, although shallow channels near the western end of the Grenada platform suggest that local drainage is toward the northwest. On its eastern end, at about $61^\circ 40'\text{W}$, this valley opens into Tobago Trough.

PARIA SHELF

Within the depths penetrated by the seismic profile equipment—0.3–0.5 sec two-way travel time—the flat continental shelf consists of nearly horizontal stratified rocks. Reflectors near the outer edge of the shelf suggest foreset bedding, and it is clear that the shelf has been built upward and northward by progradation (AA', BB', DD', JJ', Fig. 2). The shallow sediments of the central and inner shelf are characterized by well-defined, subparallel, continuous reflectors; individual beds dip gently and thicken very gradually toward the south (AA', BB', DD', Fig. 2). Although the sediments

which make up the shelf are relatively undeformed, faults of small displacement, open folds, and gentle flexures affect near-surface as well as deeper strata. Few individual structural features are of sufficient magnitude so that they can be traced from one profile to the next.

Coastline Fault System

The abrupt transition from the folded and intruded Mesozoic rocks which form the mountainous Paria-Araya Peninsulas (Maxwell and Dengo, 1951; Bucher, 1952; González de Juana *et al.*, 1968) to the nearly horizontal younger strata that comprise the shelf is best explained in terms of major faulting along the shoreline. Fault contact between rocks of the coast ranges and the shelf sediments can be demonstrated in a profile taken through Dragon's Mouth (Bassingier *et al.*, 1971, this issue of *Bulletin*). Both profiles east of $62^{\circ}30'W$ (CC' and DD') show that near-horizontal to north-dipping, commonly gently folded strata near the coast have been uplifted in relation to apparently equivalent, south-dipping sediments farther seaward, a feature that suggests that uplift of the coast ranges has taken place along several faults which form a system oriented generally east-west, parallel with the shoreline.

Carupano Sea Valley

Carupano Sea Valley occupies a structural depression bounded on the south by one or more faults of the coastline system. At $62^{\circ}50'W$ (AA', Fig. 2), this depression is a well-defined graben, perhaps 10 n. mi (18 km) across. The graben, or at least the northern bounding fault, can be recognized on the two profiles farther east (BB', Fig. 2, and CC'), so it may be inferred that the structure extends at least to $62^{\circ}15'W$. At $61^{\circ}50'W$ (DD', Fig. 2) the northern fault could not be recognized, but nearly the entire central part of the shelf is tilted southward along a pair of faults that are in line with the presumed southern boundary of the graben. Although Koldewijn (1958) has concluded that sediments derived from the coast ranges since the last glacial period have not yet been moved out of the littoral, the mountainous coastal provinces should supply sufficient detritus to fill the Carupano Sea Valley during any extended period of quiescence. Persistence of the sea valley and thickening of individual sedimentary units across faults are strong indications of continuing subsidence.

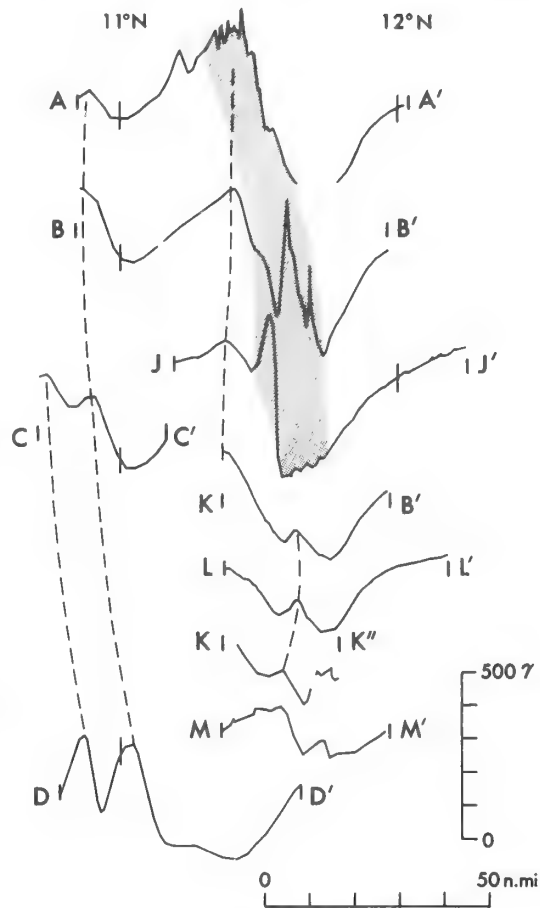


FIG. 4.—Residual magnetic anomaly profiles, Paria shelf (AA'-DD') and Grenada platform (JJ'-MM'). Dashed lines indicate correlated anomalies whose trends are shown in Figure 6. The shaded area denotes zone of short-wavelength anomalies which are attributed to shallow igneous intrusive.

Cumberland Rise

Cumberland Rise (Fig. 1) reflects a locally complex, structurally positive feature whose general trend is slightly north of east. At $62^{\circ}50'W$ (AA', Fig. 2), the predominant southward apparent dip of the shelf sediments is broken at, and in places reversed along, several faults of varying sense and amount of displacement. At $62^{\circ}30'W$ (BB', Fig. 2), an estimated 0.35 sec or more of net displacement is distributed along a series of faults south of the axis of the rise; with but one exception, motion along these faults is down-to-the-south, and displacement generally increases with depth. Far-

ther east, at $62^{\circ}20'W$ down-to-the-south displacement is manifested in abrupt, slight increases in the south dip component of the sub-surface reflectors; the only significant faults are those which form the graben associated with Carupano Sea Valley. Along $61^{\circ}50'W$ (DD', Fig. 2), the sediments dip south from a structural high on the outer shelf at $11^{\circ}20'N$; the only discernible faults would be part of the coastline system. Although topographic relief of Cumberland Rise dies out east of $62^{\circ}30'W$ (Fig. 1), the writers suggest that the anticlinal structure at $61^{\circ}50'W$, north of Dragon's Mouth (DD', Fig. 2), is on the main axis of the underlying structure. Alignment of this trend suggests kinship with an older positive structural element that includes Isla Margarita.

Tobago Trough

From seismic-refraction data collected by Lamont Geological Observatory, Edgar (1968) concluded that Tobago Trough extends southwest into the Paria-Trinidad shelf. This conclusion is supported by the nearshore bathymetry (Fig. 1) as well as by our geophysical observations. The pronounced negative gravity anomaly which occurs over the shelf north of Dragon's Mouth (DD', Fig. 3) is consistent with the

accumulation of a thick column of sediments in the trough, as postulated by Edgar (1968). In the central part of the shelf north of Dragon's Mouth, the seismic profile (DD', Fig. 2) shows 0.2 sec of sediments containing angular to sub-parallel, poorly defined, discontinuous, commonly curved or arcuate reflectors, sandwiched between sequences of the continuous, well-defined reflectors characteristic of the shelf sediments (Fig. 5). The discontinuous, curved reflectors are believed to represent foreset beds traversed at a small angle to the strike of the slope face. Structures more readily identified as foreset beds were observed at similar depths along profiles at $61^{\circ}30'W$ and $61^{\circ}10'W$, 15–30 n.mi (30–55 km) from the shoreline. The approximate limit of these beds is shown on the "structural" diagram (Fig. 6). The presence of foreset beds interbedded with the normal shelf sediments is considered to be indicative of rapid local subsidence of the central part of the shelf, and also is consistent with incursion of Tobago Trough.

The narrow, -20 to -40 mgal free-air anomaly which is developed over the southernmost part of the shelf east of $62^{\circ}30'W$ (CC', DD', Fig. 3) supports the conclusion of Edgar (1968) that a wedge of sediments, 5–7 km

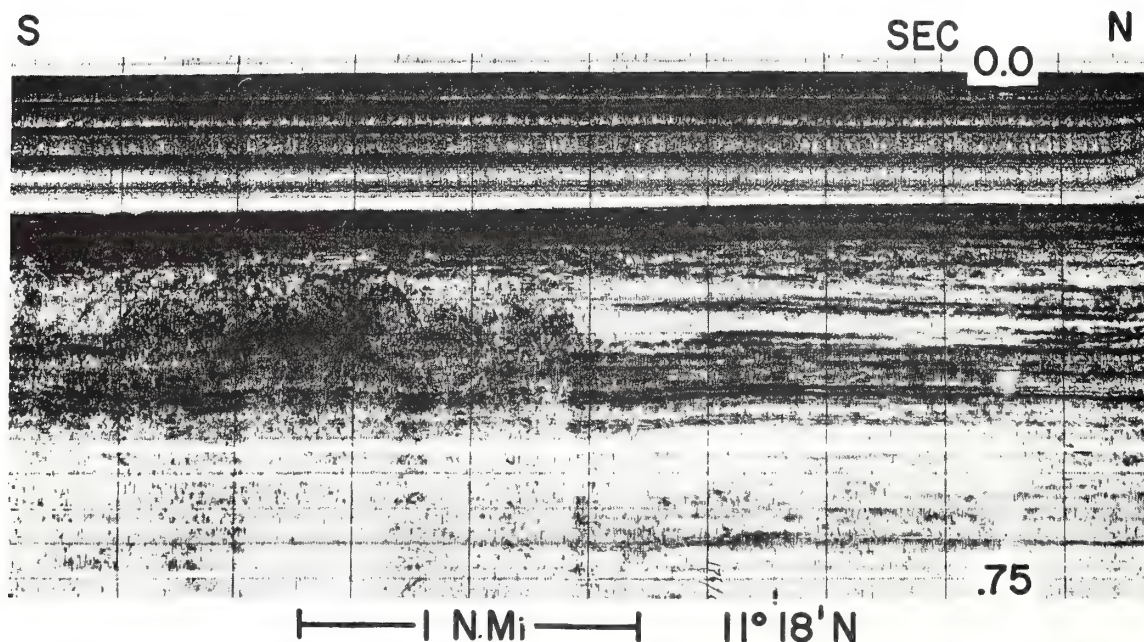


FIG. 5.—Part of seismic-reflection profile DD', showing foreset beds traversed at acute angle to strike of slope face.

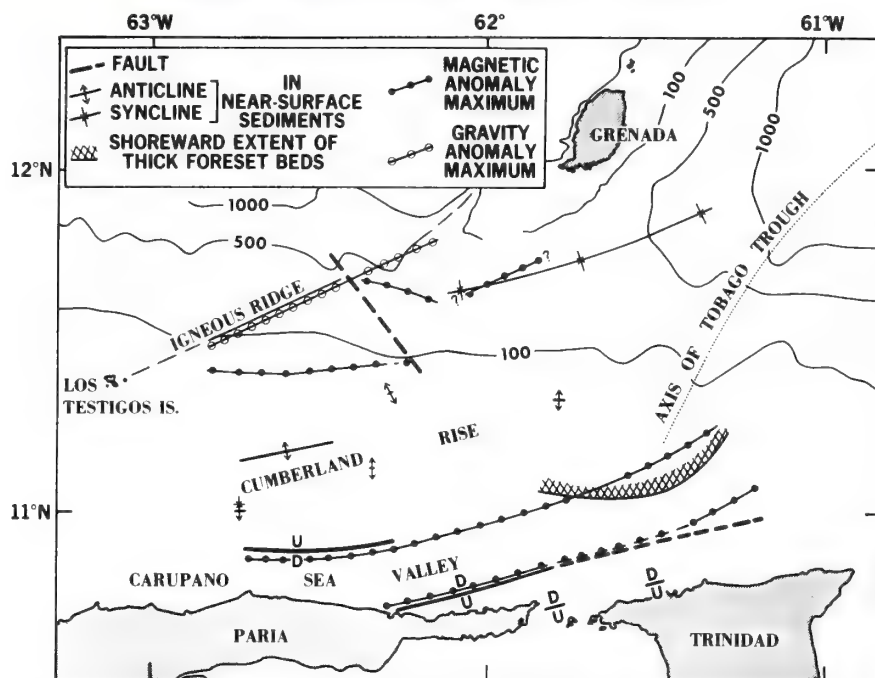


FIG. 6.—Trends and structural patterns of Paria shelf and parts of Tobago Trough and Grenada platform. (Contours are in fathoms.)

(16,400–23,000 ft) thick, extends from Tobago Trough along the Paria coast to 63°W. The Dragon's Mouth profile (DD', Fig. 3) suggests that this minimum is isolated from the broad low associated with incursion of the shelf by Tobago Trough. Bassinger *et al.* (1971) show that this low is present at 61°30'W.

Sedimentary Framework of Paria Shelf

West of 62°W the edge of the Paria shelf is built up by at least two distinct sequences of foreset bedding superimposed on each other (AA', BB', JJ', Fig. 2); the younger of these sequences forms the scarp at 11°30'N, described heretofore. An easily recognized reflecting horizon separates the two series of foreset beds; reflectors above this horizon are subparallel to angular with respect to those below it. In several localities a slope face developed on the lower sequence can be discerned beneath 0.1–0.15 sec of younger detritus (*e.g.*, BB', Fig. 2); such fossil scarps lie a few nautical miles landward of the present slope. The lower series of sediments is unconformable on broadly folded and intruded older rocks (JJ', Fig. 2). The gently graded terrace in the 200–300-fm (350–550 m) depth range is considered to be a

manifestation of this unconformity, as is the near-level surface of the "basement" ridge at 62°30'W (BB', Fig. 2; Fig. 7). The erosion surface at 200–300 fm (350–550 m) lies far below the generally accepted Pleistocene sea-level minimum, so at least an element of subsidence must be invoked to explain its position. Subsidence alone, however, does not account satisfactorily for the near-coincidence of the fossil and present foreset slope faces—a repeated event or, more likely, a cyclic series of events is required.

The structures interpreted as foreset bedding, which suggest subsidence of the central part of the shelf north of Dragon's Mouth (DD', Fig. 2), also suggest that the foreset slope face was oriented at an acute angle to the ship's track (*i.e.*, north or northwest) and that the path of sediment transport across this part of the shelf had a significant east-west component. From these inferences and the evidence of repeated or continuous subsidence of Carupano Sea Valley, it may be postulated that sediments derived from the Paria-Araya Peninsulas, and possibly from as far west as Margarita, have been transported east through Carupano Sea Valley to about 62°W, and then northeast across the

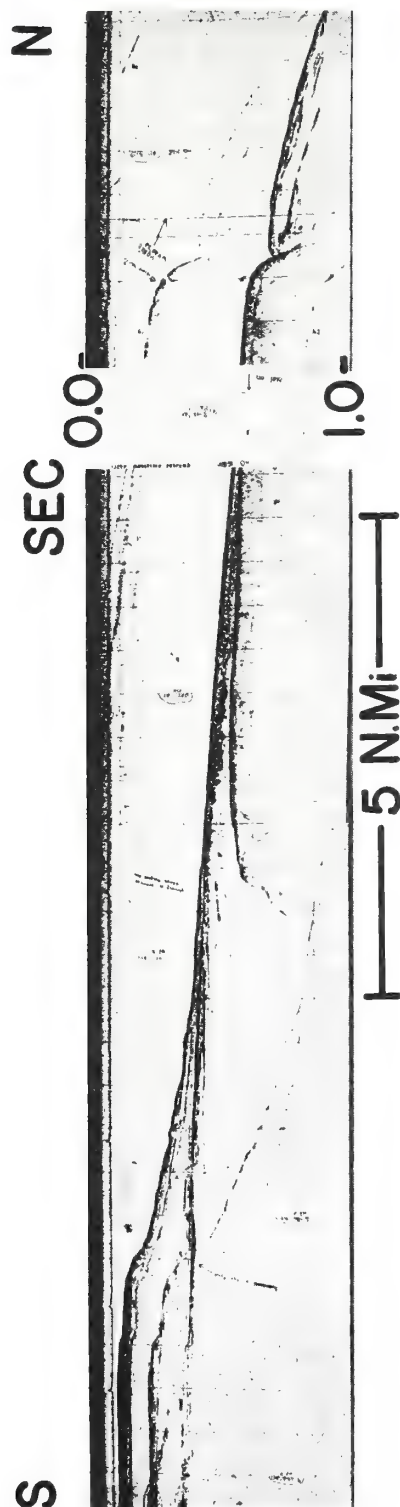


FIG. 7.—Part of seismic-reflection profile BB'. Truncated "basement" structure is interpreted to be intrusive igneous body, probably continuous with exposures on Los Testigos Islands.

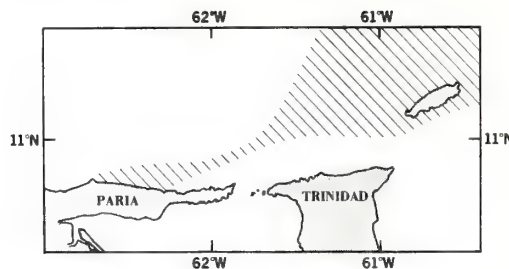


FIG. 8.—Distribution of epidote-hornblende-augite (EHA) heavy-mineral assemblage, after Koldewijn (1958).

shelf into Tobago Trough. This pattern corresponds closely with the distribution of a distinctive Holocene heavy-mineral assemblage mapped by Koldewijn (1958; Fig. 8). If this hypothesis is valid, intervals of quiescence must be postulated, during which Carupano Sea Valley was filled completely and the sediments were transported directly offshore. Detritus carried seaward and dumped over Cumberland Rise would have built the edge of the shelf upward and seaward, producing sedimentary structures like those seen in the seismic profiles from the western part of the shelf.

Trends of Lesser Antilles Arc

A broad, asymmetric magnetic-anomaly maximum can be traced for about 30 n.mi (55 km) eastward along the edge of the Paria shelf to $62^{\circ}10'W$, where it is abruptly truncated (AA', BB', JJ', Fig. 4). This anomaly is correlated with a broad, asymmetric maximum that has been mapped, east of the Grenadine platform, by J. Ewing *et al.* (1960); it probably is related to the island arc and not to the shelf. Data from outside the study area suggest that the irregular maximum which is present over the continental slope at $62^{\circ}W$ (MM', Fig. 4), and the increasing values at the northern end of the easternmost track line (DD', Fig. 4) also may be identified with this feature.

The presence of a thick wedge of sediments along the Paria coast strongly suggests that the Carupano Sea Valley depression is structurally continuous with Tobago Trough. However, a pattern of magnetic-anomaly maxima, which in the western part of the shelf seems to coincide with Carupano Sea Valley (BB', CC', DD', Fig. 4), can be traced across the axis of the trough to at least $61^{\circ}15'W$; east of $62^{\circ}30'W$ the trend swings slightly north (Fig. 6). If the anomalies are genetically related to the Caru-

pano Sea Valley depression then this structure, at depth, must extend nearly as far east as Tobago; it is not likely to be part of the present Tobago Trough.

EXTENSION OF TRENDS OF LESSER ANTILLES ARC INTO PARIA SHELF

The presence of "basement" landward of the foreset edge of the shelf at $62^{\circ}50'W$ (AA', Fig. 2) was deduced from the presence of undulating, discontinuous, strong reflectors having pronounced multiples. These reflectors coincide with a zone of short-wavelength magnetic anomalies, superimposed on a broad maximum which is believed to be related to the island arc (AA', Fig. 4); the short-wavelength anomalies are indicative of a shallow crystalline source, most probably an igneous body. A well-defined basement structure, its top presumably planed off by wave action, is present along $62^{\circ}30'W$ (BB', Fig. 2; Fig. 7), north of the foreset slope face at depths of 200–300 fm (350–550 m). In a third locality, the westernmost of four profiles that were run at right angles to the trend of the Grenada platform, possible basement crops out on the sea floor below 400 fm (730 m; JJ', Fig. 2). The fact that basement in these two profiles also is crystalline is shown by distinctive magnetic signatures which coincide with the structural features (BB', JJ', Fig. 4).

The three occurrences of crystalline basement fall on a line which, if extended toward the southwest, includes Los Testigos Islands. Maloney (1967) reported that the largest of these islands consists of a granitic intrusive surrounded by younger volcanics. We suggest that the islands and the three profile crossings define a single, essentially continuous, northeast-southwest-trending intrusive igneous body.

The investigation of the Grenada platform included four profiles run on northwest or southeast headings, normal to the long axis of the platform. The westernmost of these profiles (JJ') contains convincing evidence of "basement" structure, but the next profile (KB'), taken parallel with and about 5 n.mi (9 km) east of the first, contains no evidence of basement, even though the records show penetration of a half-second or more with good resolution. The short-wavelength magnetic anomalies attributed to the intrusive do not extend east of $62^{\circ}20'W$ (profile JJ'); instead, the broad low is broken by a distinctive, local maximum which can be traced east-southeastward for about 15 n.mi (28 km; KB', LL', KK'', Fig. 4).

The igneous ridge probably disappears at

$62^{\circ}20'W$ because of a fault. This possibility invites speculation that the fault extends south-eastward and also truncates the broad, asymmetric magnetic-anomaly maximum mapped near the edge of the shelf in the western part of the area (e.g., BB', Fig. 4). Such a fault might be confined to the intruded older sedimentary rocks and would not necessarily have any expression in the shallow strata.

The offshore basement ridge and Los Testigos Islands are so clearly on strike with the Grenada platform and the trend of the Lesser Antilles arc that truncation of the ridge at $62^{\circ}20'W$ and development of a different magnetic-anomaly pattern are presumed to represent only relatively shallow effects. The gravity anomalies show that the deeper trend of the island arc does extend into the Paria shelf. A distinctive +60 to +100 mgal free-air anomaly, which patently is related to the Grenada platform (MM', Fig. 3), can be traced southwestward through all three remaining oblique lines (LL', KB', and JJ', Fig. 3) and across the two western north-south lines (BB', AA', Fig. 3), where it coincides with the crystalline basement ridge. The regional study of Bush and Bush (1969) suggests that this anomaly continues across Los Testigos Islands to Isla Margarita where, much reduced in amplitude, it turns almost due west.

GRENADA PLATFORM

The Grenada platform—physiographically if not structurally the southern end of the Lesser Antilles arc—is a massive core complex overlain by layered sedimentary rocks that range in thickness from 0 to 0.5 sec penetration. The deeper strata usually exhibit variable, commonly comparatively steep apparent dips. The core complex is exposed on the sea floor near the western end of the platform.

A +60 to +100 mgal free-air gravity anomaly and a broad, fairly smooth magnetic-anomaly minimum were observed over the western end of Grenada platform (MM', Figs. 3, 4). The free-air anomaly indicates the presence of excess mass and tends to corroborate the existence of a dense, high seismic-velocity "root" beneath the island arc (Edgar, 1968). Observations by other investigators (e.g., J. Ewing *et al.*, 1960; Bunce *et al.*, 1970) suggest that the magnetic-anomaly profile is not atypical, and that the southern Lesser Antilles platform generally is marked by a fairly smooth, broad minimum. This minimum can be explained only by the presence of a reversely magnetized body

(G. Peter, personal commun.). Local, short-wavelength anomalies mark presumably younger intrusives.

INTER-PLATFORM BASIN

At about $62^{\circ}05'W$ northward-dipping sediments of the Paria shelf and slope nearly lap onto the intensely folded layered rocks and core complex of the Grenada platform. The two provinces are separated only by a V-shaped sea-floor valley, no more than 2 n. mi (3.7 km) wide and having perhaps 50 fm (90 m) relief. East of $62^{\circ}05'W$ this valley widens into an asymmetric, shallow basin (Fig. 1) which opens into Tobago Trough.

Most of the shallow sediments in the inter-platform basin appear to have been carried across the Paria shelf and dumped over the foreset slope face. Exhibiting a variety of structures indicative of penecontemporaneous deformation and submarine erosion, they form a wedge 0.2–0.5 sec thick which occupies the floor of the basin (KK', Fig. 2). Detritus from the Grenada platform seems to be restricted to a narrow band near its base.

SUMMARY AND CONCLUSIONS

The Paria shelf is underlain by more than 1,000 ft (0.3–0.5 sec penetration) of sediments and sedimentary rocks exhibiting subparallel, generally well-defined, continuous reflectors. In general, these beds dip gently and thicken southward; they are cut by numerous faults, commonly of small displacement. Thickening of individual beds across these faults and other evidence attest to continued or repeated epeirogenic activity.

Three major structural-physiographic elements can be delineated within the Paria shelf. Carupano Sea Valley, which extends eastward along the inner shelf parallel with the Paria-Araya shoreline, occupies a structural depression—in places a graben—bounded on the south by a zone of faults along which the coast ranges were uplifted. Cumberland Rise, a topographic and locally complex structural high north of the sea valley, is believed to reflect a positive element extending from Isla Margarita east-northeast beyond $62^{\circ}W$. The southwest extension of Tobago Trough (as shown by Edgar, 1968) is manifested (1) as a shallow embayment that extends across the shelf almost to Dragon's Mouth; (2) in a negative free-air gravity anomaly associated with the outer shelf north of Dragon's Mouth; and (3) in the oc-

currence of foreset beds intercalated with "normal" strata, interpreted as representing sudden, local subsidence of the central part of the shelf. East of $62^{\circ}30'W$ the distinctive topography of Cumberland Rise disappears, and the associated shallow structures become less complex, probably because of the accumulation of an increasingly thick blanket of trough sediments. The overall structural pattern of the shelf suggests a block that has been tilted down toward the south along the Araya-Paria-Trinidad coast, and further depressed by Tobago Trough, north of Dragon's Mouth. Our investigations do not exclude the possibility that the Carupano Sea Valley depression is a structural extension of Tobago Trough, but magnetic anomalies, which seem to be associated with the depression in the western part of the study area, extend beyond the axis of the trough nearly as far east as Tobago. East of $62^{\circ}30'W$ the trend of these anomalies develops a pronounced northward curvature, parallel with the trend of the Lesser Antilles arc.

Of the three major features which comprise the Paria shelf, only Tobago Trough is generally accepted as being part of the island arc system, but the east-northeast orientation of Cumberland Rise and the magnetic anomalies associated with Carupano Sea Valley raise the possibility that the other two elements are more closely related to the arc than to the South American continent. A broad, asymmetric magnetic-anomaly maximum over the outer shelf west of $62^{\circ}10'W$ is correlated with a similar pattern mapped by J. Ewing *et al.* (1960) north of Grenada; this pattern almost certainly is associated with the arc.

The physiography and shallow structure of the shelf, together with distribution of a Holocene heavy-mineral assemblage (Koldewijn, 1958), support a hypothesis that the principal path for sediment eroded from the Paria-Araya Peninsulas has been alongshore through Carupano Sea Valley and northeastward across the shelf into Tobago Trough. At such times as the trough or the sea valley was filled to a local base level, detritus was transported directly offshore; prograding or foreset sediments, deposited unconformably on older folded and intruded sedimentary rocks, have built the edge of the shelf upward and seaward. East of $62^{\circ}W$, sediments carried over the foreset slope face have been deposited in a comparatively shallow, asymmetric basin that opens on the east into Tobago Trough; this basin constitutes a second route by which detritus eroded from

the Paria-Araya Peninsulas can be conveyed into Tobago Trough.

Geophysical evidence indicates that Grenada platform—and by extension the southern Lesser Antilles arc—is composed of a relatively uniform, reversely magnetized, crystalline body of rock and a dense, high seismic-velocity “root.” Seismic-reflection and magnetic-anomaly data support the existence of a shallow igneous body extending from Los Testigos Islands northeast toward Grenada. Although this structure is truncated at 62°20'W (probably by faulting), gravity data substantiate extension of the Lesser Antilles trend into the Paria-Araya shelf; the intrusive body coincides with the trend.

The fact that the trends of the Lesser Antilles and Tobago Trough can be traced well into the Paria shelf implies that any recent transcurrent faulting within the area of investigation could occur only near the Paria-Araya shoreline. If, as is required by the “new global tectonics” (Isacks *et al.*, 1968), the Caribbean plate is separated from the South American continent by a fault along which great lateral displacement has taken place, this fault—if it does not predate the island arc—must occur south of 11°N. Evidence against this possibility is presented in Bassinger *et al.* (1971, this issue) and discussed by Weeks *et al.* (1971, this issue).

REFERENCES CITED

- Bassinger, B. G., R. N. Harbison, and L. A. Weeks, 1971, Marine geophysical study northeast of Trinidad-Tobago: *Am. Assoc. Petroleum Geologists Bull.*, v. 55, no. 10, p. 1730-1740.
- Bucher, W. H., 1952, Geologic structure and orogenic history of Venezuela: *Geol. Soc. America Mem.* 49, 113 p.
- Bunce, E. T., J. D. Phillips, R. L. Chase, and C. O. Bowin, 1970, Lesser Antilles Arc and the eastern margin of the Caribbean Sea: *Woods Hole Oceanog. Inst. Contrib.* 2288, 36 p.; in press, in A. E. Maxwell, ed., *The sea*, v. 4: New York, Wiley-Interscience.
- Bush, S. A., and P. A. Bush, 1969, Isostatic gravity map of the eastern Caribbean region: *Gulf Coast Assoc. Geol. Soc. Trans.*, v. 19, p. 281-285.
- Edgar, N. T., 1968, Seismic refraction and reflection in the Caribbean Sea: Ph.D. dissert., Columbia Univ., 163 p.
- Ewing, J. I., C. B. Officer, H. R. Johnson, and R. S. Edwards, 1957, Geophysical investigations in the eastern Caribbean—Trinidad shelf, Tobago trough, Barbados ridge, Atlantic Ocean: *Geol. Soc. America Bull.*, v. 68, p. 897-912.
- , J. W. Antoine, and W. M. Ewing, 1960, Geophysical measurements in the western Caribbean Sea and in the Gulf of Mexico: *Jour. Geophys. Research*, v. 65, p. 4087-4126.
- , N. T. Edgar, and J. W. Antoine, in press, Gulf of Mexico and Caribbean Sea, in A. E. Maxwell, ed., *The sea*, v. 4: New York, Wiley-Interscience.
- Ewing, W. M., J. L. Worzel, and G. L. Shurbet, 1957, Gravity observations at sea in U.S. submarines *Baracuda*, *Tusk*, *Conger*, *Argonaut* and *Medregal*: *Koninkl. Nederlandsch Geol.-Mijn. Genoot. Verh.*, *Geol. Ser.*, v. 18, p. 49-115.
- Gonzalez de Juana, C., N. G. Muñoz J., and M. Vignali C., 1968, On the geology of eastern Paria (Venezuela): 4th Caribbean Geol. Conf. Trans. p. 25-29.
- Isacks, B., J. Oliver, and L. R. Sykes, 1968, Seismology and the new global tectonics: *Jour. Geophys. Research*, v. 73, p. 5855-5899.
- Koldewijn, B. W., 1958, Sediments of the Paria-Trinidad shelf; v. 3 of Reports of the Orinoco Shelf expedition: The Hague, Mouton and Co., 109 p.
- Maloney, N. J., 1967, Geomorphology of the continental margin of Venezuela, Pt. 2, Continental terrace off Carupano: *Bol. Inst. Ocean., Univ. Oriente (Cumaná, Venezuela)*, v. 6, p. 147-155.
- Maxwell, J. C., and Gabriel Dengo, 1951, Carupano area and its relation to the tectonics of northeastern Venezuela: *Am. Geophys. Union Trans.*, v. 32, no. 2, p. 259-267.
- Officer, C. B., J. I. Ewing, J. F. Hennion, D. G. Harkrider, and D. E. Miller, 1959, Geophysical investigations in the eastern Caribbean: Summary of 1955 and 1956 cruises, in L. H. Ahrens *et al.*, eds., *Physics and chemistry of the earth*, v. 3: New York, Pergamon Press, p. 17-109.
- Weeks, L. A., R. K. Lattimore, R. N. Harbison, B. G. Bassinger, and G. F. Merrill, 1971, Structural relations among Lesser Antilles, Venezuela, and Trinidad-Tobago: *Am. Assoc. Petroleum Geologists Bull.*, v. 55, no. 10, p. 1741-1752.

Deformation of the Sea Floor off the North-west Coast of the United States

GEORGE PETER & OMAR E. DeWALD

NOAA, Atlantic Oceanographic and Meteorological Laboratories, Miami, Florida 33130

A new fracture zone separating the Tufts Abyssal Plain from the mountainous topography of the Explorer and Juan de Fuca ridges has been discovered on the basis of the magnetic anomaly offsets. North-east-south-west compression is the likely cause for the rotation, strike-slip faulting, and deformation of the small crustal blocks of the area.

THIRTEEN east-west tracklines run by NOAA ships during the past few years off the coasts of Oregon and Washington enabled us to identify the magnetic anomaly lineations and to establish their offset pattern west of the Juan de Fuca and Gorda ridges. The magnetic lineation pattern obtained (Fig. 1) reveals a new NW-SE trending fault zone which cuts the magnetic anomalies west of the Juan de Fuca Ridge, and explains the abrupt drop of the sea floor and the disappearance of the rough topography associated with the Juan de Fuca Ridge west of the proposed fault (Fig. 2). The establishment of the anomaly pattern from the Juan de Fuca Ridge to anomaly 7 (ref. 1) closes the gap that existed between the well known pattern near the coast and in the central north-east Pacific^{2,3}.

It is usually considered that magnetic anomaly lineations

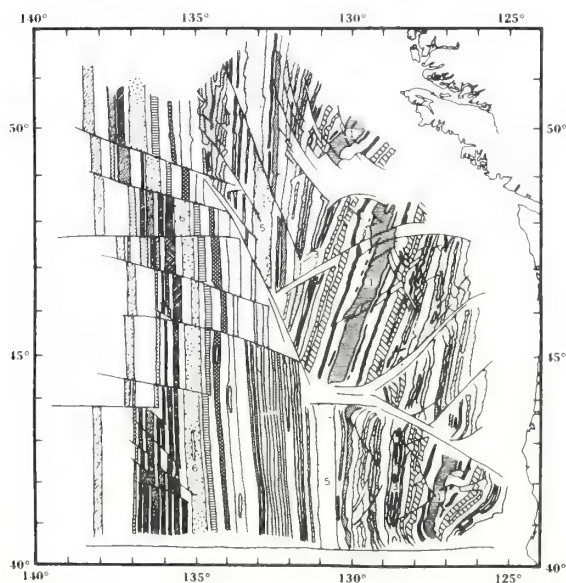


Fig. 1 Map of the sea floor magnetic anomaly lineations off the coasts of Washington and Oregon. Zip patterns demonstrate the correlation of the magnetic anomalies across the various fault offsets. Numbers (1) refer to key magnetic anomalies. Number 1 (from north to south) is associated with the centre parts of the Explorer, Juan de Fuca, and Gorda ridges.

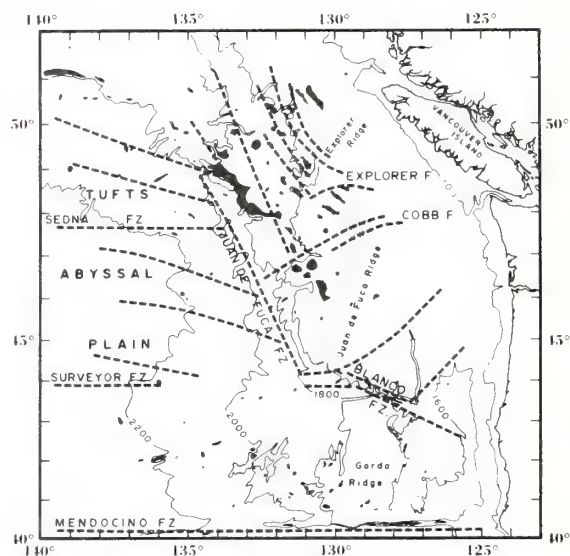


Fig. 2 Map of the magnetic anomaly offsets (dashed lines) superimposed on a sketch of the bathymetry of the sea floor west of Washington and Oregon. Zip patterns show the idealized crestal areas of the mid-oceanic ridge segments; dark patches show the major seamounts. The shelf edge is depicted by the 100 fathom isobath (1 fathom=1.83 m). For clarity, contour lines (200 fathom contour intervals) are shown only in depths greater than 1,600 fathoms. Bathymetry is after Chase *et al.*¹⁴. The new names, Juan de Fuca, Explorer, and Cobb fault zones, were approved by the Board on Geographic Names.

originate from the upper, basaltic part of the oceanic crust and represent strips of rocks which were formed at the centre of mid-oceanic ridges under the influence of the periodically reversing magnetic field of the Earth⁴. As the oceanic crust is younger and has a much simpler tectonic history than the continental crust⁵, the magnetic lineations acquired by the oceanic crust at the time of its genesis have been preserved through geologic time. Magnetic anomaly maps, therefore, show the offsets of former mid-oceanic ridges and the offsets or deformation pattern of the oceanic crust acquired after its formation.

The Juan de Fuca and Gorda ridges represent short segments of a former mid-oceanic ridge⁶ which in large part has been obliterated as it migrated eastward and collided with the North American continent^{1,7}. The origin of the two ridges and the reason for their north-easterly trend have long been a matter of controversy. Various authors have discussed whether the ridges separated and tilted north-east in adjustment to a change in the direction of sea floor spreading^{7,8}, or whether they became offset and rotated as a result of a strike-slip faulting⁹. We believe that the new data (Fig. 3) suggest a solution to this problem.

The magnetic anomaly offset pattern (Fig. 1) follows the interpretation of Pavoni¹⁰ and Peter and Lattimore⁹, and is based on the magnetic anomaly map of Mason and Raff²

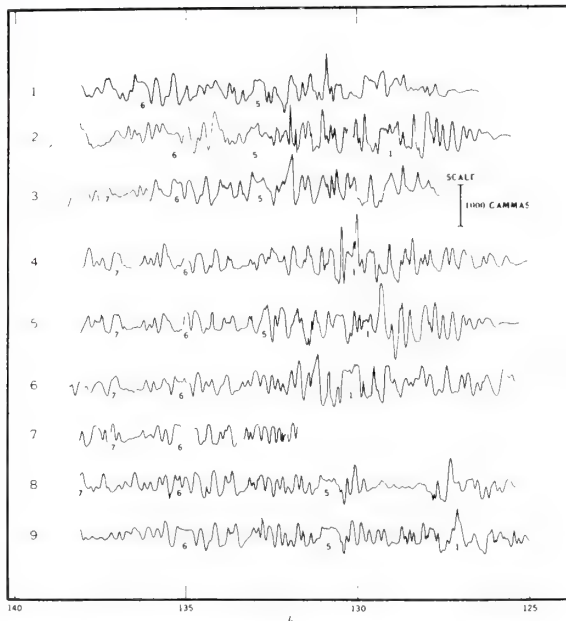
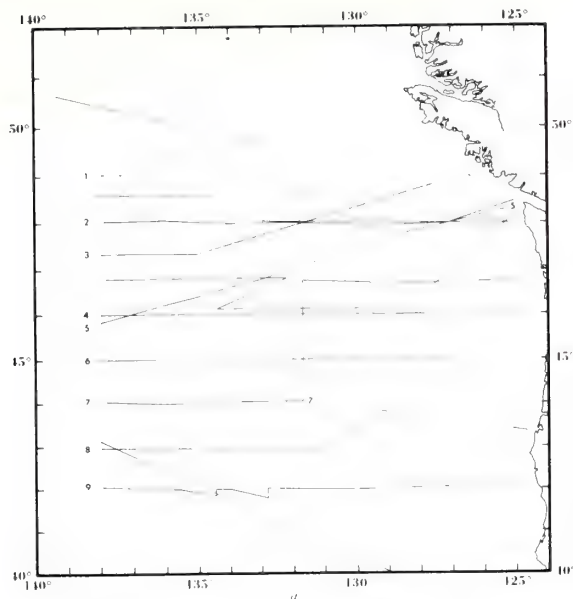


Fig. 3 a, Tracklines used for the westward extension of former magnetic anomaly maps. b, Selected east-west magnetic anomaly profiles showing identification and correlation of the magnetic anomalies. The location of the profiles is shown in a.

south of the Blanco fracture zone, east of the Juan de Fuca Ridge, and east of 134° W in the area north of 48° N. In the remaining part of Fig. 1 the magnetic lineations were established on the basis of east-west tracklines which, with the exception of a few cross lines, extend approximately along each degree latitude. A more detailed survey, therefore, may show this area structurally more complex than indicated by this figure.

The new magnetic anomaly data show that anomaly 6 has only minor offsets south of the Sedna fracture zone. The Surveyor fracture zone ends directly west of anomaly 6, and the Blanco fracture zone terminates at the southern tip of the Juan de Fuca Ridge. The magnetic anomaly pattern is continuous west of the Gorda Ridge, but anomaly 5 and a number of anomalies between 5 and 6 are missing west of the Juan de Fuca Ridge. The disappearance of the anomalies occurs along a north-west line which correlates with a sharp 300 fathom (550 m) change in the relief of the sea floor (Fig. 2). To the west of this line lies the Tufts Abyssal Plain with a gentle topographic gradient rising eastward; to the east lies the mountainous topography of the Juan de Fuca Ridge. We suggest that this demarcation line trending north-west separating the magnetic lineations and cutting the topography of the Juan de Fuca Ridge at an oblique angle represents a fracture zone, and we named it the Juan de Fuca fracture zone.

The origin of the Juan de Fuca fracture zone is most likely related to the Late Tertiary deformation¹¹ that affected this entire area. It appears in light of the new data that if the Explorer, Juan de Fuca, and Gorda ridges were continuous at the time of the formation of anomaly 5, approximately 10 m.y. ago³, then they must have been in alignment with the segment of anomaly 5 located west of the Gorda Ridge, where the anomaly sequence is uninterrupted. The missing anomalies and the well defined fault-border of the crustal fragments indicate that the deformation involved the rotation, strike-slip faulting, and overthrust of small crustal plates north of the Blanco and Juan de Fuca fault zones, rather than a gradual realignment of the ridges under the influence of a change in the direction of the sea floor spreading. If the magnetic anomalies that were offset by strike-slip faults east of the Juan de Fuca Ridge are aligned, a north-south crustal shortening of 120 km is indicated. The offset of anomaly 5 and the missing anomalies suggest a 200 km westerly displacement and consequent destruction of the crust

along the Juan de Fuca and Blanco fracture zones. Part of the north-south compression has been transmitted to the area of the Gorda Ridge, where the deformation of anomaly 3 near the coastline indicates a north-south compression of 150 km.

North-south compression indicated by the deformation pattern of the magnetic anomalies is in agreement with the relative plate motions derived for the area east of the Juan de Fuca and Gorda ridges^{7,12}. The scatter of earthquakes¹³ east of the Gorda Ridge also supports the proposed compression of that area, but to the north the distribution of the earthquakes indicates that at the present time the deformation is concentrated along the Explorer and Blanco fault zones. A more detailed discussion of the plate motions of the area will be presented in another article now in preparation.

We thank B. H. Erickson, NOAA, Pacific Oceanographic Laboratories, for providing most of the magnetic anomaly profiles.

Received July 20, 1971.

- ¹ Pitman, W. C., III, Herron, E. M., and Heirtzler, J. R., *J. Geophys. Res.*, **73**, 2069 (1968).
- ² Raff, A. D., and Mason, R. G., *Bull. Geol. Soc. Amer.*, **72**, 1267 (1961); Mason, R. G., and Raff, A. D., *Bull. Geol. Soc. Amer.*, **72**, 1259 (1961).
- ³ Pitman, W. C., III, and Hayes, D. E., *J. Geophys. Res.*, **73**, 6571 (1968).
- ⁴ Vine, F. J., and Matthews, D. H., *Nature*, **199**, 947 (1963); Vine, F. J., *Science*, **154**, 1405 (1966); Cox, A., Doell, R. R., and Dalrymple, G. B., *Science*, **144**, 1537 (1964).
- ⁵ Hess, H. H., in *Submarine Geology and Geophysics* (vol. 17, *Colston papers*) (edit. by Whittard, W. F., and Bradshaw, R.), 317 (Butterworths, London, 1965); Dietz, R. S., *Amer. J. Sci.*, **264**, 177 (1966).
- ⁶ Wilson, J. T., *Science*, **150**, 482 (1965); Menard, H. W., *Marine Geology of the Pacific*, 271 (McGraw-Hill, New York, 1964).
- ⁷ Atwater, T., *Bull. Geol. Soc. Amer.*, **81**, 3513 (1970).
- ⁸ Menard, H. W., and Atwater, T., *Nature*, **219**, 463 (1968); *ibid.*, **222**, 1037 (1969).
- ⁹ Peter, G., and Lattimore, R., *J. Geophys. Res.*, **74**, 586 (1969).
- ¹⁰ Pavoni, N., *Pure Appl. Geophys.*, **63**, 172 (1966).
- ¹¹ McManus, D. A., *Marine Geol.*, **3**, 429 (1965); Wise, D. V., *Bull. Geol. Soc. Amer.*, **74**, 357 (1963).
- ¹² Silver, E. A., *Science*, **166**, 1265 (1969).
- ¹³ Tobin, D. G., and Sykes, L. R., *J. Geophys. Res.*, **73**, 3821 (1968).
- ¹⁴ Chase, T. E., Menard, H. W., and Mammerickx, J., *The Institute of Marine Resources* (University of California, 1970).

5. MAGNETIC STRUCTURE OF THE ALEUTIAN TRENCH AND NORTHEAST PACIFIC BASIN

(June 1968)

GEORGE PETER, BARRETT H. ERICKSON, AND PAUL J. GRIM

1. Introduction

The large number of detailed magnetic surveys and exploratory tracklines made during the last decade have contributed significantly to the development of new ideas and to the understanding of the structure and evolution of the oceanic crust. Particularly significant among the methods of study of crustal structure was the Scripps Institution of Oceanography—U.S. Coast and Geodetic Survey magnetic-bathymetric survey project off the west coast of the United States (Mason, 1958; Mason and Raff, 1961; Vacquier et al., 1961; Raff and Mason, 1961). It was found that the magnetic anomalies in this area form parallel, north-south trending lineations which are frequently offset as if by lateral faults. Offsets of the magnetic lineations were found to be associated with fracture zones such as the Mendocino; investigation of other offsets led to the discovery of other major fracture zones with well-developed topographic expression. Like the magnetic lineations themselves, the minor offsets appear to lack topographic or even sub-bottom expression; these features, however, generally are considered to reflect internal structure of the oceanic crust or upper mantle. The pattern of the magnetic anomaly lineations therefore can be called the magnetic structure.

Throughout the world, similar magnetic-anomaly lineations have been found to be disposed symmetrically along either side of the axis of the mid-oceanic rises (Vine, 1966; Pitman et al., 1968; Dickson et al., 1968; Le Pichon and Heirtzler, 1968; Heirtzler et al., 1968). The axial symmetry of these magnetic-anomaly lineations and their correlation (within a central crestal zone) with dated magnetic-polarity reversals on land and with the magnetic reversals found in deep-sea cores have given strong support to the hypothesis of crustal evolution through sea-floor spreading (Dietz, 1961; Hess, 1962; Vine and Matthews, 1963; Heirtzler et al., 1966; Ninkovich et al., 1966; Vine, 1966; Cox et al., 1964; Opdyke et al., 1966; Dickson and Foster, 1966).

Detailed studies by McManus (1965), Loncarevic et al. (1966), van Andel et al. (1967), and van Andel and Bowin (1968) have provided insight into the hitherto unknown, complex geology of the crests of the mid-oceanic rises. Although this new information does not directly contradict the hypothesis of sea-floor spreading, it has raised serious questions as to its applicability. Important limitations can be placed on the mechanism of sea-floor spreading by the Y-shaped ridge-junction discovered near the Galapagos Islands (Herron and Heirtzler, 1967; Raff, 1968), by the sediment distribution over mid-oceanic ridges (Ewing and Ewing, 1967), and by the undisturbed sediments in "transform fault" zones and trenches (Ludwig et al., 1966; van Andel et al., 1967; Scholl et al., 1968).

The purpose of this paper is to describe the magnetic structure of the Northeast Pacific and the Aleutian Arc, and to discuss the questions that can be raised in regard to the application of the sea-floor spreading hypothesis within this area. All available data from the Northeast Pacific have been compiled. Magnetic and bathymetric maps for the central Northeast Pacific and the Aleutian Arc that have significant bearing on the discussion are presented, and their implications in regard to crustal genesis are discussed in some detail.

The specific areas under consideration (Fig. 1) represent part of the total systematic coverage under ESSA—Coast and Geodetic Survey project SEAMAP (Peter and Stewart, 1965; Peter, 1965; Elvers et al., 1967). Tracks for these surveys comprise a grid of north-south lines approximately spaced at 18 km intervals; irregularly spaced cross-lines were run as checks. Magnetic and bathymetric data were collected with a Varian proton-precession magnetometer and a Precision Depth Recorder, respectively. Accuracies of these measurements are discussed in Peter et al. (1965) and Elvers et al. (1967).

Primary control of the survey was obtained from LORAN-C. Lines run relatively close to the LORAN-C net provided positions along the tracklines with an estimated accuracy of ± 1 km. The uncertainty in position increases to the south, although no obvious discrepancies were noted north of 38°N . Between $35^{\circ}30'\text{N}$ and 38°N , one trackline was rejected and three others were adjusted in a north-south direction by 5 km, based on systematic discrepancies of the magnetic and bathymetric values among adjacent tracklines.

The density of tracklines and the prominence of the lineations are adequate to show all essential details on the magnetic-anomaly contour maps. The trackline density and the contour interval selected are sufficient to delineate the major topographic features. The shortcomings of the 18-km grid, however, are clearly evident in areas of irregular topography or elongated, smaller seamounts and ridges.

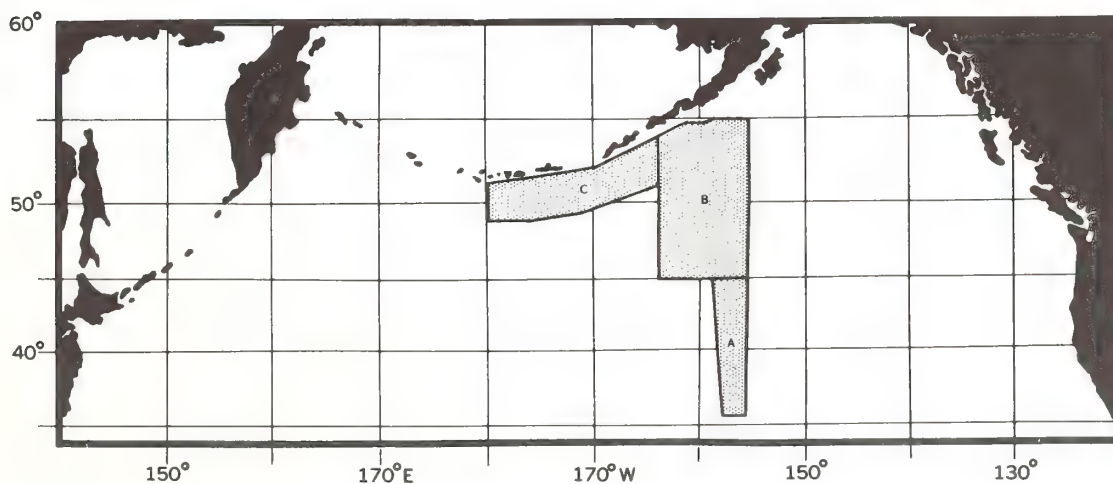


Fig. 1. Map of North Pacific Ocean: areas of detailed coverage shown in center (A, B, C).

5. MAGNETIC STRUCTURE OF THE ALEUTIAN TRENCH AND NORTHEAST PACIFIC BASIN

(June 1968)

GEORGE PETER, BARRETT H. ERICKSON, AND PAUL J. GRIM

1. Introduction

The large number of detailed magnetic surveys and exploratory tracklines made during the last decade have contributed significantly to the development of new ideas and to the understanding of the structure and evolution of the oceanic crust. Particularly significant among the methods of study of crustal structure was the Scripps Institution of Oceanography—U.S. Coast and Geodetic Survey magnetic-bathymetric survey project off the west coast of the United States (Mason, 1958; Mason and Raff, 1961; Vacquier et al., 1961; Raff and Mason, 1961). It was found that the magnetic anomalies in this area form parallel, north-south trending lineations which are frequently offset as if by lateral faults. Offsets of the magnetic lineations were found to be associated with fracture zones such as the Mendocino; investigation of other offsets led to the discovery of other major fracture zones with well-developed topographic expression. Like the magnetic lineations themselves, the minor offsets appear to lack topographic or even sub-bottom expression; these features, however, generally are considered to reflect internal structure of the oceanic crust or upper mantle. The pattern of the magnetic anomaly lineations therefore can be called the magnetic structure.

Throughout the world, similar magnetic-anomaly lineations have been found to be disposed symmetrically along either side of the axis of the mid-oceanic rises (Vine, 1966; Pitman et al., 1968; Dickson et al., 1968; Le Pichon and Heirtzler, 1968; Heirtzler et al., 1968). The axial symmetry of these magnetic-anomaly lineations and their correlation (within a central crestal zone) with dated magnetic-polarity reversals on land and with the magnetic reversals found in deep-sea cores have given strong support to the hypothesis of crustal evolution through sea-floor spreading (Dietz, 1961; Hess, 1962; Vine and Matthews, 1963; Heirtzler et al., 1966; Ninkovich et al., 1966; Vine, 1966; Cox et al., 1964; Opdyke et al., 1966; Dickson and Foster, 1966).

Detailed studies by McManus (1965), Loncarevic et al. (1966), van Andel et al. (1967), and van Andel and Bowin (1968) have provided insight into the hitherto unknown, complex geology of the crests of the mid-oceanic rises. Although this new information does not directly contradict the hypothesis of sea-floor spreading, it has raised serious questions as to its applicability. Important limitations can be placed on the mechanism of sea-floor spreading by the Y-shaped ridge-junction discovered near the Galapagos Islands (Herron and Heirtzler, 1967; Raff, 1968), by the sediment distribution over mid-oceanic ridges (Ewing and Ewing, 1967), and by the undisturbed sediments in "transform fault" zones and trenches (Ludwig et al., 1966; van Andel et al., 1967; Scholl et al., 1968).

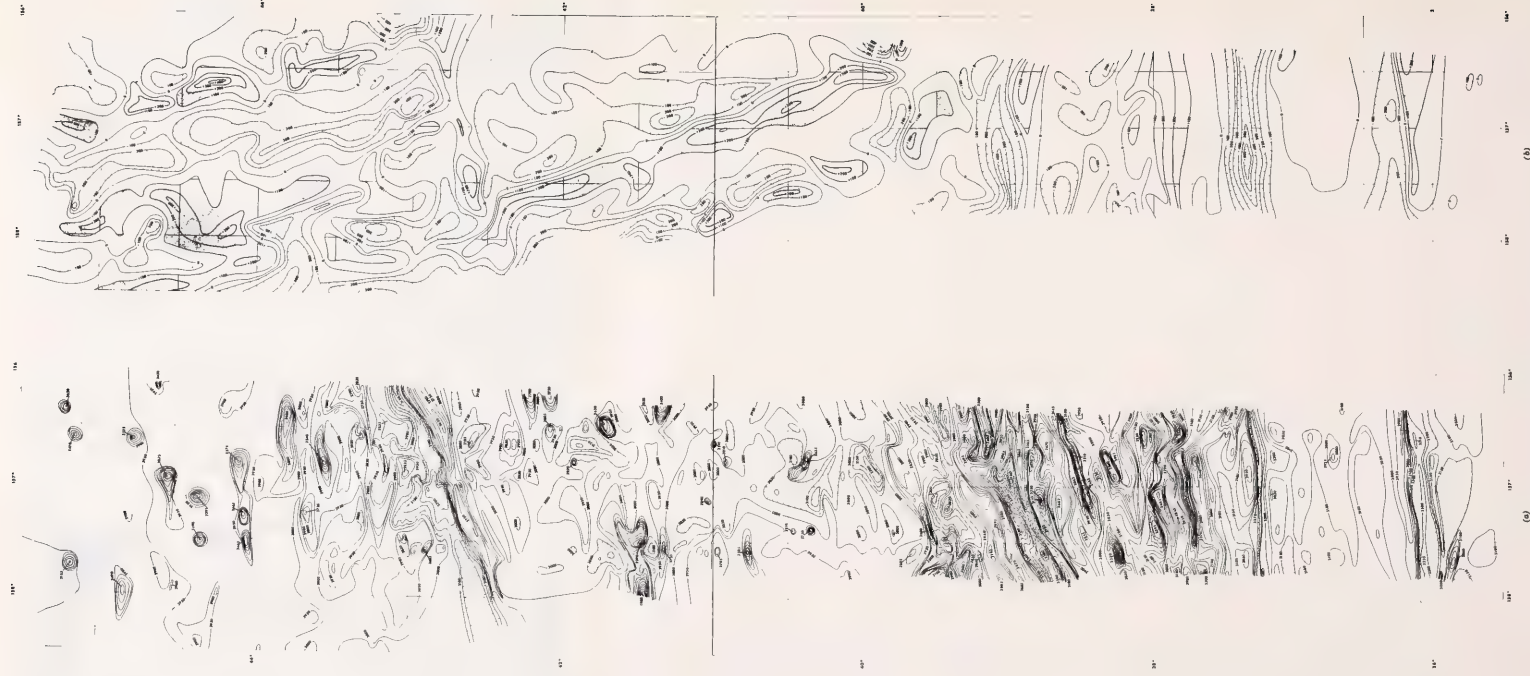


Fig. 2. (a) Bathymetric map of area A (Fig. 1). Contour interval 50 fms (1 fm = 1.83 m), except in areas of large gradients where the interval is increased. (b) Magnetic total intensity anomaly map of area A (Fig. 1). Contour interval is 100 gammas.



Fig. 2. (a) Bathymetric map of area A (Fig. 1). Contour interval 50 fms (1 fm = 1.83 m), except in areas of large gradients where the interval is increased. (b) Magnetic total intensity anomaly map of area A (Fig. 1). Contour interval is 100 gammas.

2. Central Northeast Pacific

A. Bathymetry

In area A (Figs. 1, 2a), there are three distinct bathymetric provinces separated by major fracture zones. South of the Mendocino Fracture Zone, the sea floor is comparatively smooth and has an average depth of 3100 fathoms (5670 m). This area falls under the classification of an abyssal-hill province (Hurley, 1960; Menard, 1964); there is a general east-west trend in the bottom topography which strongly contrasts with the irregular abyssal-hill topography north of the Mendocino Fracture Zone. Two east-west troughs with associated ridges on their northern side cut the ocean floor at $36^{\circ}10'N$ and $37^{\circ}20'N$. The troughs and ridges have a relief of approximately 300 fathoms (550 m). A third trough at $37^{\circ}45'N$ is bordered by ridges on both sides.

The Mendocino and Pioneer fracture zones cannot be separated. Complex elongated ridges and valleys with steep walls that resemble horsts and grabens extend from $38^{\circ}N$ to $39^{\circ}30'N$ within this zone (Fig. 3). The central

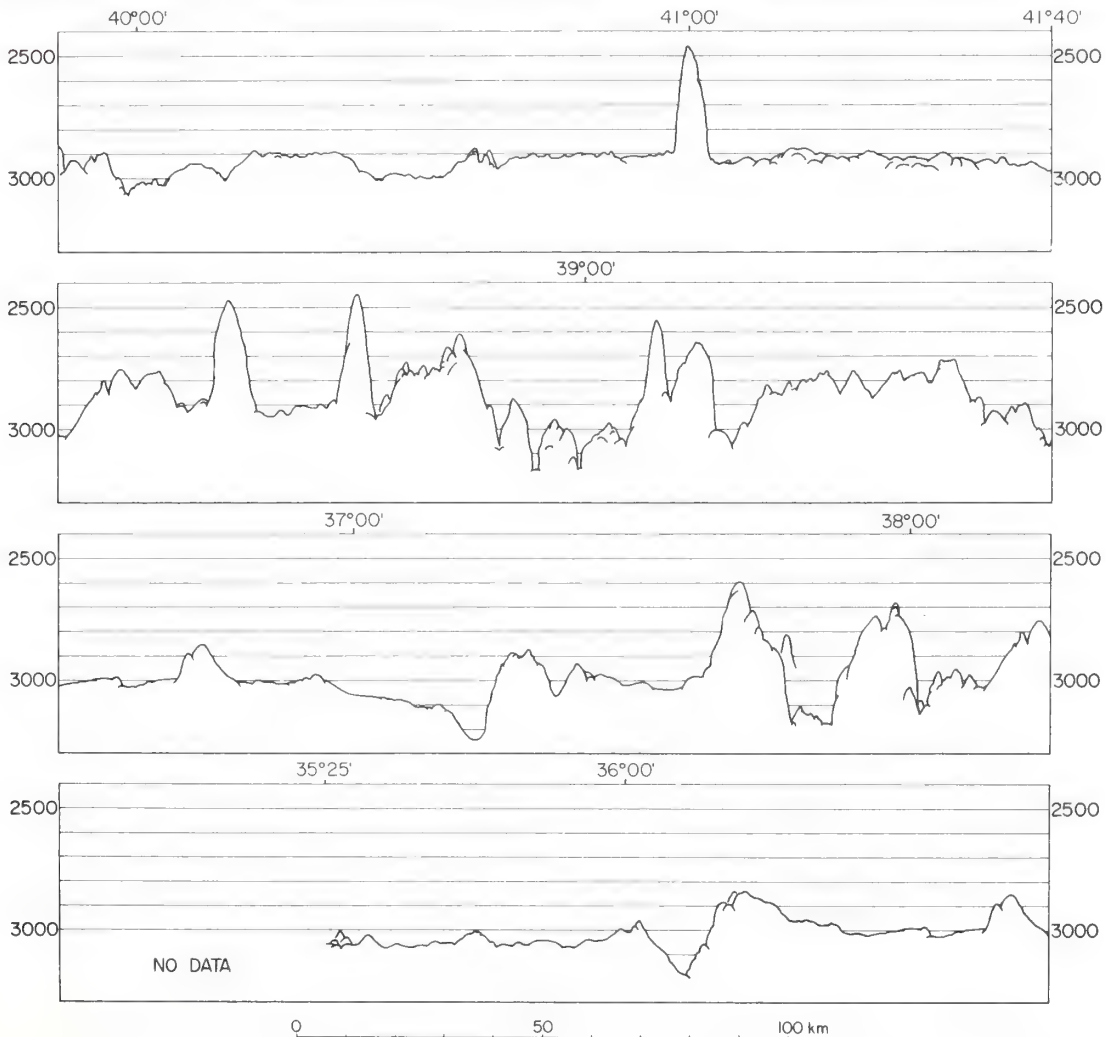


Fig. 3. PDR tracing of north-south trackline along $156^{\circ}40'W$. Depth is in fathoms (1 fm = 1.83 m).

valley of the Mendocino Fracture Zone (Menard, 1964) is the deepest part of the sea floor here. At the western end of Fig. 2a the greatest depth measured was 3525 fathoms (6450 m). In this area all the valleys and ridges of the Mendocino Fault Zone strike 070° .

Between the Mendocino and Surveyor fracture zones (Peter, 1966; Fig. 2a) the abyssal hills are more prominent and there are numerous small seamounts. The sea floor has an average depth of 3000 fathoms (5490 m); this is 100 fathoms (180 m) higher than the sea floor south of the Mendocino Fracture Zone, and 200 fathoms (360 m) lower than the base of the Mendocino ridges.

The Surveyor Fracture Zone has a strike parallel to the Mendocino Fracture Zone and is located at $42^{\circ}45'N$ (Fig. 2a). Topographically, it is a 350-fathom (650 m) high ridge, bounded on the northern side by a 200-fathom (360 m) deep trough. Elongated ridges and a generally irregular topography north of the trough appear to be related to the fracture zone. From this area northward to the Aleutian Trench the sea floor is smooth and rises gently to the north.

B. Magnetic Anomalies

The displacement of magnetic anomaly lineations (Mason, 1958; Vacquier et al., 1961) provides a method for the determination of the offsets along the submarine fracture zones. Peter (1966) previously discussed the offsets along the fracture zones of this area. Anomalies 27, 28, and 29 to the north of the Surveyor Fracture Zone and 25 and 26 to the south of it (labelled in Fig. 4) are identified from the spectrum of the world-wide magnetic-anomaly lineations (Pitman et al., 1968) in Fig. 2b. Although it has been found that east of this area the offsets of the magnetic-anomaly lineations and bottom topography generally agree in displacement (Menard, 1964), it has not been determined whether or not a particular type of bottom topography is characteristic of a specific group of magnetic lineations. It is generally agreed that there is no correlation between the individual magnetic-anomaly lineations and the bottom topography. Correlation is not found even between the magnetic data and the rugged topography of the second layer (Drake et al., 1963). Nevertheless these observations only stress the lack of direct, one-to-one correlation; Peter (1966) reported that the minor steplike elevation changes and broad (200–300 km) undulations in the sea-floor topography appear to line up with the strike of the magnetic-anomaly lineations.¹

In the area of the Surveyor Fracture Zone, the absence of correlation between the magnetic lineations and the sea-floor topography is well illustrated. Sounding and magnetic profiles suggest that this fracture zone forms a border between the smooth, south-southwest dipping, sea floor to the north and the generally horizontal, abyssal-hill province to the south. Yet the magnetic anomalies

¹ Recent studies by Talwani et al. (1968) in the area of the Reykjanes Ridge have shown that within a positive or negative magnetic anomaly lineation the variation of the amplitude of the anomaly is caused, in general, by changes of the bottom topography. Deep-tow magnetometer observations indicate correlation between trends of the magnetic anomalies and small-scale bottom irregularities (Spiess et al., 1968).



(offset by 300 km in a right lateral sense) cross this fracture zone and continue through the two entirely different bathymetric provinces without apparent change in character.

A detailed study of the Murray Fracture Zone indicates that there are elongated magnetic anomalies over the horst-graben pattern of the topography (Malahoff, 1968); in contrast to this, over this area of the Mendocino Fracture Zone magnetic anomalies are absent over even the sharpest ridges. There is a broad, magnetic low over the central part of the fracture zone, but it appears to strike east-west rather than to follow the strike of the topography.

South of the Mendocino Fracture Zone (Figs. 2a,b) the magnetic field is smooth (with the exception of three elongated anomalies over the troughs and ridges described earlier). The magnetic anomalies are strikingly different over each of these features. Over the northernmost feature a positive anomaly is present, over the central feature there is a prominent negative anomaly, and over the southernmost trough and ridge the anomaly consists of both negative and positive parts, disposed in accordance with induced magnetization in the northern hemisphere. None of the anomalies, however, is suggestive of induced magnetization due to the earth's present magnetic field. If simple vertical-sided bodies are assumed as sources, the direction of the dip of the magnetization vector, as judged by the model studies of Heirtzler et al. (1962), is different for each of these features.

3. Abyssal Plain and Trench Southwest of Kodiak

A. Bathymetry

The Aleutian Abyssal Plain (Hurley, 1960) lies between the Aleutian Trench and the Surveyor Fracture Zone (Figs. 1b, and 5). The sea floor is essentially flat, with a small southward dip of 2 m/km. A number of knolls and seamounts that vary in heights from a few hundred to over one thousand meters are distributed irregularly throughout the area. The general fabric of the sea-floor topography trends northeast-southwest in the southeastern part of Fig. 5, and northwest-southeast in the southwestern part. At 51°N weak east-west trends are observed; these give way to the northeast-southwest trends at the southern wall of the Aleutian Trench. There is no outer ridge associated with the Aleutian Trench in this area; only a small swell separates the abyssal plain and the trench.

Depths in the trench vary from 3000 fathoms (5480 m) on the east to 3800 fathoms (6960 m) on the west. Although the southern wall of the trench is relatively smooth, the northern wall is irregular with a few benches and welts which persist for great distances (Peter et al., 1965).

B. Magnetic Anomalies

In area A and most of area B (Fig. 1) the magnetic lineations generally strike N18°W. Between 47°N and 51°30'N these lineations progressively bend

(offset by 300 km in a right lateral sense) cross this fracture zone and continue through the two entirely different bathymetric provinces without apparent change in character.

A detailed study of the Murray Fracture Zone indicates that there are elongated magnetic anomalies over the horst-graben pattern of the topography (Malahoff, 1968); in contrast to this, over this area of the Mendocino Fracture Zone magnetic anomalies are absent over even the sharpest ridges. There is a broad, magnetic low over the central part of the fracture zone, but it appears to strike east-west rather than to follow the strike of the topography.

South of the Mendocino Fracture Zone (Figs. 2a,b) the magnetic field is smooth (with the exception of three elongated anomalies over the troughs and ridges described earlier). The magnetic anomalies are strikingly different over each of these features. Over the northernmost feature a positive anomaly is present, over the central feature there is a prominent negative anomaly, and over the southernmost trough and ridge the anomaly consists of both negative and positive parts, disposed in accordance with induced magnetization in the northern hemisphere. None of the anomalies, however, is suggestive of induced magnetization due to the earth's present magnetic field. If simple vertical-sided bodies are assumed as sources, the direction of the dip of the magnetization vector, as judged by the model studies of Heirtzler et al. (1962), is different for each of these features.

3. Abyssal Plain and Trench Southwest of Kodiak

A. Bathymetry

The Aleutian Abyssal Plain (Hurley, 1960) lies between the Aleutian Trench and the Surveyor Fracture Zone (Figs. 1b, and 5). The sea floor is essentially flat, with a small southward dip of 2 m/km. A number of knolls and seamounts that vary in heights from a few hundred to over one thousand meters are distributed irregularly throughout the area. The general fabric of the sea-floor topography trends northeast-southwest in the southeastern part of Fig. 5, and northwest-southeast in the southwestern part. At 51°N weak east-west trends are observed; these give way to the northeast-southwest trends at the southern wall of the Aleutian Trench. There is no outer ridge associated with the Aleutian Trench in this area; only a small swell separates the abyssal plain and the trench.

Depths in the trench vary from 3000 fathoms (5480 m) on the east to 3800 fathoms (6960 m) on the west. Although the southern wall of the trench is relatively smooth, the northern wall is irregular with a few benches and welts which persist for great distances (Peter et al., 1965).

B. Magnetic Anomalies

In area A and most of area B (Fig. 1) the magnetic lineations generally strike N18°W. Between 47°N and 51°30'N these lineations progressively bend

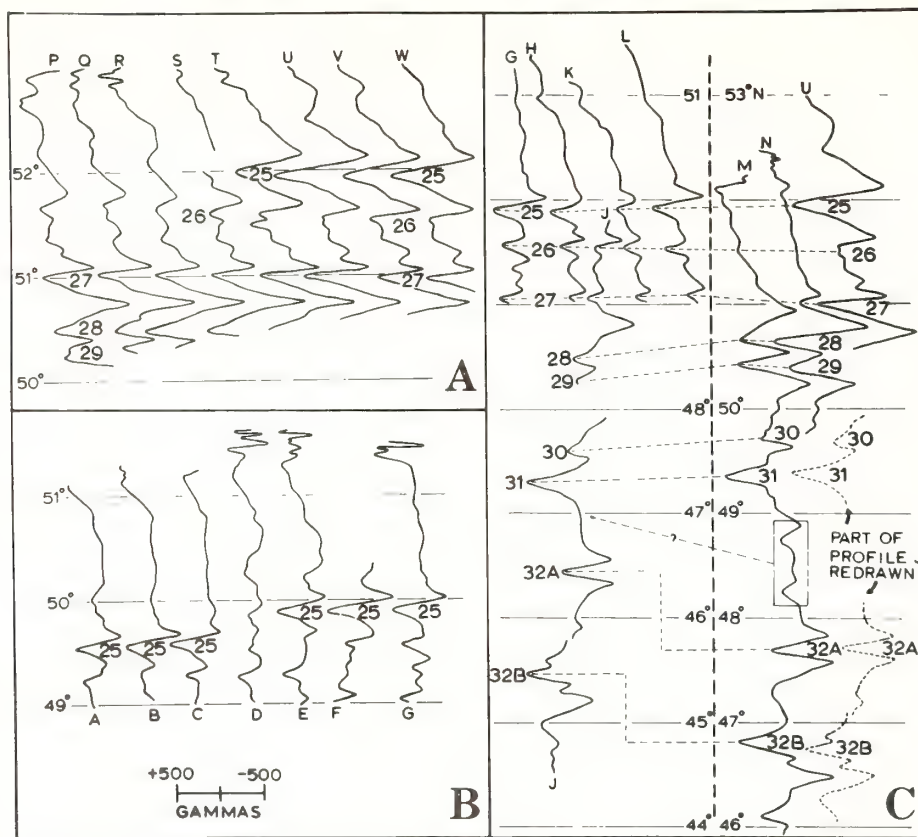


Fig. 6. Illustration of the offset of the magnetic-anomaly lineations across the Amlia and Adak fracture zones (location of profiles shown in Fig. 12) (from Grim and Erickson, 1969).

sharply westward, and their general strike becomes $N83^{\circ}W$ (Fig. 7). Anomaly 32B (see Fig. 4 for identification) bends first, at the south-west part of Fig. 7; anomaly 25 is the last lineation that clearly bends westward. The east-west lineation along $53^{\circ}30'N$ and the south-east limb that projects from it may be anomaly 24. The new strike represents an abrupt change in orientation of 65° for all these anomalies.

The control for the magnetic map is shown in Fig. 8, and discussed in detail by Elvers et al. (1967). To demonstrate the continuity of the anomalies around the bend, a number of north-south magnetic lines from this area are compared to east-west lines in Fig. 9. It is shown that along the profiles the character of the anomalies changes abruptly at the bend. The entire group of lineations is present on the westernmost profile (Fig. 9, profile 1).

One of the most pronounced differences between the east-west and north-south portions of the lineations is the higher amplitude of the anomalies along the east-west segments. Model studies (Heirtzler et al., 1962) indicate that the change in orientation of the lineations with respect to magnetic north (which changes approximately from 30 to 70° across the bend) is not sufficient to

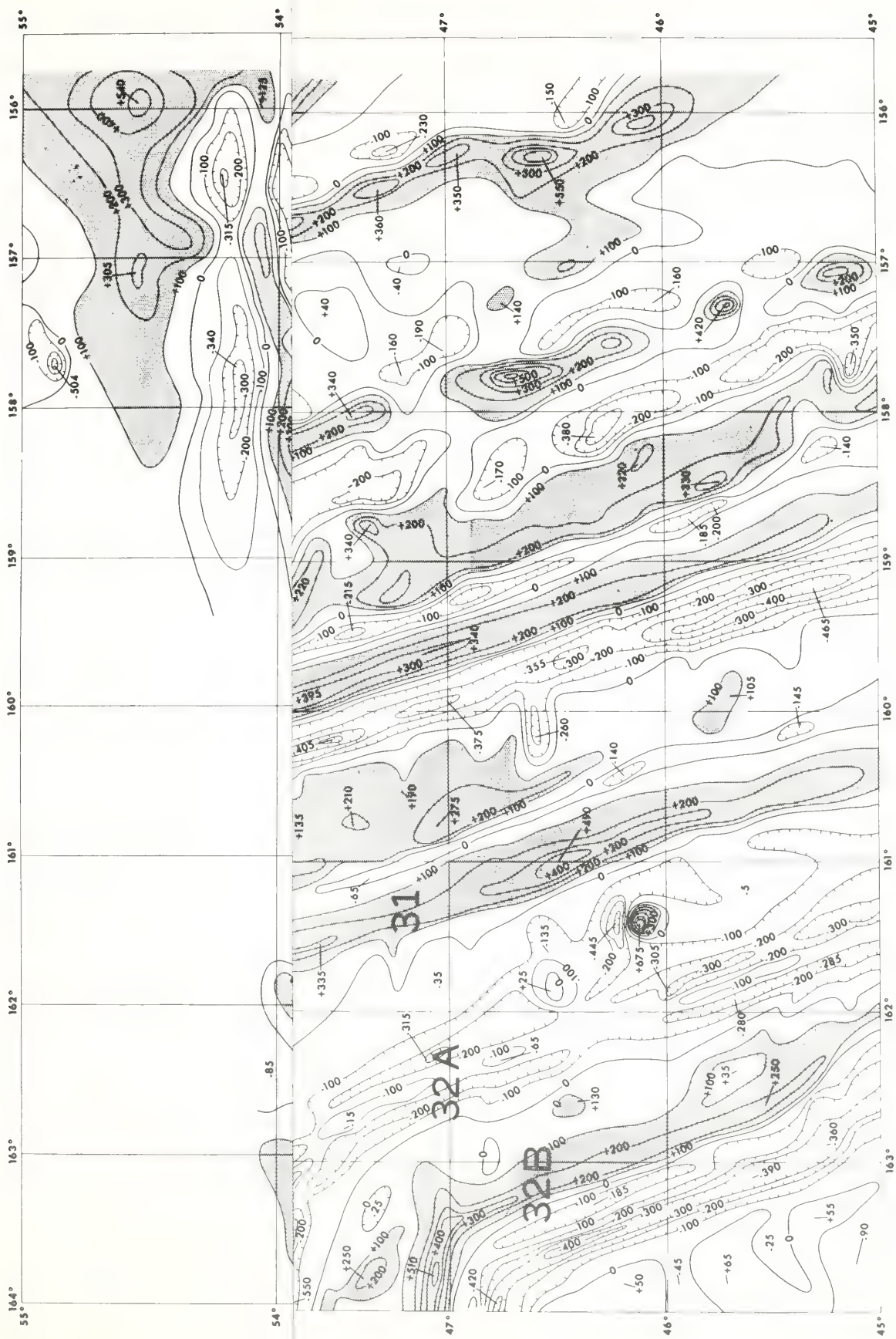


Fig. 7. Magnetic total intensity anomaly map of area B (Fig. 1). Contour interval is 100 gammas (from Elvers et al., 1967).

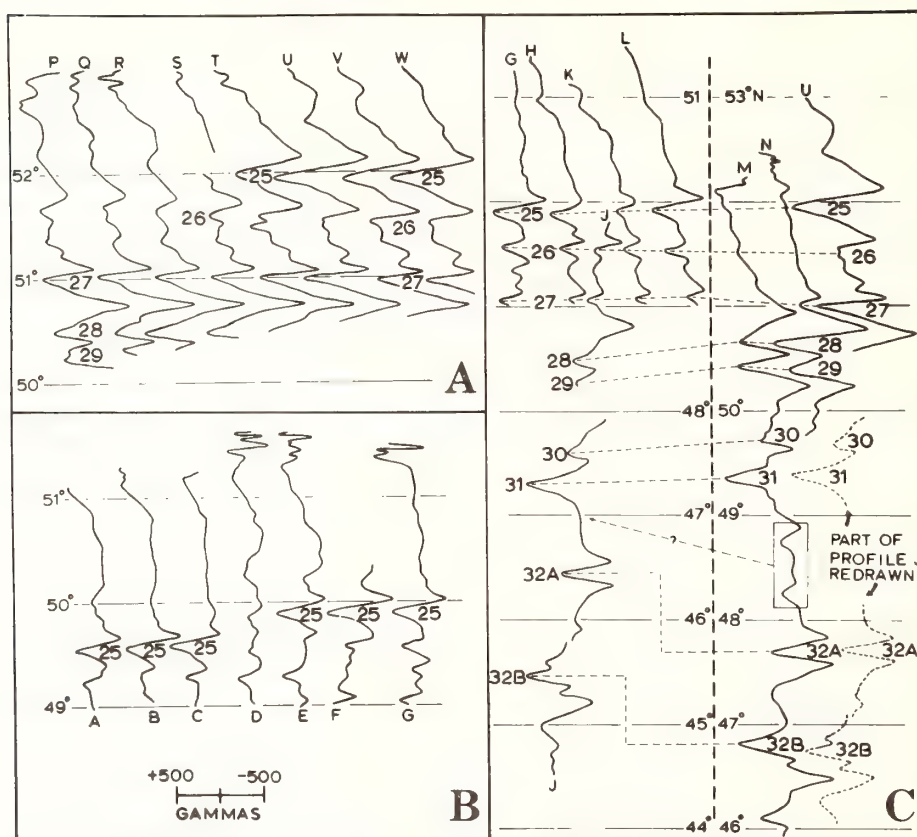


Fig. 6. Illustration of the offset of the magnetic-anomaly lineations across the Amlia and Adak fracture zones (location of profiles shown in Fig. 12) (from Grim and Erickson, 1969).

sharply westward, and their general strike becomes $N83^{\circ}W$ (Fig. 7). Anomaly 32B (see Fig. 4 for identification) bends first, at the south-west part of Fig. 7; anomaly 25 is the last lineation that clearly bends westward. The east-west lineation along $53^{\circ}30'N$ and the south-east limb that projects from it may be anomaly 24. The new strike represents an abrupt change in orientation of 65° for all these anomalies.

The control for the magnetic map is shown in Fig. 8, and discussed in detail by Elvers et al. (1967). To demonstrate the continuity of the anomalies around the bend, a number of north-south magnetic lines from this area are compared to east-west lines in Fig. 9. It is shown that along the profiles the character of the anomalies changes abruptly at the bend. The entire group of lineations is present on the westernmost profile (Fig. 9, profile 1).

One of the most pronounced differences between the east-west and north-south portions of the lineations is the higher amplitude of the anomalies along the east-west segments. Model studies (Heirtzler et al., 1962) indicate that the change in orientation of the lineations with respect to magnetic north (which changes approximately from 30 to 70° across the bend) is not sufficient to

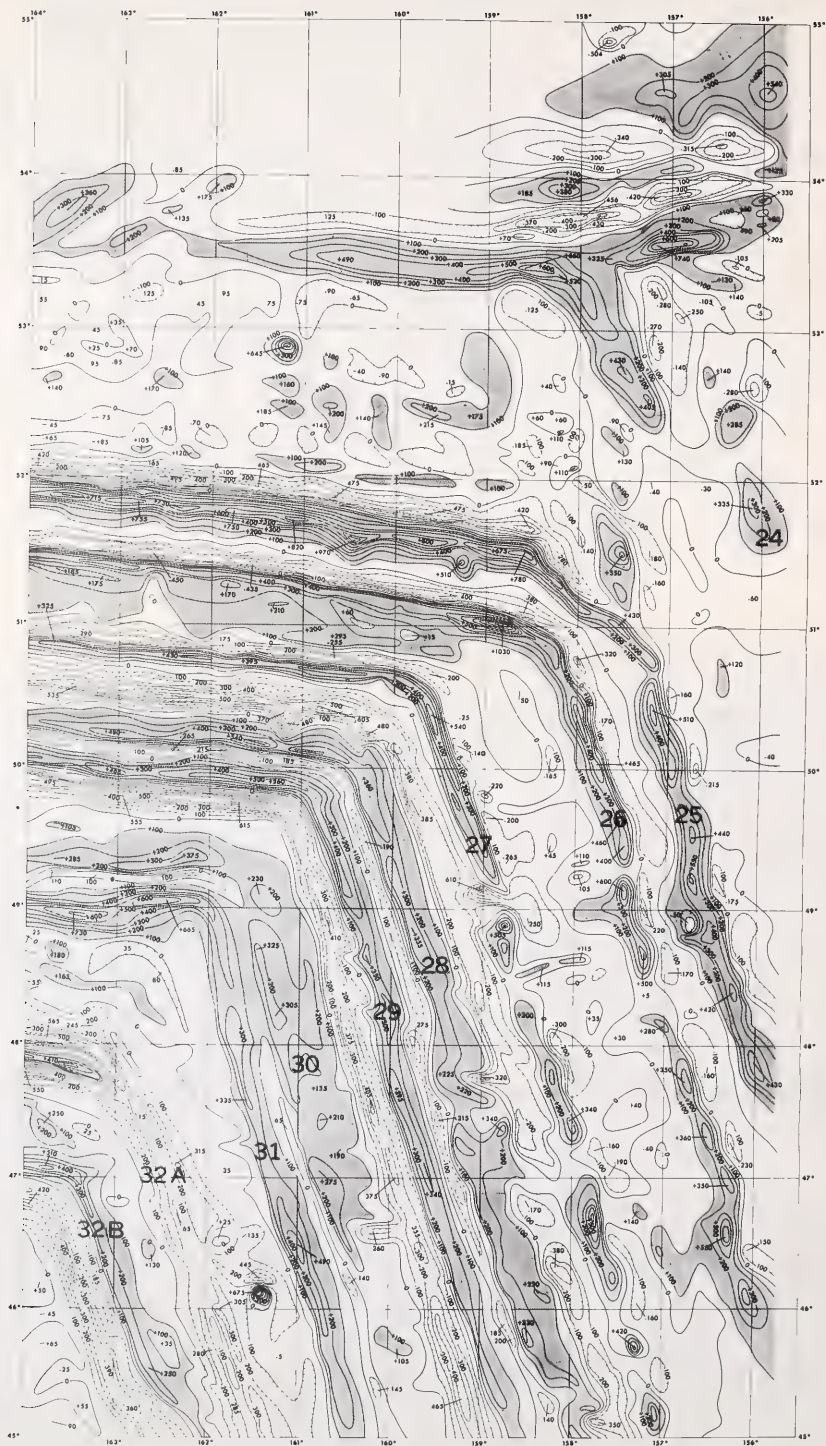


Fig. 7. Magnetic total intensity anomaly map of area B (Fig. 1). Contour interval is 100 gammas (from Elvers et al., 1967).

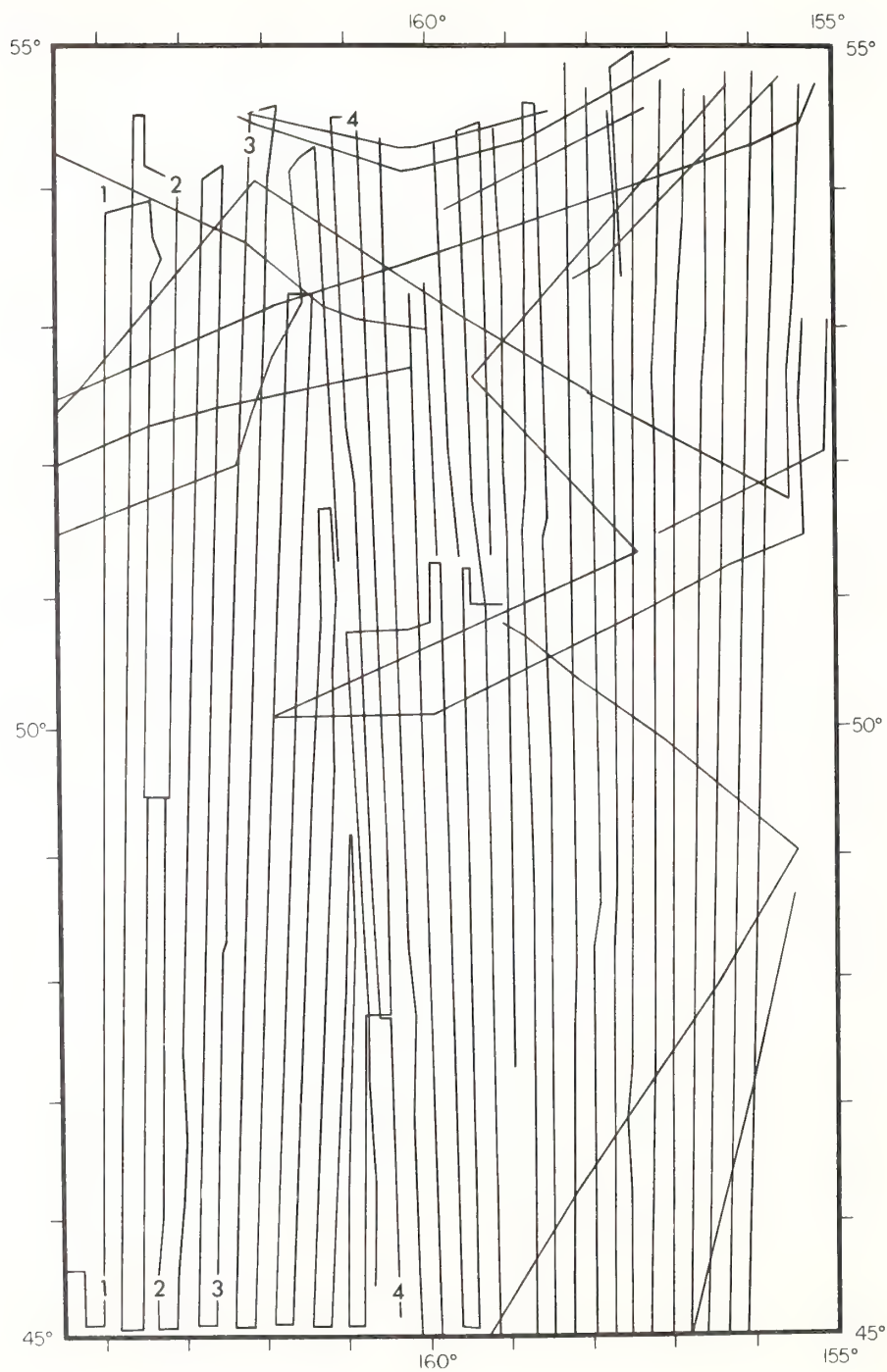


Fig. 8. Trackline chart of area B (Fig. 1). Small course changes are not shown (accuracy ± 3 km).

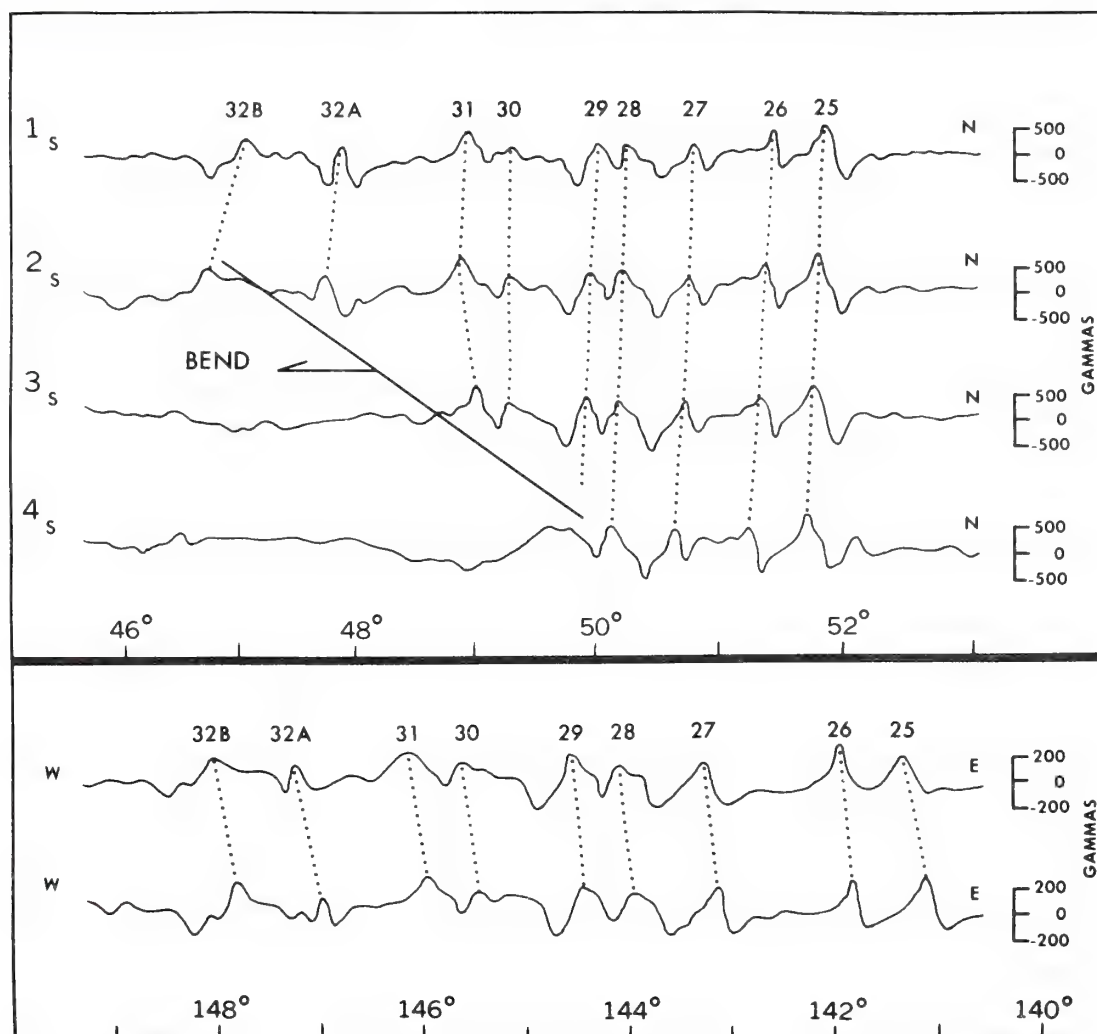


Fig. 9. Illustration of the westward bend of the magnetic-anomaly lineations. Selected north-south profiles (upper half) are compared to two east-west profiles (lower half) run along $35^{\circ}30'N$ and $36^{\circ}30'N$. Location of N-S profiles is shown in Fig. 8.

account for the increase in amplitude of the positive anomalies. The change in orientation in certain parts of the area would provide an adequate explanation for the change in amplitude of the negative lineations. In other parts, however, the change in amplitude is either greater or much less than that which would be expected from the model studies.

The decrease of distance between anomalies 26 and 27 after these lineations bend westward, is also quite prominent. By contrast, the distance between 31 and 32B increases considerably. The decreased distance between anomalies 26 and 27 seems to be at the expense of the broad, generally negative area directly east of 27; the extra distance between anomalies 31 and 32B apparently is taken up by two additional, small lineations (Fig. 6c).

A narrow, positive and negative lineation also is developed north of the east-west segment of anomaly 25. If the prominent east-west lineation along $53^{\circ}30'N$ is anomaly 24, the distance between 24 and 25 is greatly increased after the westward bend. Furthermore, if the northwest-southeast trending, positive anomaly at $52^{\circ}N$, $156^{\circ}W$, is part of anomaly 24, then there is an apparent break in this lineation at $52^{\circ}30'N$. A similar break of anomaly 32A is seen just before it bends westward. A more detailed survey would be necessary to adequately determine the smaller internal fractures and the discontinuities of these lineations.

4. Aleutian Trench and Outer Ridge ($164^{\circ}W$ to $180^{\circ}W$)

A. Bathymetry

Area C (Fig. 1) includes the Aleutian Trench and outer ridge. The weakly developed, east-west trending ridges on the outer swell southwest of Kodiak continue westward and their relief increases progressively. By $172^{\circ}W$ a typical outer ridge of moderate relief is present (Fig. 10).

At $172^{\circ}40'W$, a north-south depression cuts through the outer ridge. West of this depression there are a number of seamounts and the relief of the outer ridge is greater than it is to the east. The seamounts on the western side of this depression mark the location of the north-south trending Amlia Fracture Zone (Grim and Erickson, 1969; Hayes and Heirtzler, 1968). No indication of this fracture zone is seen in the trench; however, the change in trend of the Aleutian Arc may be related to it.

Another depression, with a less pronounced relief and a somewhat irregular shape, crosses the southern part of the outer ridge at $177^{\circ}20'W$. This depression marks the general location of the Adak Fracture Zone (Grim and Erickson, 1969). There is no appreciable difference in the topography of the outer ridge on opposite sides of this fracture zone, nor is there any evidence of a fracture zone on the trench floor. The offset of the depression between the Aleutian Terrace and the Aleutian Arc (Nichols and Perry, 1966), however, may be related to this feature. This offset—approximately 30 km—appears to be expressed as a reduction of the width of the Aleutian Terrace.

Adak Canyon to the north is approximately in line with the Adak Fracture Zone, and is probably another expression of it. The canyon separates strikingly different topography on either side. A generally smooth shelf on the east changes to chaotic topography, riddled with numerous smaller canyons, on the west. The eastern wall of Adak Canyon trends north-south; it is quite steep and has the appearance of a fault scarp.

B. Magnetic data

Westward extension of the magnetic anomaly lineations is shown in Fig. 11. Correlation of the magnetic lineations across the Amlia and Adak fracture zones is demonstrated in Fig. 6 (location of profiles is shown in Fig. 12).

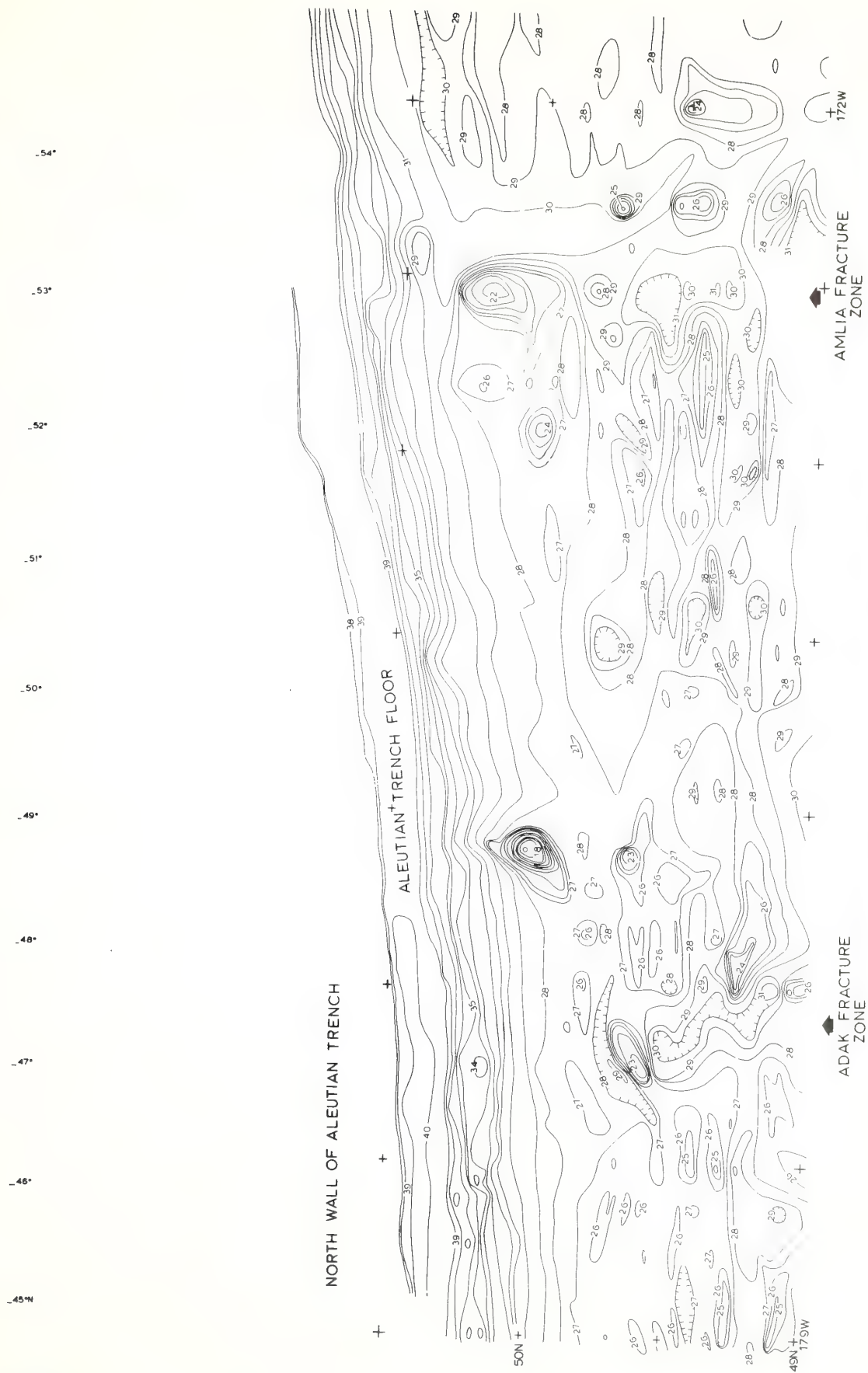
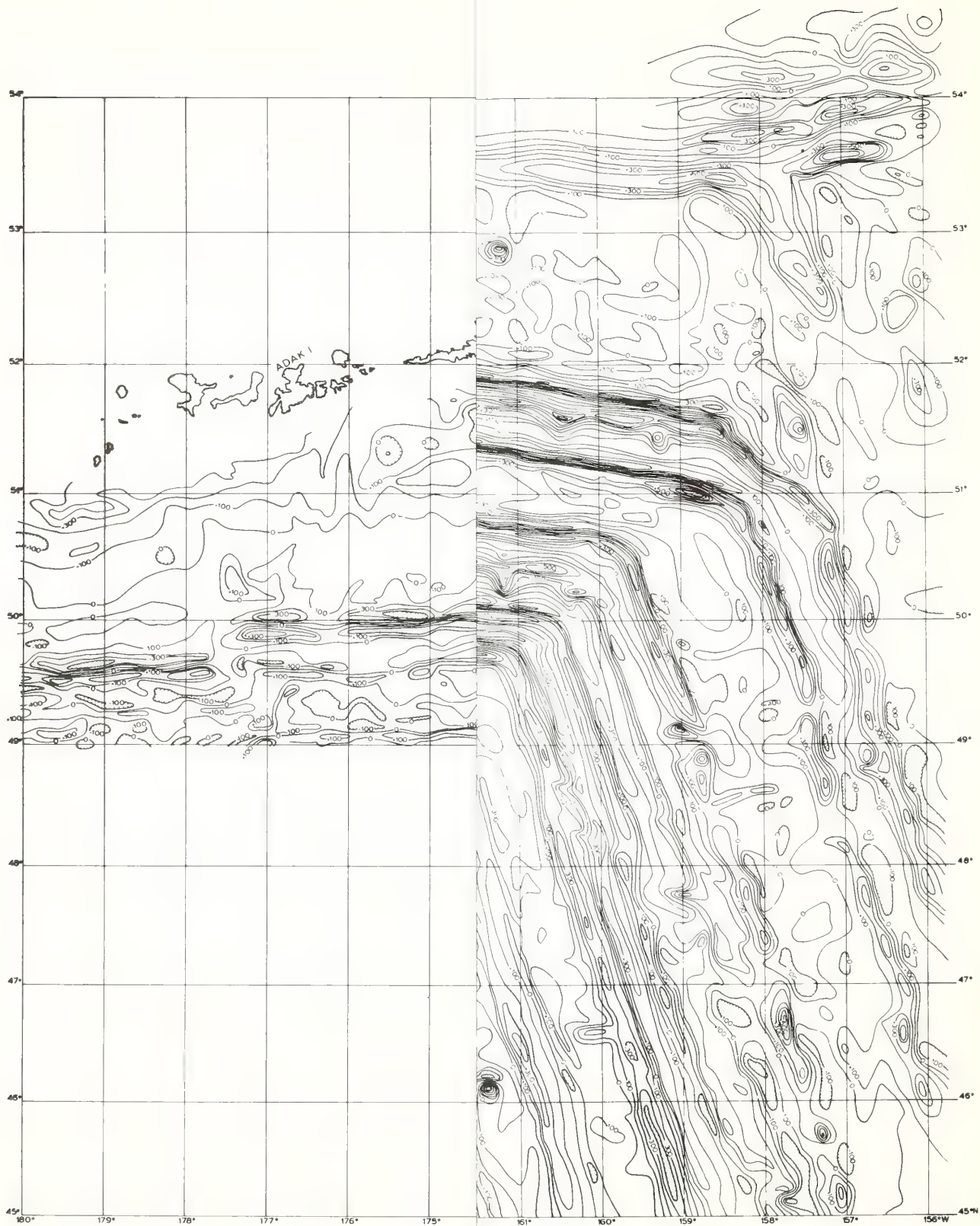


Fig. 10. Bathymetric map covering part of area C (Fig. 1). Contour labels in 100-fms (1 fm = 1.83 m); contour interval, 100 fms.



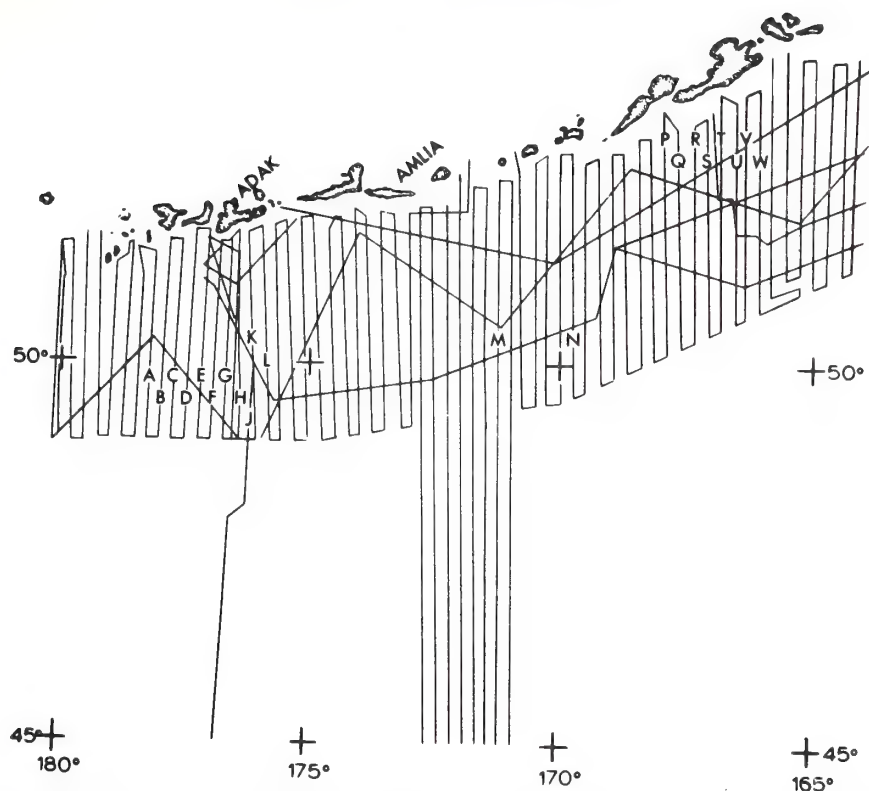


Fig. 12. Trackline chart of area C (Fig. 1) (after Grim and Erickson, 1969).

The anomalies terminate abruptly at the axis of the trench; traces of anomalies 24, 25, and 26, however, appear to cross the trench and extend over the Aleutian Terrace (Fig. 6a, profiles P, Q, and R). The east-west trend of the isogamma lines north of the trench between the Amlia and Adak fracture zones may also represent vestiges of the east-west magnetic lineations.

Generally, the magnetic field is smooth over the trench, but short-wavelength anomalies are found in shallow water near the islands where the tracklines cross the top of the Aleutian Ridge. Hayes and Heirtzler (1968) report that no traces of the lineations can be found in the Bering Sea north of the Aleutian Islands.

The location of the Amlia and Adak fracture zones was determined by the offset of magnetic lineations. The Amlia Fracture Zone offsets most lineations in a left-lateral sense by 230 km. The offset of anomalies 32A and 32B is only 140 km. The difference in offset is the result of two small anomalies (Fig. 6c, box) that are developed between anomalies 31 and 32A east of the Amlia Fracture Zone.

Anomalies 25 and 26 are not seen on profiles N and M (Fig. 6c); they seem to disappear where they cross the axis of the Aleutian Trench. Similarly, anomalies 27 and 28 disappear in the trench east of the Amlia Fracture Zone. Anomalies 29 through 32B do not cross the trench. These anomalies have the same

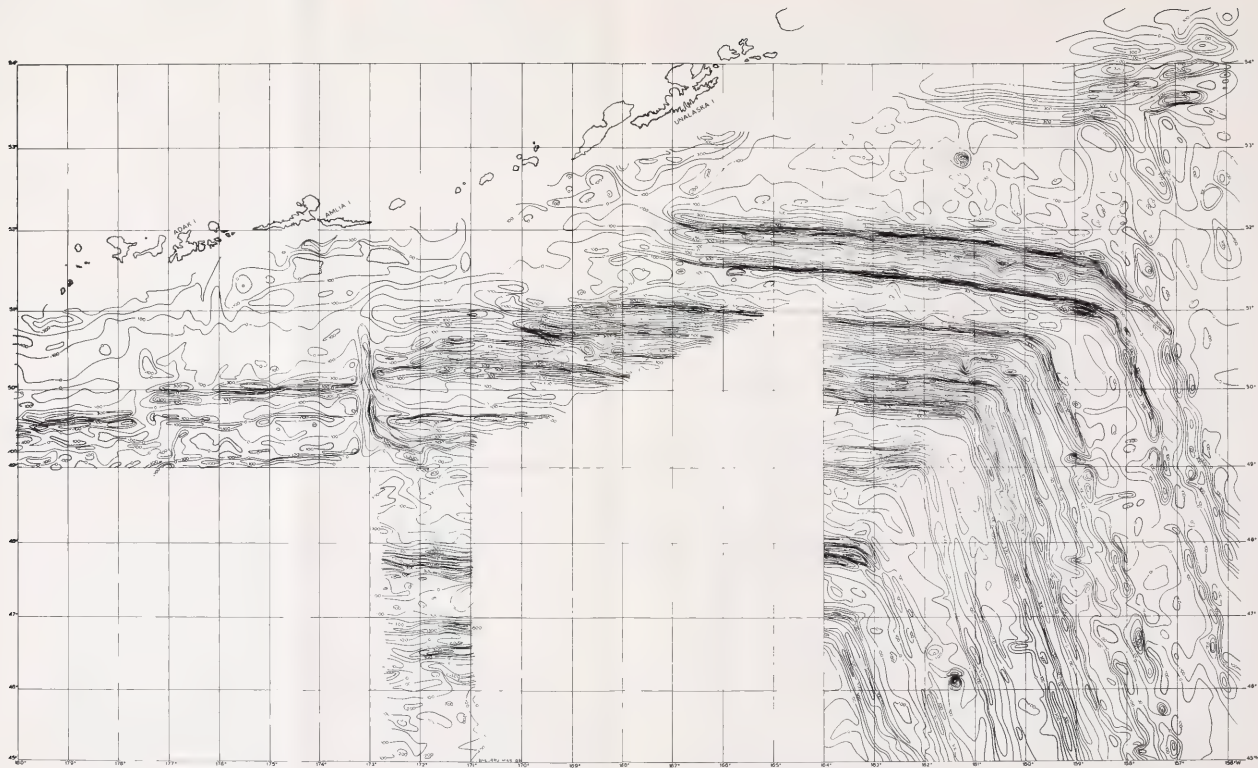


Fig. 11. Magnetic total-intensity anomaly map of areas B and C (Fig. 1). Contour interval is 100 gammas.

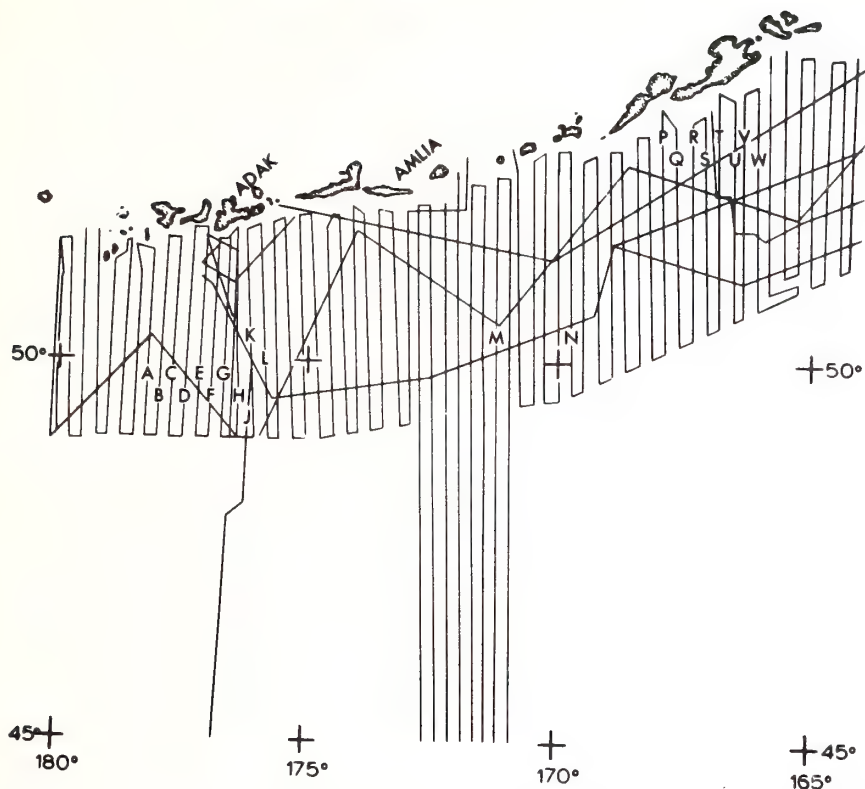


Fig. 12. Trackline chart of area C (Fig. 1) (after Grim and Erickson, 1969).

The anomalies terminate abruptly at the axis of the trench; traces of anomalies 24, 25, and 26, however, appear to cross the trench and extend over the Aleutian Terrace (Fig. 6a, profiles P, Q, and R). The east-west trend of the isogamma lines north of the trench between the Amlia and Adak fracture zones may also represent vestiges of the east-west magnetic lineations.

Generally, the magnetic field is smooth over the trench, but short-wavelength anomalies are found in shallow water near the islands where the tracklines cross the top of the Aleutian Ridge. Hayes and Heirtzler (1968) report that no traces of the lineations can be found in the Bering Sea north of the Aleutian Islands.

The location of the Amlia and Adak fracture zones was determined by the offset of magnetic lineations. The Amlia Fracture Zone offsets most lineations in a left-lateral sense by 230 km. The offset of anomalies 32A and 32B is only 140 km. The difference in offset is the result of two small anomalies (Fig. 6c, box) that are developed between anomalies 31 and 32A east of the Amlia Fracture Zone.

Anomalies 25 and 26 are not seen on profiles N and M (Fig. 6c); they seem to disappear where they cross the axis of the Aleutian Trench. Similarly, anomalies 27 and 28 disappear in the trench east of the Amlia Fracture Zone. Anomalies 29 through 32B do not cross the trench. These anomalies have the same

amplitude on both sides of the Amlia Fracture Zone; anomalies 25 through 28, which disappear in the trench, have a uniformly lower amplitude west of the Amlia Fracture Zone.

The offset of the magnetic anomalies across the Adak Fracture Zone is 30 km left-lateral. Figure 6b clearly shows the offset of anomalies 25 and 26. Data from Hayes and Heirtzler (1968) further support this offset, although these authors offer a different interpretation of the fracture pattern of this area.

The offset at $178^{\circ}30'E$ was interpreted from data published by Hayes and Heirtzler (1968). The offset at $176^{\circ}30'E$ was adopted from their interpretation.

5. Magnetic Structure of the Northeast Pacific Ocean

A. General Pattern

The Northeast Pacific constitutes an especially satisfactory area for the study of the geophysical implications of the magnetic anomalies because of the excellent survey coverage. An interpretation of the magnetic data available at the time of the writing of this article is assembled in Fig. 4. Most data are taken from published maps and profiles, unpublished data are presented through the courtesy of R. H. Higgs, U.S. Naval Oceanographic Office, and W. C. Pitman III and D. E. Hayes, Lamont-Doherty Geological Observatory.

The magnetic-anomaly lineations are numbered according to the system of Pitman et al. (1968). For most of the area shown in Fig. 4, the magnetic lines were mapped by detailed systematic surveys (18 km grid or closer); where the pattern of lineations was established from a few isolated tracklines, these tracks are indicated by black circles. For the schematic representation of the fracture zones, heavy lines are used. Dashed lines represent the possible extension of the anomalies and the fracture zones in areas in which control is poor or not available.

The magnetic lineations of the Northeast Pacific can be separated into the following three groups or "magnetic structural provinces":

1. The *coastal pattern* ("crestal anomalies" of Heirtzler and Le Pichon, 1965) is found east of anomaly 7 (or east of anomaly 10 between the Pioneer and Murray fracture zones) and is cut by numerous northwest-southeast and northeast-southwest faults.

2. The *central pattern*, between anomalies 7 and 21 (10 and 21 between the Pioneer and Murray fracture zones) consists only of north-south trending lineations. This pattern is cut by east-west faults that apparently are confined to these lineations.

3. The *western pattern* extends from anomaly 21 through anomaly 32B. It strikes northwest-southeast and bends abruptly as it approaches the Aleutian Trench. This pattern is also cut by fault zones that are nearly perpendicular to the lineations.

The orthogonal relationship between the faults and the lineations of the central and western patterns is especially striking in the case of the Surveyor

and the Mendocino fault zones; these clearly change trend toward the southwest at the beginning of the general area of the western pattern (Fig. 4).

Differences between the three patterns are further illustrated in Table I. The distance between a chosen lineation of the coastal group and one of the

TABLE I

Anomalies	Latitude	Distance (km)
5-10	52°N	775
	48°N	675
	46°N	525
	41°N	880
10-20	56°N	440
	52°N	575
	48°N	685
	45°N	740
	41°N	840
	35°N	870
	30°N	1570
25-32B	45°N	590
	41°N	585
	35°N	590

central group is highly irregular. The central anomalies gradually widen to the south; the distances among the western lineations are generally unchanged. In Table I, anomalies 10 and 20 were chosen for the measurements because they have been observed in the northern part of the area shown in Fig. 4, as well as in the area between the Pioneer and Murray fracture zones.

Although there are small internal changes, the overall width of the western lineations is the same even after they bend westward. At the Amlia Fracture Zone, however, the distance between anomalies 25 and 32B has decreased to 460 km. Westward of the Amlia Fracture Zone this distance appears to remain constant.

The large increase in the distance between anomalies 10 and 20 at 32°N is the result of the disturbed zone south of the Murray Fracture Zone that is described by Raff and Mason (1961).

Lineations 22 through 24 are somewhat irregular. As in the central group, the distances separating them increase to the south, but they strike parallel to the western group. These anomalies, therefore, can be considered to form a transitional zone between the central and western patterns. Definition of the exact nature of this transition zone must await further studies.

B. Coastal Pattern

The coastal pattern is the most complex of the three provinces. Part of the area mapped by Mason and Raff (1961) was resurveyed by Lattimore et al.

(1968) with a less dense line spacing. The similarity of the results from the two surveys proves that the complex, faulted, magnetic pattern, in fact represents complex tectonic activity in the coastal areas, and is not simply a function of the more detailed coverage as might be expected.

North of the Mendocino Fracture Zone the fault pattern is actually much more complex than can be shown in Fig. 4. There are a large number of faults between Vancouver Island and anomaly 5 along the trends shown here. Numerous small, east-west faults east of the Juan de Fuca Ridge, and northeast-southwest and northwest-southeast offsets in the Gorda Ridge area, were depicted by Pavoni (1966). Most of the faults shown here were also indicated by Raff and Mason (1961) and others.

The dashed arrow that indicates right-lateral motion along the Mendocino Fracture Zone at its eastern end (Fig. 4) represents the eastward movement of the Gorda block (area between the Mendocino and Blanco fracture zones—westward limit is approximately 135°W) which caused the separation of the Juan de Fuca and Gorda ridges postulated by Peter and Lattimore (1969). They assumed that the northeast-southwest trending magnetic lineations of this area originally were oriented north-south in conformance with the overall pattern of lineations, and that the Juan de Fuca and Gorda ridges at one time were part of a continuous ridge.

The offsets of anomalies 3 and 3' east of the Juan de Fuca Ridge argue against an original transform-fault relationship along the Blanco Fracture Zone (i.e., original offset of the two ridges) because no comparable ridge crest is present from which anomaly 3' could have originated by spreading (Pavoni, 1966; Peter and Lattimore, 1969). A relative eastward motion of the Gorda block is postulated in preference to an overall westward displacement of the crustal blocks north of the Blanco Fracture Zone. If realignment of the anomaly bands is made with respect to the anomalies of the Gorda block, a number of lineations east of the Juan de Fuca Ridge would fall under the Washington-Oregon coast, with the ridge crest and central anomalies located under Vancouver Island. Unless the continent was farther eastward at that time, these anomalies would have had to emerge from under the continent. If they were under the continent, they probably would have been "erased." This phenomenon seems to occur today along the margins of the continents.

The coastal anomaly group is not seen between the Mendocino and Pioneer fracture zones. Anomaly 9 [and possibly 8 (not shown)] occurs adjacent to the continental slope.

None of the prominent (numbered) anomalies of the coastal group are present between the Pioneer and Murray fracture zones. The somewhat distorted anomaly 10 of the central group sharply abuts the northeast-southwest trending, short-wavelength lineations that presumably belong to the coastal group. The absence of anomalies 9, 8, and 7 is a curious phenomenon which seems to occur nowhere else in the Northeast Pacific.

The northwest-southeast fault at 35°N and 123°W is quite clear on the magnetic-anomaly map of Mason and Raff (1961); the exact identity of the

coastal group of lineations is not known (triple line and double line), therefore their offset cannot be determined.

Magnetic expression of the Murray Fracture Zone toward the east ends between anomalies 9 and 7. Data are too scarce to present a good case for offset of the coastal anomalies along the extension of the Murray Fracture Zone. Small, left-lateral offsets inferred within the coastal pattern (Fig. 4), however, seem to align with left-lateral faults on the Channel Islands.

Anomalies 9, 8, and 7 are present south of the Murray Fracture Zone. Unfortunately, available data do not extend to the coastline, so only the edge of the coastal pattern is shown in Fig. 4.

C. Central Pattern

The "central pattern" has been surveyed in detail only in the area between the Pioneer and Murray fracture zones. However, since there are numerous tracklines over this pattern throughout the Northeast Pacific the north-south trend of the magnetic anomalies and the location of the east-west fracture zones (with the exception of the two northern ones) are sufficiently established.

Many of the east-west fracture zones are clearly restricted to the central pattern. Major fracture zones, like the Surveyor, Mendocino, Pioneer, and the Murray, seem to cross the western pattern as well. According to Menard (1967), some of these extend across the greater part of the Pacific basin. Even among these major fracture zones, the Surveyor and the Murray appear to terminate on the east at the eastern edge of the central pattern. The same may hold for the Mendocino and Pioneer fracture zones; this cannot be determined because south of these faults the eastern edge of the central pattern is not reached before the magnetic pattern and the faults reach the continental slope. The east-west fault at 37°N (Bassinger et al., 1969) ends east of anomaly 13, where two north-east-southwest faults seem to offset the magnetic anomalies.

The generally smaller offset of anomaly 7 at the eastern edge of the central pattern and the offsets of anomaly 6 are shown in Fig. 4 as hypothetical northwest-southeast faults. The interpretation of the offsets by these northwest-southeast faults, with the exception of the fault at 49°N and 135°W , is not necessary if differential movements (crustal compression or extension) are postulated at the eastern termination of the east-west faults.

From detailed surveys (Vacquier et al., 1961; Lattimore et al., 1968) the east-west fault at 37°N is known to terminate at 127°W against a northeast-southwest fault that, in turn, apparently cuts the crustal block between the Pioneer and Murray fracture zones. Some of the magnetic lineations are clearly offset across the east-west fault; others seem to bend and give the impression of plastic drag (Fig. 13, from Bassinger et al., 1969). Although the sediment cover is only 200 m, there is no topographic expression of this fault (L. A. Weeks, personal communication).

The western end of the east-west fault is not known. The offset of anomaly 21, designated as the westernmost of the central pattern, is generally the same as the rest of the lineations. A further puzzle is that no obvious topographic

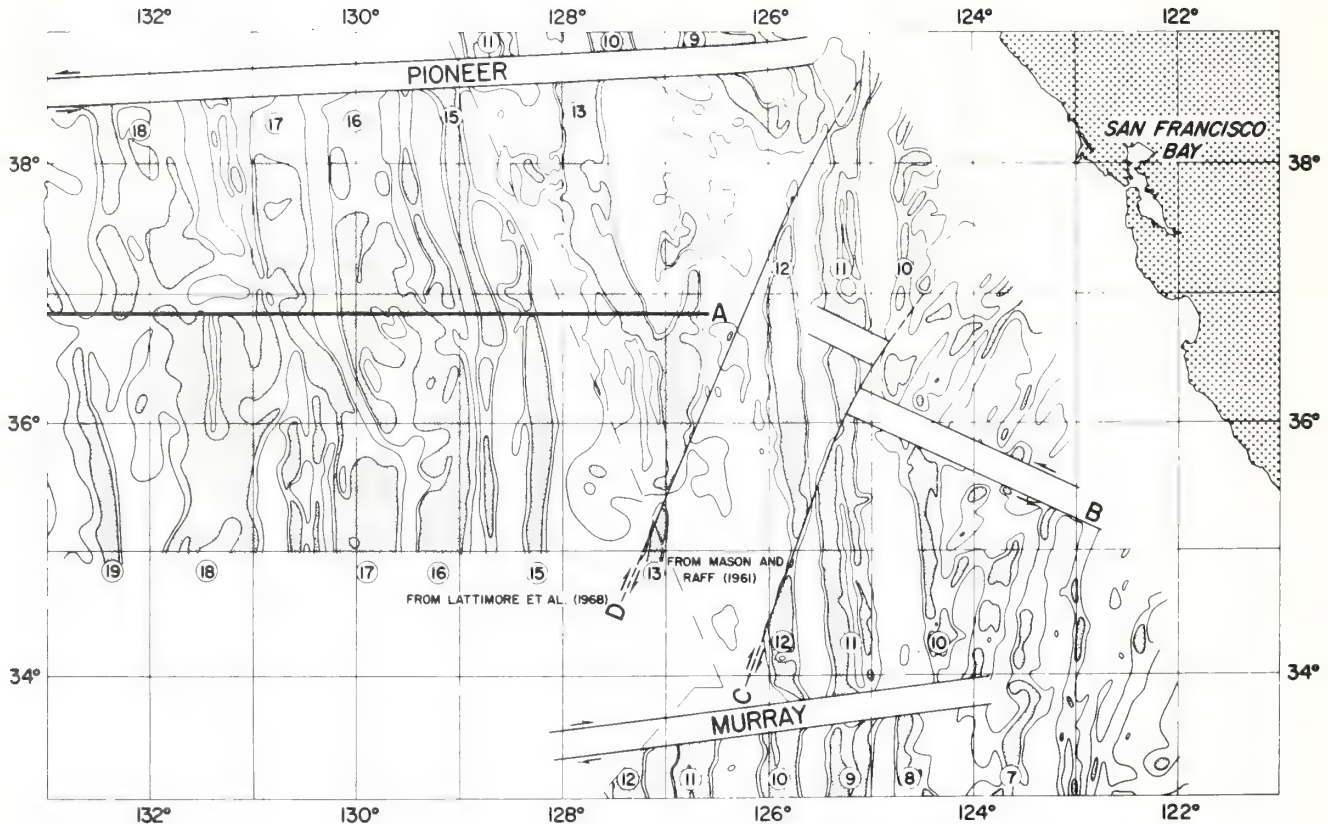


Fig. 13. Magnetic total-intensity anomaly map with interpretation of the magnetic offsets. Area is located between the Pioneer and Murray fracture zones (from Bassinger et al., 1969).

evidence exists where the faults either disappear or run into faults of different motions at the edges of the central pattern.

D. Western Pattern

The essential characteristics of the western magnetic pattern are described in the discussion of the magnetic maps for areas A, B, and C of Fig. 1. Thus only possible modes of origin of the bend in the magnetic lineations [or, as called by Elvers et al. (1967), the "Great Magnetic Bight"] are presented here.

Some of the possible explanations for the existence of the bend in the lineations are the following:

1. The magnetic lineations, as discrete geological structures within the earth's rigid crust, were straight at one time. Subsequently the crust was broken up and bent westward.
2. The magnetic lineations were straight at one time. When they were bent westward, the crustal material responsible for the lineations behaved like pliable plastic so that crustal break did not occur.

3. The magnetic anomalies were formed [as postulated by the Vine and Matthews (1963) hypothesis] along two separate, mid-oceanic ridge axes (one trending northwest-southeast, the other east-west) both of which have been obliterated since their formation.

4. The magnetic anomalies were formed [as postulated by the Vine and Matthews (1963) hypothesis] along an approximately northwest-southeast and an east-west trending, mid-oceanic ridge axis, located along anomaly 32B (Pitman and Hayes, 1968). As the younger lineations were formed these ridge crests migrated northward and eastward, leaving behind the successively younger crustal elements represented by the magnetic lineations north and east of 32B. The two ridge crests disappeared under the Aleutian Arc and the North American Continent.

5. The anomaly lineations represent a global stress or fracture pattern in the crust (possibly intruded by mantle rocks), so that the magnetic pattern (including the bend) formed "in place" (Mason, 1958; Raff and Mason, 1961; Peter, 1965 and 1966; Elvers et al., 1967).

6. The magnetic-anomaly lineations are related to geological entities located in the upper mantle and in the lower part of the oceanic crust. The magnetic bend may have formed as differentiated mantle kept filling a void created by crustal fracture. The shape of the crustal fracture and the direction of the tension that caused the fracture have determined the shape of the bend.

Arguments can be raised against both the plastic (case 2) and the rigid (case 1) behavior of the magnetic lineations. The relative straightness for thousands of kilometers, the usual fracture type offsets [although draglike phenomena are observed in places (Bassinger et al., 1969)], and the small internal fractures within individual blocks seem to support the idea that the anomalies are caused by rigid geological bodies. Yet, as Fig. 14 illustrates, the bend could not have occurred by rotation of two rigid crustal blocks. Part A (Fig. 14) represents a crustal block with two magnetic lineations. Parts B and C demonstrate that if the crust is bent as a rigid block, either crustal opening or crustal compression must occur. In the area of the bend, neither topographic nor magnetic data support such a possibility.

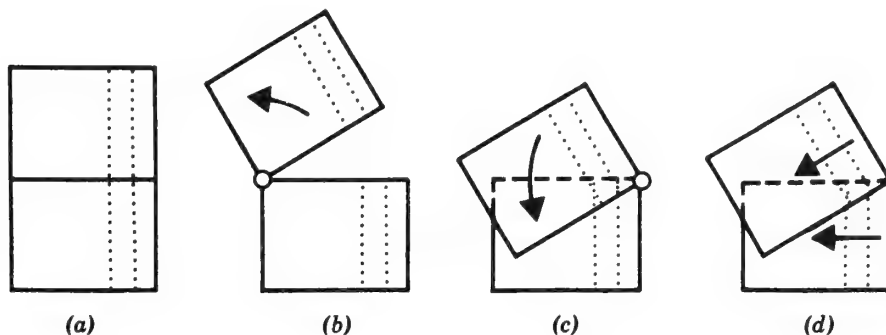


Fig. 14. Development of crustal opening and compression in case of rotation of rigid blocks.

Part D shows that overthrust of blocks must occur if the anomalies "spread" at right angles away from two segments of a ridge that forms an angle (case 3). For this case, one may consider the right edge of drawing D as the spreading source; the overlapping part is shown by dashed lines.

Case 5 is unlikely in view of the well demonstrated axial symmetry and global occurrence of the magnetic lineations.

The "migrating ridge" hypothesis (case 4) of Pitman and Hayes (1968) is a possible explanation for the formation of the bend. This, together with the last explanation above (No. 6) is treated in detail in connection with the discussion on the origin of the magnetic lineations.

6. Magnetic Structure—Origin of Magnetic Lineations

A. Proposed Hypotheses

A comprehensive summary on the possible geological origin of the magnetic lineations was given by Bullard and Mason (1963) in Volume 3 of *The Sea*. Some of their observations have a direct bearing on the origin of the magnetic lineation pattern and are shown in Table II.

TABLE II

-
- | |
|---|
| 1. There is no correlation between bottom topography and magnetic lineations. |
| 2. There is no difference in seismic velocities between areas of positive and negative lineations. |
| 3. Oceanic crust appears to be rigid; there are large displacements without distortion of the lineations. |
| 4. Orthogonal relationship between the magnetic lineations and major fracture zones may indicate common origin. |
| 5. Anomaly sharpness indicates that the upper surface of magnetic body is not deeper than 1 km below sea floor. |
| 6. Pattern disappears below continents; anomalies erased by combined effect of temperature and pressure. |
| 7. Fracture zones are younger than the magnetic pattern. |
-

Bullard and Mason (1963) listed three possible explanations for the origin of the lineations: (a) isolated magnetic bodies (such as lava flows) within the second layer; (b) elevated folds or fault blocks in the main crustal layer; and (c) zones of intrusion of mantle material.

The most commonly accepted explanation for the origin of the lineations is the Vine and Matthews (1963) hypothesis which is a corollary to the sea-floor spreading concept of Hess (1962, 1965) and Dietz (1961). According to this hypothesis, at the axis of the mid-oceanic ridges the crust is broken apart by convection currents and the basaltic material that fills the break acquires a magnetization in the direction of the existing magnetic field of the earth as it cools through the Curie point. As the earth's magnetic field periodically reverses

polarity (Cox et al., 1964), a sequence of normally and reversely magnetized rocks, symmetrical about the ridge axis, comes into existence and slowly spreads away from the ridge crest.

As another corollary of the sea-floor spreading hypothesis, Wilson (1965[a], 1965[b]) suggested that offsets of mid-oceanic ridges do not represent actual displacements, but that the opening in the crust (along which the mid-oceanic ridges and magnetic lineations subsequently formed) was offset originally. He postulated that, as the sea floor spreads away from the ridge crests, the motion along the planes which connect the offset portion of the ridge crests is actually opposite in direction to that which would be indicated by strike-slip faulting. He called this motion *transform faulting* and used it to explain both the earthquake activity concentrated along the planes which join the offset ridge crests, and the relative absence of earthquakes along the extensions of the faults that lie beyond the ridges that they join.

B. Sea-floor Spreading

Some of the data in direct support of the original sea-floor spreading and transform-fault concepts are listed in Table III; data opposed to these hypotheses are summarized in Table IV. Comparison of these two tables indicates

TABLE III

-
- | |
|---|
| 1. Magnetic lineations are generally parallel to mid-oceanic ridges. |
| 2. Magnetic lineations are symmetrical about the axis of mid-ocean ridges. |
| 3. The same spectrum of lineations and axial symmetry is present in association with all tectonically active mid-oceanic ridges. |
| 4. The sequence of positive and negative lineations which extend from the ridge-axis to a distance approximately 160 km, agrees with the sequence of normal and reverse polarities of the earth's magnetic field in the past four million years. (Measured on dated volcanic rocks on land and on deep-sea sediment cores.) |
| 5. Earthquake mechanism studies corroborate the motion required by transform faulting. |
| 6. The age of sediments (based on available samples) indicates general increase from the ridge crest to the flanks. |
-

that an important part of the facts that argue against sea-floor spreading are based on sediment structure and distribution, and on sea-floor topography. If the main source of the magnetic lineations lies within a 1- or 2-km thick basaltic layer which overlies the main "serpentinite" crustal layer (Vine and Wilson, 1965; Vine, 1966), offsets of the magnetic pattern, of either the transcurrent or transform kind, should be reflected in the sediment structure. In the Northeast Pacific, where the sediment overlying the second layer is relatively thin [145–680 m thick according to Hamilton (1967)] these offsets should be indicated on the sea floor.

TABLE IV

-
1. Over 1 km of undisturbed, horizontally bedded sediments were found in the trough of the Vema Fracture Zone which is considered to be an active transform fault.
 2. Numerous magnetic offsets, some "dated" by the magnetic time scale as less than two million years old, show no disturbance of either sea-floor topography or sub-bottom sediments.
 3. Most trenches studied are either unfilled or filled with undisturbed sediments.
 4. The topography and petrology of the upper flanks of the ridges are of a different origin from those of the ridge-crest.
 5. Magnetic lineations cross morphologic province boundaries without apparent change in character.
 6. Magnetic anomalies over the ridge-crests differ in amplitude and wavelength from those over the flanks.
 7. The magnetic structure of the Northeast Pacific indicates three phases of tectonic activity.
 8. Most faults of the Northeast Pacific do not meet the definition of transform faults.
-

If the offsets either preceded the sediment deposition or started very recently the above arguments are not necessarily valid. However, according to Vine (1966), motion along the offsets (such as transform faults) has been uniform since the Cretaceous. Based on this assumption, a geomagnetic time scale has been proposed in which anomaly 32B is "dated" as 72 million years old (Vine, 1966, Heirtzler et al., 1968).

East of the Juan de Fuca Ridge a northeast-southwest strike-slip fault offsets a group of magnetic-anomaly lineations by 100 km (Fig. 4). According to the geomagnetic time scale, the youngest lineation offset (anomaly 3) is two million years old, therefore a 5 cm/yr motion is required along the fault during Late Pliocene and Pleistocene (Peter and Lattimore, 1968). Seismic-reflection studies of this area indicated no sediment disturbance in the area of this fault (Hamilton and Menard, 1968).

On the basis of these arguments it appears that the "marine" geomagnetic time scale is questionable, and/or the magnetic lineations are likely to originate below the second layer so that their offset is not necessarily reflected in the upper part of the crustal column.

Near the axis of mid-oceanic ridges the geomagnetic time scale is supported by a number of observations (Table III), therefore its validity may be accepted within the "coastal pattern." A pause in sea-floor spreading, and consequently a rejection of the time scale outside the area of the ridge crests ("coastal pattern"), was suggested by Ewing and Ewing (1967) on the basis of the abrupt increase in sediment thickness at the edge of the ridge crests. The three different patterns in the magnetic structure (Fig. 4) strongly support the idea of three separate episodes of tectonic activity, and since the length of the pauses cannot be determined, the extrapolation of the geomagnetic time scale outside the crestal area of mid-oceanic ridges is not justified.

The suggestion that the magnetic anomalies originate below the second layer is contrary to the conclusion reached by Bullard and Mason (1963) who state that the upper surface of the magnetic bodies should be no deeper than 1 km below the sea floor. Additionally, deep-towed magnetometer data indicate large-amplitude, short-wavelength anomalies near the sea floor (Mudie and Harrison, 1967; Spiess et al., 1968; and Spiess and Mudie, Part I, Chapter 7). In order to satisfy all observations it is suggested that small intrusives (dikes) in the second layer could be responsible for the short-wavelength, large amplitude anomalies, and that the major bodies (as possible sources of these intrusives) may lie deeper.

The existence of a magnetically quiet zone at continental margins and trenches may be interpreted as support of this suggestion. Model computations, like those reported by Hayes and Heirtzler (1968), indicate that if the magnetized bodies are part of the second layer, the down-bow of the crust indicated by seismic data at the Aleutian Islands is not sufficient to account for the abrupt elimination of the anomalies over the Aleutian Trench. If, however, the magnetic bodies lie in the lower part of the crust or in the upper mantle as suggested here, the 3–6-km crustal down-warp may be sufficient to either carry the temperature of the magnetic bodies above the Curie point or cause sufficient metamorphism that their magnetization is erased (Bullard and Mason, 1963; Table II).

The crossing of the magnetic lineations over major morphologic provinces without a change in character, the apparent “drag” effect on certain lineations (mapped across fault A in Fig. 13), the relatively young offset of the magnetic lineations east of the Juan de Fuca Ridge without deformation of sediments, the irregular junction of the “central pattern” with the neighboring magnetic patterns (Fig. 4), and the abrupt termination of large east-west faults without sub-bottom or bottom topographic expression all support the probability of a deeper source of the magnetic lineations whereby the magnetic offsets do not necessarily indicate the offset of the entire crustal column. This interpretation suggests that in certain cases *small* offsets of the deeper magnetic layer can be compensated for within the overlying crustal layers in such a manner that noticeable offsets do not necessarily occur near the top of the second layer. The combination of offsets and drags of the lineations across fault A in Fig. 13 may be the result of the interaction between the deeper crustal layers that represent the proposed compensation.

Seismic refraction measurements in the Northeast Pacific (Shor, 1962; Shor et al., 1968) indicate normal oceanic crust in the areas of the “central” and “western” magnetic patterns; over the Gorda and Juan de Fuca ridges (i.e., over the “coastal pattern”) the crustal velocity is slightly higher, the mantle velocity is below normal, and the ridges appear to represent the surface expression of the upraised crust and mantle. Shor et al. (1968) concluded that the structure of the Juan de Fuca and Gorda ridges is the same as that of the East Pacific Rise. Gravity anomalies over oceanic ridges [summarized by Worzel (1965)] further reflect unique crustal structure. As Heirtzler and Le

Pichon (1965) noted, short-wavelength magnetic anomalies seem to be associated with the anomalous-mantle zone in the area of the ridge crests. It can be concluded, therefore, that the "coastal pattern" in the Northeast Pacific is associated with the anomalous crustal structure, and that it alone represents segments of the present East Pacific Rise.

Although uplifted by the present East Pacific Rise, the normal oceanic crust to the west does not appear to be a part of it structurally (Fig. 4). Both reference to the areas of the central and western magnetic patterns as "ridge flank," and the extension of the East Pacific Rise to the edge of all lineations (anomaly 32B) as proposed by many investigators, are unwarranted. It is suggested that the change of the magnetic lineations from broad, even-amplitude anomalies to short-wavelength anomalies at the edge of the "coastal pattern," is related to a change in crustal structure, rather than to more frequent reversals of the earth's field alone as Vine (1966) proposed.

A modification of the sea-floor spreading hypothesis, namely, the possibility that the ridge crest itself migrates, was raised by Pitman and Hayes (1968). These authors proposed that a Y-shaped junction of ridge crests initially existed southwest of the present bend in the anomaly lineations. Convection currents that upwelled along this junction carried the ridge crests along with them (northward and eastward) until the convection pattern was "stifled" by the Aleutian Trench. If the corollary assumptions of this hypothesis are valid, a simplified magnetic pattern (Pitman and Hayes, 1968; Fig. 4) may be explained. Modifications are necessary, however, to incorporate the detail shown in Fig. 4.

Morgan (1968) suggested that the earth's surface is broken up into large rigid blocks bounded by rises, trenches, or faults, and that these blocks rotate about each other with respect to several "poles." The mid-oceanic rises are not associated with deep-seated convection currents, but instead represent new crust created where two blocks separate. Dikes a few kilometers in width and, perhaps 100 km deep are formed in this way and magnetized according to the existing polarity of the earth's field. With continued tension, the dikes are split down the middle, new material is injected, and a symmetrical pattern of magnetic anomalies is created. Although Morgan's (1968) hypothesis may not account for all the detail of the magnetic structure derived here for the Northeast Pacific, his suggestion that the ridge crests are independent of the location of the convection cell is a significant departure from the original sea-floor spreading hypothesis.

C. Transform faults

Beyond question, many of the faults in the "coastal pattern" are *not* transform faults; many make a small angle with the ridge crests and some are bounded by other faults. Especially in the area of the Juan de Fuca Ridge, fault patterns are clearly incompatible with the concept of transform-faulting (see Morgan, 1968, Fig. 2). By definition, a transform fault must cross all magnetic lineations; none of the faults in the "coastal pattern" and only a few

in the "central pattern" meet this criterion. The Murray and Surveyor fracture zones clearly stop near the eastern edge of the "central pattern"; the other east-west faults of the "central pattern" do not extend into the westernmost lineations. The Pioneer and Mendocino fracture zones appear to cross the "western" and "central" patterns but terminate near the continental margin before the "coastal pattern" develops. The proposition that the Mendocino and Murray fracture zones may be transform faults (Wilson, 1965[a]; Vine, 1966) is also open to question on the basis of their linear extent across the entire Pacific basin (Menard, 1967).

If transform faults (cutting all three magnetic patterns) did exist in the area of Fig. 4, the "coastal pattern" could have evolved into the "central pattern" and this, in turn, into the "western pattern" through lateral spreading. The bend in the "western pattern," the development of extra lineations in part of the east-west segment of the "western pattern," and the fact that the "central pattern" does not bend, together with the arguments derived earlier, require modification of the sea-floor spreading hypothesis and its two corollaries—the Vine and Matthews (1963) and the transform-fault hypotheses (Wilson, 1965[a], 1965[b])—in their application to the East Pacific area. Present-day, transform-fault motions (Sykes, 1967) do not necessarily prove that the ridge crests were originally offset. Once the offset has taken place (e.g., by transcurrent faulting) active growth of the individual ridges would produce relative motion along the fault plane connecting the ridge crests that is in accord with transform-fault motion.

D. Interpretation

In previous portions of this paper, it is suggested that the main source of the magnetic lineations may lie below the second layer. It has been demonstrated that—because of the absence of the required overlap of lineations—the bend in the magnetic anomaly bands could not have originated by crustal spreading from two stationary ridge crests. The characteristic internal fault system of the three magnetic patterns could not be derived from one another through simple lateral spreading, and it has been suggested that the three patterns probably are associated with three episodes of tectonic activity. The interpretation of the genesis of the lineations and their offset pattern must combine these deductions with the world-wide occurrence of the magnetic lineations in association with mid-oceanic ridges, and their general symmetry with respect to the ridge crests.

These latter observations suggest that there is a definite relationship between the magnetic lineations and the ridges. Two reasonable explanations may be offered for the axial symmetry of the magnetic anomaly bands: (a) an "active" system of intrusives at the ridge crest that forces the crust aside [Vine and Wilson (1965) suggest that this takes place in the second layer]; and (b) a "passive" system of intrusives that are simply filling a void created by the opening of the crust. In the first explanation the ridge crest is directly tied to the upwelling and dynamic motion of the convection currents. The second

explanation is based on crustal tension alone, that is, there is no restriction on the mechanism that may cause the crustal tension. Among possible mechanisms are polar shift, earth-expansion, and the suggestion of Morgan (1968) that tension is produced by rotation of large crustal blocks.

Since the existence of the bend in the "western pattern" demands that the lineations cannot be pushed aside by subsequently formed younger lineations (Fig. 14d), the ridge crest is considered here not as a dynamic, moving part of the oceanic crust but as a *passive* part formed as the result of crustal tension. The mid-oceanic ridges are seen as "scars" in the earth's crust. The anomalous mantle and crustal structure below the ridge crest is believed to be caused by differentiation and volcanic processes occurring *in response* to the fracturing of the crust. It is only in the sense of "cause and effect" that the proposed "passive ridge-crest" hypothesis is different from the process of crustal generation described by Hess (1965).

If the earth's crust as a whole is under tension (earth-expansion), fracturing of the crust, differentiation processes in the upper mantle, and the filling of the void created by fracturing with differentiated mantle rocks and volcanics could account for both the existence of mid-oceanic ridges and the axial symmetry of the magnetic lineations. Figure 15b illustrates the formation of the magnetic bend according to this hypothesis: as the crust on the two sides of the fracture is pulled apart, differentiated mantle material fills the gap and becomes "welded" to the crust. Continued tension breaks this "dike" in the center where it is hottest and may be only partially solidified at depth (Morgan, 1968). With further tension, under the influence of a periodically reversing magnetic field (Vine and Matthews, 1963), magnetic lineations could be formed symmetrically about the center of the crustal break.¹

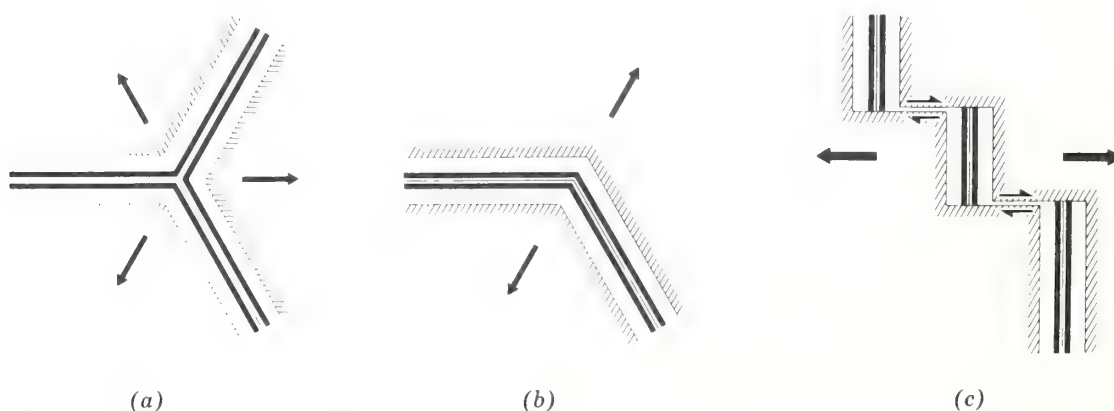


Fig. 15. Development of Y-shaped ridge junction, magnetic bend, and ridge offset through crustal tension.

¹ Symmetrical lineations can be produced not only by normally and reversely magnetized blocks, but also by nonmagnetic blocks intermixed with magnetized blocks in the formation cycle. This may be an especially attractive assumption for the older lineations.

If, in Fig. 15b, one side of the fracture is stationary and only the other side is being pulled away, the appearance is that of a "migrating ridge" such as described by Pitman and Hayes (1968) and Morgan (1968). Crustal tension in three directions (or in two directions away from a stationary block) is shown in Fig. 15a; this case is applicable to the Y-shaped ridge junction reported near the Galapagos Islands by Herron and Heirtzler (1967) and Raff (1968).

It should be noted that with a "passive" ridge crest the problem of lateral compression seen in connection with spreading (Fig. 14d) does not exist since the lineations are not spreading away from a ridge crest; they are "welded" to the lower crust and upper mantle, which are under tension and pulling apart. Thus the lineations, together with the receding crust, are moving away from the center of the ridge and give the impression of a spreading ridge. Both "active" and "passive" ridge crest hypotheses imply that the lineations are progressively older away from the center of the ridge crest.

Figure 15c illustrates how crustal tension can cause the "transform-fault" motion between the offset portions of ridge crests that Sykes (1967) noted.

Application of the observations in the preceding paragraphs to the specific case of the Northeast Pacific suggests that the "western pattern" is related to an early phase of tectonic activity, that is, to a predecessor of the East Pacific Rise. During this period, the inferred crustal opening probably followed the tectonic grain of the North American Cordillera with its westward bend in Alaska (Fig. 15b). Development of the "western pattern" was followed by a pause in the tectonic activity; during this time the opening healed over completely. Renewed crustal tension, probably with a predominant east-west component, may have been manifested in a crustal break along a "zig-zag" pattern (Fig. 15c). The intrusives represented by the anomalies of the "central pattern" would have formed in north-south openings in the crust. These openings may have been connected by east-west planes of dislocation that could be described as transform faults. During the second period of quiescence, these fractures healed over so that with renewal of east-west tensional forces the crust yielded along a slightly different pattern. The present East Pacific Rise is related to this last phase of tectonic activity. The pattern, which probably originally conformed to the north-south orientation of the "central pattern," apparently was broken up by northeast-southwest and northwest-southeast fractures subsequent to its formation. If the inferences of McManus (1965) and Peter and Lattimore (1969) are assumed, this breaking-up occurs as the result of the Late Tertiary to Recent coastal orogeny.

The deep source of the magnetic lineations postulated in this paper permits some faulting of the magnetic lineations without the disruption of bottom topography or the sedimentary section. Thus the occurrence of undisturbed sediments east of the Juan de Fuca Ridge that Hamilton and Menard (1968) reported does not present a contradiction to the proposed interpretation. The passive ridge hypothesis, coupled with earth-expansion, is especially attractive when one considers the undisturbed sediments and the lack of obvious compressional phenomena on the ocean floor at the continental margins.

7. Magnetic Structure—Origin of Aleutian Trench

A. Proposed Hypotheses

In this section the previously derived interpretation is applied to the problems of the origin of the Aleutian Trench as seen from the point of view of the two major hypotheses: the tensional- and compressional-origin hypotheses.

The hypotheses are not reviewed in detail. A comprehensive treatise on the tensional hypothesis was given by Worzel (1965); a summary of data on trenches with emphasis on their compressional, convection-current origin was given by Fisher and Hess (1963).

According to the tensional hypothesis, the trenches are considered to be down-faulted parts of the oceanic crust. The negative, isostatic anomalies that characterize the trench areas are explained in terms of mutual interaction of the island arc, trench, and outer-ridge systems. Shor (1965) suggested that the Aleutian Trench formed as a direct result of the loading of the island arc on the oceanic crust; the isostatic imbalance of the trench is attributed to the elastic behavior of the oceanic crust.

The argument for the compressional origin is also based on the negative isostatic anomalies associated with the trenches. According to this theory, static-mass imbalances in the area of the trench should be compensated for in a relatively short time; since the negative isostatic anomalies indicate that this has not occurred it is presumed that a dynamic force, such as compression caused by convection currents or drag induced by them, is preventing the trench from adjusting to isostatic equilibrium.

B. Interpretation

The mechanical conditions that might be expected to exist if the oceanic crust is moving under a curved trench driven by convection currents have been illustrated by Fisher and Hess (1963; Fig. 16). Geological structural trends similar to $f-f'$, illustrated in Fig. 16, should conform to the arcuate shape of the trench on both sides. The east-west trends of the magnetic-anomaly lineations in the vicinity of the Aleutian Trench are in sharp conflict with these logical expectations. The apparent north-south (as opposed to radial) trend of the fracture zones associated with the Aleutian Trench further implies structural independence.

Data collected in the area of the Aleutian Trench indicate that (a) traces of some magnetic lineations extend over the Aleutian Terrace; (b) those lineations that intersect the trench east of the Amlia Fracture Zone have reduced amplitudes west of the fracture zone; and (c) the fracture zones have no obvious topographic expression in the trench floor, but they may be related to changes in trend on the Aleutian Ridge.

If it is assumed that the sea floor is rigid and that it has been carried deep below the trench and island arc by a descending convection current, vestiges of the lineations and general, weak east-west trends of the anomalies

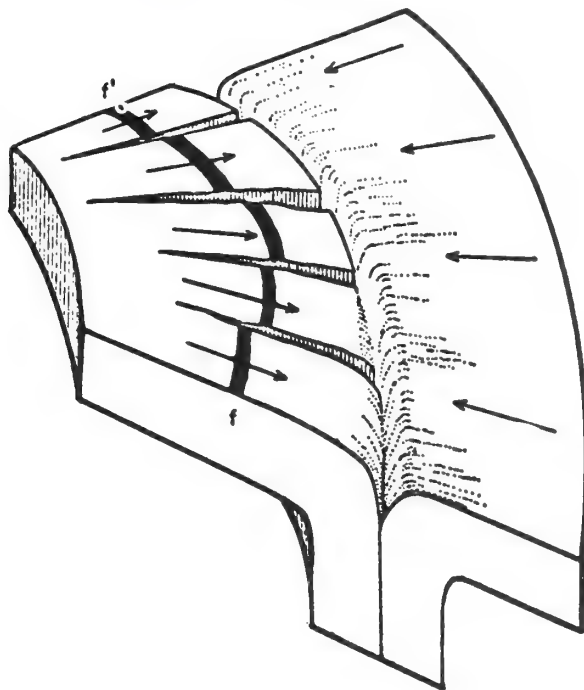


Fig. 16. Postulated mechanical situation in which the crust moves into a curved trench (from Fisher and Hess, 1963).

should not exist over the Aleutian Terrace; instead, the anomaly trends either should follow the curvature of the island arc or should not be seen at all.

The fact that anomalies 25 through 28 (the only ones that intersect the trench east of the Amlia Fracture Zone) are much reduced in amplitude west of the fracture strongly suggests that the reduction in amplitude is related to the trench formation. If the island arc and trench were superimposed on an existing, unfaulted magnetic pattern, then such loading might depress the lower part of the crust below the Curie point isotherm, or to such a temperature that metamorphism would cause alteration of mineralogy. In this manner part of the magnetization could have been erased. Before complete suppression of the anomalies took place, transcurrent faulting could have carried the crust away from the influence of the island arc, thus preserving the lineations in their diminished form. If, on the other hand, the Amlia Fracture Zone is assumed to be a transform fault and the only movement of the sea floor was northward, there is no explanation for the uniformly reduced amplitude of that particular group of anomalies.

Northward movement of the sea floor would also require that the sea-floor topography of the outer ridge be carried into the trench; the drift of guyots into the Aleutian Trench has been proposed by Menard and Dietz (1951), and the drift of guyots from the Darwin Rise to the Gulf of Alaska by Hess (1965).

Yet, the high relief of the outer ridge does not continue onto the south wall of the Aleutian Trench.

If the structures that cause the magnetic anomaly lineations lie mainly in the lower part of the crust and upper mantle, the relatively "quiet" magnetic zone of the trenches and continental margins is to be expected because crustal down-bow may be sufficient to carry the lower crust-upper mantle into such temperatures that its magnetization is erased.

Vine (1966) and others suggested that the fracture pattern off the Washington-Oregon coast is the result of the westward drift of the North American continent and the change in the direction of sea-floor spreading during the Pliocene. It was further assumed that as a result of this new direction of spreading the crust of the entire North Pacific ocean has been moving northwestward, and causing the formation of the Aleutian Trench. Recent studies of earthquake first motions by Isacks et al. (1968) support this interpretation, and together with the distribution of sediments in the North Pacific (Ewing et al., 1968), imply that the Aleutian Trench may be as young as Late Tertiary.

If the Aleutian Trench is Tertiary or younger, and the western half of the Aleutian Arc is dominated by strike-slip faulting (Isacks et al., 1968), then the existence of a well-developed trench along the western half of the arc may be questioned because no appreciable underthrusting could have taken place in the last ten million years.

Pitman and Hayes (1968) have proposed that the Aleutian Trench was formed by the underthrusting of a northward moving sea floor which ended in the Paleocene; Ewing and Ewing (1967) suggested that there was a 10-million-year pause before the renewal of sea-floor spreading in the Pliocene. These suggestions raise the question of whether or not the elapsed time before the latest phase of spreading would have been sufficient for isostatic rebound of the trench, if the cause of trench formation is underthrusting.

Whether there has been an "early" trench or not, however, the northwestward motion of the sea-floor in the last 10 million years should have created measurable differences in the development of the two halves of the Aleutian Trench.

These considerations, together with the magnetic structure of the Aleutian Arc and the Northeast Pacific, complement our earlier conclusions and suggest that the Aleutian Trench has been formed as the result of crustal downfault or down-bow rather than underthrust of the ocean floor.

Acknowledgments

The U.S. Coast and Geodetic Survey ships *Pioneer* and *Surveyor* collected the systematic SEAMAP data. For additional data and manuscripts not published at the time of writing this paper, we are indebted to R. H. Higgs, U.S. Naval Oceanographic Office, and W. C. Pitman, III, D. E. Hayes, and J. I. Ewing, Lamont-Doherty Geological Observatory. Several colleagues, especially O. E. DeWald and the late A. B. McCollum deserve credit for their help in working on SEAMAP data.

We are grateful to R. K. Lattimore and H. B. Stewart, Jr. for many helpful discussions and critical review of the manuscript.

References

- Bassinger, B. G., O. E. DeWald, and G. Peter, 1969. Interpretation of the magnetic anomalies off central California. *J. Geophys. Res.*, **74**, 1484–1487.
- Bullard, E. C., and R. G. Mason, 1963. "The magnetic field over the oceans," in *The Sea*, Vol. 3, M. N. Hill, Ed., Wiley Interscience, New York, pp. 175–217.
- Cox, A., R. R. Doell, and G. B. Dalrymple, 1964. Reversals of the Earth's magnetic field. *Science*, **144**, 1537–1543.
- Dickson, G. O., and J. Foster, 1966. The magnetic stratigraphy of a deep sea core from the North Pacific Ocean. *Earth Planet. Sci. Letters*, **1**, 458–462.
- Dickson, G. O., W. C. Pitman, III, and J. R. Heirtzler, 1968. Magnetic anomalies in the South Atlantic and ocean floor spreading. *J. Geophys. Res.*, **73**, 2087–2100.
- Dietz, R. S., 1961. Continent and ocean basin evolution by spreading of the sea floor. *Nature*, **190**, 854–857.
- Drake, C. L., J. R. Heirtzler, and J. Hirshman, 1963. Magnetic anomalies off eastern North America. *J. Geophys. Res.*, **68**, 5259–5275.
- Elvers, D. J., C. C. Mathewson, R. E. Kohler, and R. L. Moses, 1967. "Systematic ocean surveys by the USC & GSS Pioneer 1961–1963," ESSA, Operational Data Report, C & GS DR-1, 19 pp.
- Ewing, J., and M. Ewing, 1967. Sediment distribution on the mid-ocean ridges with respect to spreading of the sea floor. *Science*, **156**, 1590–1592.
- Ewing, J., M. Ewing, T. Aitken, and W. Ludwig, 1968. "North Pacific sediment layers measured by seismic profiling," in *The Crust and Upper Mantle of the Pacific Area*, Geophys. Monograph, 12, American Geophysical Union, Washington, D.C., pp. 147–173.
- Fisher, R. L., and H. H. Hess, 1963. "Trenches," in *The Sea*, Vol. 3, M. N. Hill, Ed., Wiley Interscience, New York, pp. 411–436.
- Grim, P. J., and B. H. Erickson, 1969. Fracture zones and magnetic anomalies south of the Aleutian Trench. *J. Geophys. Res.*, **74**, 1488–1494.
- Hamilton, E. L., 1967. Marine geology of the abyssal plains in the Gulf of Alaska. *J. Geophys. Res.*, **72**, 4189–4213.
- Hamilton, E. L., and H. W. Menard, 1968. Undistorted turbidites on the Juan de Fuca Ridge (abstract) *Trans. Amer. Geophys. Un.*, **49**, 208.
- Hayes, D. E., and J. R. Heirtzler, 1968. Magnetic anomalies and their relation to the Aleutian Island arc. *J. Geophys. Res.*, **73**, 4637–4646.
- Heirtzler, J. R., G. Peter, M. Talwani, and E. Zurlueh, 1962. "Magnetic anomalies caused by two dimensional structure; their computation by digital computers, and their interpretation," Tech. Rept. 5, Cv-6-62. Nonr-Geology, Columbia University, New York.
- Heirtzler, J. R., and X. Le Pichon, 1965. Crustal structure of the mid-ocean ridges, 3. Magnetic anomalies over the mid-Atlantic Ridge. *J. Geophys. Res.*, **70**, 4013–4033.
- Heirtzler, J. R., X. Le Pichon, and J. G. Baron, 1966. Magnetic anomalies over the Reykjanes Ridge. *Deep-Sea Res.*, **13**, 427–443.
- Heirtzler, J. R., G. O. Dickson, E. M. Herron, W. C. Pitman, III, and X. Le Pichon, 1968. Marine magnetic anomalies, geomagnetic field reversals, and motions of the ocean floor and continents. *J. Geophys. Res.*, **73**, 2119–2136.
- Herron, E. M., and J. R. Heirtzler, 1967. Sea-floor spreading near Galapagos. *Science*, **158**, 775–779.
- Hess, H. H., 1962. "History of ocean basins," in *Petrologic studies: A Volume in Honor of A. F. Buddington*, Geol. Soc. Amer., New York, pp. 599–620.

- Hess H. H., 1965. Mid-oceanic ridges and tectonics of the sea-floor. *Colston Papers*, **17**, 317-332.
- Hurley, R. J., 1960. The geomorphology of the abyssal plains in the Northeast Pacific Ocean (unpublished manuscript), Scripps Inst. Oceanography, San Diego, 105 pp.
- Isacks, B., J. Oliver, and L. R. Sykes, 1968. Seismology and the new global tectonics. *J. Geophys. Res.*, **73**, 5855-5899.
- Lattimore, R. K., B. G. Bassinger, and O. E. DeWald, 1968. Magnetic map from the coast of California to 133°W longitude. Misc. Geol. Inv. Map. I-531A, U.S. Geol. Surv., Washington, D.C.
- Le Pichon, X., and J. R. Heirtzler, 1968. Magnetic anomalies in the Indian Ocean and sea-floor spreading. *J. Geophys. Res.*, **73**, 2101-2117.
- Loncarevic, B. D., C. S. Mason, and D. H. Matthews, 1966. Mid-Atlantic ridge near 45° North, I, The Median Valley. *Can. J. Earth Sci.*, **3**, 327-349.
- Ludwig, W. J., J. I. Ewing, M. Ewing, S. Murauchi, N. Den, S. Asano, H. Hotta, M. Hayakawa, T. Asanuma, K. Ichikawa, and I. Noguchi, 1966. Sediments and structure of the Japan trench. *J. Geophys. Res.*, **71**, 2121-2137.
- Malahoff, A., 1968. Detailed geophysical studies of the Murray Fracture Zone (abstract). *Trans. Amer. Geophys. Un.* **49**, 213.
- Mason, R. G., 1958. A magnetic survey off the west coast of the United States between latitudes 32° and 36°N, longitudes 121° and 128°W. *Geophys. J.*, **1**, 320-329.
- Mason, R. G., and A. D. Raff, 1961. A magnetic survey off the west coast of North America, 32°N to 42°N. *Bull. Geol. Soc. Amer.*, **72**, 1259-1265.
- McManus, D. A., 1965. Blanco fracture zone, Northeast Pacific Ocean. *Marine Geol.*, **3**, 429-455.
- Menard, H. W., 1964. *Marine Geology of the Pacific*, McGraw-Hill, New York, 271 pp.
- Menard, H. W., 1967. Extension of northeastern Pacific fracture zones. *Science*, **155**, 72-74.
- Menard, H. W., and R. S. Dietz, 1951. Submarine geology of the Gulf of Alaska. *Bull. Geol. Soc. Amer.*, **62**, 1263-1285.
- Morgan, W. J., 1968. Rises, trenches, great faults, and crustal blocks. *J. Geophys. Res.*, **73**, 1959-1982.
- Mudie, J. D., and C. G. Harrison, 1967. Deep-tow profiles across Mason-Raff lineations (abstract). *Trans. Amer. Geophys. Un.*, **48**, 133.
- Nichols, H., and R. B. Perry, 1966. *Bathymetry of the Aleutian Arc, Alaska*. Six maps by U.S. Coast and Geodetic Survey, ESSA.
- Ninkovich, D., N. Opdyke, B. C. Heezen, and J. H. Foster, 1966. Paleomagnetic stratigraphy, rates of deposition and tephrochronology in North Pacific deep-sea sediments. *Earth Planet. Sci. Letters*, **1**, 476-492.
- Opdyke, N. D., B. Glass, J. D. Hays, and J. Foster, 1966. Paleomagnetic study of Antarctic deep-sea cores. *Science*, **154**, 349-357.
- Pavoni, N., 1966. Tectonic interpretation of the magnetic anomalies southwest of Vancouver Island. *Pure Appl. Geophys.*, **63**, 172-209.
- Peter, G., 1965. "Preliminary results of a systematic geophysical survey south of the Alaska Peninsula," in *Continental Margins and Island Arcs*, Geol. Surv. Canada Papers, 66-15, pp. 223-237.
- Peter, G., 1966. Magnetic anomalies and fracture pattern in the Northeast Pacific Ocean. *J. Geophys. Res.*, **71**, 5365-5374.
- Peter, G., and H. B. Stewart, Jr., 1965. Ocean Surveys: the systematic approach. *Nature*, **206**, 1017-1018.
- Peter, G., D. Elvers, and M. Yellin, 1965. Geological structure of the Aleutian Trench southwest of Kodiak Island. *J. Geophys. Res.*, **70**, 353-366.
- Peter, G., and R. Lattimore, 1969. Magnetic structure of the Juan de Fuca-Gorda ridge area. *J. Geophys. Res.*, **74**, 586-593.

- Pitman, W. C., III, and D. E. Hayes, 1968. Sea-floor spreading in the Gulf of Alaska (abstract). *Trans. Amer. Geophys. Un.*, **49**, 208.
- Pitman, W. C., III, E. M. Herron, and J. R. Heirtzler, 1968. Magnetic anomalies in the Pacific and sea-floor spreading. *J. Geophys. Res.*, **73**, 2069–2085.
- Raff, A. D., 1968. Sea-floor spreading, another rift. *J. Geophys. Res.*, **73**, 3699–3705.
- Raff, A. D., and R. G. Mason, 1961. Magnetic survey off the west coast of North America, 40°N to 52½°N. *Bull. Geol. Soc. Amer.*, **72**, 1259–1265.
- Scholl, D. W., and R. von Huene, 1968. Spreading of the ocean floor: Undeformed sediments in the Peru-Chile Trench. *Science*, **159**, 869–871.
- Shor, G. G., 1962. Seismic refraction studies off the coast of Alaska. *Bull. Seism. Soc. Amer.*, **52**, 37–55.
- Shor, G. G., 1965. Structure of the Aleutian Ridge, Aleutian Trench, and Bering Sea (abstract). *Trans. Amer. Geophys. Un.*, **46**, 196.
- Shor, G. G., P. Dehlinger, H. K. Kirk, and W. S. French, 1968. Seismic refraction studies off Oregon and northern California. *J. Geophys. Res.*, **73**, 2175–2194.
- Spiess, F. N., B. P. Luyendyk, and J. D. Mudie, 1968. Geological observations of abyssal hills using a deeply towed instrument package (abstract). *Trans. Amer. Geophys. Un.*, **49**, 213–214.
- Sykes, L. R., 1967. Mechanism of earthquakes and nature of faulting on the mid-oceanic ridges. *J. Geophys. Res.*, **72**, 2131–2153.
- Talwani, M., C. Windisch, and M. Langseth, 1968. Recent geophysical studies on the Reykjanes Ridge (abstract). *Trans. Amer. Geophys. Un.*, **49**, 201.
- Vacquier, V., A. D. Raff, and R. E. Warren, 1961. Horizontal displacement in the floor of the Pacific Ocean. *Bull. Geol. Soc. Amer.*, **72**, 1267–1270.
- van Andel, Tj. H., J. B. Corliss, and V. T. Bowen, 1967. The intersection between the Mid-Atlantic Ridge and the Vema fracture zone in the North Atlantic. *J. Marine Res.*, **25**, 343–351.
- van Andel, Tj. H., and C. O. Bowin, 1968. Mid-Atlantic ridge between 22° and 23° North latitude and the tectonics of mid-ocean rises. *J. Geophys. Res.*, **73**, 1279–1298.
- Vine, F. J., 1966. Spreading of the ocean floor: New evidence. *Science*, **154**, 1405–1415.
- Vine, F. J., and D. H. Matthews, 1963. Magnetic anomalies over oceanic ridges. *Nature*, **199**, 947–949.
- Vine, F. J., and J. T. Wilson, 1965. Magnetic anomalies over a young oceanic ridge off Vancouver Island. *Science*, **150**, 485–489.
- Wilson, J. T., 1965[a]. A new class of faults and their bearing on continental drift. *Nature*, **207**, 343–345.
- Wilson, J. T., 1965[b]. Transform faults, oceanic ridges, and magnetic anomalies southwest of Vancouver Island. *Science*, **150**, 482–485.
- Worzel, J. L., 1965. Deep structure of coastal margins and mid-oceanic ridges. *Colston Papers*, **17**, 335–359.

Bathymetry off central northwest Africa*

PETER A. RONA†

(Received 13 July, 1970; revised and accepted 3 September 1970)

Abstract—A preliminary bathymetric chart of an area about 10^6 km² extending from Cap Blanc, Mauritania, to the abyssal hills near 30°W, was constructed from about 8000 km of sounding tracks recorded by the USNS *Gibbs* in 1968 plus other earlier soundings. Major unnamed U-shaped submarine canyons attain widths of 85 km and a relief of 700 m where they cross the continental slope and upper continental rise between 20° and 25°N; narrow V-shaped canyons attain widths of 10 km and a relief of 300 m between 18° and 20°N.

Comparison of bottom morphology with patterns of atmospheric and oceanic circulation suggests that wind transport of sediment derived from North Africa is a major process in shaping the Cape Verde Plateau.

INTRODUCTION

ABOUT 8000 km of sounding tracks recorded by the USNS *J. W. Gibbs* in 1968 were combined with earlier soundings to construct a preliminary bathymetric chart which delineates the northern edge of the Cape Verde Plateau, major submarine canyons, and specific topographic features between the continental shelf and the abyssal hills near 30°W (Fig. 1). Previous bathymetric charts, based on a low density of sounding tracks, outline an unusually wide continental rise off central northwest Africa contiguous with the Cape Verde Plateau (Fig. 2) (U.S.N. OCEANOGRAPHIC OFFICE, 1952, 1961; INTERNATIONAL HYDROGRAPHIC BUREAU, 1958; HEEZEN and THARP, 1968).

Navigation on the *Gibbs* was performed by Omega with an estimated positional accuracy of ± 5 nm (ZUCCARO and RONA, 1968). Soundings were made with a 12 kHz 60° full beam width Edo UQN sonar transducer and recorded on a Raytheon 192 Precision Fathometer Recorder.

SUBMARINE CANYONS

Submarine canyons of major dimensions, either absent or less completely shown on prior charts, occur on the continental slope and upper continental rise between 18° and 26°N (Fig. 1). Seismic reflection profile *A-A'* parallel with the lower continental slope (Fig. 3) records U-shaped canyons with axes at 180, 225, 350 and 470 km which range in shoulder-to-shoulder width between 35 and 85 km and in floor-to-shoulder relief between about 350 and 780 m (Table 1). Each is underlain by a succession of buried troughs to at least 1.5 km (1.5 sec) acoustic penetration. These are directly below the canyon axis at 470 km and are offset 10–20 km south of the axes at 225, and 340 km. The sediment-water interface of the intercanyon areas (divides

*The field work was supported by the Office of Naval Research under Contract Nonr-266 (84). Reproduction in whole or in part is permitted for any purpose of the United States Government.

†NOAA Atlantic Oceanographic and Meteorological Laboratories, 901 South Miami Avenue, Miami, Florida 33130.

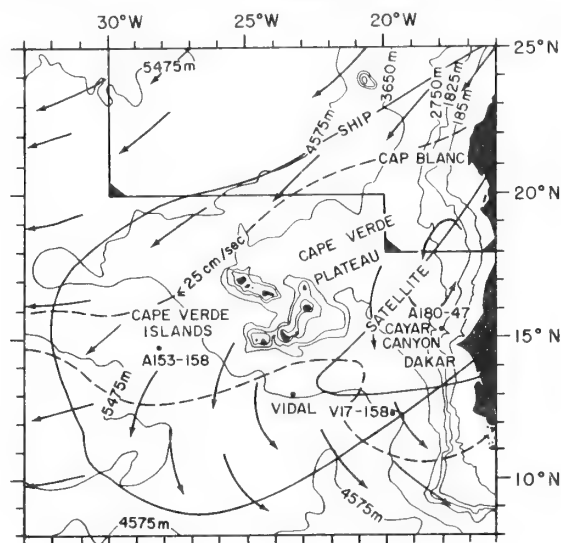


Fig. 2. Regional bathymetric chart showing the relation of the area in Fig. 1 (outlined) to the Cape Verde Plateau (U.S.N. OCEANOGRAPHIC OFFICE, 1961; DIETZ *et al.*, 1969). Directions of ocean surface currents (arrows) and a current velocity contour (≤ 25 cm/sec) (U.S.N. OCEANOGRAPHIC OFFICE, 1965, Figs. 1-5) are indicated. Envelopes are shown of most frequent dust fall occurrence (ship) (after FOLGER, 1970, Fig. 1) and of a dust storm photographed by ESSA 5 satellite on 7 June, 1967 (satellite) (PROSPERO *et al.*, 1970, Figs. 3 and 4). The locations of sediment cores (A153-158, A180-47, V17-158) (ERICSON *et al.*, 1961) and of an atmospheric dust sample collected aboard H.M.S. *Vidal* on 17 January, 1965 are also shown (FOLGER, 1970).

Table 1. Submarine canyons which cross the continental slope off Cap Blanc, Mauritania measured from precision echo-sounding records made with a 12 kHz 60° total beam width sonar transducer.

Canyon shoulder-to-shoulder distances along profile A-A' (Fig. 3) (km)	Width shoulders (km)	Width floor (km)	Depth N. shoulder (m)	Depth S. shoulder (m)	Depth floor (m)	Maximum floor-to-shoulder relief (m)
144-145	1	0.5	2200	2190	2225	35
145-205	60	15	2190	1770	2550	780
206-208	2	0.5	1790	1765	1915	150
210-245	35	10	1750	1775	2100	350
230-232	2	1	2120	2100	2210	110
265-305	40	5	1710	1885	1950	240
305-385	80	25	1885	1855	2550	695
390-425	35	10	1860	1605	2020	415
425-510	85	25	1605	1720	2290	685
470-473	3	0.5	2240	2230	2350	120
520-523	3	2	1815	1790	1900	110
531-534	3	1	1885	1900	2050	165
538-540	2	1	1945	1945	2160	215
541-542	1	0.5	1980	1940	2140	200
556-566	10	9	1805	1810	1875	70
582-585	3	1	1805	1825	1990	185
604-611	7	1	1765	1875	2065	300
622-623	1	0.5	1935	1950	2080	145
628-630	2	1	1925	1960	2070	145
649.5-650.0	0.5	0.25	1960	1920	2080	160
651-652	1	0.5	1935	1960	2060	125

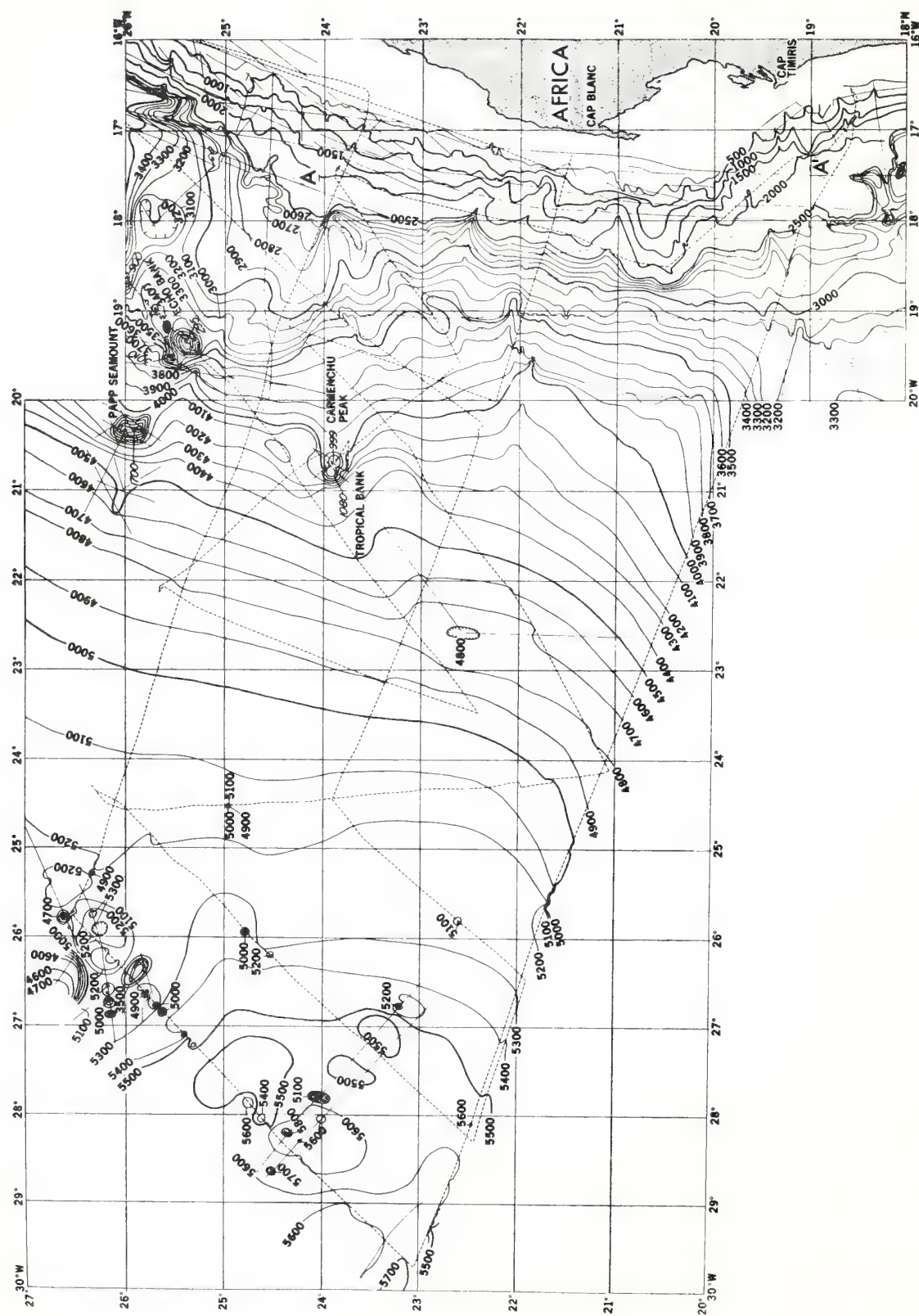


Fig. 1. The bathymetry off central northwest Africa with sounding tracks of the USNS *Gibbs* (dashed) and prior sounding tracks (dotted) of the British National Institute of Oceanography, the Russian Marine Hydrographic Institute, and the U.S. Naval Oceanographic Office (INTERNATIONAL HYDROGRAPHIC BUREAU, 1968). Soundings are in meters corrected for ships draft (+ 4 m) and vertical sounding velocity (MATTHEWS, 1939, area 12). Isobath interval is 500 m between 500 and 2500 m and 100 m at greater depths. The continental shelf break is near the 100 m isobath. (facing p. 322)

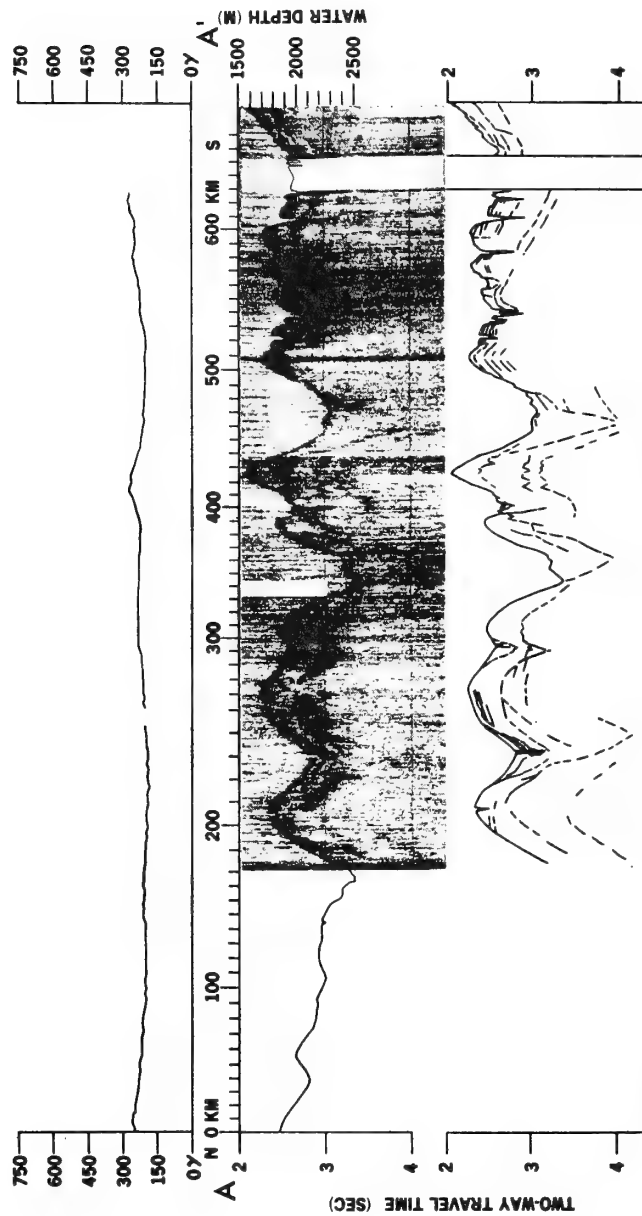


Fig. 3. Profile A-A' (Fig. 1) parallel with the lower continental slope includes a residual magnetic profile (top), an air gun seismic reflection profile (middle) and a line drawing of the seismic profile (bottom). Vertical exaggeration is about 100 : 1.

between canyons including walls) are convex-up and are generally underlain by sub-parallel convex-up strata. Smaller narrow V-shaped canyons are situated on the crests of intercanion areas at 145 and 207 km and are nearly centered within U-shaped canyons at 231 and 471 km. A succession of narrow (≤ 10 km wide), steep-walled, roughly V-shaped canyons with flat floors is present off Cap Timiris between 510 and 630 km.

SEAMOUNTS

Major seamounts known off Cap Blanc are Echo Bank and Papp Seamount based on soundings and nomenclature of the British National Institute of Oceanography (INTERNATIONAL HYDROGRAPHIC BUREAU, 1968) and Tropical Bank (INTERNATIONAL HYDROGRAPHIC BUREAU, 1958) contoured from *Gibbs* sounding tracks (Fig. 1). Tropical Bank consists of two distinct peaks at nearly equivalent depths aligned NW-SE with a common base deeper than about 2000 m below sea level, rather than a single peak as previously shown (U.S.N. HYDROGRAPHIC OFFICE, 1952). The 9-km wide summit of the southeastern peak* is nearly flat with local protuberances, possibly coral, which rise up to about 25 m above the 999-m summit (Fig. 4). This is less than the previous minimum depths of 1696 m (U.S.N. HYDROGRAPHIC OFFICE, 1952) and 1055 m (INTERNATIONAL HYDROGRAPHIC BUREAU, 1958). A bench about 0.5 km wide indents the northeast side at about 1050 m below sea level.

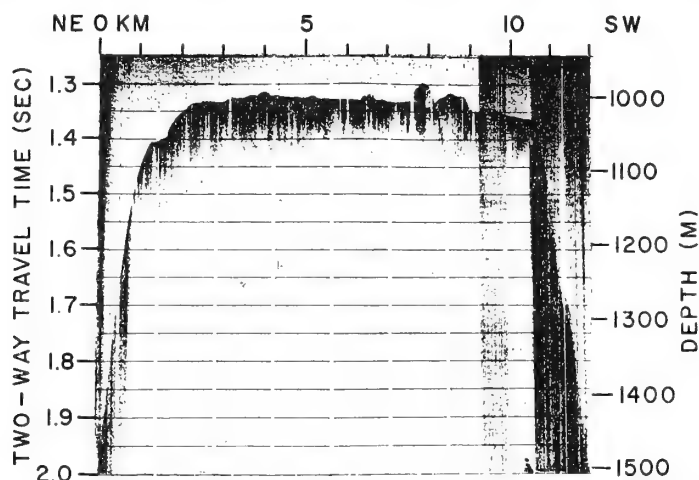


Fig. 4. Minimum depth bathymetric profile across the summit of Carmenchu Peak on Tropical Bank. A bench faces northeast at about 1050 m below sea level. Vertical exaggeration is about 20 : 1.

DISCUSSION

Knowledge of geological processes considered important in the shaping of the more thoroughly investigated continental margin off eastern North America is helpful in the interpretation of the morphology on the northwest African continental margin. Submarine canyons on the continental slope off Cape Hatteras are inferred

*I propose to name this southeastern summit of Tropical Bank 'Carmenchu Peak', in honor of Me. del Carmen Piernavieja y Oramas of Las Palmas, Canary Islands, Spain.

to have developed by depositional upbuilding of the walls (intercanyon areas), while the channels were maintained over sites of original incision by sediment transport processes (RONA, 1970). Some of the original incisions off Cap Blanc appear to have been structurally controlled at the intersections of oceanic fracture zones with the continental margin (RONA, 1969). As off Cape Hatteras, the canyons off Cap Blanc are underlain by buried troughs and the intercanyon areas by convex-up strata sub-parallel with the sediment-water interface. The similarity in the formations implies that similar processes have been active in the development of canyons on the continental slopes on both sides of the Atlantic. The scale differs, the canyons on the continental slope off Cap Blanc attaining about twice the relief and several times the width of those off Cape Hatteras (Table 1; RONA *et al.*, 1967). As canyon relief is inferred to be constructural, the differences in relief indicate that higher rates of sediment accumulation have prevailed off Cap Blanc.

The Cape Verde Plateau forms a roughly triangular salient encompassing the Cape Verde archipelago with base extending along the continental shelf from about 12° to 22°N and apex reflected as far as 1000 km seaward to the 4575-m isobath (Figs. 1 and 2). Continental rise isobaths inflect around the northern and southern flanks of the Cape Verde Plateau delineating a broad central ridge between Cap Blanc and Dakar which converges toward the Cape Verde Islands. Seismic reflection profiles reveal sediment in excess of 2 km (2 sec) with the acoustic character of stratified lutite (silt and clay size) beneath this ridge (Fig. 3; LOWRIE and ESCOWITZ, 1969, Kane 9 D,E,F). The smoothness of the residual magnetic field along the continental slope (Fig. 3) also indicates the presence of a thick sedimentary column. The 700-m relief of Cayar Canyon where it crosses the continental slope off Dakar (Fig. 2) (DIETZ *et al.*, 1968) is comparable to that of canyons off Cap Blanc (Table 1), suggesting that relatively high rates of sediment accumulation have affected the entire landward margin of the Cape Verde Plateau. Post-glacial rates of accumulation of lutite cored from the wall of Cayar Canyon are 20 cm/1000 y (ERICSON *et al.*, 1961, core A180-47, Table 5).

Wind-borne dust has frequently been observed off northwest Africa from sea-level to several kilometers above sea-level by ships (FOLGER, 1970), aircraft (PROSPERO and CARLSON, 1970), and satellites (PROSPERO *et al.*, 1970). A striking spatial correlation exists between the shapes and areas of the envelope of most frequent dust falls and the Cape Verde Plateau (Fig. 2). This correlation suggests a possible genetic relation between the pattern and volume of eolian sediment transport and sediment deposition on the Cape Verde Plateau. On the basis of similarities of composition, texture, and consideration of air parcel trajectories of the prevailing trade winds, silt and clay-sized material has been traced from North African soils to the dust envelope off northwest Africa (FOLGER, 1970; PROSPERO *et al.*, 1970), to surface sea water samples (FOLGER, 1970), and finally to deep-sea sediments (FOLGER, 1970). The ratios of clay minerals measured in tops of sediment cores from the Cape Verde Plateau (BISCAYE, 1965, cores A153-158, V17-158) are similar to those collected from the adjacent atmosphere (Fig. 2) (FOLGER, 1970, Fig. 9, Table 3). Cores recovered from the Cape Verde Plateau contain lutite (ERICSON *et al.*, 1961, A180-51, 53, 56) with the exception of those from the floor of Cayar Canyon which contain sand (A180-49, 50), probably derived from the adjacent shelf where sand predominates (MCMASTER and LACHANCE, 1968).

Oceanographic conditions immediately underlying the dust envelope favor the persistence of the fallout pattern as particles settle from the sea surface, through the water column, to the bottom. The velocity of surface currents, affecting perhaps the upper 200 m, is less than 25 cm/sec in an area over the Cape Verde Plateau (Fig. 2). The deep thermohaline circulation is predicted to be weak and diffuse on the eastern boundary of the North Atlantic (WÜST, 1957; DEFANT, 1961) and direct observations indicate negligible near bottom currents at present (LOWRIE *et al.*, 1970). The irregular topographic relief of the Cape Verde archipelago would further act to trap sediment on the bottom. The amount of atmospheric fallout might be expected to decrease away from the sediment source, which corresponds with the seaward narrowing and apparent thinning of the sedimentary apron that forms the Cape Verde Plateau. The northeast orientation of the bench observed on Tropical Bank (Fig. 4) indicates that the bench was cut by surf driven from the present prevailing wind direction and suggests that an eolian sediment transport system may have been in effect long enough to shape the Cape Verde Plateau and prograde the continental rise.

Acknowledgements—WILLIAM P. OSBORN, formerly with Hudson Laboratories of Columbia University, assisted with the bathymetric chart. HENRY S. FLEMING of U.S. Naval Research Laboratory gave helpful encouragement. Dr. A. S. LAUGHTON of the British National Institute of Oceanography provided charts of Echo Bank and Papp Seamount. Conversations with Drs. LOUIS W. BUTLER and GEORGE H. KELLER of NOAA were valuable. Dr. ROBERT S. DIETZ and PAUL J. GRIM of NOAA constructively criticized the manuscript. ERNEST L. BERGERON, Consular Agent of the U.S., facilitated matters when the *Gibbs* made port in the Canary Islands. Captain RAYMOND E. SALMAN and the officers and crew of the USNS *J. W. Gibbs* provided splendid co-operation.

REFERENCES

- BISCAYE P. E. (1965) Mineralogy and sedimentation of recent deep-sea clay in the Atlantic Ocean and adjacent seas and oceans. *Bull. Geol. Soc. Am.*, **76**, 803–831.
- DEFANT A. (1961) *Physical Oceanography*. Macmillan, New York, Vol. 1, 729 pp.
- DIETZ R. S., H. J. KNEBEL and L. H. SOMERS (1968) Cayar submarine canyon. *Bull. Geol. Soc. Am.*, **79**, 1821–1828.
- ERICSON D. B., M. EWING, G. WOLLIN and B. C. HEEZEN (1961) Atlantic deep-sea sediment cores. *Bull. Geol. Soc. Am.*, **72**, 193–286.
- FOLGER D. W. (1970) Wind transport of land-derived mineral, biogenic, and industrial matter over the North Atlantic. *Deep-Sea Res.*, **17**, 337–352.
- HEEZEN B. C. and M. THARP (1968) Physiographic diagram of the North Atlantic Ocean. *Spec. Pap. Geol. Soc. Am.*, **65**, revised.
- INTERNATIONAL HYDROGRAPHIC BUREAU (1958) *Carte Générale Bathymétrique des Océans*, 4th edition, Monaco.
- INTERNATIONAL HYDROGRAPHIC BUREAU (1968) Sheets 103, 104, 128, 129 for the *Carte Générale Bathymétrique des Océans*, Monaco.
- LOWRIE A. and E. ESCOWITZ, editors (1969) *Kane 9. U.S.N. Oceanogr. Off. Global Ocean Floor Analysis Res. Data*, Ser. 1, 1–971.
- LOWRIE A., W. JAHN and J. EGLOFF (1970) Bottom current activity in the Cape Verde and Canaries Basin, Eastern Atlantic. *Trans. Am. geophys. Un.*, **51**, 336.
- MATTHEWS D. J. (1939) *Tables of the velocity of sound in pure water and sea water*. Admiralty, Hydrographic Department, London, 52 pp.
- MCMASTER R. L. and T. P. LACHANCE (1970) Northwestern African continental shelf sediments. *Marine Geol.*, **7**, 57–67 (1969).
- PROSPERO J. M. and T. N. CARLSON (1970) Radon-222 in the North Atlantic trade winds: Its relationship to dust transport from Africa. *Science*, **167**, 974–977.
- PROSPERO J. M., E. BONATTI, C. SCHUBERT and T. N. CARLSON (1970) Dust in the Caribbean atmosphere traced to an African dust storm. *Earth Planet. Sci. Letters*, in press.

- RONA P. A. (1969) Seismic reflection profiles from northwest African continental margin between Canary and Cape Verde islands (abs.). *Trans. Am. geophys. Un.*, **50**, 211.
- RONA P. A. (1970) Submarine canyon origin on upper continental slope off Cape Hatteras. *J. Geol.*, **78**, 141–152.
- RONA P. A., E. D. SCHNEIDER and B. C. HEEZEN (1967) Bathymetry of the continental rise off Cape Hatteras. *Deep-Sea Res.*, **4**, 625–633.
- U.S.N. HYDROGRAPHIC OFFICE (1952) *Bottom Contour Chart 0305N*, 1st edition.
- U.S.N. OCEANOGRAPHIC OFFICE (1961) The world. *H. O. Misc.*, **15**, 254–257.
- U.S.N. OCEANOGRAPHIC OFFICE (1965) Oceanographic atlas of the North Atlantic Ocean, Section I Tides and Currents. *USNOO Pub. 700*. 75 pp.
- WÜST G. (1957) Stromgeschwindigkeiten und Strommengen in den Tiefen des Atlantischen Ozeans. *Wiss. Ergebn. dt. Atlant. Exped. 'Meteor'*, **6** (2), 261–420.
- ZUCCARO A. and P. A. RONA (1968) Omega navigation performance off northwest Africa during operation no. 267, April 23–May 28, 1968. *Tech. Rept. Columbia Univ. Hudson Lab.*, **153**, 36 pp. (unpublished manuscript).

deep-sea salt diapirs

The case for deep-sea salt diapirs is alive and well in spite of reports to the contrary. Leg 14 of the Deep Sea Drilling Project (February 1971 *Geotimes*) obtained evidence from 2 drilling sites off northwest Africa supporting the existence of deep-sea salt deposits. At both Sites 139 and 140, in water depths of 3,047 and 4,483 m, on the middle and lower continental rise, the sediments showed marked salinity gradients (38 to 75 ppt in 665 m penetration at Site 139; the salinity of sea water is generally about 35 ppt). These 2 sites are situated where I have interpreted the presence of possible salt diapirs from geophysical data and regional geologic considerations (Rona, 1969, *Nature*, v. 224, p. 141-143; American Association of Petroleum Geologists *Bulletin*, v. 54, p. 129-157). The diffusion rates of ions in saturated unconsolidated sediments are so high ($\frac{1}{2}$ to $\frac{1}{20}$ of diffusion rates in free solution according to Manheim (1970, *Earth and planetary science letters* 9, p. 307-309) that a signifi-

cant source concentration at depth is required to maintain the observed salinity gradients. The salinity gradients observed off northwest Africa are comparable to those in sediments over salt deposits in the Gulf of Mexico (Manheim & Sayles, 1970, *Science*, v. 170, p. 57-61).

The Leg 14 report emphasizes the drilling of a basalt body at Site 141, 200 km north of the Cape Verde Islands, that was interpreted as a salt diapir (Schneider & Johnson, 1970, *AAPG Bulletin*, v. 54, p. 2,151-2,169, figure 8). The hypothesis of deep-sea salt diapirs should not be judged on evidence from this single site but should await more evidence including publication of the Leg 14 salinity studies. The model which I postulated of the early Atlantic as an evaporite basin restricted by the Late Triassic/Jurassic positions of the drifting continents remains reasonable.

Peter A. Rona

NOAA, Atlantic Oceanographic & Meteorologic Laboratories
Miami, Fla.

Depth Distribution in Ocean Basins and Plate Tectonics

IN this article I shall show that relationships between the movement of lithospheric plates¹⁻³ and the depths of the sea floor are leading towards a quantitative theory of the distribution of oceanic depths, and that some predictions can be made. Several principal lithospheric plates have now been recognized; their relative motion over the mantle is described by a rotation of one plate relative to an adjacent plate⁴⁻⁶. The rotation requires two parameters to locate the pole of relative rotation, and one to specify the magnitude of the angular velocity. The direction of spreading is along small circles concentric about the pole of rotation and the velocity of spreading varies as the sine of the distance (measured in degrees of arc) from that pole, to a maximum at a distance of 90° along the equator of rotation. The angular velocity of rotation is the same everywhere. In the Atlantic Ocean the fracture zones between about 60° N and 10° S are very nearly small circles centred about a pole near the southern tip of Greenland (62 ± 5° N, 36 ± 2° W), and the spreading rates approximately agree with the velocities required for the opening of the North Atlantic about this pole^{1,3}.

Examination of the topography of the sea floor and spreading rates in the central region of the world system of mid-ocean ridges shows that the width of the ridge⁷, the local topography⁸, and the thickness of layer 2 of the oceanic crust⁸ seem to be related to the spreading rate in the following way. (1) Slow spreading (1-2 cm yr⁻¹) away from the ridge centre is associated with a narrow ridge, a central rift, adjacent rift mountains and a thick layer 2. (2) Fast spreading (3-4.5 cm yr⁻¹) is associated with a wide ridge, subdued topography (no central rift) and a thin layer 2. (3) The volume of lava discharged in layer 2 per unit time and unit length along the crest of the whole active system is relatively constant regardless of the spreading rate. Thus, topography and the thickness of layer 2 can be predicted if the rate of spreading is known.

An examination of topographic profiles perpendicular to various sections of the world mid-ocean ridge system supports the inference that topography is a function of spreading rate⁹. The relationship between the slope of ridge flanks and the spreading rate from the ridge crest to magnetic anomaly No. 5 at a distance corresponding to 10⁷ yr was formulated from this series of profiles so that, by knowing the spreading rate, the slope can be calculated⁹. The faster the spreading rate within an episode of spreading, the lower the topographic slope and roughness, measured over a distance corresponding to the crust generated during that episode. The decrease in

MARINE GEOPHYSICAL OBSERVATIONS OF
THE EASTERN PUERTO RICO-VIRGIN ISLANDS REGION

by

Robert B. Starr and Robert G. Bassinger

Atlantic Oceanographic Laboratories, Environmental Science Services Administration, Miami, Florida 33130

Abstract

During early May 1966, a combined bathymetric, seismic reflection profile, and total magnetic field intensity investigation was conducted of the area south and east from Puerto Rico to the Virgin Islands, using precise Hi-Fix navigation control. Except for the exceptionally shallow, flat area of the Puerto Rico-northern Virgin Islands platform, the bathymetry indicates a very irregular submarine topography of basins and block faults. The disturbed magnetic signature over the platform indicates at- or near-surface sources. South of the platform three basins with appreciably different depths were delineated. Sub-bottom reflectors within these basins indicate evidence of recent deformation. Bordering these basins to the south, a broad ridge with peaks at least as shallow as 500 fathoms, except for the shoaler Grappler Bank, extends west from St. Croix. A minor magnetic expression was evident over the ridge, but none was noted for Grappler Bank.

Introduction

The Puerto Rico-Virgin Islands shelf and St. Croix Ridge with the intervening Virgin Islands Trough¹ are at the eastern end of the Greater Antilles sector of the Antilles Arc. The area and tracklines are shown in Figure 1.

This study was conducted from the USC&GSS "Whiting" in 1966. Observations consist of 1,180 nautical miles of hydrographic soundings, continuous seismic reflection profiling, and total magnetic-field intensity observations at a nominal line spacing of 4.6 nautical miles. Ship's position was determined with HI-FIX electronic navigation. Additional lines of hydrography and magnetics were obtained by the USC&GSS "Explorer" in 1965 and one line of hydrography and seismic reflection profiling by the USNS "Lynch" in 1967.

Results

Bathymetry

For convenience of discussion, the bathymetry of the Puerto Rico-Virgin Islands region may be divided into five provinces on the basis of their morphology. From north to south these are (1) south slope of the Puerto Rico Trench (north slope of the shelf), (2) Puerto Rico-Virgin Islands shelf, (3) Virgin Islands Trough, (4) St. Croix Ridge, and (5) north margin of the Venezuelan Basin. These provinces have an east-west trend throughout the study area.

¹ The names "Virgin Islands Trough" *vice* "Virgin Islands Basin," "Grappler Seamount" *vice* "Grappler Bank," "St. Croix Ridge," "Whiting Basin," and "Whiting Seamount" were approved by the U.S. Board of Geographic Names, September 19, 1968.

The upper portion of the south slope of the Puerto Rico Trench (Fig. 2) consists of a short, steep scarp of about 20° terminating between depths of 80 and 940 fathoms. At this point the slope abruptly changes to a 3° gradient which it maintains to the limit of the tracklines. A "V"-shaped depression in this slope at about 65°05'W suggests a submarine canyon.

The Puerto Rico-Virgin Islands shelf is nearly a featureless plain except for the islands and isolated banks and reefs. The northern half, however, averages approximately 15 fathoms deeper than the shallower southern half. From our traverse west of Culebra Island, this depth difference appears to be associated with a fault. Donnelly (1965) relates this declivity between St. Thomas and Culebra to post-Pleistocene faulting.

From the character of the sounding records the steep walls of the Virgin Islands Trough appear to be much rougher than mapped, with spurs intersecting a bottom of discontinuous, relatively flat areas. Southeast of Puerto Rico a small basin (Whiting Basin) is defined by the 1,000-fathom isobath. This basin is separated from the trough by a north-south ridge connecting the Puerto Rico-Virgin Islands shelf with Whiting Seamount. East of the basin the trough deepens to a small plain at 2,200 fathoms which is partially separated from the main floor of the trough (Pl. 1). The main floor is outlined by the 2,400 fathom isobath (Pl. 1 and Fig. 2).

The St. Croix Ridge extends westward from St. Croix to Investigator Bank. West to 65°35'W, the ridge consists of an irregular row of discontinuous highs with northeast-trending spurs. Our soundings indicate that the deepest passage over the ridge occurs between 65°25'W and 65°30'W, and appears to be a little over 1,000 fathoms.

West of 65°35'W, the St. Croix Ridge has a different character from that to the east. It consists of three interconnected peaks: Whiting Seamount, Grappler Seamount, and Investigator Bank. Summits of these are much shallower than the crest of the ridge in the east; the top of Grappler Seamount is only 35 fathoms, for instance, and no consistent trend of the isobaths is apparent.

The north slope of the Venezuelan Basin appears to have a uniform gradient. Except for minor irregularities, the slope averages between 4° and 7°. It descends from the St. Croix Ridge to somewhat over 2,700 fathoms in the southeastern part of the area (Pl. 1).

Sub-Bottom Profiling Results

Seismic reflection results shown in the cross-section (Fig. 2) are form lines showing approximate penetration based on the instrument calibration velocity of 4,800 fps. The quality of the reflection records varied widely throughout the area. Penetration of the south slope of the Puerto Rico Trench was excellent. Several reflectors were observed, decreasing in number and thickness downslope (Fig. 2).

On the shallow Puerto Rico-Virgin Islands shelf, the hard bottom and multiple reflectors limited the profiler results. However, on the lines northeast of Vieques Island, sufficient penetration was obtained to identify southeast-dipping strata as far as three miles offshore (Fig. 3). Southeast of St. Thomas, an anticline was crossed with its limbs dipping northeast and southwest (Fig. 4). In addition, numerous small scarps were crossed. Similar features have been interpreted by Donnelly (1965) as fault scarps.

No significant sub-bottom reflectors were recorded along the walls of the Virgin Islands Trough owing possibly to the lack of sediment on the steep walls. The bottom of the trough, however, consists of good reflectors. These reflectors are flat lying or dip to the south away from a low, northeast-trending ridge which crosses the floor of the trough at 65°05'W. The contacts of the sediments of the trough bottom with the walls are in all cases abrupt and discontinuous. The walls appear to be fault scarps and the trough a graben (Fig. 2) as earlier suggested by Meyerhoff (1927) and Whetten (1966).

On the St. Croix Ridge, the eastern sector has southerly dipping strata on the northern ends of the spurs, but no reflectors were apparent on the main crest of the ridge (Fig. 2) or on the seamounts of the western sector. The profiler record of the top of Grappler Seamount is similar to that of the Puerto Rico-Virgin Islands shelf.

No discernible sedimentary strata were found on the northern slope of the Venezuelan Basin. However, the basin itself provided some of the deepest reflected penetrations recorded (up to 0.7 sec.). On the reflection records the boundary between the basin and the north slope can be placed at an apparent fault scarp (Fig. 2). The abrupt discontinuous contact of the basin sediments with the north slope, and the slump structures with multiple slip planes on some of the sections indicate this boundary to be a fault line. A fault at this general location has been inferred by Meyerhoff (1927) and Donnelly (1964).

Magnetics

Over the southern slope of the Puerto Rico Trench and the northern edge of the Puerto Rico-Virgin Islands shelf the magnetic anomalies are of long wave length and small amplitude (Pl. 2 and Fig. 2). This suggests that the sources of the anomalies are broad relative to their thickness and are probably at a moderate depth.

The magnetic pattern of the Puerto Rico-Virgin Islands shelf proper consists of belts of high amplitude, short wave-length anomalies (Fig. 2) which are more or less parallel to the margins of the shelf. Some of these anomalies are directly associated with known intrusives in the islands and most of them probably reflect the occurrence of near-surface intrusive bodies (Renard, 1967).

The linear magnetic low in the wall of the Virgin Islands Trough (Pl. 2) which coincides with the break in the slope east of Vieques Island suggests the possibility of a fault. This could be an extension of the major east-west fault zone of northern Puerto Rico (Briggs and Akers, 1965; Mattson, 1966).

East of 65°35'W a slight, linear, east-west magnetic high with a corresponding magnetic low to the north is apparently associated with the St. Croix Ridge. A prominent low immediately southeast of St. Croix may be

related to the coastal plain graben found there (Cederstrom, 1950; Whetten, 1966). The western sector of the ridge has noticeable anomalies which correlate with Whiting and Grappler seamounts. To the south, the northern edge of the Venezuelan Basin appears to have a relatively featureless magnetic pattern.

References

1. Briggs, R.P., and Akers, J.P., 1965, Hydrogeologic map of Puerto Rico and adjacent islands: U.S. Geol. Survey Hydrol. Inv. Atlas HA-197.
2. Cederstrom, D.J., 1950, Geology and ground-water resources of St. Croix, Virgin Islands: U.S. Geol. Survey Water Supply Paper 1067, 117 p.
3. Donnelly, T.W., 1964, Evolution of eastern Greater Antillean island arc: Am. Assoc. Petroleum Geologists Bull., v. 48, p. 680-696.
4. ———, 1965, Sea-bottom morphology suggestive of Post-Pleistocene tectonic activity of the eastern Greater Antilles: Geol. Soc. America Bull., v. 76, p. 1291-1294.
5. Mattson, P.H., 1966, Geological characteristics of Puerto Rico: p. 124-138 in Continental margins and island arcs, ed. Poole, W. H.: Geol. Survey Canada Paper 66-15, Ottawa, Queens Printer, 486 p.
6. Meyerhoff, H.A., 1927, The physiography of the Virgin Islands, Culebra, and Vieques: N.Y. Acad. Sci. Scientific Survey of Porto Rico and the Virgin Islands, v. 4, pt. 2, p. 145-219.
7. Renard, V., 1967, Virgin bank: Correlation of magnetism and gravity with geology: Ph.D. Thesis, Rice University, 111 p.
8. Whetten, J.T., 1966, Geology of St. Croix, U.S. Virgin Islands: Geol. Soc. Am. Memoir 98, p. 177-239.

GAMMAS

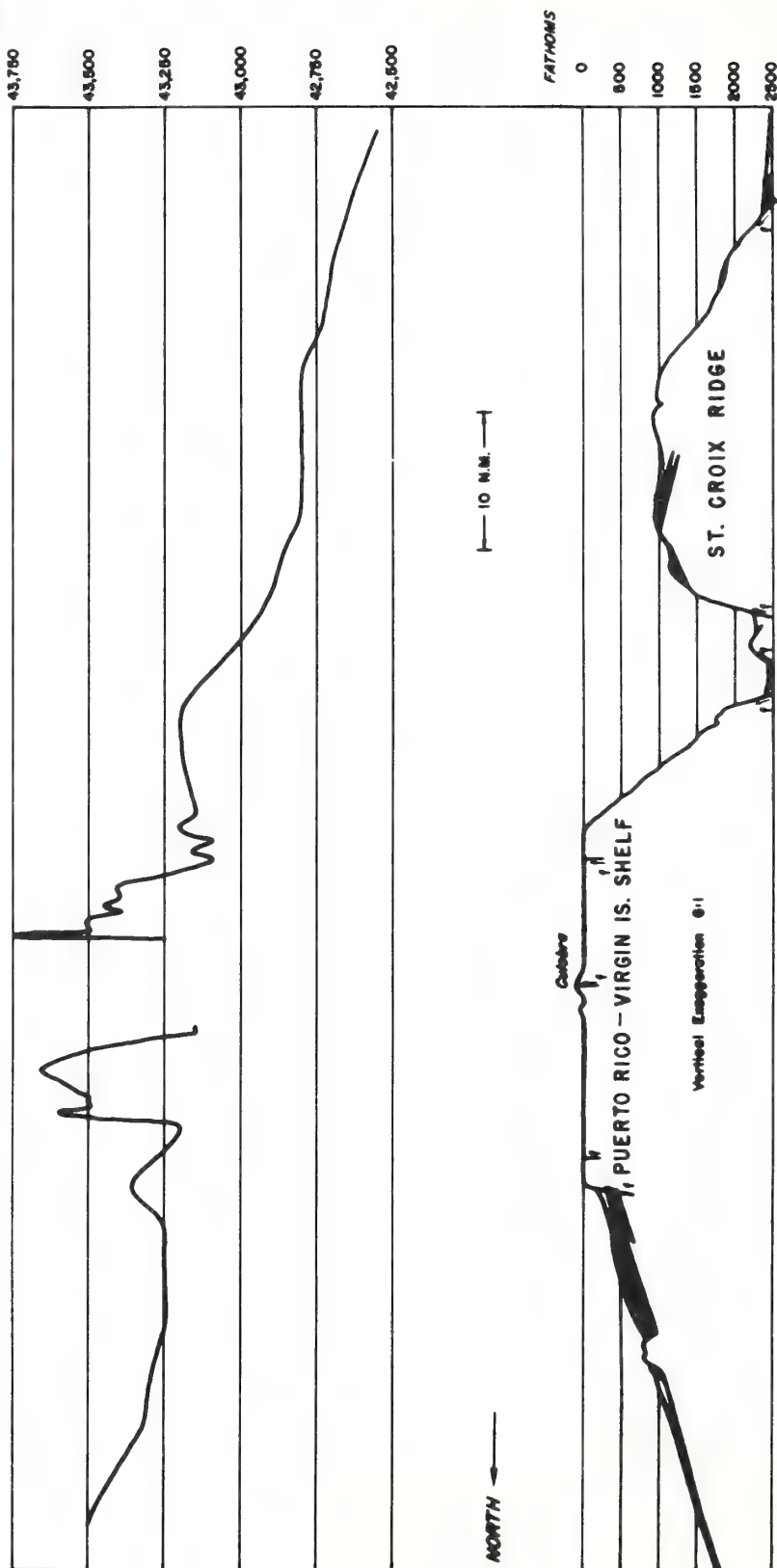


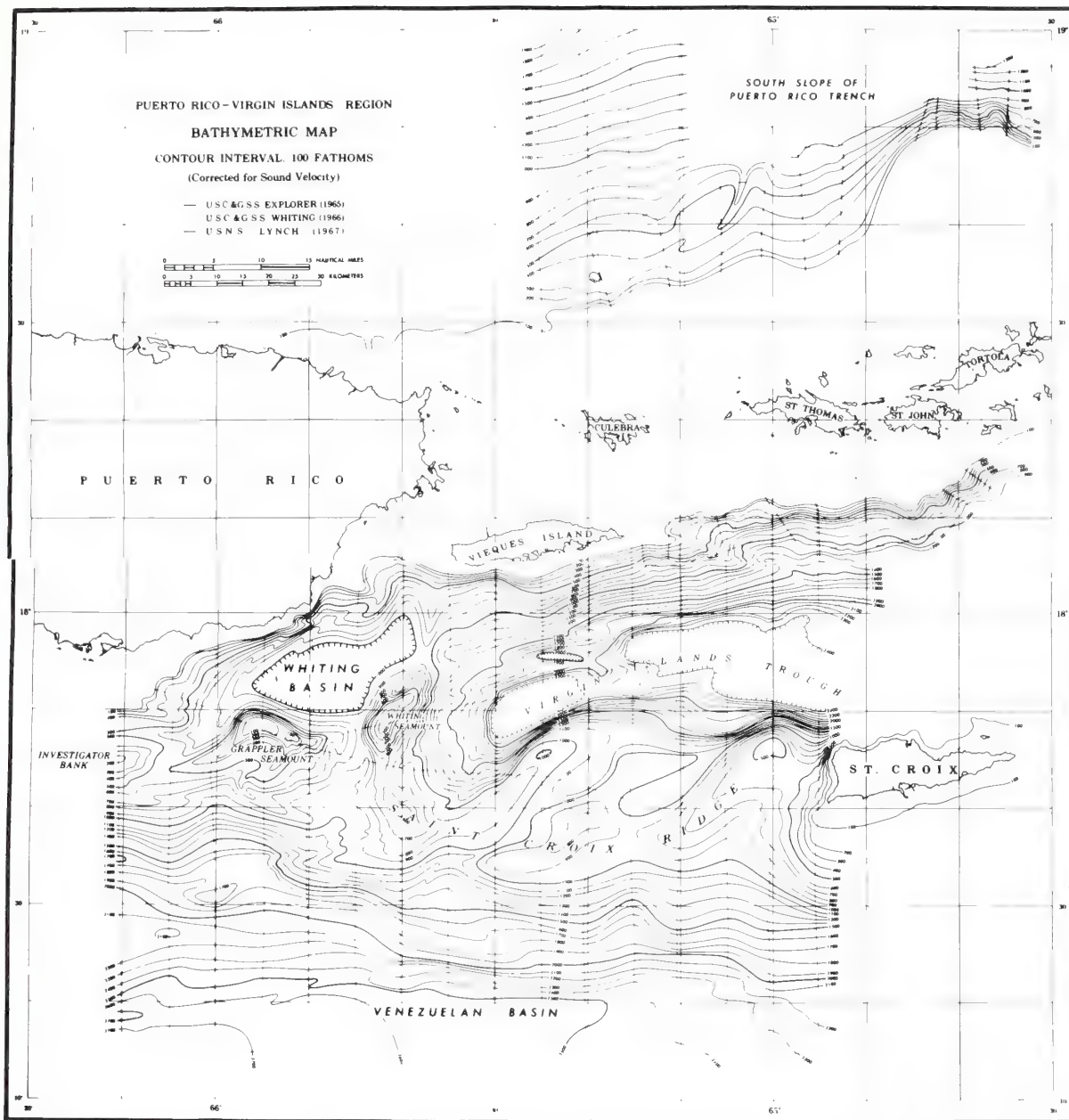
FIGURE 2—Total magnetic intensity, bathymetry, and sub-bottom reflection profile along $65^{\circ} 15' W.$ longitude.

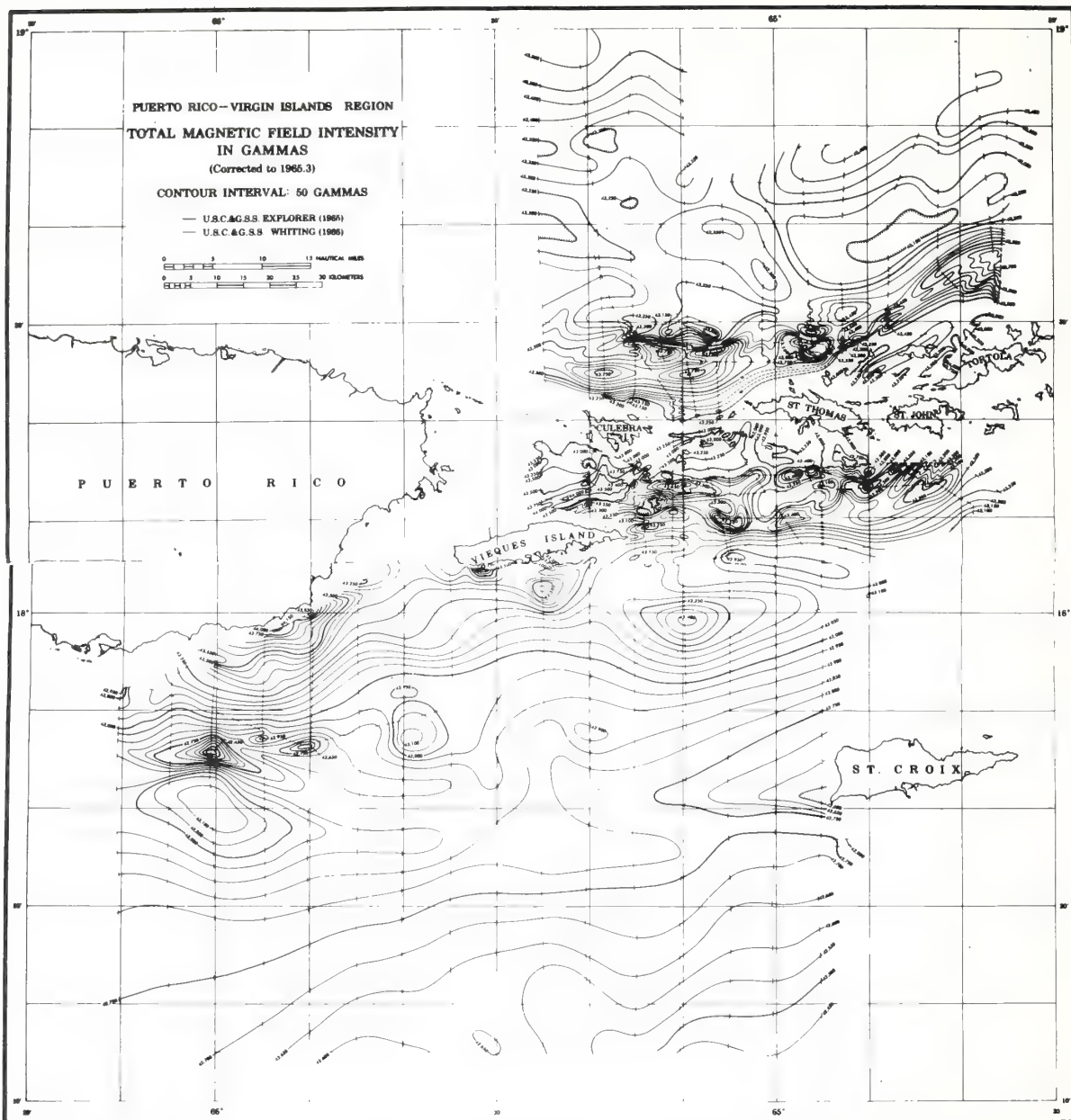


FIGURE 3—Sub-bottom reflection results northeast of Vieques.



FIGURE 4—Sub-bottom reflection results southeast of St. Thomas.





CONTINENTAL TERRACE AND DEEP PLAIN OFFSHORE CENTRAL CALIFORNIA

L. AUSTIN WEEKS* and ROBERT K. LATTIMORE

*Environmental Science Services Administration, Atlantic Oceanographic and
Meteorological Laboratories, Miami, Fla. 33130, U.S.A.*

(Received 21 April, 1970)

Abstract. Seismic-reflection profile investigations of the California continental terrace and Deep Plain, between 35°N and 39°N, support the hypothesis that the continental shelf and slope consist of alternating blocks of Franciscan and granitic-metamorphic basement overlain by varying thicknesses of younger sediments. North of 37°N, the seismic profiles confirm the distribution of turbidites shown by other workers. A significant proportion of the sediments on the middle and lower continental rise, south of 37°N, appears to be unrelated to the present Monterey deep-sea canyon system.

Near 39°N the ridge which forms the topographic axis of the Delgada deep-sea fan consists of a thin cover of acoustically-transparent sediment unconformably overlying a thick sequence of turbidites; the southern part of this ridge is composed of well-defined short reflectors of highly variable dip. The ridge is incised by a steep-walled, flat-floored valley which follows a nearly straight course across its eastern flank. Among possible explanations for this pattern is uplift of the sea floor beneath the ridge.

Our data and investigations of others indicate that acoustic basement north of 38°40'N is at least 0.5 sec (two-way travel time) shoaler than it is south of Pioneer Ridge; when present, the ridge may represent as much as 0.5 sec additional basement relief. This structural pattern probably does not extend east of 127°40'W, although the magnetic expression of the ridge persists to 127°W.

Disappearance of the distinctive abyssal hills topography from west to east within the area of investigation usually can be attributed to burial by turbidites. Normal 'pelagic' sediments form a veneer, rarely more than 0.15 sec thick, which conforms with the basement topography; some localities are devoid of discernible sediment.

1. Introduction

The first regional investigation of the sea floor off central California was part of a study of the entire California coastal margin by Shepard and Emery (1941); along with maps and descriptions of the shelf and slope, their paper includes hypotheses on the evolution of the more important physiographic features. Menard (1955) gave the name, "Deep Plain of the northeastern Pacific", to the area bounded by the Mendocino and Murray fracture zones (Figure 1), and described the area in the context of the tectonic framework of the entire northeastern Pacific basin.

Systematic marine geomagnetic observations in the area bounded by the Mendocino and Murray fracture zones have been reported by Mason (1958), Vacquier *et al.* (1961), Mason and Raff (1961) and others. A detailed bathymetric map of the continental margin, prepared by H. W. Menard, was published in Heezen and Menard (1963, Figure 12) and in more complete form in Winterer *et al.* (1968, Figure 7). Soundings and bottom samples taken across Santa Lucia Bank and the shelf offshore San Fran-

* Present address: 13720 SW 78th Ct., Miami, Fla. 33158, U.S.A.

cisco as part of a regional investigation of the continental slope have been reported by Uchupi and Emery (1963). Curray (1965) has described seismic-reflection profiles of the continental shelf and slope between Santa Lucia Bank and Cape Mendocino. In addition to these regional investigations, there is an extensive literature dealing with individual features within the Deep Plain.

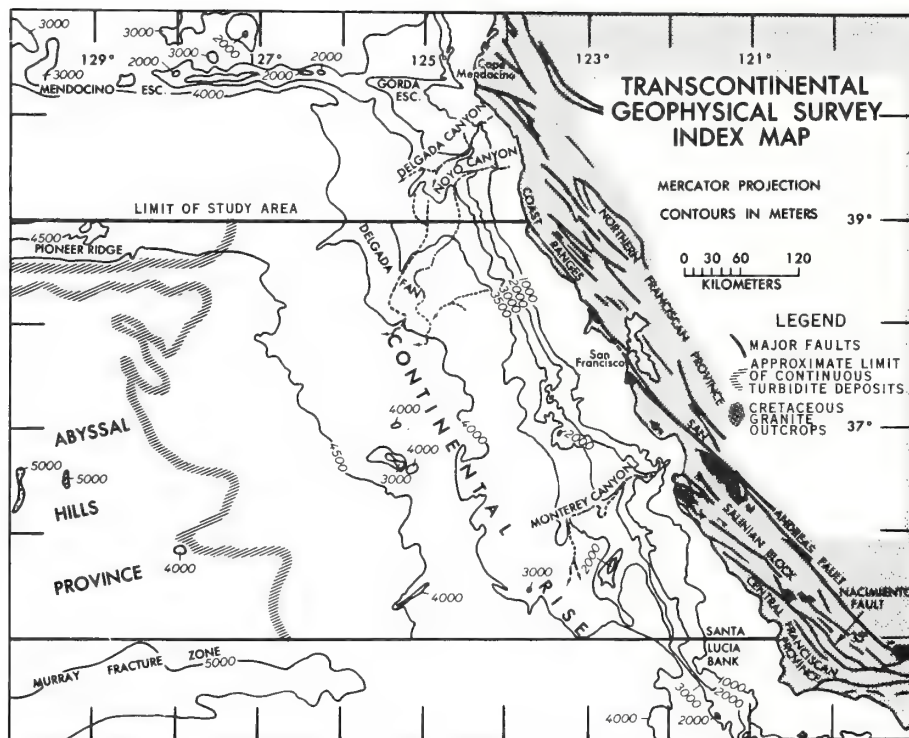


Fig. 1.

In 1965 and 1966, as part of the Environmental Science Services Administration – U.S. Coast and Geodetic Survey contribution to the international Upper Mantle Project, systematic marine geological and geophysical studies were made of the area between 35° and 39° North Latitude, extending from the California coast to 133° West Longitude – the offshore extension of the U.S. Trancontinental Geophysical Survey (TGS) (U.S. Upper Mantle Committee, 1965, p. 115). The TGS investigations included continuous geomagnetic measurements, soundings, and gravity observations along east-west lines spaced at 18-km intervals (Lattimore *et al.*, 1968a, b) as well as the collection of deep-sea cores and heat-flow measurements (Burns and Grim, 1967). The results of the TGS seismic-reflection profile reconnaissance, made by USC&GSS Surveyor in April and May, 1966, are presented in this report.

2. Methods

Continuous seismic-reflection profiles were made along a series of east-west lines, spaced at 50–60 km intervals, extending from the California coast to the base of the continental slope; at 36°N and 39°N, the lines were extended to 130°W (Figure 2). Additional traverses were run to construct a northeast-southwest profile which intersects the continental slope near Pioneer Seamount, and a northwest-southeast profile running roughly along the 4000-m isobath. The seismic profiles were made with a 20,000-joule *Rayflex* 'arcer' fired at 4-sec intervals; the return signal was subjected to a 70–120 Hz-bandpass filter. Normal survey speed was about 12 km/hr but the vessel's speed was slowed as necessary to obtain acceptable records in heavy seas.

Ship's position was determined with the U.S. Navy Satellite Navigation System, fixes being obtained at irregular intervals averaging once every two hours. This control was supplemented with LORAN and other conventional means of determining position. The probable error in any smooth-plotted ship's position is estimated to be less than 2 km.

The deepest continuous reflector on the seismic records usually was selected as the top of the basement. Beneath the sediments of the upper continental rise and in other localities where there was no distinctive reflector, the top of the basement was picked at a level below which there were no returns suggestive of bedding, so long as this level was well within the limits of penetration of the signal. 'Basement' thus represents only the shoalest acoustically-opaque rock and the nature and lithology of the basement would be expected to vary from place to place. In the continental rise, the top of the basement seems to be generally equivalent with the top of the seismic second layer as determined by refraction measurements (Mason, 1958, p. 328 and Figure 2; Menard, 1964, Figure 3.3; Winterer *et al.*, 1968, Figure 6).

3. Results and Discussions

As has been noted, the deep-sea portion of the area of the Transcontinental Geophysical Survey investigation falls within the "Deep Plain of the northeastern Pacific" (Menard, 1955, p. 1158). Generally, the Deep Plain is about 1.5 km deeper than the Ridge-and-Trough Province north of the Mendocino Escarpment, and about a half-kilometer deeper than the Baja California Seamount Province south of the Murray Fracture Zone (Menard, 1960, Figure 2); its main characteristic is that it is relatively featureless in comparison with the two provinces which adjoin it.

The results of the TGS seismic reflection observations are presented as interpretative line drawings in Figure 2. The locations of the illustrated profiles are shown on the accompanying bathymetric map (Figure 2) which has been redrawn from one prepared by the authors for the Transcontinental Geophysical Survey report (Lattimore *et al.*, 1968b).

Because of the size of the area of study and the diversity of geologic features within it, it is convenient to divide the TGS area into five provinces, and to include in the

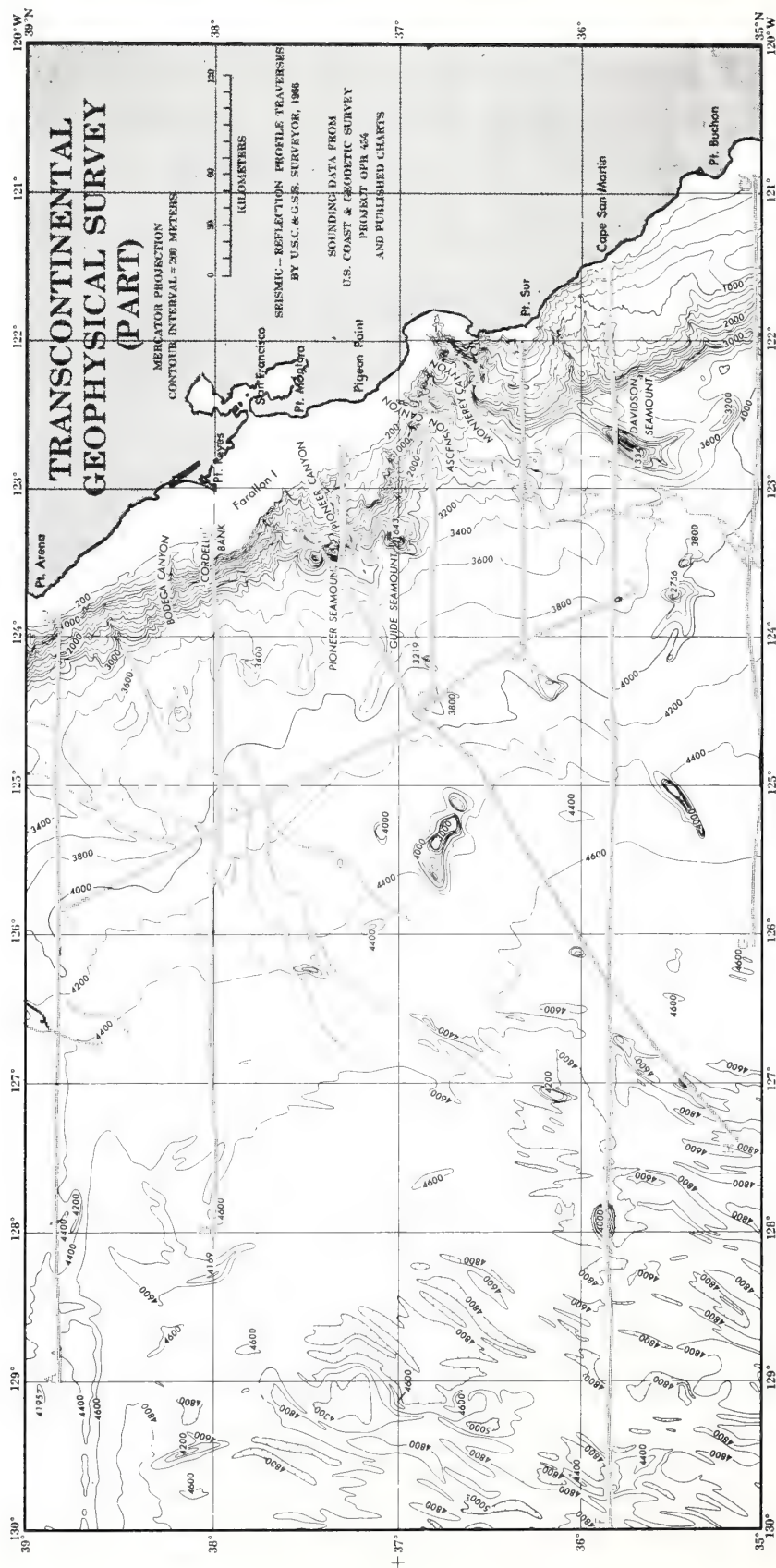


Fig. 2a.

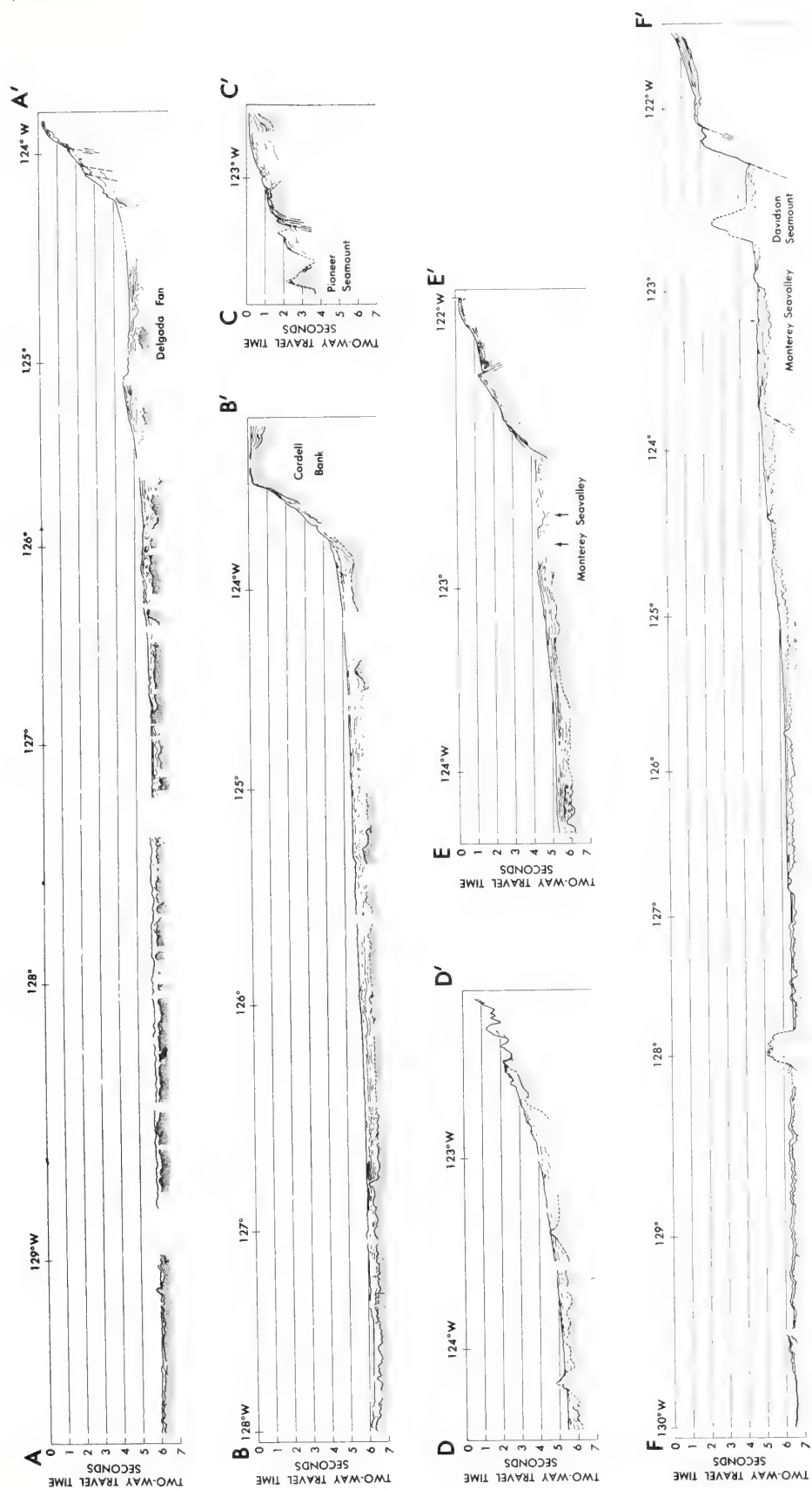


Fig. 2b.

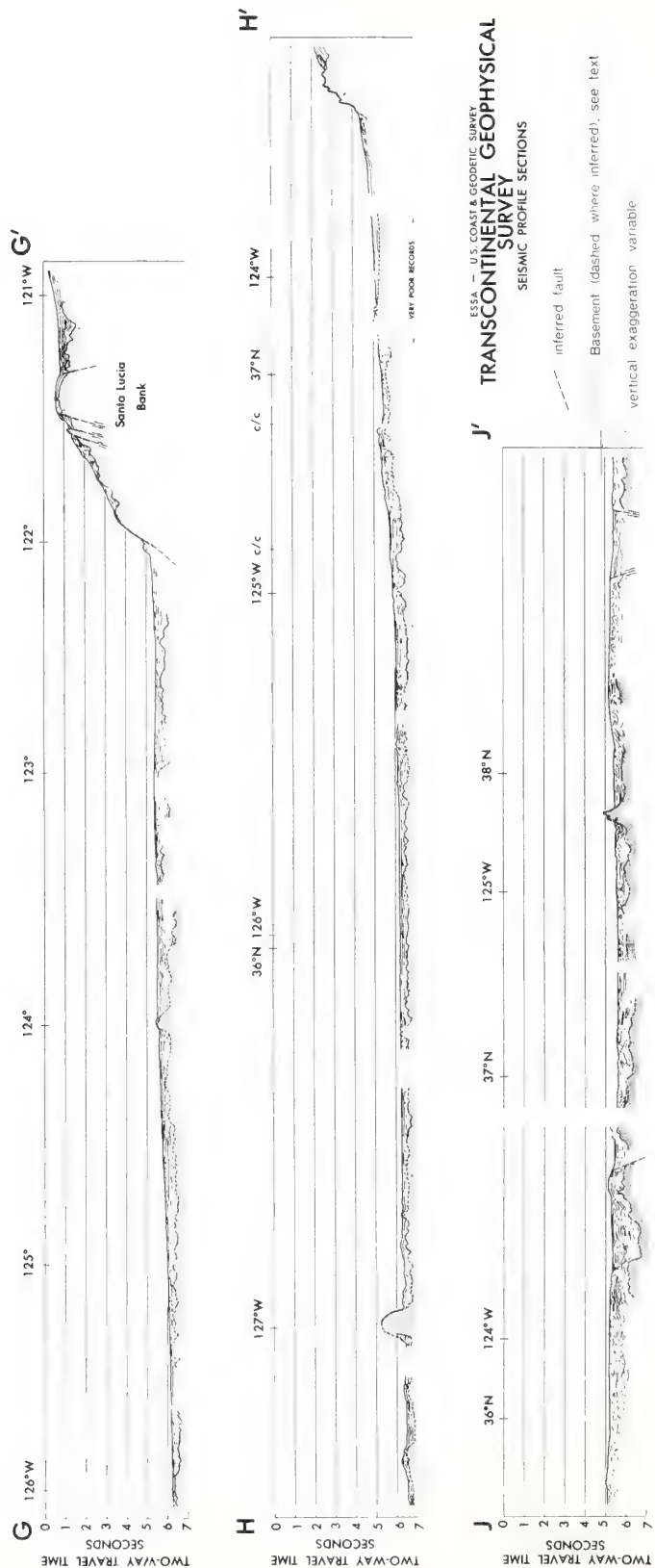


Fig. 2c.

discussion of each province a review of the results and conclusions of earlier investigators. The five areas are: (1) continental terrace (shelf and slope); (2) continental rise south of 37°N ; (3) Delgada deep-sea fan; (4) Pioneer Ridge; and (5) abyssal hills (Figure 1).

A. CONTINENTAL TERRACE

North of Cordell Bank, the TGS investigation and the study reported by Curray (1965) show that the continental shelf is composed of a thick sequence of moderately to intensely deformed strata, in some localities overlain by beds which are gently arched and cut by faults of small vertical displacement (see Curray, 1965, Figure 2). The continental slope is made up of a series of fault blocks, in which evidence of stratification can be found in the surface sediments down to depths of approximately 1800 m (AA', Figure 2).

The area from Cordell Bank south to Pioneer Seamount, which for convenience will be referred to as the Farallon platform, is characterized by an unusually wide shelf (in comparison with the shelf to the north and south) and by relatively minor incision of the shelf by sea valleys. The width and morphology undoubtedly are attributable to the presence of relatively resistant rock beneath the edge of the shelf and the upper slope (BB', Figure 2; Curray, 1965, Figure 3). A thick section of folded strata lies to landward of this resistant block; the present sea floor has been cut across both units, presumably by Pleistocene wave erosion (Curray, 1965, p. 798).

Between Pioneer Seamount and Monterey Canyon, the edge of the continental shelf is made up of at least a half-second of folded sedimentary rocks but a well-defined basement block, cut by faults, can be recognized under the middle continental slope at depths of 800 m or more (CC', DD', Figure 2; Curray, 1965, Figure 4).

From Monterey Canyon south to 35°N , the edge of the shelf consists of no more than a half-second of folded sedimentary rock (EE', FF', GG', Figure 2). These strata are overlain by younger sediments which thicken landward (to at least 0.7 sec at 36°N) and have been tilted and faulted. Off Point Sur (EE', Figure 2), at a depth of 1000 m (approximately 1.5 sec), folded strata which make up the edge of the shelf are in fault contact with a basement block that forms the middle continental slope. Off Cape San Martin (FF', Figure 2) and on Santa Lucia Bank (GG', Figure 2), the basement can be traced from beneath the edge of the shelf toward the shoreline; both basement and some of the overlying sediments are cut by faults. The continental slope is made up of fault-blocks of basement rock, in some places thinly covered by sediments.

The presence of basement beneath the outer continental shelf and upper slope was first established by Curray (1965), who concluded that basement rocks comprise an essentially continuous ridge extending from $35^{\circ}30'\text{N}$ to $39^{\circ}30'\text{N}$, with the possible exception of a zone north of Point Arena (Curray, 1965, p. 799 and Figure 1). Page (1966) suggested that, like the Coast Ranges, the California shelf and slope may be made up of blocks of a granitic-metamorphic complex alternating with blocks underlain by Franciscan rocks. The Franciscan includes a flysch sequence ranging in age

from Late Jurassic to Late Cretaceous; the granites are overlain unconformably by Upper Cretaceous and Paleocene strata (Taliaferro, 1951, p. 117). Page (1966, Figure 1) also proposed that the Salinian block – granodiorite basement bounded roughly by the Nacimiento and San Andreas faults – extends beneath the continental shelf northwest of Monterey Bay. South of Monterey Bay and west of the Nacimiento fault, sediments of the shelf are underlain by the Franciscan core complex (Page, 1966, Figure 6). The results of our investigations are entirely consistent with the hypothesis of Page (1966). Furthermore, because the trends of the Salinian block are slightly to the west of the shoreline, Franciscan basement would be expected to occur west of the shelf break, north of $36^{\circ}30'N$ (Figure 3); the presence of faulted basement blocks beneath the slope at $36^{\circ}50'N$ (DD', Figure 2) and $37^{\circ}20'N$ (CC', Figure 2) has been noted.

B. CONTINENTAL RISE SOUTH OF $37^{\circ}N$

The thalwegs of the more important sea valleys on the lower continental slope and continental rise, inferred by the authors from the TGS fathograms, are shown on the bathymetric map (Figure 2).

The existence of a tight meander in the Monterey deep-sea valley system, at $36^{\circ}15'N$, $122^{\circ}50'W$ (map, Figure 2), was first established by Shepard (1966, Figure 1); he also showed that the valley which drains southward from the meander just east of $123^{\circ}W$ does not breach the wall of the main canyon. South of $36^{\circ}N$, what is presumed to be the main channel of the Monterey system trends somewhat east of south toward the flank of Davidson Seamount, as has been shown by Dill *et al.* (1954, Figure 2); a secondary valley branches off to the southwest. South of $35^{\circ}30'N$ the main channel also swings southwestward and breaks up into a number of distributary channels.

Although the TGS investigation included east-west bathymetric profiles at approximately 18-km intervals, Pioneer Canyon could not be traced beyond the base of the continental slope. The depressions delineated by the 3800-, 4000-, and 4200-m isobaths between $36^{\circ}N$ and $37^{\circ}N$ (Figure 2) are marked by a number of valleys; although some of these are fairly well-developed, no single valley could be traced from one bathymetric profile to the next.

Throughout the area south of $37^{\circ}30'N$, two distinct types of internal structure can be recognized in the sediments of the continental rise. The first is characterized by near-horizontal, continuous reflectors which are independent of structural relief of the basement or underlying strata, and usually form a smooth sea-floor profile, concordant with the regional gradient. On the upper and middle continental rise, these sediments form floodplain-like deposits which rise tens or even hundreds of meters above the regional level of the sea floor, and extend laterally from the axes of deep-sea valleys for a hundred kilometers or more. Such deposits often are impounded by local topographic highs ($124^{\circ}25'W$, $126^{\circ}50'W$, FF', Figure 2). In the transition zone between the typical profile of the abyssal hills and the smooth profile of the continental rise, continuous reflectors can be seen to fill-in between the hills, forming broad, flat-floored valleys ($127^{\circ}20'W$, $127^{\circ}50'W$, BB', Figure 2); disappearance of the abyssal

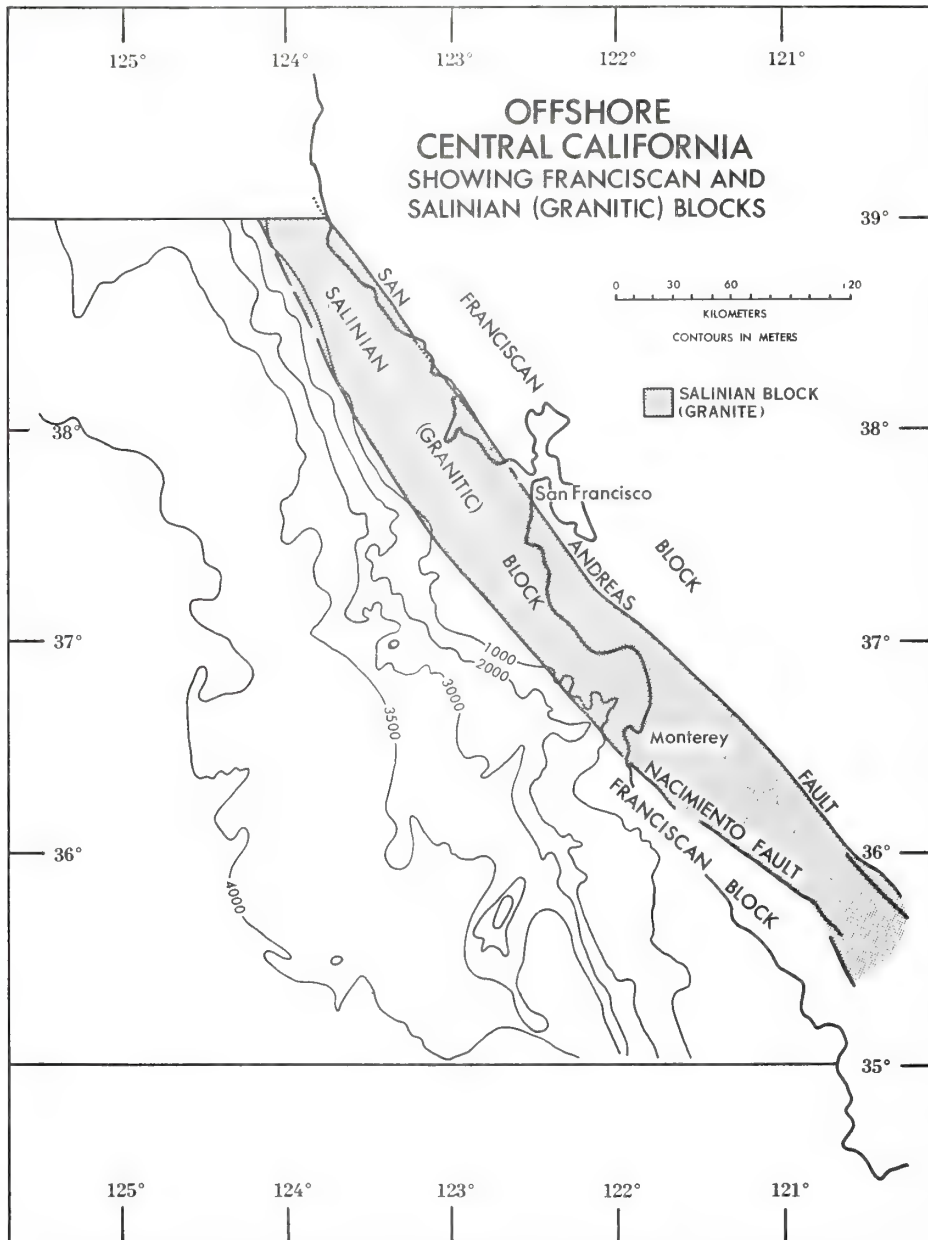


Fig. 3.

hills topography from west to east across the lower continental rise usually can be attributed to burial by this type of sediment. There is little doubt that these strata are turbidites (Hamilton, 1967, Figure 10a).

The second type of sedimentary structure is characterized by 'soft' reflectors, often

with variable dip, which commonly extend for no more than 2–3 km along the profile. Sea-floor outcrops of these strata frequently coincide with reversals or marked changes in the regional depth gradient ($124^{\circ}30'W$ – $125^{\circ}W$, HH', Figure 2) and often with a zone of 'rough' topography ($124^{\circ}40'W$ – $125^{\circ}W$, FF'; $37^{\circ}N$, JJ', Figure 2). Perhaps the most significant characteristic of these reflectors is that they are to some degree conformable with structural relief of the basement. An extensive blanket of sediments containing zones of these discontinuous-conformable reflectors occurs south of $37^{\circ}N$ at depths greater than 4000 m ($124^{\circ}15'W$ – $124^{\circ}25'W$, DD', $124^{\circ}30'W$ – $125^{\circ}30'W$, HH', Figure 2); the zones range in thickness from 0.4 sec upwards. The presence of isolated valleys in this area has been noted; despite the presence of such valleys, however, it is impossible to relate these strata to any known major deep-sea channel system. South of $36^{\circ}15'N$, similar deposits extend landward to the 3800-m isobath (JJ', Figure 2); the seismic profiles show that they are overlain by near-horizontal, floodplain-like turbidites which are associated with the Monterey deep-sea valley system. In some localities, well-bedded, horizontal strata fill in valleys and other depressions in the discontinuous-conformable sediments.

From consideration of their areal distribution, conformability, and relationship with the overlying turbidites, it seems likely that strata containing the discontinuous-conformable reflectors are composed predominantly of deposits formed in the deep ocean by some means other than turbidite sedimentation. If these deposits can be attributed to normal ('hemipelagic') sedimentary processes operating in the deep ocean, the sediment column in any given locality would consist of varying admixtures of 'normal' allogetic-abyssal and turbidite sediments; distinctive internal structures would be expected only if one process or the other were predominant. A second possibility is that the discontinuous-conformable strata originally were horizontal, and have been involved in post-depositional tectonic activity.

Regardless of the origin of the discontinuous-conformable reflectors, their nature and distribution militate against their having been derived from the present Monterey deep-sea valley system. These investigations suggest that deposits clearly associated with the Monterey system actually may comprise only a relatively small part of the blanket of sediments on the middle and lower continental rise between $35^{\circ}N$ and $37^{\circ}N$.

C. DELGADA DEEP-SEA FAN

The topographic axis of the Delgada deep-sea fan is a broad, roughly symmetrical ridge which originates at the base of the continental slope north of Delgada Canyon (Shepard and Emery, 1941, Chart IV) and extends southwest to about $38^{\circ}15'N$ (Figure 2). Two deep-sea valleys lie southeast of this ridge, between its axis and the base of the continental slope. Both valleys run generally south-southwest from where they enter the area ($39^{\circ}N$) to about $38^{\circ}N$, where they swing southwest and apparently break up into a number of smaller distributary channels; one of these channels can be traced as far as $37^{\circ}N$, $126^{\circ}30'W$ (Figure 2).

Between $39^{\circ}N$ and $38^{\circ}10'N$ the westernmost of the two deep-sea valleys follows a nearly straight course across the eastern flank of the axial ridge, and its valley seems

to have been incised into the ridge. South of $38^{\circ}15'N$, where the relief of the ridge disappears, the channel begins to meander and constructional levees are present. This valley is considered to be a member of the Delgada Canyon system (Figure 1).

Between $39^{\circ}N$ and $38^{\circ}30'N$, the eastern channel apparently occupies a broad, shallow valley, 10 km or more across, with relief on the order of 30 m. At depths greater than 3800 m, this channel has a well-defined V-shape with relief of 40 m or more. Bathymetric profiles between $38^{\circ}20'N$ and $37^{\circ}50'N$ show an asymmetric valley whose cross-sections are consistent with the meandering course shown on the map (Figure 2); levees first appear south of $38^{\circ}10'N$, at depths of about 3900 m.

Of the several sedimentary 'units' which can be distinguished in the Delgada deep-sea fan, by far the most important in terms of volume are the turbidites. These deposits cover the upper continental rise between $37^{\circ}30'N$ and $39^{\circ}N$ (BB', AA', Figure 2) and extend into the abyssal hills as far west as $128^{\circ}W$ (BB', Figure 2), in some localities beyond $128^{\circ}30'W$ (Ewing *et al.*, 1968, Figure 7). As far south as $36^{\circ}N$, turbidite strata west of $126^{\circ}30'W$ may be part of the Delgada deep-sea fan (FF', HH', Figure 2). As has been shown by Menard (1964, plate) a tongue of turbidites, 20–40 km wide, extends along the base of Pioneer Ridge at least as far west as $133^{\circ}W$. Stratified, horizontal sediments were noted on seismic-reflection profile crossings of Pioneer Ridge between $132^{\circ}W$ and $133^{\circ}W$, and Naugler and Perry (personal communication) describe a typical turbidite sequence from a core at $38^{\circ}30'N$, $132^{\circ}W$.

At $38^{\circ}50'N$ (AA', Figure 2), the western slope of the ridge which forms the topographic axis of the fan consists of 0.1–0.2 sec of sediments lying unconformably upon a thick sequence of near-horizontal strata that appear to be continuous with the turbidites at the base of the continental slope. Extensive areas of the western slope are characterized by a 'hummocky' terrain in which low (15–25 m) hills, sinusoidal in section, occur at regular 1–2 km intervals along the profile. An example of this topography can be seen in Profile AA' (Figure 2), where the hummocks are developed in near-surface sediments which lie unconformably on the turbidites. Within the uppermost 0.1–0.2 sec of these sediments only a single reflector can be discerned – a nearly continuous surface which is parallel with the present sea floor and which follows the relief of the individual hummocks. The hummocky structure and the absence of horizontal reflectors make it extremely unlikely that the near-surface sediments are turbidites; probably, they are normal deep-ocean allogenic deposits, or 'pelagic' sediments in the broad sense.

The southern end of the ridge consists of 0.4–0.6 sec of sediments in which the reflectors are discontinuous and highly contorted ($37^{\circ}55'N$ – $38^{\circ}30'N$, JJ', Figure 2). These chaotic reflectors apparently have been observed also by Truchan *et al.* (1967, p. 126) as "'cross reflections' exhibiting large apparent dips" covering an area from the Delgada Channel (probably the eastern valley) to $38^{\circ}30'N$ and $125^{\circ}35'W$. Landward of this valley, these authors noted, the sub-bottom strata are nearly horizontal.

The 'cross reflections' differ in several important respects from the discontinuous-conformable reflectors described in the preceding section. Although short, the 'cross

reflections' are distinct and well defined. In contrast with the soft, discontinuous reflectors, which may show sub-parallel orientation and commonly reflect basement relief, the 'cross reflections' may be highly angular with respect to one another, and usually are independent of relief of the basement. Significantly, the 'cross reflections' are clearly associated with a major deep-sea valley system, as has been established by Truchan *et al.* (1967, p. 126) and is illustrated in Profile JJ' (Figure 2).

The relation of the 'cross reflections' to sea floor stream channels, and their internal structure and independence of basement relief suggest that the southern part of the axial ridge (JJ', Figure 2) is composed of fossil channel levee and scour-and-fill deposits. The suggestion that these are slump deposits or submarine landslides derived from the shelf to the east is unsatisfactory in view of their distance from the base of the continental slope, their areal extent (Truchan *et al.*, 1967, p. 126) and the present gradient of the ridge, which is a maximum of 20 m/km.

To summarize the preceding paragraphs, near 39°N the ridge which forms the topographic axis of the Delgada deep-sea fan consists of a succession of turbidites overlain unconformably by 'normal' allogenic-abyssal sediments. To the south, both give way to the 'cross reflections' which may have formed by reworking of older sediments. The eastern slope of the ridge is deeply incised by a stream valley that follows a fairly straight course across it, forming an acute angle with the axis of the ridge near 38°15'N (Figure 2). Clearly, this pattern of sedimentation and valley morphology cannot be explained in terms of a static environment; some element of tectonic activity must be invoked to explain it.

Uplift of the continental shelf north of 39°N might have increased the gradient of an existing drainage system to the point that its valley would have been incised into the axial ridge; the deepened channels would have contained all sediment moved through the drainage system, so that 'normal' allogenic-abyssal sediments could have accumulated on the flanks of the ridge undiluted by turbidite deposits. An equally acceptable, alternate explanation for the incised valley and the accumulation of 'normal' deep-ocean sediments is uplift of the sea floor beneath the ridge, proper. If it may be further postulated that this uplift began in the north and progressed southward, several other major features of the area also are accounted for. The course of any major deep-sea valleys, prior to the uplift, may have been normal to the continental slope, and a thick sequence of turbidites built seaward across the continental rise. Uplift of the ridge, progressing from north to south, would have diverted the channels southward, exposing older sediments to erosion and reworking. Beyond the area of uplift the channels, once again under influence of the regional topographic gradient, would swing westward and erosional relief of the valleys would disappear. The south-eastward migration of the channels across the southern half of the ridge would account for formation of the 'cross reflections' and, particularly, for the fact that they seem to occur only to seaward of the distributary valleys (Truchan *et al.*, 1967, p. 126). The wedge of turbidites shown in Profile AA' (Figure 2) is simply an erosional remnant covered by subsequent normal deep-ocean sediments. Tectonic activity associated with uplift of the ridge also would account for displacements of the basement, often

accompanied by distortion of overlying continuous reflectors, which are found in the middle continental rise north of $37^{\circ}30'N$.

The ridges which extend westward from the base of the continental slope at approximately $37^{\circ}15'N$ and $37^{\circ}30'N$ (Figure 2) enclose a basin which may be receiving little if any terrigenous sand (Uchupi and Emery, 1963, p. 427; Wilde, 1965, Figures 9–11) despite proximity to the drainage system which empties into the Pacific through the Golden Gate. Just north of the ridge at $37^{\circ}05'N$, the sediments are no thicker than 0.3 sec (HH', Figure 2). Along the axis of the basin, at $37^{\circ}20'N$, a seismic record of marginal quality (not shown) suggests a maximum of 0.6 sec and a minimum of 0.2 sec of sediment overlying an extremely irregular basement surface. At least the upper 0.2–0.3 sec of these sediments are turbidites.

D. BASEMENT TRENDS IN THE CONTINENTAL RISE

The ridges which extend westward from the base of the continental slope at $37^{\circ}05'N$ and $37^{\circ}30'N$ are only two of at least five topographic features with marked east-west orientation which occur on the upper continental rise north of $37^{\circ}N$ (Figure 2). Profile HH' (Figure 2) suggests that the ridge at $37^{\circ}05'N$ reflects basement structure; the presence of knolls on the distal ends of the ridges at $37^{\circ}45'N$ and $38^{\circ}10'N$ supports the conclusion that the ridges are primarily basement structures.

Although there is no correlation between these east-west trends and the magnetic-anomaly pattern north of $37^{\circ}N$ (see Mason and Raff, 1961, Figure 2; Lattimore *et al.* 1968a), the ridges all seem to end at about $124^{\circ}40'W$, which coincides with the axis of the easternmost 'typical' deep-ocean magnetic anomaly lineation. This anomaly, whose north-south trend truncates the anomalies of the upper continental rise between $36^{\circ}N$ and $38^{\circ}30'N$, also coincides with the western flank of another low ridge (defined by the 4000-m isobath) that extends due south from approximately $37^{\circ}N$ to $36^{\circ}30'N$ (Figure 2). From Profiles HH' and JJ' (Figure 2), it may be seen that at least the northern tip of this north-south ridge reflects structural relief of the basement.

These observations suggest that there is, in fact, a relationship between the magnetic anomalies and the structure of the upper continental rise; for example, the crust may change from typical oceanic to intermediate at $124^{\circ}40'W$.

E. PIONEER RIDGE

The TGS seismic-reflection investigation of Pioneer Ridge was limited to a profile along the ridge at $38^{\circ}50'N$ (AA', Figure 2) and two north-south crossings west of $130^{\circ}W$ (not shown). These profiles, together with those of Ewing *et al.* (1968, Figure 7) and Winterer *et al.* (1968, Figures 2–5), yield some idea of the gross structure of this feature. West of $126^{\circ}W$, the general level of the basement north of $38^{\circ}40'N$ is about 0.5 sec higher than beneath the continental rise and abyssal hills to the south (compare AA' and BB', Figure 2; Winterer *et al.*, 1968, Figures 2a–2c). The ridge which usually occurs on the southern margin of this uplifted block, west of $127^{\circ}30'W$, represents an additional 400 m or 0.5 sec of basement relief.

West of $127^{\circ}30'W$ the basement associated with Pioneer Ridge can be described in

terms of short-wavelength features of low, regular amplitude, which are morphologically similar to the structure of the abyssal hills (AA', Figure 2; Winterer *et al.*, 1968, Figure 2d). East of 127°W, relief of the basement appears to be irregular and of greater amplitude, and the pattern more nearly resembles the basement structure found beneath the middle and upper continental rise (Figure 2).

Although the 'magnetic structure' of Pioneer Ridge extends at least as far east as 127°W (Mason and Raff, 1961, Pl. 1) topographic relief on the ridge does not extend beyond 127°40'W (Figure 2) and it is obvious from the profiles shown by Winterer *et al.* (1968, Figure 2) that the gross structure of the feature changes markedly, near the meridian. The bathymetric data compiled from the TGS investigation suggest that the low ridge at 126°W, defined by the 4000-m isobath, has an east-northeast trend (Figure 2), but the map prepared by Menard (Winterer *et al.*, 1968, Figure 7) shows this ridge as being oriented almost east-west, and Winterer *et al.* present data in support of the idea that the feature is a continuation of the Pioneer trend.

Profile AA' (Figure 2) shows that terrigenous sediments, mostly turbidites, extend along the north slope of Pioneer Ridge for about 300 km west of the base of the continental slope. At 127°W, 0.2 sec of horizontally-stratified deposits overlie thinner, acoustically-transparent beds which are conformable with the bedrock topography. West of 127°30'W acoustically transparent sediments predominate. Between 127°30'W and 128°30'W such deposits average 0.3 sec in thickness, or about double the average thickness of pelagic sediments on the abyssal hills south of the ridge. The north-south profile of Ewing *et al.* (1968, Figure 7) shows that at 128°30'W these same sediments thicken to the north. These data support the hypothesis of Winterer *et al.* (1968, p. 518) that sediments in the northern part of the Delgada fan may be at least partially derived from north of the Mendocino Escarpment.

F. ABYSSAL HILLS

At a distance of 400–500 km from the base of the continental slope the distinctive, parabolic profiles of the abyssal hills emerge from beneath a waning cover of terrigenous sediments. Within the abyssal hills province, maximum relief is found in ridges and seamounts along the northern and eastern margins; these stand 600 m or so above the surrounding sea floor (Figure 2). Otherwise, the entire province east of 133°W falls in the 4600–5400 m depth range (Lattimore *et al.*, 1968). Relief on individual hills seldom exceeds a few hundred meters, and width along the base generally is 2.5 km or less. Slope gradients approaching 10 per cent are not uncommon.

The basement structure of the abyssal hills typically is covered by a conformable mantle of acoustically-transparent sediments, undoubtedly equivalent to the 'pelagic' sediments of Hamilton (1967, p. 4202). This mantle rarely is more than 0.15 sec thick, and zones in the southwestern part of the study area are completely devoid of perceptible sediments (FF', Figure 2).

As may be expected, turbidites do not vanish abruptly from the sediment column. Almost every east-west profile contains a transition zone, up to 150 km wide, in which basement features covered with a conforming mantle of acoustically-transparent

sediments rise above horizontal, stratified sediments filling adjacent lows (FF', Figure 2). Flat-floored valleys suggesting turbidite sedimentation are common throughout the area of investigation.

4. Summary

The Transcontinental Geophysical Survey seismic-reflection profiles support the hypothesis that the gross patterns of the geology of the Coast Ranges of California are present beneath the continental shelf and slope. In particular, the broad, flat continental shelf from Pigeon Point north to Cordell Bank may be attributed to the occurrence of a crystalline ridge along the edge of the shelf; Page (1966, Figure 1) has suggested that this is an extension of the Salinian block that forms the basement beneath the Coast Ranges south of Monterey Bay. The more deeply-incised continental shelf and less precipitous upper continental slope south of Monterey Canyon are believed to reflect the presence of the Franciscan basement complex overlain by a sequence of folded and faulted sedimentary rocks, as also suggested by Page (1966, Figure 6). Basement blocks beneath the middle and lower continental slope, north of 37°N , may be a continuation of the Franciscan complex.

On the continental rise south of 37°N , the course of the Monterey deep-sea valley has been traced south and southwest from the meander at $36^{\circ}15'\text{N}$, $122^{\circ}50'\text{W}$, mapped by Shepard (1966, Figure 1). Pioneer Canyon could not be traced beyond the base of the continental slope.

Turbidites on the continental rise are characterized by near-horizontal, continuous reflectors; they tend to be concordant with the regional topographic gradient and independent of structural relief on the strata or basement beneath them. On the upper rise, south of 37°N , these sediments form floodplain-like deposits clearly associated with the distributary system of the Monterey deep-sea valley.

Below 3800–4000 m a significant proportion of the sediment column is characterized by 'soft', discontinuous reflectors which tend to be conformable with structural relief of the basement and cannot be related to any known deep-sea valley system; in places, these strata are overlain unconformably by horizontally-stratified turbidites. While the origin of these discontinuous-conformable reflectors is uncertain, it is clear that they are not related to the present Monterey deep-sea valley system.

Turbidite deposits which are related to the Delgada deep-sea fan comprise the continental rise north of $37^{\circ}30'\text{N}$; turbidites cover abyssal hills east of 128°W , and extend south of 36°N . A tongue of turbidite strata extends along the base of Pioneer Ridge at least as far west as 133°W , as shown by Menard (1964, plate). Our investigations show that turbidites occur also north of Pioneer Ridge, between $126^{\circ}50'\text{W}$ and $127^{\circ}20'\text{W}$.

Near 39°N the ridge which forms the topographic axis of the Delgada deep-sea fan consists of a sequence of turbidites overlain unconformably by 0.1–0.2 sec of normal allogenic-abyssal or 'pelagic' sediments. The southern end of this ridge is made up of 'cross reflections', probably the same as those observed by Truchan *et al.* (1967), which we interpret as having resulted from submarine scour-and-fill or rework-

ing of older sediments. The ridge is incised by a valley with steep walls and a flat floor, which follows a nearly straight course southwestward across it. Although the structure of this ridge implies a change in the sedimentary environment in response to tectonic activity, several alternative explanations can be offered which are consistent with the available data. The preferred explanation is that the ridge has undergone uplift progressing from north to south.

A pattern of abrupt changes in depth-to-basement, which is associated with the sedimentary ridge, could be related to epeirogenic activity. An alternate explanation is offered by Winterer *et al.* (1968, pp. 510–514), namely, that the structure of Pioneer Ridge extends into or beneath the sedimentary ridge.

The low east-west ridges on the upper continental rise north of 37°N are considered to be indicative of basement structure. While there is no direct correlation between these trends and the magnetic anomaly pattern (Mason and Raff, 1961, Plate 2; Lattimore *et al.*, 1968a) neither these trends nor the magnetic anomaly pattern of the upper continental rise extend west of $124^{\circ}40'\text{W}$ – the axis of the easternmost ‘typical’ deep-ocean magnetic anomaly.

A broad picture of the basement structure associated with Pioneer Ridge can be drawn from our investigations, the profile published by Ewing *et al.* (1968, Figure 7) and the report of Winterer *et al.* (1968). North of $38^{\circ}40'\text{N}$ the basement stands about 0.5 sec higher than the basement beneath the sea floor to the south. When present, the topographic ridge which runs along the southern margin of this raised block represents an additional 0.5 sec of basement relief. That this structural pattern is modified east of $127^{\circ}40'\text{W}$ is indicated by the bathymetry as well as by the seismic-reflection investigations of Winterer *et al.* (1968, Figure 2). The TGS data neither support nor contradict the inference of Winterer *et al.* (1968) that the Pioneer trend extends eastward from $127^{\circ}40'\text{W}$ beneath the sediments of the Delgada fan. Our data and that of Ewing *et al.* (1968) do substantiate the proposal of Winterer *et al.* that ‘pelagic’ sediments on Pioneer Ridge may have been derived partially from north of the Mendocino Escarpment.

Seismic-reflection observations in the abyssal hills reveal that conformable, acoustically-transparent ‘pelagic’ sediments rarely exceed 0.15 sec in thickness; in the southwestern part of the area they do not appear at all.

Acknowledgements

The authors thank S. P. Perry (ESSA, Pacific Oceanographic Research Laboratories), J. M. McAlinden and C. X. G. Fefe (U.S. Coast and Geodetic Survey) and F. M. Edvalson (U.S. Naval Oceanographic Office) for providing supplementary data on the deep-sea cores and bathymetry within the TGS area. G. F. Merrill and F. P. Saulsbury (ESSA, Atlantic Oceanographic and Meteorological Laboratories) supervised cartography and drafting of the figures. The manuscript was critically reviewed by L. W. Butler, G. H. Keller, and G. Peter (ESSA, Atlantic Oceanographic and Meteorological Laboratories).

References

- Burns, R. E. and Grim, P. J.: 1967, 'Heat Flow in the Pacific Ocean off Central California', *J. Geophys. Res.* **72**, 6239–47.
- Curry, J. R.: 1965, 'Structure of the Continental Margin off Central California', *N. Y. Acad. Sci. Trans., Ser. II* **27**, 794–801.
- Dill, R. F., Dietz, R. S., and Stewart, H.: 1954, 'Deep-Sea Channels and Delta of the Monterey Submarine Canyon', *Bull. Geol. Soc. Am.* **65**, 191–94.
- Ewing, J., Ewing, M., Aitken, T., and Ludwig, W. J.: 1968, 'North Pacific Sediment Layer Measured by Seismic Profiling'; 147–173 in Knopoff, L., Drake, C. L. and Hart, P. J. (eds.), 'Crust and Upper Mantle of the Pacific Area', *Am. Geophys. Un. Geophys. Mon.* **12**, 522 p.
- Hamilton, E. L.: 1967, 'Marine Geology of Abyssal Plains in the Gulf of Alaska', *J. Geophys. Res.* **72**, 4189–4213.
- Heezen, B. C. and Menard, H. W.: 1963, 'Topography of the Deep-Sea Floor'; 233–280 in Hill, M. N. (ed.) *The Sea* **3**, New York, Interscience, 963 p.
- Lattimore, R. K., Bassinger, B. G., and DeWald, O. E.: 1968, 'Transcontinental Geophysical Survey (35°–39°N) – Magnetic map from the Coast of California to 133°W Longitude', *U.S. Geol. Surv. Misc. Geol. Inv.*, Map I-531-A.
- Lattimore, R. K., Bush, S. A., and Bush, P. A.: 1968, 'Transcontinental Geophysical Survey (35°–39°N) – Gravity and Bathymetric Map from the Coast of California to 133°W Longitude', *U.S. Geol. Surv. Misc. Geol. Inv.*, Map I-531-B.
- Mason, R. G.: 1958, 'Magnetic Survey off the West Coast of the United States between Latitudes 32° and 36°N and Longitudes 121° and 128°W', *Geophys. J. Roy. Astron. Soc.* **1**, 320–29.
- Mason, R. G. and Raff, A. D.: 1961, 'Magnetic Survey off the West Coast of North America, 32°N Latitude to 42°N Latitude', *Bull. Geol. Soc. Am.* **72**, 1259–66.
- Menard, H. W.: 1955, 'Deformation of the Northeastern Pacific Basin and the West Coast of North America', *Bull. Geol. Soc. Am.* **66**, 1149–98.
- Menard, H. W.: 1960, 'Possible Pre-Pleistocene Deep-Sea Fans off Central California', *Bull. Geol. Soc. Am.* **71**, 1271–78.
- Menard, H. W.: 1964, *Marine Geology of the Pacific*, McGraw-Hill, New York, N.Y., 271 p.
- Page, B. M.: 1966, 'Geology of the Coast Ranges of California', 255–76, in Bailey, E. H. (ed.), 'Geology of Northern California', *Bull. Calif. Div. Mines and Geology* **190**, 508 p.
- Shepard, F. P. and Emery, K. O.: 1941, 'Submarine Topography off the California Coast: Canyons and Tectonic Interpretation', *Geol. Soc. Am. Spec. Paper* **31**, 171 p.
- Shepard, F. P.: 1966, 'Meander in Valley Crossing a Deep-Ocean Fan', *Science* **154**, 385–86.
- Taliaferro, N. L.: 1951, 'Geology of the San Francisco Bay Counties', 117–50, in 'Geologic Guidebook of the San Francisco Bay Counties', *Bull. Calif. Div. Mines* **154**, 392 p.
- Truchan, M., Windisch, C. C., and Hamilton, G. R.: 1967, 'Detailed Bathymetric and Seismic Reflection Survey of a Portion of the Delgada Deep-Sea Fan and its Channel' (abs.), *Am. Geophys. Un. Trans.* **48**, 126–27.
- Uchupi, E. and Emery, K. O.: 1963, 'The Continental Slope between San Francisco, California and Cedros Island, Mexico', *Deep-Sea Res.* **10**, 397–447.
- U.S. Upper Mantle Committee: 1965, United States program for the international Upper Mantle Project: Progress report – 1965: Washington, D.C., Nat. Acad. Sci. – Nat. Res. Council.
- Vacquier, V., Raff, A. D., and Warren, R. E.: 1961, 'Horizontal Displacements in the Floor of the Northeastern Pacific Ocean', *Bull. Geol. Soc. Am.* **72**, 1251–58.
- Wilde, P.: 1965, 'Recent Sediments of the Monterey Deep-Sea Fan', Univ. California (Berkeley), Hydraulic Eng. Lab. Tech. Rept. HEL-2-13.
- Winterer, E. L., Curry, J. R., and Peterson, M. N. A.: 1968, 'Geologic History of the Intersection of the Pioneer Fracture Zone with the Delgada Deep-Sea Fan, Northeast Pacific', *Deep-Sea Res.* **15**, 509–20.

Structural Relations Among Lesser Antilles, Venezuela, and Trinidad-Tobago¹

L. AUSTIN WEEKS,² R. K. LATTIMORE,³ R. N. HARBISON,³
B. G. BASSINGER,³ and G. F. MERRILL³

Miami, Florida 33158

Abstract More than 2,500 n. mi (4,630 km) of seismic reflection profiling, gravity, magnetics, and bathymetric data were collected in the southeastern Caribbean by the ESSA Coast and Geodetic Survey ship *Discoverer* in 1968-1969.

A review of the structural geology of the southeastern Caribbean and the South American continent in conjunction with the ESSA data supports a relatively simplistic explanation for the geologic structure. The Barbados Ridge is a greatly fractured anticlinorium, supported by "basement" rocks, and consisting of two parallel arches with a central syncline. The Lesser Antilles volcanic arc, the Tobago Trough, and the Barbados anticlinorium are traceable into the Venezuelan and Trinidadian shelves (South American continent).

An analogy between the Caribbean and Indonesian island arcs shows the validity of the concept of continuation of continental mobile belts into island arc systems. The mobile belt and the island arc system are analogous manifestations of orogeny in different crustal types. Evidence is against wrench faulting, with its implication of vast horizontal movements of individual blocks. The island arc structural belts and the mobile belts of the continent are interrelated, gradational, and interlocked.

INTRODUCTION

In 1968 the ESSA ship *Discoverer* began a continuing geophysical study of the southern Lesser Antilles, the Venezuelan and Trinidadian shelves, and the Barbados Ridge.

The primary purpose of this study is to determine the structural configuration of the Lesser Antilles island arc system and its relation to the South American continent. Previously, the senior writer and others conducted a similar study in the Andaman Sea during the International Indian Ocean Expedition in 1964 (Peter *et al.*, 1966; Weeks *et al.*, 1967). Similarities between the Andaman-Nicobar Islands and the Lesser Antilles led to a similar though expanded study of the Caribbean eastern margin.

This paper is a synthesis of the ESSA data

presented in the preceding papers in this *Bulletin* by Lattimore *et al.* (1971) and Bassinger *et al.* (1971), and of the known structural geology of the island arc system and the northeastern part of the South American continent. A structural analogy between the Lesser Antilles and Indonesian arcs is presented.

The 1969 study area was bounded by long. 58°30'-63°W and lat. 10°-12°30'N. Within that area more than 2,500 n. mi (4,630 km) were covered by seismic reflection profiling, gravimeter, magnetometer, and echo sounding observations. Additional gravimetric, magnetic, and bathymetric data were collected along various transects of the area. Figure 1 shows bathymetry and track lines within the study area.

STRUCTURAL BELTS

An interpretative cross section across the Lesser Antilles island arc system from the Venezuela basin through the Aves Ridge, Lesser Antilles, Barbados anticlinorium, and intervening troughs (Grenada Trough, Tobago Trough, Central syncline) is shown in Figure 2. The vertical scale is exaggerated to show the structural features more clearly.

Venezuela Basin

The west end of the section (Fig. 2) starts in the eastern Venezuela basin, on the west flank of the Aves Ridge. According to Edgar (1968; Fig. 3 this report), there are about 2 km (1¼ mi) of sediments, of velocity less than 5 km/sec (3.1 mi/sec), within the central part of the Venezuela basin, thickening to about 5 km (3.1 mi) on the western flank of the Aves Ridge. Sediments are thinnest within the central part of the basin and thicken toward the flanks of the basin in all directions. Ewing *et al.* (1967) showed that the sediments of the Venezuela basin are flat and undisturbed, indicating a lack of deformation or tectonic activity within the block. The basin as a unit has had a relatively stable tectonic history with only minor deformation around the edges of the plate. It is seismically inactive. Ewing *et al.* (1967) concluded that stability of the Caribbean subbasins

¹ Manuscript received, August 24, 1970; accepted, December 3, 1970.

² Consultant, 13720 SW 78th Court.

³ National Oceanic and Atmospheric Administration (NOAA), Atlantic Oceanographic and Meteorological Laboratories.

© 1971. The American Association of Petroleum Geologists. All rights reserved.

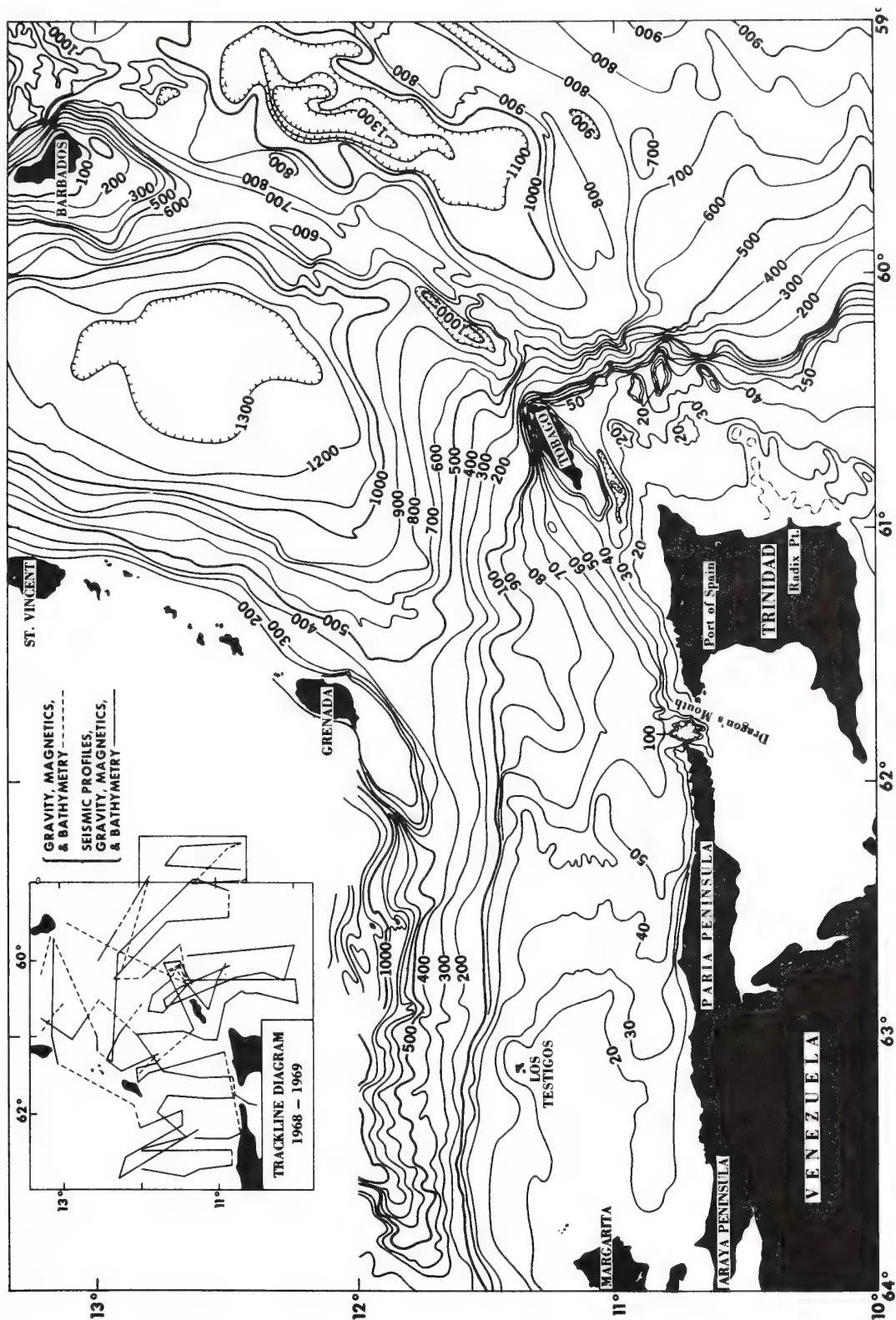


FIG. 1.—Bathymetry and trackline diagram. Contours in fm. Contour interval between 20 and 100 fm is 10 fm; below 100 fm, interval is 100 fm.

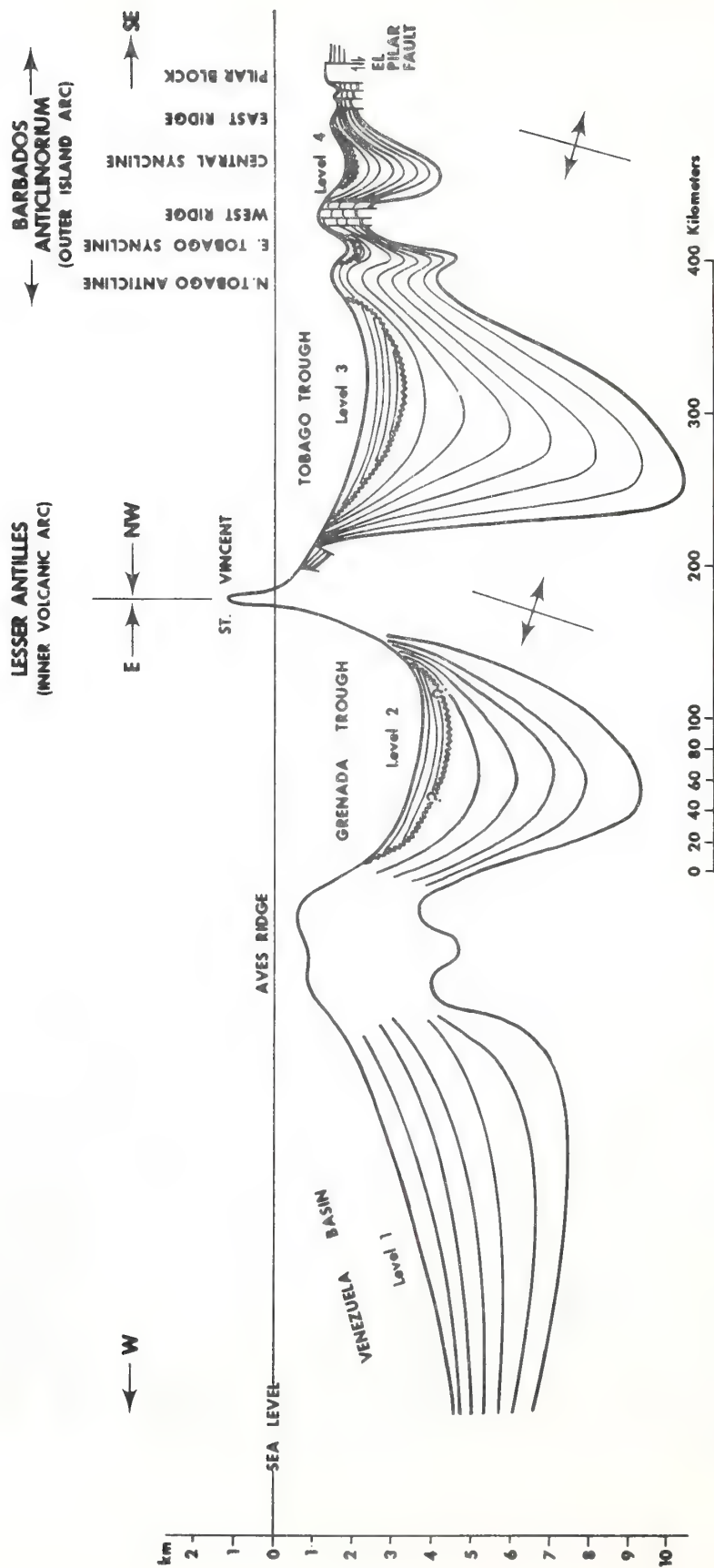


FIG. 2.—Interpretive cross section of Lesser Antilles island arc system. Levels 1–4 indicate general average increase in elevation of basins across system. No significance is implied, as levels across other island arc systems are variable. Volcanic arc is usually, but not everywhere, highest part of system. Line of section is A-A' on Figure 5.

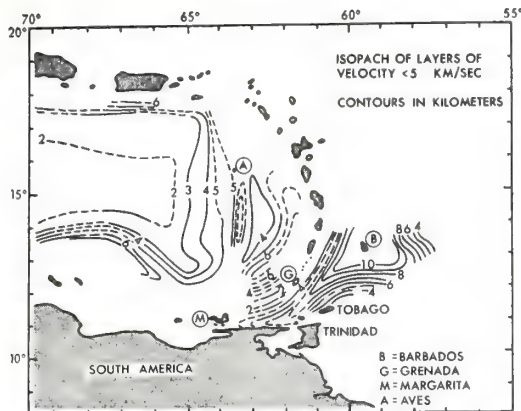


FIG. 3.—Lamont refraction data. Isopachs of less than 5 km/sec-layers are in 1-km intervals.

seems to preclude sea-floor spreading or horizontal movement, implying rather a dominant role of vertical movements instead.

Aves Ridge

The Aves Ridge is considered to be part of the island arc system, as its gross characteristics relate more to the arc than to the Venezuela basin. Sediments on the east flank of the ridge plunge unconformably beneath younger turbidites of the Grenada Trough (Edgar, 1968). The unconformable relation between older folded beds and younger relatively flat-lying deposits is characteristic of the basinal areas of the double island arc system (Fig. 2). In addition, the Carib beds of the Venezuela basin are not identified east of the western flank of the Aves Ridge. These sediments are the deep-water deposits identified over much of the Caribbean west of the Aves Ridge (Ewing *et al.*, 1967).

Bunce *et al.* (1970) showed a generalized crustal structure section from the Venezuela basin to the Atlantic Ocean. The crust thickens considerably in the eastern Venezuela basin, under the Aves Ridge and the rest of the island arc system, and does not thin again until the Atlantic Ocean is reached. Aves Ridge is, therefore, part of the thickened crust of the island arc system. Depth to mantle is roughly the same in the eastern Venezuela basin and the Atlantic Ocean, just east of the Barbados Ridge or anticlinorium.

The Aves Ridge is aseismic, nearly neutral in gravity, and approximately enclosed by the 1,000-fm (1,830 m) isobath. The only segment of the ridge above sea level is Aves Island, a

small, low 3-m (9.9 ft) maximum feature covered by calcareous sediments. Bedding strikes N70E, and dips toward the north and south (Maloney *et al.*, 1968). This strike is subparallel with strikes normal to the arc system found in Barbados and Grenada (Lesser Antilles). Dredging on the ridge has produced basalt (Hurley, 1966), glassy flows and brecciated rocks of possible eruptive origin (Marlowe, 1968), and much granite (recent cruise of R/V *Eastward*). The latter cruise dredged over 2 tons of light-colored granitic rocks from more than 50 locations along the ridge.

Aves Island has been decreasing slowly in size since the last century, and a slow epeirogenic subsidence of the whole ridge may be indicated. Such subsidence after positive elevation in tectonic trends is quite widespread (*e.g.*, Weeks *et al.*, 1967).

Grenada Trough

East of the Aves Ridge is the Grenada Trough (Fig. 2). Sedimentation in the Grenada Trough is distinct from that in the Venezuela basin. From the Grenada Trough eastward, flank sediments off the positive areas dip beneath the relatively flat sediments of the intervening Grenada and Tobago Troughs (negative areas within Barbados anticlinorium). The deeper parts of the Grenada Trough are east of the structural axis of the basin; therefore, asymmetry is eastward, toward the Atlantic Ocean. The unconformity between flank sediments dipping into the trough and the younger flat-lying beds is typical of the negative areas in the arc system. Edgar (1968; Fig. 3, this report) shows 4–7 km (2.5–4.4 mi) of sediments, a greater thickness than in the Venezuela basin.

Volcanic Arc

The volcanic arc of the Lesser Antilles forms a long graceful curve, convex toward the Atlantic. The arc is also asymmetric, with topographic slopes steeper on the west.

Volcanic activity in the Lesser Antilles has continued into recent geologic time, whereas it ceased in the Greater Antilles (except Hispaniola [MacDonald and Melson, 1969] during the Eocene (MacGillavry, 1970). MacGillavry considered that this cannot be explained by a quiescent episode of ocean-floor spreading. According to Lewis (1968, p. 44–45) the "Basaltic rocks occurring in the Lesser Antilles are directly comparable to chemical composition and mineralogy with basalts from other circum-

oceanic islands and from orogenic belts on the continental margins. Basalts of this type, characterized by a high alumina and low alkali content, are distinct from olivine tholeiites of the ocean basins and from alkali basalts of the intraoceanic islands."

Earle (1924, 1928), describing the southern Antilles, mentioned folding in Grenada that is approximately east-west, similar to strikes found on Aves Island, Barbados, and Trinidad. More recently, Martin-Kaye and Saunders (1962) described an upper Eocene sedimentary series (Tufton Hall Formation) in northern Grenada. The series consists of several hundred feet of folded, repetitively bedded graywacke and shale, with a fauna suggesting deposition at bathyal depth. It is tempting to correlate these deposits with the lower Scotland Group of Barbados (Baadsgaard, 1960), also considered to have been deposited at bathyal depth and folded with a pronounced northeast-southwest strike. Marine limestone at 180 m (600 ft) of elevation attests to later epeirogenic uplift in Grenada.

The most volcanically active segment of the arc is near the center, as the most recent volcanism is restricted to that part. The synchronous eruption of Soufrière (St. Vincent) and Pelée (Martinique) in 1902 indicates a deep common origin.

Seismically, the Lesser Antilles overlie a zone of intermediate depth earthquakes (Sykes and Ewing, 1965). Most of the hypocenters are confined to a zone about 50 km (31 mi) wide, dipping about 60°W.

Tobago Trough

East of the volcanic arc is the Tobago Trough, whose surface is about 500 fm (915 m) shallower than the Grenada Trough (Fig. 2). The trough is elliptical, asymmetrical toward the east, with the deeper parts near the Barbados anticlinorium (Fig. 1). The topographic axis is east of the structural axis, which continues southwest, depressing the Paria shelf (Figs. 1, 3). The total area of the Tobago Trough, even including the part on the Paria shelf, is less than half that of the Grenada Trough. This is a result of its termination on the north by a structural feature, herein termed the "St. Lucia-Barbados cross-warps" (Fig. 5).

The ESSA data indicate that younger, relatively flat-lying sediments unconformably overlie folded sediments which plunge under the Tobago Trough from both sides. Major contribution of sediment is from the south and per-

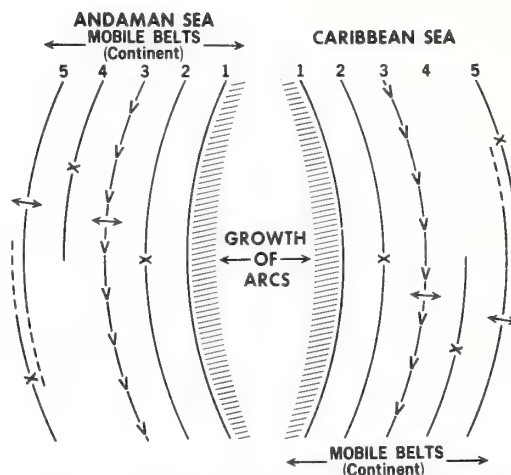


FIG. 4.—Double island arc system structural belts as seen in Andaman Sea (Indonesian Arc) and Eastern Caribbean (Lesser Antilles). See Table 1 for description of specific belts. Belts: 1. stable platform; 2. back-deep; 3. inner volcanic arc; 4. interdeep; 5. outer sedimentary arc and/or foredeep (trench).

haps southeast, with smaller amounts from the Lesser Antilles. Sediment thickness exceeds 10 km (6.2 mi, Fig. 3). Minimum thickness of sediments of similar velocities is 4 km (2.5 mi) at the southwest end of the Paria shelf, just off the Araya-Paria Peninsulas (Pilar block), reaching the maximum of more than 10 km (6.2 mi) on the northeast, just west of, and including Barbados. Tobago Trough sediments are now more than five times as thick as those in the Venezuela basin, having thickened gradually eastward across the island arc system (Fig. 3).

Barbados Anticlinorium

The Barbados anticlinorium was described earlier as a double ridge with a central syncline or trough. The Central syncline surface is somewhat above the general level of the Tobago Trough. However, the Tobago Trough is larger than the Central syncline in areal extent and volume. Sediment isopachs based on refraction data are oriented approximately east-west, with thickening northward toward Barbados (Fig. 3).

The inference of a southern source of supply for Barbados and the Tobago Trough is strong. East-west structural lineations in the Pilar block, and in some structures on Barbados itself, parallel the isopachs in every respect.

The seismic profiles suggest that the basement of the West ridge (Barbados anticlino-

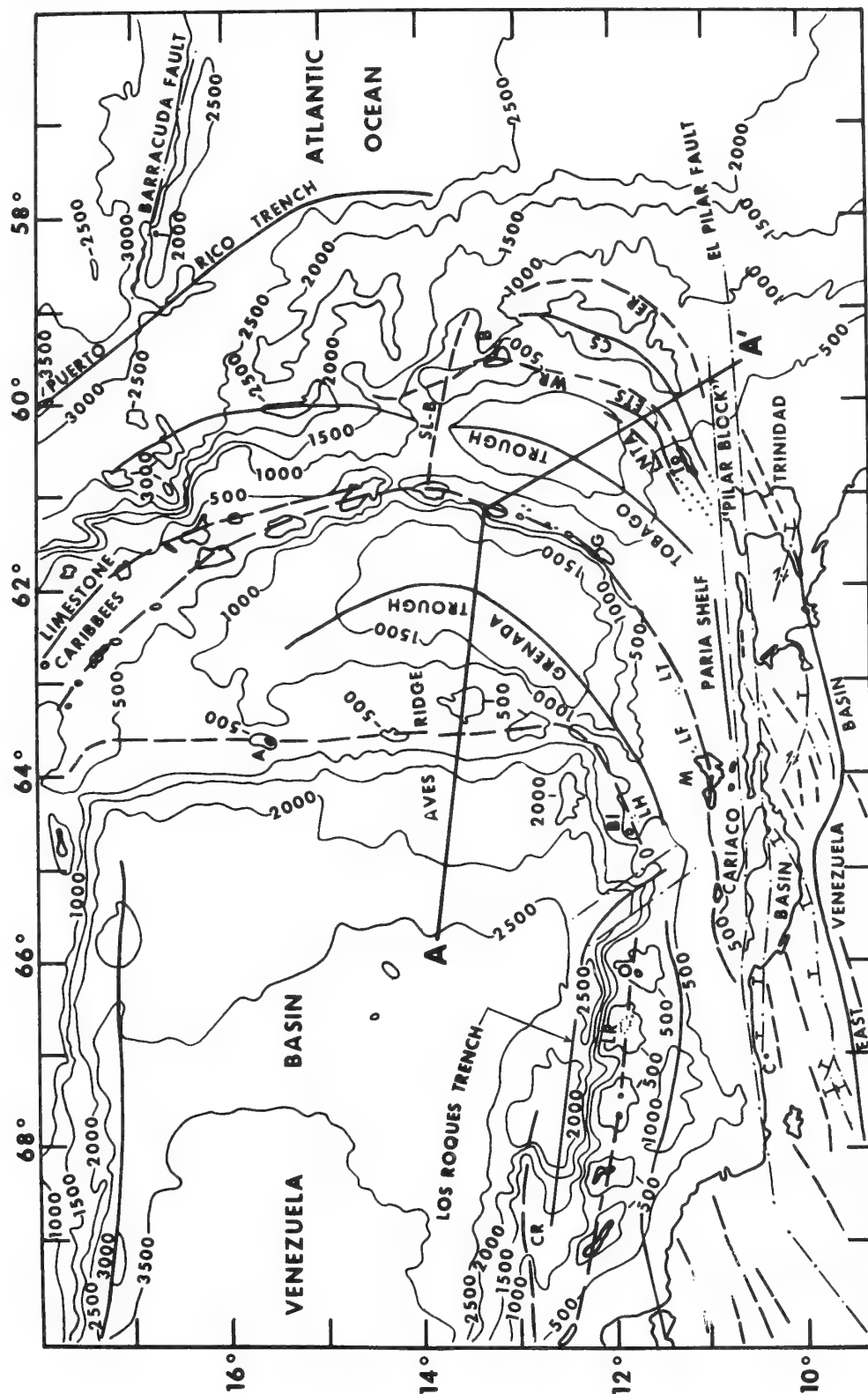


FIG. 5.—Tectonic map of southeast Caribbean. A-A' is line of section in Figure 2. Structures:

- Negative belts (troughs, basin axes, geosynclines, synclines, etc.)
- - - Positive belts (anticlinoria, anticlines, arcs, ridges, cross-warps, etc.)
- . - . Faults (fault zones, strike-slip faults, thrust faults with T on up side, etc.)

rium) plunges northward under the island of Barbados, a plausible phenomenon in view of the northward thickening of sediments (Fig. 3). The folded sediments of the East ridge and of the generally higher West ridge also plunge under the younger flat-lying sediments of the Central syncline.

Thus, the section from the Venezuela basin across the Barbados anticlinorium (Fig. 2) shows essentially a typical double island arc system. At the west is the Venezuela basin; at the east, the Atlantic basin; the apex is at the inner volcanic arc of the Lesser Antilles. Even where the outer sedimentary arc ceases to exist north of the Barbados anticlinorium, alternation of positive and negative structures prevails. Basins and ridges are approximately equidistant in their spacing. The Barbados anticlinorium is at about the same distance from the Lesser Antilles as the Aves Ridge. One cannot but believe that an overall pattern of structural "waves" is involved in the development of this double arc.

ISLAND ARC STRUCTURE, DEVELOPMENT, AND ANALOGIES WITH INDONESIAN ARC

A structural development very similar to that of the Caribbean island arc was noted in the Indonesian island arc by Weeks *et al.* (1967) and a direct comparison can be made (Fig. 4). The Indonesian arc in the Andaman Sea area and the Lesser Antilles arc of the eastern Caribbean are both double arc systems, in that both inner volcanic and outer sedimentary arcs are represented. The terminology used by the senior writer in the Andaman Sea, following that of van Bemmelen (1949), is equally applicable to the eastern Caribbean (Fig. 4; Table 1). Its advantage lies in its simplicity of terms, which are self-explanatory.

Both the Indonesian and Lesser Antilles island arc systems are characterized by inner volcanic arcs, outer sedimentary arcs, backdeeps, interdeeps, and foredeeps—present or former

trenches (Fig. 4). Table 1 lists the similarities in structure and gravity of the several arcuate belts in both the Andaman Sea and the eastern Caribbean.

The pattern of development in an island arc system is one of growth toward the ocean plate, not only normal to the arc but, in certain respects, also axially. Growth in both directions, normal and axial to the arc, occurs over a considerable period of time, or a diastrophic cycle. The cycle includes periods of orogeny and epeirogeny, as well as relaxation and/or extensional collapse. In the sense that double arcs are continuations of continental orogenic belts, the axial growth is quite evident, but axial growth within the outer island arc-foredeep belts of the system proper is becoming increasingly apparent. Axial growth explains the dual roles and interrelations between the outer sedimentary arc and the foredeep or trench (belt 5, Fig. 4).

The development of the outer sedimentary arc is of greatest interest in defining the interrelations not only of the outer sedimentary arc with the foredeep or trench, but also of the outer arc-foredeep with the orogenic belt of the continent. It is the key to the interlocking relation between the continental crust and the intermediate or oceanic crust. It is a mutual relation that is gradational in nature—axially, rather than normal to the arc system.

The writers believe that a double island arc system is a continuation of a continental mobile belt. In the Indonesian arc the orogenic belt of the Himalayas-Arakan Yoma (western Burma) continues by gradation into the Indian Ocean via the Andaman-Nicobar-Mentawai islands, or the outer sedimentary arc. At the distal end of the outer island arc the foredeep or trench becomes prominent (belt 5, Fig. 4). As shown in Table 1, the outer island arc is most completely developed where the foredeep is not and, conversely, the foredeep is best developed where the outer island arc is not. It is apparent that one cannot develop except at the expense of the other; hence, they must be mutually interrelated and gradational. The outer arc is the positive manifestation of the foredeep (negative feature). Both the foredeep and the outer island arc contain sedimentary rocks. Abyssal deposits of Barbados, the Oceanic Group (Baadsgaard, 1960), are testimony to the earlier foredeep nature of the outer arc in that area. In addition, the Eocene deposits in Barbados are flyschlike turbidites laid down under submarine conditions. The Eocene sediments of the Andaman-



Abbreviations:

CR = Curacao ridge	G = Grenada Is.
LR = Los Roques Is.	SL-B = St. Lucia-Barbados cross-warp
O = Orchila Is.	B = Barbados Is.
C = Caracas	To = Tobago Is.
Bi = Blanquilla Is.	NTA = North Tobago anticline
LH = Los Hermanos Is.	ETS = East Tobago syncline
A = Aves Is.	WR = West ridge
M = Margarita Is.	CS = Central syncline
LF = Los Frailes Is.	ER = East ridge
LT = Los Testigos Is.	

Table 1. Double Island Arc System Belts (See Fig. 4)

Feature	Area	
	<i>E. Caribbean</i>	<i>Andaman Sea</i>
1. Stable platform (a) plate from which arc system radiates (b) formerly involved in arc system, but now stable area	Venezuela basin plate and Aves Ridge	Malay Peninsula
2. Backdeep (a) basin behind, or on concave side of inner volcanic arc (b) part of arc system farthest from ocean plate	Grenada Trough on concave side of inner volcanic arc	Andaman Sea area on concave side of inner volcanic arc
3. Inner volcanic arc (a) positive gravity (b) intermediate earthquake belt (c) older feature than outer sedimentary arc (d) asymmetry toward ocean plate	Lesser Antilles	Barisan Range (Sumatra)-Narcondam and Barren Islands
4. Interdeep (a) between outer sedimentary arc and inner volcanic arc (b) absent where no outer arc present	Tobago Trough	Negative structural belt between Andaman-Nicobar Islands and Barisan-Narcondam-Barren arc
5. Outer sedimentary arc (a) negative gravity (b) occurs near continental end of island arc (c) found where trench is absent or buried (d) youngest feature of arc system (e) asymmetry toward ocean plate (f) folded, faulted, and thrust (g) shallow earthquake belt (h) structural history closely related to foredeep	Barbados anticlinorium	Andaman-Nicobar-Mentawai Islands
6. Foredeep (or Trench) (a) frontal to outer arc, where present, or to inner volcanic arc (b) negative gravity, where outer arc absent (c) trench where frontal to inner volcanic arc (d) youngest part of arc system (e) occurs along axis of outermost arc system farthest from continent (f) least expression where frontal to outer arc (older); most expression where frontal to inner volcanic arc (younger) (g) shallow earthquake belt	Depressed structural belt just in front of Barbados anticlinorium	Depressed structural belt just in front of Andaman-Nicobar-Mentawai Islands

Nicobar outer arc grade from coarse terrestrial deposits on the continental end of the belt nearest Burma to marine carbonates on the distal end of the outer arc. Infill and attendant facies changes take place from the continental end of the arc to the distal end. Hurley (1966), referring to his work in the Aleutian Trench, pointed out a similar situation there.

In Indonesia the continuation of the continental orogenic belt through the outer sedimentary arc is uninterrupted. However, in the southeastern Caribbean the Pilar block acted in some degree as a rigid wall. Toward the eastern end of the Pilar block, rigidity appears to decrease, and it is there that the outer sedimentary arc manifests itself. The analogy between the Indonesian arc and eastern Caribbean is still good, if one accepts the fact that the Pilar block is an exception to the general rule. This block is an old geologic feature which has become involved in a much younger orogenic belt-island arc development, and therefore it has acted as a partial deterrent to the more nor-

mal gradation, such as that in Indonesia and elsewhere.

The outer arc-foredeep relation is not continuous in the axial sense, but more *en échelon*, with some overlap of two structures (belt 5, Fig. 4). In both Indonesia and the eastern Caribbean it can be seen that the distal end of the outer sedimentary arc lies within or concave to the foredeep (Fig. 4). There is evidence of a buried foredeep lying outside the Andaman-Nicobar chain (Weeks *et al.*, 1967), a great distance from its more obvious expression as the Java trench. The *en échelon* expression or partial overlap of the two features is explained by the fact that the arc system is growing not only axially but also normal to the arc. Infill and elevation of the foredeep into an outer arc from the continental end are closely related to its concurrent development normal to the arc and toward the ocean basin. Undoubtedly, the development normal to the arc demands a much greater period of geologic time than axial infill and elevation. Hence, the two are still mutually

interrelated, but development in two directions creates the *en échelon* or overlap effect.

The *en échelon* effect of complete island arc systems is very evident in the western Pacific-Asian region. Arcs overlap, are concentric with each other, bifurcate, and may even be superimposed. Tectonic trends on the Asian continent exhibit remarkable proximity in some arcs, without major fracturing.

In summary, the double arc grows in two directions—normal (toward the ocean basin), and axial to the arc. Axial growth is from the continental end (mobile belt) of the outer arc toward its distal equivalent, the foredeep. The foredeep is, therefore, a younger structure than the outer sedimentary arc. Normal to the arc, the youngest feature is the outer arc or foredeep (belt 5, Fig. 4), and the oldest features are the backdeep and stable plate (belts 1, 2; Table 1, Fig. 4).

TECTONIC MAP AND INTERPRETATION

A tectonic map of the southeastern Caribbean and adjacent areas is shown in Figure 5. It is based on marine data from ESSA and other sources, and on the geology of the continent and certain islands.

The simplistic approach in the tectonic map reflects the view that the geologic history of this area can be explained without recourse to vast horizontal wrench faults or differential plate movements. Continuation of double island arc system belts into continents has been substantiated (Indonesian, Aleutian, Scotian, and Antillean). The arc belts have in places modified the structural trends of the continental margin, as on the Paria shelf.

It was noted in reviewing the geologic literature that the prevalence of cross trends in the arc system appeared to be the rule rather than the exception. These trends are more or less at right angles or normal to the arcs, and include not only faults but folds and even thrust faults. A summary of the cross trends found in the literature includes the following.

1. A fracture zone at the southeastern limit of the Los Roques Trench, north of the Netherlands Antilles, curves sharply across the interrupted arc of the Aves Ridge-Netherlands Antilles. The axis of the Eastern Venezuela basin makes a double change in trend just south of the southeastern terminus of the Los Roques Trench, and suggests the existence of a cross trend of some type, approximately at right angles to the coast near Barcelona, Venezuela.

2. Northwest-striking cross fractures, nor-

mal to the arc, occur in the Los Testigos Islands, which the ESSA data show to be a continuation of the Lesser Antilles inner volcanic arc. The islands consist of granites and volcanic rocks, Testigo Grande being a granitic intrusive body, bordered by younger volcanic rocks (Maloney, 1967). The Los Frailes Islands, along the same arc between Margarita and the Testigos, are a northwest-trending *en échelon* set of islands parallel with the eastern coast of Margarita.

3. The Los Hermanos Islands, just east of La Blanquilla Island, are oriented somewhat normal to the trend connecting the Blanquilla-Hermanos platform and the Aves Ridge. A seamount, 13 n. mi (24 km) southwest of La Blanquilla, also is oriented northwest-southeast, normal to the major trend. A basin between the seamount and the island of La Blanquilla likewise has a northwest-southeast orientation (Maloney, 1966, 1968).

4. Aves Island, the only part of the ridge above sea level, is arched with an axis approximately N70°E, and dips north and south (Maloney *et al.*, 1968). This general east-west orientation has been noted by prior workers.

5. The folds and thrusts exposed in eastern Barbados are oriented more or less east-west, normal to the outer island arc trend. The St. Lucia-Barbados cross-warp, whatever its true nature, also is normal to the arc trend.

6. In Grenada, the southernmost island of the Lesser Antilles, several anticlines and synclines have fold axes in an approximately east-west direction. These folds cross the arc trend, and are similar to those in Barbados.

7. Tobago Island consists of isoclinally folded schist and phyllite in the northern third of the island. These trends are east-northeast, contrary to the northeast strike of the island.

Undoubtedly many other examples exist, but those listed are sufficient to emphasize the fact that cross fractures and/or folds are far from uncommon.

The type of movement that has occurred along the El Pilar fault zone is very important in solving the tectonics of the region. The writers consider movement along the El Pilar and the northern fault zones to have been primarily vertical, and if any horizontal movement has occurred, it is relatively minimal. Vast horizontal movement of the magnitude of hundreds of miles is not supportable by field data.

1. Work by Potter (1968) shows that much of the literature has been theoretical, based on previous lack of field investigations. His map-

ping in the Northern Range of Trinidad has provided data for examining movement on the El Pilar fault. Evidence is good for vertical displacement of up to 6,000 ft (1,830 m) on the El Pilar and on the Brasso Seco faults, but there is *no evidence for lateral movement*. In addition, Potter noted that lateral movement since late Pliocene is not suggested by the positions of buried Plio-Pleistocene alluvial fans.

2. ESSA data from the Dragon's Mouth east to 59°W merely indicate a very clean high-angle to vertical break, between the Pilar block and the sediments on the south (Bassinger *et al.*, 1971). Lack of a wide gouge zone, expectable in a wrench fault, is quite conclusive. Although the near-vertical trace of the fault at the surface is indicated, it is not unlikely that the plane of the fault at depth may become shallower and dip north, as shown in published cross sections of Trinidad's structure (Kugler, 1961). At least this type of fault is consistent with other field data in Trinidad. The ESSA data further indicate the possibility that the El Pilar fault either becomes deeply buried or ceases to be a fracture east of 58°30'W.

3. Detailed field work along the El Pilar fault by Metz (1964) in the central Araya-Paria Peninsulas provides the evidence against large-scale strike-slip displacement. (a) The Cutacual Formation (Lower Cretaceous), only locally developed, crops out on both sides of the fault; this facies does not occur elsewhere, and therefore cannot have been displaced; (b) the same light-colored facies of the San Antonio Formation (Upper Cretaceous) also is found on either side of the fault, suggesting deposition in the same lithic province; and (c) the east-northeast-trending belt of the upper Cantil Formation (Lower Cretaceous) continues across the fault into the metamorphic belt on the north. Metz considered that, if any wrench faulting has taken place, it is minor, and recently (personal commun) Metz has even further reduced his estimate of wrench movement to 5 km (3.1 mi) or less.

4. The El Pilar and the now discounted Southern Caribbean faults have been considered as logical zones for possible right-lateral wrench movement. However, as Mencher (1963, p. 84, 85) pointed out in reference to the El Pilar, the actual field evidence for such extensive faulting and movement in Venezuela is limited and very little surface evidence of the fault exists in Trinidad. The age of the origin of the fault is uncertain, but some of the movement must be post-Cretaceous, as Cretaceous

rocks are affected, but Miocene to Holocene sediments overlapping the fault are not. Mencher concluded that, if such faults were not pre-Tertiary, they could not have played an important part in much of the tectonic history of Venezuela.

It is concluded that the El Pilar is no more than a vertical displacement fault, possibly a high-angle thrust at the surface, which continues east to about 58°30'W. It may continue even farther, but is either deeply buried or becomes inactive toward the east. If the El Pilar changes its east-west trend and becomes the frontal fault of the Barbados anticlinorium, it would indicate a reactivation of the fault as part of the arc system. This also would mean that the mobile belt continued around the eastern end of the Pilar block.

An analysis of the tectonic map (Fig. 5) shows two overall trends which have interacted. The old east-west trend, exemplified by the Pilar block and El Pilar fault, has somewhat modified and directed the arcward continuation of the continental mobile belt, with a trend more north than due east, into the island arc system. The fold and fault trends south of the Pilar block have an east-northeast trend and terminate against the block. The trends on the north have a similar east-northeast trend and terminate against the block at their southwestern ends; some are subparallel with the block. The general strike of the folds is, therefore, approximately the same north and south of the block. Only at the extreme west end of the Pilar block do trends continue around it, and it is possible that the same is true at the east end of the block.

Several extensional collapse features along the Pilar block are indicated, particularly in the Cariaco basin and the Dragon's Mouth. The abrupt turn in the southeastern part of the Los Roques Trench, the collapse of the Cariaco basin, and the abrupt twists in the axis of the Eastern Venezuela basin near 65°W long, suggest the presence of a possible tectonic cross feature. West of 66°W long, the strike of the coastal features is compatible with the merger of the continental orogenic belt-island arc system. The trends interrupted by the southeastern end of the Los Roques Trench continue west for some distance before merging with the orogenic belts of western Venezuela and Colombia (west of Fig. 5). The Pilar block seems to lose its identity, or to become involved in the trend of the merged orogenic systems from Caracas westward.

Fold and fault patterns south of the Pilar block indicate the probability that three segments of the block once stood higher in elevation, resulting in gravity-slide thrusting toward the southeast. These three areas are the Caracas (Caribbean Ranges), Cariaco (Araya-Paria Peninsulas), and North Range (Trinidad) areas. Sliding toward the southeast, normal to the folding, is suggested most strongly south of these three localities. Considerable thrusting is found in northern Guárico state, Venezuela, south of Caracas; the Serranía del Interior, south of Cariaco; and throughout Trinidad, south of the Northern Range. Wrench faults, of limited displacement, such as the Los Bajos fault of southwestern Trinidad, also occur in the Serranía del Interior, possibly merging into southeastward-directed thrusts at their limits. These faults are found south of the potentially higher areas. The high areas were undoubtedly much reduced by erosion prior to development of more recent phases of the arc system offshore.

SUMMARY

The results obtained during this study, in conjunction with the known structural geology of the region, show the following.

1. Sediments flanking the positive ridges of the southeast Caribbean island arc system are overlain unconformably by relatively undisturbed beds in the intervening troughs. In the Tobago Trough and the Central syncline (Barbados anticlinorium), an unconformity separates the folded strata of the positive elements from the flat-lying younger beds of the negative elements. Considerable elevation of the outer parts of the arc has occurred since folding ceased, as shown by the presence of reefs on Barbados at an elevation of 1,100 ft (336 m) above sea level. A period of folding was followed by one of epeirogeny.

2. Several cross features, normal to the trend of the arc system, appear to be quite common. Collapsed areas, such as in the Dragon's Mouth and the zone between the Grenada platform (Lesser Antilles) and Testigos-Margarita platform, occur within the area of study.

3. The Barbados anticlinorium, or outer sedimentary arc of the island arc system, is a feature consisting of two positive elements (West and East ridges), separated by a negative element (Central syncline). "Basement" rocks support the two ridges and lie more than 1.5 sec of acoustic penetration below the Central syncline. Other subsidiary or modifying fea-

tures, such as the North Tobago anticline and the East Tobago syncline, belong to the folded and faulted outer sedimentary arc.

4. The Lesser Antilles, or inner volcanic arc, is traceable onto the Paria shelf, continuing into the Testigos-Margarita platform. The continuation is confirmed by seismic reflection profiling and gravity data, but not by the bathymetry.

5. The Tobago Trough extends across the Paria shelf, depressing it with a large volume of sediments. The trend appears to end subparallel with the Pilar block. This observation is supported by seismic-reflection profiling, bathymetry inside the 100-fm (183 m) isobath, and refraction data. Evidence for a southern source of sediments both for the trough and Barbados is very strong.

6. Evidence shows that the Pilar block is an old structure which has partly modified the junction of the island arc system with the continent. The block is essentially a horst, bounded on the north and south by fault zones. The northern fault zone is traceable from the western end of the Araya Peninsula to the edge of the eastern Trinidadian shelf, where it cannot be distinguished from the fracture system at the junction of the East ridge and the Pilar block. In all likelihood, the fault zone north of the Pilar block consists of a series of *en échelon* fractures. Although the individual faults may strike east-northeast, the fault zone strikes essentially east-west. The El Pilar is traceable farther east, because a "basement"-sediment contact is easy to detect seismically. It is traceable east to 58°30'W, although there is considerable question as to whether it continues as a fault, because it may be deeply buried by sediments from the south.

Both the El Pilar and northern fault zones may cross the Cariaco basin and be present north and south of the coastal ranges near Caracas. This would be the most logical projection, and Figure 5 reflects this inference.

7. The evidence in the southeastern Caribbean does not support the concept of wrench faulting, with its implication of vast horizontal movements of individual blocks. The Southern Caribbean fault, long hypothesized as the southern margin of the Caribbean plate, simply does not exist. Nor is the El Pilar a wrench fault, inasmuch as most field data show its movements to have been vertical with only a small wrench component.

8. The structural geology of the region can be explained in a simplistic manner. The island

arc structural belts and the mobile belts of the continent are interrelated, gradational, and interlocked.

9. An analogy between the southeastern Caribbean and the Andaman Sea arcs shows the logic in an extension of a continental mobile belt into an island arc system. Except for the modifying influence of the Pilar block, the two island arc systems are surprisingly similar.

REFERENCES CITED

- Baadsgaard, P. H., 1960, Barbados, W. I.: exploration results 1950-1958, in *Structure of the earth's crust and deformation of rocks*: 21st Internat. Geol. Cong. Rept., Copenhagen, pt. 18, p. 21-27.
- Bassinger, B. G., R. N. Harbison, and L. A. Weeks, 1971, Marine geophysical study northeast of Trinidad-Tobago: Am. Assoc. Petroleum Geologists Bull., v. 55, no. 10, p. 1730-1740.
- Bunce, E. T., J. D. Phillips, R. L. Chase, and C. O. Bowin, 1970, The Lesser Antilles arc and the eastern margin of the Caribbean Sea: Woods Hole Oceanog. Inst. Contrib. 2288, 36 p.; in press, in A. E. Maxwell, ed., *The sea*, v. 4: New York, Wiley-Interscience.
- Earle, K. W., 1924, Geological survey of Grenada and the (Grenada) Grenadines: St. George's, Grenada, Govt. Printing Office, 9 p.
- 1928, Report on the geology of Saint Vincent and the neighbouring Grenadines: Kingston, Jamaica, Govt. Printing Office, 65 p.
- Edgar, N. T., 1968, Seismic refraction and reflection in the Caribbean Sea: Ph.D. thesis, Columbia Univ., 163 p.
- J. I. Ewing, and J. Hennion, 1971, Seismic refraction and reflection in Caribbean Sea: Am. Assoc. Petroleum Geologists Bull., v. 55, no. 6, p. 833-870.
- Ewing, J. I., M. Talwani, M. Ewing, and T. Edgar, 1967, Sediments of the Caribbean: Internat. Conf. Tropical Oceanog. Proc., Miami Univ., 1965, p. 88-102.
- Hurley, R. J., 1966, Geological studies of the West Indies: Canada Geol. Survey Paper 66-15, p. 139-150.
- Kugler, H. G., 1961, Geological map of Trinidad and geological sections through Trinidad: pub. for Petroleum Assoc. Trinidad, Zurich, Orell Fussli, and London, E. Strand.
- Lattimore, R. K., L. A. Weeks, and L. W. Mordock, 1971, Marine geophysical reconnaissance of continental margin north of Paria Peninsula, Venezuela: Am. Assoc. Petroleum Geologists Bull., v. 55, no. 10, p. 1719-1729.
- Lewis, J. F., 1968, Composition, origin and differentiation of basalt magma in the Lesser Antilles (abs.), in *Abstracts of papers: 5th Caribbean Geol. Conf., Virgin Islands, July 1-5, 1968*, p. 44-45.
- MacDonald, W. D., and W. G. Melson, 1969, A late Cenozoic volcanic province in Hispaniola: Caribbean Jour. Sci., v. 9, nos. 3-4, p. 81-90.
- MacGillavry, H. J., 1970, Geological history of the Caribbean: Nederlandse Akad. Wetensch. Proc., ser. B, v. 73, no. 1, p. 64-96.
- Maloney, N. J., 1966, Geomorphology of continental margin of Venezuela, pt. 1, Cariaco basin: Univ. Oriente, Inst. Oceanog. Bol., v. 5, no. 1, 2, p. 38-53.
- 1967, Geomorphology of continental margin of Venezuela, pt. 2, Continental terrace off Carúpano: Univ. Oriente, Inst. Oceanog. Bol., v. 6, no. 1, p. 147-155.
- C. Shubert, J. I. Marlowe, and A. T. S. Ramsay, 1968, Geology of Aves Island, Venezuela (abs.), in *Abstracts of papers: 5th Caribbean Geol. Conf., Virgin Islands, July 1-5, 1968*, p. 50-51.
- 1968, Geology of La Blanquilla Island with notes on Los Hermanos Islands, eastern Venezuela (abs.), in *Abstracts of papers: 5th Caribbean Geol. Conf., Virgin Islands, July 1-5, 1968*, p. 49-50.
- Marlowe, J. I., 1968, Geological reconnaissance of parts of Aves Ridge (abs.), in *Abstracts of papers: 5th Caribbean Geol. Conf., Virgin Islands, July 1-5, 1968*, p. 51-52.
- Martin-Kaye, P. H. A., and J. B. Saunders, 1962, An upper Eocene formation in Grenada, West Indies (abs.): 3d Caribbean Geol. Conf. Prog., Kingston, Jamaica, p. 29-30.
- Mencher, E., 1963, Tectonic history of Venezuela, in *Backbone of the Americas*: Am. Assoc. Petroleum Geologists Mem. 2, p. 73-87.
- Metz, H. L., 1964, Geology of the El Pilar fault zone, state of Sucre, Venezuela: Ph.D. thesis, Princeton Univ., 102 p.
- Peter, G., L. A. Weeks, and R. E. Bruns, 1966, A reconnaissance geophysical survey in the Andaman Sea and across the Andaman-Nicobar Island arc: Jour. Geophys. Research, v. 71, p. 495-509.
- Potter, H. C., 1968, Faulting in the Northern Range of Trinidad (abs.): 23d Internat. Geol. Cong. Rept., Prague, p. 95.
- Sykes, L. R., and M. Ewing, 1965, The seismicity of the Caribbean region: Jour. Geophys. Research, v. 70, p. 5065-5074.
- Tomblin, J. F., 1968, Geochemistry and genesis of Lesser Antillean volcanic rocks (abs.), in *Abstracts of papers: 5th Caribbean Geol. Conf., Virgin Islands, July 1-5, 1968*, p. 74-75.
- van Bemmelen, R. W., 1949, The geology of Indonesia, v. 1A: The Hague, Govt. Printing Office, 732 p.
- Weeks, L. A., R. N. Harbison, and G. Peter, 1967, Island arc system in Andaman Sea: Am. Assoc. Petroleum Geologists Bull., v. 51, no. 9, p. 1803-1815.

*Reprinted from Proceedings of the Miami Workshop
on Remote Sensing, March 29-31, 1971, 133-148.*

STUDIES OF CLOUD AND SATELLITE PARAMETERIZATION OF SOLAR IRRADIANCE AT THE EARTH'S SURFACE

Kirby J. Hanson

*National Oceanic and Atmospheric Administration
Atlantic Oceanographic and Meteorological Laboratories
Miami, Florida*

1. INTRODUCTION

If one thinks about the fact that most of the solar energy received by the earth is in tropical and subtropical latitudes and that the vast majority of this area is oceanic, it is obvious that the global distribution of solar irradiance cannot be measured but must be parameterized by some means. Since clouds modulate solar irradiance, it is logical to use cloudiness as a means of parameterization.

When clouds are *thin* (such as cirrus) they tend to attenuate the irradiance by only a small amount. An example of this can be seen from solar irradiance data at Canton Island during the four-month period from September-December, 1960. During these months the average sky coverage was 10/10th (mostly cirrus), but yet the solar irradiance was 85-90 percent of that received on clear days. When clouds are *thick*, however, the attenuation is large and the irradiance at the surface is very low. An example of this is illustrated in figures 1 and 2 which show the solar irradiance on two days at Swan Island (Caribbean). The integrated daily irradiance on the day with deep tropical convection (October 30) was only 1.2 percent of the clear-day value (October 4). Thus, the *type* of cloudiness as well as the amount is important for parameterizing surface irradiance.

However, there are certain disadvantages in using surface-observed cloudiness for parameterization. One disadvantage is that a wide range of calculated irradiance values is obtained when trying to establish the empirical relationship between irradiance and cloudiness. For example, the following empirical equations have been determined by the authors indicated below; and all have been adjusted by Quinn and Burt

(1968) to apply to Canton Island:

1. $Q = Q_0 (1.0 - 0.71C)$ (Kimball, 1928)
2. $Q = Q_A (0.803 - 0.304C - 0.458C^2)$ (Back, 1956)
3. $Q = Q_0 (1 - 0.655C)$ (Savino-Angstrom
(Budyko, 1956))
4. $Q = Q_0 (1 - 0.39C - 0.38C^2)$ (Berliand, 1960)
5. $Q = Q_0 (1 - 0.0006C_t^3)$ (Laevastu, 1960)
6. $Q = Q_0 (1 - 0.0895C_o + 0.00252a')$ (Tabata, 1964)
7. $Q = Q_A (0.884 - 0.552C_{op})$ (Quinn, 1969)

where:

- Q = total incoming solar irradiance,
 Q_0 = total incoming solar irradiance with a clear sky,
 Q_A = total solar irradiance on a horizontal surface at the top of the atmosphere,
 C = proportion of sky covered with clouds (0-1.0),
 C_t = cloud cover in tenths (1-10),
 C_o = cloud amount in Oktas (1-8),
 C_{op} = proportion of sky covered with opaque clouds (0-1.0),
 a' = midmonth solar altitude in degrees.

Oct. 4, 1966 - 670(cal/cm²)
 Oct. 30, 1966 - 8(cal/cm²)

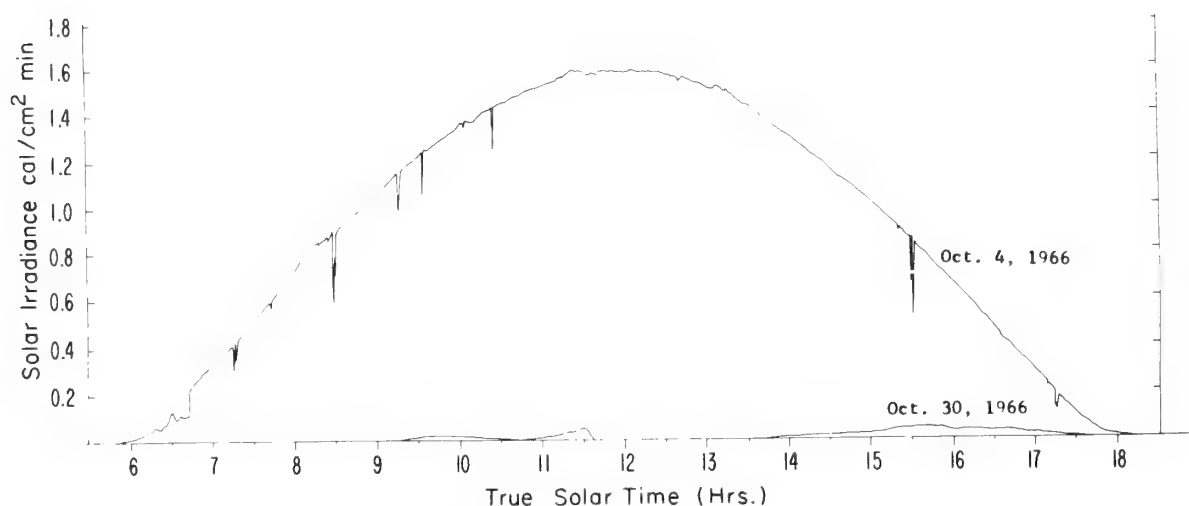


Figure 1. Solar irradiance curves for Swan Island. Values are integrated daily total irradiance (cal/cm²).

OCTOBER 4, 1966



OCTOBER 30, 1966

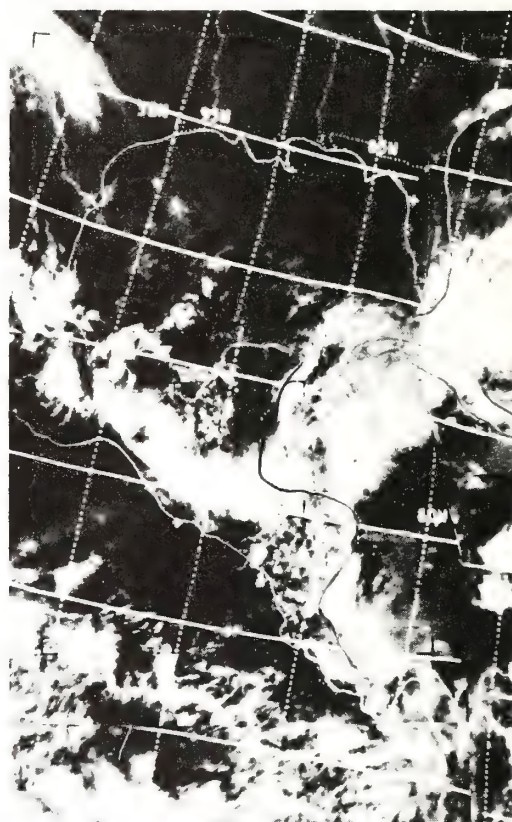


Figure 2. Satellite photos of Central America, the Gulf of Mexico, and the western Caribbean. Swan Island is located at 17°N , 84°W . The photos correspond to the two days (radiation curves) shown in figure 1.

These empirical equations have been graphed and illustrated in figure 3 to show the wide range of transmittance values for a particular value of cloud cover. Moreover, the functional relationships differ depending on the proposed formula used: in four cases a linear relationship has been found, but in others second- and third-order polynomials are illustrated.

Another difficulty with parameterization using cloudiness is that the result depends on the *time scale* over which the cloud and irradiance data are averaged. An example of this is shown in figures 4 and 5. In both illustrations, curves 3 and 5 are shown as limiting curves. Mean atmospheric transmittance and mean cloudiness averaged over *daily* periods are shown in figure 4, and averaged over *annual* periods are shown in

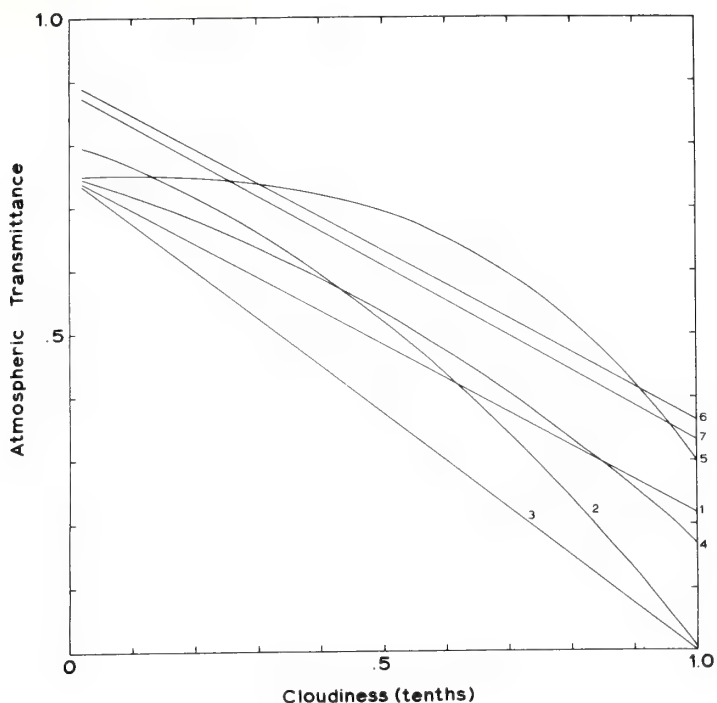


Figure 3. Atmospheric transmittance vs. cloudiness by various authors (see text) as summarized by Quinn (1968).

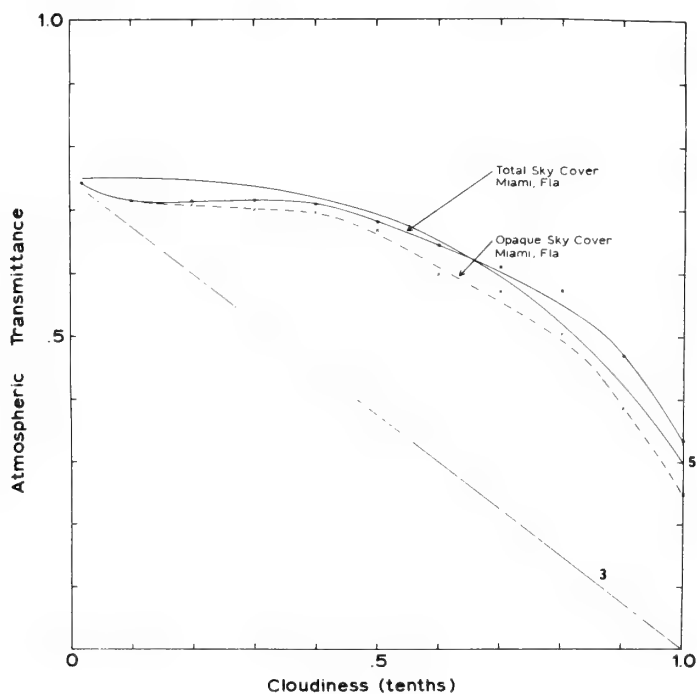


Figure 4. Atmospheric transmittance vs. cloudiness for Miami, Florida, based on daily values of irradiance and cloudiness.

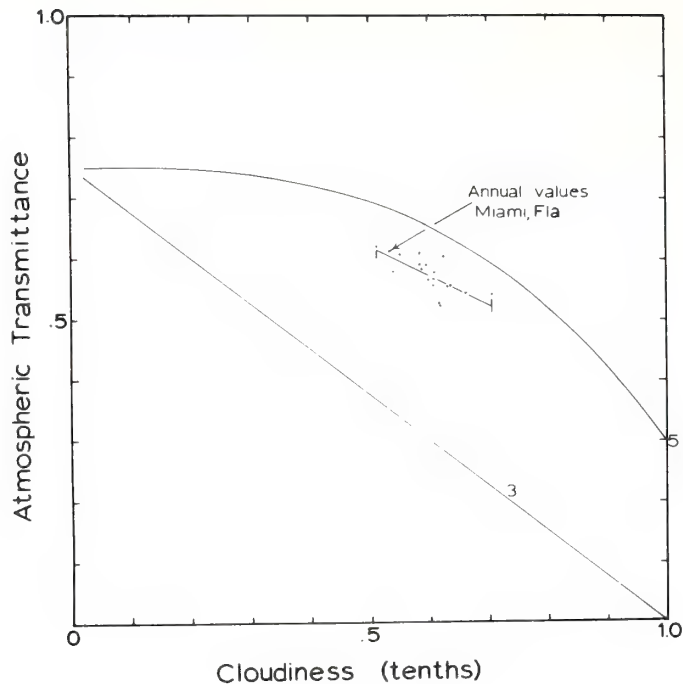


Figure 5. Atmospheric transmittance vs. cloudiness for Miami, Florida, based on annual values of irradiance and cloudiness.

figure 5. The transmittance values are obtained as the ratio of the solar irradiance at the earth's surface to the extra-terrestrial irradiance. Both figures 4 and 5 are based on data from Miami, Florida. From these figures it is clear that the *time scale* of averaging the data changes both the position and the shape of the parameterization curve. This may offer a partial explanation for the wide variety of curves in figure 3 which undoubtedly are based on a variety of time scales.

It is apparent from more than 40 years of effort by many investigators that there are certain shortcomings in quantifying solar irradiance from cloudiness. This paper is an attempt to look at the accuracies of simple parameterization techniques (which include surface-observed cloudiness) and to compare these with parameterization accuracies based on quantitative satellite data.

2. PARAMETERIZATION METHODS

There are many applications for calculated values of solar irradiance at the earth's surface and, presumably, each

of these applications has a certain requirement for accuracy. Thus, it is important to be able to state quantitatively the predictability of surface irradiance. The following sections discuss the use of simple techniques for calculating surface irradiance as well as the use of quantitative satellite data for this purpose.

2.1 Long-Term Mean Irradiance

The most simple technique for determining the surface irradiance is to use the long-term (climatic) mean irradiance.

To test the variability of observed irradiance data from the climatic mean, we have taken 18 years of data from Miami, Florida, and 15 years from Canton Island and calculated the standard deviation of the irradiance on various time scales for both locations. The results, in the left-hand columns of table 1, show (as expected) the standard deviation of irradiance to be dependent on the time scale over which the data are averaged. On a *yearly* basis at Miami, the standard deviation is 3.5 percent of the observed irradiance, whereas, on an hourly basis the standard deviation is 30.5 percent -- nearly an order of magnitude larger. For Canton Island, the standard deviation values are somewhat smaller (particularly for shorter time scales) because Canton Island is located in the equatorial dry zone (2° S. lat.) and is less affected by strongly attenuating cloudiness.

These values in the left-hand section of table 1 might be termed the "natural variance" of irradiance that occurs on various time scales. In this respect they represent an upper limit -- against which various parameterization techniques should show improvement.

2.2 Surface-Observed Cloudiness

A commonly observed meteorological parameter is total sky cover, which is the amount of sky obscured by clouds of any discernable thickness. Because it is commonly available, we have used this parameter to determine a functional relationship between cloudiness and irradiance and have calculated the variance of observed irradiance values from function-generated irradiance values. (This is commonly called "variance of the residuals after regression".) The same Miami

Table 1. Standard deviation of observed surface irradiance.

Time Scale	from long-term Mean Irradiance		from Cloud Parameterized Value		from Satellite Parameterized Value
	Miami Fla. (%)*	Canton Isl. (%)*	Miami Fla. (%)*	Canton Isl. (%)*	
Hour	30.5	-	-	-	-
Day	27.3	13.7	17.7	13.3	-
Week	14.8	9.1	8.6	8.9	-
Month	9.1	8.0	7.1	6.5	3.23
Year	3.5	4.0	3.2	3.9	-

* Percent of Mean Irradiance

1 Cox, Hastenrath (1970), $I = I_0(1 - .24C_t - .518C_t^2)$

2 Cox, Hastenrath (1970), $I = I_0(1 - .584C_t)$

3 June, 1966 - NIMBUS II (MRIR) Data

and Canton Island data were used, and the results are shown in the middle section of table 1. It can be seen that standard deviation increased with shorter time scales, and the values are *less* than those determined from the climatic mean. The major improvement in predictability (over the climatic mean) is in the *shorter* time scales. For example, for Miami, the standard deviation decreases from 27.3 to 17.7 percent on the daily time scale.

Thus, it appears that simple cloud parameterization of irradiance is most useful for applications which require calculations on time scales of a week or less.

2.3 Satellite-Observed Irradiance

Based on the principle of conservation of energy, it is possible to calculate the absorption of radiation by the *atmosphere* as a residual, in cases where satellite and surface irradiance measurements are available (Hanson et al. 1967). However, in the present case it is not atmospheric absorption that is desired, but irradiance at the surface. Thus, the residual calculation is surface irradiance -- which requires satellite irradiance measurements and a quantitative estimate of atmospheric absorption.

We have used this method to establish the accuracy with which surface irradiance may be determined. The result, with dependent data, shows that for the United States on a monthly scale (June, 1966) the standard deviation of surface irradiance is 3.2 percent (table 1). This is smaller by a factor of three than the standard deviation of the irradiance from the long-term mean. This satellite data technique is yet to be tested with independent data.

The method used in this technique is to determine the atmospheric absorption of irradiance (I_A) as a residual in

$$I_o = (1-a)I_g + I_R + I_A \quad , \quad (1)$$

where

- I_o = incident extraterrestrial solar irradiance,
- I_g = solar irradiance at earth's surface,
- I_R = irradiance reflected to space,
- a = surface reflectance (albedo).

Dividing (1) by I_0 gives:

$$1 = q_a + q_r + q_g(1-a) \quad , \quad (2)$$

where:

$q_a = I_A/I_0$, the fraction of incident sunlight absorbed in the atmosphere,

$q_r = I_R/I_0$, the fraction of incident sunlight reflected to space,

$q_g = I/I_0$, the fraction of incident sunlight transmitted by the atmosphere to the earth's surface.

The right-hand term in (2) is the fraction of the incident irradiance which is absorbed at the earth's surface; this will be denoted as q_e . Then

$$1 = q_a + q_r + q_e \quad . \quad (3)$$

Equation (3) simply shows the partitioning of solar radiation which is incident on the earth's outer atmosphere.

The following sections show how the individual irradiance terms were determined.

2.3.1 Irradiance at Upper Boundary

In this study, the irradiance, I_0 , was calculated from

$$I_0 = I_s (r_m/r)^2 \cos \zeta \quad (4)$$

The solar constant, I_s , was taken as $2.0 \text{ cal/cm}^2 \text{ min}$, r_m and r are the mean and actual earth-sun distances, and ζ is the time-integrated solar zenith angle at the subsatellite point.

2.3.2 Irradiance at the Earth's Surface

The irradiance, I_g , was obtained from measurements by the National Weather Service network of pyranometer stations which

measure the broadband (0.3-2.5 μm) solar irradiance. These data are available from the National Climatic Center (NOAA, 1966). Corrections have been made to the measurements in order to account for degradation of the sensors at some stations. The background information for determining those corrections was obtained from Stark (1971). Surface reflectance, a , values for the United States were obtained from the summer season surface reflectances reported by Kung et al. (1964). The resulting surface absorption of irradiance, q_e , over the United States is shown in the lower portion of figure 6 and is expressed as the fraction of incident extraterrestrial irradiance.

2.3.3 Irradiance at the Upper Boundary

The upwelling irradiance at satellite height, I_R , was observed by the MRIR (broadband solar) sensor on NIMBUS II. The irradiance was determined from MRIR radiance data by methods described by Raschke and Bandeen (1970). The earth's reflectance at satellite height, q_r , is given in the upper half of figure 6. There is a high negative correlation between q_e and q_r , as is evident in figure 6.

2.3.4 Irradiance in the Atmosphere

Values of atmospheric absorption, I_A , were calculated as a residual using (1) and the values of a , I_q , I_o , and I_R from the sources indicated above. The resulting q_a values are shown in the upper half of figure 7. The distribution of q_a shows high absorption in the east -- particularly the south-east -- as expected from water-vapor distribution. This latter value is shown in the lower part of figure 7 and has been calculated from mean monthly temperature and water-vapor (vertical) distributions. Optical depth of water vapor, u , was calculated from:

$$u = \frac{1}{g} \int w \, dp \quad , \quad (5)$$

where g is the acceleration of gravity at the earth's surface, w is the mixing ratio of water vapor, and p is pressure. The integration was carried out to approximately 300 mb. Optical pathlength values, τ , (in lower fig. 7) have been determined

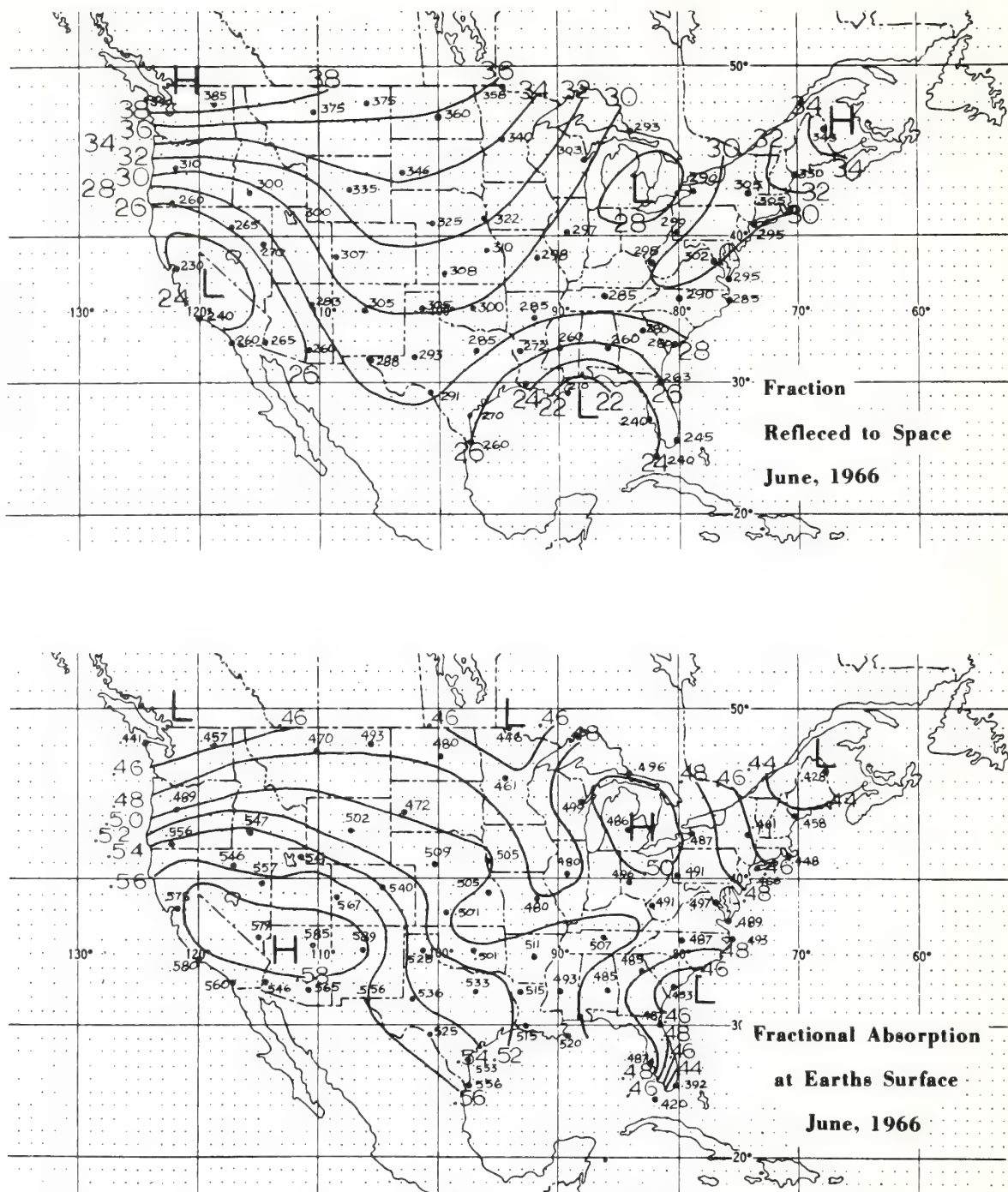


Figure 6. Distributions of fractional reflectance, q_r , of earth/atmosphere and fractional absorption of the earth's surface, q_e , for June, 1966.

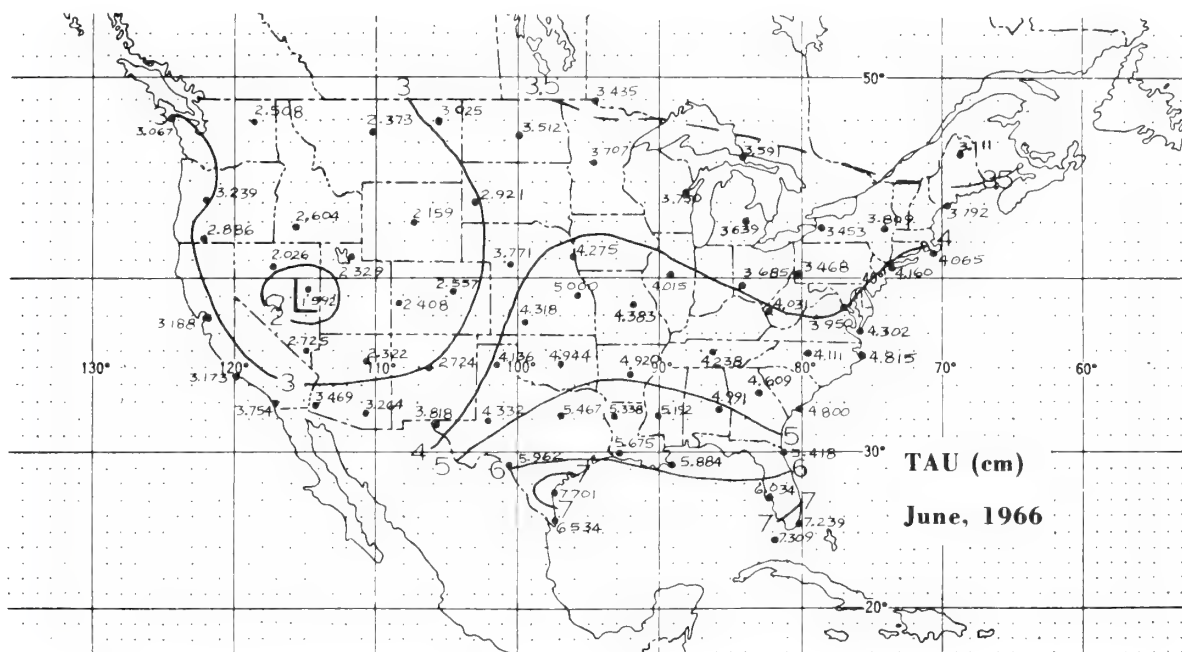
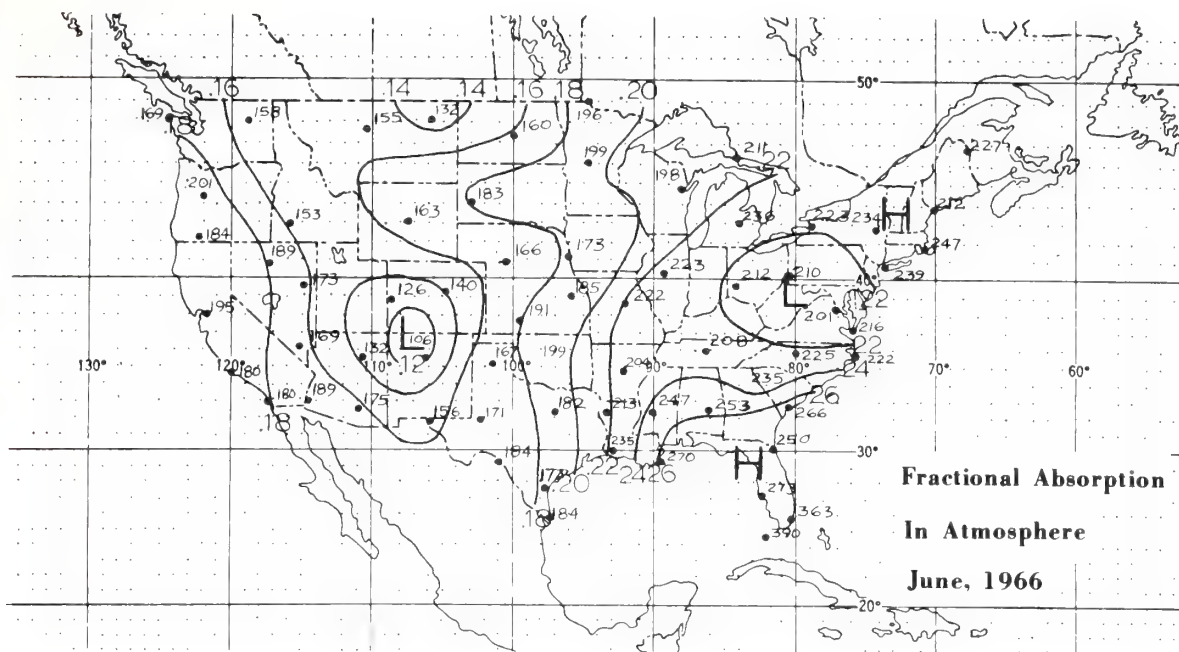


Figure 7. Distribution of fractional absorption by the atmosphere, q_a , and optical pathlength of water vapor for June, 1966.

from these u values, from the change in optical pathlength due to varying solar zenith angles, ζ , and from the effect of diffuse radiation beneath clouds. The latter effect was introduced in the following way:

$$\tau = (1-c)(.86u^* + .14(1.66u)) + c(1.66u) , \quad (6)$$

where c is the mean monthly cloudiness and u^* is the optical pathlength with clear skies,

$$u^* = u \sec \zeta . \quad (7)$$

A diffusivity factor of 1.66 has been used as the optical pathlength under diffuse light conditions due to clouds.

The resulting τ values, mapped in figure 7, show a pattern very similar to the atmospheric absorption, q_a . There are low values for optical pathlength in the western United States and higher values in the east and southeast. In comparing these two distributions, it appears that q_a values in the northeastern quarter of the United States are higher than expected from water vapor alone -- and may be a result of industrial or other pollution. The strong dependence of q_a on τ is clear from figure 7.

In figure 8, the dependence of q_a on τ is shown in a scatter diagram. The q_a values are related to τ by

$$q_a = .117 + .031\tau^{\frac{1}{2}} \ln \tau , \quad (8)$$

where the constants have been determined by least squares fit. The variance of the residuals from the function values is .00101. Thus, the standard deviation of the residuals is 3.2 percent.

In this case we have determined I_A as a residual in (1). However, it is also possible to use the measurement of I_R and a knowledge of I_o and I_A (calculated from (8)) in order to parameterize I_g over the United States. This has been done, and the calculated I_g values and observed (dependent

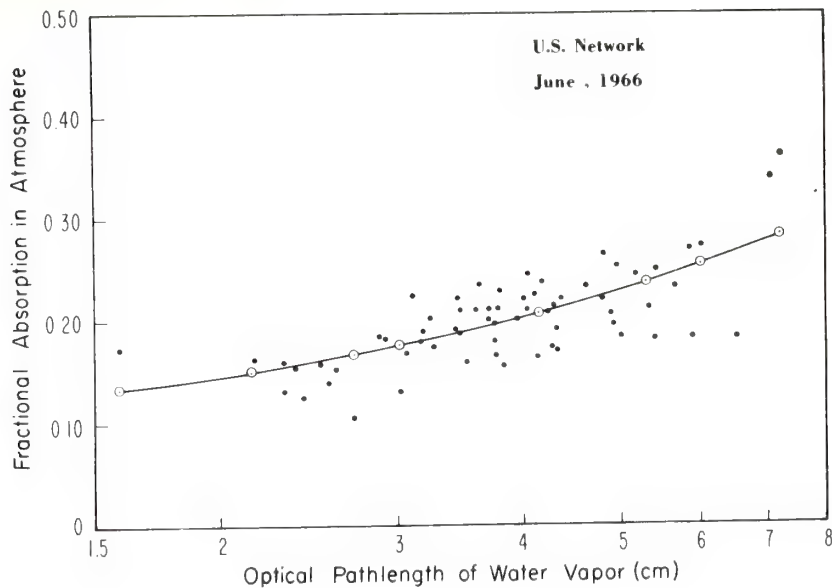


Figure 8. Fractional absorption of solar radiation by the atmosphere q_a , vs. optical pathlength of water vapor based on the U.S. network of pyranometer and radiosonde stations and on NIMBUS II broadband solar (MRIR) data for June 1966.

data) values of I_g have a standard deviation of 3.2 percent. The significance of this fact, as shown in table 1, is that the satellite parameterization of I_g shows improvement by factors of 2 and 3 over the other two techniques.

3. SUMMARY

This study has shown that there are difficulties and shortcomings with relatively simple techniques for parameterizing solar irradiance from (1) long-term climatic radiation data, and (2) cloud observations from the earth's surface. One difficulty is that there is a wide range in the results of empirically determined irradiance values (from cloudiness) depending on the equation used (i.e., the author selected). A second difficulty is that both the form and the constants of the empirical equation depend on the time scale over which the data are averaged.

In an attempt to determine the accuracy of these two parameterization techniques, we have used 18 years of data from Miami, Florida, and 15 years from Canton Island. The result (table 1) shows that the longer time scales have the smallest errors. The use of surface-observed cloudiness to parameterize the surface irradiance shows only slight improvement over the natural variance that occurs. On shorter time scales, the improvement is somewhat more significant than on the longer time scale. The use of satellite data for parameterizing surface irradiance on a monthly time scale shows improvement by a factor of about 3 over the natural variance that occurs.

4. REFERENCES

- Beriland, T.G. (1960), Metodika Klimatologicheskikh Raschetov Summarnoi Radiatsii (Method of Climatological Calculation of Global Radiation), Meteor. i Hidrol. 6, 9-12.
- Black, J.N. (1956), The distribution of solar radiation over the earth's surface, Archiv. Meteorol. Geophys. Bioklim. B7, 165-189.
- Budyko, M.I. (1956), The Heat Balance of the Earth's Surface, Gidrometeorologicheskoe Izdatel'stvo Leningrad (transl. by Office of Tech. Services, U.S. Dept. of Commerce, Washington, D.C., 1958, 259 pp).
- Cox, S., and S. Hastenrath (1970), Radiation measurements over the equatorial central Pacific, Monthly Weather Rev. 98, 823-832.
- Hanson, K.J., T.H. Vonder Haar, and V. Suomi (1967), Reflection of sunlight to space and absorption by the earth and atmosphere over the United States during the spring 1962, Monthly Weather Rev. 95, 353-362.
- Kimball, H.H. (1928), Amount of solar radiation that reaches the surface of the earth on the land and on the sea, and methods by which it is measured, Monthly Weather Rev. 56, 393-398.
- Laevastu, T. (1960), Factors affecting the temperature of the surface layer of the sea, Soc. Sci. Fennica, Commentationes Phys. Math. 25, 1-135.

NOAA (1966), Climatological Data - National Summary, Natl. Climatic Data Center, Asheville, N.C.

Quinn, W.H. (1969), A study of several approaches to computing surface insolation over tropical oceans, J. Appl. Meteorol. 8, 205-212.

Raschke, E., and W. Bandeen (1970), The radiation balance of the planet earth from radiation measurements of the satellite NIMBUS II, J. Appl. Meteorol. 9, 215-238.

Tabata, S. (1964), Insolation in relation to cloud amount and sun's altitude, Univ. of Tokyo, Geophysics Notes 17, 202-210.

Airborne Measurements of the Total Heat Flux from the Sea during Bomex

E. D. McALISTER

*University of California at San Diego
Scripps Institute of Oceanography, La Jolla, California 92037*

WILLIAM McLEISH

*Environmental Science Services Administration
Atlantic Oceanographic and Meteorologic Laboratories, Miami, Florida 33130*

ERNST A. CORDUAN

*University of California at San Diego
Scripps Institute of Oceanography, La Jolla, California 92037*

Airborne measurements of the total heat flux from the sea were successfully made during the Barbados oceanographic and meteorological experiment in May 1969. The values found at night ranged from 0.05 to 0.45 cal cm⁻² min⁻¹ and are half-hour averages over contiguous strips of ocean 1.6 km long and 75 meters wide. These are the first airborne measurements of this oceanic factor and the method used is new.

A total of 10²¹ calories of solar energy is stored during the daylight hours of one average day in the top 30 meters of the world's oceans. This energy is released during a 24-hour cycle and thus is important to the dynamics of the ocean. It represents the total energy available to the marine atmosphere from below and so has a direct bearing on meteorological predictions. No direct method of measurement of this total heat loss has previously been demonstrated.

For the past several years at Scripps Institution of Oceanography, the authors have attempted to fill this need by developing an airborne infrared-optical method. The principle of this method depends on the physical properties of water, namely its absorption coefficient for infrared radiation and its molecular heat conductivity. The system developed measures the vertical temperature gradient in the top 0.1 mm of the sea surface wherein the heat flow is dominated by molecular conduction [McAlister and McLeish, 1969]. The total heat flow may be determined from this temperature gradient and the heat conductivity of sea water. A two-wave-

length infrared radiometer was developed for this purpose.

The use of an airborne digital data reduction system was of major importance in this system. This combined with continuous calibration of detector sensitivity allowed measurement of water temperature to 0.01°C and the temperature difference between the two depths to 0.003°C. It is believed that the accuracy in reading water temperature is set by the mercury thermometer used in calibration, which could be read to 0.01°C.

This accuracy is reached only after determining atmospheric losses caused by absorption, scattering, and emission by flying at different altitudes and extrapolating the data to zero altitude, i.e., the sea surface. The radiation from the sky is continuously measured and used to remove reflected sky radiation from the beam coming from immediately below the water surface. Details of the two-wavelength radiometer, the digital data recorder, calibration, operation, calculation procedures, and the effect of sea state are described in McAlister and McLeish [1970]. The calculation procedure is repeated here and one day's records are analyzed later to illustrate the calculation

of total heat flux and sea-surface temperature.

The infrared radiance from the water surface at night I_w is the sum of two parts: $I_v(1 - r)$ from immediately below the water surface and $I_s \cdot r$ from the sky by reflection from the water surface, i.e.,

$$I_w = I_v(1 - r) + I_s \cdot r \quad (1)$$

where I_v and I_s are the underwater and sky radiation intensities and r is the reflectivity of the water surface. The radiometer compares this total with that from the reference blackbody I_B . The radiometer uses two wavelength bands, 3.4 to 4.1 μ (channel 1) and 4.5 to 5.1 μ (channel 2), which effectively isolate radiation coming from depths of 0.0075 cm and 0.0025 cm in the water. The reflectivity for the wavelengths used in channel 1 is $r_1 = 0.0268$ and in channel 2 the reflectivity is $r_2 = 0.0210$. In channel 1 the comparison of intensity from the water with that from the reference blackbody is

$$(I_{w_1} - I_{B_1}) = \frac{(I_{w_1} - I_{B_1}) - (I_{s_1} - I_{B_1}) \cdot r_1}{(1 - r_1)} = A_1 \quad (2)$$

and in channel 2 it is

$$(I_{w_2} - I_{B_2}) = \frac{(I_{w_2} - I_{B_2}) - (I_{s_2} - I_{B_2}) \cdot r_2}{(1 - r_2)} = A_2 \quad (3)$$

The difference in intensity coming from the two depths is then

$$I_{w_1} - I_{w_2} = A_1 - A_2 \quad (4)$$

The temperature difference in the water at the two depths is therefore

$$\Delta T = (A_1 - A_2)C \quad (5)$$

where

$$C = (\langle T_{B_1} \rangle - \langle T_{B_2} \rangle) / (\langle I_{B_1} \rangle - \langle I_{B_2} \rangle) \quad (6)$$

and $\langle I_{B_1} \rangle$, $\langle I_{B_2} \rangle$, $\langle T_{B_1} \rangle$, and $\langle T_{B_2} \rangle$ are the average intensities and temperatures for the two reference blackbodies during the time interval of interest. This approximate relation holds with sufficient accuracy when water temperature and the blackbody temperatures are no more than 2° or 3°C apart. After ΔT is evaluated for a particular exercise the total heat flux is calculated

by multiplying the coefficient of heat conductivity of sea water by the vertical temperature gradient.

The actual temperature at the two depths cannot be obtained as accurately as the difference in temperatures, equation 5. This is because the temperature of the water surface flown over does change a few hundredths of a degree centigrade during the half hour or more of time necessary to obtain several readings at three or more altitudes. Also, since the difference in radiation intensity coming from the two depths (equation 4) changes very little (a small fraction of 1%) for a 0.1°C change in water temperature (say, from 300.0°K to 300.1°K) the temperature difference as obtained from equation 5 is accurate.

THE TRIALS AT BARBADOS

During May of 1969 at Barbados scientists from several oceanographic institutions made use of *Scripps' Floating Instrument Platform (Flip)* to measure the latent heat flux, sensible heat flux, and the factors influencing the magnitude of these heat losses. This offered an opportunity for comparison with values measured simultaneously by the total heat flow radiometric system.

The equipment and crew were flown to Barbados in Scripps' DC-3 aircraft. The system was assembled and recalibrated to verify its condition after the flight from San Diego.

Flip was stationed 200 miles east of Barbados. Flights near it were made when weather and operating conditions permitted. These flights were at night to avoid solar interference with readings from the shorter wavelength channel (3.5 to 4.1 μ). Safety regulations that were adopted required a lateral separation of 300 meters from *Flip*. Consequently a racetrack course was flown, the downwind leg being 300 meters north of *Flip* and the upwind leg 300 meters south.

Data was tape recorded during 24 sec of each leg, which gave information on a 1.6-km strip on the sea which averaged 75 meters in width. 26,000 readings of 10 parameters were recorded during each pass. The flights were made at 50, 100, and 150 meters altitude to correct for atmospheric attenuation [McAlister and McLeish, 1970]. Usually 16 to 24 passes by *Flip* were made during a period of from

TABLE 1. Computer printout of 30-sec averages

[illegible]

40 minutes to 1 hour. These provide an average value of total heat flux from the strip of ocean 1.6 km long and 75 meters wide.

Flights were made when weather permitted a night rendezvous with *Flip*. The *Flip* was being towed to a new location from May 20 to 23, consequently no flights were made then. From May 19 to May 29, seven flights were

made as shown in Table 3. The flight on May 29 was made in cooperation with ESSA planes. *Flip* was departing Barbados on this date. During all of these flights there were scattered low clouds, 300 to 600 meters and a secondary layer at middle altitudes. These cloud conditions were uniform for all of the flights. Darkness prevented detailed cloud description.

TABLE 2. Computer printout of radiation intensity differences

CHANNEL 1			CHANNEL 2			ALT. IN METERS	$A_1 - A_2$
REC.	(S(1)-BB(1)) - ((SKY(2)-BB(1))*0.0268)	(S(2)-BB(1)) - ((SKY(2)-BB(1))*0.0210)					
	*****	*****					
2	-33.2242	34.2000	-21.7335	29.5700	-.7966		
2	-34.1212		-25.5144			150	-8.6068
3	-35.2994	40.9200	-33.3133	56.5000	-.8118		
3	-36.2524		-24.4859				-11.7626
4	-33.4234	40.8200	-38.4351	58.7800	-.8548		
4	-34.3258		-27.0927			100	-7.2331
5	-35.7298	43.2200	-42.2011	60.0800	-.8818		
5	-36.6945		-30.8148				-5.8796
6	-35.4512	43.1400	-43.1080	59.9300	-.8967		
6	-36.4084		-31.4974			50	-4.9110
7	-37.5697	45.1600	-46.0594	60.3800	-.9231		
7	-38.5841		-34.9672				-3.6169
8	-35.6011	45.9700	-35.0295	62.4800	-.9484		
8	-36.5623		-26.1607			150	-10.4016
9	-33.1563	47.0400	-33.8021	63.7200	-.9717		
9	-34.0515		-25.3289				-8.7227
10	-34.4929	47.7200	-37.3564	63.8300	-.9686		
10	-35.4242		-28.3480			100	-7.0762
11	-32.0701	47.4900	-35.5660	63.1500	-.9720		
11	-32.9360		-27.1484				-5.7875
12	-32.4824	45.6900	-40.7821	62.4700	-.9599		
12	-33.3594		-30.2761			50	-3.0833
13	-32.3531	44.1800	-40.6005	60.7600	-.9431		
13	-33.2266		-29.9654				-3.2612
14	-30.0462	45.2100	-29.6968	61.2600	-.9330		
14	-30.8574		-22.2458			150	-8.6116
15	-32.4354	44.4900	-33.4340	60.4300	-.9275		
15	-33.3111		-24.9850				-8.3261
16	-29.1978	43.6500	-32.8087	59.6500	-.9132		
16	-29.9862		-24.3693			100	-5.6169
17	-33.7277	44.3600	-37.8182	60.0800	-.9081		
17	-34.6384		-28.3429				-6.2955
18	-34.3385	42.7400	-42.2484	59.5000	-.9086		
18	-35.2656		-30.5984			50	-4.6672
19	-28.8214	42.2900	-37.4587	59.2900	-.8996		
19	-29.5995		-27.1200				-2.4795
20	-31.6429	43.7700	-31.5575	58.7800	-.9090		
20	-32.4972		-23.8523			150	-8.6449
21	-30.3818	43.5800	-30.4521	59.8700	-.9050		
21	-31.2021		-22.4997				-8.7024

EXPERIMENTAL RESULTS

The operation of the system is illustrated by a set of computer print-outs of magnetic tape records obtained during the Barbados exercises (Bomex) on May 26, 1969, and interpretation of these records. As mentioned previously the losses in the atmospheric path to the sea are determined by two flights, each at three altitudes: 50 meters, 100 meters and 150 meters. These are made in a series of flights in a racktrack course around Scripps vessel *Flip*. Successive flights of 26 sec (yielding data for ~ 1.6 km of sea surface) were made upwind 300 meters north of *Flip* and then downwind 300 meters south of *Flip*. On May 26, from 1743 to 1838 LT 20 fly-bys were made and the computer print-out of the average of a part of the 100-entry record is shown in Table 1, along with the blackbody temperatures and the water surface temperature from channel 1. Note that the water temperature is between the blackbody temperatures. Each one of the entries in this table is the average of 2600 individual readings. Notice the small variations in temperature of the blackbodies and of the water at a 0.075-mm depth, the latter being the average temperature for a 1.6-km path on the sea surface. (Details of these temperature calculations are given later.)

The computer (CDC 3600) is programmed to calculate A_1 and A_2 , the right-hand members of equations 2 and 3. Some of the steps in this calculation are printed out by the computer in Table 2. The first column is the record (flight) number, the second column is $I_{U_1} - I_{B_1}$, the third column is $I_{B_1} - I_{B_2}$. The fourth column is $I_{U_2} - I_{B_2}$ (channel 2), the fifth column is $I_{B_2} - I_{B_3}$ (channel 2), the sixth column is $T_{B_1} - T_{B_2}$ in degrees centigrade, the seventh column is flight altitude, and finally in column 8 is $A_1 - A_2$ in intensity units.

The first number in column 2 is the numerator of equation 2. The next number down (also record 2) is the above number divided by $(1 - r_1)$ which makes it A_1 . Numbers in the third and fifth column are the intensity differences in channels 1 and 2 for the temperature differences (column 6) between the two blackbodies. The first number in column 4 is the numerator of equation 3. The next number down this column is the first one divided by $(1 - r_2)$

and multiplied by the sensitivity ratio of column 3 over column 5. This number is A_2 . Column 7 is the altitude of the flight in meters. Column 8 is $A_1 - A_2$ (equation 4) for the different altitudes of flight, column 7. A progressive change in intensity difference from the two water depths (column 8) is apparent as the sea surface is approached in equal steps of 50 meters. These values of $A_1 - A_2$ are plotted against altitude in Figure 1. Each value plotted here is an average and is derived from 5200 readings in the two channels. The circled points are average values for the different flight altitudes and are derived from some 21,000 readings for the 150-meter altitude and 16,000 readings for the 100- and 50-meter altitudes.

The intercept at zero altitude shows a difference of 0.75 intensity units. Using equation 6, C (the calibration constant) is calculated from the average of the numbers in column 6 divided by the average of the numbers in column 3. This ratio is 0.0208°C per intensity unit in channel 1 for the exercise. The average temperature difference between the depths of 0.025 mm and 0.075 mm during this time interval is obtained from equation 5 and has a value of $0.75 \times 0.0208 = 0.016^\circ\text{C}$.

The heat flow equation

$$Q = K \Delta T/d \text{ per unit area}$$

gives the amount of heat energy flowing upwards as

$$= \frac{0.086 \times 0.016}{0.0050} = 0.27 \text{ cal cm}^{-2} \text{ min}^{-1}$$

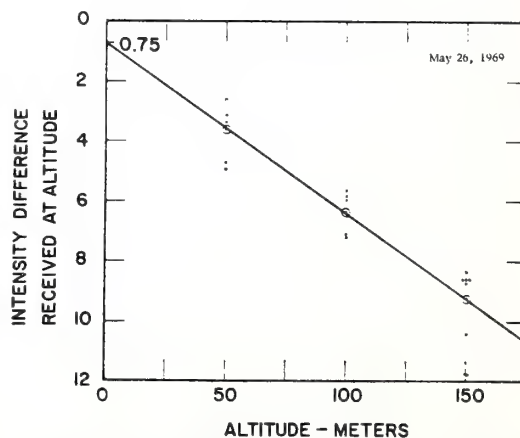


Fig. 1. Intensity difference received at altitude versus altitude.

This then is the average value of heat flux from the sea surface for the period 1743 to 1838 LT on May 26, 1969, near the latitude and longitude of *Flip*, 13.57 N and 56.33 W.

Table 3 shows the average sea-surface temperature and average heat flux obtained for the useful flights made at Barbados. Column 3 shows average values of wind speed at a 2-meter altitude as measured on *Flip* and kindly supplied by K. Davidson, University of Michigan. These are averages over the time intervals indicated in column 2. The sea-surface temperatures shown are average values for the time interval indicated. The average deviation in temperature is shown below each value. The average temperature for individual fly-bys of five of these exercises are shown in Tables 4 and 5.

The heat flux result for the May 26 exercise (calculated as shown above) is the second entry in Table 3. The May 27 results are calculated in detail in *McAlister and McLeish* [1970, page 2702]. The results for May 24 and May 29 are

obtained in exactly the same way from tape records for these dates. The May 29 exercise was flown nearer to Barbados and also nearer to vessels participating in Bomex. The strong radar pulses from these vessels interacted with our electronic system a good part of the time so that only fragmentary records were obtained. These fragments, however, did enable a value of $0.4 \text{ cal cm}^{-2} \text{ min}^{-1}$ to be calculated.

The comments column in Table 3 gives some indication of weather conditions, especially for the first three exercises listed. The negative results for May 25 were caused by radar interference nearly 100% of the time. On May 19 the wind was very gusty, so much so that the aircraft could not maintain a constant altitude, and there was no way to correct for this. In the early exercise on May 24 the power supply for the electronic system became so 'noisy' that no useful data could be obtained. The aircraft returned to Barbados, the power supply was repaired, and a late flight on that date gave the results shown in the first entry in Table 3. The

TABLE 3. Total Heat Flux Results

Date (1969)	Local Time	Sea Surface		Heat Flux Results† $\text{cal cm}^{-2} \text{ min}^{-1}$	Comments
		Wind Speed cm sec^{-1} *	Temperature $^{\circ}\text{C} \uparrow$		
May 24	1827-1858	612	27.77 ± 0.02	0.05	Intermittent rain
May 26	1740-1838	890	28.06 ± 0.02	0.27	Rain nearby
May 27	0446-0552	830	27.71 ± 0.02	0.45	Best weather
May 29	1724-1834	—	28.44	0.4	Radar interference 90% data lost
May 25	1746-1838	650	27.61 ± 0.13	Negative	Radar interference
May 19	1804-1855	795	27.96 ± 0.02	Negative	Heavy weather. Altitudes uncertain
May 24	0654-0724	770	28.08 ± 0.05	Negative	Internal interference from power supply
May 28	0553-0623	830	27.84 ± 0.07	Negative	Gusty winds; spray below 75 meters

* Data from *Flip*.

† Average over a 1.6-km strip 75 meters wide.

May 28 exercise gave no heat flux results because of wind-blown spray encountered at the 75-meter altitude. This prevented an accurate extrapolation of data to the sea surface.

The comparison of heat flux results shown in Table 3 with simultaneous measurements by others on *Flip* did not materialize. The only comparison that can be made was to data obtained on *Flip* the week before, which ranged in value from 0.15 to 0.40 cal cm⁻² min⁻¹. This range compares favorably with values in Table 3, but the measurements were not simultaneous. The May 29 value of 0.4 cal cm⁻² min⁻¹ may be compared to a simultaneously obtained value of 0.3 cal cm⁻² min⁻¹ reported in a private communication by Dr. B. Bean of ESSA. Laboratory measurements in a wind-water tunnel [McAlister and McLeish, 1969] show an experimental error in heat flux for this system of $\pm 8\%$.

SEA-SURFACE TEMPERATURES

McAlister and McLeish [1970] showed that the use of an airborne digital data recorder, con-

TABLE 4. Sea-Surface Temperatures

May 19, 1969 14.43 N, 57.32 W		May 24, 1969 13.57 N, 56.30 W	
Local Time	Surface Temp. °C	Local Time	Surface Temp. °C
1804	27.94	0700	28.05
06	0.95	04	0.09
08	0.95	08	0.16
12	0.94	12	0.20
14	0.98	17	0.05
16	28.00	20	0.04
18	27.96	22	0.06
20	0.98	24	0.07
25	28.01	0728	27.99
27	27.95		28.08 \pm .05
30	0.98		
32	0.98	1827	27.79
35	0.97	31	0.77
37	0.94	33	0.84
41	0.95	40	0.78
43	0.96	43	0.75
45	0.94	45	0.78
47	0.94	47	0.78
50	0.95	50	0.77
53	0.90	53	0.69
1855	27.92	55	0.74
	27.96 \pm 0.02	1858	27.75
			27.77 \pm .02

TABLE 5. Sea-Surface Temperatures

May 26, 1969 13.57.3 N, 56.33 W		May 27, 1969 13.58 N, 56.37 W	
Local Time	Surface Temp. °C	Local Time	Surface Temp. °C
1743	28.09	0446	27.70
46	0.07	49	0.70
49	0.11	52	0.70
52	0.08	55	0.67
55	0.10	59	0.69
57	0.10	0502	0.72
1801	0.04	06	0.69
03	0.08	08	0.69
06	0.03	11	0.70
09	0.04	14	0.73
13	0.06	17	0.75
16	0.05	20	0.75
20	0.05	24	0.74
22	0.04	27	0.73
26	0.07	30	0.72
28	0.06	33	0.74
32	0.01	37	0.71
35	0.06	40	0.73
1838	28.02	43	0.70
	28.06 \pm 0.02	46	0.74
		49	0.70
		0552	27.71
			27.71 \pm 0.02

tinuous calibration of detector sensitivity, and the data reduction methods employed provided an accuracy in temperature measurement of 0.01°C. These factors also allowed measurement of the temperature difference between the two water depths to 0.003°C. This accuracy is reached in a 30-sec averaging period, i.e., while the aircraft is flying 1.6 km at constant altitude over the ocean. (Thermistor drift found after 6-months use caused an error of 0.004 in temperature values.)

In Table 1 there are two rows for each fly-by (record number). The lower one is labeled AVG. TEMP. (average temperature) and the two temperatures on the right are of black-bodies 1 and 2 obtained from the numbers immediately above and calibration charts. The average sea-surface temperature for that 1.6 km of flight is shown to the left. These sea-surface temperatures are obtained as follows: for record 21 in Table 2 we find the entry (lower one) 31.202 which is a value for the right-hand member of equation 2, i.e., the

radiation intensity difference between the sea readings and the readings on blackbody 1. The radiometer sensitivity for record 21 is the ratio of the temperature difference between the two blackbodies and their intensity reading difference in column 3, i.e., $0.905/43.58$ or 0.0208°C per unit intensity. The product $0.0208 \times 31.202 = 0.649^{\circ}\text{C}$ is the temperature difference between the sea and blackbody 1. Table 1 shows an average temperature for blackbody 1 of 27.332°C . So $0.649 + 27.332$ or 27.981°C is the average sea-surface temperature for that record, which is printed out by the computer in Table 1 for record 21. The average sea-surface temperature for each record in Table 1 is calculated by the computer in the same way.

The effect of surface roughness and waves (i.e., sea state) on these temperature readings is discussed by *McAlister and McLeish* [1970] on page 2701. Here the studies of others and the 25° beamwidth of the radiometer that was used lead to the conclusion that as a first approximation the ocean is 'essentially flat' even up to high wind speeds. This can be visualized by noting that the radiometer beam averages the intensity received over one or two wavelengths of ocean waves so the effect of positive and negative slopes tends to cancel. If the relation between reflectivity and angle of incidence were linear, the effect of equal elements of positive and negative wave slopes would exactly cancel under conditions where the effective sky radiation is constant with angle from the zenith. For a range of $\pm 15^{\circ}$ the reflectivity versus angle is nearly linear (departs a maximum of three parts in 100 from linear). Also for a uniform overhead sky its radiation is quite uniform out to 30° from zenith. Thus the assumption of a 'flat' ocean is a good first approximation, the limits of which will have to be set by considerable experience. The distribution of wave slopes (including capillaries) is somewhat different downwind compared to upwind so that a definite lack of symmetry exists. The procedure followed in these airborne measurements of making an equal number of flights upwind and downwind is believed to cancel out this wind effect. Evidence for this belief can be seen in Figure 1 where the experimental points are seen to cluster in a group above the line and another group below this line. In Table 2 the even flights are upwind and the odd flights are downwind. Of

these ten pairs of flights six gave results where upwind and downwind were on opposite sides of the line drawn, two were nearly equal in value while two were opposed to the first six. This shows evidence of a cancellation of the wind effect as mentioned above.

With this in mind it is interesting to examine the sea surface temperatures off Barbados for the time periods shown in Table 3. Five of these flights are shown in Tables 4 and 5. Each entry in these tables gives the time of the start of each 30-sec pass and the average sea surface temperature for the strip flown over. These values were obtained from the 3.5 to $4.1\ \mu$ channel where atmospheric absorption is least. Plotting the values as a function of altitude of observation, an absorption correction of $+0.012^{\circ}\text{C}$ for each 50-meter increase in altitude was found. This correction was used to obtain values shown in Tables 4 and 5.

Most of the time *Flip* was being held against wind and current by a tug so there was little overlap in the one-mile strips of ocean from one pass to the next. In other words, each pass was most of the time over a new strip of ocean but these strips were not far apart. The latitude and longitude for each exercise are shown in these tables.

Examination of entries in these tables reveals an interesting constancy in average temperature of these one-mile strips of ocean surface under Barbados conditions. Surface temperature changes from one day to the next were noted but for periods of an hour at night the temperature stays remarkably constant. The average deviation in temperature is shown and for four of the five periods it is only $\pm 0.02^{\circ}\text{C}$. No previous measurements of sea-surface temperature have been made which show the accuracy and area coverage (a 1.6-km strip) that are reported in Tables 4 and 5. This type of temperature measurement should be better for correlation with oceanic and meteorologic factors than isolated bucket temperature measurements.

Tests are in progress to study the possibility of shipborne use of the heat flow system. Here, so near the sea surface, atmospheric attenuation is quite small and correctable from meteorological data. A protective housing and stabilized platform have been made. This usage, if found possible, would enable longer time surveys at much less expense.

LIMITATIONS OF THE PRESENT SYSTEM

The present procedure of flying at three altitudes to obtain corrections for atmospheric attenuation is very time consuming. A modification of the radiometer's optical system to view the ocean at 20° and 60° from the vertical would provide two optical path lengths to the sea from one altitude. With adequate system sensitivity they should be sufficient for attenuation corrections. This would be a major redesign of the optical system.

Daytime operation with the present wavelengths used in channel 1 is not possible because of solar energy reflected from the sea. Design of a system for day and night operation is difficult but not impossible.

Sky conditions very different from those found at Barbados have been encountered near San Diego which interfere with the operation and linearity of the preamplifier system. These conditions are a clear cold night sky with small scattered low clouds. Under these conditions the clear sky signal, $(I_{sky} - I_B)$, may be 20 times that from the water, $(I_w - I_B)$, and it may vary $\pm 50\%$ from second to second. Laboratory tests duplicating these conditions show the amplifier system to become erratic and to depart from linearity in measuring intensity differences. The sky conditions at Barbados for all exercises showed a maximum variation in sky signal of 5%. Further tests of the amplifier system show that it departs from linearity when the clear sky to cloud signal variation reaches $\pm 15\%$.

An initial solution of this electronic problem is under study. This is to attenuate the sky signal about an order of magnitude by introducing a fixed impedance to the feedback loop input of the preamplifiers when the rotating mirror brings the sky radiation onto each detector. Airborne tests of this solution are encouraging. Here it is necessary to write a new program for the tape records to bring the sky signal back to its unattenuated value before proceeding with the calculations. If this does not solve the scattered cloud problem then an improved preamplification system will be necessary. This would be a major undertaking.

SUMMARY

Participation in the Bomex trials during May 1969 resulted in airborne measurements of the total heat flow from the sea. The values found at night ranged from $0.05 \text{ cal cm}^{-2} \text{ min}^{-1}$ on May 24 to $0.45 \text{ cal cm}^{-2} \text{ min}^{-1}$ on May 27. Measurements of heat flux made from *Flip* the week before in the same location show a range from 0.15 to $0.40 \text{ cal cm}^{-2} \text{ min}^{-1}$. Thus the range of values found by conventional methods from *Flip* and the airborne system agrees well but the measurements were not simultaneous. Laboratory tests of the airborne system show an error of $\pm 8\%$.

A new order of accuracy in measurement of sea surface temperature has been demonstrated. It surpasses the accuracy of oceanographic mercury thermometry for sea surface temperature.

A redesign of the optical system is possible to shorten the time for one measurement. Also, a preamplifier improvement to include a wider range of sky conditions is under test.

These tests at Barbados have demonstrated the feasibility of airborne measurement of total heat flux with the present system. A thorough 'at sea' calibration is still lacking and further redesign is necessary before this development can be considered complete.

Acknowledgments. We are indebted to Bomex management organization and its operations team for fitting our needs so smoothly into a very complex exercise.

This research was supported by the Office of Naval Research, codes 461 and 481, Naval Oceanographic Office code 7007, and National Science Foundation, Atmospheric Sciences Section, under grants GA-1491 and GA 11975.

REFERENCES

- McAlister, E. D., and W. McLeish, Heat transfer in the top millimeter of the ocean, *J. Geophys. Res.*, **74**, 3408, 1969.
 McAlister, E. D., and W. McLeish, A radiometric system for airborne measurement of the total heat flow from the sea, *Appl. Opt.*, **9**, 2697, 1970.

(Received October 10, 1970;
 revised March 18, 1971.)

Measurements of Microwave Emission from a Foam-Covered, Wind-Driven Sea

W. NORDBERG, J. CONAWAY, DUNCAN B. ROSS¹ AND T. WILHEIT

Goddard Space Flight Center, Greenbelt, Md.

(Manuscript received 13 October 1970, in revised form 11 January 1971)

ABSTRACT

Measurements were made from aircraft of the 1.55-cm microwave emission from the North Sea and North Atlantic at surface wind speeds ranging from less than 5 to 25 m sec⁻¹. Brightness temperatures in the nadir direction increased almost linearly with wind speed from 7 to 25 m sec⁻¹ at a rate of about 1.2C (m sec⁻¹)⁻¹. At 70° from nadir the rate was 1.8C (m sec⁻¹)⁻¹. This increase was directly proportional to the occurrence of white water on the sea surface. At wind speeds <7 m sec⁻¹, essentially no white water was observed and brightness temperatures in the nadir direction were ~120K; at wind speeds of 25 m sec⁻¹ white water cover was on the order of 30% and average brightness temperatures at nadir were ~142K. Maximum brightness temperatures for foam patches large enough to fill the entire radiometer beam were 220K.

1. Introduction

Considerable interest has been devoted to the quantitative measurement of sea surface roughness, on a global scale, from spacecraft and to the possible derivation of surface winds from these measurements (NAS Summer Study, 1969). For this reason, we measured the microwave emission at 1.55 cm over the North Atlantic and the North Sea in March 1969 over a wide range of sea surface, wind and cloud conditions in order to establish a quantitative relationship between the emission and the sea state and to delineate parameters such as surface winds, foam cover, wave height and cloud cover that would affect this relationship.

Earlier measurements (Nordberg *et al.*, 1969) over the Salton Sea have shown that the microwave emission, observed at all nadir angles from 0° to 50° and at a wavelength of 1.55 cm, is considerably greater from a rough water surface than from a smooth one. Stogryn (1967) had predicted that increases in microwave emission from rough water could be observed only at nadir angles >30°. However, Stogryn's calculations were addressed primarily to the effect of the large-scale wave geometry on the emission and did not, for example, account for foam and spray. We have therefore conducted these observations at high wind speeds and extensive foam cover to investigate further this discrepancy between theory and earlier observations.

2. Description of experiment

Measurements were made from the NASA Convair 990 airborne observatory. Primary instruments carried by the aircraft were as follows:

1) A radiometer measuring horizontally polarized radiation at 1.55 cm wavelength within a 2.8° diameter field of view which was scanned perpendicularly to the aircraft's flight path over a nadir angle range of ±50°. The same instrument was used in the Salton Sea observations; it was built by the Space Division of Aerojet General Corporation (Oister and Falco, 1967).

2) A laser geodolite of the Spectra-Physics Corporation to measure the ocean wave height spectrum.

3) An infrared radiometer, similar to the Medium Resolution Infrared Radiometer (MRIR) flown on Nimbus satellites (*Nimbus III User's Guide*, 1969), to determine the sea surface temperature from emission measurements at wavelengths between 10.6 and 11.6 μ m.

4) Standard airborne navigation systems, both Doppler and inertial, with which wind speed and direction at the aircraft altitude were measured.

5) A Vinton 70-mm camera, pointing at nadir with a square field of view of about 68°, to photograph sea surface and cloud conditions.

In addition, the aircraft carried standard instrumentation for altitude, attitude, speed, and ambient temperature measurements and auxiliary cameras. A non-scanning, nadir viewing, 3-cm microwave radiometer with a field of view of about 13°×13° was provided by the Jet Propulsion Laboratory for comparison with the 1.55-cm measurements.

The aircraft was based at Shannon, Ireland. Two flights, averaging 5 hr each, were made over the North Sea, and four flights, equally long, covered a region of the North Atlantic between Iceland and Ireland. In general, passes were made over each area of interest at several altitudes between 120 and 12,000 m to differentiate the effects of atmospheric and surface emission.

¹ Present affiliation: NOAA Air-Sea Interaction Laboratory, Miami, Fla.

TABLE 1. Summary of meteorological conditions and microwave emission temperatures for six overwater flights.

Date (March 69) Time (GMT) Location	Case					
	A 10 1321 Atlantic Off Shannon	B 13 1247 Atlantic Ship J	C 13 1117 Atlantic Ship I	D 10 1430 Atlantic Ship I	E 19 1023 North Sea 57°N 3°E	F 14 1453 North Sea 59°N 1°30'E
Wind speed (m sec ⁻¹)	<5	6	13	16	17	25
Significant wave height (m)	<1	6.0†	3.9	5.0	4.0	7.8
Foam cover (%)						
Whitecaps	—	—	4.2	5.6	6.0	5.0
Streaks	—	—	3.5	6.9	17.4	27.0
Total	—	—	7.7	12.5	23.4	32.0
Temperature (°C)						
Sea surface	9	10	9	9	2	4
Air surface	10 (est.)	11	7	5	2	2
Cloud altitude (m)						
Base	2000	clear	300	800	600	150
Top	2300	clear	2100	2000	2000	5000
Brightness temperature (°K)						
High altitude*	128**	—	—	138	138	148
Low altitude	120	118	127	132	132	142

* Measured within 30 min of time shown.

** Over Irish Sea at 1212 GMT.

† All swell, no wind waves.

Surface wind speeds ranged from calm to 25 m sec⁻¹. They were obtained from surface anemometer observations and/or by extrapolation of the aircraft measured ambient wind speeds at the lowest flight altitudes under the assumption that wind speed decreased exponentially toward the surface (Ross *et al.*, 1970). Where both were available no significant discrepancy was noted. This assumption was applied to all cases shown in Table 1, except case E. In that case, examination of reduced geostrophic winds and ship reports led us to assume that the wind speed *increased* from the height of the aircraft to the surface. We are very much indebted to Prof. Vincent Cardone of New York University for pointing this out to us. A similar increase in wind speed with decreasing altitude was observed during the Salton Sea flight. However, in the absence of surface observations, it was not deemed appropriate to depart from the winds observed at 200 m, the minimum aircraft altitude, for our approximation of the surface winds. In this case, it is recognized that the true surface wind speed could be considerably higher. For the Atlantic Ocean and North Sea observations, the accuracy of the surface wind speed determinations is judged to be within 3 m sec⁻¹.

Cloud conditions, observed visually and photographically from the aircraft, ranged from clear to stratocumulus overcasts with moderate rain, over the numerous sea surface targets selected for the flights.

The 10–11 μ m equivalent blackbody temperatures were taken to be equal to the sea surface temperature when measured with the infrared radiometer at the lowest altitudes. Temperatures ranged from 10C at 50N over the Atlantic to 2C over the coldest part of the North Sea.

Sea state varied from calm, with no whitecaps, to significant wave heights of ~ 8 m with over 30% coverage by foam with extensive streaking. Significant wave heights were determined by analysis of the wave spectra observed with the laser geodolite. The foam coverage was determined from photographs of the sea surface with a digital densitometer. The method consists of numerically computing the areas on the photographs above and below a chosen brightness threshold such that whitecaps, foam streaks and undisturbed sea can be differentiated quantitatively. These parameters are listed in Table 1. Due largely to the subjective nature of the choice of the thresholds, the accuracy of this method is limited to about 15% of the value obtained. Percentages for each case are averages resulting from several consecutive photographs due to the variation in the foam cover between individual frames.

Whenever possible, sea state, temperatures and winds measured with the aircraft were compared with the observations obtained from ocean vessels I and J (59N, 19W and 53N, 20°30'W, respectively) and with analyses made by the Irish Meteorological Service at Shannon Airport. There was never any significant discrepancy among these data. A complete log of all flights, including environmental and meteorological observations was compiled by Griffie *et al.* (1969). The specific conditions for which microwave measurements are reported here are summarized in Table 1.

3. Results

Brightness temperatures measured at 1.55 cm during six low-altitude passes over the Atlantic and North Sea at wind speeds ranging from less than 5 to about 25 m sec⁻¹ were selected to illustrate their dependence on

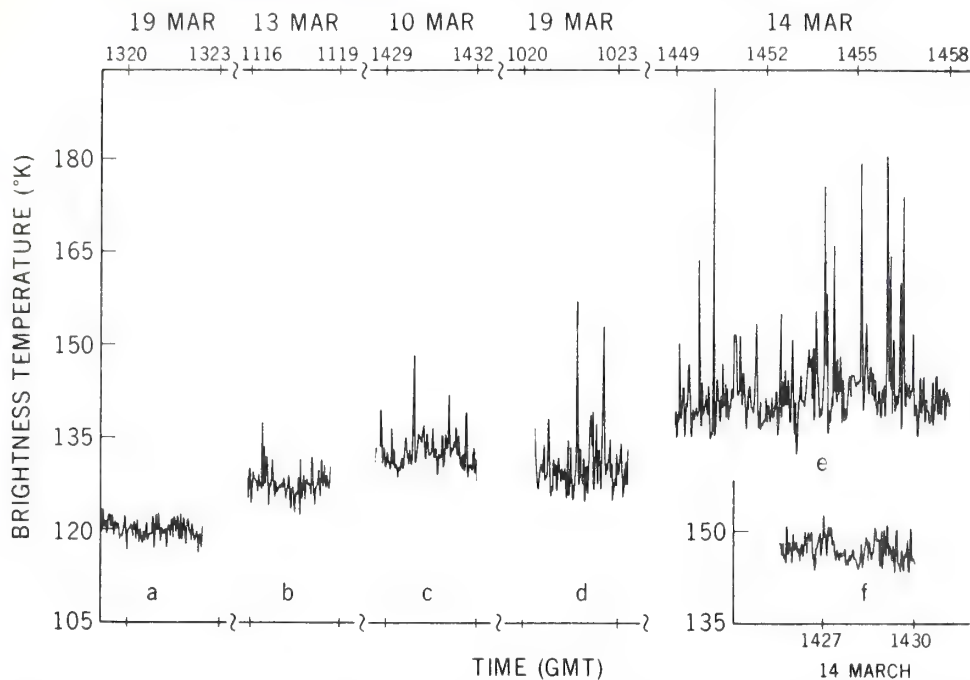


FIG. 1. Instantaneous brightness temperatures measured in the nadir direction vs time. Plot (a) corresponds to case A in Table 1, plots (b)–(e) to cases C–F. All brightness temperatures in (a)–(e) were observed from heights of ~150 m. Brightness temperatures in (f) were observed from a height ~5500 m over approximately the same location as (e).

wind speed and foam cover (Fig. 1). The recorded radiometer output was converted to radiances taking into account the calibrations performed on board the aircraft during each scan with two reference loads, one stabilized at 330K and another terminated in a liquid nitrogen dewar. Antenna and radiometer characteristics, including effects of radiation received by the antenna through side lobes outside the 2.8° diameter instantaneous field of view which were measured in the laboratory and against a known sky background prior to and after the expedition, were also taken into account in this conversion. The resulting radiances are expressed as brightness temperatures (°K) and are plotted in Fig. 1 for the nadir viewing positions only. The radiometer field of view scanned from 50° left of nadir to 50° right of nadir, once every 2 sec. Thus, the traces shown in Fig. 1 consist of one data point per 2 sec. They cover time segments corresponding to the sea, cloud and wind conditions listed in Table 1.

The plotted brightness temperatures (T_B) result from three radiation components received by the radiometer—radiation emitted to the aircraft by the sea surface, radiation emitted to the aircraft by clouds and atmospheric water vapor, and atmospheric radiation reflected toward the aircraft by the sea surface:

$$T_B = \epsilon T_W \tau_H + (1 - \epsilon) T_S \tau_H + \int_0^H T_A(h) (\partial \tau / \partial h) dh, \quad (1)$$

where T_W is the water surface temperature, T_S the sky

brightness temperature, T_A the atmosphere temperature, τ the atmosphere transmissivity, ϵ the surface emissivity, h height above surface, and H aircraft altitude. The first, second and third terms of (1) correspond to surface emission, reflected atmospheric radiation, and atmospheric emission, respectively.

The cases listed in Table 1 were chosen such that atmospheric conditions, including cloud cover, were generally similar. In each of these cases, there was no measurable precipitation from the prevailing broken stratocumulus clouds. Somewhat denser cloud cover encountered during higher wind speeds was almost compensated for by the lower atmospheric temperatures prevailing in these cases. For example, we have computed that the reflected radiation component for cases A and B of Table 1 (thin clouds but warm atmosphere) contributed ~9.5C to the measured brightness temperature, while for cases E and F (thicker clouds, but cold atmosphere) this contribution was ~11C. Thus, for the conditions listed in Table 1, the reflected component due to T_S can be assumed to be nearly constant, with variations certainly remaining smaller than 3C. Also, the directly received emitted atmospheric radiation was negligible when the aircraft was at low altitudes (150–200 m), since there were no clouds below the aircraft, and the transmissivity was very near unity between the aircraft and the surface. In those cases, the integral term in Eq. (1) approaches zero.

Measurements of T_B were also made from high altitudes (> 5000 m) for the same conditions and gener-

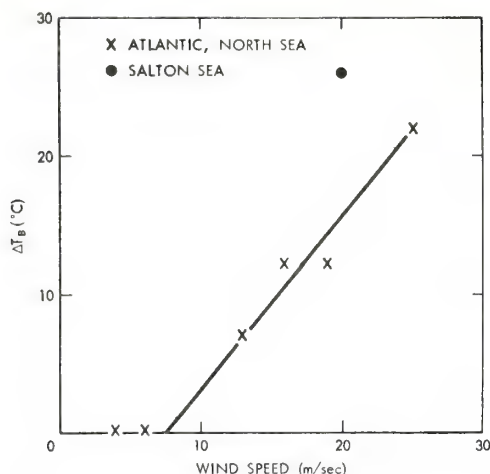


FIG. 2. Brightness temperature differences between observations made at wind speeds $< 5 \text{ m sec}^{-1}$ and higher wind speeds as a function of wind speed.

ally within less than 30 min of the times listed in Table 1. Brightness temperatures were 6–8°C higher (depending on sea surface roughness) than corresponding brightness temperatures observed at the low altitudes. In each case, these increases relative to the low-altitude passes account quite precisely for the emitted atmospheric radiation term and for the decrease of τ_H from unity to about 0.95. The comparison between low- and high-altitude observations confirms our assertion that the measurements shown in Fig. 1 were obtained under comparable atmospheric and cloud conditions.

At this wavelength, the measured brightness temperatures are essentially independent of the sea surface temperatures within the observed range, because ϵ varies inversely with the surface temperature such that ϵT_w in Eq. (1) is nearly constant. Differences between the measured brightness temperatures for the various cases of Table 1 are then almost entirely due to differences in sea surface roughness. Brightness temperature differences between the lowest wind condition (case A) and each of the other cases were computed and plotted vs surface wind speeds in Fig. 2. A systematic increase in emission with increasing wind speed is clearly evident. The rate of increase is $\sim 1.2\text{C} (\text{m sec}^{-1})^{-1}$. A qualitatively similar result was obtained from the data taken over the Salton Sea in 1968. This previously unpublished datum is from the same series of measurements discussed by Nordberg *et al.* (1969). The apparent quantitative disagreement with the 1.2C rate of increase for the North Atlantic and North Sea measurements is not deemed significant because of the large wind speed uncertainty in the Salton Sea case.

Measurements for the nadir direction only were plotted in Figs. 1 and 2. At larger nadir angles, up to 70° , we have observed proportionally larger rates of increase. Fig. 3 shows brightness temperatures as a function of nadir angle for a low and for the highest

wind speeds listed in Table 1. Although the radiometer antenna scanned only to nadir angles up to 50° , we were able to observe radiation from nadir angles up to 80° during banking of the aircraft. The two solid curves in Fig. 3 were obtained by smoothing brightness temperature averages at each nadir angle for periods of 10–20 sec during which the aircraft bank angle was held constant at 30° . The brightness temperature rate of change with wind speed increased from $1.2\text{C} (\text{m sec}^{-1})^{-1}$ at nadir to $\sim 1.8\text{C} (\text{m sec}^{-1})^{-1}$ at 70° from nadir. This is qualitatively in accord with observations by Hollinger (1970), who reported an increase from $0.8\text{C} (\text{m sec}^{-1})^{-1}$ at 30° from nadir to $1.4\text{C} (\text{m sec}^{-1})^{-1}$ at 70° from nadir, for a much lower wind speed range.

The dashed curve in Fig. 3 was computed for the atmospheric and sea surface temperature conditions observed for case B, but for a specular sea surface. The absolute brightness temperatures measured at nadir for case B were $\sim 15\text{C}$ lower than the computed temperatures (dashed curve). We believe that this discrepancy is largely due to errors in the *absolute* calibration of the radiometer and indicates that all brightness

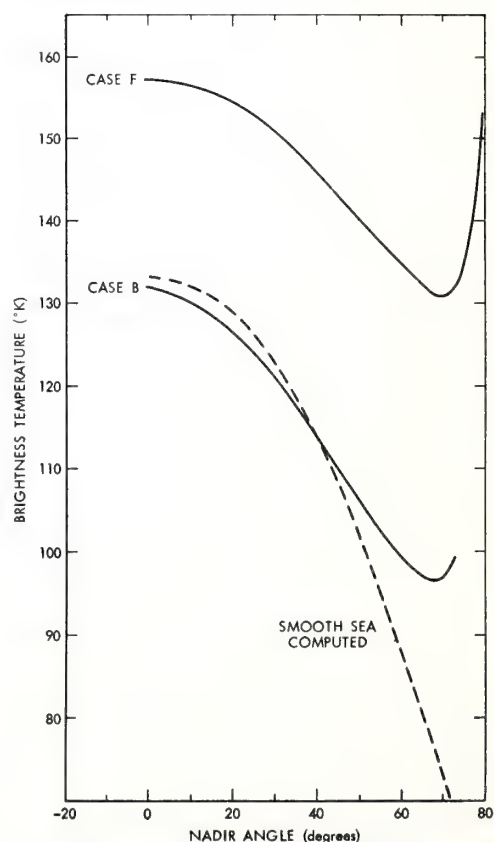


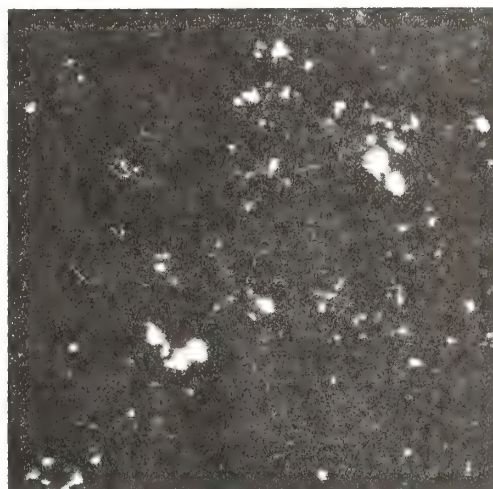
FIG. 3. Brightness temperatures averaged for 10–29 sec time periods, for each antenna scan angle during 30° aircraft banks, vs nadir angle for case B of Table 1 (lower curve) and case F of Table 1 (upper curve). Absolute brightness temperatures were normalized to computations for smooth sea (dashed curve) at nadir. The dashed curve shows computed brightness temperatures for atmospheric and sea surface temperatures encountered in case B but for a smooth, specular sea surface.

temperatures measured with this instrument should be corrected by about $+15^{\circ}\text{C}$. This correction was made for the brightness temperatures plotted for cases B and F in Fig. 3. The relative calibration of the instrument was maintained at about $\pm 1.5^{\circ}\text{C}$ throughout all flights.

Comparison of the slope of the dashed curve with the slope of curve B shows that the decrease of brightness temperatures with nadir angle is much steeper for a theoretical, specular and smooth water surface than for real water surfaces, even at low wind speeds. This suggests that the small-scale roughness introduced even by very low winds causes a considerable brightness temperature increase at large nadir angles. The slopes of curves B and F differ much less than those of curve B and the smooth water curve. This suggests that the rate of brightness temperature increase with nadir angle diminishes at the higher wind speeds. However, there remains a brightness temperature increase of at least 22°C with wind speed at all nadir angles, as shown by the offset of curve F compared to curve B. This offset could be caused by the greater emission from white water such as foam and spray which would produce nearly the same brightness temperature increase at all nadir angles, depending only on the amount of foam cover.

Fig. 2 shows that a nearly linear brightness temperature increase with wind speed occurs above a threshold of $\sim 7 \text{ m sec}^{-1}$. The measurements at 6 m sec^{-1} (case B) show no increase of T_B over the measurements at less than 5 m sec^{-1} (case A). There is no evidence of any brightness temperature difference between cases A and B despite the fact that the sea surface was very smooth for case A while extremely large swells (6 m) but no whitecaps were observed for case B. Monahan (1969a) has reported an abrupt increase in whitecap coverage and spray density at 7 m sec^{-1} and Cardone (1969) has computed that the energy available for whitecap production at wind speeds $< 7 \text{ m sec}^{-1}$ is practically negligible. This suggests that the increase of microwave emission with wind speed, shown in Fig. 2, is related mainly to the occurrence of white water (foam and spray). At lower wind speeds, where foam does not occur, the brightness temperature measured at all nadir directions is independent of wind speed. Foam has been suspected previously as a cause for increased microwave emission (Williams, 1969; Droppleman, 1970).

Further evidence of the dependence of the microwave emission on foam cover can be found in the rapid brightness temperature fluctuations with time, shown in Figs. 1c–1e. In Fig. 1d, for example, the average brightness temperature is $\sim 132\text{K}$, but, instantaneous spikes frequently reach 140K and two spikes exceed 155K . Fig. 1e, which corresponds to winds of 25 m sec^{-1} , shows many more of these spikes. In this case, the average brightness temperature is $\sim 142\text{K}$, but instantaneous spikes exceeding 150K occur about every 30 sec. Several of these spikes range between 175 and



a



b

FIG. 4. Photographs with a 70-mm camera taken in the nadir direction at surface wind speeds of 16 m sec^{-1} (a) and 25 m sec^{-1} (b), corresponding to cases D and F, respectively, in Table 1.

190K . From the photographs there is a strong implication that these spikes are caused by foam patches on the sea surface.

We have analyzed the instantaneous brightness temperatures measured at all scan angles over a period of 20 min, approximately centered on the time corresponding to Fig. 1e, to determine the amplitude and frequency of brightness temperature spikes. We found that the maximum amplitude was $\sim 220\text{K}$ for seven spikes which occurred during that period. One such spike was clearly coincident with the immense foam patch photographed in Fig. 4b. The radiometer scanned the scenes shown in Fig. 4 from left to right, with the

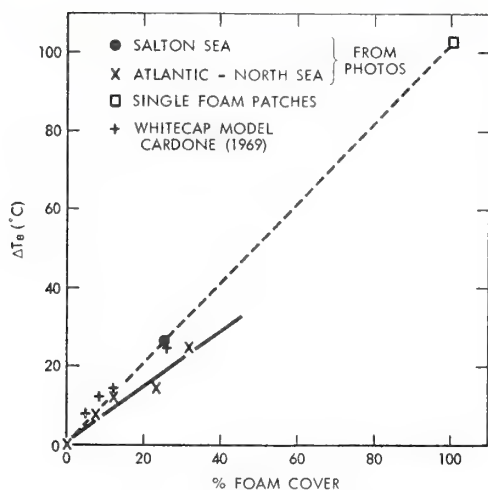


FIG. 5. Brightness temperature differences between observations made at wind speeds less than 5 m sec^{-1} and at higher wind speeds as a function of foam cover as estimated from photographs, from the analytical model of Cardone, and from single foam patches covering the entire microwave radiometer beam.

aircraft having flown from bottom to top. Since the position of the scans on the photographs are not known exactly, and since at low altitudes scans were not contiguous, the foam patches may not always have filled the antenna field of view entirely. We assume that this occurred only when the maximum brightness temperatures of 220K were measured.

The photographs of Fig. 4 were taken over sea states corresponding to the brightness temperature measurements in Figs. 1c and 1e, respectively. Aircraft altitudes ranged from 120 to 450 m. Fig. 4b was observed from 120 m and extends over about 200 m from top to bottom. The foam estimates (Table 1) were made from time series of photographs similar to those shown in Fig. 4. The increasing amounts of both foam patches and streaking with wind speed are quite apparent from Table 1. We assume that such streaking and foam patches, which were small relative to the radiometer field of view, raised the measured brightness temperatures uniformly throughout each scan, but that the largest patches of foam produced the temperature spikes which were more than 70°C above the average. It is, therefore, very important that estimates of foam coverage, as they relate to the microwave emission, include the effect of both foam patches and streaking. This has been attempted with the estimates of total foam cover listed in Table 1.

The brightness temperature spikes seen in Figs. 1d and 1e were not observed when the aircraft was at higher altitudes, where each foam patch covered an area much smaller than that resolved by the instantaneous field of view of the radiometer. Fig. 1f shows brightness temperatures measured from 5500 m in the vicinity where the photograph of Fig. 4b and the measurements shown in Fig. 1e were made. No large spikes are evident in this case. At the aircraft height of

120 m (Fig. 1e) each scan spot covered an area with a diameter of $\sim 7 \text{ m}$, while at the aircraft height of 5500 m (Fig. 1f) the diameter of the area covered was $\sim 275 \text{ m}$. In the latter case, brightness temperatures show a much smoother pattern with no significant spikes because the characteristic diameter and spacing of the largest foam patches were less than $\sim 100 \text{ m}$ (Fig. 4b) and individual patches were not resolved by the radiometer.

Brightness temperature differences were plotted vs foam coverage in Fig. 5, as determined from the photographs (solid line). There is a similar increase of brightness temperature with foam cover, as there is with wind speed. However, the rate of increase obtained from the small-scale, single foam patch measurements, each representing 100% foam cover (dashed line), is considerably greater than the rate determined from the large-scale observations derived from the photographs for less than 40% foam cover (solid line). There are two possible explanations for this discrepancy:

- 1) The estimates of streaking which account for a large portion of the white water coverage as determined from the photographs (Table 1) are subjective, though internally consistent. Thus, foam cover as determined from the photographs may have been overestimated. This is also suggested by the fact that if foam cover is taken from Cardone's (1969) model, corrected for salt water after Monahan (1969b), brightness temperature increases are consistent with the rate obtained for 100% foam cover (dashed line) which is independent of the estimates made from the photographs. The uncertainty of estimating whitewater coverage from photographs and the possibility of overestimating foam cover has been pointed out recently by Blanchard (1971).

- 2) Another possibility is that the total white water estimates made from the photographs are correct but that the effect of the streaks on the microwave emission is smaller than the effect of the whitecaps which produce the 100% foam cover spikes. In this case, the agreement with Cardone's model would be purely coincidental. Further microwave measurements under controlled conditions of foam and streaking should resolve this point.

It is noteworthy that the Salton Sea measurements made on 5 June 1968 are generally consistent with the North Sea and Atlantic measurements with regard to brightness temperature dependence on both wind speed and on foam cover.

Preliminary results from the 3-cm radiometer, flown simultaneously with the other instruments, indicate that the brightness temperature increase at this wavelength is about 8°C for a wind speed increase from calm to 13 m sec^{-1} . Beyond 13 m sec^{-1} there is only a negligible increase in brightness temperature. However, because of calibration uncertainties, the 3-cm measurements cannot be considered as firm as those at 1.55

cm. We are indebted to Messrs. F. Barath and J. Blinn of the Jet Propulsion Laboratory and A. Edgerton of Aerojet General Corporation for making this, as yet unpublished, information available to us.

4. Conclusions

There is a definite increase in the thermal emission at 1.55 cm from the sea surface with increasing wind speed. On the average, this increase amounts to about 22C in the nadir direction and 32C at 70° from nadir for a wind speed increase from 7 to 25 m sec⁻¹. For very low wind speeds, up to about 7 m sec⁻¹ when foam cover is negligible, there is no increase in brightness temperatures. Compared to calm sea states, brightness temperatures are ~100C higher when foam patches covering the radiometer field of view are observed. We conclude that the increased emission at 1.55 cm from a wind-driven sea surface is primarily due to white water cover, while the effect of the wave slope geometry is negligible. The microwave emission at 1.55 cm from the sea surface is therefore a sensitive indicator of white water coverage and of wind speed at all nadir angles, at least to 50°.

We believe that an important parameter involved in the interaction between air and the sea surface, namely, the energy expended in the production of white water, can be inferred from microwave brightness temperature measurements provided that: 1) the consistent relationship between white water occurrence and wind speed reported here is confirmed; and 2) microwave measurements are made at various wavelengths, both polarizations, and over a large range of nadir angles to separate the various effects of foam cover, cloud cover, and atmosphere and sea surface temperatures on the microwave emission.

Results from the observations reported here might provide a basis to test further developments or revisions of analytical models relating microwave emission to sea surface roughness.

Acknowledgments. There were several dozen individuals without whom these observations would not have been possible. We are unable to name all of them,

but we acknowledge their dedicated contributions gratefully. We are especially indebted to the NASA pilots and flight crew of the CV 990 observatory for carrying out the demanding flight operations that were required for these observations, to Mr. Earl Peterson of the NASA Ames Research Center for organizing the expedition, and the Irish Meteorological Service for providing excellent weather forecasts and analyses to support our flight operations.

REFERENCES

- Blanchard, D. C., 1971: Whitecaps at sea. *J. Atmos. Sci.*, **27** (in press).
- Cardone, V. J., 1969: Specification of the wind field distribution in the marine boundary layer for wave forecasting. Geophysical Science Lab., New York University, Rept. TR69-1.
- Droppleman, J. D., 1970: Apparent microwave emissivity of sea foam. *J. Geophys. Res.*, **75**, 696-698.
- Griffie, L., J. Ledgerwood, D. Hill and W. E. Marlatt, 1969: Support data for NASA Convair 990 meteorological flight IV. Dept. Atmos. Sci., Colorado State University, Ft. Collins, 83, pp.
- Hollinger, J. P., 1970: Passive microwave measurements of the sea surface. *J. Geophys. Res.*, **75**, 5209-5213.
- Monahan, E. C., 1969a: Freshwater whitecaps. *J. Atmos. Sci.*, **26**, 1026-1029.
- , 1969b: Laboratory comparisons of freshwater and salt water whitecaps. *J. Geophys. Res.*, **74**, 6961-6966.
- NAS Summer Study, 1966. Useful applications of earth-oriented satellites. Summer study on space applications, National Academy of Sciences, Washington, D. C.
- Nimbus III User's Guide*, 1969: Staff Members, Nimbus Project, NASA, Goddard Space Flight Center, Greenbelt, Md.
- Nordberg, W., J. Conaway and P. Thaddeus, 1969: Microwave observations of sea state from aircraft. *Quart. J. Roy. Meteor. Soc.*, **95**, 408.
- Oister, G., and C. V. Falco, 1967: Microwave radiometer design and development. Final Rept., Contract NAS5-9680, Aerojet-General Corp., Space Division, El Monte, Calif.
- Ross, D. R. V. Cardone and J. Conaway, 1970: Laser and microwave observations of sea surface conditions for fetch limited 35 to 50 knot winds. *IEEE Trans. Geoscience Electronics*, **GE-8** (in press).
- Stogryn, A., 1967: The apparent temperature of the sea at microwave frequencies. *IEEE Trans. Antennas Propagation*, **AP-15**, 278.
- Williams, G. F., Jr., 1969: Microwave radiometry of the ocean and the possibility of marine wind velocity determination from satellite observations. *J. Geophys. Res.*, **74**, 4591-4594.

Introductory Remarks

SEA-AIR INTERACTION INSTRUMENTATION

Problems of the interaction between the atmosphere and the ocean have confronted man ever since he left his homestead in the urge to expand his horizon and to conquer new frontiers. In his search for food and the riches of his environment, he had to master the winds, waves, and ocean currents; and these factors are primarily the result of air-sea interaction. More recently, the less obvious, but perhaps in many respects equally important, aspects of air-sea interaction have been stressed, namely, the influence of the ocean on the atmosphere in producing weather and climates. This is reflected in the present effort to gain a better understanding of the processes occurring at the sea surface and in the adjoining boundary layers in order to better parameterize the major exchanges of momentum, heat, and moisture.

The importance of the oceans to the global environment lies in the fact that more than two-thirds of the surface of this planet is covered by water with its very special and unique physical properties. This has profound effects on the atmosphere, since most of the energy received from the sun is absorbed by the water. Again, most of this absorbed energy in the water is released in the form of latent heat during the evaporation process. Thus the ocean provides a large portion of the moisture supply to the atmosphere and heats the atmosphere when the latent heat of evaporation is freed upon condensation of water vapor in the atmosphere. This heat represents the main fuel which drives the atmospheric circulation. It is therefore no surprise that large-scale experiments, such as the 1969 Barbados Oceanographic and Meteorological Experiment (BOMEX), have been conducted recently to investigate air-sea interaction processes. Others are planned for the future, such as those within the framework of the Global Atmospheric Research Program (GARP), which are designed to investigate how air-sea processes relate to large- and small-scale convective atmospheric systems.

Recently, advances have been made in several problem areas. Numerical atmospheric circulation models have been successfully coupled through air-sea interaction with ocean circulation models. Correlations between positive sea surface temperature anomalies in the Northern Pacific and dry and cold winters in the Eastern portion of the United States have been found, suggesting a strong large-

scale interaction between ocean and atmospheric circulation patterns.

Obviously, such large-scale investigations require data coverage on the global scale. Although the general climatological coverage has been obtained from data collected during the last hundred years by merchant and other ships, vast areas outside the regular shipping lanes are poorly covered. With the development of indirect sensing techniques and man-made satellites and the considerable effort spent in technology, global coverage for observing ocean surface parameters such as temperatures, salinity, waves, winds, tides, and ocean currents appears possible. Present planning for oceanographic satellites is concentrated on the feasibility of obtaining many of these parameters from space.

On the other hand, direct and indirect sensing techniques to be employed from surface platforms also need further development in order to provide ground truth and to investigate the important processes that govern air-sea exchanges. A most pressing need exists to obtain a better understanding of planetary boundary layer dynamics. Here, Doppler radar and acoustic sounding techniques seem to be the most promising tools for studying the three-dimensional structure of the boundary layer of the air. Some pertinent work on related problems may be found in the PROCEEDINGS OF THE IEEE (*Special Issue on Remote Environmental Sensing*, April 1969).

This issue, then, is organized in three parts: direct sensing of the boundary layer structure, remote sensing of the sea surface parameters, and laboratory studies of the water surface perturbed by waves and foam.

The paper by Garstang *et al.* provides an excellent summary and description of the marine atmospheric boundary layer and some of the transfer processes germane to the subcloud layer. Although some previous boundary layer observations exist, mainly over land and made from high towers, the technique described in this paper is a ship-deployed instrumented platform capable of providing unique time-series data from the atmospheric boundary layer over the ocean. Somewhat more limited in its use (nearshore areas) is a tracking system, described in the paper by Dunkel *et al.*, which permits wind profiles to be observed in the atmospheric boundary layer using rapid releases of pilot balloons. This system has been successfully

applied in an experiment just concluded over the Grand Bahama Banks. Some 400 wind profiles have been obtained in conjunction with other pertinent observations.

The next two papers deal with remote sensing of ocean waves. In his paper, Teague describes a technique by which long wavelength directional wave spectra can be observed for an area of several hundred kilometers offshore using LORAN A transmissions. This technique may prove a convenient way to monitor offshore wave conditions. The paper by Chadwick and Cooper shows that with presently available radar technology it should be possible to estimate wave heights, at least from aircraft. Through functional relationships between wind speed, fetch, and duration, possibly wind speed could be estimated by this technique.

Finally, a very important problem in the application of indirect microwave techniques is the knowledge of the emissivity of foam and bubbles, which are generated extensively by breaking waves and strong winds. Williams, in his paper, presents results of laboratory experiments that will be helpful in the interpretation of microwave data.

In closing, I would like to emphasize that the collection of papers in this issue represents a small sample of present scientific endeavors in the field of air-sea interaction. It is gratifying to see that a significant effort is now being made to bring to bear the advances in technology of the last 10 or 20 years in helping to solve our environmental problems.

—FEODOR OSTAPOFF, *Guest Editor*



Feodor Ostapoff was born in Danzig on March 19, 1925. He studied physics, mathematics, and chemistry at the University of Marburg, Marburg, Germany, and received the German equivalent of the B.S. degree in physics in 1949. He studied physical oceanography at the University of Kiel, Kiel, Germany, and received the M.S. degree in physical oceanography from New York University, New York, N. Y., in 1957.

In 1959 he joined the U. S. Weather Bureau as a Research Scientist and was engaged in Antarctic research. Since 1964 he was heavily involved in the coordination and implementation of the Federal air-sea interaction program, especially after the formation of the Environmental Science Services Administration. This program culminated in the Barbados Oceanographic and Meteorological Experiment in 1969, which he helped plan and organize. Presently he holds the position of Director of the Sea-Air Interaction Laboratory of the National Oceanographic and Atmospheric Administration.

Mr. Ostapoff is a member of the American Geophysical Union and American Meteorological Society, serving on the Committee on the Interaction of the Sea and Atmosphere. He is also a member of Sigma Xi. He also serves the Cooperative Investigations of the Caribbean and Adjacent Region (CICAR), an international program with some 15 nations participating and sponsored by the Intergovernmental Oceanographic Commission of UNESCO, as Assistant International Coordinator (Meteorology) appointed by the World Meteorological Organization.

OCEAN-ATMOSPHERE INTERACTION IN THE CARIBBEAN SEA : VIEWED FROM THE OCEANOGRAPHIC SIDE

Feodor Ostapoff

1. INTRODUCTION

The title of my paper is rather broad and while listening to my colleagues yesterday and today it became obvious that many aspects of ocean-atmosphere interactions have been discussed directly or indirectly.

Perhaps the most direct visual evidence of the effects of the atmosphere on the sea surface are the waves and wavelets which have been the subject of intense study for the past 200 years. The same driving forces establish the general circulation of the ocean. As early as 1686, Halley concluded that the surface circulation of the ocean is wind driven. Today the theory of wind driven ocean circulation has advanced to a considerable degree of sophistication. In addition the ocean is heated and cooled at the surface, in other words, its heat sources and sinks are essentially at the same geopotential, forming distinct water mass characteristics. The strength of the heat and salinity sources and sinks is determined by climatic conditions on the globe. Once the water masses are formed at the sea surface due to heating, cooling, evaporation and precipitation, ice formation and melting, they will seek their equilibrium position in the ocean according to their density. Combination of the wind driven mode and the internal pressure distribution then spreads these water masses with their specific characteristics through the oceans, modifying them through turbulent mixing. Thus, Wüst and Gordon (1964) identify in the Caribbean Sea four "core layers": the sub-tropical underwater, the sub-Antarctic intermediate water, the North Atlantic deep water, the Caribbean bottom water. In this sense then, we must recognize an ocean-atmosphere interaction process in the Caribbean Sea. Although direct effects forming the water masses occur in remote areas perhaps tens or hundreds of years earlier, these are the large-scale (in time and space) interactions.

Figure 1 (after Wyrski, 1967) illustrates the distribution of the main water masses at the sea surface and boundaries between these water masses. Clearly, the area of our topic is influenced by a very complicated and complex mechanism.

At the other end of the spectrum, we recognize small-scale interactions - perhaps it would be better to call them "first order" interactions - which act locally and are highly variable. Considerable research has been done in this field during the past few decades. The importance of this research lies in the fact that neither of the large-scale phenomena can be fully understood without an intimate knowledge of the first order interaction, nor can specific characteristics such as the sea surface temperature and salinity, the mixed layer depth and the thermocline be treated theoretically in a satisfactory way. Let us first briefly discuss these first order interactions.

2. BASIC PROCESSES ACROSS THE SEA SURFACE AND THEIR SIGNIFICANCE

The exchange across the sea surface involves a number of important quantities.

They can be classified in three main categories, as shown in Figure 2.

- (1) Momentum exchange
- (2) Heat exchange
- (3) Mass exchange

Momentum exchange is one of the most important interaction quantities from the oceanographic point of view, as discussed above. While the momentum loss by the atmosphere is of perhaps negligible consequence to the atmospheric circulation, it represents the major force which generates and maintains surface waves and drives local and major ocean currents. Indeed, the early results in ocean dynamics are based on the momentum exchange process. In this connexion we need only mention Ekman's work.

The total heat exchange can be differentiated depending on the process involved. First of all, 80% of the short-wave radiation received from the sun at the ocean surface is absorbed in the top layer of the ocean. Long-wave radiation is emitted from the ocean's surface and absorbed partially in the atmosphere. Sensible heat is exchanged by conduction due to the difference in temperatures between the two media. But most importantly, the ocean is cooled by evaporation of water, resulting in latent heat exchange. This

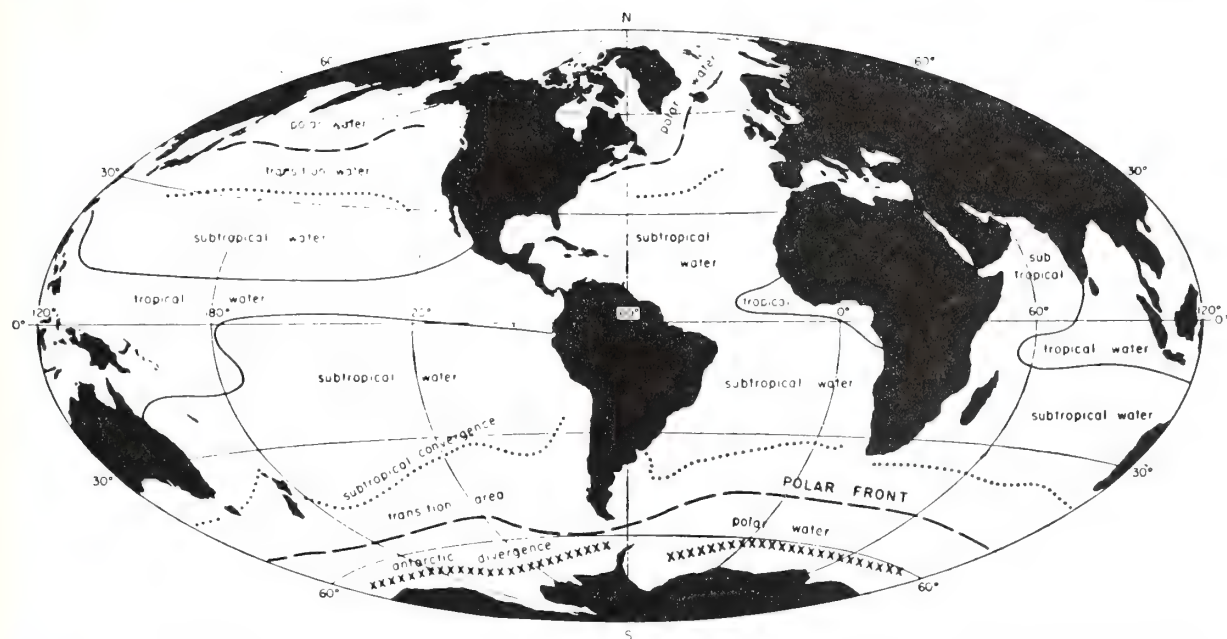


Figure 1. Distribution of the main water masses at the sea surface and boundaries between these water masses.

process and the associated water transport from the ocean to the air is of utmost importance from the energetic point of view to the generation and maintenance of the atmospheric circulation, including hurricanes and tropical storms. Evaporation and precipitation, of course, determine also to a large extent the salinity distribution in the ocean.

The most important masses exchanged at the surface are water vapour (in conjunction with the exchange of latent heat), the return of water in the form of rain (thereby releasing latent heat in the atmosphere), salt and gases. The latter are again instrumental in important physical processes in the atmosphere.

In view of the complexity and the numerous modes of interaction, we will discuss in the following only a few of the important oceanographic processes which seem particularly suited for study in the Caribbean Sea - our main topic today.

3. PRECIPITATION AND THE PRESSURE FIELD IN THE OCEAN

An often neglected but apparently important effect is that of precipitation which, in these latitudes, is more localized and more intense than in other parts of the world ocean.

Last summer, the USC&GS ship "Discoverer" (Figure 3) occupied a station some 60 miles east of Barbados for about 2 months, more or less

continuously. Three-hourly surface salinities (bucket) were observed and six-hourly STD lowerings were made. During a heavy rain shower, the surface salinity dropped abruptly by 0.7 to 1 part per thousand for about 24 hours, while the 10 metre salinity followed a longer-term trend (Figure 4).

The implication for dynamic height calculations, the basis for all geostrophic calculations, seems considerable.

Let us perform a hypothetical experiment in our minds as follows: we calculate dynamic depths for one of the regular stations which were obtained during the expedition. Then we replace the surface salinity value by a value of one part per thousand less than the original observation. Using standard oceanographic procedures, and not knowing how deep this lens is, the calculation was made for the usual standard depths of 0, 25, 50,

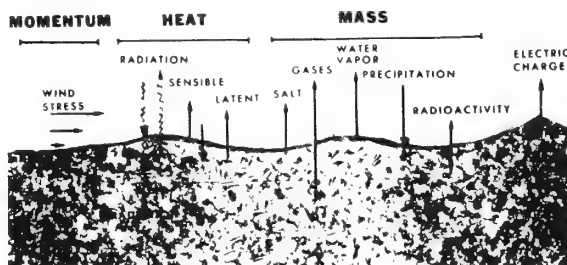


Figure 2. Air-sea interactions.



Figure 3.

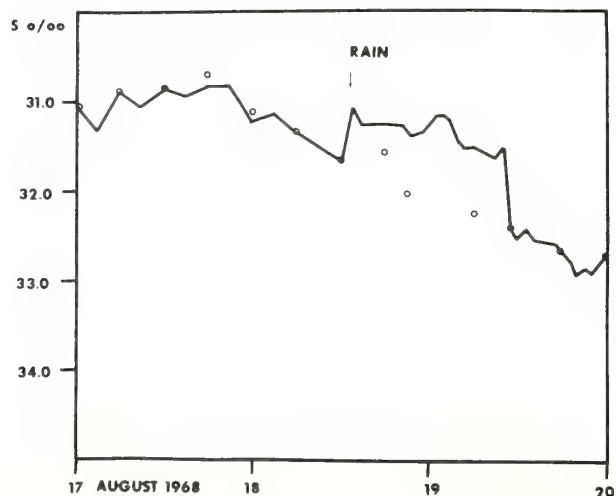


Figure 4. Surface bucket salinities (solid line) and 10 meter salinities (circles) 60 miles east of Barbados.

75, 100 metres etc. Comparing the two calculations, one finds at 25 metres a difference of 2 dyn. cm. between the two "stations". Moreover, if the two "stations" were 30 miles apart (and such variability in rain may very well occur in those latitudes) an additional "current" of about 2 knots would result in these low latitudes.

4. THE EFFECT OF HURRICANES ON TEMPERATURE STRUCTURES IN THE TOP LAYERS OF THE OCEANS

Next, I wish to discuss the effects of hurricanes on the ocean, a very pertinent subject if we consider the Caribbean Sea. Possibly, an opportunity will present itself to continue research along those lines.

In 1964, when Hurricane Hilda cross the Gulf of Mexico an opportunity arose to study the direct effects of a hurricane on the thermal structure of the open ocean. Leipper (1967) had surveyed the area prior to the passage of the hurricane. When the hurricane traversed the area a new expedition

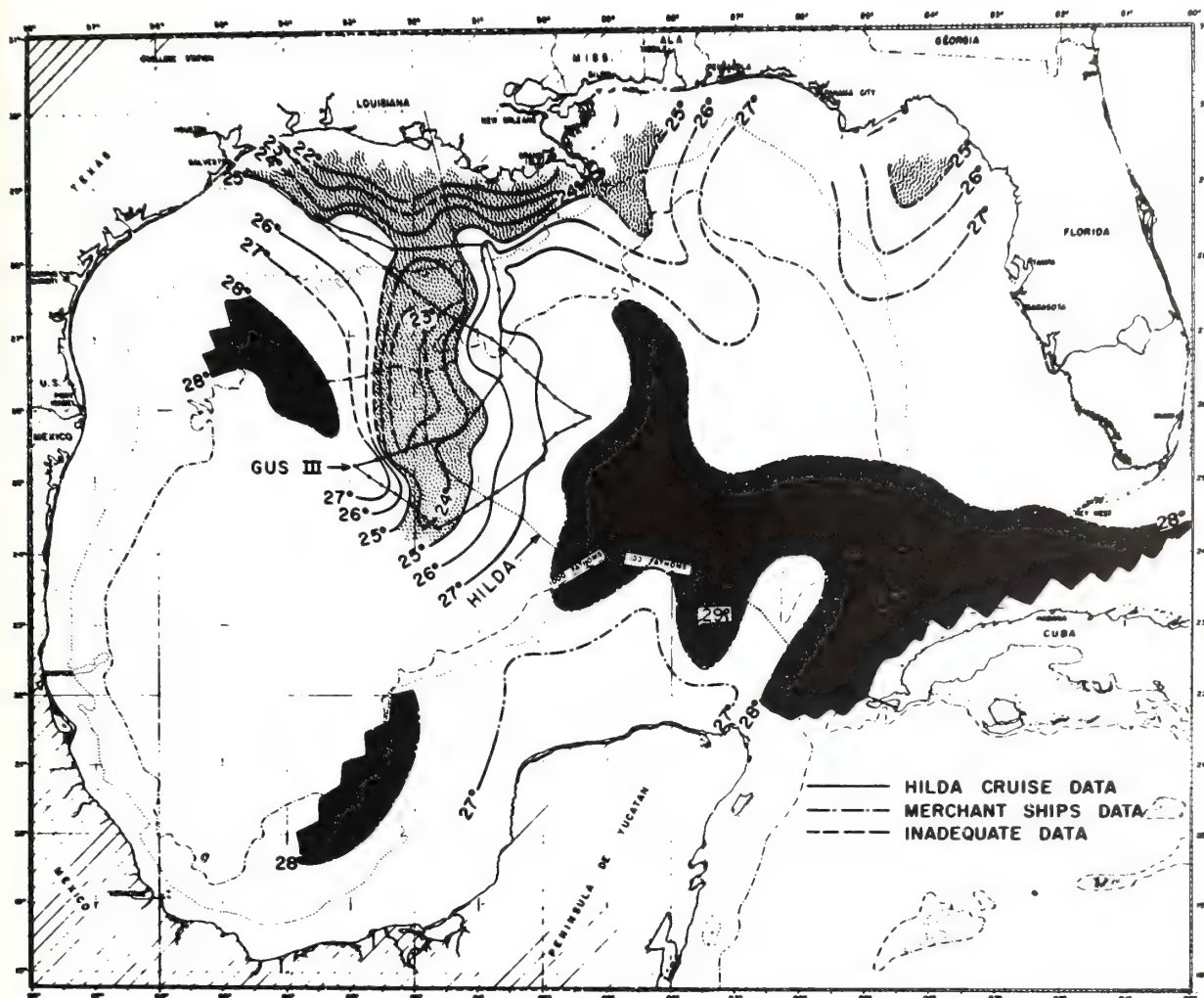


Figure 5. Sea-surface temperature, after Hilda, October 1-13 inclusive. Including Cruise Hilda and BCF data (shaded area $> 28^{\circ}$; stippled area $< 25^{\circ}$). [After Leipper, 1967]

was quickly organized and remarkable data obtained.

Figure 5 shows the sea surface temperature distribution after Hilda. The general surface temperature prior to Hilda was about 29°C . A lowering of about 6°C was observed. Even more remarkable are the vertical temperature profiles. An example is given in Figure 6.

If upwelling due to divergence induced by the wind stress is the process responsible for lowering the surface temperature, then the water may have come to the surface from about 60-80 metre depths.

Figure 7 shows the density distribution along the same cross section as in Figure 6.

The gross features of upwelling can easily be explained by Ekman's wind drift theory. The transport in the Ekman layer is outward from the centre of the storm, producing divergence from the centre up to the distance of maximum winds and convergence further out. Therefore, upward motion is indicated left and right of the eye with maximum vertical velocity at the radius of maximum winds and downward motion at the outer fringes of the storm (about twice the radius of maximum wind stress). Now, since the storm is radially symmetric, the hurricane should leave one cold water trace at the surface. However, in low latitudes and with an east-west propagation of the storm two upwelled regions may be generated

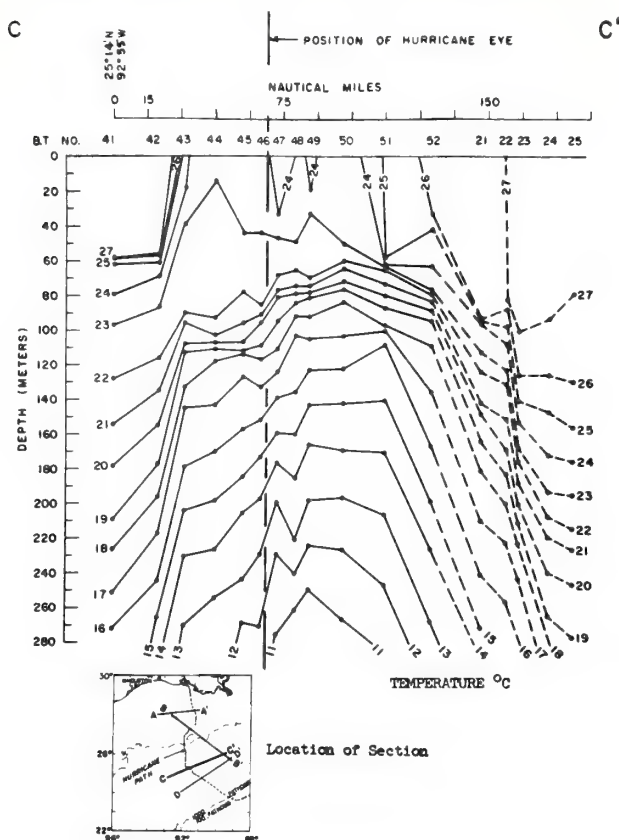
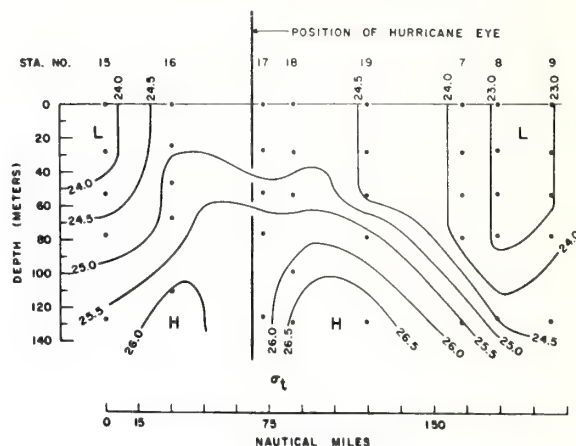


Figure 6. Depth of isotherms in section across path, after Hilda. [After Leipper, 1967]

due to the difference in Coriolis parameter (everything else being equal). For a storm of 30 miles radius of maximum winds, the Coriolis parameter could change almost by 10%. Such an effect has not been clearly observed yet, but all our measurements were taken in the Gulf of Mexico. A more elaborate transient, (although with a stationary storm) numerical model has been developed by J.J. O'Brien and R.O. Reid (1967) and J.J. O'Brien (1967) which agrees with major parts of the observations.

Present technology permits the rapid collection of sea surface temperatures from aircraft using infra-red radiation thermometers. Furthermore, expendable bathythermometers have been developed for use from aircraft. Indeed, expendable salinity-temperature probes are in the offing.

Examples of radiation temperature observation in the wake of Hurricane Betsy in 1965 are given in Figures 8 and 9. These data were obtained by J. McFadden (1967) from ESSA research aircraft. While data obtained from a ship must be



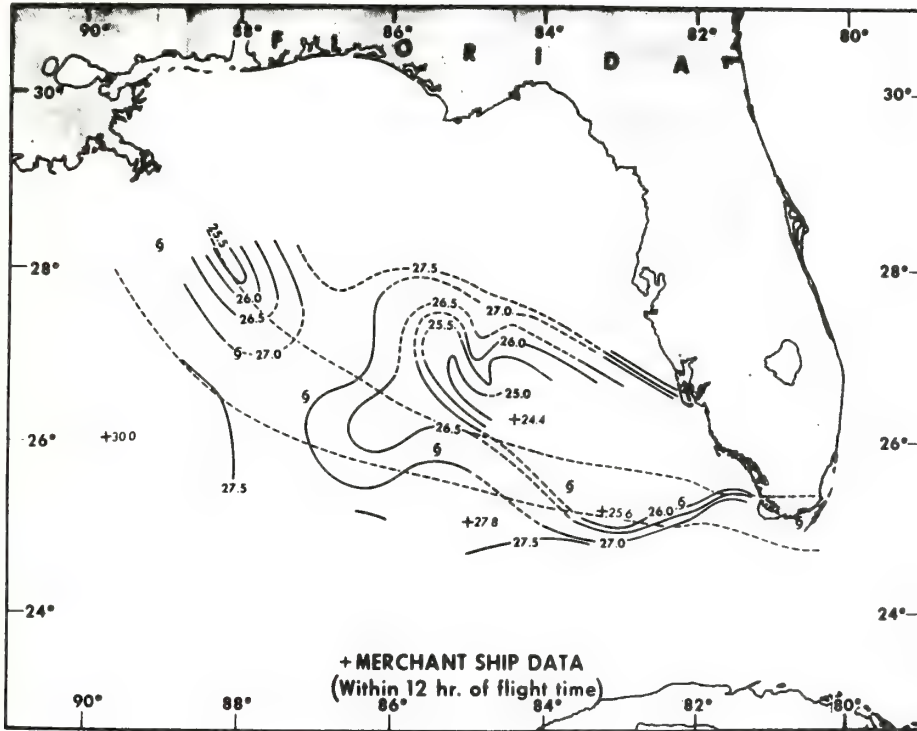


Figure 8. Sea-surface temperature distribution 10-11 September 1965. [After McFadden, 1967]

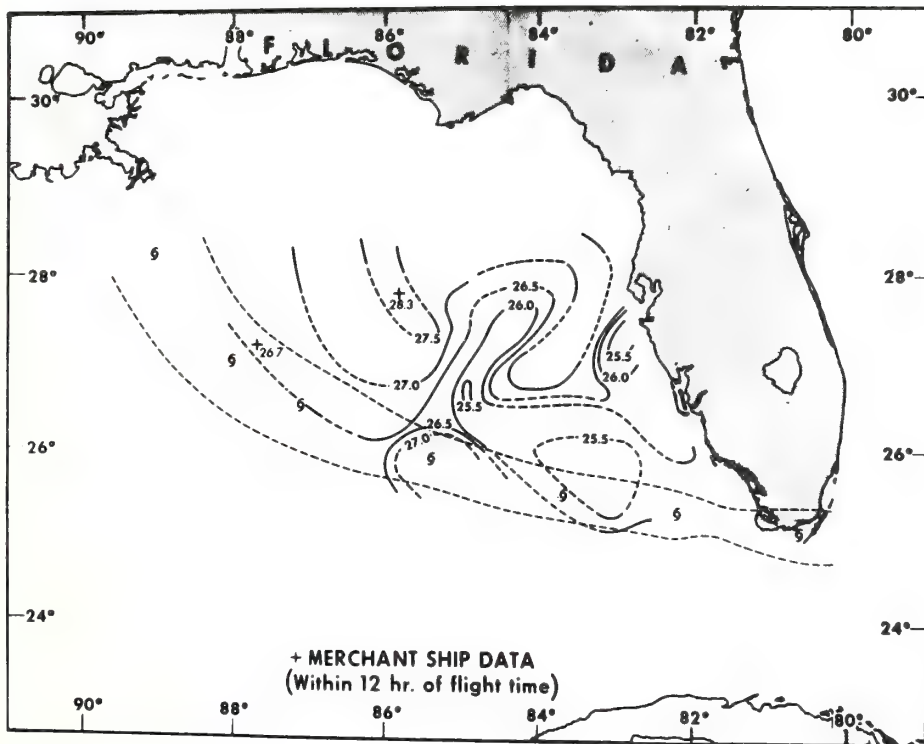


Figure 9. Sea-surface temperature distribution 15 September 1965. [After McFadden, 1967]

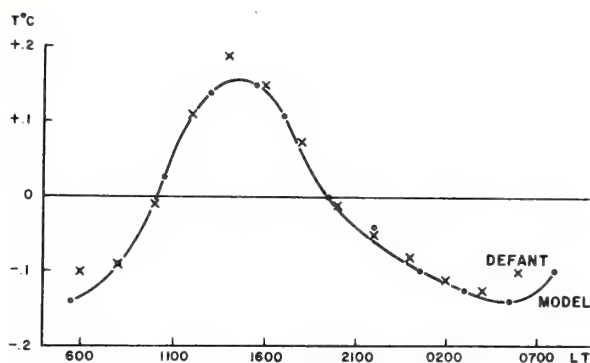


Figure 10. [After Pandolfo, 1968]

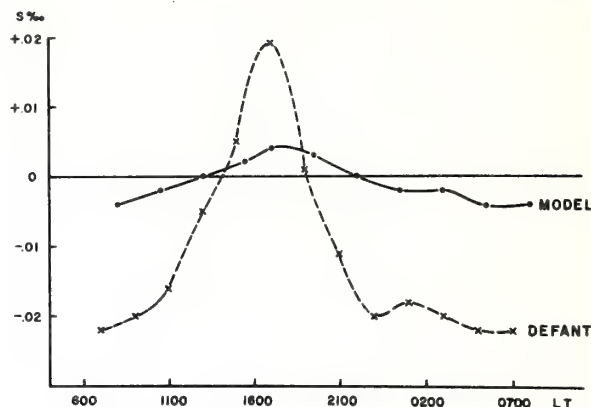


Figure 11. [After Pandolfo, 1968]

salinity. Conditions at the top and bottom of the model are prescribed.

A few examples may illustrate the presently available results although the full power of the model has not yet been explored.

The agreement between the two curves is quite satisfactory. In particular the occurrence of the maximum and minimum agrees very well, both in the salinity and temperature curves. (Figures 10 and 11). It is noteworthy that the salinity maximum follows the temperature maximum by about 3 hours. Also, the small secondary salinity maximum is reproduced in agreement with observations. This secondary maximum is related to maximum vertical mixing in the ocean, which occurs at the same time.

The observed diurnal salinity amplitude is about five times larger than the computed value. This indicates a deficiency in the model, possibly due to the fact that at this time precipitation had not been incorporated.

The vertical temperature and salinity distribution is shown in Figure 12. The initial temperature and salinity profiles were assumed linear. Again the calculated temperature profile compares quite favourably with observations obtained this summer (1968) on the Discoverer. The Discoverer data shows a mixed top layer of 15 to 17 metres. The model calculates a mixed layer depth of 20 metres. The temperature difference between 20 metres and 100 metres amounts to 4.5°C. Observations showed a difference of 3°C. The salinity profile disagrees with observations, not so much in the mixed layer as in the complete lack of the salinity maximum at about 100 metres. Clearly a single station model incorporating local processes cannot simulate such phenomena as water mass advection.

The vertical current distribution at one par-

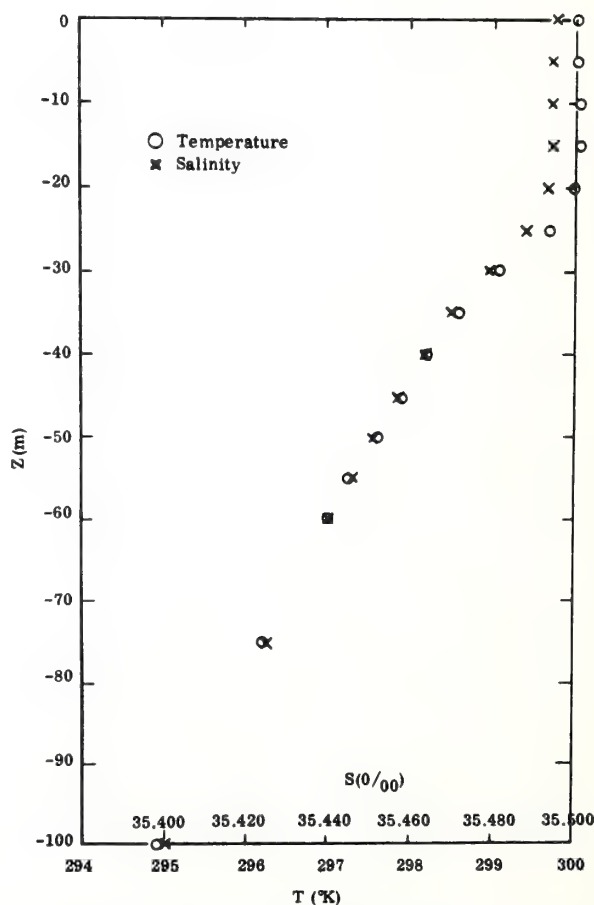


Figure 12. Oceanic temperature and salinity profiles at one time step in the run JB1 ; 0530 LST. [After Pandolfo, 1968]

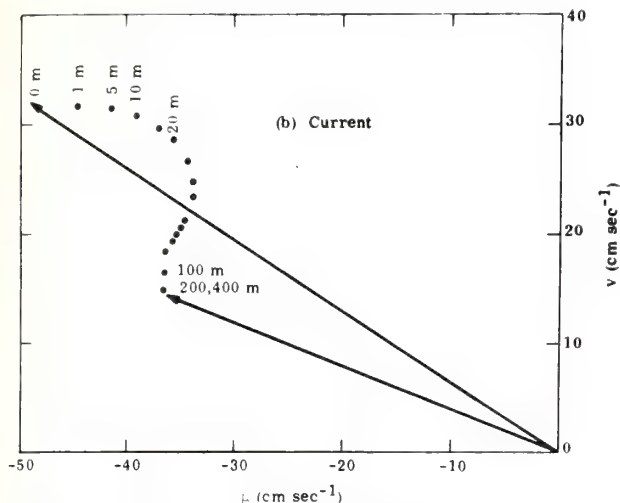


Figure 13. Wind current hodographs at one time step in the simulation run JB1; 0930 LST. [After Pandolfo, 1968]

ticular time step in the integration is shown in Figure 13. Variations with inertial periods are superimposed on the current vector.

The mean angle between surface current direction and the surface wind direction is about 30° .

This model is being further developed, principally to expand areawise and to include advective processes in the ocean and the atmosphere. An observational programme could be carried out during Cigar to utilize the model in further understanding changes occurring in the near surface layers of the ocean.

6. CLOSING REMARKS

In closing, I would like to emphasize that I have only touched briefly on a few problems which may

be interesting or important to oceanographers if we concern ourselves with the air-sea interaction problem in relationship to oceanography.

Many problems of interaction are of a fundamental nature and can be studied anywhere in the world ocean. However, we must still distinguish between climatic regimes which may favour one exchange process over the other, making the choice of an experimental area an important one if we want to isolate and study one aspect of interaction. This is certainly true as far as our sister science, meteorology is concerned, where convective processes are a predominant process in low latitudes while air mass modification may be studied better in regions where drastic differences in air masses occur. In oceanography convective mixing may be the predominant process of high latitudes where deep water masses are formed.

The Caribbean Sea has been studied extensively if we consider large-scale exchanges from the meteorological point of view. Essentially, the meteorological island network surrounding the Caribbean Sea has been utilized by applying continuity considerations. We need to mention only the works by J. Colon (1963), Malkus (1962), Hastenrath (1967) and Rasmusson (1967 and 1968). Evidently, this work could continue in support of the planned Cigar activities. Within this framework specific problems may be studied for which the Caribbean Sea may present itself as a natural laboratory.

In closing I would like to quote a few words from J. Malkus (1962) which may be worth remembering when planning our future work. She writes: "Rarely, but often enough to be of inestimable value, nature herself performs an experiment under partially controlled conditions, as we have seen in some of the trade wind cases; one of the main skills of the earth scientist lies in being able to recognize and exploit these, using them to guide his measurement programmes and as a framework within which to relate the results."

REFERENCES

- Colon, F.A. 1963. Seasonal variations in heat flux from the sea surface to the atmosphere over the Caribbean Sea. *Journ. Geoph. Res.*, **68**, 5, p. 1421-1430.
- Defant, A. 1961. *Physical Oceanography*, New York, Pergamon Press, 2 vols.
- Hastenrath, S.L. 1967. Diurnal fluctuations of the atmospheric moisture flux in the Caribbean and Gulf of Mexico area. *Journ. Geoph. Res.*, **72**, p. 4119-4130.
- Leipper, D.F. 1967. Observed ocean conditions and Hurricane Hilda, 1964. *Journ. Atmos. Sci.*, **24**, p. 182-196.
- Malkus, J.S. 1962. Large-scale interactions, *The Sea* (ed. M.N. Hill), **V**, 1, p. 88-294, Interscience Publ., New York, J. Wiley & Sons.
- McFadden, J.D. 1967. Sea surface temperatures in the wake of Hurricane Betsy (1965). *Monthly Weath. Rev.*, p. 299-302.

- O'Brien, J.J.; Reid, R.O. 1967. The non-linear response of a two layer, baroclinic ocean to a stationary, axially symmetric hurricane, Part I. Upwelling induced by momentum transfer., Journ. Atmos. Sci., p. 197-207.
- O'Brien, J.J. 1967. The non-linear response of a two layer, baroclinic ocean to a stationary, axially symmetric hurricane: Part II. Upwelling and mixing induced by momentum transfer. Journ. Atmos. Sci., p. 208-215.
- Pandolfo, J.P.; Atwater, M.A. 1968. Variations of diurnal and inertial period in a physical-numerical model of the atmosphere-ocean planetary boundary layer. Final Report, 7046-321, Contract E-120-67(N). Hartford, Conn., The Travelers Research Center, Inc.,
- Pandolfo, J.P. : Brown, P.S. Jr., 1967. Inertial oscillations in an Ekman layer containing a horizontal discontinuity surface. Journ. Mar. Res., 25, p. 10-28.
- Rasmusson, E.M. 1967. Atmospheric water vapour transport and the water balance of North America: Part I. Characteristics of the water vapour flux field. Monthly Weath. Rev., 95, p. 403-426.
- Rasmusson, E.M. 1968. Atmospheric water vapour transport and the water balance of North America: Part II. Large-scale water balance investigations. Monthly Weath. Rev. 96, p. 720-734.
- Wüst, G. : Gordon, A. 1964. Stratification and circulation in the Antillean-Caribbean basins. Part I. Spreading and mixing of the water types. New York and London, Columbia University Press, 201 p.
- Wyrtki, K. 1967. Water masses in the oceans and adjacent seas, in: International Dictionary of Geophysics (gen. ed. K. Runcorn). Pergamon Press.

U.S. DEPARTMENT OF COMMERCE
National Oceanic and Atmospheric Administration
Environmental Research Laboratories

NOAA Technical Memorandum ERL AOML-15

TESTS OF MODIFIED RADIOSONDE HYGRISTOR DUCT

Willard W. Shinnars
Gerald E. Putland
Peter B. Connors

Atlantic Oceanographic and Meteorological Laboratories
Miami, Florida
December 1971



TABLE OF CONTENTS

	PAGE
1. INTRODUCTION	1
2. AIR FLOW TESTS	3
3. FLIGHT TESTS	5
4. CONCLUSION	6
5. REFERENCES	10

TESTS OF MODIFIED RADIOSONDE HYGRISTOR DUCT

Willard W. Shinnars, Gerald E. Putland, and Peter B. Connors

To evaluate a modified configuration of the National Weather Service's radiosonde humidity duct, wind tunnel and flight tests were made by the Sea-Air Interaction Laboratory. Results indicate the new design to be greatly improved over the previous type with respect to ventilation and radiational heating.

1. INTRODUCTION

The VIZ Corporation provided the NOAA Sea Air Interaction Laboratory several newly designed hygistor housings or ducts for wind tunnel and flight tests similar to the original tests by SAIL reported in NOAA Technical Report 194-AOML 4 "Some Tests on the Radiosonde Humidity Error." The 1970 report indicated the ventilation in the area of the hygistor was reduced about 70% from ambient air flow, and the translucency and reflective characteristics of the plastic duct permitted considerable solar heating of the hygistor resulting in significant humidity errors.

The newly designed duct provides a much larger opening or air scoop than the prior design. The air passes through a restricted section holding the hygistor, and as a result the air movement is accelerated. Air entering the scoop of 58 cm^2 area passes through the restricted area of 23 cm^2 cross-section with over 100% increase in speed from the scoop area to the exit of the hygistor chamber (fig. 1). A black covering under the top and at the bottom of the hygistor section is highly effective in reducing direct and reflected solar heating of the hygistor.

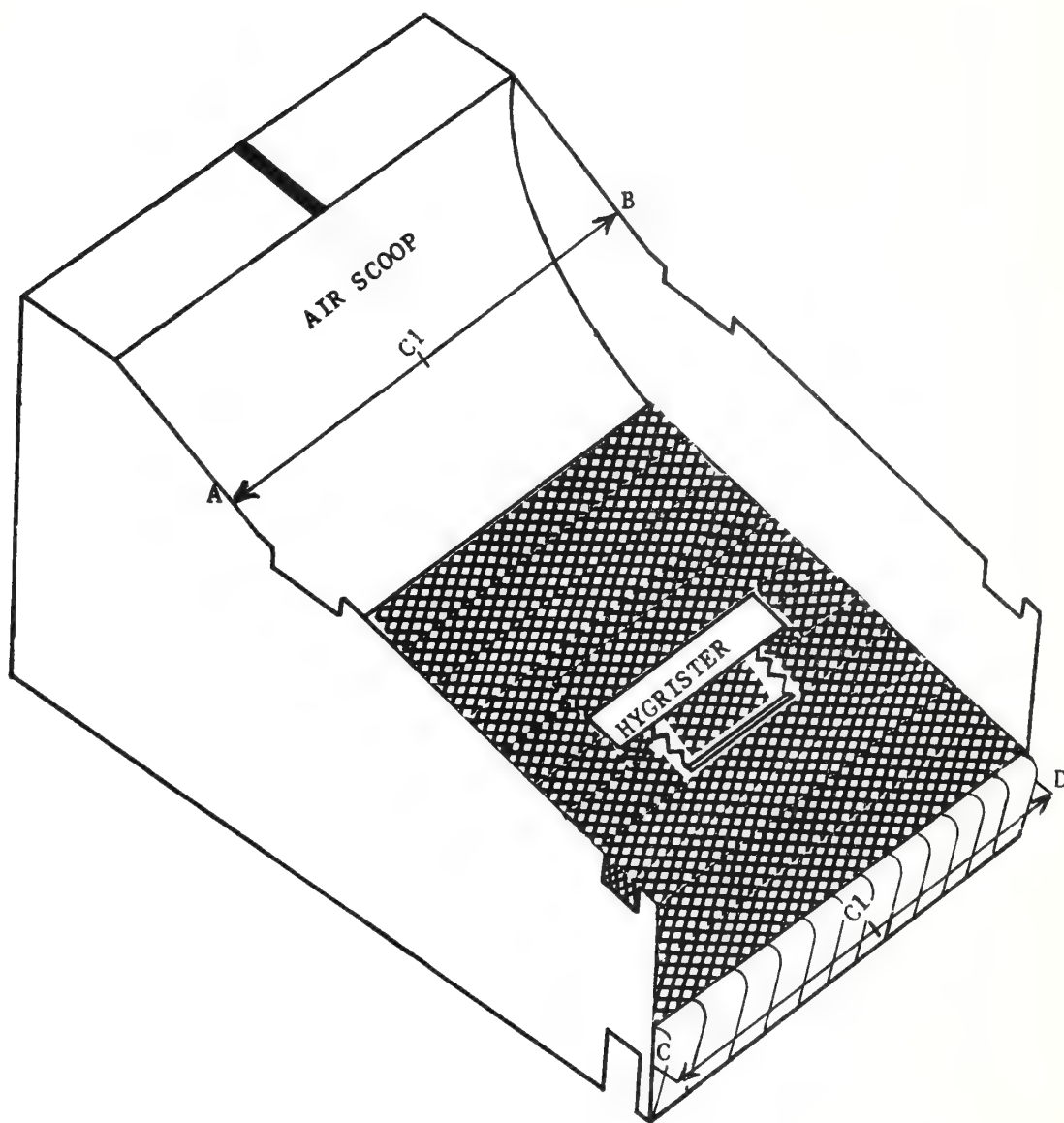


Figure 1. New design of NWS hygristor duct. Cover removed.

2. AIR FLOW TESTS

Tests were conducted in SAIL's wind-water tunnel facility, (NOAA Tech. Memo ERL AOML-12). The facility provides an air chamber 70 by 90 cm in cross-section and 610 cm in length. Air flow was 5.2 mps - about the rate of ascent of a radio-sonde. A Pitot tube and a Thermo-Systems, Inc., hot wire (constant temperature anemometer) model 1050 was used to monitor air flow rates.

The duct with a carbon hygistor in place was placed in the wind tunnel and a series of readings at 1-cm spacing were made along line A-B (fig. 1). The probe was even with the top of the side wall of the scoop. Table 1 lists these values.

Table 1. Air flow at air scoop entrance

	Cm Left				Center				Cm Right		
	5	4	3	2	1	0	1	2	3	4	5
A											
mps	1.9	2.0	2.0	2.1	2.1	2.1	2.2	2.2	2.2	2.2	2.0
	B										

The data give an average value of 2.1 mps for air entering the air scoop along A-B. This is 40% of the ambient 5.2 mps flow rate in the tunnel. Measurements were made up-wind from the duct air scoop at a distance of 7.6 cm, where a speed of 3.6 mps was recorded. At a distance of 15.2 cm upwind the speed was 4.4 mps.

Measurement of the air flow right at the hygistor posed a problem due to the probe support and connecting cables. Since the cross sectional area is nearly constant and uniform in dimensions from the air scoop to the discharge orifice, the assumption was made that the air speed at the hygistor would be essentially the same as in the discharge area. Measurements were made at 1 cm intervals from the center line along line C-D. Table 2 presents average values.

Table 2. Air flow in discharge orifice

	Cm Left			Center			Cm Right				
	5	4	3	2	1	0	1	2	3	4	5
C											
D											
mps	5.3	5.4	5.4	5.0	4.4	4.8	4.1	5.2	5.0	5.0	4.9

The mean value across the discharge orifice was 5.0 mps, over 96% of ambient flow in the wind tunnel.

Since lee or down-wind turbulence could affect the air flow through and past the duct, a 403 mc radiosonde, without the thermistor out-rigger or strap was included for a second series of measurement.

Values in Table 3 were obtained 2 cm above the air scoop at 2-cm intervals along line A-B.

Table 3. Air flow 2 cm above air scoop with radiosonde

	Cm Left		Center	Cm Right		
	4	2	0	2	4	
A						B
mps	2.9	2.6	2.4	2.4	2.6	

A mean value of 2.6 mps is obtained from the above data. The higher value at 2 cm above the orifice is consistent with the increase in speed-up wind.

Measurements across the exit orifice provide the following:

Table 4. Wind speed at discharge orifice - duct with radiosonde

	Cm Left		Center	Cm Right		
	4	2	0	2	4	
C						D
mps	5.4	4.6	4.2	5.0	5.4	

A mean value of 4.9 mps results for flow through the duct. A recheck of air flow up-wind of the duct resulted in identical values to those obtained prior to the inclusion of the full radiosonde in the tests. The 0.1 mps difference (5.0 and 4.9 mps) does not appear significant, and the experimental procedure followed does not indicate a change in ventilation rate when the duct and radiosonde are combined (i.e., without the thermistor or webbed strap in place).

3. FLIGHT TESTS

To determine the effectiveness of the new duct under operational conditions, several flights were made at Miami. Releases were made close to solar noon in order to expose the duct to maximum radiotonal effect. Air mass characteristics were typical of the trade winds, with a warm moist layer the first several hundred meters, then an inversion and relatively dry air above. Two radiosondes were flown on the same train, one with the older duct configuration and one with the new design. A further comparison was made with the vertical duct used by SAIL (Ostapoff, et al., 1970) and the new design. Figure 2 thru 6 present the comparative relative humidity values as obtained by the dual flights.

Figure 2 indicates differences as high as 20% in relative humidity with the difference varying up to 830 mb. The sonde with the new duct showed lower relative humidity above this level. Scattered clouds and the resultant shading may account for the variability at the lower level. The reversal above 825 mb, where the standard sonde indicated higher humidity, has been observed before (Brousaides and Morrissey, 1971); however, a confirmed explanation is not available.

A maximum difference of 32% in RH at 835 mb appears in figure 3 with the newly designed duct configuration giving a 97% RH value. Figures 4 and 5 are typical of comparative flights in which solar heating was substantially reduced and

ventilation of the hygistor improved relative to the standard sonde.

Figure 6 presents curves for the new NWS duct and a vertical tube used by SAIL (Ostapoff, et al., 1970). The sondes were observed to swing through a large arc during the first few minutes of flight, and it is suspected that some solar heating as well as reduced ventilation in the tube may account for the differences in RH during the early part of the flight.

4. CONCLUSION

Based on these wind tunnel and flight tests, the new National Weather Service radiosonde duct virtually eliminates the solar heating problem found in the previous duct configuration. The problem of thermal lag should also be reduced to a considerable extent with the increased ventilation rate.

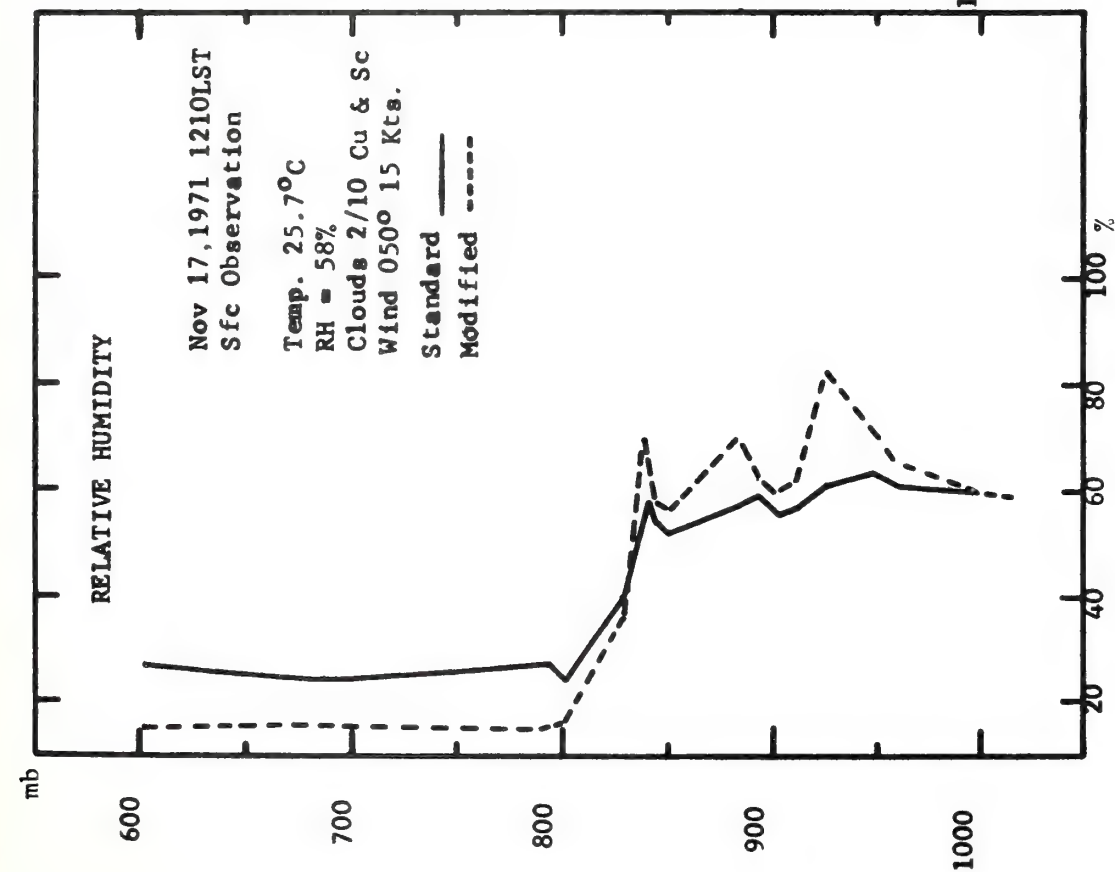


Figure 2. Relative humidity data for November 17, 1971.

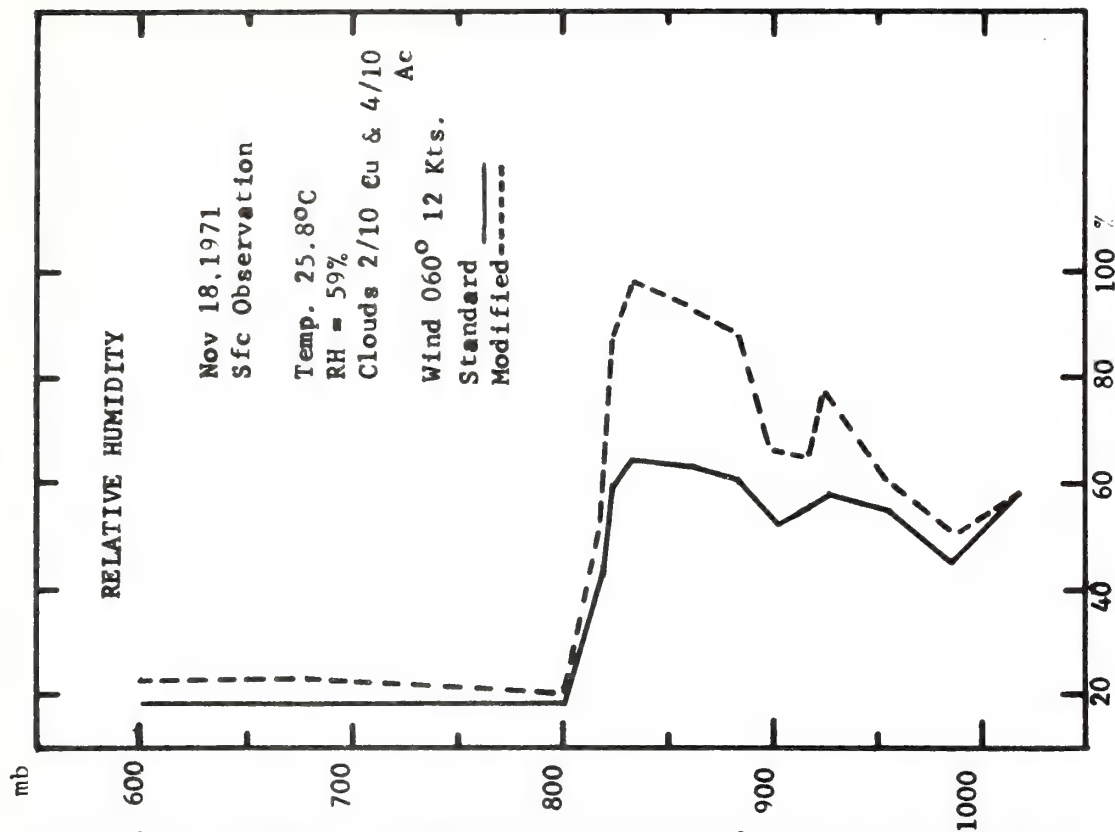


Figure 3. Relative humidity data for November 18, 1971.

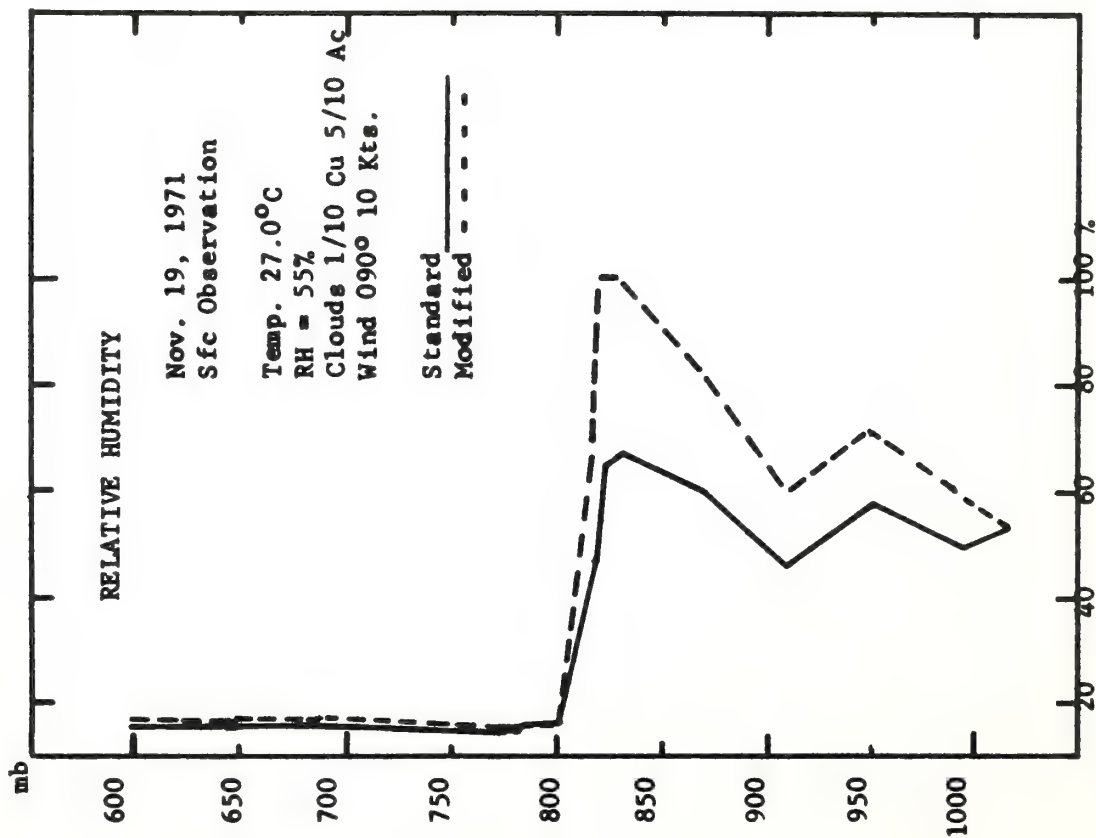


Figure 4. Relative humidity data for November 19, 1971.

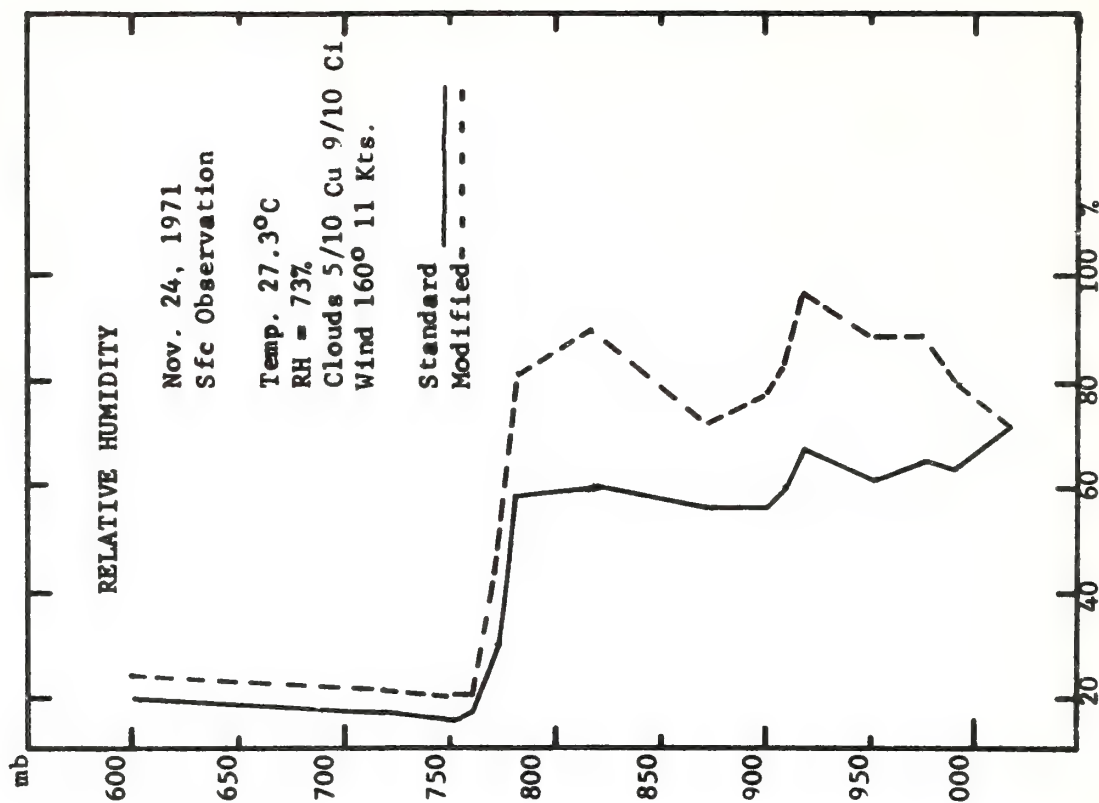


Figure 5. Relative humidity data for November 24, 1971.

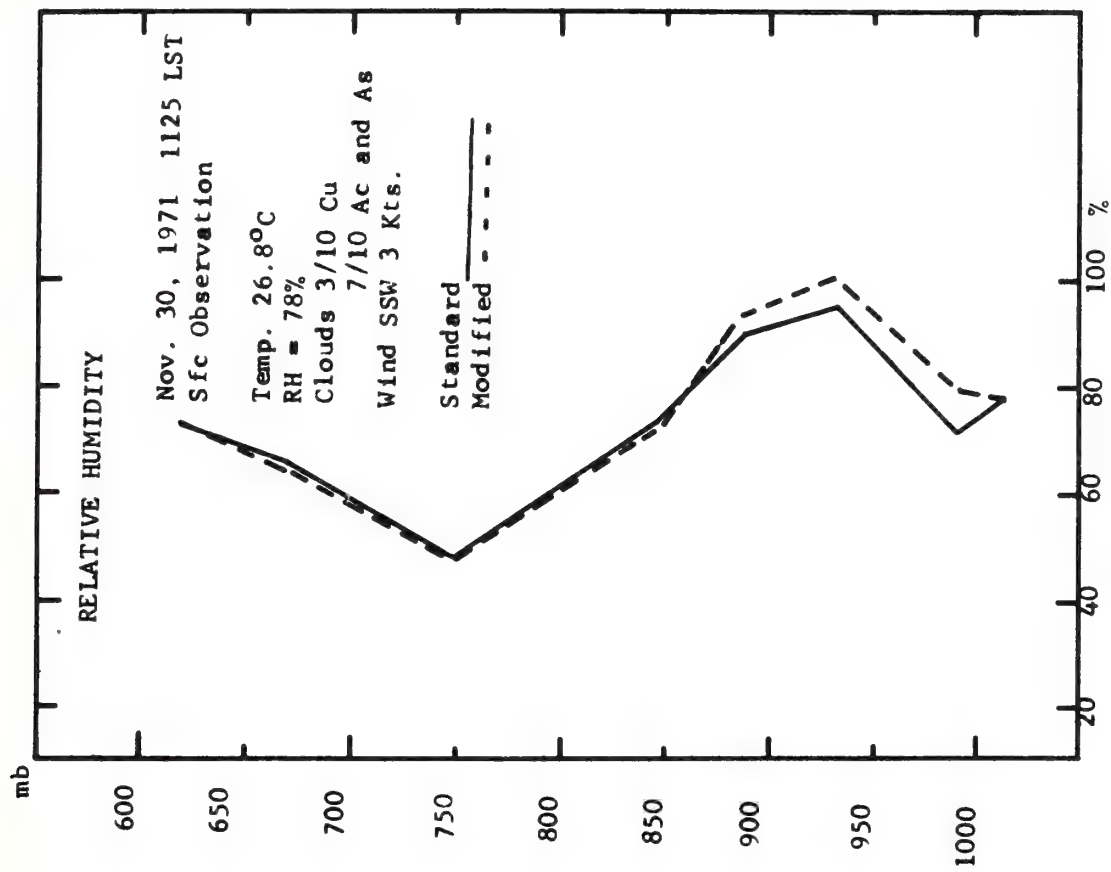


Figure 6. Relative humidity data for November 30, 1971.

5. REFERENCES

- Broussaides, F. J., and Morrissey, J. F. (1971), Improved measurements with a redesigned radiosonde humidity duct, Bulletin AMS, 2, No. 9.
- McLeish, Wm., Berles, R., Everard, W., and Putland, G. (1971), The SAIL 6-m wind-water tunnel facility, NOAA TM ERL AOML-12.
- Ostapoff, F., Shinnars, W., Augstein, E. (1970), Some tests on the radiosonde humidity error, NOAA TR ERL 194-AOML 4.

PENN STATE UNIVERSITY LIBRARIES



A000072049648